Handbook on the Physics and Chemistry of Rare Earths, **volume 16**

Elsevier, 1993

Edited by: Karl A. Gschneidner, Jr. and LeRoy Eyring
ISBN: 978-0-444-89782-4

Handbook on the Physics and Chemistry of Rare Earths, Vol. 16
edited by K.A. Gschneidner, Jr. and L. Eyring

PREFACE

Karl A. GSCHNEIDNER, Jr., and LeRoy EYRING

These elements perplex us in our rearches [sic], *baffle us in our speculations, and haunt us in our very dreams. They stretch like an unknown sea before us – mocking, mystifying, and murmuring strange revelations and possibilities.*

Sir William Crookes (February 16, 1887)

Between the publication of volume 15 of this handbook series and this volume, a Master Index (both author and subject) for volumes 1 through 15 has been issued. We hope this Master Index will serve as an aid to scholars in finding specific topics of interest and/or the accomplishments of certain authors among the extensive first 15 volumes, and that this handbook series will continue to serve rare earth scientists and engineers, and historians of science.

The review by M.Loewenhaupt and K.H. Fischer (chapter 105) focuses on one aspect of one of the most stimulating topics in the whole of lanthanide science: the dual-valence state elements Ce, Pr and Tb (valences of 3 and 4) and Sm, Eu, Tm and Yb (valences of 2 and 3). These authors bring us up to date on the status of our knowledge of valence fluctuation and heavy-fermion 4f systems as gleaned from neutron scattering experiments. The major topics include cerium-based valence fluctuation systems, cerium-based heavy-fermion materials and ytterbium-based materials. The remaining quarter of their chapter deals with samarium-, europium- and thulium-based systems. Neutron scattering is a powerful tool in understanding valence fluctuation and heavy-fermion systems. It can yield information about the magnetic structure, magnetic and non-magnetic excitations, magnons, crystal field splittings, spin–orbit transitions, and phonons. This chapter nicely complements earlier reviews that have appeared in some of our more recent volumes: volume 14 (chapters 96 and 97) and volume 15 (chapter 98), and brings up to date material published in the early volumes: volume 1 (chapters 4 and 7) and volume 2 (chapter 20).

The second review in this volume (chapter 106) by I.A. Smirnov and V.S. Oskotski deals with the thermal conductivity of rare-earth-containing materials and is the first major review on this topic. A great deal of information can be obtained on the electrical and magnetic nature of these solids, because of the varied response of the thermal conductivity to long-range magnetic order, spin-glass behavior, heavy ferm-

ions and Kondo lattices, crystalline electric fields, and superconductivity in metallic systems. The thermal conductivity of insulators and semiconductors are also reviewed. As noted by Smirnov and Oskotski, the thermal conductivity has been measured on less than 10% of the known compounds, and the thermal conductivity of many interesting rare earth phases has yet to be measured, and because of this paucity of data, many mysteries remain unanswered.

The third and fourth chapters deal with special classes of materials rather than measuring techniques as found in the first two chapters and the last one of this volume. In a brief, but powerful, review M.A. Subramanian and A.W. Sleight (chapter 107) discuss the chemistry, structure, electrical, magnetic and thermal behaviors; spectroscopic (vibrational, ultraviolet-visible and Mössbauer) properties; and luminescence of pyrochlores. Pyrochlores are ternary oxides of the general formula $A_2M_2O_7$, where A can be a divalent or trivalent cation, and M is a pentavalent cation if A is divalent or a tetravalent cation if A is trivalent. Over several hundred rare earth pyrochlores are known, many are electrical insulators, some are semiconductors, and even a few are metallic in nature.

The chapter by R. Miyawaki and I. Nakai (chapter 108) is the longest one in this volume and deals with the crystal structures of about 100 of the approximately 225 known minerals. These minerals were grouped into five classes based on the types of anionic groups found in the various structures. Within each class the minerals are arranged by the sizes of the anionic groups (isolated groups, chains, sheets or plates, and three-dimensional frameworks). The crystal chemistry of these minerals is discussed with particular emphasis on the differences between the yttrium group and the cerium group, and on the isomorphous substitution of rare earth ions by other non-rare earth ions. The chapter is well illustrated with drawings of the structures and anion coordination polyhedra around the rare earth ion.

The last chapter (chapter 109) is by D.R. Chopra on appearance potential spectroscopy (APS), which measures the probability for electronic excitation of a core level as a function of the incident electron energy. APS is based on a two-electron excitation/relaxation process and gives information on the density of unoccupied states. APS is a complementary technique to the more common Auger electron spectroscopy and X-ray photoelectron spectroscopy, and it also yields information on chemical bonding, near-neighbor configuration in the surface layer, and the chemical constituents. The author believes that when the different aspects of APS are fully exploited this technique will be accepted as a popular analytical tool for the material characterization of surfaces.

In this volume we have made one change from the previous volumes, the addition of an author index, which we believe will make this book even more useful to our readers. We plan to continue this feature in future issues.

CONTENTS

CONTENTS OF VOLUMES 1–15

VOLUME 4: Non-metallic compounds – II

1979, 1st repr. 1984; ISBN 0-444-85216-6

VOLUME 5

1982, 1st repr. 1984; ISBN 0-444-86375-3

VOLUME 6

1984; ISBN 0-444-86592-6

VOLUME 7
1984; ISBN 0-444-86851-8

VOLUME 8
1986; ISBN 0-444-86971-9

VOLUME 9
1987; ISBN 0-444-87045-8

VOLUME 10: High energy spectroscopy
1988; ISBN 0-444-87063-6

VOLUME 11: Two-hundred-year impact of rare earths on science
1988; ISBN 0-444-87080-6

VOLUME 12
1989; ISBN 0-444-87105-5

VOLUME 13
1990; ISBN 0-444-88547-1

VOLUME 14
1991; ISBN 0-444-88743-1

VOLUME 15

1991; ISBN 0-444-88966-3

Handbook on the Physics and Chemistry of Rare Earths, Vol. 16
edited by K.A. Gschneidner, Jr. and L. Eyring

Chapter 105

VALENCE-FLUCTUATION AND HEAVY-FERMION 4f SYSTEMS

M. LOEWENHAUPT and K.H. FISCHER
Institut für Festkörperforschung, Forschungszentrum Jülich GmbH, Postfach 1913, W-5170 Jülich, Germany

Contents

List of symbols

a, b	Clebsch–Gordon coefficients
AF	antiferromagnetic
b_i^+ (b_i)	slave boson creation (annihilation) operator
$\boldsymbol{B}$	magnetic field
c_m	magnetic specific heat
c_{km}^+ (c_{km})	conduction-electron creation (annihilation) operator
C	Curie constant
CF	crystal field
D	conduction-electron band width
D5, D7	diffuse neutron scattering instruments at ILL
E_k	quasi-particle energy
f_m^+ (f_m)	f-electron creation (annihilation) operator
$F(\boldsymbol{Q}, T)$	magnetic form factor
FWHM	full width at half maximum
g_j	electron Landé factor for total angular momentum
g_N	neutron g-factor
$\hbar k_0, \hbar k_1$	momentum of incoming (outgoing) neutron
H	Anderson Hamiltonian
H_{CS}	Coqblin–Schrieffer Hamiltonian
H_{CF}	crystal field Hamiltonian
H_K	Kondo Hamiltonian
H_{hf}^{4f}	hyperfine coupling constant for 4f electrons
HET	time-of-flight instrument at ISIS
HF	heavy fermion
HFR	high flux reactor of ILL
HFIR	high flux isotope reactor of ORNL
i	lattice site
ILL	Institut Laue-Langevin, Grenoble, France
Im	imaginary part
IN4, IN6, IN8	inelastic neutron scattering instruments at ILL
ISIS	intense spallation source at Rutherford Appleton Laboratory, UK
j, J	total angular momentum
J (J_{eff})	(effective) exchange coupling constant
$k = \lvert\boldsymbol{k}\rvert$	wave vector, momentum quantum number
k_B	Boltzmann constant
k_F	Fermi wave vector
k_n	wave vector defined by $\mu = k_n^2/2m^*$
l	total orbital angular momentum
l_z	z-component of l
LA	longitudinal acoustic
LLW	Lea–Leask–Wolf
m	magnetic quantum number, bare electron mass
m^*	effective electron mass
MFA	mean-field approximation
n	conduction-electron concentration
n_f	average number of f electrons per R ion
n_i	impurity concentration
N	degeneracy of 4f ground state
$N_c(\omega)$	conduction-electron density of states
$N_f(\omega)$	quasi-particle density of states
NCA	non-crossing approximation
NMR	nuclear magnetic resonance
ORNL	Oak Ridge National Laboratory, USA
$\boldsymbol{Q}$	momentum transfer
R	rare earth
R	Wilson ratio
$\boldsymbol{R}$	lattice vector
Re	real part
RKKY	Ruderman–Kittel–Kasuya–Yosida
$\boldsymbol{S}, S$	total spin (eigenvalue)
$S(\omega, \boldsymbol{Q}, T)$	scattering function
S_d	thermopower
T_C	Curie temperature
T_F	Fermi temperature
T_K	Kondo temperature
T_K^N	Kondo temperature deduced from neutron data
T_N	Néel temperature
T_{SF}	spin-fluctuation temperature
TA	transverse acoustic
U	Coulomb energy of 4f electrons
$V_k \approx V$	hopping matrix element
$\tilde{V}$	renormalized matrix element
VF	valence fluctuation
x	concentration
β	$= 1/k_B T$
$\gamma = c_m(T)/T$	Sommerfeld coefficient
γ_n	nuclear moment
$\Gamma(\boldsymbol{Q}, T)/2$	relaxation rate for Lorentzian line shape (Γ is the line width)
$\Gamma_6, \Gamma_7, \Gamma_8$	crystal field states
Δ	4f-electron level width for $U = 0$

$\tilde{\Delta}$	renormalized level width	ρ_{imp}	impurity resistivity
Δ_i	energy of crystal field level i	ρ_m	magnetic resistivity
ε_f ($\tilde{\varepsilon}_f$)	f-electron energy (renormalized)	ρ_{ul}	unitarity limit of impurity resistivity
ε_F	Fermi energy	$\boldsymbol{\sigma}$	Pauli spin matrices
ε_k	conduction electron energy	σ	spin quantum number
ε_m	energy of the maximum of the density of states $N_f(\omega)$ (Kondo peak)	$\chi(\omega)$	dynamic susceptibility
		$\chi(T)$, $\chi(\boldsymbol{Q}, T)$	static susceptibilities
Θ_D	Debye temperature	ω	band energy (excitation energy)
μ	chemical potential	$\hbar\omega$	energy transfer in neutron scattering
μ_B	Bohr magneton		
μ_{eff}	effective magnetic moment		

1. Introduction

Valence-fluctuation (VF) and heavy-fermion (HF) systems have been widely studied in the past two decades (for review articles, see: Wohlleben and Coles 1973, Wohlleben 1976, Jefferson and Stevens 1978, Robinson 1979, Grewe et al. 1980, Lawrence et al. 1981, Stewart 1984, Varma 1985, Steglich 1985, Lee et al. 1986, Moshchalkov and Brandt 1986, Newns and Read 1987, Ott 1987, Bickers 1987, Fulde et al. 1988, Schlottmann 1989, Grewe and Steglich 1991). These systems contain either lanthanide (R) elements such as Ce, Sm, Eu, Tm, or Yb or actinides such as U or Np. They can be diluted or can form concentrated alloys or compounds with other systems. In both VF and HF systems, the 4f or 5f electrons partly delocalize due to the mixing with the conduction or valence electrons of the outer shells or of the host. In this way they become itinerant in a similar way as the d electrons in transition metals.

Lanthanide VF or "intermediate valence" systems are characterized by a non-integral valence or a quantum mechanical mixture of the two ground-state configurations $(4f)^n$ and $(4f)^{n+1}$ with different valences. Due to the Coulomb interactions these states are highly correlated. The mixing with the conduction electrons leads to anomalous properties such as an isostructural phase transition with a large volume change (in SmS), strong pressure, temperature or alloying dependence and anomalies in the thermal, magnetic and transport properties.

In a "normal" compound the R ions are in a trivalent state and most of them order magnetically at low temperatures. This is in contrast to Ce compounds with the configurations $4f^1$ and $4f^0$ and the valences 3 and 4, and Sm, Eu, Tm, and Yb with the valences 3 and 2. For Yb the corresponding configurations are $4f^{13}$ and $4f^{14}$. In the solid state the second ionic configuration has nearly the same ground-state energy as the configuration with valence 3. Together with the hybridization with the conduction electrons, this leads to strong fluctuations of the 4f charge. In addition, one has an effective exchange between the spins of the 4f and the conduction electrons which leads to spin fluctuations. The corresponding exchange interaction has a profound effect on most physical properties of these alloys or compounds. It leads to the "Kondo effect" with a characteristic "Kondo" temperature T_K, which can vary between a fraction of a degree and several hundred K. In VF systems, T_K is considerably larger than in HF systems. At temperatures $T \gg T_K$ all VF and HF systems behave like systems with a stable magnetic moment (leading to a Curie or

Curie–Weiss susceptibility). At $T \ll T_K$ this moment either disappears (is "quenched") or is strongly reduced. The Kondo effect is due to the mixing of 4f and conduction electrons, the degeneracy of the f-electron ground state and the strong Coulomb repulsion between electrons in a single f-shell.

In the limit of weak hybridization of the 4f and conduction electrons, the charge fluctuations are strongly suppressed and there remain only spin fluctuations. In this "Kondo limit" the f-electron level width is small compared to the (negative) f-electron energy ε_f as well as small compared to the Coulomb energy U. At low temperatures these systems exhibit an unusually high electronic specific heat coefficient γ or a large effective mass m^* and are therefore called heavy-fermion systems.

At low temperatures ($T \ll T_K$), most HF systems order magnetically. Possible exceptions are $CeAl_3$, $CeCu_6$, $CeRu_2Si_2$, and a few other systems. However, even in these systems, one observes antiferromagnetic correlations and/or a metamagnetic transition in a magnetic field. In addition, HF systems can become superconducting. The HF superconductors presently known are $CeCu_2Si_2$, the only Ce-based system, and UPt_3, URu_2Si_2, UBe_{13}, UPd_2Al_3, and UNi_2Al_3. Some of these systems also order antiferromagnetically at a higher temperature or show in a magnetic field a transition to a metamagnetic (metastable) state. VF systems do not order magnetically and do not become superconducting. An exception is the antiferro-magnetic TmSe.

Our understanding of VF and HF compounds is based on theoretical and experimental results for *dilute* magnetic alloys (including transition metals) that are summarized in section 2.1. The basic properties involve the Kondo effect, crystal field (CF) effects and effects due to spin–spin coupling of the 4f electrons. A characteristic property of the Kondo effect is a sharp peak of the 4f-electron density of states at or very near the Fermi energy. This "Kondo resonance" builds up by strong correlations between 4f- and conduction-electron spins and is connected to a resonance in the scattering of the conduction electrons by the 4f ions. The Kondo resonance is strongest at $T = 0$, broadens considerably at T_K and vanishes at high temperatures. However, the Kondo effect is a true many-body effect, and the formation of this resonance cannot be understood in a single-electron picture. In sufficiently dilute systems it leads to a maximum of the impurity resistivity at $T = 0$ and this maximum is shifted to finite temperatures in more concentrated systems. In concentrated alloys and compounds one has in addition *collective* effects at low temperatures ($T < T_K$), the most spectacular of them being superconductivity as observed in the six systems listed above. HF superconductors have been discussed in detail by Lee et al. (1986), Moshchalkov and Brandt (1986), Fulde et al. (1988), and Grewe and Steglich (1991) and will not be considered in this chapter.

A second collective effect is the magnetic order. There is a competition between the Kondo effect, which tries to enforce a non-magnetic singlet state, and indirect magnetic interactions of the Rudermann–Kittel–Kasuya–Yosida (RKKY) type (Kittel 1963), which tend to align the 4f moments into some magnetic order and to destroy the Kondo effect. This destruction is due to the fact that the internal (or external) magnetic field lifts the degeneracy of the 4f ground state (see section 2.2).

The third collective effect (which exists only in compounds with lattice periodicity of the 4f ions) is a quasi-particle band structure at low temperatures, which exhibits

itself in the splitting of the Kondo resonance according to the symmetries of the R ion lattice. This periodic structure leads to a "coherence" of the electron waves like in other itinerant paramagnetic metals, and to a vanishing resistivity at $T=0$. This is because the local magnetic moments either disappear due to the Kondo effect or form a periodic magnetic structure far below the characteristic temperature. At temperatures $T > T_K$ the quasi-particle bands no longer exist and the coherence is destroyed since one has scattering by the local moments. At extremely high temperatures the Kondo effect disappears completely and the moments scatter incoherently, leading to the "Yosida limit" (Yosida 1957) in the resistivity.

In both diluted and concentrated systems one has a characteristic temperature that separates the magnetic high-temperature state from a non-magnetic low-temperature Fermi-liquid state (apart from the magnetic order at still lower temperatures due to a small residual magnetic moment). It turns out that many properties scale in a large concentration range as a function of this temperature. For this reason we call this characteristic temperature in all cases the "Kondo temperature", T_K, where T_K depends on the concentration of 4f ions. In this review we will briefly summarize the basic properties of VF and HF systems, focussing particularly on the presentation of neutron scattering data.

2. Survey of valence-fluctuation and heavy-fermion phenomena

2.1. *Dilute systems*

Of the various models proposed to explain the VF and HF phenomena the Anderson model is the only one that has been investigated in great detail. If one includes CF and spin–orbit coupling, this model describes most properties fairly well, despite its simplifications. In this model the conduction or valence electrons are assumed to form a single band. In R alloys and compounds this band is formed by 5d and 6s electrons, together with the conduction electrons of the other components of the system. The 4f electrons of a single R ion interact strongly via a screened Coulomb interaction. For a Ce ion this energy is of the order of $U \approx 5$ eV (Herbst et al. 1978, Johansson 1979). The exchange between these 4f electrons is usually neglected. The direct overlap of 4f wave functions between different sites is small and is also ignored. The 4f electrons hybridize with the conduction electrons, which makes them to a certain extent itinerant.

The eigenstates of an R ion in a free-electron gas can be described by spherical coordinates (assuming a large spherical box) with the quantum numbers k, l, l_z, σ, where $k = |\boldsymbol{k}|$ is the momentum, l the total orbital angular momentum, l_z its z-component and σ the spin quantum number. However, in the presence of spin–orbit coupling only the total angular momentum $j = l + \frac{1}{2}$ is conserved. For the magnetic quantum number m we have $-j \leqslant m \leqslant j$. We introduce the states $|k, j, m\rangle = a|k, l, l_z - \frac{1}{2}, \uparrow\rangle + b|k, l, l_z + \frac{1}{2}, \downarrow\rangle$, where a and b are Clebsch–Gordon coefficients. For Ce ions one has in the $4f^1$ configuration $j = \frac{5}{2}$, or a degeneracy $N = 2j + 1 = 6$. This multiplet can split in the solid by CF effects into multiplets with $N = 2$ and 4. With

these basis states the Anderson model for a single impurity reads

$$H = \sum_{k,m} \varepsilon_k c^+_{km} c_{km} + \varepsilon_f \sum_m f^+_m f_m + V \sum_{k,m} (f^+_m c_{km} + c^+_{km} f_m) + U \sum_{m>m'} f^+_m f_m f^+_{m'} f_{m'}. \tag{1}$$

Here, f^+_m creates an f-electron with quantum number $j_z = m$, c^+_{km} a conduction electron in the state $|k, \frac{5}{2}, m\rangle$; ε_k is the conduction-electron energy, ε_f the 4f-electron energy [with $\varepsilon_f \approx -2$ eV below the Fermi level for Ce (Johanssen and Rosengren 1975, Johanssen 1979, Herbst et al. 1978)] and $V_k = \langle f^1, \frac{5}{2}, m|V|f^0, k, \frac{5}{2}, m\rangle \approx V$ the hopping matrix element which usually is assumed to be constant. The parameter V_k would vary on the energy scale of the band width (of a few eV) whereas the energy scale of the Kondo effect is $k_B T_K$, corresponding to a few K. For Yb impurities one has $j = \frac{7}{2}$ and has to replace electrons by holes since for the f^{14} configuration the 4f shell is completely filled and for f^{13} it has one hole.

The parameters of the model are the band width D (with the Fermi energy assumed to be zero), the 4f-electron energy ε_f, the f-electron interaction energy U and the mixing energy V. An important new parameter is the 4f-electron level width for $U = 0$,

$$\Delta = \pi N_c(0) V^2, \tag{2}$$

where $N_c(0)$ is the conduction-electron density of states for both spin directions at the band energy $\omega = 0$. In the case of VF systems one has $|\varepsilon_f| \leqslant \Delta$, which leads to strong charge fluctuations. For HF systems one has $-\varepsilon_f \gg \Delta$ with $\varepsilon_f < 0$. In both types of systems the conduction band extends to still lower energies (Herbst et al. 1978).

For $-\varepsilon_f \gg \Delta$, $U \gg \Delta$ and $U + 2\varepsilon_f = 0$ the Anderson Hamiltonian, eq. (1), can be transformed into the Coqblin–Schrieffer (CS) Hamiltonian. In this "Kondo limit" charge fluctuations are completely suppressed and the model describes an effective 4f-electron spin j which interacts via exchange with the conduction electrons

$$H_{CS} = \sum_{k,m} \varepsilon_k c^+_{km} c_{km} - J \sum_{kk'mm'} c^+_{k'm'} f^+_m f_{m'} c_{km}. \tag{3}$$

The exchange coupling constant for electrons at the Fermi surface,

$$J = V^2 \frac{U}{\varepsilon_f(\varepsilon_f + U)}, \tag{4}$$

is negative for Ce impurities with $\varepsilon_f < 0$ and $\varepsilon_f + U > 0$. For $j = \frac{1}{2}$, $m \pm \frac{1}{2}$ (or spin $\frac{1}{2}$), the model of eqn. (3) can be identified with the Kondo Hamiltonian

$$H_K = \sum_{k,\sigma} \varepsilon_k c^+_{k\sigma} c_{k\sigma} - J \sum_{kk'\sigma\sigma'} \boldsymbol{S} c_{k'\sigma'} \boldsymbol{\sigma} c_{k\sigma}, \tag{5}$$

with the Pauli matrices $\boldsymbol{\sigma}$ and the spin quantum numbers σ, σ'. The generalization of the Kondo model, eq. (5), for a lattice (see section 2.2) describes, e.g. $CeAl_3$ and $CeCu_2Si_2$. In these systems the six-fold degeneracy of the Ce $j = \frac{5}{2}$ state is split by the CF into three doublets. At sufficiently low temperatures only the lowest doublet is effective, corresponding to $S = \frac{1}{2}$.

For the non-symmetrical Anderson model with $U + 2\varepsilon_f \neq 0$, one has in the Coqblin–Schrieffer and Kondo Hamiltonians in addition to the exchange a potential scattering term. The Kondo resonance is no longer at the Fermi energy $\varepsilon_F = 0$ but is shifted. This shift leads to a smaller resistivity $\rho(T)$, the maximum of which, however, is still at $T = 0$. The potential scattering has a dramatic effect on the thermoelectric power, which vanishes in the symmetric case $U + 2\varepsilon_f = 0$, but has a huge peak near T_K for $U + 2\varepsilon_f \neq 0$.

In the case of crystal field (CF) effects one has to add to the Hamiltonians in eqs. (1), (3) or (5) a term which for the lowest multiplet (j, m) can be written as

$$H_{CF} = \sum_{lm} B_l^m O_l^m \tag{6}$$

with the CF parameters B_l^m and where the "Stevens operator equivalents" O_l^m depend on the crystal symmetry. Magnetic excitations in CF-split systems are discussed in detail by Fulde and Loewenhaupt (1986).

Both the Anderson and the Kondo (or Coqblin–Schrieffer) model have been solved exactly for thermodynamic properties such as the 4f-electron valence, specific heat, static magnetic and charge susceptibilities, and the magnetization as a function of temperature and magnetic field $\boldsymbol{B}$ by means of the Bethe ansatz (see Schlottmann 1989, and references therein). This method also allows one to calculate the zero-temperature resistivity as a function of $\boldsymbol{B}$. Non-equilibrium properties, such as the finite temperature resistivity, thermopower, heat conductivity or dynamic susceptibility, could be calculated in a self-consistent approximation (the "non-crossing" approximation), which works well and is based on an $1/N$ expansion where N is the degeneracy of the 4f level,

$$N = 2j + 1 \tag{7}$$

[see Bickers (1987), and references therein]. Spectroscopic properties have been calculated for the ground state by means of a variation method (Gunnarsson and Schönhammer 1987).

In all theories a characteristic temperature, the Kondo temperature, emerges which is approximately

$$T_K = (D/k_B) \exp[\pi\varepsilon_f/N\Delta], \tag{8}$$

where D is the conduction-electron band width [see, e.g., Newns and Read (1987), eq. (31)]. In a more rigorous expression [Schlottman (1989), eq. (4.29)] the prefactor of the exponential in eq. (8) depends also on the quantum number j. For temperatures far above T_K all theories predict a magnetic state with a Curie susceptibility and ln T terms in the susceptibility, specific heat, resistivity, etc. Far below T_K one has the Fermi-liquid behavior with simple power laws for all quantities as a function of the temperature, the excitation energy ω, and the magnetic field B. In this regime all ln T singularities vanish. At all temperatures one has scaling: most quantities are functions of T_K, T/T_K, ω/T_K or B/T_K and do not depend explicitly on the model parameters J or U, ε_f and Δ. The ground state is a singlet, i.e. the impurity moment is "quenched" or "compensated" by the spins of the surrounding conduction electrons.

For a *non-interacting* electron gas one finds for the linear coefficient γ of the specific

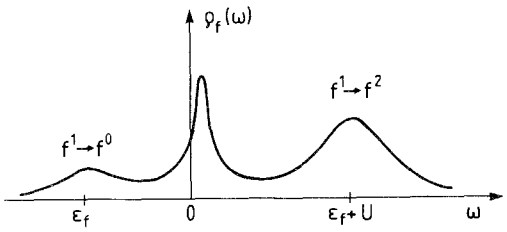

Fig. 1. Schematic 4f-electron density of states for a Ce ion in a simple metal. The energy ω is measured relative to the Fermi level. The two broad peaks are due to $4f^1 \rightarrow 4f^0$ and $4f^1 \rightarrow 4f^2$ transitions. The peak close to $\omega = 0$ is the Kondo resonance.

heat per R ion for $T \rightarrow 0$

$$\gamma = \tfrac{1}{3}\pi^2 k_B^2 N N_c(0), \tag{9}$$

where $N_c(\omega)$ is the electron density of states per R atom and per channel m. The corresponding zero-temperature susceptibility is (Newns and Read 1987):

$$\chi(0) = \tfrac{1}{3} N \mu_{eff}^2 N_c(0), \qquad \mu_{eff}^2 = g_j^2 \mu_B^2 j(j+1), \tag{10}$$

with the Landé factor g_j for the total angular momentum j and the Bohr magneton μ_B. Equations (9) and (10) lead to the Wilson ratio

$$R = \frac{\chi(0)/\mu_{eff}^2}{\gamma/\pi^2 k_B^2} = 1. \tag{11}$$

In the Kondo limit $U \rightarrow \infty, |\varepsilon_f| \gg \Delta$ one has from Bethe ansatz (Andrei and Loewenstein 1981, Andrei et al. 1983, Tsvelick and Wiegmann 1982, 1983) the exact result

$$\chi(0) = \frac{\mu_{eff}^2}{3T_K}, \qquad \gamma = \tfrac{1}{3}\pi^2 k_B^2 \frac{1}{T_K} \frac{N-1}{N} \tag{12}$$

(with a properly defined characteristic temperature T_K), which leads to the Wilson ratio $R = N/(N-1)$. Note, that for $N = 2$ R reaches its maximum value $R = 2$ and for $N \rightarrow \infty$ (which corresponds to the mean-field theory discussed below) the value $R = 1$, see eq. (11). For non-integer valences $n_f < 1$ or VF systems the correction $1/(N-1)$ to the mean-field value $R = 1$ yields a smaller value (Newns and Read 1987). For most dilute HF alloys one observes indeed R of the order of unity. The result (12) can be interpreted as the susceptibility and the coefficient γ of independent quasi-particles in a Fermi liquid. It can be compared with eq. (10) if we define a quasi-particle density of states $N_f(\omega)$ which is mostly of f-character and which replaces $N_c(0)$ in eq. (10). This leads to $N N_f(0) = T_K^{-1}$ and with $N N_c(0) \sim T_F^{-1}$ and the Fermi temperature $T_F = \hbar^2 k_F^2/2m$, to a huge effective mass, m^*, proportional to $m T_F/T_K$ or to a strongly enhanced specific heat and susceptibility in the Fermi-liquid state since $T_F/T_K \gg 1$.

The large f-electron density of states $N_f(0)$ is due to the Kondo resonance which exists in both VF and HF systems. Figure 1 shows a schematic plot of the 4f-electron density of states of a Ce ion at temperatures $T \ll T_K$ with the energy ω measured relative to the Fermi level. One has at energy $\varepsilon_f < 0$ a broad peak due to the transition of a conduction electron to the empty 4f level ($f^1 \rightarrow f^0$) and a similar broad peak

centered around the energy $\varepsilon_f + U$ due to a transition $f^1 \rightarrow f^2$. These peaks can be obtained in the lowest decoupling approximation of the equation of motion and have a width $N\Delta$, with Δ from eq. (2) (Kittel 1963). The sharp Kondo resonance appears only for $T < T_K$ and has at $T = 0$ a width of order $\pi k_B T_K / N$ (Bickers 1987). For Ce alloys the density of states $N_f(\omega)$ has its maximum at an energy $\varepsilon_m > 0$. For the symmetrical Anderson model or for the Kondo model $\varepsilon_m = 0$.

The Kondo resonance is a many-body effect. It can be traced to the fact that a sudden perturbation of an electron gas creates an infinite number of electron–hole pairs with excitation energy $\omega \rightarrow 0$. In our case the perturbation is caused by spin flip or by the exchange of a 4f and a conduction electron. In the simplest process a single conduction electron goes into the f^0 level, leading to an f^1 state and leaving a hole in the conduction-electron band. In the intermediate state and at $T = 0$, this leads to electron–hole excitations of arbitrarily small energies. At finite temperatures the Fermi surface no longer is sharp and the Kondo resonance is "washed out". A complementary picture is the result of high-temperature perturbation or T-matrix theory of the Kondo model (Fischer 1970) or of renormalization group calculations (Wilson 1975, Nozières 1974). Both approaches show that with decreasing temperature the system can be described by an increasingly strong effective exchange interaction $J_{\text{eff}}(T)$. This leads for $T \rightarrow 0$ to a singlet state which is formed by the impurity spin and spins of the surrounding conduction electrons and which leads to a disappearance of the impurity-spin degree of freedom of thermodynamic properties. Evidence for this is the transition from Curie to Pauli behavior of the susceptibility. However, there are still low-energy magnetic excitations of the 4f electrons (which form this singlet state), which are observed in inelastic neutron scattering in the form of a quasi-elastic scattering peak with a width of the order $k_B T_K$. In addition, the increasingly stronger exchange leads to increasingly stronger scattering of the conduction electrons and to a maximum in the resistivity at $T = 0$. For the symmetric Anderson model and $T = 0$ (or for the Kondo resonance at $\omega = 0$) this scattering reaches its maximum possible value for a single-scattering channel or the "unitarity" limit (Grüner and Zawadowski 1974).

The Kondo effect, including a Kondo resonance, exists also in VF systems, where one has in contrast to HF systems also sizeable charge fluctuations. In the following we list theoretical results for both systems, as obtained from the Bethe ansatz (for a review, see Schlottmann 1989) and from self-consistent perturbation theory with respect to the hopping-matrix element V, the so-called non-crossing approximation (NCA), which is essentially an expansion with respect to the inverse of the 4f-degeneracy N, eq. (7) (Keiter and Kimball 1971, Kuramoto 1983, Keiter and Czycholl 1983, Crewe 1983, Zhang and Lee 1983, 1984, Coleman 1984, 1987a, Bickers et al. 1987, Bickers 1987). The highest-order terms of this expansion can also be obtained in mean-field theory, which leads to the Wilson ratio $R = 1$. Both methods yield for thermodynamic properties fairly similar results even for $N = 4$ and $N = 6$ (see below). However, the NCA also allows for the calculation of transport properties, in contrast to the Bethe ansatz.

In this survey on VF and HF phenomena we discuss only the most important

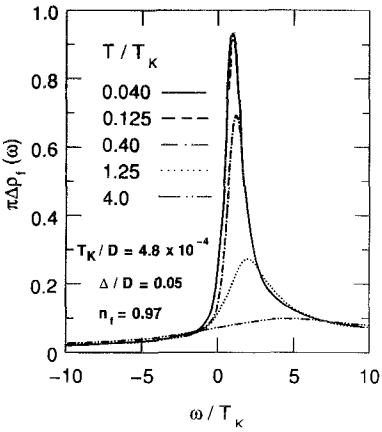

Fig. 2. Temperature dependence of the 4f-electron density of states in NCA. The density of states is normalized by $\pi\Delta$. The Kondo scale is in this case 100 times smaller than the hybridization width Δ (Bickers et al. 1987).

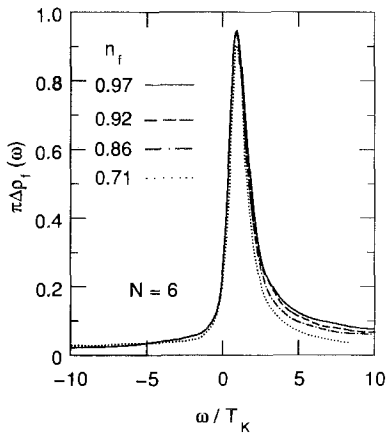

Fig. 3. The 4f density of states for $T \to 0$ and various valences (or average numbers of 4f electrons per R ion) n_f in NCA. The 4f-level degeneracy is $N = 6$ (Bickers et al. 1987).

results of both methods, and neutron data, which will be dealt with separately in section 3.

The Kondo resonance in the f-electron density of states shows a strong temperature dependence. It is largest at $T = 0$ and is already strongly reduced and broadened at temperatures $T \approx T_K$ (fig. 2). At least at $T = 0$, it is fairly insensitive to the average number, n_f, of f-electrons or holes per R ion; $n_f \approx 1$ for Ce and Yb alloys (fig. 3). Hence, VF systems with n_f distinctly lower than unity have nearly the same resonance as HF systems with $n_f \approx 1$. However, the energy scale T_K is considerably smaller in HF systems than in VF systems. The valence n_f itself depends on temperature (fig. 4). Small n_f-values increase fairly rapidly near T_K and approach at high temperatures the value of HF systems. This expresses the fact that for $T \gg T_K$ perturbation theory with respect to the hybridization V is valid and in zeroth order one can put $V = 0$. One is then dealing with an ensemble of independent ions and band electrons. The results shown in figs. 2 to 7 have been obtained by solving the NCA equations numerically for degeneracy $N = 6$, corresponding to Ce ions with $l = 3$ and $j = \frac{5}{2}$.

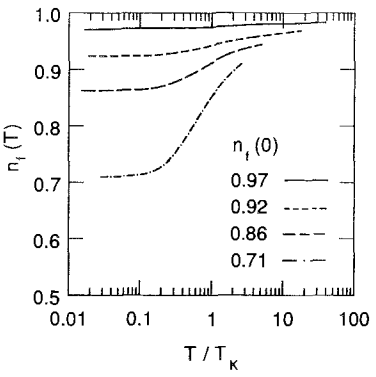

Fig. 4. Temperature dependence of the 4f-electron valence n_f in NCA (Bickers et al. 1987).

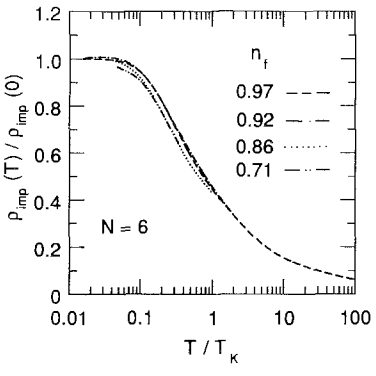

Fig. 5. Temperature dependence of the impurity resistivity for $N = 6$ and various values of the valence n_f in NCA (Bickers et al. 1987).

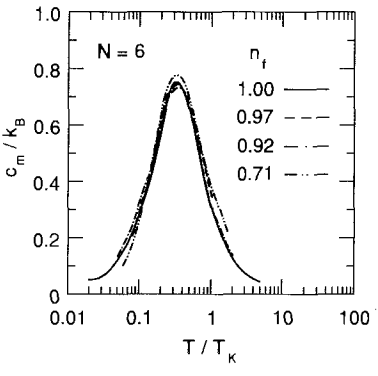

Fig. 6. Temperature dependence of the impurity (or magnetic) specific heat for $N = 6$ and various values of n_f in NCA. The result for $n_f = 1$ and the characteristic temperature T_K are calculated by means of the Bethe ansatz (Bickers et al. 1987).

The temperature dependence of the magnetic impurity resistivity $\rho_{imp}(T)$ (normalized to its value $\rho_{imp}(0)$ at $T = 0$) and of the corresponding specific heat $c_m(T)$ is plotted in figs. 5 and 6, respectively. Both $\rho_{imp}(T)$ and $c_m(T)$ scale with T/T_K and do not differ strongly for VF systems with $n_f = 0.71$ and HF systems with $n_f \approx 1$. The resistivity has its maximum at $T = 0$ and varies within about one decade around T_K as $\ln T/T_K$. It reaches its asymptotic (constant) value as given by the Born approximation only at temperatures $T > 100T_K$, i.e., outside the temperature range shown in

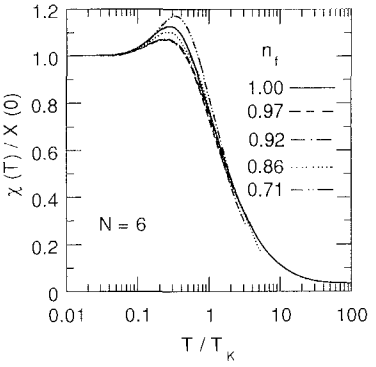

Fig. 7. Temperature dependence of the magnetic susceptibility for $N=6$ in NCA. The curve for $n_f=1$ is a Bethe-ansatz result. The susceptibility shows a weak maximum at $T/T_K \approx 0.5$ which depends on n_f (Bickers et al. 1987).

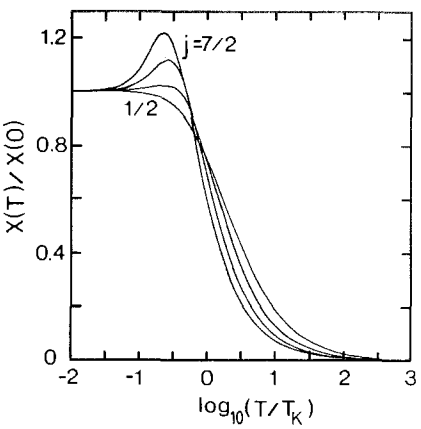

Fig. 8. Temperature dependence of the magnetic susceptibility for impurities with total angular momenta $j=\frac{1}{2},\frac{3}{2},\frac{5}{2},\frac{7}{2}$ and $n_f=1$, calculated with the Bethe ansatz for the Coqblin–Schrieffer model, eq. (3) (Rajan 1983).

fig. 5. In the Kondo limit, $n_f \to 1$, the zero-temperature resistivity $\rho_{imp}(0)$ can be calculated exactly. From the Friedel sum rule one has (Langreth 1966, Newns and Read 1987, Cox and Grewe 1988)

$$\rho_{imp}(0) = \frac{2\pi n_i}{ne^2 k_F} N \sin^2\left(\frac{\pi n_f}{N}\right). \tag{13}$$

Here n_i is the impurity concentration and n the concentration of conduction electrons.

The specific heat as a function of $\ln T/T_K$ shows a broad maximum below T_K. For $T \ll T_K$, both $\rho_{imp}(T)$ and $c_m(T)$ show Fermi-liquid behavior with $\rho_{imp}(T) = \rho_{imp}(0)\,[1 - A(T/T_K)^2]$ and $c_m(T) = \gamma T$, where $A = \pi^2(1 - 8/3N)$ to order $1/N$ (Houghton et al. 1987) and where γ is given by eq. (12).

The susceptibility $\chi(T)/\chi(0)$ with $\chi(0)$ from eq. (12) is shown in fig. 7. It is again similar for VF and HF systems, apart from a peak near T_K, which is more pronounced for VF systems. This peak depends strongly on the 4f-level degeneracy N and vanishes in the Kondo model with $N=2$ or effective spin $S=\frac{1}{2}$. Figure 8 shows this behavior for the susceptibility in the Coqblin–Schrieffer model, see eq. (3), (in which charge fluctuations are ignored) for various values of the total angular momentum j.

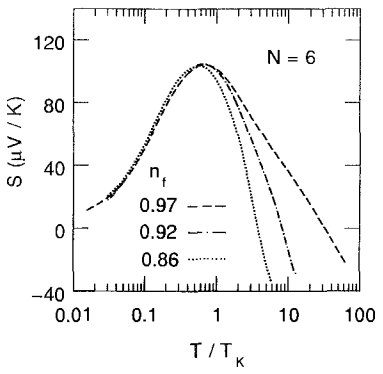

Fig. 9. Temperature dependence of the impurity thermopower $S_d(T)$ for $N = 6$ in NCA. for $T > T_K$ the thermopower depends strongly on n_f (Bickers et al. 1987).

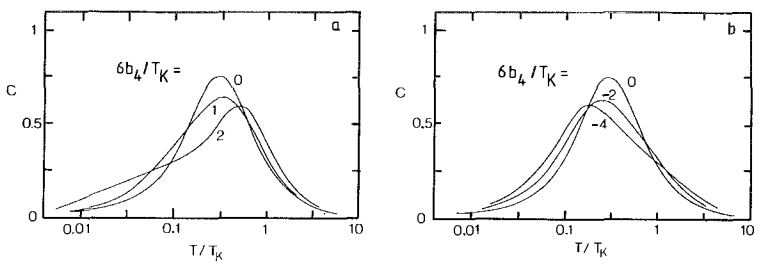

Fig. 10. Specific heat of a $j = \frac{5}{2}$ Coqblin–Schrieffer impurity as a function of temperature for various cubic CF splittings. In (a) Γ_7 and in (b) Γ_8 is the lowest lying multiplet (Kawakami and Okiji 1985).

The temperature dependence of the thermopower $S_d(T)$ of VF and HF systems is similar for $T < T_K$ but differs considerably for $T > T_K$ (fig. 9). For $N = 6$ it has a huge peak roughly at $T = T_K$ of order 100 μV/K whereas in typical metals it is of the order 1 μV/K. At low temperatures one has Fermi-liquid behavior and the exact result

$$S_d = 2\gamma \frac{\pi}{|e|N} T \cot\left(\frac{\pi n_f}{N}\right) \quad (T \to 0), \tag{14}$$

with the specific heat coefficient γ from eq. (12). The thermopower of Ce-based HF systems is positive, for Yb-based systems negative (Houghton et al. 1987, Fischer 1989b).

A crystal field (CF) can strongly modify these "standard" properties of VF or HF systems if the CF level splitting is of the order $k_B T_K$. Figures 10 and 11 show the shift and the deformation of the Kondo peak in the specific heat due to cubic CF splitting in this case. In fig. 11 one has an additional Schottky peak.

The theoretical results based on the NCA (or $1/N$ expansion) and on the Bethe ansatz presented so far are generally in rather good agreement with experimental data for dilute R systems. We present a few examples and refer for a more extended (but still rather incomplete) collection of experimental data for HF systems to Stewart (1984) and Grewe and Steglich (1991).

The impurity resistivity $\rho_{imp}(T)/\rho_{imp}(0)$ of the dilute HF system (CeLa)B_6 agrees

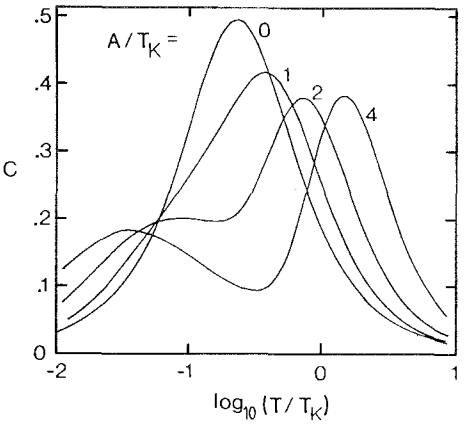

Fig. 11. Specific heat of a $j = \frac{3}{2}$ Coqblin–Schrieffer impurity as a function of temperature for various CF strenths, A, where the CF splits a quadruplet into two Kramers doublets (Desgranges and Rasul 1985, Schlottmann 1989).

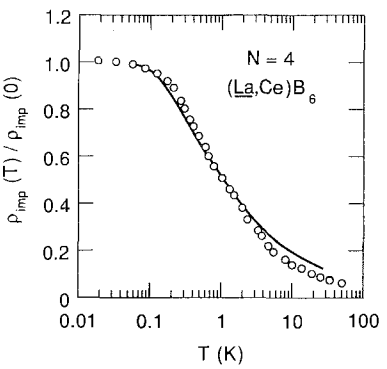

Fig. 12. Comparison of the results of the NCA for $N = 4$ with experimental data for dilute (CeLa)B_6: electrical resistivity (Bickers et al. 1987).

very well with the results of the NCA for $N = 4$ over more than three temperature decades (fig. 12). The agreement with the data for the specific heat of (CeLa)B_6 is less satisfactory. Figure 13 shows these data (including data with a magnetic field) and the theoretical results for the Coqblin–Schrieffer model with $S = \frac{3}{2}$. In fig. 14 the data for the susceptibility and specific heat of the VF system YbCuAl are compared with results from the Bethe ansatz with $N = 8$. For the specific heat the difference between YbCuAl and the non-magnetic analog LuCuAl is presented in order to eliminate phonon contributions. Part of the difference between experimental and theoretical results again can be explained by CF effects. In addition, one might have impurity interactions in this non-dilute system. The theory of neutron scattering by dilute HF and VF systems will be discussed separately in section 3.

2.2. *Concentrated systems and compounds*

The physical properties of concentrated VF and HF systems and of compounds are much less understood than those of dilute systems. In the case of transition metals in a non-magnetic host one has already for rather small concentrations (of the order of one percent) magnetic order or spin-glass structure due to direct

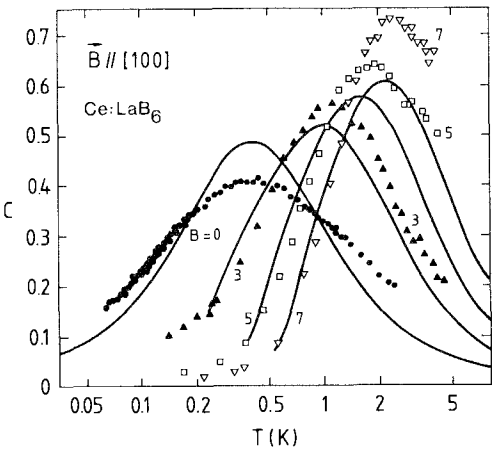

Fig. 13. Comparison of results from the Bethe ansatz for the Coqblin–Schrieffer model with $S = \frac{3}{2}$ and $T_K = 0.86$ K with the specific heat of dilute (CeLa)B_6 as a function of temperature for various magnetic fields (in T). Part of the discrepancy between theory and experiment might be due to CF effects (Schlottmann 1989).

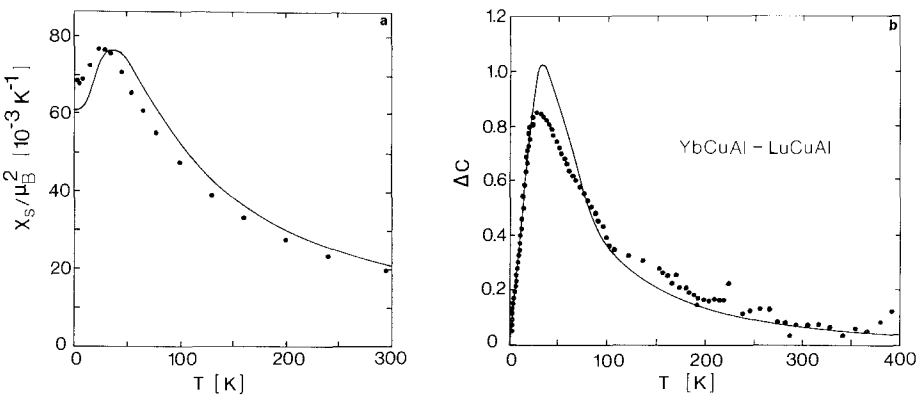

Fig. 14. Temperature dependence of (a) the susceptibility of YbCuAl and (b) the specific-heat difference between YbCuAl and the non-magnetic analog LuCuAl compared with theoretical results from the Bethe ansatz for a Coqblin–Schrieffer impurity with $N = 8$, $\Delta = 527$ K and $g_j = \frac{8}{7}$ (Schlottmann 1989).

or indirect exchange interactions. In R systems direct exchange is small, but the Rudermann–Kittel–Kasuya–Yosida (RKKY) interactions can lead to magnetic order or to spin-glass properties. As first pointed out by Doniach (1977), there is competition between the Kondo effect (which leads to the formation of singlet states and hence to a non-magnetic ground state) and the RKKY interactions. The internal fields due to these interactions tend to destroy the singlet formation or the Kondo effect. One expects a phase transition from a non-magnetic to a magnetic state as a function of concentration of the R ions or of the ratio J/D, where D is the width of the conduction-electron band. The Kondo temperature (8) with eqs. (2) and (4) can be seen to vary exponentially with the exchange constant J. One has for $N = 2$ or $S = \frac{1}{2}$ (note that $2N_c(\omega)$ is the conduction-electron density of states for both spin

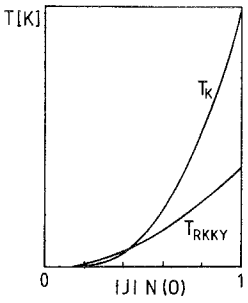

Fig. 15. Dependence of the Kondo temperature T_K and the RKKY interaction temperatures T_{RKKY} on the coupling constant (Aliev et al. 1984).

directions)

$$T_K = (D/k_B)\exp[1/J2N_c(0)] \quad (J<0) \tag{15}$$

and for the RKKY interaction (Moshchalkov and Brandt 1986)

$$T_{RKKY} = J^2/k_B D. \tag{16}$$

The dependence of both characteristic temperatures on $|J|N_c(0)$ is shown in fig. 15. One has three regimes: (a) for extremely small values of $|J|N_c(0)$ the RKKY interaction "wins" and the system has stable moments at all temperatures. (b) For somewhat larger values, but still $|J|N_c(0) \ll 1$ one has $T_K \gtrsim T_{RKKY}$. The system shows the Kondo effect but there is a delicate interplay between both interactions, and the ground state depends also on the band structure and other details if the interactions are of the same order of magnitude. (c) For $|J|N_c(0)$ of the order unity one has large Kondo temperatures, but also charge fluctuations. In this VF regime the magnetic interactions become unimportant and one has a non-magnetic ground state, as also is observed. However, strictly speaking, the Kondo model becomes invalid in this regime. More rigorous results for a one-dimensional Kondo model have been obtained by Doniach (1977), who predicted a second-order phase transition at $T=0$ from a non-magnetic Kondo to an AF state as a function of J/D. Experimentally, one indeed observes magnetic order at low temperatures ($T < T_K$) in most of the HF compounds (see section 1). In all these cases the magnetic moment is strongly reduced. At present there is no theory which predicts this behavior in detail. For the observed antiferromagnetic order, band structure effects are also important.

The various properties of VF and HF systems depend in different ways on the concentration of magnetic ions, although one has always Fermi-liquid properties (or simple power laws as function of T and $\boldsymbol{B}$) at low temperatures. The magnetic specific heat $c_m(T)$ and magnetic susceptibility $\chi(T)$ of $Ce_xLa_{1-x}Cu_6$ scale well as a function of concentration x. For $c_m(T)$ this is observed for $x=1$, 0.8, and 0.5 (Andrei et al. 1983) and for $\chi(T)$ for the concentrations $1 \leqslant x \leqslant 0.1$ (Onuki and Komatsubara 1987). The behavior of the magnetic resistivity, $\rho_m(T)$, is different. Figure 16 shows $\rho_m(T)$ for $Ce_xLa_{1-x}Cu_6$ for x between 0.094 and 1 as a function of $\ln T/T_K$. For small concentrations x the resistivity reaches its maximum at $T=0$ (compare fig. 5). With increasing concentration the maximum shifts to finite temperatures.

For $x=1$, the resistivity due to the magnetic moments vanishes at $T=0$ and one

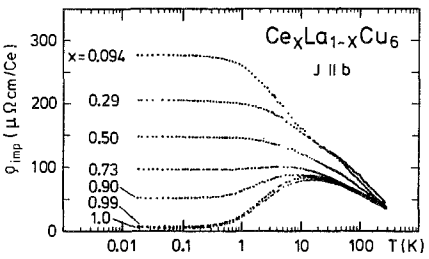

Fig. 16. Temperature dependence of the magnetic resistivity of dilute and concentrated $Ce_xLa_{1-x}Cu_6$ per mol of cerium (Onuki and Komatsubara 1987).

has

$$\rho_m(T) = A_1(T/T_K)^2. \tag{17}$$

The R ions form a periodic lattice, which leads for the 4f electrons together with the conduction electrons to the formation of "quasi-particle" bands, i.e. the electrons are in a "coherent" state. Since the magnetic moments either vanish (in the non-magnetic Kondo state) or form themselves a periodic magnetic structure (Kondo systems with magnetic order) there is no elastic scattering of the conduction electrons and therefore $\rho_m(0) = 0$. This is different at high temperatures, where even in a periodic lattice one has disordered moments, which scatter elastically. The coefficient A_1 can be calculated analytically. One finds $A_1 = j(j+1)\pi^4\rho_{ul}/9n^3$, with the resistivity in the unitarity limit $\rho_{ul} = h/(2j+1)e^2k_F$ (h is the Planck constant) (Fischer 1989a, Coleman 1987b). For small concentrations one has at low temperatures the Fermi-liquid behavior mentioned below eq. (13) and at intermediate concentrations $\rho_{imp}(T) = \rho_{imp}(0)\,[1 - A'(T/T_K)^2]$, where $\rho_{imp}(0)$ and A' depend on the R-ion concentration (Moshchalkov and Brandt 1986).

The thermopower of concentrated VF systems or compounds shows a huge Kondo peak (see fig. 9) and in addition a low-temperature peak of opposite sign (Franz et al. 1978), which can be explained by inelastic spin-flip scattering between the 4f and conduction electrons and which is due to the RKKY interactions (Fischer 1989b). The thermopower can also strongly depend on CF effects and seems to be far from universal.

The basis for our understanding of VF and HF compounds is the periodic Anderson model

$$H = \sum_{k,m} \varepsilon_k c^+_{km} c_{km} + \varepsilon_f \sum_{m,i} f^+_{im} f_{im} + V \sum_{k,m,i} [e^{i\boldsymbol{k}\boldsymbol{R}_i}\, c^+_{km} f_{im} + \text{h.c.}]$$
$$+ U \sum_{m>m',i} f^+_{im} f_{im} f^+_{im'} f_{im'}, \tag{18}$$

where one sums over all lattice sites i, in contrast to eq. (1). In the simplest approach one constructs a mean-field theory for $U \to \infty$. In this limit (which seems reasonable for Ce and Yb compounds), double occupancy of the 4f states is forbidden and one can replace the last term on the right-hand side of eq. (18) by the constraint $\Sigma_m \langle f^+_{im} f_{im} \rangle = \langle n^i_f \rangle \leqslant 1$. This constraint is taken into account by introducing a boson field b^+_i ("slave bosons") at each site i which creates a hole in the corresponding 4f orbital. In the MFA (mean-field approximation) the Bose operators b^+_i, b_i are treated

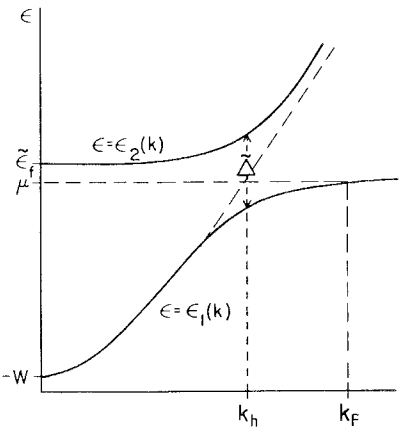

Fig. 17. Sketch of the dispersion relation $\varepsilon(k)$ for quasi-particle bands, as derived from the periodic Anderson model in a mean-field approximation (Millis and Lee 1987).

as site-independent c-numbers (Coleman 1984, 1987a, Read et al. 1984, Auerbach and Levin 1986a,b, Mills and Lee 1987, Newns and Read 1987). This leads to strongly renormalized parameters $\tilde{\varepsilon}_f$ and $\tilde{V}$ with

$$|\tilde{\varepsilon}_f| = k_B T_K, \qquad \tilde{\Delta} = \pi N_c(0)\tilde{V}^2 = \pi T_K/N \tag{19}$$

(see eq. 2) and quasi-particle bands with the dispersion

$$E_k^{\pm} = \tfrac{1}{2}\{\tilde{\varepsilon}_f + \varepsilon_k \pm [(\tilde{\varepsilon}_f - \varepsilon_k)^2 + 4\tilde{V}^2]^{1/2}\}, \tag{20}$$

as indicated in fig. 17. The chemical potential, μ, is determined by the number of quasi-particles with $\mu < \tilde{\varepsilon}_f$ for a less than half-filled band, and the wave vector k_h is defined by $\mu = k_h^2/2m$. Due to the flatness of the bands near μ and $\tilde{\varepsilon}_f$ one has a sharp Kondo resonance in the quasi-particle density of states, which is now split into two peaks. Such a split resonance has also been obtained by Kaga et al. (1988) in a somewhat different approximation. If one takes into account the conduction-electron band structure, the shape of the Kondo resonance becomes more complicated and reflects the symmetry of the crystal (see Fulde et al. 1988).

The MFA yields bands of independent quasi-particles. Fluctuation corrections to the MFA lead to interactions between these quasi-particles that are responsible for a frequency- and temperature-dependent resistivity, spin fluctuations and modifications of the mean-field result for the specific heat and susceptibility (Coleman 1987a, Auerbach et al. 1988, Millis and Lee 1987, Doniach 1987, Houghton et al. 1988). Modified models have also been considered which take into account intersite coupling or RKKY interactions explicitly (Zhang et al. 1987, Kaga and Yoshida 1988, 1989, Grewe 1988, Grewe and Welslau 1988, Grewe et al. 1988, Irkhin and Katsnelson 1989, Ohkawa and Yamamoto 1987). So far it is not clear to what extent these interactions are included if one considers quasi-particle interactions to first-order perturbation in the MFA. These approaches give a hint how low-temperature magnetic order in HF systems might be explained, but few detailed calculations have been performed (see section 3).

3. Neutron scattering and related experiments

The differential cross section for magnetic scattering is proportional to the imaginary part of the dynamic susceptibility or the magnetic excitation spectrum

$$\frac{d^2\sigma}{d\Omega\, d\omega} = \frac{k_1}{k_0}\frac{1}{2\pi}\left(\frac{g_N e^2}{mc^2}\right)^2 S(\omega, \boldsymbol{Q}, T), \tag{21a}$$

with the scattering function

$$S(\omega, \boldsymbol{Q}, T) = [1 - \exp(-\beta\hbar\omega)]^{-1}\ \mathrm{Im}\ \chi(\omega, \boldsymbol{Q}, T). \tag{21b}$$

Here, $\beta^{-1} = k_B T$, $\boldsymbol{Q}$ is the momentum transfer and $\hbar\omega$ the energy transfer, $\hbar\boldsymbol{k}_0$ and $\hbar\boldsymbol{k}_1$ are the momenta of the incoming and outgoing neutrons, and m is the bare electron mass. The Kramers–Kronig relations (White 1970) yield the sum rule

$$\chi(\boldsymbol{Q}, T) = \frac{1}{\pi}\int \frac{d\omega}{\omega}\,\mathrm{Im}\ \chi(\omega, \boldsymbol{Q}, T), \tag{22}$$

which connects Im $\chi(\omega, \boldsymbol{Q}, T)$ with the static susceptibility $\chi(\boldsymbol{Q}, T)$. The latter is often written in the form

$$\chi(\boldsymbol{Q}, T) = F^2(\boldsymbol{Q}, T)\,\chi(T), \qquad F(\boldsymbol{Q}=0) = 1, \tag{23}$$

with the magnetic form factor $F(\boldsymbol{Q}, T)$. In the limit $\omega = T = 0$ there is another exact relation between the local static susceptibility $\chi(T)$ and Im $\chi(\omega, 0, T)$, due to Shiba (1975), for dilute systems with a non-magnetic singlet ground state

$$\frac{\mu_{\mathrm{eff}}^2}{3}\left.\frac{\mathrm{Im}\ \chi(\omega, 0, T)}{\omega}\right|_{\omega=T=0} = \frac{\pi}{N}\chi^2(0), \tag{24}$$

with μ_{eff} from eq. (10).

Often one assumes that the excitation spectrum Im $\chi(\omega, \boldsymbol{Q}, T)$ can be approximated by a single relaxation process with relaxation rate $\frac{1}{2}\Gamma(\boldsymbol{Q}, T)$. This leads to a quasi-elastic line for the scattering function

$$S(\omega, \boldsymbol{Q}, T) = [1 - \exp(-\beta\hbar\omega)]^{-1}\,\chi(\boldsymbol{Q}, T)\frac{\frac{1}{2}\omega\Gamma(\boldsymbol{Q}, T)}{\omega^2 + [\frac{1}{2}\Gamma(\boldsymbol{Q}, T)]^2}, \tag{25}$$

where $\Gamma(\boldsymbol{Q}, T)$ is the line width. As discussed below, such a Lorentz function is sometimes a rather poor approximation for HF and VF systems at low temperatures. It fulfils the sum rule (22). However, the integral $\int d\omega\ \mathrm{Im}\ \chi(\omega, \boldsymbol{Q}, T)$ is not convergent. This would imply a diverging total cross section and shows that eq. (25) does not hold at high frequencies and that Im $\chi(\omega, \boldsymbol{Q}, T)$ has to decay faster than ω^{-1} for large ω. If eq. (25) holds (except in the high-frequency region), the width $\Gamma(\boldsymbol{Q}=0, T)$ of the quasi-elastic line can be expressed by the relaxation time $T_1(T)$ measured in NMR experiments. In particular, for dilute systems with a Q-independent susceptibility one has (Fulde and Loewenhaupt 1986)

$$\frac{1}{T_1} = \frac{k_B T}{\mu_B^2}\gamma_n^2 (H_{\mathrm{hf}}^{4f})^2 \lim_{\omega\to 0}[\omega^{-1}\ \mathrm{Im}\ \chi(\omega, T)], \tag{26}$$

where γ_n is the nuclear moment and H_{hf}^{4f} the hyperfine coupling constant for 4f electrons. The limit Im $\chi(\omega) \sim \omega$ for $\omega \to 0$ holds for all Fermi-liquid systems. For concentrated systems T_1 depends on a certain Q-average over Im $\chi(\omega, \boldsymbol{Q}, T)$.

At high temperatures or in the classical regime ($k_B T \gg \hbar\omega \approx \frac{1}{2}\Gamma$), the scattering function (25) has a maximum at $\omega = 0$ ("quasi-elastic" scattering). In many HF and VF systems and at low temperatures ($T \ll T_K$) the spectrum Im $\chi(\omega)$ peaks more sharply than in the Lorentzian (25), although one has still Im $\chi(\omega) \sim \omega$ for $\omega \to 0$. This leads to a "bump" or "hump" in Im $\chi(\omega)/\omega$, i.e. the maximum of this function is shifted to finite energy. Depending on $\Gamma(T)$ and T_K one might have inelastic or quasi-elastic scattering, although the difference might often be within the experimental resolution.

For non-interacting stable R ions (without hybridization with the conduction electrons), the excitation spectrum Im $\chi(\omega)$ consists of a series of δ-functions $\delta(\Delta_j - \Delta_i - \omega)$, where Δ_i is the energy of the CF level i (Fulde and Loewenhaupt 1986). The interaction of the 4f electrons of such ions with the conduction electrons of a metallic host can be described by the Kondo Hamiltonian (5) in which the exchange interaction J is replaced by $2(g_j - 1)J$ and the spin S by the total angular momentum. In addition, one has the CF term of eq. (6). For positive exchange there is no Kondo effect. Since $J/\varepsilon_F \ll 1$, where ε_F is the Fermi energy, the exchange interaction can be treated in the Born approximation. This leads to an excitation spectrum consisting of Lorentzians (25) with Korringa-like line widths $\Gamma(T)$. For two CF levels of distance $\Delta \equiv \Delta_j - \Delta_i$, one has for the quasielastic line.

$$\Gamma(T)/2 = 4\pi\alpha[(g_j - 1)JN_c(0)]^2 k_B T, \tag{27}$$

with $\alpha = 1$ for $\Delta \ll k_B T$ and $\alpha = 25/9$ for $\Delta \gg k_B T$ and for Ce with a Γ_7 ground state and a Γ_8 excited state. In addition one has for the inelastic line a term due to the decay of the CF excitations into electron–hole pairs which does not vanish for $T = 0$ (Fulde and Loewenhaupt 1986). The Korringa relation corresponds to $\alpha = 1$. For VF and HF systems the Born approximation is not sufficient and the line width $\Gamma(T)$ is no longer linear in T.

Very extended calculations of various physical properties (including Im $\chi(\omega, T)$ and $\Gamma(T)$) of HF systems have been performed by Bickers et al. (1987) and Bickers (1987) in the framework of the single-impurity Anderson model in NCA. Figure 18 shows Im $\chi(\omega)$, normalized to its maximum value and compared with a Lorentzian and experimental data for $CePd_3$ at 5 K from Galera et al. (1985a,b). For $T \geqslant T_K$ the theoretical results can be fitted by a Lorentzian whereas for $T < T_K$ the theory predicts strong deviations. Hence, for $T < T_K$ a unique line width $\Gamma(T)$ does no longer exist. One defines rather arbitrarily either the slope for $\omega \to 0$ of eq. (26) or the position of the peak of Im $\chi(\omega)$ as the effective line width. The latter definition leads to the line width presented in fig. 19 for the degeneracy $N = 6$, which shows a $T^{1/2}$ power law above T_K, increases with decreasing temperature for $T < T_K$, and for $T \to 0$ tends to $\frac{1}{2}\Gamma(0) \approx 1.4 T_K$. By contrast, the width Γ_1 defined from the slope of Im $\chi(\omega)$ for $\omega \to 0$ (see eq. (26)) extrapolates for $T \to 0$ to $\frac{1}{2}\Gamma_1(0) \approx 2.1 T_K$ (Cox et al. 1986).

The narrowing of the spectrum Im $\chi(\omega)$ for $T \to 0$, as indicated in fig. 18, leads to a "bump" in Im $\chi(\omega)/\omega$, as indicated in fig. 20. Here, the parameters are $N = 6$ and

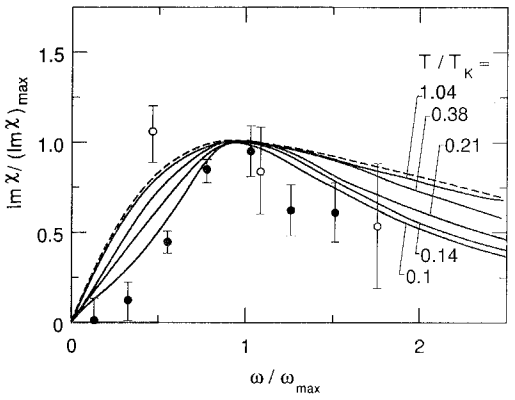

Fig. 18. Dynamic magnetic susceptibility Im $\chi(\omega)$, normalized to its maximum value, as a function of frequency ω. Solid lines result from the NCA, the dashed line corresponds to the quasi-elastic line shape eq. (25), and the dots are experimental data for $CePd_3$ (solid circles at 5 K, open circles at 280 K from Galera et al. (1985a,b)) (Bickers et al. 1987).

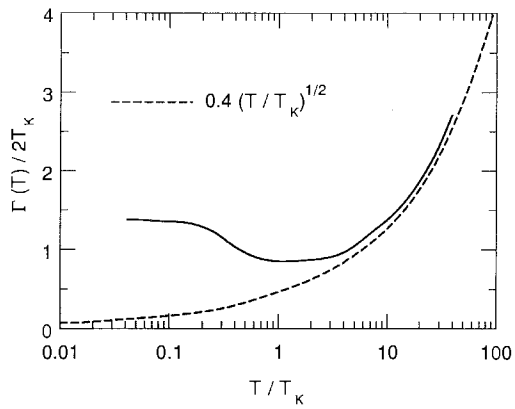

Fig. 19. Neutron scattering line width, $\Gamma(T)$, as a function of temperature from the NCA. Here, $\frac{1}{2}\Gamma$ is defined operationally as the position of the peak in Im $\chi(\omega)$, fig. 18. At high temperature one obtains a $T^{1/2}$ power law (dashed line).

$T_K = 44$ K. At low energies and $T = 0$ the NCA fails, and the correct values of Im $\chi(\omega)/\omega$ as obtained from eq. (24), are indicated as a dashed line. For $T \geqslant T_K$ the spectrum is again Lorentzian.

A simple analytic expression for Im $\chi(\omega)/\omega$ for dilute HF and VF systems at $T = 0$, based on the NCA and an additional approximation, has been proposed by Kuramoto and Müller-Hartmann (1985). It reads:

$$\text{Im } \chi(\omega) = C \frac{N\omega}{\pi \tilde{\varepsilon}_f^2} \frac{\sin \alpha}{u^2(u^2 + 4 \sin^2 \alpha)} \times \left\{ \sin \alpha \ln [(1-u^2)^2 + 4u^2 \sin^2 \alpha] + u \left[\frac{\pi}{2} - \tan^{-1} \left(\frac{1-u^2}{2u \sin \alpha} \right) \right] \right\}, \quad (28)$$

with the Curie constant $C = \frac{1}{3}(g_j \mu_B)^2 j(j+1)$, $u = \omega/\tilde{\varepsilon}_f$, $\alpha = \pi n_f / N$ and $\tilde{\varepsilon}_f$ the renormalized $4f^1$ level relative to the Fermi level, where n_f is the 4f-electron number. We showed in fig. 8 that the peak in the *static* susceptibility $\chi(T)$ depends strongly on the degeneracy N and vanishes for $N = 2$ or spin $S = \frac{1}{2}$. Unfortunately, the possibility

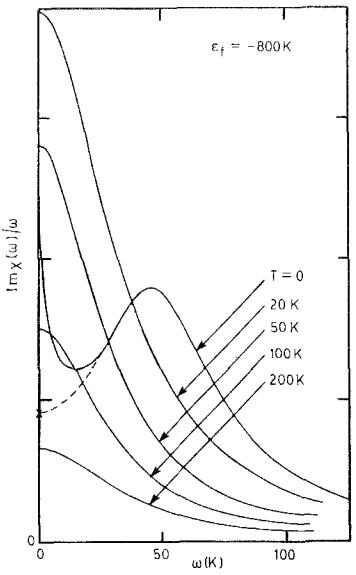

Fig. 20. Dynamic susceptibility divided by the frequency, Im $\chi(\omega)/\omega$, as a function of frequency from the NCA for $N = 6$ and $\varepsilon_f = -800$ K. The peak at $T = 0$ with a power-law divergency of Im $\chi(\omega)/\omega$ for $\omega = 0$ is an artifact of the NCA. The exact value of Im $\chi(\omega)/\omega$ for $\omega = 0$ from eq. (24) is indicated by a cross, the dashed line is an interpolation (Kuramoto and Kojima 1985).

of a similar trend in Im $\chi(\omega)/\omega$ has not yet been investigated. A simple approximation scheme based on the NCA for the single-impurity Anderson model has been proposed by Zwicknagl et al. (1990) and possibly allows to answer this question.

The width $\Gamma(T)$ at low temperatures is of the order of the Kondo temperature, T_K. In VF systems this characteristic temperature is rather high (several hundred K), which leads to a weak temperature dependence of $\Gamma(T)$ in these systems. On the other hand, the temperature region $T < T_K$ in these systems is experimentally more easily accessible. One has essentially the same features as in HF systems, such as a Lorentzian for Im $\chi(\omega)$ for $T \geq T_K$ and an inelastic peak of Im $\chi(\omega)/\omega$ for $T \ll T_K$ (Kojima et al. 1984). Earlier calculations of Schlottmann (1982) based on the Mori technique, although not completely reliable, indicate a small maximum in $\Gamma_1(T)$ (as obtained from the slope of Im $\chi(\omega)$ for $\omega \to 0$) in HF systems and a considerably stronger hump in VF systems. Possibly, this is an indication of stronger deviations from the Lorentzian at low temperatures in VF systems compared to HF systems.

The theories considered so far deal with HF or VF systems consisting of a singlet and a degenerate ground state. The Tm ion differs from the Ce, Yb, Sm, and Eu ions considered so far in that its two valence states, f^{12} and f^{13}, are both magnetic with degeneracies 13 and 8, respectively. The dynamic susceptibility of Tm-based VF systems can be well fitted by a Lorentzian with a relaxation rate $\Gamma(T)$ which below 100 K is roughly linear in T. However, the proportionality constant is considerably larger than expected for the Korringa law. At high temperatures, $\Gamma(T)$ seems to saturate, as expected for VF systems (Müller-Hartmann 1984). Similar results have been obtained by the mode–mode coupling approach (Schlottmann 1984).

A comparison of these results, which are based on a single-impurity model, with

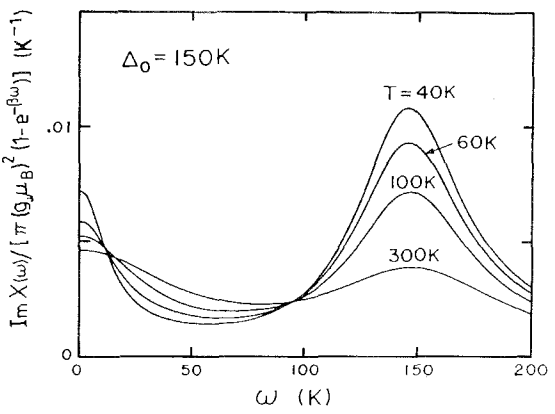

Fig. 21. Neutron scattering for a Ce^{3+} ion in a cubic crystal with the Γ_7 ground state for the parameters $T_K = 5.5$ K and the CF energy $\Delta_0 = 150$ K, calculated from a self-consistent ladder approximation (Maekawa et al. 1985a,b).

experimental data on concentrated HF and VF systems or compounds is not completely justified. However, we discussed in section 2 several physical properties that remained *qualitatively* unchanged if scaled with the characteristic temperature T_K. This is true for the static susceptibility $\chi(T)$ and possibly holds for Im $\chi(\omega, Q = 0, T)$ (Auerbach et al. 1987). However, due to the quasi-band structure Im χ now becomes Q-dependent. The Q-dependence of the static susceptibility and the width Γ has been calculated by Tachiki et al. (1987) for the Anderson lattice and compared with experimental data on $CeCu_6$, assuming a simplified band structure. Similar calculations for some typical cubic band structures, assuming a spherical Fermi surface, lead to antiferromagnetic peaks in Im $\chi(\omega, Q, T)/\chi(Q, T)$ at the zone boundary. At temperatures $T \geqslant 0.5 T_K$ the large-Q peaks can be fitted by the Lorentzian in eq. (25) with $\frac{1}{2}\Gamma = k_B T_K^N$, but at $T = 0$ and a sufficiently large Fermi momentum a shifted Lorentzian would yield a better fit (Auerbach et al. 1987). The Q-dependent dynamic susceptibility of HF systems which order magnetically at low temperatures (see section 1), has not yet been calculated. A relation between the Q-dependences of χ and Γ has been pointed out by Kuramoto (1987) and applied to $CeCu_6$.

The Kondo effect with additional CF splitting has been discussed in section 2 for the specific heat (see figs. 10 and 11). Depending on the CF parameters the Kondo peak in the specific heat can be deformed, shifted, or split into several peaks. Similar effects are observed in the dynamic susceptibility. Maekawa et al. (1985a, b) calculated the neutron scattering function $S(\omega, T)$ for a small concentration of Ce^{3+} ions in a cubic crystal with a Γ_7 ground state in the framework of the Coqblin–Schrieffer model, eq. (3). Figure 21 shows two peaks which both depend on temperature. The CF peak at $\omega \approx \Delta_0$ decreases strongly with increasing temperature. Here, Δ_0 is the crystal-field splitting. The temperature dependence of the line width $\Gamma(T)$ (fig. 22) agrees for $\Delta_0 = 150$ K fairly well with the experimental data for $Ce_{0.7}La_{0.3}Al_2$ (Loewenhaupt and Steglich 1977). In particular, the decrease of $\Gamma(T)$ at low temperatures can be explained by CF effects. However, due to the approximation made in the calculation (a self-consistent ladder approximation), the theory is not completely reliable at temperatures below the Kondo temperature. The latter is assumed to be $T_K = 5.5$ K for $\Delta_0 = 150$ K.

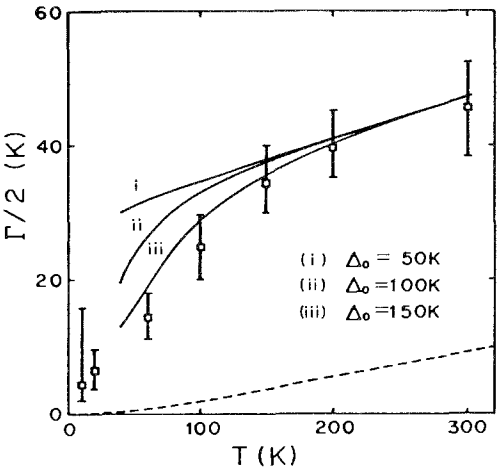

Fig. 22. Neutron-scattering line width as a function of temperature for a Ce^{3+} ion with Γ_7 ground state, $T_K = 5.5$ K and the CF energies $\Delta_0 = 50$, 100, and 150 K from a self-consistent ladder approximation. Indicated are also experimental results for $Ce_{0.7}La_{0.3}Al_2$ (Loewenhaupt and Steglich 1977) and (as dashed line) the results of second-order perturbation theory (Maekawa et al. 1985c).

An attempt to explain experimental data for the neutron scattering function $S(\omega, T)$ of the γ- and α-phases of metallic Ce on the basis of CF and spin–orbit effects (without taking into account the interaction between 4f and conduction electrons), is due to Orlov (1988). The effect of spin–orbit splitting on the dynamic susceptibility of VF systems within the framework of the NCA has been considered by Cox et al. (1986).

Up to now there is no *comprehensive* review on neutron scattering experiments involving VF and HF 4f-systems. Most of the existing reviews were given as invited talks at conferences and deal mainly with those systems investigated by the authors themselves. We list here some of these reviews in chronological order: Shapiro et al. (1978), Loewenhaupt and Holland-Moritz (1979a, b), Holland-Moritz et al. (1982), Loewenhaupt (1984a), Boucherle and Schweizer (1985), Goldman (1985), Holland-Moritz (1985), Shapiro (1986), Buyers (1986), Stassis (1986), Vettier et al. (1987), Murani (1987b), and Rossat-Mignod et al. (1988).

We should also mention the following reviews which deal at least partly with VF and HF systems in connection with NMR (Dormann 1991), ESR (Elschner and Schlott 1988), and light scattering (Zirngiebl and Güntherodt 1991).

3.1. *Cerium-based valence-fluctuation systems*

Most of the neutron scattering experiments on VF and HF 4f-systems involve Ce-based compounds. The huge amount of Ce-systems investigated in this field during the last two decades makes it impossible to discuss all of them. We were thus forced to select characteristic systems for the two groups (VF and HF) which we will discuss in more detail.

Magnetic neutron scattering can give information on the local *magnetic* properties (e.g. the existence of fast spin fluctuations in VF systems), but it cannot answer the question about the *origin* of the magnetic phenomena: are they driven by fast charge fluctuations or by the Kondo effect or by other mechanisms? As discussed in section 2,

we think that the Anderson model is the most appropriate model up to now for the description of HF and VF phenomena. The separation of the discussion on Ce-based compounds into VF and HF systems follows more from a practical point of view than from theoretical insight. We call Ce compounds VF systems if all $N = 6$ levels of the $^2F_{5/2}$ multiplet are involved in the determination of the ground state properties. We call them HF systems if only a fraction of the six states are involved. In the latter case the ground state may be a doublet ($N = 2$, this is the case for most cubic and all low symmetry systems) or a quartet ($N = 4$, this is the case for some cubic systems), often well separated from the remaining excited states. Crystal-field effects (the origin of the splitting) therefore play an important role in the discussion of HF systems, but are negligible ("wiped out") in VF systems.

For each compound we give first some information about the crystal structure and other important properties for its characterization, like valence (except for the HF systems where the valence is usually +3 or very near), susceptibility, resistivity, and specific heat. The discussion of neutron data involves all available elastic measurements (magnetic structure, ordered moments, form factor) and, of course, all inelastic measurements (quasi-elastic and inelastic magnetic scattering including magnons, crystal field and spin–orbit transitions and also phonon scattering, if related to HF and VF phenomena). We think that our list of VF compounds is more or less complete, while this is definitely not the case for the huge and still rapidly growing list of HF compounds.

3.1.1. *$CePd_3$*

$CePd_3$ is *the* archetypical valence fluctuation compound. It has a cubic crystal structure of Cu_3Au-type with $a_0 = 4.13$ Å. Early estimates for the valence from lattice-parameter systematics by Harris et al. (1972) gave a value of 3.45. This value was revised to 3.23 by Bauchspiess et al. (1982) and to 3.15 by Perez et al. (1990) employing L_{III} X-ray absorption measurements. In any case, the valence of Ce in $CePd_3$ is *considerably* different from the integer value of +3 (keeping in mind the present upper limit of 3.3 for VF Ce systems (Röhler 1987), and the obvious difficulty to define a valence in these systems at all (Baer and Schneider 1987). Thus $CePd_3$ can still be considered a typical valence fluctuator even if the f-count as deduced from the experimental data, has steadily increased over the years.

$CePd_3$ was the first compound where unusual fast spin fluctuations have been observed. The time scale of the spin fluctuations was directly measured by the width of the magnetic response deduced from an inelastic neutron scattering experiment performed on a polycrystalline sample of $CePd_3$ by Holland-Moritz et al. (1977) and (1982). Figure 23 shows the spectra of $CePd_3$ and YPd_3 at $T = 145$ and 240 K, measured on the time-of-flight spectrometer D7 situated at the cold source of the High Flux Reactor (HFR) of the Institut Laue-Langevin (ILL) in Grenoble. For this experiment unpolarized neutrons with an incident energy $E_0 = 3.5$ meV have been used. The spectra of YPd_3 (an isostructural but non-magnetic reference compound) serve to show the contribution of phonon and elastic nuclear scattering. The clearly visible additional scattering in $CePd_3$ can be interpreted as magnetic scattering from the Ce ions. Its shape, however, is completely different of what one expects from a

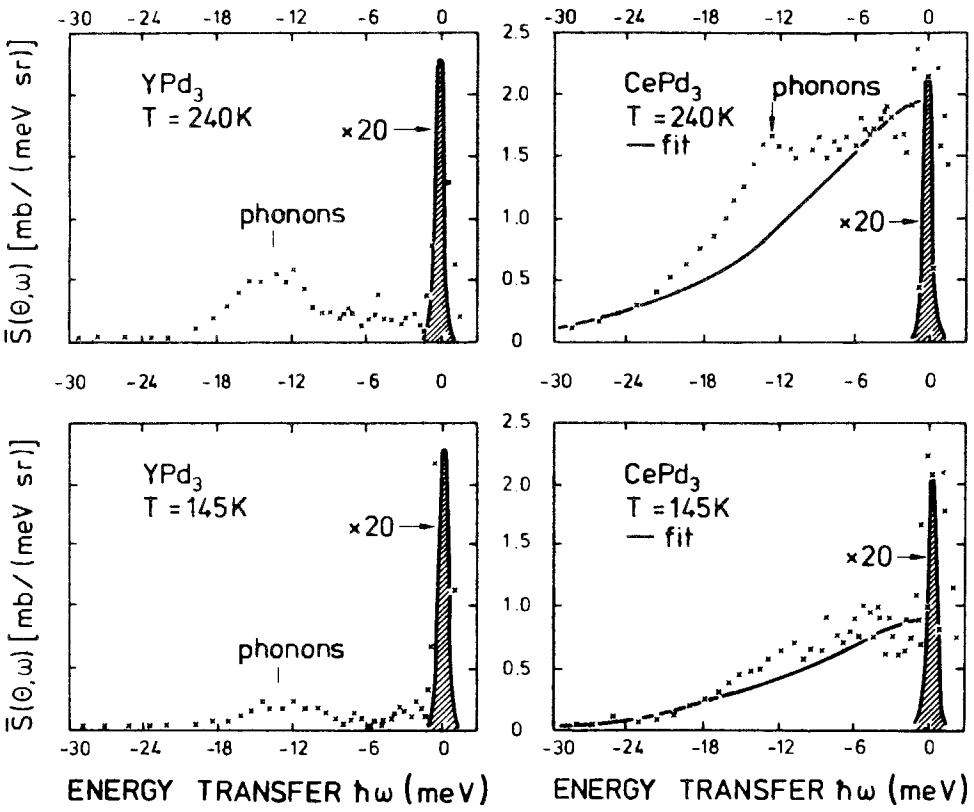

Fig. 23. Inelastic neutron spectra of YPd_3 and $CePd_3$ taken with $E_0 = 3.5$ meV at a constant scattering angle of $2\Theta = 20°$ and two different temperatures. The solid line is a fit with one broad quasi-elastic line (Holland-Moritz et al. 1982).

stable rare earth 3+ moment. Instead of a narrow ($\leqslant 1$ meV) quasi-elastic component and a sharp inelastic line around an energy transfer of order 10 meV (crystal field transition), the magnetic scattering of $CePd_3$ exhibits only a very broad ($\geqslant 10$ meV) quasi-elastic component. The underlying power spectrum is of the Lorentzian shape, see eq. (25), corresponding to a relaxational process of the spin self-correlation function in time. The solid line in fig. 23 is a fit of the magnetic scattering in $CePd_3$ with such a Lorentzian power spectrum centered at zero energy transfer. The two parameters to be determined are intensity and line width. The Q-dependence of the intensity at $T = 240$ K is shown in fig. 24. It follows the square of the free ion Ce^{3+} form factor, indicating the local character of the magnetic response. Furthermore, if extrapolated to $Q = 0$ and put on an absolute scale by a standard vanadium calibration, it corresponds within experimental error to the measured static susceptibility, including its temperature dependence (see fig. 25). For the other parameter, the line width, no Q-dependence could be detected either, consistent with the local character of the magnetic response, as already deduced from the Q-dependence of the intensity.

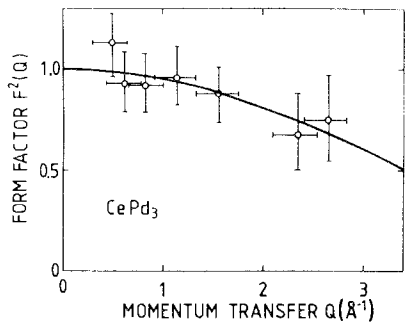

Fig. 24. Q-dependence of the inelastic magnetic scattering in $CePd_3$ deduced from the intensity in the energy window from -1 to -6 meV at $T = 240$ K (Holland-Moritz et al. 1982).

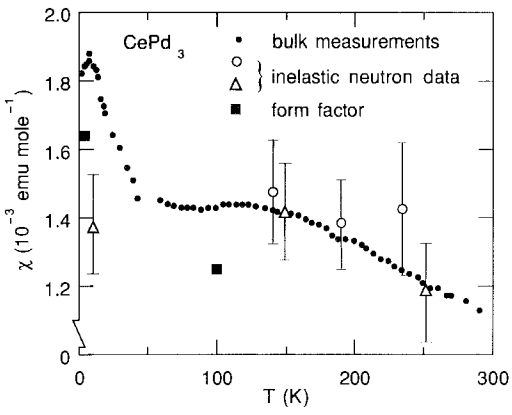

Fig. 25. Comparison of bulk susceptibility and the susceptibility of $CePd_3$ as deduced from neutron data. Open triangles from D5 neutron data by Galera et al. (1987), open circles from D7 neutron data by Holland-Moritz et al. (1982), solid squares from form factor measurements by Stassis et al. (1982). The bulk susceptibility (solid circles) was measured on the sample used by Galera et al. (1987).

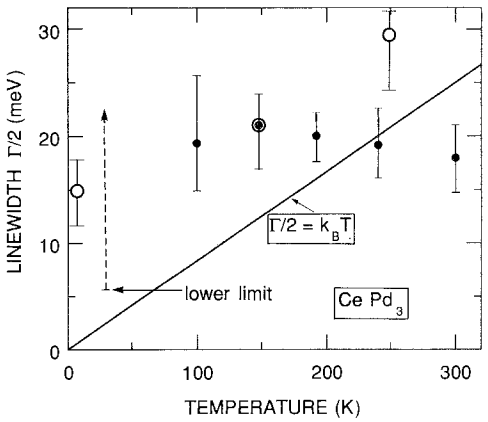

Fig. 26. Temperature dependence of the quasi-elastic line width of $CePd_3$. Solid cicles: Holland-Moritz et al. (1982); open circles: Galera et al. (1987).

The temperature dependence of the line width is shown in fig. 26. Here the filled circles indicate the line widths obtained from the D7 experiments. The line widths are nearly temperature independent from room temperature down to about 100 K with a value around 20 meV. This value of $\frac{1}{2}\Gamma$ corresponds to the unusual short relaxation time of 10^{-13} s or to a thermal energy $k_B T_{SF}$ with $T_{SF} = 232$ K, where T_{SF}

can be defined as the spin-fluctuation temperature. Here we use the expression "spin-fluctuation temperature" synonymously with "Kondo temperature". A characteristic *charge*-fluctuation temperature usually corresponds to considerably higher energies and cannot be seen directly in neutron scattering experiments. The high value of $T_{SF} = 232$ K for $CePd_3$ is consistent with the large exchange coupling constant J, as discussed in section 2.2. The constant line width in $CePd_3$, however, is in strong contrast to the much smaller absolute value and the *linear* temperature dependence (Korringa law) of the quasi-elastic line width for a stable-moment rare earth ion in a metallic compound (e.g., for $TbPd_3$ the slope of $\frac{1}{2}\Gamma(T)$ is 10^{-3} meV/K). From this we encounter the picture of *fast relaxing, local spins* to describe the spin dynamics of a valence-fluctuating system at elevated temperatures ($\geqslant$100 K). The fast relaxation prevents the observation of inelastic crystal-field transitions on an energy scale smaller than the quasi-elastic line width.

The aforementioned neutron scattering experiments on $CePd_3$, however, were unable to give conclusive information on the shape of the magnetic response below 100 K. The observable energy window in a neutron scattering experiment is confined to the incident neutron energy E_0 (for practical reasons $0.9E_0$) for processes where the neutron loses energy to the sample (positive energy transfers) and roughly to 3 to 4 times $k_B T$ for processes where the neutron gains energy from the sample (negative energy transfers). From the strong reduction of the magnetic intensity in the observable energy window of the D7 experiment for temperatures below 100 K it could only be inferred that the quasi-elastic line width must stay broad (a lower limit of 5 meV was given for $T = 30$ K) and/or that the magnetic response develops inelastic features at higher energy transfers.

To explore this region several inelastic neutron scattering experiments have been performed employing different techniques:

- time-of-flight experiments with unpolarized neutrons with different incident energies up to 115 meV on a polycrystalline sample (Severing and Murani 1990),
- triple-axis experiments with unpolarized neutrons on a single crystal (Shapiro et al. 1989),
- triple-axis experiments with a coarse energy resolution but polarized neutrons and polarization analysis on a polycrystalline sample (Galera et al. 1985a,b, 1987).

The advantage of using polarized neutrons and perform a polarization analysis lies in the *unambiguous* determination of magnetic scattering. The trade-off is usually a rather coarse energy resolution and poor counting statistics. Figure 27 shows the magnetic neutron scattering of $CePd_3$ obtained by this method on the D5 spectrometer of the ILL by Galera et al. (1987) at $T = 10$, 150, and 250 K. We have also included in the figure earlier results by the same group for $T = 5.5$ and 280 K (Galera et al. 1985a,b). At high temperatures (250 K, 280 K) the spectrum can be fitted with just one broad quasi-elastic line, confirming the aforementioned D7 results although with a somewhat larger value for the line width (30 instead of 20 meV). At $T = 150$ K there is still considerable quasi-elastic intensity with a line width of 22 meV. But, in addition a broad inelastic line at $\Delta = (55 \pm 5)$ meV with $\frac{1}{2}\Gamma = (30 \pm 5)$ meV is observed. At low temperatures (5.5 K, 10 K) this inelastic line becomes the dominant feature of the magnetic response ($\Delta = (55 \pm 5)$ meV, $\frac{1}{2}\Gamma = (24 \pm 4)$ meV). The intensity

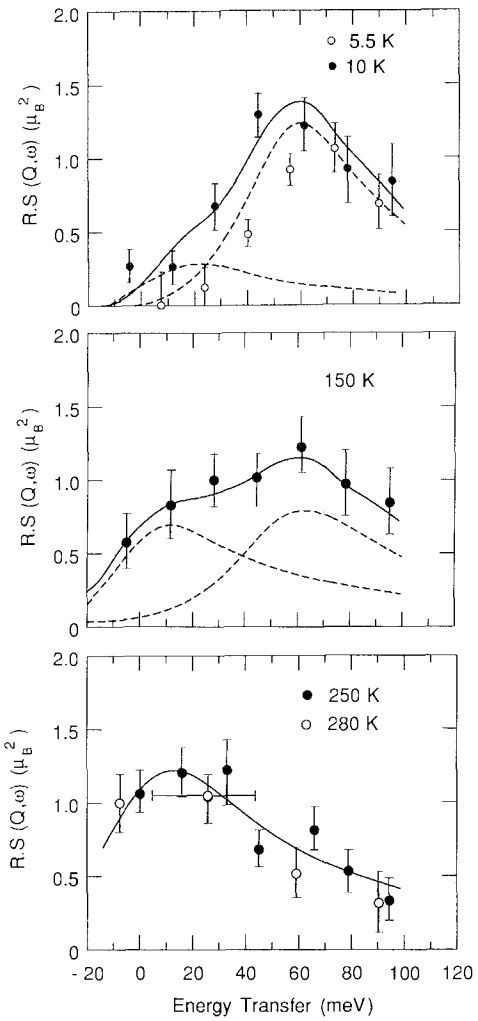

Fig. 27. Magnetic cross sections for $CePd_3$ at different temperatures and $Q = 2.57$ Å^{-1}. The lines are fits involving quasi-elastic and inelastic scattering convoluted with the energy resolution of the D5 spectrometer (FWHM $\simeq$ 40 meV). Solid circles: Galera et al. (1987); open circles: Galera et al. (1985a,b).

in the low-energy region ($\leqslant$20 meV) is drastically reduced. From the data, however, it cannot be decided whether there exists a quasi-elastic line (dashed line with $\frac{1}{2}\Gamma =$ 15 meV) or not. Galera et al. (1987) have included the quasi-elastic line in their fit and calculated from the neutron data a value of 1.4×10^{-3} emu/mol for the static susceptibility at 10 K (see fig. 25). The measured value of 1.9×10^{-3} is somewhat larger. Agreement can only be achieved if the upturn in χ below 50 K is neglected. The question, however, whether the upturn is an intrinsic property of $CePd_3$ or not, could not be satisfactorily answered up to now.

Using unpolarized neutrons, also the existence of a broad inelastic line at low temperatures was deduced from the time-of-flight data on $CePd_3$ by Severing and Murani (1990), which are shown in fig. 28. The authors claim that the intensity of

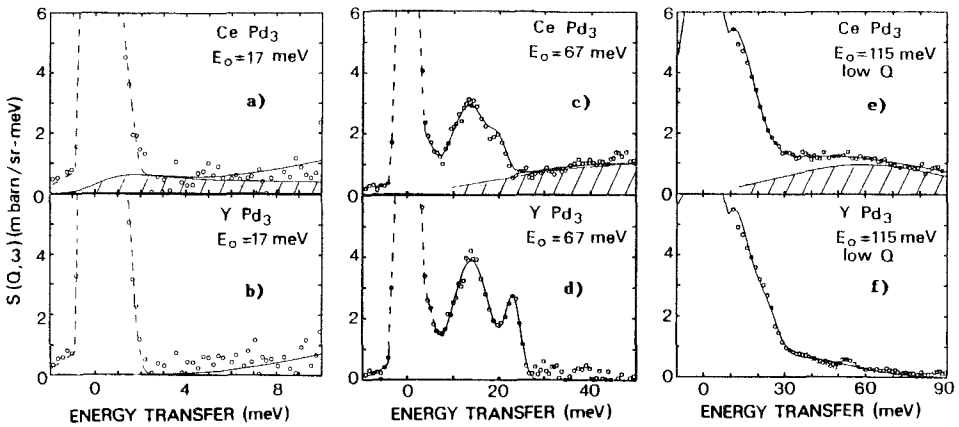

Fig. 28. $CePd_3$ and YPd_3 spectra at $T = 5$ K for three different incident energies. The average momentum transfer Q at the elastic position is 0.9, 3.4, and 4.7 $Å^{-1}$ for 17, 67, and 115 meV of incident energy, respectively. The shaded areas mark magnetic scattering (Severing and Murani 1990).

the inelastic line at 50 meV with a line width of 40 meV *alone* accounts for a static susceptibility of 1.4×10^{-3} emu/mol. They argue that there is *no* quasi-elastic scattering left at $T = 5$ K and explain the low-energy magnetic intensity as seen in fig. 28a as being totally due to magnetic scattering from an impurity phase.

Both Galera et al. (1987) and Severing and Murani (1990) agree on the observation that the low-temperature magnetic response of $CePd_3$ is dominated by the broad inelastic line ("bump or hump" as mentioned below eq. (26)) at about 50 meV energy transfer and 30 to 40 meV wide, and, furthermore, that the intensity in the quasi-elastic region is strongly reduced. This is in contrast to the findings of Shapiro et al. (1989). Their results at 10 K for a single crystal are shown in fig. 29. The sharp feature at 15.5 meV is a phonon and should be neglected in the following considerations. Magnetic scattering is observed over the *whole* energy range up to 80 meV, being strongest at low energy transfers and decaying slowly towards higher energies. Shapiro et al. (1989) could fit the magnetic part with a narrow quasi-elastic line ($\frac{1}{2}\Gamma = 3$ meV) and an overdamped inelastic line ($\Delta = 10$ meV, $\frac{1}{2}\Gamma = 15$ meV), both of Lorentzian shape. There is no indication of an inelastic structure ("hump") around 50 meV. For higher temperatures Shapiro et al. (1989) fitted their data also with a quasi-elastic and an inelastic line. The quasi-elastic line width at these temperatures is twice as large as for $T = 10$ K, the position of the overdamped inelastic line is shifted to 16 meV, comparable to its width of 10 to 15 meV. From the data itself it is not evident that there must be a quasi-elastic *and* an inelastic line (around 16 meV) in the spectra at elevated temperatures. A fit of the D7 data by Holland-Moritz et al. (1982) allowing also for an inelastic line (at 10 meV), did not improve the quality of the fit. The fit of a broad spectrum with more components reduces, of course, the width of each component. For the D7 data, line widths around 13 meV are obtained instead of 20 meV. The values given by Shapiro et al. (1989) for the quasi-elastic line

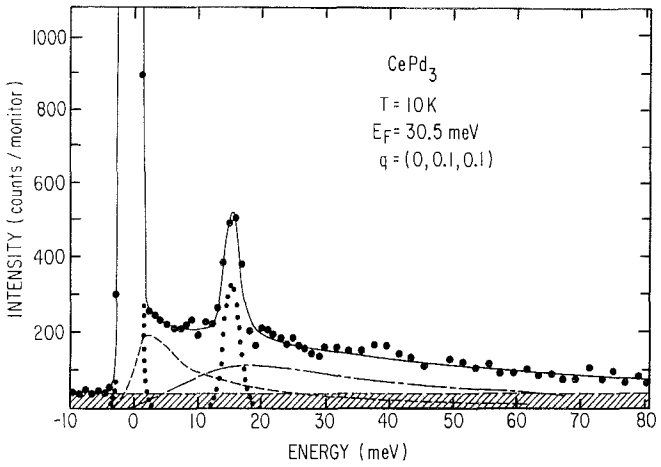

Fig. 29. Inelastic neutron spectrum measured at $T = 10$ K on a $CePd_3$ single crystal. The solid line is fit to the data which is the sum of a constant background, a Gaussian for elastic scattering and phonon scattering (15.5 meV), a narrow quasi-elastic Lorentzian of 3 meV width, and an inelastic Lorentzian at 10 meV and 15 meV wide. The excess background at high energies on account of changes in counting times was subtracted (Shapiro et al. 1989).

widths (3 meV at 10 K, 5 to 6 meV at 40 K up to 225 K), however, seem to be too small when compared to the results from the other experiments (see fig. 26).

The Q-dependence of the magnetic form factor as deduced from inelastic measurements, is often not very accurate and is limited in Q-range (see fig. 24). This leads usually only to the rather weak statement that the data are consistent with a 4f, 3d, etc., form factor. There is, however, a much more accurate method to measure the form factor over a wide Q-range, although restricted to the Q-values of nuclear Bragg reflections. Using polarized neutrons and a single crystal one can measure for each Bragg reflection the ratio R of the peak intensities for the two neutron-spin orientations, parallel and antiparallel to an external magnetic field. After minor corrections and normalization to the known nuclear structure factors one obtains the static susceptibility $\chi(\boldsymbol{Q}, T)$ and from its Fourier transform the spatial distribution of the magnetization induced by the external field. Figure 30 shows the results of such an experiment on a single crystal of $CePd_3$, performed at a polarized neutron spectrometer of the high flux isotope reactor (HIFR) at the Oak Ridge National Laboratories (ORNL) by Stassis et al. (1982) at $T = 4.2$ and 100 K. The data points at 100 K can be fitted quite well with the theoretical form factor of the Ce^{3+} free ion calculated from relativistic electronic wave functions. This implies that at 100 K the field-induced magnetization has a spatial distribution which is characteristic of the localized 4f electronic density of the Ce^{3+} ion. At 4.2 K the experimental results show deviations from the 4f form factor at low scattering angles. The induced moment must contain an additional component whose spatial distribution is more extended than that of the 4f electrons. Stassis et al. (1982) could fit their data at 4.2 K assuming that the induced moment consists of a 83% 4f–17% 5d Ce component. The extrapola-

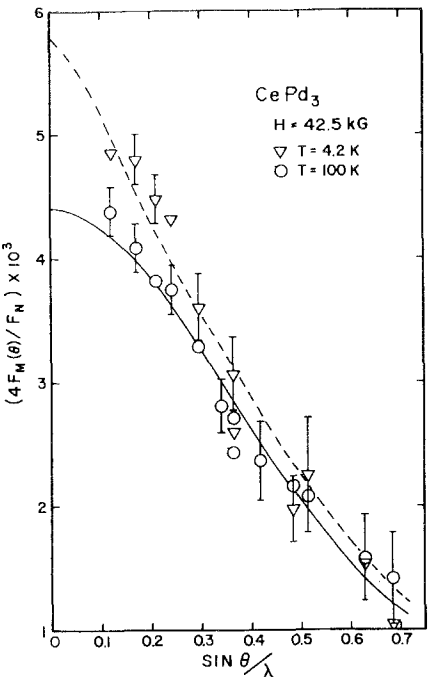

Fig. 30. Paramagnetic form factors of $CePd_3$ at 4.2 and 100 K plotted versus $\sin\theta/\lambda = Q/4\pi$. The solid line has been obtained by fitting the 100 K data to the 4f magnetic form factor of Ce^{3+}. The dashed line was obtained assuming an 83% 4f–17% 5d distribution of the induced moment (Stassis et al. 1982).

tion to $Q=0$ gives for the susceptibility 1.64×10^{-3} emu/mol at 4.2 K and 1.25×10^{-3} emu/mol at 100 K. The increase of χ at low temperatures is mainly due to the additional 5d component; the 4f component is nearly identical for the two temperatures. Both χ values deduced from the form factor extrapolation, however, are considerably smaller than the measured static bulk susceptibility (see fig. 25; χ measured on the sample which was used for the form factor measurements is similar to that shown here (Thompson et al. 1982)). The discrepancy between neutron-deduced χ and bulk χ is assumed to be due to additional contributions of s and p character, which are not detected in the neutron measurements. This discrepancy is not found in the inelastic data. They probe the 4f component only, therefore they are not tracking the upturn in χ below 50 K. Their absolute values, however, show a much larger systematic error.

Finally we discuss the influence of valence fluctuations on the phonon spectra of $CePd_3$. A detailed study has been undertaken by Severing et al. (1988). The effects associated with valence fluctuations were difficult to detect, but evident:

- a *breathing* mode had to be taken into account to reproduce the dispersion relations (see fig. 31),
- certain phonons showed unusual temperature-dependent line shifts, broadenings, and splittings (see figs. 32 and 33).

The crystallographic structure of $CePd_3$ gives rise to twelve phonon branches in each of the three main symmetry directions. The transverse modes in the [100] and [111] directions are two-fold degenerate. The results for the room-temperature

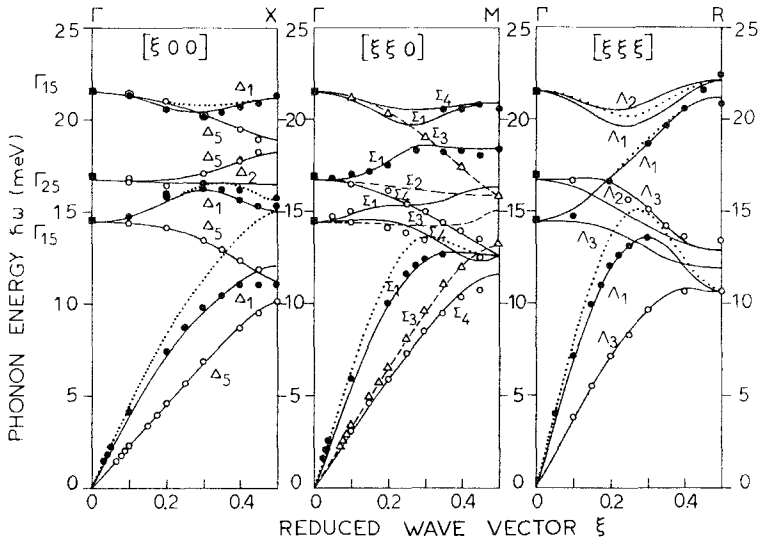

Fig. 31. Phonon dispersion curves for $CePd_3$ at room temperature. Solid symbols are longitudinal modes, open symbols transverse modes. In the [110] direction: △, transverse polarized in (110) plane; ○, transverse polarized in (100) plane. Results of Born–von Kármán fit including breathing term are shown as solid and dashed lines (the latter for △ data points). Dotted lines: if breathing term is neglected (Severing et al. 1988).

dispersion curves are shown in fig. 31. The data points are best fitted by a 16-parameter Born–von Kármán model with an additional breathing term (solid and dashed lines). The dotted lines indicate the dispersion curves as obtained with the same set of parameters but *without* breathing term. The breathing term accounts for an extra degree of freedom due to the breathing deformability of the Ce atom when undergoing valence fluctuations. Such a vibration pattern is shown in fig. 34a. It does *not* occur in "normal" compounds with Cu_3Au structure. The strongest influence of the breathing term is seen in the LA branch in the [100] direction at the zone boundary and in the LA branches of the [110] and [111] directions in the middle of the Brillouin zone. The elongation pattern for the LA mode at $\boldsymbol{q} = (0.5, 0, 0)$ is shown in fig. 34b. At these positions the phonons also exhibited an unusual temperature dependence. Examples are presented in figs. 32 and 33. The data reflect two different temperature regions: the low-temperature region ($T \leqslant 80$ K) with normal line shapes and a weak, linear decrease of the phonon energies with increasing temperature, and the region $T \geqslant 100$ K with anomalous softening, intrinsic line widths, and mode splittings. An attempt to explain the splittings has been given by Liu (1989). It should be noted that also in the magnetic response there is a considerable shift of intensity from the high-energy region (60 meV at 10 K) to the quasi-elastic region (0 to 20 meV) around this temperature, as discussed above.

However, Loong et al. (1988) concluded in another study of the phonon dispersion curves at room temperature that there are *no* significant anomalies, neither in the phonon frequencies nor in the line widths. Although the results of both groups

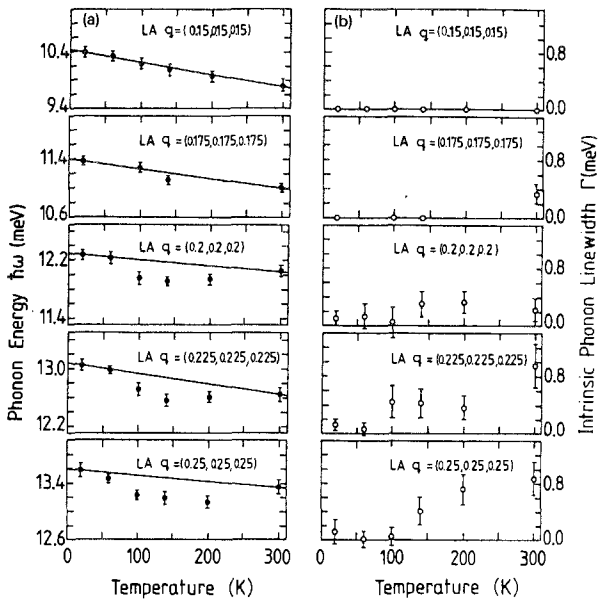

Fig. 32. (a) Phonon energies of $CePd_3$ versus temperature for several LA modes in the [111] direction. (b) Intrinsic phonon line widths of the corresponding modes versus temperature. The intrinsic line widths are fitted with a Lorentzian convoluted with a Gaussian for spectrometer resolution. Points without error bars are fits without a Lorentzian for phonons which are well described by spectrometer resolution alone (Severing et al. 1988).

[Severing et al. (1988) and Loong et al. (1988)] agree in general, there are significant differences in the interpretation of details and in their conclusions.

3.1.2. *$CeSn_3$*

The physical properties of $CeSn_3$ resemble those of $CePd_3$ in many aspects. The crystal structure is also of Cu_3Au-type, yet the nearest-neighbor Ce–Ce distance is much larger in $CeSn_3$ (4.72 Å) than in $CePd_3$ (4.13 Å). The bulk susceptibility has a broad maximum around 130 K and an upturn at low temperatures. As in $CePd_3$ there is a controversy whether the upturn is of intrinsic nature or not. Similar behavior is also observed for the resistivities (maximum around 130 K) but with a different effect on the compounds if non-magnetic impurities are added (a drastic change of $\rho(T)$ for $CePd_3$, minor effects on $\rho(T)$ for $CeSn_3$). The results of inelastic magnetic neutron scattering and of form factor measurements, which will be discussed in this section, also make both compounds look similar. There is, however, one big difference: the valence of Ce in $CeSn_3$ is near to the integral value of $+3$ [3.02, Röhler (1987)] while for $CePd_3$ the valence is *considerably* away from this value ($\geqslant 3.15$, depending on method and author). This may be the reason why no phonon anomalies have been observed for $CeSn_3$, in contrast to $CePd_3$.

First we discuss the magnetic properties. Inelastic neutron scattering experiments to study the temperature dependence of the magnetic response of $CeSn_3$ have been

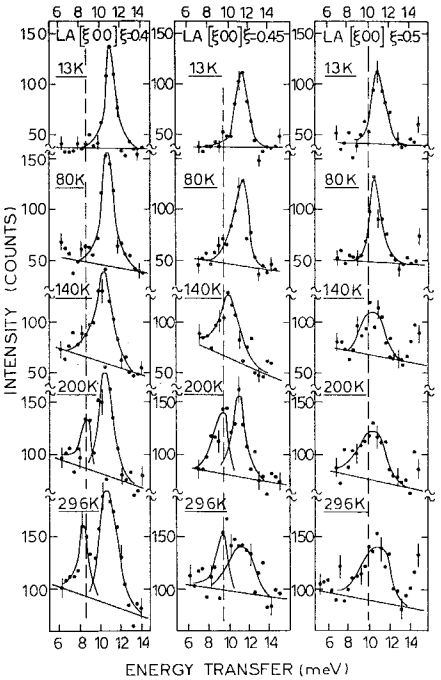

Fig. 33. Scans of several LA modes of $CePd_3$ in the [100] direction for different temperatures. The vertical dashed lines indicate the positions of the corresponding TA modes at room temperature as measured in a transverse configuration (Severing et al. 1988).

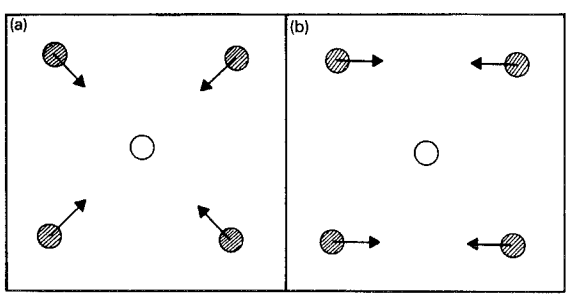

Fig. 34. Elongation pattern within the (100) plane (a) for the breathing deformation and (b) for the LA mode at $\boldsymbol{q} = (0.5, 0, 0)$. Open circle: Ce atom, hatched circles: Pd atoms (Severing et al. 1988).

performed by several groups employing different techniques (all experiments were done on polycrystalline samples):

- time-of-flight experiments with unpolarized *cold* neutrons by Holland-Moritz et al. (1982),
- time-of-flight experiments with unpolarized *thermal* neutrons with incident energies up to 82 meV by Murani (1983a, b), and
- triple-axis experiments with a coarse energy resolution but polarized neutrons and polarization analysis by Capellmann et al. (1985).

Here we present the essential neutron spectra from all three groups to allow the reader to judge by himself. All authors agree on the observation that at high temperatures the spectral response consists of only one broad quasi-elastic line of

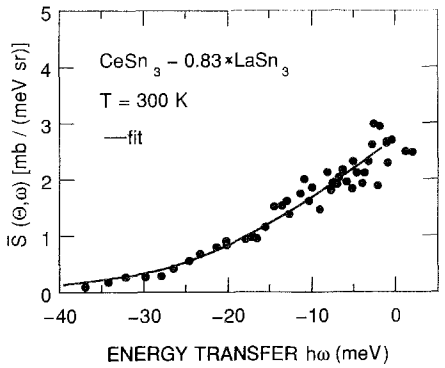

Fig. 35. Inelastic magnetic neutron spectrum of $CeSn_3$ obtained on D7 with $E_0 = 3.5$ meV at a scattering angle of 20° and at $T = 300$ K (phonons are already subtracted using an appropriate, scaled $LaSn_3$ spectrum). The solid line is a fit with one broad quasi-elastic line of Lorentzian shape. Corrections due to the Q-variation of the intensity are contained in the fitted curve, not in the data points (Holland-Moritz et al. 1982).

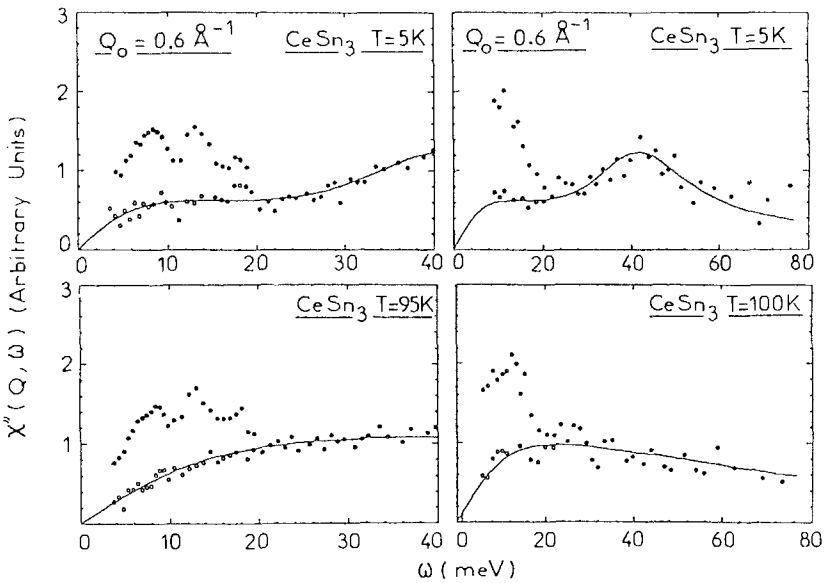

Fig. 36. The spectral response $\chi''(\omega)$ for $CeSn_3$ obtained on IN4 with $E_0 = 50$ meV (left) and 82 meV (right) at $T = 5$ and 95 K (100 K). The data have been corrected for intensity variation as a function of Q for fixed scattering angles with use of the Ce^{3+} form factor dependence. The upper points give the measured spectra and the lower points the data after phonon subtraction. The solid curves represent the best fit to the data allowing for a quasi-elastic and an inelastic line of Lorentzian shape (Murani 1983a, b).

Lorentzian shape. This was first discovered by Holland-Moritz et al. (1982). The corresponding spectrum of $CeSn_3$ at room temperature is shown in fig. 35 with the phonons already subtracted using an appropriate, scaled $LaSn_3$ spectrum. In the temperature range from 100 to 300 K, the range where cold neutrons can give valuable information, the line widths are nearly temperature independent with values around 25 meV. These values were confirmed by measurements with thermal neutrons by Murani (1983a, b), from which typical spectra at 5 and 100 K are shown in fig. 36. The phonon contribution was determined (a) by a comparison with spectra

of $LaSn_3$ and (b) by a careful analysis of the Q-dependence of the $CeSn_3$ spectra. The spectra are shown with the data points as measured (including phonon contributions) and with the phonons subtracted. Usually the inelastic neutron spectra are plotted as cross section or as scattering function $S(\omega)$ which is equal to (k_0/k_1) times the cross section with k_0 and k_1 being the incident and the final wave vector of the neutron, respectively. Murani (1983a, b), however, has plotted the $CeSn_3$ data in the form of the dynamical susceptibility $\chi''(\omega)$, which is proportional to $1-\exp(-\omega/T)$ times $S(\omega)$. This prefactor is ≈ 1 for $\omega/T \gg 1$; this means that, for energy transfers large compared to $k_B T$, $\chi''(\omega)$ and $S(\omega)$ look very much alike. On the other hand, for $\omega/T \ll 1$ the exponential in the prefactor can be expanded and we have $\chi''(\omega) \approx \omega/T$ times $S(\omega)$. For $T = 300$ K Murani (1983a, b) could fit the data with just one broad quasi-elastic line (not shown here). The solid line in fig. 36 for $T = 100$ K corresponds already to a fit with a quasi-elastic line ($\frac{1}{2}\Gamma = 23$ meV) and an inelastic line positioned at 40 meV and with half-width $\frac{1}{2}\Gamma \simeq 35$ meV. For decreasing temperatures the inelastic feature becomes more pronounced, as was also observed for $CePd_3$. At $T = 5$ K there is clearly *visible* a quasi-elastic contribution and an inelastic contribution. Murani (1983a, b) fitted the data at $T = 5$ K with a quasi-elastic line and an inelastic line at 40 meV, both having a line width of about 10–15 meV. The spectra of Capellmann et al. (1985), obtained with polarized neutrons at 30, 115, and 290 K, are presented in fig. 37. The authors have published only the experimental data with no fitting curve. Therefore we have tried to draw some theoretical curves through the data points in analogy to the curves in $CePd_3$ (fig. 27). Qualitative agreement for this interpretation of the D5 data with the results of the aforementioned experiments with unpolarized neutrons can be stated. At $T = 30$ K there is a quasi-elastic line with width around 15 meV and an inelastic line positioned at about 45 meV. For increasing temperatures both lines broaden. The spectral weight of the inelastic line is diminishing while the weight of the quasi-elastic line is increasing with temperature. At room temperature both lines have merged into one quasi-elastic line with a width of about 20–30 meV. In the interpretation of the D5 data, however, we do not agree with Capellmann et al. (1985) that there is *no* quasi-elastic intensity at low temperatures. The disagreement relies mainly on the interpretation and significance of the data point at $\omega = 0$. A similar conclusion has been drawn by Murani (1986).

The temperature dependence of the quasi-elastic line width of $CeSn_3$ is shown in fig. 38 up to room temperature. There is an increase of line width between $T = 5$ and 100 K by a factor of two. Beyond 100 K the line width stays nearly constant. Comparing fig. 26 ($CePd_3$) and fig. 38 ($CeSn_3$) it is evident that the temperature dependence and even the absolute values of the quasi-elastic line widths in these compounds are quite similar.

The Q-dependence of the inelastic magnetic scattering in $CeSn_3$ follows the free-ion Ce^{3+} form factor at all temperatures (Murani 1983a, b, Capellmann et al. 1985). Some minor deviations were only observed at $T = 5$ K by Murani.

The temperature dependence of the static susceptibility as deduced from the inelastic magnetic scattering, follows the 4f-part of the bulk susceptibility (smooth variation of $\chi(T)$ with broad maximum around 130 K, the upturn at low temperatures being neglected). The results of Murani (1983a, b) are shown in fig. 39 together with the bulk susceptibility as measured on a part of the sample used by Murani, and with the results of

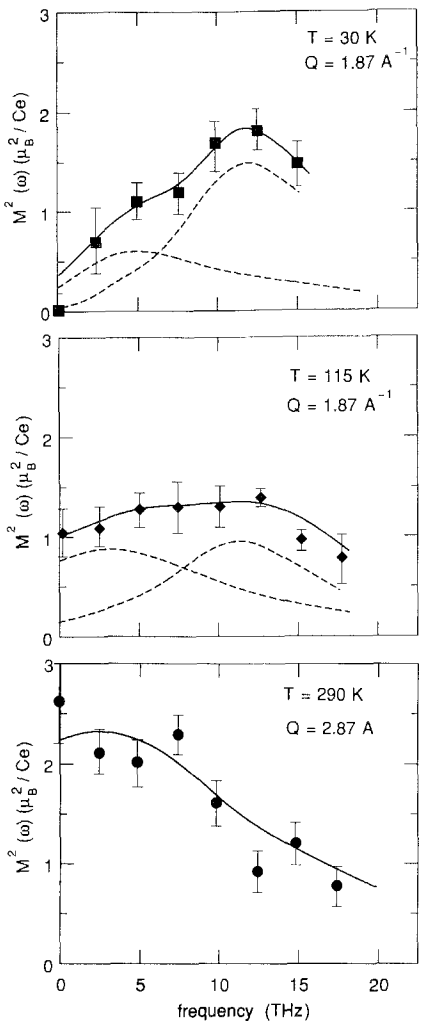

Fig. 37. Frequency dependence of the magnetic scattering of $CeSn_3$ at different temperatures obtained on D5 by Capellmann et al. (1985), data points only. The lines have been added by the present authors. Quasi-elastic and inelastic contributions are shown separately as dashed lines for $T = 30$ and 115 K. For $T = 290$ K there is only a quasi-elastic line. The energy resolution of the spectrometer is 10 THz = 41.3 meV (FWHM).

form factor measurements by Stassis et al. (1979a, b). The form factor of $CeSn_3$ shows a different behavior at low temperatures and at elevated temperatures. For temperatures of 40 K and above all data obtained on two different single crystals and for different directions of the applied magnetic field (parallel to [100] or [110]) give practically the same results. Part of the data are presented in fig. 40. The Q-dependence of the induced moment follows quite well the theoretical form factor of the Ce^{3+} free ion. The values of the static susceptibility as obtained from an extrapolation to the forward direction, however, are always lower than those of the bulk susceptibility measurements [even if compared to those measured on the crystals used by Stassis et al. (1979b)]. This discrepancy is interpreted by Stassis et al. (1979b) as an indication of an additional contribution to the bulk susceptibility of s or p electronic character, which is not detected in the neutron measurements because of the limited, finite Q-range.

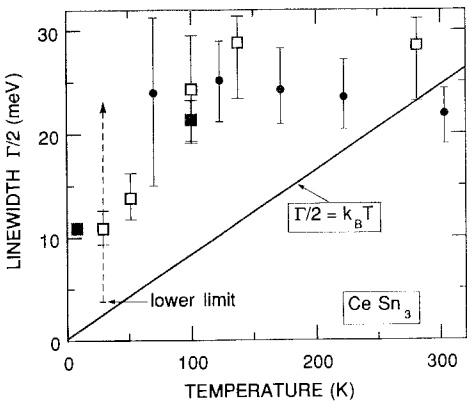

Fig. 38. Temperature dependence of quasi-elastic line width of $CeSn_3$. Solid circles: from Holland-Moritz et al. (1982); squares: from Murani (1983a, b), open and filled for $E_0 = 50$ and 82 meV, respectively.

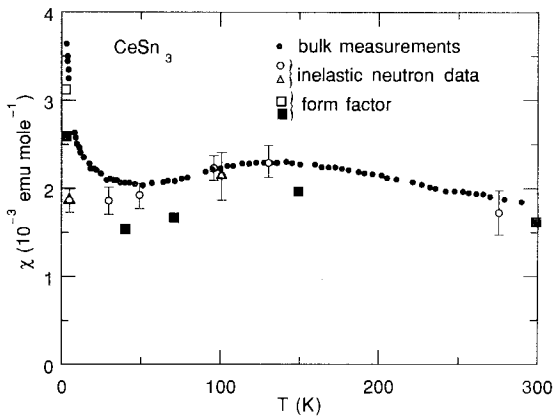

Fig. 39. Comparison of bulk susceptibility and the susceptibility of $CeSn_3$ as deduced from neutron data. Open circles and triangles: from inelastic neutron scattering by Murani (1983a, b) with $E_0 = 50$ and 82 meV, respectively. The neutron data have no absolute calibration, but are normalized to the bulk susceptibility at 130 K. Solid circles give the bulk susceptibility as measured on part of the sample used by Murani. Squares: from form factor measurements by Stassis et al. (1979b) on different single crystals, open and solid squares for 2 and 4 mm thick crystal, respectively.

At temperatures below 40 K large deviations were observed from a 4f form factor. The data obtained at 4.2 K for both crystals with the field applied in the [110] direction are plotted in fig. 41. The data do not follow a smooth curve, which is indicative of a large anisotropy in the spatial distribution of the induced magnetization. A good fit can be achieved if a Ce 5d contribution of e_g character is added coherently to the 4f component (triangles in fig. 41). The amount of the additional 5d contribution is different for the samples, which is also reflected in their different bulk susceptibility at low temperatures. Thus the occurrence of the additional 5d contribution is intimately connected with the upturn at low temperatures of the bulk susceptibility. This does not mean, however, that the upturn and the 5d contribution cannot be an intrinsic property of $CeSn_3$. Boucherle et al. (1990) investigated the form factor of stoichiometric and off-stoichiometric $CeSn_3$ at low temperatures. They

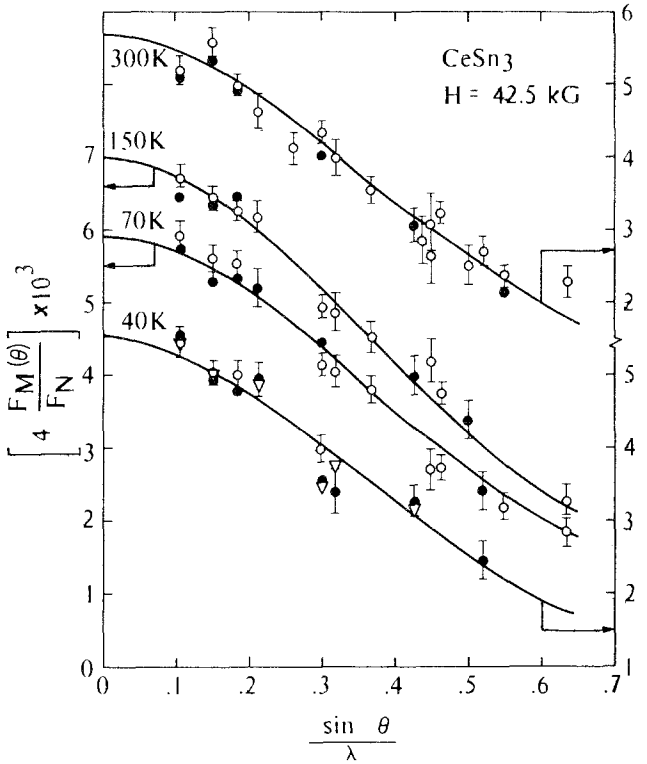

Fig. 40. Magnetic form factor data for $CeSn_3$ obtained with a 4 mm (open circles) and 2 mm (solid circles) thick crystal at 40, 70, 150, and 300 K with the field parallel to the [110] direction. The triangles are data obtained with the 2 mm thick crystal at 40 K with the field parallel to the [100] direction (Stassis et al. 1979b).

found that *only the stoichiometric* single crystal showed the additional 5d contribution, although with smaller amount (24%) than the two crystals investigated by Stassis et al. (1979b) (38% for the 4 mm and 49% for the 2 mm thick crystal). The 4f contribution was about the same for all investigated crystals. Above we said that the *inelastic* neutron scattering experiments did not reveal any significant deviation from a 4f form factor. This is not in contradiction with the form factor measurements, which show that the deviation is due to the additional 5d component. The Q-range of the inelastic data of Murani (1983a, b) is from 0.2 to 0.5 in units of $\sin(\theta)/\lambda$. The significant deviation in the form factor data of Stassis et al. (1979b), however, is seen for $\sin(\theta)/\lambda \leqslant 0.2$, outside the Q-range of Murani's data. Capellmann et al. (1985) measured the Q-dependence of the magnetic scattering with the energy window of the spectrometer set at $\omega = (0 \pm 5)$ THz. At high temperatures they state consistency with the 4f form factor, in agreement with all other experiments. At low temperatures the magnetic intensity was drastically reduced for this configuration, making any determination of the Q-dependence impossible.

In contrast to $CePd_3$, up until now, no phonon anomalies, such as unusual line shifts or line widths, have been observed in $CeSn_3$. Nevertheless, we present in fig. 42 the results of a thorough investigation of the dispersion curves of $CeSn_3$ and, for comparison, of $LaSn_3$ at room temperature by Pintschovius et al. (1980, 1983). The

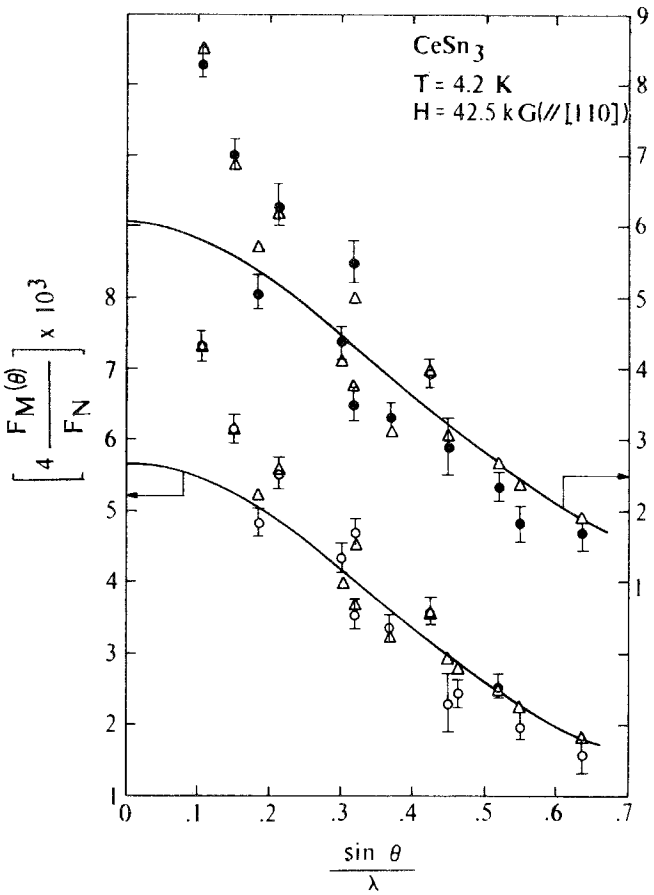

Fig. 41. Magnetic form factor data for $CeSn_3$ obtained with a 4 mm (open circles) and 2 mm (solid circles) thick crystal at 4.2 K with the field parallel to the [110] direction. The triangles are calculated values assuming the induced moment consists of a 4f and a 5d Ce component of e_g symmetry. The solid lines represent the 4f contribution (Stassis et al. 1979b).

solid lines represent a fit of the dispersion curves with a Born–von Kármán model including a breathing term usually taken as an indication of valence fluctuations. The influence, however, of the breathing term on the lattice dynamics is only moderate. Switching off the anyway weak breathing term does not change the fit significantly (dashed lines in fig. 42). Furthermore, the breathing mode constant (if not neglected) is nearly equal for both compounds, the valence fluctuating compound $CeSn_3$ and the integral valent, non-magnetic reference compound $LaSn_3$. Also a study of phonon frequency shifts induced by external pressure, gave no conclusive evidence for an unusual breathing deformability due to valence fluctuations (Blaschko et al. 1984).

The different behavior of $CeSn_3$ and $CePd_3$ concerning phonon anomalies is at first sight surprising. Both exhibit similar spin dynamics, as discussed here in detail.

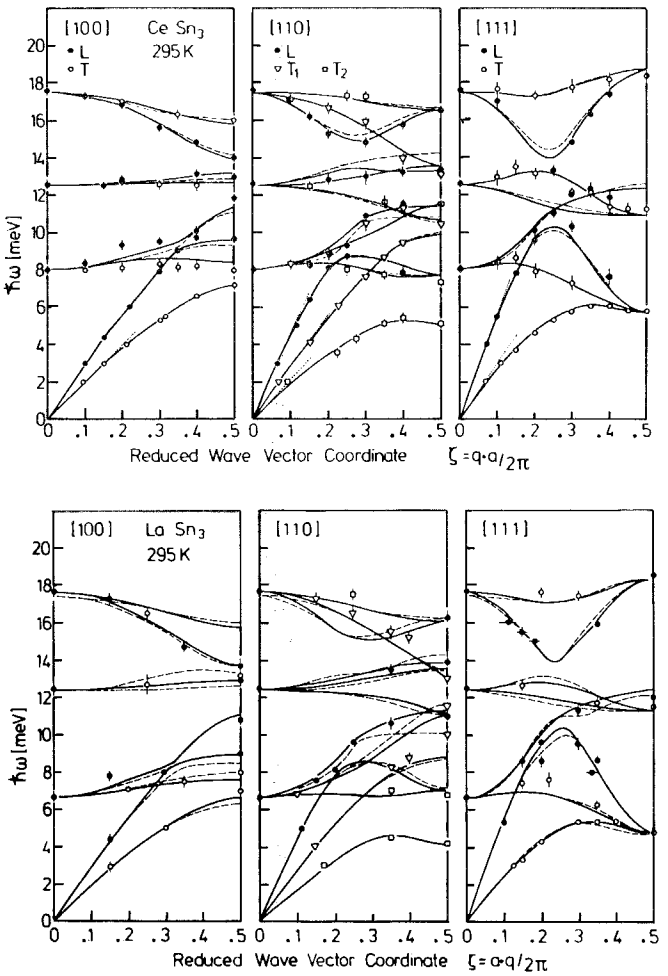

Fig. 42. Phonon dispersion curves for $CeSn_3$ (above) and $LaSn_3$ (below) at room temperature. Solid and dashed lines are the result of fits based on models which do (solid lines) and which do not (dashed lines) take into account the isotropic deformability of the rare earth ions (breathing mode). Dotted lines are the slopes of the dispersion curves of $CeSn_3$ calculated from ultrasonic data (Pintschovius et al. 1980).

The fast spin fluctuations at room temperature give a quasi-elastic line width of about 20–25 meV, corresponding to a spin-fluctuation temperature of $T_{SF} =$ 232–290 K (T_{SF} seems to be somewhat smaller for $CePd_3$ than for $CeSn_3$, compare figs. 26 and 38). T_{SF} is for both compounds of the same order as the Debye temperature ($\Theta_D = 205$ K for $CeSn_3$ and $\Theta_D = 292$ K for $CePd_3$ (Takke et al. 1981a)). There is a slight tendency that for $CeSn_3$ $\Theta_D \leqslant T_{SF}$ while for $CePd_3$ $\Theta_D \geqslant T_{SF}$. This, however, does not yet explain the absence and the presence of phonon anomalies in $CeSn_3$ and $CePd_3$, respectively. The only explanation up to date is the difference in valence (3.02 for $CeSn_3$ and $\geqslant 3.15$ for $CePd_3$). As mentioned before, charge fluctuations are

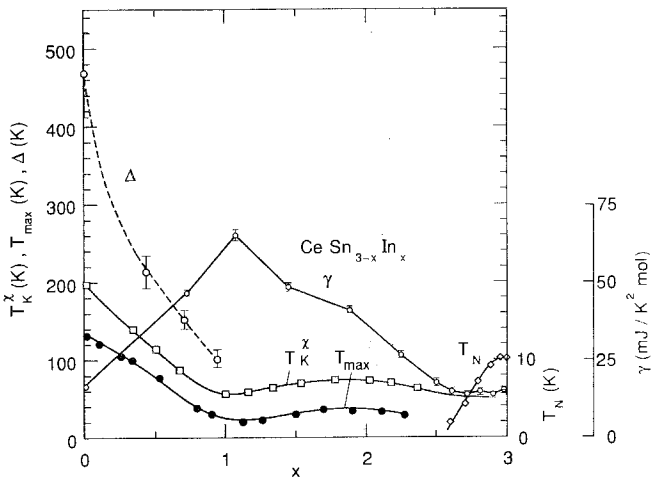

Fig. 43. Evolution of T_K^χ (Lawrence 1979) and T_{max} (Dijkman et al. 1980) from susceptibility measurements, of γ and T_N (Elenbaas et al. 1980) from specific-heat data with x for $CeSn_{3-x}In_x$. Also shown (big open circles): position Δ of hump as observed in inelastic neutron scattering by Murani (1987a, b).

always faster than the corresponding spin fluctuations and their ratio depends on the valence. In the case of Ce this means that the nearer the valence is to the integral value of 3, the larger is the ratio of charge to spin fluctuations. This would imply that the charge fluctuations are much faster in $CeSn_3$ than in $CePd_3$, and the lattice is unable to follow.

3.1.3. *$CeSn_{3-x}In_x$ and $CeIn_3$*

In connection with $CeSn_3$ we will also discuss the experiments performed on the intermetallic alloys $CeSn_{3-x}In_x$. Whereas $CeSn_3$ has weak VF properties, $CeIn_3$ behaves as a Kondo or HF compound. There have been extensive investigations of the magnetic properties (Lawrence 1979, Dijkman et al. 1980), heat capacity, and resistivity (Elenbaas et al. 1980). Some of the results of the different authors are collected in fig. 43, showing the evolution of a characteristic temperature T_K^χ [as defined by Lawrence (1979) through the scaling behavior of the effective moment $\mu^2 = T\chi/C$ by the condition $\mu^2(T_K^\chi) = 0.5$] and of T_{max} [the temperature of the maximum in $\chi(T)$]. Also shown is the evolution of the linear coefficient γ of the specific heat and the x-dependence of the antiferromagnetic ordering temperature T_N for the In-rich side. Three distinct concentration regimes seem to exist:

(1) $(0 \leqslant x \leqslant 1)$: the characteristic temperature T_K^χ and T_{max} decrease almost linearly with increasing x, accompanied by a linear increase of γ,

(2) $(1 \leqslant x \leqslant 2.6)$: γ peaks around $x \approx 1$; then there is a steady decrease of γ with x and a nearly constant characteristic temperature (with minor variations due to alloying effects, as also found in $LaSn_{3-x}In_x$); in the first two regimes no long-range magnetic ordering has been found,

(3) ($2.6 \leqslant x \leqslant 3$): γ and T_K^χ stay constant with x; long-range antiferromagnetic order appears, with T_N steeply increasing with x; $T_N = 10$ K for $CeIn_3$.

Neutron scattering investigations have been performed mainly in the first regime and for $CeIn_3$. We discuss first the results of inelastic magnetic scattering. Murani (1987a, b) has shown that the position Δ of the hump in the low-temperature spectra moves towards smaller values for increasing x (up to $x = 1$), in line with the decrease of T_K^χ and T_{max} (large, open circles in fig. 43). Let us remind that the hump in $CeSn_3$ is at an energy around 45 meV, corresponding to 522 K. This is 3.7 times T_{max} or 2.6 times T_K^χ. The hump position decreases to $\Delta = (18 \pm 2)$, (13 ± 1), and (9 ± 1) meV for $x = 0.5$, 0.75, and 1, respectively (Murani 1987a, b). This corresponds to roughly three times T_{max}. Hence there seems to be a scaling relation between the position of the hump and T_{max}, the temperature where $\chi(T)$ has a maximum. In addition to the reduction of the hump position Murani (1987a, b) claims that there is also a reduction of quasi-elastic intensity for increasing x. An experiment performed on a $CeSn_2In$ *single crystal* at $T = 5$ K by Murani et al. (1990a) reveals only an inelastic line of Lorentzian shape with $\Delta = (8 \pm 1)$ meV and $\frac{1}{2}\Gamma = (7 \pm 1)$ meV and *no* quasi-elastic scattering. The value of Δ as deduced from the single crystal experiment, is consistent within error with the value given above for the polycrystalline sample for $x = 1$. The magnetic response of the single crystal was measured at different $\boldsymbol{Q}$ values. The shape of the magnetic response seemed to be independent of $\boldsymbol{Q}$. There was, however, a slight $\boldsymbol{Q}$ dependence of the intensities, indicating the possible presence of short-range spin correlations. Temperature-dependent measurements on all samples showed the characteristic evolution of the inelastic features into a broad quasi-elastic response at elevated temperatures as usually observed for VF compounds.

Murani (1987b) also observed a change from inelastic to quasi-elastic scattering already of the *low-temperature* response when going from concentrated $CeSn_{2.25}In_{0.75}$ to dilute $Ce_{1-y}La_ySn_{2.25}In_{0.75}$ with $y = 0.2$ and 0.4. Whether this change of line shape is caused by the loss of periodicity in the dilute Ce lattice or by a reduction of the Kondo temperature for Ce ions surrounded by La ions (connected with a shift of intensity towards lower energy transfers) is not yet clear.

Preliminary inelastic neutron data for the $^2F_{5/2} \rightarrow {}^2F_{7/2}$ spin–orbit transition in $CeSn_{3-x}In_x$, obtained with high incident-neutron energies of 600 meV on the HET spectrometer of the ISIS spallation source by Murani et al. (1990b), are shown in fig. 44. The energy of the spin–orbit transition for a free Ce ion is 280 meV (see Osborn et al. 1991). An inelastic transition with about this splitting is observed for $x = 1$ to 3 ($CeSn_2In$ up to $CeIn_3$). For $x = 0.5$ there is still an inelastic transition visible, although already considerably broadened and shifted to higher energies (315 meV). In addition, a tail on the low-energy side is developing for increasing Sn concentration. This is reminiscent of the broad magnetic scattering within the $J = \frac{5}{2}$ ground-state multiplet. For $CeSn_3$ the tail is the only observed scattering intensity. No inelastic line seems visible. It is not clear whether the spin–orbit transition is totally absent in $CeSn_3$ or whether it is present but even further broadened or shifted and is thus lost in the statistical scatter of the data.

Form factor measurements have been performed on $CeSn_2In$ (Benoit et al. 1985) and $CeIn_3$ (Boucherle et al. 1983, Boucherle and Schweizer 1985). In contrast to

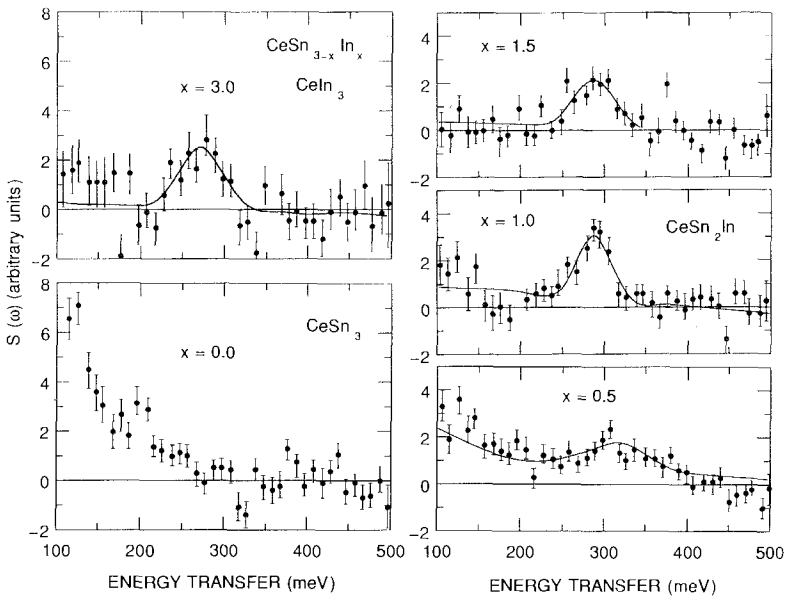

Fig. 44. Spin–orbit transition in $CeSn_{3-x}In_x$ measured at $T = 20$ K with $E_0 = 600$ meV on the HET spectrometer (redrawn from Murani et al. 1990b).

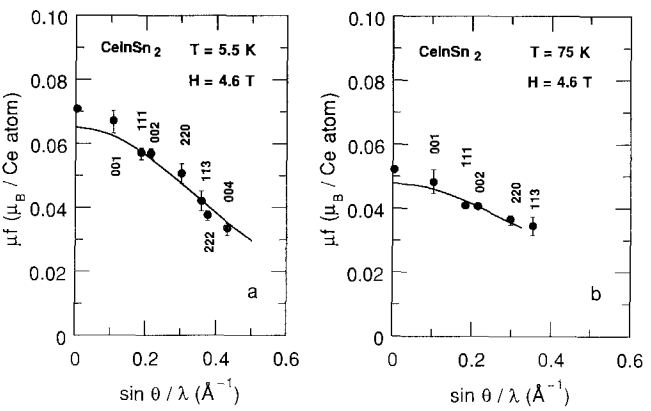

Fig. 45. Magnetic form factor of $CeSn_2In$ at $T = 5.5$ and 75 K. Solid line is 4f form factor for free Ce ion. Magnetic susceptibility measurement data on the same sample have been added at $\sin\theta/\lambda = 0$. Numbers indicate Bragg indices (Benoit et al. 1985).

$CeSn_3$ there is no *significant* 5d-like contribution at low temperatures for both compounds. Data taken at 5.5 and 75 K on a $CeSn_2In$ single crystal can be fitted essentially with a 4f form factor (solid line in fig. 45). There is a slight deviation from this line of the data point for the (001) reflection (within error bars for $T = 75$ K, just outside error bars for $T = 5.5$ K). This corresponds to a 5d contribution of at most 10% to the total magnetization density. There is also only a small upturn in the susceptibility at low temperatures measured on the same sample. No anisotropies of the form factor due to crystal field effects have been reported. The same isotropic behavior was found for $CeSn_3$ and $CePd_3$, indicating that all six levels of the $^2F_{5/2}$

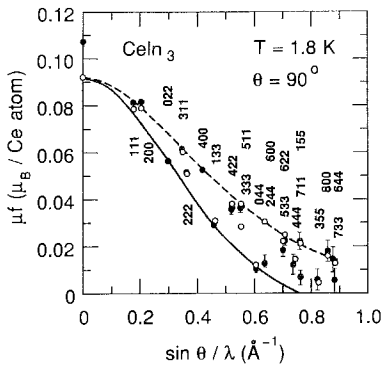

Fig. 46. Magnetic form factor for $CeIn_3$ at $T = 1.8$ K in the magnetically ordered phase. Solid circles: data points, open circles: calculated with Γ_7 ground-state wave function. Dashed and solid line: upper and lower boundary for anisotropy. Numbers indicate Bragg indices (Boucherle and Schweizer 1985).

multiplet are involved in the formation of the ground-state wave function. This is not the case for $CeIn_3$. Although $CeIn_3$ cannot be considered as a "normal" rare earth compound, it is definitely different from $CeSn_3$. There are signatures in $CeIn_3$ that its ground state is split by the cubic crystal field into a low-lying Γ_7 and an excited Γ_8 level around 10–15 meV. The form factor measured in the magnetically ordered state at 1.8 K is strongly anisotropic (fig. 46). All ($h00$) reflections lie above and all ($0kk$) reflections lie below the average 4f form factor. This is what one expects from a Γ_7 crystal field ground state (the opposite anisotropy is expected for a Γ_8 ground state or isotropic behavior for the full $J = \frac{5}{2}$ multiplet). This interpretation is strongly supported by the fact that the magnetic entropy per mol Ce is close to $R \ln 2$ at the ordering temperature (Elenbaas et al. 1980), as expected for a Γ_7 (doublet), in contrast to $R \ln 4$ for Γ_8 (quartet) or $R \ln 6$ for the full multiplet. From the slight discrepancy between the calculated and measured form factor for the two low-Q reflections (111) and (200), Boucherle et al. (1983) estimate an additional 5d contribution of 18% to the total magnetization density in $CeIn_3$. No error is quoted for this estimate, but the error must be rather large, since it relies on discrepancies for reflections where the 5d contribution is already very weak. No data are given for the more decisive reflections (001) and (011). These reflections are rather weak and thus difficult to be measured, because the nuclear scattering lengths of Ce and In are nearly equal. We are also not aware of any form factor measurements at elevated temperatures, which could give information whether the 5d contribution is still present or not.

The magnetic structure of $CeIn_3$ has been determined by Lawrence and Shapiro (1980) and by Benoit et al. (1980). $CeIn_3$ is a simple antiferromagnet with propagation vector $(\frac{1}{2}, \frac{1}{2}, \frac{1}{2})$, i.e. the Ce moments are aligned in opposite directions in adjacent (111) planes. The spin directions within the planes could not be determined from the experiments. Lawrence and Shapiro (1980) report for the Ce moments a value of $(0.65 \pm 0.1)\mu_B$ at $T = 5$ K, Benoit et al. (1980) a value of $(0.48 \pm 0.08)\mu_B$ at $T = 3$ K. Both values are somewhat smaller than the expected $0.71\mu_B$ for a Γ_7 state. Lawrence and Shapiro (1980) also investigated the critical scattering around $T_N = 10.2$ K. They observed a strong suppression of critical fluctuations and nearly mean-field behavior.

Finally, we discuss the inelastic magnetic response of $CeIn_3$. The $\Gamma_7 \rightarrow \Gamma_8$ crystal

field transition was measured by Lawrence and Shapiro (1980) as function of temperature. They observed a rather broad inelastic line at 15 meV with a width of about 10 meV at low temperatures (5 K, 15 K), shifting to 11–12 meV at elevated temperatures (50 K, 160 K). The width of the crystal field transition was originally interpreted by Lawrence and Shapiro (1980) as a measure of a spin-fluctuation energy $k_B T_{SF}$ with $T_{SF} \simeq 100$ K. This value, however, seems to be much too high for $CeIn_3$. The quasi-elastic scattering, which could not be resolved in the experiments by Lawrence and Shapiro (1980), was measured by Lassailly et al. (1985) with better energy resolution at $T = 60$, 140, and 240 K. The width and the intensity of the quasi-elastic line are strongly Q-dependent and temperature dependent. This behavior suggests that spin–spin correlations are the main origin for the spin dynamics and that line broadening due to hybridization effects is of minor importance in $CeIn_3$. The Q-dependence of the intensity is strongest for $T = 60$ K; it is still observed at 140 and 240 K, although much weaker for increasing temperatures. The Q-dependence of the line width is indicative of spin diffusion processes. A typical value for the line width in the region around 1–2 $Å^{-1}$ is 1 meV at $T = 60$ K and 2–3 meV at $T = 140$, 240 K. The value of 1 meV at 60 K is of the same order as $k_B T_N$ (10.2 K $\simeq$ 0.9 meV). Unfortunately there are no data for the quasi-elastic scattering below 60 K, which might allow to extract a residual width due to Kondo broadening in comparison to spin–spin interactions. From the data of Lassailly et al. (1985) we can estimate an upper limit for the Kondo temperature of $CeIn_3$ of $T_K \leqslant 10$ K. The increase of the line width with temperature can be understood from the increasing contribution from the Γ_8 excited state to the quasi-elastic scattering. The quasi-elastic scattering within the Γ_8 level must be considerably broader than that within the Γ_7 level. This is in line with the observation of the rather large line width of the Γ_7–Γ_8 crystal field transition. The quasi-elastic scattering is always separated from the inelastic scattering. Lassailly et al. (1985) report a value of 10 meV for the energy of the crystal field transition, in agreement with the findings of Lawrence and Shapiro (1980). In addition, Lassailly et al. (1985) claim that they have observed a *second* inelastic magnetic line around 20–25 meV. We feel, however, that this line is not of magnetic origin but most likely due to an improper subtraction of phonon scattering. It should be noted that In is a strong neutron absorber, which makes all experiments with In-containing samples rather difficult.

3.1.4. *$CeBe_{13}$*

While $CePd_3$ and $CeSn_3$ have been studied very thoroughly over the past 15 years, there are only few data available for $CeBe_{13}$, although it exhibits similar magnetic properties. $CeBe_{13}$ was classified as VF compound quite early with an (over-estimated) valence of 3.2–3.3 from lattice parameter systematics (Borsa and Olcese 1973, Krill et al. 1980). New estimates of the valence from L_{III} X-ray absorption give 3.04 (Röhler 1987), a value much more close to the integral valence of +3, similar to $CeSn_3$. The crystal structure is of cubic $NaZn_{13}$-type with the Ce ions forming a simple cubic lattice. The shortest Ce–Ce distance is 5.1 Å. There are no Ce–Ce near-neighbors since Be ions form cages around the Ce ions. The structure may be viewed as Ce ions embedded in Be metal.

The susceptibility of $CeBe_{13}$ is rather flat at low temperatures with a very broad maximum at $T_{max} = 140$ K and a paramagnetic Curie temperature $\theta_p = 200$ K (Kappler and Meyer 1979). Inelastic neutron scattering experiments have been performed by Holland-Moritz et al. (1982) on polycrystalline samples with cold neutrons (D7, $E_0 = 3.5$ meV). The spectra could be fitted with just one broad quasi-elastic line. The line width is 17 meV at room temperature and *increases* with decreasing temperatures, reaching a value of about 28 meV at 100 K. For lower temperatures it could only be stated that the magnetic response must stay broad and/or develops inclastic features. Unfortunately no inelastic neutron data are available at low temperatures with sufficiently high incident energies. There are, however, NMR data reported as function of temperature from 300 K down to 4 K (Panissod et al. 1988). NMR basically probes the imaginary part of the dynamic susceptibility, $\chi''(\omega)/\omega$, as does neutron scattering. But while NMR probes a Q-average of this quantity at low energy ($\omega \Leftrightarrow \mu$eV, nuclear Larmor frequency), neutron scattering probes it for different Q-values and in a much higher energy range (0.1 to 100 meV, depending on the spectrometer). If an electronic relaxation rate (corresponding to a quasi-elastic line width) is deduced from NMR-T_1 measurements, usually two important assumptions are made:

- there are no correlations between different spins, i.e. the magnetic response is independent of Q, and
- the magnetic response is of purely relaxational form (quasi-elastic spectrum of Lorentzian shape).

For $CeBe_{13}$ the NMR data yield a line width around 70 meV for temperatures between 4 and 50 K. It then decreases with increasing temperature to 55 meV (100 K), 35 meV (200 K), and 25 meV (300 K). This is the same behavior as observed for the line widths deduced from neutron scattering, but with larger absolute values for the NMR-deduced line widths. The discrepancy between the values for both methods increases for decreasing temperatures. It is rather unlikely that correlation effects are the origin of the discrepancies. It is more likely that the shape of $\chi''(\omega)$ changes with temperature. We therefore suspect that the magnetic response of $CeBe_{13}$ changes from a more or less quasi-elastic spectrum at high temperatures to a spectrum with quasi-elastic and inelastic features at low temperatures, as it was observed in $CePd_3$ and $CeSn_3$.

3.1.5. *(α, β, γ)-Ce and its alloys with Sc, Y, La, Th*

Ce metal in its different phases exhibits already the wide span of properties of the Ce-based compounds, ranging from well-localized moments via Kondo lattice up to heavily valence fluctuating and non-magnetic. Vice versa, the behavior of Ce compounds has been classified as β-, γ-, and α-like. Simple measurements, however, like the temperature dependence of the magnetic response of a certain phase, are hampered by the peculiarities of the phase diagram. At ambient pressure and room temperature it is possible to produce Ce samples in the β-phase (dhcp, $a_0 = 3.68$ Å, $c_0 = 11.92$ Å) and in the γ-phase (fcc, $a_0 = 5.16$ Å). At decreasing temperatures both transform into the α-phase (fcc, $a_0 = 4.85$ Å). At room temperature γ-Ce transforms upon application of a pressure of about 8 kbar into α-Ce. For more details of the

phase diagram and the description of even more phases we refer the reader to the review articles by Koskenmaki and Gschneidner (1978) and by Gschneidner and Daane (1988). To overcome the limitations of the phase diagram and allow, e.g., temperature-dependent measurements over a wide range of temperatures, a simple trick has been applied: alloying. For instance, alloying with Y *stabilizes* the β-phase, while alloying with Th *prevents* the formation of the β-phase. (Ce,Th)-alloys therefore show only the $\gamma \rightarrow \alpha$ phase transition. Further addition of La to (Ce,Th) then even allows some "fine tuning" of the $\gamma \rightarrow \alpha$ transition and eventually the suppression of the transition. Alloying, however, always introduces disorder, different local environments, etc. These effects often complicate the interpretation of work on alloys compared to experiments on chemically ordered intermetallic compounds. We therefore discuss only briefly neutron investigations performed on Ce metal and its alloys with Sc, Y, La, and Th in its different phases.

3.1.5.1. *β-phase.* In β-Ce the 4f electron can be considered as well localized. Rapid quenching to low temperatures allows one to deduce that β-Ce orders antiferromagnetically around 12–13 K (Burghardt et al. 1976). For $Ce_{1-x}Y_x$ the ordering temperature decreases with x (Panousis and Gschneidner 1972). On a polycrystalline sample of $Ce_{0.75}Y_{0.25}$ neutron diffraction experiments by Gibbons et al. (1987) yield an antiferromagnetic ordering below $T_N = 7$ K with a propagation vector of $0.5\tau_{100}$. Inelastic neutron scattering by Gibbons et al. (1989) on the same sample shows narrow quasi-elastic scattering (width is 1.3 meV at $T = 20$ K) and well-defined crystal field transitions at 8 and 16.5 meV. Gibbons et al. (1989) analyze this in terms of a Γ_7 ground state and an excited Γ_8 state at 16.5 meV (197 K) for the cubic sites and a $|\pm\frac{1}{2}\rangle$ ground state and a $|\pm\frac{3}{2}\rangle$ excited state at 8 meV (97 K) for the hexagonal sites. This model explains why the ordered moments lie in the basal plane (as found in the diffraction experiment), but predicts somewhat larger moments ($1.29\mu_B$ and $0.71\mu_B$) than found experimentally ($0.91\mu_B$ and $0.38\mu_B$ for the hexagonal and cubic sites, respectively).

3.1.5.2. *γ-phase.* The lattice and spin dynamics of a γ-Ce single crystal have been studied at room temperature by Stassis et al. (1979c). When compared to the phonon dispersion curves of Th, a relative phonon softening of some branches had been stated. Yet is was not clear whether this observation could be uniquely related to a valence-fluctuation effect. The magnetic response could be fitted with just one broad quasi-elastic line of Lorentzian shape and a width of 16 meV. Rainford et al. (1977) reported a width of 10 meV deduced from an experiment on a polycrystalline sample. Form factor measurements by Stassis et al. (1978) revealed at room temperature a 4f free-ion Ce^{3+} form factor.

For obvious reasons there are no measurements of γ-Ce at low temperatures. It is, however, believed that the residual quasi-elastic line width would only be a few meV and an inelastic crystal field transition would be observable. This can be inferred from the results of inelastic neutron scattering experiments on $Ce_{0.9-x}La_xTh_{0.1}$ (for $x = 0.14$, 0.20, 0.40) by Grier et al. (1980, 1981). The addition of La suppresses the $\gamma \rightarrow \alpha$ transition of $Ce_{0.9}Th_{0.1}$. The spectra below 110 K were

fitted with a quasi-elastic and an inelastic line of the same width. The inelastic line was interpreted as a $\Gamma_7 \rightarrow \Gamma_8$ crystal field transition with an energy around 12, 14, and 15 meV and a width around 5, 6, and 8 meV for $x = 0.40$, 0.20, and 0.14, respectively. Position and width are nearly temperature independent for all x for temperatures between 40 and 110 K. Below 40 K a moderate increase of position and line width is observed for the samples with $x = 0.40$ and 0.20, while a drastic increase is observed for the 0.14 sample ($\Delta = 21$ meV, width = 12 meV at 5 K). The different behavior of the 0.14 sample is connected to the still present $\gamma \rightarrow \alpha$ transition (although of second order instead of first order as in Ce-metal). Grier et al. (1981), however, indicate that the increase in crystal field splitting cannot be understood quantitatively on these grounds.

3.1.5.3. $\gamma \rightarrow \alpha$ *transition.* $Ce_{0.74}Th_{0.26}$ undergoes a first-order valence transition at $T = 150$ K. For this sample detailed neutron investigations have been performed. Inelastic neutron scattering experiments are reported by Shapiro et al. (1977) between 100 and 250 K using thermal neutrons and by Loong et al. (1987) between 10 and 200 K using epithermal neutrons with incident energies up to 1.2 eV. In both phases (α below, γ above 150 K) the magnetic response consists of a broad quasi-elastic spectrum with no indication of inelastic crystal field transitions. In both phases the line width increases with *decreasing* temperatures. It is typically 20 meV in the γ-phase and around 100 meV in the α-phase. At $T = 10$ K the magnetic response of the α-phase is somewhat better described by a broad *inelastic* line at $\Delta = 140$ meV and a width of 90 meV. This is reminiscent of the hump observed at low temperatures in the excitation spectra of $CePd_3$ and $CeSn_3$.

A form factor measurement by Moon and Koehler (1979) on $Ce_{0.74}Th_{0.26}$ revealed a 4f free-ion Ce^{3+} form factor in the γ-phase at $T = 180$ K and deviations from the 4f form factor at the two low-Q reflections (111) and (200) in the α-phase at $T =$ 50 K. The results at 50 K suggest that the induced moment in the α-phase has two components, one 4f-like and the other 5d-like, as also found for $CePd_3$ and $CeSn_3$.

3.1.5.4. α*-phase.* The determination of the magnetic response in α-Ce has been a challenge for neutron scatterers for many years. There is no final answer yet, but there is agreement that there *is* magnetic scattering intensity in the α-phase of Ce and that the magnetic response is very broad in energy, presumably extending up to the eV region. Fillion et al. (1985) report an inelastic scattering experiment at $T =$ 8 K with polarized neutrons and polarization analysis (D5, ILL). They obtained a weak magnetic intensity for all data points between 0 and 180 meV, followed by a steplike increase of magnetic intensity for three data points at 200, 230, and 250 meV (the upper limit of the experiment). The steplike increase of intensity between 180 and 200 meV is somewhat surprising in view of the coarse energy resolution of 150 meV (FWHM) in this region, which should produce a much smoother variation of intensity with energy transfer (even if the underlying scattering law would be a step function). Fillion et al. (1985) conclude from their data that the magnetic response in α-Ce is essentially inelastic and rule out a purely quasi-elastic response (of width around 200 meV). This is consistent with the observation of Loong et al. (1987) for

α-$Ce_{0.74}Th_{0.26}$ at $T = 10$ K. Furthermore, the tail of the inelastic magnetic response in α-$Ce_{0.74}Th_{0.26}$ seems to extend well beyond 500 meV. A similar conclusion concerning the extent of the response to high energy transfers was drawn by Murani et al. (1990b) from the results of an experiment with $E_0 = 2$ eV on a $Ce_{0.93}Sc_{0.07}$ sample. Exploiting the hysteretic nature of the $\alpha \leftrightarrow \gamma$ transition Murani et al. (1990b) managed to measure the magnetic response of the same sample in the α- and in the γ-phase at the same temperature (125 K). A difference spectrum reveals the narrow ($\leqslant 50$ meV) response of the γ-phase and a very broad response of the α-phase, again extending to energy transfers far beyond 500 meV.

3.2. *Cerium-based heavy-fermion systems*

It seems that there are no "normal" Ce compounds. As a consequence we should discuss in this section all neutron scattering experiments on all those Ce compounds which are not mentioned in the previous section. Yet, this is an impossible task. Therefore, the list of Ce-based HF compounds dealt with in this section, and subdivided into superconducting, non-ordering, antiferromagnetic-ordering and ferromagnetic-ordering compounds, is far from being complete. As already mentioned in the beginning of section 3.1, we have taken the degeneracy of the ground state as criterion whether a Ce compound is a VF ($N = 6$) or a HF ($N = 2$ or 4) system. Note: this is not a common definition. Usually the HF systems have much lower Kondo temperatures than the VF systems. Because of this small Kondo energy the RKKY interaction no longer can be ignored. Hence, in HF systems one has to consider also spin–spin interactions, which in VF systems practically are absent (the 5d–4f coupling seen in the form factor of some VF compounds takes place *on site* on each Ce ion). The spin–spin interactions in HF systems produce either long-range magnetic order or short-range spin correlations. In both cases the magnetic response is drastically modified at low temperatures compared to the spectrum of non-interacting Kondo spins. Spin correlations can best be identified by $\boldsymbol{Q}$-dependent measurements on single crystals. Magnetic order is easily seen in neutron diffraction on polycrystalline samples if the ordered moments are sufficiently large ($\geqslant 0.2\mu_B$). Very small ordered moments ($10^{-2}\mu_B$) can only be detected by diffraction from single crystals. A *non-interacting* $S = \frac{1}{2}$ Kondo spin ($N = 2$) shows a quasi-elastic magnetic response of Lorentzian shape (eq. 25) down to $T = 0$. By setting the residual width $\frac{1}{2}\Gamma_0$ equal to $k_B T_K^N$ we define a neutron-deduced Kondo temperature T_K^N, which should agree with the (not very precisely) defined transition of the static susceptibility from a Curie–Weiss law to Pauli behavior. In more concentrated systems and/or for $S > \frac{1}{2}$ ($N \geqslant 4$) the connection between magnetic response and Kondo temperature is much more complicated (see theoretical part at beginning of section 3). Inelastic features are often seen in the low-temperature magnetic response. They can be due to (in increasing order of energy for a typical Ce compound):

- magnons in a magnetically ordered phase or pseudo-magnons due to spin correlations above the ordering temperature or in nearly ordering systems,
- Kondo or VF response for $N \geqslant 4$,
- crystal field transitions,
- spin–orbit transitions.

However, it is often very difficult to identify the individual sources for inelasticity (compare, e.g., the discussion of results for $CeRu_2Si_2$ from single crystal and polycrystal data).

3.2.1. *Superconducting ($CeCu_2Si_2$)*

So far the only known cerium HF superconducting compound is $CeCu_2Si_2$ (Steglich et al. 1979a). The superconducting properties of Ce- and U-based HF compounds are discussed in detail by Grewe and Steglich (1991). The appearance of superconductivity depends strongly on stoichiometry (copper-deficient samples are *not* superconducting while copper-excess samples have $T_c \simeq 0.5$ to 0.7 K) and, for the nominally stoichiometric samples, on sample preparation, like, e.g., on annealing temperature, cooling rate, etc. $CeCu_2Si_2$ has the tetragonal $ThCr_2Si_2$ structure with $a = 4.09$ Å and $c = 9.91$ Å. For this symmetry we expect a CF splitting of the $^2F_{5/2}$ Ce^{3+} ground state into three doublets. An early inelastic neutron scattering investigation on a nominally stoichiometric polycrystalline sample by Horn et al. (1981a) revealed a CF level scheme with a doublet at 12 meV as first excited state and a second doublet at 31 meV. This level scheme was questioned since specific heat, magnetic susceptibility and resistivity data of $CeCu_2Si_2$ seem to favor a quasi-quartet located around 32 meV (Steglich 1985). The latter scheme is supported by recent neutron investigations by Goremychkin and Osborn (1991b) (quasi-quartet at 30 meV), while neutron investigations by Holland-Moritz et al. (1989a) on copper-deficient $CeCu_{1.8}Si_2$ (0–21–33 meV) and on copper-excess $CeCu_{2.2}Si_2$ (0–17–33 meV) seemed to confirm the first proposed scheme. Even experiments with polarized neutrons (Stassis et al. 1986, Johnson et al. 1985) were not able to locate unambiguously the position of the first excited state. In any case, all data agree on the fact that the ground state of $CeCu_2Si_2$ is a doublet, well separated (at least 12 meV) from the excited states, with a total CF splitting of about 31 meV. No long-range magnetic order could be detected down to 30 mK by neutron diffraction on a polycrystalline sample (Horn et al. 1981a). Also no significant spatial spin correlations were found in a polarized neutron experiment by Johnson et al. (1985) at 70 mK. The magnetic response, integrated in this experiment over an energy window of ± 20 meV, is essentially Q-independent, showing the local character of the underlying magnetism. From form factor measurements on a (Cu-rich) $CeCu_2Si_2$ single crystal by Stassis et al. (1985) it was concluded that the induced magnetization at 4.2 K is predominantly of 4f electronic character. No indication of a 5d contribution was found in $CeCu_2Si_2$ in contrast to the situation in VF $CeSn_3$ at low temperatures.

The temperature dependence of the quasi-elastic line width of $CeCu_2Si_2$ was investigated by Horn et al. (1981a) and Stassis et al. (1986) between 5 K and room temperature. The results are shown in fig. 47. The line width follows roughly a $T^{1/2}$ law with an extrapolated residual width of about 1 meV for $T \to 0$. Data on Cu-deficient and Cu-excess samples for decreasing temperatures show a change from the quasi-elastic line shape ($T = 1.5$ K: $\frac{1}{2}\Gamma \simeq 0.8$ meV) to an inelastic line shape below 1 K (Holland-Moritz et al. 1989a). From the low-temperature data a Kondo temperature of about 8 K can be estimated. A similar result for T_K was obtained from the

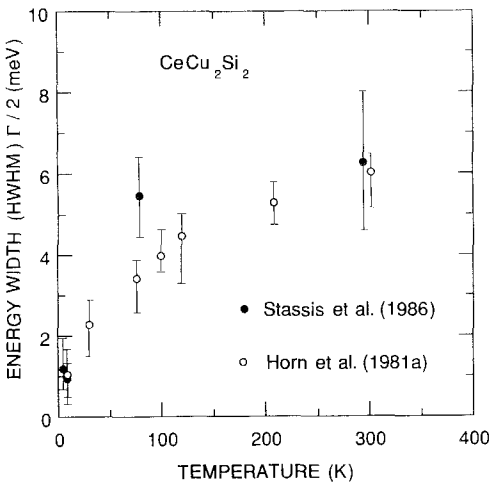

Fig. 47. Temperature dependence of the quasi-elastic line width of $CeCu_2Si_2$. Open circles from Horn et al. (1981a), solid circles from Stassis et al. (1986).

analysis of a polarized neutron scattering experiment by Uemura et al. (1986) at $T = 2.5$ K performed at different external magnetic fields between 0 and 2 T.

Finally, we want to note that when passing the superconducting transition temperature no change in the inelastic magnetic response was observed (Holland-Moritz et al. 1989a). Also the search for anomalies in the phonon density-of-states did not reveal any indications for a strong coupling between the phonons and the Ce 4f electrons (Gompf et al. 1987). The phonon spectra of both $CeCu_2Si_2$ and its non-superconducting reference compound $LaCu_2Si_2$ turned out to be similar.

In view of the detailed results obtained on a single crystal of $CeCu_6$ (existence of spin correlations, discrimination between single-site quasi-elastic and intersite inelastic scattering; see section 3.2.2) it would be of great importance to perform similar experiments on $CeCu_2Si_2$ single crystals. This may then shed some light on the origin of the *inelastic* line observed in $CeCu_2Si_2$ at low temperatures yielding an unphysical degeneracy of six when fitted with the Kuramoto–Müller-Hartmann formula (eq. 28) (Holland-Moritz et al. 1989a). For a doublet ground state with $S_{\text{eff}} = \frac{1}{2}$ a *quasi-elastic* line shape is expected in the Kondo limit down to the lowest temperature. Inelasticity in this case requires the existence of spin correlations, as in $CeCu_6$ and $CeRu_2Si_2$, or of a gap.

3.2.2. *Non-ordering (CeAl$_3$, CeCu$_6$, CeRu$_2$Si$_2$, CeNi$_2$Ge$_2$, CePt$_2$Si$_2$)*

For one of these compounds ($CeAl_3$) magnetic ordering with very small ordered moments had been proposed, but the bulk of the present experimental evidence is against this suggestion.

$CeAl_3$ crystallizes in the hexagonal Ni_3Sn structure with $a = 6.545$ Å and $c = 4.609$ Å (Taylor 1971). For this symmetry the Ce^{3+} ground state splits into three doublets, with the pure wave functions $|\pm\frac{1}{2}\rangle$, $|\pm\frac{3}{2}\rangle$, and $|\pm\frac{5}{2}\rangle$. There are only two inelastic transitions (between $|\pm\frac{1}{2}\rangle$ and $|\pm\frac{3}{2}\rangle$ and between $|\pm\frac{3}{2}\rangle$ and $|\pm\frac{5}{2}\rangle$) with non-zero matrix elements of $\frac{16}{3}$ and $\frac{10}{3}$, respectively. Murani et al. (1977) and Murani

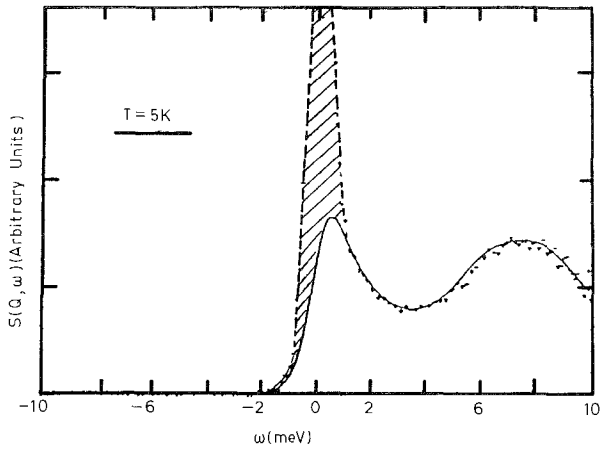

Fig. 48. Scattering function $S(\omega)$, for $CeAl_3$ at $T = 5$ K. The continuous line represents a fit with a quasi-elastic and two inelastic peaks of Lorentzian shape centered at 6 and 8 meV, respectively (Murani 1987b).

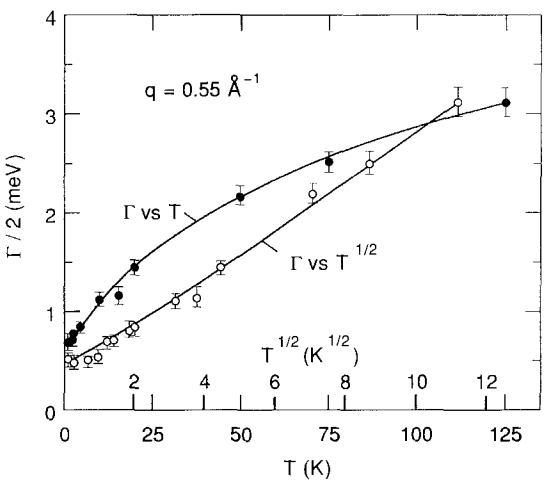

Fig. 49. Temperature dependence of the quasi-elastic line width of $CeAl_3$ plotted versus T and $T^{1/2}$ (Murani et al. 1980).

(1987b) observed at $T = 5$ K on a polycrystalline sample of $CeAl_3$ two CF transitions at $\Delta_1 = 6$ meV and $\Delta_2 = 8$ meV, although not well separated from each other (see fig. 48). If there are really two transitions from the ground state then the ground state has to be the $|\pm\frac{3}{2}\rangle$ doublet. This implies that the quasi-elastic scattering, which is also observed in $CeAl_3$, must originate from J^z matrix elements (all $J^{\pm}$ matrix elements are zero for this doublet). The temperature dependence of the quasi-elastic line width has been measured by Murani et al. (1980) between 60 mK and 125 K. The results are shown in fig. 49 on a T and $T^{1/2}$ scale. For $T \geqslant 1$ K the line width follows nicely a $T^{1/2}$ law and is constant below 1 K with $\frac{1}{2}\Gamma = 0.5$ meV, yielding $T_K^N = 6$ K for $CeAl_3$. The line shape is quasi-elastic down to the lowest measured temperature, as expected for a $S_{eff} = \frac{1}{2}$ ground state doublet. The value of the Kondo temperature of the ground-state doublet as deduced from the neutron data is in fairly

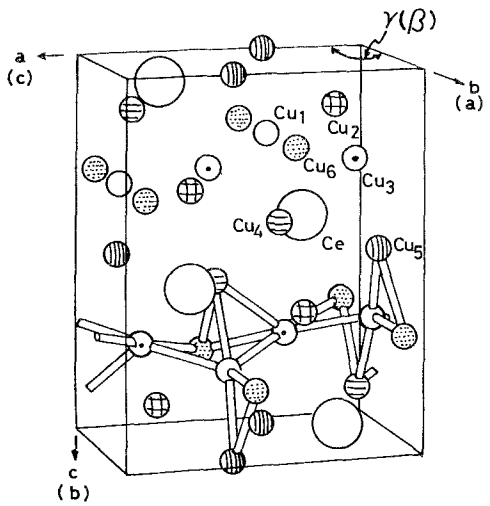

Fig. 50. Crystal structure of $CeCu_6$. The axes are marked in the orthorhombic notation (the monoclinic notation is given in parentheses) (from Onuki et al. 1985a).

good agreement with T_K values obtained from susceptibility measurements on small-sized single crystals of $CeAl_3$ [$T_K^\chi = 4.6$ K (Jaccard et al. (1988)] and from specific heat data [$\gamma = 1620$ mJ/K^2 mol (Andres et al. 1975)]. On the other hand, there is a discrepancy between the spin-relaxation rates obtained from the quasi-elastic line widths of the neutron data and those deduced from NMR, from which the existence of ferromagnetic correlations is inferred (Lysak and MacLaughlin 1985).

The inter-multiplet transition $^2F_{5/2} \rightarrow {}^2F_{7/2}$ was observed by Osborn et al. (1990), who find, surprisingly, *two*, equal intense, lines at 260 and 291 meV with rather large widths of 49 meV compared to an estimated resolution of 12 meV. The unusual large splitting and line width of the excited $^2F_{7/2}$ multiplet compared to the much lower crystal field splitting ($\leqslant 8$ meV) and the small residual quasi-elastic line width of 0.5 meV of the ground-state $^2F_{5/2}$ multiplet are discussed by Osborn et al. (1990) in terms of hybridization-mediated enhanced exchange between f and conduction electrons.

$CeCu_6$ has an orthorhombic crystal structure at room temperature [$a = 8.11$ Å, $b = 5.10$ Å, $c = 10.16$ Å (Cromer et al. 1960)] and becomes monoclinic below $T \simeq 220$ K [$a^* = 5.08$ Å, $b^* = 10.12$ Å, $c^* = 8.07$ Å, $\beta = 91.36°$ at 65 K (Asano et al. (1986)]. The crystal structure is shown in fig. 50. It should be noted that most publications on $CeCu_6$ use the orthorhombic notation even at low temperatures. To avoid confusion we use a, b, and c for the orthorhombic and ($a^* = b$, $b^* = c$, $c^* = a$) for the monoclinic notation. In both structures the low local symmetry of the Ce ions splits the ground state into three doublets. Walter et al. (1986) propose a CF level scheme 0–5.5–11 meV, while Goremychkin and Osborn (1991a) find a slightly different scheme: 0–7–13.8 meV. Again, the ground-state doublet is well separated from the excited states, which is important for the discussion of the low-temperature properties. The temperature dependence of the quasi-elastic line width measured on a polycrystalline sample in the temperature region from 1.5 to 120 K follows a $T^{1/2}$

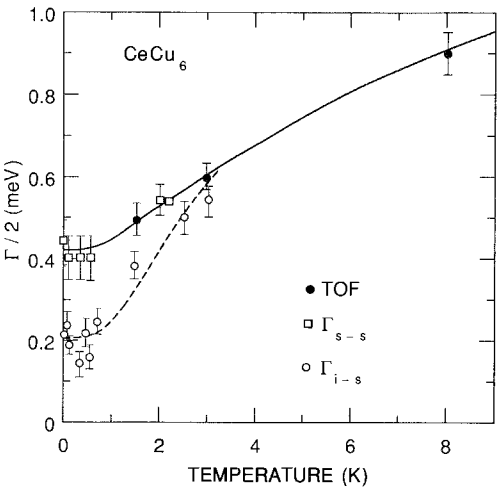

Fig. 51. Temperature dependence of the line widths for the quasi-elastic single-site contributions (open squares, $\Gamma_{s\text{-}s}$) and for the inelastic inter-site contributions (open circles, $\Gamma_{i\text{-}s}$) obtained on a $CeCu_6$ single crystal (Rossat-Mignod et al. 1988). Also shown are the quasi-elastic line widths measured on a polycrystalline sample by a time-of-flight (TOF) technique (IN6, solid circles) (Walter et al. 1986).

law with a residual width of about 0.5 meV (Walter et al. 1986). There is no long-range order nor superconductivity down to 10 mK. Below 3 K, however, *short-range* spin correlations become observable. A full account of detailed neutron scattering experiments performed on a single crystal of $CeCu_6$ in the low-temperature region (25 mK to 5 K) is given by Rossat-Mignod et al. (1988).

We will now discuss the essential findings. The anisotropic magnetic behavior seen in susceptibility and magnetization (Amato et al. 1987) is also reflected in the different magnetic response for $\boldsymbol{Q}$ along the main symmetry directions. Energy scans for $\boldsymbol{Q}$ along the b^* direction do not show any sizeable magnetic intensity, which indicates that the ground-state doublet has an Ising-type anisotropy along the b^*-axis with negligible *transverse* fluctuations (note: neutrons sample only fluctuations perpendicular to $\boldsymbol{Q}$). Energy scans with $\boldsymbol{Q}$ along the a^* and c^* direction, however, show magnetic scattering with a maximum around 0.2–0.3 meV, originating from *longitudinal* fluctuations along the b^*-axis. Rossat-Mignod et al. (1988) subdivide the magnetic response into a single-site, $\boldsymbol{Q}$-independent, Kondo-type contribution and an inter-site, $\boldsymbol{Q}$-dependent contribution from antiferromagnetic spin correlations.

The single-site fluctuations can be described by a quasi-elastic line of Lorentzian shape. At 25 mK the half line width is $\frac{1}{2}\Gamma_{s\text{-}s} = (0.42 \pm 0.04)$ meV, defining a Kondo temperature of $T_K^N = (5 \pm 0.5)$ K. For increasing temperatures $\Gamma_{s\text{-}s}$ fits well to the quasi-elastic line width deduced from time-of-flight measurements on polycrystalline $CeCu_6$ samples, as shown in fig. 51. The single-site contribution amounts to about 90% of the spectral weight if integrated over q-space within a Brillouin zone. The remaining 10% stems from the inter-site correlations, which are strongly peaked in q-space and inelastic in energy. The correlations are commensurate along c^* with propagation vector $\boldsymbol{k}_1 = (0, 0, 1)$ and incommensurate along a^* with $\boldsymbol{k}_2 = (0.85, 0, 0)$. Furthermore, the correlation lengths are anisotropic: $\xi(a^*) = (9 \pm 1)$ Å, extending up to second neighbors, and $\xi(c^*) = (3.5 \pm 0.5)$ Å, extending only up to the first neighbor. The temperature dependence of the correlations lengths is shown in fig. 52.

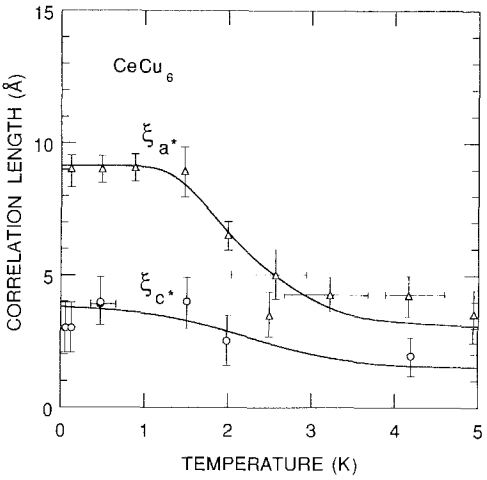

Fig. 52. Magnetic correlation lengths along the a^* and c^* directions as a function of temperature for $CeCu_6$ (Rossat-Mignod et al. 1988).

The widths of the inelastic inter-site response $\Gamma_{i\text{-}s}$ is also strongly $\boldsymbol{Q}$-dependent but with the product [intensity times width] being roughly constant. The minimal values for the position and the width in energy at $T = 25$ mK measured at $\boldsymbol{Q} = (0, 0, 0.9)$ and $(1.15, 0, 0)$ are $\hbar\omega_0 \simeq \frac{1}{2}\Gamma_{i\text{-}s} \simeq 0.2$ meV. With increasing temperature $\Gamma_{i\text{-}s}$ stays roughly constant up to $T = 1$ K, but increases strongly above 1 K (see fig. 51). Thus the width becomes much larger than the energy, which means that the inelastic character of the inter-site excitations is lost. $\Gamma_{i\text{-}s}$ and $\Gamma_{s\text{-}s}$ become equal above 3 K, where also the magnetic correlations begin to collapse (see fig. 52). The inter-site correlations can also be suppressed by the application of an external field. Figure 53 shows the evolution of the inelastic magnetic intensities in magnetic field along the easy b^*-axis. The intensity measured at $\boldsymbol{Q} = (-1.5, 0, 0)$ corresponds to the single-site contribution. At $\boldsymbol{Q} = (0, 0, 0.9)$ and $(-1.15, 0, 0)$ both the single-site and the inter-site contributions are measured. From the suppression of the inter-site contribution with field a metamagnetic-like transition at 2.5 T is deduced by Rossat-Mignod et al. (1988). This is supported by the recent observation of a metamagnetic transition in magnetization measurements along the c (b^*) direction by Schröder et al. (1992). Although less significant, there is also a decrease of single-site intensity with increasing field, which can be correlated with the decrease of the linear term, γ, of the specific heat in $CeCu_6$, when a magnetic field is applied in the c (b^*) direction (Amato et al. 1987).

The low Kondo temperature of $T_K^N = 5$ K and the presence of magnetic correlations at low temperatures indicates that $CeCu_6$ is near to a magnetic instability. Negative pressure (i.e. by appropriate alloying to expand the lattice) usually drives a Kondo system towards the magnetic limit. Long-range magnetic order was predicted from specific-heat data on $CeCu_{6-x}Au_x$ by Germann and Löhneysen (1989) for $x > 0.1$ and was verified by neutron diffraction on polycrystalline $CeCu_{5.5}Au_{0.5}$ (Chattopadhyay et al. 1990). Surprisingly, the magnetic Bragg peaks of $CeCu_{5.5}Au_{0.5}$ do not appear at the positions of the short-range correlations of $CeCu_6$. The crystal field level scheme of $CeCu_{5.5}Au_{0.5}$ (Stroka et al. 1992) is only slightly modified

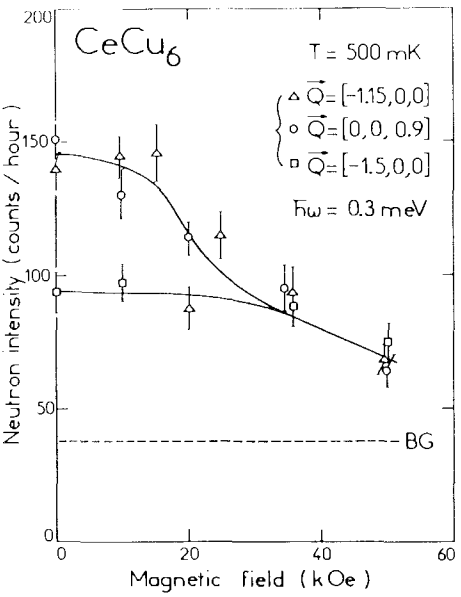

Fig. 53. Magnetic intensities measured on $CeCu_6$ at $T = 0.5$ K as a function of magnetic field applied along the b^* direction. The scattering vectors were chosen to follow intensities on the peaks associated with the wave vectors $\boldsymbol{k}_1 = (0, 0, 1)$ (circles), $\boldsymbol{k}_2 = (0.85, 0, 0)$ (triangles), and in between (squares) (Rossat-Mignod et al. 1988).

(0–8–14 meV) compared to $CeCu_6$ (0–7–13 meV) and does not account for the different magnetic ordering phenomena at low temperatures. It is rather the subtle interplay between RKKY exchange and Kondo energy which produces long-range magnetic order in $CeCu_{5.5}Au_{0.5}$ and short-range correlations in $CeCu_6$.

$CeRu_2Si_2$ has a tetragonal $ThCr_2Si_2$ structure with $a = 4.197$ Å and $c = 9.797$ Å (Hiebl et al. 1983). The crystal field splitting has not yet been determined, but it seems likely that the ground state is a doublet, well separated ($\leqslant 20$ meV) from the two excited doublets (Grier et al. 1988, Severing et al. 1989a). $CeRu_2Si_2$ neither becomes superconducting nor orders magnetically down to 20 mK in zero field. The two maxima in the specific heat at 11 and 84 K can be attributed to a Kondo effect on the ground-state doublet ($T_K = 24$ K) and to a Schottky anomaly from an excited state at 220 K (Besnus et al. 1985), respectively. The low-temperature susceptibility is strongly anisotropic ($\chi_c \simeq 15\chi_{a,b}$) and at $T = 1.5$ K a metamagnetic transition occurs at $H_c = 8$ T (Haen et al. 1987).

Severing et al. (1989b) performed inelastic neutron scattering experiments on a polycrystalline sample of $CeRu_2Si_2$ and report a *linear* temperature dependence of the quasi-elastic line width between 50 and 250 K. Below 50 K the magnetic response becomes Q-dependent and at 1.5 K the spectra are better fitted with a broad inelastic line ($\Delta \simeq \frac{1}{2}\Gamma \simeq 1$–$1.15$ meV, depending on Q) than with a quasi-elastic line. A fit with the analytic function of Kuramoto and Müller-Hartmann (eq. (28)) looks also acceptable but yields an unrealistic large degeneracy of (3.85 ± 0.74) for the ground state in contrast to the expected value of 2 for a doublet. No attempt has been made by Severing et al. (1989b) to fit the low-temperature spectra by a superposition of a (Q-independent) quasi-elastic and a (Q-dependent) inelastic line. However, this has been

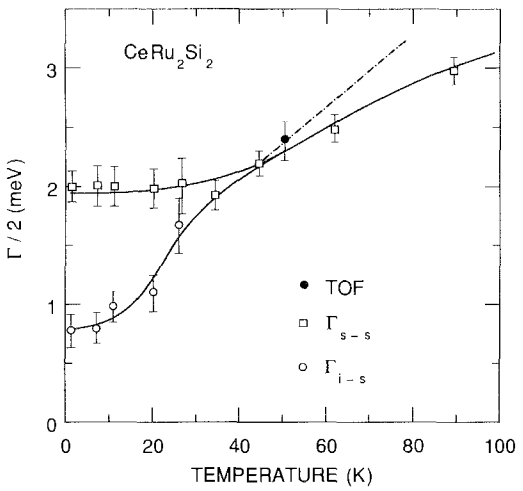

Fig. 54. Temperature dependence of the line widths for the quasi-elastic single-site contributions (open squares, $\Gamma_{s\text{-}s}$) and for the inelastic inter-site contributions (open circles, Γ_s) obtained on a $CeRu_2Si_2$ single crystal (Regnault et al. 1990). Also shown is the quasi-elastic line width measured at $T = 50$ K on a polycrystalline sample and the slope towards higher temperatures is drawn as a dash-dotted line [from IN4/IN6 time-of-flight (TOF) data (Severing et al. 1989)].

done by Rossat-Mignod et al. (1988), Jacoud et al. (1989), and Regnault et al. (1990), who analyzed their data obtained on a *single crystal* of $CeRu_2Si_2$ in analogy to the situation in $CeCu_6$. The quasi-elastic part then originates from single-site fluctuations, its residual line width being $\frac{1}{2}\Gamma \simeq 2$ meV, as shown in fig. 54. This yields $T_K^N = 23$ K, in good agreement with estimates from other measurements. Inter-site correlations develop below 50 K and are identified by additional $\boldsymbol{Q}$-dependent inelastic magnetic intensity. At low temperatures the spectral weight of this intensity is about 40% of the total intensity (for comparison: 10% in $CeCu_6$). The inelastic intensity is peaked at the incommensurate wave vectors $\boldsymbol{q}_1 = (0.3, 0, 0)$ and $\boldsymbol{q}_2 = (0.3, 0.3, 0)$, indicating competing in-plane couplings between first- and second-nearest neighbors. The temperature dependence of the anisotropic correlation lengths $\xi_{a,b}$ and ξ_c is shown in fig. 55. Position and line width of the corresponding inelastic response are slightly dispersive with the minimum for both at $\boldsymbol{q}_1$ and $\boldsymbol{q}_2$. The range of values at $T = 1.4$ K is $\Delta = 1.2$–1.6 meV and $\frac{1}{2}\Gamma = 0.8$–2 meV. The temperature dependence of the inelastic line width at $\boldsymbol{q}_2$ is shown in fig. 54 together with that of the quasi-elastic line width. Both widths merge above 30 K. The polycrystalline data from Severing et al. (1989b) agree with the single crystal data around 50 K, but give a slightly steeper and linear increase towards higher temperatures (dash-dotted line in fig. 54).

As in $CeCu_6$, the magnetic correlations in $CeRu_2Si_2$ can be suppressed by the application of an external field (in the c direction). The field dependence of the magnetic signal up to 10 T at $T = 1.5$ K is reproduced in fig. 56. The inter-site contribution disappears above the metamagnetic transition at 8.3 T and at the highest

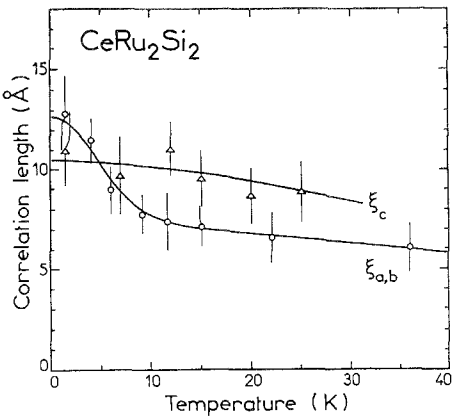

Fig. 55. Magnetic correlation lengths along the *a* and *c* directions as a function of temperature for $CeRu_2Si_2$ (Regnault et al. 1990).

field the scattering becomes $\boldsymbol{Q}$-independent and purely quasi-elastic. The single-site response measured at $\boldsymbol{Q} = (0.9, 0.9, 0)$ is only little affected by the application of the external field. Comparing figs. 51–53 with figs. 54–56, respectively, it is evident that the behavior of the two non-ordering HF compounds $CeCu_6$ and $CeRu_2Si_2$ is similar except for an increase of the characteristic energy scale from $CeCu_6$ to $CeRu_2Si_2$ by roughly a factor of five. This is also reflected in the *decrease* of γ from 1600 mJ/K^2 mol for $CeCu_6$ to 350 mJ/K^2 mol for $CeRu_2Si_2$.

$CeRu_2Si_2$ is also close to a magnetic instability. Alloying [(Ce,La)Ru_2Si_2: Mignot et al. (1990), $CeRu_2(Si,Ge)_2$: Mignot et al. (1991)] that corresponds to *negative* pressure produces long-range magnetic order at low temperatures with roughly the same incommensurate wave vector $\boldsymbol{q}_1 = (0.31, 0, 0)$ that describes the short-range

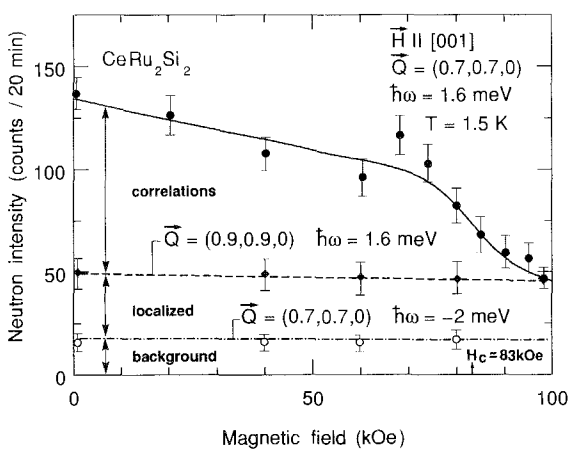

Fig. 56. Magnetic intensities measured on $CeRu_2Si_2$ at $T = 1.5$ K as a function of a magnetic field applied along the *c* direction. The scattering vectors were chosen to follow intensities on the peak associated with the wave vector $\boldsymbol{q}_2 = (0.3, 0.3, 0)$, and in the flat region at (0.9, 0.9, 0). The background was determined at (0.7, 0.7, 0) but with $\hbar\omega = -2$ meV instead of +1.6 meV (Rossat-Mignod et al. 1988).

correlations in the pure compound. An inelastic neutron study of a single crystal of $Ce_{0.8}La_{0.2}Ru_2Si_2$ ($T_N = 5.7$ K) by Jacoud et al. (1992) at $T = 1.5$ K shows that single-site fluctuations ($\frac{1}{2}\Gamma_{s\text{-}s} = 0.7$ meV, i.e. $T_K^N = 8$ K) are even present in the long-range ordered state.

$CeNi_2Ge_2$ is tetragonal with $a = 4.150$ Å and $c = 9.854$ Å (Knopp et al. 1988a). Like $CeRu_2Si_2$ it does not order nor becomes superconducting and seems to have a doublet ground state. Yet the CF splitting itself has not been determined. The low-temperature specific-heat data taken at $B = 4$ T (to suppress coherence effects in zero field) can be quantitatively fitted with an $S_{eff} = \frac{1}{2}$ impurity Kondo model, yielding $T_K = 29$ K [$\gamma = 300$ mJ/K^2 mol (Knopp et al. 1988a)]. Knopp et al. (1988a) also report on the temperature dependence of the quasi-elastic part of the magnetic response measured on a polycrystalline sample on IN6 with $E_0 = 3.15$ meV and on IN4 with $E_0 = 12.5$ meV between 5 and 200 K. They can describe all spectra with just one quasi-elastic line of Lorentzian shape. For $T \geqslant 40$ K the line width increases smoothly with temperature, reaching 6 meV at 200 K. At 30 K there is a shallow minimum ($\frac{1}{2}\Gamma \simeq 3.5$ meV) and again a smooth increase of the line width towards the low-temperature limit ($\frac{1}{2}\Gamma_0 = 4$ meV). For an $S = \frac{1}{2}$ Kondo system, however, no minimum in the $\Gamma(T)$ curve is expected. It is therefore likely that the observed minimum is an artifact of the fitting procedure caused by the restriction of just one quasi-elastic Lorentzian line. A similar difficulty was discussed for the polycrystalline data of $CeRu_2Si_2$. There the fit of the magnetic response with just one function also led to inconsistencies. Again, single crystal data are necessary to elucidate the situation in $CeNi_2Ge_2$.

$CePt_2Si_2$ has a tetragonal $CaBe_2Ge_2$-type structure with $a = 4.25$ Å and $c = 9.79$ Å (Hiebl and Rogl 1985). Although its valence is near +3 (Röhler 1987), its properties seem to lie in-between those of HF and VF compounds. The resistivity and susceptibility show a broad maximum around 76 and 60 K, respectively. Single crystal data show that the behavior of $CePt_2Si_2$ is anisotropic with even different temperatures for the maxima in the ***a*** and ***c*** directions: 55 and 85 K for the resistivity curves, 55 and 65 K for the susceptibility curves (Gignoux et al. 1988a). Specific heat data are interpreted by Ayache et al. (1987) in terms of an $S_{eff} = \frac{1}{2}$ Kondo contribution with $T_K = 70$ K and a Schottky peak near 90 K arising from a doublet ground state and an excited doublet at $\Delta = 240$ K (20.7 meV). The low-temperature specific heat yields a linear coefficient, γ, around 100 mJ/K^2 mol (with a maximum of 130 mJ/K^2 mol at $T = 1.4$ K). From all this one would expect a magnetic response consisting of a quasi-elastic line with residual width of about 6–8 meV and inelastic CF transitions around 20 meV. Two groups have performed inelastic neutron scattering experiments on polycrystalline samples of $CePt_2Si_2$. Both observe at all temperatures between 5 and 200 K only a rather broad (15–20 meV) magnetic response with no indications of well-defined inelastic CF transitions (Grier et al. 1988, Gignoux et al. 1988b). The unusual temperature dependence of the spectral width, showing a minimum around 100 K, however, seems to indicate that the magnetic response must contain inelastic features reminiscent of CF transitions, although presumably considerably broadened. This point should be checked by neutron scattering on single crystals.

3.2.3. *Antiferromagnetic ordering ($CeAl_2$, CeB_6, $CeCu_2$, $CePb_3$, CeT_2M_2)*

Most of the HF compounds show magnetic order at low temperatures and from these compounds again the majority orders antiferromagnetically. Even in the ordered state the specific-heat data show a rather large linear-T term, although typically reduced by a factor of 10 [$CeAl_2$: 130 to 180 mJ/K^2 mol, CeB_6: 260 mJ/K^2 mol, $CeCu_2$: 82 mJ/K^2 mol (Bredl 1987)] if compared to a non-ordering Ce compound with similar T_K ($CeCu_6$: 1600 mJ/K^2 mol). An exception is $CePb_3$ with $\gamma = 1400$ mJ/K^2 mol (Lin et al. 1987). Most of the antiferromagnetically ordering HF compounds exhibit in addition a metamagnetic transition and have rather complicated phase diagrams in the H–T and p–T planes. Usually the ordered magnetic moment is reduced if compared to the free CF ground-state moment ("Kondo compensation"). In some cases, however, the exact CF ground state is not known or modified by other interactions (e.g. quadrupolar, CeB_6). This makes a comparison, of course impossible. Inelastic neutron scattering experiments cover

- the ordered region (magnons),
- quasi-elastic scattering above T_N, and
- crystal field transitions including CF-phonon interactions.

$CeAl_2$ has a cubic Laves-phase structure with $a = 8.06$ Å. The Ce ions form a diamond lattice, which can be viewed as two interpenetrating fcc lattices shifted by $(\frac{1}{4}, \frac{1}{4}, \frac{1}{4})$. The local cubic symmetry is expected to split the $J = \frac{5}{2}$ Ce^{3+} ground state into a low-lying Γ_7 doublet and an excited Γ_8 quartet. Instead of the expected *single* inelastic $\Gamma_7 \rightarrow \Gamma_8$ transition, however, *two* inelastic transitions were observed in $CeAl_2$ by neutron scattering (Loewenhaupt et al. 1979) and this was explained by a formation of a bound state between the crystal field transition and a phonon (Thalmeier and Fulde 1982, Thalmeier 1984). The influence of this strong coupling on the lattice dynamics (unusual frequency shifts and line broadenings with temperature) has been reported on by Reichardt and Nücker (1984) and Loewenhaupt et al. (1987). Reviews of this phenomenon can be found in Fulde and Loewenhaupt (1986) and Thalmeier and Lüthi (1991) and will therefore not be discussed further in this chapter. The energies of the two CF transitions are about 9 and 17 meV and the energy of the interacting phonon varies between 11 (at 6 K) and 13 meV (at 300 K). Hence, the low-temperature properties of $CeAl_2$ are mainly determined by the Γ_7 ground-state doublet. The Kondo temperature is estimated to be $T_K = (5 \pm 2)$ K (Steglich et al. 1979b) analysing the residual quasi-elastic line width and specific-heat data on diluted (La,Y) and concentrated $CeAl_2$. The Kondo temperature is of the same order as the antiferromagnetic ordering temperature $T_N = 3.8$ K. The ordering is incommensurate with wave vectors of the form $(\frac{1}{2} + \delta, \frac{1}{2} - \delta, \frac{1}{2})$ where $\delta = 0.11$ (Barbara et al. 1977, 1979). Barbara et al. proposed a single-q collinear structure with the moments in the (111) direction and a long-period sinusoidal modulation ($\delta^{-1} \cong 9$ atomic layer spacings) of the *value* of the moments. The absence of higher-order satellites down to $\frac{1}{10}T_N$ was taken as evidence for the existence of Kondo compensated moments (at the nodes of modulation) even for $T \rightarrow 0$. Any moment value between zero and $0.89\mu_B$ can be realized in this structure, with an average value of $0.63\mu_B$. The average value corresponds to the free Γ_7 value ($0.71\mu_B$) reduced by 10%. A triple-q structure was proposed by Shapiro et al. (1979) to explain the observation of intensity at the $(\frac{1}{2}, \frac{1}{2}, \frac{1}{2})$ position. This latter model, however, was disproved by Barbara et al. (1980)

and Boucherle et al. (1981), who showed that the $(\frac{1}{2}, \frac{1}{2}, \frac{1}{2})$ intensity belongs to another phase of $CeAl_2$ which can be stabilized by defects or pressure. To account for the pressure effects a complicated T–p phase diagram was proposed by Schefzyk et al. (1984).

For a long time the question of the magnetic structure of $CeAl_2$ seemed to be settled in favor of the single-q collinear modulated structure proposed by Barbara et al. (1977). Recently, however, Forgan et al. (1990) produced in an applied field a single-domain $CeAl_2$ single crystal and reported that even in this state there are two (coupled) modulations. This excludes a single-q structure. They therefore propose a double-q, spiral structure which is non-chiral (i.e. the moments in different sublattices rotate in different senses). Furthermore, there are no zero moments in this structure. All moment values for the spiral structure lie between $0.53\mu_B$ and $0.75\mu_B$, with the same average value of $0.63\mu_B$ as given for the sinusoidally modulated structure.

The magnetic excitations (magnons) in the ordered state at $T = 1.2$ K have been measured in zero field on a (multi-domain) single crystal by Osborn et al. (1987). The spectra consist of broadened bands which can be characterized by two (overlapping) Gaussian peaks. The two bands were interpreted as originating from an acoustic magnon branch centred at 0.7 meV and with a FWHM of 0.4 meV, and from an optic magnon branch centered at 1.2 meV and with a FWHM of 0.8 meV. Both branches show little dispersion except near the ordering wave vectors, where the acoustic branch softens. A complete softening could not be observed, presumably due the presence of several domains. Therefore, the reported value of 0.45 meV for the magnon gap may not be the true gap value (if there is a gap at all). The results of specific-heat measurements at low temperatures (Steglich et al. 1979b) yield a linear term in T with $\gamma = 130$ mJ/K^2 mol and a T^3 term, indicating the presence of *gapless* antiferromagnetic magnons. At $T_N = 3.8$ K the entropy is only $\frac{1}{2}R \ln 2$, reaching the full value of $R \ln 2$ for a doublet above 15 K. This shows the existence of short-range spin correlations in $CeAl_2$ far above the ordering temperature, which was also inferred from the Q-dependence of the quasi-elastic response measured with relaxed energy resolution (D7; Steglich et al. 1979b). An experiment with improved energy resolution (IN6; Loewenhaupt 1984b) shows that the low-energy response ($\leqslant 2$ meV) contains at $T = 5$ K besides the quasi-elastic also an inelastic component. This reminds one of the situation for the non-ordering HF compounds $CeCu_6$ and $CeRu_2Si_2$, as reported by Rossat-Mignod et al. (1988) and discussed in section 3.2.2. Unfortunately, there are no investigations of the short-range order in $CeAl_2$ above T_N using a single crystal, which might then be directly compared with the other results.

The evolution of the quasi-elastic line width with temperature was reported by Horn et al. (1981b). Above 15 K ($\frac{1}{2}\Gamma = 0.5$ meV) up to room temperature ($\frac{1}{2}\Gamma = 5$ meV) they found a $T^{1/2}$ law, as in other HF compounds. Below 15 K the quasi-elastic line width is temperature independent (Steglich et al. 1979b) if measured with moderate energy resolution (but we have to keep in mind that the magnetic response in this temperature region is Q-dependent and develops additional inelastic features). These complications do not arise for dilute samples of the type $Ce_{1-x}M_xAl_2$ with M = La, Y for $x \leqslant 0.6$ and with M = Sc for $x \leqslant 0.4$ (Horn et al. 1981b). For all samples a $T^{1/2}$ law has been measured in the temperature range from 2.5 to 60 K.

Dilution with La (producing *negative* chemical pressure) reveals smaller line widths compared to $CeAl_2$, while for Y and Sc diluted samples (*positive* chemical pressure) the line widths become larger. For $Ce_{1-x}Sc_xAl_2$ and $x \geqslant 0.5$ the strong lattice pressure even seems to drive the Ce ions into a VF state (Loewenhaupt et al. 1981), showing a considerably larger and nearly temperature-independent quasi-elastic line width (for $x = 0.5$: $\frac{1}{2}\Gamma \simeq 20$ meV).

CeB_6 crystallizes in the cubic CaB_6 structure with $a = 4.135$ Å. This structure can be viewed as a bcc CsCl structure with Ce^{3+} ions at the body centered positions and boron octahedra at the cube corners. The Kondo behavior of the *dilute* system (CeLa)B_6 ($T_K = 1$ K) has been nicely demonstrated by resistivity (see fig. 12) and specific-heat (see fig. 13) measurements. The behavior of the full compound CeB_6, on the other hand, was considered to be mysterious for quite some time (see, e.g. Komatsubara et al. 1983). The clue for a better although not yet complete understanding of the magnetic properties of CeB_6 was the observation of an unexpected large (47 meV) crystal field splitting with a Γ_8 ground state and a Γ_7 excited state and an additional splitting of the Γ_8 quartet deduced indirectly from an energy shift of the $\Gamma_8 \rightarrow \Gamma_7$ transition at temperatures below 20 K (Zirngiebl et al. 1984, Loewenhaupt et al. 1985). Strong quadrupolar interactions yield in zero field at $T_Q = 3.3$ K a transition to long-range antiferro-quadrupolar ordering, followed at $T_N = 2.3$ K by a transition to a non-collinear, commensurate, double-q magnetic structure (Effantin et al. 1985). The latter transition is suppressed by a magnetic field at 1.5 T whereas the former transition is shifted to higher temperatures in high magnetic fields. A similar phase diagram is found for dilute $Ce_{0.75}La_{0.25}B_6$, but with reduced $T_Q \simeq T_N \simeq 1.6$ K and an increased metamagnetic transition field of 2.6 T (Erkelens et al. 1987). The ordered magnetic moment ($0.28\mu_B$) of CeB_6 is strongly reduced compared to the free Γ_8 moment ($1.57\mu_B$). The entropy determined from specific-heat data is only $R \ln 2$ at T_N, it reaches $R \ln 3$ around 10 K, but $R \ln 4$ not below 50 K (Peysson et al. 1986). This led Kunii (1988) to propose a somewhat peculiar splitting of the Γ_8 quartet into a ground-state doublet and two excited singlets at 0.78 meV (9 K) and 8.2 meV (95 K). Any splitting of the Γ_8 state in the paramagnetic phase, however, has not yet been observed directly.

The temperature dependence of the quasi-elastic line width seems to follow a $T^{1/2}$ law (D7 data, Horn et al. 1981c) between 5 K ($\frac{1}{2}\Gamma = 0.4$ meV) and 280 K ($\frac{1}{2}\Gamma = 2$ meV). Figure 57 shows these results together with those of a later experiment with better energy resolution (IN6 data, Neuhaus 1987). A closer inspection of the low-temperature region, however, reveals instead of the overall $T^{1/2}$ dependence (dotted line in fig. 57) a *kink* in the $\Gamma(T)$ curve at $T = 20$ K, separating a steep linear increase below 20 K from a flat linear increase above 20 K. From the residual widths one obtains $T_K^N = 3$ to 4.5 K depending on the extrapolation scheme ($T^{1/2}$ or linear). Also shown in fig. 57 are the results for dilute $Ce_{0.5}La_{0.5}B_6$, which give in general lower values for the line widths. The residual width yields $T_K^N = 2.3$ K for linear extrapolation and a kink around 15 K. The reduced Kondo temperature is in line with $T_K = 1$ K for the dilute limit of (CeLa)B_6. The kink in both curves is a further (indirect) indication of the Γ_8 splitting in the paramagnetic state. It may be smaller in $Ce_{0.5}La_{0.5}B_6$ than in CeB_6. Down to $T_N = 2.3$ K, including the antiferro-quadrupolar

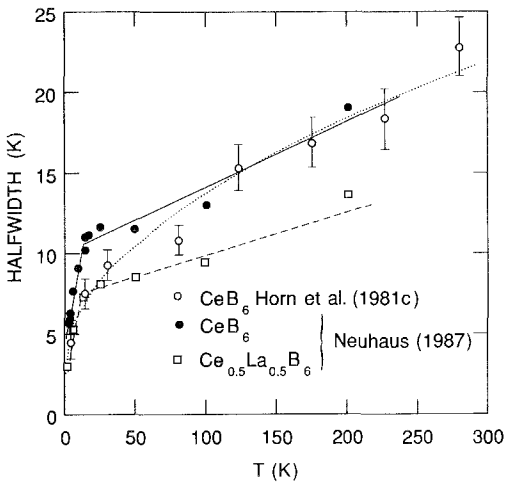

Fig. 57. Temperature dependence of the quasi-elastic line width for CeB_6 and $Ce_{0.5}La_{0.5}B_6$ (open circles: Horn et al. 1981c, other symbols: Neuhaus 1987).

ordered region below T_Q, the magnetic response of CeB_6 is quasi-elastic (Neuhaus 1987). These results obtained for a polycrystalline sample agree with the observation of Regnault et al. (1988) that there is no inelastic feature in the magnetic spectrum of a single crystal in zero field at T = 2.3 K. Application of 4 T, however, produces dispersive magnetic excitations in the antiferro-quadrupolar phase at $T = 2.3$ K with energies up to 1 meV (Regnault et al. 1988). In the magnetically ordered phase at $T = 1.5$ K, well below T_N, the magnon density of states measured on the polycrystalline sample peaks at 0.5 and 1 meV, which can be interpreted as originating from acoustic and optic magnon branches. These inelastic features soften towards T_N and disappear above T_N (Neuhaus 1987).

$CeCu_2$ crystallizes in an orthorhombic $CeCu_2$-type structure with $a = 4.43$ Å, $b = 7.06$ Å, and $c = 7.47$ Å (Larson and Cromer 1961). The electrical resistivity (ln T law) and other properties classify this compound as Kondo lattice (Gratz et al. 1985, Onuki et al. 1985b). Below $T_N = 3.5$ K, $CeCu_2$ orders in a simple antiferromagnetic structure (fig. 58) with the moments of the two Ce ions of the primitive unit cell in opposite directions and along the c-axis (Trump et al. 1991, Nunez et al. 1992). Surprisingly, this structure is much simpler than those of the "normal" RCu_2 compounds [see, e.g. Lebech et al. (1987)] and of the other antiferromagnetic Ce HF compounds discussed in this section. The susceptibility and the magnetization are very anisotropic in the ordered as well as in the paramagnetic phase of $CeCu_2$, with the easy axis in the a direction, the hard axis in the b direction, and the c direction in between. The strong magnetic anisotropy is mainly due to single-ion crystal field effects. The low-symmetry crystal field splits the $J = \frac{5}{2}$ ground state of Ce^{3+} into three doublets. Inelastic neutron scattering experiments on a polycrystalline sample yield a level scheme 0–9–23 meV, from which, however, only the position of the 23 meV level could be determined directly (Loewenhaupt et al. 1988). The position of the first excited level was inferred only indirectly from the temperature dependence of the intensity of the 23 meV transition and from the evolution of the entropy with

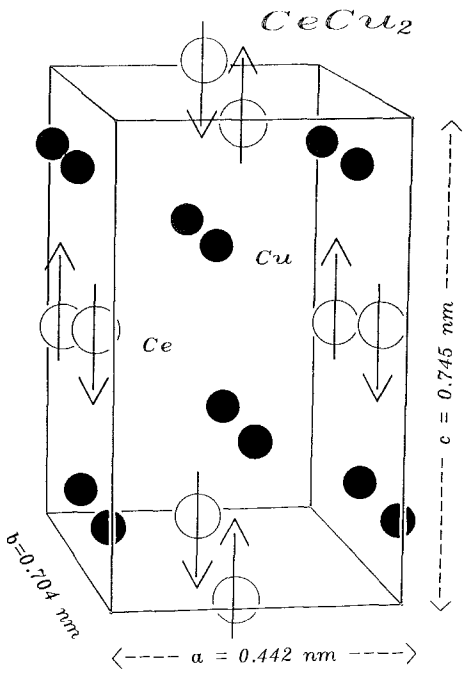

Fig. 58. Magnetic structure of $CeCu_2$ (Trump et al. 1991).

temperature [$\frac{2}{3}$ R ln 2 at T_N, R ln 2 at 16 K, R ln 4 around 50 K (Loewenhaupt et al. 1990)]. Furthermore, there seems to be a strong coupling between the crystal field transition from the first to the second excited level (23 − 9 = 14 meV) and a phonon around 14 meV (Loewenhaupt et al. 1988, 1990). This is a similar situation as the CF–phonon bound state in $CeAl_2$, except that in $CeCu_2$ the involved CF transition connects *excited* levels and hence this effect can only be observed at elevated temperatures.

The magnons have been measured at $T = 1.2$ K, well below T_N, on a single crystal of $CeCu_2$ in all main symmetry directions (Trump 1991). There are again two magnon branches: an acoustic and an optic branch. The acoustic magnons exhibit at the Γ-point a small gap of 0.06 meV [in agreement with specific heat data of Takayanagi et al. (1990)], followed by a steep increase in energy at low q-values and with an extended flat portion towards the zone boundary with energies around 0.5 meV. The optic branch is strongly dispersive with energies between 0.8 and 1.5 meV. The magnon dispersion curves can be fitted with an anisotropic Heisenberg model with dominant antiferromagnetic exchange for short distances and weaker ferromagnetic exchange of long-range character. Above T_N the low-energy magnetic response becomes quasi-elastic with a mainly Gaussian line shape at low temperatures and changing around 50 K to a mainly Lorentzian line shape at higher temperatures (Loewenhaupt et al. 1990). A good fit of the spectra is obtained allowing for a superposition of both types of line shapes with an increasing ratio of Lorentzian to Gaussian intensity with increasing temperatures. The Gaussian width is nearly inde-

pendent of temperature ($\frac{1}{2}\Gamma = 0.8$ meV). It is interpreted as being due to short-range spin correlations, which show up also in the Q-dependence of the quasi-elastic intensity and in strong contributions to the specific heat above T_N (Takayanagi et al. 1990). The Lorentzian width increases linearly with temperature ($T = 5$ K: $\frac{1}{2}\Gamma = 0.4$ meV, $T = 200$ K: $\frac{1}{2}\Gamma = 1.4$ meV) and is identified with life-time effects of single-ion relaxation processes of the Ce paramagnetic moments. The residual width of Lorentzian shape may be reminiscent of the Kondo effect ($T_K^N = 4$ K), although strongly modified by the presence of spin correlations.

$CePb_3$ has a simple cubic Cu_3Au structure with $a = 4.87$ Å. This compound has drawn much attention since Lin et al. (1985) reported that it exhibits, besides its HF properties and magnetic ordering at $T_N \simeq 1.1$ K, a magnetic-field-induced superconducting transition. The observation of superconductivity in $CePb_3$, however, turned out to be an impurity effect. The magnetic ordering was investigated in zero field on a multi-domain single crystal by Vettier et al. (1986). At $T = 30$ mK, well below $T_N = 1.16$ K, they observe magnetic Bragg peaks at eight incommensurate positions around the X-point $(0, 0, \frac{1}{2})$, corresponding to propagation vectors of the form $(\mu_1, \mu_2, \frac{1}{2})$ with $\mu_1 = 0.135$ and $\mu_2 = 0.058$. *Assuming* a single-q structure (although couplings between different components cannot be ruled out), they propose a sinusoidally modulated structure with a modulation amplitude of $m_0 = (0.55 \pm 0.10)\mu_B$ and the moments along the (001) direction. This type of structure is similar to the single-q modulated structure proposed by Barbara et al. (1977) for $CeAl_2$, which, however, was disproved by Forgan et al. (1990). As in $CeAl_2$, there were no higher-order harmonics observed in $CePb_3$, indicating a pure sine-wave modulation of the moments in a single-q structure and hence the presence of Kondo compensated zero moments at the nodes. For this structure, however, the moment directions (001) do not coincide with the axis of easy magnetization (111). It is therefore more likely that the magnetic structure of $CePb_3$ is of triple-q type rather than of single-q type (Welp 1988). Unfortunately, the validity of the assumption of a single-q structure was not yet checked in a diffraction experiment on a single-domain $CePb_3$ crystal. Neutron diffraction under pressure reveals a transition from the incommensurate structure at 0.7 GPa to a simple type-II structure, which corresponds to alternating ferromagnetic [111]-planes (Morin et al. 1988). T_N decreases to 0.6 K at 0.7 GPa, followed by an increase and a possible maximum around 1.3 GPa with $T_N \simeq 1$ K (Kirsch et al. 1992).

Inelastic neutron scattering experiments on the single crystal at $T = 200$ mK (Vettier et al. 1986) revealed a broadened $\Gamma_7 \rightarrow \Gamma_8$ transition at 1.5 THz (= 6.2 meV), in agreement with inelastic neutron data on a polycrystalline sample at $T = 4$ K [$\Delta = (5.8 \pm 0.2)$ meV with $\frac{1}{2}\Gamma = (1.9 \pm 0.2)$ meV] by Renker et al. (1987). From intensity considerations it was concluded that Γ_7 is the ground state. The temperature dependence of the Lorentzian quasi-elastic line width was reported by Balakrishnan et al. (1989) for temperatures between 2 and 128 K. It follows a $T^{1/2}$ law with a residual width of only 0.17 meV, yielding a Kondo temperature of $T_K^N = 2$ K. No evidence could be found for any Q-dependence (beyond the single-ion magnetic form factor) of the magnetic intensity over the range 0.2 to 2.4 $Å^{-1}$ at any investigated temperature. This is surprising in view of the results for the other ordering compounds, as discussed in this section, but it is in line with the single-ion Kondo

behavior of the whole series (Ce,La)Pb_3 from the very dilute limit to the full compound (Lin et al. 1987).

CeT_2Si_2 compounds crystallize in the tetragonal $ThCr_2Si_2$ structure. The magnetic ordering has been investigated with neutron diffraction for T = Au, Ag, Pd, and Rh by Grier et al. (1984), where also the lattice parameters can be found. All four compounds order antiferromagnetically with $T_N = 10$ K for T = Au, Ag, and Pd and $T_N = 39$ K for T = Rh and ordered moments of $1.29\mu_B$ (Au), $0.73\mu_B$ to $0.93\mu_B$ (Ag, assuming sine-wave or square-wave modulation), and $0.62\mu_B$ (Pd). Although the structures of these compounds are different in detail, they have in common that there are ferromagnetic planes with the moments perpendicular to the planes but along the direction of antiferromagnetic coupling or modulation. The fourth compound, $CeRh_2Si_2$, shows a second phase transition around 27 K and a different antiferromagnetic type of ordering (of which the low-temperature structure is not yet clear). The first three compounds (Au, Ag, Pd) show well-defined crystal field transitions (Severing et al. 1989a) with a doublet ground state sufficiently separated from the next excited doublet ($\geqslant 8.8$ meV) and total splittings of about 20 meV. The Lorentzian quasi-elastic line width follows above T_N roughly a $T^{1/2}$ law, with values for the line widths at 10 K increasing from Au (0.15 meV) to Ag (0.45 meV) to Pd (0.9 meV). This yields Kondo temperatures T_K^N of 1.7 K (Au), 5 K (Ag), and 10 K (Pd). It should be noted that for the first two compounds, where $T_K \ll T_N$, an additional quasi-elastic line with Gaussian shape was necessary to fit the measured spectra in the low-temperature region. These Gaussian contributions are also observed in the quasi-elastic response of other magnetically ordering polycrystalline Kondo compounds and can be associated with (critical) spin fluctuations which occur as precursors of the magnetic order. In the ordered state the spectra become inelastic with typically two peaked regions (in the energy range up to 3 meV), originating from the density of states of the acoustic and optic magnon branches (Grier et al. 1988, Severing et al. 1989b, Loidl et al. 1989). For $CeRh_2Si_2$ there exist only inelastic neutron data with low incident energies (Severing et al. 1989b). The quasi-elastic line width is around 3 to 4 meV above T_N and the magnetic intensity in the available energy window ($\leqslant 2$ meV) decreases rapidly below T_N. The experimental conditions did not allow to determine the CF level scheme nor to characterize the magnetic response in the ordered state.

CeT_2Ge_2 compounds have the same crystal structure as the CeT_2Si_2 compounds discussed above. There is a trend that the hybridization between the f-electrons and the conduction electrons is smaller for the Ge-based compounds when compared to the corresponding Si-based compounds. Direct comparison is possible for T = Au, Ag, and Cu because there exist inelastic neutron scattering data at least for the quasi-elastic response for all systems. If magnetic ordering effects [$T_N = 15$, 5, 4.1 K for CeT_2Ge_2 with T = Au, Ag, Cu, respectively (Böhm et al. 1988, Knopp et al. 1989)] are taken into account by an additional *Gaussian* quasi-elastic line above T_N and the Kondo relaxation effects by a *Lorentzian* quasi-elastic line, then the following results are obtained for the residual Lorentzian line widths: $\frac{1}{2}\Gamma \leqslant 0.1$ meV (Au, Loidl et al. 1989), 0.15 meV (Ag, Knopp et al. 1987, 1988b), and 0.35 meV (Cu, Knopp et al.

1989). This yields Kondo temperatures, T_K^N, of $\leqslant 1$, 2, and 4 K for the Ge-based compounds while $T_K^N = 1.7$, 5, and 8 K was obtained for the Si-based compounds (see previous discussion). This underlines the trend of increasing hybridization when going from Ge to Si and also from Au to Ag to Cu within both series. For $CeAg_2Ge_2$ and $CeCu_2Ge_2$ only one inelastic crystal field transition was observed at 11 meV and at 16.5 meV, respectively, and interpreted as a transition from a doublet ground state to an excited quasi-quartet (Knopp et al. 1987, 1989). From this proposed level scheme a moment of about $1.6\mu_B$ is expected for the ground state. This value is roughly observed for the ordered moment in $CeAg_2Ge_2$ (Knopp et al. 1988b), but only half this value is found in $CeCu_2Ge_2$ (Knopp et al. 1989). The reduction of the moment in the latter compound seems to be related to the observation of quasi-elastic intensity of Lorentzian shape well below T_N besides inelastic intensity from the magnon density of states (Knopp et al. 1989). This latter point, however, needs further clarification from single crystal data to separate intensity due to low-lying magnon modes from true quasi-eleastic scattering. Finally, we should mention a very interesting investigation of the evolution of the magnetic ordering when $CeCu_2Ge_2$ is alloyed with the non-ordering compound $CeNi_2Ge_2$ (Steglich et al. 1990). These alloying experiments are expected to cover the whole span from local-moment magnetism with ordered moments of the order of μ_B (although reduced by the Kondo effect) to heavy-fermion band magnetization with possibly very small ordered moments of the order of 10^{-1} to $10^{-2}\mu_B$ (Steglich 1991).

3.2.4. *Ferromagnetic ordering (CeAg, $CeSi_x$, $CeRu_2Ge_2$)*

CeAg has a cubic CsCl structure with $a = 3.77$ Å at room temperature and undergoes a martensitic phase transition into a tetragonal phase around 15 K (Ihrig and Methfessel 1976). A new interpretation of this phase transition was proposed later by Morin (1988) in terms of a quadrupolar ordering. The cubic crystal field ground state is Γ_8, well separated from the Γ_7 excited state at 23 meV (Frick et al. 1983). The tetragonal distortion or the quadrupolar ordering may split the Γ_8 quartet into two doublets. This splitting, however, was not observed directly. It must be rather small, if it exists at all. At $T_C = 5.3$ K CeAg orders ferromagnetically with a moment of only $0.7\mu_B$ [from magnetization data extrapolated to $T = 0$ K (Takke et al. 1981b)] or $0.8\mu_B$ [from neutron diffraction at $T = 1.8$ K (Schmitt et al. 1978)]. Single crystal magnetization data yield a somewhat larger saturation moment of $1.25\mu_B$ (Morin 1988). In any case, the experimentally observed magnetic moment is smaller than the value for a free Γ_8 ground state ($1.57\mu_B$). The reduction is thought to be due to the Kondo effect and not to the possible splitting of the Γ_8 ground state (Takke et al. 1981b). Application of pressure first increases the Curie temperature, T_C, towards a maximum ($T_{C,max} = 7.6$ K at $p = 0.7$ GPa) followed by a decrease and reaching the zero pressure value of T_C at $p \simeq 2.5$ GPa, as inferred from resistivity measurements (Eiling and Schilling 1981). Inelastic neutron scattering on a CeAg polycrystal under pressure reveals an increase of the residual quasi-elastic line width from 0.55 meV at zero pressure to 1.1 meV at 2.3 GPa (Frick et al. 1983). If other contributions to the line width can be neglected one obtains $T_K^N = 6$ K at zero

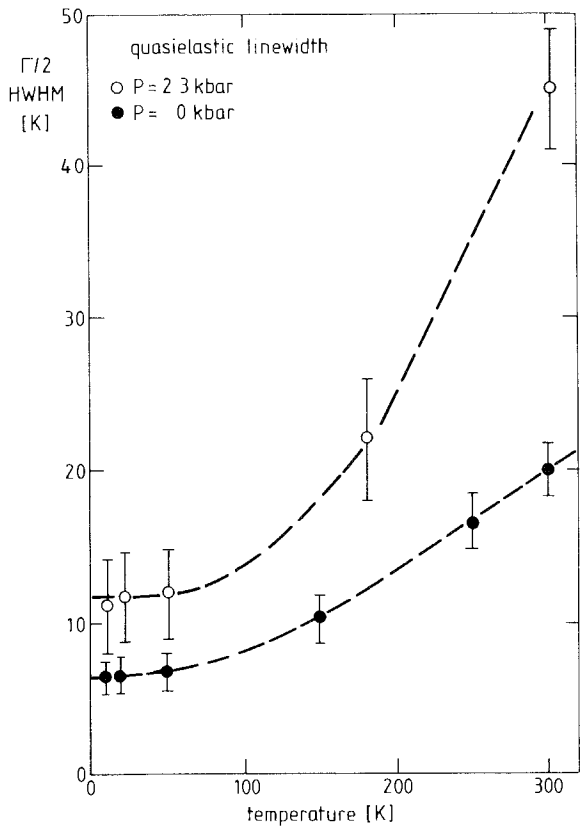

Fig. 59. Temperature dependence of the quasi-elastic line width of CeAg measured at normal pressure (solid circles) and at $p = 2.3$ GPa (open circles). Lines are only guides for the eye (Frick et al. 1983).

pressure and $T_K^N = 12$ K at 2.3 GPa. The Curie temperature is about the same for both pressures and should therefore not have a large influence on the line width. The temperature dependence of the quasi-elastic line width for both pressures is shown in fig. 59. It differs from the usual behavior of Kondo systems ($T^{1/2}$ law or linear): a flat portion at low temperature is followed by a steep increase at elevated temperatures above 100 K. The reason for this different behavior is not yet clear. Unfortunately, the relaxed energy resolution (D7) does not allow one to identify and to separate different contributions with Gaussian or Lorentzian shape to the quasi-elastic response.

$CeSi_x$ crystallizes in a tetragonal α-$ThSi_2$-type structure for $1.8 \leqslant x \simeq 2$ and in an orthorhombic α-$GdSi_2$-type structure for $1.6 < x < 1.8$ [see Kohgi et al. (1990a) and references therein]. For $1.85 < x \simeq 2$ the compound shows HF behavior with no magnetic ordering down to 0.1 K while for $x < 1.85$ it becomes ferromagnetic with Curie temperature around 10 K. The Kondo mechanism is also effective in the ferromagnetically ordered regime, leading to finite magnon line widths [$x = 1.7$, Hippert et al. (1988); $x = 1.8$, Kohgi et al. (1987)] and reduced ordered moments ($0.45\mu_B$). There is a smooth variation of the crystal field splitting over the whole series. It increases monotonously from $CeSi_{1.7}$ (0–15–28 meV) to $CeSi_2$

(0–25–48 meV) (Kohgi et al. 1990b, 1991, Galera et al. 1989). The residual quasi-elastic line width of the non-ordering $CeSi_x$ compounds also increases with x [$x = 1.85$: $\frac{1}{2}\Gamma_0 = 1.7$ meV, $x \simeq 2$: $\frac{1}{2}\Gamma_0 = 3.5$ meV (Galera et al. 1989)], yielding Kondo temperatures, T_K^N, of 19 and 40 K, respectively. The increase of T_K is in line with the decrease of the linear coefficient, γ, of the specific heat from 234 mJ/K^2 mol for $x = 1.85$ to 104 mJ/K^2 mol for $x \simeq 2$ (Yashima et al. 1982). All conclusions concerning the line widths (magnons, quasi-elastic, CF transitions), however, should be critically looked at, because it is rather difficult to separate the contribution from the Kondo effect from lattice-disorder effects, even if similar experiments on corresponding $CeGe_x$ compounds are used for comparison [magnons: Hippert et al. (1988); CF: Kohgi et al. (1990b), Lahiouel et al. (1987)]. There are also doubts whether stoichiometric $CeSi_2$ exists at all. Dhar et al. (1987) give an upper limit of $x \simeq 1.95$.

$CeRu_2Ge_2$ belongs to the large group of CeT_2M_2 compounds with a $ThCr_2Si_2$-type structure. But unlike the other members, which are antiferromagnets or non-ordering HF and VF compounds, $CeRu_2Ge_2$ orders ferromagnetically with $T_C = 7.5$ K (Böhm et al. 1988) (note: at 8.5 K there is a second transition of yet unknown origin). The low-temperature specific heat (Böhm et al. 1988) contains a linear T term with a rather low γ-value of only 20 mJ/K^2 mol and a $T^{3/2}\exp(-\Delta/T)$ term indicative of ferromagnetic magnons with a gap ($\Delta = 10$ K). From the high-temperature specific heat Felten et al. (1987) propose a CF level scheme 0–43–65 meV. Inelastic neutron scattering has only been performed with low incident-neutron energies and was thus not able to determine the crystal field splitting. Loidl et al. (1989) report the temperature dependence of the quasi-elastic Lorentzian line width. It shows a *linear* temperature dependence with small values, similar to the antiferromagnet $CeAu_2Ge_2$. Also the residual width is small and resolution-limited ($\frac{1}{2}\Gamma_0 < 0.1$ meV). From this: $T_K^N < 1$ K. It therefore seems that the low-temperature properties of $CeRu_2Ge_2$ are dominated by RKKY-type interactions and not by Kondo fluctuations.

3.3. *Ytterbium-based systems*

Making a particle–hole inversion one can connect the properties of Ce-based VF compounds with those of Yb-based VF compounds. Ce^{3+} ($4f^1$) and Yb^{3+} ($4f^1 = 4f^{14-1}$) have a magnetic ground state with one electron or one hole in the f-shell, and Ce^{4+} and Yb^{2+} have no f-electron or a magnetic-inactive filled f-shell, respectively. The average valence in VF Ce compounds, however, never covers the full range from +3 to +4 (3.3 being the maximum, see section 3.1.1) while it does so for Yb compounds (from +3 to +2, of course). Also the magnetic ground state multiplets of Ce^{3+} and Yb^{3+} are not identical due to Hund's rule for the coupling of L and S to J ($J = |L - S|$ for the light rare earths and $J = |L + S|$ for the heavy rare earths). Thus for Ce^{3+} the ground state multiplet is $^2F_{5/2}$ ($N = 6$) with the excited $^2F_{7/2}$ state at about 280 meV while for Yb^{3+} the ground state multiplet is $^2F_{7/2}$ ($N = 8$) with the excited $^2F_{5/2}$ at about 1300 meV.

The number of Yb-based systems investigated by neutron scattering is smaller than that of the Ce-based systems. Also the division into VF and HF Yb-based

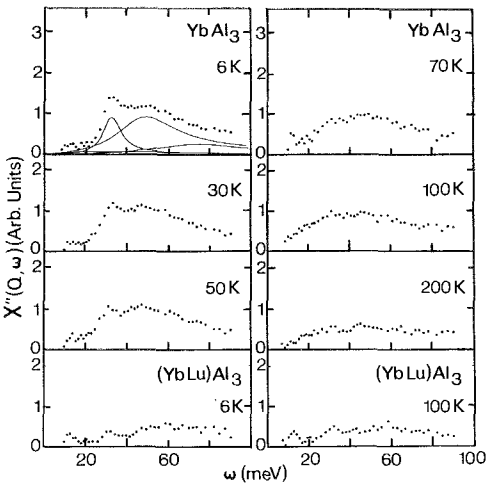

Fig. 60. Magnetic spectral response of $YbAl_3$ and $Yb_{0.5}Lu_{0.5}Al_3$ at various temperatures for $Q = 1.3$ Å^{-1}, corrected for the Yb^{3+} form factor. The continuous curves in the 6 K spectrum are a decomposition of the response into a weak, broad quasi-elastic line and three inclastic lines (Murani 1985a, b).

systems is not as straightforward as for the Ce-based systems. In most cases CF and VF effects are of comparable strength in Yb systems, and therefore the interpretation of the magnetic response as seen by neutron scattering is often controversial.

3.3.1. *$YbAl_3$*

$YbAl_3$ has a cubic Cu_3Au structure with $a = 4.20$ Å. The lattice parameter, if compared with the neighboring $TmAl_3$ and $LuAl_3$, indicates that Yb is more or less trivalent in this compound (Havinga et al. 1973). Walter et al. (1991) derive a somewhat smaller average valence of (2.85 ± 0.1) when considering a variety of valence dependent properties. $YbAl_3$ does not order magnetically but seems to become superconducting at $T_c = 0.94$ K (Havinga et al. 1970). The superconductivity, however, is believed to be caused by impurity phases and not by $YbAl_3$ itself, as mentioned in footnote 13 in the paper by Walter et al. (1991). The temperature dependence of the susceptibility (with maximum around 120 K) and of the resistivity (with steep slope around 120 K) resemble those of the VF compounds $CePd_3$ and $CeSn_3$ (Havinga et al. 1973).

Inelastic neutron scattering experiments on a polycrystalline sample of $YbAl_3$ were reported by Murani (1985a, b) employing unpolarized neutrons with incident energies of 50 and 115 meV. Figure 60 shows the magnetic spectral response $\chi''(\omega)$ of $YbAl_3$ at various temperatures between 6 and 200 K and, for comparison, of the dilute sample $Yb_{0.5}Lu_{0.5}Al_3$ at 6 and 100 K. The phonon scattering (exhibiting a strong peak at 13 meV and two weaker structures at 22 and 33 meV) has been subtracted from the original data in the usual way. The shape of the magnetic response of $YbAl_3$ at elevated temperatures (70 to 200 K) can fairly well be described by a broad quasi-elastic line centered at zero energy transfer with a half width of (40 ± 10) meV. As in the case of the VF-Ce compounds, there is a drastic change of the shape of the magnetic response for decreasing temperatures. The intensity in the low-energy region ($\leqslant 30$ meV) is reduced and an inelastic feature develops. At $T = 6$ K it seems that

there is a gap in the magnetic excitation spectrum with a resolution limited step-like increase of intensity at 32 meV and a rather smooth decrease of intensity towards higher energies. In the absence of theoretical models Murani (1985a, b) has decomposed the low-temperature spectral response into a very weak, broad quasi-elastic component and three inelastic Lorentzians at different finite energies and with different widths (32 meV, sharp; 46 meV, broad; 70 meV, very broad; see solid lines in fig. 60). In contrast to $YbAl_3$, the shape of the magnetic response of the dilute sample $Yb_{0.5}Lu_{0.5}Al_3$ does not show any change with temperature. At $T = 6$ and 100 K it can be described by a broad quasi-elastic line with an even larger width than the high-temperature spectra of $YbAl_3$. This indicates that the gap in $YbAl_3$ at low temperatures must be connected with collective properties of the well-ordered lattice of the full compound. On the other hand, the existence of the gap in $YbAl_3$ has been questioned by Walter et al. (1991), who performed an inelastic neutron investigation with cold neutrons. Instead, these authors claim to have observed a Kondo resonance in $YbAl_3$ at 18 meV (if extrapolated to $T = 0$). Unfortunately, the evidence for the 18 meV excitation is only indirect. Because of the low incident energy of the cold neutrons ($E_0 = 3$ meV, IN6) the relevant energy region can only be covered at elevated temperatures ($T \geqslant 50$ K) and the response at low temperatures can only be *extrapolated* from these high-temperature data. If there is magnetic intensity in the gap below 30 meV, it must be only a small fraction of the total magnetic scattering intensity of $YbAl_3$, as can be inferred from fig. 60.

Preliminary experiments on the $^2F_{7/2} \rightarrow {}^2F_{5/2}$ spin–orbit transition by Osborn and Goremychkin (1991) locate this transition at (1374 ± 12) meV and find an unusually large FWHM of 340 meV. The large width is taken as evidence for the strong hybridization of the f-shell with the conduction band.

3.3.2. *$YbCu_2Si_2$ and $YbPd_2Si_2$*

$YbCu_2Si_2$ [valence 2.9 (Röhler 1987), $\gamma = 135$ mJ/K^2 mol (Sales and Viswanathan 1976)] was the first Yb-based VF compound to be investigated by inelastic neutron scattering (Holland-Moritz et al. 1978). It showed the typical broad, nearly temperature-independent response which was first analyzed with a quasi-elastic line only, with width around 6–10 meV. Subsequent measurements with different incident neutron energies and a more careful phonon subtraction led to inconsistencies if only a quasi-elastic line was used to fit the magnetic part of the spectra (Holland-Moritz 1982). Better consistency for all data was obtained assuming a crystal field splitting of the $J = \frac{7}{2}$ ground-state multiplet of Yb^{3+} into four doublets. This is expected for the tetragonal symmetry of the Yb ions in this crystal structure ($ThCr_2Si_2$-type, $a = 3.92$ Å, $c = 9.99$ Å (Rogl 1984)). The excited doublets were placed at 18, 23, and 31 meV. The low-energy part was fitted with a quasi-elastic line of width 4–5 meV in the temperature range from 5 to 300 K (Holland-Moritz et al. 1982). The spectra at $T = 5$ K, taken with $E_0 = 12.5$ and 51.5 meV, are shown in fig. 61. Unfortunately, the magnetic part of the high-energy spectrum is considerably masked by phonon and multi-phonon scattering. No attempts were made at that time to fit the low-energy part of the magnetic response (<10 meV) with an inelastic line instead of a quasi-elastic line.

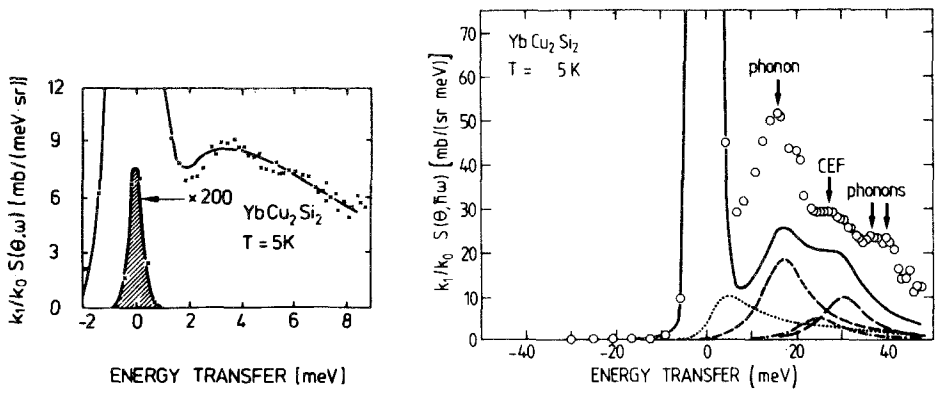

Fig. 61. Inelastic neutron spectra of polycrystalline $YbCu_2Si_2$ at $T = 5$ K taken with $E_0 = 12.5$ meV (left) and 51.5 meV (right) on IN4. The solid line is the magnetic part obtained from a complete fit (magnetic plus phonon) of the measured spectrum. Right spectrum: the quasi-elastic (dotted line) and the three crystal field transitions (dashed lines) are shown separately (Holland-Moritz et al. 1978, 1982).

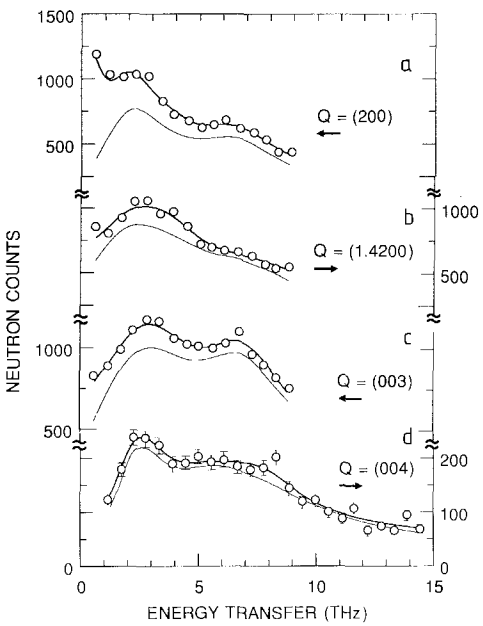

Fig. 62. Inelastic neutron scattering cross section of single crystal $YbCu_2Si_2$ at $T = 4.3$ K and at four different wavevector transfers (IN8). Thin line is the magnetic contribution and the thick line is the sum of the magnetic and phonon parts, fitted to the data. Note the different scale for (d). The count rate is lower because a different configuration was used to access the higher energy transfers (Currat et al. 1989).

An inelastic neutron scattering study on a *single crystal* of $YbCu_2Si_2$ was performed at $T = 4.3$ K by Currat et al. (1989) on a triple-axis instrument (IN8, ILL) covering a range of energy transfers between 8 and 50 meV. The results are shown in fig. 62 for different $\boldsymbol{Q}$-vectors along the two principal directions *a* and *c*. The magnetic part of the response is indicated by the thin lines under the data points (the thick lines through the data points are the sum of magnetic and phonon scattering, the latter being obtained by scaling of data measured at equivalent lattice vectors with high

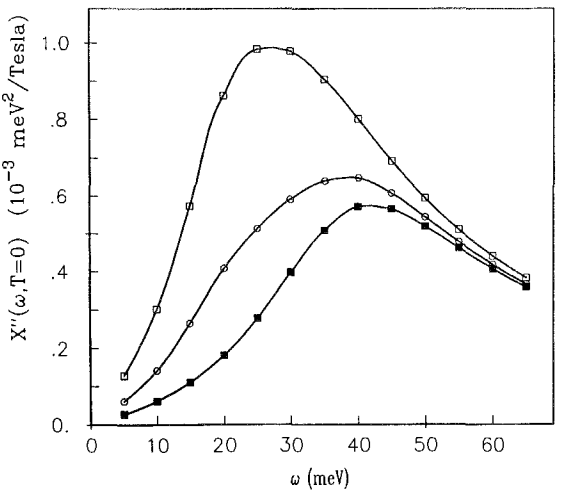

Fig. 63. Calculation of $\chi''(\omega, T=0)$ for $YbCu_2Si_2$. Open squares: $\chi''_{\parallel}(\omega)$, solid squares: $\chi''_{\perp}(\omega)$, open circles: $\chi''_{av}(\omega) = \frac{1}{3}(\chi''_{\parallel} + 2\chi''_{\perp})$. Due to the large value of $T_0 = 200$ K used in the calculation no crystal field transitions are seen (Zwicknagl et al. 1990).

Q-values). Although the static susceptibility of $YbCu_2Si_2$ is rather anisotropic at low temperatures [$\chi_{\parallel} : \chi_{\perp} \simeq 3:1$ (Shimizu et al. 1987)] the magnetic response for the measured $\boldsymbol{Q}$-vectors is only slightly different, exhibiting two broad inelastic peaks around 12–16 and 30 meV. This supports the interpretation of Holland-Moritz et al. (1982) of the powder spectra in fig. 61 in terms of a characteristic temperature of 50 K (=quasi-elastic line width) for the ground-state doublet (this region is not covered by the single crystal experiment) and strong transition matrix elements to the first and third excited doublets at 18 and 32 meV (corresponding to the peaks around 12–16 and 30 meV in the single crystal data).

This interpretation of the magnetic response is, however, in contrast to the assumptions made by Zevin et al. (1988a, b) and by Rasul and Schlottmann (1989a, b) to explain the unusual temperature dependence of the 4f quadrupole moment in $YbCu_2Si_2$ measured using the Mössbauer effect (Bonville and Hodges 1985, Tomala et al. 1990). These theories assume a considerably larger characteristic temperature ($\simeq 200$ K) and a crystal field level scheme with pure $|\pm J_z\rangle$ states, with $|\pm\frac{7}{2}\rangle$ being lowest. In the absence of spin and charge fluctuations this would yield only one crystal field transition with a non-zero matrix element for neutron scattering at low temperatures, namely from the ground-state doublet to the first excited doublet $|\pm\frac{5}{2}\rangle$, at 4 meV (Rasul and Schlottmann 1989a, b) or at 10 meV (Zevin et al. 1988a, b). Zwicknagl et al. (1990) calculated the magnetic response including crystal field *and* strong spin and charge fluctuations. Their results for $\chi''_{\parallel}(\omega)$, $\chi''_{\perp}(\omega)$, and $\chi''_{av}(\omega) = \frac{1}{3}(\chi''_{\parallel} + 2\chi''_{\perp})$ are shown in fig. 63. In this model the two broad inelastic peaks observed in the neutron scattering experiments are *not* related to crystal field transitions but to electronic transitions due to the assumed large characteristic energy (temperature) of this VF system. The crystal field anisotropy is reflected in the different position of the broad peak for $\chi''_{\parallel}(\omega)$ and $\chi''_{\perp}(\omega)$. This model, however, does not explain the low-energy response ($\lesssim 6$ meV, see fig. 61) and the presence of two broad inelastic peaks in the single crystal spectra for all $\boldsymbol{Q}$-vectors (see fig. 62).

$YbPd_2Si_2$ exhibits similar physical properties as $YbCu_2Si_2$: $ThCr_2Si_2$ structure [$a = 4.09$ Å, $c = 9.87$ Å (Rogl 1984)], a valence around 2.9 (Röhler 1987), a maximum in the susceptibility around 40 K, and a large specific heat $\gamma = 203$ mJ/K^2 mol. From specific heat and NMR measurements by Besnus et al. (1988) and from Mössbauer effect measurements by Bonville et al. (1990) it was concluded that $YdPd_2Si_2$ has a characteristic temperature of about 65 K, involving, however, only the two low-lying doublets ($N = 4$) which are well separated in energy from the two other doublets. No specific values for the splittings are given except that the splitting between the two low-lying doublets is small compared to 65 K while the separation between the quasi-quartet ground state and the remaining two excited doublets is large compared to 65 K. Inelastic neutron scattering experiments are reported by Weber et al. (1989b) for polycrystalline $YbPd_2Si_2$ in the temperature range from 1.5 to 250 K. For temperatures between 100 and 250 K the VF-typical broad quasi-elastic response with width 11–13 meV is observed. At $T \simeq 50$ K an inelastic excitation at 21 meV becomes visible; its intensity increases with decreasing temperature. In the same temperature range ($T < 50$ K) the quasi-elastic line width decreases rapidly and at $T = 5$ K the quasi-elastic response is transformed to a second *inelastic* feature at about 4.7 meV. The width of this inelastic low-energy excitation fits well to the temperature dependence of the quasi-elastic line width for $T > 5$ K. Weber et al. (1989b) note that a simple explanation of their observations on the basis of a crystal field model is not possible. They speculate that the existence of a high-energy and of a low-energy excitation may be due to a different relaxation behavior along different crystallographic axes. This can only be checked by an experiment on a single crystal. We want to offer here, however, another explanation on the ground of the aforementioned description given by Besnus et al. (1988) and Bonville et al. (1990, 1991). Then the high-energy excitation (21 meV) is a crystal field transition from the quasi-quartet ground state to one or both of the high-lying doublets. It is visible in the experiment because the transition energy (21 meV) is larger than the characteristic energy (65 K $\approx$ 6 meV). The transition energies within the quasi-quartet are smaller than the characteristic energy, leading to the observation of a quasi-elastic line with residual width (5 meV) of the order of the characteristic energy. Finally, at low temperatures ($T = 5$ K) the quasi-elastic line transforms into an inelastic feature, although involving only $N = 4$ states of the total $N = 8$ states of Yb^{3+}. For an interpretation of the inelastic neutron spectra of $YbPd_2Si_2$ (and $YbAgCu_4$) see also Polatsek and Bonville (1992).

3.3.3. *YbCuAl*

YbCuAl is also one of the earliest VF compounds studied with inelastic neutron scattering and whose neutron data were compared with NMR data (Mattens et al. 1980, MacLaughlin et al. 1979, Murani et al. 1985). It crystallizes in a hexagonal Fe_2P-type structure with $a = 6.92$ Å and $c = 4.00$ Å. The valence found from the lattice parameters is close to 3, from L_{III} absorption spectra a value of 2.95 is obtained. The susceptibility has a maximum around 30 K and the specific heat, γ, is 260 mJ/K^2 mol. YbCuAl shows the typical broad quasi-elastic line with a width of 6–10 meV in the temperature range from 30 to 250 K, directly obtained from the neutron data

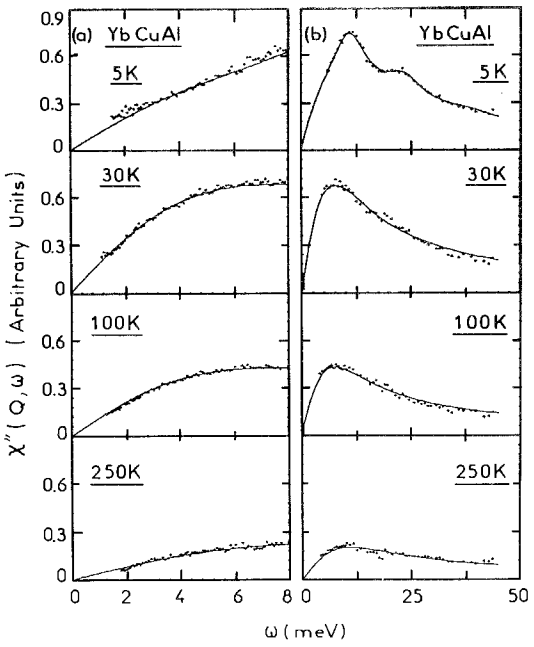

Fig. 64. Imaginary part of the magnetic susceptibility, $\chi''(\omega)$, for polycrystalline YbCuAl obtained after phonon correction at different temperatures and for $E_0 =$ 12.6 meV (left) and 50.7 meV (right). The solid lines through the data points represent fits with quasi-elastic Lorentzians (plus two inelastic Lorentzians at $T = 5$ K) (Murani et al. 1985).

and deduced from NMR data assuming relaxational behavior and the absence of correlations. Again, at low temperatures ($T = 5$ K) inelastic features seem to appear in the magnetic response, yet on top of a still present broad quasi-elastic response (fig. 64). No simple explanation of the inelastic features could be given, a crystal field description has been ruled out (Murani et al. 1985).

From the analysis of Mössbauer effect and susceptibility data Bonville et al. (1990) estimate a characteristic temperature of 90 K and a rather small total crystal field splitting of only 20 K. Adopting these values it is tempting to relate the broad inelastic features at 10 and 23 meV in the magnetic response of YbCuAl at $T = 5$ K to the two broad maxima for $\chi''_{\parallel}(\omega)$ and $\chi''_{\perp}(\omega)$ in the model of Zwicknagl et al. (1990) as originally calculated for $YbCu_2Si_2$ (see fig. 63). We should, however, note that there is some ambiguity about the origin of the two broad peaks in the neutron scattering data since their position coincides also with sharp maxima in the phonon density of states. Yet the very detailed analysis of Murani et al. (1985) seems to prove their magnetic origin. Unfortunately, no single crystals of this compound are available to investigate the direction dependence of the magnetic response which is predicted in the model of Zwicknagl et al. (1990).

Preliminary experiments on diluted samples $Yb_{1-x}Y_xCuAl$ with $x = 0.2$ and 0.7 still show the inelastic peaks below $T = 30$ K (Murani 1987b).

3.3.4. *$YbXCu_4$ (X = Ag, Au, Pd, and In)*

The $YbXCu_4$ compounds crystallize in the cubic $AuBe_5$ structure, Strukturbericht notation C15b. In this structure the Yb and X ions form well ordered sub-lattices.

The local symmetry of the Yb ion is cubic and the Yb–Yb distance is rather large and of the order of 5 Å. The compounds with X = Au and Pd appear to order antiferromagnetically at 0.6 and 0.8 K, respectively, whereas $YbAgCu_4$ does not show any sign of magnetic order down to 0.45 K (Rossel et al. 1987). $YbInCu_4$ undergoes a first-order valence transition around 40–50 K with no sign of magnetic order at low temperatures (Felner et al. 1987, Yoshimura et al. 1988, Kojima et al. 1989). All compounds are in a nearly trivalent state at room temperature. While the compounds with X = Ag, Au, and Pd stay trivalent down to low temperatures, the valence transition in $YbInCu_4$ yields at $T = 45$ K a sudden change in valence by about 0.1 f-electron to about 2.9.

Inelastic neutron scattering experiments on polycrystalline samples using time-of-flight techniques with incident energies between 3 and 67 meV have been reported for the compounds with X = Ag, Au, and Pd by Severing et al. (1990a) and for X = In, covering the valence transition, by Severing at al. (1990b).

The results for $YbAuCu_4$ and $YbPdCu_4$ resemble those obtained for Ce-based HF or Kondo lattices, which show magnetic order at low temperatures. Inelastic crystal field transitions are well separated from quasi-elastic scattering. For $YbAuCu_4$ a crystal field level scheme is deduced from the neutron data. The level sequence is Γ_7–Γ_8 (3.89 meV)–Γ_6 (6.88 meV) and the crystal field parameters in LLW notation are $W = -(0.225 \pm 0.004)$ meV and $x = -(0.945 \pm 0.005)$. The spectra of $YbPdCu_4$ are also interpreted in a crystal field scheme, but the inelastic transitions are considerably broader while the quasi-elastic line is even narrower than for $YbAuCu_4$. The unusual width of the inelastic transitions is explained by the presence of a large amount of *disordered* $Yb_{1-x}Pd_{1+x}Cu_4$ phase, Strukturbericht notation C15, which does not exhibit the cubic site symmetry of the Yb ions, as in the ordered C15b phase. The narrower quasi-elastic line width reflects the weaker hybridization in the compound with X = Pd with respect to X = Au. The overall crystal field splitting is of the same order for both compounds.

The magnetic response of the third compound, $YbAgCu_4$, is markedly different. Although an interpretation of the spectra in terms of crystal field theory cannot be ruled out, it would require a much larger overall splitting for $YbAgCu_4$ than for the other two compounds. This is just opposite to the trend observed in the isostructural, stable-moment compounds $ErXCu_4$, where the overall crystal field splitting *decreases* in the sequence X = Pd → Au → Ag. Thus, Severing et al. (1990a) have put forward an interpretation of the temperature dependence of the magnetic response of $YbAgCu_4$ in terms of theories describing the magnetic relaxation behavior of unstable 4f moments. Figure 65 shows the spectra of $YbAgCu_4$ at $T = 5$ K measured with neutrons of incident energies of 12.5 and 50 meV and fitted with the analytic function for $\chi''(\omega)$ in the $T \to 0$ limit given by Kuramoto and Müller-Hartmann (eq. 28). The variables in the function are α/π, the ratio of the 4f occupancy to the degeneracy of the ground state (n_f/N), and the characteristic energy parameter $\tilde{\varepsilon}_f$ (the position of the renormalized 4f level relative to the Fermi level). The low-energy part of the spectrum (< 6 meV) was excluded from the fitting range, since, as Kuramoto and Müller-Hartmann point out, their analytic function *underestimates* the real spectrum by as much as 20% for $\omega \to 0$. The resulting fit parameters are $\alpha/\pi = 0.147$ (±15%)

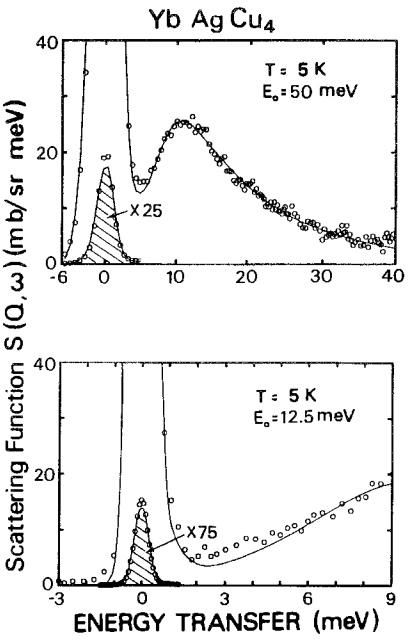

Fig. 65. Inelastic neutron spectra of $YbAgCu_4$, at $T = 5$ K with $E_0 = 50$ and 12.5 meV (IN4). The spectra are fitted with the analytic function for $\chi''(\omega)$ by Kuramoto and Müller-Hartmann (eq. 28). Elastic incoherent scattering is marked by the hatched area (Severing et al. 1990a).

and $\tilde{\varepsilon}_f/k_B = 96$ K ($\pm 8\%$). Assuming $n_f = 1$, a value of $N = 6.8 \pm 1$ for the ground-state degeneracy is obtained. Within the uncertainty, the value of N is consistent with the full degeneracy of the $2J + 1 = 8$ of an Yb^{3+} ion. This indicates that the overall crystal field splitting is small compared to the characteristic energy, in agreement with the aforementioned trend for the crystal field splittings in this series. Hence, crystal field transitions are not resolved in the magnetic spectra of $YbAgCu_4$.

For increasing temperatures the inelastic feature of the magnetic response of $YbAgCu_4$ merges into a broad quasi-elastic line around $T \approx 75$ K. Figure 66 shows the temperature dependence of the inelastic ($T < 75$ K) and of the quasi-elastic ($T \geqslant 75$ K) line width of $YbAgCu_4$ and of the quasi-elastic line width of the more stable-moment compounds $YbAuCu_4$ and $YbPdCu_4$. A forced fit of the spectra of $YbAgCu_4$ for $T < 75$ K with a quasi-elastic line yields increasing line widths for decreasing temperatures (filled data points in fig. 66). For $T \geqslant 75$ K the quasi-elastic line width increases slightly with temperature. This produces a minimum of the line width at a temperature $T_0 \approx 75$ K, which is interpreted in the theory of Bickers et al. (1987) as a characteristic temperature equal to the position of the Kondo resonance measured from the Fermi level. Employing different (single-ion) theories for the interpretation of the inelastic neutron data including susceptibility and specific-heat data, yields characteristic temperatures (energies) around 100 K for $YbAgCu_4$, as collected in table III of the paper of Severing et al. (1990a). The relatively good agreement between the variously determined values for the characteristic temperature suggests that the observed magnetic response of $YbAgCu_4$ can be understood in terms of an intermediate-valent, single-ion model. The quasi-elastic line width of the magnetically ordering compounds $YbAuCu_4$ and $YbPdCu_4$ follows roughly a $T^{1/2}$

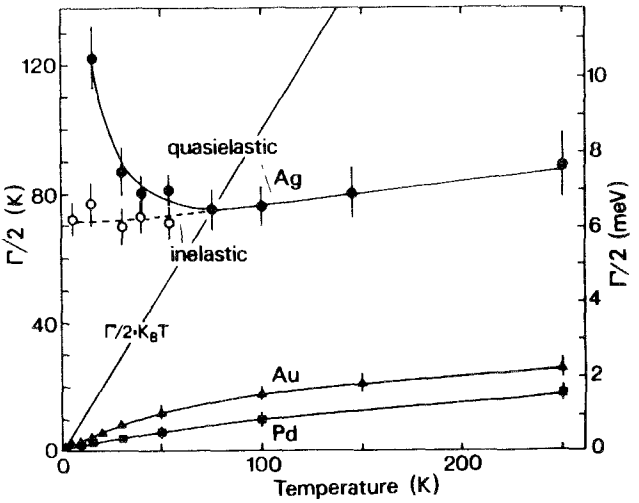

Fig. 66. Temperature dependence of the quasi-elastic Lorentzian line width of $YbPdCu_4$ (solid squares), $YbAuCu_4$ (solid triangles), and $YbAgCu_4$ (solid circles). The open circles represent the width of an alternative fit of the $YbAgCu_4$ data below 75 K with an inelastic Lorentzian (Severing et al. 1990a).

power law. The characteristic (Kondo) temperatures are much smaller than for $YbAgCu_4$ and of order 1 K, a value of the same order as the RKKY interactions in these compounds.

$YbInCu_4$ exhibits the features of both types of $YbXCu_4$ compounds discussed above:

- an intermediate-valent behavior similar to $YbAgCu_4$ below T_v, the valence-transition temperature, and
- a behavior similar to $YbAuCu_4$ and $YbPdCu_4$ for temperatures above T_v (Severing et al. 1990b).

For comparison, also the magnetic response of $YbInNi_4$ has been studied. The spectra of $YbInNi_4$, measured between 5 and 50 K, can be analyzed in terms of an ordinary crystal field splitting with a level sequence 0–2.9–4.1 meV. Quasi-elastic and inelastic lines are well separated. This is also the case for the spectra of $YbInCu_4$ at $T = 50$ and 75 K (above T_v). A similar level scheme is deduced with the level sequence 0–3.2–3.8 meV. Below T_v, however, the spectra of $YbInCu_4$ are completely different. In the intermediate-valent phase the crystal field transitions and the quasi-elastic scattering are absent (except for a small amount due to magnetic impurities) and, instead, a broad inelastic line centered around 40 meV and with a width of 18 meV appears. Measurements at various temperatures in the intermediate-valent phase (5, 20, 35 K) show that the magnetic signal is nearly temperature independent in this state.

3.3.5. *$YbBe_{13}$, YbPd, and Yb_3Pd_4*

These three Yb compounds have in common that they order magnetically at low temperatures ($T_N = 1.28$, 0.5, and 3.1 K for $YbBe_{13}$, YbPd, and Yb_3Pd_4, respectively) and that they show well-defined crystal field splittings, as deduced from inelastic neutron scattering on polycrystalline samples by Walter et al. (1985) and by Walter

and Wohlleben (1987). The behavior of these Yb compounds is similar to the behavior of Ce-based Kondo and HF compounds.

$YbBe_{13}$ has a cubic $NaZn_{13}$ structure (as $CeBe_{13}$) with $a = 10.195$ Å. The crystal field level scheme is Γ_7–Γ_8 (3.2 meV)–Γ_6 (4.4 meV), corresponding to LLW parameters $W = 0.154$ meV and $x = 0.911$ (Walter et al. 1985). The quasi-elastic line width shows a linear temperature dependence with a residual width of only 0.2 meV (2 K). The absolute values and the slope ($\approx$1 meV/300 K) of the quasi-elastic line width, although being small on the scale of non-ordering Yb-based VF compounds, are anomalously large if compared to the stable-moment $TbBe_{13}$ compound (slope <0.1 meV/300 K). Walter et al. (1985) take this as an indication of the presence of hybridization of 4f and 5d electrons in $YbBe_{13}$, as in the case of Ce-based Kondo compounds with valence very near to +3. Near the magnetic phase transition the quasi-elastic line is more of Gaussian than of Lorentzian ($T \geqslant 39$ K) shape.

A similar behavior as for $YbBe_{13}$ is observed for cubic YbPd (CsCl structure, $a =$ 3.44 Å) and trigonal Yb_3Pd_4 (Pb_3Pd_4 structure, $a = 12.917$ Å, $c = 5.664$ Å) by Walter and Wohlleben (1987). Yet, surprisingly, for both compounds nearly the same (cubic) level scheme is deduced from the neutron data [Γ_8–Γ_7 (4–5 meV)–Γ_6 (12–13 meV)]. Unfortunately, all results are obtained only with low-energy neutrons (3 meV) and on (partially) multi-phase samples. We therefore hesitate to believe that the authors have really observed some novel features, like two different quasi-elastic line widths or "magnetophonons", unless these are confirmed by new experiments. Also the interpretation of part of the data in terms of "selection rules" for matrix elements between the non-magnetic $4f^{14}$ configuration and the various crystal field states of the $4f^{13}$ configuration has been questioned on theoretical grounds (Schmidt and Müller-Hartmann 1989).

3.3.6. *YbX (X = N, P, As, and Sb)*

YbX compounds with X = N, P, As, and Sb have a cubic rocksalt structure and a nearly integral +3 valence for the Yb ions. Details of their physical properties depend on sample preparation and stoichiometry (see, e.g. Dönni et al. 1990a). Their main properties are:

- a large crystal field splitting with the level sequence Γ_6–Γ_8–Γ_7 and the first excited state at least 13 meV above the ground state,
- antiferromagnetic order with small Néel temperatures ($\leqslant$1 K), being much lower than expected from the RKKY exchange interaction, and
- reduced ordered magnetic moments ($\leqslant 0.9\mu_B$), much lower than expected for a Γ_6 ground state ($1.33\mu_B$)

The crystal field splitting has been investigated by two groups [Dönni et al. (1990a–c) for X = N, P and Sb and by Kohgi et al. (1990c) for X = N, P, and As]. They agree on the level sequence Γ_6–Γ_8–Γ_7, but disagree on the position of the exited Γ_7 level and on the interpretation of the resulting crystal field parameters. For YbN, Dönni et al. (1990b) and Kohgi et al. (1990c) observe a 6–7 meV *additional splitting* of the $\Gamma_6 \rightarrow \Gamma_8$ transition with a stronger peak at 30 (31.7) meV and a weaker peak at 37 (38) meV. The temperature dependence of this unusual splitting is investigated in more detail by Ohoyama et al. (1992). Returning to the discussion of the level

scheme, we have to mention that there is no matrix element for the $\Gamma_6 \rightarrow \Gamma_7$ transition, so that the position of the Γ_7 level can only be obtained by the observation of the $\Gamma_8 \rightarrow \Gamma_7$ transition at elevated temperatures when the Γ_8 level is sufficiently populated. Dönni et al. (1990b) place the Γ_7 level at 81 meV while Kohgi et al. (1990c) place it at 50 meV due to differences in the interpretation of the high-temperature spectra (phonon scattering). Similarly for YbP, Dönni et al. (1990a) give Γ_6–Γ_8 (19 meV)–Γ_7 (43 meV) while Kohgi et al. (1990c) give Γ_6–Γ_8 (20 meV)–Γ_7 (35 meV) For YbAs there are only published data by Kohgi et al. (1990c), who propose a level sequence Γ_6–Γ_8 (18 meV)–Γ_7 (42 meV). Finally, for YbSb there are only data by Dönni et al. (1990c). They again observe a splitting of the $\Gamma_6 \rightarrow \Gamma_8$ transition with a stronger peak at 13 meV and a weaker peak at 18 meV and place the Γ_7 level at 39 meV. The splitting of the $\Gamma_6 \rightarrow \Gamma_8$ transition in YbN and YbSb may be of similar origin as that observed in $CeAl_2$ (crystal field–phonon interaction).

In any case the ground-state Γ_6 doublet is well separated from the first excited Γ_8 quartet. The magnetic moment connected with Γ_6 is $1.33\mu_B$. In contrast to this expectation the ordered moments of YbN, YbP, and YbAs as deduced from neutron diffraction by Dönni et al. (1990c) are only $0.39\mu_B$, $1.03\mu_B$, and $0.86\mu_B$. YbSb does not show magnetic ordering down to 7 mK. Slightly different results are obtained from specific-heat (Ott et al. 1985) and Mössbauer effect measurements (Bonville et al. 1988) indicating the aforementioned sample dependence. Similar slight differences were also found for the values of the ordering temperatures by the different groups.

3.4. *Samarium-based systems*

Sm ions show low-lying spin–orbit coupled states which have to be included in the discussion of the magnetic response measured by inelastic neutron scattering when considering VF systems. The energy levels of 2+ and 3+ free and CF-split Sm ions are shown schematically in fig. 67. The following states have to be taken into account:

- For Sm^{2+} ($4f^6$): the non-magnetic $J=0$ ($^7F_0$) ground state and the $J=1$ ($^7F_1$) excited state at 36.4 meV (free-ion value); there is no splitting in cubic CF fields for both states.
- For Sm^{3+} ($4f^5$): the $J=\frac{5}{2}$ ($^6H_{5/2}$) ground state and the $J=\frac{7}{2}$ excited state at 130 meV; a cubic CF splits the ground state into a doublet and a quartet (same as for Ce^{3+}).

The strongest magnetic scattering stems from the $^7F_0 \rightarrow {}^7F_1$ transition with an inelastic magnetic cross section of 7.3 b. The second-largest cross section is the quasi-elastic scattering within the $^7F_1$ excited state (2.72 b). Its observation, however, depends on its population, hence on temperature and valence. Both these cross sections belong to the Sm^{2+} ion. On the other hand, the *total* magnetic scattering intensity from the $^6H_{5/2}$ ground state of Sm^{3+} is only 0.43 b (nine times smaller than for the $J=\frac{5}{2}$ ground state of Ce^{3+}). When the state is split by a crystal field the intensity is further divided into a quasi-elastic and an inelastic part. Besides the low

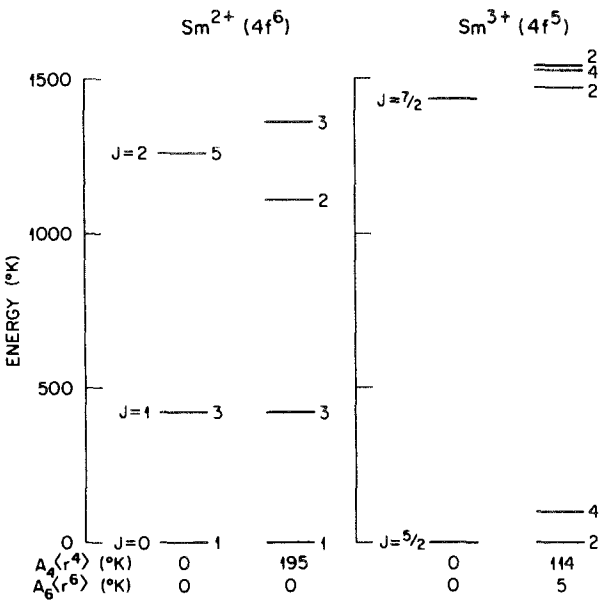

Fig. 67. Energy levels for free Sm ions and for Sm ions in crystal fields expected for SmS (with the CF parameters given below the scheme). Degeneracies are shown to the right of the levels (Moon et al. 1978).

magnetic intensities there is another handicap for neutron investigations of Sm compounds: the rather high absorption cross section. This requires the use of isotope enriched samples. Therefore only few systems have been investigated. Mostly, also the quality of the data is not good enough to identify all expected contributions to the magnetic response. The situation is similar for Eu-based VF compounds.

3.4.1. *SmS and* $Sm_{0.75}Y_{0.25}S$

SmS and YS have a simple NaCl structure with $a = 5.97$ and 5.50 Å, respectively. SmS undergoes a first-order, isostructural phase transition around 0.65 GPa (6.5 kbar) at room temperature from the semiconducting, "black" Sm^{2+} state to the metallic, "gold", mixed-valent state. At the phase transition the volume shrinks by 15% ($a_0 = 5.66$ Å in the gold phase). From the lattice parameter a ratio of 20/80 for the Sm^{2+}/Sm^{3+} mixing is estimated. Lattice pressure in the $Sm_{1-x}Y_xS$ alloys drives the Sm ions already at ambient pressure into the VF state for $x \geqslant 0.15$. The alloy $Sm_{0.75}Y_{0.25}S$, which was the only one investigated by neutron scattering, has a mixing ratio of $\simeq 40/60$ for Sm^{2+}/Sm^{3+} at room temperature, increasing to $\sim 70/30$ at 2 K (with the dominant change around 200 K).

The $^7F_0 \rightarrow {}^7F_1$ excitation at 26 meV in SmS at ambient pressure was studied in detail by Shapiro et al. (1975) on a single crystal and by Mook et al. (1978a) on a polycrystalline sample as function of temperature. All data (dispersion, intensities) could be satisfactorily explained by the paramagnetic singlet–triplet model in MF–RPA (mean field–random phase approximation) assuming sharp transitions which are only limited by resolution. Applying pressure, the situation is unchanged up to 0.6 GPa (McWhan et al. 1978). At 0.65 GPa in the VF phase, however, there is no evidence for *sharp* transitions from either the Sm^{2+} or the Sm^{3+} configuration. Yet,

the accuracy of the experiments was not sufficient to detect *broadenend* transitions, which are expected in a VF system. These were observed in the VF alloy $Sm_{0.75}Y_{0.25}S$. Mook et al. (1978a) report a broad $^7F_0 \rightarrow {}^7F_1$ transition (FWHM $\simeq$ 15 meV) centered around 32 meV. The temperature dependence of its intensity is claimed to be inconsistent with the expected temperature dependence for the singlet–triplet model (which worked so well for SmS). Mook et al.'s findings, however, are revised by recent experiments by Holland-Moritz et al. (1988). Due to better experimental resolution they observe a fine structure (four peaks) of the broad $^7F_0$–$^7F_1$ transition with individual line widths of only 2 meV and a temperature dependence of the total intensity consistent with the expectations of the singlet–triplet model. The fine structure is explained in terms of a resonant coupling of optical phonons to the dispersive magnetic exciton built from the localized $^7F_0 \rightarrow {}^7F_1$ transition by magnetic intersite coupling. Clearly, single crystal data are necessary to approve or disapprove this explanation. On the same polycrystalline sample of $Sm_{0.75}Y_{0.25}S$ Weber et al. (1989a) could also detect quasi-elastic scattering above $T = 100$ K. It stems from the $^6H_{5/2}$ ground state of the Sm^{3+} component and from transitions within the excited $^7F_1$ state of the Sm^{2+} component. Its width is about (7 ± 2) meV, and temperature independent between 100 and 250 K. As in other VF compounds, the broad quasi-elastic magnetic response at elevated temperatures may become inelastic at low temperatures, but the experimental conditions (cold neutrons with $E_0 = 3.15$ meV) do not allow to draw any decisive conclusions from the data below 100 K. Also no indication of a crystal field splitting of the $^6H_{5/2}$ state could be detected in this experiment. This shows that the low-energy magnetic response in $Sm_{0.75}Y_{0.25}S$ resembles strongly those of typical Ce- and Yb-based VF compounds.

Because of the drastic difference in the shape of the magnetic form factors of Sm^{2+} (monotonous decrease with Q) and Sm^{3+} (maximum at finite Q) interesting effects were expected from form factor measurements in VF-Sm compounds. The results of Moon et al. (1978), however, indicate no visible change of the form factor of SmS when going from the 2+ low-pressure to the VF high-pressure phase, as presented in fig. 68. Also, more precise data from a single crystal of $Sm_{0.76}Y_{0.24}S$ (Moon et al. 1978, 1983) can only be fitted assuming an unreasonably small fraction of Sm^{3+} in the VF state. Moon et al. (1978, 1983) argue that the Curie term, which gives rise to the finite Q maximum in the Sm^{3+} form factor, is strongly suppressed in the VF state. This assumption is in line with susceptibility data of these Sm systems and futhermore supported by the observation of a broad quasi-elastic (or possibly inelastic) line in $Sm_{0.75}Y_{0.25}S$, as discussed above.

In contrast to the more subtle effects on the magnetic form factor and the difficulty to observe the influence on the inelastic magnetic response there are strong phonon anomalies associated with the VF state in SmS under pressure and in $Sm_{0.75}Y_{0.25}S$. Figure 69 shows the acoustic phonon dispersion curves of SmS at room temperature in the 2+ ("black", semiconducting) state at ambient pressure and in the VF ("gold", metallic) state at 0.7 GPa. While there is little change in the [100] and [110] direction Mook et al. (1982) observe a dramatic softening of the LA branch in the middle of the [111] direction. This is shown in detail in fig. 70. The unusual behavior of the LA mode in the [111] direction is even more pronounced in the VF alloy

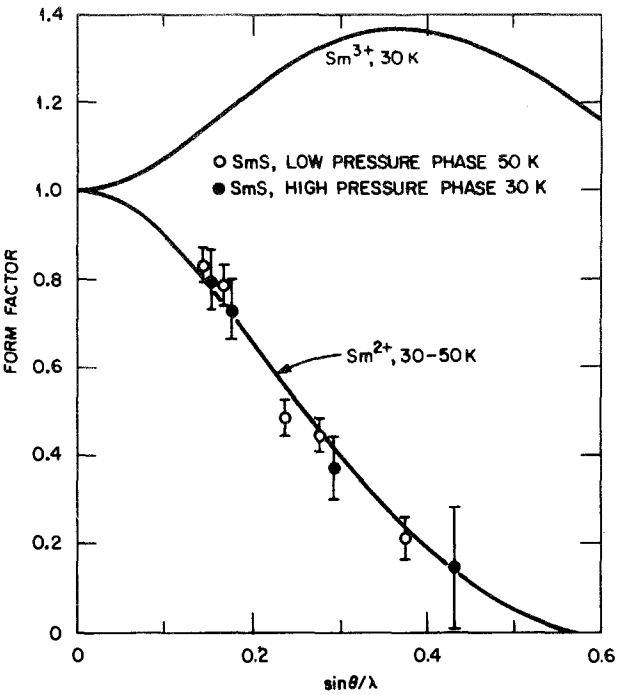

Fig. 68. Form factor of the high-pressure (VF) phase of SmS compared with the low-pressure results and the ionic calculations. The Sm^{3+} calculation is based on $A_4\langle r^4\rangle = 114$ K, $A_6\langle r^6\rangle = 5$ K and $J_{cx} = 7$ K (Moon et al. 1978).

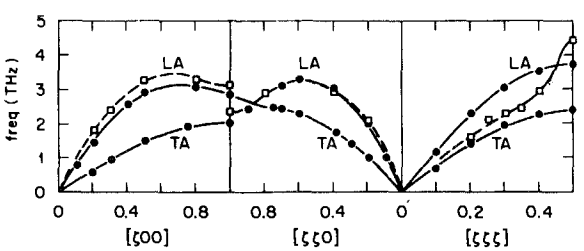

Fig. 69. Phonon dispersion curves for SmS. The solid circles show measurements done at standard pressure. The open squares show measurements done at 0.7 GPa, where SmS is in the VF phase (Mook et al. 1982).

$Sm_{0.75}Y_{0.25}S$, as measured by Mook et al. (1978b) and shown in fig. 71. Here the LA mode lies partly even *below* the TA mode. In addition, the phonons exhibit intrinsic line widths. Temperature dependent measurements by Mook and Nicklow (1979) reveal that the largest phonon softening and the largest phonon line widths are observed around 200 K, where $Sm_{0.75}Y_{0.25}S$ shows the steepest change in valence or Sm^{2+}/Sm^{3+} mixing. These findings could be explained quite satisfactorily by lattice dynamical models which take into account the peculiarities of the NaCl structure and the VF character of the Sm ions ("breathing" modes). The models were developed by Grewe and Entel (1979), Bennemann and Avignon (1979), Bilz et al. (1979), Wakabayashi (1980) and Mishchenko and Kikoin (1991).

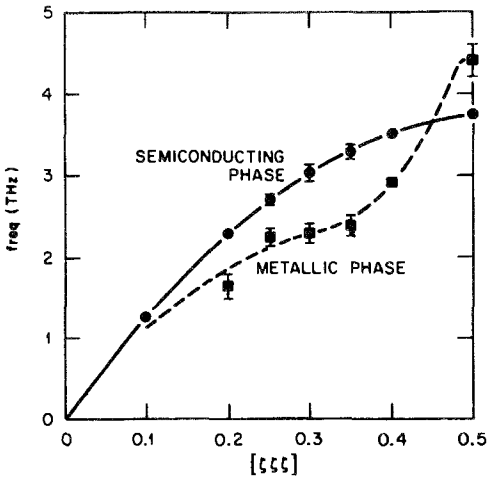

Fig. 70. LA phonon dispersion curves for the [111] direction for metallic (VF) and semiconducting SmS (Mook et al. 1982).

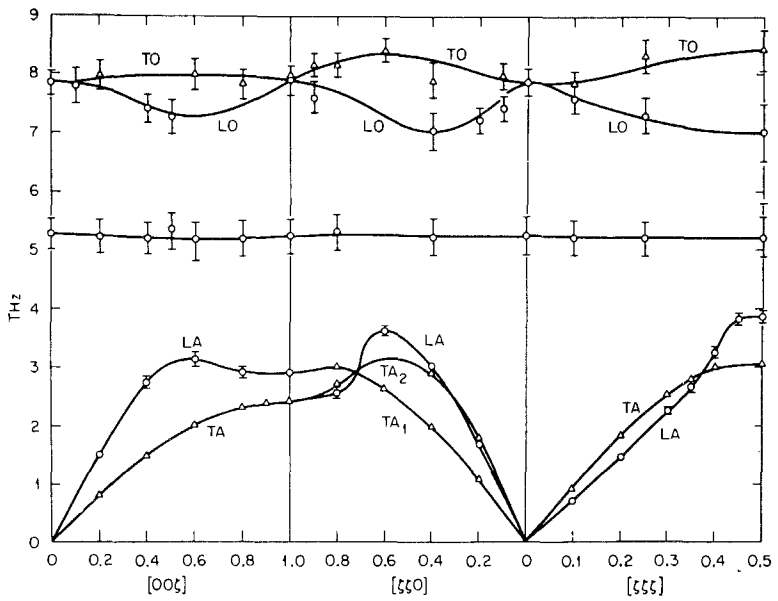

Fig. 71. Phonon dispersion curves for $Sm_{0.75}Y_{0.25}S$ measured at room temperature. The flat mode near 5 THz is the local Y mode (Mook et al. 1978b).

3.4.2. *SmB_6*

SmB_6 crystallizes in the cubic CaB_6 structure with $a = 4.13$ Å (Alekseev et al. 1989). Its valence is $\simeq 2.6$ (lattice parameter, Mössbauer isomer shift, L_{III} absorption edge). The resistivity of SmB_6 is small at room temperature but increases drastically below 30 K (by a factor of 10^4, depending on sample quality). Thus we can call SmB_6 a small-gap VF semiconductor with an activation energy of around 3 meV. Czycholl

(1982) has calculated in the alloy approximation of the Anderson lattice model the dynamical magnetic response for SmB_6. At low temperatures he obtains an inelastic feature due to excitations across the hybridization gap. For increasing temperatures the inelastic feature weakens and quasi-elastic intensity appears. The whole response becomes quasi-elastic at sufficiently high temperatures (a few hundred K). This is what one typically observes for *metallic* VF compounds (e.g. $CePd_3$, $CeSn_3$) but it could not be verified for SmB_6 since the inelastic neutron scattering experiments are strongly hampered by poor statistics. The only available data (Holland-Moritz and Kasaya 1986, Alekseev et al. 1992) show at $T = 5$ K a very weak inelastic line with intensity of only 0.1 b and positioned around 15 meV. It seems to be of magnetic origin but shows some peculiar Q-dependence (it broadens and merges for increasing Q into the 11 meV phonon line). We think that this inelastic line is a CF transition within the $^6H_{5/2}$ ground-state multiplet of Sm^{3+} interacting with the large phonon density of states around 11 meV. Extrapolation of the CF parameters of CeB_6, PrB_6, and NdB_6 (Loewenhaupt and Prager 1986) would yield for Sm^{3+} a Γ_8 ground state and a Γ_7 excited state around 11 meV. The quasi-elastic scattering could not be detected in the above experiments due to insufficient energy resolution. Also the $^7F_0 \rightarrow {}^7F_1$ transition from the Sm^{2+} state was hardly visible, presumably due to strong line broadening. Its position is estimated to lie between 30 and 40 meV (Alekseev et al. 1992), close to the free-ion value of 36 meV.

More successful than these measurements on polycrystalline samples of SmB_6 searching for the magnetic excitations, were measurements of the phonon dispersion relations on a single crystal of double isotope $^{154}Sm^{11}B_6$ by Alekseev et al. (1989, 1992). Figure 72 shows the data and their interpretation. Starting from the dispersion of LaB_6 (Smith et al. 1985) the strong softening of the SmB_6 modes can only be explained if VF-specific breathing (Γ_1^+) and dipole (Γ_{15}^-) modes are added to the usual phonon modes. In addition there is a flat mode at 4.75 THz $\hat{=}$ 20 meV. Temperature-dependent measurements indicate that the flat mode does not exist at $T = 1.8$ K.

3.5. *Europium-based systems*

In Eu-based VF systems the two valence states Eu^{2+} and Eu^{3+} have to be considered when discussing neutron scattering experiments. They yield:

- for Eu^{2+} ($4f^7$) a spin-only $^8S_{7/2}$ ground-state multiplet with negligible CF splitting and a rather large magnetic cross section of 38 b (same as Gd^{3+}), and
- for Eu^{3+} ($4f^6$) a $J = 0$ $^7F_0$ non-magnetic ground-state multiplet and a $J = 1$ $^7F_1$ magnetic excited state at 46 meV (free-ion value), both being connected by an inelastic spin–orbit transition with 7.3 b (same as Sm^{2+}).

These properties would suggest that Eu VF compounds are good candidates for the study of the magnetic response with neutrons. A huge handicap, however, is the large absorption cross section of natural Eu (2450 b for $E_0 = 30$ meV). The use of an isotope (^{153}Eu: 390 b for 30 meV) improves the situation somewhat but reduces drastically the number of investigated compounds (presently: two), even if there exists a much larger number of interesting Eu VF compounds.

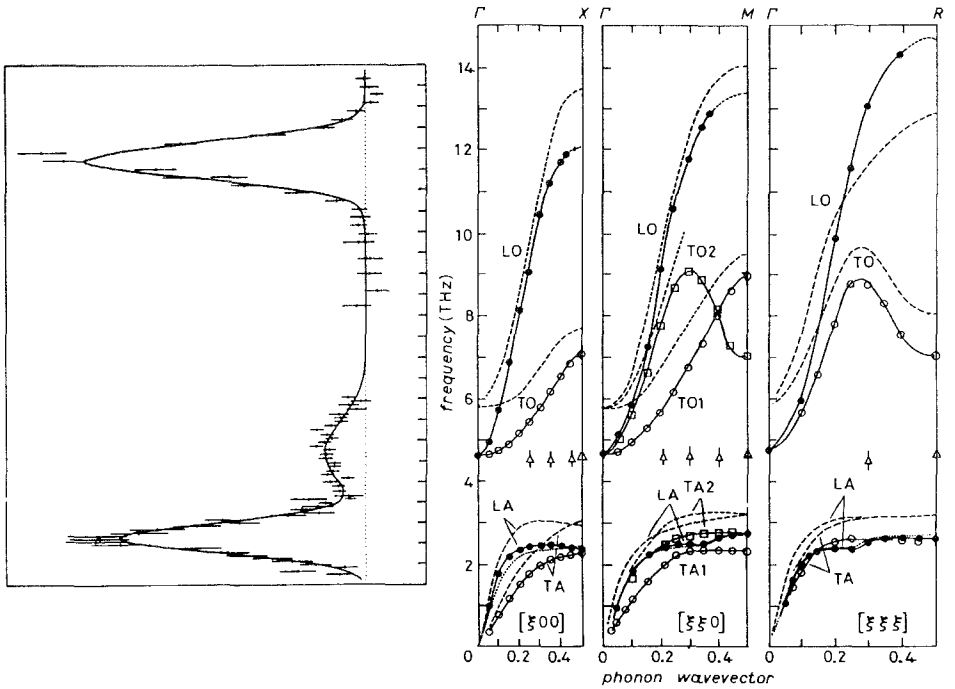

Fig. 72. Phonon dispersion curves for SmB_6 (lines connecting the experimental points are only to guide the eye). Dashed lines are the phonon branches for LaB_6 from Smith et al. (1985), dotted lines are the calculated LA branch obtained by adding dipole and monopole electronic modes to the dynamic model of LaB_6. Left figure: scan for $\boldsymbol{q} = (0.3, 0.3, 0)$, the solid line is the best fit with three Gaussians (Alekseev et al. 1989).

3.5.1. *$EuNi_2P_2$*

$EuNi_2P_2$ has a tetragonal $ThCr_2Si_2$ structure with $a = 3.938$ Å and $c = 9.469$ Å (at room temperature). The valence changes only slightly with temperature: 2.53 at 16 K, 2.47 at 53 K and 2.35 at room temperature (from Mössbauer data) (Perscheid et al. 1985). The only inelastic neutron experiments, performed on a polycrystalline sample with ^{153}Eu isotope, are reported by Holland-Moritz et al. (1989b). Only the response from the Eu^{2+} state could be detected as function of temperature between 5 and 270 K. There was no indication of the $^7F_0 \rightarrow {}^7F_1$ transition of the Eu^{3+} state in the spectra with $E_0 = 50$ meV. This transition would have been observed if it had an energy of 38 meV or less (as in $EuPd_2Si_2$). But it would lie outside the accessible energy range if its energy would be around 46 meV or larger (corresponding to the free-ion value of the $^7F_0 \rightarrow {}^7F_1$ transition). It is thus not clear whether this Eu^{3+} transition was not observed due to intrinsic effects (e.g. line broadening) or due to experimental limitations.

We now discuss the Eu^{2+} response in more detail. Between 100 and 270 K a temperature-independent broad quasi-elastic response with $\frac{1}{2}\Gamma \simeq 6$ meV is observed. Its intensity corresponds roughly to the fraction of Eu^{2+} ions. Its Q-dependence is consistent with the Eu^{2+} magnetic form factor. Below 100 K the magnetic response

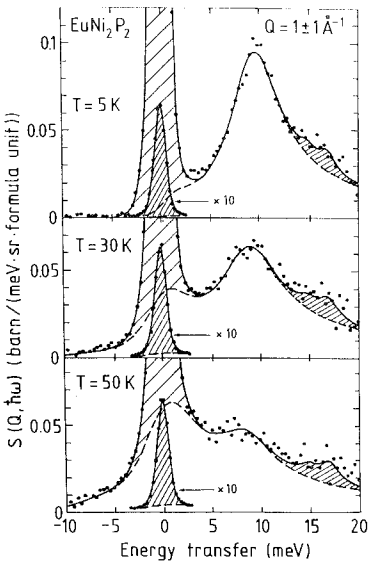

Fig. 73. Inelastic neutron spectra of $EuNi_2P_2$ at $T = 5$, 30, and 50 K obtained with $E_0 = 30$ meV. The hatched areas represent the elastic nuclear and the inelastic phonon scattering. The magnetic response (dashed or solid line) involves a quasi-elastic and an inelastic line of Lorentzian shape (Holland-Moritz et al. 1989b).

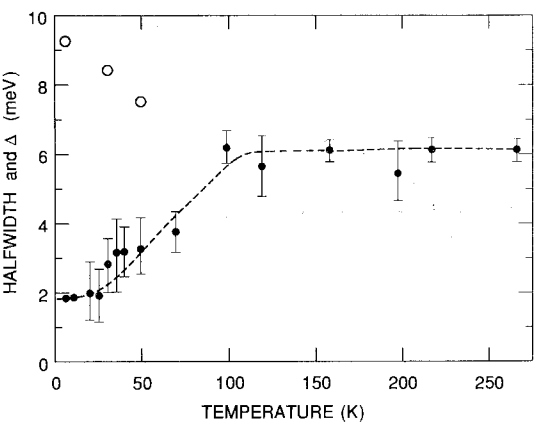

Fig. 74. Temperature dependence of the quasi-elastic magnetic line width (solid circles) and of the position Δ of the inelastic line (open circles) in $EuNi_2P_2$ (Holland-Moritz et al. 1989b).

splits into a quasi-elastic line and an inelastic line, as shown in fig. 73. For decreasing temperatures the quasi-elastic component narrows and decreases in intensity while the inelastic line gains intensity and moves to higher energies. The temperature dependence of the line width of the quasi-elastic line and of the position of the inelastic line are reproduced in fig. 74. This behavior is similar to that found for TmSe. Deviations of the Q-dependence of the intensity from the Eu^{2+} form factor at low temperatures (at $T = 5$ K, especially for the inelastic lines for $Q \leqslant 1$ Å^{-1}) were also reported by Holland-Moritz et al. (1989b) and assumed to be due to 5d electrons (similar to $CeSn_3$).

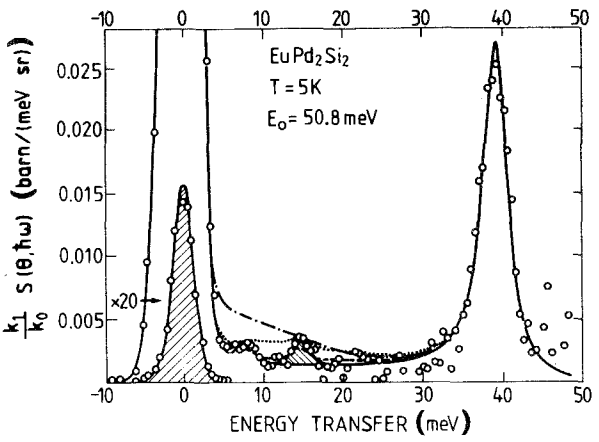

Fig. 75. Inelastic neutron spectrum of $EuPd_2Si_2$ at $T = 5$ K obtained with $E_0 = 50.8$ meV (Holland-Moritz et al. 1987).

3.5.2. *$EuPd_2Si_2$*

$EuPd_2Si_2$ crystallizes in the $ThCr_2Si_2$ structure with $a = 4.10$ Å and $c = 9.88$ Å (Rogl 1984). As is found in many other VF Eu compounds, the valence changes considerably with temperature. It is around 2.75 at 15 K and 2.3 at room temperature, showing the largest change around $T = 150$ K. The only inelastic neutron scattering experiment was performed by Holland-Moritz et al. (1987) for different temperatures between 5 and 250 K on a polycrystalline sample enriched with ^{153}Eu isotope. The low-temperature spectra ($T < 100$ K) are dominated by the response from the Eu^{3+} state: the $^7F_0 \rightarrow {}^7F_1$ transition (see fig. 75). The energy of this transition is considerably lower than the free-ion value (38 meV in $EuPd_2Si_2$ compared to 46 meV) and its line width is only 2 meV. The response of the Eu^{2+} state cannot be seen directly in the spectra. It can only be deduced indirectly. Assuming an upper limit of 2.85 for the valence at 5 K and a quasi-elastic shape for the Eu^{2+} response a lower limit of 25 meV for the line width is estimated by Holland-Moritz et al. (1987) (if this line exists at all at low temperatures). On the other hand, the spectra at high temperatures ($T \geqslant 200$ K) are dominated by the response from the Eu^{2+} state: quasi-elastic scattering with $\frac{1}{2}\Gamma \simeq 4$ meV. No inelastic intensity from the $^7F_0 \rightarrow {}^7F_1$ transition is visible in this temperature region.

This yields a picture of $EuPd_2Si_2$ for the two temperature regions, below and above the steep valence change, of a VF system with not too fast spin fluctuations in both regions (2 to 4 meV, if the inelastic and the quasi-elastic line width are taken as measure). Furthermore, only the magnetic response of the dominant valence state is observed in each region. At intermediate temperatures (100 to 200 K) where the steep valence change takes place, it seems that the response of both valence states is observed simultaneously. Both signals change, however, dramatically within a small temperature region. The quasi-elastic line broadens with *decreasing* temperature (200 K: 4 meV, 120 K: 22 meV) and becomes undetectable below 100 K. The inelastic $^7F_0 \rightarrow {}^7F_1$ transition broadens (5 K: 2 meV, 140 K: 4 meV) and shifts (5 K: 38 meV, 140 K: 36 meV) with *increasing* temperature and becomes undetectable above 140 K.

3.6. *Thulium-based systems*

The peculiarity of Tm-based VF systems is the fact that both valence states have magnetic ground-state multiplets [Tm^{2+} ($4f^{13}$): $^2F_{7/2}$ ($N = 8$), same as Yb^{3+}, and Tm^{3+} ($4f^{12}$): $^3H_6$ ($N = 13$)]. The CF ground state of Tm^{2+} is at least a doublet, Tm^{3+} may have a CF singlet ground state. A large number of neutron investigations has been performed on TmSe and will be discussed here in detail. As far as other Tm compounds are concerned, we are only aware of neutron data on the Kondo-lattice TmS (Lassailly et al. 1983, Holtzberg et al. 1985) and on pressure dependent neutron scattering experiments on TmTe (Walter et al. 1992).

3.6.1. *TmSe*

Stoichiometric TmSe has a simple rocksalt structure with $a = 5.71$ Å at room temperature. The sample preparation has been a problem from the beginning, especially for growing large single crystals. The valence is estimated to be around 2.6 (L_{III} edges). Non-stoichiometric Tm_xSe shows the tendency towards $+3$ for decreasing x in connection with a decreasing lattice parameter [$x = 0.87$: $a = 5.63$ Å (Batlogg et al. 1979)].

Bjerrum-Møller et al. (1977) investigated the magnetic structure of a stoichiometric single crystal of TmSe by neutron diffraction. Surprisingly, they found a simple type-I antiferromagnetic structure below $T_N = 3.2$ K, yet with a rather small ordered moment of $(1.7 \pm 0.2)\mu_B$. Applying a magnetic field of about 0.4 T, they observed a first-order phase transition from the antiferromagnetic state to a ferromagnetic state. The H–T phase diagram can be understood using a classical spin Hamiltonian with a weak and antiferromagnetic nearest-neighbor exchange, a strong and ferromagnetic next-nearest-neighbor exchange, and a small anisotropy term. Bonnet et al. (1986) measured the magnetic form factor in the antiferromagnetic state (1.6 K, 0.28 T), in the ferromagnetic state (1.6 K, 1.6 T) and in the paramagnetic state (8 K, 1.6 T). While for the latter two states of TmSe they observe a purely f-like form factor, the form factor in the antiferromagnetic state deviates at low angles. This shows that only in the antiferromagnetic state the outer electrons of Tm (5d) are polarized (i.e. coupled to the 4f-magnetization), similar to the observations for VF Ce compounds (see section 3.1).

Neutron diffraction studies as function of external pressure were reported by Ribault et al. (1980) and Debray et al. (1981). The AF type-I structure is stable up to pressures of 3 GPa (with T_N first increasing with increasing pressure, passing a maximum around 1.5 GPa, and then decreasing). For higher pressures (> 3 GPa) the structure changes to type-II AF. In the region between 1.5 and 3 GPa there seems to exist a mixture of both structure types (depending on the sample). The type-II structure is also observed at ambient pressure for under-stoichiometric TmSe [sample 2, Shapiro et al. (1978)] with $T_N \sim 4.7$ K. But even at 1.6 K the long-range order in this sample it not fully developed (correlation length $\simeq 100$ Å).

The interpretation of the dynamical response of TmSe is still rather controversial. It seems that the response of stoichiometric TmSe consists at low temperatures (but

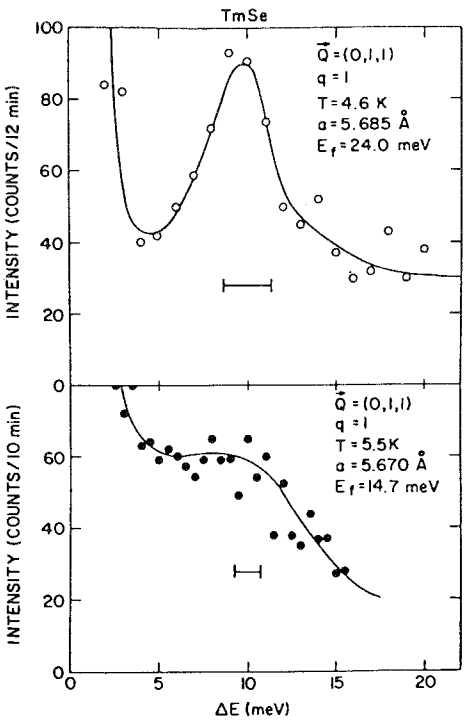

Fig. 76. Inelastic neutron spectra measured on two single crystals of TmSe at low temperatures. The top portion is for stoichiometric TmSe and the lower portion is for $Tm_{0.99}Sc$. The concentrations were determined from the room temperature lattice constants. The lattice constants given in the figures are those at the low temperatures (Shapiro and Grier 1982).

above $T_N = 3.2$ K) of a narrow quasi-elastic line ($\frac{1}{2}\Gamma \simeq 0.5$ meV at $T = 5$ K) well separated from an inelastic line at $\Delta = 10$ meV. This was observed on a polycrystalline sample (Loewenhaupt and Holland-Moritz 1979b) and on a single crystal (Shapiro and Grier 1982) with room temperature lattice parameters of 5.711 and 5.714 Å, respectively. In all other experiments the sharp 10 meV inelastic line was not observed [sample 2, Shapiro et al. (1978), also Furrer et al. (1981)], presumably due to the under-stoichiometry of the investigated sample. The sensitivity of the 10 meV line on the stoichiometry is shown in fig. 76, comparing the low-temperature inelastic response of a single crystal of stoichiometric TmSe ($a = 5.714$ Å) with that of slightly under-stoichiometric $Tm_{0.99}Se$ ($a = 5.690$ Å). The lattice constants given in parentheses are those at room temperature. In the latter sample the inelastic structure is already considerably broadened. We now return to the discussion of the magnetic response of the stoichiometric compound in more detail: its Q, temperature and magnetic field dependence. Figure 77 shows the inelastic spectrum of TmSe at $T =$ 4.6 K for several Q values along the [100] direction. Shapiro and Grier (1982) observe a slight dispersion (2 meV) and a drastic intensity variation within a Brillouin zone, which deviates from the single-ion Tm magnetic form factor. They explain their findings within a model of Fedro and Sinha (1981). In this model the 10 meV line is an excitation across a hybridization gap originating from the coupling between the localized f-electrons and bandlike d-electrons (as shown schematically in the inset to fig. 77). This interpretation has been doubted by Holland-Moritz (1983). He has

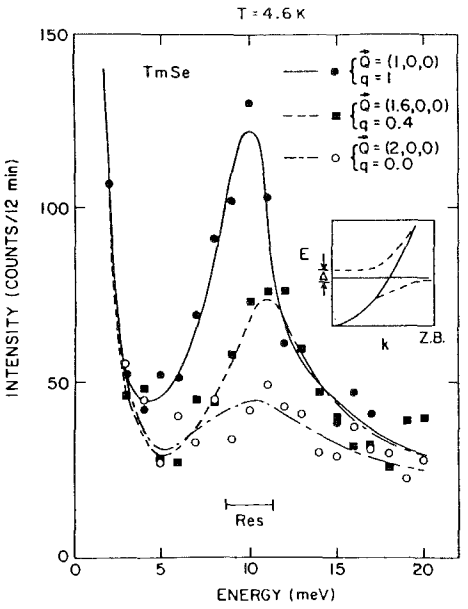

Fig. 77. Inelastic neutron spectra of TmSe measured at $T = 4.6$ K for different values of q along the [q00] direction. The inset is a schematic form of uncoupled f and d bands (solid lines) and the result when they are coupled giving rise to a hybridization gap Δ (Shapiro and Grier 1982).

observed an inelastic line also in the low-temperature spectra of $TmSe_{0.85}Te_{0.15}$ and *dilute* $Tm_{0.05}Y_{0.95}Se$ and $Tm_{0.05}La_{0.95}Se$, favoring a *single-ion origin* of the excitation. A model on this basis has been put forward by Mazzaferro et al. (1981) and Schlottmann (1984).

No measurable effect on the 10 meV line is observed when TmSe is cooled below $T_N = 3.2$ K (Holland-Moritz and Loewenhaupt 1979, Shapiro and Grier 1982). The quasi-elastic line, however, becomes inelastic ($\Delta = 1$ meV), indicative of magnon-like excitations within the ground state. A field dependent measurement of the magnetic spectra at $T = 1.9$ and 4.2 K by Loewenhaupt and Bjerrum-Møller (1981) reveals a strong field response of the magnon-like excitation while the 10 meV line is only slightly affected even in fields of 10 T (fig. 78). The ground-state splitting can be described by an effective spin $S = \frac{1}{2}$ and an effective g-factor $g = 3.8$. The assumption of a doublet ground state ($N = 2$) is supported by specific-heat data, which show that the entropy has reached $0.5R \ln 2$ at T_N and $R \ln 2$ around 8 K (Berton et al. 1981). The temperature dependence of the magnetic response above T_N is almost identical for the polycrystalline sample and the single crystal (fig. 79). It shows a broadening and a shift of the inelastic line and a broadening of the quasi-elastic line. For temperatures around 80 to 120 K both lines merge into one broad quasi-elastic line with $\frac{1}{2}\Gamma \simeq 7$ meV. Its width stays constant up to room temperature. The evolution of the quasi-elastic line width and of the position of the inelastic line (if present) is shown in fig. 80 for TmSe and, as comparison, for $TmSe_{0.85}Te_{0.15}$ and the dilute alloys $Tm_{0.05}Y_{0.95}Se$ and $Tm_{0.05}La_{0.95}Se$. There seems to exist a correlation between the position of the inelastic line at low temperatures and the width of the (merged) quasi-elastic line at elevated temperatures.

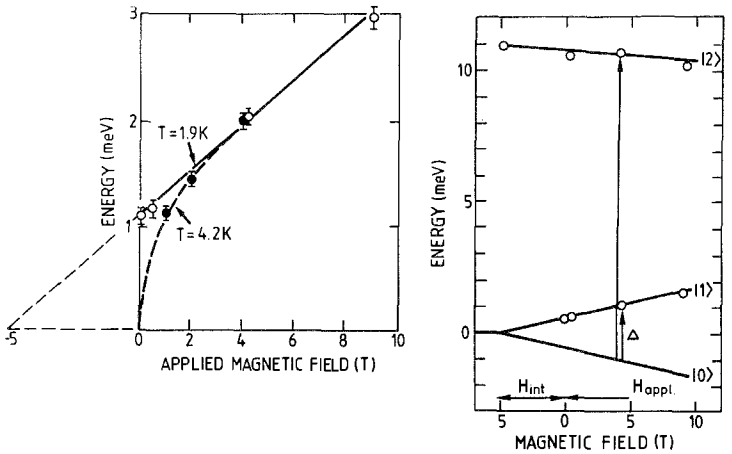

Fig. 78. Left: magnetic field dependence of the low-energy excitation in TmSe at $T = 1.9$ K (below T_N) and at 4.2 K (above T_N). The extrapolation of the excitation energy for the data at 1.9 K (dashed line) yields the value of the internal field in the ordered state. Right: proposed level scheme for stoichiometric TmSe at low temperature. Levels 0 and 1 are singlets, the degeneracy of level 2 is unknown, but expected to be large (Loewenhaupt and Bjerrum-Møller 1981).

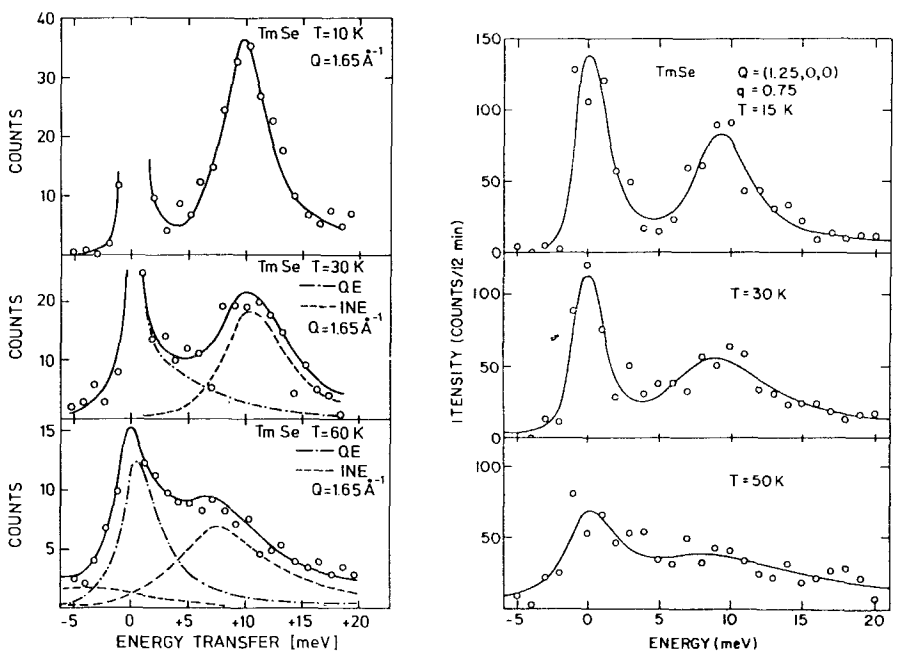

Fig. 79. Inelastic neutron spectra at different temperatures for stoichiometric TmSe in the form of a polycrystalline sample (left, from Loewenhaupt and Holland-Moritz 1979b) and of a single crystal (right, from Shapiro and Grier 1982).

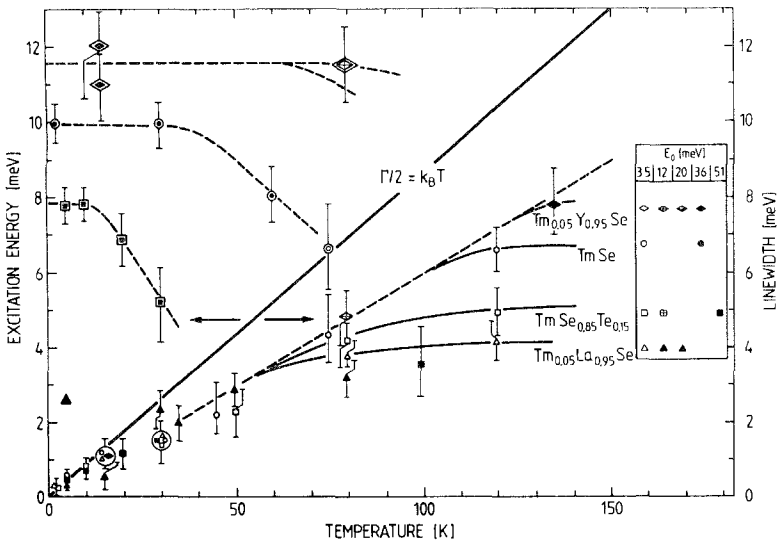

Fig. 80. Temperature dependence of the quasi-elastic line widths (lower right part) and of the excitation energies (upper left part) of TmSe and $TmSe_{0.85}Te_{0.15}$ and of dilute $Tm_{0.05}Y_{0.95}Se$ and $Tm_{0.05}La_{0.95}Se$ (Holland-Moritz 1983).

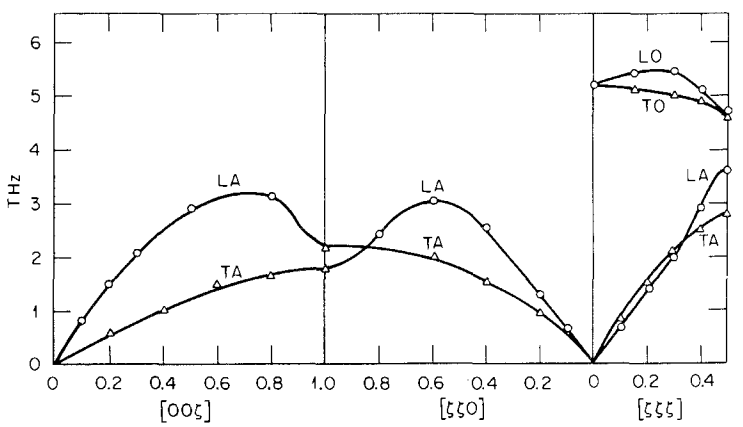

Fig. 81. Phonon dispersion curves for (under-stoichiometric) TmSe (Mook and Holtzberg 1981).

Finally, we want to mention that also phonon anomalies have been observed in TmSe (Mook and Holzberg 1981) and in dilute $Tm_{0.05}Y_{0.95}S$ (Holland-Moritz and Severing 1986), similar to those found in SmS under pressure and in $Sm_{0.75}Y_{0.25}S$. The phonon dispersion curves of TmSe are shown in fig. 81. Unfortunately, the investigated large crystal had a room temperature lattice constant of 5.682 Å, indicative of an under-stoichiometric sample.

4. Summary

This chapter deals with valence-fluctuation and heavy-fermion 4f systems, such as Ce, Sm, Eu, Tm and Yb alloys and compounds. Sections 1 and 2 summarize the most important physical properties of these systems, based on the main theoretical results achieved so far and on representative data.

In the main part (section 3) we summarize neutron scattering data of VF and HF systems. By means of neutrons one can measure the magnetic structure of a system (elastic magnetic scattering) and magnetic and non-magnetic excitations such as relaxational modes (quasi-elastic excitations), magnons, crystal field, and spin–orbit transitions, and phonons. Some of these excitations have been observed in all VF or HF systems. Both VF and HF systems exhibit a quasi-elastic line due to spin fluctuations or the Kondo effect. Both expressions are used synonymously, but in VF systems the quasi-elastic line is quite broad, corresponding to a high characteristic energy, and is fairly temperature independent. Here one speaks in general about spin fluctuations. In HF systems the quasi-elastic line is narrower, temperature dependent, and has, at low temperatures, an halfwidth $\frac{1}{2}\Gamma \simeq k_B T_K^N$. A typical quasi-elastic line can be fitted by a Lorentzian and corresponds to a single relaxation time. In most *HF compounds* the line becomes $\boldsymbol{Q}$-dependent at low temperatures, indicating spin correlations that at still lower temperatures often lead to magnetic order. These spin correlations, on the other hand, lead already to deviations from the Lorentz shape above the spin-ordering temperature. In *VF compounds* spin correlations do not play a role, but the high-temperature quasi-elastic line also changes shape and becomes narrower and inelastic at low temperatures.

Ce-based HF systems have been investigated by many groups, whereas few data exist for the corresponding VF systems and for Yb-, Sm-, Eu-, and Tm-based VF and HF systems. As a consequence, our survey over Ce-based VF and Yb, Sm, Eu, and Tm systems is rather complete, whereas for Ce-based HF systems we could only select representative examples. Part of this strong research activity on Ce compounds is due to the fact that $CeCu_2Si_2$ becomes superconducting, and it is an enormous challenge to find other superconducting HF systems. In addition, one has in these systems a variety of magnetic structures, such as ferromagnetic, antiferromagnetic and spiral order and metamagnetism. In many cases the detection of these structures is hampered by moments that are strongly reduced by the Kondo effect.

In addition to the Kondo effect one has in HF systems strong crystal field effects, and the corresponding 4f-levels can be determined by neutron scattering experiments. The interplay between Kondo and CF effects varies from system to system, and the corresponding information is part of the content of this chapter. Since in HF systems the Kondo temperature is typically rather small, one observes at low temperature mainly the properties of the lowest CF level.

Valence fluctuations couple to phonons, and our review gives a rather complete survey of the corresponding anomalies. In addition, one has phonon anomalies due to the CF–phonon interaction, since a lattice deformation around an R ion modifies the crystalline electric field. Finally, we mention the spin–orbit interaction, which is

modified in VF and HF systems due to the hybridization between f and conduction electrons. The few neutron scattering experiments on spin–orbit transitions in VF and HF systems show unexpected splittings, line shifts, and line broadenings if compared to the free-ion case.

References

Alekseev, P.A., A.S. Ivanov, B. Dorner, H. Schober, K.A. Kikoin, A.S. Mishchenko, V.N. Lazukov, E.S. Konovalova, Y.B. Paderno, A.Y. Rumyantsev and I.P. Sadikov, 1989, Europhys. Lett. **10**, 457.

Alekseev, P.A., A.S. Ivanov, V.N. Lazukov, I.P. Sadikov and A. Severing, 1992, Physica B **180** + **181**, 281.

Aliev, F.G., N.B. Brandt, V.V. Moshchalkov and S.M. Chudinov, 1984, J. Low Temp. Phys. **57**, 61.

Amato, A., D. Jaccard, J. Flouquet, F. Lapierre, J.L. Tholence, R.A. Fisher, S.E. Lacy, J.A. Olsen and N.E. Phillips, 1987, J. Low Temp. Phys. **68**, 371.

Andrei, N., and J.H. Loewenstein, 1981, Phys. Rev. Lett. **46**, 356.

Andrei, N., K. Furuya and J.H. Loewenstein, 1983, Rev. Mod. Phys. **55**, 331.

Andres, K., J.E. Graebner and H.R. Ott, 1975, Phys. Rev. Lett. **35**, 1779.

Asano, H., M. Umino, Y. Onuki, T. Komatsubara, F. Izumi and N. Watanabe, 1986, J. Phys. Soc. Jpn. **55**, 454.

Auerbach, A., and K. Levin, 1986a, Phys. Rev. Lett. **57**, 877.

Auerbach, A., and K. Levin, 1986b, Phys. Rev. B **34**, 3524.

Auerbach, A., J.H. Kim and K. Levin, 1987, Physica B **148**, 50.

Auerbach, A., J.H. Kim and K. Levin, 1988, Phys. Rev. Lett. **60**, 623.

Ayache, C., J. Beille, E. Bonjour, R. Calemczuk, G. Creuzet, D. Gignoux, A. Najib, D. Schmitt, J. Voiron and M. Zerguine, 1987, J. Magn. & Magn. Mater. **63–64**, 329.

Baer, Y., and W.-D. Schneider, 1987, in: Handbook on the Physics and Chemistry of Rare Earths, Vol. 10, eds K.A. Gschneidner Jr and L. Eyring (North-Holland, Amsterdam) p. 1.

Balakrishnan, G., D. Mck. Paul and N.R. Bernhoeft, 1989, Physica B **156–157**, 815.

Barbara, B., J.X. Boucherle, J.L. Bouevoz, M.F. Rossignol and J. Schweizer, 1977, Solid State Commun. **24**, 481.

Barbara, B., M.F. Rossignol, J.X. Boucherle, J. Schweizer and J.L. Bouevoz, 1979, J. Appl. Phys. **50**, 2300.

Barbara, B., M.F. Rossignol, J.X. Boucherle and C. Vettier, 1980, Phys. Rev. Lett. **45**, 938.

Batlogg, B., H.R. Ott, E. Kaldis, W. Thöni and P. Wachter, 1979, Phys. Rev. B **19**, 247.

Bauchspiess, K.R., W. Boksch, E. Holland-Moritz, H. Launois, R. Pott and D. Wohlleben, 1982, in: Valence Fluctuations in Solids, eds L.M. Falicov, W. Hanke and M.B. Maple (North-Holland, Amsterdam) p. 417.

Bennemann, K.H., and M. Avignon, 1979, Solid State Commun. **31**, 645.

Benoit, A., J.X. Boucherle, P. Convert, J. Flouquet, J. Palleau and J. Schweizer, 1980, Solid State Commun. **34**, 293.

Benoit, A., J.X. Boucherle, J. Flouquet, J. Sakurai and J. Schweizer, 1985, J. Magn. & Magn. Mater. **47–48**, 149.

Berton, A., J. Chassy, B. Cornut, J. Flouquet, J. Odin, J. Peyard and F. Holtzberg, 1981, Phys. Rev. B **23**, 3504.

Besnus, M.J., J.P. Kappler, P. Lehmann and A. Meyer, 1985, Solid State Commun. **55**, 779.

Besnus, M.J., M. Benakki, A. Braghta, H. Danan, G. Fischer, J.P. Kappler, A. Meyer and P. Panissod, 1988, J. Magn. & Magn. Mater. **76–77**, 471.

Bickers, N.E., 1987, Rev. Mod. Phys. **59**, 846.

Bickers, N.E., D.L. Cox and J.W. Wilkins, 1987, Phys. Rev. B **36**, 2036.

Bilz, H., G. Güntherodt, W. Kleppmann and W. Kress, 1979, Phys. Rev. Lett. **43**, 1988.

Bjerrum-Møller, H., S.M. Shapiro and R.J. Birgeneau, 1977, Phys. Rev. Lett. **39**, 1021.

Blaschko, O., G. Krexner, L. Pintschovius, W. Assmus and G. Ernst, 1984, Solid State Commun. **51**, 971.

Böhm, A., R. Caspary, U. Habel, L. Pawlak, A. Zuber, F. Steglich and A. Loidl, 1988, J. Magn. & Magn. Mater. **76–77**, 150.

Bonnet, M., J.X. Boucherle, J. Flouquet, F. Holtzberg, D. Jaccard, J. Schweizer and A. Stunault, 1986, Physica B **136**, 428.

Bonville, P., and J.A. Hodges, 1985, J. Magn. & Magn. Mater. **47–48**, 152.

Bonville, P., J.A. Hodges, F. Hulliger, P. Imbert, G. Jehanno, J.B. Marimon da Cunha and H.R. Ott, 1988, J. Magn. & Magn. Mater. **76–77**, 473.

Bonville, P., J.A. Hodges, P. Imbert, D. Jaccard, J. Sierro, M.J. Besnus and A. Meyer, 1990, Physica B **163**, 347.

Bonville, P., J. Hammann, J.A. Hodges, P. Imbert, G. Jehanno, M.J. Besnus and A. Meyer, 1991, Z. Phys. B **82**, 267.

Borsa, F., and G. Olcese, 1973, Phys. Stat. Solidi (a) **17**, 631.

Boucherle, J.X., and J. Schweizer, 1985, Physica B **130**, 337.

Boucherle, J.X., J.L. Buevoz, S. Horn, M. Loewenhaupt, H. Scheuer, J. Schweizer and F. Steglich, 1981, Solid State Commun. **38**, 669.

Boucherle, J.X., J. Flouquet, Y. Lassailly, J. Palleau and J. Schweizer, 1983, J. Magn. & Magn. Mater. **31–34**, 409.

Boucherle, J.X., G. Fillion, J. Flouquet, F. Givord, P. Lejay and J. Schweizer, 1990, Physica B **163**, 635.

Bredl, C.D., 1987, J. Magn. & Magn. Mater. **63–64**, 355.

Burghardt, P., K.A. Gschneidner Jr, D.C. Koskenmaki, D.K. Finnemore, J.O. Moorman, S. Legvold, C. Stassis and T.A. Vyrostek, 1976, Phys. Rev. B **14**, 2995.

Buyers, W.J.L., 1986, Physica B **137**, 53.

Capellmann, H., P.J. Brown, S.M. Johnson, K.R.A. Ziebeck and J.G. Booth, 1985, J. Magn. & Magn. Mater. **49**, 137.

Chattopadhyay, T., H. v. Löhneysen, T. Trappmann and M. Loewenhaupt, 1990, Z. Phys. B **80**, 159.

Coleman, P., 1984, Phys. Rev. B **29**, 3035.

Coleman, P., 1987a, Phys. Rev. B **35**, 5072.

Coleman, P., 1987b, J. Magn. & Magn. Mater. **63–64**, 245.

Cox, D.L., and N. Grewe, 1988, Z. Phys. B **71**, 321.

Cox, D.L., N.E. Bickers and J.W. Wilkins, 1986, J. Magn. & Magn. Mater. **54-57**, 333.

Cromer, D.T., A.C. Larson and R.B. Roof, 1960, Acta Crystallogr. **13**, 913.

Currat, R., R.G. Lloyd, P.W. Mitchell, A.P. Murani and J.W. Ross, 1989, Physica B **156–157**, 812.

Czycholl, G., 1982, Phys. Rev. B **25**, 3413.

Debray, D., R. Kahn, D.L. Decker, A. Werner, M. Loewenhaupt, E. Holland-Moritz and D.K. Ray, 1981, in: Valence Fluctuations in Solids, eds L.M. Falicov, W. Hanke and M.B. Maple (North-Holland, Amsterdam) p. 183.

Desgranges, H.-U., and J.W. Rasul, 1985, Phys. Rev. B **32**, 6100.

Dhar, S.K., K.A. Gschneidner Jr, W.H. Lee, P. Klavins and R.N. Shelton, 1987, Phys. Rev. B **36**, 341.

Dijkman, W.H., F.R. de Boer, P.F. de Chatel and J. Aarts, 1980, J. Magn. & Magn. Mater. **15–18**, 970.

Doniach, S., 1977, Physica B **91**, 231.

Doniach, S., 1987, Phys. Rev. B **35**, 1814.

Dönni, A., P. Fischer, A. Furrer, P. Bonville, F. Hulliger and H.R. Ott, 1990a, Z. Phys. B **81**, 83.

Dönni, A., P. Fischer, A. Furrer, W. Bacsa and P. Wachter, 1990b, Z. Phys. B **80**, 269.

Dönni, A., A. Furrer, P. Fischer, F. Hulliger, P. Wachter and H.R. Ott, 1990c, J. Magn. & Magn. Mater. **90–91**, 143.

Dormann, E., 1991, in: Handbook on the Physics and Chemistry of Rare Earths, Vol. 14, eds K.A. Gschneidner Jr and L. Eyring (North-Holland, Amsterdam) p. 63.

Effantin, J.M., J. Rossat-Mignod, P. Burlet, H. Bartholin, S. Kunii and T. Kasuya, 1985, J. Magn. & Magn. Mater. **47–48**, 145.

Eiling, A., and J.S. Schilling, 1981, Phys. Rev. Lett. **46**, 364.

Elenbaas, R.A., C.J. Schinkel and C.J.M. van Deudekom, 1980, J. Magn. & Magn. Mater. **15–18**, 979.

Elschner, B., and M. Schlott, 1988, J. Magn. & Magn. Mater. **76–77**, 444.

Erkelens, W.A.C., L.P. Regnault, P. Burlet, J. Rossat-Mignod, S. Kunii and T. Kasuya, 1987, J. Magn. & Magn. Mater. **63–64**, 61.

Fedro, A.J., and S.K. Sinha, 1981, in: Valence Fluctuations in Solids, eds L. M. Falicov, W. Hanke and M. B. Maple (North-Holland, Amsterdam) p. 329.

Felner, I., I. Nowik, D. Vaknin, U. Potzel, J. Moser, G.M. Kalvius, G. Wortmann, G. Schmiester, G. Hilscher, E. Gratz, C. Schmitzer, N. Pillmayr, K.G. Prasad, H. de Waard and H. Pinto, 1987, Phys. Rev. B **35**, 6956.

Felten, R., G. Weber and H. Rietschel, 1987, J. Magn. & Magn. Mater. **63–64**, 383.

Fillion, G., R.M. Galera, D. Givord, J. Pierre, J. Schweizer and C. Vettier, 1985, J. Appl. Phys. **57**, 3179.

Fischer, K.H., 1970, Springer Tracts Mod. Phys. **54**, 1.

Fischer, K.H., 1989a, Z. Phys. B **74**, 475.
Fischer, K.H., 1989b, Z. Phys. B **76**, 315.
Forgan, E.M., B.D. Rainford, S.L. Lee, J.S. Abell and Y. Bi, 1990, J. Phys.: Condens. Matter **2**, 10211.
Franz, W., E. Griessel, F. Steglich and D. Wohlleben, 1978, Z. Phys. B **31**, 7.
Frick, B., M. Loewenhaupt, D. Debray and W. Just, 1983, Z. Phys. B **52**, 223.
Fulde, P., and M. Loewenhaupt, 1986, Adv. Phys. **34**, 589.
Fulde, P., J. Keller and G. Zwicknagl, 1988, Solid State Phys. **41**, 1.
Furrer, A., W. Bührer and P. Wachter, 1981, Solid State Commun. **40**, 1011.
Galera, R.M., D. Givord, J. Pierre, A.P. Murani, J. Schweizer, C. Vettier and K.R.A. Ziebeck, 1985a, J. Magn. & Magn. Mater. **52**, 103.
Galera, R.M., D. Givord, J. Pierre, A.P. Murani, C. Vettier and K.R.A. Ziebeck, 1985b, J. Magn. & Magn. Mater. **47–48**, 139.
Galera, R.M., A.P. Murani, J. Pierre and K.R.A. Ziebeck, 1987, J. Magn. & Magn. Mater. **63–64**, 594.
Galera, R.M., A.P. Murani and J. Pierre, 1989, Physica B **156–157**, 801.
Germann, A., and H. v. Löhneysen, 1989, Europhys. Lett. **9**, 367.
Gibbons, E.P., E.M. Forgan and K.A. McEwen, 1987, J. Phys. F **17**, L101.
Gibbons, E.P., E.M. Forgan, K.A. McEwen and A.P. Murani, 1989, Physica B **156–157**, 777.
Gignoux, D., D. Schmitt and M. Zerguine, 1988a, Phys. Rev. B **37**, 9882.
Gignoux, D., D. Schmitt, M. Zerguine and A.P. Murani, 1988b, J. Magn. & Magn. Mater. **76–77**, 401.
Goldman, A.I., 1985, Physica B **135**, 9.
Gompf, F., E. Gering, B. Renker, H. Rietschel, U. Rauchschwalbe and F. Steglich, 1987, J. Magn. & Magn. Mater. **63–64**, 344.
Goremychkin, E.A., and R. Osborn, 1991a, report RAL-91-072 and to be published in Phys. Rev. B.
Goremychkin, E.A., and R. Osborn, 1991b, report RAL-91-073 and to be published in Phys. Rev. B.
Gratz, E., E. Bauer, B. Barbara, S. Zemirli, F. Steglich, C.D. Bredl and W. Lieke, 1985, J. Phys. F **15**, 1975.
Grewe, N., 1983, Z. Phys. B **52**, 193; **53**, 2711.
Grewe, N., 1988, Solid State Commun. **66**, 1053.
Grewe, N., and P. Entel, 1979, Z. Phys. B **33**, 331.
Grewe, N., and F. Steglich, 1991, in: Handbook on the Physics and Chemistry of Rare Earths, Vol. 14, eds K.A. Gschneidner Jr and L. Eyring (North-Holland, Amsterdam) p. 343.
Grewe, N., and B. Welslau, 1988, Solid State Commun. **65**, 437.
Grewe, N., H.J. Leder and P. Entel, 1980, in: Festkörperplobleme XX. Advances in Solid State Physics, ed. H. Treusch (Vieweg, Braunschweig) p. 413.
Grewe, N., T. Pruschke and H. Keiter, 1988, Z. Phys. B **71**, 75.
Grier, B.H., S.M. Shapiro, C.F. Majkrzak and R.D. Parks, 1980, Phys. Rev. Lett. **45**, 666.
Grier, B.H., R.D. Parks, S.M. Shapiro and C.F. Majkrzak, 1981, Phys. Rev. B **24**, 6242.
Grier, B.H., J.M. Lawrence, V. Murgai and R.D. Parks, 1984, Phys. Rev. B **29**, 2664.
Grier, B.H., J.M. Lawrence, S. Horn and J.D. Thompson, 1988, J. Phys. C **21**, 1099.
Grüner, G., and A. Zawadowski, 1974, Rep. Progr. Phys. **37**, 1497.
Gschneidner Jr, K.A., and A.H. Daane, 1988, in: Handbook on the Physics and Chemistry of Rare Earths, Vol. 11, eds K.A. Gschneidner Jr and L. Eyring (North-Holland, Amsterdam) p. 409.
Gunnarsson, O., and K. Schönhammer, 1987, in: Handbook on the Physics and Chemistry of Rare Earths, Vol. 10, eds K.A. Gschneidner Jr and L. Eyring (North-Holland, Amsterdam) p. 103.
Haen, P., J. Flouquet, F. Lapierre, P. Lejay, J.M. Mignot, A. Ponchet and J. Voiron, 1987, J. Magn. & Magn. Mater. **63–64**, 320.
Harris, I.R., M. Norman and W.E. Gardner, 1972, J. Less-Common Met. **29**, 299.
Havinga, E.E., H. Damsma and M.H. Vanmaaren, 1970, J. Phys. & Chem. Solids **31**, 2653.
Havinga, E.E., K.H.J. Buschow and H.J. van Daal, 1973, Solid State Commun. **13**, 621.
Herbst, J.E., R.E. Watson and J.W. Wilkins, 1978, Phys. Rev. B **17**, 3089.
Hiebl, K., and P. Rogl, 1985, J. Magn. & Magn. Mater. **50**, 39.
Hiebl, K., C. Howarth, P. Rogl and M.J. Sienko, 1983, J. Magn. & Magn. Mater. **37**, 287.
Hippert, F., B. Hennion, F.L. Chui, M. Kohgi and T. Satoh, 1988, J. Magn. & Magn. Mater. **76–77**, 417.
Holland-Moritz, E., 1982, in: Valence Instabilities, eds P. Wachter and H. Boppart (North-Holland, Amsterdam) p. 347.
Holland-Moritz, E., 1983, J. Magn. & Magn. Mater. **38**, 253.

Holland-Moritz, E., 1985, J. Magn. & Magn. Mater. **46-47**, 127.

Holland-Moritz, E., and M. Kasaya, 1986, Physica B **136**, 424.

Holland-Moritz, E., and M. Loewenhaupt, 1979, J. Phys. Colloq. (Paris) **40**, C5-359.

Holland-Moritz, E., and A. Severing, 1986, Z. Phys. B **63**, 313.

Holland-Moritz, E., M. Loewenhaupt, W. Schmatz and D. Wohlleben, 1977, Phys. Rev. Lett. **38**, 983.

Holland-Moritz, E., D. Wohlleben and M. Loewenhaupt, 1978, J. Phys. Colloq. (Paris) **39**, C6-835.

Holland-Moritz, E., D. Wohlleben and M. Loewenhaupt, 1982, Phys. Rev. B **25**, 7482.

Holland-Moritz, E., E. Braun, B. Roden, P. Perscheid, E.V. Sampathkumaran and W. Langl, 1987, Phys. Rev. B **35**, 3122.

Holland-Moritz, E., E. Zirngiebl and S. Blumenröder, 1988, Z. Phys. B **70**, 395.

Holland-Moritz, E., W. Weber, A. Severing, E. Zirngiebl, H. Spille, W. Baus, S. Horn, A.P. Murani and J.L. Ragazzoni, 1989a, Phys. Rev. B **39**, 6409.

Holland-Moritz, E., W. Weber, G. Michels, W. Schlabitz, A. Mewis, C. Sauer and H. Mutka, 1989b, Z. Phys. B **77**, 105.

Holtzberg, F., J. Flouquet, P. Haen, F. Lapierre, Y. Lassailly and C. Vettier, 1985, J. Appl. Phys. **57**, 3152.

Horn, S., E. Holland-Moritz, M. Loewenhaupt, F. Steglich, H. Scheuer, A. Benoit and J. Flouquet, 1981a, Phys. Rev. B **23**, 3171.

Horn, S., F. Steglich, M. Loewenhaupt and E. Holland-Moritz, 1981b, Physica B **107**, 103.

Horn, S., F. Steglich, M. Loewenhaupt, H. Scheuer, W. Felsch and K. Winzer, 1981c, Z. Phys. B **42**, 125.

Houghton, A., N. Read and H. Won, 1987, Phys. Rev. B **35**, 5123.

Houghton, A., N. Read and H. Won, 1988, Phys. Rev. B **37**, 3782.

Ihrig, H., and S. Methfessel, 1976, Z. Phys. B **24**, 381.

Irkhin, V.Yu., and M.I. Katsnelson, 1989, Z. Phys. B **75**, 67.

Jaccard, D., R. Cibin, A. Bezinge, J. Sierro, K. Matho and J. Flouquet, 1988, J. Magn. & Magn. Mater. **76–77**, 255.

Jacoud, J.L., L.P. Regnault, J. Rossat-Mignod, C. Vettier, P. Lejay and J. Flouquet, 1989, Physica B **156–157**, 818.

Jacoud, J.L., L.P. Regnault, J.M. Mignot, J. Rossat–Mignod, J. Flouquet and P. Lejay, 1992, J. Magn. & Magn. Mater. **108**, 131.

Jefferson, J.M., and K.W.H. Stevens, 1978, J. Phys.: Condens. Matter **11**, 3919.

Johansson, B., 1979, Phys. Rev. B **20**, 1315.

Johansson, B., and A. Rosengren, 1975, Phys. Rev. B **11**, 2836.

Johnson, S.M., J.A.C. Bland, P.J. Brown, A. Benoit, H. Capellmann, J. Flouquet, H. Spille, F. Steglich and K.R.A. Ziebeck, 1985, Z. Phys. B **59**, 401.

Kaga, H., and T. Yoshida, 1988, Phys. Rev. B **38**, 12047.

Kaga, H., and T. Yoshida, 1989, Physica C **159**, 727.

Kaga, H., H. Kubo and T. Fujiwara, 1988, Phys. Rev. B **37**, 341.

Kappler, J.P., and A. Meyer, 1979, J. Phys. F **9**, 143.

Kawakami, N., and A. Okiji, 1985, J. Magn. & Magn. Mater. **52**, 220.

Keiter, H., and G. Czycholl, 1983, J. Magn. & Magn. Mater. **31**, 477.

Keiter, H., and J.C. Kimball, 1971, Int. J. Magn. **1**, 233.

Kirsch, T., A. Eichler, P. Morin and U. Welp, 1992, Z. Phys. B **86**, 83.

Kittel, C., 1963, in: Quantum Theory of Solids (Wiley, New York) ch. 18, p. 360.

Knopp, G., H. Spille, A. Loidl, K. Knorr, U. Rauchschwalbe, P. Felten, G. Weber, F. Steglich and A.P. Murani, 1987, J. Magn. & Magn. Mater. **63–64**, 88.

Knopp, G., A. Loidl, R. Caspary, U. Gottwick, C.D. Bredl, H. Spille, F. Steglich and A.P. Murani, 1988a, J. Magn. & Magn. Mater. **74**, 341.

Knopp, G., A. Loidl, K. Knorr, H. Spille, F. Steglich and A.P. Murani, 1988b, J. Magn. & Magn. Mater. **76–77**, 420.

Knopp, G., A. Loidl, K. Knorr, L. Pawlak, M. Duczmal, R. Caspary, U. Cottwick, H. Spille, F. Steglich and A.P. Murani, 1989, Z. Phys. B **77**, 95.

Kohgi, M., F. Hippert, L.-P. Regnault, J. Rossat-Mignod, B. Hennion, T. Satoh, F.L. Chui, T. Miura and H. Takei, 1987, Jpn. J. Appl. Phys. **26**, 559.

Kohgi, M., M. Ito, T. Satoh, H. Asano, T. Ishigaki and F. Izumi, 1990a, J. Magn. & Magn. Mater. **90–91**, 433.

Kohgi, M., T. Satoh, K. Ohoyama, M. Ari and R. Osborn, 1990b, Physica B **163**, 137.

Kohgi, M., K. Ohoyama, A. Oyamada, T. Suzuki and M. Arai, 1990c, Physica B **163**, 625.

Kohgi, M., T. Satoh, K. Ohoyama and M. Arai, 1991, Physica B **169**, 501.
Kojima, H., Y. Kuramoto and M. Tachiki, 1984, Z. Phys. B **54**, 293.
Kojima, K., H. Hayashi, A. Minami, Y. Kasamatsu and T. Hihara, 1989, J. Magn. & Magn. Mater. **81**, 267.
Komatsubara, T., N. Sato, S. Kunii, I. Oguro, Y. Furukawa, Y. Onuki and T. Kasuya, 1983, J. Magn. & Magn. Mater. **31–34**, 368.
Koskenmaki, D.C., and K.A. Gschneidner Jr, 1978, in: Handbook on the Physics and Chemistry of Rare Earths, Vol. 1, eds K.A. Gschneidner Jr and L. Eyring (North-Holland, Amsterdam) p. 337.
Krill, G., J.P. Kappler, M.F. Ravet, A. Amamou and A. Meyer, 1980, J. Phys. F **10**, 1031.
Kunii, S., 1988, J. Magn. & Magn. Mater. **76–77**, 337.
Kuramoto, Y., 1983, Z. Phys. B **53**, 37.
Kuramoto, Y., 1987, Solid State Commun. **63**, 467.
Kuramoto, Y., and H. Kojima, 1985, J. Magn. & Magn. Mater. **47–48**, 329.
Kuramoto, Y., and E. Müller-Hartmann, 1985, J. Magn. & Magn. Mater. **52**, 122.
Lahiouel, R., R.M. Galera, J. Pierre, E. Siaud and A.P. Murani, 1987, J. Magn. & Magn. Mater. **63–64**, 98.
Langreth, D.C., 1966, Phys. Rev. **150**, 712.
Larson, A.C., and D.T. Cromer, 1961, Acta Crystallogr. **14**, 73.
Lassailly, Y., C. Vettier, F. Holtzberg, J. Flouquet, C.M.E. Zeyen and F. Lapierre, 1983, Phys. Rev. B **28**, 2880.
Lassailly, Y., S.K. Burke and J. Flouquet, 1985, J. Phys. C **18**, 5737.
Lawrence, J.M., 1979, Phys. Rev. B **20**, 3770.
Lawrence, J.M., and S.M. Shapiro, 1980, Phys. Rev. B **22**, 4379.
Lawrence, J.M., P.S. Riseborough and R.D. Parks, 1981, Rep. Progr. Phys. **44**, 1.
Lebech, B., Z. Smetana and V. Sima, 1987, J. Magn. & Magn. Mater. **70**, 97.
Lee, P.A., T.M. Rice, J.W. Serene, L.J. Sham and J.W. Wilkins, 1986, Comments Condens. Mater. Phys. **12**, 99.
Lin, C.L., J. Teter, J.E. Crow, T. Mihalisin, J. Brooks, A.I. Abou-Aly and G.R. Stewart, 1985, Phys. Rev. Lett. **54**, 2541.
Lin, C.L., A. Wallash, J.E. Crow, T. Mihalisin and P. Schlottmann, 1987, Phys. Rev. Lett. **58**, 1232.
Liu, S.H., 1989, Phys. Rev. B **39**, 1403.
Loewenhaupt, M., 1984a, in: Moment Formation in Solids, ed. W.J.L. Buyers (Plenum, New York) p. 215.
Loewenhaupt, M., 1984b, unpublished data.
Loewenhaupt, M., and H. Bjerrum-MØller, 1981, Physica B **108**, 1349.
Loewenhaupt, M., and E. Holland-Moritz, 1979a, J. Magn. & Magn. Mater. **14**, 227.
Loewenhaupt, M., and E. Holland-Moritz, 1979b, J. Appl. Phys. **50**, 7456.
Loewenhaupt, M., and M. Prager, 1986, Z. Phys. B **62**, 195.
Loewenhaupt, M., and F. Steglich, 1977, in: Crystal Field Effects in Metals and Alloys, ed. A. Furrer (Plenum, New York) p. 198.
Loewenhaupt, M., B.D. Rainford and F. Steglich, 1979, Phys. Rev. Lett. **72**, 1709.
Loewenhaupt, M., S. Horn and F. Steglich, 1981, Solid State Commun. **39**, 295.
Loewenhaupt, M., J.M. Carpenter and C.-K. Loong, 1985, J. Magn. & Magn. Mater. **52**, 245.
Loewenhaupt, M., W. Reichardt, R. Pynn and E. Lindley, 1987, J. Magn. & Magn. Mater. **63–64**, 73.
Loewenhaupt, M., M. Prager, E. Gratz and B. Frick, 1988, J. Magn. & Magn. Mater. **76–77**, 415.
Loewenhaupt, M., E. Gratz, N. Pillmayr and H. Müller, 1990, Physica B **163**, 427.
Loidl, A., G. Knopp, H. Spille, F. Steglich and A.P. Murani, 1989, Physica B **156–157**, 794.
Loong, C.-K., B.H. Grier, S.M. Shapiro, J.M. Lawrence, R.D. Parks and S.K. Sinha, 1987, Phys. Rev. B **35**, 3092.
Loong, C.-K., J. Zarestky, C. Stassis, O.D. McMasters and R.M. Nicklow, 1988, Phys. Rev. B **38**, 7365.
Lysak, M.J., and D.E. MacLaughlin, 1985, Phys. Rev. B **31**, 6963.
MacLaughlin, D.E., F.R. de Boer, J. Bijvoet, P.F. de Chatel and W.C.M. Mattens, 1979, J. Appl. Phys. **50**, 2094.
Maekawa, S., S. Takahashi, S. Kashiba and M. Tachiki, 1985a, J. Appl. Phys. **57**, 3169.
Maekawa, S., S. Takahashi, S. Kashiba and M. Tachiki, 1985b, J. Phys. Soc. Jpn. **54**, 1955.
Maekawa, S., S. Takahashi, S. Kashiba and M. Tachiki, 1985c, J. Magn. & Magn. Mater. **52**, 149.
Mattens, W.C.M., F.R. de Boer, A.P. Murani and G.H. Lander, 1980, J. Magn. & Magn. Mater. **15–18**, 973.
Mazzaferro, J., C.A. Balseiro and B. Alascio, 1981, Phys. Rev. Lett. **47**, 274.
McWhan, D.B., S.M. Shapiro, J. Eckert, H.A.

Mook and R.J. Birgeneau, 1978, Phys. Rev. B **18**, 3623.

Mignot, J.-M., J.L. Jacoud, L.P. Regnault, J. Rossat-Mignod, P. Haen, P. Lejay, Ph. Boutrouille, B. Hennion and D. Pettigrand, 1990, Physica B **163**, 611.

Mignot, J.-M., Ph. Boutrouille, L.P. Regnault, P. Haen and P. Lejay, 1991, Solid State Commun. **77**, 317.

Millis, A.J., and P.A. Lee, 1987, Phys. Rev. B **35**, 3394.

Mishchenko, A.S., and K.A. Kikoin, 1991, J. Phys.: Condens. Matter **3**, 5937.

Mook, H.A., and F. Holtzberg, 1981, in: Valence Fluctuations in Solids, eds L. M. Falicov, W. Hanke and M. B. Maple (North-Holland, Amsterdam) p. 113.

Mook, H.A., and R.M. Nicklow, 1979, Phys. Rev. B **20**, 1656.

Mook, H.A., T. Penny, F. Holtzberg and M.W. Shafer, 1978a, J. Phys. Colloq. (Paris) **39**, C6-837.

Mook, H.A., R.M. Nicklow, T. Penny, F. Holtzberg and M.W. Shafer, 1978b, Phys. Rev. B **18**, 2925.

Mook, H.A., D.B. McWhan and F. Holtzberg, 1982, Phys. Rev. B **25**, 4321.

Moon, R.M., and W.C. Koehler, 1979, J. Appl. Phys. **50**, 2089.

Moon, R.M., W.C. Koehler, D.B. McWhan and F. Holtzberg, 1978, J. Appl. Phys. **49**, 2107.

Moon, R.M., S.H. Liu and K. Werner, 1983, J. Magn. & Magn. Mater. **31–34**, 387.

Morin, P., 1988, J. Magn. & Magn. Mater. **71**, 151.

Morin, P., C. Vettier, J. Flouquet, M. Konczykowski, Y. Lassailly, J.M. Mignot and U. Welp, 1988, J. Low Temp. Phys. **70**, 377.

Moshchalkov, V.V., and N.B. Brandt, 1986, Sov. Phys. Usp. **29**, 725.

Müller–Hartmann, E., 1984, Z. Phys. B **57**, 281.

Murani, A.P., 1983a, J. Phys. F **16**(33), 6359.

Murani, A.P., 1983b, Phys. Rev. B **28**, 2308.

Murani, A.P., 1985a, Phys. Rev. Lett. **54**, 1444.

Murani, A.P., 1985b, J. Magn. & Magn. Mater. **47–48**, 142.

Murani, A.P., 1986, J. Magn. & Magn. Mater. **61**, 212.

Murani, A.P., 1987a, Phys. Rev. B **36**, 5705.

Murani, A.P., 1987b, in: Theoretical and Experimental Aspects of Valence Fluctuations and Heavy Fermions, eds L.C. Gupta and S.K. Malik (Plenum, New York) p. 287.

Murani, A.P., K. Knorr and K.H.J. Buschow, 1977, in: Crystal Field Effects in Metals and Alloys, ed. A. Furrer (Plenum, New York) p. 268.

Murani, A.P., K. Knorr, K.H.J. Buschow, A. Benoit and J. Flouquet, 1980, Solid State Commun. **36**, 523.

Murani, A.P., W.C.M. Mattens, F.R. de Boer and G.H. Lander, 1985, Phys. Rev. B **31**, 52.

Murani, A.P., R. Currat, A. Severing and R. Raphel, 1990a, Physica B **163**, 717.

Murani, A.P., W.G. Marshall, A.D. Taylor and R. Osborn, 1990b, ISIS experimental report ULS 85/1, p. A164.

Neuhaus, W., 1987, Berichte der KFA Jülich, Jül-2165.

Newns, D.M., and N. Read, 1987, Adv. Phys. **36**, 799.

Nozières, P., 1974, J. Low Temp. Phys. **17**, 31.

Nunez, V., R. Trump, P.J. Brown, T. Chattopadhyay, M. Loewenhaupt and F. Tasset, 1992, J. Phys.: Condens. Matter **4**, 1115.

Ohkawa, F.J., and T. Yamamoto, 1987, Physica B **148**, 84.

Ohoyama, K., M. Kohgi, T. Nakane, M. Arai, A.D. Taylor, A. Oyamada and T. Suzuki, 1992, Physica B **180** + **181**, 250.

Onuki, Y., and T. Komatsubara, 1987, J. Magn. & Magn. Mater. **63–64**, 281.

Onuki, Y., Y. Shimizu, M. Nishihara, Y. Machii and T. Komatsubara, 1985a, J. Phys. Soc. Jpn. **54**, 1964.

Onuki, Y., Y. Machii, Y. Shimizu, T. Komatsubara and T. Fujita, 1985b, J. Phys. Soc. Jpn. **54**, 3562.

Orlov, V.G., 1988, Solid State Commun. **67**, 689.

Osborn, R., and E.A. Goremychkin, 1991, ISIS report 1991, Vol. II, p. A208.

Osborn, R., M. Loewenhaupt, B.D. Rainford and W.G. Stirling, 1987, J. Magn. & Magn. Mater. **63–64**, 70.

Osborn, R., K.A. McEwen, E.A. Goremychkin and A.D. Taylor, 1990, Physica B **163**, 37.

Osborn, R., S.W. Lovesey, A.D. Taylor and E. Balcar, 1991, in: Handbook on the Physics and Chemistry of Rare Earths, Vol. 14, eds K.A. Gschneidner Jr and L. Eyring (North-Holland, Amsterdam) p. 1.

Ott, H.R., 1987, in: Progress in Low Temperature Physics, Vol. XI, ed. D.F. Brewer (Elsevier, Amsterdam) p. 215.

Ott, H.R., H. Rudiger and F. Hulliger, 1985, Solid State Commun. **55**, 113.

Panissod, P., M. Benakki and A. Qachaou, 1988, J. Phys. Colloq. (Paris) **49**, C8-685.

Panousis, N.T., and K.A. Gschneidner Jr, 1972, Phys. Rev. B **5**, 4767.

Perez, I., G. Liang, J.B. Zhou, H. Jhans, S.A. Shaheen and M. Croft, 1990, Physcia B **163**, 618.

Perscheid, B., E.V. Sampathkumaran and G. Kaindl, 1985, J. Magn. & Magn. Mater. **47 + 48**, 410.

Peysson, Y., C. Ayache, J. Rossat-Mignod, S. Kunii and T. Kasuya, 1986, J. Phys. (Paris) **47**, 113.

Pintschovius, L., E. Holland–Moritz, D. Wohlleben, S. Stöhr and J. Liebertz, 1980, Solid State Commun. **34**, 953.

Pintschovius, L., E. Holland–Moritz, D. Wohlleben, S. Stöhr, J. Liebertz, W. Assmus, C. Stassis, C.-K. Loong, J. Zarestky and R.M. Moon, 1983, Solid State Commun. **47**, 663.

Polatsek, G., and P. Bonville, 1992, Z. Phys. B **88**, 189.

Rainford, B.D., B. Buras and B. Lebech, 1977, Physica B **86–88**, 41.

Rajan, V.T., 1983, Phys. Rev. Lett. **51**, 308.

Rasul, J.W., and P. Schlottmann, 1989a, Phys. Rev. B **39**, 3065.

Rasul, J.W., and P. Schlottmann, 1989b, Phys. Rev. Lett. **62**, 1325.

Read, N., D.M. Newns and S. Doniach, 1984, Phys. Rev. B **30**, 3841.

Regnault, L.P., W.A.C. Erkelens, J. Rossat–Mignod, C. Vettier, S. Kunii and T. Kasuya, 1988, J. Magn. & Magn. Mater. **76–77**, 413.

Regnault, L.P., J.L. Jacoud, J.M. Mignot, J. Rossat–Mignod, C. Vettier, P. Lejay and J. Flouquet, 1990, Physica B **163**, 606.

Reichardt, W., and N. Nücker, 1984, J. Phys. F **14**, L135.

Renker, B., E. Gering, F. Gompf, H. Schmidt and H. Rietschel, 1987, J. Magn. & Magn. Mater. **63 + 64**, 31.

Ribault, M., J. Flouquet, P. Haen, F. Lapierre, J.M. Mignot and F. Holtzberg, 1980, Phys. Rev. Lett. **45**, 1295.

Robinson, J.M., 1979, Phys. Rev. Rep. **51**, 1.

Rogl, P., 1984, in: Handbook on the Physics and Chemistry of Rare Earths, Vol. 7, eds K.A. Gschneidner Jr and L. Eyring (North-Holland, Amsterdam) p. 1.

Röhler, J., 1987, in: Handbook on the Physics and Chemistry of Rare Earths, Vol. 10, eds K.A. Gschneidner Jr and L. Eyring (North-Holland, Amsterdam) p. 453.

Rossat–Mignod, J., L.P. Regnault, J.L. Jacoud, C. Vettier, P. Lejay, J. Flouquet, E. Walker, D. Jaccard and A. Amato, 1988, J. Magn. & Magn. Mater. **76–77**, 376.

Rossel, C., K.N. Yang, M.B. Maple, Z. Fisk, E. Zirngiebl and J.D. Thompson, 1987, Phys. Rev. B **35**, 1914.

Sales, B.C., and R. Viswanathan, 1976, J. Low Temp. Phys. **23**, 449.

Schefzyk, R., W. Lieke, F. Steglich, T. Goto and B. Lüthi, 1984, J. Magn. & Magn. Mater. **45**, 229.

Schlottmann, P., 1982, Phys. Rev. B **25**, 2371.

Schlottmann, P., 1984, Phys. Rev. B **29**, 4468.

Schlottmann, P., 1989, Phys. Rep. **181**, 1.

Schmidt, H.J., and E. Müller–Hartmann, 1989, Z. Phys. B **75**, 331.

Schmitt, D., P. Morin and J. Pierre, 1978, J. Magn. & Magn. Mater. **8**, 249.

Schröder, A., H.G. Schlager and H. v. Löhneysen, 1992, J. Magn. & Magn. Mater. **108**, 47.

Severing, A., and A.P. Murani, 1990, Physica B **163**, 699.

Severing, A., W. Reichardt, E. Holland–Moritz, D. Wohlleben and W. Assmus, 1988, Phys. Rev. B **38**, 1773.

Severing, A., E. Holland–Moritz, B.D. Rainford, S.R. Culverhouse and B. Frick, 1989a, Phys. Rev. B **39**, 2557.

Severing, A., E. Holland–Moritz and B. Frick, 1989b, Phys. Rev. B **39**, 4164.

Severing, A., A.P. Murani, J.D. Thompson, Z. Fisk and C.-K. Loong, 1990a, Phys. Rev. B **41**, 1739.

Severing, A., E. Gratz, B.D. Rainford and K. Yoshimura, 1990b, Physica B **163**, 409.

Shapiro, S.M., 1986, Physica B **136**, 365.

Shapiro, S.M., and B.H. Grier, 1982, Phys. Rev. B **25**, 1457.

Shapiro, S.M., R.J. Birgeneau and E. Bucher, 1975, Phys. Rev. Lett. **34**, 470.

Shapiro, S.M., J.D. Axe, R.J. Birgeneau, J.M. Lawrence and R.D. Parks, 1977, Phys. Rev. B **16**, 2225.

Shapiro, S.M., H. Bjerrum–MØller, J.D. Axe, R.J. Birgeneau and E. Bucher, 1978, J. Appl. Phys. **49**, 2101.

Shapiro, S.M., E. Gurewitz, R.D. Parks and L.D. Kupferberg, 1979, Phys. Rev. Lett. **43**, 1748.

Shapiro, S.M., C. Stassis and G. Aeppli, 1989, Phys. Rev. Lett. **62**, 94.

Shiba, H., 1975, Prog. Theor. Phys. **54**, 967.

Shimizu, T., H. Yasuoka, Z. Fisk and J.L. Smith, 1987, J. Phys. Soc. Jpn. **56**, 4113.

Smith, H.G., G. Dolling and T. Goto, 1985, Solid State Commun. **53**, 15.

Stassis, C., 1986, Physica B **137**, 61.
Stassis, C., C.-K. Loong, G.R. Kline, O.D. McMasters and K.A. Gschneidner Jr, 1978, J. Appl. Phys. **49**, 2113.
Stassis, C., C.-K. Loong, O.D. McMasters and R.M. Moon, 1979a, J. Appl. Phys. **50**, 2091.
Stassis, C., C.-K. Loong, B.N. Harmon, S.H. Liu and R.M. Moon, 1979b, 303.
Stassis, C., T. Gould, O.D. McMasters, K.A. Gschneidner Jr and R.M. Moon, 1979c, Phys. Rev. B **19**, 5746.
Stassis, C., C.-K. Loong, J. Zarestky, O.D. McMasters, R.M. Moon and J.R. Thompson, 1982, J. Appl. Phys. **53**, 7890.
Stassis, C., J.D. Axe, C.F. Majkrzak, B. Batlogg and J.P. Remeika, 1985, J. Appl. Phys. **57**, 3087.
Stassis, C., B. Batlogg, J.P. Remeika, J.D. Axe, G. Shirane and Z.J. Uemura, 1986, Phys. Rev. B **33**, 1680.
Steglich, F., 1985, in: Theory of Heavy Fermions and Valence Fluctuations, eds T. Kasuya and T. Saso (Springer, Berlin) p. 23, and references therein.
Steglich, F., 1991, J. Magn. & Magn. Mater. **100**, 186.
Steglich, F., J. Aarts, C.D. Bredl, W. Lieke, D. Meschede, W. Franz and H. Schäfer, 1979a, Phys. Rev. Lett. **43**, 1892.
Steglich, F., C.D. Bredl, M. Loewenhaupt and K.D. Schotte, 1979b, J. Phys. Colloq. (Paris) **40**, C5-301.
Steglich, F., U. Alheim, C. Schank, C. Geibel, S. Horn, M. Lang, G. Sparn, A. Loidl and A. Krimmel, 1990, J. Magn. & Magn. Mater. **84**, 271.
Stewart, G.R., 1984, Rev. Mod. Phys. **56**, 755.
Stroka, B., A. Schröder, T. Trappmann, H. v. Löhneysen, M. Loewenhaupt and A. Severing, 1992, Z. Phys. B, in print.
Tachiki, M., S. Takahashi and T. Koyama, 1987, Jpn. J. Appl. Phys. Suppl. **26**(3), 493.
Takayanagi, S., I. Umehara, K. Sato, Y. Onuki and N. Wada, 1990, J. Magn. & Magn. Mater. **90–91**, 479.
Takke, R., M. Niksch, W. Assmus, B. Lüthi, R. Pott, R. Schefzyk and D. Wohlleben, 1981a, Z. Phys. B **44**, 33.
Takke, R., N. Dolezal, W. Assmus and B. Lüthi, 1981b, J. Magn. & Magn. Mater. **23**, 247.
Taylor, K.N.R., 1971, Adv. Phys. **20**, 551.
Thalmeier, P., 1984, J. Phys. F **17**, 4153.
Thalmeier, P., and P. Fulde, 1982, Phys. Rev. Lett. **49**, 1588.
Thalmeier, P., and B. Lüthi, 1991, in: Handbook on the Physics and Chemistry of Rare Earths, Vol. 14, eds K.A. Gschneidner Jr and L. Eyring (North-Holland, Amsterdam) p. 225.
Thompson, J.R., S.T. Sekula, C.-K. Loong and C. Stassis, 1982, J. Appl. Phys. **53**, 7893.
Tomala, K., D. Weschenfelder, G. Czjzek and E. Holland-Moritz, 1990, J. Magn. & Magn. Mater. **89**, 143.
Trump, R., 1991, Dissertation, University of Cologne (unpublished).
Trump, R., S. Thierfeld, M. Loewenhaupt and T. Chattopadhyay, 1991, J. Appl. Phys. **69**, 4699.
Tsvelick, A.M., and P.B. Wiegmann, 1982, J. Phys. F **15**, 1707.
Tsvelick, A.M., and P.B. Wiegmann, 1983, J. Phys. F **16**, 2281 and 2321.
Uemura, Y.J., C.F. Majkrzak, G. Shirane, C. Stassis, G. Aeppli, B. Batlogg and J.P. Remeika, 1986, Phys. Rev. B **33**, 6508.
Varma, C.M., 1985, Comments Solid State Phys. **11**, 221.
Vettier, C., P. Morin and J. Flouquet, 1986, Phys. Rev. Lett. **56**, 1980.
Vettier, C., P. Burlet and J. Rossat-Mignod, 1987, J. Magn. & Magn. Mater. **63–64**, 18.
Wakabayashi, N., 1980, Phys. Rev. B **22**, 5833.
Walter, U., and D. Wohlleben, 1987, Phys. Rev. B **35**, 3576.
Walter, U., Z. Fisk and E. Holland-Moritz, 1985, J. Magn. & Magn. Mater. **47–48**, 159.
Walter, U., D. Wohlleben and Z. Fisk, 1986, Z. Phys. B **62**, 325.
Walter, U., E. Holland-Moritz and Z. Fisk, 1991, Phys. Rev. B **43**, 320.
Walter, U., E. Holland-Moritz and U. Steigenberger, 1992, Z. Phys. B **89**, 169.
Weber, W., E. Holland-Moritz and K. Fischer, 1989a, Europhys. Lett. **8**, 257.
Weber, W., E. Holland-Moritz and A.P. Murani, 1989b, Z. Phys. B **76**, 229.
Welp, U., 1988, Dissertation, University of Konstanz, unpublished.
White, R.M., 1970, in: Quantum Theory of Magnetism (McGraw-Hill, New York).
Wilson, K.G., 1975, Rev. Mod. Phys. **47**, 773.
Wohlleben, D., 1976, J. Phys. Colloq. (Paris) C4-231.
Wohlleben, D., and B.R. Coles, 1973, in: Magnetism, Vol. 5, ed. H. Suhl (Academic Press, New York) p. 3.
Yashima, H., N. Sato, H. Mori and T. Satoh, 1982, Solid State Commun. **43**, 595.
Yoshimura, K., T. Nitta, M. Mekata, T. Shimizu,

T. Sakakibara, T. Goto and G. Kido, 1988, Phys. Rev. Lett. **60**, 851.
Yosida, K., 1957, Phys. Rev. **107**, 396.
Zevin, V., G. Zwicknagl and P. Fulde, 1988a, Phys. Rev. Lett. **60**, 3221.
Zevin, V., G. Zwicknagl and P. Fulde, 1988b, J. Magn. & Magn. Mater. **76–77**, 475.
Zhang, F.C., and T.K. Lee, 1983, Phys. Rev. B **28**, 33.
Zhang, F.C., and T.K. Lee, 1984, Phys. Rev. B **30**, 1556.
Zhang, F.C., T.K. Lee and Z.B. Su, 1987, Phys. Rev. B **35**, 4728.
Zirngiebl, E., and G. Güntherodt, 1991, in: Handbook on the Physics and Chemistry of Rare Earths, Vol. 14, eds K.A. Gschneidner Jr and L. Eyring (North-Holland, Amsterdam) p. 163.
Zirngiebl, E., B. Hillebrands, S. Blumenröder, G. Güntherodt, M. Loewenhaupt, J.M. Carpenter, K. Winzer and Z. Fisk, 1984, Phys. Rev. B **30**, 4052.
Zwicknagl, G., V. Zevin and P. Fulde, 1990, Z. Phys. B **79**, 365. Erratum: 1991, Z. Phys. B **83**, 153.

Handbook on the Physics and Chemistry of Rare Earths, Vol. 16
edited by K.A. Gschneidner, Jr. and L. Eyring

Chapter 106

THERMAL CONDUCTIVITY OF RARE EARTH COMPOUNDS

I.A. SMIRNOV and V.S. OSKOTSKI
Russian Academy of Sciences, A.F. Ioffe Physico-Technical Institute, St. Petersburg, Russia

Contents

Symbols and abbreviations

a	lattice constant	H_{cr}	critical magnetic field for destroying superconductivity
(ac)	crystal plane		
a, c	crystal axes	H_{c1}, H_{c2}	low and high critical magnetic field
A_d	de Gennes factor	H_s	magnetic field of κ saturation
C	heat capacity	H_{s0}	high magnetic field for suppression of carriers
CJTE	cooperative Jahn–Teller effect		
C_e	electron heat capacity	I	exchange integral
d	density	$\boldsymbol{J}$	total angular moment
D	thermal diffusivity	$\boldsymbol{k}$	electron wave vector
DKL	dilute Kondo lattice	k_0	Boltzmann constant
e	electron charge	l	free path length of phonons
f	Fermi function	L	Lorentz number
F	Fermi integral	$\boldsymbol{L}$	orbital moment
g	Landé factor	LA	longitudinal acoustic
$g(\varepsilon_F)$	electron density of states at Fermi level	LO	longitudinal optic
		L_{cf}	Lorentz number of the crystal field effect
$\hbar$	$h/2\pi$, h is the Planck constant		
H	magnetic field	L_{eff}	effective Lorentz number
HFS	heavy-fermion system	L_N	nonparabolic Lorentz number
HTSC	high-temperature superconductivity	L_0	Sommerfeld value of the Lorentz number

${}^{n}_{k}L^{n}$	generalised Fermi integral
m	electron mass
m^*	effective electron mass
m_h^*	effective mass of heavy electrons
m_l^*	effective mass of light electrons
M	atomic mass
MPL	magnetic percolation limit
MPT	magnetic phase transition
MTLS	magnetic two-level system
n	normal state of a metal
n_c	electron number from a level in a conduction band
N	normal process of phonon scattering
N	degeneracy of an f-level
NM	nonmagnetic
N_a	number of free electrons per atom
$\boldsymbol{q}, \boldsymbol{q}_1, \boldsymbol{q}_2, \boldsymbol{q}_3$	phonon wave vectors
Q	electron number for an f-level
r	atomic radius
R	rare earth element
R	electrical resistivity
REC	rare earth compound
$\boldsymbol{S}$	spin moment
SOPT	spin-orientation phase transition
T	temperature
TA	transverse acoustic
TO	transverse optic
T_c	superconduction critical temperature
T_C	Curie temperature
T_f	temperature of "freezing"
T_{fer}	ferroelectric phase transition temperature
T_K	Kondo temperature
T_{JT}	Jahn–Teller phase transition temperature
T_N	Néel temperature
T_s	spin-reorientation temperature
T_{1s}, T_{2s}	temperatures of the beginning and the end of the reorientation process
T^*	high-temperature limit of coherent interaction between heavy fermions
U	Umklapp-process of phonon scattering
v	mean phonon velocity
W	thermal resistivity
W_e	electron thermal resistivity
W_i	ideal electron thermal resistivity due to scattering by phonons
W_L	lattice thermal resistivity
W_0	electron thermal resistivity due to scattering by impurities and defects
x	concentration
x_{MPL}	magnetic percolation limit of concentration
α	thermal electromotive force
α_N	nonparabolic thermal electromotive force
β	$= k_0 T \varepsilon_g^*$
γ	electronic specific heat coefficient
δ	linear expansion coefficient
Δ	resonance energy of phonons
$\Delta\kappa_{res}$	change of thermal conductivity due to resonance scattering of phonons
ε_F	Fermi energy
ε_g	width of a forbidden band
ε_g^*	effective width of a forbidden band
ϑ_0	angle of magnetic moment rotation
Θ	Debye temperature
Θ_1	low Debye temperature
Θ_2	high Debye temperature
κ	thermal conductivity
κ_b	bipolar thermal conductivity
κ_c	electron thermal conductivity
κ_{exc}	exciton thermal conductivity
κ_L	lattice thermal conductivity
κ_m	magnon thermal conductivity
κ_{MPL}	magnetic percolation limit of thermal conductivity
κ_{phot}	photon thermal conductivity
κ_{tot}	total thermal conductivity
λ	phonon wave length
μ	$= \varepsilon_F / k_0 T$, residual Fermi level
μ_B	Bohr magneton
ν	electron band density of states
ρ	electrical resistivity
ρ_i	ideal electrical resistivity
ρ_{magn}	magnon electrical resistivity
ρ_{ph}	electrical resistivity due to phonon scattering
ρ_{spd}	electrical resistivity due to spin-disorder scattering
ρ_{tot}	total electrical resistivity
ρ_0	residual electrical resistivity
σ	electrical conductivity
τ	relaxation time of phonons
τ_b	boundary relaxation time of phonons
τ_c	colloid relaxation time of phonons
τ_d	point defect relaxation time of phonons

τ_D	dislocation relaxation time of phonons	τ_p	paramagnetic-ion relaxation time of phonons
τ_e	conduction-electron relaxation time of phonons	τ'_R	molecular impurity relaxation time of phonons
τ_{ff}	four-phonon relaxation time of phonons	τ''_R	quasilocal vibrational relaxation time of phonons
τ_N	normal-process relaxation time of phonons	τ_U	Umklapp-process relaxation time of phonons
		ω	phonon frequency

1. Introduction

Rare earth compounds (RECs) include a wide set of new classes of materials with unusual and sometimes unique properties. By now several thousand of RECs have been synthesized: oxides (Arsen'ev et al. 1983), chalcogenides, hydrides, borides, carbides, phosphides, pnictides, halogenides (Kost et al. 1983), zirconates, hafnates, niobates, tantalates, antimonates (Arsen'ev et al. 1985), carbonates, oxalates, nitrates, titanates (Komissarova et al. 1984), silicates, germanates, phosphates, arsenates, vanadates (Bondar' et al. 1983), sulphates, selenates, tellurates, chromates and others. Luckily for the authors, thermal conductivity has been measured by now in no more than hundred RECs. The main feature of RECs is that they include the lanthanide ions with the unfilled inner shells containing from zero (La-$4f^0$) to 14 (Lu-$4f^{14}$) electrons. The ions with the unfilled inner shells have noncompensated momenta, therefore one expects magnetic ordering in compounds with such ions. However, because of the specificity of filling and behaviour of the 4f shells (see table 4) not all RECs are magnetics. So, one can separate the RECs in two groups: magnetics and nonmagnetics. The 4f-shells do not overlap in RECs (the radius of the 4f shell is ~ 0.3 Å, which is ~ 0.1 of the interatomic distance) and they form localized atomic-like states with concentration $\sim 10^{22}$ cm^{-3} (Smirnov 1981). The 4f levels are involved in some RECs:

(a) in a forbidden band (lanthanide semiconductors) in which they are present as "impurity levels" (Smirnov 1981, Smirnov and Oskotski 1978). [These "impurity levels" are unique, because in the usual semiconductors (Ge, Si, A_3B_5, A_2B_6) it is impossible to create such a large concentration of impurity levels. In lanthanide semiconductors the 4f levels determine the main kinetic effects, optics and unusual phase transitions] or,

(b) in a conduction band, forming systems with Kondo impurities, concentrated Kondo lattices, heavy fermions and intermediate valencies of lanthanide ions depending on the position of the 4f levels relative to the Fermi level (and on the lanthanide ion concentration) (see section 5).

All of the above listed nonstandard classes of lanthanide materials show their specific character in nonstandard behaviour of physical parameters. For example,

(1) coexistence is possible of magnetism and intermediate valency (Matlak and Nolting 1983), magnetism and superconductivity (see section 8.3), magnetism and ferroelectricity (Venevtsev and Lubimov 1990):

(2) it is possible to induce by a magnetic field the Kondo effect (Sandalov and Podmarkov 1985) and superconductivity (Buzdin and Moschalkov 1986), and, by powerful optical pumping, magnetic phase transitions in magnetically ordered lanthanide compounds (Golovenchits et al. 1981, Golovenchits and Sanina 1982);

(3) induced ferromagnetism (arising as a result of competition between the exchange interaction effect and the crystal field effect) is observed (Guertin and Foner 1978, Bucher et al. 1972);

(4) in systems with heavy fermions destruction of the superconductivity by introducing nonmagnetic impurities occurs and, on the other hand, the superconduction transition temperature (T_c) increases with increasing magnetic ion concentration (Buzdin and Moshchalkov 1986);

(5) in a number of systems there is a "re-entrant" superconductivity (with two and even three superconduction transition temperatures);

(6) all systems have unusual dependences (on temperature, magnetic and electric fields, and pressure) of the various parameters of transport, optical, magnetic and other effects.

From the history of thermal conductivity (κ) investigations in solids one can see that κ has always "responded" on the appearance of new effects. We will try to review the unusual character of κ in RECs. Unfortunately, κ of many interesting RECs has not yet been measured and many mysteries have no answer at this moment. This review is the first major review devoted to κ of RECs. There is only one prior review devoted to κ and other thermal properties of rare earth chalcogenides (Smirnov 1972), in which data are collected up to 1972.

This review is not a reference book on κ of RECs. Here we are trying to show on typical examples how the unusual properties of RECs reveal themselves in the behaviour of κ. Naturally, because of the limited size of this review, we could not analyse all literature data on κ of RECs. Before we analyse the specific behaviour of κ in RECs, we will briefly discuss in the next section the usual (classical) regularities in the behaviour of κ of standard solids. This should help readers to understand what new features are added to the whole picture of the behaviour of the thermal conductivity by the results on κ of RECs. This review is mainly devoted to discussing the experimental work.

2. Brief summary of thermal conductivity of solids

The total thermal conductivity κ_{tot} of insulators, metals and semiconductors consists of the following contributions:

insulators: $\kappa_{tot} = \kappa_L$,
metals: $\kappa_{tot} = \kappa_L + \kappa_e$,
semiconductors: $\kappa_{tot} = \kappa_L + \kappa_e + \kappa_b + \kappa_{ph} + \kappa_{exc}$,

where κ_L is the lattice, κ_e is the electron, κ_b the bipolar, κ_{ph} the photon and κ_{exc} the exciton contribution to the thermal conductivity. A contribution κ_m, the magnon

thermal conductivity, is possible in magnetic insulators, metals and semiconductors at low temperatures due to heat transport by spin waves. At present the main theoretical propositions of the thermal conductivity κ of solids are obtained, comprehended and described in Oskotski and Smirnov (1972), Berman (1976), Smirnov and Tamarchenko (1977) and other monographs, and many reviews.

2.1. *Thermal conductivity of a crystal lattice*

A thermal flow is carried by phonons and its value and temperature behaviour depend on the contribution of different scattering mechanisms. $\kappa_L(T)$ of semiconductors and insulators is similar, while κ_L of metals is significantly smaller in the low-temperature region because of strong phonon–electron scattering (fig. 1). At low temperatures ($T \ll \Theta$, Θ is the Debye temperature) phonons are scattered, mainly, by crystal boundaries and $\kappa_L \propto T^3$. At $T > \Theta$ phonon–phonon scattering results in a temperature dependence $\kappa_L \propto T^{-1}$. At $T < \Theta$ exists a temperature region with $\kappa_L \propto \exp(\Theta/aT)$. In metals at $T \ll \Theta$ due to phonon–electron scattering $\kappa_L \propto T^2$. As it has been noted above, different temperature dependences could occur in other temperature regions of $\kappa_L(T)$ due to contributions from different scattering mechanisms.

For three-phonon interactions one distinguishes two types of collisions: normal processes (N processes), in which the total momentum is conserved and the direction of flow does not change (these processes lead to infinite thermal conductivity); and Umklapp processes (U processes), in which the sum of the wave vectors is not conserved and changes sharply, leading to a finite thermal resistivity of a crystal. In U processes the following conditions are fulfilled:

$$\omega_1 + \omega_2 = \omega_3, \tag{1}$$

$$\boldsymbol{q}_1 + \boldsymbol{q}_2 = \boldsymbol{q}_3 = 2\pi \boldsymbol{b}, \tag{2}$$

where ω is an angular frequency, $\boldsymbol{q}_1$, $\boldsymbol{q}_2$ and $\boldsymbol{q}_3$ are phonon wave vectors, and $\boldsymbol{b}$ is a reciprocal lattice vector. The theory of lattice thermal conductivity meets with difficulties with N processes, especially at low temperatures, when long-wavelength phonons prevail and N processes are the main type of phonon–phonon scattering. Although N processes themselves do not produce a thermal resistance, they influence κ_L indirectly by redistributing phonons of different modes. Three-phonon N and U processes are mainly anharmonic processes. However, processes of higher orders are

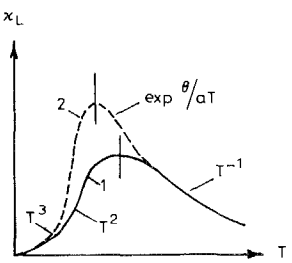

Fig. 1. Schematic shape of the temperature dependence of κ_L for metals (1) and insulators (semiconductors) (2).

possible when simultaneously four of more phonons interact (Oskotski and Smirnov 1972, Berman 1976, Smirnov and Tamarchenko 1977). To satisfy condition (2), interacting phonons are to have wave vectors near $\pi \boldsymbol{b}$. At $T > \Theta$ there are many such phonons, and U processes occur often, their number increases proportional to T, and $\kappa_L \propto T^{-1}$. At $T \ll \Theta$ the number of phonons with wave vectors near $\pi \boldsymbol{b}$ decreases exponentially giving rise to a fast increase of κ_L by the law $\kappa_L \propto \exp(\Theta/aT)$ (a is a coefficient of order two). At low and medium temperatures the acoustic phonons of the spectrum participate in the heat transport and scattering processes. At high temperature optical phonons are excited. Then κ_L can increase due to additional heat transport by optical phonons, or decrease due to additional scattering of acoustic phonons by optical ones (Blackman 1935, Gurevich 1959, Leroux-Huqou and Veyssie 1965, Devyatkova and Smirnov 1962, Slack 1979).

Usually theoretical analysis of κ_L data is carried out in the Debye model in the relaxation-time approximation, where κ_L has the form

$$\kappa_L = GT^3 \int_0^{\Theta/T} \frac{x^4}{\tau^{-1} \sinh^2(\frac{1}{2}x)} \, dx. \tag{3}$$

Here $x = \hbar\omega/k_0 T$, G is a constant, τ^{-1} is the sum of the reciprocal relaxation times of phonons in different scattering processes: $\tau^{-1} = \Sigma \tau_i^{-1}$, where $\tau_i = \tau_b, \tau_d, \tau_e, \tau_D, \tau_c, \tau'_R, \tau''_R, \tau_p, \tau_U, \tau_N, \tau_F$, the relaxation times of phonon scattering, correspondingly, on crystal boundaries, point defects and impurities, conduction electrons, dislocations, colloids, molecular impurities, quasi-local vibrations, paramagnetic ions, U, N and four-phonon processes. Each τ^{-1} has its own frequency and temperature dependence (Oskotski and Smirnov 1972, Berman 1976, Smirnov and Tamarchenko 1977). In fig. 2 the temperature regions are marked in which the various scattering mechanisms are significant. Callaway (1959) has shown how it is possible to account in eq. (3) for the relaxation time of N processes. Holland (1963) has proposed a mechanism which, for τ_N^{-1} and τ_R^{-1}, takes into account some details of phonon spectra and the separated heat flows transferred by transverse and longitudinal acoustic phonons. To conform

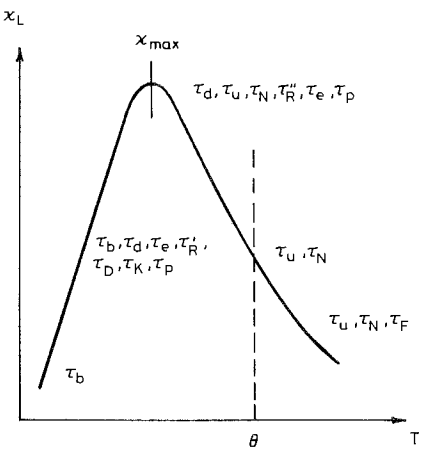

Fig. 2. Schematic shape of the temperature dependence of κ_L for solids. The temperature regions are marked, where various phonon scattering processes play an appreciable role. Θ is the Debye temperature.

experimental and theoretical values of κ_L, according to eq. (3) one has to introduce a great number of fitting constants (for example, Al-Edani and Dubey (1986) have introduced twenty constants for κ_L of GdS). The more mechanisms of phonon scattering are introduced, the greater is the number of fitting constants. Sometimes some of the constants can be evaluated by independent theoretical calculations or measured experimentally. In this review we will try to use this method of analysis as seldom as possible and limit ourselves only to the physical nature of the behaviour of $\kappa_L(T)$. Thus, analysing experimental data on $\kappa_L(T)$ of RECs we consider the results "standard" if $\kappa_L(T)$ has a value and a temperature dependence predicted by the theory for ordinary solids (Oskotski and Smirnov 1972, Berman 1976, Smirnov and Tamarchenko 1977), and "nonstandard" if there are deviations from the theory.

2.2. *Electron contribution to the thermal conductivity*

The electron thermal conductivity of metals and semiconductors is determined by the Wiedemann–Franz law

$$\kappa_e = LT/\rho, \tag{4}$$

where L is the Lorentz number and ρ is the electrical resistivity. In the low-temperature region ($T < \Theta/10$) the electron thermal resistivity, $W_e = 1/\kappa_e$, can be presented in the form (Smirnov and Tamarchenko 1977)

$$W_e = W_0 + W_i, \tag{5}$$

where W_0 is the thermal resistivity caused by electron scattering by impurities and defects ($W_0 = \rho_0/L_0 T$, with ρ_0 the residual electrical resistivity, L_0 the Sommerfeld value of the Lorentz number and $L_0 = \frac{1}{3}(k_C/e)^2\pi^2 = 2.45 \times 10^{-8}$ W Ω/K^2) and W_i is the ideal thermal resistivity caused by electron scattering of phonons (Oskotski and Smirnov 1972, Berman 1976, Smirnov and Tamarchenko 1977)

$$W_i = B\left(\frac{T}{\Theta}\right)^2\left[I_5\frac{\Theta}{T} + \frac{D}{\varepsilon_F}\frac{\Theta}{T}\left(\frac{2\pi^2}{3}I_5\frac{\Theta}{T} - \frac{1}{3}I_7\frac{\Theta}{T}\right)\right]. \tag{6}$$

Here B and D are constants, ε_F is the Fermi energy, and I_5 and I_7 are integrals of the type

$$I_n(x) = \int_0^x \frac{z^n\,dz}{(e^z - 1)(1 - e^{-z})}. \tag{7}$$

These integrals are tabulated in Smirnov and Tamarchenko (1977). Equation (5) is obtained by analogy with the case of the electrical resistivity $\rho_{tot} = \rho_0 + \rho_i$ (where ρ_i is the ideal electrical resistivity caused by electron scattering by thermal vibrations).

At low temperatures $W_L \propto T^2$, so eq. (5) can be presented in the form

$$W_e = \rho_0/L_0 T + \alpha T^2 = \beta/T + \alpha T^2, \tag{8}$$

$$W_e T = \alpha T^3 + \beta. \tag{9}$$

The temperature dependence, $W_e = f(T^3)$, is a straight line with a slope of α. The intercept on the W_e-axis is β. The parameter α must be a constant for a certain class of materials and independent of sample purity (Smirnov and Tamarchenko 1977). The constant β, on the other hand, changes from sample to sample and depends indirectly (through ρ_0) on its purity. Figure 3 shows schematically the temperature dependence of the different contributions to eq. (8). Since W_i increases and W_0 decreases with T, W_e has a minimum at a certain temperature. The Lorentz number of metals of any purity for $T \gg \Theta$, and in samples with impurities and defects for $T \ll \Theta$, is a constant and equals L_0. At $T = 0$ for pure metals $L = 0$ (see fig. 4 and eq. (10)). In the intermediate temperature range, L is determined by the temperature and the purity of the sample. At temperatures both lower as well as higher than Θ the ratio L/L_0 in metals could be presented in the form (Oskotski and Smirnov 1972)

$$\frac{L}{L_0} = \left[\frac{\rho_0}{4A_0} + \left(\frac{T}{\Theta}\right)^5 I_5\left(\frac{\Theta}{T}\right)\right] \Big/ \left[\frac{\rho_0}{4A_0} + \chi\left(\frac{T}{\Theta}, \frac{D}{\varepsilon_F}\right)\right], \tag{10}$$

where the function

$$\chi\left(\frac{T}{\Theta}, \frac{D}{\varepsilon_F}\right) = \left(\frac{T}{\Theta}\right)^5 \left\{\left[1 + \frac{3}{2\pi^2}\frac{\varepsilon_F}{D}\left(\frac{\Theta}{T}\right)^2\right] I_5\left(\frac{\Theta}{T}\right) - \frac{1}{2\pi^2} I_7\left(\frac{\Theta}{T}\right)\right\},$$

with I_5 and I_7 integrals of the type (7), A_0 is a constant which depends on an interaction constant between electrons and the lattice, the lattice constant, ε_F, atomic mass and Θ. D is also a constant. According to Olsen and Rosenberg (1953)

$$D/\varepsilon_F = 2^{-1/3} N_a^{-2/3}, \tag{11}$$

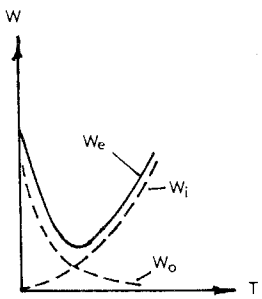

Fig. 3. The temperature dependence of different contributions to eq. (8).

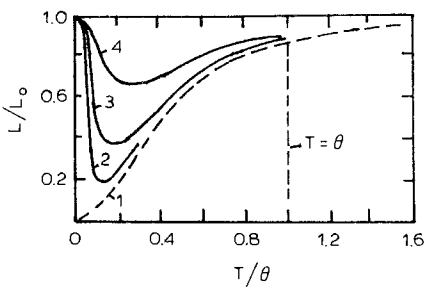

Fig. 4. The dependence of L/L_0 on T/Θ (Oskotski and Smirnov 1972) calculated using eq. (10) for $N_a = 1$. Curve 1: $\rho_0/4A = 0$, curve 2: 0.0038, curve 3: 0.0191, curve 4: 0.0957.

where N_a is the number of free electrons on an atom. For $T/\Theta > 0.6$ (Olsen and Rosenberg 1953)

$$\rho_i = \rho_{tot} - \rho_0 = A_0 T/\Theta. \tag{12}$$

The parameter $\rho_0/4A_0$ in eq. (10) is a measure of the purity of a material. For very pure metals $\rho_0/4A_0 = 0$. Figure 4 shows, e.g., dependences $L/L_0 = f(T/\Theta)$ calculated using eq. (10) for a number of values of $\rho_0/4A_0$. A decrease of L compared to L_0 is connected with the inelastic character of electron scattering by phonons in this temperature region. At very low temperatures in metals with impurities and for $T > \Theta$ electrons are scattered elastically (Smirnov and Tamarchenko 1977). In some metals (e.g., monovalent and noble ones) for $T > 0$ one finds that $L < L_0$. One connects this effect with an additional inelastic scattering mechanism – electron–electron scattering (Smirnov and Tamarchenko 1977). In the thermal conductivity theory any deviation of L from L_0 indicates the presence of some new elastic or inelastic scattering mechanism for the current carriers.

A more complicated behaviour of the Lorentz number is observed in semiconductors. L/L_0 behaves differently for elastic and inelastic scattering of electrons and in the presence of complicated energy band and interband scattering.

The Lorentz number of a semiconductor with a parabolic band, due to elastic scattering of electrons can be written as (Oskotski and Smirnov 1972, Smirnov and Tamarchenko 1977)

$$L = \left[\frac{(r+\frac{7}{2})F_{r+5/2}(\mu^*)}{(r+\frac{3}{2})F_{r+1/2}(\mu^*)} - \frac{(r+\frac{5}{2})^2 F^2_{r+3/2}(\mu^*)}{(r+\frac{3}{2})^2 F^2_{r+1/2}(\mu^*)}\right]\left(\frac{k_0}{e}\right)^2, \tag{13}$$

where F represents the Fermi integral $F_m(\mu^*) = \int_0^\infty x^m (e^{\mu^*} + 1)^{-1}\, dx$ (the integrals are tabulated in Smirnov and Tamarchenko (1977)). μ^* is a reduced Fermi level, $\mu^* = \varepsilon_F/k_0 T$ [μ^* is determined from experimental data on the thermal electromotive force, α, by the equation

$$\alpha = \left(\frac{k_0}{e}\right)\left(\frac{(r+\frac{5}{2})F_{r+3/2}(\mu^*)}{(r+\frac{3}{2})F_{r+1/2}(\mu^*)} - \mu^*\right) \tag{13a}$$

(Oskotski and Smirnov 1972)], r is a scattering parameter (r is an exponent in the dependence of electron relaxation time on energy, e.g., $r = 0.5$ and -0.5, respectively, for scattering by optical and acoustic phonons). In nondegenerated samples ($\mu^* < 0$, $|\mu| \gg 1$) the Lorentz number is equal to

$$L = (r + 2.5)(k_0/e)^2 \tag{14}$$

and depends only on the scattering parameter. In the case of strong degeneration ($\mu^* \gg 1$) $L = L_0$. Figure 5 (curve 1) shows the dependence $L/(k_0/e)^2 = f(\mu^*)$ for $r = -0.5$.

In the case of a nonparabolic band described by the Kane model (Kane 1957) for the elastic scattering mechanism of electrons by acoustic vibrations, the Lorentz

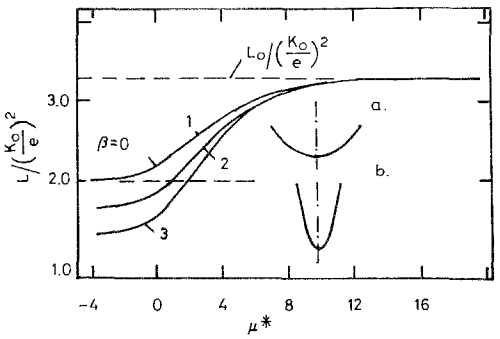

Fig. 5. The dependences $L/(k_0/e)^2 = f(\mu^*)$ calculated by eq. (13) (curve 1) and eq. (15) (curves 2 and 3) for $r = -0.5$. Curve 1: $\beta = 0$, parabolic band (a); curve 2: $\beta = 0.05$, nonparabolic band (b); curve 3: $\beta = 0.2$, nonparabolic band (b).

number has a more complicated form (Oskotski and Smirnov 1972)

$$L_N = \left(\frac{k_0}{e}\right)^2 \frac{{}^2_{-2}L^1\ {}^0_{-2}L^1 - \left({}^1_{-2}L^1\right)^2}{{}^0_{-2}L^1}, \tag{15}$$

where ${}^n_k L^m(z, \mu^*)$ are generalised Fermi integrals:

$${}^n_k L^m(z, \mu^*) = \int_0^\infty \left(-\frac{\partial f}{\partial z}\right) z^n [z(1+\beta z)]^m (1+2\beta z)^k \, dz. \tag{16}$$

These integrals are tabulated in Smirnov and Tamarchenko (1977). Here $\beta = k_0 T \varepsilon_g^*$, $z = \varepsilon/k_0 T$, f is the Fermi function and ε_g^* is the effective width of the forbidden band of interaction, which is near to the real forbidden band width, ε_g, for a number of narrow-band semiconductors. μ^* is also determined from α by equations taking account of the band nonparabolicity. For $r = -0.5$

$$\alpha_N = (k_0/e) \frac{{}^1_{-2}L^1 - \mu^*\ {}^0_{-2}L^1}{{}^0_{-2}L^1}. \tag{15a}$$

Figure 5 (curves 2 and 3) shows the dependences $L/(k/e)^2 = f(\mu^*)$ calculated using eq. (15) for a number of parameters β. A nonparabolic band appreciably changes the L value except for the case of strong degeneration.

All inelastic scattering mechanisms of electrons (electron–electron scattering, scattering by optical lattice vibrations, intervalley transitions and so on) lead to a decreasing Lorentz number compared with the case of elastic scattering. For example, in degenerated semiconductors (and metals) we always have $L < L_0$ (Oskotski and Smirnov 1972, Smirnov and Tamarchenko 1977).

In materials with a complex electron band structure (subbands of "heavy" and "light" carriers) strong interband scattering (e.g., s–d) is possible at a certain position of the chemical potential relative to the bottom of the "heavy" subband. This scattering strongly influences the value of L (fig. 6) (Kolomoets 1966). The value of

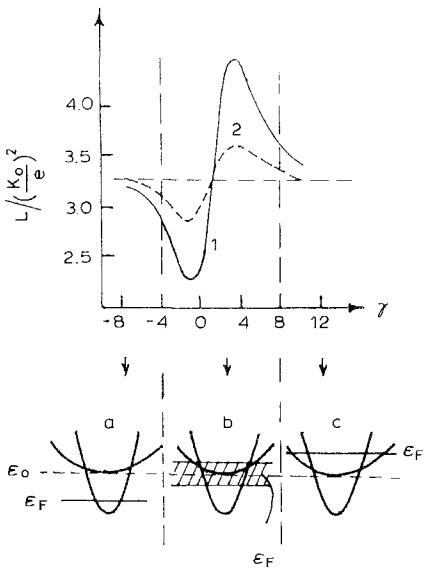

Fig. 6. The dependence of the Lorentz number on γ for the case of high degeneration of current carriers at $S = 32$ (1), 8 (2). (a), (b), and (c) depict different positions of the Fermi level, ε_F, relative to the bottom of the band of heavy carriers (ε_0), $\gamma = (\varepsilon_F - \varepsilon_0)/k_0 T$.

L depends on the parameter S:

$$S = \frac{|M_{lh}|^2 m_h^{*3/2}}{|M_l|^2 m_l^{*3/2}}, \tag{17}$$

where M_{lh} and M_l are matrix elements of transitions between states of corresponding subbands and m_h^* and m_l^* are the effective masses of heavy and light carriers.

Let us consider briefly other contributions to the thermal conductivity. Bipolar thermal conductivity, κ_{bip}, appears in semiconductors in the region of the intrinsic conductivity due to diffusion of electron–hole pairs from the hot to the cold end of a sample.

The photon contribution, κ_{phot}, to the thermal conductivity, κ_{tot}, can be significant at medium and high temperatures in materials which are semi-transparent and transparent in the infrared region. In insulators $\kappa_{phot} \propto T^3$, and in semiconductors $\kappa_{phot}(T)$ shows a curve with a maximum. At low temperatures $\kappa_{phot} = 0$. At high temperatures, due to the intrinsic conductivity, the concentration of carriers increases exponentially, and the absorption coefficient increases in semiconductors so that κ_{phot} decreases to zero. The magnon component, κ_m, of the thermal conductivity will be considered in detail in section 3.4. Exciton thermal conductivity (κ_{exc}) – diffusion of excitons from the hot to the cold end with a consecutive recombination – could be expected at high temperatures. This has been predicted by Pikus (1956).

The following information about defects in solids can be obtained from $\kappa(T)$ measurements:

(1) Type of defects: vacancies, bivacancies, complexes, clusters, impurity atoms, dislocations, isotopes and so on.

(2) A value for the impurity and defect concentrations down to small values ($\sim 10^{12}$–10^{13} cm^{-3}).
(3) Kinetics of ordering processes of defects in solids.
(4) Kinetics of the formation and decay of bivacancies, complexes and clusters.

From analysis of $\kappa_L(T)$ one can obtain information about the contributions of different phonon groups (optical or acoustic) to the heat transport and about the nature of phonon interactions with free carriers. The electron component of the thermal conductivity contains information on the scattering mechanism and its character (elastic or inelastic), and allows one to determine the kind of energy band structure (parabolic, nonparabolic), the presence of additional subbands with light and heavy carriers, and the nature of the electron interaction with phonons and other electrons. From data on the bipolar thermal conductivity one can determine the forbidden-band width at medium and high temperatures. Useful information on material properties can be obtained from κ_{phot}, κ_{exc} and κ_m.

In recent years a new class of materials – rare earth compounds (RECs) – has been investigated intensively. These materials possess nonstandard physical properties, including the thermal conductivity. New features were observed in κ_L, κ_e and κ_m. Analysing data on the thermal conductivity of RECs, in this review we will try to attract more attention to nonstandard effects characteristic of the solids containing ions with f-electrons.

We will consider in more detail results for κ_L, κ_e, κ_m. Table 1 shows materials, effects and parameters, which can be analysed using experimental data on κ_L, κ_e and κ_m. This review is devoted, mainly, to the discussion of situations enumerated in table 1.

TABLE 1
Effects influencing the thermal conductivity of rare earth compounds.

κ_{tot}	= κ_L	+ κ_e	± κ_m
Superconducting systems with heavy fermions	Influence of magnetic phase transitions	Systems with Kondo impurities	Magnon heat transport
High-temperature superconducting systems	Phonon scattering on spin disorder	Concentrated Kondo lattices; systems with heavy fermions	Phonon scattering by magnons
Systems with coexistence of magnetism and superconductivity	Phonon scattering on paramagnetic rare earth ions	Systems with intermediate valency of rare earth ions	Scattering of current carriers by magnons
	Influence of Jahn–Teller effect	Electron scattering on spin disorder	
	Spin glasses	Scattering of current carriers on ground state levels split by crystal field	
	Rare earth glasses		
	Systems with homogeneous and nonhomogeneous intermediate valency of rare earth ions		

3. Influence of the magnetic structure on the thermal conductivity of lanthanide compounds

One can divide the influence of magnetic properties on thermal conductivity into three temperature regions (fig. 7):
- Region 1 ($T > T_N$, T_C, T_s). Phonons and electrons are scattered by disordered spins (spin–disorder scattering).
- Region 2 ($T \simeq T_N$, T_C, T_s). Thermal conductivity can change sharply.
- Region 3 ($T < T_N$, T_C, T_s). There is electron and phonon scattering by magnons and heat transfer by magnons.

Let us consider the behaviour of κ of lanthanide compounds in these regions.

3.1. *Electron scattering by spin disorder in the paramagnetic region ($T > T_N$, T_C, T_s) and its influence on the thermal conductivity of lanthanide materials*

In great detail the influence of electron scattering by spin disorder has been investigated by Gratz and Zuckerman (1982a, b), Gratz and Novotny (1983), Gratz (1982), Bauer et al. (1985a, b, 1986, 1987) and Gratz et al. (1985). Experimental data on the thermal conductivity of RAl_2 (R = Y, La, Ce, Pr, Nd, Sm, Gd, Tb, Yb, Dy, Ho, Er, Tm, Lu), $LaCu_6$, $Ce_xLa_{1-x}Cu_6$ have been analysed. Let us consider data for RAl_2. The compounds RAl_2 crystallise in a cubic lattice of $MgCu_2$-type. RAl_2 with R = Y, La, Yb, Lu are nonmagnetics. $CeAl_2$ is antiferromagnetic ($T_N = 3.8$ K)

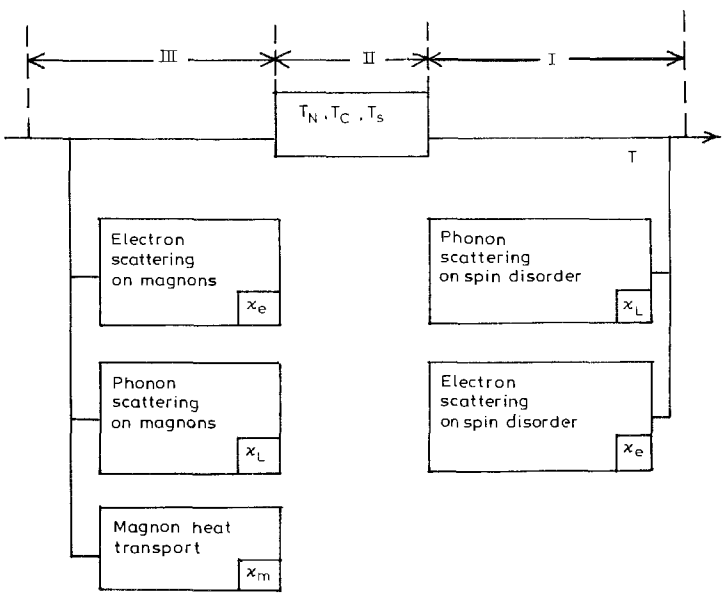

Fig. 7. The influence of certain scattering or transport mechanisms on the contributions to thermal conductivity (the symbol is given in the lower right corner of each rectangle) in three temperature regions. T_N, T_C and T_s are the Néel, Curie and spin reorientation temperatures, respectively.

(Barbara et al. 1977). Other compounds are ferromagnetics with T_C in the range 6–168 K. The R atoms (excluding Ce, Eu and Yb) have valency +3. RAl_2 are metals. The measured κ is equal to

$$\kappa_{tot} = \kappa_L + \kappa_e. \tag{18}$$

At temperatures $T \ll \Theta$ thermal phonons in metals are mainly scattered by conduction electrons. According to a theory of Klemens (1969), the predominant phonon–electron scattering is given by

$$\kappa_L = bT^2. \tag{19}$$

At these temperatures κ_e is determined by conduction electron scattering on static defects (Klemens 1969) and

$$\kappa_e = aT. \tag{20}$$

So, at $T \ll \Theta$

$$\kappa_{tot} = aT + bT^2 \quad \text{or} \quad \kappa_{tot}/T = a + bT. \tag{21}$$

The coefficients a and b can be evaluated from the dependence $\kappa_{tot}/T = f(T)$. Figure 8 shows such a dependence for YAl_2 (Bauer et al. 1986). The resulting b shows that the contribution of κ_L to κ_{tot} is about 5% at 20 K. For higher temperatures a numerical calculation has been done using approximate theoretical equations (Klemens 1969). It turns out that, at 300 K, κ_L contributes only about 2% to κ_{tot}. So, practically the experimental value of κ_{tot} for RAl_2 is equal to κ_e.

The influence of the electron-spin disorder scattering on κ_e in the paramagnetic region (i.e. the magnetic contribution to the thermal conductivity) is estimated by comparing $\kappa_{tot} \simeq \kappa_e$ of the magnetic and nonmagnetic compounds of the RAl_2 family. YAl_2 is chosen as a nonmagnetic reference material. In the paramagnetic region (Dekker 1965) $\rho(T)$ can be represented as

$$\rho(T) = \rho_o + \rho_{ph} + \rho_{magn}, \tag{22}$$

where the terms are the residual, the lattice and the magnon electrical resistivity, respectively.

$$\rho_{magn} = \rho_{spd} \propto \text{const.}(g-1)^2 J(J+1) = \text{const. } A_d, \tag{23}$$

where ρ_{spd} is the electrical resistivity due to spin-disorder scattering (Dekker 1965), g the Landé factor, J the total angular momentum, and A_d the de Gennes factor.

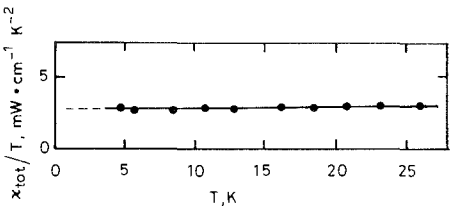

Fig. 8. κ_{tot}/T as a function of T in YAl_2 (Bauer et al. 1986).

The electronic thermal resistivity $W_e = 1/\kappa_e$ in the paramagnetic region for RAl_2 can be written as:

(a) for nonmagnetic compounds (NM) (YAl_2, $LuAl_2$)

$$W_e = W_{e,d}^{NM} + W_{e,ph}^{NM}, \tag{24}$$

(b) for magnetic compounds (M) ($GdAl_2$, etc.)

$$W_e^M = W_{e,d}^M + W_{e,ph}^M + W_{e,magn}. \tag{25}$$

The indices (e,d), (e,ph), (e,magn) indicate free-carrier scattering by defects, phonons and magnons, respectively.

The difference $(W_e^M - W_e^{NM})$ corresponds to the contribution to the electronic thermal resistivity from electron scattering by the disordered spins

$$\Delta W = W_e^M - W_e^{NM} = (W_{e,d}^M - W_{e,d}^{NM}) + (W_{e,ph}^M - W_{e,ph}^{NM}) + W_{e,magn}. \tag{26}$$

Let us suppose that $W_{e,ph}^M$ and $W_{e,ph}^{NM}$ are equal in all related RAl_2 compounds, then

$$\Delta W = (W_{e,d}^M - W_{e,d}^{NM}) + W_{e,magn}. \tag{27}$$

$W_{e,d}$ in magnetic and nonmagnetic compounds is proportional to T^{-1} [see eq. (20)]: $W_{e,d}^M = B^M/T$, $W_{e,d}^{NM} = B^{NM}/T$, where $B = 1/a$ [see eq. (20)]. According to Bauer et al. (1986)

$$W_{e,magn} = W_{spd} \approx \text{const.}(g-1)^2 J(J+1)/T = \text{const. } A_d/T. \tag{28}$$

So, finally we have

$$\Delta W = (B^M - B^{NM})/T + \text{const. } A_d/T. \tag{29}$$

Experimentally ΔW is determined as the difference $1/\kappa^M - 1/\kappa^{NM}$, where κ^{NM} is the thermal conductivity of YAl_2 (see, e.g., fig. 9). Figures 10 and 11 show the dependence of ρ_{spd}, eq. (23), and $\Delta W'T$, eq. (30), on the de Gennes factor

$$\Delta W'T = \Delta WT - (B^M - B^{NM}) = W_{spd}\,T. \tag{30}$$

As one can see in these figures, the experimental dependences $\rho_{spd}(A_d)$ and $W_{spd}(A_d)$

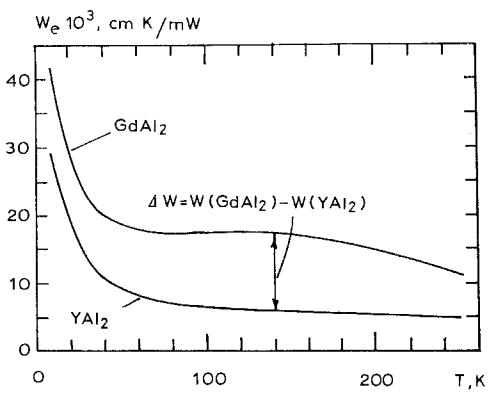

Fig. 9. $W_e = 1/\kappa^{NM}$ and $W_e = 1/\kappa^M$ as functions of T, respectively, for YAl_2 and $GdAl_2$ (Bauer et al. 1986).

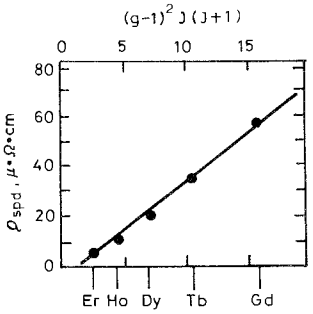

Fig. 10. The dependence of ρ_{spd} on the de Gennes factor for compounds RAl_2 (Bauer et al. 1986).

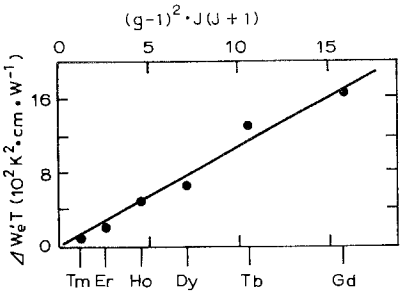

Fig. 11. The dependence of $\Delta W_e T$ on the de Gennes factor for compounds RAl_2 (Bauer et al. 1986).

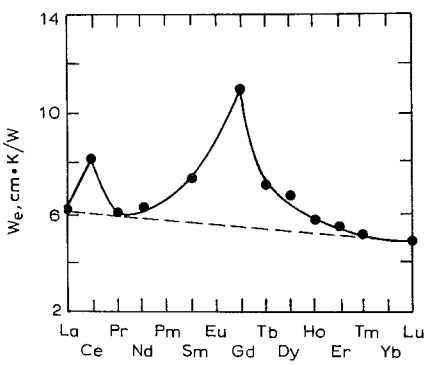

Fig. 12. The dependence of W of compounds RAl_2 on the atomic number of the lanthanides at $T = 270$ K (Bauer et al. 1985a, b, 1986).

agree well with the theory for RAl_2 for the heavy lanthanide elements [cf. eq. (23) (Dekker 1965) and eq. (28) (Bauer et al. 1986)].

Experimental data for W, as shown in fig. 12, show a large influence of electron–spin disorder scattering on κ_e of RAl_2. The dotted line is considered as a reference, corresponding to W of a hypothetical nonmagnetic material. Additional scattering of electrons by disordered spins causes an increase in W compared to the reference value. $GaAl_2$ has the largest W. W decreases from $GdAl_2$ in both directions to nonmagnetic $LaAl_2$ and $LuAl_2$. "A jump" of W is observed for $CeAl_2$. $CeAl_2$, unlike other RAl_2, is a Kondo material with peculiar physical properties. The experimental data shown in fig. 13 confirm the theoretical dependence, eq. (29).

Table 2 shows data for ρ_{spd} (obtained from electrical conductivity data) (Gratz and

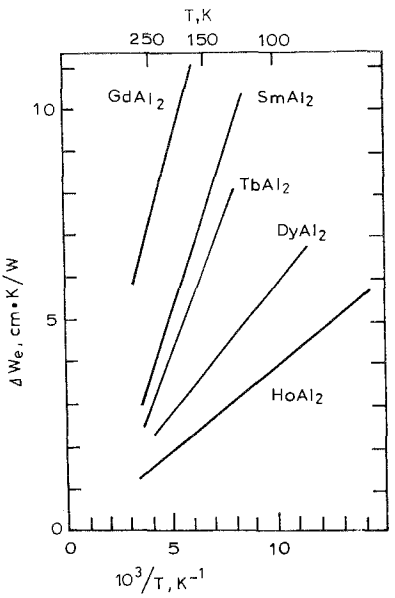

Fig. 13. The dependence $\Delta W(1/T)$ for compounds RAl_2 (Bauer et al. 1985a, b, 1986).

TABLE 2
Electrical resistivity due to spin-disorder scattering of electrons.

RAl_2	$GdAl_2$	$TbAl_2$	$DyAl_2$	$HoAl_2$	$ErAl_2$	$TmAl_2$
ρ^*_{spd} (μΩ cm)	43.7	32.8	16.6	13.2	5.5	1.7
ρ_{spd} (μΩ cm)	59.0	35.0	23.5	13.5	6.5	1.5

ρ^*_{spd}: calculated from the Wiedemann–Franz law.
ρ_{spd}: experimental results.

Zuckerman 1982a,b, Gratz 1982, Gratz and Novotny 1983, Gratz et al. 1985, Bauer et al. 1985a,b, 1986) and ρ^*_{spd} (calculated using the Wiedemann–Franz law from experimental $\Delta W'$). $\rho_{spd} = L_0 \Delta W' T$ (Bauer et al. 1986). As one can see in table 2, the agreement between ρ_{spd} and ρ^*_{spd} is good.

3.2. *Electron scattering by spin disorder in the paramagnetic region in Kondo systems (electrical conductivity, thermal conductivity)*

The theoretical dependence $\rho(T)$ has been obtained by Coornut and Coqblin (1972) for compounds with concentrated Kondo lattices and carrier scattering by disordered spins (ρ_{spd}), taking into account the crystal field effect. According to this calculation the temperature dependence $\rho_{spd}(\ln T)$ could be divided into two regions separated by a maximum at a temperature approximately equal to the value of the splitting by the crystal field.

$CeAl_2$ is a prototype of materials with concentrated Kondo lattices. For $T_N > 3.8$ K (the paramagnetic region) strong scattering of carriers by disordered spins is observed

(Bauer et al. 1986). Figure 14 shows the dependence $\rho_{spd} = f(\ln T)$ [$\rho_{spd} = \rho(CeAl_2) - \rho(YAl_2)$], which agrees well with the conclusions of Coornut and Coqblin (1972). It turns out that the dependence $\Delta W T = f(\ln T)$ [$\Delta W = W(CeAl_2) - W(YAl_2)$] for $CeAl_2$ has the same shape as ρ_{spd} (Bauer et al. 1986) (fig. 14). Similar dependences $\Delta W(T)$ have also been obtained in other systems with concentrated Kondo lattices: $CeCu_2$ (Gratz et al. 1985) and $CeCu_6$ (Bauer et al. 1987). All this allows us to conclude that the observed behaviour $\Delta W T = f(\ln T)$ is typical for compounds with Kondo lattices and electron scattering by disordered spins.

So, the influence of electron scattering by spin disorder on κ_e of RECs has been considered in sections 3.1 and 3.2. We have failed to find data on the influence in the temperature region $T > T_N$, T_C of phonon scattering by spin disorder on κ_L.

3.3. *Magnetic phase transitions (temperature region 2: $T \approx T_N$, T_C, T_s)*

Magnetic phase transitions (MPTs) can be divided in two groups (Belov et al. 1976, 1979, Belov 1972):

- group 1: MPTs of the order–disorder type. These transitions are connected with the destruction of ferro- and antiferromagnetic ordering (observed transitions: ferromagnetic–paramagnetic and antiferromagnetic–paramagnetic at temperatures T_C and T_N, respectively).
- group 2: MPTs of the order–order type. These transitions are connected with a magnetic structure type change (e.g., ferromagnetic–antiferromagnetic, collinear antiferromagnetic–noncollinear antiferromagnetic and so on). Such transitions resemble structural transitions in crystals and sometimes they are called magneto-structural phase transitions.

The spin-orientation transitions can be distinguished by their unique features from the large family of magneto-structural phase transitions. Unfortunately, the thermal conductivity of RECs has not been investigated for all groups of magnetic phase transitions. Reliable data are available for the MPT of the order–disorder type and for the spin-orientation phase transition (SOPT).

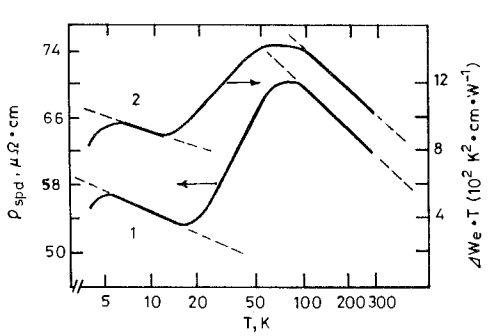

Fig. 14. Dependence of ρ_{spd} (1) and $\Delta W_e T$ (2) on $\ln T$ for $CeAl_2$ (Bauer et al. 1986). $\rho_{spd} = \rho(Ce\ Al_2) - \rho(YAl_2)$. $\Delta W_e = W_e(CeAl_2) - W_2(YAl_2)$.

3.3.1. *Thermal conductivity of magnetic lanthanide materials in the region* $T \approx T_N$, T_C

In this region there are no specific effects in the thermal conductivity of lanthanide magnetic materials. Their κ behaviours are analogous to the κ of other magnetic materials. Very often the phase transition from the paramagnetic to the ferromagnetic or antiferromagnetic state does not manifest itself in the temperature dependence of κ_L and κ_e. However, there are cases where at T_N and T_C appreciable variations are observed in the temperature dependence and the value of κ_L and κ_e. There are qualitative considerations (which, however, are not always confirmed experimentally), why a variation of κ_L and κ_e is observed at T_N and T_C. It is important to know which scattering and transfer mechanisms prevail near T_N and T_C and which variations of these mechanisms are connected with the reconstruction of a magnetic system. For example, if for $T > T_N$ (T_C) there is a very strong electron scattering by disordered spins in a material with $\kappa_{tot} \simeq \kappa_e$, then an increase of the value κ_{tot} is possible at the transition temperature T_N (T_C).

Let us consider some examples of κ_L and κ_e behaviour of RECs at T_C and T_N:

(1) EuO (insulator, $\kappa_{tot} = \kappa_L$). No variation of κ_L is observed at T_C (fig. 15) (Salamon et al. 1974, Martin and Dixon 1972). It is interesting to note that in EuO a strong decrease of the thermal diffusivity, D, at T_C is observed (Salamon et al. 1974). This decrease is fully compensated for in κ_L by an increase of the heat capacity, C, in this temperature range ($\kappa_L = DCd$, d is the density of the material). For $T \leqslant T_C$ in EuO there is no additional heat transfer by magnons (because of strong magnon–magnon interaction), phonon–magnon scattering is low and κ_L is determined mainly by phonon–phonon scattering.

(2) $PrAl_2$, $SmAl_2$ [metals, $\kappa_{tot} = \kappa_e$ (Bauer et al. 1987, (Müller et al. 1983)] (see fig. 16). κ_{tot} changes at T_C in $PrAl_2$ and does not change in $SmAl_2$. Possibly, this is connected with a different influence of electron scattering by the spin system on the thermal conductivity (for $T > T_C$ electrons are scattered by disordered spins, for $T < T_C$ by the disordered spin system). This situation has been discussed above.

(3) DyS [poor metal, $\kappa_{tot} = \kappa_L + \kappa_e$ (Novikov et al. 1975)] (see fig. 17). Anomalies in $\kappa_L(T)$ and $\kappa_e(T)$ are observed at $T = T_N$. The behaviour of $\kappa_e(T)$ of DyS near T_N is analogous to that in $PrAl_2$ (cf. figs. 16 and 17) and could be explained by electron scattering by the spin subsystem. It is more complicated, however, to explain the behaviour of $\kappa_L(T)$ of DyS near T_N.

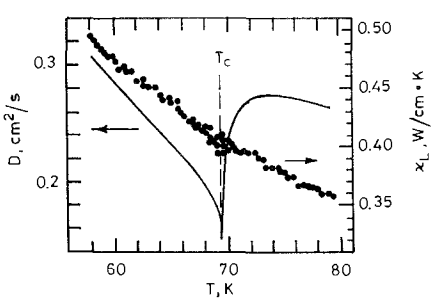

Fig. 15. Dependence $\kappa_{tot}(T) = \kappa_L(T)$ and $D(T)$ for a monocrystal of EuO. $T_C = 69.33$ K (Salamon et al. 1974).

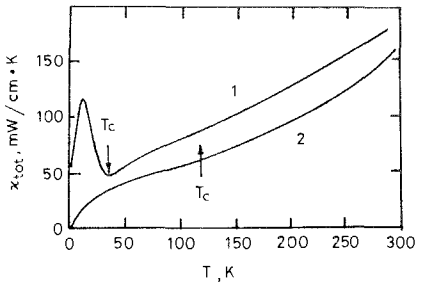

Fig. 16. Dependence $\kappa_{tot}(T) \simeq \kappa_L(T)$ for $PrAl_2$ (1) and $SmAl_2$ (2). T_C is the Curie temperature (Bauer et al. 1986).

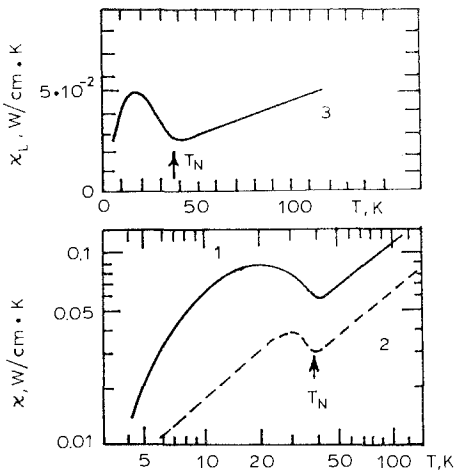

Fig. 17. Temperature dependence of the thermal conductivity of DyS. Curve 1: κ_{tot}, 2: κ_e, 3: κ_L (Novikov et al. 1975).

3.3.2. *Behaviour of the thermal conductivity of lanthanide materials at a SOPT*

At a SOPT the orientation of the magnetic moments relative to the crystallographic axes changes under influence of external parameters (temperature, magnetic field, pressure) (Belov et al. 1976, 1979, Belov 1972). If the SOPT occurs at a variation of temperature or magnetic field, it is called, correspondingly, spontaneous or induced transition. Transitions with spin reorientations are characterised by the ordering parameter θ_0, the angle of magnetic moment rotation relative to the crystal axes. A SOPT could be of the first (θ changes abruptly) or of the second kind (θ changes gradually). A great number of SOPTs are observed in RECs (orthoferrites, ferrites-garnets, intermetallics) (Belov et al. 1976, 1979). The nature and characteristic features of the SOPTs have been investigated most completely in the orthoferrites $RFeO_3$. The crystal symmetry of orthoferrites is described by the orthorhombic space group $D_{2h}^{16} - P_{bnm}^{17}$. The orthoferrites have a distorted perovskite structure.

The most frequent reorientational transitions in the lanthanide orthoferrites are transitions with spin and magnetic momentum reorientations in the (*ac*) crystal plane. At the temperatures T_{1s} and T_{2s}, which correspond to the beginning and to the end of the reorientation process, one observes phase transitions of second kind. The values of T_{1s} and T_{2s} in $RFeO_3$ vary over a wide range depending on the atomic number of the lanthanide (Belov et al. 1976). At T_{1s} and T_{2s} there are anomalies

of the elastic modulus, the heat capacity, the magnetic susceptibility, the frequencies of soft spin modes become zero, and so on (Belov et al. 1976, 1979). The character of the transitions changes significantly in (*ac*)-reorientation in an external magnetic field H. When applying H along the *a*- and *c*-axes of a crystal the temperature of the first phase transition is shifted and the other disappears (Belov et al. 1976). To our regret, we could not find data on measurements of κ in a magnetic field for this phase transition type.

The influence of a SOPT on κ has been investigated in single crystals of $SmFeO_3$, $Sm_{0.6}Gd_{0.4}FeO_3$ and $Sm_{0.65}Er_{0.15}Tb_{0.2}FeO_3$ (Barilo et al. 1984). Figure 18 shows data on $\kappa(T)$, $\theta_0(T)$ and $\Delta v/v_t = f(T)$ (the relative variation of the sound velocity) in $Sm_{0.6}Gd_{0.4}FeO_3$. Analogous results are obtained for two above-mentioned compositions as well. For $SmFeO_3$ and $Sm_{0.65}Er_{0.15}Tb_{0.2}FeO_3$ $T_{1s} = 454$ and 303 K and $T_{2s} = 487$ and 358 K, respectively (Barilo et al. 1984).

$RFeO_3$ are insulators and the experimentally measured $\kappa_{tot} = \kappa_L$. As one can see in fig. 18a, at the temperatures T_{1s} and T_{2s} κ has minima. At T_{1s} spins are oriented along the *a*-axis, at T_{2s} along the *c*-axis (fig. 18b). Anomalous behaviour of $\kappa(T)$ of $Sm_{0.6}Gd_{0.4}FeO_3$ in the SOPT region is connected with unusual behaviour of the sound velocity (fig. 18c). Both anomalies are due to a strong spin–phonon interaction.

As an example of the SOPT influence on κ_L we have listed the most impressive experimental data. However, for other types of SOPTs κ_L could behave differently at $T = T_s$: from sharp changes of the κ_L value to the complete absence of an effect.

Besides data on the influence of the SOPT on κ_L of $RFeO_3$ there is information

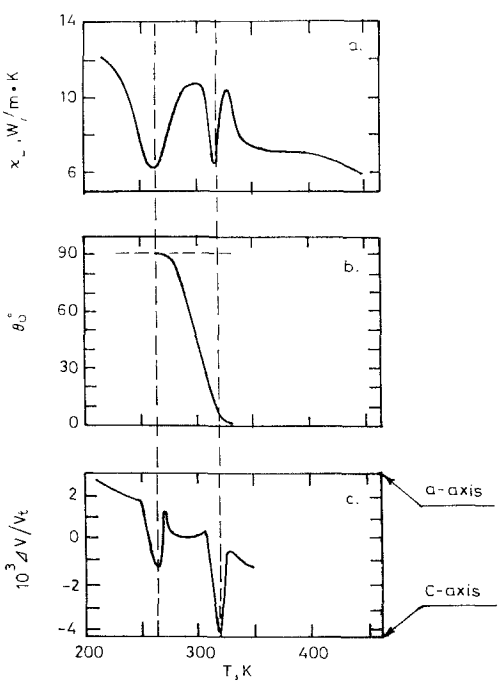

Fig. 18. Properties of $Sm_{0.6}Gd_{0.4}FeO_3$ in the SOPT region as functions of T (Barilo et al. 1984). (a) κ_L. (b) θ_0, the angle between the *c*-axis and $\boldsymbol{F}$, the light magnetisation vector in the spin-reorientation regions. (c) $\Delta v/v_t$. The dashed lines indicate T_{1s} and T_{2s}.

in the literature on the behaviour in the SOPT region in RCu_2 (R = Sm, Ho, Dy, Er, Tm) (Gratz et al. 1990, Gratz and Novotny 1985). Theoretical calculations of κ_L near the SOPT have been carried out by Buchelnikov et al. (1987).

3.4. *Phonon–magnon scattering, heat transfer by magnons in lanthanide compounds ($T < T_N, T_C$)*

Magnetic materials – insulators and semiconductors – at $T < T_C$ (T_N) can display two effects:

(1) A decrease of κ_L as a result of phonon scattering by magnons.

(2) An additional thermal conductivity due to magnon heat transfer (κ_m).

Since in metals $\kappa_L \ll \kappa_e$, it is difficult to analyse the influence of phonon–magnon scattering on κ_L. In practice, one can consider only the contribution κ_m. Electron–magnon scattering has to decrease the value κ_e in these metals. In magnetic lanthanide insulators a phonon–magnon scattering effect or an additional heat transfer by magnons could prevail. It is possible that both effects are comparable. As a rule, κ_m contributes at lower temperatures while phonon–magnon scattering contributes at higher temperatures (near T_C (T_N)).

Let us first consider data on the thermal conductivity of insulating magnetic lanthanide materials. Strong phonon–magnon scattering occurs when magnon and phonon dispersion branches intersect. They perturb one another, branches split, and an effective gap Δ appears between them (fig. 19) (Rives et al. 1969, Sheard 1976, Kittel 1958). As a result, the contribution to the heat transfer of phonons with the energy of the intersection decreases. In an external magnetic field the magnon dispersion branch shifts to higher frequencies. The distribution of phonons carrying the heat has a maximum near energy $4k_0T$. If the intersection of the phonon and magnon branches at $H = 0$ occurs at an energy less than $4k_0T$, then the thermal conductivity first decreases and then increases with increasing H (curve 1 of fig. 20). At different mutual dispositions of the dispersion curves variant 2 of fig. 20 is possible. In the works of Rives et al. (1969), Sheard (1976), Dixon (1976, 1981), Dixon et al. (1974) and Dixon and Landau (1976) some versions of phonon–magnon scattering are considered: one phonon–one magnon, two magnons–one phonon.

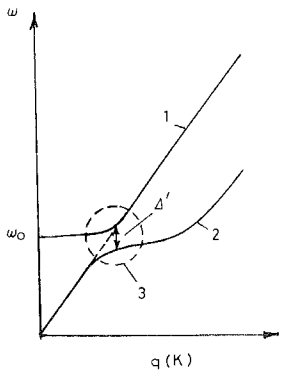

Fig. 19. Schematic shape of magnon (1) and phonon (2) dispersion curves for a hypothetic ferromagnet (Rives et al. 1969, Sheard 1976). (3) The region of strong phonon–magnon interaction.

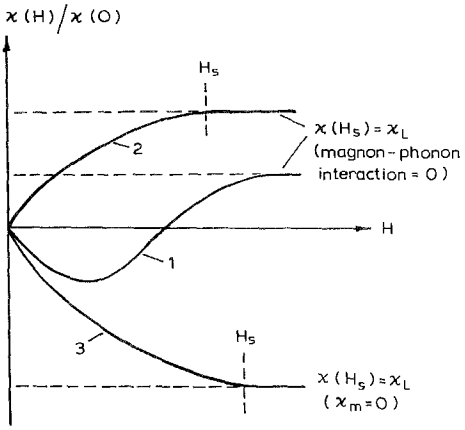

Fig. 20. Scheme of the dependence of $\kappa(H)/\kappa(0)$ on magnetic field. H_s is the field in which $\kappa(H)/\kappa(0)$ saturates ($g\beta H_s \gg k_0 T$). Curves 1 and 2: strong phonon–magnon interaction, 3: magnon heat transport.

In a high magnetic field ($H > H_s$) the ratio $\kappa(H)/\kappa(0)$ saturates (fig. 20), and the influence of phonon–magnon scattering on κ_L completely disappears, and $\kappa(H_s)$ becomes equal to κ_L. As a rule, $\kappa_L(H_s)$ is larger than $\kappa_L(H = 0)$, since at $H = 0$ phonon–magnon scattering decreases κ_L. A high magnetic field ($H > H_s$) could suppress κ_m as well (fig. 20, curve 3) (Rives et al. 1969, Martin and Dixon 1972, McCollum et al. 1964). Then $\kappa(H_s) = \kappa_L$. When analysing experimental data on the thermal conductivity of lanthanide magnetic materials in a magnetic field one has to keep in mind that:

(1) If heat transfer is to occur by magnons or phonon–magnon scattering it is necessary to reach magnetic fields $H \geqslant H_s$. At weak magnetic fields one could erroneously take phonon–magnon scattering for κ_m (fig. 20, curves 1, 2 at $H \ll H_s$).

(2) Zeeman splitting of paramagnetic levels occurs in magnetic fields. At low temperatures a decrease of κ_L due to resonance phonon scattering by these levels is possible.

The contribution of κ_m to κ and the influence of phonon–magnon scattering on κ_L have been studied for a great number of lanthanide magnetics. References on pioneer studies are found in Dixon and Landau (1976), Charap (1964), Slack and Oliver (1971), Martin and Dixon (1972). In this review we will consider data on κ of the lanthanide insulating magnetic materials $GdCl_3$ ($T_C = 2.2$ K), EuO ($T_C \approx 69$ K), $HoPO_4$ ($T_N \approx 1.39$ K) and the garnets DyAlG ($T_N = 2.5$ K) and YIG ($T_C \approx 545$–560 K), and for these materials we will analyse the influence of κ_m and phonon–magnon scattering on their thermal conductivity.

In the ferromagnet $GdCl_3$ and the antiferromagnet $HoPO_4$ heat transfer by magnons is insignificant. The dependence $\kappa(H)/\kappa(0)$ (figs. 21a, b) is analogous to curves 1 and 2 in fig. 20.

By contrast, in EuO the effect of phonon–magnon scattering is small and the heat at low temperatures is transferred mainly be magnons. At $T = 0.93$ K the contribution of κ_m to κ in EuO is about 75%, fig. 22. This value is a record for the investigated magnetics at the present time. However, simple dependences like those shown in figs. 21 and 22 (Dixon and Landau 1976, Walton et al. 1973, Metcalfe and Rosenberg

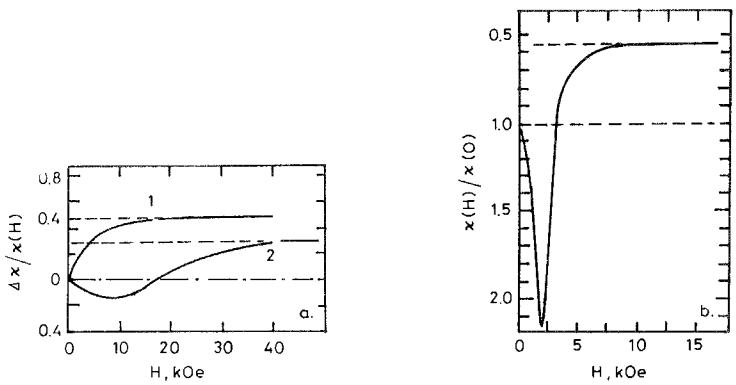

Fig. 21. (a) Dependence $\Delta\kappa/\kappa(H)$ for $GdCl_3$ (Rives et al. 1969). Curve 1: 1.3 K, 2: 0.46 K, $T_C = 2.2$ K, $\Delta\kappa = \kappa(H) - \kappa(0)$. (b) Dependence $\kappa(H)/\kappa(0)$ for $HoPO_4$ (Parsons 1976). $T = 0.54$ K.

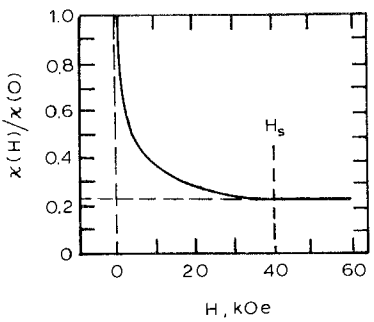

Fig. 22. Dependence $\kappa(H)/\kappa(0)$ for EuO (Martin and Dixon 1974). $T = 0.93$ K.

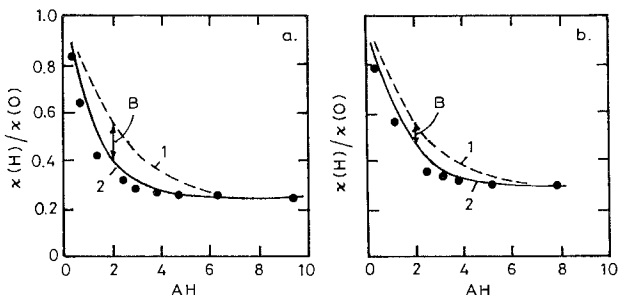

Fig. 23. Dependence $\kappa(H)/\kappa(0)$ for YIG (Walton et al. 1973) at temperatures 0.458 K (a) and 0.273 K (b). $A = \mu_B/k_0 T$. Curve 1: according to a theory without taking into account phonon–magnon scattering and magnon heat transport. Curve 2: according to a theory which takes into account phonon–magnon scattering and magnon heat transport. B is the contribution from phonon–magnon scattering.

1979) are not always observed in experiments. For example, in garnets, parallel with the prevailing heat transfer by magnons, the effect of magnon–phonon scattering plays a significant role and its contribution increases with temperature (figs. 23a, b) (Dixon and Landau 1976, Walton et al. 1973).

Peculiarities in the phonon and magnon dispersion curves can have influence on the considered effects (Slack and Oliver 1971). Figures 24a, b shows dependences $\kappa(H, T)$ for $GdCl_3$ (Dixon 1976, 1981) and DyAlG (Dixon and Landau 1976), respectively, and helps to illustrate more clearly our considerations on the contribution of κ_m and the role of phonon–magnon scattering in κ of lanthanide magnetic materials. At low temperatures in a magnetic field $H = H_s$ one observes in $GdCl_3$ an increase $(+\Delta\kappa)$ and in DyAlG a decrease $(-\Delta\kappa)$ of the thermal conductivity. In $GdCl_3$ phonon–magnon scattering is excluded as scattering mechanism and in DyAlG κ_m is suppressed.

Theoretical calculations have been carried out by Callaway (1959) of the two parts of $\kappa_L(T)$ with $T < T_C$, T_N and $T > T_C$, T_N in a high magnetic field. It turns out that both parts can be described by using common constants in the theoretical formulae for phonon scattering by crystal boundaries, point defects and phonons (with taking into account the U and N processes). This points out that $\kappa(H_s, T)$ obtained at low temperatures in both materials is equal to the real κ_L.

Let us consider experimental data on the thermal conductivity of the magnetic lanthanide metals. As it has been noted at the beginning of this section, it is rather complicated to separate κ_m from the experimentally measured κ_{tot}. In these metals

$$\kappa_{tot} = \kappa_L + \kappa_e + \kappa_m. \tag{31}$$

The main difficulties arise in the separation of κ_L. At very low temperatures (where κ_m is most manifested) phonons are scattered, mainly, by crystal boundaries and κ_L decreases rapidly with decreasing temperature ($\kappa_L \propto T^3$). Therefore, at these

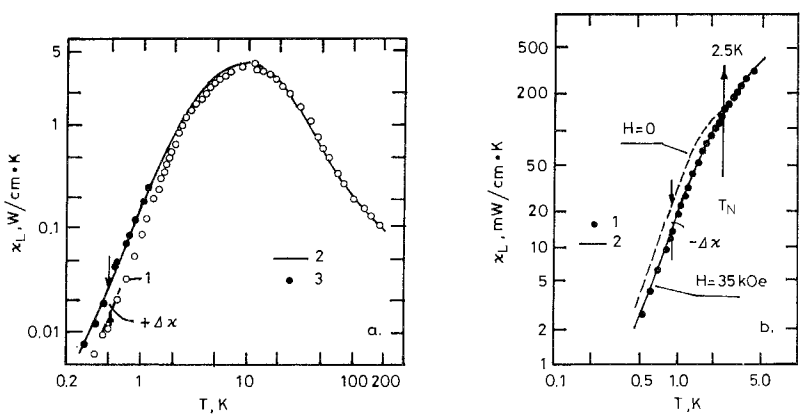

Fig. 24. (a) The temperature dependence of the thermal conductivity for $GdCl_3$ (Dixon 1976, 1981) at $H = 0$ (1) and $H = 3.5$ kOe (3). The solid line (2) represents a calculation according to Callaway (1959) taking into account phonon scattering by crystal boundaries, point defects and phonons (U and N processes). The heat flow and magnetic field are directed along the c-axis of the crystal. (b) The temperature dependence of the thermal conductivity for DyAlG (Dixon and Landau 1976) at $H = 0$ (dotted line) and $H = 35$ kOe (points 1). $H \parallel [111]$, heat flow $\parallel [100]$. The solid line (2) represents a calculation taking into account phonon scattering by crystal boundaries, point defects and phonons (U and N processes). The curve for $H = 0$ is given for averaged experimental values.

temperatures more often $\kappa_L \ll \kappa_e$ (see, e.g., section 3.1). κ_e is calculated in the first approximation by the Wiedemann–Franz law

$$\kappa_e = L_0 T/\rho, \tag{32}$$

where L_0 is the Sommerfeld value of Lorentz number. So, κ_m in magnetic metals is calculated using the scheme:

(1) κ_L is supposed to be negligible in comparison with κ_e.

(2) L_{eff} is calculated from the dependence

$$L_{eff} = \kappa_{tot} T/\rho. \tag{33}$$

If L_{eff} exceeds L_0, it is considered that there is a contribution of κ_m to κ_{tot}.

(3) κ_e^0 is calculated using eq. (32).

(4) κ_m is determined by

$$\kappa_m = \kappa_{tot} - \kappa_e^0. \tag{34}$$

Let us consider, for example, the separation of κ_m in the alloy ErNi ($T_C \approx 105$ K) (Mori et al. 1984). Figures 25a, b, c illustrate the procedure of the determination of κ_m. One could expect a decreased κ_e in the magnetic lanthanide metals due to electron–magnon scattering. However, we have not succeeded in finding reliable literature data on this question.

Another way for a direct separation of κ_m in magnetic metals exists, but for some reason nobody has used it. It is possible to suppress κ_m in a strong magnetic field ($H > H_s$) and determine κ_e, and then to calculate κ_m. In principle, the magnetic field could influence κ_e as well, but because of the low mobility of current carriers in the lanthanide metals it is practically impossible to reach a sufficiently high magnetic field (H_{s0}) for the suppression of carriers ($H_{s0} > H_s$).

4. Thermal conductivity of spin glasses

A spin glass is a new magnetic state differing from the ferro- and antiferromagnetic state. A spin glass is formed by introducing magnetic impurities into a nonmagnetic

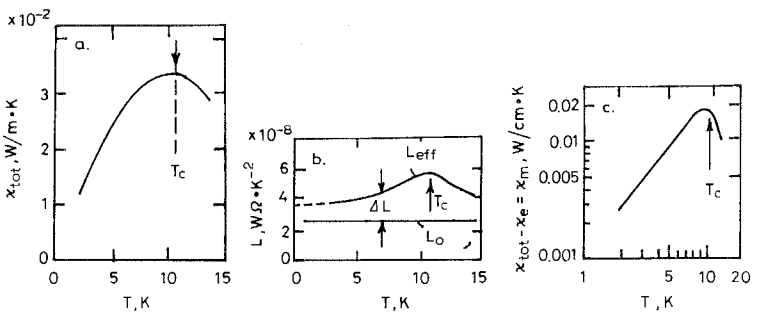

Fig. 25. The temperature dependence for ErNi: (a) of the total thermal conductivity (Mori et al. 1984), (b) of the effective Lorentz number calculated using eq. (33) and (c) of κ_m calculated using eq. (34).

(or weakly magnetic) matrix. In spin glasses the orientation of impurity spins varies randomly in space, just as atoms are randomly arranged in glasses (Maletta 1982, Fisher 1983, 1985, Mydosh 1978, Korenblit and Shender 1984, Maletta and Zinn 1989). The resulting magnetic structure is called "spin glass" (fig. 26). The spin-glass state is the result of competition between ferro- and antiferromagnetic interaction in a disordered system. The macroscopic moment is zero. Spin waves in spin glasses are not observed. Therefore κ_m equals zero. Spin glasses can be metals or insulators. By structure they can be crystalline (metals and insulators) or amorphous materials (metallic glasses). Classical spin-glass systems are alloys: CuMn, AuFe, ZnMn, AuCr, AuMn, AgMn, MoFe, RhMn, PdFe, PtCo and others (Fisher 1983). There are also a great number of spin glasses based on rare earth elements: rare earth metal alloys, metal and insulator crystals, and metallic amorphous systems (Fisher 1983, 1985, Mydosh 1978, Durand and Poon 1979).

Figure 27 shows a scheme of the formation of metallic spin glasses (Mydosh 1978). A small number of magnetic impurity ions in a nonmagnetic matrix forms an impurity Kondo system. At a critical concentration x_{cr} (in metal systems on the average equal to 50 ppm) the system changes to a spin-glass state. At higher concentrations

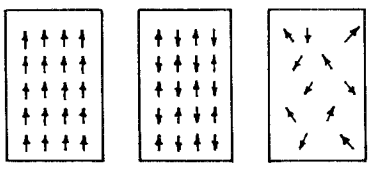

Fig. 26. Schematic picture of the magnetic moments in ferromagnetic (FM), antiferromagnetic (AM) and spin glass (SG) systems.

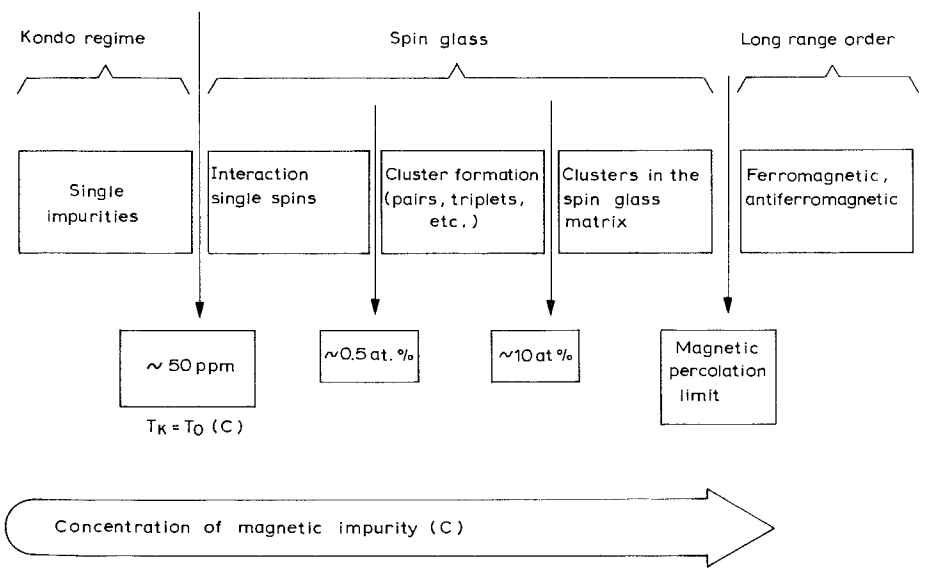

Fig. 27. Scheme of formation of metallic spin glasses (Mydosh 1978).

($x > x_{MPL}$, magnetic percolation limit) the system becomes magnetically ordered. The scheme of fig. 27 shows that interpretation of experimental data on thermal conductivity (specially on κ_e) is rather complicated, because two influences on the Lorentz number are mixed: an effect which is specific to the spin-glass character, and the Kondo effect (see section 5).

ρ in metal spin glasses varies with temperature (at low temperatures) as $T^{3/2}$ (more often) and as T^2 (more seldom). Patterson (1978) and Sharma and Tripathi (1980) have calculated the Lorentz number theoretically for metallic spin glasses with taking the temperature dependencies of ρ into account. It turns out that at low temperatures

$$L/L_0 \simeq 0.98 \quad (\text{at } \rho \sim T^{3/2}) \quad \text{(Patterson 1978)}, \tag{35}$$

$$L/L_0 \simeq 0.55\text{–}0.44 \quad (\text{at } \rho \sim T^2) \quad \text{(Sharma and Tripathi 1980)}. \tag{36}$$

Unfortunately, we were unable to find experimental studies on the thermal conductivity of lanthanide metallic spin glasses which attempted to verify eqs. (35) and (36). Figure 28 shows experimental data for the metallic spin-glass alloys AgCr. As one can see, the experimental and theoretical results agree rather well (Ducastel and Pitsi 1986).

Let us consider data on the thermal conductivity in spin-glass insulators. In them $\kappa_{tot} = \kappa_L$. A typical representative of spin-glass insulators is $Eu_xSr_{1-x}S$. When doping the Heisenberg ferromagnet EuS (Curie temperature $T_C = 16.6$ K, lattice of NaCl-type) with nonmagnetic Sr (SrS is diamagnetic with NaCl-type lattice) the ferromagnet order is destroyed and a spin glass is formed. According to the magnetic phase diagram of $Eu_xSr_{1-x}S$ (Maletta 1982) (fig. 29a):

(a) for $x > 0.7$ the system behaves like a simple dilute Heisenberg ferromagnet (region I);
(b) for $x_c < x < 0.7$ the system is in a reentrant or "frustrated" ferromagnetic state (region II);
(c) for $x_p < x < x_c \simeq 0.51$ spin-glass behaviour is found (region III);
(d) for $x < x_p$ superparamagnetism of isolated Eu clusters is observed ($x_p = 0.136$) (region IV).

The thermal conductivity of the $Eu_xSr_{1-x}S$ system in the temperature region 0.06–30 K and in magnetic fields up to 7 T has been measured by Arzoumanian et al. (1983, 1984), Löhneysen et al. (1986) and Lecomte et al. (1983, 1984, 1986). The compositions in the different regions of the magnetic phase diagrams have been investigated: I ($x = 1$), II ($x = 0.54$), III ($x = 0.25$, 0.40 and 0.44), IV ($x = 0.1$, 0.017, 0.005) (fig. 29a). Figures 30 and 31 show data on $\kappa_{tot}(T)$ for $Eu_xSr_{1-x}S$ single crystals from all phase-diagram regions.

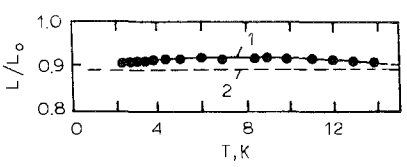

Fig. 28. The temperature dependence of L/L_0 for the metallic spin glass AgCr (1) (Ducastel and Pitsi 1986) and (2) calculation using eq. (35).

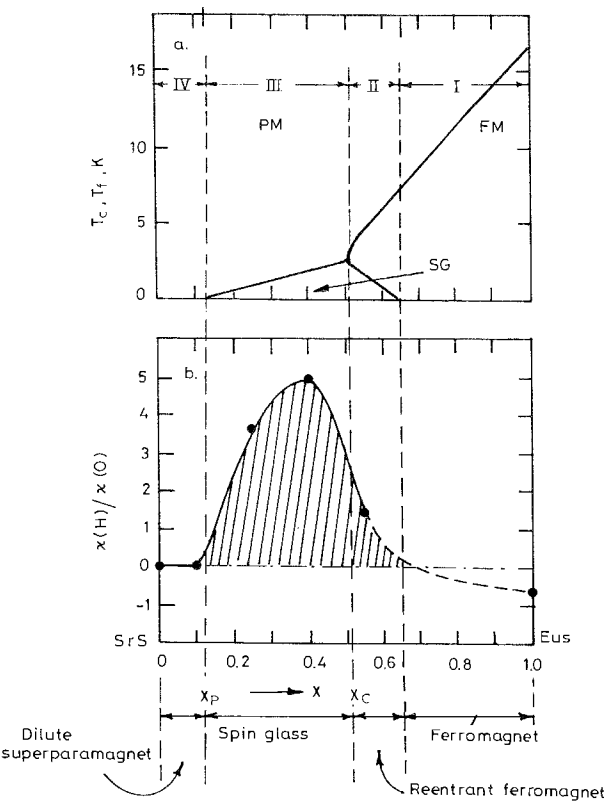

Fig. 29. (a) Magnetic phase diagram for $Eu_xSr_{1-x}S$ (Maletta 1982). (b) Dependence of $\kappa(H)/\kappa(0)$ on $x = 1.6$ K and $H = 6$ T (based on the experimental data of Belov (1972) and Belov et al. (1979).

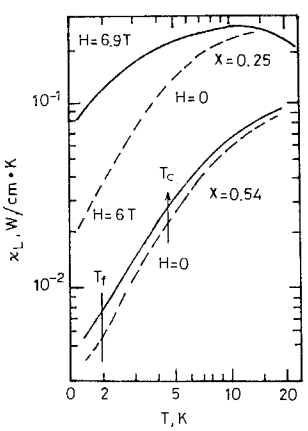

Fig. 30. The temperature dependence of κ_{tot} for $Eu_xSr_{1-x}S$ single crystals ($x = 0.25$ and 0.54) (Lecomte et al. 1983).

Let us consider data for κ measured in zero magnetic field ($H = 0$). Some regularities can be noted:

(1) No anomalies of κ_L near T_f (the "freezing" temperature for the spin-glass system) have been observed (for compositions with $x = 0.44$ and 0.54 the values T_f

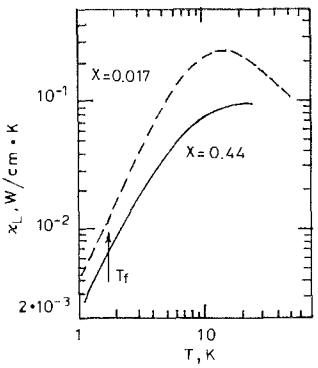

Fig. 31. The temperature dependence of κ_{tot} for $Eu_xSr_{1-x}S$ single crystals ($x = 0.44$ and 0.017) (Arzoumanian et al. 1983, 1984).

are essentially equal, respectively 1.8 and 2 K). The same effect has been observed also in the thermal conductivity of metallic amorphous spin glasses (see, e.g. Herlach et al. 1981).

(2) No anomalies of κ_L have been observed at $T_C \simeq 4.5$ K for samples with $x = 0.54$.

(3) At low temperatures (for the samples with $x = 0.25$, 0.44 and 0.54) κ_L obeys a dependence $T^{1.8-2}$ and not T^3, as would be expected for phonon scattering by crystal boundaries.

(4) Data on the temperature dependence of κ_L can be described satisfactorily in the model of a magnetic two-level system (MTLS) (Arzoumanian 1983, 1984). This model explains well the behaviour of $\kappa_L(T)$ in metal spin glasses (see, e.g., Herlach et al. 1983). The most interesting data on $\kappa_L(T)$ have been obtained in magnetic fields (along the heat flux) (figs. 29b, 30, 32, 33). In the spin-glass region III ($x = 0.25$, 0.4) at low temperatures an anomalously large increase of κ in a magnetic field is observed (fig. 29b). For compositions in region IV ($x = 0.005$ and 0.017) a magnetic field does not have an influence on the κ value (figs. 29b, 32). In region II ($x = 0.54$) the ratio $\kappa(H)/\kappa(0)$ increases but not so much as in the spin-glass region (cf. data for $x = 0.44$ in fig. 29b). In EuS (region I) the value of $\kappa(T)$ in a magnetic field does not increase, but, on the contrary, decreases (figs. 29b, 32, 34, 35) (Lecomte et al. 1984,

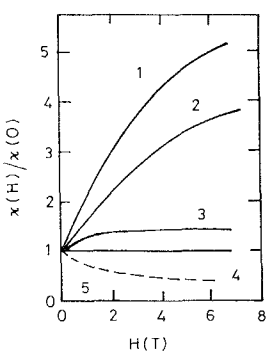

Fig. 32. Magnetic field dependence of the thermal conductivity of $Eu_xSr_{1-x}S$ (1–4) (Löhneysen et al. 1986) and EuS (5) (Lecomte et al. 1984) at 1.6 K plotted as $\kappa(H)/\kappa(0)$; $x = 0.4$ (1), 0.25 (2), 0.54 (3), 0.005 (4).

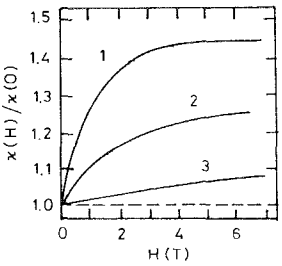

Fig. 33. Magnetic field dependence of the thermal conductivity for $Eu_{0.54}Sr_{0.46}S$ at three fixed temperatures $T = 1.65$ K (1), 3.85 K (2), 13.5 K (3) (Lecomte et al. 1983).

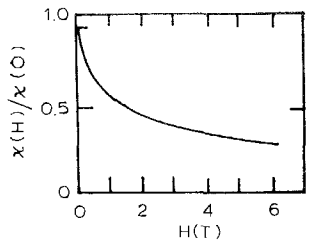

Fig. 34. The magnetic field dependence $\kappa(H)/\kappa(0)$ for EuS at $T = 1.65$ K (Lecomte et al. 1984).

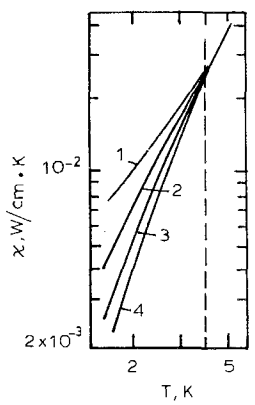

Fig. 35. The temperature dependence of the thermal conductivity of EuS in various magnetic fields: $H = 0$ T (1), 0.77 T (2), 3.22 T (3), 6.45 T (4) (Lecomte et al. 1984).

1986, McCollum et al. 1964). A thermal conductivity which decreases in magnetic fields at low temperature, is not unique. This effect has been discussed in section 3.4.

The effect of a giant increase of the thermal conductivity in a magnetic field in the spin-glass region needs special explanation. It cannot be explained, for example, by an increase in the heat capacity C, because, on the contrary, C in magnetic field decreases (fig. 36) (Löhneysen et al. 1986). More probably, the strong increase of κ_{tot} in a magnetic field is connected with field-induced magnon heat transport.

As it has been noted above, one does not observe spin waves in a spin glass, and hence κ_m is absent. The magnetic field, however, orders the spin arrangement (fig. 37) and κ_m arises. A sufficiently high magnetic field must lead to "freezing" κ_m (like in the case of EuS) and the ratio $\kappa(H)/\kappa(0)$ must begin to decrease at $H > H_{cr}$ (fig. 38). However, experiments in such high field have not yet been carried out. Arzoumanian et al. (1983) and Lecomte et al. (1983) have given another explanation of the observed

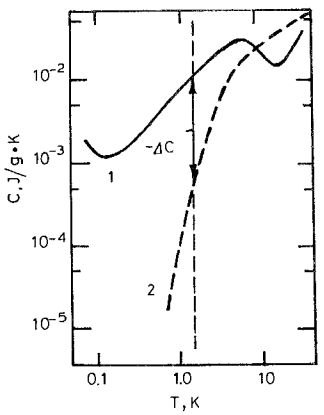

Fig. 36. The heat capacity C of $Eu_{0.54}Sr_{0.46}S$ as a function of temperature, T, in two magnetic fields: $H = 0$ T (1), 6.6 T (2) (Löhneysen et al. 1986).

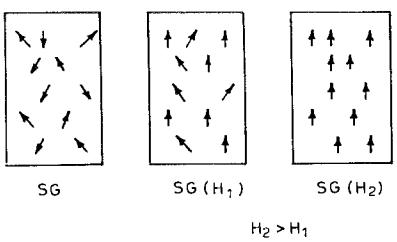

Fig. 37. Magnetic moments in spin glasses in various magnetic fields: $H = 0$ (1), H_1 (2), H_2 (3); $H_2 > H_1$.

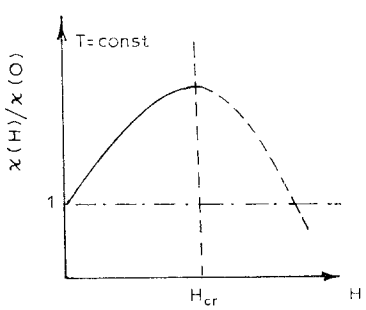

Fig. 38. Schematic shape of the dependence of $\kappa(H)/\kappa(0)$.

effect. The increase of the ratio $\kappa(H)/\kappa(0)$ in the spin-glass region is connected with decreasing phonon–magnon scattering, since spins order in the magnetic field. However, this contradicts, according to Lecomte et al. (1986), the experimental data on the absence of the influence of a magnetic field on samples with $x = 0.1$ and 0.017 outside the spin-glass region. Both hypotheses need further experimental and theoretical study.

5. Thermal conductivity of systems with heavy fermions, intermediate valency of lanthanide ions, dilute and concentrated Kondo lattices

5.1. *Main principles, theoretical premises*

As it has been noted already in the Introduction the systems noted in the section title are among the most interesting and unusual materials known. They are, as a rule, metals. Figures 39a, b, c show schemes of their electron structures and figs. 39a′, b′, c′ show, as an example, schematically the unusual behaviour of $\rho(T)$ of these classes of materials (almost all physical parameters behave anomalously). One can conclude from the band pictures that peculiarities of the behaviour of κ in these materials must reveal themselves mainly in κ_e (especially in the temperature dependence of the Lorentz number). Considerable difficulties arise, however, in the separation of κ_L and κ_e from κ_{tot}. In many cases the contribution κ_L to κ_{tot} is rather significant over a wide temperature interval, due to low mobilities (and consequently not a small ρ). An incomplete exclusion of κ_L could give rise to an overstated value L if calculated according to the Wiedemann–Franz law $[L = (\kappa_{tot} - \kappa_L)T/\rho]$. Unfortunately, the separation of κ_L and κ_e with a high enough precision is a rare case, and experimentalists are satisfied with approximate methods not always yielding a true temperature dependence $L(T)$. The more reliable data on $L(T)$ can be obtained in the low- and superlow-temperature regions ($T < 4$ K and $T < 1$ K, respectively), where one could consider $\kappa_L \ll \kappa_e$ with a high precision.

In a number of theoretical works the behaviour of $\kappa_e(T)$ and $L(T)$ of systems with concentrated (CKL) and dilute (DKL) Kondo lattices have been investigated (Fisher 1971, Nakamura et al. 1987, Bhattacharjee and Coqblin 1988, Cox and Grewe 1988,

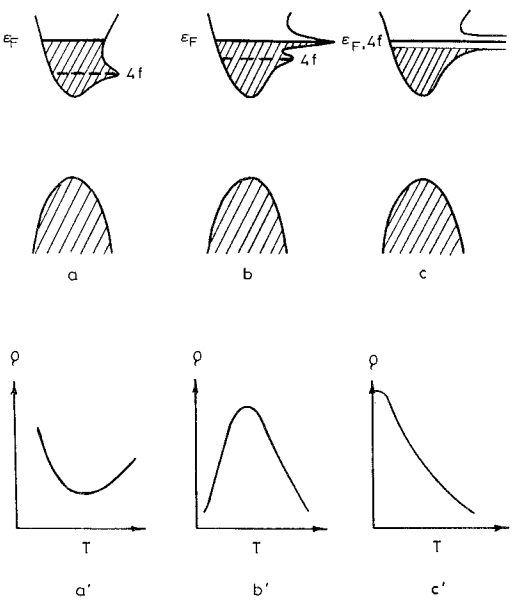

Fig. 39. Schematic shape of the electron band structure (a, b, c) and $\rho(T)$ (a′, b′, c′) for metals with Kondo impurities (a, a′), concentrated Kondo systems (including systems with heavy fermions) at $T < T_K$ (b, b′) and for compounds with homogeneous intermediate valency of rare earth ions (c, c′).

Belitsky and Goltsev 1991, Bhattacharjee et al. 1989, Raki et al. 1990), and the specific behaviour of $L(T)$ intrinisic only in these systems has been predicted (or explained, if experimental data had been obtained previously). Analysing experimental data on $L(T)$ of CKL and DKL systems one must remember that in normal metals $L = L_0$ due to the scattering of electrons by static defects, and $L < L_0$ in the low-temperature region due to

(a) inelastic scattering by long-wavelength acoustic phonons (see section 2, fig. 4) and

(b) scattering of electrons by split crystal field ground state levels of paramagnetic rare earth ions (see section 6.2). L can be larger or smaller than L_0 at interband scattering of the current carriers in the presence of a complex band structure with heavy and light bands (see section 2, fig. 6). The last case is close to the situation in the class of materials considered in this section and reminds one of the situation shown in figs. 39b, c.

Discussing results on κ of heavy-fermion systems one must distinguish two temperature regions: a low-temperature one, $T < T_K$, and a high-temperature one, $T > T_K$. The Kondo temperature, T_K, corresponds to the delocalization of f-electrons due to Kondo interaction with free electrons:

$$T_K = (\varepsilon_F/k_0) \exp[1/2Ig(\varepsilon_F)]. \tag{37}$$

$g(\varepsilon_F)$ is the state density at the Fermi level, ε_F, I is the exchange integral of the s–f interaction. T_K is usually of the order of only a few or dozens K. The region $T < T_K$, in its turn, is divided in two intervals: $T < T^*$ and $T^* \leqslant T \leqslant T_K$. Here T^* is the temperature below which one must consider the interaction between heavy fermions as being coherent. In this temperature region the law $\rho \propto DT^2$ ($\rho = \rho_0 + DT^2$) is fulfilled. (In systems with heavy fermions D is about two orders larger than in normal metals.) T^* is smaller than T_K. For example, in $CeAl_3$ $T_K \simeq 5$ K and $T^* \simeq 350$ mK (Flouquet et al. 1985). At $T < T_K$ a peak in the state density arises due to the Abrikosov–Suhl resonances (fig. 39b). At $T \simeq T_K$ the peak spreads out, and its amplitude sharply decreases. At $T \gg T_K$ the singularity in the state density disappears and the system turns into a Kondo impurity state. The theoretical formulae describing the variation of L/L_0 with temperature and magnetic field in the region $T < T^*$ are taken from Belitsky and Goltsev (1991). These formulae take into account scattering of current carriers by the usual impurities (defects, impurity atoms) [eq. (38)] and by so called "exchange energy defects" [eq. (39)]. The first defects do not give rise to, and the second defects give rise to, a change of the local exchange integral between localized f-electrons and conduction electrons. An example of a defect of the second type are substitutional impurities – nonmagnetic rare earth ions in a Kondo lattice.

$$L(T, H) = 1 + \frac{16}{15} \frac{q_0}{n_c} \frac{\pi^2 T^2}{T_0^2} [1 + \tfrac{4}{3} J(J+1)(g\mu_B H/T_0)^2], \tag{38}$$

$$L(T, H) = 1 + \frac{16}{15} \frac{\pi^2 T^2}{T_0^2} [1 - \tfrac{1}{3} J(J+1)(g\mu_B H/T_0)^2], \tag{39}$$

where $q_0 = Q/N$ (N is the degeneracy of the f-level, Q the number of electrons in the

f-level), Nn_c is the number of electrons in one level in the conduction band, T_0 is like by nature to T^*,

$$T_0 = (n_c/\nu_0)\exp(1/\nu_0 I), \tag{40}$$

where ν_0 is the band-electron state density.

It follows from eqs. (38) and (39) that in the coherent region at low temperatures $L > L_0$, which is in contrast to normal metals with impurities, where $L = L_0$. Such an effect is only possible in a Kondo lattice. For the standard metals another equation for L/L_0 is used, the correction to L_0 is proportional to T/ε_F and is small. Unfortunately, at present there is no clear physical explanation for the fact that L exceeds L_0 in Kondo systems at low temperatures. In the extreme case of strong inelastic fermion–fermion scattering eq. (39) turns into

$$L(0, 0)/L_0 = 36/\pi^2 - 3 \simeq 0.648. \tag{41}$$

This was shown in some other works [see, e.g., Cox and Grewe (1988)]. With decreasing temperature L/L_0 increases, reaches $L = L_0$, and then behaves according to eqs. (38) or (39). Such a behaviour is the result of competition of different scattering mechanisms for current carriers (inelastic fermion–fermion, elastic scattering by static defects and the peculiar scattering characteristic for a Kondo lattice). For $T > T_K$ one expects that in the Kondo-impurity region $L < L_0$ (fig. 40), see Nakamura et al. (1987), Bhattacharjee and Coqblin (1988), Cox and Grewe (1988). Thus, we have schematically presented the dependence $L/L_0 = f(T)$ for the heavy-fermion system in fig. 41.

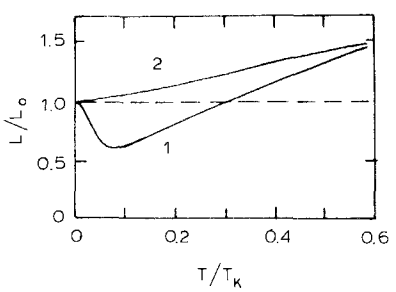

Fig. 40. Calculated temperature dependence of L/L_0 for heavy-fermion systems based on Ce. x is the concentration of Ce. Curve 1: concentrated Kondo system ($x = 0.98$), 2: dilute Kondo system ($x = 0.2$) (Nakamura et al. 1987).

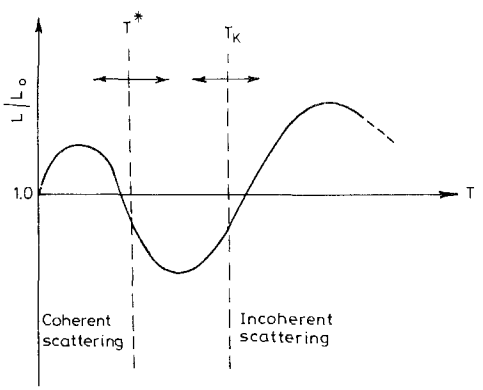

Fig. 41. Schematic shape of the temperature dependence of L/L_0 for a heavy-fermion system.

5.2. *Experimental results*

To date κ has been investigated in a large number of CKL and DKL systems. Table 3 gives a list of the most important compounds investigated. It includes also data on the classical heavy-fermion systems UBe_{13} and UPt_3 to make the picture complete. We will discuss κ of these compounds in section 8.2, analysing κ of the superconducting heavy-fermion systems. Also presented in table 3 are the crystal structures, the values of γ, the electron specific-heat coefficient ($C_e = \gamma T$), which gives information on the electron state density (and hence on the value of the effective mass) at the Fermi level. (For nonmagnetic materials γ is defined as $\gamma = \lim(C/T)$, while for magnetic materials γ is defined by extrapolation to zero temperature from above the ordering temperature.) According to a contemporary classification (De Visser et al. 1987) the compounds can be separated into two groups: the true heavy-fermion systems ($\gamma \geqslant 400$ mJ/mol K^2, $m^*/m \approx 10^2$–10^3) and CKLs with "half-heavy" fermions ($\gamma \leqslant 400$–200 mJ/mol K^2) (in standard metals $\gamma \sim 1$–10 mJ/mol K^2). The κ of a number of DKL systems has been measured: in $Ce_xLa_{1-x}Cu_6$ (Bauer et al. 1987), $Ce_xLa_{1-x}Al_2$ (Steglich 1976, Moeser and Steglich 1975) and $CePd_3$, a compound with an intermediate valence (Schneider and Wohlleben 1981). All systems with heavy and "half-heavy" fermions can be divided into three groups: nonmagnetics, magnetics and superconductors (see table 3). The most typical representative of these

TABLE 3
Cerium and uranium materials related to concentrated Kondo lattice systems for which the thermal conductivity has been measured.

Compound	γ, mJ/mol K^2	Crystal structure	State	Refs.*
$CeAl_3$	1620	hexagonal	nonmagnetic	[1–6]
$CeCu_6$	1600	orthorhombic	nonmagnetic	[7–9]
$CeCu_2Si_2$	1100	tetragonal	superconducting	[3, 10–13]
UBe_{13}	1100	cubic	superconducting	[9, 4, 5, 14, 15]
UPt_3	422	hexagonal	superconducting	[5, 10, 16–20]
$CeRu_2Si_2$	350	tetragonal	nonmagnetic	[5, 21]
CeB_6	~255	orthorhombic	antiferromagnet	[5, 23, 24]
$CeAl_2$	135	cubic	antiferromagnet	[3, 24]
$CeCu_2$	82	orthorhombic	antiferromagnet	[25]
$CePt_2Si_2$	80–86	tetragonal	nonmagnetic	[26–28]

*References: [1] Flouquet et al. (1985), [2] Ott et al. (1984a), [3] Sparn et al. (1985), [4] Jaccard and Flouquet (1987), [5] Flouquet et al. (1986), [6] Andres et al. (1975), [7] Brück et al. (1986), [8] Peysson et al. (1986b), [9] Jaccard and Flouquet (1985), [10] Steglich et al. (1985a), [11] Franz et al. (1979), [12] Franz et al. (1978), [13] Schneider et al. (1983), [14] Jaccard et al. (1985a), [15] Ravex et al. (1987), [16] De Visser et al. (1987), [17] Jaccard et al. (1985b), [18] Sulpice et al. (1986), [19] Franse et al. (1985), [20] Steglich et al. (1985b), [21] Amato et al. (1989), [22] Peysson et al. (1985), [23] Marcenat et al. (1990), [24] Bauer et al. (1986), [25] Gratz et al. (1985), [26] Bhattachrjee et al. (1989), [27] Raki et al. (1990); [28] Ayache et al. (1989).

groups are: $CeAl_3$ [nonmagnetic; although Berth et al. (1987) have observed in $CeAl_3$ weak magnetic ordering], $CeAl_2$, CeB_6 (magnetics) and $CeCu_2Si_2$ (superconductor). Data on κ of the first two groups are considered in this section, data on superconductors will be discussed in section 8. Let us note some general features of these systems.

(1) Ce has an integer valence in all compounds listed in table 3.
(2) At low ($T < 4$ K) and superlow ($T < 1$ K) temperatures $\kappa_L \ll \kappa_e$ and thus the experimental κ_{tot} is equal to κ_e.
(3) At elevated temperatures one cannot neglect the contribution of κ_L in metals with a small free path length for electrons.
(4) κ_{tot} of heavy-fermion systems, as a rule, is much smaller than κ_{tot} of related rare earth compounds which are not heavy fermions (see, e.g., figs. 42 and 12).

5.2.1. *Nonmagnetic heavy-fermion systems*

In the classical heavy-fermion compound $CeAl_3$ ($T_K \simeq 5$ K, $T^* \simeq 0.35$ K) (Jaccard and Flouquet 1985, 1987, Sparn et al. 1985) at $T < 1$ K (the region $T \leqslant T^*$) L/L_0 behaves according to the theoretical dependence (38) (fig. 43). At $\simeq 50$ mK there is a maximum ($L/L_0 \sim 1.1$) and near 350 mK a minimum (connected with inelastic fermion–fermion scattering). At $T > 1$ K the ratio L/L_0 tends to one and then, in the

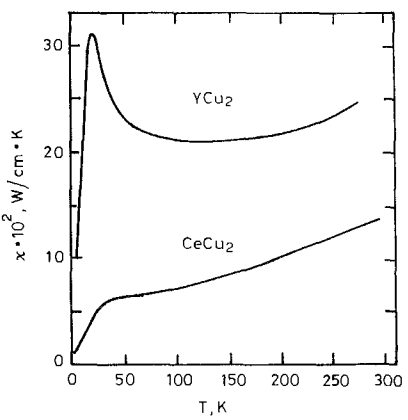

Fig. 42. The temperature dependence of κ_{tot} in $CeCu_2$ and YCu_2 (Gratz et al. 1985).

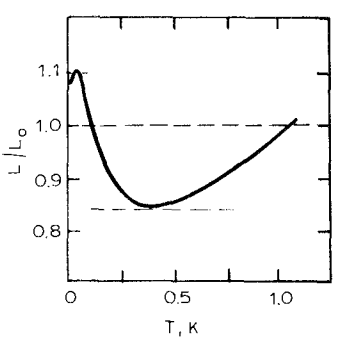

Fig. 43. The temperature dependence of L/L_0 in $CeAl_3$ (Sparn et al. 1985, Jaccard and Flouquet 1987).

Kondo-impurity region, L/L_0 exceeds one. At $T < 1$ K it is assumed that $\kappa_L \ll \kappa_e$, as has been noted above.

The increase of L/L_0 at $T < 500$ mK occurs due to intensifying (with decrease of temperature) current carrier scattering by static defects (since ρ_0 becomes more important than D/T^2) and the specific effect of L/L_0 increases (over one), which is characteristic for the heavy-fermion systems (Belitsky and Goltsev 1991). In this temperature interval $\kappa_L \propto T^{-1}$ (fig. 44) (Flouquet et al. 1985). In $CeAl_3$ κ_L and κ_e have been separated between 0.1 and 50 K (fig. 45) (Ott et al. 1984a). κ_e is calculated using the Wiedemann–Franz law under the supposition that $L = L_0$. It turns out, that the contribution κ_L to κ_{tot} at $T > 1$ K is rather large, but it becomes negligible at $T \lesssim 1$K. If at $T \gtrsim 5$ K ($T > T_K$) the ratio L/L_0 begins to exceed one, as is expected according to the theory for the Kondo-impurity region (Nakamura et al. 1987, Bhattacharjee and Coqblin 1988, Cox and Grewe 1988), then the κ_L contribution to κ_{tot} of $CeAl_3$ is small.

An interesting result should be noted. The separation of the lattice thermal conductivity carried out above gives for $CeAl_3$ $\kappa L \propto T$, and not T^2 (as for phonon scattering by electrons) as well as not T^3 (as for boundary scattering).

$CeCu_2Si_2$ is another classical nonmagnetic heavy-fermion superconductor ($T_c \simeq 0.6$ K, $T_K \simeq 10$ K, $T^* \simeq 1$ K) (Sparn et al. 1985, Steglich et al. 1985a, Franz et al.

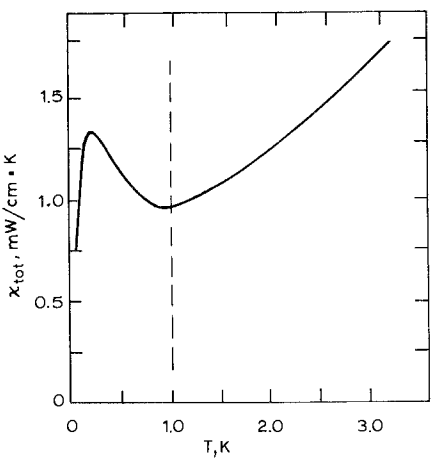

Fig. 44. The temperature dependence of κ_{tot} in $CeAl_3$ (Sparn et al. 1985, Jaccard and Flouquet 1987). $\kappa_L \ll \kappa_e$ at $T < 1$ K.

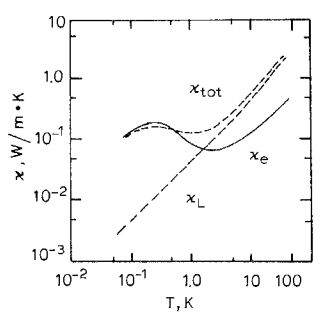

Fig. 45. The temperature dependence of the various contributions to κ in $CeAl_3$ (Ott et al. 1984a).

1978, 1979, Schneider et al. 1983). The low-temperature data on κ used for the analysis of $L(T)/L_0$ are obtained at a magnetic field ($H = 2.5$ T) in which the sample is in the normal state (fig. 46) (Sparn et al. 1985). As one can see, up to $T \simeq 0.7$ K the ratio $L/L_0 = 1$ and then L/L_0 becomes >1. The "excess" $\Delta\kappa$ of κ_e in comparison with the calculated curve (curve 1) is connected by Sparn et al. (1985) with the neglect of the κ_L contribution to κ_{tot}. $\Delta\kappa$ is proportional to T^2 and at 1 K $\Delta\kappa \simeq 0.2$ mW/K cm, which coincides with κ_L extrapolated from the high-temperature region for $CeCu_2Si_2$ obtained by Franz et al. (1978). (Similar behaviour of $L(T)/L_0$ is observed in the heavy-fermion superconductor UPt_3 (De Visser et al. 1987).) Franz et al. (1978) have attempted to separate κ_L and κ_e of $CeCu_2Si_2$ in the interval 1.5–300 K (fig. 47). The contribution κ_L to κ_{tot} turns out to be rather large over the whole temperature interval. $L(T)/L_0$ calculated for $CeCu_2Si_2$ from $\kappa_e(T)$ (fig. 47) and $\rho(T)$ (Franz et al. 1978) is shown in fig. 48. In region I, where $CeCu_2Si_2$ can be considered as CKL system, the ratio $L/L_0 < 1$. In region III, corresponding to a Kondo-impurity system, $L/L_0 > 1$, which agrees well with theoretical predictions (Nakamura et al. 1987, Bhattacharjee and Coqblin 1988, Cox and Grewe 1988, Belitsky and Goltsev 1991, Bhattacharjee et al. 1989) and with the scheme of the behaviour of $L(T)/L_0$ (fig. 41).

$CeRu_2Si_2$ ($T_K \simeq 24$ K, $T^* \simeq 700$ mK) is a "half-heavy" fermion system. It is

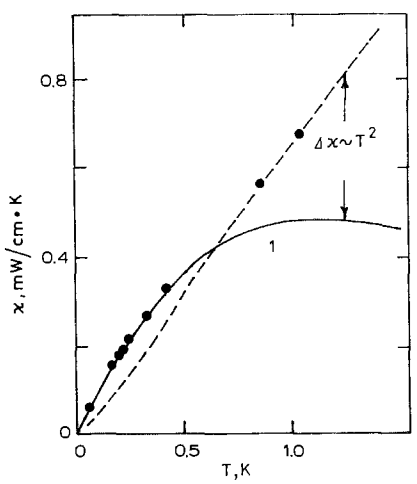

Fig. 46. The temperature dependence of κ in polycrystalline $CeCu_{2.02}Si_{1.98}$ (Sparn et al. 1985). The solid line gives κ_e calculated using the Wiedemann–Franz law with $L = L_0$. The dotted line gives the experimental result at $H = 0$, points the experiment result at $H = 2.5$ T.

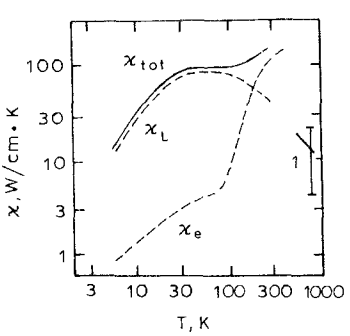

Fig. 47. Experimental (κ_{tot}) and calculated (κ_L and κ_e) thermal conductivities as functions of temperature in the polycrystalline sample $CeCu_2Si_2$ (Franz et al. 1978). Curve 1: κ_L calculated according to Leibfried and Schlömann (1954).

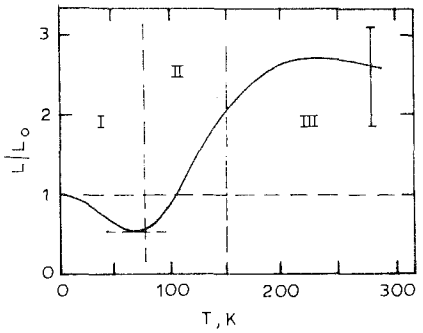

Fig. 48. The temperature dependence of L/L_0 in $CeCu_2Si_2$ (Franz et al. 1978). I is the coherent state region, II the intermediate region, and III the Kondo-impurity region.

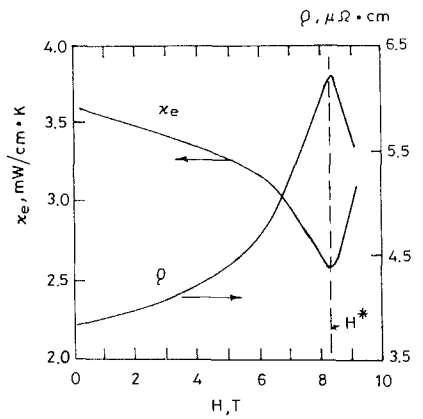

Fig. 49. The magnetic field dependence of κ_e and ρ in a single crystal of $CeRu_2Si_2$ (Amato et al. 1989). κ, $\rho \perp c$, $\boldsymbol{H} \| \boldsymbol{c}$, $T = 640$ mK.

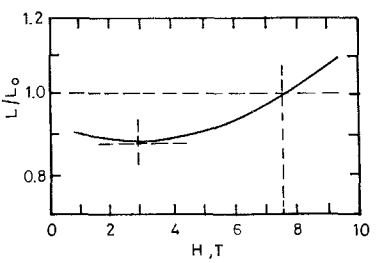

Fig. 50. The magnetic field dependence of L/L_0 in a single crystal of $CeRu_2Si_2$ (Amato et al. 1989). κ, $\rho \perp c$, $\boldsymbol{H} \| c$, $T = 640$ mK.

isostructural with $CeCu_2Si_2$, but it is not a superconductor. $CeRu_2Si_2$ undergoes a metamagnetic-like transition at $T < 10$ K in an applied magnetic field $H^* \simeq 8$ T along the c-axis. It turns out that the maximum of $\rho(H^*)$ coincides with the minimum of $\kappa_e(H^*)$ (fig. 49) (Amato et al. 1989). At low temperatures ($T < 1$ K) $\kappa_L \ll \kappa_e$. Figure 50 shows the dependence $L(H)/L_0$ for $T < T^*$ ($T^* = 640$ mK) for $CeRu_2Si_2$. $L/L_0 < 1$ up to $H \simeq 7$ T, which suggests the presence of strong inelastic fermion–fermion scattering characteristic for a heavy-fermion system. The increase of L/L_0 at $H > 7$ T can be explained, possibly, in the framework of the theories developed by Nakamura et al. (1987), Cox and Grewe (1988) and Belitski and Goltsev (1991).

5.2.2. *Magnetic heavy-fermion systems*

An evaluation of the κ_L contribution to κ_{tot} has been carried out for $CeCu_2$ ($T_K \simeq 17$ K, $T_N = 3.5$ K) by the method considered in section 3.2 (Gratz et al. 1985). It turns out that in a rather wide temperature interval $\kappa_L \ll \kappa_e$. Figure 51 shows the dependence $L(T)/L_0$ of $CeCu_2$ in the temperature interval 3.5–300 K (Gratz et al. 1985). At low temperatures (but for $T > T_N$) there is a maximum $L/L_0 \simeq 1.11$ at about 20 K. A minimal value of $L/L_0 = 0.8$ is reached at $\simeq 80$ K. Thus, $CeCu_2$ has a $L(T)/L_0$ dependence which is typical for a heavy-fermion system (cf. with $L(T)/L_0$ for $CeAl_3$, fig. 43).

In $CeAl_2$ ($T_K \simeq 5$ K, $T_N \simeq 3.8$ K) $\kappa_L \ll \kappa_e$ only at $T < 4$ K (i.e. for $T \leqslant T_N$) (Sparn et al. 1985). Figure 52 shows $L(T)/L_0$ of $CeAl_2$ at $T > 5$ K. $L/L_0 = 1$ at $T = 0.8$ and 4 K. Between 0.8 and 4 K the ratio $L/L_0 < 1$, which is probably caused by inelastic scattering of the current carriers by magnons. This conclusion is confirmed by the results of Marcenat et al. (1990) on κ of CeB_6. CeB_6 is a typical representative of CKL systems. In contrast to classical nonmagnetic Kondo systems, it undergoes two magnetic phase transitions, at $T_1 = 3.3$ K and $T_2 = 2.4$ K. Three phases are distinguished (Effantin et al. 1985):

–phase I ($T > T_1$, paramagnetic),

– phase II ($T_2 < T < T_1$, antiferro-quadropolar ordered phase) [a partial magnetic ordering is observed when applying a magnetic field (Effantin et al. 1985)],

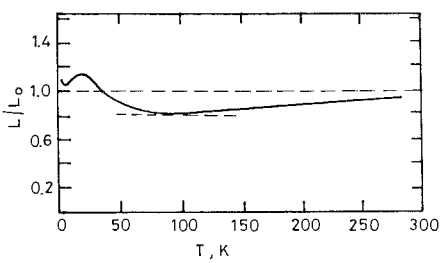

Fig. 51. The temperature dependence of L/L_0 in $CeCu_2$ (Gratz et al. 1985).

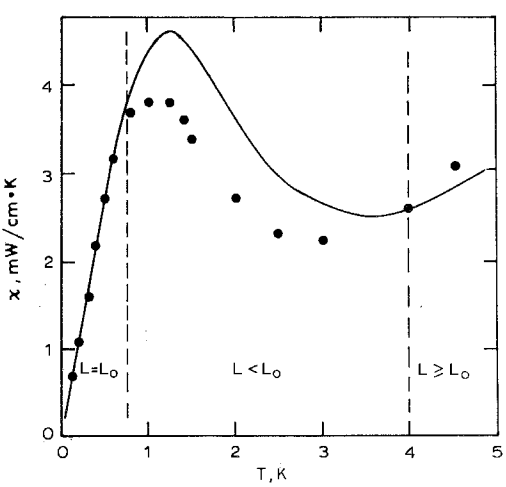

Fig. 52. The temperature dependence of κ in a $CeAl_2$ single crystal (Marcenat et al. 1990). The solid line gives the calculation with $L = L_0$, points the experimental result; the heat flow is along [100].

– phase III ($T < T_2$, antiferromagnetic, $T_2 = T_N$).

Figure 53 shows experimental data on $\kappa_{tot}(T, H)$ of CeB_6 (Marcenat et al. 1990). An evaluation of $L(T, H)/L_0$ for CeB_6 was carried out for the temperature region $T < T_N$, where $\kappa_L \ll \kappa_e$. It turns out that experimental data on $\kappa_e(T, H)$ can be well described (see fig. 54) by the following equation

$$\kappa_e^{-1} = \rho_0(H)/L_0\, T + [\rho(H) - \rho_0(H)]/0.45 L_0\, T, \tag{42}$$

where the first term arises due to electron scattering by static defects and the second term is connected with inelastic electron scattering by magnons (i.e. $L/L_0 = 0.45$). L/L_0 does not depend on temperature (between 0.3 and 1.4 K) and on magnetic field (between 0 and 7 T).

Let us note an interesting feature in the behaviour of $\kappa_{tot}(H)$ of CeB_6 not connected with $L(T, H)/L_0$ but rather pertaining to the subject of section 3. In zero magnetic field κ_{tot} does not change at $T = T_1$, but has a minimum at $T = T_N$ (figs. 53 and 55). Two peaks are clearly seen in the temperature dependence of the heat capacity of CeB_6 – a large peak at T_N and a small one at T_1 (fig. 56) (Peysson et al. 1985). A "weighted" redistribution of these peaks occurs in a magnetic field. At a field $H = 8$ T the peak at T_N disappears and only one large peak at T_1 remains (fig. 57). The minimum of $\kappa_{tot}(T, H)$ at $H = 7$ T shifts to T_1 (fig. 55).

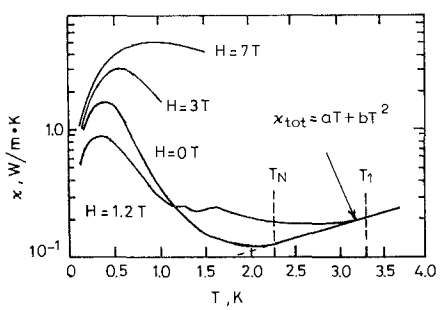

Fig. 53. The temperature dependence of κ_{tot} for CeB_6 single crystals in various magnetic fields H (Marcenat et al. 1990). H and $\nabla T \| [110]$. For $T > T_N$ $\kappa_{tot} = aT + bT^2$.

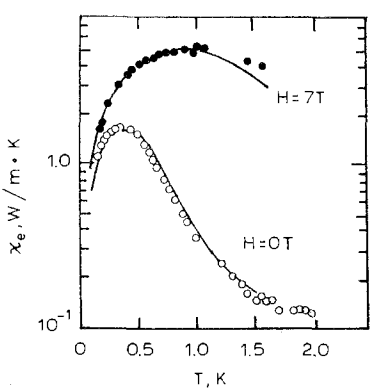

Fig. 54. The temperature dependence of κ_e in CeB_6 single crystals (Marcenat et al. 1990) at $H = 0$ and 7 T. H and $\nabla T \| [110]$. Points give the experimental results, the solid line gives the calculation using eq. (42) (the same good agreement of experiment and theory has been obtained by Marcenat et al. (1990) for the curves in fig. 53 at $H = 1.2$ and 3 T). Not all experimental points of Marcenat et al. (1990) are shown.

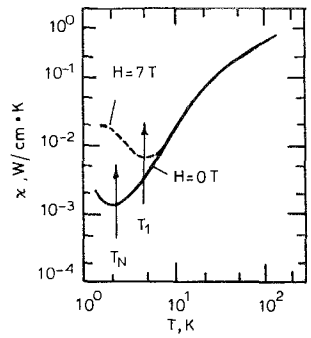

Fig. 55. The temperature dependence of κ_{tot} in CeB_6 (Peysson et al. 1985) at $H = 0$ and 7 T.

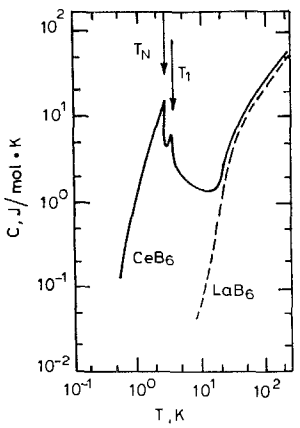

Fig. 56. The temperature dependence of the heat capacity (C) of CeB_6 (Peysson et al. 1985). Data on $C(T)$ for LaB_6 are shown for comparison.

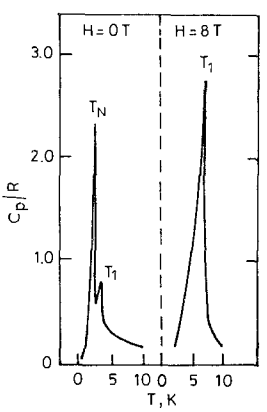

Fig. 57. The temperature dependence of the heat capacity (C) of CeB_6 at two magnetic fields (Peysson et al. 1985).

5.2.3. *Lorentz-number anisotropy in heavy-fermion systems*

Over the last few years measurements of the thermal conductivity of the heavy-fermion systems $CeCu_2Si_2$ (Schneider et al. 1983) and $CePt_2Si_2$ (Bhattacharjee et al. 1989, Raki et al. 1990) have been carried out on single crystals and the anisotropy of L/L_0 has been analysed. Unfortunately, in these works κ_L and κ_e have not been

separated. Therefore, it is only possible to draw general conclusions about the $L(T)/L_0$ anisotropy:

(1) Anisotropy of the Lorentz number is strongly revealed at low temperatures.

(2) Anisotropy of $L(T)/L_0$ is observed experimentally in $CeCu_2Si_2$ (L/L_0 along [100] is greater than along [001]) and in $CePt_2Si_2$ (L/L_0 along [001] is greater than along [110]).

(3) Theory agrees with experiment only qualitatively (Bhattacharjee et al. 1989, Raki et al. 1990).

5.2.4. *Lorentz number in dilute Kondo systems*

Let us consider $La_{1-x}Ce_xAl_2$ (Steglich 1976, Moeser and Steglich 1975) and $La_{1-x}Ce_xCu_6$ (Bauer et al. 1987) as examples of dilute Kondo systems. The terminal compounds of the $La_{1-x}Ce_xAl_2$ system are $LaAl_2$, a superconductor ($T_c = 3.3$ K), and $CeAl_2$, a CKL system. Ce at concentrations of $x = 0.0099$ and 0.0150 is used as Kondo impurity in $LaAl_2$ (Moeser and Steglich 1975). At such concentrations of Ce impurities superconductivity is not observed. Figure 58 shows the dependence $L(T)/L_0$ for $La_{1-x}Ce_xAl_2$ obtained by Moeser and Steglich (1975) taking into account the contribution of κ_L to κ_{tot}. As in the case of CKL, the maximum of $L(T)/L_0$ (with $L > L_0$) is observed in the low-temperature region. A similar dependence is observed in $La_{1-x}Ce_xCu_6$, where Ce ($x = 0.03$ and 0.1) also is a Kondo impurity (fig. 59) (Bauer et al. 1987, Onuki et al. 1985a, b). The contribution of κ_L to κ_{tot} is taken into account in the calculation of $L(T)/L_0$ as in the previous case (Bauer et al. 1987). So, one can draw the general conclusion that the presence of a maximum in $L(T)/L_0$ (with $L > L_0$) is the same necessary indication of a dilute Kondo system as is the presence of a minimum in $\rho(T)$. However, in the case of $L(T)/L_0$ one must keep in mind that the presence of a large amount of non-Kondo impurities in the sample, along with the Kondo impurities, could give rise to the disappearance of the maximum in $L(T)/L_0$ (with $L > L_0$) due to the strong influence of current carrier scattering by static defects.

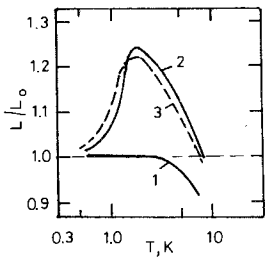

Fig. 58. The temperature dependence of L/L_0 in $La_{1-x}Ce_xAl_2$ (Moeser and Steglich 1975) for various values of the concentration, x: ($r = 52$) (1), 0.0099 ($r = 79$) (2), 0.0150 ($r = 47$) (3), where $r = \rho(300\text{ K})/\rho(12\text{ K})$.

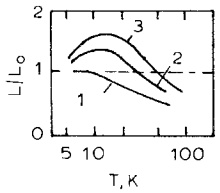

Fig. 59. The temperature dependence of L/L_0 of $Ce_xLa_{1-x}Cu_6$ (Bauer et al. 1987) for various x values: 0 (1), 0.03 (2), 0.1 (3).

5.2.5. *Thermal conductivity of systems with an intermediate valence*

One could expect nonstandard behaviour of $L(T)/L_0$ in these systems too. Unfortunately, this case has not been discussed theoretically and it is not possible to draw any conclusions from the analysis of experimental data on thermal conductivity. In the classical compounds with an intermediate valence of the lanthanide atoms (SmB_6, TmSe) $\kappa_L \gg \kappa_e$ (especially in the low-temperature region). The contribution of κ_L to κ_{tot} has not been taken into account during investigations of metals from this class of materials [e.g., $CePd_3$ (Schneider and Wohlleben 1981)].

6. Influence of paramagnetic lanthanide ions on the thermal conductivity of ordered and disordered systems

As it has been noted in the Introduction, a principal special feature of ions with partly filled inner shells (d- and f-elements are related here) is the existence of nonzero spin ($\boldsymbol{S}$), orbital ($\boldsymbol{L}$) and total ($\boldsymbol{J}$) momenta (see table 4). A crystal electric field removes the degeneration of the orbital momentum orientations and instead of one energy level in a crystal there is a system of levels. The magnitude of the splitting is determined by the value of the electric field gradient, the electron shell configuration and its location inside the ion. In a magnetic field, H, additional splitting of the levels (the so-called Zeeman splitting) is possible. The energy difference between the split levels equals $\Delta E = g\mu_B H$, where g is the Landé factor and μ_B the Bohr magneton.

Lattice vibrations can transfer an ion from one level to another with the absorption of a phonon. Thus paramagnetic rare earth ions with unfilled inner shells are defects which reduce the thermal conductivity of a crystal lattice. There are two approaches for an evaluation of the variation of the thermal conductivity of compounds with

TABLE 4

Electron configurations, spin (S), orbital (L) and total (J) momenta of lanthanide ions R^{3+}, R^{4+} and R^{2+}.

Ion	$4f^n$	S	L	J	Ground term
La^{3+}, Ce^{4+}	$4f^0$	0	0	0	$^1S_0$
Ce^{3+}	$4f^1$	$\frac{1}{2}$	3	$\frac{5}{2}$	$^2F_{5/2}$
Pr^{3+}	$4f^2$	1	5	4	$^3H_4$
Nd^{3+}	$4f^3$	$\frac{3}{2}$	6	$\frac{9}{2}$	$^4J_{9/2}$
Pm^{3+}	$4f^4$	2	6	4	$^5J_4$
Sm^{3+}	$4f^5$	$\frac{5}{2}$	5	$\frac{5}{2}$	$^6H_{5/2}$
Eu^{3+}, Sm^{2+}	$4f^6$	3	3	0	$^7F_0$
Gd^{3+}, Eu^{2+}	$4f^7$	$\frac{7}{2}$	0	$\frac{7}{2}$	$^8S_{7/2}$
Tb^{3+}	$4f^8$	3	3	6	$^7F_6$
Dy^{3+}	$4f^9$	$\frac{5}{2}$	5	$\frac{15}{2}$	$^6H_{15/2}$
Ho^{3+}	$4f^{10}$	2	6	8	$^5J_8$
Er^{3+}	$4f^{11}$	$\frac{3}{2}$	6	$\frac{15}{2}$	$^4J_{15/2}$
Tm^{3+}	$4f^{12}$	1	5	6	$^3H_6$
Yb^{3+}	$4f^{13}$	$\frac{1}{2}$	3	$\frac{7}{2}$	$^2F_{7/2}$
Lu^{3+}, Yb^{2+}	$4f^{14}$	0	0	0	$^1S_0$

paramagnetic ions: a resonance approach (Orbach 1960, 1962, McClintok et al. 1967, McClintok and Rosenberg 1968, Oskotski and Smirnov 1971, 1972, Oskotski et al. 1972, 1982, Luguev et al. 1975b, Vasil'ev et al. 1984b, Smirnov et al. 1985, 1989) and a coherent one taking into account the formation of spin–phonon excitations in the crystal spectrum (Elliot and Parkinson 1967, Iolin 1970, Kokshenev 1985). Both theoretical approaches give roughly the same result – essentially a decrease of the thermal conductivity of crystals containing paramagnetic ions. The resonance is more obvious and we will use it in the following.

We will also consider separately the influence of internal crystal field and external magnetic field on κ of compounds with lanthanide ions.

6.1. *Phonon scattering by paramagnetic levels split by a lattice crystal field*

Let us consider the two-level scheme (fig. 60) (Smirnov et al. 1989) and a phonon energy distribution function which is a product of the Planck function and the phonon density function (phonon spectrum) (fig. 61). A phonon with a resonance energy $\hbar\omega = \Delta$ can be absorbed in an intermediate process (fig. 60). Because of that a narrow band of phonons (shaded in fig. 61) is in practice no longer involved in the heat transport process, decreasing κ by $(-\Delta\kappa_{res})$ (fig. 62). To absorb a phonon it is necessary to have Δ less than Θ_D (i.e. the energy Δ lies inside the phonon spectrum). The f-shells are found deeply in atoms, screened by outer shells and their splitting by a crystal field is small ($\sim$100 K), which is just inside the phonon spectra.

Phonons can be scattered as well by the levels of the d-shell split by the crystal field. But interactions of the crystal field with the d- and f-shells are significantly different. The d-shells are external and the crystal field acts on them stronger than the spin–orbit interaction. The d-levels in crystals are split according to the following scheme. The orbital eigenstates formed by a crystal field from states with different

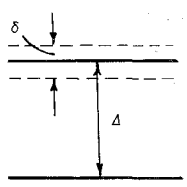

Fig. 60. The two-level system. Δ is the splitting by the lattice crystal field, δ is the spread of the levels with temperature, $\delta \propto T^{-1/2}$ (Oskotski et al. 1972, Luguev et al. 1975b).

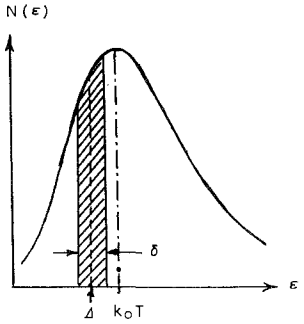

Fig. 61. The phonon energy distribution function.

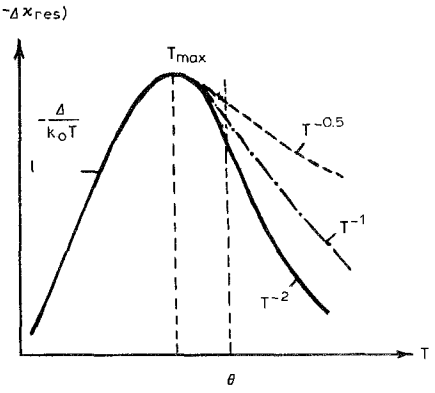

Fig. 62. Theoretical temperature dependence of $-\Delta\kappa_{res}$ for the two-level model.

projections of the orbital momentum are distant from one another by ~1000 K. These levels are degenerate according to the orientations of the total spin of the d-shell. The spin–orbit interaction removes this degeneration and splits the levels by ~100 K (this is inside the phonon spectrum). For this to occur an eigenstate has to have a nonzero average orbital momentum. So, the paramagnetic levels influence κ_L only in special cases. It must as well be noted that crystals with d-elements are often ferromagnetics with high T_C and the crystal field does not split the levels.

In f-elements the spin–orbit interaction is essentially stronger than the lattice–orbit one. This leads to the splitting of states with a total momentum $\boldsymbol{J} = \boldsymbol{L} + \boldsymbol{S}$ and to a more simple level structure than in the case of the d-elements. Only ions with $\boldsymbol{L} \neq 0$ and $\boldsymbol{J} \neq 0$ can interact with phonons. This condition is not satisfied for the ions La^{3+}, Ce^{4+}, Lu^{3+}, Yb^{2+} ($\boldsymbol{L} = \boldsymbol{J} = 0$), Eu^{3+}, Sm^{2+} ($\boldsymbol{J} = 0$), Gd^{3+} and Eu^{2+} ($\boldsymbol{L} = 0$) (see table 4). First studies of the influence of paramagnetic lanthanide ions (PLnIs) on κ_L were performed at low temperatures on holmium and cerium ethylsulphates with hexagonal symmetry (McClintock et al. 1967, McClintock and Rosenberg 1968, Morton and Rosenberg 1962). In this case the paramagnetic levels are split in the lattice crystal field by some degrees and could be split further by an external magnetic field (for details see section 6.1.6.6). The typical splitting in cubic crystals is about 100 K, so the effect on κ_L is essential at medium and high temperatures. In this section we are mainly considering the experimental data concerning the influence of PLnIs on κ_L in crystals of cubic symmetry.

6.1.1. *Temperature dependence of* $-\Delta\kappa_{res}$

The temperature dependence of $-\Delta\kappa_{res}$ – the reduction of the thermal conductivity due to resonance phonon scattering due to PLnIs – has a resonance form (fig. 62) in the two-level model (fig. 60) (Oskotski and Smirnov 1971, Oskotski et al. 1972, Luguev et al. 1975b, Smirnov et al. 1989, Smirnov 1972, Golubkov et al. 1973, Vasil'ev et al. 1978). The temperature region $T > T_{max}$, $T > \Theta$ is the most informative (Luguev et al. 1975b, Smirnov et al. 1989). The temperature dependence and absolute value of $-\Delta\kappa_{res}$ depends on:

(1) The lanthanide ion concentration.

TABLE 5
The temperature dependence of $-\Delta\kappa_{res}$ in the high-temperature region on the concentrations and arrangements of the PLnIs in the lattice.

Small concentration of PLnIs	High concentration of PLnIs		
	Ordered arrangement of PLnIs in the lattice	Disordered arrangement of PLnIs in the lattice	
		Phonon–phonon scattering is greater than phonon–impurity one	Phonon–phonon scattering is less than phonon–impurity one
I	II	III	IV
T^{-2}	$T^{-0.5}$	T^{-1}	$T^{-0.5}$

(2) The arrangement of lanthanide ions in the crystal lattice.
(3) The relative contribution of the different mechanisms of phonon scattering (table 5).

6.1.2. *Methods for separating* $-\Delta\kappa_{res}$

There are two methods for separating $-\Delta\kappa_{res}$: a theoretical one and an experimental one. Theoretically $-\Delta\kappa_{res}$ is determined in the Callaway model as the difference of $\kappa_L(1)$ and $\kappa_L(2)$, where $\kappa_L(1)$ is calculated taking into account phonon scattering by sample boundaries, defects and phonons (N and U processes), and $\kappa_L(2)$ is calculated taking into account the same processes plus resonance scattering of phonons by the split paramagnetic levels of the lanthanide ions (Oskotski et al. 1982, Vasil'ev et al. 1978, 1984b, Neelmani and Verma 1972, Arutyunyan et al. 1986, 1987):

$$-\Delta\kappa_{res} = \kappa_L(2) - \kappa_L(1). \tag{43}$$

Experimentally $-\Delta\kappa_{res}$ is determined as differences between κ_L of crystals containing PLnIs and that of crystals with the same concentration of lanthanide ions with zero $\boldsymbol{L}$ or $\boldsymbol{J}$. For example:

$$-\Delta\kappa_{res} = \kappa_L(\mathrm{PrS}) - \kappa_L(\mathrm{LaS}),$$

$$-\Delta\kappa_{res} = \kappa_L(\mathrm{TbS}) - \kappa_L(\mathrm{GdS}),$$

$$-\Delta\kappa_{res} = \kappa_L(\mathrm{ErS}) - \kappa_L(\mathrm{LuS}).$$

All lanthanide elements can be grouped around three reference elements: around La — Ce, Pr, Nd (group I); around Gd — Sm, Eu (group II) and Tb, Dy, Ho (group III); and around Lu — Er, Tm, Yb (group IV). The errors in the evaluation of $-\Delta\kappa_{res}$ are small, because the properties of the reference elements and the corresponding compounds do not differ too much, and the differences in their masses and ionic radii are small. The maximum differences in the atomic mass and ionic radii are:

Group I $\Delta M = M(\mathrm{Nd}) - M(\mathrm{La}) = 5.34$ g,
$\Delta r = r(\mathrm{Nd}) - r(\mathrm{La}) = -0.066$ Å.
Group II $\Delta M = M(\mathrm{Sm}) - M(\mathrm{Gd}) = -6.85$ g,
$\Delta r = r(\mathrm{Sm}) - r(\mathrm{Gd}) = 0.026$ Å.
Group III $\Delta M = M(\mathrm{Ho}) - M(\mathrm{Gd}) = 7.68$ g,
$\Delta r = r(\mathrm{Ho}) - r(\mathrm{Gd}) = -0.044$ Å.
Group IV $\Delta M = M(\mathrm{Er}) - M(\mathrm{Lu}) = -7.74$ g,
$\Delta r = r(\mathrm{Er}) - r(\mathrm{Lu}) = 0.033$ Å.

For example, for the substitution of Pr by Sc in PrS the values of ΔM and Δr are much higher: $\Delta M = 95.951$ g, $\Delta r = 0.183$ Å.

6.1.3. *Arrangement of PLnIs in a crystal lattice*

PLnIs can be arranged in a crystal lattice in different ways (fig. 63). In all cases the appearance of $-\Delta\kappa_{\mathrm{rcs}}$ can be expected. Crystals where PLnIs are the main ions, and not defects, are of special interest. Here, in an ideal lattice without impurities an additional thermal resistance W_2 appears due to phonon scattering by the paramagnetic levels of the PLnIs.

6.1.4. *Choice of materials for investigation*

Let us analyse all cases of table 5. For this purpose experimental data on $\kappa(T)$ are presented for the different groups of materials:

- Small concentrations of PLnIs (these ions are impurities): $Y_{1-x}Ln_xAl_5O_{12}$ (Ln = Gd, Tb, Dy, Er, Tm, Lu) (Oskotski et al. 1972, Vasil'ev et al. 1984a, b, Smirnov et al. 1985, Arutyunyan et al. 1987, Dzhabbarov et al. 1978, Parfen'eva et al. 1979, Smirinov et al. 1988). These compounds are insulators ($\kappa_{\mathrm{tot}} = \kappa_{\mathrm{L}}$), and they have a cubic lattice with the space group O_h^{10}-Ia3d.
- Large concentration of PLnIs – they form the matrix of a compound with ordered arrangement of PLnIs in a lattice:
  (a) PrS (LaS is the reference material) (Vasil'ev et al. 1978, Oskotski et al. 1982, Smirnov et al. 1988, 1989). This is a metal ($\kappa_{\mathrm{tot}} = \kappa_{\mathrm{L}} + \kappa_{\mathrm{e}}$) with a cubic lattice of NaCl-type.
  (b) $PrTe_{1.33}$ ($LaTe_{1.33}$ is the reference material) (Luguev et al. 1975b, Smirnov et al. 1985, 1988, 1989, Oskotski et al. 1982, Vasil'ev et al. 1976). This is a degenerated semiconductor ($\kappa_{\mathrm{tot}} = \kappa_{\mathrm{L}} + \kappa_{\mathrm{e}}$) with a cubic lattice of Th_3P_4-type.
- Large concentration of PLnIs – disordered arrangement of PLnIs in a lattice:
  (a) $PrTe_{1.5}$ ($LaTe_{1.5}$ is the reference material) – a defect lattice, where the phonon–phonon scattering is stronger than the phonon–defect one (Luguev et al. 1975b, 1978, Oskotski et al. 1982, Smirnov et al. 1985, 1988, 1989, Vasil'ev et al. 1976). These are insulators ($\kappa_{\mathrm{tot}} = \kappa_{\mathrm{L}}$) with cubic structure of Th_3P_4-type.
  (b) Glasses – a solid where there is complete disorder. The phonon–phonon scattering is less than the phonon–impurity one. $Pr_2S_3(Ga_2O_3)_2$ [$La_2S_3(Ga_2O_3)_2$ as the reference material] (Smirnov et al. 1985, 1988, 1989, 1990, Parfen'eva et al. 1990a); PrP_5O_{14} (LaP_5O_{14} as the reference material) (Parfen'eva et al. 1990b).

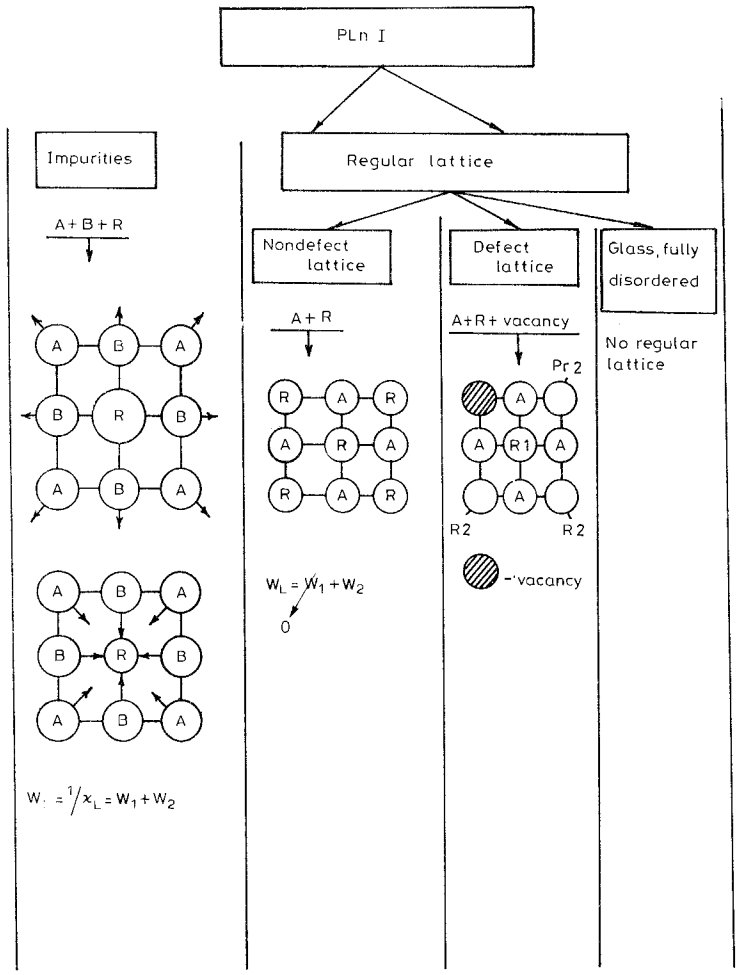

Fig. 63. Schematic arrangement of PLnIs in a crystal lattice. A and B are the lattice ions, R represents lanthanide ions. W_1 is the usual defect thermal resistance, and W_2 is the thermal resistance due to resonance phonon scattering on PLnIs.

In all these materials the lanthanide ions have a valence of +3. All the compounds have a cubic structure. In the investigated temperature range there are no magnetic transitions.

6.1.5. *Schemes of level splitting in a lattice crystal field for selected materials*

Data on level splitting of the ground states of Pr, Er, Ho, Dy ions in a lattice field of crystals PrS, Pr_2Te_3, Pr_3Te_4 and garnets have been obtained from neutron scattering (Turberfield et al. 1971, Parfen'eva et al. 1990b), optical measurements (Slack and Oliver 1971), and from an analysis of the Schottky heat capacity (C_{Sch}) (fig. 64) (Vasil'ev et al. 1983, Mitarov et al. 1975). Figure 64 shows that only a few

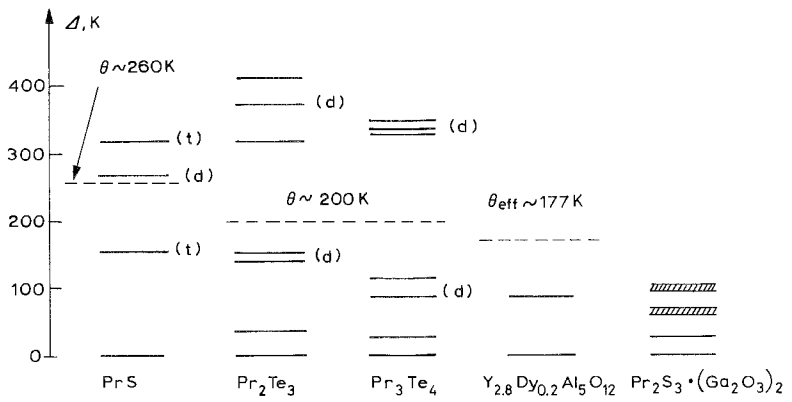

Fig. 64. Splitting of the levels in a crystal field for PrS (Vasil'ev et al. 1983, Turberfield et al. 1971); Pr_2Te_3 and Pr_3Te_4 (Mitarov et al. 1975); $Y_{2.8}Dy_{0.2}Al_5O_{12}$ (Slack and Oliver 1971); and $Pr_2S_3(Ga_2O_3)_2$ (Parfen'eva et al. 1990b). d stands for doublet, t for triplet. Only levels with an energy less than θ give contributions to phonon scattering.

low-energy levels in the garnets are capable of scattering phonons. The ions Dy^{3+} in $Y_3Al_5O_{12}$, Er^{3+} in $Er_3Al_5O_{12}$ and Ho^{3+} in $Ho_3Al_5O_{12}$ have eight levels (Slack and Oliver 1971).

Difficulties have arisen with regard to the level scheme of the glass $Pr_2S_3(Ga_2O_3)_2$. The average energy position of the broadly spread first excited level has been determined from an analysis of the C_{Sch} data using the model of Bhattacharjee and Coqblin (1982) for the paramagnetic ions in the amorphous material. This quantity is approximately equal to 30 K (Smirnov et al. 1990). The energy positions of the next excited levels in the $Pr_2S_3(Ga_2O_3)_2$ glass have been successfully determined from experimental inelastic neutron scattering data (Smirnov et al. 1990). The temperature dependence of the neutron spectrum indicates the existence in the disordered glass structure of a certain principal type of a nearest-neighbour environment of ions Pr^{3+} (with a statistical distribution) producing a crystal field potential. So on the basis of C_{Sch} and neutron scattering data it has been possible to suggest an approximate energy level scheme for $Pr_2S_3(Ga_2O_3)_2$ glass of 0, 30, 60–72, 96–108 K, which is shown in fig. 64.

6.1.6. *Analysis of experimental thermal conductivity data*

It has been necessary to establish from an analysis of experimental data on the thermal conductivity of many materials with PLnIs the following:

(1) Do the theoretical temperature dependences of $-\Delta\kappa_{res}(T)$ for low and high temperatures ($T >$, $< \Theta$) given in fig. 62 and table 5 agree with experiment?

(2) Is the observed effect of κ_L decreasing analogous to a Schottky effect in the heat capacity?

(3) How is T_{max} [in the dependence $-\Delta\kappa_{res} = f(T)$] connected with Δ_1, the distance to the first excited level?

(4) How much influence does a defect of the lattice have on the value of $-\Delta\kappa_{res}$?

Below we consider separately for high and low temperatures, the experimental data on the thermal conductivity of compounds with PLnIs.

6.1.6.1. *Regions of high temperatures.* $T > T_{max}$, $T > \Theta$.

(a) Lanthanide ions are impurities (Oskotski and Smirnov 1971, Oskotski et al. 1972, 1982, Vasil'ev et al. 1984a, b, Smirnov et al. 1988, 1989, Parfen'eva et al. 1979). Figure 65 shows the dependence of κ_L on the atomic number of Ln^{3+} in $Y_{2.8}Ln_{0.2}Al_5O_{12}$ (Ln = Gd, Tb, Dy, Er, Tm, Lu) at 300 K (Smirnov et al. 1988, 1989). The results can be approximated by two straight lines: line A for paramagnetic ions and line B for nonparamagnetic ions. Similar dependences $\kappa_L = f(Ln^{3+})$ were obtained in the temperature range 100–300 K for all investigated PLnI impurities. Figure 66 shows data on $\kappa_L(T)$ for $Y_{2.8}Dy_{0.2}Al_5O_{12}$.

Figure 67 shows a comparison of κ_L of magnetic (ErAlG), nonmagnetic (YAlG, GdAlG, LuAlG) garnets and YAlG with various concentrations of Er impurity (Slack and Oliver 1971). Data on κ_L of YAlG with Er impurity have also appeared in Arutyunyan et al. (1987, 1984), Petrunin et al. (1989). One can see that κ_L of the

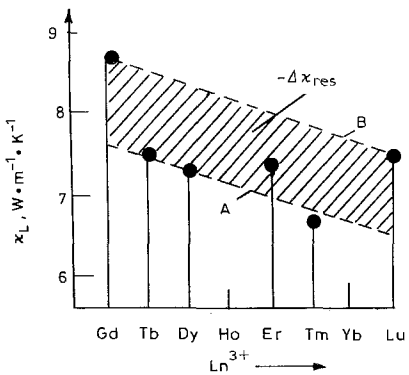

Fig. 65. Dependence of κ_L on the atomic number of the impurity ion R for $Y_{2.8}R_{0.2}Al_5O_{12}$ at $T = 300$ K (Smirnov et al. 1988, 1989).

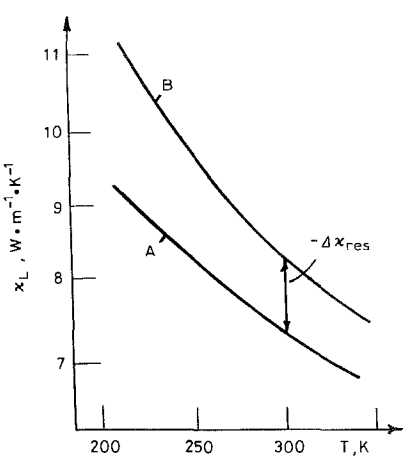

Fig. 66. The temperature dependence of κ_L for $Y_{2.8}Dy_{0.2}Al_5O_{12}$. Curve A gives the experiment and B data obtained with the procedure of fig. 65.

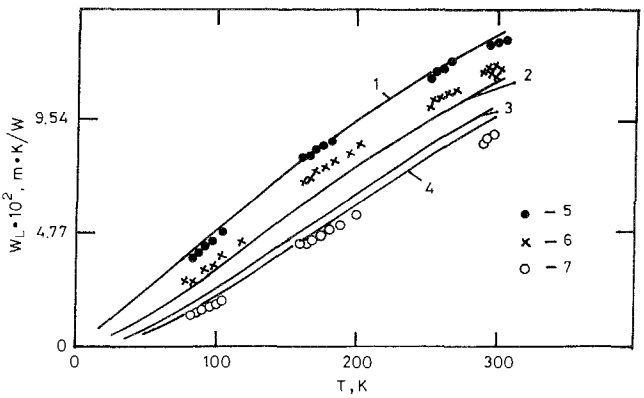

Fig. 67. The temperature dependence of the thermal resistance of the crystal lattice, $W_L = 1/\kappa_L$, for $R_3Al_5O_{12}$ (R = Er (1), La (2), Gd (3), Y (4)) (Slack and Oliver 1971), and $Y_{3-x}Er_xAl_5O_{12}$ ($x = 0.32$ (5), 0.148 (6), 0 (7)) (Oskotski et al. 1972).

crystals with Er impurities becomes smaller than the κ_L of the nonmagnetic garnets. From these figures one can see that in garnets with PLnIs the value of $-\Delta\kappa_{res}$ is sufficiently large at all investigated temperatures. Figure 68 shows the dependence $-\Delta\kappa_{res} = f(T)$ in $Y_{2.8}R^{3+}_{0.2}Al_5O_{12}$ (R^{3+} = Dy or Tb). It turns out, that $(-\Delta\kappa) \propto T^{-2}$, as predicted by the theory (see table 5, column I).

(b) Large concentrations of PLnIs (ordered arrangement of PLnIs in a lattice) (Luguev et al. 1975b, Oskotski et al. 1982, Smirnov et al. 1985, 1988, 1989, Vasil'ev et al. 1976, 1978, Neelmani and Verma 1972, Arutyunyan et al. 1986, 1987, Slack and Oliver 1971). (In this section experimental data on κ_L in Pr_3Te_4 are discussed. Data for PrS will be described in section 6.1.6.2.)

Figure 69 shows experimental data on $\kappa_L(T)$ in Pr_3Te_4, La_3Te_4 and $-\Delta\kappa_{res}$ as the difference $\kappa_L(Pr_3Te_4) - \kappa_L(La_3Te_4)$. It turns out that $(-\Delta\kappa_{res}) \propto T^{-0.5}$ (see fig. 70), as it is predicted by theory (table 5, column II). Arutyunyan et al. (1987) have

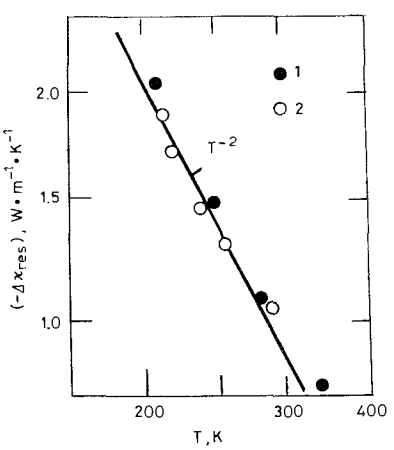

Fig. 68. The temperature dependence of $-\Delta\kappa_{res}$ for $Y_{2.8}R^{3+}_{0.2}Al_5O_{12}$. R = Dy (1) and Tb (2).

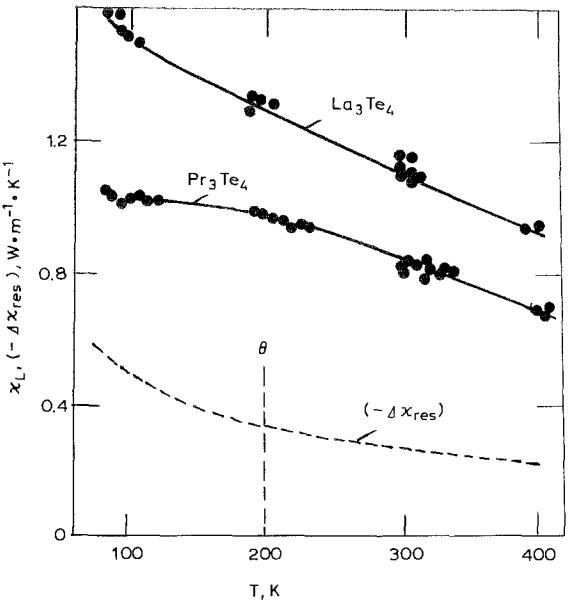

Fig. 69. The temperature dependence of κ_L for La_3Te_4, Pr_3Te_4 and $-\Delta\kappa_{res}$ (Luguev et al. 1975b, Oskotski et al. 1982, Smirnov et al. 1988, 1989).

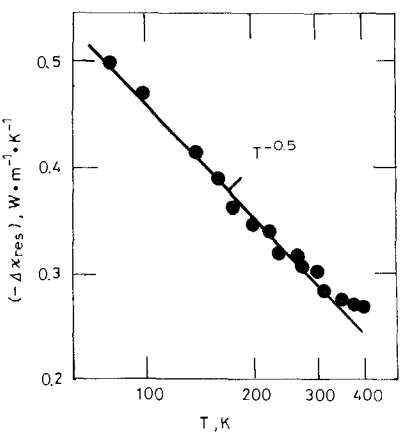

Fig. 70. The temperature dependence of $-\Delta\kappa_{res}$ for Pr_3Te_4 (Smirnov et al. 1988, 1989).

observed a similar temperature dependence, $(-\Delta\kappa_{res}) \propto T^{-0.6}$, in the temperature range 200–1000 K in $Y_{3-x}Er_xAl_5O_{12}$ for $x = 0.9$ and 1.5, which are sufficiently large that these samples cannot be considered as small impurity concentrations (Luguev et al. 1975b).

Unusual temperature dependences $(-\Delta\kappa_{res}) \propto T^{-2}$ must be noted for EuAlG and DyAlG in the temperature range 20–300 K (Slack and Oliver 1971) and $T^{-1.4}$ in ErAlG (Arutyunyan et al. 1987) in the range 200–1000 K, which do not agree with the theory of Luguev et al. (1975b). These observations need a special explanation.

(c) High PLnI concentration. Disordered arrangement of PLnIs in a lattice (phonon–phonon scattering is stronger than the phonon–impurity one) (Luguev et al.

1975b, 1978, Oskotski et al. 1982, Smirnov et al. 1985, 1988, 1989, Vasil'ev et al. 1976).

The R_2Te_3 phase has a defect lattice with $\sim 10^{21}$ cm^{-3} vacant sites (every ninth R-site is empty). The vacancies are statistically distributed (Golubkov et al. 1973). Figure 71 shows data on $\kappa_L(T)$ for Pr_2Te_3, La_2Te_3 and $-\Delta\kappa_{res} = \kappa(Pr_2Te_3) - \kappa(La_2Te_3)$. $(-\Delta\kappa_{res}) \propto T^{-1}$ (fig. 72), as is predicted by the theory (table 5, column III).

(d) High PLnI concentration. Disordered arrangement of PLnIs in a lattice (phonon–phonon scattering is less than the phonon–impurity one) (Smirnov et al. 1985, 1988, 1989, 1990, Parfen'eva et al. 1990a, b). (Data in this section concern both high- and low-temperature ranges.) These scattering conditions are satisfied in glasses. Figure 73 gives κ_L in the glasses $La_2S_3(Ga_2O_3)_2$, $La_2S_3(Ga_2O_3)_3$ (group 1) and $Pr_2S_3(Ga_2O_3)_2$, $Pr_2S_3(Ga_2O_3)_3$ (group 2) and $-\Delta\kappa_{res} = \kappa_L$ (glass with Pr) $- \kappa_L$ (glass with La) (the difference between the averaged values of the curves in fig. 73 of the second and first group). Figure 74 shows the temperature dependence of the heat capacity of the glasses $La_2S_3(Ga_2O_3)_2$ and $Pr_2S_3(Ga_2O_3)_2$ in a plot of C/T^3 versus ln T. The presence of resonant scattering of phonons by the PLnI (Pr^{3+}) in these glasses is indicated by the following experimental facts:

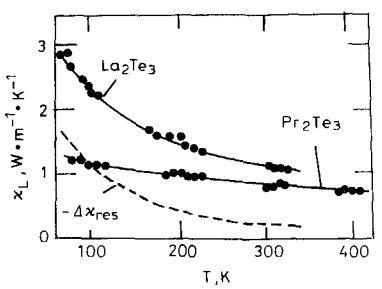

Fig. 71. The temperature dependence of κ_L for La_2Te_3, Pr_2Te_3 and $-\Delta\kappa_{res}$res (Smirnov et al. 1988, 1989).

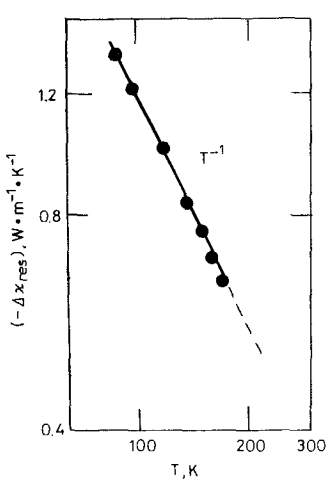

Fig. 72. The temperature dependence of $-\Delta\kappa_{res}$ for Pr_2Te_3 (Smirnov et al. 1988, 1989).

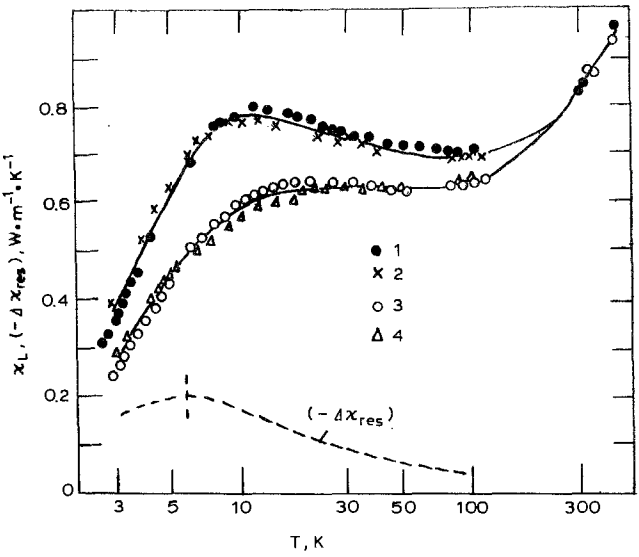

Fig. 73. The temperature dependence of κ_L and $-\Delta\kappa_{res}$ of the glasses $R_2S_3(Ga_2O_3)_2$ (R = La (1), Pr (3)) and $R_2S_3(Ga_2O_3)_3$ (R = La (2), Pr (4)). (Smirnov et al. 1988, 1989).

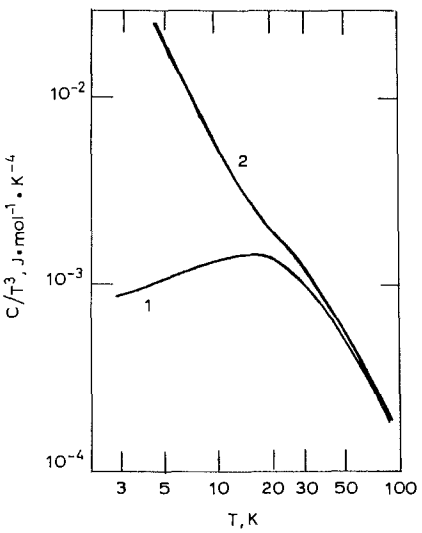

Fig. 74. The temperature dependence of C/T^3 for the glasses $Pr_2S_3(Ga_2O_3)_2$ (1) and $La_2S_3(Ga_2O_3)_2$ (2) (Smirnov et al. 1989).

(1) In $Pr_2S_3(Ga_2O_3)_2$ a Schottky contribution to the heat capacity is observed (fig. 74).

(2) A considerable variation of glass composition (from $R_2S_3(Ga_2O_3)_2$ to $R_2S_3(Ga_2O_3)_3$ does not have much influence on the κ_L value. But κ_L of glasses with Pr and La differ greatly.

(3) The dependence $(-\Delta\kappa_{res}(T)) \propto T^{-0.52}$ (fig. 75) agrees well with the prediction of the theory (see fig. 62 and table 5, column IV).

The $\kappa_L(T)$ of glasses of the intermediate compositions $(Pr_2S_3)_y(La_2S_3)_{1-y}(Ga_2O_3)_2$ ($y = 0.1$, 0.3 and 0.5) has been measured by Smirnov et al. (1992a) (fig. 76).

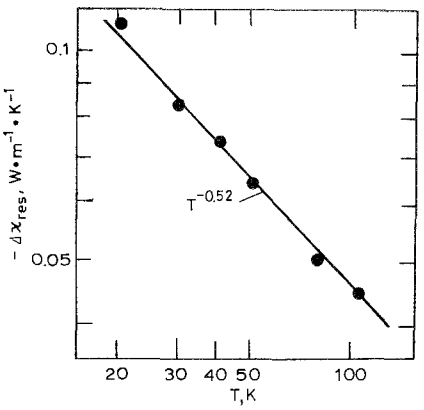

Fig. 75. The temperature dependence of $-\Delta\kappa_{res}$ for $Pr_2S_3(Ga_2O_3)_2$ (Smirnov et al. 1988, 1989).

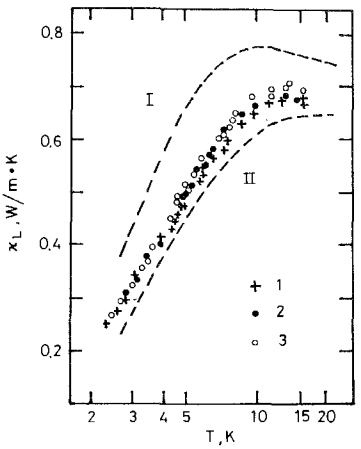

Fig. 76. The temperature dependence of κ_L for $(Pr_2S_3)_y(La_2S_3)_{1-y}(Ga_2O_3)_2$ (Smirnov et al. 1992a) for the values $y = 0.1$ (1), 0.3 (2), 0.5 (3). Curve I is for $La_2S_3(Ga_2O_3)_2$, curve II for $Pr_2S_3(Ga_2O_3)_2$.

The glass $(Gd_2S_3)_{0.3}(La_2S_3)_{0.7}(Ga_2S_3)_2$ has been used as a reference material, because in this glass there is no resonance phonon scattering from the paramagnetic levels of Gd^{3+} ions with $L = 0$.

Figure 77 shows data on the heat capacity of $(Pr_2S_3)_{0.3}(La_2S_3)_{0.7}(Ga_2O_3)_2$. An additional contribution to the heat capacity is observed in the Pr glass in comparison with the La glass. There is good agreement of experimental data (points 1 in fig. 77) with the sum of the partial contributions of the experimental values of C of the glasses $Pr_2S_3(Ga_2O_3)_2$ and $La_2S_3(Ga_2O_3)_2$, i.e. $0.3C[Pr_2S_3(Ga_2O_3)_2] + 0.7C[La_2S_3(Gd_2O_3)_2]$ (the solid curve 2 in fig. 77). This proves that the observed additional contribution to the heat capacity, ΔC, is due to the Schottky-effect, i.e. $\Delta C = C_{Sch}$.

$(-\Delta\kappa_{res})$ has been determined for this glass with $x = 0.3$ using the relation

$$(-\Delta\kappa_{res}) = \kappa_L[(Pr_2S_3)_{0.3}(La_2S_3)_{0.7}(Ga_2O_3)_2] - \kappa_0. \tag{44}$$

The value of κ_0 (fig. 78) is obtained by correcting the κ_L reference curve of $(Gd_2S_3)_{0.3}(La_2S_3)_{0.7}(Ga_2O_3)_2$ by taking into account the dependence of the thermal

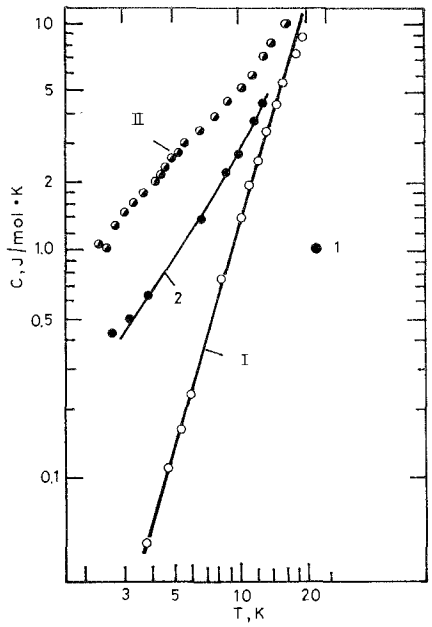

Fig. 77. The temperature dependence of the heat capacity for $(Pr_2S_3)_{0.3}(La_2S_3)_{0.7}(Ga_2O_3)_2$ (Smirnov et al. 1992a). Points (1) give experimental results, the solid line (2) is calculated from the formula $0.3C[Pr_2S_3(Ga_2O_3)_2] + 0.7C[La_2S_3(Ga_2O_3)_2]$. Curve I represents heat capacity of $La_2S_3(Ga_2O_3)_2$, II the heat capacity of $Pr_2S_3(Ga_2O_3)_2$.

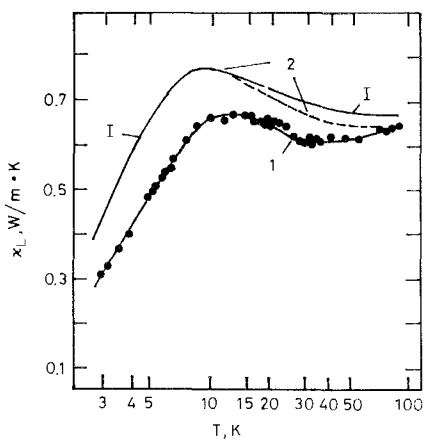

Fig. 78. The temperature dependence of κ_L for $(Pr_2S_3)_{0.3}(La_2S_3)_{0.7}(Ga_2O_3)_2$ (1) and $(Gd_2S_3)_{0.3}(La_2S_3)_{0.7}(Ga_2O_3)_2$ (2) (Smirnov et al. 1992a). The solid line (I) represents values of κ_0 (the correction of the reference curve for $(Gd_2S_3)_{0.3}(La_2S_3)_{0.7}(Ga_2O_3)_2$ taking into account the dependence of the lattice thermal conductivity on the mass and the ionic radius of the lanthanide ion).

conductivity of the mass and the ionic radius of the lanthanide ion (Smirnov et al. 1991a). The resulting $(-\Delta\kappa_{res}) \propto T^{-0.5}$ (for $T > T_{max}$ in the range 5–50 K) agrees well with theory (table 5, column IV).

Resonance scattering of phonons by Pr ions has also been observed in the phosphate-glass PrP_5O_{14}, during an investigation of its thermal conductivity (LaP_5O_{14} has been used as the reference material) (fig. 79) (Parfen'eva et al. 1990b). The thermal conductivity of phosphate glasses is much smaller than that of $R_2S_3(Ga_2O_3)_2$ and has nearly the same value and temperature dependence as the thermal conductivity of quartz glass (Zeller and Pohl 1971).

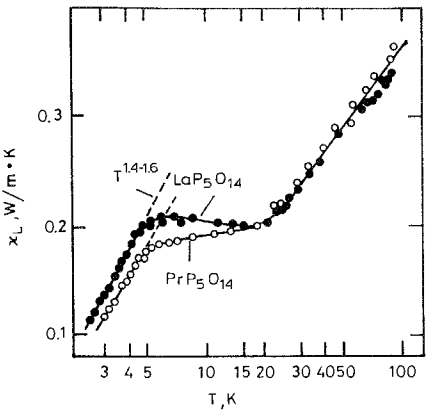

Fig. 79. The temperature dependence of κ_L for the glasses LaP_5O_{14} and PrP_5O_{14} (Parfen'eva et al. 1990b).

A Schottky contribution to the heat capacity of PrP_5O_{14} has also been observed (fig. 80).

The temperature dependence $\kappa_L(T)$ and $C(T)$ for LaP_5O_{14} show that phonon scattering by PLnIs is observed in the temperature range where their thermal properties could be explained by using a two-level model (Karpov and Parshin 1985).

6.1.6.2. *Influence of PLnIs on* κ_L. *Low temperatures* ($T \leqslant T_{max}$, $T < \Theta$).

(a) PLnIs are impurities (Vasil'ev et al. 1984a, b, Arutyunyan et al. 1987).

Analysis of the experimental data on κ_L of solid solutions of garnets $Y_{2.8}R_{0.2}Al_5O_{12}$ (R = Gd, Dy, Er, Tm, Lu) has been carried out using the Callaway

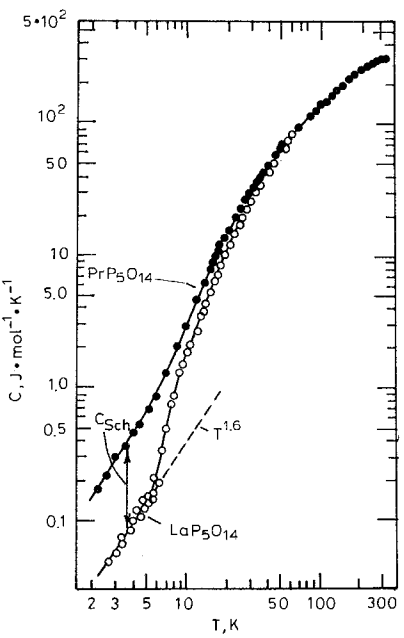

Fig. 80. The temperature dependence of the heat capacity of the glasses LaP_5O_{14} and PrP_5O_{14} (Parfen'eva et al. 1990b).

model (Callaway 1959) in the temperature range 2–100 K (Vasil'ev et al. 1984a, b). For nonmagnetic solid solutions with R = Gd, Lu scattering of phonons by boundaries, point defects, phonons (N and U processes) are taken into account. The results of the calculations are shown in fig. 81 (solid lines come from theory, points show experimental data). It is noted that all three curves for garnets with Gd and Lu impurities are calculated by the variation of only one parameter of the phonon–defect scattering, taking into account the concentration and the mass of the substituted atoms. The other parameters for the curves 1–3 in fig. 81 are identical. Similar calculations have been carried out for $Y_{1-x}R_xAl_5O_{12}$ ($x = 0.2$) with impurities PLnIs R = Er, Dy, Tm (Vasil'ev et al. 1984a, b). The scattering of phonons by paramagnetic ions has been accounted for in these cases together with a consideration of the above scattering mechanisms. The results for $Y_{2.8}Dy_{0.2}Al_5O_{12}$ are shown in fig. 82. An analogous analysis of the experimental data for magnetic garnets and garnets with paramagnetic ions has been carried out by Neelmani and Verma (1972) and Arutyunyan et al. (1986, 1987).

Figure 83 shows the results of a comparison of the values of $-\Delta\kappa_{res}$ for $Y_{2.8}Dy_{0.2}Al_5O_{12}$ obtained by calculations (for $T < 100$ K) and from experimental data (for $T > 100$ K). Curve 1 in fig. 83 presents the differences between the experimental values κ_L (points in fig. 82) and values calculated as described above without taking into account the phonon scattering by paramagnetic ions (curve 1 in fig. 82). Curve 2 in fig. 83 presents the experimental data shown in fig. 68 (points 1). As one can see, the coincidence of the two ($-\Delta\kappa_{res}$) curves is good in actual magnitude and also for the temperature dependences in the low- and high-temperature ranges.

(b) A high concentration of PLnIs (ordered arrangement of PLnIs in a lattice) (Smirnov et al. 1988, 1989, Vasil'ev et al. 1978).

Figure 84 shows data on κ_L of LaS and PrS and $-\Delta\kappa_{res} = \kappa_L(PrS) - \kappa_L(LaS)$. LaS and PrS are metals. For them $\kappa_{tot} = \kappa_L + \kappa_e$, where κ_L is calculated from the Wiedemann–Franz law, and the Lorentz number is determined by eq. (4) (Oskotski and Smirnov 1972, Smirnov and Tamarchenko 1977, Wilson 1965). The influence of

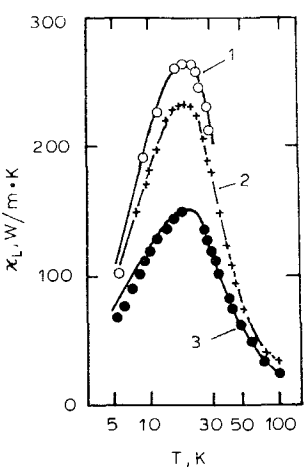

Fig. 81. The temperature dependence of κ_L for the solid alloys $Y_{3-x}R_xAl_5O_{12}$. R = Gd, $x = 0.2$ (1), R = Lu, $x = 0.1$ (2), $x = 0.2$ (3). Solid lines are calculated using the Callaway model, the points are experimental data (Vasil'ev et al. 1984a, b).

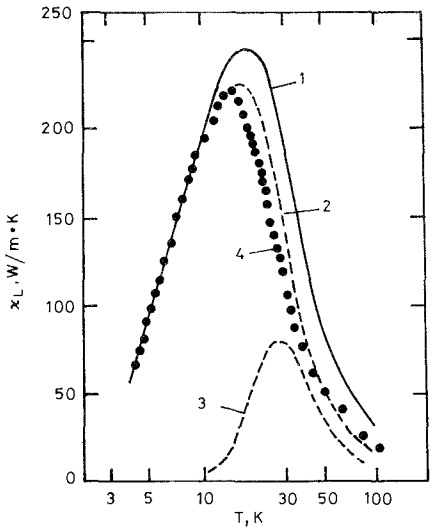

Fig. 82. The temperature dependence of κ_L for $Y_{2.8}Dy_{0.2}Al_5O_{12}$ (Vasil'ev et al. 1984a, b). Curve 1: a calculation without resonance, 2: a calculation with resonance, 3: $-\Delta\kappa_{res}$ as difference between 1 and 2, 4: experimental points.

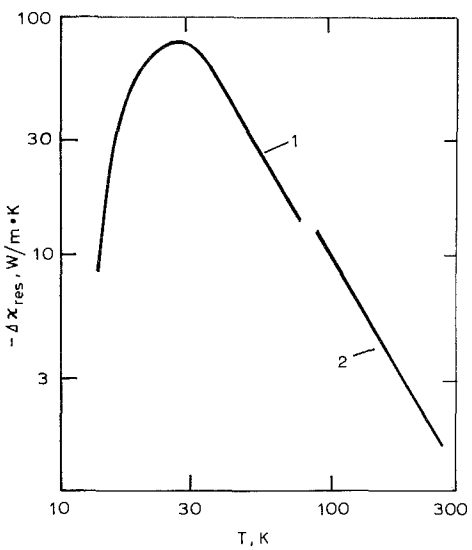

Fig. 83. The temperature dependence of $-\Delta\kappa_{res}$ for $Y_{2.8}Dy_{0.2}Al_5O_{12}$. Curve 1 is the low-temperature part, $-\Delta\kappa_{res} = \kappa_L$ (the experimental curve 4 from fig. 82) $-\kappa_L$ (the calculated curve 1 of fig. 82), curve 2 is the high-temperature part ($T > 100$ K), $-\Delta\kappa_{res}$ – the experimental data from fig. 68.

the crystal field effect on κ_e has not been taken into account in the separation of the lattice thermal conductivity from κ_{tot} of PrS and Pr_3Te_4 (see section 6.2). Evaluations have shown that taking this effect into account hardly changes the value of $-\Delta\kappa_{res}$ and does not affect the main conclusions. A theoretical analysis of κ_L of PrS in the Callaway model, with resonant phonon scattering by paramagnetic Pr^{3+} taken into account, was carried out by Vasil'ev et al. (1978) (fig. 85). The solid line in fig. 85 is from experiment, and the dotted line a calculation using the equations of Oskotski et al. (1972), Luguev et al. (1975b) and Vasil'ev et al. (1978). The theoretical and experimental curves are matched at the point T_{max}. One can see that the experimental

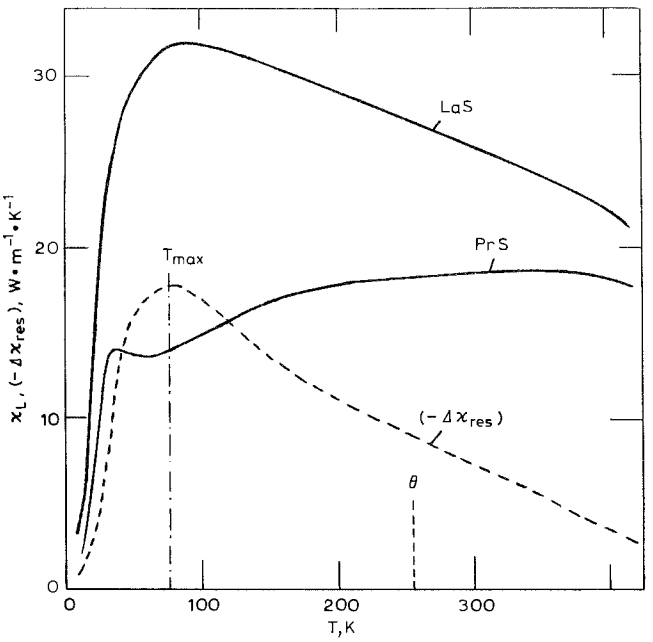

Fig. 84. The temperature dependence of κ_L for LaS, PrS and $-\Delta\kappa_{res}$ (Vasil'ev et al. 1978).

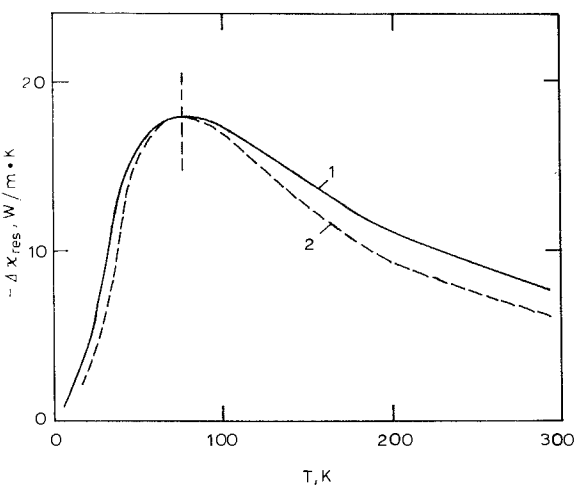

Fig. 85. The temperature dependence of $-\Delta\kappa_{res}$ for PrS (Vasil'ev et al. 1978). Curve 1 experiment, 2 theoretical calculation.

and theoretical temperature dependences of $-\Delta\kappa_{res}$ agree well at $T < T_{max}$ and $T > T_{max}$.

On the basis of the analysis of the experimental data on $\kappa_L(T)$ and $-\Delta\kappa_{res}(T)$ of a large group of lanthanide materials one may conclude that theory and experiment agree sufficiently well at both low ($T < T_{max}$, $T \leqslant \Theta$) and high ($T > T_{max}$, $T > \Theta$) temperatures.

6.1.6.3. *Is the effect of resonant phonon scattering by paramagnetic impurities on κ_L an analogue of the Schottky effect in the heat capacity?* Let us compare the temperature dependences of C_{Sch} and $-\Delta\kappa_{res}$ in crystals (PrS) and glasses ($Pr_2S_3(Ga_2O_3)_2$).

(a) Crystals. Figure 86 shows values of C of PrS and LaS and $C_{Sch} = C(PrS) - C(LaS)$ (Vasil'ev et al. 1983). The experimental data $C_{Sch}(T)$ agree with the theoretical results using the level splitting of the ground state of Pr^{3+} in PrS obtained in neutron studies (fig. 87) (Turberfield et al. 1971). It follows from fig. 87 that:

(1) The shapes of temperature dependences of C_{Sch} and $-\Delta\kappa_{res}$ for high and low temperatures are similar.
(2) The temperatures of the maxima of C_{Sch} and $-\Delta\kappa_{res}$ coincide.
(3) The effect of $-\Delta\kappa_{res}$ and the Schottky-effect differ in sign: κ_L decreases, whereas C increases (fig. 88).

So, one can draw the conclusion that the effect of resonant phonon scattering by

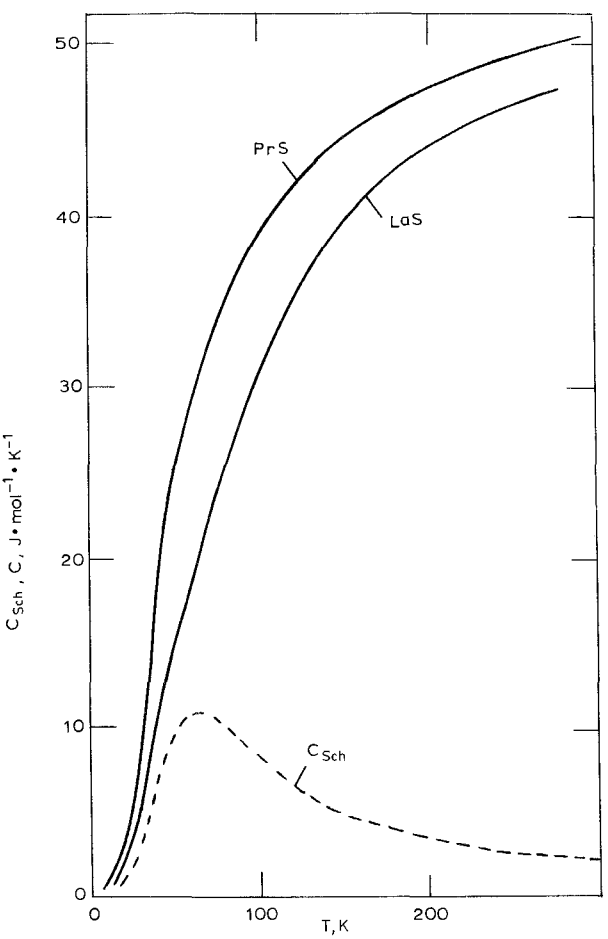

Fig. 86. The temperature dependence of the heat capacity of PrS and LaS, and the Schottky contribution C_{Sch} (Vasil'ev et al. 1983).

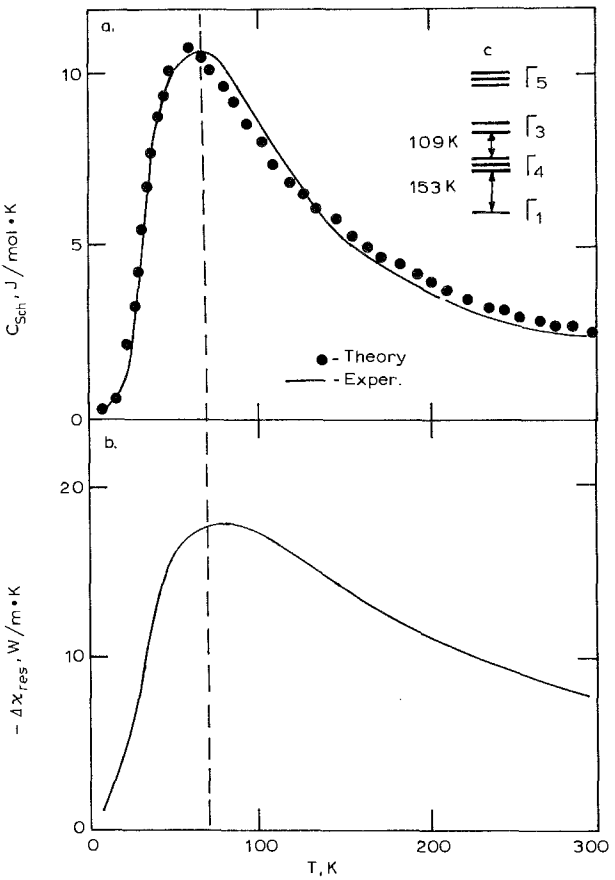

Fig. 87. The temperature dependence (a) of C_{Sch} (Vasil'ev et al. 1983) and (b) of $-\Delta\kappa_{res}$ (Smirnov et al. 1988, 1989) for PrS. (c) Crystal field levels of Pr^{3+} in PrS obtained from neutron data (Turberfield et al. 1971).

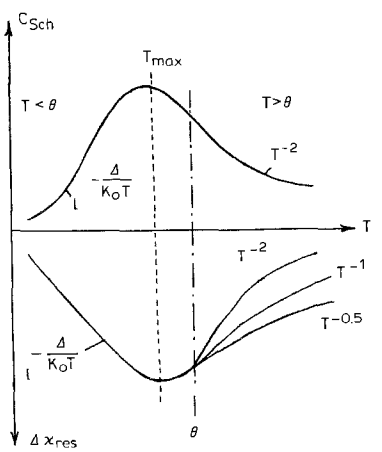

Fig. 88. A schematic representation of the temperature dependences of C_{Sch} and $-\Delta\kappa_{res}$ for a two-level system.

levels of the paramagnetic ions split in a crystal field is an analogue of the Schottky effect in the heat capacity.

(b) Glasses. The above-stated conclusion is also confirmed by measurements of C_{Sch} and $-\Delta\kappa_{res}$ in the glass $Pr_2S_3(Ga_2O_3)_2$. However, in glasses there are some peculiarities (Smirnov et al. 1992a). The maximum temperatures of C_{Sch} and $-\Delta\kappa_{res}$ do not coincide (fig. 89) and the value $\Delta T = T_{max}(C_{Sch}) - T_{max}(-\Delta\kappa_{res})$ increases with increasing broadening of the split levels, γ_0 (fig. 90). When $\gamma_0 = 0$ (no broadening, crystal case) $\Delta T \to 0$. In the $Pr_2S_3(Ga_2S_3)_2$ glass where $\Delta T \simeq 10$ K, this corresponds to $\gamma_0 \simeq 0.5$.

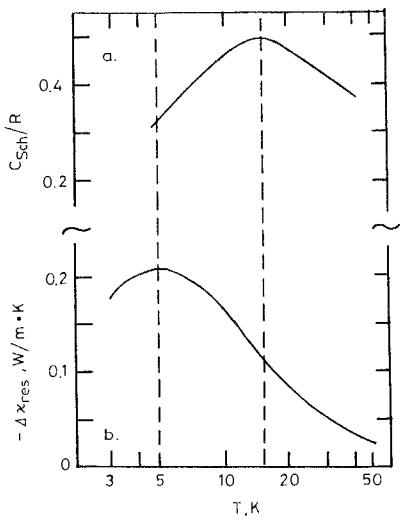

Fig. 89. The temperature dependence (a) of C_{Sch} and (b) of $-\Delta\kappa_{res}$ for the glass $Pr_2S_3(Ga_2O_3)_2$ (Smirnov et al. 1992a).

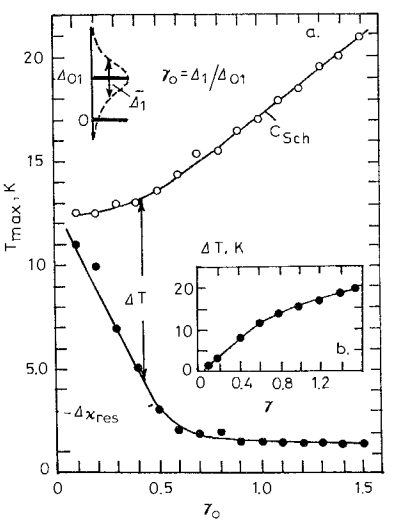

Fig. 90. (a) The theoretical dependence of the position of the maximum of C_{Sch} and $-\Delta\kappa_{res}$ in the glass $Pr_2S_3(Ga_2O_3)_2$ on the broadening of the lowest split levels, γ (Smirnov et al. 1992a). (b) The dependence of ΔT on γ.

6.1.6.4. *Connection of T_{max} in $-\Delta\kappa_{res}(T)$ with Δ_1, the separation of the first excited level from the ground state.* Figure 91 shows data on $T_{max} = f(T)$ for a number of materials with PLnIs. It turns out that $T_{max} \simeq \frac{2}{3}\Delta_1/k$. So, it is possible to exclude from the heat transfer (thermal conductivity) of a solid that or another phonon group (cf. fig. 61), and to construct a material with certain thermal properties by selection of PLnIs.

6.1.6.5. *Influence of lattice defects on the $-\Delta\kappa_{res}$ value.*

(a) *Defects in solids.* Let us consider as a model defect system Pr_2Te_3–Pr_3Te_4 (and as a reference system La_2Te_3–La_3Te_4). In these systems:

(1) A continuous transition takes place from a defect free lattice Ln_3Te_4 to a defect one [the defects (vacancies) are in the cation subsystem]. In Ln_2Te_3 the vacancy concentration reaches $\sim 10^{21}$ cm^{-3} (Golubkov et al. 1973).

(2) The same type of crystal structure (Th_3P_4) is kept through the entire system: the lattice constant changes insignificantly (from 9.485 Å in Pr_3Te_4 to 9.482 Å in Pr_2Te_3) (Golubkov et al. 1973).

(3) The energy of the crystal field levels of the ground state of Pr^{3+} ions varies insignificantly through the system (cf. fig. 64) (Mitarov et al. 1975).

Let us consider in more detail the experimental data on $-\Delta\kappa_{res}$ of the system Pr_2Te_3–Pr_3Te_4 obtained for $T > T_{max}$, $T > \Theta$ (these have been partly discussed earlier). Let us analyse data on κ_L of this system at 100 K (Luguev et al. 1975b, 1978, Oskotski et al. 1982, Smirnov et al. 1988, 1989, Vasil'ev et al. 1976). A summary of the data is shown schematically in fig. 92 (Smirnov et al. 1988, 1989). It turns out that $-\Delta\kappa_{res}$ of the heavily defect lattice Pr_2Te_3 significantly exceeds $-\Delta\kappa_{res}$ of the defect-free lattice Pr_3Te_4 (fig. 92). The $-\Delta\kappa_{res}$ value increases continuously with an increase of the number of defects in the lattice. This effect can be explained with the help of the diagrams in figs. 92b, c, which are analogous to fig. 61.

In Pr_3Te_4 (figs. 92b, b') all Pr ions (let us designate them Pr2) have the same environment. Phonons with an energy Δ_1 do not take part in the heat transport (fig. 92b'). The ions Pr1 and Pr2 are nonequivalent in Pr_2Te_3 (fig. 92c, c'), since Pr1 in contrast to Pr2 has a vacancy as a neighbour (cf. scheme of the crystal lattice in

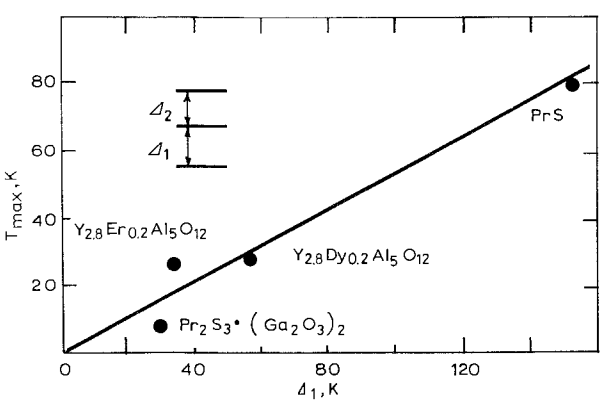

Fig. 91. Dependence of T_{max} on Δ_1 (energy of the first crystal field level) for a number of investigated materials (Smirnov et al. 1988, 1989).

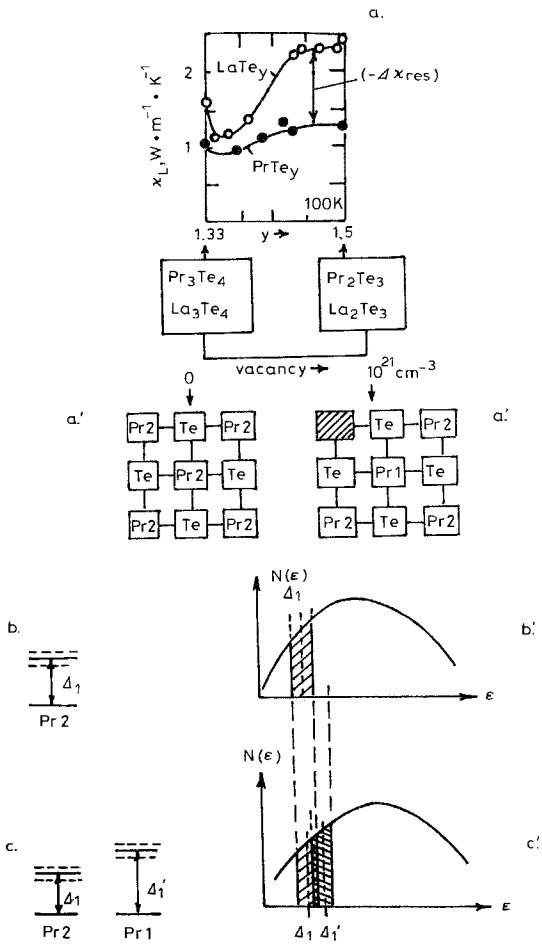

Fig. 92. A schematic presentation of the influence of crystal lattice defects on $-\Delta\kappa_{res}$ in the system Pr_2Te_3–Pr_3Te_4. Details are explained in the text.

fig. 92a'). They are in different crystal fields and as a result there are two types of levels, Δ_1 and Δ_1' (fig. 92c). This leads to "spreading" of the resonance band and to more phonons not taking part in heat transport (fig. 92c').

(b) *Glasses.* As has been noted above, in glasses, where there is short-range order, but no long-range order, a more significant decrease of κ_L due to resonance phonon scattering by PLnIs than in Pr_2Te_3–Pr_3Te_4 is observed. Short-range order in glasses will split the levels of Pr (Smirnov et al. 1990). Due to the absence of long-range order in glasses the first excited level, in contrast to crystals, is separated from the ground state by a value which varies from ion to ion according to the Gauss law (Bhattacharjee and Coqblin 1982)

$$p(\Delta) = \frac{1}{\pi^{1/2} A} \exp\left[-\frac{(\Delta - \Delta_{01})^2}{2A^2} \right], \tag{45}$$

where Δ_{01} is the average position of the excited level and A the halfwidth of the

distribution function (fig. 93). The large effect of resonant phonon scattering by PLnIs in glasses can be explained qualitatively using the scheme of levels shown in figs. 94a, b (as has been done for the system Pr_2Te_3–Pr_3Te_4). A strong spreading of the first excited level is a consequence of a system of close lying levels (Δ_1, Δ_1', Δ_1'' and so on) of different Pr ions with different environments (fig. 94a). This can lead to a broader resonance band than in the Pr_2Te_3–Pr_3Te_4 system, and as a result more phonons not taking part in heat transport (see fig. 94b).

6.1.6.6. *Phonon scattering by paramagnetic levels split by a magnetic field.* As noted at the beginning of this section, an additional splitting of levels can occur in a magnetic field (the so-called Zeeman splitting). This allows one to vary the resonant phonon energy and this leads to a contribution of certain phonon groups to the thermal conductivity with the help of a magnetic field. The results on the influence of a magnetic field at low temperatures on κ_L of materials with PLnIs are now classical and have been described in reviews and books (Oskotski and Smirnov 1972, Berman 1976). This effect was observed for the first time in holmium ethylsulphate,

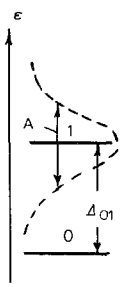

Fig. 93. Positions of the first excited level in a glass (dashed line).

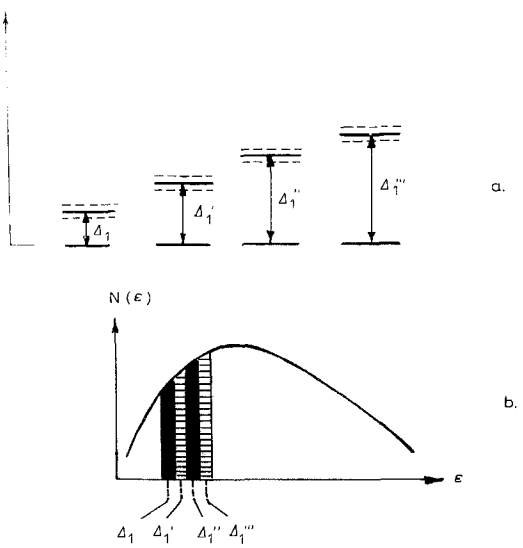

Fig. 94. Scheme illustrating the influence of phonon scattering by PLnIs in a glass.

$Ho(C_2H_5SO_4)\cdot 9H_2O$ (Morton and Rosenberg 1962, McClintok et al. 1967), and then in cerium ethylsulphate (McClintok and Rosenberg 1968). To date $\kappa_L(H)$ has been measured in a large number of materials with paramagnetic ions.

Let us consider briefly the results on $\kappa_L(H)$ in holmium ethylsulphate (Morton and Rosenberg 1962, McClintok et al. 1967). Holmium ethylsulphate is an insulator with hexagonal symmetry; according to spectroscopic data the lowest energy level is a doublet. A singlet lies higher by 8.6 K. The g-factor is large ($g = 15.4$ for ground doublet splitting by a magnetic field along the hexagonal axis). This allows a large splitting in moderate magnetic fields. The magnetic field splits the ground doublet as shown in fig. 95. Phonons can cause transitions, A, between the split doublet levels, and, B_1 and B_2, between the doublet and singlet levels. At $H = 0$ a transition D_0 is possible. The energy of resonant phonons for transition A is $\hbar\omega = g\mu_B H$, for transitions B_1 and B_2 this energy is $\hbar\omega = D_0 \pm \frac{1}{2}g\mu_B H$. Bands with finite widths appear in the phonon spectrum at frequencies corresponding to the transitions A, B_1 and B_2, giving decreased contributions to the thermal conductivity due to resonant scattering (figs. 95c, d, e), i.e. the situation is analogous to that discussed above. Figure 95a shows the dependence of the thermal conductivity of holmium ethylsul-

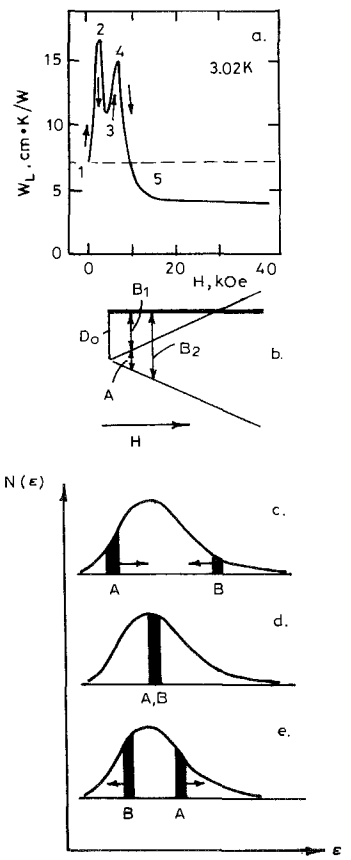

Fig. 95. Properties of holmium ethylsulphate. (a) The magnetic field dependence of the thermal resistivity. (b) Dependence of the energy levels on magnetic field. (c, d, e) Schemes of contributions of different parts of the phonon spectrum to κ_L (maxima of curves are near $\hbar\omega \approx k_0 T$).

phate on a magnetic field H. At low temperatures ($T < 8.6$ K, when $k_0 T \simeq \frac{1}{2} D_0$) in weak H there are two clear peaks in the dependence $W_L(H)$. Let us try to explain this effect qualitatively using the scheme in figs. 95c, d, e. First we divide the curve $W_L(H)$ (fig. 95a) into four parts: 1–2, 2–3, 3–4, and 4–5. For weak magnetic fields the band A lies in the range of small frequencies, the bands B_1 and B_2 lie on the right side of the phonon distribution function, $N(\varepsilon)$ (fig. 95c). This corresponds to a position of $W_L(H)$ near point 1 in fig. 95a. With increasing H the band A shifts to the right and the band B_1 shifts to the left (fig. 95c). This leads to an increase in the number of phonons with a small contribution to κ_L. At the same time the band B_2 shifts to the right and its contribution to κ_L is insignificant. So, κ_L decreases (W_L increases). This decrease continues until the moment when bands A and B_1 coincide (fig. 95d). This process corresponds to the part 1–2 of the $W_L(H)$ dependence (fig. 95a). If the intensities of resonant scattering of phonons in the bands A and B_1 are high, their superposition (fig. 95d) leads to a decrease in the sum of the intensities of scattering and $W_L(H)$ decreases (part 2–3 in fig. 95a). With a further increase in H, the bands A and B_1 are separating from each other (fig. 95e). This leads at first to a sharp increase of $W_L(H)$ (part 3–4 in fig. 95a) and then to a smooth decrease of $W_L(H)$ (part 4–5 in fig. 95a). At greater values of H the resonant bands shift to a frequency range where there are small number of phonons, so $W_L(H)$ ceases to depend on H. At the same time the transitions between levels which have occurred without a magnetic field, disappear and $W_L(H)$ at high H is less than at $H = 0$.

6.2. *Influence of the crystal field effect on the electron part of the thermal conductivity*

Up to now we have discussed the influence of the crystal field effect on κ_L (due to phonon resonance scattering by the rare earth ions) and the heat capacity (Schottky effect). It is known that the crystal field can significantly influence the behaviour of the elastic constants (Lüthi et al. 1973), the thermal expansion coefficient (Ott and Lüthi 1976), the magnetostriction and thermoemf (Sierro et al. 1975), the electrical conductivity (Lüthi et al. 1973, Friederich and Fert 1974, Andersen et al. 1974) and the electron part of the thermal conductivity κ_e (Smirnov and Tamarchenko 1977, Wong 1978, Matz et al. 1982, Müller et al. 1982).

Let us consider very briefly the influence of a crystal field on κ_e. (In a somewhat different way this phenomenon has been considered in section 3.1 when discussing spin–phonon scattering and its influence on κ_e in the paramagnetic region.) A theory of this effect has been elaborated on by Wong (1978), Fulde and Peschel (1972), Bhattacharjee and Coqblin (1988) and was experimentally verified with RSb (R = La, Er, Tm) by Wong (1978), with $PrCu_5$ by Wong (1978) and Matz et al. (1982), with $PrPt_5$ by Wong (1978), with $LaAl_3$ and $PrAl_3$ by Müller et al. (1982) and with (La, Pr)Sn by Sütsch and Umlauf (1981). It has been supposed by Wong (1978), Matz et al. (1982) and Müller et al. (1982) that at low temperatures in the investigated alloys $\kappa_L \ll \kappa_e$ and therefore $\kappa_{tot} = \kappa_e$. (The question whether such a supposition and method of separation of κ_L and κ_e is right, has been discussed in section 3.1.) For these temperatures

$$W_e = 1/\kappa_e = W_0 + W_i = A/T + BT^2 \quad \text{or} \quad \kappa_e/T = (A + BT^3)^{-1} \tag{46}$$

(Smirnov and Tamarchenko 1977). Here $A = \rho_0/L$, ρ_0 is the residual electrical resistance and W_i the ideal thermoresistance due to electron scattering by lattice vibrations.

Figure 96 shows, as an example, the experimental data for $PrPt_5$ with the effect of the crystal lattice field, and as a reference material $LaPt_5$ without such effect (it turns out that for $LaPt_5$ the second term in eq. (46) is insignificant). Values κ_e for $PrPt_5$, calculated with the theoretical formulae of Wong (1978) taking into account the crystal lattice field effect by using the experimental data of the energy level splittings shown in fig. 96b, are presented as well. κ_e decreases appreciably due to the crystal field effect. A good agreement of experiment and theory is noted.

Figure 97 shows data on $L_{cf}/L_0 = f(T)$ in $PrAl_3$. L_{cf} is the so-called Lorentz number of the crystal field effect. It is determined by the equation

$$L_{cf} = \rho_{cf}/W_{cf}\,T, \tag{47}$$

where ρ_{cf} and W_{cf} are the "magnetic" parts of the electrical and thermal electronic resistance which depend upon the crystal field effect. ρ_{cf} and W_{cf} are determined as differences of ρ and W_e in $PrAl_3$ and $LaAl_3$:

$$\rho_{cf} = \rho(PrAl_3) - \rho(LaAl_3), \tag{48}$$

$$W_{cf} = W_e(PrAl_3) - W_e(LaAl_3). \tag{49}$$

At low temperatures $L_{cf} < L_0$, which points out the inelastic character of the current carrier scattering at Γ_1–Γ_6 transfer. With increasing temperature the doublet Γ_6 becomes occupied (fig. 97b) and this, probably, results in the elastic character of the scattering at higher temperatures. The fact that L_{cf} exceeds L_0 for $T > 20$ K could be due to the neglect of the κ_L contribution to the thermal conductivity.

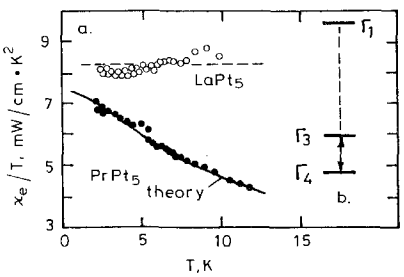

Fig. 96. (a) The temperature dependence of κ_L/T for $LaPt_5$ and $PrPt_5$. Solid line is a theoretical calculation of κ_e for $PrPt_5$ taking into account the crystal lattice field. (b) The energy level splitting in $PrPt_5$ (Wong 1978).

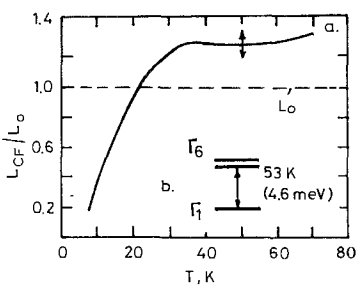

Fig. 97. (a) The temperature dependence of the ratio L_{cf}/L_0 for $PrAl_3$. (b) The energy level splitting in $PrAl_3$ (Müller et al. 1982).

7. Thermal conductivity of lanthanide compounds with structural phase transitions initiated by the cooperative Jahn–Teller effect (CJTE)

According to the Jahn–Teller theorem (Jahn and Teller 1937) any structure (besides linear) with an electron ground state degenerate in the orbital quantum number is unstable and tends to reduce the symmetry, to split the ground state and to remove the degeneracy. The Jahn–Teller effect manifests itself as a phase transition of first or second order at a transition temperature T_{JT} (we are using T_{JT} instead of the usual T_c, since we are using T_c for the superconduction transition temperature). The Jahn–Teller effect has been observed experimentally in solids on defects and as cooperative effect on basic atoms. The CJTE is investigated using different methods: resonance, electronic, optical, acoustic, magnetic, thermal (Sturge 1967, Gehring and Gehring 1975). It manifests itself distinctly in the temperature dependence of the thermal conductivity. The most convenient materials for investigation of the CJTE are compounds with lanthanide elements. In lanthanide paramagnetic ions, because of the strong localization of f-shell inside the ion and its weak interaction with the crystal lattice (see section 6), the Jahn–Teller splitting of levels ($2W$ in fig. 98a) turns out to be small and T_{JT} equals a few degrees [in the case of d-elements this interaction is much stronger, and T_{JT} can be of the order of 1000 K; in $MgMn_2O_3$, e.g., $T_{JT} \simeq 1000$ K (Sturge 1967, Gehring and Gehring 1975)]. At these temperatures many scattering mechanisms are insignificant, which considerably simplifies the investigation of the influence of a CJTE.

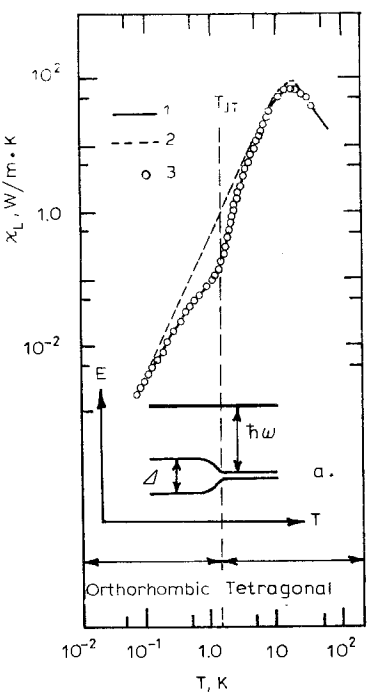

Fig. 98. (a) Energy levels in the tetragonal and orthorhombic phase of $TmVO_4$. (b) The temperature dependence of κ_L for single crystals of $TmVO_4$ (Daudin and Salce, 1982). Curve 1 gives the calculation according to Callaway (1959) taking into account the various scatterings: (I) phonons by phonons (U and N processes), crystal boundaries, point defects, dislocations and (II) resonance scattering by split levels of the ground state and first excited level. Curve 2 gives the calculation according to Callaway (1959) taking into account scattering I but not scattering II. Curve 3 gives the experimental values of κ_L from Daudin and Salce (1982).

The CJTE is observed in a great number of lanthanide compounds: zircons RXO_4 (R = Tm, Tb, Dy; X = V, P, As), intermetallic compounds (TmGd, TmZn, CeAg and others), compounds with lanthanide impurities (LaSb : Dy) DySb, $PrAlO_3$ and others (Sturge 1967, Gehring and Gehring 1975, Ray et al. 1981, Bloch and Davidov 1982, Harley et al. 1973). Experimentally the influence of the CJTE on κ_L has been investigated, mainly, in the insulators RXO_4. The structural transition from tetragonal to orthorhombic symmetry occurs in these crystals at decreasing temperature to T_{JT} (to a few Kelvins) and the two-fold degenerate ground state splits in two (see fig. 98a). The first measurements of $\kappa(T)$ in $TmVO_4$ and $DyVO_4$ have been carried out by Parsons and Rosenberg (1972). Then $\kappa(T)$ of these crystals and also of $TbVO_4$, $HoPO_4$ and $TmAsO_4$ has been measured by Parsons (1976), Daudin et al. (1980, 1981a, b, 1984) and Daudin and Salce (1982). These authors and Parsons and Rosenberg (1972) have discussed the influence of a magnetic field on the thermal conductivity of these crystals. Published data on $\kappa(T, H)$ have been analysed theoretically by Daudin et al. (1984) and Mutscheller and Wagner (1984a, b, 1986, 1987).

The classical subject of CJTE studies is $TmVO_4$. It has no additional phase transitions besides the CJTE ($T_{JT} = 2.15$ K). Figure 98b shows experimental data on κ (T) in $TmVO_4$ (Daudin and Salce 1982). Since $TmVO_4$ is an insulator, the experimentally measured κ_{tot} equals κ_L. Figure 98a shows the energy levels of $TmVO_4$ in the high-temperature (tetragonal symmetry) and in the low-temperature (orthorhombic symmetry) phase (Cooke et al. 1972). At $T < T_{JT}$ the doubly degenerate ground state splits into two levels with $2W \simeq 3$ K (Cooke et al. 1972). The distance to the next excited level is practically the same in both phases and equals ~ 50 K (Knoll 1971). At $T = T_{JT}$ a sharp change in the value and of the temperature dependence of κ_L of $TmVO_4$ is observed (fig. 98b). Near T_{JT} (for $T < T_{JT}$) $\kappa_L \propto T^{5.5 \pm 0.5}$ (fig. 99). Figure 98a (Daudin and Salce 1982) shows the results of a theoretical analysis of $\kappa_L(T)$ for $TmVO_4$ using the Callaway model (Callaway 1959) taking two groups of phonon scatterers into account: the first one is the scattering of phonons by phonons (U and N processes), crystal boundaries, point defects and dislocations; and the second one the resonance phonon scattering by the split levels of the ground state and by the first excited level. There is a direct analogy with the case of phonon scattering by the paramagnetic levels of lanthanide ions split by the lattice crystal field (see section 6).

Comparing experimental data and theoretical curves of κ_L one can draw the following conclusions:

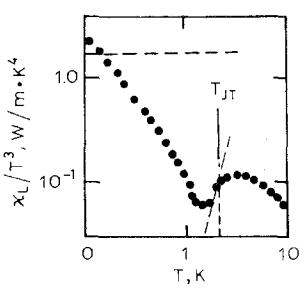

Fig. 99. The temperature dependence of κ_L/T^3 for a single crystal of $TmVO_4$ (Daudin and Salce 1982). Dashed lines show calculated values of κ_L for boundary scattering (the so-called Casimir limit).

(1) At $T \sim T_{JT}$ strong scattering of phonons by the split ground state occurs. With decreasing temperature this scattering at first increases in the narrow temperature region corresponding in fig. 98a to the region of the transition from the unsplit doublet to the one split by $2W$, and then vanishes due to "freezing" of the resonance phonons (see fig. 99, $T < T_{JT}$). Consequently, the main scatterer of phonons is not the sample grain boundaries, but the boundaries of the Jahn–Teller domains. The Jahn–Teller domains are the regions in which the equivalent orthorhombic axes are directed along different second-order axes in the basal plane of the tetragonal crystal cell. In $TmVO_4$ the orthorhombic axes a' and b' are rotated by 45° relative to the axes a and b of the nondistorted lattice (Kazey and Sokolov 1986). The sample grain boundaries begin to scatter phonons only at $T \sim 100$ mK (see figs. 99 and 100).

(2) At $T > T_{JT}$ (approximately to 6 K, i.e. $\sim 3T_{JT}$) κ_L continues to experience the influence of phonon resonance scattering on the above mentioned level system (see fig. 98b).

A similar effect has been observed in the measurement of the linear expansion coefficient δ in $TmVO_4$ (Kazey and Sokolov 1986). The contribution to the value of δ from the CJTE does not vanish at $T \simeq T_{JT}$, but continues up to $T \sim 3T_{JT}$. Kazey and Sokolov (1986) have connected such a behaviour of $\delta(T)$ with the presence of significant distortions in the tetragonal crystal lattice of $TmVO_4$ at $T > T_{JT}$.

Other explanations of the observed decrease of κ_L in $TmVO_4$ in the region $T > T_{JT}$ have been proposed – the influence of a soft mode, pseudospin thermal conductivity and so on (Daudin and Salce 1982).

A strong increase of κ_L has been observed on applying a magnetic field H along the c-axis of a crystal of $TmVO_4$ ($H \parallel c$) over a wide temperature region $T < T_{JT}$ to $T > T_{JT}$ (figs. 100, 101) (Daudin and Salce 1982, Daudin et al. 1984). κ_L increases

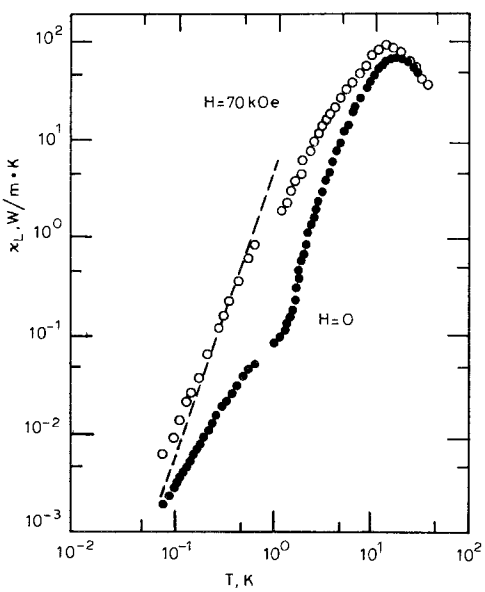

Fig. 100. The temperature dependence of κ_L for a single crystal of $TmVO_4$ at $H = 0$ and 70 kOe, $H \parallel c$ (Daudin et al. 1984). The dashed line gives the calculated κ_L due to grain boundary scattering.

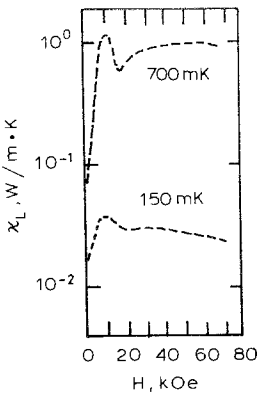

Fig. 101. The magnetic-field dependence of κ_L for a single crystal of $TmVO_4$ (Daudin et al. 1984). Data are given for the temperatures 150 and 700 mK.

with H up to 20–30 kOe, and then becomes saturated (fig. 101). The magnetic field strongly influences the structural phase transitions induced by the CJTE (Gehring and Gehring 1975, Cooke et al. 1972, Kazey and Sokolov 1986, Vekhter et al. 1987, Melcher et al. 1973). Three cases can be realized (Vekhter et al. 1987):

(1) Full suppression of the transition. The external field splits or mixes the electron states in such a way that the local Jahn–Teller distortions are reduced, T_{JT} decreases (sometimes it reaches zero).

(2) The external field increases local distortions, and causes a homogeneous distortion and makes the phase transition indistinct.

(3) The phase transition in the external field remains, but the temperature interval of the ordered phase increases.

The effects observed in $TmVO_4$ can be explained, more probably, on the basis of the first supposition.

In addition, a reorientation of the Jahn–Teller domains occurs in the magnetic field, and at some critical mean field H_{cr} the sample reaches a single domain state (Cooke et al. 1972, Kazey and Sokolov 1986, Melcher et al. 1973). H_{cr} in $TmVO_4$ is, apparently, equal to $\sim$70 kOe, because at this mean field the following condition is fulfilled: phonons are scattered on the sample grain boundaries but not on the boundaries which separate the domains (fig. 100, dashed line).

It is necessary to note that, as the conclusion of this section, all the above-mentioned peculiarities of $\kappa_L(T)$ behaviour found in $TmVO_4$ are observed as well in other investigated compounds of the family of rare earth zircons.

8. Thermal conductivity of rare earth superconductors

8.1. *Main principles*

Let us consider qualitatively some conclusions of the theory of thermal conductivity of standard superconductors which may be useful in analysing κ data of rare earth

superconductors. This theory has been developed by Geilikman (1958), Geilikman and Kresin (1958, 1959, 1972) and Bardeen et al. (1959).

The most important properties of superconducting electrons are that they do not transport energy and do not interact with phonons. At $T < T_c$ the number of heat transporting electrons decreases by an exponent determined by the energy gap $\Delta(T)$ at the Fermi surface and the electron thermal conductivity

$$\kappa_e^s \sim \exp[-\Delta(T)/T]. \tag{50}$$

The relative contributions to the total thermal conductivity, κ_{tot}^s, from κ_e^s and κ_L^s in the superconductivity region and their temperature dependences are determined, mainly, by $\Delta(T)$ and T_c (superconducting and normal states are marked, respectively, by the indices s and n).

Let us consider the case of a metal with $\kappa_L^n \ll \kappa_e^n$.

(a) The value T_c is small and electrons are mainly scattered by defects. The electron thermal conductivity in a normal state $\kappa_e^n \propto T$. In the superconducting state at $T < T_c$ the value κ_e^s decreases rapidly due to the decreasing number of normal electrons. At very low temperatures, when κ_e^s is practically negligible, κ_L^s shows up. κ_L^s is somewhat larger than κ_L^n at the same temperature due to absence of phonon–electron scattering. It is possible at very low temperature to reach the region $\kappa_L^s \propto T^3$, where boundary scattering dominates (see fig. 102).

(b) The value T_c is not so small and electrons are scattered by defects and lattice vibrations. At $T < T_c$, κ_e^s decreases at first (as in the previous case) and then can increase slightly due to a weakening of the electron–phonon scattering. At very low temperatures κ_L^s can show up on the background of the small κ_e^s (fig. 103).

In the case $\kappa_L^n \gg \kappa_e^n$ at $T < T_c$ the κ_L^s becomes greater than the κ_L^n due to a decrease of the phonon–electron scattering (fig. 104). A combination of variants of figs. 102–104 is possible.

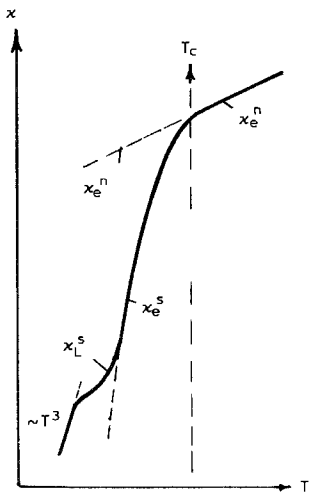

Fig. 102. Schematic shape of the temperature dependence of κ_L^s, κ_e^n and κ_e^s for a metal when electron–impurity interaction is the main electron scattering mechanism. $\kappa_L \ll \kappa_e$.

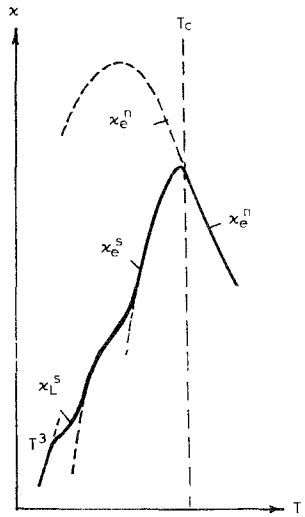

Fig. 103. Schematic shape of the temperature dependences of κ_L^s, κ_c^n and κ_c^s for a metal when electron–impurity and electron–phonon interactions are the main electron scattering mechanisms. $\kappa_L \ll \kappa_e$.

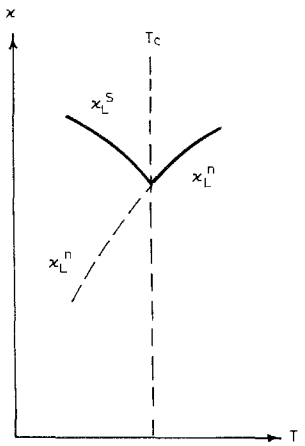

Fig. 104. Schematic shape of the temperature dependences of κ_{tot}^n and κ_{tot}^s for the case $\kappa_L \gg \kappa_e$.

An external magnetic field $H > H_{cr}$ (critical field) destroys superconductivity and transfers the superconductor to the normal state. For pure metals H_{cr} can be small.

In superconductors of the second kind at $T < T_c$ in a mixed state (in a magnetic field between H_{c1} and H_{c2}, where H_{c1} is the lower and H_{c2} the upper critical field) a new effect in the thermal conductivity is possible: phonon and electron scattering by Abrikosov vortex lines penetrating the superconductor (Red'ko and Chakalski 1987).

8.2. *Thermal conductivity of heavy-fermion systems*

Steglich et al. (1979) have observed in $CeCu_2Si_2$ a new effect in solid state physics: heavy-fermion superconductivity (HFS) with $T_c = 0.56$ K. In the following years the

HFS has also been observed in UBe_{13} ($T_c = 0.854$ K) (Ott et al. 1983) and UPt_3 ($T_c = 0.520$ K) (Stewart et al. 1984). For the sake of completeness we will consider data on the thermal conductivity of all three heavy-fermion superconductors.

HFS has a number of distinguishing features. Let us note some of them:

(1) In these systems triplet superconductivity is possible with a parallel orientation of the electron spins in a pair with total spin 1 (superconductivity in HFS-systems is connected with Cooper pairs, formed by fermions with a very large effective mass ($m^*/m_0 \sim 100$–1000, m_0 is the free-electron mass)).

(2) A non-phonon mechanism of superconductivity is possible (Gudak 1985).

(3) The heavy-fermion superconductors of the second kind (such as $CeCu_2Si_2$, UBe_{13} and UPt_3) have a ratio $H_c(0)/T_c(0)$ significantly higher than the classical superconductors. According to the theory $H_c(0)/T_c(0)$ does not depend on the type of superconductor. So, at $T_c = 1$ K the magnetic field $H_c(0)$ which destroys superconductivity (paramagnetic limit) is 16 kOe. $H_c(0)$ values in excess of the paramagnetic limit is a characteristic of HFS systems. For example, in $CeCu_2Si_2$ it is two times and in UBe_{13} it is more than six times as large.

Magnetic impurities suppress superconductivity and nonmagnetic impurities weakly influence T_c in classical superconductors. In HFS systems even nonmagnetic impurities suppress superconductivity. For example, the higher the concentration of Ce^{3+} ions in the alloy $Ce_xLa_{1-x}Cu_2Si_2$, the higher is T_c (Buzdin and Moshchalkov 1986). So, a highly unusual situation arises: a decrease of the number of magnetic centres leads to a sharp decrease of T_c.

Can one obtain from the thermal conductivity some independent information about the nature of superconductivity in HFS systems? It turns out that from the temperature dependence of κ_e^s at $T \ll T_c$ one can decide if there is triplet or singlet coupling in the HFS system. For triplet coupling a vanishing energy gap occurs only at points on the Fermi surface, whereas for singlet coupling vanishing energy gaps can form entire lines on the Fermi surface (Volovik and Gor'kov 1984, 1985, Varma 1985, Schmitt-Rink et al. 1986). This is the only way to determine the coupling type at the present time (Volovik and Gor'kov 1984, 1985). One can obtain indirectly information about the behaviour of the gap, Δ, from the temperature dependences of the heat capacity and the thermal conductivity of HFS systems (see table 6 and fig. 105) (Varma 1985).

Let us consider the experimental data on the thermal conductivity of $CeCu_2Si_2$ (Sparn et al. 1985, Steglich et al. 1985a, b, Franz et al. 1978, 1979, Schneidner et al.

TABLE 6
Influence of the superconducting-gap shape on the thermal properties of semiconductors.

Properties at $T \ll T_c$	Quasi-particle spectrum has a gap over the entire Fermi surface (fig. 105a)	Gap vanishes at points on the Fermi surface (fig. 105b)	Gap vanishes at lines on the Fermi surface (fig. 105c)
Heat capacity	$\propto \exp(-\Delta/T)$	$\propto (T/\Delta)^3$	$\propto (T/\Delta)^2$
Thermal conductivity κ_e^s	$\propto \exp(-\Delta/T)$	$\propto (T/\Delta)^3$	$\propto (T/\Delta)^2$

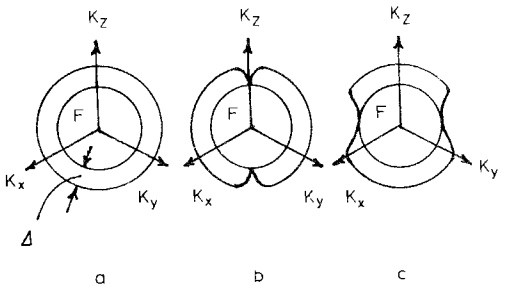

Fig. 105. Schematic shape of the superconducting gap $\Delta(k)$ in momentum space (Buzdin and Moshchalkov 1986) (a) in a standard superconductor; and in a heavy-fermion superconductor with (b) vanishing gaps at some points and (c) on lines on the Fermi surface.

1983), UBe_{13} (Sparn et al. 1985, Jaccard and Flouquet 1987, Flouquet et al. 1986, Jaccard et al. 1985a, b, Ravex et al. 1987, Alekseevski et al. 1986) and UPt_3 (De Visser et al. 1987, Floquet et al. 1986, Steglich et al. 1985a, Jaccard et al. 1985b, Sulpice et al. 1986, Franse et al. 1985). At $T \ll T_c$ all three compounds have $\kappa_L^n \ll \kappa_e^n$ and the κ_e^s dependence on T has the form

$$\kappa_e^s = \alpha T^2 + \beta T \tag{51}$$

The values of α and β are given in table 7. The temperature dependence $\kappa_e^s \propto T^2$ which is observed in all three compounds, corroborates the presence of singlet coupling (see tables 8 and 6), however, the temperature dependence of the heat capacity $C \propto T^3$ (see table 8) in $CeCu_2Si_2$ and UBe_{13} contradicts this conclusion (see table 6). Experimental data on the absorption coefficient of ultrasound in UPt_3 (Bishop et al. 1984) and on the reciprocal time of the spin relaxation in $CeCu_2Si_2$ (MacLaughlin et al. 1984) and UBe_{13} (Clark et al. 1984) confirm the conclusion about singlet coupling.

At present there is no clear understanding of the nature of the linear term in κ_e^s. In a number of works the appearance of this term is connected with the presence of impurities in the samples (or the nonsuperconducting phase), because the contribution

TABLE 7
Experimental values of the coefficients α and β in the dependence $\kappa_e^s = \beta T + \alpha T^2$ for $T < T_c$.

Compound	α (mW/K^3 cm)	Refs.*	β (mW/K^2 cm)	Refs.*
$CeCu_2Si_2$	2.8	[1]	0.7	[1][a]
	1.8	[2]		
UBe_{13}	0.38	[1]	0.03	[4][a]
	0.53	[3]		
UPt_3	19.5	[1, 5, 6]	0.55	[1, 6–8]
	20	[7, 8]		
URu_2Si_2	0.96	[9]	0.2	[9]

[a]The contribution βT for $CeCu_2Si_2$ and UBe_{13} has also been observed by Franse et al. (1984) and Jaccard and Flouquet (1987).

*References: [1] Jaccard et al. (1985a), [2] Steglich et al. (1985b), [3] Alekseevski et al. (1986), [4] Ravex et al. (1987), [5] Steglich et al. (1984), [6] Jaccard et al. (1985b), [7] Sulpice et al. (1986), [8] Schmitt-Remi et al. (1986), [9] Lopez de la Torre et al. (1988).

TABLE 8
Experimental temperature dependences of C and κ_c^s for $T < T_c$.

Property	$CeCu_2Si_2$	Refs.*	UPt_3	Refs.*	UBe_{13}	Refs.*
C	T^3	[1]	T^2	[1, 2]	T^3	[3]
κ_e^s	T^2	[4–6]	T^2	[1, 4, 7]	T^2	[4, 8–10]

*References: [1] Steglich et al. (1985a), [2] Sulpice et al. (1986), [3] Ott et al. (1984b), [4] Jaccard et al. (1985a), [5] Steglich et al. (1985b), [6] Franse et al. (1984), [7] Jaccard et al. (1985b), [8] Sparn et al. (1985), [9] Varma (1985), [10] Alekseevski et al. (1986).

of the linear term to the thermal conductivity decreases with increasing purity of the material. A linear term is also observed in the heat capacity at $T \ll T_c$ in a number of works [e.g., in UBe_{13} (Ravex et al. 1987) and UPt_3 (Sulpice et al. 1986)]. Figures 106 and 107 show, e.g., data on κ_L^s of UPt_3 (Schmitt-Rink et al. 1986, Clark et al.

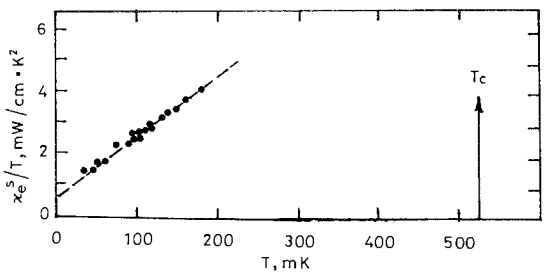

Fig. 106. The temperature dependence of κ_e^s/T for UPt_3 (Schmitt-Rink et al. 1986, Clark et al. 1984).

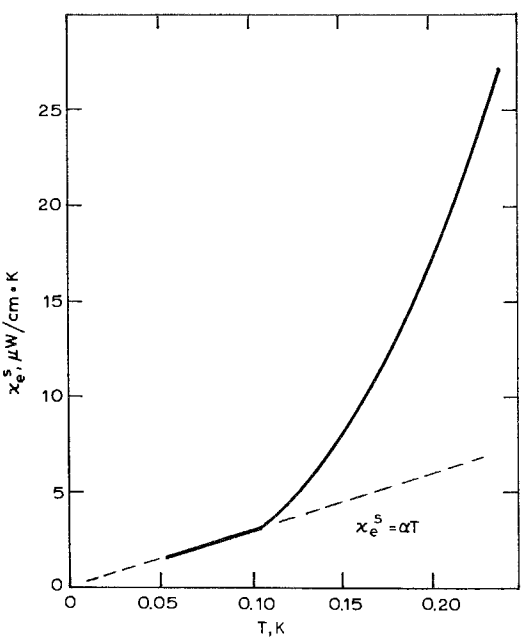

Fig. 107. The temperature dependence of κ_e^s/T for UBe_{13} (Volovik and Gor'kov 1984, 1985).

1984) and UBe_{13} (Volovik and Gor'kov 1984), which illustrate the T^2 and T dependences in the low-temperature region.

8.3. *Thermal conductivity of rare earth compounds in which superconductivity and magnetism coexist*

For a long time it was thought that superconductivity and magnetism could not coexist (Ginzburg 1957). A small amount of magnetic impurities (up to $\sim 1\%$) destroys superconductivity (Matthias et al. 1958, 1959, Suhl et al. 1959). Superconductivity is destroyed also during a phase transition from the superconducting to the magnetic state. However, at the beginning of the 1970s two classes of ternary compounds, $R_xMo_6X_8$ ($x = 1$ or 1.2, X = S, Se) and RRh_4B_4, in which magnetism and superconductivity coexist, were discovered by Hamaker et al. (1979) and Fischer et al. (1979). Several dozens of magnetic superconductors are known at the present time. In the system $R_xMo_6X_8$ (rhombohedral-hexagonal crystal structure with rhombohedral angle near 80°) all compounds with R from La to Lu (excluding Ce and Eu) are superconductors (Fischer et al. 1975, Shelton et al. 1976). Coexistence of magnetism and superconductivity is observed in $R_{1.2}Mo_6S_8$ (R = Gd, Tb, Dy, Er) (Ishikawa and Fischer 1977, Moncton et al. 1978) and $R_xMo_6Se_8$ ($x = 1$, 1.2; R = Gd, Er) (McCallum et al. 1977a, b). In the system RRh_4B_4 (tetragonal crystal structure) superconductivity is observed in compounds with R = Y, Nd, Sm, Er, Tm, Lu and superconductivity coexists with magnetism in compounds with R = Nd, Sm, Er, Tm (Matthias et al. 1977, Vandenberg and Matthias 1977).

Different electrons are responsible for magnetism and superconductivity in the case of their coexistence. Superconductivity arises because of the formation of Cooper pairs of outer shell electrons, while magnetism is connected with the magnetic moments of the inner electron shells of the lanthanide ions. As has been shown by Buzdin et al. (1984), competition between superconductivity and ferromagnetism leads to the appearance of a new type of magnetic order in the superconducting phase – a magnetic domain structure, which is an average between ferromagnetism and antiferromagnetism (Buzdin and Moshchalkov 1986).

Since then extensive investigations of the physical properties of systems with coexistence of superconductivity and magnetism have been carried out. The thermal conductivity of the RRh_4B_4 system (R = Sm, Er, Tm, Lu) (Ott et al. 1980, Hamaker et al. 1981a, b, Odoni and Ott 1979, Odoni et al. 1981) has been investigated in detail. Table 9 gives some parameters of these materials which are necessary for a discussion of the results on κ. T_{c1} and T_{c2} are, respectively, the high and the second critical superconducting temperatures. As one can see from table 9, the width of the temperature interval of coexistence of superconductivity and magnetism is small: ~ 0.5–1 K for $TmRh_4B_4$ and $SmRh_4B_4$ and ~ 0.05 K for $ErRh_4B_4$. The last interval has been fixed only by means of precise measurements of the magnetic susceptibility and the linear expansion coefficient (Ott et al. 1978, Woolf et al. 1979). Therefore one can try to search for an influence of this effect on κ only in $TmRh_4B_4$ and $SmRh_4B_4$. Nevertheless, we will consider in this section, to make the picture complete, all four compounds from table 9. $LuRh_4B_4$ can be considered a reference

TABLE 9
Data on T_{c1}, T_{c2}, T_C and T_N for some compounds RRe_4B_4.

Compound	T_{c1} (K)	Refs.*	T_{c2} (K)	Refs.*	T_C (K)	Refs.*	T_N (K)	Refs.*
$SmRh_4B_4$	2.72	[1]					0.87	[1, 2]
	2.68	[2]						
$ErRh_4B_4$	8.7	[3–5]	0.98	[3, 4]	0.93	[3, 4, 6]		
$TmRh_4B_4$	9.8	[7, 8]			0.4	[7, 8]		
$LuRh_4B_4$	11.6	[4]						

*References: [1] Hamaker et al. (1979), [2] Ott et al. (1980), [3] Ott et al. (1978), [4] Woolf et al. (1979), [5] Odoni and Ott (1979), [6] Fertig et al. (1977), [7] Hamaker et al. (1981a), [8] Hamaker et al. (1981b).

material, because it undergoes only the superconducting transition. Figure 108 shows the temperature dependence of κ_{tot} of $LuRh_4B_4$ (Odoni et al. 1981). κ_L and κ_e are separated into the normal and superconducting state contributions by calculation. At $T \sim T_c$ a sharp increase of κ_L^n (κ_L^s) occurs due to decreasing phonon scattering by the electrons, and a decrease of κ_e^n (κ_e^s) occurs. At the lowest temperatures the thermal conductivity in the superconducting state (κ^s) is only due to κ_L^s. At $T < 2.5$ K $\kappa^s = \kappa_L^s$ and is proportional to T^3, which is typical for boundary phonon scattering. $ErRh_4B_4$ is a prototype of compounds with two superconducting transition temperatures (T_{c1} and T_{c2}) – "reentrant" superconductors (see table 9 and fig. 109). Figures 110 and 111 show the $\kappa(T)$ dependences. Unlike $LuRh_4B_4$, the contribution of κ_L to κ_{tot} is small near T_c. However, at low temperatures κ_{tot} becomes equal to κ_L^s and proportional to $T^{2.8}$ (as in the case of $LuRh_4B_4$ (see figs. 110 and 111a)). At $T < 1.2$–1.4 K κ_{tot} increases with decreasing temperature and at $T \sim T_c$ (T_{c2}) it has a maximum. At $T < T_c$ (T_{c2}) the behaviour of the thermal conductivity changes radically. Now the main heat carriers are not phonons (κ_L decreases sharply again due to strong phonon–electron scattering), but electrons, $\kappa_L \ll \kappa_e$ and $\kappa_{tot} = \kappa_e$. This conclusion is proved by the temperature dependence of $\kappa_{tot} = \kappa_e \propto T$, which is typical for electron scattering by static defects and impurities. On extrapolation of T to zero, $\kappa_e(T)$ tends

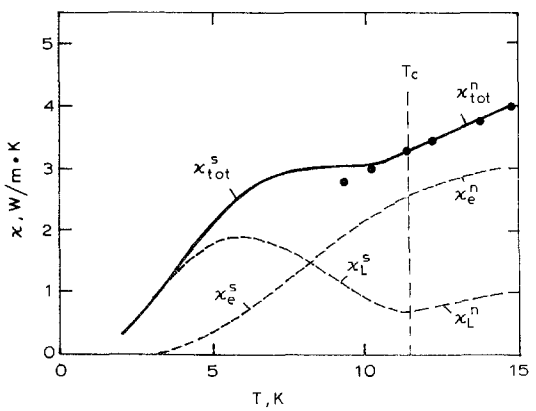

Fig. 108. The temperature dependence of κ for $LuRh_4B_4$ (Odoni et al. 1981). Solid line is the experimental κ_{tot} at $H = 0$, points give the experimental κ_{tot} at $H = 5$ kOe, dashed lines show calculated values κ_e^n, κ_e^s, κ_L^n and κ_L^s.

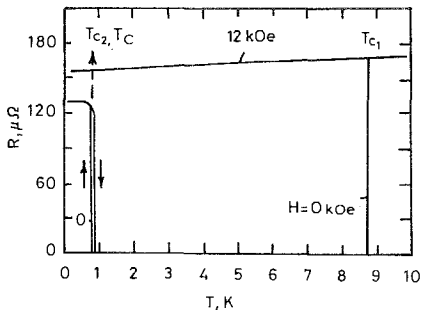

Fig. 109. The temperature dependence of the electrical resistivity, R, for $ErRh_4B_4$ without a magnetic field and in a longitudinal magnetic field $H = 12$ kOe (Ott et al. 1978).

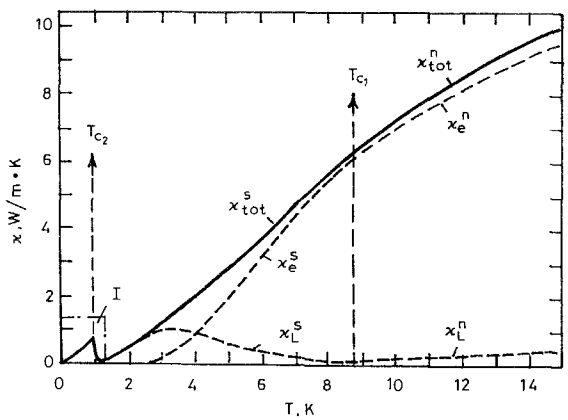

Fig. 110. The temperature dependence of κ for $ErRh_4B_4$ (Odoni et al. 1981). The solid line is the experimental value. The dashed line gives the calculated κ^n_e, κ^s_e, κ^n_L and κ^s_L.

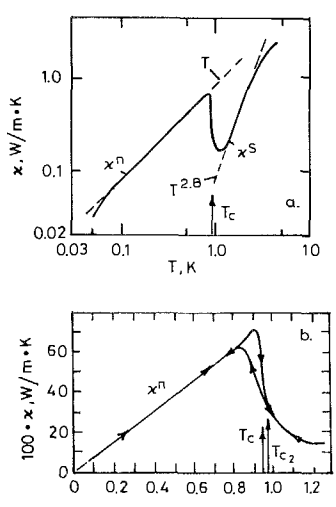

Fig. 111. (a) The temperature dependence of κ for $ErRh_4B_4$ in region I of fig. 110 (Odoni and Ott 1979). (b) A more detailed picture near the phase transition.

to zero (fig. 111b). Besides, $\kappa_{tot}(T)$ can be described well by the Wiedemann–Franz law with $L = L_0$. Near the phase transition $\kappa(T)$ of $ErRh_4B_4$ shows hysteresis (fig. 111b), similar to the case of $R(T)$ (fig. 109).

Figures 112–115 show $\kappa(T)$ and R(T) dependences for $SmRh_4B_4$ and $TmRh_4B_4$ with the coexistence of superconductivity with antiferro- and ferromagnetic ordering, respectively (Hamaker et al. 1979, 1981a, b, Ott et al. 1980). At $H = 0$ in the regions of superconductivity (II), of superconductivity and magnetism coexistence (I), and also at the points T_c (0.4 K for $TmRh_4B_4$) and T_N (0.87 K for $SmRh_4B_4$) no anomalies in κ^s behaviour are observed except for the decrease of the value n in the dependence $\kappa^s \propto T^n$ in the region of superconductivity and magnetism coexistence from $\simeq 2.8$ (typical for κ_L^s) to $\simeq 1$ ($\kappa^s \propto T$) with decreasing temperature. Ott et al. (1980) have connected this effect with the appearance of a magnon contribution against a background of small κ_L.

In the normal state [which requires a field ~ 2 kOe for $SmRh_4B_4$ (fig. 112) and ~ 3 kOe for $TmRh_4B_4$ to quench superconductivity (fig. 114)] $\kappa^n \propto T$, as in the case

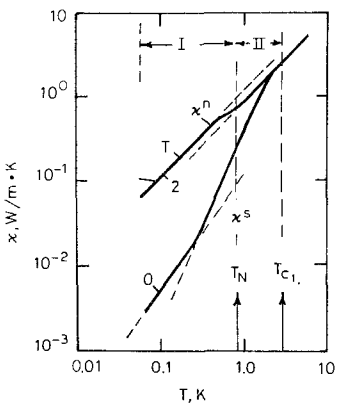

Fig. 112. The temperature dependence of κ for $SmRh_4B_4$ without a magnetic field and in a longitudinal magnetic field. The numbers by the curves are the values of H in kOe (Hamaker et al. 1981b).

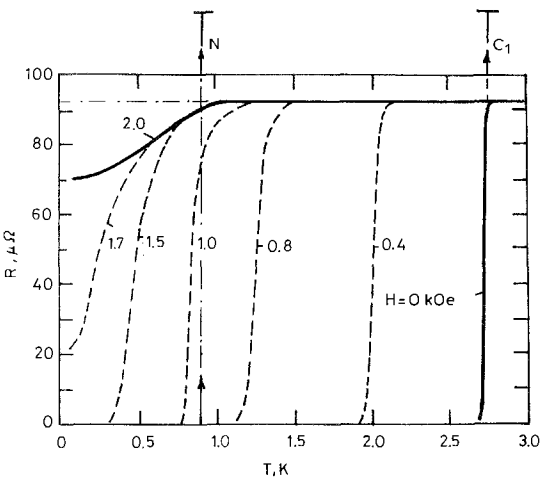

Fig. 113. The temperature dependence of the electrical resistivity, R, for $SmRh_4B_4$ without a magnetic field and in a longitudinal magnetic field. The numbers by the curves are the values of H in kOe (Hamaker et al. 1979, Ott et al. 1980).

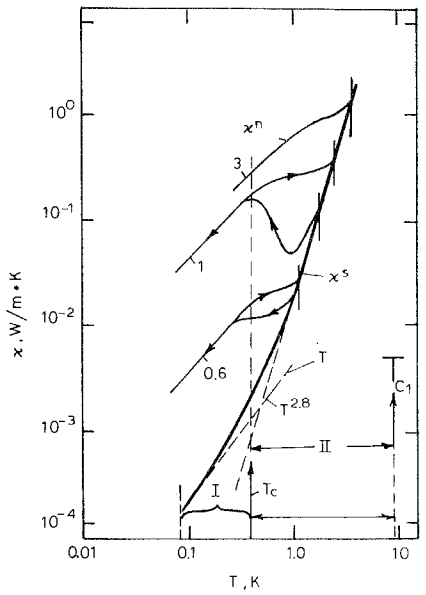

Fig. 114. The temperature dependence of κ for $TmRh_4B_4$ without a magnetic field and in a longitudinal magnetic field. The numbers by the curves are the values of H in kOe (Hamaker et al. 1981a, b).

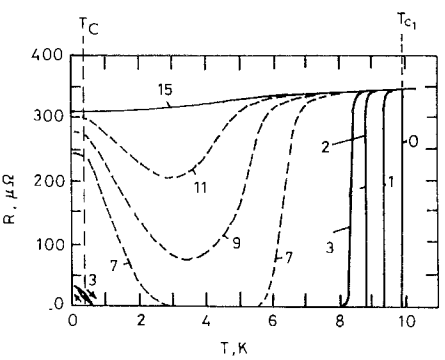

Fig. 115. The temperature dependence of the electrical resistivity, R, for $TmRh_4B_4$ without a magnetic field and in a longitudinal magnetic field. The numbers by the curves are the values of H in kOe (Hamaker et al. 1981a, b).

of $ErRh_4B_4$, and this can also be explained by the prevailing contribution of κ_e at these temperatures.

It is interesting to observe the influence of a magnetic field on κ in the presence of the specific magnetic domain structure typical for the magnetism/superconduction coexistence region. Anomalous behaviour of κ in a magnetic field has been observed in $TmRh_4B_4$ (fig. 114):

(1) A weak magnetic field strongly influences both the value and the temperature dependence of the thermal conductivity.

(2) Large hysteresis is observed in the dependence $\kappa(T)$ for $T > T_c$, which disappears at $T \simeq T_c$, and for $T < T_c$ κ_s is proportional to T.

(3) The phase transition temperature shifts with a magnetic field to higher temperature. At $H = 3$ kOe, $\kappa(T)$ of $TmRh_4B_4$ behaves like $\kappa(T)$ of $ErRh_4B_4$ in the interval $T_c \leqslant T \leqslant T_{c2}$ in zero magnetic field (see fig. 111).

So, the unusual behaviour of $\kappa(T)$ of $TmRh_4B_4$ in a magnetic field can be explained by a series of phase transitions induced by the magnetic field. This field leads to magnetic ordering, which starts the destruction of superconductivity.

8.4. *Some words on the thermal conductivity of high-temperature superconducting rare earth compounds*

In the past few years investigation of high-temperature superconductors (HTSC) has become one of the fashionable branches of solid state physics. More than a hundred papers have been published on the thermal conductivity of HTSCs (this is only an insignificant part of the several thousand papers on other physical properties of HTSCs). Nevertheless, because of the limited size of this review we cannot discuss in detail even the principal articles on κ for HTSCs. Recently several reviews and a number of general articles have been devoted to this aspect of HTSCs (Fischer et al. 1988, Kirichenko et al. 1990, Jezowski and Klamut 1990, Uher 1989, 1990, Regueiro and Castle 1990, Florent'ev et al. 1990). One can find references to the majority of published works on κ of HTSCs in these review articles. The theory of κ in HTSCs is considered by Tewordt and Wölkhausen (1989). Investigations of κ in HTSCs containing rare earth elements (system 1–2–3: $RBa_2Cu_3O_{7-\delta}$ (R = Y, Eu, Gd, Ho, Sm, Er, Dy); system 2–1–4: $R_{2-x}Sr_xCuO_4$) can be separated into four stages:

(1) Imperfect, often multiphase, ceramic samples have been measured. Everyone associated with these papers has strived to measure something and to publish it as soon as possible. These data are not trustworthy at present.

(2) Measurements have been carried out on well prepared and certified ceramic samples of high density. These results are trustworthy.

(3) Measurements have been carried out on small single crystals (plates with sizes $\sim 0.5 \times 0.5$ mm). Some difficulties have arisen. First, many of the single crystals that have been prepared are imperfect. Second, the classical, precise methods for κ measurements were developed for large samples. Thus, it has been necessary to develop a new technique, but significant errors are associated with it.

(4) The quality of single crystals has been improved, and their dimensions have grown (but not enough to use the classical methods of κ measurement). The precision of the new methods has increased due to technological progress. The anisotropy of the thermal conductivity has been investigated. The κ of single crystals is 8–10 times higher than the κ of ceramic samples.

A number of peculiarities of $\kappa(T)$ has been observed in HTSCs. Let us consider some of them.

(1) In contrast to classical superconductors $\kappa_L \gg \kappa_e$ in HTSCs (in polycrystalline HTSCs it is 10–25%, in single crystals 30–50%).

(2) A nonstandard temperature dependence of $\kappa(T)$ is observed for $T > T_c$ and $T < T_c$ (fig. 116). For $T > T_c$ $\kappa \simeq$ const. For $T < T_c$, the value of κ initially increases with decreasing T, passes through a maximum and then decreases. Between 10 and 1 K, $\kappa \propto T^2$; at $T < 1$ K a linear temperature dependence ($\kappa \propto T$) is observed in some samples. For the greatest part the peculiarities of κ_{tot} in HTSCs are connected with κ_L, because, as has been noted above, $\kappa_L > \kappa_e$. Independence of κ_L of T for $T > T_c$

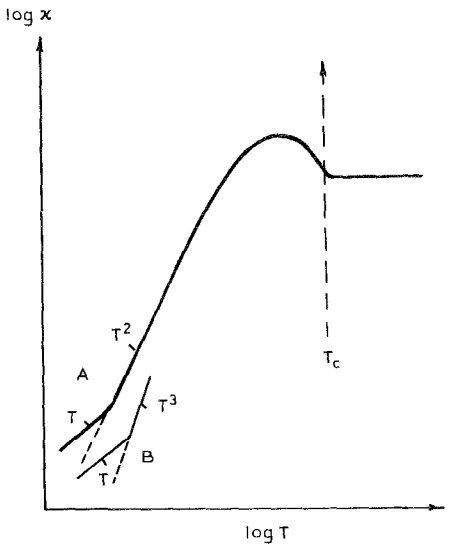

Fig. 116. Schematic shape of κ for a HTSC (on a logarithmic scale). Curves A and B are possible temperature dependences of κ for different groups of materials and samples.

can be explained either by strong phonon–electron scattering or phonon–defect scattering. Oxygen vacancies, twins and structural inhomogeneities serve as defects. The increase of κ_L for $T < T_c$ can be explained by a decreasing phonon–electron scattering in the superconductivity region (cf. figs. 116 and 104). There is another explanation of this effect. Ginzburg (1989a, b) hypothesised that the convective heat transport by normal current carriers, which is negligible in classical superconductors, becomes significant in HTSCs. For $T < T_c$, κ increases at first and then, as the normal carriers "condense", decreases. The higher the contribution of κ_e to κ_{tot}, the higher the maximum of κ. The $\kappa_L \propto T^2$ dependence at low temperatures in crystals can be explained by phonon scattering by conduction electrons (in superconductors by normal carriers), dislocations and in glasses or heavily disordered systems by resonance phonon scattering of two-level systems, see section 9.1. An estimation of Regueiro and Castello (1990) shows that the second version is more likely in the case of HTSCs, because at these temperatures in the investigated HTSC samples there are no longer any normal carriers, and a model taking phonon scattering by dislocations into account leads to an unrealistically high dislocation density. By the way, the same temperature dependence $\kappa \propto T^2$ has been observed in superconducting heavy-fermion systems (section 8.2). However, for these materials it is $\kappa_e(T)$, and for HTSCs it is $\kappa_L(T)$. Very likely, the oxygen vacancies are responsible for the structure "disorder" in HTSCs. The dependence $\kappa \propto T$ has been observed in a number of HTSC samples at superlow temperatures. Mostly this is connected with scattering of normal electrons on static defects. In this temperature region, κ_L becomes insignificant and κ_e is appreciable ($\kappa_e \propto T$). It is not clear where the normal electrons come from [according to the estimate of Kirichenko et al. (1990) and Uher (1990) they make up ~15% in the 1–2–4 HTSCs]. Either they are inherent to HTSCs due to the high anisotropy of the gap in the electron exciting spectrum, or they are present

because of impurities. As noted earlier, the linear term of $\kappa(T)$ has been observed in the superconducting heavy-fermion systems and in the systems in which superconductivity and magnetism coexist. In the first case, as in the case of HTSCs, this term is connected with scattering of normal current carriers by defects, and in the second case with the contribution κ_m to κ_{tot}. Probably, structural defects are responsible for the linear term in $\kappa_L(T)$ of HTSCs. It should be remembered that in 1–2–3 systems the linear term is not observed up to $T \simeq 50$ mK (Regueiro and Castello 1990). A different interpretation of the low-temperature data on κ of a number of HTSCs is given in some works (Uher 1990, Florent'ev et al. 1990, Sparn et al. 1989). The $\kappa(T)$ dependence is approximated by the equation $\kappa(T) = aT + bT^3$. The second term is connected with boundary scattering of phonons.

Probably, additional independent experiments are necessary to explain the origins of the different κ behaviour of HTSCs at low temperatures.

Concluding this section, we present in fig. 117 the experimental $\kappa_{tot}(T)$ of the 1–2–3 system for a polycrystalline sample (the average κ_{tot} value) and for a single crystal (the maximum κ_{tot} value known at the present time) (Florent'ev et al. 1990).

9. Thermal conductivity of rare earth glasses and crystalline materials with glass-like behaviour of $\kappa_L(T)$

9.1. *Thermal conductivity of rare earth glasses*

Glasses based on the rare earth elements have been investigated intensively in the last fifteen years because of their interesting and prospective practical spectral-luminescent properties [see, e.g., Reisfeld and Bornstein (1977), Reisfeld et al. (1977, 1979), Kamarzin et al. (1983a, b), Sokolov et al. (1988)]. However, data on the thermal conductivity in the literature are scarce: Smirnov et al. (1985, 1988, 1989, 1991a), Parfen'eva et al. (1990a, b, c), Guessons and Mazuer (1982). The unusual thermal conductivity and heat capacity of glasses and amorphous systems at superlow, low and high temperatures has attracted the attention of theoreticians and experimentalists [see, e.g., Anderson et al. (1972), Phillips (1972, 1987), Karpov and Parshin (1983, 1985), Pohl and De Yoreo (1985), Jagannathan et al. (1989), Galperin et al. (1988), Krasny et al. (1990), Freeman and Anderson (1986), Love and Anderson (1990)]. Rare earth glasses possess all peculiarities of $\kappa(T)$ and $C(T)$ inherent in usual glasses but they show also a new effect – resonance scattering of phonons by the paramagnetic lanthanide ions [see Smirnov et al. (1985, 1988, 1989, 1992a), Parfen'eva et al. (1990a, b)], which has been discussed in detail in section 6.

Below we will consider briefly the main results on the thermal conductivity of rare earth glasses which in principle can be explained in the framework of contemporary theory (Anderson et al. 1972, Karpov and Parshin 1983, 1985). We will discuss separately the data for insulating and metallic rare earth glasses.

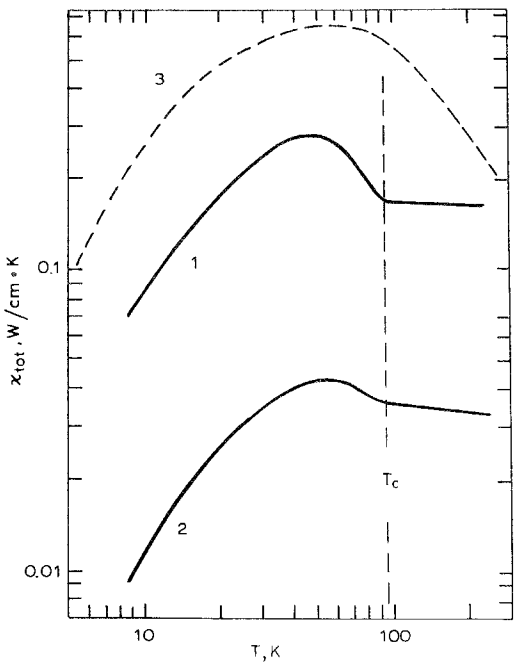

Fig. 117. The temperature dependence of κ_{tot} for a single crystal sample of $Y_{0.98}Yb_{0.02}Ba_2Cu_3O_{7-x}$ (1) and for a polycrystalline $YBa_2Cu_3O_{7-x}$ (2). Data for CuO are shown for comparision (3) (Florent'ev et al. 1990).

9.1.1. *Thermal conductivity of insulating rare earth glasses*

According to the existing theory the temperature dependence of κ_L in insulating glasses can be represented as a kind of staircase (fig. 118) (Karpov and Parshin 1983, 1985, Galperin et al. 1988). At low temperatures ($T < 0.1$–5 K) the heat is transported, mainly, by the thermal phonons scattered by two-level systems. Here κ_L is proportional to T^2 (region I in fig. 118). The first "step" (region II, $T \sim 5$–10 K), where $\kappa_L =$ const., is connected with resonance scattering of thermal phonons by anharmonic oscillators, which show Van Hove singularities (Galperin et al. 1988) in their densities of states. In region III the increase of κ_L is connected with "subthermal" phonons with energies much less than the energy of the phonons scattered resonantly by the

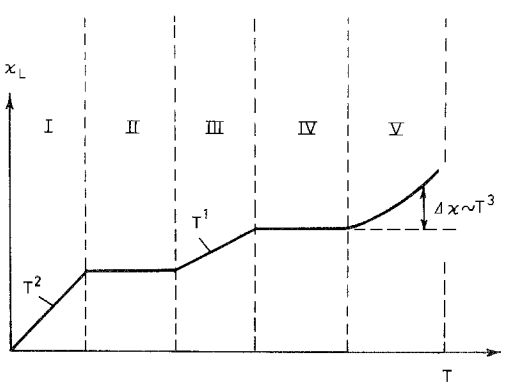

Fig. 118. Schematic shape of the theoretical temperature dependence of κ_L for glasses.

two-level systems. Here κ_L is proportional to T. The second "step" (region IV) is connected with phonon scattering by boundaries of clusters and structural units of the glass. In this region the conditions that the free path length l is constant and that l does not depend on temperature must be fulfilled. The increase in thermal conductivity in region V (fig. 118, $\Delta\kappa$) is connected with the appearance of photon thermal conductivity. (The heat capacity of glasses in region I has a temperature dependence $C \propto T$, which with increasing temperature turns into the standard dependence $C \propto T^3$ and then at high temperatures into $C = \text{const.}$)

The experimental data on κ_L of rare earth glasses are based, mainly, on $R_2S_3(Ga_2S_3)_x$ (R = La, Ce, Pr, Nd; $x = 2$ or 3) glasses (Smirnov et al. 1985, 1988, 1989, 1991a, Parfen'eva et al. 1990a–c). In the system R_2S_3–R_2O_3–Ga_2O_3–Ga_2S_3 (R = lanthanide) glass formation is observed over a wide region (Sokolov et al. 1988, Guittard et al. 1986). Figure 119 shows as example the glass formation region for R = La.

Glasses based on Ga_2S_3 are formed with lanthanides from La to Er (Loireau-Lorach et al. 1976), and glasses based on Ga_2O_3 are formed with lanthanides from La to Nd (Sokolov et al. 1988). Lanthanides following Nd can enter into a glass composition together with some light lanthanides. The width of the glass formation region of the system $(R_2O_3)(Ga_2X_3)_x$ (X = S, O) depends on R and decreases to the side of the heavy lanthanides (Loireau-Lorach et al. 1976).

Data on κ_L of the above-mentioned rare earth glasses are related to the regions III–V distinguished in fig. 118. Let us consider κ_L of $La_2S_3(Ga_2O_3)_2$ (fig. 120)

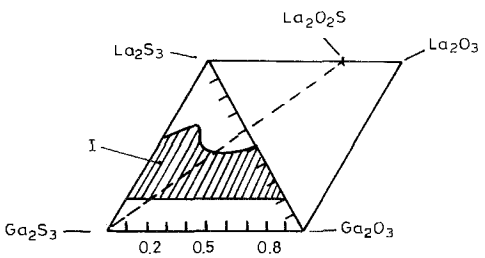

Fig. 119. The glass region (I) in the system La_2S_3–La_2O_3–Ga_2O_3–Ga_2S_3 (Sokolov et al. 1988, Guittard et al. 1986).

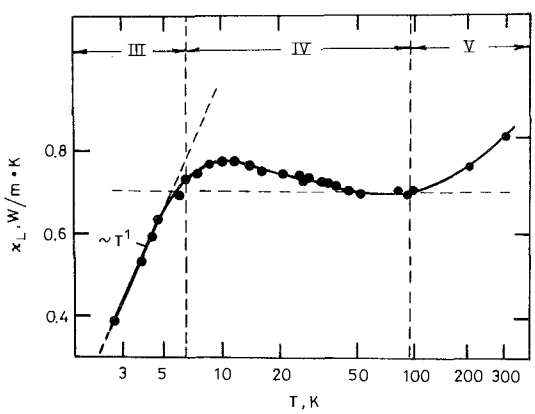

Fig. 120. The temperature dependence of κ_L for $La_2S_3(Ga_2O_3)_2$ (Parfen'eva et al. 1990c).

(Smirnov et al. 1992a, Parfen'eva et al. 1990c). The temperature dependence of κ_L in the interval 3–5 K ($\kappa_L \propto T$) is typical for region III (fig. 118) [In this temperature interval the heat capacity $C \propto T^3$ (Smirnov et al. 1992a)]. The free path length of phonons l ($l = 3\kappa_L/Cv$) (Smirnov et al. 1991a) calculated from experimental data on κ_L, C and the sound velocity v at $T \geqslant 30$–40 K begins to saturate (fig. 121), which is typical for region IV. And finally in the interval 100–400 K the law $\Delta\kappa \propto T^3$ is fulfilled, which is typical for region V. The low-temperature plateau in the dependence $\kappa_L(T)$ typical for insulating glasses is realized for $R_2S_3(Ga_2O_3)_x$ at lower temperatures ($T < 4$ K).

As shown above (see fig. 73) a variation of the concentration x from 2 to 3 in glasses $R_2S_3(Ga_2O_3)_x$ (with $R^{3+} = La^{3+}$, Pr^{3+}) practically does not influence the value of κ_L. On the other hand, substitution of La^{3+} by Ce^{3+} or Nd^{3+} (at constant x) changes κ_L significantly in region IV (but has little effect on the value of κ_L in region III) (fig. 122). (The large influence of substitution of La^{3+} by Pr^{3+} on κ_L caused by strong resonance scattering of phonons by the paramagnetic levels of Pr is discussed in section 6.1.).

In region IV κ_L decreases linearly with the lanthanide atomic number (fig. 122b), which shows that there is some decrease of the structural unit sizes with decreasing ionic radius of the lanthanide ion. This effect is purely geometrical and is not connected with the decrease of κ_L due to resonance phonon scattering on the paramagnetic levels of Ce^{3+} and Nd^{3+}. This is confirmed by the absence of the Schottky effect in the heat capacity of these glasses in the discussed temperature region (Smirnov et al. 1992a). The split excited levels of the ground states of the ions Ce and Nd lie high and do not scatter the phonons. An analogous influence on κ_L is observed for the partial substitution of La^{3+} by Gd^{3+} in the glass $(Gd_2S_3)_{0.3}(La_2S_3)_{0.7}(Ga_2O_3)_2$ (fig. 123) (the Gd^{3+} ion has $L = 0$ and, consequently, resonance phonon scattering is absent). From figs. 120 and 122 one can see that $\kappa_L(T)$ of the considered glasses is somewhat different from the classical temperature depend-

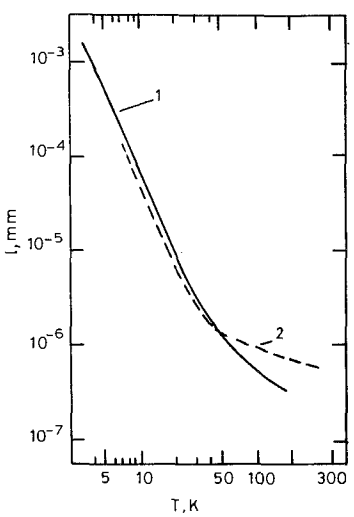

Fig. 121. The temperature dependence of the phonon free path length in the glass $La_2S_3(Ga_2O_3)$ (1) (Smirnov et al. 1992b) and in fused quartz (2) (Zeller and Pohl 1971).

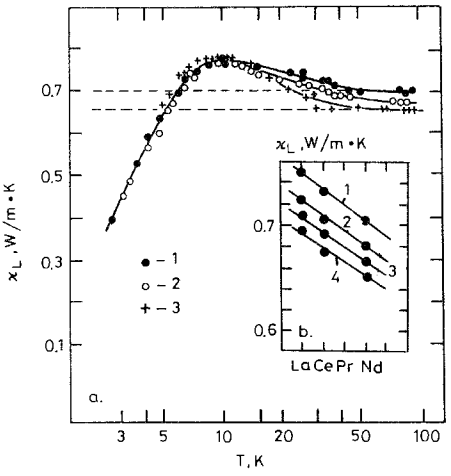

Fig. 122. (a) The temperature dependence of κ_L for the glasses $R_2S_3(Ga_2O_3)_2$ (R = La (1), Ce (2), Nd (3)) (Parfen'eva et al. 1990c, Smirnov et al. 1992b). (b) Dependence of $\kappa_L(T)$ on the atomic number of R in the glasses $R_2S_3(Ga_2O_3)_2$. $T = 20$ K (1), 30 K (2), 40 K (3), 100 K (4).

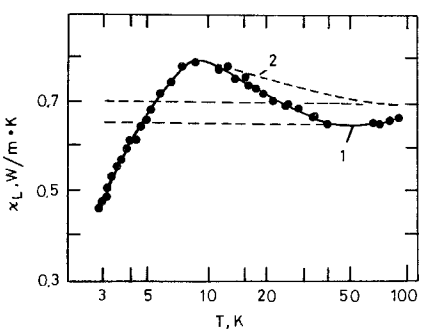

Fig. 123. The temperature dependence of κ_L for the glass $(Gd_2S_3)_{0.3}(La_2S_3)_{0.7}(Ga_2O_3)_2$ (1) (Smirnov et al. 1992b) and for the glass $(La_2S_3)(Ga_2O_3)_2$ (dashed line 2). For $T < 10$ K, κ_L of both glasses coincide.

ence of the insulating glasses. In the rare earth glasses a small peak in κ_L (characteristic for crystalline solids) is observed near 10 K. This peak becomes more pronounced for substitution of La by a heavy lanthanide.

In all above-mentioned glasses the La ions are substituted isovalently. For the nonisovalent substitution of La ions κ_L of the glasses decreases much stronger. For example, when one considers $\kappa_L(T)$ of the glass $(2EuS)_{0.5}(La_2S_3)_{0.5}(Ga_2O_3)_2$ (fig. 124) (Smirnov et al. 1992a), with the La^{3+} ion substituted by Eu^{2+} ions. In this glass, apparently, not only variation of the short-range order parameters occurs, but also formation of ionic vacancies as additional phonon scattering centres (Smirnov et al. 1992a) (the resonance phonon scattering effect on Eu^{2+} levels is absent, because Eu^{2+} has $L = 0$). All these glasses belong to the glasses with a "large" κ_L value. The classical insulating glasses (of quartz-type) have a κ_L which is 2–3 times smaller. Besides, these glasses have a noncharacteristic (for the classical insulating amorphous solids) small maximum of κ_L in the low-temperature region (see figs. 120, 122 and 123). This could point to the presence of small crystalline regions in the glasses of $R_2S_3(Ga_2O_3)_x$-type (although according to X-ray data these materials are ideal glasses).

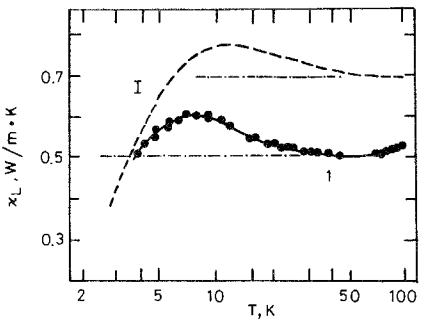

Fig. 124. The temperature dependence of κ_L for the glass $(2EuS)_{0.5}(La_2S_3)_{0.5}(Ga_2O_3)_2$ (1) (Smirnov et al. 1992b), for the glass $La_2S_3(Ga_2O_3)_2$ (I).

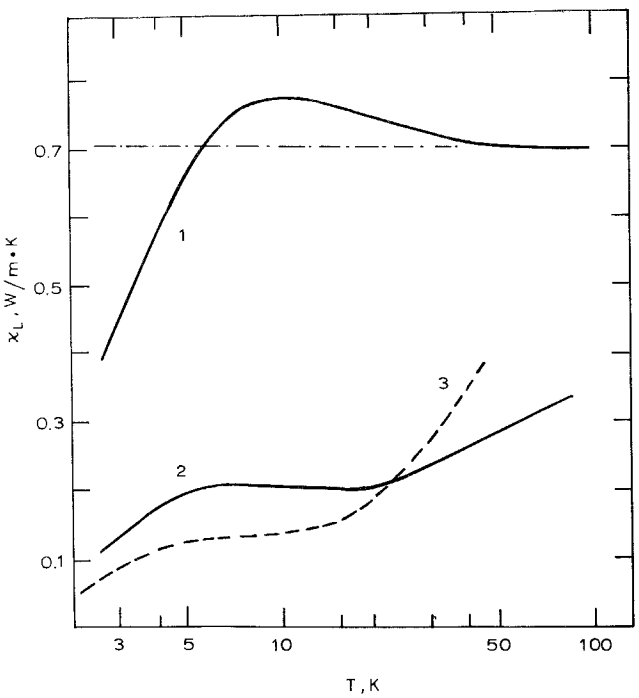

Fig. 125. The temperature dependence of κ_L for the glasses $La_2S_3(Ga_2O_3)_2$ (1), LaP_5O_{14} (2) (Parfen'eva et al. 1990c, Smirnov et al. 1992b) and fused quartz (3) (Zeller and Pohl 1971).

However, in the family of rare earth glasses representatives may be found which have similar properties (both in magnitude and temperature dependence of κ_L) as the classical insulating glasses. The glasses LaP_5O_{14} and PrP_5O_{14}, which were discussed in section 6.1 (see also fig. 125) are an example.

9.1.2. *Thermal conductivity of metallic rare earth glasses*

There are only a few papers devoted to investigation of the thermal conductivity of metallic rare earth glasses (Guessons and Mazuer 1982). No peculiarities (compared with standard metallic glasses) have been connected with the presence of the rare earth elements. The "glass" behaviour of metallic glasses must display itself in both

the value and the temperature dependence of κ_L (as it is for insulating glasses). The metallic glasses differ from the insulating ones by:

(a) the presence of electron thermal conductivity ($\kappa_{tot} = \kappa_L + \kappa_e$); and

(b) the presence of phonon–electron scattering decreases the value of κ_L and influences its temperature dependence (Löhneysen et al. 1981).

This causes difficulties in the separation of κ_L from κ_{tot}. It is known that it is not easy to separate κ_L from κ_{tot} with a great deal of precision in normal (crystalline) metals, because $\kappa_e \gg \kappa_L$. For metal glasses this task is even more difficult because κ_L is smaller than in crystalline metals. According to the experimental temperature dependence of κ_L all metallic glasses can be divided in two groups (Matey and Anderson 1977a, b):

(a) a group with a plateau ($\kappa_L = \text{const.}$) in the region 1–10 K; and

(b) a group without such a plateau.

It should be kept in mind that the plateau of κ_L in the region 1–10 K is typical for insulating glasses. In a number of works (Love and Anderson 1990, Matey and Anderson 1977a, b, Zaitlin and Anderson 1975, Dreyfus et al. 1968) attempts have been made to explain qualitatively the absence of the plateau in metallic glasses (in this model the plateau can be absent under certain conditions in the insulating glasses). According to the model the low-frequency phonons (L, with frequency less than 10^{11} Hz) contribute to κ_L only at low temperatures, and high-temperature phonons (H) contribute only at high temperatures. The presence or absence of the plateau in $\kappa_L(T)$ depends on the relative contributions of the L and H phonons (see fig. 126b). The plateau is observed for a large ratio of L and H contributions (Matey and Anderson 1977a, b). Unfortunately, there are very few experimental data on κ_L of the metallic rare earth glasses. Love and Anderson (1990) give data on $\kappa(T)$ of the glasses $Ce_{100-x}Al_x$ ($x = 12$, 43, 70, 77 and 86). These glasses belong to the second group, they have no plateau in the region 1–10 K. Figure 126 shows, as example, $\kappa(T)$ of two glasses of this system (Love and Anderson 1990).

9.2. *Thermal conductivity of crystalline materials with "glass-like" behaviour of $\kappa_L(T)$*

During the last few years many cases were observed where κ_L of crystals behaves as κ_L of glasses in some narrow, or over a wide, temperature range. As is known,

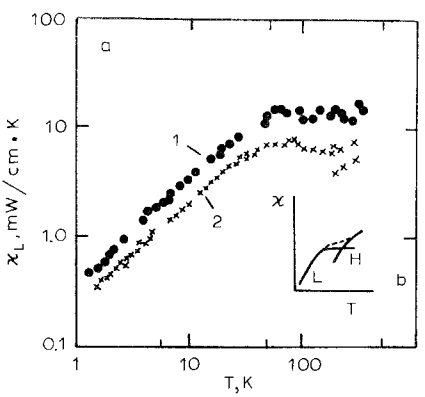

Fig. 126. (a) The temperature dependence of κ_L for the metallic glasses $Ce_{23}Al_{77}$ (1) and $Ce_{57}Al_{43}$ (2) (Guessons and Mazuer 1982). (b) Schematic shape of the contributions to κ_L of different phonon groups (L and H) (Matey and Anderson 1977a, b).

the distinctive features of glasses are a small κ_L and a characteristic temperature dependence of κ_L. The small κ_L value in amorphous (and in some crystalline) materials is caused by strong phonon scattering. Different types of scatterers can be responsible for one or another temperature dependences of κ_L. Let us consider what factors in crystals could result in decreasing κ_L and a change in its temperature dependence. Let us divide them in three groups:

(a) first group: factors leading to "amorphous" behaviour of κ_L over the whole temperature region;

(b) second group: factors leading to "amorphous" behaviour of κ_L in separate temperature regions;

(c) third group: factors leading to the "amorphous" behaviour of κ_L only at high temperatures.

Let us consider some of these factors. Factors in the first group are: a high concentration of point defects (e.g., vacancies) strongly distorting the crystal lattice (Smirnov et al. 1973, 1992b), a decrease of crystallite sizes to some critical value (Spear et al. 1981) (this effect is essential, as a rule, in thin films), large fluctuation of composition, a crystal lattice with a great number of atoms in the elementary cell (Slack et al. 1971, Cahill et al. 1989, Golikova and Tadzhiev 1986, Berezin et al. 1974, Petrov et al. 1969, 1975, Golikova et al. 1974), the presence in ferroelectric crystals of sporadic regions with a local electric polarization (De Yoreo et al. 1985) and so on. A rule was established empirically for ferroelectrics (De Yoreo et al. 1985): if the dielectric constant and refraction coefficient sharply change at the point of the ferroelectric phase transition (T_{fer}), then $\kappa_L(T)$ behaves as in a normal crystal. If at the point T_{fer} these parameters do not change sharply, then $\kappa_L(T)$ behaves as in amorphous materials. Effects characteristic for the second group [where "amorphisation" is revealed as regions with $\kappa_L = \text{const.}$ on the curves $\kappa_L(T)$] can be initiated by doping with impurities that have a much larger mass than the matrix mass [this leads to local modes in the phonon spectrum and resonance phonon scattering on them (Cahill et al. 1989)], by phonon scattering on colloids and large clusters of impurity atoms (De Goër 1986), by phonon scattering by inhomogeneities of the crystal lattice which are caused by irradiation with small doses of neutrons, electrons, ions, γ-rays (at large doses full amorphisation can be reached) (Oskotski and Smirnov 1972, De Goër 1986, De Goër et al. 1986), by phonon scattering on disordered crystal regions, crystallographic domains, soft modes arising at various phase transitions [see, e.g., Andres et al. (1984, 1985), Salce and Boatner (1986)], by strong acoustic phonon scattering by optical phonons (Oskotski and Smirnov 1972) and so on. The third group is related to the case (possible only at high temperatures) when the phonon free path length reaches interatomic distances, i.e. becomes less than a phonon wavelength (the minimal mean free path of phonons in a crystal must be of the order of the phonon wavelength) – the so-called case of minimal thermal conductivity (Slack 1979). In this case the κ_L of crystal and amorphous materials are about the same in magnitude and κ_L ceases to depend on temperature (Slack 1979). Let us consider a few of the most interesting examples of "glass" behaviour of $\kappa_L(T)$ in crystalline rare earth compounds.

9.2.1. *"Amorphisation" of κ_L arising due to a complex crystallographic structure*

Let us consider data on $\kappa_L(T)$ of RB_{66} (R = Y, Gd) (Slack et al. 1971, Cahill et al. 1989, Golikova and Tadzhiev 1986, Türkes et al. 1986, Raychaudhuri et al. 1980). The crystal lattice of RB_{66} is cubic and is rather complicated (Richards and Kasper 1969). The elementary cell of YB_{66} (lattice constant $a = 23.440$ Å) consists of 1584 boron atoms and 24 yttrium atoms. Inside the cell the boron and yttrium atoms are disorderly arranged (i.e. the structure is nearly amorphous). This complicated character of the lattice causes the "glassy" behaviour of $\kappa_L(T)$ in these compounds (Slack et al. 1971, Cahill et al. 1989, Petrov et al. 1969, 1975) over the entire investigated temperature interval (1–1000 K). Figures 127 and 128 show $\kappa_L(T)$ of YB_{66}, $YB_{61.7}$ and GdB_{66} (Cahill et al. 1989, Golikova and Tadzhiev 1986) [YB_{66} and GdB_{66} are

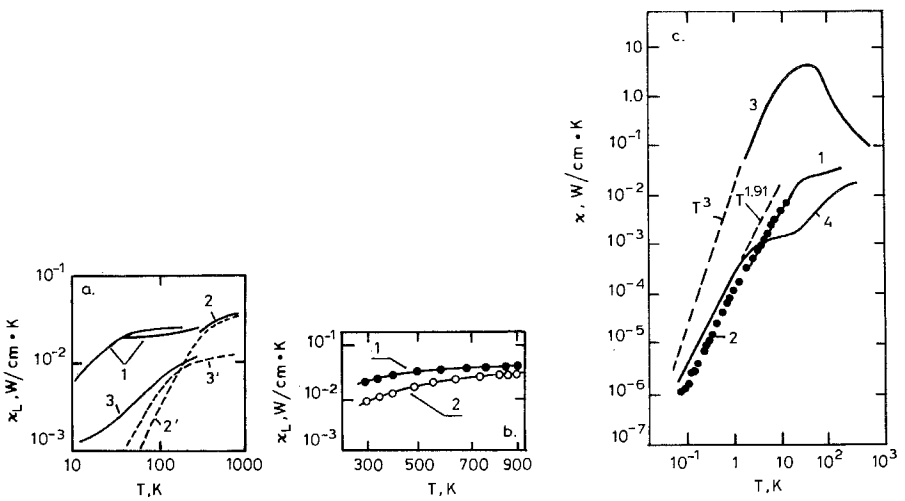

Fig. 127. (a) The temperature dependence of κ_L for YB_{66} (1) and GdB_{66} (2) (Golikova and Tadzhiev 1986, Richards and Kasper 1969). Data on κ_L of fused quartz are shown for comparison (3). The dashed lines give the minimal thermal conductivity (at $l = \lambda$) for GdB_{66} (2′) and fused quartz (3′) (Petrov et al. 1969, Smirnov et al. 1972). (b) κ_L for YB_{66} (1) and for amorphous boron (2) (Richards and Kasper 1969). (c) κ_L for YB_{66} (1, 2), β-boron (3) and fused quartz (4) (the low-temperature region) (Golikova and Tadzhiev 1986, Raychaudhuri et al. 1980).

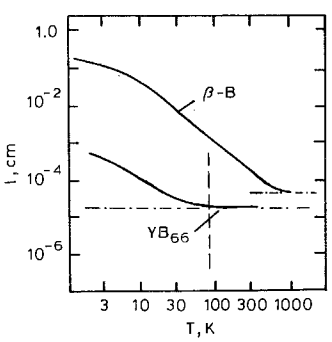

Fig. 128. The temperature dependence of the free path length, l, in YB_{66} (Cahill et al. 1989). Data for the crystal β-boron are shown for comparison (at 1 K l is approximately equal to the sample size).

semiconductors with $\rho_{300} \sim 10^4\ \Omega$ cm (Golikova and Tadzhiev 1986), therefore $\kappa_{tot} = \kappa_L$]. At all temperatures $\kappa_L(T)$ behaves as in classical insulating glasses (fused quartz, amorphous boron).

The plateau in the dependence $\kappa_L(T)$ of YB_{66} occurs at a higher temperature than in the case of a classical insulating glass. This is connected with the large value of Θ in YB_{66} (in YB_{66} $\Theta \simeq 1340$ K, in fused quartz $\Theta \simeq 500$ K). The higher the value of Θ, the higher the temperature region of the plateau (Cahill et al. 1989).

The free path length of acoustical phonons in YB_{66} tends to a constant value already at $T \geqslant 80$ K (fig. 128) (Slack et al. 1971). In addition to $\kappa_L(T)$, the "amorphous" character of YB_{66} has been observed in the temperature dependences of the electrical resistance, the thermoemf and the heat capacity (Cahill et al. 1989, Golikova and Tadzhiev 1986). Thus, in these compounds not only the phonon spectrum is "amorphisised", but the electron spectrum as well. As has been noted above, the "amorphous" behaviour of $\kappa_L(T)$ in YB_{66} is observed over the wide temperature interval 1–1000 K. The "amorphisation" is also observed in the behaviour of $\kappa_L(T)$ of a similar material, the tetrahedral crystal β-B with 105 atoms in the elementary cell (Petrov et al. 1969). However, in this case the amorphisation reveals itself only at high enough temperatures. At low temperatures $\kappa_L(T)$ behaves just as in normal crystalline solids (it has maximum at low temperatures). It is very likely that the large number of atoms in the elementary cell of YB_{66} is the cause of the more complete "amorphisation" of YB_{66} in comparison with β-B. At high temperatures in YB_{66} (as in classical insulating glasses) the condition $l = \lambda$ begins to be fulfilled [the so-called case of minimal thermal conductivity (Slack (1979)] (see fig. 127a, dashed lines).

9.2.2. *"Amorphisation" of κ_L due to the strong phonon scattering by lattice defects*

An unusual situation arises in lanthanide compounds with an inhomogeneous variable valency of the lanthanide ions with phonon scattering by crystal lattice defects. We will consider as an example Sm_3S_4. [In Sm_3S_4, $\rho_{300} \simeq 10\ \Omega$ cm. The electronic contribution to κ_{tot} is insignificant over the whole temperature interval, hence one can consider $\kappa_{tot} = \kappa_L$ (Smirnov et al. 1972)]. This compound contains the ions Sm^{2+} and Sm^{3+} in the ratio 1:2 ($Sm^{2+}Sm_2^{3+}S_4$), statistically distributed through the cation sublattice. Because of the appreciable difference in the ionic radii of Sm^{2+} and Sm^{3+} one of them can be considered as an "impurity" (let us call it an A-type defect), scattering phonons and decreasing κ_L. The ions Sm^{2+} and Sm^{3+} exchange electrons by hops, which change the valencies (hopping conductivity). With increasing temperature the frequency of hops increases (but the ratio of Sm^{2+} and Sm^{3+} concentration remains constant). At the valency variation the radii of the ions change, deforming the lattice around them. The deformation cloud fluctuating in the lattice from one ion to another ion (let us call it a type-B defect) is the cause of additional scattering of phonons, decreasing the thermal conductivity. Both defects of A- and B-type decrease the κ_L to values approaching the thermal conductivity of a glass. At high temperatures, when the "concentration" of B-type defects increases appreciably, strong phonon–defect scattering can lead to an "amorphous" temperature dependence of $\kappa_L(T)$ ($\kappa_L = \text{const}$). This is observed experimentally (fig. 129). [At

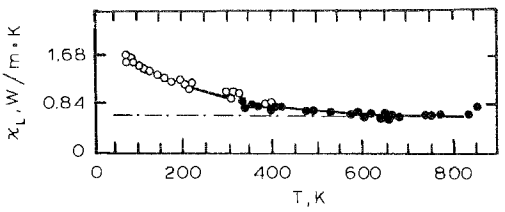

Fig. 129. The temperature dependence of κ_L for Sm_3S_4 (Türkes et al. 1986). Points show measurements for different experimental sets.

the highest temperatures, when $l \simeq \lambda$, $\kappa_L(T)$ is probably influenced by the effect of "minimal thermal conductivity" (Slack 1979).]

Ytterbium hydride YbH_x $(2 < x < 3)$ also belongs to the compounds with inhomogeneous variable valency of the lanthanide ions. In YbH_x there are different ions, Yb^{2+} and Yb^{3+} in the ratio 1:2 (Smirnov et al. 1992b). YbH_x has a face centred cubic lattice. κ_e is small over the entire temperature range investigated, so $\kappa_{tot} = \kappa_L$. but YbH_x differs from Sm_3S_4 having besides the A- and B-type defects a rather large concentration of vacancies in the hydrogen sublattice (let us call them C-type defects). The concentration of hydrogen vacancies decreases as x varies from 2 to 3 (at $x = 2$ it is $\simeq 33\%$, at $x = 3$ it is 0). Figure 130 shows the $\kappa_L(T)$ dependence for the two compounds from the system YbH_x with $x = 2.41$ and 2.57. The vacancy (C-type defect) concentrations are, respectively, ~ 20 and $\sim 14\%$. One can see that the value and the temperature dependence of $\kappa_L(T)$ (at low temperatures $\kappa_L \propto T^{1.4-1.6}$) is similar to $\kappa_L(T)$ of classical insulating glasses (see fig. 129). Thus, only the combined influence of the three types of defects (A, B and C) results in the full "amorphisation" of $\kappa_L(T)$. When the concentration of C-type defects decreases, κ_L of YbH_x increases and tends toward κ_L of Sm_3S_4 (curve 4 in fig. 130).

Data on $\rho(T)$ and $\alpha(T)$ of YbH_x compositions support the above conclusion of "amorphisation" as well. There are many experiments showing the "amorphous" character in the thermal conductivity behaviour in some temperature regions, but we cannot discuss them because of space limitations on this review.

This section was devoted to the thermal conductivity of rare earth glasses with

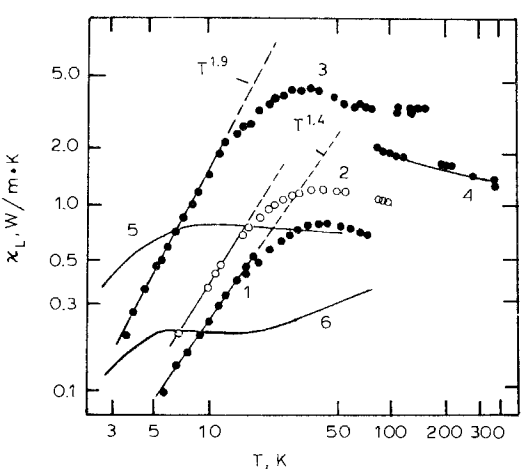

Fig. 130. The temperature dependence κ_L for YbH_x with $x = 2.41$ (1), 2.57 (2) and 2.63 (3) (Andres et al. 1984) (phonons are scattered by defects of A, B and C type), for Sm_3S_4 (4) (Türkes et al. 1986) (phonons are scattered by defects of A and B type), for the glasses $La_2S_3(Ga_2O_3)_2$ (5) and LaP_5O_{14} (6) (see fig. 125).

different distortions of the crystal structure (so-called crystal inhomogeneities). In section 4 the thermal conductivity of spin glasses with magnetic inhomogeneities has been discussed.

10. Thermal conductivity of rare earth compounds at high temperatures

Up to now the discussion of the thermal conductivity of rare earth compounds has been primarily devoted to low and superlow temperatures. The thermal conductivity of rare earth compounds at medium and high temperatures has been discussed partly in the sections devoted to glasses (section 9) and to phonon scattering by lanthanide ions (section 6). In this section we consider the behaviour of κ of these materials at high temperatures, i.e. at $T \geqslant \Theta$. Unfortunately, for many of these experiments the measurements have not been exact enough, and the samples have been of poor quality, because the main purpose of the measurements has been for technical applications. For this reason it is necessary to carry out complex purposeful investigations of the thermal conductivity on samples of high quality at high temperatures. Optical phonons can contribute to κ_L (or decrease κ_L due to additional phonon scattering) in this temperature region. κ_L can vary due to a change in the sample volume with temperature. "Amorphisation" of κ_L is also observed when one reaches the conditions for "minimal thermal conductivity" (see section 9).

In the high-temperature region one can expect peculiarities of κ_e due to variation of the Lorentz number near an electron zone boundary of a material (see section 2) and to other scattering mechanisms of electrons. Peculiarities can arise in κ_{tot} due to bipolar, photon and exciton contributions and possible heat transport by induced vacancy diffusion. Known experimental data on κ of rare earth compounds confirm the regularities observed in other types of materials. However, many effects are original, have their own distinctive features. We will separate these results into two groups:

(1) experimental data, and

(2) interesting possible effects which have not yet been observed experimentally.

10.1. *Phonon spectrum peculiarities and κ_L of rare earth compounds*

Phonon spectra of compounds with rare earth ions with intermediate valency exhibit anomalies (Mook and Holtzberg 1981, Mook and Nicklow 1978, Alekseev et al. 1989, Kikoin and Mishchenko 1988) which are capable of affecting the behaviour of $\kappa_L(T)$ at medium and high temperatures, but, unfortunately, such experiments have not yet been carried out. Let us consider, for example, features of the phonon spectra of $Sm_{0.75}Y_{0.25}S$ (Mook and Holtzberg 1981, Mook and Nicklow 1978) and SmB_6 (Alekseev et al. 1989), which are typical representatives of compounds with intermediate valency (figs. 131b, 132b). In these compounds:

(1) the longitudinal acoustic (along [111] in both compounds) and optical (in $Sm_{0.75}Y_{0.25}S$) modes are strongly softened (compare spectra a and b in figs. 131 and 132) (in all known crystals LA-phonons have higher energy than TA-phonons near

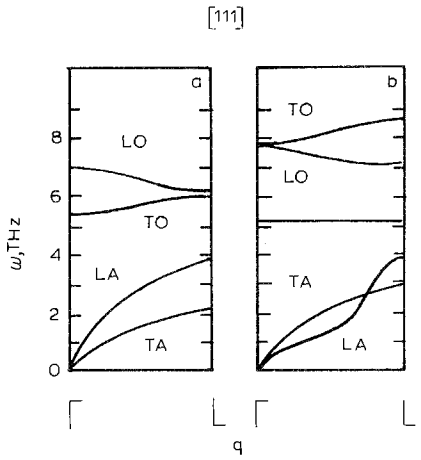

Fig. 131. Phonon spectra (a) of semiconducting SmS and (b) of $Sm_{0.75}Y_{0.25}$ (Mook and Holtzberg 1981, Mook and Nicklow 1978, Kikoin and Mishchenko 1988).

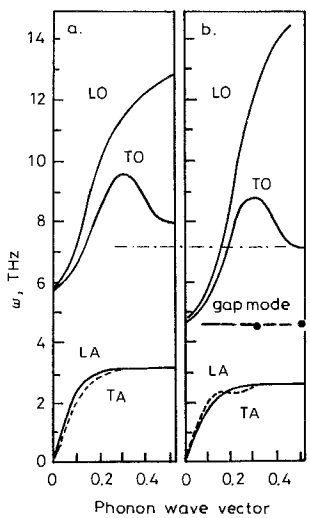

Fig. 132. Phonon spectra (a) of LaSb and (b) of SmB_6 (Alekseev et al. 1989).

the zone centre. The LO mode of $Sm_{0.75}Y_{0.25}S$ has a lower energy than the TO mode over the entire Brillouin zone (Mook and Nicklow 1978, Mook and Holtzberg 1981). This is rather unusual – such an effect has been observed only in $Sm_{0.75}Y_{0.25}S$ (Mook and Holtzberg 1981, Mook and Nicklow 1978) and YbS (Roedhammer et al. 1978).

(2) In both compounds a nondispersive mode arises between LA and LO modes (figs. 131b and 132b). Alekseev et al. (1989) and Kikoin and Mishchenko (1988) have suggested that this mode is typical for compounds with intermediate valency of the lanthanide ions. Mook and Nicklow (1978), on the other hand, have contended that this mode is connected with local vibrations of the Y ions.

The above noted features of the phonon spectra must manifest themselves in both

the magnitude and the temperature dependence of κ_L. Let us hope that future experiments will prove this supposition.

The hexaborides of the rare earth elements show interesting properties. RB_6 crystallizes in the CaB_6 structure, where the cations and the B6-octahedrons form a lattice of CsCl-type (fig. 133). In such a lattice two Debye temperatures are observed: a low-temperature one ($\Theta_1 \simeq 150$ K) connected with the "soft" metal sublattice and a high-temperature one ($\Theta \simeq 600$ K) related to the "hard" boron sublattice (Paderno et al. 1991, Schell et al. 1982, Smith et al. 1985, Takegahara and Kasuya 1985, Peysson et al. 1986a, Klochkov and Shvarzman 1982, Korsukova et al. 1987). The vibrations of the lattices depend upon each other. The phonon spectra of RB_6 have some peculiarities (see, e.g., fig. 132) (Alekseev et al. 1989, Paderno et al. 1991, Schell et al. 1982, Smith et al. 1985, Takegahara and Kasuya 1985, Peysson et al. 1986a). The principal one is the nondispersive behaviour of the LA and TA modes at energies higher than $\simeq 150$ K. All this can be reflected in the $\kappa_L(T)$ behaviour. Impurities and defects can decrease κ_L significantly at low and medium temperatures, because they are scattered, mainly, by long-wavelength phonons; and the short-wavelength acoustic phonons do not transport heat, since their group velocity $\partial\omega/\partial q \simeq 0$ (see figs. 131 and 132). This has been proven experimentally for SmB_6 (Konovalova et al. 1984) and for LaB_6 (Neshpor et al. 1976). Figure 134 shows, as an example, data on κ_L of single crystal and polycrystalline samples of SmB_6. It is difficult to say now which phonons are responsible for κ_L in RB_6 at high temperatures (Konovalova et al. 1984, Neshpor et al. 1976, Tanaka 1974, Markov et al. 1978, Aivazov et al. 1979, 1980, Bryushkova et al. 1985). κ_L is rather high in RB_6 at high temperatures. For example, $\kappa_L \simeq 15$ W/m K in LaB_6 at 1300 K (Tanaka 1974).

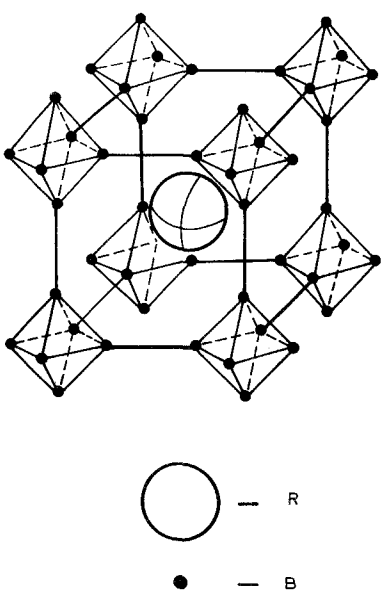

Fig. 133. Crystal structure of RB_6.

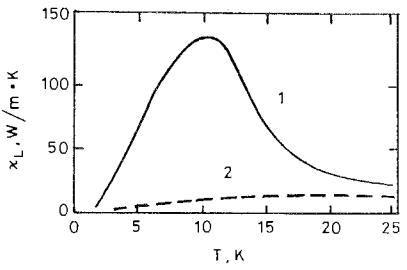

Fig. 134. The temperature dependence of κ_L for single crystal (1) and polycrystalline (2) samples of SmB_6 (Konovalova et al. 1984).

One could suppose a contribution of the optical phonons to κ_L at high temperatures (Slack 1979, Devyatkova and Smirnov 1962), but this is not too likely.

It is possible that in RB_6 there are two types of phonon spectra due to the presence of two sublattices: the "low-temperature" spectrum (connected with metal atoms) and the "high-temperature" spectrum (connected with boron atoms). The boron sublattice vibrations give an insignificant contribution to κ_L at low temperatures. However, this contribution becomes the main one at high temperatures. Unfortunately, it is difficult to draw from the literature data a simple conclusion about the influence of the different sublattices in RB_6 on κ_L, because measurements of the thermal conductivity have been carried out often on poorly characterised samples over narrow temperature intervals. Difficulties also arise in the separation of κ_L from the experimental κ_{tot}.

10.2. *Phonon–electron scattering at $T \geqslant \Theta$*

Only phonons with q less than $2k$ (k is the absolute value of the electron wave vector) can interact with electrons. In nondegenerate semiconductors the wave vector of most electrons is much smaller than the wave vector of the thermal phonons at not very low temperatures. Therefore, only the longest-wavelength phonons can interact with electrons giving rise to a small contribution to the thermal conductivity.

The electron wave vectors at the Fermi level in metals are more likely, rather than the wave vectors of phonons, to make a significant contribution to the heat transport. These phonons can interact with electrons, and thus, an effect of phonon–electron scattering is to be expected in metals at all temperatures. One fails, however, to observe phonon–electron scattering in pure metals at high temperatures because of the complexity of the κ_L separation. One can separate κ_e and κ_L and observe phonon–electron scattering in rare earth metals and metal-like compounds which contain rare earth elements, due to the low mobility of electrons which increases ρ considerably and hence decreases κ_e) (Oskotski and Smirnov 1971, Khusnutdinova et al. 1971, Luguev et al. 1975a).

Let us consider, as an example, $\kappa_L(T)$ of the model system La_3Te_4–La_2Te_3 (or otherwise $LaTe_x$ with $1.33 \leqslant x \leqslant 1.5$) (Luguev et al. 1975) (this system has been considered already to some extent in section 6). κ_L is separated from κ_{tot} by the standard method (Oskotski and Smirnov 1972, Luguev et al. 1975a). κ_L of this system presents a surprise again (as noted in section 6). One might expect a decrease of κ_L

with variation of the composition from $LaTe_{1.33}$ to $LaTe_{1.5}$, due to an increase in the number of vacancies in the La lattice. However, the opposite is observed (fig. 135). One can explain the unusual behaviour of $\kappa_L(x)$ in this system only by considering additional phonon–electron scattering. Figure 136 shows the dependence of the thermal resistance of the crystal lattice, $W_L = 1/\kappa_L$, on temperature for three compositions of the $LaTe_x$ system. A calculation has been carried out on the basis of the Callaway (1959) model. One can see that due to phonon–electron scattering κ_L of $LaTe_{1.33}$ (and nearby compositions) is smaller than κ_L of $LaTe_{1.5}$ (fig. 135).

We note that the minimum of κ_L (in isotherms of $\kappa_L(x)$) in the $LaTe_x$ system is smoothed out as temperature increases and the phonon–electron scattering decreases compared to other scattering mechanisms (Oskotski and Smirnov 1972, Luguev et al. 1975a).

A large contribution to W_L from phonon–electron scattering is observed in LaS and GdS up to ~ 700 K (Khusnutdinova et al. 1971).

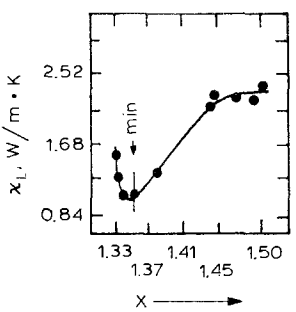

Fig. 135. The temperature dependence of κ_L for the system $LaTe_x$ ($1.33 \leqslant x \leqslant 1.5$) (Luguev et al. 1975a). $T = 100$ K.

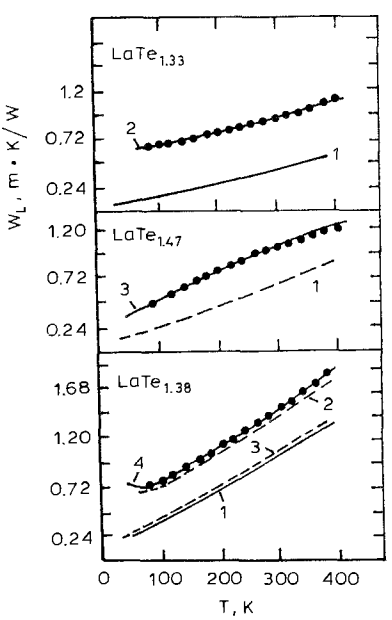

Fig. 136. The temperature dependence of the lattice thermal resistance, $W_L = 1/\kappa_L$, in $LaTe_{1.33}$, $LaTe_{1.47}$ and $LaTe_{1.38}$. Solid lines are the result of calculation, points of experiment. The phonon scattering processes considered in the calculations are: (1) phonons by phonons, (2) phonons by phonons plus phonons by electrons, (3) phonons by phonons plus phonons by defects, (4) phonons by phonons plus phonons by electrons plus phonons by defects.

10.3. κ_e *of rare earth compounds at high temperatures*

As has been noted in section 2, one can obtain from an analysis of data on κ_e information about scattering mechanisms of electrons in a material, the electron spectrum, and so on. Let us consider some examples of such an analysis in the high-temperature region. Difficulties arise in the separation of κ_L and κ_e from κ_{tot} for metals and metal-like rare earth materials. At $T > \Theta$ one usually supposes $L = L_0$ and calculates κ_e by the Wiedemann–Franz law. However, because of a large κ_e value and a small κ_L value both estimated contributions have large errors associated with them. Over the last thirty years a great number of measurements at high temperatures have been carried out on the hexaborides of rare earth elements and their solid solutions (Neshpor et al. 1976, Tanaka 1974, Markov et al. 1978, Aivazov et al. 1979, 1980, L'vov et al. 1963, 1965, Samsonov et al. 1975, Samsonov 1964). [The thermal conductivity of hexaborides has been measured at low temperatures by Konovalova et al. (1984), Flachbart et al. (1982a, b) and Peysson et al. (1985, 1986c).] The problem of separation of κ_e and κ_L arises in this case as well.

Bryushkova et al. (1985) have carried out an evaluation of the L/L_0 ratio for the hexaborides and their solid solutions for temperatures from 300 to 2000 K. The classical method of separation of κ_e and κ_L by analysis of the dependence $\kappa_{tot} = f(\sigma)$ (σ is the electrical conductivity, $\sigma = 1/\rho$) at constant temperature has been used (Smirnov and Tamarchenko 1977). Such an evaluation has been completed for RB_6 (fig. 137) and the solid solutions $La_xEu_{1-x}B_6$ and $La_xGd_{1-x}B_6$ (fig. 138). One can determine L/L_0 of $La_xGd_{1-x}B_6$ in the temperature region 1000–2000 K using data on $\kappa_{tot}(T)$ (fig. 139) and ρ (fig. 140) (see also fig. 141). The ratio L/L_0 is smaller than one between 300 and 1500 K. This is probably connected with inelastic scattering of carriers by optical vibrations of the crystal lattice. The resultant dependence $L(T)/L_0$ is typical for metals with a large Θ value (see section 2). Data of Neshpor et al. (1976) seem to contradict the above ideas on $L(T)/L_0$.

More interesting results are obtained from an analysis of κ_e of rare earth compounds carried out for the sake of determining the features of the electron zone

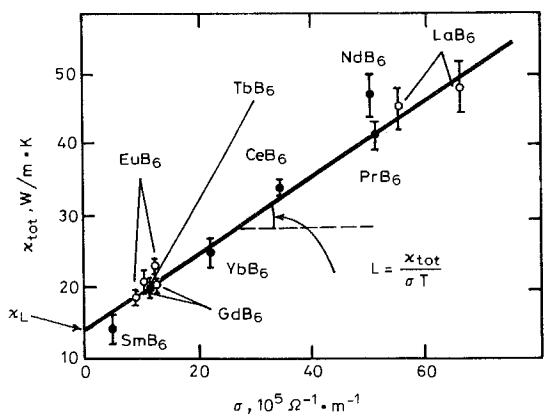

Fig. 137. κ_{tot} for RB_6 as a function of σ at 300 K (Bryushkova et al. 1985). $\kappa_{tot} = \kappa_L + L\sigma T$.

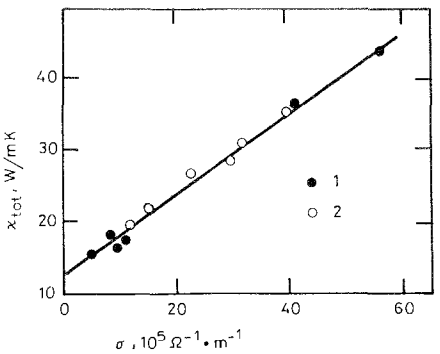

Fig. 138. κ_{tot} as a function of σ for $La_xEu_{1-x}B_6$ (1) and $La_xGd_{1-x}B_6$ (2) at $T = 300$ K (Bryushkova et al. 1985).

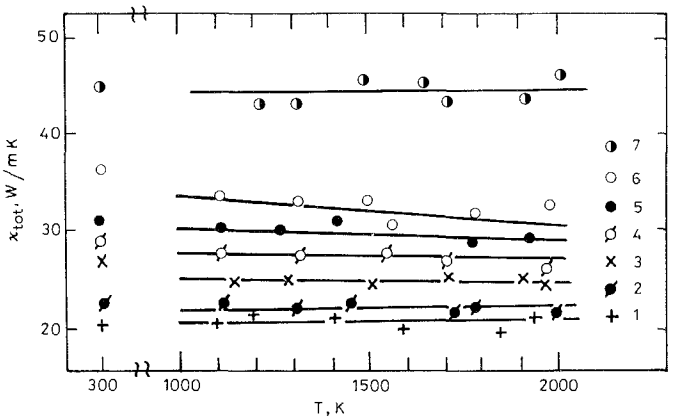

Fig. 139. The temperature dependence of κ_{tot} for $La_xGd_{1-x}B_6$ at $x = 0$ (1), 0.1 (2), 0.3 (3), 0.5 (4), 0.7 (5), 0.9 (6), 1 (7) (Bryushkova et al. 1985).

boundary in SmS (Shadrichev et al. 1976, Oskotski and Smirnov 1977, Sergeeva et al. 1972), in Ce_3Se_4, Nd_3S_4 (Smirnov et al. 1972), in GdS, ErS (Vasil'ev et al. 1975) and in LaSb (Goncharova et al. 1968). Let us consider data on the thermal conductivity of semiconducting n-type SmS (Shadrichev et al. 1976, Oskotski and Smirnov 1977, Zhuze et al. 1973, Smirnov 1972). Unfortunately, the data on κ of SmS and a number of its solid solution alloys obtained at low temperatures ($T < 100$ K) (Benbachir et al. 1985), do not give any information on the material parameters.

SmS (crystal structure of NaCl-type) has a homogeneity region, approximately, from 50 to 54 at% Sm, which does not extend to the S-side (Oskotski and Smirnov 1977, Zhuze et al. 1973, Smirnov 1972) where it changes from a semiconductor to a semimetal (figs. 142a, b). With increasing temperature the Fermi level in SmS can change its position and "scan" the conduction band. If the conduction band in SmS is complex [which consists of s- and d-subbands (see Golubkov et al. 1973), and the s-subband is lower than the d-subband], then the Lorentz number undergoes sharp changes as the Fermi level approaches the bottom of the d-band. This can lead to increasing as well as decreasing L/L_0 values (see section 2). Oskotski and Smirnov

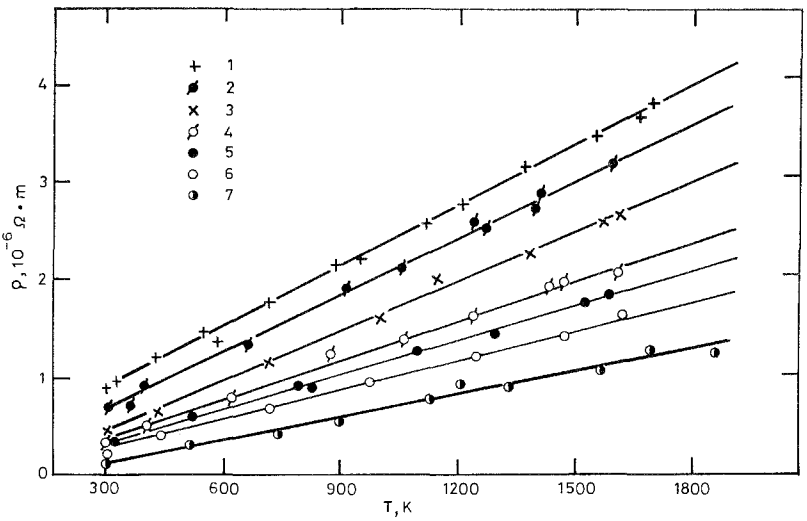

Fig. 140. The temperature dependence of ρ for $La_xGd_{1-x}B_6$ at various x. Designations (1)–(7) see the figure caption of fig. 139.

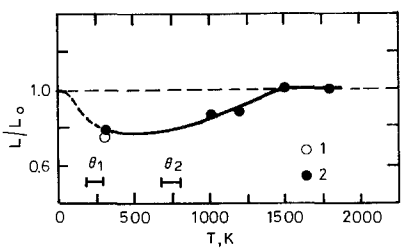

Fig. 141. The temperature dependence of the ratio L/L_0 for the hexaborides of lanthanides (1) and the solid solution alloy $La_xGd_{1-x}B_6$ (2). Θ_1 and Θ_2 are the two Debye temperatures.

(1977) have carried out an analysis of $\kappa_e(T)$ for two samples of SmS from the homogeneity region (figs.142b, c). Experimental values of L (see fig. 143a) have been calculated by using the equation

$$L_{exp} = (\kappa_{tot} - 1/W_L^0)/\sigma T, \tag{52}$$

where κ_{tot} and σ are measured experimentally, W_L^0 is determined by extrapolation of W_L from the low-temperature region $T < 300$ K (fig. 142c) to the high-temperature region. Curve 1 of fig. 142c is calculated for all temperatures by

$$W_L = 1/(\kappa_{tot} - L\sigma T), \tag{53}$$

where L is determined by standard formulae for the single-band model (taking into account the electron gas degeneration) for the scattering of carriers by acoustic vibrations of the crystal lattice (Oskotski and Smirnov 1972, 1977, Smirnov and Tamarchenko 1977). According to Oskotski and Smirnov (1977) a deviation of the W_L values from W_L^0 at $T > 300$ K can be attributed to neglecting the interband scattering. The L_{exp} value (fig. 143a) can only be explained by interband scattering

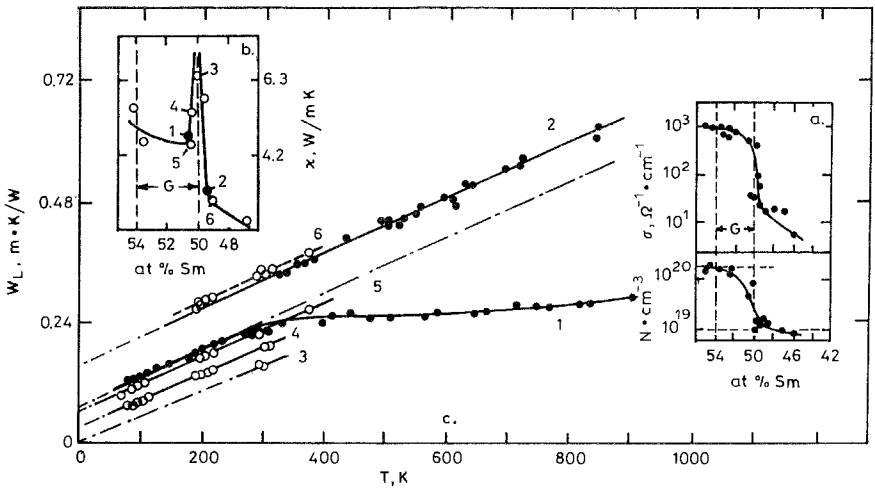

Fig. 142. The dependence on the Sm concentration of the electrical conductivity σ and the current carrier concentration n (a), κ_L (b) and W_L (c) in the homogeneity region of SmS, where 1 through 6 are the sample numbers. (a) and (b) are the result of measurements at 300 K (Shadrichev et al. 1976, Oskotski and Smirnov 1977, Zhuze et al. 1973, Smirnov 1972). The interval G gives the homogeneity limits.

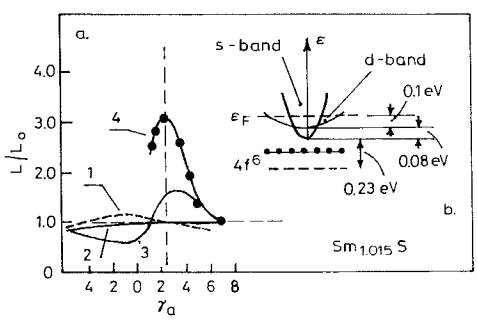

Fig. 143. (a) Dependence of L/L_0 on γ for the sample $Sm_{1.015}S$ (Shadrichev et al. 1976, Oskotski and Smirnov 1977, Zhuze et al. 1973). Curve 1: calculation for a model with the heavy-electron band lower than the light-electron band (here the interband interaction does not influence L/L_0). Curves 2 and 3: calculation for a model with the light-electron band lower than the heavy-electron band (2 without and 3 with the interband interaction taken into account). Curve 4: experimental data. (b) Schematic shape of the conduction band of $Sm_{1.015}S$. Solid circles give impurity levels. Values of energy distances have been obtained from analysis of data on κ_L (Shadrichev et al. 1976).

of electrons from the "light" lower s-band into the "heavy" upper d-band. The Fermi level lies in the d-band. The theoretical L/L_0 ratio (fig. 143a) depends upon the parameter S (see section 2, eq. (17)). Curve 3 in fig. 143a is calculated with $S = 8$. For the experimental L/L_0 value to agree with the theoretical one it is necessary to take a larger S value.

10.4. *Other effects*

We will now consider some effects in the κ of rare earth compounds, some of which have already been observed, others will probably be seen in later experiments in the high-temperature region. A theoretical analysis of experimental data has been carried out in the Callaway model for κ_L and GdS and LaS (crystal lattice of the NaCl-type) in the temperature region 300–800 K taking into account the contribution to the heat transport from longitudinal and transverse acoustic modes (Dubey 1981, Al-Edani and Dubey 1986). In GdS and LaS, as in other compounds with NaCl-structure (Singh and Verma 1972), heat is transported, mainly, by the transverse acoustic phonons. Slack (1979) has shown that κ_L of solids at high temperatures can significantly depend on a volume variation. This conclusion has been proven experimentally many times in solid Ar, Ne, Kr and Xe [comparative measurements have been carried out at constant pressure and constant volume (Clayton and Batchelder 1973, Weston and Daniels 1984)]. Anomalous volume variations have been observed in a number of rare earth compounds either at phase transitions [e.g., in SmS at a hydrostatic pressure of $\simeq 6.5$ kbar at 300 K (Smirnov and Oskotski 1978)] or over a wide enough temperature interval [e.g., in $Sm_{0.83}Gd_{0.17}S$, where the lattice constant changes from 5.7 to 5.83 Å in the temperature interval 300–900 K (Jayaraman et al. 1975)]. Unfortunately, experiments on the influence of a volume variation on κ_L in rare earth compounds have not been carried out yet.

The photon contribution κ_{phot} can give a significant contribution to κ_{tot} in semitransparent (or transparent) IR-radiation materials. Hence, it is necessary to be convinced that κ_{phot} is absent, before an analysis of the possible heat transport contributions by vacancies, excitons and so on is made. This makes the conclusions of Pillai and George (1988, 1991) connecting an additional thermal conductivity of $RCoO_3$ (R = La, Nd, Gd) in the temperature range 300–1100 K with the exciton contribution, κ_{exc}, somewhat tentative, because the κ_{phot} contribution has not been considered. The thermal conductivity of PrF_3, LaF_3, $LaF_3 + Nd^{3+}$ single crystals have been measured between 300 and 1400 K by Remizova (1975, 1978). These materials are transparent in the IR part of the spectrum [e.g., LaF_3 is fully transparent between 0.13 and 13 μm (Remizova 1978)]. An experimental and theoretical evaluation of κ_{phot} is given. κ_{phot} gives the major contribution to κ_{tot} (e.g., at 1400 K κ_{phot} is $\simeq 85\%$ of κ_{tot} in LaF_3). However, an additional thermal conductivity remains after subtraction of κ_{phot} and κ_L from κ_{tot}. Remizova (1975, 1978) explains its origin by the ionic conductivity of F^- ions, which have a high mobility due to a great number of defects (Sher et al. 1966). It seems more realistic to explain the additional thermal conductivity in LaF_3 and PrF_3 by vacancy heat transport (Zinov'ev and Masharov 1973, Strzhemechny and Kalnoy 1983), because (as has been noted above) there are a great number of Schottky defects in these compounds with the concentration increasing with temperature (Sher et al. 1966). Heat transport by vacancies has been observed in the premelting region in solid Kr and Ar by Bondarenko et al. (1982) and in Pt by Zinov'ev et al. (1968) and Slack (1964).

11. Conclusion

Investigation of the thermal conductivity of RECs has contributed much new information, and thus extended our knowledge on the thermal conductivity of solids as a separate scientific branch of solid state physics. This new information is obtained because of the specific influence of the 4f-levels of the lanthanide ions on κ. The limited size of this review does not allow us to discuss the κ of a large group of RECs introduced into technological applications over the last few years. These are: medium and high-temperature thermoelectric materials, hydrogen absorbers, laser materials, new materials for powerful tiny magnets, new luminescent materials, oxides, coating materials, superlow-temperature materials and so on. The κ of some of the materials listed above has been considered in this review when discussing certain thermal conductivity effects. Other topics not fully reviewed include numerous works on the thermal conductivity of the high-temperature superconductors, and papers devoted to the thermal conductivity of elementary rare earth metals.

In the process of writing this review it has become clear that the many-sided theoretical interpretations and critical analyses of the published data demand a new extensive review.

The investigation of the thermal conductivity of the rare earth compounds is still far from completion. There are many interesting problems and mysteries awaiting solutions.

References

Aivazov, M.I., T.I. Bryushkova, V.S. Mkrtchyan and V.A. Rubanov, 1979, Tekh. Vys. Temp. **17**, 330.

Aivazov, M.I., S.B. Aleksandrovich, T.I. Bryushkova, V.S. Mkrtchyan and V.A. Rubanov, 1980, Tekh. Vys. Temp. **18**, 429.

Al-Edani, M.C., and K.S. Dubey, 1986, Phys. Status Solidi b **137**, 449.

Alekseev, P.A., A.S. Ivanov, B. Dorner, H. Shober, K.A. Kikoin, E.S. Konovalova, A.S. Mishchenko, V.N. Lazukov, Y.B. Paderno, A.Y. Rumyantsev and I.P. Sadikov, 1989, Europhys. Lett. **10**, 457.

Alekseevski, N.E., A.V. Mishin, A.S. Rudenko and A.A. Sorokin, 1986, Pis'ma Zh. Eksp. & Teor. Fiz. **43**, 533.

Amato, A., D. Jaccard, J. Sierro, P. Haen, P. Lejay and J. Flouquet, 1989, J. Low Temp. Phys. **77**, 195.

Andersen, H.N., P.E. Gregers-Hansen, E. Holm, H. Smith and O. Vogt, 1974, Phys. Rev. Lett. **32**, 1321.

Anderson, P.W., B.I. Halperin and C.M. Varma, 1972, Philos. Mag. **25**, 1.

Andres, E.E., I.V. Volchok, A.I. Zvyagin and S.V. Startsev, 1984, Fiz. Nizk. Temp. **10**, 398.

Andres, E.E., I.V. Volchok, A.I. Zvyagin, V.B. Kokshenev and S.V. Startsev, 1985, Fiz. Nizk. Temp. **11**, 769.

Andres, K., J.E. Graebner and H.R. Ott, 1975, Phys. Rev. Lett. **35**, 1779.

Arsen'ev, P.A., L.M. Kovba, Kh.S. Bagdasarov, B.F. Dzhurinski, A.V. Potemkin, B.I. Pokrovski, F.M. Spiridonov, V.A. Antonov and V.V. Ilyukhin, 1983, Rare Earth Compounds (Systems with Oxides of I–III Elements) (Nauka, Moscow) p. 278. In Russian.

Arsen'ev, P.A., V.B. Glushkova, A.A. Evdokimov, E.K. Keller, V.B. Kravchenko, M.V. Kravchinskaya, V.A. Krzhizhanovskaya, A.K. Kuznetsov, Kh.M. Kurbanov, A.V. Potemkin, P.A. Tikhonov and M.N. Tsnitlin, 1985, Rare Earth Compounds (Zirconates, Hafnates, Niobates, Tantalates, Antimonates) (Nauka, Moscow) p. 270. In Russian.

Arutyunyan, S.R., Kh.S. Bagdasarov, A.P. Dodokin and A.M. Kevorkov, 1984, Kvant. Elektron. **11**, 1284.

Arutyunyan, S.R., Kh.S. Bagdasarov, A.P. Dodokin and A.M. Kevorkov, 1986, Fiz. Tverd. Tela **28**, 957.

Arutyunyan, S.R., Kh.S. Bagdasarov, A.P. Dodokin and A.M. Kevorkov, 1987, Fiz. Tverd. Tela **29**, 1874.

Arzoumanian, C., A.M. de Goër, B. Salce and F. Holtzberg, 1983, J. Phys. (Paris) Lett. **44**, L39.

Arzoumanian, C., B. Salce, A.M. de Goër and F. Holtzberg, 1984, in: Phonon Scattering in Condensed Matter, eds W. Eisenwenger, K. Laßman and S. Döttinger (Springer, Berlin) p. 460.

Ayache, C., M. Raki, B. Salce, D. Schmitt, A.K. Bhattacharjee and B. Coqblin, 1988, J. Phys. Colloq. (Paris) **49**, C8-791.

Barbara, B., J.X. Boucherle, J.L. Buevoz, M.F. Rossignol and J. Schweizer, 1977, Solid State Commun. **24**, 481.

Bardeen, J., G. Rickayzen and L. Tewordt, 1959, Phys. Rev. **113**, 982.

Barilo, S.N., S.P. Ges, L.E. Soshnikov and T.V. Smirnova, 1984, Phys. Status Solidi b **122**, 47.

Bauer, E., E. Gratz and G. Adam, 1985a, in: Proc. Conf. on Electronic Structure and Properties of Rare Earths and Actinide Intermetallics, eds G. Helscher, G. Wiesinger, E. Gratz, C. Schmitzer, P. Weinberger and R. Grösssinger (North-Holland, Amsterdam) pp. 81–83.

Bauer, E., E. Gratz, H. Kirchmayr, N. Pillmayr and H. Novotny, 1985b, J. Less-Common Met. **111**, 369.

Bauer, E., E. Gratz and G. Adam, 1986, J. Phys. F **16**, 493.

Bauer, E., E. Gratz and Y. Peysson, 1987, J. Magn. & Magn. Mater. **63–64**, 303.

Belitsky, V.I., and A.V. Goltsev, 1991, Physica B **172**, 459.

Belov, K.P., 1972, Ferrits in High Magnetic Fields (Nauka, Moscow). In Russian.

Belov, K.P., A.K. Zvezdin, A.M. Kadomtseva and R.Z. Levitin, 1976, Usp. Fiz. Nauk **119**, 447.

Belov, K.P., A.K. Zvezdin, A.M. Kadomtseva and R.Z. Levitin, 1979, Orientational Transitions in Rare Earth Magnetics (Nauka, Moscow). In Russian.

Benbachir, K., J. Mazuer and J.P. Senateur, 1985, Solid State Commun. **54**, 965.

Berezin, A.A., O.A. Golikova, M.M. Kazanin, T. Khomidov, D.N. Mirlin, A.V. Petrov, U.S. Umarov and V.K. Zaitsev, 1974, J. Non-Cryst. Solids **16**, 237.

Berman, R., 1976, Thermal Conductivity in Solids (Clarendon Press, Oxford).

Berth, S., H.R. Ott, F.N. Gydax, B. Hitti, E. Lippelt, A. Schenck, C. Baines, B. van den Brandt, T. Konter and S. Mango, 1987, Phys. Rev. Lett. **59**, 2991.

Bhattacharjee, A.K., and B. Coqblin, 1982, in: Crystalline Electric Field Effect in f-Electron Magnetism (Plenum, New York) p. 1.

Bhattacharjee, A.K., and B. Coqblin, 1988, Phys. Rev. B **38**, 338.

Bhattacharjee, A.K., B. Coqblin, M. Raki, L. Forro, C. Ayache and D. Schmitt, 1989, J. Phys. (Paris) **50**, 2781.

Bishop, D.J., C.M. Varma, B. Batlogg, E. Bucher, Z. Fisk and J.L. Smith, 1984, Phys. Rev. Lett. **53**, 1009.

Blackman, M., 1935, Philos. Mag. **19**, 989.

Bloch, J.M., and D. Davidov, 1982, Phys. Rev. B **26**, 3631.

Bondar', I.A., N.V. Vinogradova and L.N. Dem'yanets, Zh.A. Ezhova, V.V. Ilyukhin, V.Yu. Kara–Ushanov, L.N. Komissarova, E.V. Lazarevski, B.N. Litvin, P.P. Mel'nikov, D.A. Murashov, V.M. Orlovski, K.K. Palkina, M.A. Petrova, I.A. Rozanov, N.N. Chudinova and A.A. Fotier, 1983, Rare Earth Compounds (Silicates, Germanates, Phosphates, Arsenates, Vanadates) (Nauka, Moscow) p. 284. In Russian.

Bondarenko, A.I., V.G. Manzhely, V.A. Popov, M.A. Strzhemechny and V.G. Gavrilko, 1982, Fiz. Nizk. Temp. **8**, 1215.

Brück, E., A. Nowack, N. Hohn, H. Paulus and A. Freimuth, 1986, Z. Phys. B **63**, 1.

Bryushkova, T.I., B.A. Merisov and V.S. Mkrtchyan, 1985, Tekh. Vys. Temp **23**, 1016.

Buchelnikov, V.D., Yu.A. Kuzavko and V.G. Shavrov, 1987, Fiz. Nizk. Temp. **13**, 1074.

Bucher, E., J.P. Maita and A.S. Cooper, 1972, Phys. Rev. B **6**, 2709.

Buzdin, A.I., and V.V. Moshchalkov, 1986, Exotic Superconductors (Znanie, Moscow) p. 64. In Russian.

Buzdin, A.I., L.N. Bulaevski, M.L. Kulich and S.V. Panyukov, 1984, Usp. Fiz. Nauk **144**, 597.

Cahill, D.G., H.E. Fischer, S.K. Watson, R.O. Pohl and G.A. Slack, 1989, Phys. Rev. B **40**, 3254.

Callaway, J., 1959, Phys. Rev. **113**, 1046.

Charap, S.N., 1964, Phys. Rev. Lett. **13**, 237.

Clark, W.G., Z. Fisk, K. Glover, M.D. Lan, D.E. Mac Laughlin, J.L. Smith and C. Tien, 1984, in: Proc. LT-17 Conference (North-Holland, Amsterdam) p. 227.

Clayton, F., and D.N. Batchelder, 1973, J. Phys. C **6**, 1213.

Cooke, A.J., S.J. Swithenby and M.R. Wells, 1972, Solid State Commun. **10**, 265.

Coornut, B., and B. Coqblin, 1972, Phys. Rev. B **5**, 4541.

Cox, D.L., and N. Grewe, 1988, Z. Phys. B **71**, 321.

Daudin, B., and B. Salce, 1982, J. Phys. C **15**, 463.

Daudin, B., A.M. de Göer and S.H. Smith, 1980, in: Phonon Scattering in Condensed Matter, ed. H.J. Maris (Plenum, New York) p. 93.

Daudin, B., R. Lagnier and B. Salce, 1981a, J. Magn. & Magn. Mater. **25**, 197.

Daudin, B., B. Salce and S.H. Smith, 1981b, J. Phys. Colloq. (France) **42**, Suppl. 12, C6-277.

Daudin, B., W. Mutscheller and M. Wagner, 1984, Phys. Status Solidi b **122**, 73.

David, G., D.G. Cahill and R.O. Pohl, 1987, Phys. Rev. B **35**, 4067.

De Goër, A.M., 1986, in: Phonon Scattering in Condensed Matter, Vol. V, eds E.A. Anderson and J.P. Wolfe (Springer, Berlin) pp. 6–14.

De Goër, A.M., N. Devismes and B. Salce, 1986, in: Phonon Scattering in Condensed Matter, Vol. V, eds A.C. Anderson and J.P. Wolfe (Springer, Berlin) pp. 70–72.

De Visser, A., A. Menovsky and J.J.M. Franse, 1987, Physica B **147**, 80.

De Yoreo, J.J., R.O. Pohl and G. Burns, 1985, Phys. Rev. B **32**, 5780.

Dekker, A.J., 1965, J. Appl. Phys. **36**, 906.

Devyatkova, E.D., and I.A. Smirnov, 1962, Fiz. Tverd. Tela **4**, 2507.

Dixon, G.S., 1976, in: Phonon Scattering in Solids, eds L.J. Challis, V.W. Rampton and A.F.G. Wyatt (Plenum, New York) pp. 246–248.

Dixon, G.S., 1981, J. Phys. C **14**, 2147.

Dixon, G.S., and D.P. Landau, 1976, Phys. Rev. B **13**, 3121.

Dixon, G.S., J.J. Martin and N.D. Love, 1974, AIP Conf. Proc. **18**, 1073.

Dreyfus, B., N.C. Fernandes and R. Maynard, 1968, Phys. Rev. Lett. A **26**, 647.

Dubey, K.S., 1981, J. Thermal Anal. **20**, 447.

Ducastel, R., and G. Pitsi, 1986, Phys. Status Solidi b **134**, 799.

Durand, J., and S.J. Poon, 1979, J. Phys. Colloq. (Paris) C5-231.

Dzhabbarov, I., S.I. Ivanov, V.V. Medved, L.S. Parfen'eva and I.A. Smirnov, 1978, Fiz. Tverd. Tela **20**, 297.

Effantin, J.M., J. Rossat-Mignod, P. Burlet, H. Bartholin, S. Kunii and T. Kasuya, 1985, J. Magn. & Magn. Mater. **47–48**, 145.

Elliot, R.J., and J.B. Parkinson, 1967, Proc. Phys. Soc. **92**, 1024.

Fertig, W.A., D.C. Johnston, L.E. de Long, R.W. McCallum, M.P. Maple and B.T. Matthias, 1977, Phys. Rev. Lett. **38**, 987.

Fischer, H.E., S.K. Watson and D.G. Cahill, 1988, Comments Condens. Matter. Phys. **14**, 65.

Fischer, K.H., 1971, Phys. Status Solidi b **46**, 11.

Fischer, K.H., 1983, Phys. Status Solidi b **116**, 357.

Fischer, K.H., 1985, Phys. Status Solidi b **130**, 13.

Fischer, Ø., A. Treyvaud, R. Chevrel and W. Sergent, 1975, Solid State Commun. **17**, 721.

Fischer, Ø., M. Ishikawa, M. Pelizzone and A. Treyvaud, 1979, J. Phys. Colloq. (Paris) **40**, C5-89.

Flachbart, K., M. Reiffers, S. Janos, Y.B. Paderno, V.I. Azorenko and E.S. Konovalova, 1982a, J. Less-Common Met. **88**, L3.

Flachbart, K., M. Reiffers, S. Janos, Y.B. Paderno, V.I. Azorenko and E.S. Konovalova, 1982b, J. Less-Common Met. **88**, L11.

Florent'ev, V.V., A.V. Inyushkin, A.N. Taldenkov, O.K. Mel'nikov and A.B. Bykov, 1990, Sverkhprovodimost Fiz. Chim. Tekh. **3**, 2302.

Flouquet, J., P. Haen, C. Marcenat, P. Lejay, A. Amato, D. Jaccard and E. Walker, 1985, J. Magn. & Magn. Mater. **52**, 85.

Flouquet, J., P. Haen, F. Lapierre, D. Jaccard and G. Remenyl, 1986, J. Magn. & Magn. Mater. **54–57**, 322.

Franse, J.J.M., P.M. Frings, A. de Visser, A. Menovski, T.T.M. Palstra, P.M. Kes and J.A. Mydosh, 1984, Physica B **126**, 116.

Franse, J.J.M., A. Menovsky, A. de Visser, C.D. Bredl, U. Gottwick, W. Lieke, H.M. Mayer, U. Rauchschwalbe, G. Sparn and F. Steglich, 1985, Z. Phys. B **59**, 15.

Franz, W., A. Grießel, F. Steglich and D. Wohlleben, 1978, Z. Phys. B **31**, 7.

Franz, W., F. Steglich and D. Wohlleben, 1979, J. Phys. Colloq. (Paris) C5-40; C5-342.

Freeman, J.J., and A.C. Anderson, 1986, in: Phonon Scattering in Condensed Matter, Vol. V, eds A.C. Anderson and J.P. Wolfe (Springer, Berlin) pp. 32–34.

Friederich, A., and A. Fert, 1974, Phys. Rev. Lett. **33**, 1214.

Fulde, P., and I. Peschel, 1972, Adv. Phys. **21**, 1.

Galperin, Y.M., V.G. Karpov and V.N. Solov'ev, 1988, Fiz. Tverd. Tela **30**, 3636.
Gehring, G.A., and K.A. Gehring, 1975, Rep. Prog. Phys. **38**, 1.
Geilikman, B.T., 1958, Zh. Eksp. Teor. Fiz. **34**, 1042.
Geilikman, B.T., and B.Z. Kresin, 1958, Dokl. Akad. Nauk SSSR **123**, 259.
Geilikman, B.T., and B.Z. Kresin, 1959, Zh. Eksp. & Teor. Fiz. **36**, 959.
Geilikman, B.T., and B.Z. Kresin, 1972, Kinetic and Nonstationar Effects in Superconductors (Nauka, Moscow). In Russian.
Ginzburg, V.L., 1957, Sov. Phys.-JETP **4**, 153.
Ginzburg, V.L., 1989a, Pis'ma Zh. Eksp. & Teor. Fiz. **49**, 50.
Ginzburg, V.L., 1989b, J. Supercond. **2**, 323.
Golikova, O.A., and A. Tadzhiev, 1986, J. Non-Cryst. Solids **87**, 64.
Golikova, O.A., V.K. Zaitsev, N.M. Orlov, A.V. Petrov, L.S. Stil'bans and E.N. Tkalenko, 1974, Phys. Status Solidi a **21**, 405.
Golovenchits, E.I., and V.A. Sanina, 1982, Fiz. Tverd. Tela **24**, 375.
Golovenchits, E.I., V.A. Sanina and T.A. Shaplygina, 1981, Zh. Eksp. & Teor. Fiz. **80**, 1911.
Golubkov, A.V., E.V. Goncharova, V.P. Zhuze, G.M. Loginov, V.M. Sergeeva and I.A. Smirnov, 1973, Physical Properties of Rare Earth Chalcogenides (Nauka, Leningrad). In Russian.
Goncharova, E.V., V.P. Zhuze, V.V. Zhdanova, T.B. Zhukova, I.A. Smirnov and E.V. Shadrichev, 1968, Fiz. Tverd. Tela **10**, 1322.
Gratz, E., 1982, Phys. Scr. T **1**, 97.
Gratz, E., and H. Novotny, 1983, in: Proc. Int. Conf. on Magnetism of Rare Earths and Actinides, Bucharest, 1983, eds. E. Burzo and H. Rogalski, p. 17.
Gratz, E., and H. Novotny, 1985, Physica B **130**, 75.
Gratz, E., and M.J. Zuckermann, 1982a, J. Magn. & Magn. Mater. **29**, 181.
Gratz, E., and M.J. Zuckermann, 1982b, Transport Properties of Rare Earth Intermetallic Compounds, in: Handbook on the Physics and Chemistry of Rare Earths, Vol. 5, eds K.A. Gschneidner Jr and L. Eyring (North-Holland, Amsterdam) pp. 117–216.
Gratz, E., E. Bauer, B. Barbara, S. Zemirli, F. Steglich, C.D. Bredl and W. Lieke, 1985, J. Phys. F **15**, 1975.
Gratz, E., E. Bauer, H. Novotny, H. Müller, S. Zemirli and B. Barbara, 1987, J. Magn. & Magn. Mater. **63–64**, 200.
Gratz, E., N. Pillmayr, E. Bauer, H. Müller, B. Barbara and M. Loewenhaupt, 1990, J. Phys. Condens. Matter **2**, 1485.
Gudak, O., 1985, Pis'ma Zh. Eksp. & Teor. Fiz. **42**, 244.
Guertin, R.P., and S. Foner, 1978, Phys. Lett. A **68**, 116.
Guessons, A., and J. Mazuer, 1982, J. Phys. (Paris) Lett. **43**, L801.
Guittard, M., A.M. Loireau–Lorach, F. Berguer, S. Barnier and J. Flahaut, 1986, Mater. Res. Bull. **62**, 191.
Gurevich, V.L., 1959, Fiz. Tverd. Tela **1**, 147.
Hamaker, H.C., L.D. Woolf, H.B. Mac Kay, Z. Fisk and M.B. Maple, 1979, Solid State Commun. **32**, 289.
Hamaker, H.C., H.B. Mac Kay, M.S. Torikachvili, L.D. Woolf and M.B. Maple, 1981a, J. Low Temp. Phys. **44**, 553.
Hamaker, H.C., H.B. Mac Kay, L.D. Woolf, M.B. Maple, W. Odoni and H.R. Ott, 1981b, Phys. Lett. A **81**, 91.
Harley, R.T., W. Hayes, A.M. Perry and S.P.R. Smith, 1973, J. Phys. C **6**, 2382.
Herlach, D.M., E.F. Wassermann and J. Kästner, 1981, Phys. Rev. B **24**, 204.
Herlach, D.M., E.F. Wassermann and R. Willnecker, 1983, Phys. Rev. Lett. **50**, 529.
Holland, M.G., 1963, Phys. Rev. **132**, 2461.
Iolin, E.M., 1970, Fiz. Tverd. Tela **12**, 1159.
Ishikawa, A., and Ø. Fischer, 1977, Solid State Commun. **24**, 747.
Jaccard, D., and J. Flouquet, 1985, J. Magn. & Magn. Mater. **47–48**, 45.
Jaccard, D., and J. Flouquet, 1987, Helv. Phys. Acta **60**, 108.
Jaccard, D., J. Flouquet, Z. Fisk, J.L. Smith and H.R. Ott, 1985a, J. Phys. (Paris) Lett. **46**, L811.
Jaccard, D., J. Flouquet, P. Lejay and J.L. Tholence, 1985b, J. Appl. Phys. **57**, 3082.
Jagannathan, A., R. Orbach and O. Entin–Wohlman, 1989, Phys. Rev. B **39**, 13465.
Jahn, H.A., and E. Teller, 1937, Proc. Roy. Soc. London A **161**, 220.
Jayaraman, A., P.D. Dernier and L.D. Longinotti, 1975, High Temp.–High Pressures **7**, 1.
Jezowski, A., and J. Klamut, 1990, in: Studies of High Temperature Superconductors, ed. A. Norwkar (Nove Science Publ., New York) pp. 263–309.
Kamarzin, A.A., A.A. Mamedov, V.A. Smirnov,

A.A. Sobol, V.V. Sokolov and I.A. Shcherbakov, 1983a, Kvant. Electron. **10**, 1560.

Kamarzin, A.A., A.A. Mamedov, V.A. Smirnov and V.V. Sokolov, 1983b, Fiz. Tverd. Tela **25**, 1664.

Kane, E.O., 1957, J. Phys. & Chem. Solids **1**, 249.

Karpov, V.G., and D.A. Parshin, 1983, Pis'ma Zh. Eksp. & Teor. Fiz. **38**, 536 [JETP Lett. **38**, 648].

Karpov, V.G., and D.A. Parshin, 1985, Zh. Eksp. & Teor. Fiz. **88**, 2212 [Sov. Phys.-JETP, **61**, 1308].

Kazey, Z.A., and V.I. Sokolov, 1986, Zh. Eksp. & Teor. Fiz. **91**, 1799.

Khusnutdinova, V.Y., V.S. Oskotski, I.A. Smirnov and V.M. Sergeeva, 1971, Phys. Status Solidi b **48**, 353.

Kikoin, K.A., and A.S. Mishchenko, 1988, Zh. Eksp. & Teor. Fiz. **94**, 237.

Kirichenko, Y.A., K.V. Rusanov and E.G. Tyurina, 1990, Sverkhprovodimost Fiz. Khim. Tekh. **3**, 1385.

Kittel, C., 1958, Phys. Rev. **110**, 836.

Klemens, P.G., 1969, Thermal Conductivity (Academic Press, London).

Klochkov, L.A., and E.I. Shvarzman, 1982, in: High Temperature Borides and Silicides (IPM AN USSR, Kiev) pp. 82–87. In Russian.

Knoll, K.D., 1971, Phys. Status Solidi b **45**, 553.

Kokshenev, V.B., 1985, Phys. Status Solidi b **132**, 375.

Kolomoets, N.V., 1966, Fiz. Tverd. Tela **8**, 999.

Komissarova, L.N., V.M. Shatski and G.Ya. Pushikina, L.G. Shchorbakova, L.G. Mamsurova and G.E. Sukhanova, 1984, Rare Earth Compounds (Carbonates, Oxalates, Nitrates, Titanates) (Nauka, Moscow) p. 234. In Russian.

Konovalova, E.S., Y.B. Paderno, N.I. Perepelitsa, E.M. Dudnik, S. Janos, K. Flachbart and M. Reiffers, 1984, Fiz. Tverd. Tela **26**, 2138.

Korenblit, I.Y., and E.F. Shender, 1984, Izv. Vyssh. Uchebn. Zaved. Fiz. **27**(10), 23.

Korsukova, M.M., L. Lundstrom and L.E. Tergenius, 1987, Solid State Commun. **63**, 187.

Kost, M.E., A.L. Shilov and V.N. Mikheeva, S.I. Uspenskaya, V.I. Novokshonov, K.E. Mironov, M.N. Abdusalyamoba, A.A. Eliseev, G.M. Kus'micheva and G.B. Seifer, 1983, Rare Earth Compounds (Hydrides, Borides, Carbides, Phosphides, Pnictides, Chalcogenides, Pseudochalcogenides) (Nauka, Moscow) p. 268. In Russian.

Krasny, V.P., N.P. Kovalenko and V.V. Mikho, 1990, Physica B **162**, 122.

Lecomte, G.V., H. v. Löhneysen and W. Zinn, 1983, J. Magn. & Magn. Mater. **38**, 235.

Lecomte, G.V., H. v. Löhneysen and W. Zinn, 1984, in: Phonon Scattering in Condensed Matter, eds W. Eisewenger, K. Laßman and S. Döttinger (Springer, Berlin) p. 466.

Lecomte, G.V., H. v Löhneysen, J. Wosnitza and W. Zinn, 1986, in: Phonon Scattering in Condensed Matter, eds A.C. Anderson and J.P. Wolfe (Springer, Berlin) p. 251.

Leibfried, G., and E. Schlömann, 1954, Nachr. Akad. Wiss. Göttingen A **2**, 71.

Leroux–Huqou, P., and J.J. Veyssie, 1965, Phys. Status Solidi **8**, 561.

Lockwood, A., C. Wood, J. Vandersande, A. Zoltan, L. Danielson, V. Rawag and D. Wittenberg, 1986, J. Less-Common Met. **126**, 113.

Löhneysen, H.v., D.M. Herlach, E.F. Wassermann and K. Samwer, 1981, Solid State Commun. **39**, 591.

Löhneysen, H.v., R. van den Berg, J. Wosnitza, G.V. Lecomte and W. Zinn, 1986, J. Magn. & Magn. Mater. **54–57**, 189.

Loireau–Lorach, A.M., M. Guittard and J. Flahaut, 1976, Mater. Res. Bull. **11**, 1489.

Lopez de la Torre, M.A., S. Vieira, R. Villar, M.B. Maple and M.S. Torikachvili, 1988, Physica C **153–155**, 457.

Love, M.S., and A.C. Anderson, 1990, Phys. Rev. **42**, 1845.

Luguev, S.M., V.S. Oskotski, L.N. Vasil'ev, V.N. Bystrova, T.I. Komarova and I.A. Smirnov, 1975a, Fiz. Tverd. Tela **17**, 2941.

Luguev, S.M., V.S. Oskotski, V.M. Sergeeva and I.A. Smirnov, 1975b, Fiz. Tverd. Tela **17**, 2697.

Luguev, S.M., T.I. Komarova, V.N. Bystrova and I.A. Smirnov, 1978, Izv. Akad. Nauk SSSR Neorg. Mater. **14**, 46.

Lüthi, B., M.E. Mullen, K. Andres, E. Bucher and J.P. Maita, 1973, Phys. Rev. B **8**, 2639.

L'vov, S.N., V.F. Nemchenko and Y.B. Paderno, 1963, Dokl. Akad. Nauk SSSR **149**, 1371.

L'vov, S.N., V.F. Nemchenko and Y.B. Paderno, 1965, in: High Temperature Inorganic Compounds (in Russian) (Naukova Dumka, Kiev) pp. 445–450.

MacLaughlin, D.E., C. Tien, L.C. Gupta, A. Aarts, F.R. de Boer and Z. Fisk, 1984, Phys. Rev. B **30**, 1577.

Maletta, H., 1982, J. Appl. Phys. **53**, 2185.

Maletta, H., and W. Zinn, 1989, Spin glasses, in:

Handbook on the Physics and Chemistry of Rare Earths, Vol. 12, eds K.A. Gschneidner Jr and L. Eyring (North-Holland, Amsterdam) pp. 213–356.
Marcenat, C., D. Jaccard, J. Sierro, J. Flouquet, J. Onuki and T. Komatsubara, 1990, Physica B **163**, 147.
Markov, Yu.M., G.N. Trokhina, E.E. Zernova and V.V. Maksimovski, 1978, Izv. Akad. Nauk SSSR Neorg. Mater. **14**, 79.
Martin, J.J., and G.S. Dixon, 1972, Phys. Status Solidi b **54**, 707.
Matey, J.R., and A.C. Anderson, 1977a, Phys. Rev. B **16**, 3406.
Matey, J.R., and A.C. Anderson, 1977b, J. Non-Cryst. Solids **23**, 129.
Matlak, S., and B. Nolting, 1983, Solid State Commun. **47**, 11.
Matthias, B.T., H. Suhl and E. Gorenzwit, 1958, Phys. Rev. Lett. **1**, 449.
Matthias, B.T., H. Suhl and E. Gorenzwit, 1959, Phys. Rev. Lett. **2**, 92.
Matthias, B.T., E. Gorenzwit, J.M. Vandenberg and H. Barz, 1977, Proc. Nat. Acad. Sci. US **74**, 1334.
Matz, W., B. Lippold, E.A. Goremychkin, A. Andreeff, H. Greissman and T. Frauenheim, 1982, in: Crystalline Electric Field Effects in f-Electron Magnetism, eds R.P. Guertin, W. Suski and Z. Zołnierek (Plenum, New York) pp. 69–82.
McCallum, R.W., D.C. Johnston, R.N. Shelton, W.A. Fertig and M.B. Maple, 1977a, Solid State Commun. **24**, 501.
McCallum, R.W., D.C. Johnston, R.N. Shelton and M.B. Maple, 1977b, Solid State Commun. **24**, 391.
McClintok, P.V.E., and H.M. Rosenberg, 1968, Proc. Roy. Soc. London A **302**, 419.
McClintok, P.V.E., I.P. Morton, R. Orbach and H.M. Rosenberg, 1967, Proc. Roy. Soc. London A **298**, 359.
McCollum, D.C., R.L. Wild and J. Callaway, 1964, Phys. Rev. A **136**, 426.
Melcher, R.L., E. Putte and B.A. Scott, 1973, Phys. Rev. Lett. **31**, 307.
Metcalfe, M.J., and H.M. Rosenberg, 1979, Phys. Lett. A **33**, 211.
Mitarov, R.G., V.V. Tikhonov, L.N. Vasil'ev, V.S. Oskotski, A.V. Golubkov and I.A. Smirnov, 1975, Fiz. Tverd. Tela **17**, 496.
Moeser, J.N., and F. Steglich, 1975, Z. Phys. B **21**, 165.
Moncton, D.E., G. Shirane, W. Thomlinson, M. Ishikawa and Ø. Fischer, 1978, Phys. Rev. Lett. **41**, 1133.
Mook, H.A., and F. Holtzberg, 1981, in: Valence Fluctuations in Solids, eds L.M. Falikov, W. Hanke and M.B. Maple (North-Holland, Amsterdam) p. 113.
Mook, H.A., and R.M. Nicklow, 1978, Phys. Rev. B **18**, 2925.
Mori, K., Y. Ishikava and K. Sato, 1984, J. Phys. Soc. Jpn. **53**, 664.
Morton, I.P., and H.M. Rosenberg, 1962, Phys. Rev. Lett. **8**, 200.
Müller, H., E. Hegenbarth, W. Matz, E. Mrosau and A. Schmeltzer, 1982, in: Crystalline Electric Field Effects in f-Electron Magnetism, eds R.P. Guertin, W. Suski and Z. Zołnierek (Plenum, New York) pp. 98–93.
Müller, H., E. Hegenbarth and S. Mahmoud, 1983, Phys. Status Solidi b **115**, K69.
Mutscheller, W., and M. Wagner, 1984a, in: Phonon Scattering in Condensed Matter, eds W. Eisenmenger, K. Lassman and S. Döttinger (Springer, Berlin) p. 298.
Mutscheller, W., and M. Wagner, 1984b, Solid State Commun. **50**, 577.
Mutscheller, W., and M. Wagner, 1986, Phys. Status Solidi b **134**, 39.
Mutscheller, W., and M. Wagner, 1987, Phys. Status Solidi b **144**, 507.
Mydosh, J.A., 1978, J. Magn. & Magn. Mater. **7**, 237.
Nakamura, A., N. Kawakami and A. Okiji, 1987, Phys. Lett. A **120**, 241.
Neelmani, and G.S. Verma, 1972, Phys. Rev. B **6**, 3509.
Neshpor, V.S., B.A. Fridlender, V.N. Paderno, Y.B. Paderno and M.A. Nerus, 1976, Techn. Vys. Temp. **14**, 903.
Novikov, V.I., V.P. Zhuze, V.M. Sergeeva and S.S. Shalyt, 1975, Zh. Eksp. & Teor. Fiz. **68**, 2159.
Odoni, W., and H.R. Ott, 1979, Phys. Rev. Lett. A **70**, 480.
Odoni, W., G. Keller and H.R. Ott, 1981, Physica B **108**, 1227.
Olsen, J.L., and H.M. Rosenberg, 1953, Adv. Phys. **2**, 28.
Onuki, Y., Y. Shimizu, T. Komatsubara, A. Sumiyama, Y. Oda, H. Hagano, T. Fujita, Y. Maeno, K. Satoh and T. Ohtsuka, 1985a, J. Magn. & Magn. Mater. **52**, 344.
Onuki, Y., Y. Shimizu, M. Nishihara, Y. Mashii and T. Komatsubara, 1985b, J. Phys. Soc. Jpn. **54**, 1964.
Orbach, R., 1960, Philos. Mag. **5**, 1303.
Orbach, R., 1962, Phys. Rev. Lett. **8**, 393.

Oskotski, V.S., and I.A. Smirnov, 1971, Fiz. Tverd. Tela **13**, 1635.

Oskotski, V.S., and I.A. Smirnov, 1972, Crystal Defects and Thermal Conductivity (Nauka, Leningrad). In Russian.

Oskotski, V.S., and I.A. Smirnov, 1977, Semiconductor–metal phase transition in samarium monosulphate, in: Rare Earth Semiconductors, eds V.P. Zhuze and I.A. Smirnov (Nauka, Leningrad) pp. 105–145. In Russian.

Oskotski, V.S., L.S. Parfen'eva and I.A. Smirnov, 1972, in: Proc. Int. Conf. on Phonon Scattering in Solids, ed. H.J. Albany, Paris, pp. 254–259.

Oskotski, V.S., L.N. Vasil'ev and I.A. Smirnov, 1982, in: Synthesis and Properties of Rare Earth Compounds (AN USSR, Sverdlovsk) pp. 86–94. In Russian.

Ott, H.R., and B. Lüthi, 1976, Phys. Rev. Lett. **36**, 600.

Ott, H.R., W.A. Fertig, D.C. Johnston, M.B. Maple and B.T. Matthias, 1978, J. Low Temp. Phys. **33**, 159.

Ott, H.R., W. Odoni, H.C. Hamaker and M.B. Maple, 1980, Phys. Lett. A **75**, 243.

Ott, H.R., H. Rudiger, Z. Fisk and J.L. Smith, 1983, Phys. Rev. Lett. **50**, 1595.

Ott, H.R., O. Marti and F. Hulliger, 1984a, 607.

Ott, H.R., H. Rudiger, T.M. Rice, K. Ueda, Z. Fisk and J.L. Smith, 1984b, Phys. Rev. Lett. **52**, 1915.

Paderno, Y.B., N.Y. Shitsevalova and V.B. Muratov, et al., 1991, Borides, preprint 91 - NI (IPM AN USSR, Kiev). In Russian.

Parfen'eva, L.S., I. Dzhabbarov, S.I. Ivanov, I.A. Smirnov and V.V. Medved, 1979, in: Refractory Rare Earth Compounds, ed. K.E. Mironov (Nauka, Novosibirsk) pp. 139–141. In Russian.

Parfen'eva, L.S., I.A. Smirnov, V.V. Tikhonov, V.S. Iskotski and V.V. Sokolov, 1990a, in: Physics and Chemistry of Rare Earth Semiconductors (Nauka, Novosibirsk) pp. 106–108. In Russian.

Parfen'eva, L.S., I.A. Smirnov, V.V. Tikhonov and K.M. Khalmedov, 1990b, in: Abstracts 5th All-Union Conf. on Physics and Chemistry of Rare Earth Semiconductors (Universitet, Saratov) p. 31.

Parfen'eva, L.S., V.V. Sokolov, I.A. Smirnov, V.V. Popov, N.N. Efremova and L.D. Finkelshtein, 1990c, in: Physics and Chemistry of Rare Earth Semiconductors, ed. K.E. Mironov (Nauka, Novosibirsk) pp. 109–111. In Russian.

Parsons, M.W.S., 1976, in: Phonon Scattering in Solids, eds L.J. Challis, V.W. Rampton and A.F.G. Wyatt (Plenum, New York) pp. 240–242.

Parsons, M.W.S., and H.M. Rosenberg, 1972, in: Proc. Int. Conf. on Phonon Scattering in Solids, ed. H.F. Albany (CERN Saclay, Paris) pp. 326–329.

Patterson, J.D., 1978, Phys. Status Solidi b **90**, K85.

Petrov, A.V., M.S. Germaidze, O.A. Golikova, A.Y. Kiskachi and V.N. Matveev, 1969, Fiz. Tverd. Tela **11**, 907.

Petrov, A.V., V.M. Orlov, V.K. Zaitsev and V.A. Feigelman, 1975, Fiz. Tverd. Tela **17**, 3703.

Petrunin, G.I., V.G. Popov and M.I. Timoshechkin, 1989, Fiz. Tverd. Tela **31**(7), 139.

Peysson, Y., C. Ayache, B. Salce, J. Rossat–Mignod, S. Kunii and T. Kasuya, 1985, J. Magn. & Magn. Mater. **47–48**, 63.

Peysson, Y., B. Daudin, M. Dubus and R.E. Benenson, 1986a, Phys. Rev. B **34**, 8367.

Peysson, Y., B. Salce, C. Ayache and E. Bauer, 1986b, J. Magn. & Magn. Mater. **54–57**, 423.

Peysson, Y., B. Salce and A.M. de Goër, 1986c, in: Phonon Scattering in Condensed Matter, Vol. V, eds A.C. Anderson and J.P. Wolfe (Springer, Berlin) pp. 251–253.

Phillips, W.A., 1972, J. Low Temp. Phys. **7**, 351.

Phillips, W.A., 1987, Rep. Progr. Phys. **50**, 1657.

Pikus, G.E., 1956, Zh. Tekh. Fiz. **26**, 36.

Pillai, C.G.S., and A.M. George, 1988, Proc. Nat. Acad. Sci. India, Sect. A **54**, 824.

Pillai, C.G.S., and A.M. George, 1991, Int. J. Thermophys. **12**, 207.

Pohl, R.O., and J.J. de Yoreo, 1985, in: Physics of Disordered Materials, eds D. Adler, H. Fritzsche and S.R. Ovshinsky (Plenum, New York) pp. 529–540.

Raki, M., L. Forro, C. Ayache, D. Schmitt, A.K. Bhattacharjee and B. Coqblin, 1990, Physica B **163**, 93.

Ravex, A., J. Flouquet, J.L. Tholence, D. Jaccard and A. Meyer, 1987, J. Magn. & Magn. Mater. **63–64**, 400.

Ray, D.K., K. Westerholt, S. Methfessel and S.K. Ghatak, 1981, Solid State Commun. **38**, 783.

Raychaudhuri, A.K., J.M. Peech and R.O. Pohl, 1980, in: Phonon Scattering in Condensed Matter, ed. H.J. Maris (Plenum, New York) pp. 45–48.

Red'ko, N.A., and B.K. Chakalski, 1987, Zh. Eksp. Teor. Fiz **92**, 1090.

Regueiro, M.D.N., and D. Castello, 1990, invited talk in: Int. Conf. LT-19, Brighton, England, p. 631.
Reisfeld, R., and A. Bornstein, 1977, Chem. Phys. Lett. **47**, 194.
Reisfeld, R., A. Bornstein, J. Flahaut, M. Guittard and A.M. Loireau–Lozach, 1977, Chem. Phys. Lett. **47**, 408.
Reisfeld, R., A. Bornstein, J. Bodenheimer and J. Flahaut, 1979, J. Lumin. **18-19**, 253.
Remizova, L.A., 1975, Tekh. Vys. Temp. **13**, 207.
Remizova, L.A., 1978, Tekh. Vys. Temp. **16**, 773.
Richards, S.M., and J.S. Kasper, 1969, Acta Crystallogr. B **25**, 237.
Rives, J.E., G.S. Dixon and D. Walton, 1969, J. Appl. Phys. **40**, 1555.
Roedhammer, P., W. Reichardt and F. Holtzberg, 1978, Phys. Rev. Lett. **40**, 465.
Salamon, M.B., P.R. Garnier, B. Golding and E. Buechler, 1974, J. Phys. & Chem. Solids **35**, 851.
Salce, B., and L.A. Boatner, 1986, in: Phonon Scattering in Condensed Matter, eds A.C. Anderson and J.P. Wolfe (Springer, Berlin) pp. 272–274.
Samsonov, G.V., 1964, Refractory Compound of Less-Common Metals with Nonmetals (Metallurgiya, Moscow). In Russian.
Samsonov, G.V., T.I. Serebryakova and V.A. Neronov, 1975, Borides (Atomizdat, Moscow). In Russian.
Sandalov, I.S., and A.N. Podmarkov, 1985, Zh. Eksp. & Teor. Fiz. **88**, 1321.
Schell, G., H. Winter, H. Rietschel and F. Gompf, 1982, Phys. Rev. B **25**, 1589.
Schmitt-Rink, S., K. Miyake and C.M. Varma, 1986, Phys. Rev. Lett. **57**, 2575.
Schneider, H., and D. Wohlleben, 1981, Z. Phys. B **44**, 193.
Schneider, H., Z. Kletowski, F. Oster and D. Wohlleben, 1983, Solid State Commun. **48**, 1093.
Sergeeva, V.M., E.V. Goncharova, N.F. Kartenko, M.A. Demina, I.A. Smirnov, R.N. Andryushin and Y.K. Misyurev, 1972, Izv. Akad. SSSR Neorg. Mater. **8**, 2114.
Shadrichev, E.V., L.S. Parfen'eva, V.I. Tamarchenko, O.S. Gryaznov, V.M. Sergeeva and I.A. Smirnov, 1976, Fiz. Tverd. Tela **18**, 2380.
Sharma, K.C., and R.S. Tripathi, 1980, Phys. Status Solidi b **102**, K161.
Sheard, F.W., 1976, in: Phonon Scattering in Solids, eds L.J. Challis, V.W. Rampton and A.F.G. Wyatt (Plenum, New York) pp. 154–162.
Shelton, R.N., R.W. McCallum and H. Adrian, 1976, Phys. Lett. A **56**, 213.
Sher, A., R. Solomon, K. Lee and M.W. Muller, 1966, Phys. Rev. **144**, 593.
Sierro, J., E. Bucher, L.D. Longinotti, H. Takayama and P. Fulde, 1975, Solid State Commun. **17**, 79.
Singh, D.P., and G.S. Verma, 1972, Phys. Rev. B **6**, 4013.
Slack, G.A., 1964, J. Appl. Phys. **35**, 339.
Slack, G.A., 1979, Solid State Phys. **34**, 1.
Slack, G.A., and D.M. Oliver, 1971, Phys. Rev. B **4**, 592.
Slack, G.A., D.M. Oliver and F.H. Horn, 1971, Phys. Rev. B **4**, 1741.
Smirnov, I.A., 1972, Phys. Status Solidi a **14**, 363.
Smirnov, I.A., 1981, Zh. Vses. Khim. Ova. **26**, 602.
Smirnov, I.A., and V.S. Oskotski, 1978, Usp. Fiz. Nauk **124**, 241.
Smirnov, I.A., and V.I. Tamarchenko, 1977, Electronic Thermal Conductivity in Metals and Semiconductors (Nauka, Leningrad). In Russian.
Smirnov, I.A., L.S. Parfen'eva, V.Y. Khusnutdinova and V.M. Sergeeva, 1972, Fiz. Tverd. Tela **14**, 844.
Smirnov, I.A., L.S. Parfen'eva and V.M. Sergeeva, 1973, Neorg. Mater. **9**, 485.
Smirnov, I.A., V.S. Oskotski and L.S. Parfen'eva, 1985, J. Less-Common Met. **111**, 353.
Smirnov, I.A., V.S. Oskotski and L.S. Parfen'eva, 1988, in: Actual Problems of Physics and Chemistry of Rare Earth Semiconductors (AN USSR, Makhachkala) pp. 4–23. In Russian.
Smirnov, I.A., V.S. Oskotski and L.S. Parfen'eva, 1989, High Temp.–High Pressures **21**, 237.
Smirnov, I.A., V.V. Tikhonov, P.A. Alekseev, V.N. Lazukov, L.N. Vasil'ev, V.V. Sokolov and L.S. Parfen'eva, 1990, in: Abstracts 5th All-Union Conf. on Physics and Chemistry of Rare Earth Semiconductors (Universitet, Saratov) p. 33.
Smirnov, I.A., L.S. Parfen'eva, V.S. Oskotski, L.N. Vasil'ev, V.V. Tikhonov, K.M. Khalmedov, V.V. Sokolov, P.A. Alekseev and V.N. Lazukov, 1992a, to be published.
Smirnov, I.A., L.S. Parfen'eva, T.B. Zhukova, K.M. Khalmedov, V.S. Oskotski, I.N. Kulikova, E.A. Sovestnov and V.A. Shaburov, 1992b, to be published.
Smith, H.G., G. Dolling and T. Goto, 1985, Solid State Commun. **53**, 15.
Sokolov, V.V., A.A. Kamarzin, X. Bach and

S. Methfessel, 1988, in: IVth Int. Soviet–West Germany Symp. on Studies of Rare Earth Compound (Tbilisi) pp. 192–196.

Sparn, G., W. Lieke, U. Gottwick, F. Steglich and N. Grewe, 1985, J. Magn. & Magn. Mater. **47–48**, 521.

Sparn, G., M. Baenitz, S. Horn, F. Steglich, W. Assmus, T. Wolf, A. Kapitulnic and Z.X. Zhao, 1989, Physica C **162–164**, part 1, 508.

Spear, W.E., G. Willeke, P.G. le Comber and A.E. Fitzgerald, 1981, J. Phys. Colloq. (Paris) **42**, C4-257.

Steglich, F., 1976, Z. Phys. B **23**, 331.

Steglich, F., J. Aarts, C.D. Bredl, W. Lieke, D. Meschede, W. Franz and H. Schäfer, 1979, Phys. Rev. Lett. **43**, 1982.

Steglich, F., C.D. Bredl, W. Lieke, U. Rauchschwalbe and G. Sparn, 1984, Physica B **126**, 82.

Steglich, F., U. Ahlheim, J.J.M. Franse, N. Grewe, D. Rainer and U. Rauchschwalbe, 1985a, J. Magn. & Magn. Mater. **52**, 54.

Steglich, F., U. Rauchschwalbe, U. Gottwick, H.M. Mayer, G. Sparn, N. Grewe, U. Poppe and J.J.M. Franse, 1985b, J. Appl. Phys. **57**, 3054.

Stewart, G.R., Z. Fisk, J.O. Willis and J.L. Smith, 1984, Phys. Rev. Lett. **52**, 679.

Strzhemechny, M.A., and S.E. Kalnoy, 1983, Fiz. Nizk. Temp. **9**, 318.

Sturge, M.D., 1967, Solid State Phys. **20**, 92–211.

Suhl, H., B.T. Matthias and E. Gorenzwit, 1959, J. Phys. & Chem. Solids **19**, 346.

Sulpice, A., P. Candit, J. Chaussy, J. Flouquet, D. Jaccard, P. Lejay and J.L. Tholence, 1986, J. Low Temp. Phys. **62**, 39.

Sütsch, P., and E. Umlauf, 1981, J. Low Temp. Phys. **42**, 11.

Takegahara, K., and T. Kasuya, 1985, Solid State Commun. **53**, 21.

Tanaka, T., 1974, J. Phys. C **7**, L177.

Tewordt, L., and T. Wölkhausen, 1989, Solid State Commun. **70**, 839.

Turberfield, K.C., L. Passell, R.J. Birgeneau and E. Bucher, 1971, J. Appl. Phys. **42**, 1746.

Türkes, P.R.H., E.T. Swartz and R.O. Pohl, 1986, in: Proc. Int. Conf. on the Physics and Chemistry of Boron and Boron-Rich Solids, Albuquerque, 1985, eds D. Emin, T. Aselage, C.L. Beckel, I.A. Howard and C. Wood, AIP Conf. Proc. **140**, 346.

Uher, C., 1989, Invited Talk, 3rd Ann. Conf. on Superconductivity and Applications, Buffalo, NY.

Uher, C., 1990, in: Int. Conf. on Transport Properties of Superconductors, Rio de Janeiro, April 29–May 4.

Vandenberg, J.M., and B.T. Matthias, 1977, Proc. Nat. Acad. Sci. USA **74**, 1336.

Varma, C.M., 1985, J. Appl. Phys. **57**, 3064.

Vasil'ev, L.N., I.N. Kulikova, L.S. Parfen'eva, N.N. Stepanov and E.V. Shadrichev, 1975, Fiz. Tverd. Tela **17**, 2928.

Vasil'ev, L.N., S.M. Luguev and V.S. Oskotski, 1976, Fiz. Tverd. Tela **18**, 906.

Vasil'ev, L.N., T.I. Komarova, L.S. Parfen'eva and I.A. Smirnov, 1978, Fiz. Tverd. Tela **20**, 1077.

Vasil'ev, L.N., A.V. Gorobets, A.V. Golubkov, V.S. Oskotski, I.A. Smirnov and V.V. Tikhonov, 1983, Phys. Status Solidi a **80**, 237.

Vasil'ev, L.N., I. Dzhabbarov, V.S. Oskotski, L.S. Parfen'eva, V.V. Popov and I.A. Smirnov, 1984a, Fiz. Tverd. Tela **26**, 2710.

Vasil'ev, L.N., I. Dzhabbarov, L.S. Parfen'eva, V.S. Oskotski and I.A. Smirnov, 1984b, High Temp.–High Pressures **16**, 45.

Vekhter, B.G., V.N. Golubev and M.D. Kaplan, 1987, Pis'ma Zh. Eksp. & Teor. Fiz. **45**, 136.

Venevtsev, Yu.N., and V.N. Lubimov, eds, 1990, Magnetoferroelectric Materials (Nauka, Moscow) p. 181. In Russian.

Volovik, G.E., and L.P. Gor'kov, 1984, Pis'ma Zh. Eksp. & Teor. Fiz. **39**, 550.

Volovik, G.E., and L.P. Gor'kov, 1985, Zh. Eksp. & Teor. Fiz. **88**, 1412.

Walton, D., J.E. Rives and Q. Khalid, 1973, Phys. Rev. B **8**, 1210.

Weston, H.T., and W.B. Daniels, 1984, Phys. Rev. B **29**, 2709.

Wilson, A.H., 1965, The Theory of Metals, 2nd Ed. (Cambridge University Press, Cambridge).

Wong, Y.H., 1978, Phys. Rev. B **17**, 3899.

Woolf, L.D., D.C. Johnston, H.B. Mac Kay, R.W. McCallum and M.B. Maple, 1979, J. Low Temp. Phys. **35**, 651.

Zaitlin, M.P., and A.C. Anderson, 1975, Phys. Rev. B **12**, 4475.

Zeller, R.C., and R.O. Pohl, 1971, Phys. Rev. B **4**, 2029.

Zhuze, V.P., E.V. Goncharova, N.E. Kartenko, T.I. Komarova, L.S. Parfen'eva, V.M. Sergeeva and I.A. Smirnov, 1973, Phys. Status Solidi a **18**, 63.

Zinov'ev, V.A., and S.I. Masharov, 1973, in: Thermophysical Properties of Materials (Nauka, Moscow) pp. 49–51. In Russian.

Zinov'ev, V.A., R.P. Krentsis and P.V. Geld, 1968, Fiz. Tverd. Tela **10**, 2820.

Handbook on the Physics and Chemistry of Rare Earths, Vol. 16
edited by K.A. Gschneidner, Jr. and L. Eyring

Chapter 107

RARE EARTH PYROCHLORES

M.A. SUBRAMANIAN
E.I. du Pont de Nemours and Company, Wilmington, DE, 19880-0328, USA

A.W. SLEIGHT
Department of Chemistry, Oregon State University, Corvallis, OR, 97331-4003, USA

Contents

1. Introduction

The occurrence of the pyrochlore structure is very common since the vast majority of the elements in the periodic table are found in this structure. The ideal pyrochlore formula is $A_2M_2X_7$, where A and M are cations and X is an anion such as oxygen or fluorine. However, defect structures such as $A_2M_2X_6$ and AM_2X_6 are well known. The oxidation states for the $A_2M_2O_7$ formulation are generally $A_2^{2+}M_2^{5+}O_7$ or $A_2^{3+}M_2^{4+}O_7$. It is the latter formulation that this chapter will mainly address, i.e., those pyrochlores where the A cation is a trivalent rare earth: $R_2^{3+}M_2^{4+}O_7$. All the rare earths are known to occupy the A sites, and eighteen different tetravalent cations can occupy the M site. In addition, many rare earth pyrochlores with more complex formulations, such as $R_2^{3+}M^{3+}M^{5+}O_7$, are known.

Since there are over a hundred different rare earth compounds with the pyrochlore structure, there exists a wide diversity of properties. Some rare earth pyrochlores are

electrical insulators; others are low-activation-energy semiconductors. In rare cases, $A_2^{3+}M_2^{4+}O_7$ pyrochlores may possess metallic properties. Ferroelectricity is observed for compounds with the pyrochlore structure, but this does not occur in the $R_2^{3+}M_2^{4+}O_7$ phases. In addition to diamagnetism and paramagnetism, ferromagnetism is also observed for some $R_2M_2O_7$ compounds.

Superconductivity might be expected to occur in the pyrochlore structure considering the wide variety of compositions and properties found for compounds with this structure. However, superconductivity has not been observed at any temperature for any compound with this structure, regardless of whether or not a rare earth element is present.

An interesting aspect of the pyrochlore structure is the unique coordination found for the rare earth at the A cation site. Although this environment is sometimes viewed as a distorted cube, two oxygens are much closer than the remaining six. These are in fact among the shortest R–O distances ever observed, and such rare earth cations are in the highest electric field gradient ever observed.

Despite the wide occurrence of the pyrochlore structure, compounds with this structure type have been reviewed only once before (Subramanian et al. 1983). The appendix presents a bibliography on rare earth pyrochlores with an organization very different from that which directly follows.

2. Pyrochlore structure

2.1. *Crystallography*

The space group for the ideal pyrochlore structure is Fd3m. One has a choice of four origins for the pyrochlore structure. Both the A and M cations are at inversion centers, and either of these cation sites can be used as the origin. The generally preferred description has the M cation at the origin, and this decription is given in table 1. In addition to the systematic absences of the space group, there are systematic absences based on the positions occupied for the pyrochlore structure. These additional conditions apply to even indices only and are: h, k and l must be equal to $4n+2$ or $4n$, or $h+k+l$ must be equal to $4n$. This causes the 442 reflection, e.g., to be forbidden even though it is allowed for the Fd3m space group. However, the 442 reflection becomes allowed when anisotropic thermal motions are considered.

For the ideal $A_2M_2O_7$ pyrochlore structure, all A cations are equivalent and all

TABLE 1
Atomic positions in space group Fd3m for $R_2M_2O_7$ pyrochlores.

Atom	Position	Coordinates
R	16d	$\frac{1}{2}, \frac{1}{2}, \frac{1}{2}$
M	16c	0, 0, 0
O	48f	$x, \frac{1}{8}, \frac{1}{8}$
O	8b	$\frac{1}{8}, \frac{1}{8}, \frac{1}{8}$

M cations are equivalent, but there are two types of oxygen. Thus, it is sometimes preferred to write the pyrochlore formula as $A_2M_2O_6O'$. The oxygen referred to as O′ is in a special position and is sometimes missing from the structure. There is only one positional parameter for the pyrochlore structure, and this is for the more abundant oxygen species. This parameter, x(O), would be 0.3125 for a regular octahedral oxygen environment around M and would be 0.375 for a regular cubic oxygen environment around A. In fact for $R_2M_2O_7$ pyrochlores, x(O) is found to range from 0.319 to 0.343 (Barker et al. 1970, McCauley 1980, Subramanian et al. 1983, Chakoumakos 1984).

Several structural refinements for the pyrochlore structure have been published based on single crystal data; however, for $R_2M_2O_7$ pyrochlores, structures are based on refinements of powder data obtained by either X-ray or neutron diffraction. Since there is only one positional parameter to refine, the structures are generally highly overdetermined even when powder data are used. The results of the structural refinements on $R_2M_2O_7$ pyrochlores are summarized in table 2.

2.2. *Description of structure*

Two different descriptions of the pyrochlore structure are useful. One description views the structure as derived from the fluorite structure (Aleshin and Roy 1962, Longo et al. 1969), and the other views the pyrochlore structure as a network structure (Sleight 1968a). The relationship to the fluorite structure is shown in fig. 1. For x(O) equal to 0.375, we have the fluorite structure except that A and M cations are ordered on the fluorite cation sites and there are ordered oxygen vacancies. The oxygen vacancies are such that the A cation coordination number remains eight, but the M cation coordination number drops to six. In practice, the oxygen positional parameter always decreases considerably, so that the coordination around M approaches octahedral. This reduced value of x(O) causes the coordination around the A cation to deviate very significantly from cubic. The A cation now has two very close distances ($\sim$2.3 Å), lying on the three-fold axis; and there are six more distant oxygens ($\sim$2.5 Å). The fluorite-related description of the pyrochlore structure is especially useful to understand the order–disorder transformation and ranges of stoichiometry that exist, for example, for phases in the R_2O_3–ZrO_2 systems.

The network description of the pyrochlore structure has become more popular, partly because it leads to a natural description of defect pyrochlores such as $A_2M_2O_6$ and AM_2O_6. In this description, the structure is viewed as made up of two networks which interpenetrate (Sleight 1968a). One network, A_2O', is the same as the networks found in Cu_2O. The O′ is tetrahedrally coordinated by A, and the A cation has a coordination number of only two. The other network, MO_3, is made up of octahedrally coordinated M cations. These octahedra are linked together by corners to form a three-dimensional network with cubic symmetry. Figure 2 shows how these two networks interpenetrate. The strongest interaction between these two networks is between the A^{3+} cations and the O^{2-} anions from the MO_3 network. For $R_2^{3+}M_2^{4+}O_7$ pyrochlores, the network charges are $(R_2O)^{4+}$ and $(MO_3)^{4-}$. Thus, the structure can be viewed as made up of two covalent networks with ionic bonding

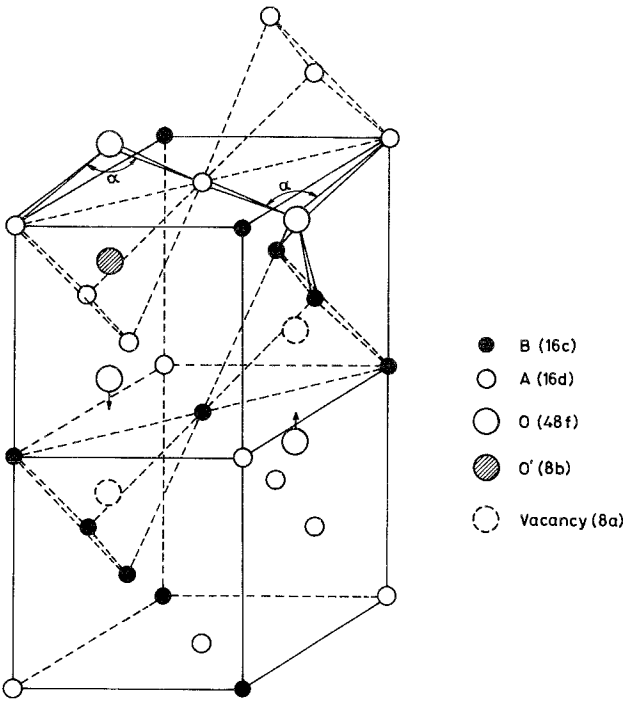

Fig. 1. Pyrochlore structure as derived from the fluorite structure. The cation positions for $\frac{1}{4}$ of the unit cell are shown. The shifts of (48f) oxygen towards the (8a) vacant site are indicated.

between the two networks. Although R–O bonding is usually considered more ionic than covalent, one must remember that R–O′ distances in the pyrochlore structure are only about 2.3 Å. Mössbauer results are also compatible with this description, since they show that the highest electric field gradient ever observed for rare earth cations is found when such cations reside at the A site of the pyrochlore structure (Bauminger et al. 1974, 1976). This unusual environment at the A site also results in very anisotropic thermal parameters for A cations since they cannot readily vibrate against such close oxygens. The coordination of the M cation is frequently described as octahedral, but in fact, the coordination is actually trigonal antiprismatic.

2.3. *Order–disorder and nonstoichiometry*

When M cations are large enough to adopt eight-fold coordination to oxygen, order–disorder transformations and significant ranges of stoichiometry are observed for the pyrochlore structure (Perez Y Jorba 1962, Faucher and Caro 1975). In fact, Zr and Hf are the only M cations large enough for these related phenomena to be exhibited (Roth 1956, Michel et al. 1974, 1976, Collongues et al. 1961, 1965). Figure 3 shows the R_2O_3–ZrO_2 phase diagram for R = Gd and Sm (Collongues 1963). Two-phase regions, which presumably must exist, are not shown between the pyrochlore and disordered fluorite region. Thus, it is reasonable to assume that the stability field for a single-phase pyrochlore is somewhat smaller than indicated in fig. 3.

TABLE 2
Oxygen x(48f) parameters for $R_2M_2O_7$ pyrochlores (B_0 origin).

Compound	x(48f)	Ref.
$Sm_2Ti_2O_7$	0.327	Knop et al. (1965, 1969)
$Eu_2Ti_2O_7$	0.327	
$Gd_2Ti_2O_7$	0.322	
$Dy_2Ti_2O_7$	0.323	
$Er_2Ti_2O_7$	0.331	
$Lu_2Ti_2O_7$	0.330	
$Y_2Ti_2O_7$	0.328	
$Er_2Mn_2O_7$	0.328	Subramanian et al. (1988)
$Y_2Mn_2O_7$	0.327	
$Sm_2Mo_2O_7$	0.343	Hubert (1975a,b)
$Eu_2Mo_2O_7$	0.322	
$Tb_2Mo_2O_7$	0.3363	Greedan et al. (1991)
$Y_2Mo_2O_7$	0.3382	Reimers et al. (1988)
$Nd_2Ru_2O_7$	0.330	Sleight and Bouchard (1972)
$Lu_2Ru_2O_7$	0.336	
$Pr_2Ru_2O_7$	0.325	
$Nd_2Ru_2O_7$	0.328	
$Sm_2Ru_2O_7$	0.329	
$Dy_2Ru_2O_7$	0.332	
$Y_2Ru_2O_7$	0.333	Kanno (1992)
$Sm_2Pt_2O_7$	0.325	Hoekstra and Siegel (1968)
$Eu_2Pt_2O_7$	0.329	
$Er_2Pt_2O_7$	0.334	
$Y_2Pt_2O_7$	0.329	
$La_2Sn_2O_7$	0.325	Brisse and Knop (1968)
$Sm_2Sn_2O_7$	0.333	
$Eu_2Sn_2O_7$	0.335	
$Gd_2Sn_2O_7$	0.332	
$Er_2Sn_2O_7$	0.335	
$Y_2Sn_2O_7$	0.338	
$Sc_2Si_2O_7$	0.325	Reid et al. (1977)
$In_2Si_2O_7$	0.329	

Pyrochlore microdomains have been observed in samples quenched from a region reported to be single-phase disordered fluorite.

3. Pyrochlore composition

3.1. $A_2^{3+}M_2^{4+}O_7$

One might expect that any M^{4+} cation that can take on octahedral coordination to oxygen could form an $R_2^{3+}M_2^{4+}O_7$ compound with a pyrochlore structure for

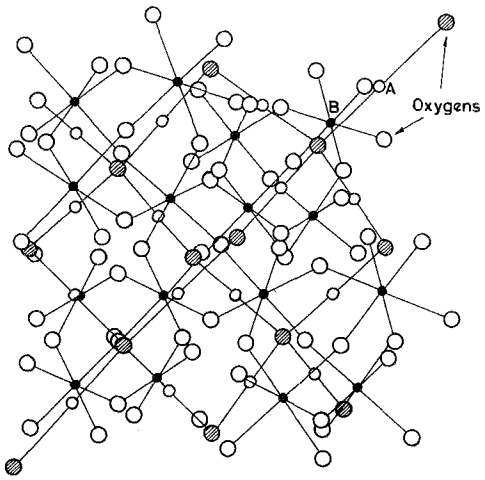

Fig. 2. The pyrochlore structure as interpenetrating networks of A_2O and M_2O_6.

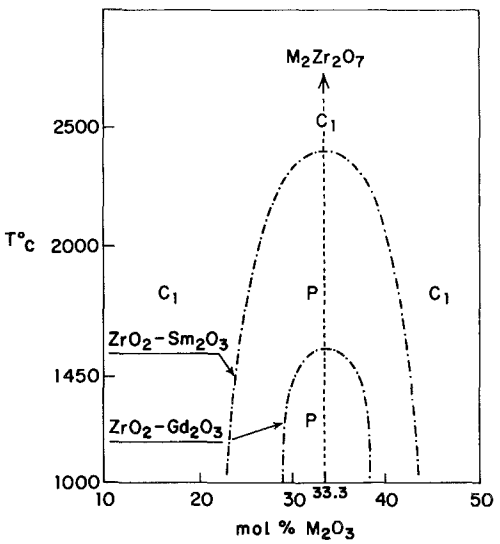

Fig. 3. R_2O_3–ZrO_2 phase diagram for R = Sm or Gd. P denotes pyrochlore and C_1 disordered fluorite.

any R^{3+} cation. However, there are some further constraints as is obvious from the stability field shown in fig. 4. The size ratio R/M must be neither too large nor too small.

Table 3 gives a complete listing of all known $R_2^{3+}M_2^{4+}O_7$ pyrochlores with their room-temperature cell dimensions. Nearly all M^{4+} cations which take on octahedral coordination in binary oxides are represented. However, attempts to use Nb^{4+} or W^{4+} have failed to date. Some of the phases listed in table 3 require high pressure for their synthesis. In some cases, the pressure was required to stabilize the coordination number, e.g., Si^{4+}. In other cases, the pressure was required to stabilize the oxidation state, e.g., Cr^{4+}. Some of the obvious gaps in table 3 could presumably be

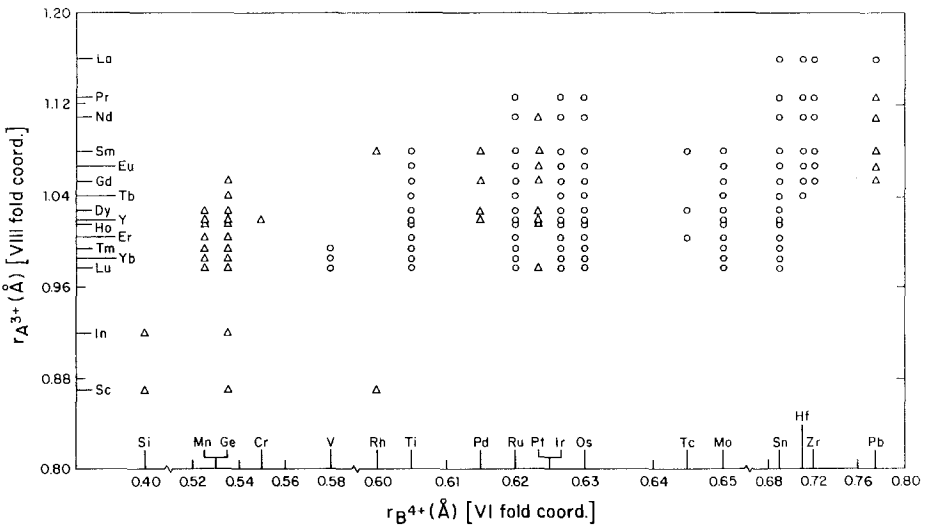

Fig. 4. Stability field diagram for $A_2^{3+}M_2^{4+}O_7$ (R = rare earth, Sc or In) pyrochlores. Δ denotes high-pressure synthesis.

eliminated if there was a particular interest in examining the missing compound, e.g., where M is Tc, Rh or Pd. On the other hand, attempts to expand the series where M is V or Cr have failed (Subramanian et al. 1983).

3.2. *Complex formulations*

Rare earths are found in pyrochlores other than the simple $R_2^{3+}M_2^{4+}O_7$ formulation. A trivial example would be an $R_{2-x}^{3+}A_x^{3+}M_2O_7$ solid solution where A^{3+} might be Bi, Tl or In. In fact, such solid solutions where A^{3+} is Bi or Tl have been of some interest because $Bi_2^{3+}M_2^{4+}O_7$ and $Tl_2^{3+}M_2^{4+}O_7$ pyrochlores are metallic when M is Ru or Ir, whereas analogous $R_2M_2O_7$ pyrochlores are semiconducting (Sleight and Bouchard 1972). Pyrochlore solid solutions of the type $R_{2-x}Bi_xTi_2O_7$ have been reported by Bamberger et al. (1985).

Another group of complex pyrochlores containing rare earth cations might be viewed as solid solutions between $R_2^{3+}M_2^{4+}O_7$ and $A_2^{2+}M_2^{5+}O_7$ (table 4).

Such phases appear to have a narrow homogeneity range close to $(A^{2+}R^{3+})(M^{5+}M^{4+})O_7$. Thus, they have been referred to as compounds rather than solid solutions. Still other formulations based on rare earths partially occupying the A site are $(A^+R^{3+}Sb_2^{5+})O_7$ and $(Cd^{2+}R^{3+})(Fe_{1/2}^{3+}Nb_{3/2}^{5+})O_7$ (table 4).

Very extensive series of rare earth pyrochlores exist based on substitutions at the M site: $R_2(M^{3+}M^{5+})O_7$ and $R_2(M_{4/3}^{3+}W_{2/3}^{6+})O_7$. In the $A_2^{3+}(M^{3+}M^{5+})O_7$ series, A^{3+} may be Bi^{3+} as well as a rare earth; M^{3+} may be Cr, Fe, Ga or a rare earth; and M^{5+} may be Nb, Ga, or Sb (table 4).

Pyrochlores containing Ce^{4+} are also reported (McCauley and Hummel 1980): $(CaCe)Ti_2O_7$ and $(CdCe)Ti_2O_7$ (table 4). Wakiya et al. (1991) have reported a cubic

TABLE 3
Cell dimensions for $R_2^{3+}M_2^{4+}O_7$-pyrochlores.

Rare earth (R)	Metal															
	Ti	V	Cr	Mn	Zr	Mo	Tc	Ru	Rh	Pd	Hf	Os	Ir	Pt	Si	Ge
La					10.805						10.773					
Pr					10.715						10.680	10.408	10.406	10.419		
Nd					10.678			10.355			10.630	10.391	10.383	10.378		
Sm	10.233				10.594	10.409	10.352	10.330	10.302	10.307	10.546	10.323	10.318	10.313		
Eu	10.196				10.554	10.372		10.280			10.506	10.302	10.290	10.286		
Gd	10.185				10.528	10.337		10.255		10.236	10.475	10.275	10.266	10.261		9.985
Tb	10.152					10.293		10.228			10.449	10.245	10.222	10.222		
Dy	10.124			9.929		10.257	10.246	10.200		10.155		10.217	10.217	10.202		9.929
Ho	10.100			9.905		10.238		10.170				10.190	10.183	10.170		9.903
Er	10.087			9.869		10.204	10.194	10.152		10.103		10.167	10.158	10.144		9.864
Tm	10.054	9.973		9.847		10.183		10.118				10.147	10.136	10.118		9.845
Yb	10.030	9.945		9.830		10.158		10.098		10.049		10.124	10.115	10.095		9.829
Lu	10.018	9.928		9.815		10.140		10.085				10.106	10.095	10.076		9.813
Y	10.095		10.096	9.901		10.232		10.079		10.126		10.188	10.180	10.164		9.897
Sc								10.142	9.800	9.804				9.851	9.287	9.600
In										9.919				9.962	9.413	9.711

TABLE 4
Complex pyrochlores containing a rare earth cation.

Compound	a_0 (Å)	Ref.*	Compound	a_0 (Å)	Ref.*
$R_2(M^{3+}Sb^{5+})O_7$			**$R_2(M^{3+}_{4/3}W^{6+}_{2/3})O_7$**		
$Pr_2(CrSb)O_7$	10.405	[1]	$Gd_2(V_{4/3}W_{2/3})O_7$	10.234	[7]
$Nd_2(CrSb)O_7$	10.370	[1]	$Tb_2(V_{4/3}W_{2/3})O_7$	10.207	[7]
$Sm_2(CrSb)O_7$	10.340	[1]	$Dy_2(V_{4/3}W_{2/3})O_7$	10.191	[7]
$Eu_2(CrSb)O_7$	10.330	[1]	$Ho_2(V_{4/3}W_{2/3})O_7$	10.165	[7]
$Gd_2(CrSb)O_7$	10.300	[1]	$Er_2(V_{4/3}W_{2/3})O_7$	10.137	[7]
$Tb_2(CrSb)O_7$	10.260	[1]	$Tm_2(V_{4/3}W_{2/3})O_7$	10.118	[7]
$Dy_2(CrSb)O_7$	10.250	[1]	$Yb_2(V_{4/3}W_{2/3})O_7$	10.393	[7]
$Ho_2(CrSb)O_7$	10.220	[1]	$Lu_2(V_{4/3}W_{2/3})O_7$	10.078	[7]
$Er_2(CrSb)O_7$	10.200	[1]	$Y_2(V_{4/3}W_{2/3})O_7$	10.164	[7]
$Yb_2(CrSb)O_7$	10.160	[1]			
$Y_2(CrSb)O_7$	10.215	[1]	$Gd(Mn_{4/3}W_{2/3})O_7$	10.363 (92.87)	[8, 9]
$Pr_2(FeSb)O_7$	10.405	[1]	$Dy(Mn_{4/3}W_{2/3})O_7$	10.291 (92.73)	[8, 9]
$Nd_2(FeSb)O_7$	10.375	[1]			
$Sm_2(FeSb)O_7$	10.305	[1]	$Ho(Mn_{4/3}W_{2/3})O_7$	10.264 (92.67)	[8, 9]
$Eu_2(FeSb)O_7$	10.295	[1]			
$Gd_2(FeSb)O_7$	10.265	[1]	$Er(Mn_{4/3}W_{2/3})O_7$	10.215 (92.62)	[8, 9]
$Tb_2(FeSb)O_7$	10.230	[1]			
$Dy_2(FeSb)O_7$	10.210	[1]	$Tm(Mn_{4/3}W_{2/3})O_7$	10.165 (92.58)	[8, 9]
$Ho_2(FeSb)O_7$	10.191	[1]			
$Er_2(FeSb)O_7$	10.160	[1]	$Yb(Mn_{4/3}W_{2/3})O_7$	10.135 (92.53)	[8, 9]
$Yb_2(FeSb)O_7$	10.135	[1]			
$Y_2(FeSb)O_7$	10.180	[1]	$Gd(Fe_{4/3}W_{2/3})O_7$	10.337 (92.88)	[10]
$Nd_2(NdSb)O_7$	10.820	[2, 3]	$Dy(Fe_{4/3}W_{2/3})O_7$	10.279 (92.77)	[10]
$Sm_2(SmSb)O_7$	10.720	[2, 3]			
$Eu_2(EuSb)O_7$	10.668	[2, 3]	$Ho(Fe_{4/3}W_{2/3})O_7$	10.245 (92.69)	[10]
$Gd_2(GdSb)O_7$	10.638	[2, 3]			
$Tb_2(TbSb)O_7$	10.550	[2, 3]	$Er(Fe_{4/3}W_{2/3})O_7$	10.219 (92.61)	[10]
$Dy_2(DySb)O_7$	10.522	[2, 3]			
$Ho_2(HoSb)O_7$	10.495	[2, 3]	$Tm(Fe_{4/3}W_{2/3})O_7$	10.175 (92.60)	[10]
$Er_2(ErSb)O_7$	10.448	[2, 3]			
$Tm_2(TmSb)O_7$	10.410	[2, 3]	$Yb(Fe_{4/3}W_{2/3})O_7$	10.145 (92.50)	[10]
$Yb_2(YbSb)O_7$	10.368	[2, 3]			
$Lu_2(LuSb)O_7$	10.359	[2, 3]	$Y(Fe_{4/3}W_{2/3})O_7$	10.232 (92.68)	[10]
$Y_2(YSb)O_7$	10.487	[2, 3]			
$Nd_2(GaSb)O_7$	10.37	[1]			
$Gd_2(GaSb)O_7$	10.26	[1]	**$R_2(M^{2+}_{2/3}M^{5+}_{4/3})O_7$**		
$Y_2(GaSb)O_7$	10.18	[1]	$Y_2(Mn_{2/3}Mo_{4/3})O_7$	10.30 (91.88)	[11]
$Bi_2(YNb)O_7$	10.95	[4]	$Y_2(Mn_{2/3}Nb_{4/3})O_7$		[11]
$Bi_2(LuNb)O_7$	10.83	[4]	$Y_2(Mn_{2/3}Ta_{4/3})O_7$		[11]
$La_2(ScNb)O_7$	10.672	[5]	**$(RCd)(M^{3+}W^{6+})O_7$**		
$Nd_2(ScNb)O_7$	10.534	[5]	$(GdCd)(VW)O_7$	10.244	[8]
$Sm_2(ScNb)O_7$	10.497	[5]	$(TbCd)(VW)O_7$	10.255	[8]
$Ho_2(ScNb)O_7$	10.332	[6]	$(DyCd)(VW)O_7$	10.218	[8]
$Sm_2(ScTa)O_7$	10.466	[6]	$(HoCd)(VW)O_7$	10.201	[8]

TABLE 4 (cont'd)

Compound	a_0 (Å)	Ref.*
$(ErCd)(VW)O_7$	10.184	[8]
$(TmCd)(VW)O_7$	10.174	[8]
$(YbCd)(VW)O_7$	10.162	[8]
$(LuCd)(VW)O_7$	10.150	[8]
$(YCd)(VW)O_7$	10.205	[8]
$(GdCd)(CrW)O_7$	10.194	[8]
$(TbCd)(CrW)O_7$	10.176	[8]
$(DyCd)(CrW)O_7$	10.165	[8]
$(HoCd)(CrW)O_7$	10.152	[8]
$(ErCd)(CrW)O_7$	10.134	[8]
$(TmCd)(CrW)O_7$	10.126	[8]
$(YbCd)(CrW)O_7$	10.115	[8]
$(LuCd)(CrW)O_7$	10.104	[8]
$(YCd)(CrW)O_7$	10.149	[8]
$(GdCd)(MnW)O_7$	10.249	[8]
$(TbCd)(MnW)O_7$	10.226	[8]
$(DyCd)(MnW)O_7$	10.217	[8]
$(HoCd)(MnW)O_7$	10.200	[8]
$(ErCd)(MnW)O_7$	10.182	[8]
$(TmCd)(MnW)O_7$	10.174	[8]
$(YbCd)(MnW)O_7$	10.161	[8]
$(LuCd)(MnW)O_7$	10.153	[8]
$(YCd)(MnW)O_7$	10.203	[8]
$(GdCd)(FeW)O_7$	10.252	[8]
$(TbCd)(FeW)O_7$	10.233	[8]
$(DyCd)(FeW)O_7$	10.222	[8]
$(HoCd)(FeW)O_7$	10.206	[8]
$(ErCd)(FeW)O_7$	10.194	[8]
$(TmCd)(FeW)O_7$	10.184	[8]
$(YbCd)(FeW)O_7$	10.170	[8]
$(LuCd)(FeW)O_7$	10.159	[8]
$(YCd)(FeW)O_7$	10.205	[8]
$(RCd)(Fe^{3+}_{1/2}Nb^{5+}_{3/2})O_7$		
$(CdLa)(Fe_{1/2}Nb_{3/2})O_7$	10.429	[12]
$(CdNd)(Fe_{1/2}Nb_{3/2})O_7$	10.381	[12]
$(CdSm)(Fe_{1/2}Nb_{3/2})O_7$	10.354	[12]
$(CdGd)(Fe_{1/2}Nb_{3/2})O_7$	10.341	[12]
$(CdDy)(Fe_{1/2}Nb_{3/2})O_7$	10.317	[12]
$(CdHo)(Fe_{1/2}Nb_{3/2})O_7$	10.303	[12]
$(CdEr)(Fe_{1/2}Nb_{3/2})O_7$	10.297	[12]
$(CdTm)(Fe_{1/2}Nb_{3/2})O_7$	10.285	[12]
$(CdYb)(Fe_{1/2}Nb_{3/2})O_7$	10.278	[12]
$(CdLu)(Fe_{1/2}Nb_{3/2})O_7$	10.275	[12]
$(CdY)(Fe_{1/2}Nb_{3/2})O_7$	10.305	[12]
$(RA)(M^{4+}Nb^{5+})O_7$		
$(CaLa)(TiNb)O_7$	10.374	[12]
$(CdLa)(TiNb)O_7$	10.350	[12]
$(PbLa)(TiNb)O_7$	10.383	[12]
$(CdNd)(TiNb)O_7$	10.315	[12]
$(CaSm)(TiNb)O_7$	10.318	[12]
$(CdSm)(TiNb)O_7$	10.278	[12]
$(PbSm)(TiNb)O_7$	10.369	[12]
$(CaEr)(TiNb)O_7$	10.219	[12]
$(CaLa)(ZrNb)O_7$	10.610	[13]
$(SrLa)(ZrNb)O_7$	10.642	[13]
$(BaLa)(ZrNb)O_7$	10.710	[13]
$(CdLa)(ZrNb)O_7$	10.530	[13]
$(PbLa)(ZrNb)O_7$	10.668	[13]
$(CaSm)(ZrNb)O_7$	10.518	[13]
$(SrSm)(ZrNb)O_7$	10.651	[13]
$(CdSm)(ZrNb)O_7$	10.431	[13]
$(PbSm)(ZrNb)O_7$	10.620	[13]
$(CaEr)(ZrNb)O_7$	10.371	[13]
$(CaLa)(HfNb)O_7$	10.600	[13]
$(SrLa)(HfNb)O_7$	10.635	[13]
$(BaLa)(HfNb)O_7$	10.700	[13]
$(CdLa)(HfNb)O_7$	10.518	[13]
$(PbLa)(HfNb)O_7$	10.662	[13]
$(CaSm)(HfNb)O_7$	10.593	[13]
$(SrSm)(HfNb)O_7$	10.579	[13]
$(BaSm)(HfNb)O_7$	10.537	[13]
$(CdSm)(HfNb)O_7$	10.438	[13]
$(PbSm)(HfNb)O_7$	10.652	[13]
$(CaEr)(HfNb)O_7$	10.316	[13]
$(RA)(M^{4+}M^{5+})O_7$		
$(CaLa)(SnNb)O_7$	10.450	[13]
$(SrLa)(SnNb)O_7$	10.562	[13]
$(BaLa)(SnNb)O_7$	10.600	[13]
$(CdLa)(SnNb)O_7$	10.410	[13]
$(PbLa)(SnNb)O_7$	10.580	[13]
$(CaSm)(SnNb)O_7$	10.541	[13]
$(SrSm)(SnNb)O_7$	10.444	[13]
$(CdSm)(SnNb)O_7$	10.480	[13]
$(PbSm)(SnNb)O_7$	10.538	[13]
$(CaEr)(SnNb)O_7$	10.385	[13]
$(CaLa)(TiTa)O_7$	10.365	[13]
$(CdLa)(TiTa)O_7$	10.334	[13]
$(PbLa)(TiTa)O_7$	10.376	[13]
$(CaSm)(TiTa)O_7$	10.295	[13]
$(CdSm)(TiTa)O_7$	10.247	[13]
$(PbSm)(TiTa)O_7$	10.337	[13]
$(CaEr)(TiTa)O_7$	10.222	[13]
$(CdNd)(TiTa)O_7$	10.30	[13]
$(PbCe)(TiTa)O_7$	10.34	[13]

TABLE 4 (cont'd)

Compound	a_0 (Å)	Ref.*	Compound	a_0 (Å)	Ref.*
$(PbPr)(TiTa)O_7$	10.39	[13]	$\mathbf{(RM^{2+})(Pb^{4+}Bi^{5+})O_7}$		
$(PbNd)(TiTa)O_7$	10.39	[13]	$(LaCa)(PbBi)O_7$	10.889	[14]
$(PbSm)(TiTa)O_7$	10.36	[13]	$(NdCa)(PbBi)O_7$	10.842	[14]
$(PbEu)(TiTa)O_7$	10.36	[13]	$(SmCa)(PbBi)O_7$	10.810	[14]
$(PbBi)(TiTa)O_7$	10.39	[13]	$(EuCa)(PbBi)O_7$	10.794	[14]
$(ZnNd)(TiTa)O_7$	10.26	[13]	$(GdCa)(PbBi)O_7$	10.783	[14]
$(CaLa)(HfTa)O_7$	10.600	[13]	$(HoCa)(PbBi)O_7$	10.746	[14]
$(SrLa)(HfTa)O_7$	10.631	[13]	$(ErCa)(PbBi)O_7$	10.720	[14]
$(BaLa)(HfTa)O_7$	10.661	[13]	$(LaSr)(PbBi)O_7$	10.982	[14]
$(CdLa)(HfTa)O_7$	10.520	[13]	$(NdSr)(PbBi)O_7$	10.920	[14]
$(PbLa)(HfTa)O_7$	10.660	[13]	$(SmSr)(PbBi)O_7$	10.891	[14]
$(CaSm)(HfTa)O_7$	10.498	[13]	$(GdSr)(PbBi)O_7$	10.860	[14]
$(CdSm)(HfTa)O_7$	10.371	[13]	$(DySr)(PbBi)O_7$	10.831	[14]
$(PbSm)(HfTa)O_7$	10.570	[13]	$(LaBa)(PbBi)O_7$	11.119	[14]
$(CaEr)(HfTa)O_7$	10.430	[13]			
$(CaLa)(SnTa)O_7$	10.448	[13]	$\mathbf{(A^{2+}Ce^{4+})Ti_2O_7}$		
$(SrLa)(SnTa)O_7$	10.540	[13]	$(CdCe)Ti_2O_7$	10.136	[15]
$(BaLa)(SnTa)O_7$	10.572	[13]	$(CaCe)Ti_2O_7$	10.211	[15]
$(CdLa)(SnTa)O_7$	10.389	[13]			
$(PbLa)(SnTa)O_7$	10.564	[13]	$\mathbf{(RNa^{+})(Ti^{4+}Nb^{5+})O_6F}$		
$(CaLa)(SnTa)O_7$	10.448	[13]	$(CeNa)(TiNb)O_6F$	10.374	[16]
$(CaSm)(SnTa)O_7$	10.430	[13]	$(Pra)(TiNb)O_6F$	10.365	[16]
$(CdSm)(SnTa)O_7$	10.332	[13]	$(NdNa)(TiNb)O_6F$	10.347	[16]
$(PbSm)(SnTa)O_7$	10.450	[13]	$(EuNa)(TiNb)O_6F$	10.309	[16]
$(CaEr)(SnTa)O_7$	10.388	[13]	$(GdNa)(TiNb)O_6F$	10.304	[16]
$(CaEr)(ZrTa)O_7$	10.440	[13]	$(YbNa)(TiNb)O_6F$	10.255	[16]
			$(YNa)(TiNb)O_6F$	10.262	[16]
$\mathbf{(RMn^{2+})(Mn^{2+}Sb^{5+})O_6}$					
$(EuMn)(MnSb)O_6$	10.270	[13]	$\mathbf{(RCd^{2+})(Ti^{4+})_2O_6F}$		
$(GdMn)(MnSb)O_6$	10.254	[13]	$(NdCd)(Ti)_2O_6F$	10.240	[16]
$(DyMn)(MnSb)O_6$	10.204	[13]	$(EuCd)(Ti)_2O_6F$	10.198	[16]
$(HoMn)(MnSb)O_6$	10.190	[13]	$(GdCd)(Ti)_2O_6F$	10.184	[16]
$(YbMn)(MnSb)O_6$	10.140	[13]	$(YbCd)(Ti)_2O_6F$	10.119	[16]
$(YMn)(MnSb)O_6$	10.184	[13]	$(YCd)(Ti)_2O_6F$	10.140	[16]

*References: [1] Montmory and Bertaut (1961); [2] Nath (1970); [3] Faurie et al. (1976); [4] Smolenskii et al. (1974); [5] Alpress and Rossell (1979); [6] Filipev et al. (1982); [7] Subramanian et al. (1979); [8] Subramanian et al. (1983); [9] Bazuev et al. (1983); [10] Basile et al. (1977); [11] Bazuev et al. (1984, 1985, 1987, 1989); [12] Fedorov et al. (1976); [13] Belyaev et al. (1972a, b, 1978), Belyaev and Sharmova (1975); [14] Subramanian (1990); [15] McCauley and Hummel (1980); [16] Grannec et al. (1974).

pyrochlore of the type $Ca_{2x}Ce_{2-2x}Sn_2O_7$ over the range $0.35 \leqslant x \leqslant 0.43$. The assumption is that these phases all contain both Ce^{3+} and Ce^{4+}.

Although pyrochlores of the type $(A^{1+}R^{3+})_2M_2O_7$ have been reported for M = Nb, Ta and V (Chincholkar 1972a, b), such phases apparently have not actually been prepared (Sleight 1974b).

4. Electrical properties

Pyrochlores of the type $R_2^{3+}M_2^{4+}O_7$ where M is from group four (Si, Ge, Sn, Pb, Ti, Zr, and Hf) are electrical insulators, as expected for these d^0 or d^{10} electronic configurations. When the d shell is partially filled, semiconducting properties are normally observed with generally low activation energies (table 5). Except for the low-spin d^6 situation, the conduction mechanism is most likely electron hopping between the M sites. For $Pt^{4+}(5d^6)$, the t_{2g} band is filled and the activation energy is presumably related to excitation into the empty e_g band. The fact that the conduction mechanism of the Pt^{4+} compounds differs from the others is supported by the

TABLE 5
Electrical data.

Compound	ρ (Ω cm)[a]	E_a (eV)[b]	Ref.*
$Pr_2Ru_2O_7$(p)[c]	1.0	0.2	[1]
$Nd_2Ru_2O_7$(c)	1.6	0.11	[1]
$Eu_2Ru_2O_7$(c)	1.2	0.3	[1]
$Gd_2Ru_2O_7$(c)	0.2	0.1	[1]
$Yb_2Ru_2O_7$(c)	1	0.12	[1]
$Y_2Ru_2O_7$(p)	10	0.3	[1]
$Nd_2Ir_2O_7$(c)	28×10^{-2}	0.08	[1]
$Sm_2Ir_2O_7$(c)	3.5×10^{-2}	0.08	[1]
$Eu_2Ir_2O_7$(c)	7.0×10^{-2}	0.09	[1]
$Dy_2Ir_2O_7$(c)	2.0×10^{-1}	0.07	[1]
$Y_2Ir_2O_7$(p)	30	0.17	[1]
$Gd_2Os_2O_7$(p)	1×10^{-2}	0.01	[2]
$Nd_2Pt_2O_7$(c)	2×10^{-1}	0.14	[2]
$Gd_2Pt_2O_7$(c)	7×10^{-2}	0.3	[2]
$Sm_2Mo_2O_7$(p)	6×10^{-2}	0.01	[3]
$Eu_2Mo_2O_7$(p)	5×10^{-2}	0.01	[4]
$Gd_2Mo_2O_7$(p)	1×10^{-2}	0.01	[4]
$Dy_2Mo_2O_7$(p)	3×10^{-2}	0.02	[4]
$Er_2Mo_2O_7$(p)	2×10^{-2}	0.05	[4]
$La_2Pb_2O_7$(p)	1010	0.5	[5]
$Gd_2Ti_2O_7$(p)	3.7×10^3	0.25	[1]
$Dy_2Mn_2O_7$(p)	1×10^6	0.37	[3]
$Ho_2Mn_2O_7$(p)	8×10^7	0.45	[3]
$Er_2Mn_2O_7$(p)	3×10^7	0.47	[3]
$Tm_2Mn_2O_7$(p)	2×10^7	0.48	[3]
$Lu_2Mn_2O_7$(p)	2×10^8	0.51	[3]
$Y_2Mn_2O_7$(p)	3×10^6	0.38	[3]

[a] Resistivity at 298 K.

[b] Activation energy determined from the temperature dependence of the electrical resistivity data.

[c] c means data from single crystal; p means data taken from powder compact.

*References: [1] Sleight and Gillson (1970); [2] Shaplygin and Lazarev (1973); Lazarev and Shaplygin (1978a, b); [3] Subramanian et al. (1980b); [4] Greedan et al. (1987); [5] Sleight (1969).

properties when A^{3+} is not a rare earth. Such compounds are metallic for Ru^{4+}, Rh^{4+}, Os^{4+} and Ir^{4+} but semiconducting for Pt^{4+} (Sleight 1968b, Subramanian et al. 1983). Mixing narrow d bands with the broad post-transition metal 6s or 6p bands broadens the t_{2g} band to allow metallic conductivity, but it does not destroy the gap between the t_{2g} and e_g bands. More evidence for a hopping model for the cases other than Pt^{4+} comes from the sign of the Seebeck coefficient and the Hall coefficient. Both measurements were made on $Eu_2Ru_2O_7$ crystals and opposite signs were observed (Sleight and Gillson 1970). This should not be the case for classical semiconductors and is very strong evidence in favor of electron hopping.

Mixed oxides of Ru^{4+} and Ir^{4+} are frequently metallic as are RuO_2 and IrO_2. The more localized electron behavior observed when these cations are located in the pyrochlore structure is presumably due to structural considerations. The M–O–M bond angle in pyrochlores is not the most favorable for delocalization of t_{2g} electrons. The most favorable angle would be 180°, whereas this angle tends to be about 130° in the pyrochlore structure. This is a significant deviation from 180° and is therefore presumably adequate to cause an activated hopping process in the absence of mixing with post-transition metal s or p bands.

Pyrochlores of the type $R_2^{3+}M_2^{4+}O_7$ are very close to the delocalized-electron limit when M^{4+} is $4d^{1-5}$ or $5d^{1-5}$. Thus, it is not surprising that there has been some controversy as to whether these compounds are metallic or low-activation-energy semiconductors. Lazarev and Shaplygin (1978a,b) have argued that $R_2M_2O_7$ (M = Os, Ru and Ir) compounds are metallic based on infrared spectra and the high room-temperature conductivities. However, their arguments are not convincing. Crystals of many of these compounds have been grown hydrothermally, and four-probe electrical resistivity measurements invariably show electrical resistivity decreasing with increasing temperature (Sleight and Gillson 1970). Furthermore, thermoelectric-power measurements always show a value too high for a metallic compound, e.g., +440 for $Eu_2Ru_2O_7$, +320 for $Y_2Ru_2O_7$ and +50 for $Y_2Ir_2O_7$ (Sleight and Gillson 1970). Spectroscopic studies (XPS, UPS, and HREELS) have also been used to substantiate localized electrons for $R_2Ru_2O_7$ pyrochlores and delocalized electrons for $Bi_2Ru_2O_7$ (Cox et al. 1983, 1986). Magnetic susceptibility studies on $R_2Ru_2O_7$ pyrochlores further confirm localized d-electrons (Leonard et al. 1962, Rosset and Ray 1962, Greedan 1991). Ehmann and Kemmler-Sack (1985) conclude from infrared spectra that $R_2Ru_2O_7$ pyrochlores are semiconducting.

Several workers have attempted to find the metal–insulator transition in $Bi_{2-x}R_xRu_2O_7$ pyrochlore solid solutions. Spectroscopic studies (Cox et al. 1986) on the $Bi_{2-x}Gd_xRu_2O_7$ system indicate a transition at about $x = 1.55$, and electrical resistivity data on the $Bi_{2-x}Y_xRu_2O_7$ system suggest a very similar value (Kanno 1992). The transition is not well-defined in either case.

The partial substitution of Ag^+ or Cu^+ for A in $A_2Ru_2O_7$ pyrochlores has been reported (Bouchard 1971, Haouzi et al. 1986) to have a significant effect on the electrical properties of these materials. Such a substitution seems reasonable because both Cu_2O and Ag_2O have the same structure as the A_2O' network of the pyrochlore structure. No pyrochlore of the type $Cu_2M_2O_7$ or $Ag_2M_2O_7$ has ever been reported, but partial substitution of Ag^+ or Cu^+ on the A site can occur. For example, it has been reported that substitution of Cu^+ for Nd^{3+} can occur in the

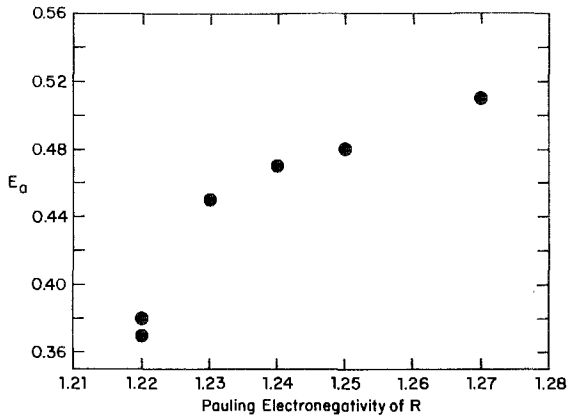

Fig. 5. Activation energy (from electrical resistivity data) versus the Pauling electronegativity value of R for the $R_2Mn_2O_7$ pyrochlores.

$Nd_{2-x}Cu_xRu_2O_{7-x}$ system up to a value of x of about 0.375. Such a substitution apparently leads to metallic behavior (Haouzi et al. 1986). Presumably, the proximity of the Cu 4s and 3d bands has a similar effect on the Ru 4d band as do the 6s or 6p bands of Tl, Pb, and Bi.

For $R_2M_2O_7$ pyrochlores where the M cation has the electronic configuration d^2 (e.g., Mo^{4+}), d^3 (e.g., Mn^{4+}), d^4 (e.g., Ru^{4+}) or d^5 (e.g., Ir^{4+}), there is a trend toward greater delocalization of the d-electrons as the R cation becomes more electropositive (Subramanian et al. 1980b, Greedan et al. 1987, Subramanian et al. 1988, Sleight and Gillson 1971). This trend is illustrated for the $R_2Mn_2O_7$ series in fig. 5. An analogous situation exists for AMO_3 compounds with the perovskite structure. For pyrochlores of the type $R_2Mo_2O_7$, the increased delocalization apparently results in metallic conductivity for the larger rare earth cations.

Oxygen ion conductivity has also been studied in various pyrochlores, such as $Gd_2Zr_2O_7$ (van Dijk et al. 1983). The structure of this compound takes on a disordered fluorite structure if the compound is quenched from high temperatures. Such a compound may be represented as $MO_{1.75}$, indicating a high level of oxygen vacancies relative to the ideal MO_2 fluorite formula. Higher ionic conductivity is observed for the ordered pyrochlore form, where ideally there are no oxygen vacancies. This suggests that the defect concentration in the pyrochlore modification can remain significant. At 1000 K, a conductivity of 68 $(\Omega\,\mathrm{cm})^{-1}$ is reported for $Gd_2Zr_2O_7$ (van Dijk et al. 1983).

5. Magnetic and specific heat properties

Ferromagnetism has been reported for $R_2M_2O_7$ pyrochlores where M is V (Bazuev et al. 1977, Shin-ike et al. 1977, Soderholm and Greedan 1979, Soderholm et al. 1980, 1982), Mn (Fujinika et al. 1979, Subramanian et al. 1988, Reimers et al. 1991) or Mo (Subramanian et al. 1980b, Mandiram and Gopalakrishman 1980, Ranganathan et al. 1983, Sato et al. 1986, Ali et al. 1989, Greedan 1991). However, the magnetic properties are complex, which, at least in part, is due to frustration. The M cations

may be viewed as clustered into tetrahedral units which share corners to form infinite, intersecting chains. Antiferromagnetic M–M interactions would be expected to dominate via M–O–M superexchange. However, these interactions are frustrated by the tetrahedral arrangement. Spins at two points of the tetrahedron may couple in a antiparallel fashion, but it is then impossible for the remaining two atoms of the tetrahedron to align their spins antiparallel to the first two. This frustration of the antiferromagnetic interaction apparently frequently allows the ferromagnetic interaction, which might be expected to be weaker, to dominate.

The only $R_2V_2O_7$ pyrochlores reported are for R = Tm, Yb and Lu (Shin-ike et al. 1977). These three compounds are ferromagnetic, as indicated in table 6. In addition, magnetic properties have been investigated in the solid solutions $Lu_{2-x}Y_xV_2O_7$, $Lu_{2-x}Sc_xV_2O_7$, and $R_2V_{2-x}Mo_xO_7$ (table 6).

Pyrochlores of the type $A_2Mn_2O_7$ are known for Dy, Ho, Eu, Tm, Yb, Lu, Y, Sc, In and Tl (Subramanian et al. 1988). All exhibit ferromagnetic behavior (table 6). On the other hand, there are indications that these compounds do not possess a spontaneous moment in the absence of an applied field.

Pyrochlores of the type $R_2Mo_2O_7$ are reported for R = Nd–Lu and Y. However, ferromagnetism apparently only occurs in the case of the three largest rare earth cations, i.e. Nd, Sm and Gd (Greedan 1991). The highest electrical conductivity also occurs for these ferromagnetic pyrochlores, which are possibly best described as metals. It is interesting that $R_2Mo_2O_7$ pyrochlores are the only known examples of magnetic order based on Mo^{4+} oxides. Spin-glass behavior is reported for $Y_2Mo_2O_7$ (Sato and Greedan 1987). Specific heat and neutron diffraction studies on $Y_2Mo_2O_7$ indicate no magnetic order down to 4.2 K. Solid solutions of the type $La_{2-x}Y_xMo_2O_7$ have also been prepared, and their magnetic properties have been determined (table 6).

Ferromagnetism has also been reported for pyrochlores of the type $R_2Cr^{3+}Sb^{5+}O_7$ (table 6).

The magnetic properties of $R_2Ru_2O_7$ pyrochlores were investigated for R = Pr, Nd, Gd, Tb, Dy, Ho and Y. The magnetic contribution of Ru^{4+} is less than expected and has been attributed to a high degree of covalency in these compounds. Specific heat measurements on $Y_2Ru_2O_7$, $Nd_2Ru_2O_7$, $Eu_2Ir_2O_7$ and $Lu_2Ir_2O_7$ also indicate no magnetic ordering down to 4.2 K (Blacklock et al. 1980, Blacklock and White 1980).

The magnetic properties of $R_2M_2O_7$ have also been studied where M is a diamagnetic cation such as Ti^{4+} (Townsend and Crossley 1968), Zr^{4+}, Sn^{4+} (Mitina et al. 1970) or Ga^{3+}–Sb^{5+} (Blöte et al. 1969). Magnetic-ordering temperatures have sometimes been detected at very low temperatures: 1.4 K for $Dy_2Ti_2O_7$, 1.3 K for $Ho_2Ti_2O_7$, 1.25 K for $Er_2Ti_2O_7$, 0.21 K for $Yb_2Ti_2O_7$, 0.37 K for $Nd_2Zr_2O_7$, 0.91 K for $Nd_2Sn_2O_7$ and 1.2 K for Nd_2GaSbO_7.

6. Spectroscopy

6.1. *Vibrational spectroscopy*

Theoretical analysis of the normal vibrations of the pyrochlore structure predicts 26 normal modes (McCaffrey et al. 1971, McCauley 1973, Vandenborre et al. 1981).

TABLE 6
Magnetic data for some $R_2M_2O_7$ compounds: M = V, Mn or Mo.

Compound	T_c (K)	θ_c (K)	μ_{eff}	μ_{sat}	Ref.*
$Tm_2V_2O_7$	71.4	+10			[1–4]
$Yb_2V_2O_7$	73.2	+11			
$Lu_2V_2O_7$	72.5	+83.3	1.92	0.93	
$Y_{0.40}Lu_{1.60}V_2O_7$	70	+79	1.96	0.95	
$Y_{0.80}Lu_{1.20}V_2O_7$	71.5	+90.2	1.90	0.98	
$Sc_{0.20}Lu_{1.80}V_2O_7$	69	+93	1.94	1.00	
$Sc_{0.40}Lu_{1.60}V_2O_7$	67	+83	1.96	0.93	
$Sc_{0.60}Lu_{1.40}V_2O_7$	56	+74	2.12	0.77	
$Sc_{0.80}Lu_{1.20}V_2O_7$	46	+62	2.24		
$Sc_{1.00}Lu_{1.00}V_2O_7$	36	+49	2.34		
$Tb_2Mn_2O_7$	38				
$Dy_2Mn_2O_7$	40	+33	14.4		[5, 6]
$Ho_2Mn_2O_7$	37	+33	14.4		
$Er_2Mn_2O_7$	35	+40	13.3		
$Tm_2Mn_2O_7$	30	+56	10.4		
$Yb_2Mn_2O_7$	35	+41	7.6		
$Lu_2Mn_2O_7$	23	+70	4.9		
$Y_2Mn_2O_7$	20	+50	5.4		
$Sc_2Mn_2O_7$	15				
$Nd_2Mo_2O_7$	96	+115		2.1	[4, 7]
$Sm_2Mo_2O_7$	93	+121		2.3	
$Gd_2Mo_2O_7$	83			1.5	
$Tb_2Mo_2O_7$	7(?)	+17	(21.8)		
$Dy_2Mo_2O_7$		+10	(26.7)		
$Ho_2Mo_2O_7$		+5	(27.0)		
$Er_2Mo_2O_7$		−12	(22.7)		
$Tm_2Mo_2O_7$		−32	(14.6)		
$Yb_2Mo_2O_7$		−25	(4.1)		
$Y_2Mo_2O_7$		−61	(1.06)		
Pr_2CrSbO_7		+7			[8]
Nd_2CrSbO_7		+8			
Sm_2CrSbO_7		+12			
Eu_2CrSbO_7		+4			
Gd_2CrSbO_7		+12			
Tb_2CrSbO_7		+15			
Dy_2CrSbO_7		+16			
Ho_2CrSbO_7		+10			
Er_2CrSbO_7		+10			
Tm_2CrSbO_7		+6			
Yb_2CrSbO_7		+10			
Y_2CrSbO_7		+15			

*References: [1] Soderholm et al. (1982); [2] Shin-ikc et al. (1977); [3] Soderholm and Greedan (1979); [4] Greedan (1991); [5] Subramanian et al. (1988); [6] Troyanchuk and Derkachenko (1988); [7] Sato et al. (1986); [8] Bongers and van Meurs (1967).

Seven of these are IR active, and six are Raman active. Trends in the position of these bands are discussed by Vandenborre et al. (1983) and Subramanian et al. (1983). Raman spectroscopy has been particularly useful in studying order–disorder phenomena in pyrochlores (Michel et al. 1976).

6.2. *UV–visible spectroscopy*

Interatomic electronic transitions can give rise to very complex absorption spectra dependent on the rare earth cation or the transition metal cation present. In addition, charge transfer bands are found at high energies. These charge transfer bands are generally in the UV; however in some cases, such as the $R_2Pb_2O_7$ pyrochlores, the charge transfer band extends well into the visible region. Most of the information available for electronic absorption spectroscopy in pyrochlores is found in publications concerned with luminescent properties.

6.3. *Luminescent properties*

McCauley (1969) studied the luminescence of Eu^{3+} in $R_2M_2O_7$ pyrochlores where M was Ti, Zr, Hf, Sn or a mixture of Sn and Ti. Brixner (1984) described the luminescence of Eu^{3+}, Tb^{3+} and Ti^{4+} in the pyrochlore $La_2Hf_2O_7$. The absorption and luminescence spectra of Nd^{3+} in $Y_2Ti_2O_7$ and $Gd_2Ti_2O_7$ single crystals were given by Antonov et al. (1977). Berdowski and Blasse (1986) have reported on the luminescence and energy-transfer properties of $Eu_2Ti_2O_7$ and $Gd_2Ti_2O_7$:Eu.

6.4. *Mössbauer spectroscopy*

Mössbauer studies of Fe in the R_2FeSbO_7 series (Knop et al. 1968, Snee et al. 1977, Sundararajan et al. 1983) and of Sn in the $R_2Sn_2O_7$ series (Belyaev et al. 1969, Loebenstein et al. 1970, Calage and Pannetier 1977, Snee et al. 1977) give rise to similar conclusions. In both cases, the isomer shift is essentially constant as the rare earth is varied. On the other hand, there are definite trends with the quadrupole splitting as the rare earth cation is varied (fig. 6). Clearly the environment of the M cation is becoming closer to ideal octahedral as the rare earth cation increases in size. This is to be expected since the oxygen positional parameter, x(O), decreases steadily towards its octahedral value of 0.3125 as the rare earth cation size increases.

Mössbauer studies have also been carried out for Eu, Gd, and Dy in various $R_2M_2O_7$ pyrochlores (Bauminger et al. 1974, 1976, Cashion et al. 1973, Dunlap et al. 1978a, b, Kmiec et al. 1975, Chien and Sleight 1978). The unusual environment for the rare earth cation in the pyrochlore structure leads to a very pronounced lattice vibrational anisotropy, which can be estimated from the Mössbauer data. Also, the highly anisotropic environment leads to a very large electric field gradient at the rare earth cation site. In fact, $R_2Ti_2O_7$ pyrochlores have the largest electric field gradient ever observed for a rare earth ion (Bauminger et al. 1974, 1976). The electric field gradient increases regularly with decreasing unit-cell edge in the $Eu_2M_2O_6O'$ series where M is Pb, Zr, Hf, Sn, Mo and Ti. This can be attributed to a decreasing

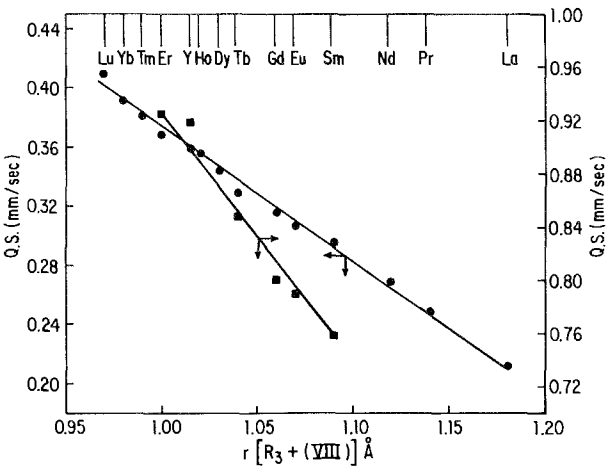

Fig. 6. Variation of the quadrupole splitting versus ionic radius of rare earth for $R_2Sn_2O_7$ (circles) and R_2FeSbO_7 (squares) pyrochlores.

Eu–O′ distance along the three-fold axis. The isomer shifts of ^{151}Eu in $Eu_2M_2O_7$ pyrochlores relative to Eu_2O_3 are negative where M is Pb, Zr, Hf, Sn, Mo and Ti, but are positive where M is Pt, Ir and Ru (Chien and Sleight 1978).

The question of magnetic order in $Y_2Ru_2O_7$ has been addressed by ^{99}Ru studies (Gibb et al. 1973). The conclusion was that this compound is magnetically ordered at 4.2 K, but other interpretations of the data are possible.

Appendix. Bibliography on rare earth $R_2M_2O_7$ pyrochlores

Reviews	Subramanian et al. (1983), Greedan (1991)
Structural papers	Jona et al. (1955), Sleight (1968a), Longo et al. (1969), Barker et al. (1970), McCauley (1980), Subramanian et al. (1983, 1988), Chakoumakos (1984), Darriet et al. (1971), Nikiforov et al. (1972), Nyman et al. (1978), Pannetier and Lucas (1970), O'Keefe et al. (1980)

$R_2M_2O_7$ pyrochlores (M = 3d transition element)

$R_2Ti_2O_7$ pyrochlores

Synthesis	Knop et al. (1965), Roth (1956), Brixner (1964), Knop et al. (1969), Collongues et al. (1965), Bocquillon et al. (1971), Mizutani et al. (1974), Shcherbakova et al. (1979)
Crystal growth	Garton and Wanklyn (1968), Becker and Will (1969, 1970), Kato and Utsunomiya (1970)
Electrical properties	Brixner (1964), Uematsu et al. (1979), Knop et al. (1969)
Magnetic properties	van Geuns (1966), Flood (1974), Cashion et al. (1968), Townsend and Crossley (1968)
Infrared spectra	Knop et al. (1969), Klee and Weitz (1969), McCaffrey et al. (1971), Vandenborre et al. (1983)
Raman spectra	Sheetz and White (1976); Vandenborre et al. (1983)
Mössbauer spectra	Bauminger et al. (1974), Dunlop et al. (1978a,b), Bauminger et al. (1976), Chien and Sleight (1978)

Luminescent	McCauley (1969), Antonov et al. (1977)
$R_2V_2O_7$ pyrochlores	
Synthesis	Bazuev et al. (1976), Kitayama and Katsura (1976), Bazuev et al. (1977, 1978), Shin-ike et al. (1977, 1979), Greedan (1979), Soderholm and Greedan (1979), Molodkin et al. (1978)
Electrical properties	Shin-ike et al. (1977)
Magnetic properties	Bazuev et al. (1977), Shin-ike et al. (1977), Soderholm and Greedan (1979), Soderholm et al. (1980, 1982), Greedan et al. (1986)
$Ln_2Cr_2O_7$ pyrochlores	
Synthesis	Fujinika et al. (1979)
$Ln_2Mn_2O_7$ pyrochlores	
Synthesis	Fujinika et al. (1979), Subramanian et al. (1988)
Crystal growth	Subramanian et al. (1988).
Electrical properties	Fujinika et al. (1979), Subramanian et al. (1988)
Magnetic properties	Fujinika et al. (1979), Subramanian et al. (1988), Troyanchuk and Derkachenko (1988), Reimers et al. (1991)

$R_2M_2O_7$ pyrochlores (M = 4d transition element)

$R_2Zr_2O_7$ pyrochlores	
Synthesis	Roth (1956), Klee and Weitz (1969), Collongues (1963), Perez Y Jorba (1962), Michel et al. (1976)
Order-disorder	Perez Y Jorba (1962), Michel et al. (1976)
Infrared	Klee and Weitz (1969), Gundovin et al. (1975)
Raman spectra	Vandenborre et al. (1981, 1983), Gundovin et al. (1975), Sheetz and White (1976)
Electrical	Steele et al. (1968), Chappey and Guillou (1975), Fomina and Pal'guev (1977), Shinozaki et al. (1979), van Dijk et al. (1980, 1983), van Dijk (1981), van Dijk and Burggraaf (1981)
Magnetic and specific heat studies	Blöte et al. (1969)
$R_2Mo_2O_7$ pyrochlores	
Synthesis	McCarthy (1971), Hubert (1974, 1975a, b), Subramanian et al. (1980)
Electrical	Hubert (1974, 1975), Subramanian et al. (1980b), Mandiram and Gopalakrishman (1980)
Magnetic	Ranganathan et al. (1983), Sato et al. (1986), Greedan et al. (1987), Ali et al. (1989), Reimers et al. (1988, 1990), Greedan et al. (1991), Greedan (1991)
$R_2Tc_2O_7$ pyrochlores	
Synthesis	Muller et al. (1964)
$R_2Ru_2O_7$ pyrochlores	
Synthesis	Bertaut et al. (1959), Lazarev and Shaplygin (1978a, b), Bouchard and Gillson (1971)
Crystal growth	Sleight and Bouchard (1972)
Electrical properties	Sleight and Bouchard (1972), Bouchard and Gillson (1971), Lazarev and Shaplygin (1978a, b), Ehmann and Kemmler-Sack (1985), Haouzi et al. (1986), Kanno (1992)
Magnetic properties	Leonard et al. (1962), Rosset and Ray (1962), Greedan (1991)
Infrared	Kochergina et al. (1978), Ehmann and Kemmler-Sack (1985)
Mössbauer	Chien and Sleight (1978)
XPS, UPS and HREELS	Cox et al. (1983, 1986)
Specific heat studies	Blacklock et al. (1980), Blacklock and White (1980)

$R_2Rh_2O_7$ pyrochlores

Synthesis	Lazarev and Shaplygin (1978a, b)

$R_2Pd_2O_7$ pyrochlores

Synthesis	Sleight (1968b), Lazarev and Shaplygin (1978a)
Electrical properties	Sleight (1968b), Lazarev and Shaplygin (1978a, b)

$R_2M_2O_7$ pyrochlores (M = 5d transition element)

$R_2Hf_2O_7$ pyrochlores

Synthesis	Klee and Weitz (1969), Spiridinov et al. (1968), Besson et al. (1966)
Infrared	Gundovin et al. (1975)
Luminescent	Brixner (1984)

$R_2Os_2O_7$ pyrochlores

Synthesis	Shaplygin and Lazarev (1973)
Electrical properties	Lazarev and Shaplygin (1978a, b)

$R_2Ir_2O_7$ pyrochlores

Synthesis	Sleight and Bouchard (1972), Montmory and Bertaut (1961), Lazarev and Shaplygin (1978a, b)
Crystal growth	Sleight and Bouchard (1972)
Electrical properties	Sleight and Bouchard (1972), Bouchard and Gillson (1971), Lazarev and Shaplygin (1978a, b)
Mössbauer	Chien and Sleight (1978)
Specific heat	Blacklock et al. (1980), Blacklock and White (1980)

$R_2Pt_2O_7$ pyrochlores

Synthesis	Sleight and Bouchard (1972), Sleight (1968), Hoekstra and Gallagher (1968), Hoekstra and Siegel (1968)
Crystal growth	Ostorero and Makram (1974)
Electrical properties	Sleight (1968), Lazarev and Shaplygin (1978a, b)
Infrared	Hoekstra and Gallagher (1968)

$R_2M_2O_7$ pyrochlores (M = Group IVa element)

$R_2Si_2O_7$ pyrochlores

Synthesis	Reid and Ringwood (1974), Reid et al. (1977), Bocquillon et al. (1977), Chateau and Loriers (1979)

$R_2Ge_2O_7$ pyrochlores

Synthesis	Shannon and Sleight (1968), Bocquillon et al. (1978), Bocquillon and Padiour (1980)

$R_2Sn_2O_7$ pyrochlores

Synthesis	Whinfrey et al. (1960), Whinfrey and Tauber (1961)
Infrared/Raman	McCaffrey et al. (1971), Brisse and Knop (1968), Vandenborre et al. (1983)
Electrical	Brisse and Knop (1968)
Magnetic properties	van Geuns (1966)
Specific heat	Blöte et al. (1969)
Mössbauer (Sn)	Belyaev et al. (1969), Loebenstein (1970), Calage and Pannetier (1977)
Mössbauer (Ln)	Cashion et al. (1973), Kmiec et al. (1975), Chien and Sleight (1978), Bauminger et al. (1976)

$R_2Pb_2O_7$ pyrochlores

Synthesis	Brisse (1967), Sleight (1969)

References

Aleshin, E., and R. Roy, 1962, J. Am. Ceram. Soc. **45**, 18.

Ali, N., M.P. Hill, S. Labroo and J.E. Greedan, 1989, J. Solid State Chem. **83**, 178.

Allpress, J.G., and H.J. Rossell, 1979, J. Solid State Chem. **27**, 105.

Antonov, V.A., P.A. Arsen'ev and D.S. Petrova, 1977, Phys. Status Solidi **41**, K127.

Bamberger, C.E., H.W. Dunn, G.M. Begun and S.A. Landry, 1985, J. Solid State Chem. **58**, 114.

Barker, W.W., J. Graham, O. Knop and F. Brisse, 1970, Crystal chemistry of oxide pyrochlores, in: The Chemistry of Extended Defects in Non-metal Solids, eds L. Eyring and M. O'Keeffe (North Holland, Amsterdam).

Basile, F., P. Poix and D. Michel, 1977, Ann. Chim. **2**, 283.

Bauminger, E.R., A. Diamant, I. Felner, I. Nowik and S. Ofer, 1974, Phys. Lett. A **50**, 321, and references therein.

Bauminger, E.R., A. Diamant, I. Felner, I. Nowik, A. Mustachi and S. Ofer, 1976, J. Phys. Colloq. (Paris) **C6**, 49.

Bazuev, G.V., and A.S. Borukhovich, 1983, Russ. J. Phys. Chem. **57**, 1714.

Bazuev, G.V., O.V. Makarova, V.Z. Oboldin and G.P. Shveikin, 1976, Dokl. Akad. Nauk SSSR **230**, 869.

Bazuev, G.V., A.A. Samokhvalov, Yu.N. Morozov, I.I. Matveenko, V.S. Babushkin, T.I. Arbuzova and G.P. Shveikin, 1977, Sov. Phys.-Solid State **19**, 1913.

Bazuev, G.V., O.V. Makarova and G.P. Shveikin, 1978, Russ. J. Inorg. Chem. **23**, 345.

Bazuev, G.V., O.V. Makarova and G.P. Shveikin, 1983, Russ. J. Inorg. Chem. **28**, 1088.

Bazuev, G.V., O.V. Makarova and G.P. Shveikin, 1984, Russ. J. Inorg. Chem. **29**, 504.

Bazuev, G.V., O.V. Makarova and G.P. Shveikin, 1985, Russ. J. Inorg. Chem. **30**, 1253.

Bazuev, G.V., V.G. Zubkov and G.P. Shveikin, 1987, Russ. J. Inorg. Chem. **31**, 1377.

Bazuev, G.V., O.V. Makarova and N.A. Kirsanov, 1989, Russ. J. Inorg. Chem. **34**, 13.

Becker, W.J., and G. Will, 1969, Z. Naturforsch. B **24**, 259.

Becker, W.J., and G. Will, 1970, Z. Kristallogr. **131**, 278.

Belyaev, I.N., and A.G. Sharmova, 1975, Izv. Akad. Nauk SSSR Neorg. Mater. **11**, 269.

Belyaev, I.N., I.S. Lyubutin, L.N. Dem'yanets, T.V. Dmitrieva and L.P. Mitina, 1969, Sov. Phys.-Solid State **11**, 424.

Belyaev, I.N., L.N. Aver'yanova, L.A. Solov'ev, V.M. Ezhov and Yu.I. Gol'tsov, 1972a, Sov. Phys.-Crystallogr. **17**, 98.

Belyaev, I.N., L.N. Aver'yanova, V.M. Ezhov and D.V. Balashov, 1972b, Russ. J. Inorg. Chem. **17**, 1490.

Belyaev, I.N., M.L. Sholokhovich and N. Khan, 1978, Russ. J. Inorg. Chem. **23**, 1112.

Berdowski, P.A.M., and G. Blasse, 1986, J. Solid State Chem. **62**, 317.

Bernard, D., 1976, Ph.D. Thesis (University of Rennes, France).

Bertaut, E.F., F. Forrat and M.C. Montmory, 1959, C.R. Hebd. Séances Acad. Sci. C (Paris) **249**, 829.

Besson, J., C. Deportes and G. Robert, 1966, C.R. Hebd. Séances Acad. Sci. C (Paris) **262**, 527.

Blacklock, K., and H.W. White, 1979, J. Chem. Phys. **71**, 5287.

Blacklock, K., and H.W. White, 1980, J. Chem. Phys. **72**, 2191.

Blacklock, K., H.W. White and E. Gurmen, 1980, J. Chem. Phys. **72**, 1966.

Blöte, H.W.J., R.F. Wielinga and W.J. Huiskamp, 1969, Physica **43**, 549.

Bocquillon, G., and J. Padiour, 1980, Mater. Res. Bull. **15**, 1069.

Bocquillon, G., F. Queyrous, C. Susse and R. Collongues, 1971, C.R. Hebd. Séances Acad. Sci. C (Paris) **272**, 572.

Bocquillon, G., C. Chateau, C. Loriers and J. Loriers, 1977, J. Solid State Chem. **20**, 1.

Bocquillon, G., J. Mougrion and J. Loriers, 1978, C.R. Hebd. Séances Acad. Sci. C (Paris) **287**, 5.

Bongers, P.F., and E.R. van Meurs, 1967, J. Appl. Phys. **38**, 944.

Bouchard, R.J., 1971, US patent 3847829.

Bouchard, R.J., and J.L. Gillson, 1971, Mater. Res. Bull. **6**, 669.

Brisse, F., 1967, Ph.D. Thesis (Dalhousie University, Halifax, Canada).

Brisse, F., and O. Knop, 1968, Can. J. Chem. **46**, 859.

Brixner, L.H., 1964, Inorg. Chem. **3**, 1065.

Brixner, L.H., 1984, Mater. Res. Bull. **19**, 143.

Bystrom, A., 1945, Ark. Kemi Mineral. Geol. A **18**, 1.

Calage, Y., and J. Pannetier, 1977, J. Phys. & Chem. Solids **38**, 711.

Cashion, J.D., A.H. Cook, M.J.M. Leask, T.L. Thorp and M.R. Wells, 1968, J. Mater. Sci. **3**, 402.

Cashion, J.D., D.B. Prowse and A. Vas, 1973, J. Phys. C **6**, 2611.

Chakoumakos, B.C., 1984, J. Solid State Chem. **53**, 120.

Chappey, B., and M. Guillou, 1975, C.R. Hebd. Séances Acad. Sci. C (Paris) **280**, 1117.

Chateau, C., and J. Loriers, 1979, C.R. Hebd. Séances Acad. Sci. C (Paris) **288**, 421.

Chien, C.L., and A.W. Sleight, 1978, Phys. Rev. B **18**, 2031.

Chincholkar, V.S., 1972a, J. Inorg. Nucl. Chem. **34**, 2973.

Chincholkar, V.S., 1972b, Chem. Commun. **723**.

Collongues, R., 1963, Ann. Chim. **8**, 395.

Collongues, R., M. Perez Y Jorba and J. Lefevre, 1961, Bull. Soc. Chim. France, p. 70.

Collongues, R., F. Queyrous, M. Perez Y Jorba and J.S. Gilles, 1965, Bull. Soc. Chim. France **4**, 1141.

Cox, P.A., R.G. Edgall, J.B. Goodenough, A. Hamnett and C.C. Naish, 1983, J. Phys. C **16**, 6221.

Cox, P.A., J.B. Goodenough, P.J. Tavener, D. Telles and R.G. Egdell, 1986, J. Solid State Chem. **16**, 360.

Darriet, P.J., M. Rat, J. Galy and P. Hagenmuller, 1971, Mater. Res. Bull. **6**, 1305.

Dunlap, B.D., G.K. Shenoy, J.M. Friedt, M. Meyer and G.J. McCarthy, 1978a, Phys. Rev. B **18**, 1936.

Dunlap, B.D., G.K. Shenoy, J.M. Friedt, M. Meyer and G.J. McCarthy, 1978b, J. Appl. Phys. **49**, 1936.

Ehmann, A., and S. Kemmler-Sack, 1985, Mater. Res. Bull. **20**, 437.

Faucher, M., and P. Caro, 1975, J. Solid State Chem. **12**, 1.

Faurie, J.P., G. Boulon and M.C. Delaigue, 1976, J. Solid State Chem. **17**, 7.

Fedorov, N.F., T.A. Tunik, R.N. Razumovski and L.I. Mikhaitova, 1976, Russ. J. Inorg. Chem. **21**, 47.

Filipev, V.S., Ya.E. Cherner, O.A. Bunina and V.F. Seregin, 1982, Sov. Phys.-Crystallogr. **27**, 364.

Flood, D.J., 1974, J. Appl. Phys. **45**, 4041.

Fomina, L.N., and S.F. Pal'guev, 1977, Russ. J. Inorg. Chem. **22**, 177.

Fujinika, H., N. Kinomura, M. Koizumi, Y. Miyamoto and S. Kume, 1979, Mater. Res. Bull. **14**, 1133.

Garton, G., and B.M. Wanklyn, 1968, J. Mater. Sci. **3**, 395.

Gibb, T.C., R. Greatrex, N.N. Greenwood and P. Kaspi, 1973, J.C.S. Dalton, 1253.

Grannec, J., H. Baudry, J. Ravez and J. Portier, 1974, J. Solid State Chem. **10**, 66.

Greedan, J.E., 1979, Mater. Res. Bull. **14**, 13.

Greedan, J.E., 1991, in: Magnetic Properties of Non-Metals, Vol III/27 of Landolt–Bornstein, New Series, ed. H.P.J. Wijn (Springer, Berlin) in press.

Greedan, J.E., M. Sato, Xu Yan and F.S. Razavi, 1986, Solid State Commun. **59**, 895.

Greedan, J.E., M. Sato, N. Ali and W.R. Datars, 1987, J. Solid State Chem. **68**, 300.

Greedan, J.E., J.N. Reimers, C.V. Stager and S.L. Penny, 1991, Phys. Rev. B. **43**, 5682.

Gundovin, N.V., F.M. Spiridinov, L.N. Komissarova and K.I. Petrov, 1975, Russ. J. Inorg. Chem. **20**, 325.

Haouzi, A., J. Muller and J.C. Joubert, 1986, Mater. Res. Bull. **21**, 1489.

Hoekstra, H.R., and F. Gallagher, 1968, Inorg. Chem. 7, 2553.

Hoekstra, H.R., and S. Siegel, 1968, Inorg. Chem. 7, 141.

Horowitz, H.S., J.M. Longo and J.T. Lewandowski, 1981, Mater. Res. Bull. **16**, 489.

Hubert, P.H., 1974, Bull. Soc. Chim. France, p. 2385.

Hubert, P.H., 1975, Bull. Soc. Chim. France, pp. 475, 2463.

Jona, F., G. Shirane and R. Pepinsky, 1955, Phys. Rev. **98**, 903.

Kanno, R., 1992, private communication.

Kato, M., and T. Utsunomiya, 1970, Bull. Tokyo Inst. Technol. **98**, 23.

Kitayama, K., and J. Katsura, 1976, Chem. Lett. (Japan) 815.

Klee, W.E., and G. Weitz, 1969, J. Inorg. Nucl. Chem. **31**, 2367.

Kmiec, K., K. Latka, T. Matlax, K. Ruebenbauer and K. Tomalya, 1975, Phys. Status Solidi b **68**, K125.

Knop, O., F. Brisse, L. Castelliz and Sutarno, 1965, Can. J. Chem. **43**, 2812.

Knop, O., F. Brisse, R.E. Meads and J. Bainbridge, 1968, Can. J. Chem. **46**, 3829.

Knop, O., F. Brisse and L. Castelliz, 1969, Can. J. Chem. **47**, 971.

Kochergina, L.L., V.V. Fomichev, E.E. Antomova and K.I. Petrov, 1978, Russ. J. Inorg. Chem. **24**, 824.

Lazarev, V.B., and I.S. Shaplygin, 1978a, Mater. Res. Bull. **13**, 229.
Lazarev, V.B., and I.S. Shaplygin, 1978b, Russ. J. Inorg. Chem. **23**, 163.
Leonard, R.A., E.F. Bertaut, M.C. Montmory and R. Pauthenet, 1962, J. Appl. Phys. **335**, 1205.
Loebenstein, H.M., R. Zilber and H. Zmora, 1970, Phys. Lett. A **33**, 453.
Longo, J.M., P.M. Raccah and J.B. Goodenough, 1969, Mater. Res. Bull. **4**, 191.
Mandiram, A., and J. Gopalakrishman, 1980, Indian J. Chem. A **19**, 1042.
McCaffrey, J.F., N.T. McDevitt and C.M. Phillippi, 1971, J. Opt. Soc. Am. **61**, 209.
McCarthy, G.J., 1971, Mater. Res. Bull. **6**, 31.
McCauley, R.A., 1969, Ph.D. Thesis (Pennsylvania State University, PA).
McCauley, R.A., 1973, J. Opt. Soc. Am. **63**, 721.
McCauley, R.A., 1980, J. Appl. Phys. **51**, 290.
McCauley, R.A., and F.A. Hummel, 1980, J. Solid State Chem. **33**, 99.
Michel, D., M. Perez, Y. Jorba and R. Collongues, 1974, Mater. Res. Bull. **9**, 1457.
Michel, D., M. Perez, Y. Jorba and R. Collongues, 1976, J. Raman Spectrosc. **5**, 163.
Mitina, L.P., I.N. Belyaev, L.N. Dem'yanets, T.V. Dmitrieva and I.S. Lyubutin, 1970, Sov. Phys.-Crystallogr. **15**, 150.
Mizutani, N., A. Kitazawa and M. Kato, 1974, J. Chem. Soc. Jpn. (Ind. Chem. Sect.) **9**, 1623.
Molodkin, A.K., V.G. Remizov, Yu.E. Bogatov, V.N. Belan and V.M. Skorikov, 1978, Russ. J. Inorg. Chem. **23**, 631.
Montmory, M.C., and E.F. Bertaut, 1961, C.R. Hebd. Séances Acad. Sci. C (Paris) **252**, 4171.
Muller, O., W.B. White and R. Roy, 1964, J. Inorg. Nucl. Chem. **26**, 2075.
Nath, D.K., 1970, Inorg. Chem. **9**, 2714.
Nikiforov, L.G., 1972, Sov. Phys.-Crystallogr. **17**, 347.
Nyman, H., S. Andersson, B.G. Hyde and M. O'Keeffe, 1978, J. Solid State Chem. **26**, 123.
O'Keeffe, M., and B.G. Hyde, 1980, Philos. Trans. R. Soc. London **295**, 553.
Ostorero, J., and H. Makram, 1974, J. Cryst. Growth **24/25**, 677.
Pannetier, J., and J. Lucas, 1970, Mater. Res. Bull. **5**, 797.
Perez Y Jorba, M., 1962, Ann. Chim. **7**, 479.
Ranganathan, R., G. Rangarajan, R. Srinivasan, M.A. Subramanian and G.V. Subba Rao, 1983, J. Low Temp. Phys. **52**, 481.
Reid, A.F., and A.E. Ringwood, 1974, Nature (London) **252**, 681.
Reid, A.F., C. Li and A.E. Ringwood, 1977, J. Solid State Chem. **20**, 219.
Reimers, J.N., J.E. Greedan and M. Sato, 1988, J. Solid State Chem. **72**, 390.
Reimers, J.N., J.E. Greedan, S.L. Penny and C.V. Stager, 1990, J. Appl. Phys. **67**, 5967.
Reimers, J.N., J.E. Greedan, R. Kremer, E. Gmelin and M.A. Subramanian, 1991, Phys. Rev. B. **43**, 3387.
Rosset, J., and K. Ray, 1962, J. Chem. Phys. **37**, 1017.
Roth, R.S., 1956, J. Res. Nat. Bur. Stand. **56**, 17.
Sato, M., and J.E. Greedan, 1987, J. Solid State Chem. **67**, 248.
Sato, M., Xu Yan and J.E. Greedan, 1986, Z. Anorg. Allg. Chem. **540/541**, 177.
Shannon, R.D., 1976, Acta Crystallogr. A **32**, 751.
Shannon, R.D., and A.W. Sleight, 1968, Inorg. Chem. **7**, 1649.
Shaplygin, I.S., and V.B. Lazarev, 1973, Mater. Res. Bull. **8**, 761.
Shcherbakova, L.G., L.G. Mamsurova and G.E. Sukhanova, 1979, Russ. Chem. Rev. **48**, 228.
Sheetz, B.E., and W.B. White, 1976, Proc. 12th Rare Earth Research Conference, Vol. II (Denver Research Institute, Denver, CO) p. 524.
Shin-ike, T., G. Adachi and J. Shiokawa, 1977, Mater. Res. Bull. **12**, 1149.
Shin-ike, T., G. Adachi, J. Shiokawa, M. Shimada and M. Koizumi, 1979, Mater. Res. Bull. **14**, 1323.
Shinozaki, K., M. Miyauchi, K. Kuroda, O. Sakurai, N. Mizutani and M. Kato, 1979, J. Am. Ceram. Soc. **62**, 538.
Sleight, A.W., 1968a, Inorg. Chem. **7**, 1704.
Sleight, A.W., 1968b, Mater. Res. Bull. **3**, 699.
Sleight, A.W., 1969, Inorg. Chem. **8**, 1807.
Sleight, A.W., 1974a, Mater. Res. Bull. **9**, 1177.
Sleight, A.W., 1974b, Mater. Res. Bull. **9**, 1185.
Sleight, A.W., and R.J. Bouchard, 1972, Proc. 5th Mater. Res. Symp., NBS Special Publication, Vol. 364, p. 227.
Sleight, A.W., and J.L. Gillson, 1970, unpublished.
Sleight, A.W., and J.L. Gillson, 1971, Mater. Res. Bull. **6**, 781.
Smolenskii, G.A., V.A. Isupov, G.I. Golovshchikova and A.G. Tutov, 1974, Izv. Akad. Nauk SSSR Neorg. Mater. **12**, 297.
Snee, T.J., R.E. Meads and W.G. Barker, 1977, J. Phys. C **10**, 1761.
Soderholm, L., and J.E. Greedan, 1979, Mater. Res. Bull. **14**, 1449.

Soderholm, L., J.E. Greedan and M.F. Collins, 1980, J. Solid State Chem. **35**, 385.

Soderholm, L., C.V. Stager and J.E. Greedan, 1982, J. Solid State Chem. **43**, 175.

Spiridinov, F.M., V.A. Stepanov, L.N. Komissarova and V.I. Spitsyn, 1968, J. Less.-Common. Met. **14**, 435.

Steele, B.D.H., B. Powell and P. Moody, 1968, Proc. Br. Ceram. Soc. **10**, 87.

Subramanian, M.A., 1981, Ph.D. Thesis (IIT Madras, India).

Subramanian, M.A., 1990, Mater. Res. Bull. **25**, 107.

Subramanian, M.A., G. Aravamudan and G.V. Subba Rao, 1979, Mater. Res. Bull. **14**, 1457.

Subramanian, M.A., G. Aravamudan and G.V. Subba Rao, 1980a, Bull. Mater. Sci. (India) **2**, 201.

Subramanian, M.A., G. Aravamudan and G.V. Subba Rao, 1980b, Mater. Res. Bull. **15**, 1401.

Subramanian, M.A., G. Aravamudan and G.V. Subba Rao, 1983, Prog. Solid State Chem. **15**, 55.

Subramanian, M.A., C.C. Torardi, D.C. Johnson, J. Pannetier and A.W. Sleight, 1988, J. Solid State Chem. **72**, 24.

Sundararajan, M.D., A. Narayanasamy, T. Nagarajan, G.V. Subba Rao, A.K. Singh and L. Haggstrom, 1983, Solid State Commun. **48**, 657.

Towsend, M.G., and W.A. Crossley, 1968, J. Phys. Chem. Solids **29**, 593.

Troyanchuk, I.O., and V.N. Derkachenko, 1988, Sov. Phys.-Solid State **30**, 2003.

Uematsu, K., K. Shinozaki, O. Sakurai, N. Mizutani and M. Kato, 1979, J. Am. Ceram. Soc. **62**, 219.

Van Dijk, T., 1981, Ph.D. Thesis (Twente University of Technology, Enschede, The Netherlands).

Van Dijk, T., and A.J. Burggraaf, 1981, Phys. Status Solidi a **63**, 229.

Van Dijk, T., K.J. de Vries and A.J. Burggraaf, 1980, Phys. Status Solidi a **58**, 115.

Van Dijk, T., K.J. de Vries and A.J. Burggraaf, 1983, Solid State Ionics **17**, 159.

Van Geuns, J.R., 1966, Thesis (University of Leiden, The Netherlands).

Vandenborre, N.T., E. Husson and H. Brusset, 1981, Spectrochim. Acta A **37**, 113.

Vandenborre, N.T., E. Husson, J.P. Chatry and D. Michel, 1983, J. Raman Spectrosc. **14**, 63.

Wakiya, N., N. Kieda, A. Saiki, K. Shonozaki and N. Mizutani, 1991, J. Solid State Chem. **92**, 320.

Whinfrey, C.G., and A. Tauber, 1961, J. Am. Chem. Soc. **83**, 755.

Whinfrey, C.G., D.W. Eckart and A. Tauber, 1960, J. Am. Chem Soc. **82**, 2695.

Handbook on the Physics and Chemistry of Rare Earths, Vol. 16
edited by K.A. Gschneidner, Jr. and L. Eyring

Chapter 108

CRYSTAL STRUCTURES OF RARE EARTH MINERALS

Ritsuro MIYAWAKI
Ceramic Technology Department, Government Industrial Research Institute, Nagoya, Kita, Nagoya 462, Japan

Izumi NAKAI
Department of Chemistry, The University of Tsukuba, Ibaraki 305, Japan

Contents

List of symbols

Ln	chemical symbol for La–Lu	JCPDS	the card number of JCPDS (Joint Committee for Powder Diffraction Standards)
Z	number of structural formula in a unit cell		
Dx	calculated density		
Dm	observed density	AP	atomic parameters
		ID	interatomic distances
		IL	illustration

1. Introduction

1.1. *Rare earth minerals*

So far, a total of about 200 distinct species of rare earth minerals have been described. A large number of carbonates, phosphates, silicates, niobates, fluorides, etc. are known as rare earth minerals. However, no sulfide of the rare earths has been reported as a mineral species. The rare earth minerals are defined as minerals containing rare earth elements as essential constituents (Levinson 1966). However, in order to judge this criterion, it is necessary to obtain structural as well as compositional information about the mineral. In addition, the determination of a chemical formula for a mineral also requires structural information in many cases, because order or disorder of certain atoms in the crystal structure cannot be determined by chemical analysis alone. Therefore, minerals with significant contents of rare earths are treated as rare earth minerals in this text, even if the rare earth content appears "unessential" to the mineral.

The rare earth minerals always contain a variety of rare earth elements. The study of the elemental distribution of rare earths in minerals and rocks has been a subject of geochemistry and mineral chemistry for many years. Their distribution basically follows the Oddo–Harkins rule (Oddo 1914, Harkins 1917): i.e., a lanthanide with even atomic number is more abundant than the neighboring lanthanides with odd atomic number in natural minerals. From the view point of the distribution of rare

earth elements, rare earth minerals can be classified into the following three groups: a group with a predominance of the Y-group rare earths with relatively small ionic radii; a group rich in the Ce-group rare earths with relatively large ionic radii; and a transitional group composed of minerals with both Y-group dominant and Ce-group dominant species: e.g., gadolinite-(Y) and gadolinite-(Ce). By international convention, the correct name of a rare earth mineral is written with the group name followed by the chemical symbol of the dominant rare earth element in parentheses: e.g., again gadolinite-(Y) and gadolinite-(Ce) (Nickel and Mandarino 1987, Bayliss and Levinson 1988).

1.2. *Crystal structures of rare earth minerals*

Crystal structures have been reported for about half of the known rare earth minerals. The structure analyses have revealed that many of them are solid solutions of the rare earth ions and other heterovalent ions, such as Na^{+}, Ca^{2+} and Th^{4+}, that have ionic radii comparable to those of the rare earth ions; some of the rare earth minerals have independent crystallographic sites for rare earth atoms. It is known that the similarity of ionic radii and electronegativities are important factors for isomorphous substitutions, whereas the similarity of chemical properties is sometimes not so significant. On the other hand, when an ion is substituted by another ion with a different valence, charge balance always must be compensated. Studies of the isomorphous substitution between trivalent rare earth ions and other heterovalent ions observed in natural rare earth minerals are important for understanding the behavior of rare earth elements in solids.

Crystallographic studies are impeded by the fact that some rare earth minerals always occur in the metamict state, which is an amorphous state mainly caused by radiation damage to the crystal structure caused by radioactive decay of elements such as uranium and thorium. Crystallographic data and crystal structures of metamict minerals were therefore determined using samples recrystallized by annealing. In such cases, we must note that there is some doubt about the identity of the crystal structure of the recrystallized phase and the original structure of pre-metamict minerals.

Although many structural classifications of minerals have already been proposed, none has focused on rare earth minerals. In view of the importance of the rare earths as natural resources as well as to earth sciences, we have started to review their structures as a series "Crystal Structures of Rare Earth Minerals" (abbreviated as CSRM) yearly updated in "Rare Earths", the Journal of the Rare Earth Society of Japan (Miyawaki and Nakai 1987, 1988, 1989, 1990, 1991). We attempt in this series to provide the complete data necessary for understanding the crystal structures of the rare earth minerals. The present text is based on the CSRM, with permission of the society. In this text, we summarize our most up-to-date knowledge on the crystal structures of rare earth minerals. Thus, this will serve as a structural data base of rare earth minerals. We will continue to publish the CSRM, so that any new data, suggestions, corrections and criticisms are welcome and will be reflected in the next CSRM. Please send all correspondences to R.M.

A complementary review, entitled "Compositional and Phase Relations among Rare Earth Minerals", was recently written by Burt (1989). In this review, the

compositional and phase relations and isomorphous substitutions in rare earth minerals are clearly illustrated in figures with graphical vector representations of mineral compositional spaces.

1.3. *Explanation of the text*

We cite a total of 226 rare earth minerals, from which 104 crystal structures are known and are introduced here. The minerals are classified on the basis of their structures, and minerals without structural data are classified on the basis of their crystallographic data. The mineral species cited in this text are selected from "Glossary of Mineral Species" (Fleischer and Mandarino 1991) and "Mineral Reference Manual" (Nickel and Nichols 1991); some are new minerals described after the publications of the Glossary and the Manual. We also included several unnamed minerals and inadequately described minerals. Some of the crystal structures reported here have been determined using artificial substances. They should be isostructural with natural minerals, but they may differ in chemical composition; an example is garnet.

The literature survey of the crystal structures has been done using "Structure Reports", "Chemical Abstracts", "Mineralogical Abstracts" and "The American Mineralogist". Descriptions of minerals were also searched using "A Manual of New Mineral Names" (Embrey and Fuller 1980), "Dana's System of Mineralogy" (Palache et al. 1944), "Mineralogy" (Kostov 1968), "Mineralogische Tabellen" (Strunz 1978), "The American Mineralogist" and "Systematics of Minerals" (Hölzel 1989).

The newest, therefore probably most reliable, data have been preferentially used in the discussion of the structures, compared with earlier data, if any. Most of the illustrations are original with us. The literature has been covered up to February, 1992.

In the tables the data are presented in the following format: the mineral name is given in the heading. A synonym, variety and/or discredited name, if any, is also given, in parentheses. A mineral name written in capital letters represents a well-described mineral or one approved by the Commission on New Minerals and Mineral Names of the International Mineralogical Association (IMA). A mineral name in lower case is a synonym, variety or discredited name. The chemical formula, and then the structural formula, are given below the mineral name. The chemical symbol "Ln" is used for La–Lu, and "R" stands for rare earths including yttrium.

The crystal data are given as follows: in the first column, crystal system, space group, Z (number of structural formula units in the unit cell), the calculated density, Dx, and observed density, Dm, in the second column the lattice parameters, a, b, c in Å, and α, β, γ, and in the third column the source of the material, reference, and the card number of JCPDS (Joint Committee for Powder Diffraction Standards). The entries AP and ID indicate the tables for the atomic parameters and interatomic distances, respectively.

Most of the figures of the crystal structures were drawn by one of the authors (R.M.) using the atomic parameters reported in the literature. The anion coordinations around the rare earth atoms are represented by polyhedra in some figures for carbonate minerals. In other cases, the coordination polyhedra of rare earths are not drawn explicitly; instead, metal–oxygen bonds are drawn by light lines. Carbonate

ions are expressed by black triangles, and phosphate ions, silicate ions, etc. by tetrahedra shaded with single lines. Octahedral groups such as TiO_6, NbO_6 are illustrated with octahedra shaded with double lines.

Rare earth minerals are roughly classified in the following five classes based on the types of anionic groups found in their crystal structures. However, a group of minerals whose structures are related to each other, are put together in preference to the types of the anionic groups.

Class 1: structures with triangular anionic groups – carbonates.
Class 2: structures with tetrahedral anionic groups – phosphates, silicates, etc.
  (A) structures with isolated tetrahedral anionic groups – phosphates, arsenates, vanadates and silicates.
  (B) structures with linked tetrahedral anionic groups – silicates.
Class 3: structures with tetrahedral and octahedral anionic groups – aluminosilicates and titanosilicates.
Class 4: structures with octahedral anionic groups – complex oxides containing octahedrally coordinated titanium, niobium, tantalum.
Class 5: structures without anionic groups – fluorides and simple oxides.

In each class, the rare earth minerals are basically arranged according to the sizes of the anionic groups: i.e., in the order of isolated anionic groups, one-dimensional chains, columns, two-dimensional sheets, plates, and three-dimensional frameworks.

Section 3 discusses some crystal-chemical aspects of rare earth minerals. Our interest has been centered on the following two points: the difference between Y-group and Ce-group rare earths and isomorphous substitution of rare earth ions with other ions. We have developed our discussion based on the knowledge obtained from the structural data.

2. Crystal structures of rare earth minerals

2.1. *Class 1: structures with triangular anionic groups – carbonates*

The carbonate ion is the only ion with a triangular shape found in the crystal structures of rare earth minerals, although braitschite-(Ce), a unique borate of rare earths, might contain BO_3. The carbonate ion is always isolated from other carbonate ions in the structures. The rare earth atoms of carbonate minerals tend to have higher coordination numbers than those in the other oxysalt minerals.

TENGERITE-(Y)
$Y_2(CO_3)_3 \cdot nH_2O$ ($n = 2$–3)
$Y_2(CO_3)_3 \cdot nH_2O$ ($n = 2$–3)

Sys. orthorhombic	$a = 6.078(4)$ Å	source: synthetic $Y_2(CO_3)_3 \cdot nH_2O$ ($n = 2$–3)
S.G. $Bb2_1m$	$b = 9.157(2)$ Å	Ref.: Miyawaki et al. (1993)
$Z = 4$	$c = 15.114(6)$ Å	JCPDS: #25-1010, #27-0091, #24-1419
$Dx = 3.18$ g/cm^3		
AP: table 1	ID: table 2	IL: fig. 1

KIMURAITE-(Y)
$CaY_2(CO_3)_4 \cdot 6H_2O$
$CaY_2(CO_3)_4 \cdot 6H_2O$

Sys. orthorhombic	$a = 9.2545(8)$ Å	source: Saga, Japan
S.G. Imm2, Immm,	$b = 23.976(4)$ Å	Ref: Nagashima et al. (1986)
I222, or $I2_12_12_1$	$c = 6.0433(7)$ Å	JCPDS: #40-0473
$Z = 4$		
$Dx = 2.98$ g/cm^3		

LOKKAITE-(Y)
$CaY_4(CO_3)_7 \cdot 9H_2O$
$CaY_4(CO_3)_7 \cdot 9H_2O$

Sys. orthorhombic	$a = 39.35(2)$ Å	source: Saga, Japan
S.G. Bm2m	$b = 6.104(4)$ Å	Ref.: Nagashima et al. (1986)
$Z = 4$	$c = 9.26(1)$ Å	JCPDS: #25-0170

The crystal structure of tengerite-(Y) (Miyawaki et al. 1993) is built up of corrugated sheets of nine-coordinated Y-polyhedra and CO_3 triangles (fig. 1). The sheets are connected directly by other CO_3 triangles to form a three-dimensional structure.

Outlines of the crystal structures of kimuraite-(Y) and lokkaite-(Y) were revealed by X-ray crystal structure analyses (Miyawaki and Nakai, unpublished data). The two minerals have corrugated sheets, which are similar to those in tengerite-(Y). However, the arrangements of the sheets are different among the three structures (fig. 2): the corrugated sheets in the structure of kimuraite-(Y) are isolated by calcium ions and water molecules, while lokkaite-(Y) is intermediate between tengerite-(Y) and kimuraite-(Y). This structural relationship among these minerals is reflected in their lattice parameters. The lattice parameters parallel to the plane of the corrugated sheets, a and b of tengerite-(Y), c and a of kimuraite-(Y), and b and c of lokkaite-(Y),

TABLE 1
Atomic parameters of tengerite-(Y)[a].

	x	y	z	B (Å^2)
Y	0.4984(5)	0	0.34223(5)	0.93[b]
C1	0.256(1)	0.257(3)	0.1957(5)	0.70(11)
C2	0.276(3)	0.064(2)	0.5	1.18[b]
O1	0.332(2)	0.129(1)	0.2201(7)	0.75(16)
O2	0.1068(10)	0.253(3)	0.1343(4)	0.82(8)
O3	0.311(2)	0.375(1)	0.2292(7)	0.79(17)
O4	0.473(2)	0.012(2)	0.5	1.18(20)
O5	0.186(2)	0.097(2)	0.421(1)	2.08[b]
O6	0.183(3)	0.414(2)	0.411(1)	2.28(35)

[a] MoKα, $R = 0.045$ (765 refl.).
[b] B_{eq}.

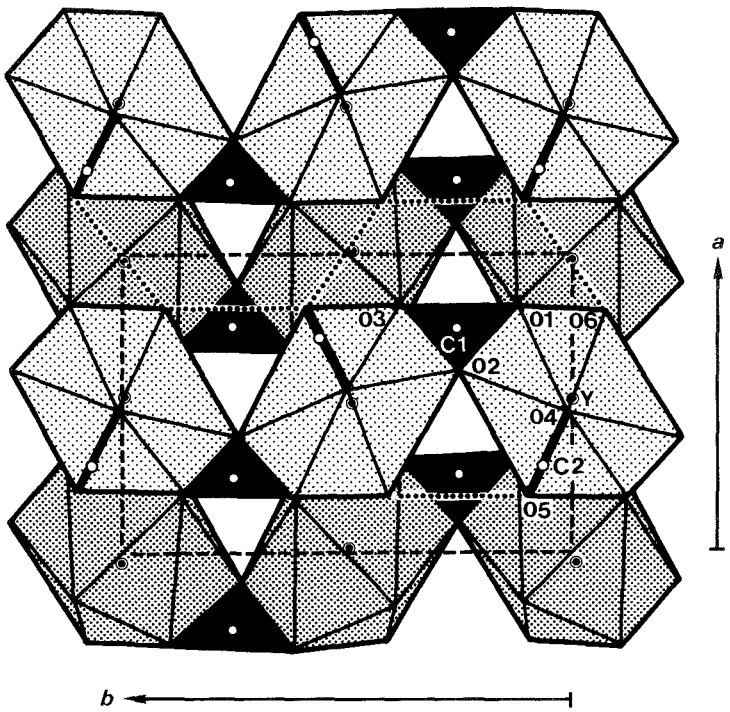

Fig. 1. The crystal structure of tengerite-(Y): projection onto (001) showing the corrugated sheets.

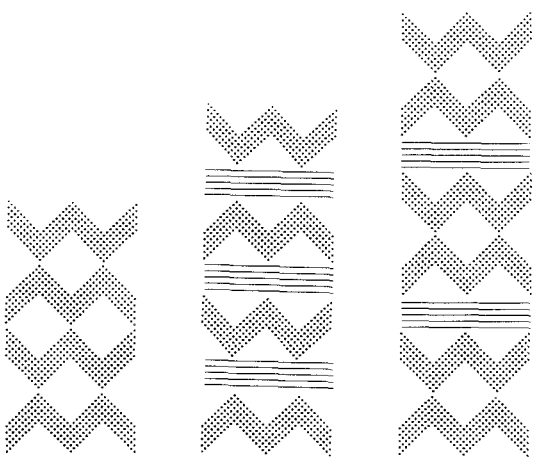

Tengerite-(Y)
$Y_2(CO_3)_3 \cdot 2\text{-}3H_2O$
a= 6.078
b= 9.157
c=15.114

Kimuraite-(Y)
$CaY_2(CO_3)_4 \cdot 6H_2O$
c= 6.0433
a= 9.2545
b=23.976

Lokkaite-(Y)
$CaY_4(CO_3)_7 \cdot 9H_2O$
b= 6.104
c= 9.26
a=39.35

Fig. 2. Schematic illustrations of the crystal structures of tengerite-(Y), kimuraite-(Y), and lokkaite-(Y). The dot pattern indicates the corrugated sheets of rare earth atoms and carbonate ions, and the straight lines indicate the layers of calcium atoms and water molecules.

TABLE 2
Interatomic distances for tengerite-(Y) in Å.

Y–O6	2.34(2)	C1–O3	1.24(2)
Y–O3	2.36(1)	C1–O2	1.30(1)
Y–O2	2.37(3)	C1–O1	1.31(3)
Y–O4	2.392(2)	mean	1.28
Y–O1	2.41(1)		
Y–O5	2.42(2)	C2–O4	1.29(2)
Y–O2′	2.44(3)	C2–O5	1.34(2) ×2
Y–O3′	2.45(1)	mean	1.32
Y–O1′	2.53(1)		
mean	2.41		

are close to 6.1 and 9.2 Å, respectively. On the other hand, the lattice parameters perpendicular to the corrugated sheets; *c* of tengerite-(Y), *b* of kimuraite-(Y), *a* of lokkaite-(Y), are different from each other; the ratio of these axes is very close to that of the number of cations in each chemical formula, namely 2:3:5.

KAMPHAUGITE-(Y)
$CaY(CO_3)_2(OH)\cdot H_2O$
$CaY(CO_3)_2(OH)\cdot H_2O$

Sys. tetragonal	$a = 7.434(1)$ Å	source: Hørtekollen, Oslo, Norway
S.G. $P4_12_12$	$c = 21.793(3)$ Å	Ref.: Rømming et al. (1992)
$Z = 8$		
$Dx = 3.11$ g/cm^3		
AP: table 3	ID: table 4	IL: fig. 3

Kamphaugite-(Y) is a new mineral, which is chemically related to tengerite-(Y), kimuraite-(Y) and lokkaite-(Y) (Raade and Brastad 1992). However, the crystal structure analysis (Rømming et al. 1992) revealed that kamphaugite-(Y) has corrugated sheets different from those in tengerite-(Y). The structure (fig. 3) is built of corrugated sheets parallel to (001), which consist of CO_3 triangles with alternating nine-coordinated Y and eight-coordinated Ca polyhedra. Zeolitic water is in the space between the corrugated sheets.

LANTHANITE-(La)
$La_2(CO_3)_3\cdot 8H_2O$
$La_2(CO_3)_3\cdot 8H_2O$

Sys. orthorhombic	$a = 9.504(4)$ Å	source: Bastnäs, Västmanland, Sweden
S.G. Pbnb	$b = 16.943(6)$ Å	Ref.: Dal Negro et al. (1977)
$Z = 4$	$c = 8.937(5)$ Å	JCPDS: #25-1400
$Dx = 2.78$ g/cm^3		
AP: table 5	ID: table 6	IL: fig. 4

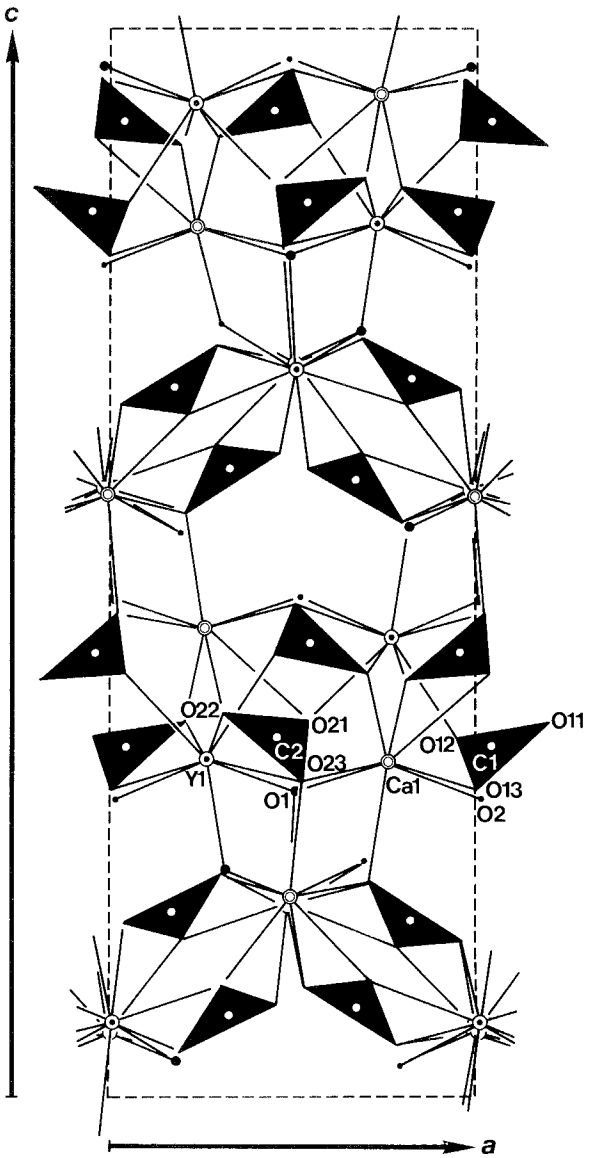

Fig. 3. Projection of the crystal structure of kamphaugite-(Y) onto (010).

LANTHANITE-(Ce)
$Ce_2(CO_3)_3 \cdot 8H_2O$
$Ce_2(CO_3)_3 \cdot 8H_2O$

Sys. orthorhombic	$a =$ 9.482(6) Å	source: Snowdonia, North Wales, UK
S.G. Pbnb	$b =$ 16.938(11) Å	Ref.: Bevins et al. (1985)
$Z =$ 4	$c =$ 8.965(3) Å	JCPDS: #38-0377
Dx = 2.79 g/cm^3		
Dm =2.76 g/cm^3		

TABLE 3
Atomic parameters of kamphaugite-(Y)[a].

	x	y	z	U(Å^2)
Y1[b]	0.99024(10)	0.76810(9)	0.56887(3)	0.0087(2)
Ca1[c]	0.9975(2)	0.2618(2)	0.5633(1)	0.0074(4)
C1	0.6734(11)	0.5487(11)	0.5767(4)	0.013(2)
C2	0.3251(10)	0.9596(11)	0.5864(4)	0.009(2)
O1	0.8126(7)	1.0108(8)	0.5357(3)	0.012(1)
O2	0.0146(9)	0.3030(8)	0.2776(3)	0.019(1)
O11	0.6910(8)	0.7035(9)	0.6021(3)	0.015(1)
O12	0.5441(9)	0.4521(9)	0.5873(3)	0.025(2)
O13	0.8047(8)	0.5036(9)	0.5387(3)	0.022(2)
O21	0.4672(9)	1.0420(8)	0.6029(3)	0.022(2)
O22	0.2867(9)	0.8083(8)	0.6096(3)	0.018(1)
O23	0.2109(8)	1.0255(8)	0.5468(3)	0.016(1)

[a] MoKα, $R = 0.067$, $R_w = 0.081$ (2566 refl.).
[b] 0.90(1)Y, 0.10(1)Gd.
[c] 0.93(1)Ca, 0.07(1)Y.

TABLE 4
Interatomic distances for kamphaugite-(Y) in Å.

Y1–O1	2.309(6)	Ca1–O22	2.348(7)
Y1–O1	2.350(6)	Ca1–O11	2.356(7)
Y1–O11	2.388(7)	Ca1–O13	2.361(7)
Y1–O22	2.395(7)	Ca1–O1	2.395(6)
Y1–O21	2.415(7)	Ca1–O23	2.395(7)
Y1–O12	2.473(7)	Ca1–O23	2.438(6)
Y1–O13	2.491(7)	Ca1–O2	2.517(7)
Y1–O23	2.566(6)	Ca1–O21	2.781(7)
Y1–O2	2.593(7)	mean	2.449
mean	2.442		
C1–O12	1.22(1)	C2–O22	1.26(1)
C1–O11	1.28(1)	C2–O21	1.27(1)
C1–O13	1.32(1)	C2–O23	1.31(1)
mean	1.27	mean	1.28

LANTHANITE-(Nd) (=coutinite)
$Nd_2(CO_3)_3 \cdot 8H_2O$
$Nd_2(CO_3)_3 \cdot 8H_2O$

Sys. orthorhombic	$a =$ 9.476 Å	source: Curitiba, Parana, Brazil
S.G. Pbnb	$b =$ 16.940 Å	Ref.: Roberts et al. (1980)
$Z =$ 4	$c =$ 8.942 Å	JCPDS: #30-0678
Dx = 2.82 g/cm^3		
Dm = 2.81 g/cm^3		

TABLE 5
Atomic parameters of lanthanite-(La)[a].

	x	y	z	B_{eq} (Å^2)
R1	0.25	0.25037(2)	0.75	0.84
R2	0.25	0.28122(2)	0.25	0.79
C1	0.25	0.1066(4)	0.25	1.82
C2	0.4975(6)	0.7165(3)	0.5428(6)	1.23
O1	0.25	0.0340(4)	0.25	5.44
O2	0.3423(4)	0.1469(2)	0.3232(4)	1.40
O3	0.5072(4)	0.7948(2)	0.1875(4)	1.56
O4	0.6164(4)	0.7620(3)	0.9791(5)	1.72
O5	0.3845(4)	0.7919(3)	0.9770(5)	1.66
W1	0.1478(6)	0.4059(3)	0.3781(5)	2.61
W2	0.6773(5)	0.3784(3)	0.1140(5)	2.16
W3	0.8837(4)	0.1209(2)	0.1844(5)	1.88
W4	0.6089(8)	0.4957(4)	0.3874(9)	5.31
H11	0.686(8)	0.044(5)	0.653(8)	6.49
H12	0.641(8)	0.096(4)	0.512(9)	6.06
H21	0.334(8)	0.134(4)	0.506(9)	4.04
H22	0.252(12)	0.081(4)	0.618(8)	8.09
H31	0.379(7)	0.423(4)	0.745(12)	4.55
H32	0.515(9)	0.134(4)	0.324(8)	5.54

[a] MoKα, $R = 0.025$ (1022 refl.).

TABLE 6
Interatomic distances for lanthanite-(La) in Å.

R1–O3	2.495(4) ×2	R2–O4	2.518(4) ×2
R1–O5	2.499(4) ×2	R2–O3	2.518(4) ×2
R1–W3	2.591(4) ×2	R1–O2	2.525(4) ×2
R1–W2	2.592(5) ×2	R2–W1	2.591(5) ×2
R1–O4	2.742(4) ×2	R2–O5	2.760(4) ×2
mean	2.584	mean	2.582
C1–O1	1.232(9)	C2–O5	1.274(7)
C1–O2	1.290(5) ×2	C2–O4	1.277(7)
mean	1.271	C2–O3	1.309(6)
		mean	1.287

CALKINSITE-(Ce)
$Ce_2(CO_3)_3 \cdot 4H_2O$
$Ce_2(CO_3)_3 \cdot 4H_2O$

Sys. orthorhombic	$a = 9.57 \pm 0.02$ Å	source: Bearpaw Mts., MT, USA
S.G. $P2_122_1$	$b = 12.65 \pm 0.08$ Å	Ref.: Pecora and Kerr (1953)
$Z = 4$	$c = 8.94 \pm 0.02$ Å	JCPDS: #6-0076
Dm $= 3.28 \pm 0.01$ g/cm^3		

MOYDITE-(Y)
$Y[B(OH)_4](CO_3)$
$Y[B(OH)_4](CO_3)$

Sys. orthorhombic	$a = 9.089(1)$ Å	source: Papineau, Que., Canada
S.G. Pbca	$b = 12.244(1)$ Å	Ref.: Grice and Ercit (1986)
$Z = 8$	$c = 8.926(1)$ Å	JCPDS: #40-0508
AP: table 7	ID: table 8	IL: fig. 6

The crystal structure of lanthanite-(La) was independently analyzed by Shinn and Eick (1968) and Dal Negro et al. (1977). Although both lanthanite-(La) and tengerite-(Y) are sesqui-type hydrous rare earth carbonates, their crystal structures are quite different from each other. The crystal structure of lanthanite-(La) has two rare earth sites, which are ten-coordinated by the oxygen atoms of the carbonate ions and water molecules. The La polyhedra share corners and edges to form platy sheets parallel to the *ac*-plane (fig. 4). Lanthanite-(La) is a highly hydrated mineral ($8H_2O$) and the sheets are connected only by hydrogen bonds. This structural feature accounts for the presence of the perfect cleavage parallel to (010) in lanthanite-(La).

TABLE 7
Atomic parameters of moydite-(Y)[a].

	x	y	z	U_{eq}
Y	0.0146(1)	0.4991(1)	0.2272(1)	0.0083(1)
B	0.0032(24)	0.2490(16)	0.2415(30)	0.0149(24)
C	0.2622(10)	0.5454(7)	0.0268(8)	0.0113(22)
O1	−0.2792(5)	0.4688(5)	−0.1692(6)	0.0132(16)
O2	−0.1267(7)	0.4550(6)	0.0164(6)	0.0166(18)
O3	0.3680(7)	0.5565(6)	−0.0617(7)	0.0202(20)
O4	0.1019(7)	0.3172(6)	0.1534(6)	0.0155(21)
O5	−0.0944(7)	0.3256(6)	0.3258(6)	0.0159(21)
O6	0.0879(7)	0.1796(7)	0.3505(7)	0.0176(23)
O7	−0.0844(7)	0.1700(6)	0.1538(7)	0.0165(21)

[a] MoKα, $R = 0.051$, $R_w = 0.037$ (1278 refl.).

TABLE 8
Interatomic distances for moydite-(Y) in Å.

Y–O3	2.270(6)	B–O4	1.456(24)
Y–O2	2.341(6)	B–O7	1.477(23)
Y–O1	2.364(5)	B–O5	1.494(23)
Y–O7	2.431(8)	B–O6	1.504(24)
Y–O4	2.455(8)	mean	1.483
Y–O2	2.465(6)		
Y–O1	2.491(5)	C–O3	1.252(10)
Y–O6	2.496(8)	C–O2	1.290(10)
Y–O5	2.505(7)	C–O1	1.292(9)
mean	2.424	mean	1.278

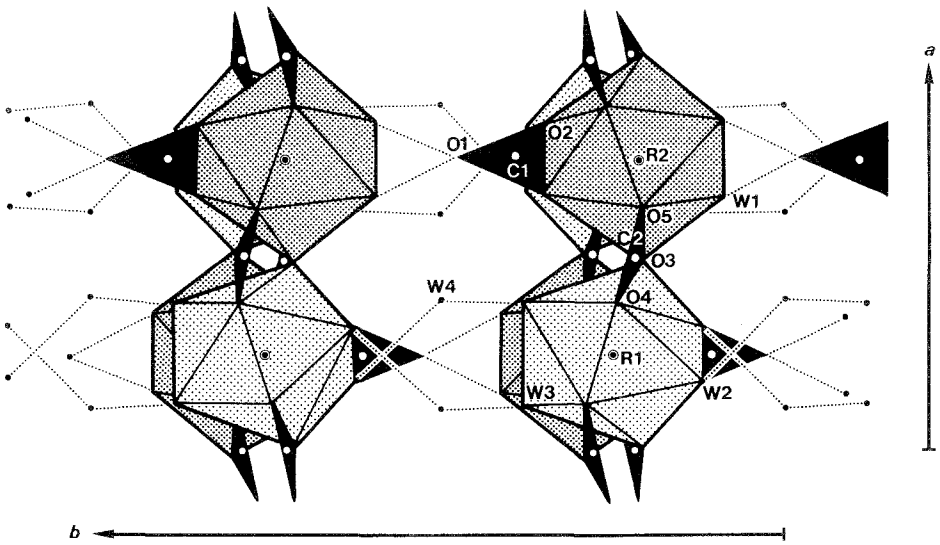

Fig. 4. Projection of the crystal structure of lanthanite-(La) onto (001) showing the connection of the sheets by hydrogen bonds (light dot lines).

Calkinsite-(Ce) was described as a new mineral from Montana, USA, by Pecora and Kerr (1953), but its crystal structure is still unknown. A comparison of the lattice parameters of calkinsite-(Ce) and lanthanite-(La) suggests a close structural relationship between these minerals. The similarity of the *a*- and *c*-axes of calkinsite-(Ce) and lanthanite-(La) shows the presence of lanthanite-type platy sheets in the crystal structure of calkinsite-(Ce) (fig. 5). Calkinsite-(Ce) shows perfect {010} cleavage.

Moydite-(Y) is a rare borocarbonate mineral of rare earths, described by Grice et al. (1986). The crystal structure was determined by Grice and Ercit (1986). Moydite-(Y) has a layered structure (fig. 6), with sheets of corner-sharing YO_9 polyhedra parallel to the *ac*-plane, reinforced by CO_3 triangles. Successive sheets are linked via edge-sharing along the *b*-axis by isolated $B(OH)_4$ tetrahedra, accounting for the {010}

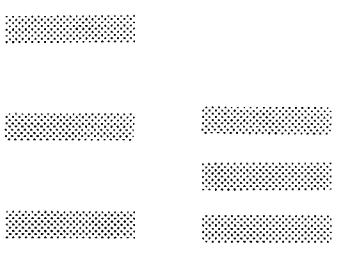

Fig. 5. Schematic illustrations of the crystal structures of lanthanite-(La) and calkinsite-(Ce). The dots indicate the platy sheets of rare earth atoms and carbonate ions. The water molecules are located in the spaces between the sheets.

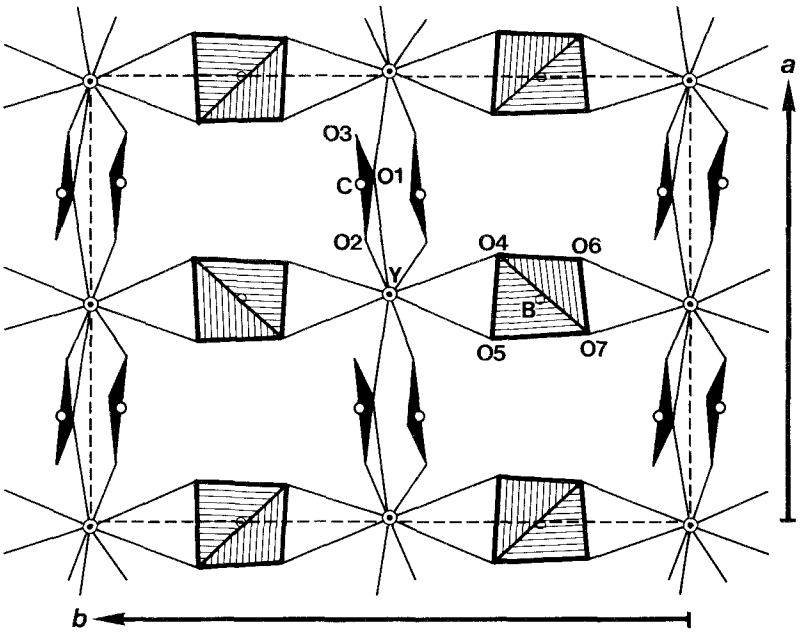

Fig. 6. The crystal structure of moydite-(Y).

cleavage. Grice and Ercit (1986) pointed out that the crystal structures of moydite-(Y) and lanthanite-(La) are closely related to each other. As is mentioned by them, the cell dimensions of moydite-(Y), $a = 9.089(1)$, $b = 12.244(1)$, and $c = 8.926(1)$ Å, resemble those of lanthanite-(La), $a = 9.504(4)$, $b = 16.943(6)$, and $c = 8.937(5)$ Å, in the *ac*-plane because four large La or Y polyhedra, having a cluster diameter of 4.5 Å, define the dimensions of this plane in the two respective structures. In the structure of lanthanite-(La) (Dal Negro et al. 1977), the *b* dimension is controlled by two La polyhedra, two carbonate groups, and two water molecules, whereas in moydite-(Y) the *b* dimension is only $\frac{3}{4}$ that of lanthanite because only two Y polyhedra and two borate tetrahedra need to be accomodated. Chemically, a marked difference is that moydite-(Y) contains smaller Y-group rare earths, whereas lanthanite-(La) contains larger Ce-group rare earths.

DONNAYITE-(Y)
$NaCaSr_3Y(CO_3)_6 \cdot 3H_2O$
$NaCaSr_3Y(CO_3)_6 \cdot 3H_2O$

Sys. triclinic	$a =$ 9.000(1) Å	source: Mont St. Hilaire, Que., Canada
S.G. P1	$b =$ 8.999(1) Å	Ref.: Chao et al. (1978)
$Z =$ 1	$c =$ 6.793(1) Å	JCPDS: #29-1445
Dx = 3.266 g/cm^3	$\alpha = 102.77(1)°$	
Dm = 3.30(1) g/cm^3	$\beta = 116.28(1)°$	
	$\gamma = 59.99(1)°$	

McKELVEYITE-(Y)
$NaCaBa_3Y(CO_3)_6 \cdot 3H_2O$
$NaCaBa_3Y(CO_3)_6 \cdot 3H_2O$

Sys. triclinic	$a =$ 9.170(3) Å	source: Green River Formation, WY, USA
S.G. P1	$b =$ 9.169(3) Å	Ref.: Chao et al. (1978)
$Z =$ 1	$c =$ 7.075(2) Å	JCPDS: #18-0901
	$\alpha =$ 102.50(3)°	
	$\beta =$ 115.63(3)°	
	$\gamma =$ 59.99(3)°	

Donnayite-(Y) from Quebec, Canada was first described by Chao et al. (1978). Their single crystal X-ray diffraction study suggests that donnayite-(Y) is isomorphous with weloganite, $Na_2(Sr,Ca)_3Zr(CO_3)_6 \cdot 3H_2O$. In the crystal structure of weloganite, the six carbonate groups and three water molecules are linked together by six cations with coordinations 10 (for the three Sr), 9 (for the Zr) and 6 (for the two Na) (Grice and Perrault 1975). Chao et al. (1978) further extended the isomorphous relationship to mckelveyite-(Y), which was described as a new mineral from Wyoming, USA by Milton et al. (1965), with chemical formula $Na_{1.9}Ba_{4.0}Ca_{1.1}Sr_{0.2}R_{1.5}(CO_3)_9 \cdot 5H_2O$ and crystallographic data: trigonal, space group $P\bar{3}$, $a = 9.174 \pm 0.002$, $c = 19.154 \pm 0.007$ Å. Later, Desautels (1967) proposed a new space group, P3 or P3m1, based on morphological evidence. The isomorphism, suggested by the strong similarity of its powder diffraction pattern (Milton et al. 1965) with those of donnayite-(Y) and weloganite, was confirmed by an X-ray study of a single crystal. The cell parameters of the three minerals are compared in table 9. They also recalculated the chemical formula of mckelveyite-(Y), $NaCaBa_3Y(CO_3)_6 \cdot 3H_2O$, and indicated that mckelveyite-(Y) is the Ba-analogue of donnayite-(Y).

Although crystal structure analyses of these two minerals have not been carried out, Chao et al. (1978) assumed that the Na and Ca atoms are ordered in the two distinct positions occupied by the Na atoms in the weloganite structure (Grice and Perrault 1975), because the Na:Ca ratios in donnayite-(Y) and mckelveyite-(Y) are both very close to 1:1.

TABLE 9
Comparison of crystal data of donnayite-(Y), weloganite and mckelveyite-(Y).

	Donnayite-(Y) $NaCaSr_3Y(CO_3)_6 \cdot 3H_2O$	Weloganite $Na_2Sr_3Zr(CO_3)_6 \cdot 3H_2O$	mckelveyite-(Y) $NaCaBa_3Y(CO_3)_6 \cdot 3H_2O$
S.G.	P1	P1	P1
Z	1	1	1
a (Å)	9.000(1)	8.966(1)	9.170(3)
b (Å)	8.999(1)	8.980(2)	9.169(3)
c (Å)	6.793(1)	6.730(1)	7.075(2)
α (°)	102.77(1)	102.72(2)	102.50(3)
β (°)	116.28(1)	116.65(1)	115.63(3)
γ (°)	59.99(1)	60.06(1)	59.99(3)

BASTNÄSITE-(Ce)
$Ce(CO_3)F$
$Ce(CO_3)F$

Sys. hexagonal	$a = 7.16_2$ Å	source: Mountain Pass, CA., USA
S.G. $P\bar{6}2c$	$c = 9.78_7$ Å	Ref.: Donnay and Donnay (1953)
$Z = 6$		JCPDS: #11-0340
$Dx = 5.02$ g/cm^3		
$Dm = 4.78 \pm 0.1$ g/cm^3		
AP: table 10	ID: table 11	IL: fig. 7

BASTNÄSITE-(La)
$La(CO_3)F$
$La(CO_3)F$

Sys. hexagonal	$a =$	source:
S.G. $P\bar{6}2c$	$c =$	Ref.: Levinson (1966)
$Z = 6$		

BASTNÄSITE-(Y)
$Y(CO_3)F$
$Y(CO_3)F$

Sys. hexagonal	$a = 6.57$ Å	source: Kazakhstan
S.G. $P\bar{6}2c$	$c = 9.48$ Å	Ref.: Mineev et al. (1970)
$Z = 6$		JCPDS: #25-1009
$Dm = 3.9$–4.0 g/cm^3		

TABLE 10
Atomic parameters of bastnäsite-(Ce)[a].

	x	y	z
Ce	0.333	0	0
C	0.245	0.333	0.25
O1	0.067	0.333	0.25
O2	0.333	0.333	0.138
F1	0	0	0
F2	0.333	0.667	0

[a] Prediction.

TABLE 11
Interatomic distances for bastnäsite-(Ce) in Å.

Ce–O1	2.49 ×2	C–O1	1.27
Ce–O2	2.74 ×6	C–O2	1.27 ×2
Ce–F1	2.39	mean	1.27
Ce–F2	2.39 ×2		
mean	2.60		

HYDROXYLBASTNÄSITE-(Ce)
$Ce(CO_3)(OH)$
$Ce(CO_3)(OH)$

Sys. hexagonal	$a = 7.23 \pm 0.02$ Å	source: CIS
S.G. $P\bar{6}2c$	$c = 9.98 \pm 0.05$ Å	Ref.: Kirillov (1964)
$Z = 6$		JCPDS: #17-0503
Dm = 4.745 g/cm^3		

HYDROXYLBASTNÄSITE-(Nd)
$Nd(CO_3)(OH)$
$Nd(CO_3)(OH)$

Sys. hexagonal	$a = 7.191(1)$ Å	source: Montenegro, Yugoslavia
S.G. $P\bar{6}2c$	$c = 9.921(2)$ Å	Ref.: Maksimović and Pantó (1985); Farkas et al. (1985)
$Z = 6$		JCPDS: #38-0400
Dx = 4.89 g/cm^3		

hydroxylbastnäsite-(La)
$La(CO_3)(OH)$
$La(CO_3)(OH)$

Sys. hexagonal	$a =$	source: Hungary, Yugoslavia
S.G. $P\bar{6}2c$	$c =$	Ref.: Maksimović and Pantó (1983)
$Z = 6$		JCPDS: #29-0744

THORBASTNÄSITE
$Th(Ca,Ce)(CO_3)_2F_2 \cdot 3H_2O$
$(Th,Ca,Ce)(CO_3)F \cdot nH_2O$

Sys. hexagonal	$a = 6.99 \pm 0.02$ Å	source: Eastern Siberia, Russia
S.G. $P\bar{6}2c$	$c = 9.71 \pm 0.02$ Å	Ref.: Pavlenko et al. (1965)
$Z = 6$		JCPDS: #18-1362
Dx = 5.70 g/cm^3		
Dm = 4.04 g/cm^3		

PARISITE-(Ce)
$CaCe_2(CO_3)_3F_2$
$CaCe_2(CO_3)_3F_2$

Sys. trigonal (hex.)	$a = 7.17_6$ Å (order)	source: Muzo, Colombia, etc.
S.G. R3	$a = 7.12_4$ Å (disorder)	Ref.: Donnay and Donnay (1977)
$Z = 18$	$c = 84.1_1$ Å	JCPDS: #33-0269
Dx = 4.29 (order), 4.35 (disorder) g/cm^3		
Dm = 4.05 ± 0.1, 4.26 ± 0.1, 4.39 ± 0.1, 4.41 ± 0.1 g/cm^3		
AP: table 12		

TABLE 12
Atomic parameters of parisite-(Ce)[a].

	x	*y*	*z*
Ce1	0.333	0	0
Ce2	0.333	0	0.108
Ce3	0.333	0	0.167
Ce4	0.333	0	0.275
Ca1	0.333	0	0.054
Ca2	0.333	0	0.221
C1	0.245	0.333	0.138
C2	0.245	0.333	0.304
C3, C4, C5, C6	not determined		
O1	0.067	0.333	0.138
O2	0.067	0.333	0.304
O3	0.333	0.333	0.124
O4	0.333	0.333	0.151
O5	0.333	0.333	0.291
O6	0.333	0.333	0.317
O7, O8, O9, O10, O11, O12, O13, O14, O15, O16, O17, O18	not determined		
F1	0	0	0
F2	0	0	0.333
F3	0	0	0.667
F4	0	0	0.108
F5	0	0	0.441
F6	0	0	0.775
F7	0	0	0.167
F8	0	0	0.500
F9	0	0	0.834
F10	0	0	0.275
F11	0	0	0.608
F12	0	0	0.942

[a] Prediction.

parisite-(Nd)
$CaNd_2(CO_3)_3F_2$
$CaNd_2(CO_3)_3F_2$

Sys. trigonal (hex.)	$a =$	source: Baiyun Obo, China
S.G. R3	$c =$	Ref.: Zhang and Tao (1986)
$Z =$		
$Dm = 4.2–4.5$ g/cm^3		

RÖNTGENITE-(Ce)
$Ca_2Ce_3(CO_3)_5F_3$
$Ca_2Ce_3(CO_3)_5F_3$

Sys. trigonal (hex.)	$a = 7.13_1$ Å	source: Narsarsuk, Greenland, etc.
S.G. R3	$c = 69.4_1$ Å	Ref.: Donnay and Donnay (1953)
$Z = 9$		JCPDS: #35-0579
$Dx = 4.19$ g/cm^3		
AP: table 13		

SYNCHYSITE-(Ce)
$CaCe(CO_3)_2F$
$CaCe(CO_3)_2F$

Sys. monoclinic,	$a = 7.10_7$ Å	source: Narsarsuk, Greenland, etc.
pseudo-hex.	$c = 54.7_2$ Å	Ref.: Donnay and Donnay (1953)
S.G.		JCPDS: #18-0284
$Z = 18$		
$Dx = 3.99$ g/cm^3		
$Dm = 4.05 \pm 0.1$,		
4.15 ± 0.1 g/cm^3		

SYNCHYSITE-(Nd)
$CaNd(CO_3)_2F$
$CaNd(CO_3)_2F$

Sys. ortho, pseudo-hex.	$a = 4.039(2)$ Å	source: Bohemia, Czechoslovakia
S.G.	$b = 6.984(5)$ Å	Ref.: Scharm and Kühn (1983)
$Z = 12$	$c = 54.27(4)$ Å	JCPDS: #35-0589
$Dx = 4.14$ g/cm^3		

SYNCHYSITE-(Y) (=doverite)
$CaY(CO_3)_2F$
$CaY(CO_3)_2F$

Sys. pseudo-orthorhombic	$a = 4.07 \pm 0.02$ Å	source: Dover, NJ, USA
S.G.	$b = 7.06 \pm 0.02$ Å	Ref.: Smith et al. (1960)
$Z = 2$	$c = 9.12 \pm 0.02$ Å	JCPDS: #29-0393, #14-0570
$Dx = 3.61–3.72$ g/cm^3		
$Dm = 3.89–4.1$ g/cm^3		

TABLE 13
Atomic parameters of röntgenite-(Ce)[a].

	x	y	z
Ce1	0.333	0	0
Ce2	0.333	0	0.131
Ce3	0.333	0	0.263
Ca1	0.333	0	0.066
Ca2	0.333	0	0.197
C1	0.245	0.333	0.298
C2, C3, C4, C5	not determined		
O1	0.067	0.333	0.298
O2	0.333	0.333	0.282
O3	0.333	0.333	0.314
O4, O5, O6, O7, O8, O9, O10, O11, O12, O13, O14, O15	not determined		
F1	0	0	0
F2	0	0	0.333
F3	0	0	0.667
F4	0	0	0.131
F5	0	0	0.464
F6	0	0	0.798
F7	0	0	0.263
F8	0	0	0.596
F9	0	0	0.930

[a] Prediction.

CORDYLITE-(Ce)
$BaCe_2(CO_3)_3F_2$
$BaCe_2(CO_3)_3F_2$

Sys. hexagonal
S.G. $P6_3/mmc$ or $P\bar{6}2c$
$Z = 2$
$Dx = 3.97$ g/cm^3
AP: table 14

$a = 5.098(1)$ Å
$c = 23.050(5)$ Å

source: Mont St. Hilaire, Que., Canada
Ref.: Chen and Chao (1975)
JCPDS: #27-0034

TABLE 14
Atomic parameters of cordylite-(Ce).

	x	y	z
R	0.333	0.667	0.143
R′	0.667	0.333	0.857
R″	0.667	0.333	0.643
R‴	0.333	0.667	0.357
Ba	0	0	0
Ba′	0	0	0.5
$CO_3$1	0.667	0.333	0.25
$CO_3$1′	0.333	0.667	0.75
$CO_3$2	0.667	0.333	0.07
$CO_3$2′	0.333	0.667	0.93
$CO_3$2″	0.333	0.667	0.57
$CO_3$2‴	0.667	0.333	0.43
F	0	0	0.143
F′	0	0	0.857
F″	0	0	0.643
F‴	0	0	0.357

HUANGHOITE-(Ce)
$BaCe(CO_3)_2F$
$BaCe(CO_3)_2F$

Sys.	trigonal (hex.)	$a = 5.070 \pm 0.003$ Å	source: China
S.G.	R3m	$c = 38.408 \pm 0.005$ Å	Ref.: Qian et al. (1982)
$Z =$	6		JCPDS: #15-0286
Dm =	4.51–4.67 g/cm^3		
AP:	table 15	ID: table 16	IL: fig. 10

zhonghuacerite-(Ce)
$Ba_2Ce(CO_3)_3F$
$Ba_2Ce(CO_3)_3F$

Sys.	trigonal (hex. subcell)	$a = 5.07$ Å	source: Baiyun Obo, China
S.G.		$c = 9.82$ Å	Ref.: Zhang and Tao (1981)
$Z =$	1		JCPDS: #39-0396
Dx =	4.66 g/cm^3		
Dm =	4.20–4.40 g/cm^3		

CEBAITE-(Ce)
$Ba_3Ce_2(CO_3)_5F_2$
$Ba_3Ce_2(CO_3)_5F_2$

Sys.	monoclinic	$a = 21.2$ Å	source: Baiyun Obo, China
S.G.	Cm	$b = 5.06$ Å	Ref.: Li and Hashimoto (1984);
$Z =$	4	$c = 13.1$ Å	Li and Fan (1982);
Dm =	4.66, 4.31, 4.44 g/cm^3	$\beta = 95°$	Zhang and Tao (1983)
AP:	table 17	ID: table 18	IL: fig. 11

TABLE 15
Atomic parameters of huanghoite-(Ce)[a].

	x	*y*	*z*
Ba1	0	0	0
Ba2	0	0	0.50095(21)
Ce1	0	0	0.25534(7)
Ce2	0	0	0.74515(6)
C1	0	0	0.12721(129)
C2	0	0	0.39361(131)
C3	0	0	0.60860(126)
C4	0	0	0.87351(153)
O1[b]	0.29366(494)	0.14960(474)	0.12689(49)
O2[b]	0.29832(435)	0.14859(442)	0.39479(43)
O3[b]	0.13850(475)	0.28614(488)	0.60822(47)
O4[b]	0.14752(433)	0.29018(438)	0.87240(45)
F1	0	0	0.31700(78)
F2	0	0	0.68490(91)

[a] MoKα, $R = 0.041$ (324 refl.).
[b] Maybe at the special position; 9 b m ($x, 2x, z$; $x, -x, z$; $-2x, -x, z$).

TABLE 16
Interatomic distances for huanghoite-(Ce) in Å[a].

Ba1–O3	2.798(19) ×3	Ba2–O4	2.923(23) ×3
Ba1–O2	2.861(17) ×3	Ba2–O4	2.944(24) ×3
mean	2.830	Ba2–O1	2.972(25) ×3
		Ba2–O1	2.996(26) ×3
Ba1–F1	2.994(7) ×3	mean	2.959
Ba1–F2	3.010(8) ×3		
mean	3.002		
[mean	2.916]		
Ce1–O4	2.522(18) ×3	Ce2–O1	2.478(20) ×3
Ce1–O3	2.630(27) ×3	Ce2–O2	2.620(25) ×3
Ce1–O3	2.674(26) ×3	Ce2–O2	2.625(24) ×3
mean	2.609	mean	2.574
Ce1–F1	2.368(30)	Ce2–F2	2.314(35)
[mean	2.585]	[mean	2.548]
C1–O1	1.290(22) ×3	C2–O2	1.311(19) ×3
C3–O3	1.257(22) ×3	C4–O4	1.275(19) ×3

[a] Recalculated by RM. [mean] is an average of both M–O and M–F distances.

TABLE 17
Atomic parameters of cebaite-(Ce)[a].

	x	y	z		x	y	z
Ba1	0	0	0	O8	0.098	0	0.869
Ba2	0	0.500	0.500	O9	0.492	0.500	0.613
Ba3	0.200	0.500	0.100	O10	0.016	0	0.329
Ba4	0.200	0	0.600	O11	0.021	0.281	0.128
Ba5	0.300	0.500	0.400	O12	0.487	0.781	0.814
Ba6	0.300	0	0.900	O13	0.127	0.281	0.384
Ce1	0.102	0	0.285	O14	0.381	0.781	0.558
Ce2	0.402	0.500	0.685	O15	0.220	0.781	0.235
Ce3	0.102	0.500	0.785	O16	0.280	0.281	0.765
Ce4	0.402	0	0.185	O17	0.321	0.281	0.028
C1	0.051	0.500	0.143	O18	0.187	0.781	0.914
C2	0.457	0	0.799	O19	0.427	0.281	0.284
C3	0.157	0.500	0.399	O20	0.091	0.781	0.658
C4	0.351	0	0.543	O21[c]	0.021	0.719	0.128
C5	0.250	0	0.250	O22[c]	0.487	0.219	0.814
C6	0.250	0.500	0.750	O23[c]	0.127	0.719	0.384
C7	0.351	0.500	0.043	O24[c]	0.381	0.219	0.558
C8	0.157	0	0.899	O25[c]	0.220	0.219	0.235
C9	0.457	0.500	0.299	O26[c]	0.280	0.719	0.765
C10	0.051	0	0.643	O27[c]	0.321	0.719	0.028
O1	0.110	0.500	0.173	O28[c]	0.187	0.219	0.914
O2	0.398	0	0.769	O29[c]	0.427	0.719	0.284
O3	0.216	0.500	0.429	O30[c]	0.091	0.219	0.658
O4	0.292	0	0.513	F1	0.126	0	0.117
O5	0.309	0	0.280	F2	0.426	0.500	0.517
O6	0.191	0.500	0.720	F3	0.126	0.500	0.617
O7	0.410[b]	0.500	0.073	F4	0.426	0	0.017

[a]High-resolution electron microscopy.
[b]0.041, given in the original paper must be mistyped.
[c]These atoms, given in the original paper, are symmetrically equivalent to other atoms: O21 = O11, O22 = O12, O23 = O13, O24 = O14, O25 = O15, O26 = O16, O27 = O17, O28 = O18, O29 = O19, O30 = O20.

baiyuneboite-(Ce)
$NaBaCe_2(CO_3)_4F$
$NaBaCe_2(CO_3)_4F$

Sys. hexagonal	$a = 5.0875(15)$ Å	source:
S.G. $P6_3/mmc$	$c = 23.1680(1)$ Å	Ref.: Fu et al. (1987)
$Z = 2$		
AP: table 19	ID: table 20	IL: fig. 12

A prediction of the structural scheme of bastnäsite-(Ce), parisite-(Ce), synchysite-(Ce) and cordylite-(Ce) was reported by Oftedal (1929, 1931a, b), and later Donnay and Donnay (1953) studied the crystal structures of bastnäsite-(Ce), parisite-(Ce) and synchysite-(Ce), and confirmed the prediction of Oftedal (1931a, b). They also discov-

TABLE 18
Interatomic distances for cebaite-(Ce) in Å[a].

Ba1–O7	2.21	Ba2–O14	2.92 ×2	Ba3–O1	2.21	Ba4–O4	2.34
Ba1–O11	2.21 ×2	Ba2–O9	2.94 ×2	Ba3–O15	2.28 ×2	Ba4–O20	2.73 ×2
Ba1–O8	2.81	Ba2–O20	3.05 ×2	Ba3–O18	2.81 ×2	Ba4–O16	2.99 ×2
Ba1–O12	2.81 ×2	Ba2–O13	3.39 ×2	Ba3–O17	3.02 ×2	Ba4–O6	2.99 ×2
mean	2.51	Ba2–O19	3.41 ×2	mean	2.63	Ba4–O13	3.41 ×2
		Ba2–O10	3.42 ×2			Ba4–O3	3.42 ×2
Ba1–F1	2.96	mean	3.19	Ba3–F1	3.00	mean	3.04
Ba1–F4	3.00 ×2	Ba2–F3	2.96	[mean	2.68]	Ba4–F3	3.00 ×2
mean	2.99	Ba2–F2	3.00 ×2			[mean	3.03]
[mean	2.67]	mean	2.99				
		[mean	3.15]				
Ba5–O3	1.85	Ba6–O17	2.21 ×2	Ce1–O10	1.96	Ce2–O9	2.20
Ba5–O14	2.94 ×2	Ba6–O16	2.28 ×2	Ce1–O13	1.97 ×2	Ce2–O14	2.20 ×2
Ba5–O4	2.94 ×2	Ba6–O18	2.66 ×2	Ce1–O15	2.86 ×2	Ce2–O12	2.76 ×2
Ba5–O15	2.99 ×2	Ba6–O2	2.81	Ce1–O11	2.93 ×2	Ce2–O2	2.76 ×2
Ba5–O5	2.99 ×2	mean	2.44	Ce1–O1	2.94 ×2	mean	2.48
Ba5–O19	3.39 ×2	Ba6–F4	2.96	mean	2.60	Ce2–F2	2.30
mean	2.94	[mean	2.51]	Ce1–F1	2.30	[mean	2.45]
Ba5–F2	2.96			[mean	2.57]		
[mean	2.94]						
Ce3–O6	2.14	Ce4–O19	1.97 ×2	C1–O1	1.28	C2–O2	1.28
Ce3–O20	2.19 ×2	Ce4–O5	2.42	C1–O11	1.28 ×2	C2–O12	1.28 ×2
Ce3–O12	2.73 ×2	Ce4–O11	2.91 ×2	mean	1.28	mean	1.28
Ce3–O18	2.76 ×2	Ce4–O17	2.93 ×2				
Ce3–O8	2.76 ×2	Ce4–O7	2.94 ×2	C3–O3	1.28	C4–O4	1.28
mean	2.56	mean	2.66	C3–O13	1.28 ×2	C4–O14	1.28 ×2
Ce3–F3	2.30	Ce4–F4	2.30	mean	1.28	mean	1.28
[mean	2.53]	[mean	2.62]				
C5–O5	1.28	C6–O6	1.28	C7–O7	1.28		
C5–O15	1.28 ×2	C6–O16	1.28 ×2	C7–O17	1.28 ×2		
mean	1.28	mean	1.28	mean	1.28		
C8–O8	1.28	C9–O10	1.28	C10–O9	1.28		
C8–O18	1.28– ×2	C9–O19	1.28 ×2	C10–O20	1.40 ×2		
mean	1.28	mean	1.28	mean	1.36		

[a]Calculated by RM. [mean] is an average of both M–O and M–F distances.

ered a new member of this mineral group during their investigation and reported it as a new mineral, röntgenite-(Ce) (Donnay 1953). They have predicted all the atomic coordinates in bastnäsite-(Ce) and also that of some atoms in parisite-(Ce) and röntgenite-(Ce) by reference to ionic radii and the symmetries, and reported

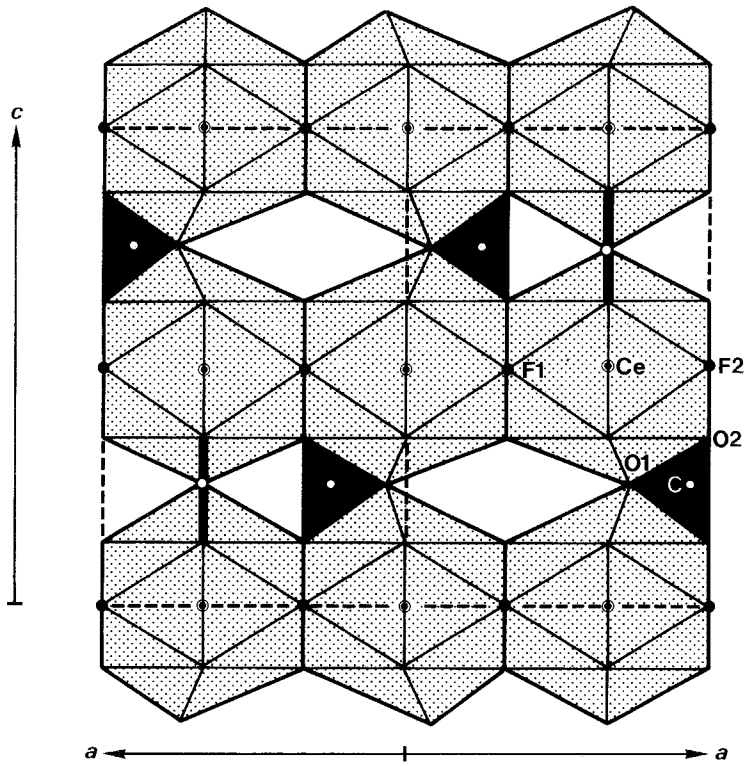

Fig. 7. Projection of the crystal structure of bastnäsite-(Ce) onto (110) showing the connection of the sheets by carbonate ions.

on the relationships among bastnäsite-(Ce), parisite-(Ce), röntgenite-(Ce) and synchysite-(Ce).

The projections of the crystal structure of bastnäsite-(Ce) are given in fig. 7. The structure shows that the cerium atom is coordinated by three fluorine atoms and eight oxygen atoms of the carbonate ions, in which the Ce–O1 distance, 2.49 Å, is shorter than the Ce–O2 distance, 2.74 Å. The Ce polyhedra share faces to form a sheet of cerium and fluorine, and share corners to form a three-dimensional structure. Donnay and Donnay (1953) have pointed out that the difference between the two kinds of Ce–O distances indicates the considerable strength of the shorter Ce–O1 bond accounting for the observed lack of (0001) cleavage in spite of the sheet structure.

Hydroxylbastnäsite-(Ce) is known as an (OH)-analog of bastnäsite-(Ce). On the other hand, the crystal structure of synthetic $Nd(CO_3)(OH)$ was reported by Christensen (1973); the crystal structure of $Nd(CO_3)(OH)$ (fig. 8) has a lower symmetry, $P\bar{6}$, with lattice parameters $a = 12.32$, $c = 9.88$ Å, in spite of the close structural similarity with bastnäsite-(Ce).

Pavlenko et al. (1965) described a new variety of the bastnäsite series, thorbastnäsite

TABLE 19
Atomic parameters of baiyuneboite-(Ce)[a].

	x	*y*	*z*
Ce	0.33333(0)[b]	0.66667(0)[b]	0.35388(11)
Ba	0[b]	0[b]	0[b]
Na	0.33333(0)[b]	0.66667(0)[b]	0.75000(0)[b]
C1	0[b]	0[b]	0.68056(172)
C2	0.66667(0)[b]	0.33333(0)[b]	0.43383(158)
O1	0.14459(192)	0.28918(0)	0.67737(60)
O2	0.52300(239)	0.04600(0)	0.43485(58)
F	0.33333(0)[b]	0.66667(0)[b]	0.25000(0)[b]

[a]MoKα, $R = 0.049$ (437 refl.).
[b]Special positions.

TABLE 20
Interatomic distances for baiyuneboite-(e) in Å.

Ce–O2	2.515(10) ×3	Ba–O2	2.969(13)	×12
Ce–O1	2.657(10) ×6	Na–O1	2.368(10)	×6
mean	2.610	Na–F	2.943(0)	×3
Ce–F	2.407(3)	[mean	2.560]	
[mean	2.589]			
C1–O1	1.279(2)	C2–O2	1.269(1)	

from Eastern Siberia, Russia, and gave it the formula, $Th(Ca,R)(CO_3)_2F_2 \cdot 3H_2O$. However, based on the reported space group $P\bar{6}2c$, which is the same as that of bastnäsite-(Ce), it is impossible to divide the rare earth site into two independent sites, Th and (Ca,R). Moreover, because of this crystallographic restriction, the number of water molecules, 3, may be variable, with partial occupancy of water molecules. Thus, the chemical formula for thorbastnäsite must be $(Th,Ca,R)(CO_3)F \cdot nH_2O$, suggesting an isomorphous substitution in the rare earth site: $2R^{3+} \rightleftarrows Th^{4+} + Ca^{2+}$. However, the crystal structure of bastnäsite-(Ce) (fig. 7) does not have enough space for water molecules; therefore, the presence of water molecules in thorbastnäsite is doubtful. The similar cell dimensions of thorbastnäsite and bastnäsite-(Ce) imply a lack of any additional sites for water molecules.

Synchysite-(Ce), parisite-(Ce) and röntgenite-(Ce) have sheets of cerium and fluorine atoms which are similar to those in bastnäsite. The crystal structures of synchysite-(Ce), parisite-(Ce) and röntgenite-(Ce) have calcium atoms just above or below the cerium in the direction of the *c*-axis; however, the stacking of calcium layers is distinct in each mineral (fig. 9).

Dexpert et al. (1972) proposed that bastnäsite-(Ce) is structurally related to vaterite, $Ca(CO_3)$. Furthermore, Dal Negro et al. (1975) suggested that bastnäsite-type sheet structures (the sheets of cerium and fluorine atoms) can be derived from vaterite-type sheets by the replacement of calcium with cerium and by the introduction of

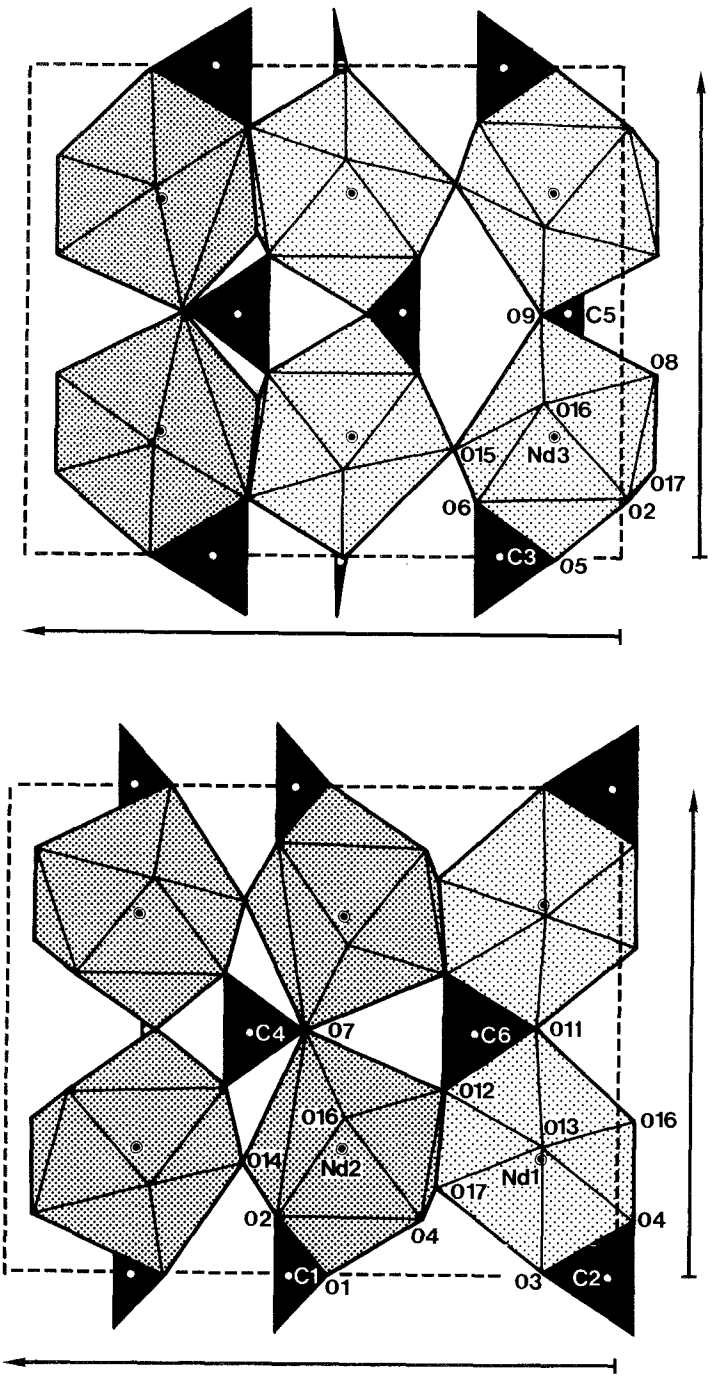

Fig. 8. The crystal structure of $Nd(CO_3)(OH)$.

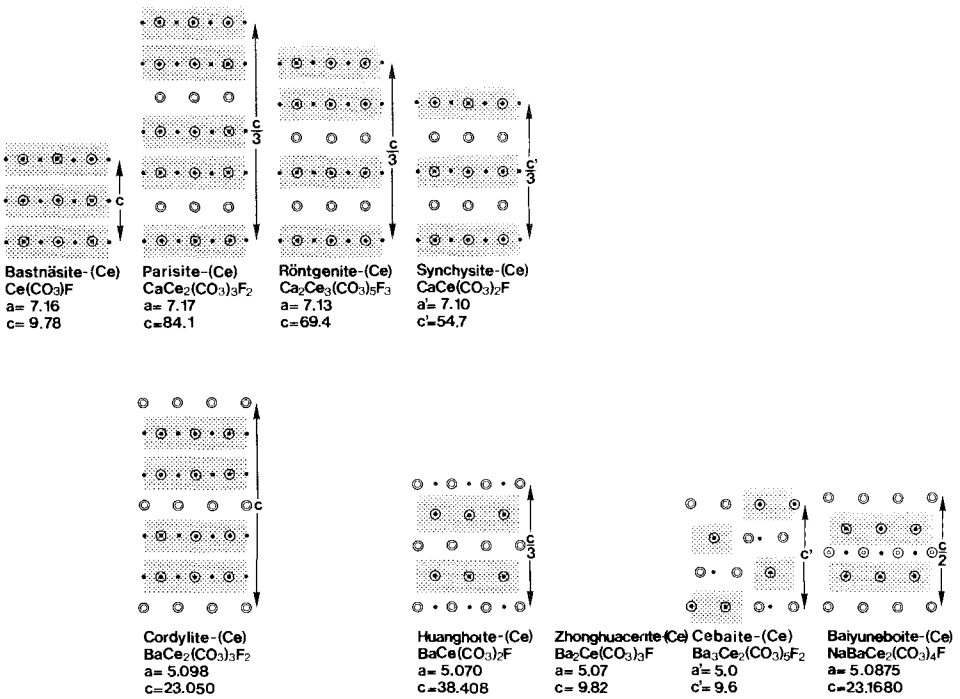

Fig. 9. Schematic illustrations of the crystal structures of the bastnäsite-group minerals and the cordylite-group minerals. The dots indicate the sheets of rare earth atoms and carbonate ions. ◉: rare earths, ◎: calcium, barium or sodium, •: fluorine.

fluorine atoms. They pointed out that this introduction causes an extension of the cell perpendicular to the sheet, and that the environments of the calcium atoms in parisite-(Ce), röntgenite-(Ce) and synchysite-(Ce) are similar to that in vaterite. They concluded that these structural features explain the co-existence of bastnäsite-type sheets and vaterite-type sheets in the crystal structures of parisite-(Ce), röntgenite-(Ce) and synchysite-(Ce).

The structural scheme of cordylite-(Ce) is similar to that of parisite-(Ce) and cordylite-(Ce), and is a Ba-analogue of parisite-(Ce) from the viewpoint of chemical composition. However, the arrangement of barium atoms is different from that of the calcium atoms in parisite-(Ce): i.e., the barium atoms are placed just above or below the fluorine atoms in cordylite-(Ce), whereas the calcium atoms are just above or below the cerium atoms in parisite-(Ce). The differences in crystallographic data between the two minerals may be caused by this difference in their crystal structures.

The crystal structure of huanghoite-(Ce) was analyzed by Qian at al. (1982). In the crystal structure of huanghoite-(Ce) (fig. 10), both the cerium atoms at the two independent sites are coordinated by nine oxygen atoms and a fluorine atom, and form irregular polyhedra. On the other hand, the two kinds of barium atoms show different shapes of coordination polyhedra, i.e., Ba1 forms an icosahedron with six

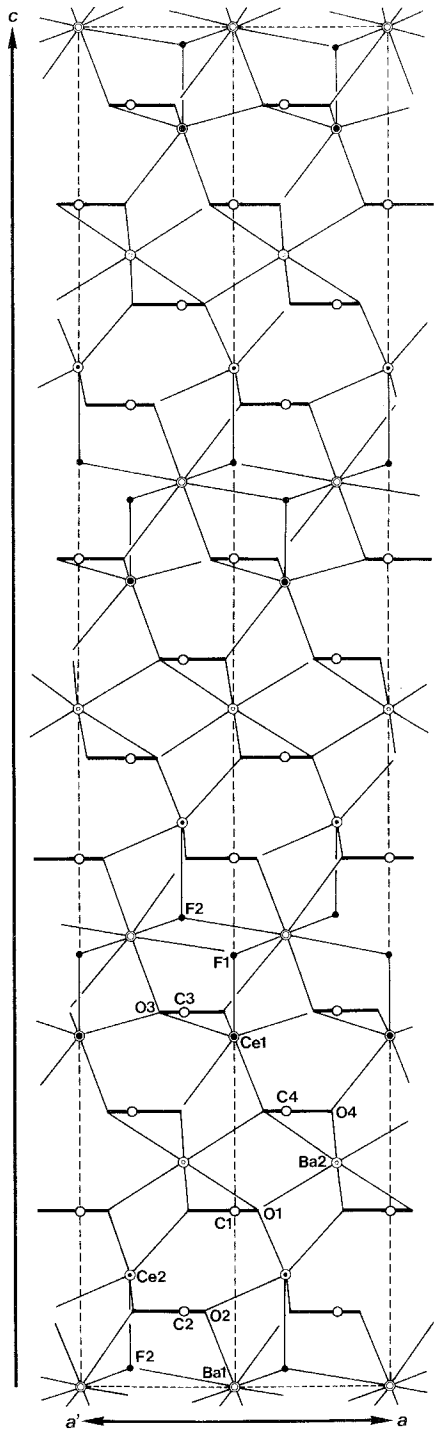

Fig. 10. The crystal structure of huanghoite-(Cc).

oxygen atoms and six fluorine atoms, whereas Ba2 forms a distorted hexagonal prism with twelve oxygen atoms. It was determined that huanghoite-(Ce) has a superstructure with subcell dimension $a = 5.070$, $c' = 9.602$ ($=\frac{1}{4}c$) Å. The length of the a-axis, 5.070 Å, is closely related to that of cordylite-(Ce), 5.098 Å. Furthermore, the crystal structures of huanghoite-(Ce) and cordylite-(Ce) are related to each other. In both structures, barium atoms are placed just above or below the fluorine atoms. The cerium and barium layers alternate in the structure of huanghoite-(Ce), Ba–, Ce–, Ba–, Ce–, ..., in contrast to the pattern in the structure of cordylite-(Ce), Ba–, Ce–, Ce–, Ba–, Ce–, Ce–, ...

Zhonghuacerite-(Ce) is another barium rare earth fluorocarbonate, and was described by Zhang and Tao (1981). The chemical composition and the lattice parameters of zhonghuacerite-(Ce) suggest some relationship to huanghoite-(Ce).

Cebaite-(Ce) was originally described by Wang et al. (1973) as an unnamed mineral. Later, Zhang and Tao (1983) gave new data on cebaite-(Ce), and showed it to be an independent mineral species. Li and Hashimoto (1984) determined the crystal structure of cebaite-(Ce) using high-resolution electron microscopy, based on matching of the theoretical and observed contrasts in images. The basic structure of cebaite-(Ce) (fig. 11) is the same as that of huanghoite-(Ce). Although the crystal system of cebaite-(Ce) is monoclinic, the structure possesses a trigonal (hex.) subcell corresponding to that of huanghoite-(Ce) (light broken line in fig. 11). In contrast to the crystal structure of huanghoite-(Ce), that of cebaite-(Ce) does not have alternating Ce and Ba layers. In the structure of cebaite-(Ce), each heavy-atom layer contains both Ce and Ba atoms. The fluorine atoms are approximately above or below the cerium

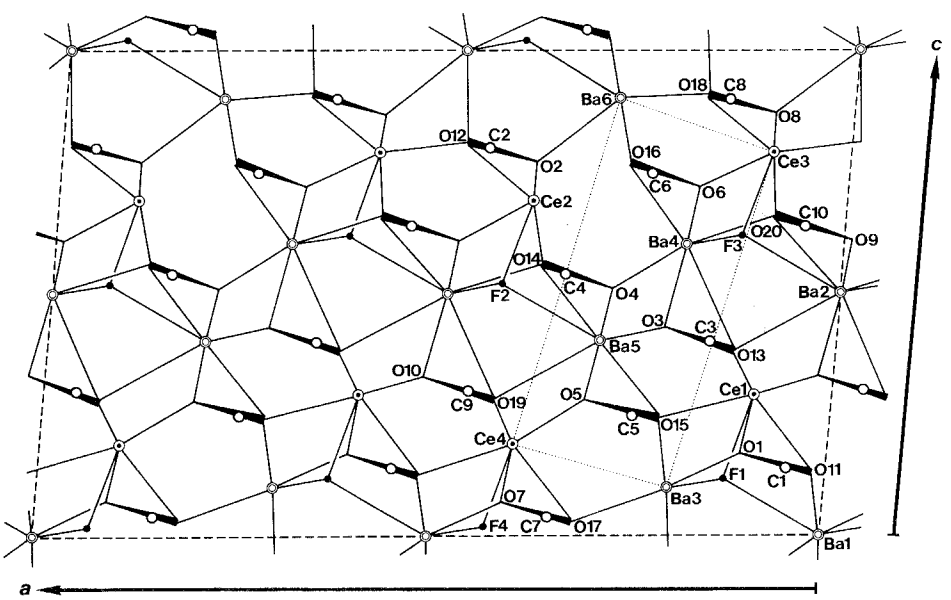

Fig. 11. The crystal structure of cebaite-(Ce).

TABLE 21
Comparison of crystal data of baiyuneboite and related minerals.

Name	Formula	Crystal system	Lattice parameters
baiyuneboite-(Ce)	$NaBaCe_2(CO_3)_4F$	hexagonal	$a = 5.0875(15)$, $c = 23.1680(1)$ Å
huanghoite-(Ce)	$BaCe(CO_3)_2F$	trigonal	$a = 5.070(3)$, $c = 38.408(5)$ Å
cordylite-(Ce)	$BaCe_2(CO_3)_3F_2$	hexagonal	$a = 5.098(1)$, $c = 23.050(5)$ Å
zhonghuacerite-(Ce)	$Ba_2Ce(CO_3)_3F$	hexagonal	$a = 5.07$, $c = 9.82$ Å (subcell)
cebaite-(Ce)	$Ba_3Ce_2(CO_3)_5F_2$	monoclinic	$a = 21.2$, $b = 5.06$, $c = 13.11$ Å, $\beta = 95°$

atom as in the other cerium–barium fluorocarbonates, such as cordylite-(Ce) and huanghoite-(Ce). Due to the different arrangement of the cerium atoms, the arrangement of fluorine atoms in cebaite-(Ce) is also different from those in huanghoite-(Ce) and cordylite-(Ce).

Baiyuneboite-(Ce) is a new mineral described by Fu and Su (1987). The crystal structure (Fu et al. 1987) is not a true "layer structure", but it can be tentatively expressed as consisting of three kinds of layers, i.e., a layer of CeO_9F polyhedra, a layer of BaO_{12} distorted hexagonal prisms and a layer of NaO_6F_3 polyhedra (fig. 12). These layers are stacked in a sequence "–Ba–Ce–Na–Ce–Ba–" in the 001 direction. The CO_3 triangles are parallel to the (001) plane and are located between the metal layers. This structure is closely related to those of huanghoite-(Ce), $BaCe(CO_3)_2F$ (Qian et al. 1982), cordylite-(Ce), $BaCe_2(CO_3)_3F_2$ (Chen and Chao 1975), zhonghuacerite-(Ce), $Ba_2Ce(CO_3)_3F$ (Zhang and Tao 1981), and cebaite-(Ce) $Ba_3Ce_2(CO_3)_5F_2$ (Li and Hashimoto 1984). The lattice parameters of these minerals are compared in table 21. The *a* parameters for these minerals are very close [*b* for cebaite-(Ce)] to each other, namely 5.1 Å. The crystal structures are known for huanghoite-(Ce), cebaite-(Ce), and partially for cordylite-(Ce). Huanghoite-(Ce) and cordylite-(Ce) have a layer stacking similar to that of baiyuneboite-(Ce), but the stacking sequence is –Ce–Ba–Ce–Ba– for huanghoite-(Ce) and –Ba–Ce–Ce–Ba– for cordylite-(Ce), while Ba and Ce are in the same layer in the structure of cebaite-(Ce). The crystal structure of cordylite-(Ce) has not been fully determined and the strong similarity of the cell parameters and the space group for baiyuneboite-(Ce) and cordylite-(Ce) may require a full determination of the structure of cordylite-(Ce). These minerals are also structurally related to the bastnäsite group minerals.

ANCYLITE-(Ce)
$(Ce,Sr,Ca)(CO_3)(OH,H_2O)$
$(Ce,Sr,Ca)(CO_3)(OH,H_2O)$

Sys. orthorhombic	$a = 5.03(1)$ Å	source: Mont St. Hilaire, Que., Canada
S.G. Pmcn	$b = 8.53(1)$ Å	Ref.: Dal Negro et al. (1975)
$Z = 4$	$c = 7.29(1)$ Å	JCPDS: #29-0384
$Dx = 4.15$ g/cm^3		
$Dm = 4.1$ g/cm^3		
AP: table 22	ID: table 23	IL: fig. 13

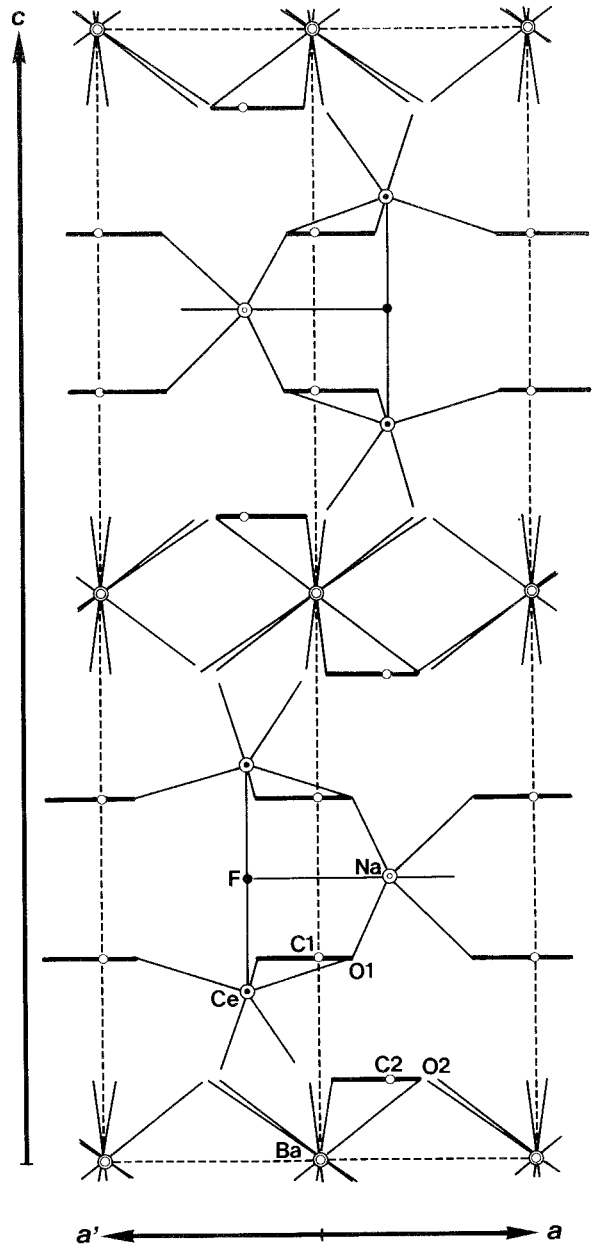

Fig. 12. The crystal structure o baiyuneboite-(Ce).

TABLE 22
Atomic parameters of ancylite-(Ce)[a].

	x	y	z	B_{eq} (Å^2)
M	0.25	0.3399(1)	0.6476(1)	0.80
C	0.75	0.1905(14)	0.8099(18)	0.79
O1	0.75	0.3181(12)	0.7210(16)	1.81
O2	0.5297(14)	0.1218(8)	0.8520(10)	1.55
O3	0.25	0.4135(14)	0.9749(14)	2.43

[a] MoKα, $R = 0.059$ (498 refl.). M: La, Ce, Sr, Ca. O3: OH, H_2O.

TABLE 23
Interatomic distances for ancylite-(Ce) in Å.

M–O3	2.468(11)	C–O1	1.268(9)
M–O3	2.502(10)	C–O2	1.291(8) ×2
M–O1	2.579(2) ×2	mean	1.283
M–O2	2.595(7) ×2		
M–O2	2.648(7) ×2		
M–O2	2.768(7) ×2		
mean	2.615		

calcioancylite-(Ce) (=weibyeite)
$(Ce,Ca,Sr)(CO_3)(OH,H_2O)$
$(Ce,Ca,Sr)(CO_3)(OH,H_2O)$

Sys.	$a =$	source: Cleveland, NC, USA
S.G.	$b =$	Ref.: White and Nelen (1987)
$Z =$	$c =$	

CALCIOANCYLITE-(Nd)
$(Nd,Ca)(CO_3)(OH,H_2O)$
$(Nd,Ca)_2Nd(Ca,Nd)(CO_3)_4(OH,H_2O)_4$

Sys. monoclinic	$a =$ 4.976(2) Å	source: Baveno, Piedmont, Italy
S.G. Pm11	$b =$ 8.468(2) Å	Ref.: Orlandi et al. (1990)
$Z =$ 1	$c =$ 7.212(2) Å	
Dx = 4.08 g/cm^3	$\beta = 90.04(3)°$	
Dm > 4.02 g/cm^3		
AP: table 24	ID: table 25	

TABLE 24
Atomic parameters of calcioancylite-(Nd)[a].

	x	y	z	U
M1[b]	1/4	0.3399[f]	0.3524[f]	0.0132(8)[g]
M2[c]	1/4	0.1677(5)	0.8517(6)	0.0149(10)[g]
M3[d]	3/4	0.6609(2)	0.6448(2)	0.0102(7)[g]
M4[e]	3/4	0.8440(3)	0.1445(4)	0.0082(5)[g]
C1	3/4	0.191(4)	0.177(4)	0.017(7)
C2	3/4	0.312(4)	0.699(4)	0.017(7)
C3	1/4	0.817(3)	0.805(4)	0.007(6)
C4	1/4	0.687(3)	0.314(4)	0.011(6)
O11	3/4	0.325(2)	0.272(3)	0.012(5)
O12	3/4	0.194(2)	0.790(2)	0.008(3)
O13	1/4	0.695(3)	0.705(3)	0.033(6)
O14	1/4	0.831(3)	0.241(3)	0.028(6)
O21	0.529(3)	0.125(2)	0.143(2)	0.015(4)
O22	0.520(3)	0.383(2)	0.649(3)	0.018(4)
O23	0.480(3)	0.885(2)	0.847(2)	0.023(4)
O24	0.473(3)	0.622(2)	0.353(2)	0.021(4)
O31	1/4	0.412(3)	0.036(3)	0.023(5)
O32	1/4	0.082(2)	0.526(3)	0.016(4)
O33	3/4	0.590(2)	0.981(3)	0.020(5)
O34	3/4	0.899(2)	0.463(2)	0.015(4)

[a] MoKα, $R = 0.044$, $R_w = 0.036$ (1531 refl.).
[b] M1: 70.0% R – 30.0% Ca.
[c] M2: 40.4% R – 59.6% Ca.
[d] M3: 63.3% R – 36.7% Ca.
[e] M4: 100.0% R.
[f] Fixed.
[g] U_{eq}.

GYSINITE-(Nd)
$(Nd,Pb)(CO_3)(OH,H_2O)$
$(Nd,Pb)(CO_3)(OH,H_2O)$

Sys. orthorhombic	$a = 5.0028(8)$ Å	source: Shaba, Zaïre
S.G. Pmcn	$b = 8.555(1)$ Å	Ref.: Chabot and Sarp (1985)
$Z = 4$	$c = 7.2392(8)$ Å	JCPDS: #39-0364
$Dx = 5.18$ g/cm^3		
AP: table 26	ID: table 27	

The crystal structures of ancylite-(Ce) and gysinite-(Nd) were determined by Dal Negro et al. (1975) and by Chabot and Sarp (1985), respectively. These two minerals are isostructural, and the crystal structures (fig. 13) consist of carbonate ions (C, O1 and O2), O3 of the hydroxyl ion or water molecule, with the metal (M) site occupied by rare earth elements and strontium, calcium [ancylite-(Ce)] or lead [gysinite-(Nd)]. In both crystal structures, the M site is surrounded by ten oxygen atoms, and the

TABLE 25
Interatomic distances for calcioancylite-(Nd) in Å.

M1–O31	2.359(21)		M2–O31	2.457(24)	
M1–O32	2.518(18)		M2–O32	2.459(19)	
M1–O22	2.552(18)	×2	M2–O12	2.537(3)	×2
M1–O11	2.557(5)	×2	M2–O21	2.545(16)	×2
M1–O24	2.636(16)	×2	M2–O23	2.656(16)	×2
M1–O21	2.738(17)	×2	M2–O22	2.696(16)	×2
mean	2.584		mean	2.578	
M3–O34	2.409(17)		M4–O34	2.345(19)	
M3–O33	2.500(20)		M4–O33	2.451(22)	
M3–O24	2.537(16)	×2	M4–O23	2.555(16)	×2
M3–O13	2.542(5)	×2	M4–O14	2.585(6)	×2
M3–O22	2.617(17)	×2	M4–O21	2.625(16)	×2
M3–O23	2.741(18)	×2	M4–O24	2.772(15)	×2
mean	2.578		mean	2.587	
C1–O21	1.258(21)	×2	C2–O12	1.193(32)	
C1–O11	1.325(38)		C2–O22	1.346(20)	×2
mean	1.280		mean	1.295	
C3–O13	1.259(36)		C4–O24	1.270(19)	×2
C3–O23	1.316(21)	×2	C4–O14	1.332(34)	
mean	1.297		mean	1.291	

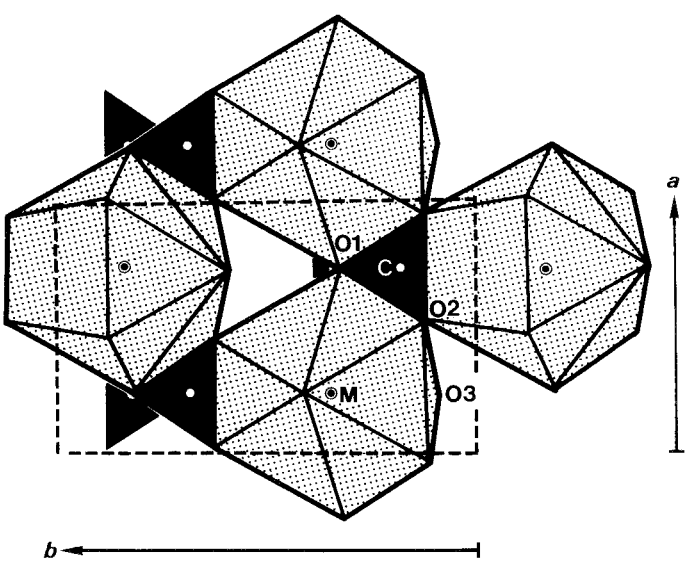

Fig. 13. Projection of the crystal structure of ancylite-(Ce) onto (001).

TABLE 26
Atomic parameters of gysinite-(Nd)[a].

	x	y	z	$100U$ (Å^2)[b]
M[c]	0.25	0.3400(3)	0.6491(2)	1.44(4)
C	0.75	0.178(6)	0.810(4)	1.5(6)
O1	0.75	0.318(4)	0.724(4)	2.6(6)
O2	0.527(3)	0.122(2)	0.852(3)	1.7(3)
O3[d]	0.25	0.405(5)	0.970(5)	4.1(9)

[a] MoKα, $R = 0.065$, $R_w = 0.071$ (368 refl.).
[b] $T = \exp[-2\pi^2 U(2 \sin\theta/\lambda)^2]$.
[c] M: 0.08La + 0.59Nd + 0.33Pb.
[d] O3: 0.67OH + 0.33H_2O.

TABLE 27
Interatomic distances for gysinite-(Nd) in Å.

M–O3	2.385(37)	C–O2	1.249(24) ×2
M–O3	2.463(37)	C–O1	1.356(53)
M–O1	2.566(6) ×2	mean	1.285
M–O2	2.579(17) ×2		
M–O2	2.660(16) ×2		
M–O2	2.747(16) ×2		
mean	2.595		

ten-coordinated M polyhedra share faces, edges and corners to form a three-dimensional structure.

The ideal formulae for ancylite-(Ce) and gysinite-(Nd) can be expressed as $(R^{3+},M^{2+})(CO_3)(OH,H_2O)$, which assumes the presence of the two end-member compositions: $R(CO_3)(OH)$ and $M^{2+}(CO_3)\cdot H_2O$. Sawyer et al. (1973) synthesized $R(CO_3)(OH)$, which is isostructural with ancylite-(Ce). On the other hand, monohydrocalcite, $Ca(CO_3)\cdot H_2O$ is not isostructural with ancylite-(Ce) (Taylor 1975). So far, no phase with a formula $M^{2+}(CO_3)\cdot H_2O$, which is isostructural with ancylite-(Ce), has ever been reported. In addition, no occurrence of ancylite-(Ce) with a ratio R/M^{2+} less than one has yet been found. Thus, the synthetic $R(CO_3)(OH)$ is one end-member of the ancylite series, but $M^{2+}(CO_3)\cdot H_2O$ may not be another. Chabot and Sarp (1985) gave the general formula $M^{3+}_{1-y}M^{2+}_y CO_3(OH)_{1-y}\cdot yH_2O$, for ancylite-(Ce) and gysinite-(Nd). Thus, gysinite-(Nd) should be called ancylite-(Nd).

$R(CO_3)(OH)$, synthesized by Sawyer et al. (1973), can be described as a polymorph of hydroxylbastnäsite. This synthetic $R(CO_3)(OH)$ and hydroxylbastnäsite are related as are aragonite and vaterite, the polymorphs of $CaCO_3$, respectively.

Dal Negro et al. (1975) suggested that the crystal structure of ancylite-(Ce) can be compared to that of the orthorhombic carbonates, aragonite, strontianite, and witherite. These minerals belong to the same space group, Pmcn, and the cell dimensions of the a- and b-axis in ancylite-(Ce) are very close to the corresponding ones in strontianite ($a = 5.090(2)$, $b = 8.358(2)$, $c = 5.997(4)$ Å). In addition, the mean M–O

bond distance, 2.61 Å, is very close to the mean Sr–O bond length in strontianite (2.64 Å). Thus, the crystal structure of ancylite-(Ce) can be derived ideally from that of aragonite, $CaCO_3$, by replacing the calcium atoms with rare earth elements and introducing additional hydroxyl ions. The introduction of the hydroxyl ions into the compact structure of aragonite results in a relative shifting of the superposed carbonate ions and tilting of the angles between the carbonate triangles and the (001) plane.

The bastnäsite-type fluorocarbonate RCO_3F is related to the vaterite type of calcium carbonate (Mayer 1969), similar to the relation found between the ancylite-type hydroxyl carbonate and aragonite-type carbonate. However, Dal Negro et al. (1975) suggested that no family of minerals similar to that for the vaterite–bastnäsite series can exist for the aragonite–ancylite series. The introduction of the F anion in the vaterite structure affects only the *c* direction; in this way vaterite-type layers (normal to *c*) can concur syntaxially with bastnäsite layers as in parisite-(Ce) ($2CeCO_3F \cdot CaCO_3$), röntgenite-(Ce), ($3CeCO_3F \cdot 2CaCO_3$), and synchysite-(Ce), ($CeCO_3F \cdot CaCO_3$). Syntaxy phenomena, which are common among these minerals, can be explained in the same manner. On the other hand, the introduction of hydroxyl ions or water molecules into the aragonite-type structure affects both the *b* and *c* cell parameter, and this makes the coexistence of aragonite-type layers with ancylite-type layers impossible.

A Ca-analogue of ancylite-(Ce) is known as calcioancylite-(Ce). Recently, a new member of the ancylite group, calcioancylite-(Nd), was described by Orlandi et al. (1990). They analyzed the crystal structure, and revealed that it is monoclinic, not orthorhombic. Their structure analysis confirmed the main features of the crystal structure of ancylite-(Ce) (Dal Negro et al. 1975), but provided evidence for a different distribution of alkaline earths and rare earths over the M sites. This result confirms the structure refinement of ancylite-(Ce) reported by Szymanski and Chao at the Annual Meeting of the American Crystallographic Association, Hamilton (Canada) in 1986. Orlandi et al. (1990) concluded that all "ancylites" and "calcioancylites" seem to be monoclinic, and that the different chemical compositions give rise to different ordering patterns over the M sites. They also reported that "weibyeite", a discredited mineral, from Baveno, is a calcioancylite-(Ce) after their reexamination.

SCHUILINGITE-(Nd)
$PbCuNd(CO_3)_3(OH) \cdot 1.5H_2O$
$PbCuNd(CO_3)_3(OH) \cdot 1.5H_2O$

Sys.	orthorhombic	$a = 7.418(9)$ Å	source: Shaba, Zaïre
S.G.	$P2_1cn$	$b = 18.87(2)$ Å	Ref.: Piret and Deliens (1982)
$Z =$	4	$c = 6.385(7)$ Å	JCPDS: #35-0545
Dx =	4.74 g/cm^3		
Dm =	5.2 ± 0.1 g/cm^3		

Schuilingite-(Nd) was originally described as a hydrous carbonate of lead, copper and calcium (Vaes 1947). Later, Guillemin and Pierrot (1957) gave the chemical formula $Pb_3Cu_2Ca_6(CO_3)_8(OH)_6 \cdot 6H_2O$ for schuilingite-(Nd) and classified it as "class 16, type 2", carbonates containing hydroxyl or halogen, $A_mB_n(XO_3)_pZ_q$ type 2″,

in Dana's System of Mineralogy (Palache et al. 1944). Recently, Piret and Deliens (1982) proposed the chemical formula $PbCuR(CO_3)_3(OH)\cdot 1.5H_2O$ and reported the crystallographic data based on a new chemical analysis and X-ray study of the specimen from Shaba, Zaïre. They also carried out single crystal structure analysis, but atomic coordinates (x, y, z) of the metal atoms were only obtained with $R = 0.159$: i.e., Pb(0.241, 0.526, 0.111), R(0.728, 0.806, 0.872), Cu(0.265, 0.643, 0.582).

BIJVOETITE-(Y)
$Y_2(UO_2)_4(CO_3)_4(OH)_6\cdot 11H_2O$
$Y_2(UO_2)_4(CO_3)_4(OH)_6\cdot 11H_2O$

Sys. orthorhombic	$a = 21.22(3)$ Å	source: Shaba, Zaïre
S.G. C2ma, Cm2b or Cmma	$b = 45.30(7)$ Å	Ref.: Deliens and Piret (1982)
$Z =$ 16	$c = 13.38(2)$ Å	JCPDS: #35-0551
Dx = 3.907 g/cm^3		
Dm = 3.95 ± 0.15 g/cm^3		

Bijvoetite-(Y) was described as a new mineral from Shinkolobwe, Shaba, Zaïre (Deliens and Piret 1982). Its structure is not known.

BURBANKITE
$(Na,Ca)_3(Sr,Ba,Ce)_3(CO_3)_5$
$(Na,Ca,\square)_3(Sr,Ba,Ca,Ce)_3(CO_3)_5$

Sys. hexagonal	$a = 10.512(2)$ Å	source: Bearpaw Mt., MT, USA
S.G. $P6_3mc$	$c = 6.492(2)$ Å	Ref.: Effenberger et al. (1985)
$Z =$ 2		JCPDS: #26-1374
Dx = 3.54 g/cm^3		
Dm = 3.50 g/cm^3		
AP: table 28	ID: table 29	IL: fig. 14

TABLE 28
Atomic parameters of burbankite[a]

	x	y	z	U_{eq}
M1[b]	0.52310(8)	0.47690	0.3131(2)	0.017
M2[c]	0.84172(1)	0.15828	0[d]	0.014
C1	0.7992(2)	0.2008	0.5378(6)	0.015
C2	0	0	0.8302(11)	0.017
C3	1/3	2/3	0.4854(20)	0.015
O1	0.3770(3)	0.0824(2)	0.6318(4)	0.022
O2	0.9297(2)	0.0703	0.3340(5)	0.027
O3	0.4042(1)	0.5958	0.4880(9)	0.022
O4	0.7750(2)	0.2250	0.3536(5)	0.021

[a] MoKα, $R = 0.026$, $R_w = 0.022$ (933 refl.).
[b] M1: 0.59Na + 0.30Ca.
[c] M2: 0.53Sr + 0.17Ba + 0.15Ca + 0.15R.
[d] Invariant, fixes the origin.

TABLE 29
Interatomic distances of burbankite in Å.

M1–O4	2.374(2) ×2	M2–O1	2.570(2) ×2
M1–O1	2.395(2) ×2	M2–O4	2.597(3)
M1–O3	2.445(3)	M2–O1	2.695(2) ×2
M1–O3	2.491(5)	M2–O2	2.696(2)
M1–O1	2.715(2) ×2	M2–O2	2.723(2) ×2
mean	2.488	M2–O3	2.778(1) ×2
		mean	2.683
C1–O4	1.274(4)	C2–O2	1.280(2) ×3
C1–O1	1.291(3) ×2	C3–O3	1.290(1) ×3
mean	1.285		

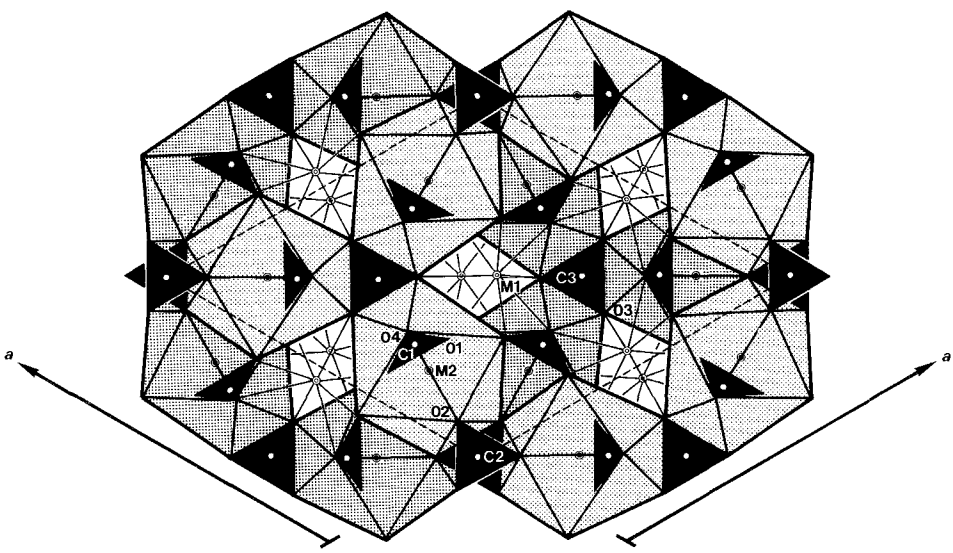

Fig. 14. The crystal structure of burbankite.

The crystal structure of burbankite was determined by Voronkov and Shumyatskaya (1968). The structure (fig. 14) consists of two independent sites M1 and M2 for large cations, and three distinct carbonate ions C1, C2 and C3. Rare earth elements occupy the ten-coordinated M2 site, together with divalent strontium, barium and calcium. The M2 polyhedra are directly connected by the carbonate ions C2 and C3 at the corners of the polyhedra forming a sheet of six-membered rings parallel to the (0001) plane. On the other hand, the M2 polyhedra share edges in the direction of the *c*-axis forming a three-dimensional structure with channels normal to the sheets. The two M2 polyhedra related by translational symmetry in the direction of the *c*-axis do not share edges and apices, and the carbonate ions C1,

TABLE 30
Atomic parameters of remondite-(Ce)[a].

	x	y	z	B
M1[b]	−0.8413(1)	0.8413(1)	0	1.03(2)
M2[c]	−0.3185(1)	0.8405(1)	0.0029(5)	1.06(2)
M3[d]	−0.8404(1)	−0.6816(1)	0.0008(5)	1.08(2)
Na1	−0.5232(7)	−0.0464(6)	−0.3094(10)	1.5(1)
Na2	−0.5226(6)	0.5234(6)	−0.3105(10)	1.5(2)
Na3	−0.9537(7)	0.5230(6)	−0.3096(10)	1.6(2)
C1	0.0000(14)	0.0003(13)	−0.3334(19)	1.1(2)
C2	−0.6684(12)	−0.3341(12)	0.0258(15)	1.2(3)
C3	−0.6059(13)	0.1958(12)	−0.0335(15)	1.1(3)
C4	−0.1996(10)	−0.3939(10)	−0.0342(13)	0.7(2)
C5	−0.1985(11)	0.1951(12)	−0.0353(14)	0.9(3)
O1	0.0686(13)	−0.0726(12)	−0.3329(25)	2.3(4)
O2	0.0660(12)	−0.8603(10)	−0.3393(27)	2.4(4)
O3	−0.1402(13)	−0.0708(13)	−0.3413(28)	2.6(4)
O4	−0.5977(12)	0.5954(12)	0.0263(17)	1.9(3)
O5	−0.5996(12)	−0.1911(10)	0.0215(20)	1.9(3)
O6	−0.8078(12)	0.5971(12)	0.0243(17)	2.0(3)
O7	−0.7763(11)	0.7782(11)	−0.3489(16)	1.4(2)
O8	−0.7748(11)	−0.5527(10)	−0.3480(18)	1.5(3)
O9	−0.4441(11)	−0.7780(11)	−0.3466(18)	1.5(3)
O10	−0.6328(11)	−0.9232(10)	−0.1316(20)	1.6(3)
O11	0.9238(10)	−0.7100(10)	−0.1310(19)	1.6(3)
O12	−0.2916(10)	−0.3696(10)	−0.1328(18)	1.5(2)
O13	0.9238(10)	0.6315(10)	−0.1279(19)	1.5(3)
O14	−0.6292(11)	−0.7089(10)	−0.1322(18)	1.6(3)
O15	−0.2902(11)	−0.9211(10)	−0.1295(19)	1.6(3)

[a] MoKα, $R = 0.074$, $R_w = 0.091$ (2391 refl.).
[b] M1: 1.114(3). [c] M2: 0.947(3). [d] M3: 0.962(3).

which are obliquely situated between the polyhedra, connect the polyhedra. The channel contains M1 cations, Na and Ca, which form an eight-coordinated polyhedron composed of a combination of distorted triangular prisms with four-sided pyramids constructed on two of the side faces of the prism (see fig. 94j), in other words, a distorted tetragonal antiprism (see fig. 94i).

Voronkov and Shumyatskaya (1968) proposed $Na_3(Sr_2Ce)(CO_3)_5$ as an end member for burbankite. They pointed out that the occupancy of Na in the M2 site is possibly less than one, after their structure analysis, and the number of Na atoms in all the chemical compositions of known varieties of burbankite was less than six per unit cell. Naturally occurring burbankites can be considered as solid solutions of the two end members $Na_3[(Sr,Ca,Ba)_2R](CO_3)_5$ and $Na_2Ca(Sr,Ca,Ba)_3(CO_3)_5$ with isomorphous substitution of $Na^+ + R^{3+} \rightleftarrows Ca^{2+} + (Sr,Ca,Ba)^{2+}$. It should be noted here that rare earth elements with relatively small ionic radii, such as Y, Yb, may occupy the eight-coordinated M1 site (mean M1–O distance = 2.48 Å).

The crystal structure of burbankite was refined by Effenberger et al. (1985). The

structure is basically the same as that reported by Voronkov and Shumyatskaya (1968). Their structure analysis and electron microprobe analysis indicated that Na and Ca atoms occupy the smaller M1 site, and Sr, Ba and R atoms occupy the M2 site, and vacancies can occur at the M1 site. They also suggested that there would be no vacancy at the M2 site. Furthermore, they reported that it is not necessary for the M2 site to be occupied by R atoms to stabilize the burbankite-type structure, with reference to synthetic isotypic phases without any trivalent cations.

KHANNESHITE
$(Na,Ca)_3(Ba,Sr,Ce,Ca)_3(CO_3)_5$
$(Na,Ca)_3(Ba,Sr,Ce)_3(CO_3)_5$

Sys. hexagonal	$a = 10.65 \pm 0.01$ Å	source: Khanneshin, Afghanistan
S.G. $P6_3mc$	$c = 6.58 \pm 0.01$ Å	Ref.: Eremenko and Bel'ko (1982)
$Z = 2$		JCPDS: #35-0700
Dx = 3.94 g/cm^3		
Dm =3.8–3.9 g/cm^3		

REMONDITE-(Ce)
$Na_3(Ce,Ca,Na,Sr)_3(CO_3)_5$
$Na_3(Ce,Ca,Na,Sr)_3(CO_3)_5$

Sys. monoclinic	$a = 10.412(4)$ Å	source: Nlende, Kribi, Cameroun
S.G. $P2_1$	$b = 10.414(4)$ Å	Ref.: Ginderow (1989)
$Z = 2$	$c = 6.291(3)$ Å	
Dx = 3.46 g/cm^3	$\gamma = 119.80(5)°$	
AP: table 30	ID: table 31	

Remondite-(Ce) is a new mineral described by Cesbron et al. (1988). This mineral belongs to an $A_3B_3(CO_3)_5$ structural group with A = (Na,Ca,□) and B = (Ca,Sr,Ba,R), which includes burbankite and khanneshite. Chemically, remondite-(Ce) is a rare earth analogue of burbankite, but the crystal system is monoclinic (pseudo-hexagonal) in contrast to burbankite and khanneshite, which are hexagonal. The crystal structure of remondite-(Ce) was solved by Ginderow (1989). The occupancy parameters of the M sites suggest that the cations Ce, Ca, Na, and Sr are ordered in the three M sites. The crystal structure of remondite-(Ce) is practically isostructural with that of burbankite. The atomic parameters of remondite-(Ce) by Ginderow (1989) and those of burbankite by Effenberger et al. (1985) are related as follows:

$$x_{\text{remondite-(Ce)}} = x_{\text{burbankite}},$$

$$y_{\text{remondite-(Ce)}} = y_{\text{burbankite}},$$

$$z_{\text{remondite-(Ce)}} = \tfrac{1}{2} - z_{\text{burbankite}}.$$

Khanneshite was described as a new mineral from Khanneshin, Afghanistan, and as a Ba-analogue of burbankite by Eremenko and Bel'ko (1982), but a structure analysis has not yet been reported.

TABLE 31
Interatomic distances for remondite-(Ce) in Å.

M1–O13	2.467(8)	M2–O9	2.487(11)
M1–O10	2.473(8)	M2–O12	2.496(12)
M1–O7	2.494(11)	M2–O15	2.498(11)
M1–O11	2.626(12)	M2–O14	2.602(11)
M1–O15	2.634(12)	M2–O10	2.608(13)
M1–O1	2.641(16)	M2–O3	2.710(16)
M1–O2	2.653(15)	M2–O1	2.725(10)
M1–O3	2.690(16)	M2–O2	2.727(14)
M1–O5	2.710(14)	M2–O4	2.756(9)
M1–O6	2.742(15)	M2–O5	2.785(13)
mean	2.613	mean	2.639
M3–O11	2.471(12)	Na1–O7	2.356(10)
M3–O8	2.497(11)	Na1–O9	2.367(16)
M3–O14	2.504(13)	Na1–O10	2.386(15)
M3–O12	2.614(12)	Na1–O15	2.395(12)
M3–O13	2.649(13)	Na1–O5	2.397(11)
M3–O3	2.681(15)	Na1–O5	2.470(13)
M3–O2	2.691(15)	Na1–O15	2.711(14)
M3–O1	2.692(11)	Na1–O10	2.726(14)
M3–O4	2.732(9)	mean	2.476
M3–O6	2.757(14)		
mean	2.629		
Na2–O8	2.349(13)	Na3–O8	2.375(16)
Na2–O9	2.366(13)	Na3–O7	2.376(10)
Na2–O12	2.373(11)	Na3–O13	2.384(15)
Na2–O14	2.385(11)	Na3–O11	2.390(11)
Na2–O4	2.395(16)	Na3–O6	2.398(12)
Na2–O4	2.513(14)	Na3–O6	2.491(13)
Na2–O14	2.709(11)	Na3–O13	2.694(14)
Na2–O12	2.718(11)	Na3–O11	2.727(14)
mean	2.476	mean	2.479
C1–O2	1.260(15)	C2–O6	1.260(15)
C1–O3	1.268(17)	C2–O4	1.275(22)
C1–O1	1.279(23)	C2–O5	1.292(15)
mean	1.269	mean	1.276
C3–O9	1.267(15)	C4–O12	1.272(17)
C3–O10	1.287(16)	C4–O8	1.274(14)
C3–O14	1.296(19)	C4–O13	1.318(15)
mean	1.283	mean	1.288
C5–O15	1.257(12)		
C5–O7	1.270(15)		
C5–O11	1.309(12)		
mean	1.279		

EWALDITE
$Ba(Ca,Y,Na,K)(CO_3)$
$Ba(Ca,Y,Na,K,Sr,U,\square)(CO_3)_2$

Sys.	hexagonal	$a = 5.284(7)$ Å	source: Green River Formation, WY, USA
S.G.	$P6_3mc$	$c = 12.78(1)$ Å	Ref.: Donnay and Preston (1971)
$Z =$	2		
Dx =	3.37 g/cm^3		
Dm =	3.25(5) g/cm^3		
AP:	table 32	ID: table 33	IL: fig. 15

Donnay and Preston (1971) determined atomic parameters of the two cation sites, Ba and (Ca,R), and those of one of the two carbonate ions, C1 and O1, of ewaldite, but those of the other carbonate ion could not be determined by their analysis. They assumed that the second carbonate ion would lie at $z = 0.665$, and could partially occupy $\frac{1}{6}$ of the sites of four general (twelve-fold) positions or be positionally disordered, based on the examinations of the difference electron-density map and information from the infrared spectrum. The crystal structure of ewaldite, including their prediction of the position of the O2 site of the second carbonate ion, is given in fig. 15. In the structure, the Ca, R, Na, and K atoms occupy the site octahedrally coordinated by six oxygen atoms with three (Ca,R)–O distances of 2.364(19) Å, and the Ba atom is surrounded by nine oxygen atoms. The two types of cations lie on the three-fold axes and are interleaved by carbonate groups parallel to the basal plane. Thus, the structure consists of eight layers of Ba, (Ca,R) and two kinds of carbonate ions. The sequence of the layers in the cell, in conventional notation, is ABCBACBC (quadruple hexagonal close-packed), corresponding to the chemical

TABLE 32
Atomic parameters of ewaldite-(Y)[a].

	x	y	z	B (Å^2)
Ba	0.3333	0.6667	0	
Ca,R	0.3333	0.6667	0.305(1)	
C1	0	0	0.422(3)	2.3(7)
O1	0.137(3)	−0.137(3)	0.425(1)	2.7(3)
C2			0.665	
O2			0.665	
O3			0.665	
O4			0.665	

[a] MoKα, $R = 0.065$ (298 refl.).

TABLE 33
Interatomic distances for ewaldite-(Y) in Å.

Ba–O1	2.821(15) ×6	Ca,R–O1	2.364(19) ×3
C1–O1	1.263(30) ×3		

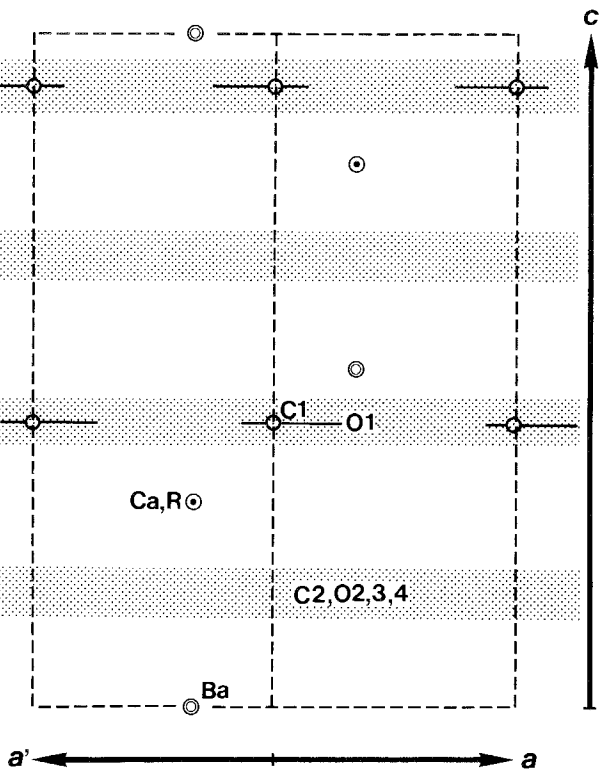

Fig. 15. Schematic illustration of the crystal structure of ewaldite.

sequence Ba–CO_3(2)–(Ca,R)–CO_3(1)–Ba–CO_3(2)–(Ca,R)–CO_3(1) – repeated along the 6_3 axis.

Despite the existence of a relationship between the lattice parameters of ewaldite and burbankite: $2a_{ewal} = a_{burb}$, $\frac{1}{2}c_{ewal} = c_{burb}$, and their chemical composition (both are carbonates of barium, calcium, rare earths, sodium and so on), there is no apparent structural similarity between the two.

CARBOCERNAITE
$(Sr,Ce,Ba)(Ca,Na)(CO_3)_2$
$(Sr,Ce,Ba)(Ca,Na)(CO_3)_2$

Sys.	orthorhombic	$a = 5.214(3)$ Å	source: Baiyun Obo, China
S.G.	$Pmc2_1$	$b = 6.430(3)$ Å	Ref.: Shi et al. (1982)
$Z =$	2	$c = 7.301(12)$ Å	JCPDS: #25-0175, #14-0273
Dx =	3.64 g/cm^3		
Dm =	3.53 g/cm^3		
AP:	table 34	ID: table 35	IL: fig. 16

Carbocernaite was described as a new mineral from the Kola Peninsula, Russia by Bulakh et al. (1961). They suggested that the mineral is very similar to burbankite in chemical composition, and that the structures may be related to each other because

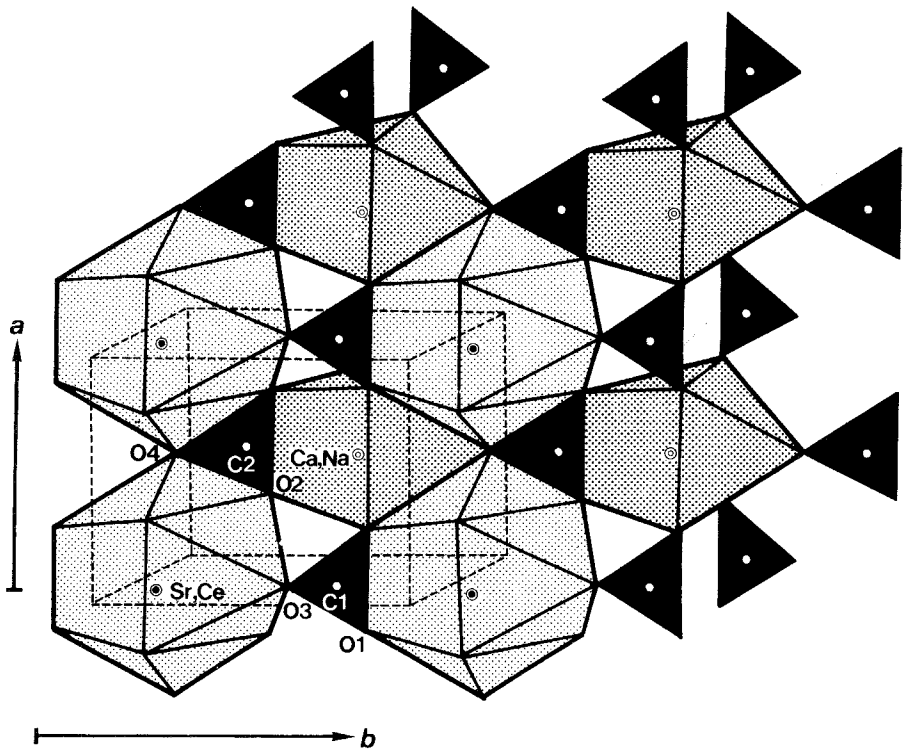

Fig. 16. Illustration of the crystal structure of carbocernaite showing the alternate arrangements of the sheets of (Sr,Ce) and those of Ca,Na).

the lattice parameters of these minerals show a relationship: i.e., $2a_{carb}(6.41\ Å) = c_{burb}(12.78\ Å)$ and $c_{carb}(5.23\ Å) = a_{burb}(5.284\ Å)$.

The crystal structure analysis was performed by Voronkov and Pyatenko (1967a), and revealed the ideal formula $AB(CO_3)_2$ (A = Na, Ca, B = R, Sr, Ca, Ba) for carbocernaite. The structure was confirmed by Shi et al. (1982). The coordination numbers are as follows: A cations = 7, B cations = 10. The B-polyhedra join along the triangular faces to form zigzag chains, and the chains form corrugated sheets parallel to the (100) plane by sharing corners (fig. 16). The corrugated sheets are arranged alternately with sheets of the seven-coordinated A-polyhedra, which play a cementing role. The corrugated sheets are structurally different from the sheet of tengerite-(Y).

It follows from the generalized formula $AB(CO_3)_2$ of carbocernaite that, in principle, two types of compounds characterized by the simplest compositions, $A^{2+}B^{2+}(CO_3)_2$ and $A^{+}B^{3+}(CO_3)_2$, may have the carbocernaite structure. However, Voronkov and Pyatenko (1967a) pointed out that the $A^{2+}B^{2+}(CO_3)_2$-type compounds, such as $CaCa(CO_3)_2 = Ca(CO_3)$ (calcite, aragonite or vaterite), $CaSr(CO_3)_2$ (aragonite type),$CaBa(CO_3)_2$ (barytocalcite), do not have the carbocernaite-type structure. So far, carbocernaite is the only known phase that has the formula $A^{+}B^{3+}(CO_3)_2$ and its structure is different from any other carbonate structure

TABLE 34
Atomic parameters of carbocernaite[a].

	x	*y*	*z*	*B*
Sr,Ce	0	0.1168(4)	0.2555(11)	1.41(6)
Ca,Na	0.5	0.4844(14)	0.5495(10)	1.86(21)
C1	0	0.4176(40)	0.8436(38)	0.95(47)
C2	0.5	0.0343(49)	0.5782(45)	1.68(62)
O1	0.2097(26)	0.4907(24)	0.2951(20)	2.02(33)
O2	0.2850(33)	0.1288(27)	0.5452(23)	2.49(34)
O3	0	0.2313(43)	0.9204(41)	3.15(57)
O4	0.5	0.1433(41)	0.1462(36)	2.62(53)

[a]MoKα, R = 0.062 (313 refl.).

TABLE 35
Interatomic distances for carbocernaite in Å[a].

Sr,Ce–O3	2.542		Ca,Na–O1	2.352 ×2
Sr,Ce–O3	2.555		Ca,Na–O1	2.396 ×2
Sr,Ce–O2	2.586	×2	Ca,Na–O4	2.496
Sr,Ce–O1	2.657	×2	Ca,Na–O2	2.547 ×2
Sr,Ce–O2	2.657	×2	mean	2.441
Sr,Ce–O4	2.732	×2		
mean	2.636			
C1–O1	1.292	×2	C2–O4	1.245
C1–O3	1.323		C2–O2	1.298 ×2
mean	1.302		mean	1.280

[a]Calculated by RM.

without water or additional anions. Although a relationship between carbocernaite and burbankite was suggested as mentioned above, the structural features of these minerals do not show any similarity.

KAMOTOITE-(Y)
$U_4Y_2O_{12}(CO_3)_3 \cdot 14.5H_2O$
$U_4Y_2O_{12}(CO_3)_3 \cdot 14.5H_2O$

Sys. monoclinic	$a = 21.22(1)$ Å	source: Shaba, Zaïre
S.G. $P2_1/a$	$b = 12.93(1)$ Å	Ref.: Deliens and Piret (1986b)
$Z = 4$	$c = 12.39(1)$ Å	JCPDS: #40-0482
Dx = 3.94 g/cm^3	$\beta = 115.3(1)°$	
Dm = 3.93 g/cm^3		

Deliens and Piret (1986b) described a new rare earth mineral, kamotoite-(Y), for which they gave the chemical formula $4UO_3 \cdot Y_2O_3 \cdot 3CO_2 \cdot 14.5H_2O$. There is a possibility of the uranium and rare earth atoms being disordered, i.e., $(U,Y)_6O_{12}(CO_3)_3 \cdot 14.5H_2O$, because of the similarity of the ionic radii of uranium and the Y-group of rare earth ions. The structure is not known.

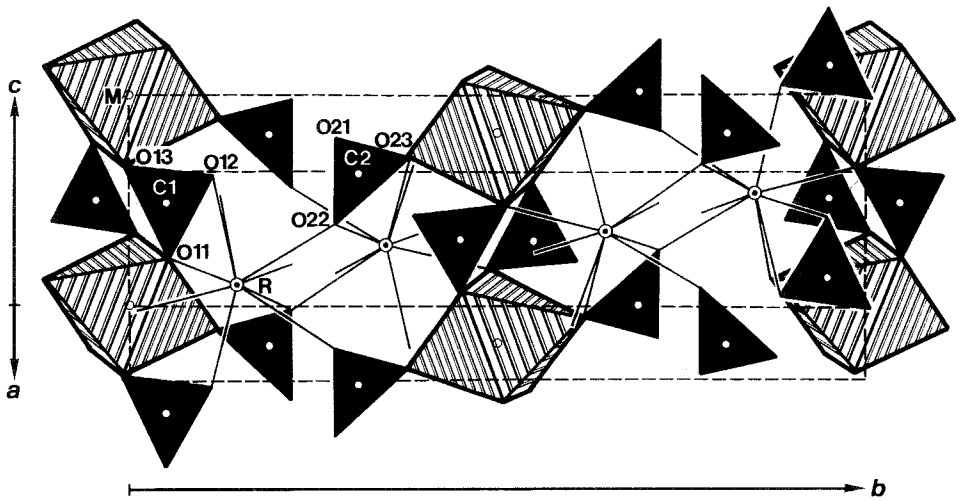

Fig. 17. The crystal structure of sahamalite-(Ce).

SAHAMALITE-(Ce) $(Mg,Fe)Ce_2(CO_3)_4$ $(Mg,Fe)Ce_2(CO_3)_4$		
Sys. monoclinic	$a = 5.894(1)$ Å	source: Mountain Pass, CA, USA
S.G. $P2_1/a$	$b = 16.116(3)$ Å	Ref.: Pertlik and Preisinger (1983)
$Z = 2$	$c = 4.612(1)$ Å	JCPDS: #6-0189
Dx = 4.30 g/cm^3	$\beta = 106.54(1)°$	
Dm = 4.30 g/cm^3		
AP: table 36	ID: table 37	IL: fig. 17

The mineral sahamalite-(Ce) was originally described by Jaffe et al. (1953), and its crystal structure was determined by Pertlik and Preisinger (1983). In the crystal structure of sahamalite-(Ce) (fig. 17), slightly distorted MO_6 octahedra (M = Mg,Fe) are joined by carbonate groups over common corners forming $[M(CO_3)_4]^{6-}$ chains parallel to [001]. Three chains are connected by R atoms in nine-coordination with oxygen. Each R polyhedron has one common edge with each of the carbonate groups. The whole structure represents a three-dimensional network.

DAQINGSHANITE-(Ce) $(Sr,Ca,Ba)_3Ce(PO_4)(CO_3)_3$ $(Sr,Ca,Ba)_3Ce(PO_4)(CO_3)_3$		
Sys. trigonal	$a = 10.058 \pm 0.002$ Å	source: Baiyun Obo, China
S.G. R3m	$c = 9.225 \pm 0.003$ Å	Ref.: Ximen and Peng (1985a)
$Z = 3$		JCPDS: #37-0455
Dx = 3.71 g/cm^3		
Dm = 3.81 g/cm^3		
AP: table 38	ID: table 39	IL: fig. 18

TABLE 36
Atomic parameters of sahamalite-(Ce)[a].

	x	y	z
M[b]	0	0	0
R[c]	0.08173(6)	0.34587(2)	0.30511(8)
C1	0.3084(10)	0.0463(4)	0.6120(13)
C2	0.5228(11)	0.3115(4)	0.8183(14)
O11	0.2825(9)	0.0454(3)	0.3273(11)
O12	0.4182(9)	0.1072(3)	0.7634(11)
O13	0.2273(9)	0.9855(3)	0.7392(11)
O21	0.6813(9)	0.2787(3)	0.0429(11)
O22	0.0286(9)	0.7784(3)	0.4454(12)
O23	0.0943(9)	0.8769(3)	0.1511(12)

[a]MoKα, $R = 0.043$, $R_w = 0.045$ (1453 refl.).
[b]M: 0.86Mg + 0.14Fe.
[c]R: 0.5Ce + 0.5La.

TABLE 37
Interatomic distances for sahamalite-(Ce) in Å.

R–O22	2.487(6)	M–O11	2.039(4) ×2
R–O21	2.498(5)	M-O13	2.053(6) ×2
R–O22	2.505(5)	M–O23	2.123(5) ×2
R–O11	2.509(5)	mean	2.072
R–O12	2.524(5)		
R–O13	2.551(5)		
R–O21	2.565(5)		
R–O12	2.670(6)		
R–O23	2.732(5)		
mean	2.560		
C1–O12	1.270(7)	C2–O22	1.283(8)
C1–O11	1.278(8)	C2–O23	1.289(9)
C1–O13	1.301(8)	C2–O21	1.294(7)
mean	1.283	mean	1.289

Daqingshanite-(Ce) is a unique rare earth strontium phosphocarbonate mineral described by Ren et al. (1983). Their preliminary study of the crystal structure showed that it has a calcite-type structure similar to that of huntite, $Mg_3Ca(CO_3)_4$. This was confirmed in a structure analysis by Ximen and Peng (1985a). In the crystal structure (fig. 18), Ce and Sr atoms occupy individual independent sites to form ten- and nine-coordinated polyhedra with irregular shapes, respectively. The cation ordering of daqingshanite-(Ce) conforms to intralayer two-dimensional ordering, as in the huntite-type structure. The distribution of anions in the structure is also ordered, and also belongs to an intralayer two-dimensional ordering with an 1 : 3 ratio of the

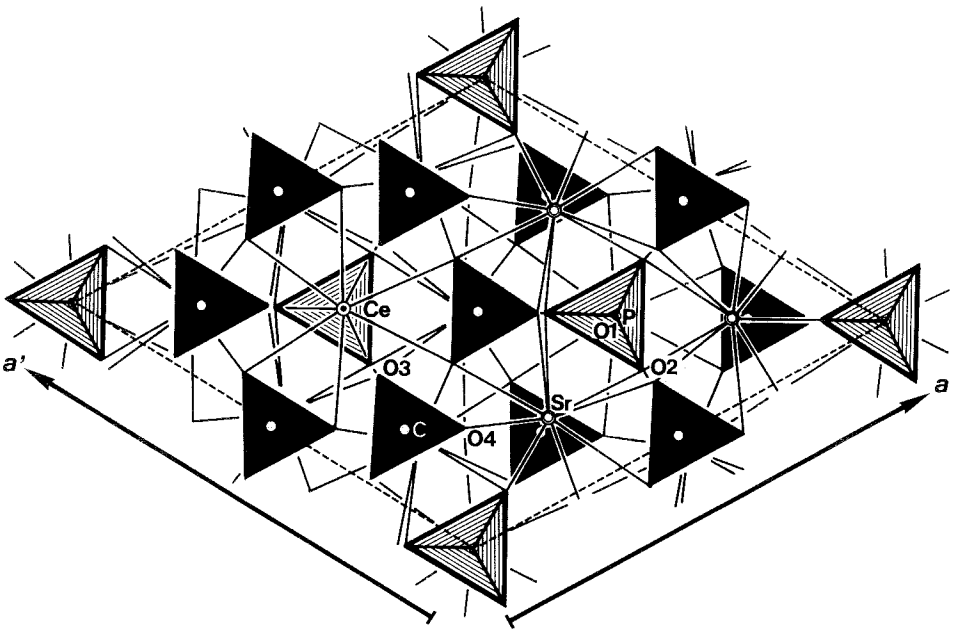

Fig. 18. The crystal structure of daqingshanite-(Ce).

TABLE 38
Atomic parameters of daqingshanite-(Ce)[a].

	x	*y*	*z*
Ce	0	0	0
Sr	0.4833(2)	−0.4833(2)	0.0449(5)
P	1/3	2/3	0.2481(25)
C	0.3334(36)	0.1667(18)	0.2168(55)
O1	1/3	2/3	0.4174(91)
O2	0.2540(8)	0.5079(36)	0.1818(55)
O3	0.1881(26)	0.0940(13)	0.2016(31)
O4	0.4038(23)	0.0906(21)	0.2463(26)

[a]MoKα, $R = 0.079$ (427 refl.).

TABLE 39
Interatomic distances for daqingshanite-(Ce) in Å.

Ce–O1	2.300	Sr–O2	2.562
Ce–O3	2.479 ×3	Sr–O4	2.576 ×2
Ce–O4	2.672 ×6	Sr–O2	2.592(25) ×2
mean	2.577	Sr–O4	2.771 ×2
		Sr–O3	2.808 ×2
C–O3	1.273(38)	mean	2.673
C–O4	1.306(31) ×2		
mean	1.295	P–O2	1.512(25) ×3
		P–O1	1.562(88)
		mean	1.525

two kinds of anion groups. A site occupancy refinement indicated that about 30% of the P sites were vacant and a portion of the PO_4 groups may be replaced by CO_3 groups.

SHABAÏTE-(Nd)
$CaNd_2(UO_2)(CO_3)_4(OH)_2 \cdot 6H_2O$
$CaNd_2(UO_2)(CO_3)_4(OH)_2 \cdot 6H_2O$

Sys. monoclinic	$a = 9.208(5)$ Å	source: Shaba, Zaïre
S.G. P2, Pm or P2/m	$b = 32.09(3)$ Å	Ref.: Deliens and Piret (1989)
$Z = 5$	$c = 8.335(4)$ Å	
Dx = 3.18 g/cm^3	$\beta = 90.3(1)°$	
Dm = 3.13(10) g/cm^3		

Deliens and Piret (1989) described a new rare earth mineral, shabaïte-(Nd), $CaNd_2(UO_2)(CO_3)_4(OH)_2 \cdot 6H_2O$. There is a possibility that the calcium and rare earth atoms are disordered, i.e., $(Nd,Ca)_3(UO_2)(CO_3)_4(OH)_2 \cdot 6H_2O$. The crystal structure is not known.

ASTROCYANITE-(Ce)
$Cu_2Ce_2(UO_2)(CO_3)_5(OH)_2 \cdot 1.5H_2O$
$Cu_2Ce_2(UO_2)(CO_3)_5(OH)_2 \cdot 1.5H_2O$

Sys. hexagonal	$a = 14.96$ Å	source: Shaba, Zaïre
S.G. P6/mmm, P6mm, P622, $P\bar{6}2m$ or $P\bar{6}m2$	$c = 26.86$ Å	Ref.: Deliens and Piret (1990)
$Z = 12$		
Dx = 3.95 g/cm^3		
Dm = 3.80 g/cm^3		

Astrocyanite-(Ce) is a new mineral described by Deliens and Piret (1990). It occurs as bright blue millimeter-sized rosettes in a uraninite matrix in the Cu–Co deposit of East Kamoto, southern Shaba, Zaïre, associated with other uranium and rare earth secondary minerals such as kamotoite-(Y), shabaïte-(Nd) and françoisite-(Nd).

BRAITSCHITE-(Ce)
$(Ca,Na_2)_7Ce_2B_{22}O_{43} \cdot 7H_2O$
$(Ca,Na_2)_7Ce_2B_{22}O_{43} \cdot 7H_2O$

Sys. hexagonal	$a = 12.156 \pm 0.001$ Å	source: Grand Co., UT, USA
S.G.	$c = 7.377 \pm 0.005$ Å	Ref.: Raup et al. (1968)
$Z = 1$		JCPDS: #21-0158
Dx = 2.837 g/cm^3		
Dm = 2.903 ± 0.002 g/cm^3		

Braitschite-(Ce) was first described by Raup et al. (1968). They also reported the possibility of another chemical formula, $(Ca,Na_2)_6Ce_2B_{24}O_{45} \cdot 6H_2O$, which fits the hexagonal symmetry requirements. Further studies on the chemical formula and crystal structure of the mineral have not yet been reported.

2.2. *Class 2: structures with tetrahedral anionic groups – phosphates, silicates, etc.*

2.2.1. *Structures with isolated tetrahedral anionic groups – phosphates, arsenates, vanadates and silicates*

The structural roles of phosphate, arsenate and vanadate ions are similar to each other in the crystal structures of rare earth minerals. Like the carbonate ion, these anions almost always exist as isolated anions in the crystal structures, and do not form infinite anionic groups such as chains. A few silicates structurally related to the phosphates are also included in this section.

XENOTIME-(Y)
YPO_4
YPO_4

Sys. tetragonal	$a = 6.878 \pm 0.003$ Å	source: Hitterö, Norway
S.G. $I4_1/amd$	$c = 6.036 \pm 0.003$ Å	Ref.: Krstanović (1965)
$Z = 4$		JCPDS: #11-0254, #9-0377
AP: table 40	ID: table 41	IL: fig. 19

The crystal structure of xenotime-(Y) was determined by Vegard (1927) and Strada and Schwendiman (1934). It is isostructural with that of zircon, $ZrSiO_4$. The yttrium atoms form eight-coordinated polyhedra which connect isolated PO_4 tetrahedra. According to these results, the high stability of xenotime-(Y) against metamictization compared with zircon could be ascribed to the fact that the Y–O distances in xenotime-(Y) are more regular than the Zr–O distances in zircon. Krstanović (1965) redetermined the atomic parameters of the oxygen atoms in the crystal structure of xenotime-(Y) (fig. 19). The result shows that the Y–O distances are also not regular in xenotime-(Y) and the different behavior toward metamictization of these minerals cannot be explained on the basis of the cation–anion distances alone.

TABLE 40
Atomic parameters of xenotime-(Y)[a].

	x	*y*	*z*
Y	0	0.75	0.125
P	0	0.25	0.625
O	0	0.064	0.234

[a]X-ray: ?, $R = 0.10$.

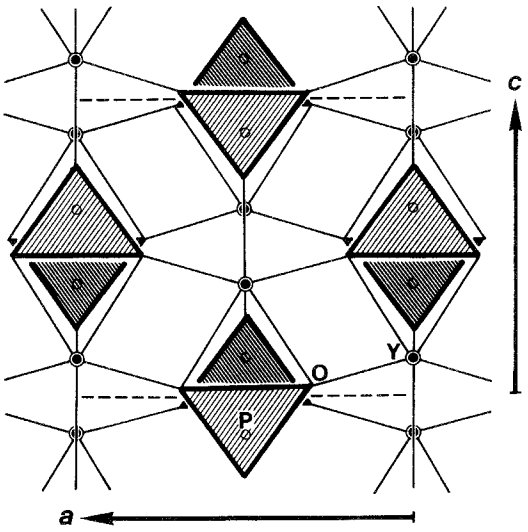

Fig. 19. The crystal structure of xenotime-(Y).

TABLE 41
Interatomic distances for xenotime-(Y) in Å.

Y–O	2.27 ×4	P–O	1.50 ×4
Y–O	2.56 ×4		
mean	2.42		

CHERNOVITE-(Y)
$Y(As,P)O_4$
$Y(As,P)O_4$

Sys. tetragonal	$a = 6.99_3$ Å	source: Binnatal, Switzerland
S.G. $I4_1/amd$	$c = 6.16_7$ Å	Ref.: Graeser et al. (1974)
$Z = 4$		JCPDS: #26-0999, #13-0429
$Dx = 4.93$ g/cm^3		

WAKEFIELDITE-(Y)
YVO_4
YVO_4

Sys. tetragonal	$a = 7.10$ Å	source: Wakefield, Que., Canada
S.G. $I4_1/amd$	$c = 6.30$ Å	Ref.: Hogarth and Miles (1969)
$Z = 4$		JCPDS: #17-0341
$Dx = 4.26$ g/cm^3		

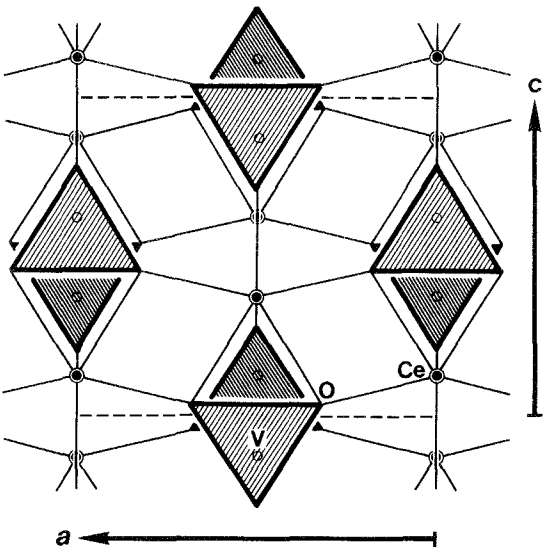

Fig. 20. The crystal structure of wakefieldite-(Ce).

TABLE 42
Atomic parameters of wakefieldite-(Ce)[a].

	x	y	z	B_{eq}
Ce[b]	0	3/4	1/8	0.74
V[c]	0	3/4	5/8	0.84
O	0	0.0716(4)	0.2067(4)	1.37

[a] MoKα, $R = 0.014$, $R_w = 0.013$ (140 refl.).
[b] 0.93Ce + 0.07Y.
[c] 0.92V + 0.08As.

WAKEFIELDITE-(Ce) (= kusuite)
$CeVO_4$
$CeVO_4$

Sys.	tetragonal	$a = 7.354(3)$ Å	source: Tifernine, Anti-Atlas, Morocco
S.G.	$I4_1/amd$	$c = 6.488(4)$ Å	Ref.: Baudracco-Gritti et al. (1987)
$Z =$	4		JCPDS: #29-0398, #12-0757
Dx =	4.80 g/cm^3		
Dm =	4.76 g/cm^3		
AP:	table 42	ID: table 43	IL: fig. 20

The structure of chernovite-(Y) (Graeser et al. 1974) and wakefieldite-(Y) (Hogarth and Miles 1969) were assumed to be isostructural with that of xenotime-(Y) because of the close similarity of the X-ray powder diffraction patterns. The crystal structure of wakefieldite-(Ce) (Baudracco-Gritti et al. 1987) (fig. 20) is isostructural with that of zircon. Therefore, wakefieldite-(Ce) is a Ce–V-analogue of xenotime-(Y). Although kusuite (Ce^{3+},Pb^{2+},Pb^{4+})VO_4 was described by Deliens and Piret (1977) as a Ce,Pb-

TABLE 43
Interatomic distances for wakefieldite-(Ce) in Å.

Ce–O	2.425(3) ×4	V–O	1.706(3) ×4
Ce–O	2.518(3) ×4		
mean	2.472		

TABLE 44
Atomic parameters of monazite-(Ce)[a].

	x	*y*	*z*
Ce	0.275	0.658	0.100
P	0.261	0.658	0.575
O1	0.250	0.492	0.400
O2	0.417	0.650	0.808
O3	0.083	0.667	0.692
O4	0.250	0.825	0.400

[a] CuKα and MoKα, $R_{h0l} = 0.16$ (55 refl.), $R_{hk0} = 0.19$ (58 refl.).

TABLE 45
Interatomic distances for monazite-(Ce) in Å.

Ce–O1	2.29	P–O3	1.57
Ce–O4	2.30	P–O1	1.61[a]
Ce–O2	2.31	P–O2	1.62
Ce–O1	2.34	P–O4	1.62
Ce–O4	2.34	mean	1.61
Ce–O3	2.37		
Ce–O3	2.65		
Ce–O2	2.96		
mean	2.45		
Ce–O2	3.31		

[a] Recalculated by RM.

analogue of wakefieldite, the mineral name "kusuite" was changed into plumboan wakefieldite-(Ce) in accordance with the new nomenclature of the rare earth minerals by the IMA Commission on New Minerals and Mineral Names (Deliens and Piret 1986a, Nickel and Mandarino 1987).

MONAZITE-(Ce) (=kularite)
$CePO_4$
$CePO_4$

Sys. monoclinic	$a = 6.77 \pm 0.01$ Å	source: Ishikawa-yama, Fukushima, Japan
S.G. $P2_1/n$	$b = 6.99 \pm 0.01$ Å	Ref.: Ueda (1967)
$Z = 4$	$c = 6.45 \pm 0.01$ Å	JCPDS: #29-0403, #11-0556
$Dm = 5.20$ g/cm^3	$\beta = 103°38'$	
AP: table 44	ID: table 45	IL: fig. 21

MONAZITE-(La)
$LaPO_4$
$LaPO_4$

Sys. monoclinic	$a =$ 6.84 Å	source: synthetic $LaPO_4$
S.G. $P2_1/n$	$b =$ 7.07 Å	Ref.: Carron et al. (1958)
$Z =$ 4	$c =$ 6.45 Å	JCPDS: #35-0731, #12-0283
Dx = 5.13 g/cm^3	$\beta = 103.85°$	

MONAZITE-(Nd)
$NdPO_4$
$NdPO_4$

Sys. monoclinic	$a =$ 6.745(4) Å	source: Pta. Glogstafel, Val Formazza, Italy
S.G.	$b =$ 6.964(4) Å	
$Z =$ 4	$c =$ 6.435(4) Å	Ref.: Graeser and Schwander (1987)
Dx = 5.43 g/cm^3	$\beta = 103.65(4)°$	

GASPARITE-(Ce)
$CeAsO_4$
$CeAsO_4$

Sys. monoclinic	$a =$ 6.973(3) Å	source: Penninic region, Alps, Italy and Switzerland
S.G. $P2_1/n$	$b =$ 7.137(4) Å	
$Z =$ 4	$c =$ 6.738(6) Å	Ref.: Graeser and Schwander (1987)
Dx = 5.63 g/cm^3	$\beta = 104.69(5)°$	JCPDS: #15-0772

CHERALITE
$(Th,Ca,Ce)(P,Si)O_4$
$(Th,Ca,Ce)(P,Si)O_4$

Sys. monoclinic	$a =$ 6.717 ± 0.005 Å	source: Travancore, India
S.G. $P2_1/n$	$b =$ 6.920 ± 0.005 Å	Ref.: Finney and Rao (1967)
$Z =$ 4	$c =$ 6.434 ± 0.005 Å	JCPDS: #33-1095
Dm = 5.20 g/cm^3	$\beta = 103°50' \pm 05'$	
AP: table 46	ID: table 47	IL: fig. 22

TABLE 46
Atomic parameters of cheralite[a].

	x	y	z	B (Å^2)
Ce	0.2198(2)	0.1596(2)	0.3991(2)	1.08(2)
P	0.1960(8)	0.1630(9)	0.8858(9)	0.83(7)
O1	0.2473(36)	0.5064(38)	0.4426(37)	2.56(41)
O2	0.0238(32)	0.1044(30)	0.6906(33)	1.84(30)
O3	0.3740(29)	0.2221(28)	0.7898(31)	1.56(27)
O4	0.1114(30)	0.3337(35)	−0.0011(31)	1.93(28)

[a] MoKα, $R = 0.084$ (615 refl.).

TABLE 47
Interatomic distances for cheralite in Å.

Ce–O3	2.403(25)	P–O3	1.527(25)
Ce–O1	2.418(25)	P–O1	1.529(25)
Ce–O2	2.429(25)	P–O2	1.544(25)
Ce–O1	2.498(25)	P–O4	1.564(25)
Ce–O3	2.517(25)	mean	1.541
Ce–O4	2.539(25)		
Ce–O4	2.555(25)		
Ce–O2	2.564(25)		
Ce–O4	2.778(25)		
mean	2.522		
Ce–O2	3.154(25)		
Ce–O3	3.764(25)		
Ce–O1	3.945(25)		

BRABANTITE (=cathophorite)
$CaTh(PO_4)_2$
$(Ca,Al,Mg,R,U)Th(PO_4)_2$

Sys. monoclinic	$a = 6.726 \pm 0.006$ Å	source: Brabant farm, Karibib, Namibia
S.G. $P2_1$	$b = 6.933 \pm 0.005$ Å	Ref.: Rose (1980)
$Z = 2$	$c = 6.447 \pm 0.012$ Å	JCPDS: #31-0311, #35-0465
Dx = 5.26 g/cm^3	$\beta = 103°53' \pm 16'$	
Dm = 4.72 g/cm^3		

TOMBARTHITE-(Y)
$Y(Si,H_4)O_{3-x}(OH)_{1+2x}$
$Y(Si,H_4)O_{3-x}(OH)_{1+2x}$

Sys. monoclinic	$a = 7.12$ Å	source: Høgetveit, Evje, Norway
S.G. $P2_1/n$	$b = 7.29$ Å	Ref.: Neumann and Nilssen (1968)
$Z = 4$	$c = 6.71$ Å	JCPDS: #21-1314
Dx = 3.68 g/cm^3	$\beta = 102°41'$	
Dm = 3.51 g/cm^3		

karnasurite-(Ce) (=kozhanovite)
$(Ce,La,Th)(Ti,Nb)(Al,Fe)(Si,P)_2O_7(OH)_4 \cdot 3H_2O$
$(Ce,La,Th)(Ti,Nb)(Al,Fe)(Si,P)_2O_7(OH)_4 \cdot 3H_2O$

Sys. hexagonal (?)	$a =$	source: Mt. Karnasurt, Lovozero, Kola
S.G. X-ray amorphous	$c =$	Peninsula, Russia
$Z =$		Ref.: Kuz'menko and Kozhanov (1959),
Dm = 2.89–2.95 g/cm^3		Vlasov et al. (1959)

The crystal structure of monazite-(Ce) was determined by Kokkoros (1942) and was confirmed by the X-ray powder diffraction study of Mooney (1948); later, Ueda (1953) reinvestigated the structure. Refinements of the crystal structure of monazite-(Ce) were independently reported by Ueda (1967) and by Ghouse (1968). The crystal structure of cheralite was determined by Finney and Rao (1967).

The crystal structure of monazite-(Ce) (fig. 21) shows close relationships to that of xenotime-(Y) (fig. 19). The characteristic difference between monazite-(Ce) and xenotime-(Y) is the predominance of Ce among the rare earth elements in monazite-(Ce) and that of Y in xenotime-(Y). This difference reflects on the two crystal structures. Although Ueda (1967) reported the coordination number of cerium atom as nine, the longest Ce–O distance, 3.31 Å, is too long to be included in the direct coordination. Therefore, the cerium atoms are regarded as eight-coordinated in the crystal structure of monazite-(Ce), as reported by Ghouse (1968). The mean Ce–O distance is 2.45 Å for eight-coordination, which is slightly larger than the mean Y–O distance in xenotime, 2.42 Å. The arrangements of the PO_4 tetrahedra, which are connected by rare earth atoms in both structures, are distinct due to differences in the volumes and shapes of the rare earth polyhedra. The compact tetragonal crystal structure of xenotime-(Y) suggests that xenotime-(Y) may be a high-pressure phase of the monoclinic structure of monazite-(Ce).

Gasparite-(Ce) is an arsenate analogue of monazite-(Ce), described by Graeser and Schwander (1987).

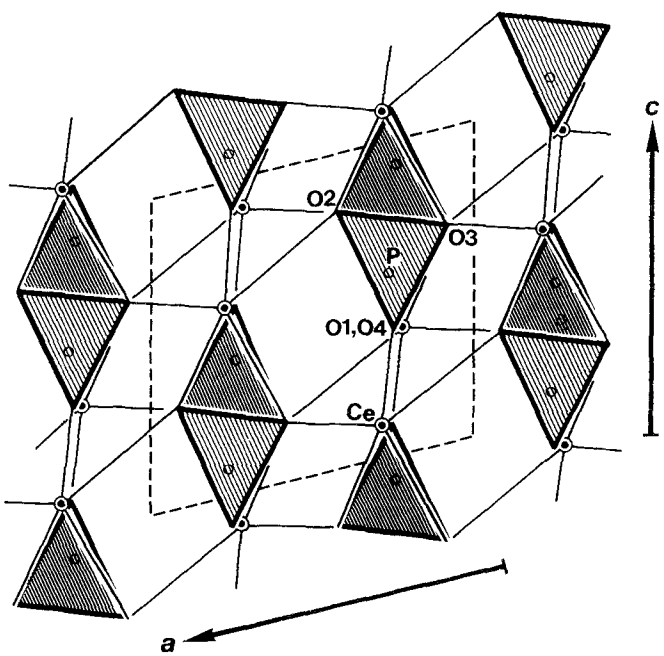

Fig. 21. Projection of the crystal structure of monazite-(Ce) onto (010).

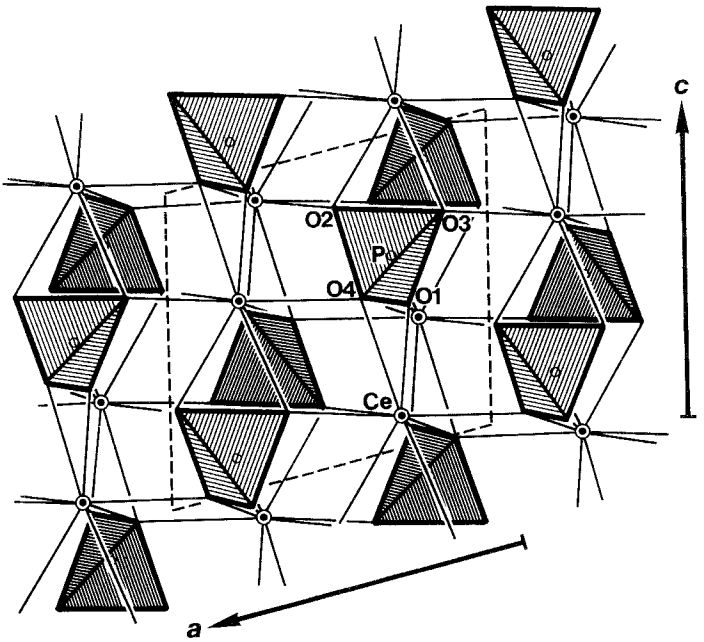

Fig. 22. Projection of the crystal structure of cheralite onto (010).

The crystal structure of cheralite (fig. 22) is isotypic with that of monazite-(Ce). It can be seen in the structure that the isomorphous substitution of thorium and calcium atoms for cerium atoms causes tilting of the PO_4 tetrahedra due to the difference in the ionic radii between them. A reexamination of the type of material of cheralite was done by Bowles et al. (1980).

Brabantite (Rose 1980) is related to cheralite. However, the difference in the space groups between brabantite, $P2_1$, and cheralite, $P2_1/n$, suggests ordering of Ca and Th in the crystal structure of brabantite. Cathophorite (Lingaitukuang), described by Wang (1978), is identical to brabantite.

Tombarthite-(Y) was described by Neumann and Nilssen (1968) with the chemical formula $Y_4(Si,H_4)_4O_{12-x}(OH)_{4+2x}$, indicating partial substitution of four hydrogen atoms for a silicon atom. They reported that the X-ray powder diffraction data could be indexed on the basis of the crystal data of monazite-(Ce); however, a crystal structure analysis of tombarthite-(Y) has not yet been reported. One of the ideal end members of tombarthite-(Y), $YSiO_3(OH)$, can be regarded as a Y,Si-analogue of monazite-(Ce).

Karnasurtite-(Ce) had previously been named as kozhanovite without a description. Karnasurtite-(Ce) is X-ray amorphous; after being heated to 900°C, it gives a diffraction pattern similar to that of huttonite, $ThSiO_4$ (Kuz'menko and Kozhanov, 1959, Vlasov et al. 1959).

VITUSITE-(Ce)
$Na_3Ce(PO_4)_2$
$Na_3Ce(PO_4)_2$

Sys.	orthorhombic	$a = 14.091(4)$ Å	source: Lovozero, Kola Peninsula, Russia
S.G.	$Pca2_1$	$b = 5.357(1)$ Å	Ref.: Karpov et al. (1980)
$Z =$	8	$c = 18.740(3)$ Å	JCPDS: #33-1232
Dx =	3.76 g/cm^3		
Dm =	3.60 g/cm^3		
AP:	tables 48, 49	ID: tables 50, 51	IL: fig. 23a,b

The crystal structure of vitusite-(Ce) was determined by Karpov et al. (1980). They reported two structural models (fig. 23), which are mutually related by displacement along a quarter of the *a*-axis. They also reported that the presence of a superstructure was indicated by very weak reflections having pseudo-intervals along the *b*-axis, but the cell dimension of the superstructure could not be determined. They pointed out

TABLE 48
Atomic parameters of vitusite-(Ce): model 1[a].

	x	*y*	*z*	*B* (Å^2)
Ce1	0.134	0.489	0	2.12
Ce2	0.118	0.060	0.223	1.78
Na1	0.369	−0.006	0.255	1.38
Na2	0.118	0.495	0.474	1.01
Na3	0.454	−0.002	0.076	1.62
Na4	0.296	0.510	0.154	0.89
Na5	0.234	0.004	0.420	1.06
Na6	0.464	0.476	0.314	1.02
P1	0.013	0.517	0.149	0.33
P2	0.488	−0.011	0.404	0.16
P3	0.225	0.531	0.319	0.19
P4	0.229	−0.005	0.076	0.20
O1	0.474	0.491	0.076	0.22
O2	0.127	0.534	0.142	1.60
O3	0.489	0.249	0.190	1.66
O4	0.475	0.701	0.190	1.15
O5	0.260	0.005	0.157	0.92
O6	0.126	0.040	0.071	1.76
O7	0.271	0.750	0.039	1.74
O8	0.272	0.229	0.039	1.52
O9	0.130	0.414	0.316	0.33
O10	0.259	0.519	0.402	1.63
O11	0.318	0.464	0.275	1.08
O12	0.230	0.793	0.294	1.02
O13	0.388	0.116	0.423	4.42
O14	0.480	0.010	0.324	0.15
O15	0.036	0.820	0.448	3.70
O16	0.462	0.711	0.423	2.34

[a]Mo, $R = 0.126$ (1833 refl.).

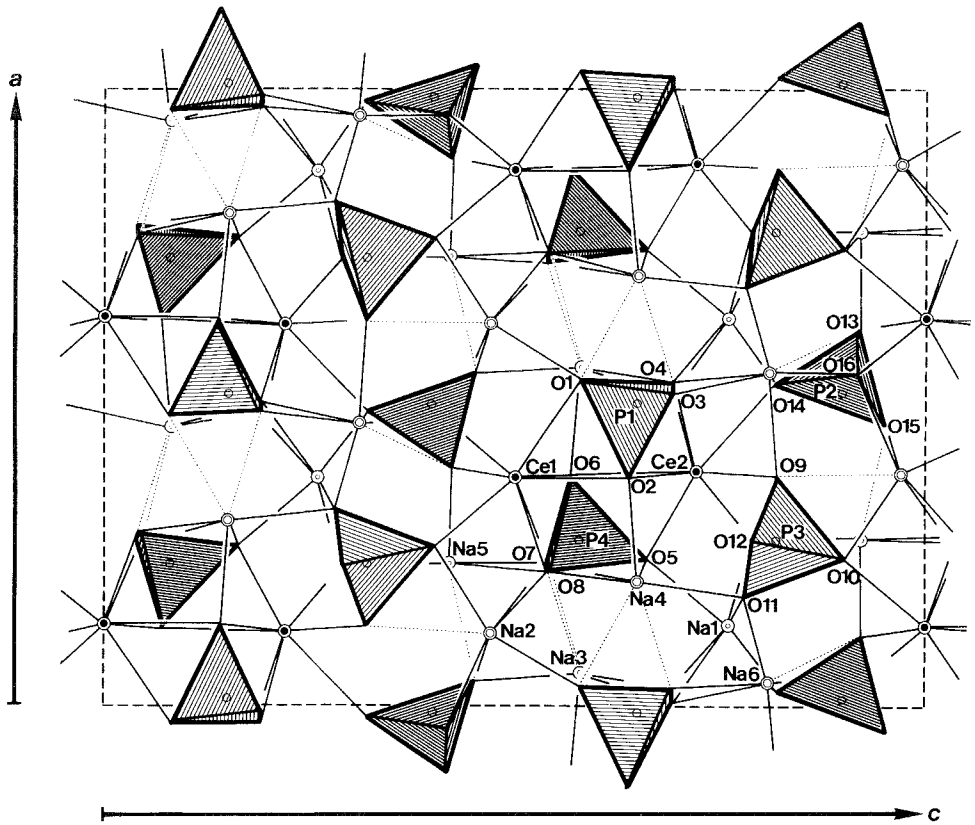

Fig. 23. The crystal structure of vitusite-(Ce); (a) projection of model I onto (010).

that the structure of vitusite-(Ce) shows a similarity to that of β-K_2SO_4, whose cell dimensions a and c are half the corresponding dimensions of vitusite-(Ce). In the crystal structure of vitusite-(Ce), the two independent cerium sites are coordinated by eight oxygen atoms of PO_4 tetrahedra forming a three-dimensional framework, and the sodium atoms are located in the cavities in the framework. Karpov et al. (1980) described the coordination number of sodium atoms as six, except for the four-coordinated one at the Na6 site in "model 2". However, the irregular coordination numbers of Na3 and Na4 are unreasonable, because such one-sided coordinations are observed only in covalent molecular groups with a lone pair of electrons, such as in NH_3. We recalculated the interatomic distances using the atomic parameters of Karpov et al. (1980) and the computer program BADTEA (Finger and Prince 1975), and reconsidered the coordination numbers of the sodium atoms in vitusite-(Ce). The coordination numbers for the sodium atoms are calculated under the assumption that all the oxygen atoms within 3.13 Å, which is the maximum bond length for a Na–O bond reported by Donnay and Allmann (1970), are bonding to the sodium atoms. The results are as follows: Na1, 7; Na2, 7; Na3, 8; Na4, 8; Na5, 7;

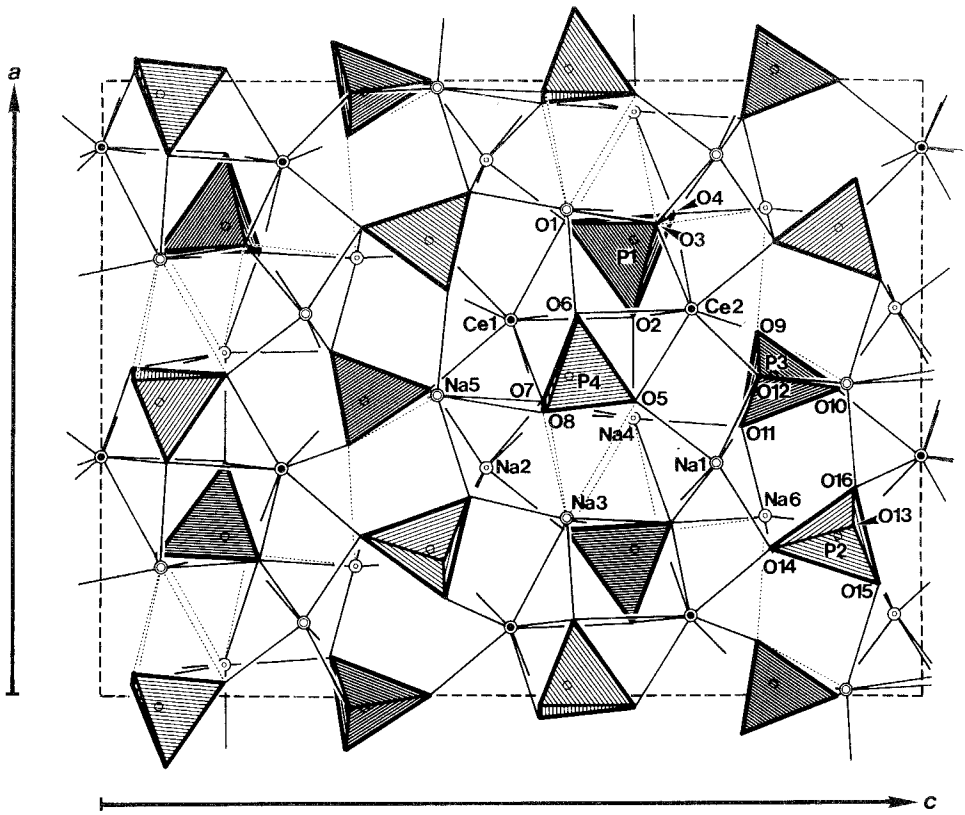

Fig. 23. (b) projection of model II onto (010).

Na6, 8 for "model 1"; Na1, 6; Na2, 7; Na3, 9; Na4, 9; Na5, 8; Na6, 8 for "model 2". The additional bonds are indicated by light broken lines in fig. 23.

Karpov et al. (1980) demonstrated the isomorphism $3Ca \rightleftarrows 3Na + Ce$ after refinement of the multiplicities, which permitted the introduction of calcium atoms into the Na2 site of "model 1" and in the Na1 site of "model 2". This isomorphous substitution requires a change of the number of atoms from three to four, and vice versa. The substitution $2Ca \rightleftarrows Na + Ce$, which is usually observed in rare earth minerals, does not require any change of the number of atoms. However, Karpov et al. (1980) did not refer to the latter type of substitution, and any concrete values of the result of the refinement of multiplicities are lacking in their paper. Therefore, it is impossible to decide which kind of substitution occurs in the structure.

Karpov et al. (1980) reported that the pseudo-hexagonal symmetry of the principal structural block, i.e., six-membered units of PO_4 tetrahedra surrounding the Na and Ce atoms, is typical of the structures of compounds of $A_xB_y(TO_4)_{(x+y)/2}$ (T: S, V, and Si) type, such as aphthitalite (glaserite) $K_3Na(SO_4)_2$, larnite β-Ca_2SiO_4, and synthetic $Na_3La(VO_4)_2$.

TABLE 49
Atomic parameters of vitusite-(Ce): model 2[a].

	x	y	z	B (Å^2)
Ce1	0.385	0.013	0	1.30
Ce2	0.369	0.439	0.224	1.19
Na1	0.617	0.509	0.253	1.36
Na2	0.370	−0.018	0.474	1.15
Na3	0.705	0.515	0.072	1.22
Na4	0.546	0.966	0.151	1.13
Na5	0.485	0.468	0.410	0.65
Na6	0.711	0.010	0.314	0.86
P1	0.264	0.985	0.147	0.46
P2	0.736	0.502	0.403	0.34
P3	0.477	0.966	0.317	0.47
P4	0.479	0.498	0.074	0.32
O1	0.726	0.001	0.074	1.09
O2	0.378	0.020	0.146	1.12
O3	0.728	0.254	0.180	1.85
O4	0.721	0.772	0.185	1.67
O5	0.515	0.493	0.154	0.76
O6	0.376	0.488	0.076	1.20
O7	0.517	0.743	0.037	1.06
O8	0.526	0.274	0.036	1.40
O9	0.407	0.157	0.299	2.74
O10	0.499	0.018	0.403	0.94
O11	0.560	0.071	0.281	1.93
O12	0.480	0.685	0.296	1.65
O13	0.719	0.206	0.423	1.55
O14	0.758	0.485	0.324	0.93
O15	0.321	0.499	0.448	2.00
O16	0.655	0.655	0.421	2.51

[a] Mo, $R = 0.133$ (1592 refl.).

CERVANDONITE-(Ce)
$Ce(Fe,Ti,Al)_3SiAs(Si,As)O_{13}$
$Ce(Fe,Ti,Al)_3SiAs(Si,As)O_{13}$

Sys. monoclinic	$a = 11.3$ Å	source: Pizzo Cervandone, Italy;
S.G. C2, Cm or C2/m	$b = 19.5$ Å	Scherbadung, Switzerland
$Z = 6$	$c = 7.2$ Å	Ref.: Armbruster et al. (1988)
$Dx = 4.9$ g/cm^3	$\beta = 121°$	

Armbruster et al. (1988) described a new rare earth arsenosilicate mineral, cervandonite-(Ce). They presumed that arsenic dominantly exists in the As^{5+} state in this mineral, and reported a tetrahedral $Si–As^{5+}$ solid solution with variations of the Fe^{3+}/Fe^{2+} ratio for charge balance.

TABLE 50
Interatomic distances for vitusite-(Ce) in Å: model 1[a].

Ce1–O16	2.31	Ce2–O5	2.37	Na1–O14	2.03	Na2–O15	2.15
Ce1–O10	2.38	Ce2–O4	2.47	Na1–O12	2.35	Na2–O1	2.31
Ce1–O13	2.48	Ce2–O12	2.51	Na1–O5	2.39	Na2–O10	2.41
Ce1–O7	2.49	Ce2–O3	2.54	Na1–O4	2.49	Na2–O7	2.41
Ce1–O8	2.50	Ce2–O9	2.58	Na1–O3	2.49	Na2–O8	2.43
Ce1–O1	2.67	Ce2–O14	2.74	Na1–O11	2.65	Na2–O16	2.64
Ce1–O2	2.67	Ce2–O6	2.85	Na1–O11	2.95	Na2–O9	3.00
Ce1–O6	2.75	Ce2–O2	2.96	mean	2.48	mean	2.48
mean	2.53	mean	2.63				
Na3–O6	2.43	Na4–O11	2.30	Na5–O13	2.25	Na6–O11	2.18
Na3–O3	2.57	Na4–O2	2.40	Na5–O8	2.54	Na6–O16	2.40
Na3–O15	2.59	Na4–O7	2.53	Na5–O7	2.61	Na6–O9	2.41
Na3–O1	2.65	Na4–O8	2.65	Na5–O12	2.62	Na6–O14	2.51
Na3–O4	2.68	Na4–O5	2.70	Na5–O10	2.64	Na6–O4	2.62
Na3–O1	2.73	Na4–O5	2.75	Na5–O10	2.80	Na6–O3	2.65
Na3–O8	2.93	Na4–O4	2.80	Na5–O15	3.01	Na6–O14	2.88
Na3–O7	2.98	Na4–O1	2.90	mean	2.64	Na6–O13	3.01
mean	2.70	mean	2.63			mean	2.58
P1–O1	1.48	P2–O15	1.48	P3–O12	1.48	P4–O6	1.47
P1–O4	1.50	P2–O14	1.51	P3–O9	1.48	P4–O8	1.56
P1–O3	1.51	P2–O16	1.57	P3–O11	1.59	P4–O5	1.58
P1–O2	1.61	P2–O13	1.60	P3–O10	1.63	P4–O7	1.60
mean	1.53	mean	1.54	mean	1.55	mean	1.55

[a]Recalculated by RM.

APATITE group (FLUORAPATITE, HYDROXYLAPATITE, CHLORAPATITE)
$Ca_5(PO_4)_3(F,OH,Cl)$
$(Ca,Na,Ce,Nd)_2(Ca,Nd,Sm)_3[(P,Si)O_4]_3(F,OH,Cl)$

Sys. hexagonal	$a = 9.4052$ Å	source: Pajarito, NM, USA, etc.
S.G. $P6_3/m$	$c = 6.9125$ Å	Ref.: Hughes et al. (1991)
$Z = 2$		JCPDS: #9-0432, #25-0166, #15-0876, #35-0496, #24-0214, #33-0271
AP: table 52	ID: table 53	IL: fig. 24

The crystal structure of R–Sr-apatite was determined by Borisov and Klevtsova (1963). They revealed an ordering of the rare earth, strontium and calcium atoms, and proved the isomorphous replacement $2Ca^{2+} \rightleftarrows R^{3+} + (Na,K)^{+}$. Hughes et al. (1991) analyzed the crystal structures of four R-bearing apatite samples, and suggested the isomorphous substitutions $Ca + P \rightleftarrows R + Si$ and $2Ca \rightleftarrows R + Na$ in R-bearing apatites. The crystal structure of R-bearing apatite (fig. 24) consists of nine-coordinated Ca1 sites, seven-coordinated Ca2 sites, PO_4 tetrahedra and the (F,OH) sites. Borisov and Klevtsova (1963) reported that rare earth atoms with larger ionic radii occupy

TABLE 51
Interatomic distances for vitusite-(Ce) in Å; model 2[a].

Ce1–O13	2.37	Ce2–O9	2.13	Na1–O12	2.29	Na2–O10	2.26
Ce1–O16	2.38	Ce2–O12	2.45	Na1–O5	2.35	Na2–O1	2.31
Ce1–O10	2.45	Ce2–O5	2.46	Na1–O14	2.39	Na2–O8	2.32
Ce1–O7	2.46	Ce2–O14	2.47	Na1–O4	2.40	Na2–O7	2.47
Ce1–O8	2.53	Ce2–O4	2.48	Na1–O3	2.49	Na2–O13	2.54
Ce1–O1	2.64	Ce2–O2	2.68	Na1–O11	2.53	Na2–O15	2.72
Ce1–O2	2.74	Ce2–O3	2.70	mean	2.41	Na2–O15	2.90
Ce1–O6	2.91	Ce2–O6	2.79			mean	2.50
mean	2.56	mean	2.52				
Na3–O15	2.35	Na4–O2	2.39	Na5–O10	2.42	Na6–O11	2.24
Na3–O6	2.41	Na4–O7	2.48	Na5–O15	2.42	Na6–O13	2.30
Na3–O3	2.48	Na4–O11	2.51	Na5–O12	2.43	Na6–O14	2.64
Na3–O4	2.54	Na4–O5	2.57	Na5–O16	2.60	Na6–O4	2.74
Na3–O1	2.62	Na4–O8	2.73	Na5–O7	2.63	Na6–O3	2.84
Na3–O1	2.77	Na4–O4	2.75	Na5–O8	2.74	Na6–O16	2.87
Na3–O8	2.91	Na4–O5	2.86	Na5–O9	2.88	Na6–O14	2.90
Na3–O7	2.99	Na4–O1	2.92	Na5–O10	2.96	Na6–O9	2.92
Na3–O5	3.09	Na4–O3	3.04	mean	2.64	mean	2.68
mean	2.68	mean	2.69				
P1–O1	1.47	P2–O16	1.45	P3–O9	1.46	P4–O6	1.45
P1–O3	1.51	P2–O15	1.46	P3–O11	1.46	P4–O8	1.54
P1–O4	1.60	P2–O14	1.52	P3–O12	1.56	P4–O7	1.58
P1–O2	1.62	P2–O13	1.65	P3–O10	1.66	P4–O5	1.58
mean	1.55	mean	1.52	mean	1.54	mean	1.54

[a]Recalculated by RM.

TABLE 52
Atomic parameters of R-bearing apatite[a].

	x	*y*	*z*
Ca1	2/3	1/3	−0.0012(1)
Ca2	−0.01140(4)	0.23885(4)	1/4
P	0.36881(7)	0.39692(7)	1/4
O1	0.4821(2)	0.3233(2)	1/4
O2	0.4671(2)	0.5853(2)	1/4
O3	0.2557(1)	0.3396(2)	0.0721(2)
F	0	0	1/4

[a]Mo, $R = 0.015$, $R_w = 0.018$ (419 refl.).

TABLE 53
Interatomic distances for R-bearing apatite in Å.

Ca1–O1	2.424(1) ×3	Ca2–F	2.3019(4)
Ca1–O2	2.467(2) ×3	Ca2–O3	2.357(2) ×2
Ca1–O3	2.827(2) ×3	Ca2–O2	2.401(2)
mean	2.573	Ca2–O3	2.518(1) ×2
		Ca2–O1	2.639(1)
		mean	2.465
P–O1	1.534(2)		
P–O2	1.535(2)		
P–O3	1.537(1) ×2		
mean	1.536		

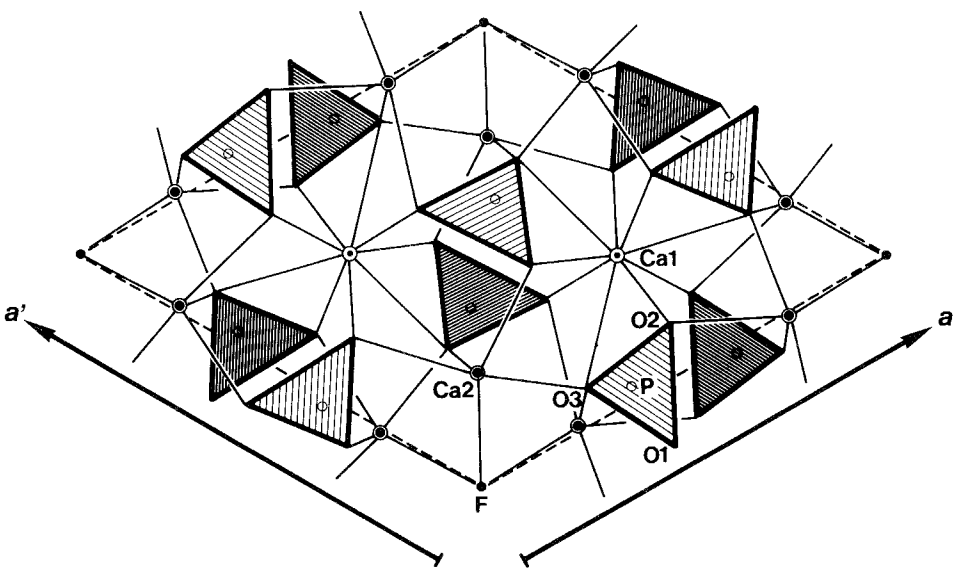

Fig. 24. The crystal structure of R-bearing apatite.

the seven-coordinated sites rather than the nine-coordinated sites. On the other hand, Hughes et al. (1991) reported that the rare earth atoms occupy both Ca sites and the ratios (R in the Ca2 site)/(R in the Ca1 site) in the four crystals studied vary between 1.76 and 3.00. They revealed that La–Pr should preferentially substitute in the seven-coordinated Ca2 site, whereas Pm*–Sm should selectively substitute in the nine-coordinated Ca1 site, on the basis of bond-valence calculations for substituent rare earth elements in the apatite structures. Their calculations also indicated that Nd can readily substitute in either Ca site.

* Although Pm was included in their calculation, this element is an artificial radionuclide.

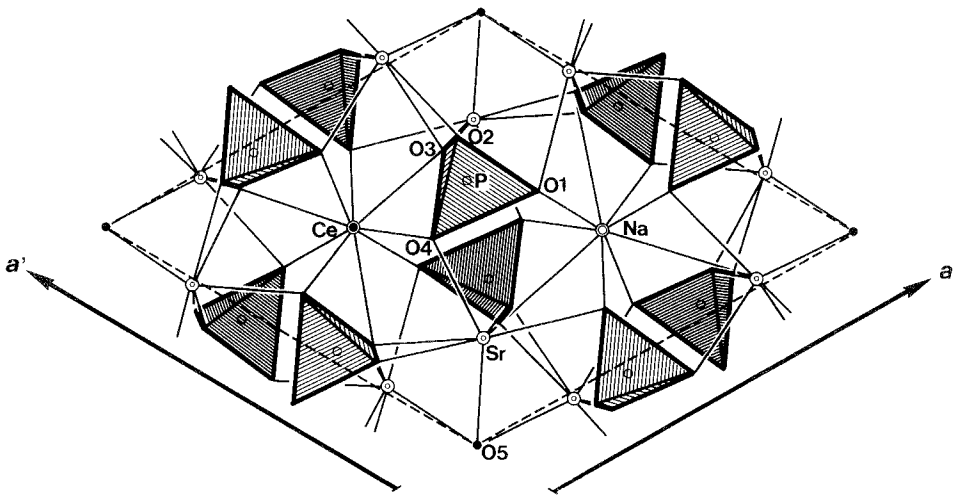

Fig. 25. The crystal structure of belovite-(Ce).

BELOVITE-(Ce)
$Sr_3NaCe(PO_4)_3(OH)$
$Sr_3NaCe(PO_4)_3(OH)$

Sys. trigonal (hex.)	$a = 9.692(3)$ Å	source: Mt. Karnasurt, Lovozero, Russia
S.G. $P\bar{3}$	$c = 7.201(1)$ Å	Ref.: Nadezhina et al. (1987)
$Z = 2$		JCPDS: #31-1350
AP: table 54	ID: table 55	IL: fig. 25

An over-all view of the crystal structure of belovite-(Ce) (fig. 25) (Klevtsova and Borisov 1964) shows a similarity to that of apatite (fig. 24). However, cerium atoms occupy the nine-coordinated sites in contrast to the rare earths in apatite, and the symmetry of belovite-(Ce), $P\bar{3}$, is lower than that of apatite, $P6_3/m$.

The refinement of the crystal structure of belovite-(Ce) (Nadezhina et al. 1987) confirmed the cation distribution reported by Klevtsova and Borisov (1964): i.e., the cerium atom is at the nine-coordinated cation site.

TABLE 54
Atomic parameters of belovite[a].

	x	y	z	B
Ce[b]	0.3333	0.6666	0.5148(2)	1.06
Na[c]	0.3333	0.6666	0	1.73
Sr[d]	0.2383(1)	−0.0176(1)	0.2439(2)	1.17
P	0.4021(4)	0.3720(4)	0.2518(4)	0.91
O1	0.4895(9)	0.1510(8)	0.736(1)	1.23
O2	0.319(1)	0.257(1)	0.092(1)	2.32
O3	0.366(1)	0.273(1)	0.433(1)	1.52
O4	0.537(1)	0.120(1)	0.230(1)	1.72
O5	0	0	0.293(3)	3.32

[a] Mo, $R = 0.048$ (651 refl.).
[b] Ce: 1.45Ce + 0.35Sr.
[c] Na: 1.0Na + 0.5Ca + 0.4Ce.
[d] Sr: 5.55Sr + 0.15Ce + 0.1Ca.

TABLE 55
Interatomic distances for belovite in Å.

Ce–O1	2.508(8) ×3	Na–O4	2.449(9) ×3
Ce–O4	2.571(9) ×3	Na–O1	2.581(9) ×3
Ce–O3	2.691(9) ×3	Na–O2	3.141(9) ×3
mean	2.590[a]	mean	2.724[a]
Sr–O5	2.425(4)	P–O2	1.52(1)
Sr–O2	2.483(9)	P–O4	1.53(1)
Sr–O4	2.512(9)	P–O1	1.54(1)[b]
Sr–O3	2.513(9)	P–O3	1.55(1)
Sr–O2	2.611(8)	mean	1.54[a]
Sr–O1	2.790(8)		
Sr–O3	2.795(8)		
mean	2.590[a]		

[a]Recalculated by RM.
[b]The value 11.52(1) in the original paper may be a misprint.

lessingite-(Ce)
$Ca_2Ce_3(SiO_4)_3(OH,F)$
$(Ce,Ca)_5(SiO_4)_3(OH,F)$

Sys. hexagonal	$a = 9.664(3)$ Å	source: Kyshtym, Urals, Russia
S.G. $P6_3$	$c = 7.090(1)$ Å	Ref.: Kalsbeek et al. (1990)
$Z = 2$		
Dx = 4.48 g/cm^3		
AP: table 56	ID: table 57	

BRITHOLITE-(Ce) (= beckelite)
$(Ce,Ca,Na)_5[(Si,P)O_4]_3(OH,F)$
$(Ce,Ca,Na)_5[(Si,P)O_4]_3(OH,F)$

Sys. hexagonal	$a = 9.629(1)$ Å	source: Naujakasik, Ilímaussaq, Greenland
S.G. $P6_3$	$c = 7.059(2)$ Å	Ref.: Kalsbeek et al. (1990)
$Z = 2$		JCPDS: #17-0724
Dx = 4.33 g/cm^3		
AP: table 58	ID: table 59	IL: fig. 26

Gay (1957) reported that the crystal system of lessingite-(Ce) is hexagonal, and gave the lattice parameters, $a = 9.67$, $c = 7.08$ Å. Li et al. (1981) determined the crystal structure of lessingite-(Ce) from China and reported that it is monoclinic and pseudo-hexagonal and that the crystal structure is basically isostructural with that of apatite. Recently, Kalsbeek et al. (1990) refined the crystal structures of lessingite-(Ce) and britholite-(Ce) from the type localities, Kyshtym, Urals, Russia and Naujakasik, Ilimaussaq, Greenland, respectively. They reported that the two minerals are isostructural, and are hexagonal with space group $P6_3$. In the structures (fig. 26), the rare earth elements occupy a seven-coordinated site and two nine-coordinated sites

TABLE 56
Atomic parameters of lessingite-(Ce)[a].

	sof[b]	x	y	z	B (Å^2)
R1	0.732(3)	0.33333	0.66667	−0.0047(2)	0.942(8)[c]
R1a	0.721(4)	0.66667	0.33333	−0.0011(2)	1.61(1)[c]
R2	0.828(2)	0.23851(5)	−0.01142(5)	0.2500	1.263(6)[c]
Si	1.004(6)	0.4007(2)	0.3726(2)	0.2507(8)	0.92(2)[c]
O1		0.3235(6)	0.4878(5)	0.253(2)	1.47(6)
O2		0.5942(6)	0.4688(6)	0.232(1)	1.54(8)
O3		0.316(1)	0.2400(9)	0.419(1)	2.3(1)
O3a		0.3632(7)	0.2636(7)	0.059(1)	1.37(7)
O4		0	0	0.205(2)	3.2(3)

[a] MoKα, $R = 0.039$, $R_w = 0.059$ (1121 refl.).
[b] Site occupancy factor.
[c] B_{eq}.

with different site occupancy factors. They suggested that the lowering of the space group symmetry, $P6_3$, relative to the apatite structure, $P6_3/m$, originates in differences in the oxygen positions. The isomorphous substitution of Si for P, together with distortions of the seven- and nine-coordination polyhedra in the structures, may contribute to the change of space group. Their results may suggest that lessingite-(Ce) and britholite-(Ce) belong to one mineral species.

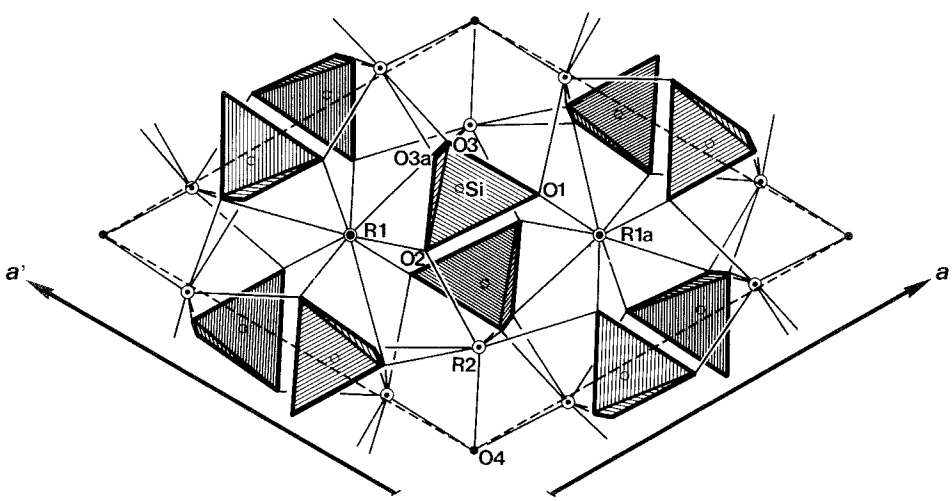

Fig. 26. The crystal structure of britholite-(Ce) which is isostructural with that of lessingite-(Ce).

TABLE 57
Interatomic distances for lessingite-(Ce) in Å.

R1–O1	2.48(1) ×3	R1a–O2	2.417(7) ×3
R1–O2	2.573(7) ×3	R1a–O1	2.43(1) ×3
R1–O3	3.086(9) ×3	R1a–O3a	2.695(7) ×3
mean	2.71	mean	2.51
R2–O4	2.384(2)	Si–O1	1.620(7)
R2–O3a	2.408(7)	Si–O2	1.625(5)
R2–O3	2.428(9)	Si–O3	1.641(9)
R2–O2	2.455(5)	Si–O3a	1.644(8)
R2–O3	2.467(9)	mean	1.633
R2–O3a	2.672(6)		
R2–O1	2.730(4)		
mean	2.506		

TABLE 58
Atomic parameters of britholite-(Ce)[a].

	sof[b]	x	y	z	B (Å^2)
R1	0.771(3)	0.33333	0.66667	−0.0028(1)	1.56(1)[c]
R1a	0.654(2)	0.66667	0.33333	0.0015(1)	1.21(1)[c]
R2	0.789(1)	0.23654(4)	−0.01176(3)	0.2500	1.407(6)[c]
Si	1.048(4)	0.4014(1)	0.3729(1)	0.2506(5)	0.95(2)[c]
O1		0.3254(4)	0.4886(4)	0.252(2)	1.66(5)
O2		0.5927(5)	0.4697(4)	0.2718(8)	1.72(6)
O3		0.3218(6)	0.2461(6)	0.422(1)	2.33(9)
O3a		0.3677(6)	0.2651(5)	0.0609(9)	1.61(7)
O4		0	0	0.201(2)	4.5(3)

[a] MoKα, $R = 0.033$, $R_w = 0.055$ (965 refl.).
[b] Site occupancy factor.
[c] B_{eq}.

TABLE 59
Interatomic distances for britholite-(Ce) in Å.

R1–O2	2.387(5) ×3	R1a–O1	2.431(9) ×3
R1–O1	2.461(9) ×3	R1a–O2	2.609(6) ×3
R1–O3	3.037(6) ×3	R1a–O3a	2.647(6) ×3
mean	2.628	mean	2.562
R2–O4	2.326(2)	Si–O2	1.603(4)
R2–O3	2.409(7)	Si–O1	1.610(5)
R2–O3a	2.428(6)	Si–O3	1.614(7)
R2–O2	2.457(3)	Si–O3a	1.624(7)
R2–O3	2.505(6)	mean	1.613
R2–O3a	2.668(5)		
R2–O1	2.736(3)		
mean	2.504		

Sr-containing BRITHOLITE-(Ce)
$(Ce,Ca,Sr)_5[(Si,P)O_4]_3(OH,F)$
$(Ce,Ca,Sr)_2(Ce,Ca)_3[(Si,P)O_4]_3(OH,F)$

Sys.	hexagonal	$a = 9.638(1)$ Å	source: Khibiny alkaline massif, Kola Peninsula, Russia
S.G.	$P6_3/m$	$c = 7.081(1)$ Å	Ref.: Genkina et al. (1991)
$Z =$	2		
Dm =	4.025 g/cm^3		
AP:	table 60	ID: table 61	

On the other hand, Genkina et al. (1991) independently analyzed the crystal structure of Sr-containing britholite-(Ce). They reported that the space group is $P6_3/m$, which is in contrast to the result of Kalsbeek et al. (1990), $P6_3$, and which confirms the result of Ito (1968) for artificial $Ca_2Y_3(SiO_4)_3(OH)$. It is worth noting that the O4 site is statistically occupied by anions such as F^-, $(OH)^-$ or O^{2-}. Genkina et al. (1991) pointed out that the Ce and Ca atoms partly occupy both the nine-coordinated A1 and seven-coordinated A2 site, whereas the larger Sr atoms occupy only the A1 site. On the other hand, Borisov and Klevtsova (1963) reported that the larger R and Sr atoms preferentially occupy the seven-coordinated site rather than nine-coordinated site in R–Sr-apatite. Genkina et al. (1991) explained the difference in the cation distributions between phosphate (apatite-type) and silicate (britholite-type) by the environments of the cation sites which are affected by the charge of the tetrahedral anionic groups. They suggested that the isomorphous substitution $Ca^{2+} + P^{5+} \rightleftarrows R^{3+} + Si^{4+}$ leads to a change in the immediate environments of the A1 and A2 sites by the tetrahedral anionic group, SiO_4 or PO_4.

TABLE 60
Atomic parameters of Sr-containing britholite-(Ce)[a].

	x	y	z	B_{iso}
A1[b]	0.3333	0.6667	0.9959(1)	1.09(3)
A2[c]	0.7479(0)	0.9877(0)	0.25	1.22(3)
Si	0.9709(3)	0.3722(3)	0.25	0.72(7)
O1	0.5932(11)	0.1245(12)	0.25	2.0(1)
O2	0.3421(13)	0.0871(9)	0.0701(11)	3.0(1)
O3	0.5117(11)	0.6739(13)	0.25	1.7(1)
O4[d]	0	0	0.177(6)	2.8(1)

[a] Mo, $R = 0.0354$ (465 refl.).
[b] $Ce_{0.40}Ca_{0.35}Sr_{0.25}$.
[c] $Ce_{0.86}Ca_{0.14}$.
[d] F^-, $(OH)^-$ or O^{2-}. This anion occupies its position statistically, with coordinates (0, 0, 0.177), or in the specularly reflected position (0, 0, 0.323).

TABLE 61
Interatomic distances for Sr-containing britholite-(Ce) in Å.

A1–O3	2.464(4) ×2	A2–O2	2.405(7) ×2
A1–O3	2.468(8)	A2–O4	2.429(9)
A1–O1	2.480(6)	A2–O1	2.435(14)
A1–O1	2.481(8)	A2–O2	2.586(4) ×2
A1–O1	2.484(6)	A2–O3	2.729(9)
A1–O2	2.862(9)	mean	2.500
A1–O2	2.867(12)		
A1–O2	2.868(9)	Si–O1	1.602(11)
mean	2.604	Si–O2	1.606(6) ×2
		Si–O3	1.609(3)
		mean	1.606

BRITHOLITE-(Y) (=abukumalite, pravdite)
$(Y,Ca,Na)_5[(Si,P)O_4]_3(OH,F)$
$(Y,Ca,Na)_5[(Si,P)O_4]_3(OH,F)$

Sys. hexagonal	$a = 9.40$ Å	source: synthetic $Ca_2Y_3(SiO_4)_3(OH)$
S.G. $P6_3/m$	$c = 6.81$ Å	Ref.: Ito (1968)
$Z = 2$		JCPDS: #31-0315

Pravdite occurs in a metamict state. Nurlybayev (1962) reported that some of the lines in the X-ray powder diffraction pattern of the annealed sample correspond to those of karnasurtite-(Ce). However, the mineral name "pravdite" was discredited by the IMA Commission on New Minerals and Mineral Names (Nickel and Mandarino 1987), because it is regarded as an altered britholite (Tarkhanova et al. 1964). A non-metamict beckelite from Vietnam is hexagonal with $a = 9.61(1)$ Å and $c = 7.05(1)$ Å, $(Ce,Ca,Na,Mn)_{10.63}(Si,Al,Fe)_{5.37}O_{22.89}F_{4.29} \cdot 2.72H_2O$ (Feldman et al. 1987). Beckelite was suggested to be probably britholite-(Ce) by Embrey and Fuller (1980).

TRITOMITE-(Ce)
$Ca_2Ce_3(Si_2B)O_{13}$
$(Ce,Ca,Th)_5(Si,B)_3(O,OH,F)_{13}$

Sys. hexagonal	$a = 9.35$ Å	source: Låven Island, Brevik, Langesundfjord, Norway
S.G.	$c = 6.88$ Å	
$Z = 2$		Ref.: Jaffe and Molinski (1962)
$Dm = 4.2$ g/cm^3		JCPDS: #14-0174

TRITOMITE-(Y) (=spencite)
$Y_3(Ce,Th)^{4+}Ca(Si_2B)O_{13}$
$(Y,Ca,Th)_5(Si,B)_3(O,OH,F)_{13}$

Sys. hexagonal	$a = 9.32$ Å	source: Cranberry Lake, Sussex Co., NJ, USA
S.G.	$c = 6.84$ Å	Ref.: Jaffe and Molinski (1962)
$Z =$		JCPDS: #27-1063, #14-0138
Dm = 3.40 g/cm^3		

MELANOCERITE-(Ce) (thorian- =caryocerite ?)
$(Ce,Ca)_5(Si,B)_3O_{12}(OH,F)\cdot nH_2O$ (?)
$(Ce,Ca)_5(Si,B)_3O_{12}(OH,F)\cdot nH_2O$ (?)

Sys. hexagonal	$a = 9.35$ Å	source: Kjeö, Barkevik, Langesundfjord, Norway
S.G.	$c = 6.88$ Å	Ref.: Vlasov (1966);
$Z =$		Fleischer and Mandarino (1991)
		JCPDS: #38-0457

Tritomite-(Ce) was classified in the cerite group together with törnebohmite-(Ce), lessingite-(Ce), beckelite, kainosite-(Y), nordite-(Ce), hellandite-(Y) and steenstrupine-(Ce) by Kostov (1968). Frondel (1961) considered that tritomite-(Ce) may be related to the datolite group, to which gadolinite-(Y) and hingganite-(Y), among others, belong. The lattice parameters of tritomite-(Ce) suggest that it may have a structural relationship to apatite, as shown in the classification by Strunz (1978). On the other hand, Jaffe and Molinski (1962) stated that the relation of tritomite-(Ce) to the datolite group is uncertain, although possible.

The mineral names abukumalite and spencite are synonyms for britholite-(Y) and tritomite-(Y), respectively (Levinson 1966). Tritomite, melanocerite and caryocerite, a Th-analogue of melanocerite, resemble each other. They are considered as either identical or separate species by different authors and their identity is under question (Boggs 1980).

RETZIAN-(Ce)
$Mn_2Ce(AsO_4)(OH)_4$
$Mn_2Ce(AsO_4)(OH)_4$

Sys. orthorhombic	$a = 5.670 \pm 0.004$ Å	source: Nordmarks Odalfält, Värmland, Sweden
S.G. Pban	$b = 12.03 \pm 0.01$ Å	Ref.: Moore (1967)
$Z = 2$	$c = 4.863 \pm 0.004$ Å	JCPDS: #20-0731
AP: table 62	ID: table 63	IL: fig. 27

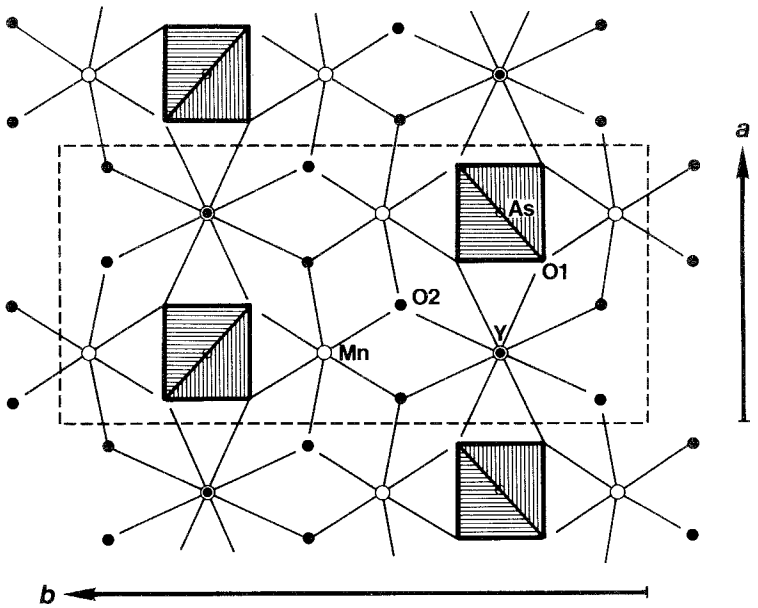

Fig. 27. The crystal structure of retzian-(Ce).

RETZIAN-(La)
$Mn_2La(AsO_4)(OH)_4$
$Mn_2La(AsO_4)(OH)_4$

Sys. orthorhombic	$a = 5.670(7)$ Å	source: Ogdensburg, Sussex Co., NJ, USA
S.G. Pban	$b = 12.01(1)$ Å	Ref.: Dunn et al. (1984)
$Z = 2$	$c = 4.869(8)$ Å	JCPDS: #38-0380
Dx = 4.49 g/cm^3		
Dm > 4.2 g/cm^3		

RETZIAN-(Nd)
$Mn_2Nd(AsO_4)(OH)_4$
$Mn_2Nd(AsO_4)(OH)_4$

Sys. orthorhombic	$a = 5.690(5)$ Å	source: Ogdensburg, Sussex Co., NJ, USA
S.G. Pban	$b = 12.12(1)$ Å	Ref.: Dunn and Sturman (1982)
$Z = 2$	$c = 4.874(3)$ Å	JCPDS: #35-0686
Dx = 4.45 g/cm^3		
Dm > 4.2 g/cm^3		

The crystal structure of retzian-(Ce) was determined by Moore (1967). The structure (fig. 27) consists of sheets built of Mn^{2+}-centered oxygen octahedra and R^{3+} centered oxygen square antiprisms. Inside the sheets, ribbons of the Mn-octahedra formed by linkages of their edges are held by the R-square antiprisms. AsO_4 tetrahedra are situated between the sheets. Despite the similarity of the chemical formulae of retzian-

TABLE 62
Atomic parameters of retzian-(Ce)[a].

	M^b	x	y	z	B
Y	1.18	0.25	0.25	0	0.06 ± 0.09
As	1	0.75	0.25	0.5	0.44 ± 0.14
Mn	0.90	0.25	0.5548 ± 0.0008	0	0.81 ± 0.16
O1	1	0.5769 ± 0.0048	0.3198 ± 0.0036	0.3045 ± 0.0054	1.09 ± 0.48
O2[c]	1	0.5783 ± 0.0044	0.5770 ± 0.0034	0.2010 ± 0.0049	1.08 ± 0.47

[a] Mo, $R = 0.062$ (120 refl.).
[b] Occupancy.
[c] (OH).

TABLE 63
Interatomic distances for retzian-(Ce) in Å.

Y–O2	2.50 ± 0.06 ×4	Mn–O2	2.10 ± 0.06 ×2
Y–O1	2.52 ± 0.06 ×4	Mn–O1	2.12 ± 0.06 ×2
mean	2.51	Mn–O1	2.33 ± 0.06 ×2
As–O	1.60 ± 0.06 ×4	meam	2.18

(Ce) and flinkite, $Mn_2^{2+}Mn^{3+}(AsO_4)(OH)$, the structure of retzian-(Ce) is not closely related to that of flinkite.

Although Moore (1967) assumed the chemical formula $Mn_2Y(AsO_4)(OH)_4$ for the sample in his crystal structure analysis, he did not analyze the chemical composition of the sample. Recently, Dunn and Sturman (1982) made a redefinition of retzian-(Ce) using the type of material from the Moss Mine, Sweden, and redefined the formula as $Mn_2CeAsO_4(OH)_4$. Retzian-(La) (Dunn et al. 1984) and -(Nd) (Dunn and Sturman 1982) were also described and they were approved by the IMA Commission on New Minerals and Mineral Names.

FLORENCITE-(Ce)
$CeAl_3(PO_4)_2(OH)_6$
$CeAl_3(PO_4)_2(OH)_6$

Sys. trigonal (hex.)	$a = 6.979(4)$ Å	source: Diamantina, Minas Gerais, Brazil
S.G. $R\bar{3}m$	$c = 16.25(1)$ Å	Ref.: Lefebvre and Gasparrini (1980)
$Z = 3$		JCPDS: #8-0143

FLORENCITE-(La)
$LaAl_3(PO_4)_2(OH)_6$
$LaAl_3(PO_4)_2(OH)_6$

Sys. trigonal (hex.)	$a = 6.987(2)$ Å	source: Shituru, Shaba, Zaïre
S.G. $R\bar{3}m$	$c = 16.248(6)$ Å	Ref.: Lefebvre and Gasparrini (1980)
$Z = 3$		JCPDS: #38-0347
$Dm = 3.52(2)$ g/cm^3		

FLORENCITE-(Nd)
$NdAl_3(PO_4)_2(OH)_6$
$NdAl_3(PO_4)_2(OH)_6$

Sys. trigonal (hex.)	$a = 6.992(1)$ Å	source: Sausalito, Marin Co., CA, USA
S.G. $R\bar{3}m$	$c = 16.454(7)$ Å	Ref. Fitzpatrick (1986)
$Z = 3$		JCPDS: #39-0333

ARSENOFLORENCITE-(Ce)
$CeAl_3(AsO_4)_2(OH)_6$
$CeAl_3(AsO_4)_2(OH)_6$

Sys. trigonal (hex.)	$a = 7.029$ Å	source: South Australia and Queensland, Australia
S.G. $R\bar{3}m$	$c = 16.517$ Å	Ref.: Nickel and Temperly (1987)
$Z = 3$		
$Dx = 4.091$ g/cm^3		
$Dm = 4.096$ g/cm^3		

KEMMLITZITE
$(Sr,Ce)Al_3(AsO_4)[(P,S)O_4](OH)_6$
$(Sr,Ce)Al_3(AsO_4)[(P,S)O_4](OH)_6$

Sys. trigonal (hex.)	$a = 7.072 \pm 0.001$ Å	source: Kemmlitz, Saxony, Germany
S.G.	$c = 16.51 \pm 0.01$ Å	Ref.: Hak et al. (1969)
$Z = 3$		JCPDS: #22-1248
$Dx = 3.601$ g/cm^3		
$Dm = 3.63$ g/cm^3		

Florencite-(Ce), -(La), -(Nd), and arsenoflorencite-(Ce) are members of the crandallite group (Fleischer and Mandarino 1991) with a chemical formula: $AB_3(XO_4)_2(OH,F)_6$; A = Ba, Bi, Ca, Ce, La, Nd, Pb, Sr, Th; B = Al, Fe; X = As, P, Si. Crystal structure analyses of these minerals have not been reported yet, but the crystal data suggest that they have the alunite, $KAl_3[SO_4]_2(OH)_6$, type structure.

Arsenoflorencite-(Ce) is an arsenate analogue of florencite-(Ce), described by Nickel and Temperly (1987).

Kemmlitzite may be an As-analogue of svanbergite, $SrAl_3(PO_4)(SO_4)(OH)_6$, suggesting an isomorphous substitution $Sr^{2+} + S^{6+} \rightleftarrows Ce^{3+} + P^{5+}$. The crystal structure is unknown. If it is in the beudantite group, the structure is presumably similar to that of alunite and florencite-(Ce) (D.M. Burt, personal communication).

CHURCHITE-(Y) (=weinschenkite)
$YPO_4 \cdot 2H_2O$
$YPO_4 \cdot 2H_2O$

Sys. monoclinic	$a = 5.61$ Å	source: Cornwall, England
S.G. A2/a or Aa	$b = 15.14$ Å	Ref.: Claringbull and Hey (1953)
$Z = 4$	$c = 6.19$ Å	JCPDS: #8-0167
$Dm = 3.263$ g/cm^3	$\beta = 115.3°$	

CHURCHITE-(Nd)
$NdPO_4 \cdot 2H_2O$
$NdPO_4 \cdot 2H_2O$

Sys. monoclinic	$a = 6.19$ Å	source: Kazakhstan, Russia
S.G. C2/c	$b = 15.14$ Å	Ref.: Podporina et al. (1983);
$Z = 4$	$c = 5.61$ Å	Claringbull and Hey (1953)
$Dx = 3.84$ g/cm^3	$\beta = 115.1°$	JCPDS: #39-1385

Churchite-(Y) was originally described as a hydrated phosphate of Ce-group rare earths by Church (1865a, b) and named by Williams (1865). On the other hand, weinschenkite was described as a hydrated phosphate of yttrium by Laubmann (1923), but, unfortunately, this mineral name was also used for a variety of hornblende, $Ca_2(Fe,Mg)_4Al(Si_7Al)O_{22}(OH,F)_2$ by Murgoci (1922). Strunz (1942) gave the lattice parameters for weinschenkite and noted its structural similarity to that of gypsum, $CaSO_4 \cdot 2H_2O$ (JCPDS #33-311: monoclinic, C2/c, $a = 6.2845(11)$, $b = 15.2079(15)$, $c = 5.6776(7)$ Å, $\beta = 114.09(1)°$, $Z = 4$). Claringbull and Hey (1953) reexamined the chemical compositions, X-ray powder diffraction patterns, and optical and physical properties of churchite-(Y) and weinschenkite, and revealed that the two minerals are identical, i.e., a hydrated phosphate of yttrium. Milton and Bastron (1971) redefined the name as "churchite-(Y)" for the hydrated phosphate of yttrium, and it was approved by the IMA Commission on New Minerals and Mineral Names. A crystal structure analysis of churchite-(Y) has not been reported but it is isostructural with gypsum, $CaSO_4 \cdot 2H_2O$.

VYUNTSPAKHKITE-(Y)
$Y_4Al_3Si_5O_{18}(OH)_5$
$Y[(Al,\square)(\square,Al,Si)](SiO_4)[(OH),O]_2$

Sys. monoclinic	$a = 5.830(2)$ Å	source: Kola Peninsula, Russia
S.G. $P2_1/a$	$b = 14.763(4)$ Å	Ref.: Yakubovich et al. (1984)
$Z = 4$	$c = 6.221(2)$ Å	JCPDS: #35-0708
$Dx = 4.02$ g/cm^3	$\beta = 123.05(2)°$	
AP: table 64	ID: table 65	IL: fig. 28

The crystal structure of vyuntspakhkite-(Y) was determined by Yakubovich et al. (1984). The structural formula is written as $Y_4[(Al_{2.5}\square_{1.5})(\square_{2.5}(Al,Si)_{1.5}](SiO_4)_4[(OH)_{3.5},O_{0.5}]_2$ and an idealized formula is $Y_4Al_2AlSi_5O_{18}(OH)_5$. The structure (fig. 28) consists of two types of layers: a layer composed of M tetrahedra and Al trigonal bi-pyramids, and a layer of Si tetrahedra and eight-coordinated Y polyhedra. They reported that the Al and the M sites cannot be simultaneously occupied because of the short distance between the two sites, 1.68(1) Å. They also pointed out that the layer of Si tetrahedra and Y polyhedra is similar to that of SO_4 tetrahedra and eight-coordinated Ca polyhedra in the crystal structure of gypsum, $CaSO_4 \cdot 2H_2O$. The layers in the structure of vyuntspakhkite-(Y) are connected by the cations at the Al and M sites, in contrast to the layers in the crystal structure of gypsum, which are joined by hydrogen bonds.

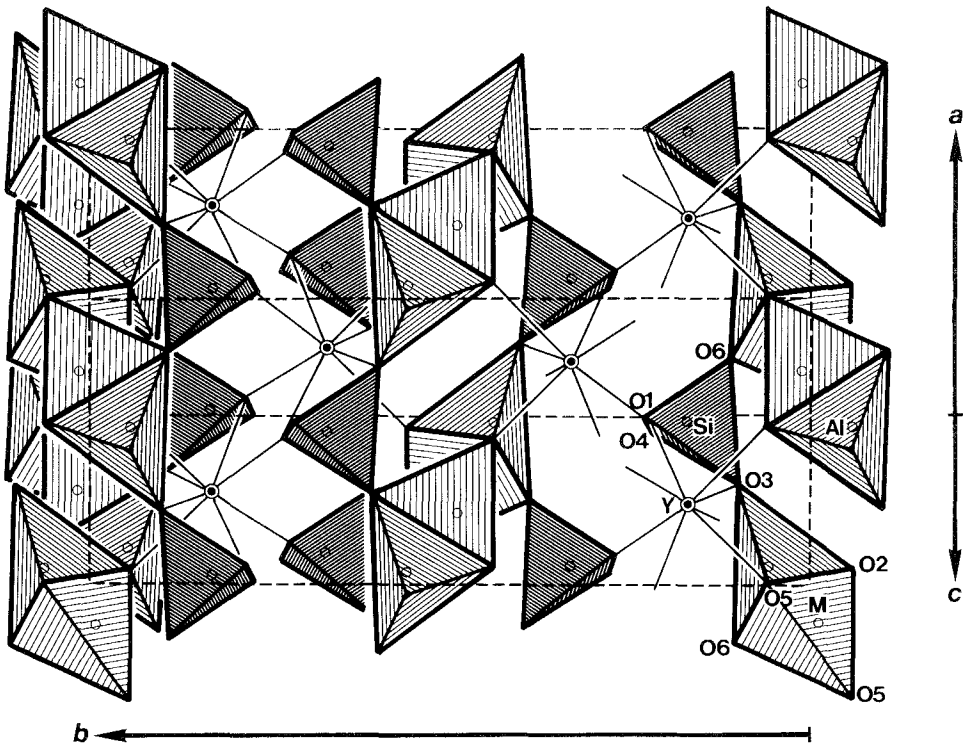

Fig. 28. The crystal structure of vyuntspakhkite-(Y). The M site and the Al site cannot be occupied simultaneously.

TABLE 64
Atomic parameters of vyuntspakhkite-(Y)[a].

	x	y	z	B (Å^2)
Y	0.0857(2)	0.17436(5)	0.6921(1)	0.92(2)
Si	0.0902(7)	0.1675(2)	0.1944(6)	0.70(6)
Al[b]	0.092(1)	0.4376(3)	0.211(1)	0.3(1)
M[c]	0.051(2)	0.4936(6)	0.679(2)	0.45(2)
O1	0.260(2)	0.2268(5)	0.451(1)	0.6(2)
O2[d]	0.059(2)	0.5629(5)	0.177(2)	0.8(2)
O3	0.086(2)	0.8974(5)	0.732(1)	1.4(2)
O4	0.404(2)	0.2773(6)	0.929(1)	1.2(2)
O5[e]	0.262(2)	0.9427(6)	0.437(2)	1.9(3)
O6	0.226(2)	0.6057(8)	0.872(2)	2.7(3)

[a] MoKα, $R = 0.04$ (922 refl.).
[b] Al: 0.625Al. [c] M: 0.125Al + 0.250Si.
[d] O2: 1.000(OH). [e] O5: 1.000(OH).

TABLE 65
Interatomic distances for vyuntspakhkite-(Y) in Å.

Y–O1	2.208(8)	Si–O1	1.604(7)
Y–O4	2.224(8)	Si–O4	1.614(8)
Y–O4	2.349(9)	Si–O6	1.620(13)
Y–O1	2.354(9)	Si–O3	1.640(11)
Y–O2	2.414(9)	mean	1.619
Y–O5	2.441(11)		
Y–O3	2.491(8)	Al–O6	1.755(14)
Y–O6	2.519(9)	Al–O3	1.811(14)
mean	2.375	Al–O2	1.859(8)
		Al–O5	1.869(10)
M–O2	1.59(1)	Al–O2	2.070(10)
M–O5	1.77(2)	mean	1.873
M–O5	1.79(1)		
M–O6	1.97(1)		
mean	1.78		

KOLBECKITE (=eggonite, sterrettite)
$Sc(PO_4) \cdot 2H_2O$
$Sc(PO_4) \cdot 2H_2O$

Sys. monoclinic	$a = 8.88$ Å	source: Potash Sulfur Springs, Garland, Co., AR, USA
S.G. $P2_1/n$	$b = 10.08$ Å	Ref.: Hey et al. (1982)
$Z = 4$	$c = 5.42$ Å	JCPDS: #38-0431
	$\beta = 90°51'$	

Hey et al. (1982) reviewed the curious history of eggonite, kolbeckite and sterrettite, $ScPO_4 \cdot 2H_2O$, and described two new occurrences of this mineral. Kolbeckite is related to phosphosiderite, $FePO_4 \cdot 2H_2O$.

RHABDOPHANE-(Ce)
$Ce(PO_4) \cdot nH_2O$
$Ce(PO_4) \cdot nH_2O$

Sys. hexagonal	$a = 7.055 \pm 0.003$ Å	source: synthetic $CePO_4$
S.G. $P6_222$	$c = 6.439 \pm 0.005$ Å	Ref.: Mooney (1950)
$Z = 3$		JCPDS: #35-0614
$Dx = 4.193$ g/cm^3		
AP: table 66	ID: table 67	IL: fig. 29

TABLE 66
Atomic parameters of rhabdophane-(Ce)[a].

	x	y	z
Ce	0.5	0	0
P	0.5	0	0.5
O	0.446	0.147	0.360

[a] CuKα.

TABLE 67
Interatomic distances for rhabdophane-(Ce) in Å.

Ce–O	2.34 ×4	As–O	1.56 ×4
Ce–O	2.66 ×4		
mean	2.50		

RHABDOPHANE-(La)
$La(PO_4) \cdot nH_2O$
$La(PO_4) \cdot nH_2O$

Sys. hexagonal	$a = 6.98 \pm 0.03$ Å	source: Salisbury, CT, USA
S.G. $P6_222$	$c = 6.39 \pm 0.03$ Å	Ref.: Muto et al. (1959)
$Z = 3$		JCPDS: #12-0277

RHABDOPHANE-(Nd)
$Nd(PO_4) \cdot nH_2O$
$Nd(PO_4) \cdot nH_2O$

Sys. hexagonal	$a = 6.960 \pm 0.003$ Å	source: Fowey Consols Mine, Cornwall, England
S.G. $P6_222$	$c = 6.372 \pm 0.006$ Å	Ref.: Bowles and Morgan (1984)
$Z = 3$		

BROCKITE
$(Ca,Th,Nd)(PO_4) \cdot H_2O$
$(Ca,Th,Nd)(PO_4) \cdot H_2O$

Sys. hexagonal	$a = 6.98 \pm 0.03$ Å	source: Wet Mts., Custer Co., CO, USA
S.G. $P6_222$	$c = 6.40 \pm 0.03$ Å	Ref.: Fisher and Meyrowitz (1962)
$Z = 3$		JCPDS: #15-0248
$Dx = 4.0$ g/cm^3		
$Dm = 3.9 \pm 0.2$ g/cm^3		

NINGYOITE
$(U,Ca,Ce)(PO_4) \cdot nH_2O$
$(U,Ca,Ce)(PO_4) \cdot nH_2O$

Sys. orthorhombic	$a = 6.78 \pm 0.03$ Å	source: Ningyo, Tottori, Japan
S.G. P222	$b = 12.10 \pm 0.05$ Å	Ref.: Muto et al. (1959)
$Z = 6$	$c = 6.38 \pm 0.03$ Å	JCPDS: #12-0273

SARYARKITE-(Y)
$Ca(Y,Th)Al_5(SiO_4)_2[(P,S)O_4]_2(OH)_7 \cdot 6H_2O$
$(Ca,Y,Th)_2Al_5[(Si,P,S)O_4]_4(OH)_7 \cdot 6H_2O$

Sys. tetragonal	$a = 8.213 \pm 0.002$ Å	source:
S.G. $P42_12$ or $P4_22_12$	$c = 6.55 \pm 0.01$ Å	Ref.: Krol et al. (1964)
$Z = 1$*		JCPDS: #16-0712
$Dx = 3.35$ g/cm^3		
$Dm = 3.07–3.15$ g/cm^3		

* $Z = 4$ given in the original paper is in error (E.H. Nichel, personal communication).

STILLWELLITE-(Ce)
$CeBSiO_5$
$CeBSiO_5$

Sys. trigonal (hex.)	$a = 6.85 \pm 0.03$ Å	source: CIS
S.G. $P3_1$	$c = 6.70 \pm 0.03$ Å	Ref.: Voronkov and Pyatenko (1967b)
$Z = 3$		JCPDS: #25-1447, #26-0349
$Dm = 4.70$ g/cm^3		
AP: table 68	ID: table 69	IL: fig. 30

The crystal structure of rhabdophane-(Ce) was analyzed by Mooney (1950) using samples synthesized using the precipitation method. In the crystal structure (fig. 29), alternating cerium atoms and PO_4 tetrahedra build columns extending along the *c*-axis. These columns are linked to four neighboring columns forming a three-dimensional framework with cylindrical open channels at (00*z*). Mooney (1950) presumed the presence of neutral molecules, such as zeolitic water, in the channels, and he gave possible positions, 0, 0, $\frac{1}{2}$; 0, 0, $\frac{5}{6}$; 0, 0, $\frac{1}{6}$ for the molecules with occupancies less than or equal to one half, after the consideration of the interatomic distances between these sites and the nearest oxygen atoms. However, the distance between the molecule and the cerium atom, 3.69 Å, seems too long to be included in the bonds. The cerium atoms are coordinated by eight oxygen atoms of PO_4 tetrahedra forming slightly distorted cubes.

Brockite is a Ca, Th-analogue of rhabdophane-(Ce), described by Fisher and Meyrowitz (1962). Its chemical and crystallographic data suggest the presence of the isomorphous substitution of $2R^{3+} \rightleftarrows Ca^{2+} + Th^{4+}$ in the crystal structure of brockite.

Muto et al. (1959) reported that ningyoite has a pseudo-hexagonal lattice, and that the X-ray powder pattern resembles that of rhabdophane-(Ce). The space group, P222, suggested by Muto et al. (1959) may be due to the possibility of ordering of uranium, calcium and rare earth atoms in the structure.

Krol et al. (1964) reported that the X-ray powder diffraction pattern of saryarkite-(Y) is very similar to that of rhabdophane-(Ce). The symmetry of saryarkite-(Y) is not hexagonal but tetragonal.

The crystal structure of stillwellite-(Ce) was reported by Voronkov et al. (1965) and by Voronkov and Pyatenko (1967b) (fig. 30). The structural feature without the BO_4 tetrahedra is very similar to that of rhabdophane-(Ce) (Voronkov and Pyatenko 1967b): e.g., in the crystal structure of stillwellite-(Ce), there are columns of alternating cerium atoms and SiO_4 tetrahedra which are very similar to those of cerium atoms and PO_4 tetrahedra in rhabdophane-(Ce). The clear difference between the two structures is the presence of infinite helical chains of BO_4 tetrahedra situated at the origin of the unit cell in the crystal structure of stillwellite-(Ce), which correspond to the cylindrical open spaces in rhabdophane-(Ce). The cerium atoms in stillwellite-(Ce) are coordinated by nine oxygen atoms, which connect the units of the Ce,SiO_4-columns and BO_4 chains forming a three-dimensional architecture.

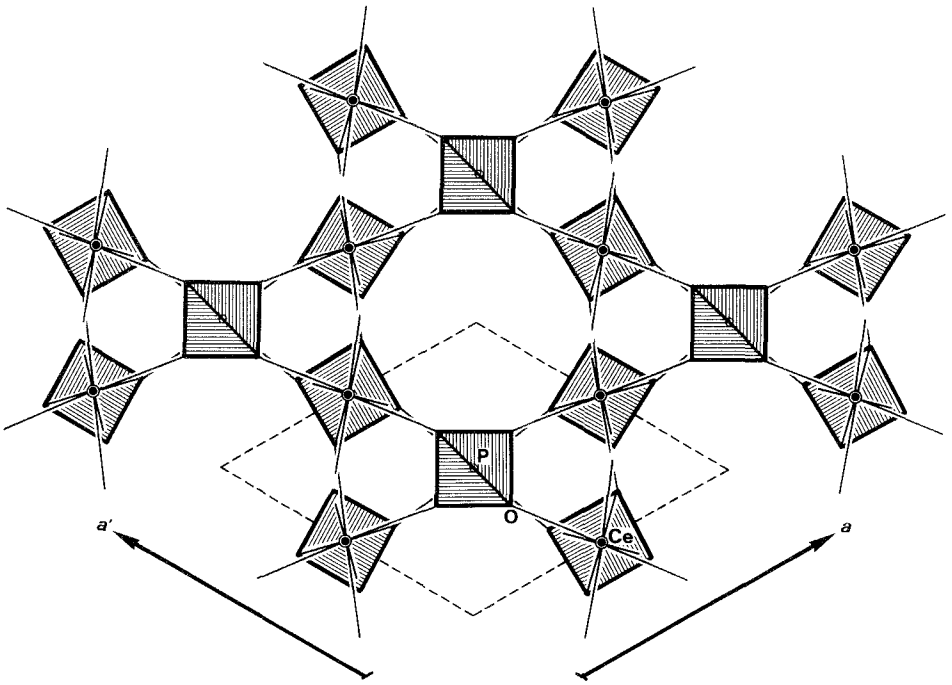

Fig. 29. The crystal structure of rhabdophane-(Ce). Zeolitic water may be located in the space at (0, 0, z).

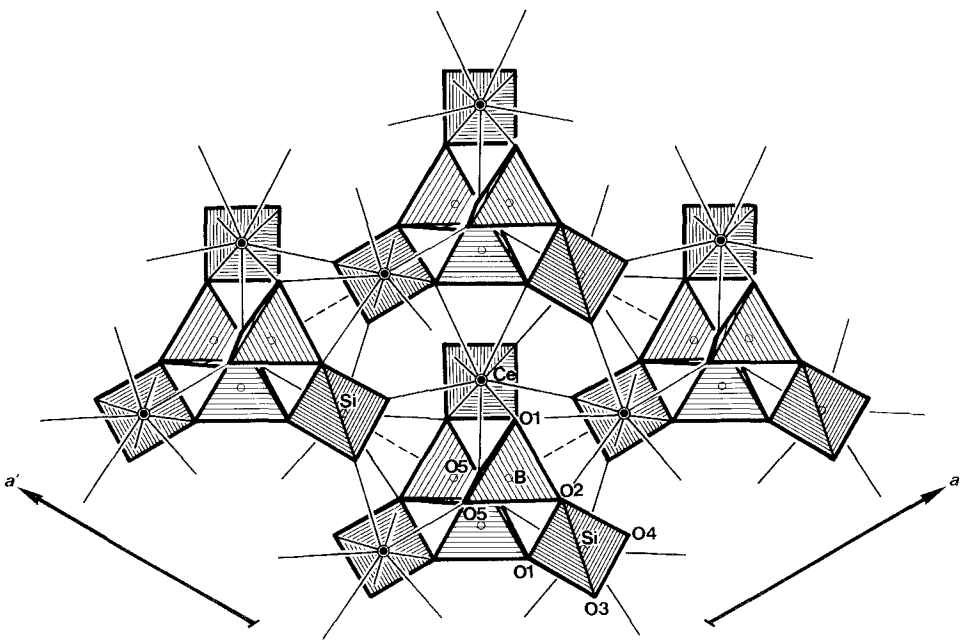

Fig. 30. The crystal structure of stillwellite-(Ce).

TABLE 68
Atomic parameters of stillwellite-(Ce)[a].

	x	y	z
Ce	0.587	0	0
Si	0.585	0	0.5
B	0.113	0	0.973
O1	0.339	0.194	0.023
O2	0.195	0.339	0.310
O3	0.613	0.464	0.320
O4	0.464	0.614	0.014
O5	0.051	0.051	0.781

[a]X-ray is not specified, $R_{hk0} = 0.092$, $R_{0kl} = 0.128$.

TABLE 69
Interatomic distances for stillwellite-(Ce) in Å.

Ce–O3	2.35	Si–O3	1.60
Ce–O4	2.36	Si–O4	1.60
Ce–O5	2.59	Si–O1	1.64
Ce–O4	2.62	Si–O2	1.64
Ce–O1	2.63	mean	1.62
Ce–O3	2.63		
Ce–O2	2.64	B–O2	1.45
Ce–O2	2.72	B–O5	1.45
Ce–O1	2.73	B–O5	1.47
mean	2.59	B–O1	1.49
		mean	1.47

AGARDITE-(Y)
$YCu_6(AsO_4)_3(OH)_6 \cdot 3H_2O$
$(Y,Ca)Cu_6[AsO_3(O,OH)]_3(OH)_6 \cdot 3H_2O$

Sys. hexagonal
S.G. $P6_3/m$ or $P6_3$
$Z = 2$
Dx = 3.66 ± 0.04 g/cm^3
Dm = 3.72 ± 0.05 g/cm^3

$a = 13.55 \pm 0.05$ Å
$c = 5.87 \pm 0.02$ Å

source: Bou-Skour, Morocco
Ref.: Dietrich et al. (1969)
JCPDS: #25-0183

AGARDITE-(La)
$LaCu_6(AsO_4)_3(OH)_6 \cdot 3H_2O$
$(La,Ca)Cu_6[AsO_3(O,OH)]_3(OH)_6 \cdot 3H_2O$

Sys. hexagonal
S.G. $P6_3/m$ or $P6_3$
$Z = 2$

$a =$
$c =$

source: Kamariza, Greece
Ref.: Fehr and Hochleitner (1984)

agardite-(Ce)
$CeCu_6(AsO_4)_3(OH)_6 \cdot 3H_2O$
$(Ce,Ca)Cu_6[AsO_3(O,OH)]_3(OH)_6 \cdot 3H_2O$

Sys. hexagonal	$a = 13.605(5)$ Å	source:
S.G. $P6_3/m$	$c = 5.917(1)$ Å	Ref.: Hess (1983)
$Z = 2$		
$Dx = 3.66$ g/cm^3		
AP: table 70	ID: table 71	IL: fig. 32

Unnamed Ca-analogue of AGARDITE-(Y)
$CaCu_6[AsO_3(OH)]_3(OH)_6 \cdot 3H_2O$
$(Ca,Y)Cu_6[AsO_3(OH,O)]_3(OH)_6 \cdot 3H_2O$

Sys. hexagonal	$a = 13.583(2)$ Å	source: Setoda, Hiroshima, Japan
S.G. $P6_3/m$	$c = 5.895(1)$ Å	Ref.: Aruga and Nakai (1985)
$Z = 2$		
$Dx = 3.61$ g/cm^3		
AP: table 72	ID: table 73	IL: fig. 31

TABLE 70
Atomic parameters of agardite-(Ce)[a].

	x	y	z	U (Å^2)
Ln	0.66667	0.33333	0.25	0.0086(4)
As	0.49393(5)	0.14946(5)	0.75	0.0071(3)
Cu	0.41091(5)	0.31377(4)	0.5023(1)	0.0105(3)
O1	0.5728(3)	0.1792(3)	0.5172(5)	0.0133(11)
O2	0.3914(4)	0.3990(4)	0.25	0.0132(17)
O3	0.4132(4)	0.2137(4)	0.75	0.0112(15)
OH1	0.3692(4)	0.3765(4)	0.75	0.0110(15)
OH2	0.4388(4)	0.2432(4)	0.25	0.0162(19)
OW	0.1644(22)	0.1551(23)	0.4614(60)	0.199(22)

[a] MoKα, $R = 0.037$ (1317 refl.).

TABLE 71
Interatomic distances for agardite-(Ce) in Å.

Ln–O1	2.418(4) ×6	Cu–O2	1.988(4)
Ln–OH2	2.704(8) ×3	Cu–OH2	1.913(4)
mean	2.513	Cu–OH1	1.919(4)
		Cu–O3	2.011(4)
As–O1	1.667(3) ×2	Cu–O1	2.315(6)
As–O2	1.703(8)	Cu–OW	2.96(3)
As–O3	1.712(7)	mean	2.18
mean	1.687		

TABLE 72
Atomic parameters of the unnamed Ca-analogue of agardite-(Y)[a].

	x	y	z	B_{eq} (Å^2)
Y[b]	0.66667	0.33333	0.25	0.79
Cu	0.41184(9)	0.31497(9)	−0.0021(2)	0.89
As	0.3438(1)	0.4948(8)	0.25	0.65
O1[c]	0.1989(7)	0.4125(8)	0.25	0.84
O2[c]	0.3920(8)	0.4011(8)	0.25	0.92
O3[d]	0.5725(5)	0.1808(5)	−0.016(1)	1.13
O4[e]	0.4400(9)	0.2444(8)	0.25	1.39
O5[e]	0.3766(8)	0.0090(8)	0.25	0.90
O6[f]	0.156(4)	0.007(4)	−0.065(7)	15(1)[g]

[a]MoKα, $R = 0.077$, $R_w = 0.056$ (1087 refl.).
[b]Y: Ca,Y,Fe,Ce,La,Nd.
[c]O1, O2:O.
[d]O3: (O,OH).
[e]O4, O5: OH.
[f]O6: H_2O.
[g]Isotropic temperature factor.

TABLE 73
Interatomic distances for the unnamed Ca-analogue of agardite-(Y) in Å.

Y–O3	2.395(6) ×6	Cu–O4	1.908(9)
Y–O4	2.687(11) ×3	Cu–O5	1.924(6)
mean	2.489	Cu–O2	1.991(9)
		Cu–O1	2.011(8)
As–O3	1.659(6) ×2	Cu–O3	2.321(8)
As–O2	1.689(13)	Cu–O6	3.14(7)
As–O1	1.710(8)	mean	2.216
mean	1.679		

GOUDEYITE
$AlCu_6(AsO_4)_3(OH)_6 \cdot 3H_2O$
$(Al,Y,Ca)Cu_6(AsO_4)_3(OH)_6 \cdot 3H_2O$

Sys. hexagonal	$a = 13.472(1)$ Å	source: Pershing Co., NV, USA
S.G. $P6_3/m$ or $P6_3$	$c = 5.902(4)$ Å	Ref.: Wise (1978)
$Z = 2$		JCPDS: #29-0526
Dm = 3.50 ± 0.03 g/cm^3		

PETERSITE-(Y)
$YCu_6(PO_4)_3(OH)_6 \cdot 3H_2O$
$(Y,Ca)Cu_6(PO_4)_3(OH)_6 \cdot 3H_2O$

Sys. hexagonal	$a = 13.288(5)$ Å	source: Secaucus, Hudson Co., NJ, USA
S.G. $P6_3/m$ or $P6_3$	$c = 5.877(5)$ Å	Ref.: Peacor and Dunn (1982)
$Z = 2$		JCPDS: #35-0556
Dx = 3.40 g/cm^3		
Dm = 3.41 g/cm^3		

Agardite-(Y), -(La), goudeyite and petersite-(Y) are known to belong to the mixite group (mixite, $BiCu_6(AsO_4)_3(OH)_6 \cdot 3H_2O$), and these minerals crystallize in the hexagonal space group $P6_3/m$ or $P6_3$ with similar lattice parameters. Therefore, they were presumed to be isostructural. Aruga and Nakai (1985) determined the crystal structure of Ca-rich agardite, a Ca-predominant variety of agardite-(Y), which was introduced as an unnamed Ca-analogue of agardite by Dunn (1985).

In the crystal structure of Ca-rich agardite (fig. 31), each copper atom is octahedrally coordinated by five oxygen atoms of the AsO_4 tetrahedra and by a zeolitic water molecule forming a column along the direction of the *c*-axis. The columns are linked by AsO_4 tetrahedra forming a three-dimensional framework with tunnel-like spaces for the Y site. The coordination form of the Y site, which is occupied by calcium, yttrium and lanthanide atoms, can be described in terms of a nine-coordinated tricapped trigonal prism (see fig. 94m).

Aruga and Nakai (1985) revealed that the charge compensation required by the substitution of Ca^{2+} for trivalent rare earths, is accomplished by the concomitant substitution of OH^- for O^{2-} at the O3 site of the AsO_4 tetrahedra. Therefore, the general formula for the mixite group could be expressed as $(A^{3+},A^{2+})Cu_6[XO_3(O,OH)]_3(OH)_6 \cdot 3H_2O$.

Fehr and Hochleitner (1984) described agardite-(Ce) from Lavrion, Greece, together with agardite-(La), but the mineral name "agardite-(Ce)" has not been submitted to or approved by the IMA Commission on New Minerals and Mineral Names. The crystal structure of agardite-(Ce) was reported by Hess (1983) under the name of chlorotile, which was discredited by the IMA Commission on New Minerals and Mineral Names in 1970. The structure (fig. 32) is isostructural with that of the unnamed Ca-analogue of agardite (Aruga and Nakai 1985). Hess (1983) reported

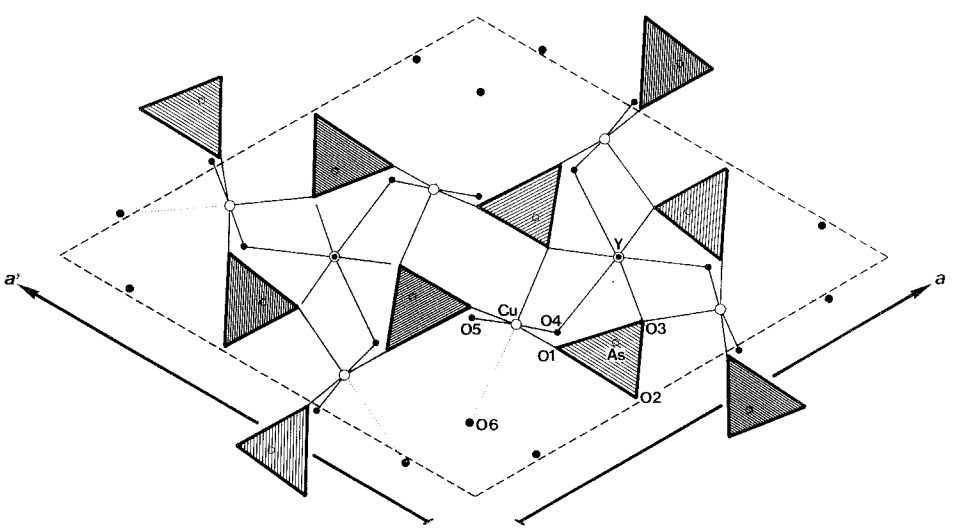

Fig. 31. The crystal structure of the unnamed Ca-analogue of agardite-(Y). The Y site is largely substituted by Ca, and the O3 site by (OH).

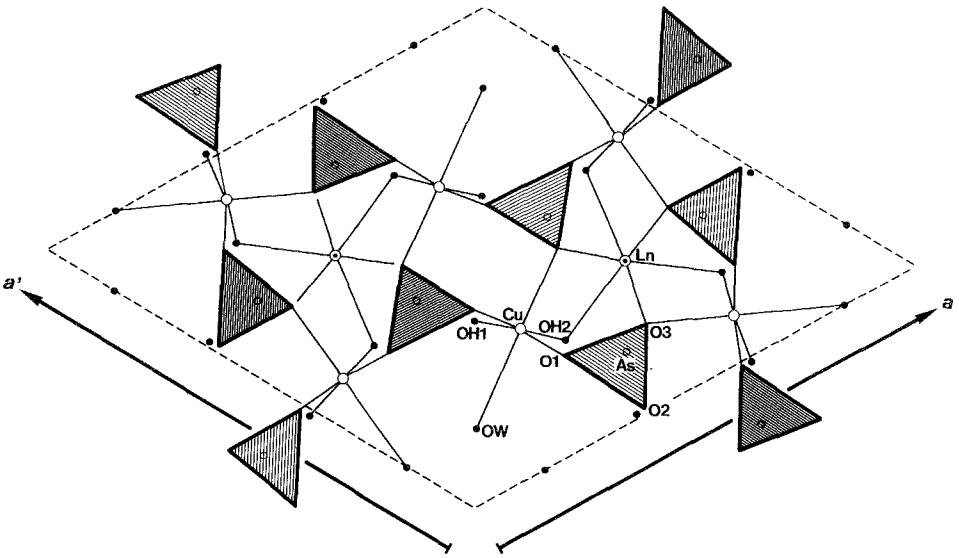

Fig. 32. The crystal structure of agardite-(Ce).

that the site occupancy at the Ce site was 70% when only the scattering factor of Ce had been used in the refinement calculation. He also suggested that isomorphous substitution of Ce with Ca or the other rare earth atoms may occur at the Ce site. He discussed the charge compensation system for the substitution of a trivalent Ce ion and a divalent Ca ion, i.e., $Ce^{3+} + OH^- \rightleftarrows Ca^{2+} + H_2O$ and $2Ce^{3+} \leftrightarrows Ca^{2+} + Ce^{4+}$. However, Aruga and Nakai (1985) revealed the coupled substitution of $Ce^{3+} + O^{2-} \leftrightarrows Ca^{2+} + OH^-$ in the Ca-analogue of agardite, based on a bond-valence calculation.

FRANÇOISITE-(Nd)
$Nd[(UO_2)_3O(OH)(PO_4)_2] \cdot 6H_2O$
$Nd[(UO_2)_3O(OH)(PO_4)_2] \cdot 6H_2O$

Sys. monoclinic	$a =$ 9.298(2) Å	source: Kamoto, Shaba, Zaïre
S.G. $P2_1/c$	$b =$ 15.605(4) Å	Ref.: Piret et al. (1988)
$Z =$ 4	$c =$ 13.668(2) Å	
Dx = 4.63 g/cm^3	$\beta =$ 112.77(1)°	
AP: table 74	ID: table 75	IL: fig. 33

Françoisite-(Nd) is a new mineral described by Piret et al. (1988), who also solved the crystal structure. Tetrahedral PO_4 groups and uranium–oxygen polyhedra are connected to each other by sharing oxygen edges or apexes forming $[(UO_2)_3O(OH)(PO_4)_2]_n^{3n-}$ layers, as in the dumontite ($Pb_2(UO_2)_3(PO_4)_2(OH)_4 \cdot 3H_2O$)–phosphuranylite ($Ca(UO_2)_3(PO_4)_2(OH)_2 \cdot 6H_2O$) structural group. These layers are parallel to (010) and are linked by tricapped trigonal prisms (see fig. 94m) of $NdO_4(H_2O)_5$ and water molecules forming a three-dimensional structure (fig. 33).

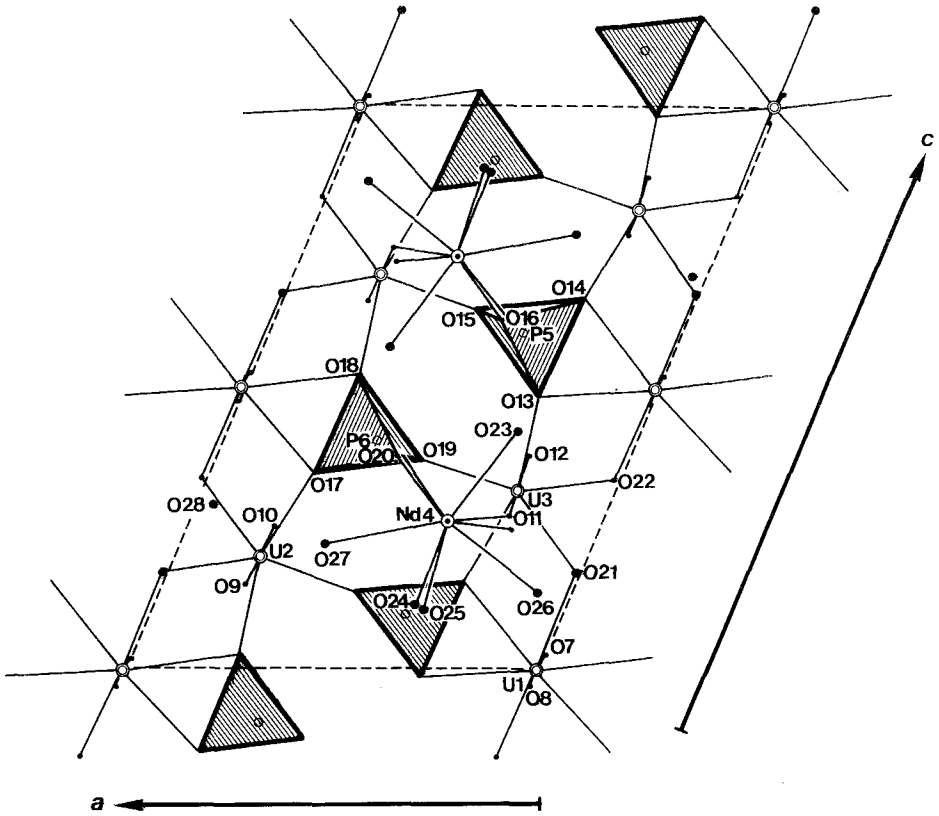

Fig. 33. The crystal structure of françoisite-(Nd).

CHUKHROVITE-(Y)
$Ca_3YAl_2(SO_4)F_{13} \cdot 10H_2O$
$Ca_3YAl_2(SO_4)F_{13} \cdot 10H_2O$

Sys. cubic — $a = 16.80 \pm 0.005$ Å — source: Central Kazakhstan
S.G. — Ref.: Ermilova et al. (1960)
$Z = 8$ — JCPDS: #14-0061
$Dm = 2.353$ g/cm^3

chukhrovite-(Ce)
$Ca_3CeAl_2(SO_4)F_{13} \cdot 10H_2O$
$Ca_3CeAl_2(SO_4)F_{13} \cdot 10H_2O$

Sys. cubic — $a = 16.80 \pm 0.005$ Å — source: Oberwolfach, Black Forest, Germany
S.G. — Ref.: Walenta (1978)
$Z = 8$

TABLE 74
Atomic parameters of françoisite-(Nd)[a].

	x	*y*	*z*	*U*
U1	0.0111(2)	0.2085(1)	−0.0002(2)	0.0104(8)
U2	−0.2094(2)	0.2423(1)	0.2002(1)	0.0095(10)
U3	0.2361(2)	0.2450(1)	0.3174(1)	0.0116(10)
Nd4	0.6245(3)	−0.0052(3)	0.2348(2)	0.0204(15)
P5	0.389(1)	0.186(1)	0.103(1)	0.011(3)
P6	−0.368(1)	0.186(1)	−0.094(1)	0.015(3)
O7	0.003(6)	0.322(2)	0.016(4)	0.046(11)
O8	0.011(4)	0.093(2)	−0.011(3)	0.023(8)
O9	−0.202(4)	0.350(2)	0.155(3)	0.021(8)
O10	−0.220(3)	0.134(2)	0.247(2)	0.007(7)
O11	0.232(4)	0.353(3)	0.273(3)	0.036(10)
O12	0.253(4)	0.137(3)	0.373(3)	0.041(10)
O13	0.283(3)	0.194(2)	−0.014(2)	0.008(7)
O14	0.274(3)	0.202(2)	0.158(3)	0.018(8)
O15	0.521(3)	0.250(2)	0.136(2)	0.013(7)
O16	0.457(4)	0.098(3)	0.122(3)	0.028(9)
O17	−0.254(3)	0.205(2)	−0.146(3)	0.017(8)
O18	−0.260(4)	0.193(3)	0.024(3)	0.026(9)
O19	−0.494(3)	0.256(2)	−0.121(2)	0.012(7)
O20	−0.437(4)	0.097(3)	−0.120(3)	0.028(9)
O21[b]	0.012(3)	0.190(2)	0.171(2)	0.003(6)
O22	0.017(3)	0.233(2)	−0.159(2)	0.020(7)
O23[c]	0.700(3)	−0.002(3)	0.078(2)	0.029(8)
O24[c]	0.632(6)	−0.094(4)	0.382(5)	0.067(16)
O25[c]	0.648(5)	0.092(4)	0.389(4)	0.048(12)
O26[c]	0.911(4)	−0.006(4)	0.362(3)	0.045(10)
O27[c]	0.367(6)	−0.002(7)	0.274(4)	0.102(18)
O28[c]	0.039(4)	0.021(3)	0.199(3)	0.041(10)

[a] MoKα, $R = 0.061$ (1430 refl.).
[b] OH.
[c] H_2O.

Chukhrovite-(Y) and -(Ce) were described by Ermilova et al. (1960) and Walenta (1978), respectively. Chukhrovite, $(Ca_3R)Al_2(SO_4)F_{13} \cdot 10H_2O$ and synthetic $Ca_4AlSi(SO_4)F_{13} \cdot 12H_2O$ are isostructural. The crystal structure of synthetic $Ca_4(AlSi)(SO_4)F_{13} \cdot 12H_2O$ was determined by Mathew et al. (1981) under the name of synthetic chukhrovite. However, the mineral name "chukhrovite" may not be used for this synthetic phase, because $(Ca_3R)Al_2(SO_4)F_{13} \cdot 10H_2O$ (=chukhrovite) and $Ca_4AlSi(SO_4)F_{13} \cdot 12H_2O$ (=the synthetic phase) are the end members of the solid solution in the $[Ca_3(Y,Ce,Ca)](Al,Si)_2(SO_4)F_{13} \cdot 12H_2O$ system with isomorphous substitution $R + Al \rightleftarrows Ca + Si$; an independent name would need to be given to the latter phase if it were discovered in nature.

TABLE 75
Interatomic distances for françoisite-(Nd) in Å[a].

U1–O7	1.79	U2–O9	1.80
U1–O8	1.80	U2–O10	1.83
U1–O22	2.22	U2–O22	2.27
U1–O21	2.35	U2–O15	2.32
U1–O17	2.50	U2–O21	2.39
U1–O14	2.57	U2–O18	2.40
U1–O13	2.62	U2–O17	2.43
U1–O18	2.67	mean	2.21[b]
mean	2.32[b]	Nd4–O20	2.34
U3–O11	1.79	Nd4–O16	2.36
U3–O12	1.82	Nd4–O24	2.42
U3–O22	2.21	Nd4–O23	2.51
U3–O19	2.32	Nd4–O25	2.53
U3–O13	2.37	Nd4–O26	2.56
U3–O21	2.42	Nd4–O10	2.58
U3–O14	2.43	Nd4–O11	2.61
mean	2.19[b]	Nd4–O27	2.65
		mean	2.51[b]
P5–O16	1.49	P6–O20	1.51
P5–O15	1.51	P6–O17	1.52
P5–O13	1.53	P6–O19	1.53
P5–O14	1.55	P6–O18	1.54
mean	1.52[b]	mean	1.53[b]

[a]ESDs are about 0.03 Å.
[b]Calculated by RM.

TABLE 76
Atomic parameters of $Ca_4AlSi(SO_4)F_{13} \cdot 12H_2O$[a].

	x	y	z	B (Å^2)
Ca	0.29171(2)	0.29171	0.29171	
M[b]	0.5	0.5	0.5	
S	0.125	0.125	0.125	
O	0.07396(7)	0.07396	0.07396	
F1	0.375	0.375	0.375	
F2	0.22049(6)	0.33649(6)	0.45070(6)	
W	0.15481(8)	0.24744(10)	0.30479(8)	
H1	0.126(1)	0.222(1)	0.271(1)	3.5(5)
H2	0.135(1)	0.231(2)	0.345(2)	5.5(7)

[a]MoKα, $R = 0.025$, $R_w = 0.028$ (481 refl.).
Crystal data: cubic, Fd3, $a = 16.710(2)$ and $Z = 8$.
[b]M: 0.5Al + 0.5Si.

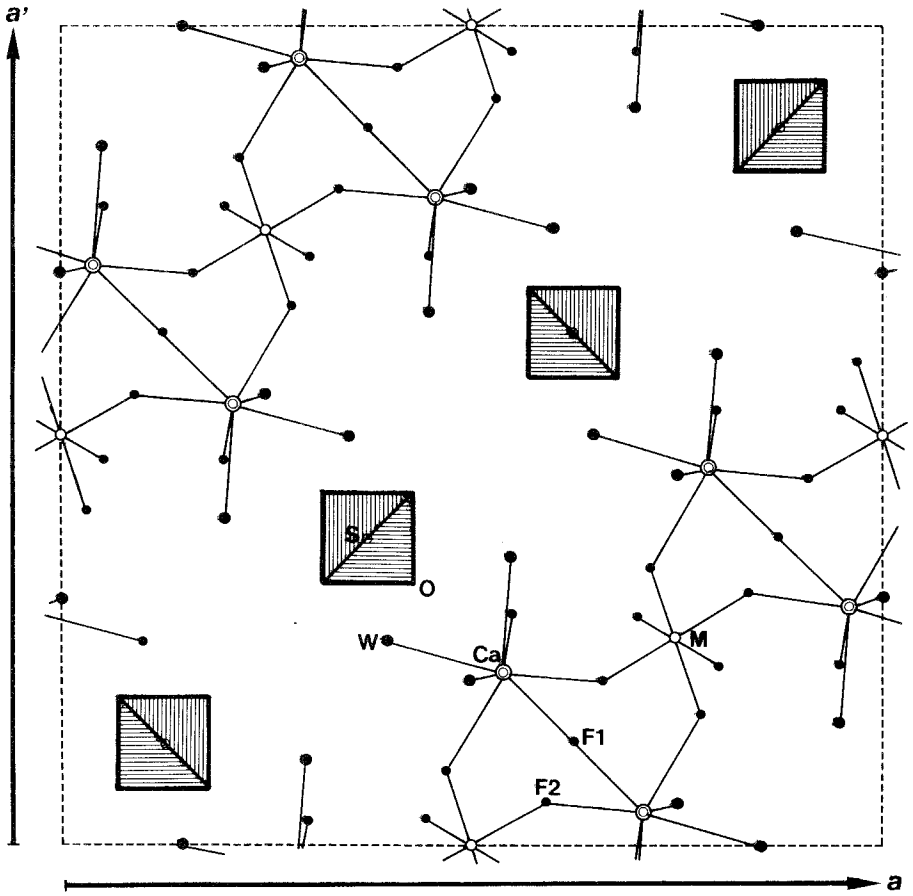

Fig. 34. The crystal structure of $Ca_4AlSi(SO_4)F_{13} \cdot 12H_2O$.

The structure (fig. 34, tables 76, 77) of synthetic $Ca_4AlSi(SO_4)F_{13} \cdot 12H_2O$ consists of SO_4 tetrahedra, $(Al,Si)F_6$ (= MF_6) octahedra and seven-coordinated Ca polyhedra (Mathew et al. 1981). The Ca polyhedra are monocapped octahedra coordinated by three water molecules (W), the three F2 atoms of the three different MF_6 octahedra and one F1 atom shared by the neighboring Ca atoms. The SO_4 tetrahedra lie in the cavities of the three-dimensional framework of the MF_6 octahedra and Ca polyhedra, and are linked to the framework by hydrogen bonds between the twelve water molecules and the four oxygen atoms of the SO_4 tetrahedra. Mathew et al. (1981) stated that this appears to be the first example of hydration number twelve observed for the SO_4 ion in the crystalline state. Another unusual feature of the structure is that all four faces of the SO_4 ion are linked to faces of four different calcium polyhedra via hydrogen bonds. They pointed out that any variation in the Al/Si ratio from one would be restricted by the F1 content unless other modes of

TABLE 77
Interatomic distances for $Ca_4AlSi(SO_4)F_{13} \cdot 12H_2O$ in Å.

Ca–F2	2.361(1) ×3	M–F2	1.735(1) ×6
Ca–F1	2.411(1)	S–O	1.477(1) ×4
mean	2.374		
Ca–W	2.414(1) ×3		

substitution are invoked, because the geometry and large bond strength involving F1 ions do not allow partial occupancy at the F1 site.

The rare earth atoms contained in natural samples presumably occupy the largest Ca site with as charge compensation mechanism the coupled substitution $Ca^{2+} + Si^{4+} \rightleftarrows R^{3+} + Al^{3+}$, which could change the Al/Si ratio without vacancies at the F1 site. In addition, the replacement of F1 by O^{2-} proposed by Mathew et al. (1981) for the charge compensation of the substitution of Si^{4+} for Al^{3+} is also adaptable to that of Ca^{2+} with R^{3+}. However, the problem of the difference in numbers of water molecules, 10 and 12 between the two phases, has not yet been solved.

IIMORIITE-(Y)
$Y_2(SiO_4)(CO_3)$
$Y_2(SiO_4)(CO_3)$

Sys. triclinic	$a =$ 6.573(1) Å	source: Bokan Mt., AK, USA
S.G. P1 or $P\bar{1}$	$b =$ 6.651(1) Å	Ref.: Foord et al. (1984)
$Z =$ 2	$c =$ 6.454(1) Å	JCPDS: #35-0640
Dx = 4.91 g/cm³	$\alpha =$ 116.44°	
Dm = 4.47 g/cm³	$\beta =$ 92.34°	
	$\gamma =$ 95.63°	

Iimoriite-(Y) was first described by Kato and Nagashima (1970) as $Y_5(SiO_4)_3(OH)_3$ from Fukushima, Japan, and they suggested that iimoriite-(Y) had a superstructure with $P\bar{1}$ symmetry. Recently, Foord et al. (1984) reinvestigated the iimoriite-(Y) samples from Alaska, USA and from the type locality. They gave the revised ideal formula $Y_2(SiO_4)(CO_3)$ for iimoriite-(Y), and reported the absence of a superstructure.

In their paper, they mentioned that a complete crystal structure analysis of iimoriite-(Y) had been carried out by Campana et al. (in preparation). It seems that the paper has not yet been published.

2.2.2. *Structures with linked tetrahedral anionic groups – silicates*

Silicate ions form a diortho group (Si_2O_7), ring, chain, sheet or three-dimensional framework in the crystal structures of rare earth minerals. A remarkable difference between structures of silicates and phosphates is due to the fact that phosphate ions do not form such anionic groups in the structures, except for canaphite, $CaNa_2P_2O_7 \cdot 4H_2O$ (Rouse et al. 1988).

YTTRIALITE-(Y) [high-temperature y-phase]
$(Y,Th)_2Si_2O_7$
$(Y,Th)_2Si_2O_7$

Sys.	monoclinic	$a =$ 7.50 ± 0.03 Å	source: synthetic $(Y,Th)_2Si_2O_7$
S.G.	$P2_1/m$	$b =$ 8.06 ± 0.03 Å	Ref.: Batalieva and Pyatenko (1972)
$Z =$	2	$c =$ 5.02 ± 0.02 Å	JCPDS: #24-1427, #24-1428
Dm = 4.0 g/cm^3		$\beta = 112°00' \pm 30'$	
AP:	table 78	ID: table 79	IL: fig. 35

THORTVEITITE
$(Sc,Y)_2Si_2O_7$
$(Sc,Y)_2Si_2O_7$

Sys.	monoclinic	$a =$ 6.650(1) Å	source: Iveland, Setesdalen, Norway
S.G.	C2/m	$b =$ 8.616(1) Å	Ref.: Bianchi et al. (1988)
$Z =$	2	$c =$ 4.686(1) Å	JCPDS: #20-1037, #19-1125
		$\beta = 102.20(1)°$	
AP:	table 80	ID: table 81	IL: fig. 36

KEIVIITE-(Y)
$Y_2Si_2O_7$
$Y_2Si_2O_7$

Sys.	monoclinic	$a =$ 6.845(5) Å	source: Kola Peninsula, Russia
S.G.	C2/m	$b =$ 8.960(5) Å	Ref.: Voloshin et al. (1985)
$Z =$	2	$c =$ 4.734(3) Å	JCPDS: #38-0440
Dx = 4.48 g/cm^3		$\beta = 101.65(5)°$	
Dm = 4.45 g/cm^3			

TABLE 78
Atomic parameters of yttrialite-(Y) [high-temperature y-phase][a].

	x	y	z
Y1	0	0	0
Y2	0.5	0	0
Si1	0.120	0.25	0.588
Si2	0.709	0.25	0.548
O1	0.190	0.25	0.310
O2	0.508	0.25	0.264
O3	0.880	0.25	0.430
O4	0.190	0.090	0.800
O5	0.688	0.090	0.736

[a] Mo, $R_{hk0} = 0.089$ (39 refl.), $R_{h0l} = 0.16$ (59 refl.).

TABLE 79
Interatomic distances for yttrialite-(Y) [high-temperature y-phase] in Å.

Y1–O	2.15 ×2	Y2–O	2.28 ×2
Y1–O	2.33 ×2	Y2–O	2.38 ×2
Y1–O	2.62 ×2	Y2–O	2.40 ×2
mean	2.37	mean	2.35
Si1–O	1.63 ×2	Si2–O	1.60
Si1–O	1.67 ×2	Si2–O	1.64
mean	1.65	Si2–O	1.64 ×2
		mean	1.63

TABLE 80
Atomic parameters of thortveitite[a].

	x	*y*	*z*
M[b]	0	0.30503(3)	0.5
Si	0.22108(11)	0	−0.08762(15)
O1	0	0	0
O2	0.38654(28)	0	0.22171(38)
O3	0.23655(26)	0.15499(17)	−0.28174(30)

[a] MoKα, $R = 0.021$, $R_w = 0.029$ (849 refl.).
[b] Sc,Y.

TABLE 81
Interatomic distances for thortveitite in Å.

M–O3	2.124(2) ×2	Si–O1	1.608(1)
M–O2	2.162(1) ×2	Si–O2	1.624(2)
M–O3	2.234(2) ×2	Si–O3	1.631(2) ×2
mean	2.173	mean	1.623

KEIVIITE-(Yb)
$Yb_2Si_2O_7$
$Yb_2Si_2O_7$

Sys. monoclinic	$a =$ 4.715(1) Å		source: Kola Peninsula, Russia
S.G. A2/m	$b =$ 8.870(3) Å		Ref.: Yakubovich et al. (1986)
$Z =$ 2	$c =$ 6.805(3) Å		JCPDS: #37-0458, #25-1345
Dx = 6.04 g/cm^3	$\beta = 102.01(3)^\circ$		
Dm = 5.95 g/cm^3			
AP: table 82	ID: table 83		IL: fig. 37

TABLE 82
Atomic parameters of keiviite-(Yb)[a].

	x	y	z	B_{iso}
Yb	0	0.80653(7)	0.5	0.53(1)
Si	0.4127(9)	0.5	0.7188(5)	0.76(5)
O1	0.5	0.5	0.5	1.5(2)
O2	0.716(2)	0.5	0.881(1)	0.9(1)
O3	0.220(2)	0.6506(8)	0.735(1)	1.1(1)

[a] MoKα, $R = 0.0404$ (841 refl.).

TABLE 83
Interatomic distances for keiviite-(Yb) in Å.

Yb–O3	2.204(7) ×2	Si–O2	1.614(11)
Yb–O2	2.224(7) ×2	Si–O1	1.625(4)
Yb–O3	2.293(7) ×2	Si–O3	1.631(8) ×2
mean	2.240	mean	1.625

THALENITE-(Y)
$Y_2Si_3O_{10}(OH)$
$Y_2Si_3O_{10}(OH)$

Sys. monoclinic	$a = 10.343 \pm 0.005$ Å	source: CIS
S.G. $P2_1/n$	$b = 7.294 \pm 0.006$ Å	Ref.: Kornov et al. (1972)
$Z = 4$	$c = 11.093 \pm 0.008$ Å	JCPDS: #38-0439
Dx = 4.34 g/cm^3	$\gamma = 96°55' \pm 30'$	
AP: table 84	ID: table 85	IL: fig. 38

F-analogue of THALENITE-(Y)
$Y_3Si_3O_{10}F$
$Y_3Si_3O_{10}F$

Sys. monoclinic	$a = 7.318(2)$ Å	source: Kola Peninsula, Russia
S.G. $P2_1/n$	$b = 11.134(3)$ Å	Ref.: Yakubovich et al. (1988)
$Z = 4$	$c = 10.379(3)$ Å	
Dx = 4.29 g/cm^3	$\beta = 97.24(2)°$	
AP: table 86	ID: table 87	

Yttrialite-(Y) occurs in the metamict state, and two crystalline phases obtained by annealing were reported (Proshchenko 1962, Lima de Faria 1964, Batalieva et al. 1969): i.e., a low-temperature α-phase and a high-temperature y-phase. On the other hand, α-, β-, γ- and δ-phases are reported for artificial compounds with the formula $Y_2Si_2O_7$ by Ito and Johnson (1968) and by Felsche (1970). Batalieva and Pyatenko (1972) suggested that the 4–11% of ThO_2 content in yttrialite-(Y) is "the special characteristic" of this mineral, and that the y-phase could be synthesized only in the presence of a small amount of ThO_2. They obtained crystals of yttrialite-(Y) using

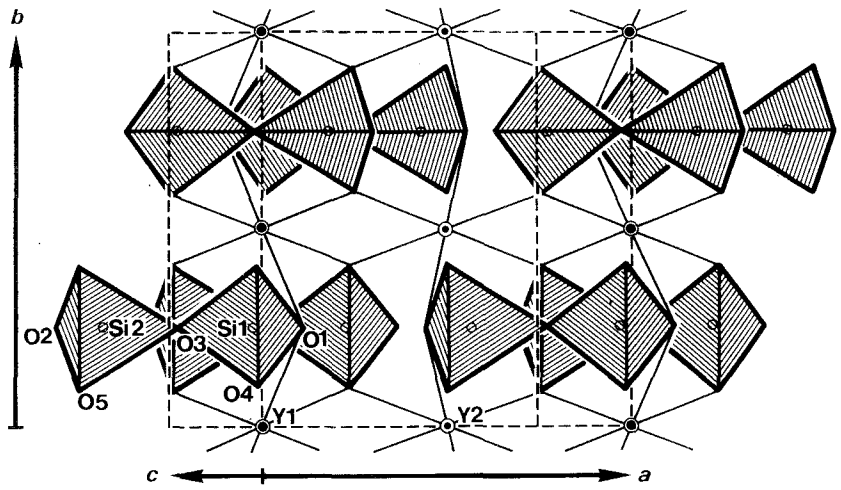

Fig. 35. The crystal structure of yttrialite-(Y).

as the starting material $Y_2Si_2O_7 + ThO_2$ in a weight ratio of 96:4, and determined the crystal structure of the y-phase of yttrialite-(Y).

The crystal structure of yttrialite-(Y) (y-phase) (fig. 35) consists of a layer of distorted Y octahedra parallel to the *ac*-plane. The layers are connected by the Si tetrahedra of the diortho groups. Batalieva and Pyatenko (1972) suggested a similarity in the structural features of tilleyite, $Ca_5(Si_2O_7)(CO_3)_2$, cuspidine, $Ca_4(Si_2O_7)(F,OH)_2$, and yttrialite-(Y). It is worth noting that both crystallographically independent Y sites (Y1 and Y2) have a low coordination number, 6, which is the lowest coordination number ever reported for a rare earth atom in the structure of a rare earth mineral. The low coordination numbers cause shortening of the Y–O interatomic distances, a mean Y1–O distance of 2.37 Å and a Y2–O distance of 2.35 Å, to strengthen the interactions.

Batalieva and Pyatenko (1972) pointed out that the crystal structure of y-phase yttrialite-(Y) is similar to that of $Gd_2Si_2O_7$, which is closely related to δ-$Y_2Si_2O_7$ in its X-ray powder diffraction patterns and lattice parameters. Although the crystal structure of yttrialite-(Y) (y-phase) does not have a closely packed structure, those of β- and γ-$Y_2Si_2O_7$ have a close packing of the oxygen atoms.

The crystal structure of thortveitite was first determined by Zachariasen (1930) and refined by Cruickshank et al. (1962). Smolin et al. (1973) reinvestigated the crystal structure using synthetic crystals of $Sc_2Si_2O_7$. Recently, Bianchi et al. (1988) made a reexamination of four natural samples of thortveitite by electron microprobe analyses and single crystal structure determination. The structure consists of layers of Sc octahedra and diortho groups of Si tetrahedra connecting the layers (fig. 36). This structure apparently resembles that of yttrialite-(Y) (y-phase), although the former has a distorted hexagonal packing of the oxygen atoms and is isotypic with that of β-$Y_2Si_2O_7$ (Batalieva and Pyatenko 1967). The analytical data reported by

TABLE 84
Atomic parameters of thalenite-(Y)[a].

	x	*y*	*z*	*B*
Y1	0.312	0.905	0.230	1.45
Y2	−0.017	0.237	0.534	1.80
Y3	0.497	0.301	0.402	1.86
Si1	0.111	0.232	0.245	1.57
Si2	0.209	0.493	0.039	1.36
Si3	0.741	0.023	0.085	1.33
O1	0.981	0.260	0.318	1.35
O2	0.119	0.023	0.231	1.01
O3	0.365	0.469	0.018	2.07
O4[b]	0.123	0.235	0.114	1.83
O5	0.230	0.340	0.325	1.63
O6	0.369	0.023	0.414	2.07
O7	0.362	0.012	0.026	2.19
O8	0.690	0.181	0.391	0.99
O9	0.700	0.211	0.143	1.65
O10	0.893	0.042	0.047	1.94
O11[c]	0.440	0.196	0.218	1.14

[a] MoKα, $R = 0.11$ for $\sin\theta/\lambda < 0.85$ refl.
[b] The atomic parameters of the O4 site include misprints, since the interatomic distances recalculated using these values are not identical with the distance given in the original paper (see the next table).
[c] O11 = (OH).

Bianchi et al. (1988) indicate extensive substitution of Y and Ln for Sc, as well as non-negligible amounts of Zr and Hf; the charge balance is maintained by multiple substitution of Ca, Mg and Mn in the M site and of Al for Si. There is no evidence for disorder involving the Si_2O_7 group and the Si–O–Si angle is exactly 180°.

Keiviite-(Yb) and -(Y) were described as new minerals by Voloshin et al. (1983a, 1985). Yakubovich et al. (1986) determined the crystal structure of keiviite-(Yb) using a polysynthetically twinned sample, which consisted of keiviite-(Yb) and another phase of $R_2Si_2O_7$, i.e., $Er_2Si_2O_7$ having a different structure from that of keiviite-(Yb). The crystal structure of keiviite-(Yb) (fig. 37) is isostructural with that of thortveitite (fig. 36).

Thalenite-(Y) is usually described with the chemical formula $Y_2Si_2O_7$, and it had been thought that the crystal structure contains diortho Si_2O_7 groups as in the structure of yttrialite-(Y). Kornev et al. (1972) analyzed the crystal structure of thalenite-(Y), and revealed the chemical formula to be $Y_3Si_3O_{10}(OH)$ rather than $Y_2Si_2O_7$. The structure (fig. 38) contains triortho Si_3O_{10} groups in contrast to the diortho Si_2O_7 groups found in the crystal structures of the high-temperature y-phase of yttrialite-(Y), thortveitite and keiviite-(Yb). Y1 forms a seven-coordinated polyhedron on the open side of the triortho Si_3O_{10} group making up a layer of Si and Y.

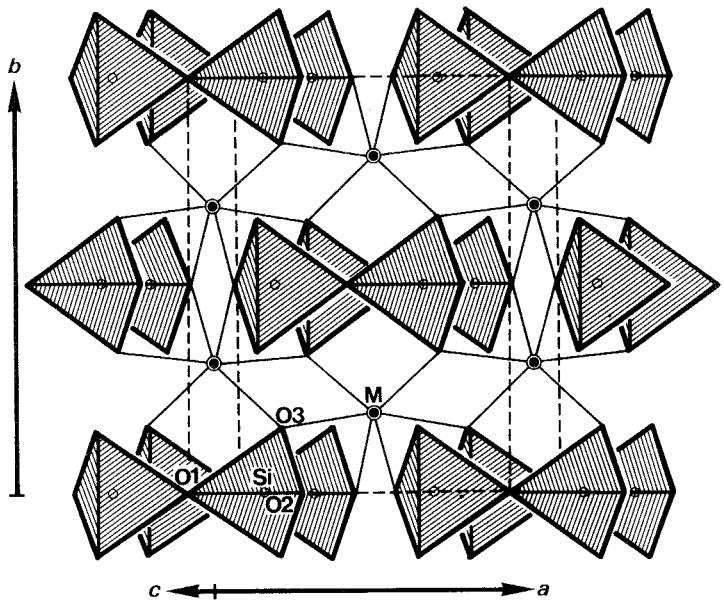

Fig. 36. The crystal structure of thortveitite.

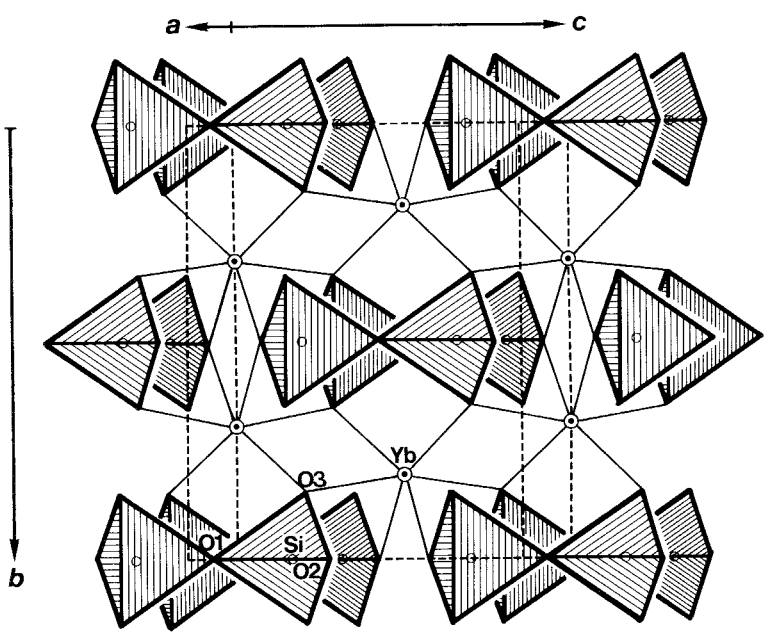

Fig. 37. The crystal structure of keiviite-(Yb).

TABLE 85
Interatomic distances for thalenite-(Y) in Å[a].

Y1–O1	2.21	Y2–O11	2.22
Y1–O9	2.22	Y2–O3	2.25
Y1–O6	2.27	Y2–O7	2.29
Y1–O2	2.27	Y2–O3[b]	2.31
Y1–O8	2.36	Y2–O9	2.32
Y1–O11	2.37	Y2–O1	2.40
Y1–O7	2.43	Y2–O7	2.58
mean	2.30	mean	2.34
Y3–O10	2.21	Y2–O2	3.32[b]
Y3–O11	2.23	Si1–O4	1.46[c]
Y3–O10	2.24	Si1–O2	1.54
Y3–O8	2.28	Si1–O1	1.60
Y3–O6	2.29	Si1–O5	1.64
Y3–O2	2.43	mean	1.56
Y3–O4	2.66[c]	(Si1–O4	1.60)[c]
Y3–O5	2.94	Si2–O6	1.60
mean	2.41	Si2–O8	1.61
(Y3–O4	2.78)[c]	Si2–O3	1.66
Si3–O9	1.62	Si2–O4	2.15[c]
Si3–O10	1.62	mean	1.76
Si3–O7	1.63	(Si2–O4	1.65)[c]
Si3–O5	1.66		
mean	1.63		

[a] Recalculated by RM.
[b] Probably, the Y2–O2 distance 2.32 Å given in the original paper, is a mistype of Y2–O3 distance.
[c] The interatomic distances concerning the O4 site recalculated using the original atomic parameters are not identical with the distances given in the original paper, whose values are given in parentheses.

Between these layers, seven-coordinated Y2 and eight-coordinated Y3 polyhedra make up another layer. It is worth noting that the coordination numbers of the Y polyhedra, 7 and 8, in thalenite-(Y) are higher than those in diortho silicates of yttrium, 6, e.g., the high-temperature y-phase of yttrialite-(Y).

Fitzpatrick and Pabst (1986) suggested that yttrialite-(Y) may be identical with metamict thalenite-(Y) in their description of thalenite-(Y) from Arizona. Yttrialite-(Y) is known only as a metamict mineral. The crystal structure of thalenite-(Y) reported by Kornev et al. (1972) does not resemble the structure of the high-temperature y-phase of yttrialite-(Y).

Recently, Yakubovich et al. (1988) reported the crystal structure of thalenite from the Kola Peninsula. Their chemical analysis gave as the ideal formula $Y_3Si_3O_{10}F$ for their specimen. Further, their structural analysis disclosed that the F^- ion occupies an independent anion site in the structure. Consequently, their specimen is

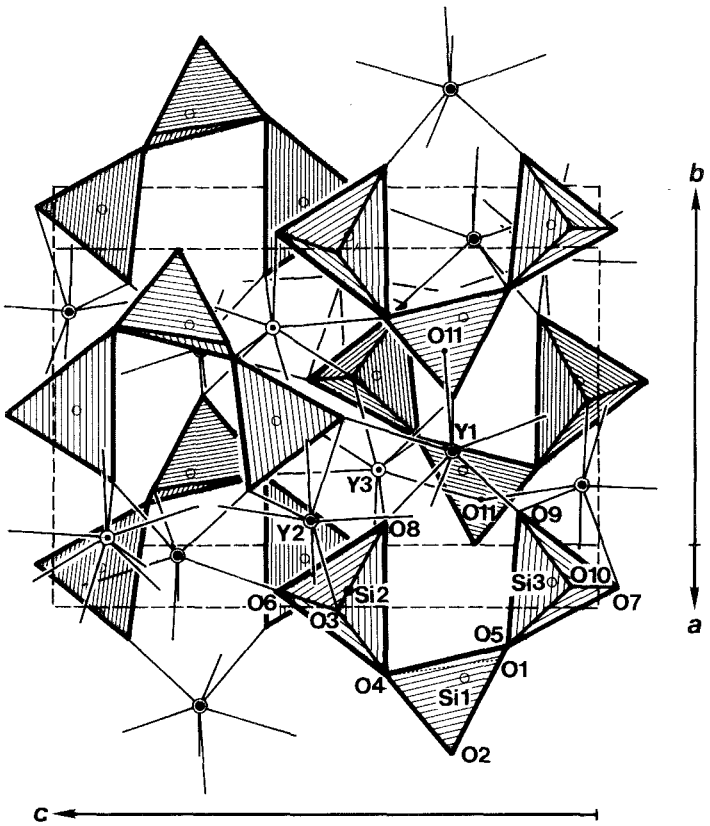

Fig. 38. The crystal structure of thalenite-(Y).

TABLE 86
Atomic parameters of F-analogue of thalenite-(Y)[a].

	x	*y*	*z*	*B*
Y1	0.90512(9)	0.22965(6)	0.31144(6)	0.30(1)
Y2	0.23710(9)	0.53235(6)	−0.01781(6)	0.34(1)
Y3	0.30073(9)	0.40225(6)	0.49650(6)	0.50(1)
Si1	0.2325(3)	0.2453(2)	0.1112(2)	0.72(5)
Si2	0.4941(3)	0.0383(2)	0.2080(2)	0.72(5)
Si3	0.0231(3)	0.0861(2)	0.7408(2)	0.70(5)
O1	0.2698(7)	0.3192(4)	0.9832(4)	1.0(1)
O2	0.0164(7)	0.2286(5)	0.1211(4)	1.0(1)
O3	0.4662(7)	0.0226(5)	0.3611(4)	1.3(1)
O4	0.3193(7)	0.1089(4)	0.1231(4)	1.1(1)
O5	0.3434(7)	0.3238(5)	0.2313(4)	1.2(1)
O6	0.0244(7)	0.4121(4)	0.3710(4)	1.0(1)
O7	0.0128(7)	0.0243(5)	0.3611(4)	1.0(1)
O8	0.1864(7)	0.3941(4)	0.6922(4)	1.1(1)
O9	0.2075(7)	0.1440(5)	0.6974(4)	1.2(1)
O10	0.0403(7)	0.0506(4)	0.8919(4)	1.1(1)
F	0.1943(6)	0.2162(4)	0.4403(4)	1.5(1)

[a] MoKα, $R = 0.0405$, $R_w = 0.0358$ (2284 refl.).

TABLE 87
Interatomic distances for F-analogue of thalenite-(Y) in Å.

Y1–O1	2.214(5)	Y2–O7	2.288(5)
Y1–O2	2.232(5)	Y2–O3	2.292(5)
Y1–O9	2.246(5)	Y2–O9	2.316(5)
Y1–O6	2.264(5)	Y2–O3	2.339(5)
Y1–O8	2.341(5)	Y2–O1	2.390(5)
Y1–O7	2.451(6)	Y2–O7	2.589(5)
mean	2.291	mean	2.369
Y1–F	2.366(5)	Y2–F	2.235(5)
[mean	2.302]	[mean	2.350]
Y3–O10	2.236(6)	Si1–O1	1.609(6)
Y3–O10	2.256(5)	Si1–O2	1.610(6)
Y3–O6	2.265(6)	Si1–O4	1.647(6)
Y3–O8	2.295(5)	Si1–O5	1.647(6)
Y3–O2	2.402(6)	mean	1.628
Y3–O4	2.706(5)		
Y3–O5	2.945(5)		
mean	2.444		
Y3–F	2.258(5)		
[mean	2.420]		
Si2–O8	1.623(6)	Si3–O10	1.607(5)
Si2–O6	1.628(6)	Si3–O9	1.610(6)
Si2–O3	1.638(5)	Si3–O7	1.625(6)
Si2–O4	1.660(6)	Si3–O5	1.652(6)
mean	1.637	mean	1.624

not thalenite-(Y), $Y_3Si_3O_{10}OH$, but a distinct new species according to the rules of mineralogical nomenclature. These two minerals are isostructural with each other, and $Y_3Si_3O_{10}F$ is considered as the F-analogue of thalenite-(Y), $Y_3Si_3O_{10}OH$ (Kornev et al. 1972). A clear mineralogical definition is necessary for this species.

HIORTDAHLITE II
$(Na,Ca)_4Ca_8Zr_2(Y,Zr,Ln,Na)_2(Si_2O_7)_4O_3F_5$
$(Na,Ca)_4Ca_6(Ca,Y)_2Zr_2(Y,Na)_2(Si_2O_7)_4O_2(F,O)_2F_4$

Sys.	triclinic	$a =$ 11.012(6) Å	source: Kipawa River, Canada
S.G.	$P\bar{1}$	$b =$ 10.342(3) Å	Ref.: Merlino and Perchiazzi (1987)
$Z =$	1	$c =$ 7.359(3) Å	JCPDS: #27-0668
Dx =	3.287 g/cm^3	$\alpha =$ 89.92(2)°	
Dm =	3.256 g/cm^3	$\beta =$ 109.21(5)°	
		$\gamma =$ 90.06(3)°	
AP:	table 88	ID: table 89	IL: fig. 39

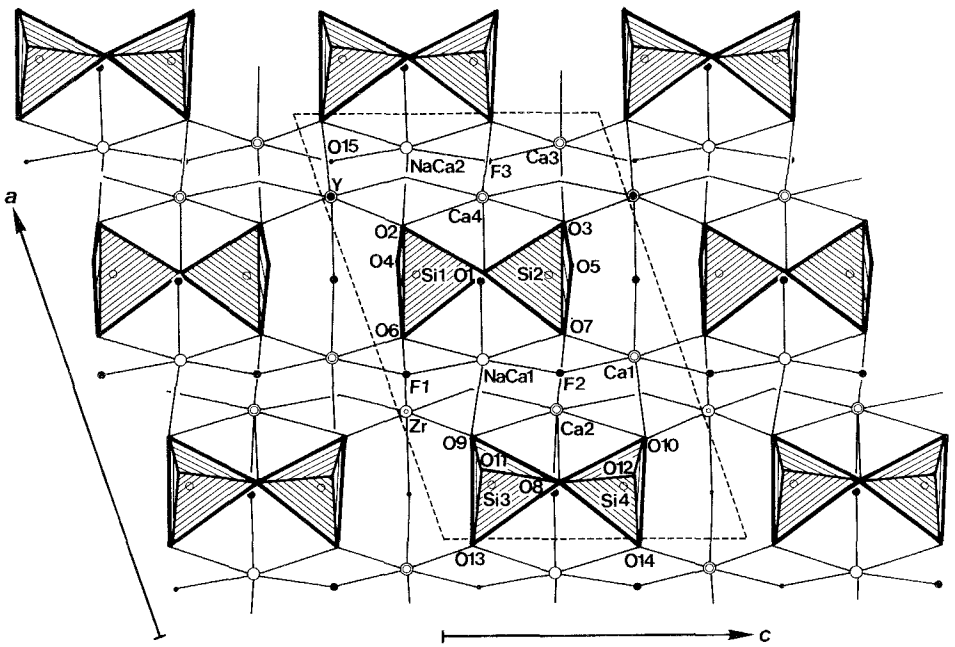

Fig. 39. The crystal structure of hiortdahlite II.

Hiortdahlite II is a member of the whole family of minerals related to cuspidine, $Ca_4Si_2O_7(F,OH)_2$, and låvenite, $Na_2(Mn,Ca,Fe)(Zr,Nb)(Si_2O_7)(O,F)_2$, which have crystal structures characterized by "octahedral walls". It is very difficult to distinguish the various phases from each other by means of X-ray powder diffraction patterns, because of the similar assembly of the common structural units in all the minerals of this family. Merlino and Perchiazzi (1985) and Merlino and Perchiazzi (1987) analyzed the crystal structures of hiortdahlite I, $Na_4Ca_8Zr_2(Nb,Mn,Ti,Fe,Mg,-Al)_2(Si_2O_7)_4O_3F_5$, and hiortdahlite II, and revealed the difference in the structures and chemical compositions. The crystal structure of hiortdahlite II (fig. 39) consists of Si_2O_7 diortho groups and two symmetry-independent octahedral walls; a wall built up by alternating Ca1, Zr, NaCa1 octahedra and a Ca2 polyhedron parallel to $(\bar{2}10)$ and another wall built up from Ca3, Ca4, Y and NaCa2 octahedra parallel to (210). The rare earth atoms occupy parts of the octahedrally six-coordinated Y and Ca3 sites. The refined site occupancies given by Merlino and Perchiazzi (1987) are listed in table 88.

TABLE 88
Atomic parameters of hiortdahlite II[a].

	x	y	z	B_{eq}
Ca1	0.4269(3)	0.3709(3)	0.8425(5)	1.67
Ca2	0.3039(4)	0.0979(4)	0.5267(5)	2.00
Ca3[b]	0.9297(3)	0.1281(3)	0.8457(4)	1.53
Ca4	0.8030(3)	0.3988(3)	0.5264(4)	1.22
Zr	0.3002(2)	0.0985(2)	1.0251(3)	2.00
Y[c]	0.8053(2)	0.4039(2)	0.0272(3)	1.50
NaCa1[d]	0.4217(5)	0.3766(5)	0.3371(7)	2.09
NaCa2[e]	0.9203(5)	0.1218(5)	0.3316(7)	2.21
Si1	0.6227(4)	0.1725(5)	0.2184(6)	1.46
Si2	0.6205(4)	0.1745(4)	0.6575(6)	1.23
Si3	0.1265(4)	0.3190(4)	0.2223(6)	1.32
Si4	0.1216(4)	0.3210(4)	0.6563(6)	1.06
O1	0.6250(15)	0.1706(17)	0.4413(19)	6.08
O2	0.7377(11)	0.2733(10)	0.2282(18)	2.60
O3	0.7438(12)	0.2612(12)	0.7655(18)	3.20
O4	0.6571(11)	0.0292(11)	0.1741(17)	2.40
O5	0.6450(13)	0.0295(12)	0.7380(18)	3.55
O6	0.4785(10)	0.2133(12)	0.0981(16)	2.51
O7	0.4843(11)	0.2340(11)	0.6366(18)	2.70
O8	0.1340(17)	0.2987(15)	0.4456(20)	5.47
O9	0.2409(10)	0.2272(10)	0.2105(16)	2.25
O10	0.2393(11)	0.2325(11)	0.7891(16)	2.71
O11	0.1587(12)	0.4700(10)	0.2009(17)	2.67
O12	0.1484(13)	0.4658(12)	0.7055(19)	4.13
O13	0.9874(11)	0.2702(11)	0.0908(17)	2.97
O14	0.9828(11)	0.2688(11)	0.6434(18)	2.80
O15	0.1123(10)	0.0157(11)	0.9408(15)	1.92
F1[f]	0.6116(9)	0.4949(10)	0.9333(14)	1.88
F2	0.3913(10)	0.5081(9)	0.5761(14)	2.67
F3	0.8906(9)	−0.0005(9)	0.5827(15)	2.81

[a] MoKα, $R = 0.069$ (1793 refl.).
[b] Ca3: 0.80Ca + 0.20Y.
[c] Y: 0.68Y + 0.32Na.
[d] NaCa1: 0.43Ca + 0.57Na.
[e] NaCa2: 0.50Ca + 0.50Na.
[f] F1: 0.50F + 0.50O.

LEPERSONNITE-(Gd)
$CaGd_2(UO_2)_{24}(CO_3)_8Si_4O_{12} \cdot 60H_2O$
$CaGd_2(UO_2)_{24}(CO_3)_8Si_4O_{12} \cdot 60H_2O$

Sys. orthorhombic	$a = 16.23(3)$ Å	source: Shaba, Zaïre
S.G. Pnnm or Pnn2	$b = 38.74(9)$ Å	Ref.: Deliens and Piret (1982)
$Z =$ 2	$c = 11.73(3)$ Å	JCPDS: #35-0522
Dx = 4.01 g/cm^3		
Dm = 3.97 ± 0.05 g/cm^3		

Lepersonnite-(Gd) was described as a new mineral from Shaba, Zaïre, together with bijvoetite-(Y) (Deliens and Piret 1982). Its structure is not known.

TABLE 89
Interatomic distances for hiortdahlite II in Å.

Ca1–F1	2.301(12)	Ca2–F3	2.261(10)
Ca1–F1	2.309(10)	Ca2–O7	2.350(12)
Ca1–O7	2.310(14)	Ca2–O4	2.476(13)
Ca1–F2	2.345(11)	Ca2–O5	2.565(15)
Ca1–O6	2.410(12)	Ca2–O9	2.572(12)
Ca1–O10	2.436(12)	Ca2–O10	2.662(13)
mean	2.352	Ca2–O8	2.728(10)
		mean	2.516
Ca3–O15	2.227(11)	Ca4–F2	2.239(11)
Ca3–O13	2.251(12)	Ca4–O14	2.313(12)
Ca3–F3	2.271(11)	Ca4–O11	2.344(12)
Ca3–O14	2.289(14)	Ca4–O12	2.398(15)
Ca3–O15	2.316(12)	Ca4–O2	2.446(12)
Ca3–O3	2.375(13)	Ca4–O3	2.508(15)
mean	2.288	mean	2.375
Zr–O5	2.112(13)	Y–F1	2.224(10)
Zr–O15	2.134(11)	Y–O11	2.259(13)
Zr–O4	2.139(13)	Y–O2	2.298(14)
Zr–O10	2.148(11)	Y–O12	2.300(13)
Zr–O9	2.157(12)	Y–O3	2.343(13)
Zr–O6	2.204(11)	Y–O13	2.353(12)
mean	2.149	mean	2.296
NaCa1–F2	2.281(11)	NaCa2–F3	2.334(11)
NaCa1–F1	2.318(12)	NaCa2–O15	2.388(12)
NaCa1–F2	2.335(12)	NaCa2–F3	2.348(13)
NaCa1–O9	2.450(11)	NaCa2–O2	2.464(12)
NaCa1–O7	2.550(13)	NaCa2–O13	2.625(14)
NaCa1–O6	2.659(14)	NaCa2–O14	2.649(13)
mean	2.432	mean	2.468
Si1–O4	1.591(13)	Si2–O7	1.582(13)
Si1–O6	1.600(11)	Si2–O5	1.602(13)
Si1–O2	1.623(13)	Si2–O3	1.603(12)
Si1–O1	1.632(16)	Si2–O1	1.609(16)
mean	1.612	mean	1.599
Si3–O13	1.600(11)	Si4–O12	1.546(13)
Si3–O9	1.603(12)	Si4–O14	1.594(13)
Si3–O11	1.620(12)	Si4–O8	1.617(17)
Si3–O8	1.631(16)	Si4–O10	1.624(11)
mean	1.614	mean	1.595

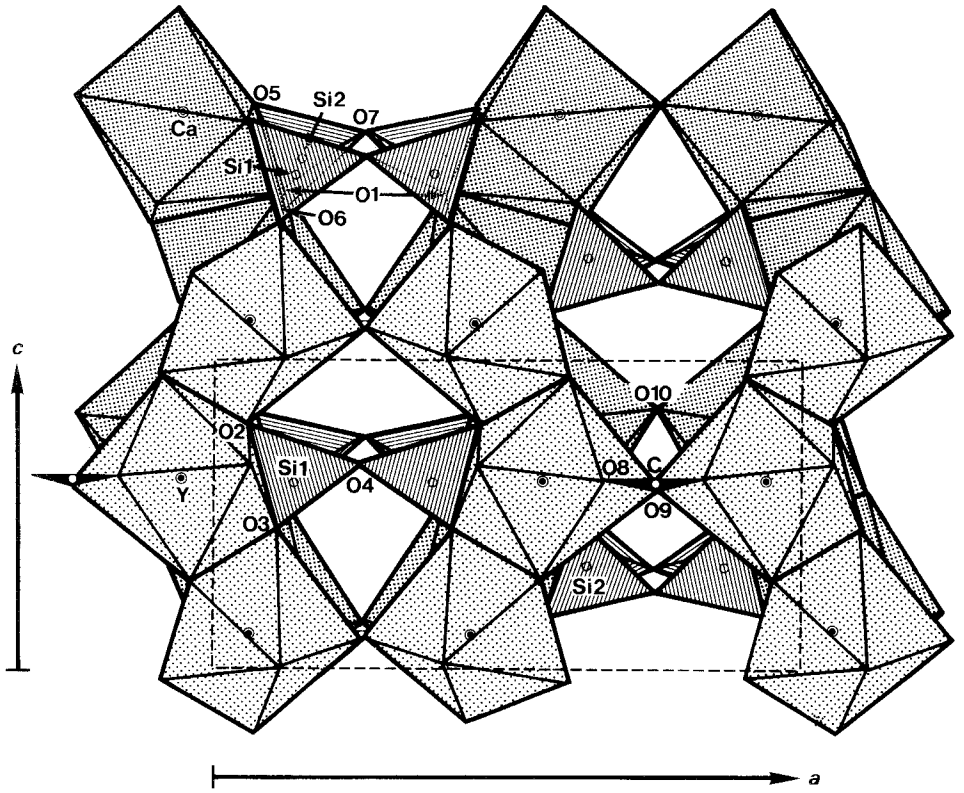

Fig. 40. Projection of the crystal structure of kainosite-(Y) onto (010) showing the six-membered rings of Y polyhedra.

KAINOSITE-(Y) (=cenosite)
$Ca_2Y_2Si_4O_{12}(CO_3)\cdot H_2O$
$Ca_2Y_2[(Si,Al)_4(O,OH)_{12}](CO_3)\cdot H_2O$

Sys. orthorhombic	$a = 13.011(1)$ Å	source: Baveno, Novara, Italy
S.G. Pmnb	$b = 14.310(1)$ Å	Ref.: Giuseppetti et al. (1989)
$Z = 4$	$c = 6.757(1)$ Å	JCPDS: #14-0332
AP: table 90	ID: table 91	IL: fig. 40

The crystal structure of kainosite-(Y) was determined by Volodina et al. (1963), and refined by themselves (Rumanova et al. 1967). The structure was further refined by Giuseppetti et al. (1989), who confirmed the result reported by Rumanova et al. (1967), and found the hydrogen positions of the water molecule. The following chemical formula was given, based on the activation analysis: $Ca_2[Y_{1.53}Y_{0.08}Dy_{0.10}Er_{0.09}Gd_{0.07}La_{0.01}Ce_{0.02}Nd_{0.01}Sm_{0.01}(Pr + Eu)_{0.01}Tb_{0.02}$-$Ho_{0.01}Tm_{0.01}Lu_{0.01}Fe_{0.02}]$-$[(Si_{3.87}Al_{0.13})O_{12}]CO_3H_2O$, or simply, $Ca_2(Y_{1.53}Ln_{0.47})[(Si_{3.87}Al_{0.13})O_{12}]CO_3H_2O$.

In the crystal structure of kainosite-(Y), the Y (rare earth) atom and calcium atom independently occupy two crystallographic sites. Both cations are coordinated by

TABLE 90
Atomic parameters of kainosite-(Y)[a].

	x	y	z	B_{eq}
Y	0.0568(0)	0.2187(0)	0.1117(0)	0.99(1)
Ca	0.0772(1)	0.4523(0)	0.3001(1)	1.28(1)
Si1	0.1307(1)	0.1469(1)	0.6112(1)	0.99(2)
Si2	0.1312(1)	0.4309(1)	0.8389(1)	1.01(2)
C	1/4	0.1243(3)	0.1129(7)	1.46(9)
O1	0.1127(2)	0.0353(1)	0.5569(3)	1.37(5)
O2	0.0524(2)	0.1707(1)	0.7927(3)	1.21(5)
O3	0.0954(2)	0.2164(2)	0.4382(3)	1.37(5)
O4	1/4	0.1600(2)	0.6729(5)	1.45(7)
O5	0.0525(2)	0.4196(2)	0.6540(3)	1.27(5)
O6	0.1111(2)	0.3613(1)	0.0190(3)	1.32(5)
O7	1/4	0.4266(2)	0.7571(5)	1.31(7)
O8	0.1639(2)	0.0817(2)	0.1148(4)	1.69(5)
O9	1/4	0.2142(2)	0.1078(5)	1.65(7)
O10W	1/4	0.3810(3)	0.3625(6)	2.10(9)
H1	1/4	0.319	0.335	3.00
H2	1/4	0.369	0.506	3.00

[a] MoKα, $R = 0.022$ (1578 refl.).

TABLE 91
Interatomic distances for kainosite-(Y) in Å.

Y–O6	2.249	Ca–O8	2.244
Y–O2	2.263	Ca–O6	2.345
Y–O3	2.263	Ca–O2	2.438
Y–O8	2.405	Ca–O5	2.457
Y–O2	2.453	Ca–O10	2.505
Y–O5	2.453	Ca–O5	2.511
Y–O3	2.481	Ca–O1	2.728
Y–O9	2.515	Ca–O1	2.972
mean	2.385	mean	2.525
Si1–O3	1.603	Si2–O6	1.594
Si1–O4	1.618	Si2–O5	1.624
Si1–O2	1.630	Si2–O7	1.643
Si1–O1	1.655	Si2–O1	1.670
mean	1.626	mean	1.633
C–O8	1.275 ×2		
C–O9	1.288		
mean	1.279		

eight oxygen atoms forming D_{2d} dodecahedra. The Ca dodecahedron is larger and more distorted than the Y dodecahedron. These polyhedra share their edges and corners forming individual six-membered rings (fig. 40).

A characteristic feature of the structure is alternating independent sheets composed of Ca polyhedra and of Y polyhedra, which are parallel to the (100) plane and are

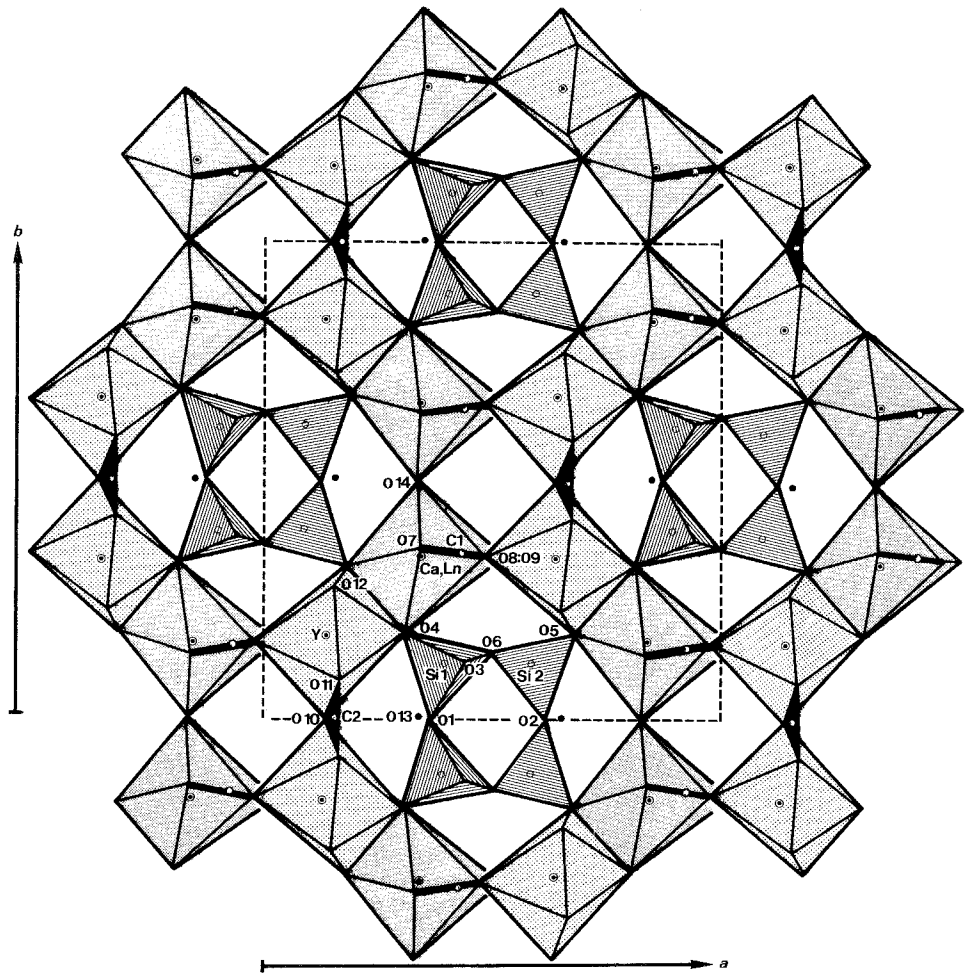

Fig. 41. The checkered pattern of the crystal structure of caysichite-(Y).

arranged along the *b*-axis. The SiO_4 tetrahedra form isolated Si_4O_{12} rings, which are nearly in the (001) plane, and across the (010) sheets, and lie in the "hexagonal" holes made up of the large-cation polyhedra. The CO_3 triangles lie almost in the (001) plane; the triangles are located at the same *z* level as the tetrahedral rings. The hydrogen bonds, which are provided by the water molecules, O10, are directly involved in the architectural pattern through the O9 ... H1–O10–H2 ... O7 bonds, which lie in the (100) plane at $x = \frac{1}{4}, \frac{3}{4}$. Consequently, the structure of kainosite-(Y) becomes a three-dimensional network.

Giuseppetti et al. (1989) pointed out that the short edge of the YO_8 polyhedron, O2–O3, is shared with the Si1 tetrahedron, and that the shortest O8–O9 edge is shared with the CO_3 triangle. This is an important example showing that the shape of the coordination polyhedron of the rare earth elements tends to be restricted by neighboring rigid polyhedra such as SiO_4 and CO_3, which share their edges with the rare earth polyhedron.

TABLE 92
Atomic parameters of caysichite-(Y)[a].

	x	y	z	B (Å^2)
Y	0.1403(1)	0.1710(1)	0.0422	0.96[f]
Ca,Ln[b]	0.1471(1)	0.1647(1)	0.4574(1)	1.19[f]
Si1	0.3990(2)	0.1103(2)	0.0880(3)	0.30[f]
Si2	0.4069(2)	0.1118(2)	0.4039(3)	0.10[f]
C1	0.0681(9)	0.1527(9)	0.7562(13)	0.89(19)
C2	0.1622(12)	0	0.1851(18)	0.68(26)
O1	0.3672(9)	0	0.0618(11)	0.23[f]
O2	0.3774(9)	0	0.4311(11)	0.80[f]
O3	0.4390(6)	0.1228(6)	0.2457(8)	0.62[f]
O4	0.3092(6)	0.1808(7)	0.0559(8)	0.54[f]
O5	0.3187(6)	0.1831(6)	0.4555(9)	0.70[f]
O6	0.4953(7)	0.1382(7)	−0.0054(9)	1.19[f]
O7	0.1632(8)	0.1381(9)	0.7701(12)	2.41(20)
O8	0.0226(7)	0.1597(7)	0.6407(9)	1.26(15)
O9	0.0200(6)	0.1635(7)	0.8693(9)	1.09(14)
O10	0.1391(11)	0	0.0583(14)	1.59(21)
O11	0.1721(6)	0.0809(7)	0.2538(9)	0.69(13)
O12[c]	0.1520(7)	0.2780(6)	0.2482(9)	0.89[f]
O13[d]	0.3478(19)	0	0.7445(28)	6.50[f]
O14[e]	0.1698(14)	0	0.5297(17)	2.62[f]

[a] MoKα, $R = 0.06$ (959 refl.).
[b] Ca,Ln: $Ca_{0.75}Ln_{0.25}$.
[c] O12: H_2O.
[d] O13: H_2O.
[e] O14: $(H_2O)_{0.5}(OH)_{0.5}$.
[f] B_{eq}.

CAYSICHITE-(Y)
$Y_2Ca_2Si_4O_{10}(CO_3)_3 \cdot 4H_2O$
$Y_2(Ca,Gd)_2Si_4O_{10}(CO_3)_3(H_2O,OH) \cdot 3H_2O$

Sys.	orthorhombic	$a = 13.27(1)$ Å	source: Evans Lou Mine, Que., Canada
S.G.	$Ccm2_1$	$b = 13.91(1)$ Å	Ref.: Mellini and Merlino (1978)
$Z =$	4	$c = 9.73(1)$ Å	JCPDS: #26-1394
Dx =	3.029 g/cm^3		
Dm =	3.03 g/cm^3		
AP:	table 92	ID: table 93	IL: fig. 41

The crystal structure of caysichite-(Y) (Mellini and Merlino 1978) is built up of double columns of alternating Y and (Ca,Ln) polyhedra parallel to the c-axis (fig. 41): in each column Y and (Ca,Ln) polyhedra alternately share an edge and a corner with carbonate groups wedged between two succeeding corner-sharing polyhedra. Each double column is connected to four other double columns building up a three-dimensional framework. The double-column connection defines a checkered pattern of channels. The four-repeat UUDD (up–up–down–down)-type double chains of Si–O tetrahedra occupy the channels. Therefore, in the conventional classification of silicates, caysichite-(Y) belongs to the chain silicates. Both the Y polyhedron and the (Ca,Ln) polyhedron are eight-coordinated $\Delta(D_{2d})$ dodecahedra (see fig. 94h). The (Ca,Ln) dodecahedron is larger and more distorted than that of yttrium, which is similar to those of calcium and yttrium in kainosite-(Y).

TABLE 93
Interatomic distances for caysichite-(Y) in Å.

Y–O4	2.249(8)	Ca,Ln–O5	2.293(8)
Y–O5	2.265(9)	Ca,Ln–O11	2.324(8)
Y–O9	2.322(9)	Ca,Ln–O9	2.373(9)
Y–O8	2.375(9)	Ca,Ln–O14	2.418(6)
Y–O10	2.382(8)	Ca,Ln–O4	2.421(9)
Y–O11	2.446(8)	Ca,Ln–O8	2.433(17)
Y–O12	2.505(9)	Ca,Ln–O12	2.572(9)
Y–O7	2.680(16)	Ca,Ln–O7	3.100(14)
mean	2.403	mean	2.492
Si1–O3	1.576(8)	Si2–O3	1.606(8)
Si1–O1	1.610(5)	Si2–O6	1.610(9)
Si1–O4	1.617(9)	Si2–O5	1.615(9)
Si1–O2	1.631(8)	Si2–O2	1.626(5)
mean	1.608	mean	1.614
C1–O8	1.280(16)	C2–O10	1.270(14)
C1–O9	1.280(16)	C2–O11	1.315(15) ×2
C1–O7	1.286(14)	mean	1.300
mean	1.282		

Mellini and Merlino (1978) revealed the anion chemistry in caysichite-(Y) using the method of Donnay and Allmann (1970). The result shows that the oxygen atoms O12, O13, and O14, which do not belong to silicate or carbonate ions, are H_2O, H_2O and (H_2O,OH), respectively, and yields the chemical formula $Y_4(Ca,Ln)_4(OH)(H_2O)_5[Si_8O_{20}](CO_3)_6 \cdot 2H_2O$. The formula cited above in this text has been rearranged from the viewpoint of crystallography.

CERITE-(Ce)
$(Ce,Ca)_9(Fe,Mg)(SiO_4)_6[SiO_3(OH)](OH)_3$
$Ce_9(\square,Ca)(Fe^{3+},Mg)(SiO_4)_6[SiO_3(OH)](OH)_3$

Sys.	trigonal (hex.)	$a = 10.779(6)$ Å	source: Mountain Pass, CA, USA
S.G.	R3c	$c = 38.061(7)$ Å	Ref.: Moore and Shen (1983a)
$Z =$	6		JCPDS: #11-0126
Dm =	4.78 g/cm^3		
AP:	table 94	ID: table 95	IL: fig. 42

STEENSTRUPINE-(Ce)
$Na_{14}Ce_6Mn^{2+}Mn^{3+}Fe_2^{3+}Zr(PO_4)_7Si_{12}O_{36}(OH)_2 \cdot 3H_2O$
$Na_{14}Ce_6Mn^{2+}Mn^{3+}Fe_2^{3+}Zr(PO_4)_7(Si_6O_{18})_2(OH)_2 \cdot 3H_2O$

Sys.	trigonal (hex.)	$a = 10.460(4)$ Å	source: Tunugdliarfik, Ilimaussaq, South Greenland
S.G.	$R\bar{3}m$	$c = 45.479(15)$ Å	Ref.: Moore and Shen (1983b)
$Z =$	3		
Dm =	3.40–3.47 g/cm^3		
AP:	table 96	ID: table 97	IL: fig. 43

The structure of cerite-(Ce) (fig. 42) consists of two types of rods running parallel to the *c*-axis (Moore and Shen 1983a). One rod is partly disordered at (00*z*) and includes the M octahedra, Ca polyhedra, $SiO_3(OH)$ tetrahedra and $(OH)^-$ groups which are bonded to the R ions. The other rod at (*x*, *y*, *z*), which is fully occupied, is based on the corner-, edge-, and face-linkages of $(Si1)O_4$ and $(Si2)O_4$ tetrahedra and $(R1)O_8OH$, $(R2)O_8OH$ and $(R3)O_8OH$ polyhedra. Omitting the bond to OH, the anhydrous RO_8 group is a dodecahedron with maximal point symmetry of D_{2d}. The OH^- ligands bond through a rhombus-shaped window in this dodecahedron. Moore and Shen (1983a) reported that the structure of cerite-(Ce) is based on the same structural principle as whitlockite, $Ca_9Mg(PO_4)_6[PO_3(OH)]\square_3$ (Calvo and Gopal 1975). They also suggested that cerite-(Ce) probably has a F^- analogue, and is related to a substantial family of rare earth silicates with rhombohedral structures such as cappelenite-(Y), okanoganite-(Y) and steenstrupine-(Ce).

The crystal structure of steenstrupine-(Ce) was determined by Moore and Shen (1983b), and a clear chemical formula was given for the first time. The structure (fig. 43) has a feature similar to that of cerite-(Ce), consisting of types of rods parallel to the *c*-axis. Rod I at (00*z*), etc. has the sequence M1–Na1–OH–M3–M2–□1–T–□1–M2–M3–OH–Na1 and rod II at $(\frac{1}{3}\frac{1}{6}z)$, etc., has the sequence Na3–P–P–Na3–Si2–Na2–R–Si1–Si1–R–Na2–Si2. In rod I, T is a disordered PO_4 group and the sequence Na1–M1–Na1 is a face-sharing octahedral trimer and M3–M2 a face-sharing octahedral dimer. A Si_6O_{18} six-membered ring occurs with approximate point symmetry C3i. It is suggested that the apical oxygens in the six-ring can be hydroxylated, balancing the removal of the large Na2 and Na3 cations of low charge: $Na^+_{12} \rightleftarrows \square_{12}$ as $[Si_6O_{18}]^{12-}_2 \rightleftarrows [Si_6O_{12}(OH)_6]^{6-}_2$.

The difference in the arrangement of polyhedra in the rods of the two structures affects only the lengths of the *c*-axes, i.e. the ratio of the *c*-axis lengths of steenstrupine-(Ce) to that of cerite-(Ce) is about 12 : 10, whereas the *a*-axis lengths of both minerals are comparable to each other. The rare earth atoms exist dominantly in the eight-coordinated R site, and occupy neither the eight-coordinated Na1 site nor the eight-coordinated Na2 site. The polyhedra of Na1 and Na2 are larger than the R polyhedra.

ILIMAUSSITE-(Ce)
$Ba_2Na_4CeFeNb_2Si_8O_{28} \cdot 5H_2O$
$Ba_2Na_4CeFeNb_2Si_8O_{28} \cdot 5H_2O$

Sys.	hexagonal	$a = 10.80 \pm 0.04$ Å	source: Ilimaussaq, Greenland
S.G.	$P6_3/mcm$, $P6_3cm$ or $P\bar{6}c2$	$c = 20.31 \pm 0.07$ Å	Ref.: Semenov et al. (1968)
			JCPDS: #21-0399
$Z =$	3		
Dm =	3.6 g/cm^3		

Ilimaussite-(Ce) was described by Semenov et al. (1968). They suggested a relationship to cerite [R3c, $a = 10.779$, $c = 38.061$ Å, see cerite-(Ce)] based on similarities between the two sets of crystal data.

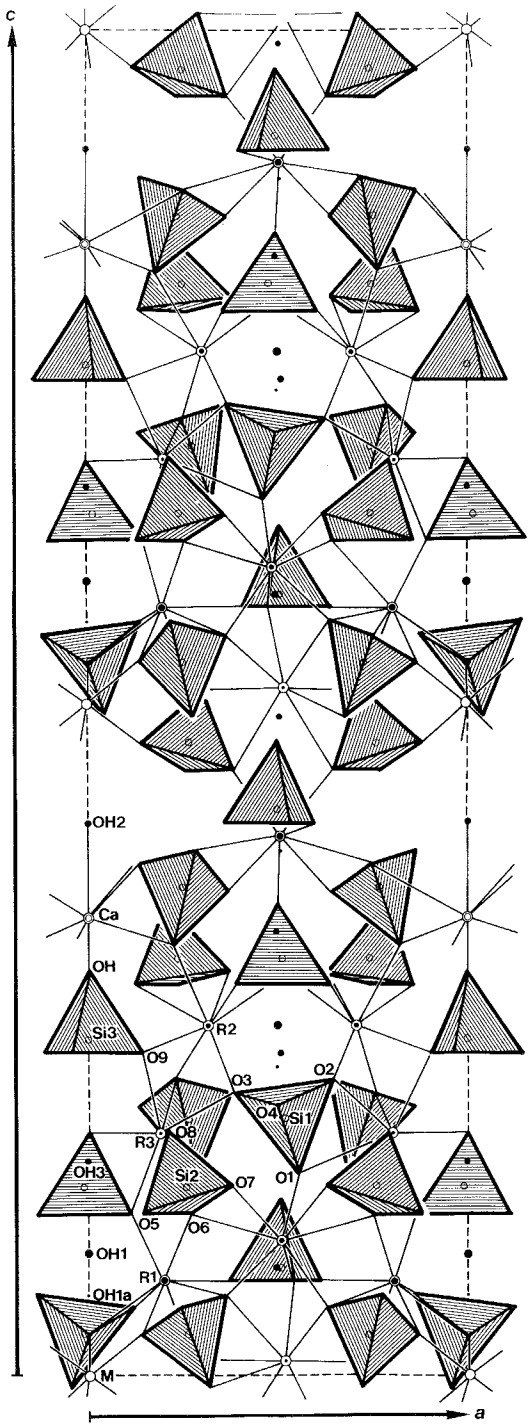

Fig. 42. The crystal structure of cerite-(Ce). Only half of the unit cell ($0 < y < 0.5$) is drawn.

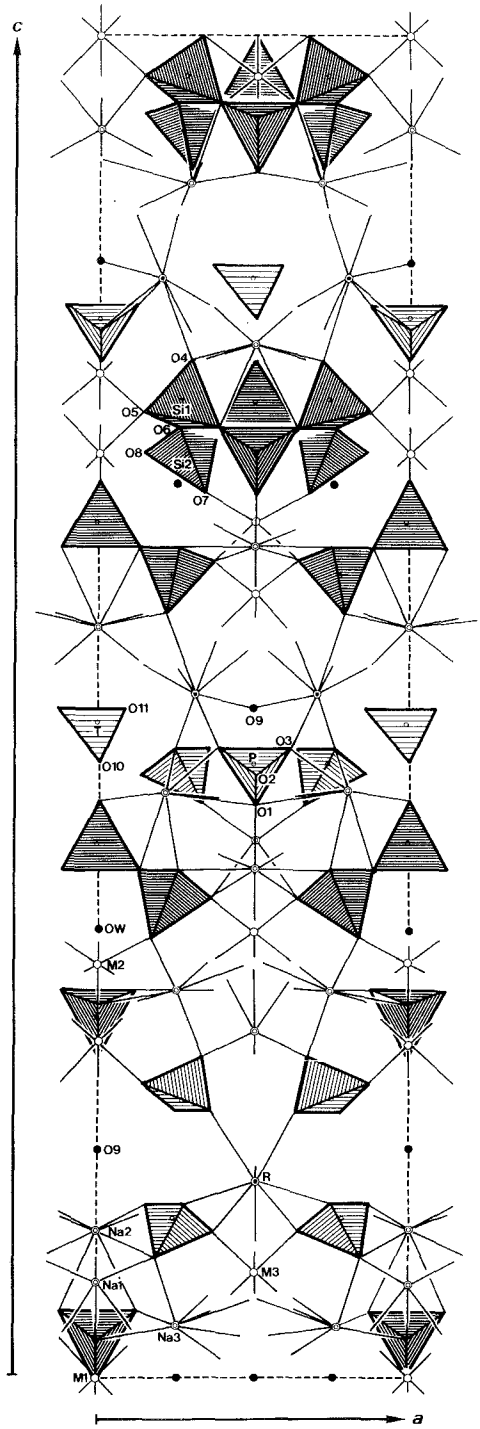

Fig. 43. The crystal structure of steenstrupine-(Ce). Only half of the unit cell ($0 < y < 0.5$) is drawn.

TABLE 94
Atomic parameters of cerite-(Ce)[a].

	K_b	x	y	z
R1	0.940(5)	0.2552(1)	0.1318(1)	0.0683(2)
R2	0.890(5)	0.1435(1)	0.2621(1)	0.4329(2)
R3	0.879(5)	0.2592(1)	0.1357(1)	0.1762(2)
Ca	0.169(9)	0	0	0.3444(13)
M	1.460(8)	0	0	0
Si1	1	0.3164(4)	0.1471(4)	0.3641(2)
Si2	1	0.1499(4)	0.3255(5)	0.1376(2)
Si3	0.862(7)	0	0	0.2524(2)
O1	1	0.2653(14)	0.0907(15)	0.3232(3)
O2	1	0.2764(9)	0.0034(9)	0.3871(3)
O3	1	0.2578(12)	0.2478(12)	0.3796(3)
O4	1	0.0857(10)	0.1785(10)	0.0334(3)
O5	1	0.2415(11)	0.2645(11)	0.1177(3)
O6	1	−0.0140(10)	0.2640(10)	0.1236(3)
O7	1	0.1682(9)	0.0743(10)	0.4655(3)
O8	1	0.1396(10)	0.2824(9)	0.1788(2)
O9	1	0.1602(11)	0.0392(12)	0.2398(3)
OH	0.866(9)	0	0	0.2967(5)
OH1a	0.097(8)	0	0	0.0638(37)
OH1	1	0	0	0.0900(5)
OH2	1	0	0	0.4090(5)
OH3	0.936(9)	0	0	0.1633(5)

[a] MoKα, $R = 0.032$ (1711 refl.).
[b] K, the site multiplicity, was based on Ce^{3+} for R, Mg^{2+} for M, Si^{4+} for Si3, Ca^{2+} for Ca and O^{-} for the oxygens.

TABLE 95
Interatomic distances for cerite-(Ce) in Å.

R1–O5	2.411(7)	R2–O2	2.397(7)
R1–O8	2.455(7)	R2–O3	2.421(7)
R1–O4	2.494(7)	R2–O7	2.465(7)
R1–O4	2.505(7)	R2–O7	2.496(7)
R1–O6	2.533(7)	R2–O9	2.513(7)
R1–O2	2.629(7)	R2–O1	2.546(7)
R1–O3	2.824(7)	R2–O5	2.659(7)
R1–O9	2.906(7)	R2–O6	2.871(7)
mean	2.595	mean	2.546
R3–O6	2.457(7)	M–O7	2.049(10) × 3
R3–O8	2.492(7)	M–O4	2.096(10) × 3
R3–O3	2.540(7)	mean	2.072
R3–O2	2.549(7)		
R3–O8	2.582(7)	Ca–OH	1.82(5)
R3–O9	2.640(7)	Ca–OH2	2.46(5)
R3–O5	2.669(7)	Ca–O1	2.64(4) × 3
R3–O1	2.953(7)	Ca–O3	3.04(5) × 3
mean	2.610	mean	2.67
Si1–O4	1.609(8)	Si2–O8	1.620(8)
Si1–O3	1.616(8)	Si2–O5	1.623(8)
Si1–O2	1.638(8)	Si2–O7	1.628(8)
Si1–O1	1.662(8)	Si2–O6	1.636(8)
mean	1.631	mean	1.627
Si3–O9	1.631(8) × 3		
Si3–OH	1.686(7)		
mean	1.645		

TABLE 96
Atomic parameters of steenstrupine-(Ce)[a].

	x	y	z	F[b]	K[b]	Occ.[b]
R	0.1311	0.2622(1)	0.18329(2)	Ce^{3+}	0.919(6)	
M1	0	0	0	Y^{3+}	0.89(2)	$Th_{0.42}Zr_{0.41}Ti_{0.10}Al_{0.07}$
M2	0	0	0.3137(1)	Fe^{2+}	1	$Mn_{0.745}Ca_{0.255}$
M3	0	0	0.2450(1)	Fe^{2+}	1	$Fe_{0.845}Mn_{0.155}$
Na1	0	0	0.0702(2)	Ca^{2+}	1	$Na_{0.735}Ca_{0.265}$
Na2	0.2742(7)	0.1371	0.4375(1)			
Na3	0.3330(7)	0.1665	0.2884(1)			
Si1	0.1580	0.3160(5)	0.3994(1)			
Si2	0.2966(5)	0.1483	0.3639(1)			
P	0.3600(4)	0.1800	0.2129(1)	P	1	$P_{0.77}Si_{0.23}$
T	0	0	0.4941(3)	P	0.88	
O1	0.4388(25)	0.2194	0.2416(3)			
O2	0.1844(10)	0.0922	0.2154(2)			
O3	0.3967(12)	0.3227(10)	0.1950(2)			
O4	0.1369	0.2738(14)	0.4334(3)			
O5	0.2448	0.4896(41)	0.3920(4)			
O6	0.2521(14)	0.2501(14)	0.3838(2)			
O7	0.2180(16)	0.1090	0.3340(3)			
O8	0.4758(37)	0.2379	0.3635(3)			
O9	0	0	0.1655(5)	O	1	OH^-
O10	0	0	0.4586(26)	O	0.67(14)	
O11	0.1380(34)	0.1528(41)	0.4969(14)	O	0.82(6)	
OW	0.3333	0.1667	0.6667	O	0.73(5)	H_2O

[a] MoKα, $R = 0.073$ (1740 refl.).
[b] Occupancies: F, form factors; K, site occupancies.

TABLE 97
Interatomic distances for steenstrupine-(Ce) in Å.

R–O11	2.45(6) (×1/2)	M1–O8	2.21(1) ×6
R–O9	2.51(1)		
R–O3	2.52(1) ×2	M2–O7	2.18(2) ×3
R–O4	2.56(1)	M2–O5	2.39(2) ×3
R–O2	2.57(1) ×2	mean	2.29
R–O3	2.58(1) ×2		
R–O11	2.72(12) (×1/2)	M3–O5	2.09(1) ×3
mean	2.56	M3–O2	2.15(1) ×3
		mean	2.12
Na1–O1	2.28(1) ×3		
Na1–O8	2.51(2) ×3	Si1–O4	1.59(1)
mean	2.40	Si1–O5	1.61(1)
		Si1–O6	1.62(1) ×2
Na2–O3	2.45(1) ×2	mean	1.61
Na2–O4	2.49(1) ×2		
Na2–O6	2.77(2) ×2	Si2–O7	1.54(2)
Na2–O1	3.14(2) ×2	Si2–O8	1.62(1)
mean	2.71	Si2–O6	1.63(1) ×2
		mean	1.61
Na3–O7	2.32(2)		
Na3–O1	2.33(2)	P–O1	1.49(1)
Na3–O6	2.62(2) ×2	P–O3	1.57(1) ×2
Na3–O5	2.69(1) ×2	P–O2	1.59(1)
Na3–O8	2.71(2) ×2	mean	1.56
mean	2.59		
		T–O11	1.53(3) ×3
		T–O10	1.61(12)
		mean	1.55

TABLE 98
Atomic parameters of phosinaite[a].

	x	y	z	B_{iso}
Ce	0	0.5	0.1394(2)	0.82(4)
Ca	0.0205(9)	0.2506(5)	0.5026(3)	1.99(8)
Ca,Na	0.0183(14)	0.2659(4)	0.1876(6)	3.85(15)
Na1	0	0	0.451(1)	3.58(28)
Na2	0	0	0.160(1)	4.43(32)
Na3	0.5	0.5	0.127(1)	3.06(25)
Na4	0.5	0	0.172(1)	3.25(26)
Na5	0.5	0	0.458(1)	3.19(27)
Na6	0.539(2)	0.259(1)	0.183(1)	4.37(26)
Na7	0.265(1)	0.141(1)	0.330(1)	1.93(16)
Na8	0.226(2)	−0.150(1)	0.002(1)	5.41(32)
Si1	0.3104(9)	0.3889(4)	0.3203(6)	2.19(13)
Si2	0.2552(9)	0.5885(4)	0.3642(5)	1.85(10)
P1	0.2342(9)	−0.1179(3)	0.3061(4)	1.49(10)
P2	0.2690(10)	0.1250(4)	0.0250(5)	1.99(11)
O1	0.256(2)	0.405(1)	0.196(1)	2.98(31)
O2	0.236(2)	0.297(1)	0.374(1)	2.88(29)
O3	0.537(3)	0.385(1)	0.326(1)	5.78(50)
O4	0.249(2)	0.479(1)	0.359(1)	3.03(21)
O5	0.787(2)	0.358(1)	0.471(1)	3.02(33)
O6	0.873(2)	0.396(1)	0.268(1)	4.18(40)
O7	0.585(2)	0.159(1)	0.353(1)	2.81(31)
O8	0.792(2)	0.149(1)	0.186(1)	3.11(33)
O9	0.756(2)	0.014(1)	0.314(1)	2.82(29)
O10	0.938(2)	0.150(1)	0.370(1)	3.05(34)
O11	0.955(3)	0.356(1)	0.035(1)	4.94(46)
O12	0.283(3)	0.158(1)	0.145(1)	4.11(38)
O13	0.743(3)	−0.023(1)	0.014(1)	5.00(43)
O14	0.602(3)	0.339(1)	0.027(2)	6.51(55)

[a] Mo, $R = 0.072$ (1117 refl.).

OKANOGANITE-(Y)
$(Na,Ca)_3Y_{12}Si_6B_2O_{27}F_{14}$
$(Na,Ca)_3Y_{12}Si_6B_2O_{27}F_{14}$

Sys.	trigonal (hex.)	$a = 10.72(1)$ Å	source: Okanogan Co., WA, USA
S.G.	R3, R$\bar{3}$, R32, R3m, R$\bar{3}$m, R3c or R$\bar{3}$c	$c = 27.05(8)$ Å	Ref.: Boggs (1980)
			JCPDS: #35-0483
$Z =$	3		
Dx =	4.37 g/cm^3		
Dm =	4.35 g/cm^3		

Okanoganite-(Y) was described by Boggs (1980). The crystal structure has not yet been reported. However, the similarity of the crystal systems and lengths of the *a*-axis of okanoganite-(Y) and cerite-(Ce) suggests some structural relationship between the two.

TABLE 99
Interatomic distances for phosinaite in Å.

Ce–O1	2.413(15)	Ca–O10	2.259(14)	Ca,Na–O11	2.322(17)		
Ce–O1	2.413(15)	Ca–O7	2.275(15)	Ca,Na–O6	2.336(17)		
Ce–O6	2.328(15)	Ca–O5	2.336(16)	Ca,Na–O8	2.411(16)		
Ce–O6	2.328(15)	Ca–O2	2.340(15)	Ca,Na–O12	2.515(18)		
Ce–O11	2.501(16)	Ca–O5	2.528(17)	Ca,Na–O1	2.650(16)		
Ce–O11	2.501(16)	Ca–O2	2.644(15)	Ca,Na–O2	2.800(15)		
Ce–O13	2.628(17)	mean	2.397	Ca,Na–O10	2.888(14)		
Ce–O13	2.628(17)			mean	2.565		
mean	2.468						
Na1–O10	2.449(13)	Na2–O13	2.574(19)	Na3–O1	2.412(15)	Na4–O9	2.540(14)
Na1–O10	2.449(13)	Na2–O13	2.574(19)	Na3–O1	2.412(15)	Na4–O9	2.540(14)
Na1–O9	2.463(14)	Na2–O9	2.597(15)	Na3–O13	2.560(19)	Na4–O13	2.619(18)
Na1–O9	2.463(14)	Na2–O9	2.597(15)	Na3–O13	2.560(19)	Na4–O13[a]	2.619(18)
Na1–O4	2.657(16)	Na2–O8	2.691(13)	Na3–O14	2.738(20)	Na4–O12	2.839(15)
Na1–O4	2.657(16)	Na2–O8	2.691(13)	Na3–O14	2.738(20)	Na4–O12	2.839(15)
mean	2.523	mean	2.621	mean	2.570	mean	2.666
Na5–O9	2.559(14)	Na6–O14	2.270(20)	Na7–O9	2.271(14)	Na8–O8	2.293(15)
Na5–O9	2.559(14)	Na6–O8	2.418(18)	Na7–O12	2.321(15)	Na8–O11	2.330(22)
Na5–O4	2.580(16)	Na6–O12	2.453(19)	Na7–O7	2.361(15)	Na8–O14	2.464(24)
Na5–O4	2.580(16)	Na6–O3	2.534(20)	Na7–O2	2.374(13)	Na8–O13	2.518(18)
Na5–O5	2.727(15)	Na6–O7	2.579(16)	Na7–O10	2.420(15)	Na8–O1	2.541(15)
Na5–O5	2.727(15)	mean	2.451	Na7–O5	2.439(14)	mean	2.429
Na5–O7	2.734(14)			mean	2.364		
Na5–O7	2.734(14)						
mean	2.650						
Si1–O2	1.573(13)	Si2–O5	1.571(14)	P1–O7	1.537(14)	P2–O14	1.446(20)
Si1–O1	1.608(13)	Si2–O6	1.581(17)	P1–O8	1.537(13)	P2–O12	1.508(15)
Si1–O3	1.637(16)	Si2–O3	1.613(17)	P1–O9	1.537(13)	P2–O13	1.525(15)
Si1–O4	1.671(13)	Si2–O4	1.637(12)	P1–O10	1.556(14)	P2–O11	1.575(17)
mean	1.627	mean	1.601	mean	1.542	mean	1.514

[a]O10 in the original paper may be mistyped.

PHOSINAITE
$Na_{11}(Na,Ca)_2Ca_2Ce_{0.67}(Si_4O_{12})(PO_4)_4$
$Na_{11}(Na,Ca)_2Ca_2Ce_{0.67}(Si_4O_{12})(PO_4)_4$

Sys. orthorhombic	$a = 7.234(3)$ Å	source: Khibiny, Kola Peninsula, Russia
S.G. $P2_12_12$	$b = 14.670(4)$ Å	Ref.: Krutik et al. (1981)
$Z = 2$	$c = 12.231(4)$ Å	JCPDS: #27-0666
AP: table 98	ID: table 99	IL: fig. 44

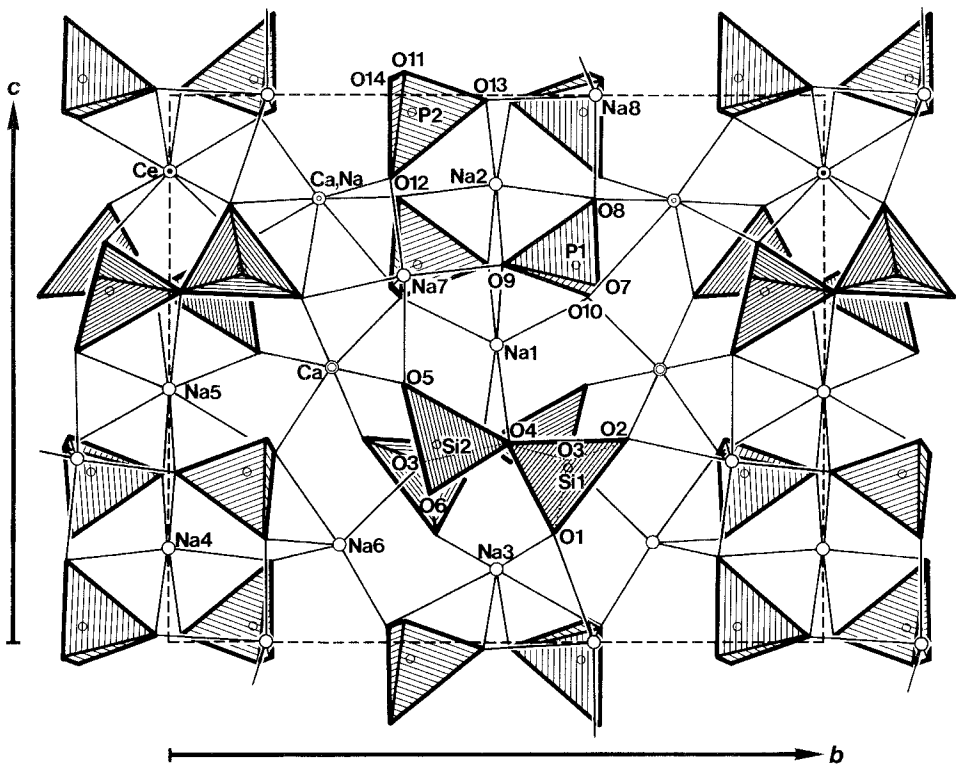

Fig. 44. The crystal structure of phosinaite.

In the structure of phosinaite (fig. 44) Si atoms form a four-membered ring of SiO_4 tetrahedra (Krutik et al. 1981). Four isolated PO_4 tetrahedra are linked by the polyhedra of Na7 and Na8. These tetrahedra are sandwiched by layers of Ce, Ca (Ca,Na) and the other Na polyhedra parallel to [100]. Two thirds of the Ce sites are occupied and the total charge is balanced. Therefore, the chemical formula $Na_{11}(Na,Ca)_2Ca_2Ce_{0.67}(Si_4O_{12})(PO_4)_4$ was given. It was revealed that the phosinaite structure has linked tetrahedral anionic groups. Krutik et al. (1981) reported that clinophosinaite $Na_3Ca[SiO_3](PO_4)$ is a monoclinic analogue of phosinaite and contains practically no rare earths. The presence of Ce in phosinaite reduces its contents of Ca and Na in comparison with clinophosinaite, corresponding to isomorphic replacement according to the scheme $Na + Ca \rightleftarrows Ce^{3+}$. Apparently Ce has an ordering influence on the whole structure; the two statistically distributed P2 tetrahedra in clinophosinaite are replaced by a fairly precisely fixed P2 tetrahedron in phosinaite (Krutik et al. 1981).

TABLE 100
Atomic parameters of cascandite[a].

	x	*y*	*z*
M1[b]	0.0027(1)	0.6629(1)	0.9128(1)
M2[c]	−0.0019(1)	0.6421(1)	0.4062(1)
Si1	0.2163(1)	0.0402(1)	0.0886(2)
Si2	0.2102(1)	0.0666(1)	0.5229(2)
Si3	0.2055(1)	0.8366(1)	0.7399(2)
OA1	0.1160(3)	0.4490(3)	0.8729(5)
OA2	0.1176(3)	0.4462(3)	0.4203(5)
OA3	0.1279(4)	0.6930(4)	0.2416(5)
OB1	0.1295(4)	0.1568(3)	−0.0262(5)
OB2	0.1479(4)	0.2006(3)	0.6291(5)
OB3	0.1113(4)	0.7139(3)	0.6736(5)
OC1	0.1571(4)	0.0538(4)	0.2871(5)
OC2	0.1507(4)	0.9458(3)	0.5940(5)
OC3	0.1815(4)	0.8981(3)	0.9601(5)
H	0.13	0.18	0.86

[a] MoKα, $R = 0.042$ (1526 refl.).
[b] M1: Ca. [c] M2: Sc.

TABLE 101
Interatomic distances for cascandite in Å.

M1–OB1	2.312(4)	M2–OB3	2.044(3)
M1–OB3	2.336(4)	M2–OA3	2.057(4)
M1–OA3	2.370(4)	M2–OB2	2.070(4)
M1–OA1	2.391(4)	M2–OA1	2.173(4)
M1–OA2	2.542(3)	M2–OA2	2.192(4)
M1–OA1	2.570(4)	M2–OA2	2.253(3)
mean	2.420	mean	2.131
M1–OC3	3.055(4)		
M1–OC3	3.090(4)		
Si1–OC1	1.614(4)	Si2–OB2	1.610(4)
Si1–OA1	1.617(4)	Si2–OC1	1.624(4)
Si1–OB1	1.628(4)	Si2–OC2	1.628(4)
Si1–OC3	1.639(4)	Si2–OA2	1.642(4)
mean	1.624	mean	1.626
Si3–OB3	1.604(4)		
Si3–OA3	1.609(4)		
Si3–OC2	1.627(4)		
Si3–OC3	1.647(4)		
mean	1.622		

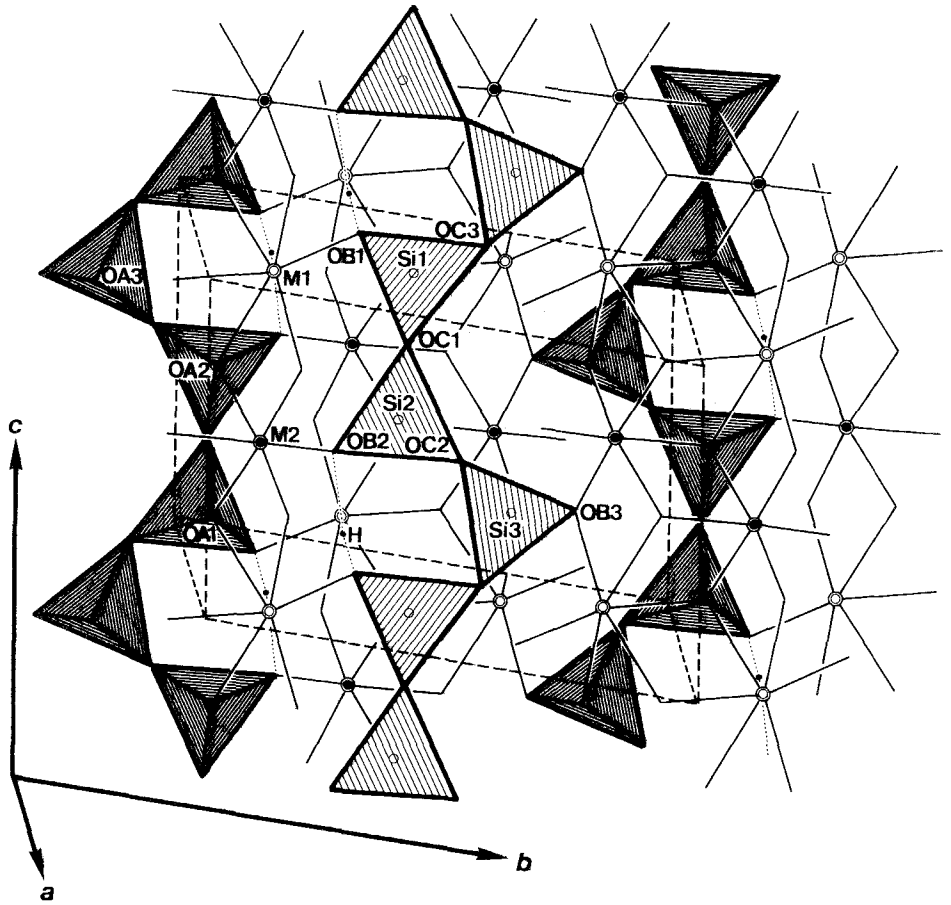

Fig. 45. The crystal structure of cascandite.

CASCANDITE		
$Ca(Se,Fe)Si_3O_9(OH)$		
$Ca(Se,Fe)Si_3O_8(OH)$		
Sys. triclinic	$a =$ 9.791(8) Å	source: Baveno, Italy
S.G. $C\bar{1}$	$b =$ 10.420(9) Å	Ref.: Mellini and Merlino (1982)
$Z = 4$	$c =$ 7.076(6) Å	JCPDS: #34-0169, #35-0541
	$\alpha =$ 98.91(8)°	
	$\beta =$ 102.63(8)°	
	$\gamma =$ 84.17(8)°	
AP: table 100	ID: table 101	IL: fig. 45

A new pyroxenoid mineral, cascandite, was described by Mellini et al. (1982), and its crystal structure was analyzed by Mellini and Merlino (1982). The structure of cascandite is similar to those of pectolite, $NaCa_2Si_3O_8(OH)$, and serandite, $Na(Mn,Ca)_2Si_3O_8(OH)$. The structure is composed of octahedral double chains, formed by two strands of edge-sharing octahedra, and tetrahedral single chains with

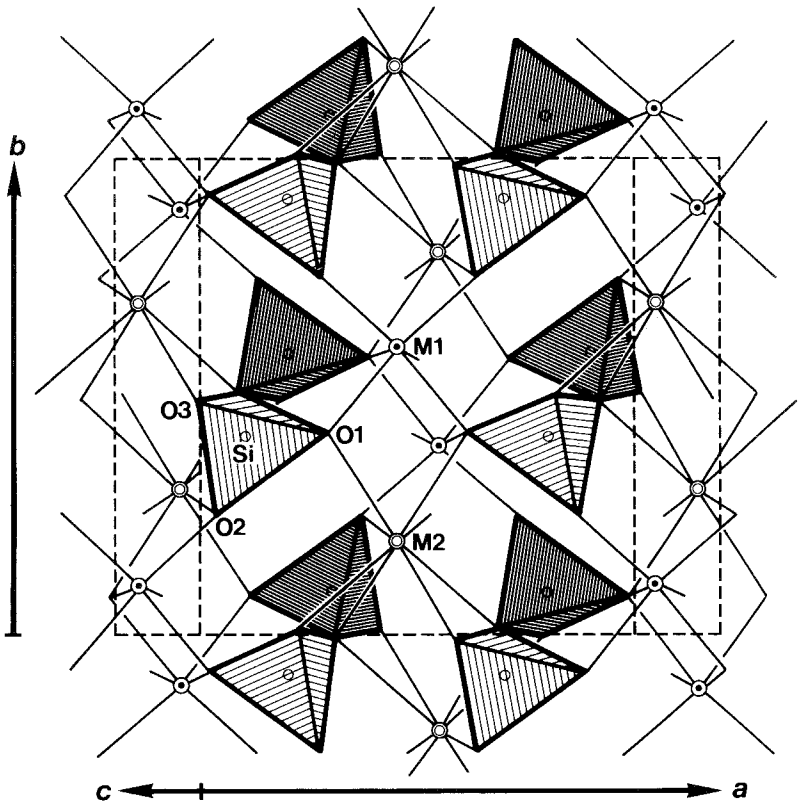

Fig. 46. The crystal structure of jervisite.

a repeat period of three SiO_4 tetrahedra (fig. 45). Scandium atoms occupy the smaller octahedral M2 site, and calcium atoms occupy the larger M1 site. Mellini and Merlino (1982) calculated the valence-bond balance and the two next neighboring oxygen atoms (OC3) were included into the coordination about the M1 atom, yielding a coordination number of 8 for the calcium site.

JERVISITE
$(Na,Ca,Fe)(Sc,Mg,Fe)Si_2O_6$
$(Na,Ca,Fe)(Sc,Mg,Fe)Si_2O_6$

Sys. monoclinic	$a =$ 9.8438(4) Å	source: synthetic $NaScSi_2O_6$
S.G. C2/c	$b =$ 9.0439(4) Å	Ref.: Hawthorne and Grundy (1973)
$Z = 4$	$c =$ 5.3540(2) Å	JCPDS: #21-1369, #35-0542
	$\beta = 107.215(2)°$	
AP: table 102	ID: table 103	IL: fig. 46

Jervisite is a scandium pyroxene and a natural analogue of the synthetic phase $NaScSi_2O_6$ (Mellini et al. 1982). The crystal structure of $NaScSi_2O_6$, the synthetic jervisite, was analyzed by Hawthorne and Grundy (1973). In the crystal structure (fig. 46), the Na atom occupies the M2 site which is considered as a very distorted square antiprism, and the Sc atom occupies the M1 site which is a distorted octahedra.

TABLE 102
Atomic parameters of jervisite[a].

	x	y	z	B_{eq}
M1[b]	0	0.89627(6)	1/4	0.42(1)
M2[c]	0	0.3036(2)	1/4	1.31(2)
Si	0.29130(6)	0.08731(6)	0.2439(1)	0.40(1)
O1	0.1182(1)	0.0785(2)	0.1455(3)	0.51(2)
O2	0.3591(2)	0.2479(2)	0.3072(3)	0.70(2)
O3	0.3504(2)	0.0082(2)	0.0179(3)	0.66(2)

[a] MoKα, $R = 0.028$ (781 refl.).
[b] M1: Sc. [c] M2: Na.

TABLE 103
Interatomic distances for jervisite in Å.

M1–O2	2.017(2) ×2	M2–O2	2.411(6) ×2
M1–O1	2.105(5) ×2	M2–O3	2.461(4) ×2
M1–O1	2.183(2) ×2	M2–O1	2.490(2) ×2
mean	2.102	M2–O3	2.894(3) ×2
		mean	2.564
Si–O2	1.592(2)		
Si–O1	1.630(3)		
Si–O3	1.653(2)		
Si–O3	1.653(3)		
mean	1.632		

EUDIALYTE (=barsanovite, eucolite)
$\{(Ca,Ce)_6Zr_3Fe_3(Si_3O_9)_2(Si_9O_{27})_2\}\{Na,K)_{16}(OH,Cl)_4\}$
$(Ca,Ce)_6Zr_3(Fe,\square)_3Si_{21}(Si,\square)_9(\square,K)_3(\square,Al)(\square,Mn)_3(Na,\square)_{46}O_{69}(O,\square)_6(OH,\square)_6(Cl,\square)_4$

Sys. trigonal (hex.)	$a = 14.257(3)$ Å	source:
S.G. R3m	$c = 30.05(2)$ Å	Ref.: Rastsvetaeva and Andrianov (1987)
$Z = 3$		JCPDS: #8-0355, #25-0814
Dx = 2.87 g/cm^3		
Dm = 2.74 g/cm^3		
AP: table 104	ID: table 105	IL: fig. 47

eucolite (= a variety of EUDIALYTE)
$\{Ca_6Zr_3Fe_3(Si_3O_9)_2(Si_9O_{27})_2\}\{(Na,K,Sr,R)_{16}(OH,Cl)_4\}$
$Ca_6Zr_3(\square,Fe)_3Si_{24}(Si,\square)_3(Ti,\square)(Nb,Al,\square)(Fe,Mn,\square)_3 -$
$(Na,K,Sr,R,Mg)_3(\square,Sr,Mg)_3(Na,\square)_{36}O_{69}(O,\square)_6(OH,\square)_6(Cl,\square)_2$

Sys. trigonal (hex.)	$a = 14.255(2)$ Å	source: Mt. Chasnochorr, Khibinskii, CIS
S.G. R3m	$c = 29.919(5)$ Å	Ref.: Rastsvetaeva et al. (1988)
$Z = 3$		
Dm = 3.0 g/cm^3		
AP: table 107	ID: table 106	IL: fig. 47

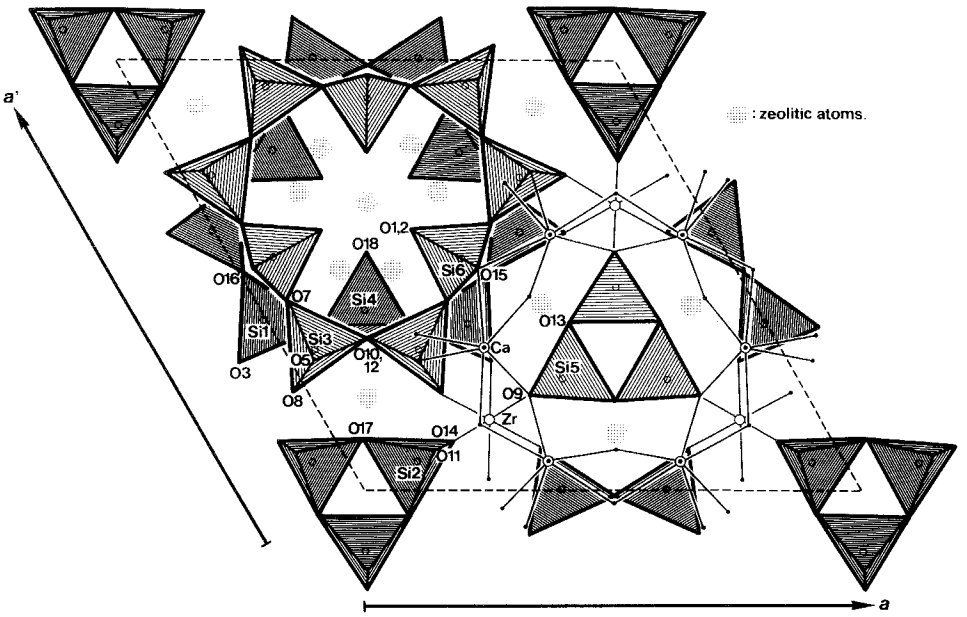

Fig. 47. The framework of the crystal structure of eudialyte.

The crystal structure of eudialyte (fig. 47) was reported as consisting of three- and nine-membered rings of Si tetrahedra (Golyshev et al. 1971, Giuseppetti et al. 1971, Golyshev et al. 1973). The additional Si and OH sites with partial occupancies are located at the centers of the rings. The rings are connected by large cations such as Zr, Fe, Na, and Ca. The rare earth elements may occupy the Ca site of six-coordination or the Na sites of seven- or eight-coordination.

Rastsvetaeva and Andrianov (1987) reexamined the crystal structure, especially the zeolitic part. Their analysis revealed incomplete occupancy of the Fe site and suggested that the Na4 and OH3 sites of Golyshev et al. (1973) should be changed to K and Cl sites, respectively. Moreover, they located 18 additional positions corresponding to Si9, Al, Mn, Na4–Na15, OH2, OH3, Cl3 and Cl4 in the zeolitic cavities. The Si6–(O1, O7, O7, O15) tetrahedron and Si10–(O2, O7, O7, O15) tetrahedron are related to each other and have disordered orientations. The crystallochemical formula of eudialyte, with separation of the framework and the zeolitic parts, is $\{Ca_6Zr_3[Si_3O_9]_2[Si_9O_{27}]_2\}^{24-}$–$\{(Na_{14.3}K_{1.3}Sr_{0.3})\ (Fe^{2+}_{1.9}Mn^{2+}_{0.5}Fe^{3+}_{0.1})\ (Si_{1.3}Al_{0.3}H_{0.4})(OH_{2.1}Cl_{1.7})\}^{24+}$.

Rastsvetaeva et al. (1988) analyzed the crystal structure of eucolite, a variety of eudialyte, characterized by a high content of heavy multivalent cations such as Fe, Mn, R, Nb, and Ca. The framework of Si, Zr, and Ca polyhedra remains unchanged in the structure of this variety, while the composition and distribution of the atoms

TABLE 104
Atomic parameters of eudialyte (=barsanovite, eucolite)[a].

	x	y	z	B	Occupancies		x	y	z	B	Occupancies
Zr	0.3335(1)	0.1667(1)	0.1667(1)	0.75(1)		Na14	0.125(1)	0.250(2)	0.334(1)	3.2(15)	1.0(2)/9
Fe[b]	0.0026(2)	0.5014(1)	−0.0002(1)	0.40(1)	5.8(1)/9	Na15[b]	0.561(4)	0.125(4)	0.005(4)	6.1(19)	0.5(1)/9
Ca	0.4063(1)	0.3331(1)	0.3335(1)	0.51(1)		O1[b]	0.2136(9)	0.6067(7)	0.2734(5)	3.1(3)	3.8(2)/9
Si1	0.6087(1)	0.6031(1)	0.0972(1)	0.63(3)		O2	0.2148(4)	0.6074(3)	0.2505(2)	1.9(1)	5.4(1)/9
Si2	0.1409(2)	0.0704(1)	0.0832(1)	0.55(4)		O3	0.4021(5)	0.3019(4)	0.1258(1)	1.6(1)	
Si3	0.2697(1)	0.3274(1)	0.2365(1)	0.56(3)		O4	0.6195(4)	0.0319(4)	0.0453(1)	1.3(1)	
Si4[b]	0.2093(1)	0.4183(1)	0.0760(1)	0.76(4)		O5	0.0457(4)	0.3006(4)	0.2890(1)	0.8(1)	
Si5	0.5267(2)	0.2634(1)	0.2510(1)	0.55(4)		O6	0.1001(4)	0.3799(4)	0.1073(1)	0.8(1)	
Si6	0.4586(1)	0.5414(1)	0.2584(1)	0.54(4)	7.5(1)/9	O7	0.5580(4)	0.6179(4)	0.2267(1)	1.6(1)	
Si7	0.3333	0.6667	0.0852(3)	0.8(1)	1.6(1)/3	O8	0.2627(4)	0.2294(3)	0.2072(1)	1.6(1)	
Si8	0.3333	0.6667	0.2451(2)	0.3(1)	1.3(1)/3	O9[b]	0.4423(2)	0.2209(1)	0.2908(1)	0.7(1)	
Si9	0.3333	0.6667	0.0548(2)	0.8(2)	1.1(1)/3	O10	0.1788(1)	0.3576(2)	0.2184(1)	1.3(1)	
Si10	0.4451(2)	0.5549(2)	0.2664(2)	0.6(1)	1.4(1)/9	O11[b]	0.1839(6)	0.0918(4)	0.1334(2)	1.4(1)	
K	0.1886(3)	0.0943(2)	0.2841(1)	1.0(1)	3.6(1)/9	O12	0.1784(3)	0.3567(4)	0.0290(2)	0.8(1)	
Al	0.3333	0.6667	0.2816(3)	1.4(3)	0.9(1)/3	O13[b]	0.6045(2)	0.3958(2)	0.2540(2)	0.8(1)	
Mn[b]	0.1869(1)	0.3736(2)	0.3315(1)	0.7(1)	1.6(1)/9	O14	0.2336(3)	0.1168(2)	0.0465(1)	1.2(1)	
Na1[b]	0.4378(3)	0.2190(2)	0.0550(1)	1.4(1)	6.8(1)/9	O15	0.4842(3)	0.5157(3)	0.3053(2)	1.1(1)	
Na2[b]	0.1076(2)	0.2154(3)	0.1547(2)	2.5(1)	6.4(1)/9	O16[b]	0.0121(3)	0.5062(2)	0.1170(1)	0.9(1)	
Na3	0.5749(2)	0.1498(4)	0.1699(2)	2.3(1)	6.3(1)/9	O17	0.0614(3)	0.1227(4)	0.0771(2)	1.1(1)	
Na4	0.4169(2)	0.5831(2)	0.1609(2)	2.9(1)	4.5(1)/9	O18[b]	0.2750(2)	0.5496(3)	0.0678(1)	3.1(1)	
Na5[b]	0.0782(3)	0.1566(5)	0.1742(2)	1.2(1)	2.5(1)/9	O19	0.4752(6)	0.2376(4)	0.2016(2)	1.4(1)	
Na6	0.4925(7)	0.7040(8)	0.1713(3)	2.2(2)	3.8(2)/18	OH1	0.3333	0.6667	0.1386(3)	1.0(3)	1.6(1)/3
Na7	0.1055(5)	0.2110(7)	0.3394(3)	1.7(2)	1.5(1)/9	OH2	0	0	0.3370(6)	2.6(4)	1.1(1)/3
Na8	0.5507(3)	0.1014(4)	0.1821(2)	1.4(2)	2.6(1)/9	OH3	0.285(2)	0.571(3)	0.3289(7)	4.7(7)	2.4(2)/9
Na9	0.2266(5)	0.1133(3)	0.2782(2)	1.6(2)	3.8(1)/9	OH4	0.3333	0.6667	0.1929(5)	1.4(4)	1.3(1)/3
Na10	0.188(2)	0.094(1)	0.2972(4)	1.7(1)	1.8(1)/9	Cl1	0.6667	0.3333	0.1030(3)	4.1(2)	1.6(1)/3
Na11	0.4730(8)	0.2365(6)	0.0459(2)	2.0(1)	2.2(1)/9	Cl2	0	0	0.2443(2)	4.1(1)	2.2(1)/3
Na12	0.188(2)	0.594(2)	0.146(1)	3.3(6)	0.7(1)/9	Cl3	0.6667	0.3333	0.0473(5)	4.1(2)	1.0(1)/3
Na13	0.3333	0.6667	0.2958(7)	2.4(4)	0.7(1)/3	Cl4	0	0	0.1916(8)	2.9(8)	0.4(1)/3

[a]X-ray is not specified, $R = 0.0250$ (1680 refl.).
[b]Maybe at the special position: 9 b m (x, $2x$, z; x, $-x$, z; $-2x$, $-x$, z). The slight discrepancies of atomic coordinates from the condition for the special position affect the interatomic distances in table 105.

TABLE 105
Interatomic distances for eudialyte in Å[a].

Zr–O19	2.040(7)	Fe^{b}–O5	2.029(5)	Ca–$O9^{b}$	2.294(3)		
Zr–O8	2.049(6)	Fe^{b}–O5	2.031(5)		2.300(3)		
Zr–O8	2.050(6)	Fe^{b}–O4	2.056(5)	Ca–O14	2.345(4)		
Zr–O3	2.072(5)	Fe^{b}–O4	2.058(5)	Ca–O12	2.366(5)		
Zr–O3	2.073(5)	mean	2.044	Ca–O5	2.379(6)		
Zr–O11	2.101(7)			Ca–O4	2.402(6)		
mean	2.064			Ca–O15	2.417(5)		
				mean	2.368		
Si1–O3	1.569(6)	Si2–O14	1.589(4)	Si3–O8	1.612(5)	$Si4^{b}$–O12	1.604(6)
Si1–O4	1.593(4)	$Si2–O11^{b}$	1.599(7)	Si3–O5	1.612(4)	$Si4^{b}–O18^{b}$	1.640(4)
Si1–O6	1.623(7)		1.599(7)	Si3–O7	1.645(4)		1.640(4)
$Si1–O16^{b}$	1.636(4)	Si2–O17	1.649(5)	Si3–O10	1.649(3)	$Si4^{b}$–O6	1.657(5)
	1.639(4)	Si2–O17	1.650(6)	mean	1.630	$Si4^{b}$–O6	1.660(5)
mean	1.606	mean	1.622			mean	1.640
$Si5–O9^{b}$	1.586(4)	Si6–O15	1.545(7)	$Si7–O18^{b}$	1.536(5)	Si8–O2	1.472(5)
	1.586(4)	Si6–O7	1.600(4)		1.537(5)	$Si8–O1^{b}$	1.705(13)
Si5–O19	1.615(7)	Si6–O7	1.600(4)	$Si7–O18^{b}$	1.536(5)		1.705(13)
$Si5–O13^{b}$	1.642(3)	Si6–O2	1.647(5)		1.537(5)	Si8–O2	1.472(5)
	1.646(3)	$Si6–O1^{b}$	1.677(12)	$Si7–O18^{b}$	1.537(5)	$Si8–O1^{b}$	1.705(13)
$Si5–O13^{b}$	1.643(4)		1.677(12)		1.537(5)		1.705(13)
	1.647(4)	mean[c]	1.601	Si7–OH1	1.605(13)	Si8–O2	1.473(5)
mean	1.623			mean[c]	1.547	$Si8–O1^{b}$	1.706(13)
							1.706(13)
						Si8–OH4	1.569(16)
						mean[c]	1.569
$Si9–O18^{b}$	1.496(4)	$Si10–O1^{b}$	1.299(12)				
	1.496(4)		1.299(12)				
$Si9–O18^{b}$	1.498(4)	Si10–O2	1.382(6)				
	1.498(4)	Si10–O15	1.517(8)				
$Si9–O18^{b}$	1.498(4)	Si10–O7	1.837(6)				
	1.498(4)	Si10–O7	1.837(6)				
Si9–OH2	1.537(19)	mean[c]	1.635				
mean[c]	1.502						
K–O5	2.605(5)	$Al–O1^{b}$	1.498(11)	Mn^{b}–O4	2.047(6)		
K–O5	2.605(6)		1.498(11)	Mn^{b}–O4	2.050(6)		
K–O12	2.788(7)	Al–O2	1.736(7)	Mn^{b}–O5	2.159(5)		
K–OH2	2.819(11)	$Al–O1^{b}$	1.498(11)	Mn^{b}–O5	2.161(5)		
K–O8	2.852(4)		1.498(11)	Mn^{b}–OH3	2.439(37)		
K–O8	2.852(5)	Al–O2	1.736(7)	mean[c]	2.125		
K–O9	3.139(5)	$Al–O1^{b}$	1.500(11)				
mean[c]	2.808		1.500(11)				
		Al–O2	1.737(7)				
K–C12	2.618(5)	Al–OH3	1.848(29)				
[mean[c]	2.788][d]	Al–OH3	1.848(29)				
		Al–OH3	1.848(29)				
		mean[c]	1.682				

TABLE 105 (cont'd)

Na1[b]–O4	2.520(6)	Na2[b]–O11[b]	2.566(6)	Na3–O19	2.505(6)	Na4–OH1	2.169(5)
Na1[b]–O4	2.523(5)		2.570(9)	Na3–O19	2.505(10)	Na4–OH4	2.276(8)
Na1[b]–O14	2.534(5)	Na2[b]–O11[b]	2.568(7)	Na3–O16[b]	2.554(6)	Na4–O16[b]	2.315(6)
Na1[b]–O3	2.605(6)		2.572(10)		2.554(6)		2.315(6)
Na1[b]–O3	2.606(6)	Na2[b]–O10	2.597(6)	Na3–O3	2.566(6)	Na4–O7	2.684(7)
Na1[b]–O15	2.653(7)	Na2[b]–O17	2.598(8)	Na3–O3	2.566(7)	Na4–O7	2.684(7)
Na1–OH3	3.032(30)	Na2[b]–O8	2.639(7)	Na3–O13[b]	2.630(8)	Na4–O2	2.759(9)
	3.044(33)	Na2[b]–O8	2.641(7)		2.630(8)	Na4–O6	3.024(6)
Na1[b]–OH3	3.033(30)	Na2[b]–O6	2.791(8)	mean	2.544	Na4–O6	3.024(6)
	3.045(33)	Na2[b]–O6	2.793(7)			mean[c]	2.675
mean[c]	2.612	mean	2.650				
Na1[b]–Cl3	2.836(4)	Na2[b]–Cl4	2.881(10)	Na3–Cl1	3.029(8)		
Na1[b]–Cl1	3.173(5)	[mean[c]	2.653][d]	[mean[c]	2.593][d]		
mean[c]	3.043						
[mean[c]	2.662][d]						
Na5[b]–O11[b]	2.448(7)	Na6–OH4	2.156(11)	Na7–O5	2.396(12)	Na8–O16[b]	2.406(7)
	2.451(10)	Na6–OH1	2.278(11)	Na7–O5	2.396(9)		2.406(7)
Na5[b]–O11[b]	2.451(8)	Na6–O10	2.407(9)	Na7–OH2	2.606(9)	Na8–O13[b]	2.534(8)
	2.454(11)	Na6–O7	2.509(13)	Na7–O4	2.683(8)		2.534(8)
Na5[b]–O8	2.498(8)	Na6–O6	2.577(11)	Na7–O4	2.683(11)	Na8–O3	2.705(7)
Na5[b]–O8	2.500(7)	Na6–O2	2.762(11)	Na7–O18[b]	2.922(8)	Na8–O3	2.705(7)
Na5[b]–O10	2.815(7)	Na6–O6	3.119(10)		2.927(8)	Na8–O7	2.708(7)
Na5[b]–O17	2.948(9)	mean[c]	2.423	Na7–O18[b]	2.922(11)	Na8–O7	2.708(8)
mean	2.611				2.927(11)	Na8–O19	2.713(7)
Na5[b]–Cl4	2.003(9)			mean[c]	2.664	Na8–O19	2.713(10)
Na5[b]–Cl2	2.859(8)					mean	2.649
mean[c]	2.728						
[mean[c]	2.625][d]						
Na9–O5	2.514(7)	Na10–O12	2.470(19)	Na11–OH3	2.564(3)	Na12–OH1	1.808(25)
Na9–O5	2.514(7)	Na10–OH2	2.611(24)	Na11–OH3	2.564(3)	Na12–OH4	2.281(28)
Na9–O8	2.589(7)	Na10–O5	2.615(15)	Na11–O15	2.592(9)	Na12–O16[b]	2.340(26)
Na9–O8	2.589(7)	Na10–O5	2.615(26)	Na11–O4	2.595(10)		2.340(26)
Na9–O9[b]	2.690(7)	mean[c]	2.578	Na11–O4	2.595(12)	Na12–O18[b]	2.869(28)
	2.690(7)			Na11–O3	2.932(8)		2.872(28)
Na9–O12	2.730(9)	Na10–C12	2.813(22)	Na11–O3	2.932(10)	Na12–O18[b]	2.869(32)
mean	2.604	[mean[c]	2.614][d]	Na11–O14	2.956(11)		2.872(32)
Na9–C12	2.978(7)			mean[c]	2.750	Na12–O6	2.901(27)
[mean[c]	2.645][d]			Na11–C13	2.392(10)	Na12–O6	2.901(34)
				Na11–C11	2.943(10)	mean[c]	2.730
				mean[c]	2.731		
				[mean[c]	2.748][d]		

TABLE 105 (cont'd)

Na13–OH3	1.544(34)	Na14–O5	2.108(23)	Na15–OH3	1.420(65)
Na13–OH3	1.545(34)	Na14–O5	2.108(28)	Na15–O4	2.215(76)
Na13–OH3	1.545(34)	Na14–O4	2.450(20)	Na15–O4	2.243(88)
Na13–O1[b]	1.624(15)	Na14–O4	2.450(30)	Na15–O5	2.855(72)
	1.624(15)	Na14–OH2	3.088(25)	Na15–O5	2.877(84)
Na13–O2	1.998(15)	mean[c]	2.347	Na15–O1[b]	2.957(94)
Na13–O1[b]	1.624(15)				2.960(94)
	1.624(15)			Na15–O1[b]	2.976(86)
Na13–O2	1.998(15)				2.978(86)
Na13–O1[b]	1.625(15)			mean[c]	2.634
	1.625(15)				
Na13–O2	1.999(15)			Na15–C13	2.869(69)
Na13–OH4	3.092(26)			[mean[c]	2.645]
mean[c]	1.915				
Na13–C13	2.549(26)				
[mean[c]	1.961][d]				

[a]Recalculated by RM.
[b]Atoms may be at the special positions. Reconsideration is necessary.
[c]Mean values weighted by occupancies.
[d][mean]: an average of both M–O and M–Cl distances.

in the zeolitic cavities are individual and influence the properties of the mineral in a definite way. The characteristic composition of eucolite primarily involves the transformation of the configuration of the nine-membered rings and the adjacent microregions. The complexity of the composition also leads to a large number of positions having heavy isomorphic impurities which are concentrated in a microregion adjoining one of the nine-fold rings. The absence of similar concentrations in the microregion of the second zeolitic chamber strengthens the acentricity of the eucolite structure. The chemical formula separated into framework and zeolitic parts, given by Rastsvetaeva et al. (1988), is $\{Ca_6Zr_3[Si_3O_9]_2[Si_9O_{27}]_2\}^{24-}$–$\{[Na_9(Na,K,Sr,R,Mg)_6][Fe^{2+}_{1.2}(Fe^{2+},Fe^{3+},Mn)_{1.8}][Si_{1.1}(Nb,Al,Ti,H)_{0.9}][(OH)_{3.1}$-$Cl_{1.4}]\}^{24+}$.

Rastsvetaeva et al. (1990) analyzed the crystal structure of potassium oxonium eudialyte, in which a large part of the sodium is replaced by H_3O^+ or potassium. They reported that coordination polyhedra of iron atoms in the shape of a plane square and a five-pointed square pyramid were not observed in the structure of their eudialyte specimen, whereas they were found in those of eudialyte (Rastsvetaeva and Andrianov 1987) and eucolite (Rastsvetaeva et al. 1988). The octahedron is the coordination polyhedron for the iron atoms in potassium–oxonium eudialyte, in which the cation position is split into two parts (Fe^{3+} and M) 0.71(2) Å apart. They pointed out that it is important to note the relative orderliness of the zeolitic part in potassium–oxonium eudialyte compared with the other varieties of eudialyte. The number of sites for zeolitic atoms with a fixed number of positions for framework atoms, 26, varies from 31 to 16 in the crystal structures of the varieties of eudialyte (Rastsvetaeva et al. 1990). The number of the site for the zeolitic atoms in potassium–

TABLE 106
Interatomic distances for eucolite in Å[a].

Zr–O3	2.07(1) ×2	Fe–O4	2.05(1) ×2	Ca–O9	2.28(1)		
Zr–O8	2.07(1) ×2	Fe–O5	2.05(1) ×2	Ca–O14	2.33(1)		
Zr–O19	2.07(1) ×2	Fe–OH5	2.54(10)	Ca–O12	2.35(1)		
Zr–O11	2.10(1) ×2	Fe–OH3	2.58(1)	Ca–O5	2.36(1)		
mean	2.08	mean	2.22	Ca–O4	2.38(1)		
				Ca–O15	2.42(1)		
				mean	2.35		
Si1–O3	1.60(1)	Si2–O14	1.53(1)	Si3–O5	1.60(1)	Si4–O12	1.57(1)
Si1–O4	1.60(1)	Si2–O11	1.58(1)	Si3–O8	1.60(1)	Si4–O18	1.59(1)
Si1–O6	1.61(1)	Si2–O17	1.65(1)	Si3–O10	1.61(1)	Si4–O6	1.65(1) ×2
Si1–O16	1.63(1)	Si2–O17	1.66(1)	Si3–O7	1.67(1)	mean	1.62
mean	1.61	mean	1.61	mean	1.62		
Si5–O19	1.61(1)	Si6–O2	1.59(1)	Si7–O18	1.58(3) ×3	Si8–OH4	1.49(4)
Si5–O9	1.64(1)	Si6–O15	1.59(1)	Si7–OH1	1.63(1)	Si8–O1	1.61(2) ×3
Si5–O13	1.64(1) ×2	Si6–O7	1.63(1)	mean	1.59	mean	1.58
mean	1.63	Si6–O1	1.66(2)			Si8–O2	1.52(1) ×3
		mean	1.62			mean	1.55
Si9–O18	1.52(1) ×3	Ti–OH5	1.72(9) ×3	M1–OH3	1.90(1) ×3	M2–O4	2.07(1) ×2
Si9–OH2	1.64(3)	Ti–O18	1.77(1) ×3	M1–O2	2.04(1) ×3	M2–O5	2.10(1) ×2
mean	1.55	mean	1.75	mean	1.97	M2–OH3	2.11(1)
Si9–OH5	2.07(8) ×3	Ti–OH2	1.03(3)	M1–O1	1.68(2) ×3	mean	2.09
mean	1.77			mean	1.87		

M3–O4	2.52(1) ×2	M4–O5	2.50(1) ×2	Na1–O5	2.60(1) ×2	Na2–O8	2.59(1) ×2
M3–O15	2.58(1)	M4–O9	2.61(1)	Na1–O12	2.62(1)	Na2–O11	2.59(1) ×2
M3–OH3	2.65(1) ×2	M4–O8	2.62(1) ×2	Na1–OH2	2.67(2)	Na2–O10	2.60(1)
M3–O3	2.81(1) ×2	M4–O12	2.65(1)	Na1–O8	2.97(1) ×2	Na2–O17	2.65(1)
M3–O14	2.92(1)	mean	2.58	Na1–O9	3.07(1)	Na2–O6	2.84(1) ×2
mean	2.68	M4–Cl2	2.93(1)	mean	2.79	mean	2.66
M3–Cl1	2.89(1)	[mean][c]	2.63	Na1–OH5	2.58(9) ×2		
[mean][c]	2.71			mean	2.74		
Na3–O19	2.53(1) ×2	Na4–OH1	2.20(2)	Na5–O11	2.45(1) ×2	Na6–OH1	2.22(1)
Na3–O16	2.54(1)	Na4–O16	2.27(2)	Na5–O8	2.47(1)	Na6–O10	2.29(1)
Na3–O3	2.60(1) ×2	Na4–OH4	2.39(2)	Na5–O10	2.82(1)	Na6–O2	2.49(1)
Na3–O13	2.61(1)	Na4–O2	2.74(3)	Na5–O17	2.91(1)	Na6–O2	2.71(2)
Na3–O7	3.04(1) ×2	Na4–O7	2.76(2) ×2	mean	2.62	Na6–O7	2.81(2)
mean	2.69	Na4–O6	2.96(2) ×2			Na6–O6	3.05(1)
		mean	2.63			mean	2.60
						Na6–OH4	1.86(1)
						Na6–O1	2.95(2)
						mean[b]	2.55
Na7–OH1	2.07(3)	Na8–O16	2.45(1)	Na9–O16	2.53(4)	Na10–O19	2.51(2) ×2
Na7–OH4	2.23(3)	Na8–O13	2.56(1)	Na9–O18	2.83(4) ×2	Na10–O3	2.55(2) ×2
Na7–O16	2.52(4)	Na8–O7	2.61(1) ×2	Na9–O6	2.94(3) ×2	Na10–O16	2.75(3)
Na7–O6	2.67(4)	Na8–O19	2.69(1) ×2	Na9–O2	3.08(3)	Na10–O13	2.93(3)
Na7–O7	2.67(3)	Na8–O3	2.71(1) ×2	mean	2.86	mean	2.63
Na7–O2	2.70(3)	mean	2.63	Na9–OH1	1.61(4)	Na10–Cl1	2.57(3)
mean	2.48			Na9–OH4	2.19(4)	[mean][c]	2.62
				[mean][c]	2.62		

[a]Recalculated by RM. [b]Mean of the 8 distances. [c]Mean of the distances to oxygen and chlorine.

TABLE 107
Atomic parameters of eucolite[a].

	x	y	z	B	Occupancies		x	y	z	B	Occupancies
Zr	0.3295(1)	0.1647(1)	0.1667(1)	0.74(1)		O1	0.214(2)	0.607(1)	0.2685(5)	2.9(4)	0.34
Fe^{2+}	0.0039(3)	0.5021(2)	0.0009(1)	0.69(3)	0.44	O2	0.2105(6)	0.6053(4)	0.2498(2)	1.1(1)	0.67
Ca	0.4060(1)	0.3322(1)	0.3332(1)	0.64(1)		O3	0.4009(5)	0.2987(4)	0.1252(2)	1.9(1)	
Si1	0.6090(1)	0.6039(1)	0.0967(1)	0.83(3)		O4	0.6231(4)	0.0355(4)	0.0446(1)	1.2(1)	
Si2	0.1407(2)	0.0702(1)	0.0809(1)	0.92(4)		O5	0.0450(4)	0.3001(4)	0.2892(1)	1.3(1)	
Si3	0.2664(1)	0.3264(1)	0.2367(1)	0.62(3)		O6	0.1033(4)	0.3858(5)	0.1061(2)	1.8(1)	
Si4	0.2097(1)	0.4192(1)	0.0738(1)	0.67(4)		O7	0.5679(4)	0.6108(4)	0.2265(2)	2.1(1)	
Si5	0.5268(2)	0.2634(1)	0.2502(1)	0.75(4)		O8	0.2576(4)	0.2284(4)	0.2072(2)	1.7(1)	
Si6	0.4587(1)	0.5412(1)	0.2565(1)	1.03(4)		O9	0.4359(5)	0.2177(4)	0.2900(2)	1.8(1)	
Si7	1/3	2/3	0.0865(2)	0.4(1)	0.60	O10	0.1785(2)	0.3569(3)	0.2192(2)	1.4(1)	
Si8	1/3	2/3	0.2467(7)	1.3(3)	0.28	O11	0.1833(6)	0.0915(4)	0.1308(2)	2.0(1)	
Si9	1/3	2/3	0.0554(4)	1.4(3)	0.21	O12	0.1787(3)	0.3574(4)	0.0281(2)	1.6(1)	
Ti	0	0	0.3684(4)	1.0(2)	0.16	O13	0.6055(3)	0.3948(3)	0.2543(2)	1.4(1)	
M1	1/3	2/3	0.2956(1)	1.4(1)	0.71(Nb,Al)	O14	0.2286(4)	0.1143(3)	0.0447(2)	1.5(1)	
M2	0.1838(1)	0.3675(1)	0.3301(1)	0.96(3)	0.53(Fe,Mn)	O15	0.4804(3)	0.5159(3)	0.3055(2)	1.3(1)	
M3	0.4649(1)	0.2324(1)	0.0480(1)	1.06(3)	1 (Na,R)	O16	0.0143(5)	0.5072(4)	0.1152(2)	1.5(1)	
M4	0.2258(5)	0.1129(4)	0.2797(2)	2.7(1)	0.36(Sr,Mg)	O17	0.0621(3)	0.1241(4)	0.0744(3)	1.8(1)	
Na1	0.1876(6)	0.0938(4)	0.2895(3)	1.5(2)	0.58	O18	0.2735(3)	0.5470(4)	0.0676(4)	5.3(2)	
Na2	0.1083(3)	0.2167(5)	0.1543(3)	3.1(1)	0.62	O19	0.4753(5)	0.2377(4)	0.2006(2)	1.7(1)	
Na3	0.5690(3)	0.1381(4)	0.1723(2)	1.7(1)	0.60	OH1	1/3	2/3	0.1411(4)	1.3(3)	0.66
Na4	0.4194(8)	0.5806(8)	0.1606(9)	2.8(4)	0.13	OH2	0	0	0.334(1)	3.0(1)	0.32
Na5	0.0805(4)	0.1611(6)	0.1704(3)	1.8(2)	0.36	OH3	0.2688(4)	0.5368(5)	0.3310(3)	1.9(2)	0.57
Na6	0.4793(8)	0.7247(14)	0.1837(4)	3.1(2)	0.23	OH4	1/3	2/3	0.197(1)	0.9(6)	0.27
Na7	0.179(3)	0.554(3)	0.162(1)	3.0(6)	0.09	OH5	0.209(8)	0.605(6)	0.009(2)	1.7(9)	0.04
Na8	0.5523(4)	0.1044(6)	0.1809(3)	1.0(2)	0.27	Cl1	2/3	1/3	0.0971(3)	3.6(1)	0.73
Na9	0.204(3)	0.602(2)	0.147(1)	4.6(9)	0.19	Cl2	0	0	0.2497(4)	3.6(2)	0.64
Na10	0.592(1)	0.184(2)	0.157(1)	1.8(4)	0.11						

[a]X-ray is not specified, $R = 0.0273$ (1640 refl.).

TABLE 108
Atomic parameters of ashcroftine-(Y)[a].

	Occ.	x	y	z
Y1	1	0.3556(1)	0.1152(1)	0.1468(1)
Y2	1	0.2679(1)	0.1618(1)	0
K1	1	0.2704(5)	0	1/2
K2	1	0.3057(4)	0	0
Na1	1	1/2	0	1/4
Si1	1	0.2414(1)	0.1510(1)	0.4128(2)
Si2	1	0.2697(2)	0.0635(1)	0.2945(2)
Si3	1	0.2188(2)	0.0630(1)	0.1339(2)
C1	1	0.4002(9)	0	0.1582(15)
C2	1	0.3709(11)	0.0923(10)	1/2
O1	1	0.2371(4)	0.0935(4)	0.3644(5)
O2	1	0.2235(4)	0.0619(4)	0.2264(5)
O3	1	0.3018(3)	0.1780(4)	0.4034(5)
O4	1	0.2682(4)	0.0970(4)	0.0958(5)
O5	1	0.3247(4)	0.0958(4)	0.2695(5)
O6	1	0.1595(4)	0.0875(5)	0.1160(8)
O7	1	0.1912(4)	0.1912	0.3848(6)
O8	1	0.2297(6)	0.1322(5)	1/2
O9	1	0.2807(6)	0	0.3205(8)
O10	1	0.2200(7)	0	0.1033(8)
O11	1	0.4261(5)	0.0469(5)	0.1713(7)
O12	1	0.3529(7)	0	0.1315(10)
O13	1	0.3596(5)	0.0693(4)	0.4353(5)
O14	1	0.3932(6)	0.1411(6)	1/2
OH1	1	0.2473(5)	0.2473	1/2
OW1[b]	1	0.1264(7)	0.1264	0.2782(9)
OW2[b]	1	1/2	0	0
K1D	0.30	0.2158(10)	0.2158	0.2057(21)
Na1D	0.45	0.4181(10)	0	0.3924(15)
Na2D	0.28	0.3900(17)	0	0.3585(25)
Na3D	0.42	0	0	0
T1D	0.38Si	0.1336(4)	0.1336	0.0622(8)
T2D	0.39Si	0.0986(5)	0.0986	0.0905(11)
ϕ1D	$0.49OH^-$	0.1859(9)	0.1859	0.0772(21)
ϕ2D	$0.30OH^-$	0.0532(10)	0.0532	0.1270(26)
ϕ3D	$0.13H_2O$	0.1441(37)	0.1086(41)	0
ϕ4D	$0.54O^{2-}$	0.0983(12)	0.0983	0
ϕ5D	$0.36H_2O$	0.1036(29)	0	0
ϕ6D	$0.50OH^-$	0.1733(15)	0.1733	0

[a] MoKα, $R = 0.058$ (1774 refl.).
[b] H_2O.

TABLE 109
Interatomic distances for ashcroftine-(Y) in Å.

Y1–O5	2.321(8)	Y2–OH1	2.21(1)	K1–O13	2.94(1) ×4	K2–O12	2.57(2) ×2
Y1–O3	2.321(8)	Y2–O4	2.29(1) ×2	K1–O9	3.15(1) ×2	K2–O10	2.74(2) ×2
Y1–O4	2.322(9)	Y2–ϕ6D	2.29(4)	K1–O8	3.32(1) ×2	K2–O14	2.86(2) ×2
Y1–O5	2.363(9)	Y2–O3	2.30(1) ×2	K1–O1	3.36(1) ×4	K2–O4	3.01(1) ×4
Y1–O13	2.382(10)	Y2–ϕ1D	2.46(3) ×2	mean	3.18	mean	2.84
Y1–O11	2.395(11)	Y2–O14	2.55(2)				
Y1–O14	2.580(2)	mean	2.35	Na1–O11	2.51(1) ×8		
Y1–O12	2.779(2)						
mean	2.433						
Si1–O3	1.595(9)	Si2–O5	1.591(10)	Si3–O6	1.571(11)		
Si1–O8	1.617(6)	Si2–O9	1.611(6)	Si3–O4	1.586(10)		
Si1–O7	1.619(10)	Si2–O1	1.622(10)	Si3–O10	1.603(6)		
Si1–O1	1.622(9)	Si2–O2	1.629(10)	Si3–O2	1.624(9)		
mean	1.613	mean	1.613	mean	1.596		
C1–O12	1.23(2)	C2–O13	1.29(1) ×2				
C1–O11	1.30(3) ×2	C2–O14	1.29(3)				
mean	1.28	mean	1.29				
K1D–ϕ1D	2.47(5)	Na1D–O11	2.26(2) ×2	Na2D–O13	2.26(4) ×2	Na1D–Na2D	0.90(3)
K1D–O7	3.24(4)	Na1D–O13	2.30(2) ×2	Na2D–O11	2.39(3) ×2	Na3D–ϕ5D	2.49(1) ×4
K1D–OW1	3.29(4)	Na1D–OW2	2.74(2)	Na2D–O9	2.67(4)	Na3D–ϕ2D	2.86(1) ×8
K1D–O3	3.21(4) ×2	mean	2.37	mean	2.39	mean	2.74
mean	3.08						
T1D–O6	1.54(2) ×2	T2D–O6	1.55(2) ×2	T1D–ϕ3D	1.33(5) ×2		
T1D–ϕ4D	1.67(2)	T2D–ϕ4D	1.58(2)	T1D–ϕ6D	1.78(3)		
T1D–ϕ1D	1.79(2)	T2D–ϕ2D	1.67(3)				
mean	1.64	mean	1.59				

TABLE 110
Atomic parameters of miserite[a].

	x	y	z	B (Å^2)
R	0.00757(16)	0.60253(10)	0.15005(24)	1.72(4)
Ca,K[b]	0	0	0.5	1.22(10)
K	0.32021(29)	0.99315(18)	0.15955(44)	1.46(6)
Ca1	0.40066(21)	0.26328(14)	0.51548(31)	1.13(5)
Ca2	0.40829(21)	0.25742(13)	0.02070(29)	0.83(5)
Ca3	0.36304(22)	0.61689(14)	0.07902(31)	1.16(5)
Ca4	0.00483(21)	0.40187(12)	0.34005(33)	1.04(5)
Ca5	0.64636(22)	0.38063(14)	0.40674(31)	1.13(6)
Si1	0.28670(27)	0.44355(17)	0.29577(39)	0.77(8)
Si2	0.71369(27)	0.55740(17)	0.27878(39)	0.77(6)
Si3	0.70028(34)	0.90456(20)	0.32885(49)	0.73(6)
Si4	0.61346(27)	0.10334(17)	0.33692(39)	0.74(7)
Si5	0.76951(26)	0.18751(17)	0.14196(40)	0.69(6)
Si6	0.90073(17)	0.81847(18)	0.11888(39)	0.84(6)
Si7	0.23322(31)	0.80826(21)	0.28473(44)	0.75(5)
Si8	0.09730(34)	0.18089(22)	0.30029(49)	0.68(7)
O1	0.12345(90)	0.45144(66)	0.13560(120)	1.14(11)
O2	0.40191(99)	0.35875(65)	0.26502(121)	1.18(11)
O3	0.34456(94)	0.52995(57)	0.29881(139)	1.35(12)
O4	0.73283(95)	0.57700(58)	0.50477(141)	1.57(15)
O5	0.59977(119)	0.63990(72)	0.17052(183)	1.29(14)
O6	0.88067(79)	0.55533(49)	0.29494(120)	1.26(13)
O7	0.67354(78)	0.46506(48)	0.20091(112)	1.94(13)
O8	0.60037(95)	0.83471(58)	0.24654(140)	1.51(12)
O9	0.60012(93)	0.00046(56)	0.29928(111)	1.57(12)
O10	0.80172(71)	0.90022(44)	0.19590(105)	1.44(12)
O11	0.20706(93)	0.10629(58)	0.43929(129)	1.30(11)
O12	0.44704(93)	0.15462(58)	0.27408(128)	1.58(12)
O13	0.69893(92)	0.11796(57)	0.19834(126)	1.46(12)
O14	0.71489(86)	0.11252(49)	0.56477(122)	1.84(13)
O15	0.65205(76)	0.27387(47)	0.13538(121)	1.35(12)
O16	0.93578(95)	0.18125(58)	0.29619(141)	1.58(12)
O17	0.22355(75)	0.83779(46)	0.07440(120)	1.48(12)
O18	0.85352(91)	0.72919(56)	0.11145(135)	1.26(11)
O19	0.06830(94)	0.80492(57)	0.27437(139)	1.62(12)
O20	0.34777(91)	0.71819(56)	0.34867(134)	1.42(12)
O21	0.14822(90)	0.27164(56)	0.37394(134)	1.18(11)
O22	0.09514(92)	0.15516(56)	0.08265(124)	1.38(12)
OH	0.88014(71)	0.35558(45)	0.03173(106)	1.51(21)
F	0.11449(73)	0.63584(44)	0.46082(105)	2.81(18)
W[c]	0	0	0	7.07(99)

[a] CuKα, $R = 0.062$ (2755 refl.).
[b] Ca,K: 0.54(2)Ca + 0.26(3)K.
[c] W: 0.53(4)H_2O.

TABLE 111
Interatomic distances for miserite in Å[a].

R–F	2.217	Ca,K–O10	3.007	K–O9	2.663	Ca1–O21	2.358
R–O6	2.231	Ca,K–O11	3.158	K–O17	2.806	Ca1–O12	2.439
R–O1	2.248	Ca,K–O14	3.187	K–O14	2.948	Ca1–O20	2.449
R–O18	2.227	Ca,K–O16	3.241	K–O11	2.958	Ca1–O8	2.486
R–OH	2.277	Ca,K–O13	3.340	K–O22	2.980	Ca1–O2	2.532
R–O1	2.440	Ca,K–O19	3.416	K–O13	2.986	Ca1–O4	2.592
mean	2.273	mean	3.225	K–W	2.996	Ca1–O5	2.640
				K–O10	3.000	mean	2.528
				K–O12	3.051		
				K–O8	3.252		
				mean	2.962		
Ca2–O5	2.253	Ca3–OH	2.241	Ca4–O21	2.227	Ca5–F	2.218
Ca2–O2	2.295	Ca3–O7	2.279	Ca4–OH	2.302	Ca5–O7	2.267
Ca2–O8	2.314	Ca3–O3	2.334	Ca4–F	2.406	Ca5–O2	2.402
Ca2–O15	2.366	Ca3–O5	2.345	Ca4–O6	2.484	Ca5–O3	2.449
Ca2–O18	2.432	Ca3–O15	2.430	Ca4–O1	2.521	Ca5–O15	2.491
Ca2–O12	2.494	Ca3–O20	2.449	Ca4–O4	2.567	Ca5–O20	2.506
mean	2.359	mean	2.346	Ca4–O6	2.601	mean	2.389
				mean	2.444		
Si1–O3	1.617	Si2–O5	1.604	Si3–O8	1.603	Si4–O12	1.611
Si1–O2	1.624	Si2–O4	1.611	Si3–O9	1.620	Si4–O13	1.621
Si1–O4	1.631	Si2–O7	1.613	Si3–O11	1.633	Si4–O14	1.634
Si1–O1	1.632	Si2–O6	1.640	Si3–O10	1.641	Si4–O9	1.668
mean	1.626	mean	1.617	mean	1.624	mean	1.634
Si5–O15	1.592	Si6–O18	1.598	Si7–O20	1.620	Si8–O11	1.596
Si5–O13	1.615	Si6–O22	1.607	Si7–O17	1.635	Si8–O22	1.606
Si5–O17	1.625	Si6–O10	1.635	Si7–O14	1.640	Si8–O16	1.619
Si5–O16	1.641	Si6–O19	1.647	Si7–O19	1.653	Si8–O21	1.625
mean	1.618	mean	1.622	mean	1.637	mean	1.612

[a]The errors are 0.009 Å.

oxonium eudialyte, 20, is lower than those in eudialyte, 30, and eucolite, 26. They explained the cause of the ordering of the zeolitic atoms by the replacement of sodium by the larger K and H_3O^+. They concluded that the crystal structure and crystal-chemical formula of potassium–oxonium eudialyte confirm its individuality, the crystallization under relatively lower temperature hydrothermal condition with higher potassium alkalinity.

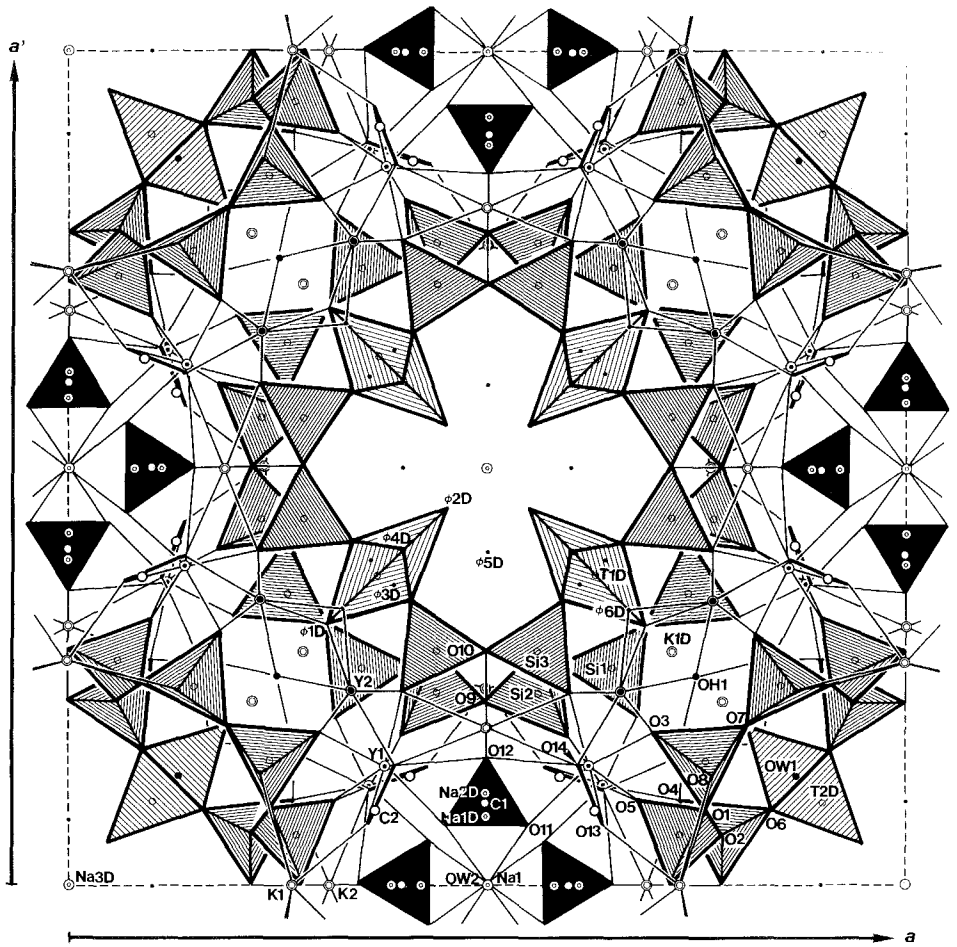

Fig. 48. The crystal structure of ashcroftine-(Y).

ASHCROFTINE-(Y)

$K_5Na_5(Y,Ca)_{12}(OH)_2(CO_3)_8(Si_{28}O_{70})\cdot 8H_2O$

$K_5Na_5(Y,Ca)_{12}(OH)_2(CO_3)_8(Si_{28}O_{70})\cdot 8H_2O$

Sys.	tetragonal	$a = 23.994(6)$ Å	source: Narsaruk, Greenland
S.G.	I4/mmm	$c = 17.512(5)$ Å	Ref.: Moore et al. (1987)
$Z =$	4		JCPDS: #22-0508
Dx =	2.60 g/cm^3		
Dm =	2.61(5) g/cm^3		
AP:	table 108	ID: table 109	IL: fig. 48

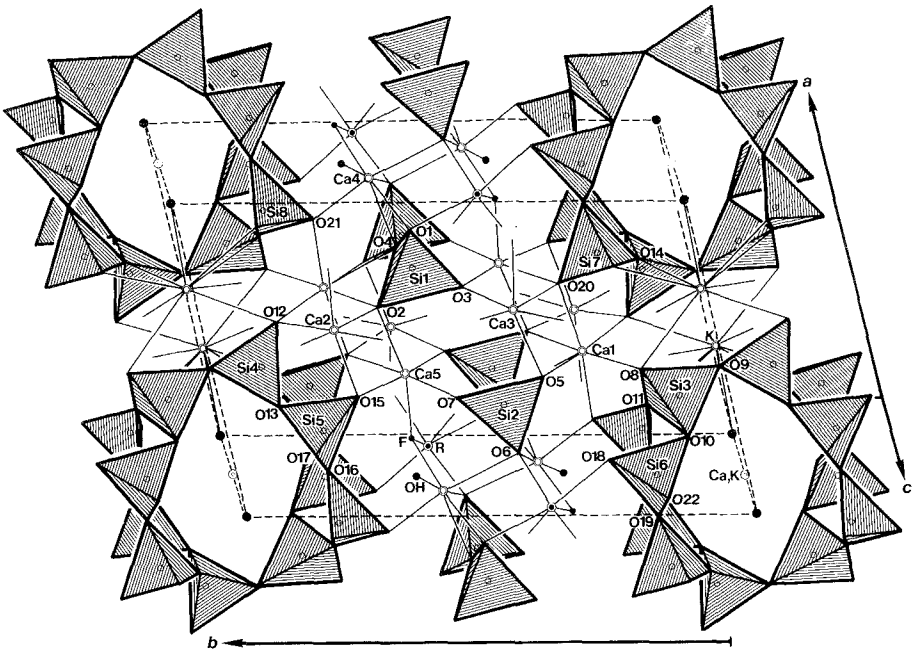

Fig. 49. The crystal structure of miserite.

Moore et al. (1987) determined the crystal structure of ashcroftine-(Y). It is based on at least 39 atoms in an asymmetric unit. Of these, 27 are ordered and make up a $[K_8Na_2Y_{24}(OH)_4(CO_3)_{16}(Si_{48}O_{128})\cdot 10H_2O]^{18-}$ framework, which is called the "healthy part" according to their expression. The remaining 12 atoms are located in a disordered region, the "pathological part", which consists of partially occupied T(D) = (Si,B), Si; Na(D), K(D), and $\phi(D) = O^{2-}$, OH^-, H_2O sites (fig. 48): all atoms are suffixed by D to indicate their disordered nature. The underlying polyanion is a giant $[Si_{48}O_{128}]$ ball whose connections define a polyhedron, hence the mineral is called a *balosilicate* by them. Breaks in the ball admit an extensive circumjacent disordered region and together define the $^1_\infty[Si_{56}O_{140}]$ tubular inosilicate with channels and bulges oriented parallel to [001]. All terminal oxygens point outside, away from the central channel. The ordered carbonate fraction defines, among other things, ordered $[Na(CO_3)_4]$ clusters. The entire ordered region is called the *curd*. The large balls are encrusted with a border region, the *limbus*, with Y–O, Na–O, and K–O bonds. The disordered region is called the *whey*. X-ray analysis only offers an average structure of the *whey*.

MISERITE
$Ca_{10}(Ca,K,\square)K_2Y_2Si_{16}O_{44}(OH)_2F_2 \cdot nH_2O$ $(n < 1)$
$Ca_{10}(Ca,K,\square)K_2Y_2Si_{16}O_{44}(OH)_2F_2 \cdot nH_2O$ $(n < 1)$

Sys.	triclinic	$a =$ 10.100(5) Å	source: Kipawa Lake, Que., Canada
S.G.	$P\bar{1}$	$b =$ 16.014(7) Å	Ref.: Scott (1976)
$Z =$	1	$c =$ 7.377(5) Å	JCPDS: #22-0806
Dm =	2.926(2) g/cm^3	$\alpha =$ 96°25(3)′	
		$\beta =$ 111°09(3)′	
		$\gamma =$ 76°34(2)′	
AP:	table 110	ID: table 111	IL: fig. 49

The crystal structure of miserite (fig. 49) is characterized by a large tunnel parallel to the *c*-axis formed by linkages of three-membered subchains of the Si tetrahedra, where all tetrahedra share three corners (Scott 1976). This tunnel displays almost perfect mm symmetry and is crosslinked by the K atoms forming a wall parallel to the *ac*-plane, adjacent tunnels being displaced vertically by exactly $\frac{1}{2}c$. Edge-sharing columns of Ca polyhedra with six- or seven-coordination bonded to each other, to the six-coordinated R polyhedron, and to the isolated diortho group (Si_2O_7) form a slab infinite in extent in *a* and *c*, which falls between the walls and connects them in the *b* direction. Inside the tunnel, there are sites for zeolitic water molecules and (Ca,K) sites which are partially occupied. Scott (1976) reported that this structure has no simple structural relationship to any other known structure of silicates, and is classified in Zoltai's Type 5 (mixed type) as the first member of this type (Zoltai 1960).

AGRELLITE
$Na(Ca,Ce,Na)_2Si_4O_{10}F$
$Na(Ca,Ce,Na)_2Si_4O_{10}F$

Sys.	triclinic	$a =$ 7.759(2) Å	source: Villedieu Témiscaming Co., Que., Canada
S.G.	$P\bar{1}$	$b =$ 18.946(3) Å	Ref.: Ghose and Wan (1979)
$Z =$	4	$c =$ 6.986(1) Å	JCPDS: #22-1230, #29-1188
Dx =	2.887 g/cm^3	$\alpha =$ 89.88(2)°	
Dm =	2.902 g/cm^3	$\beta =$ 116.65(2)°	
		$\gamma =$ 94.32(2)°	
AP:	table 112	ID: table 113	IL: fig. 50

The crystal structure of agrellite (fig. 50) has a pseudo-*C*-centered lattice (Ghose and Wan 1979). The structure consists of silicate tubes parallel to the *c*-axis cross-linked by sodium atoms to sodium silicate layers, and calcium polyhedral layers, both parallel to the (010) plane, alternating along the *b*-axis, forming a three-dimensional framework. The silicate tube consists of two centrosymmetrically related single silicate chains; each single chain is formed by corner-sharing four-membered tetrahedral rings [Si(1)–Si(2)–Si(3)–Si(4)]. Although the structure of agrellite is very similar to that of miserite, agrellite has no diortho group of Si tetrahedra, and the diameter of the tube is much smaller than that in miserite.

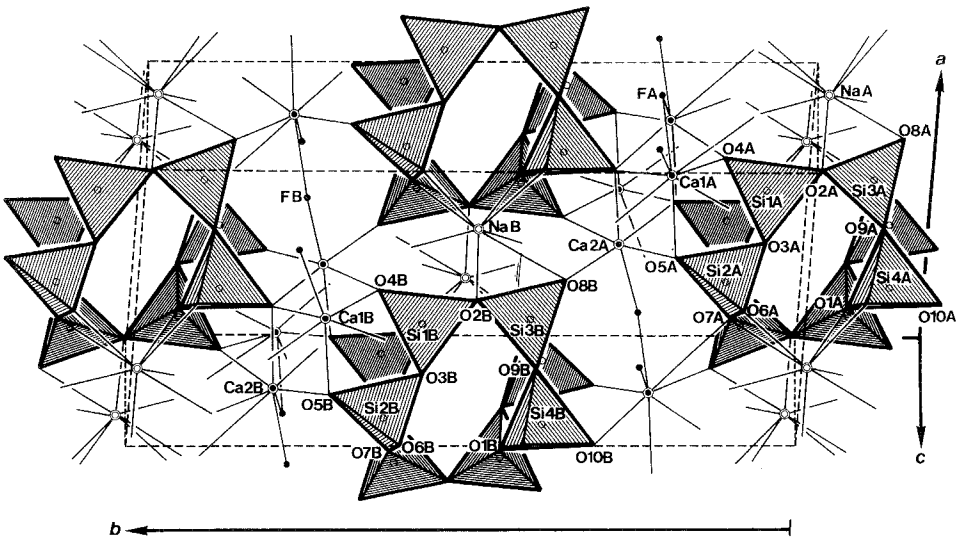

Fig. 50. The crystal structure of agrellite.

Rare earth elements partially occupy the Ca sites in the structure. Ghose and Wan (1979) suggested that the eight-coordinated Ca1A site contains most of the rare earth atoms, whereas the slightly larger eight-coordinated Ca2B and smaller six-coordinated Ca1B and Ca2A sites contain very small amounts of the rare earth atoms. The charge compensation, accompanied by the isomorphous substitution of R^{3+} for Ca^{2+} in the Ca sites, may be accomplished by the coupled substitution $2Ca^{2+} \rightleftarrows R^{3+} + Na^{+}$.

GADOLINITE-(Y)
$Y_2Fe^{2+}Be_2Si_2O_{10}$
$Y_2(Fe^{2+},\square)Be_2Si_2O_8(O,O)_2$

Sys. monoclinic	$a = 10.000(2)$ Å	source: Miyazuma-kyo, Yokkaichi, Mie, Japan
S.G. $P2_1/a$	$b = 7.565(2)$ Å	Ref.: Miyawaki et al. (1984)
$Z = 2$	$c = 4.768(1)$ Å	JCPDS: #26-1134, #22-0990
	$\beta = 90.31(2)°$	
AP: table 114	ID: table 115	IL: fig. 51

GADOLINITE-(Ce)
$Ce_2Fe^{2+}Be_2Si_2O_{10}$
$Ce_2(Fe^{2+},\square)Be_2Si_2O_8(O,OH)_2$

Sys. monoclinic	$a = 4.82 \pm 0.02$ Å	source: Skien, Norway
S.G. $P2_1/c$	$b = 7.58 \pm 0.02$ Å	Ref.: Segalstad and Larsen (1978)
$Z = 2$	$c = 10.01 \pm 0.03$ Å	JCPDS: #29-1409
Dx = 4.90 g/cm^3	$\beta = 90°28' \pm 16'$	

TABLE 112
Atomic parameters of agrellite[a].

	x	y	z	U
Ca1A[b]	0.99796(14)	0.21554(5)	0.99620(15)	1.16(3)
Ca1B[c]	0.54176(12)	0.28461(4)	0.01966(13)	0.92(3)
Ca2A[d]	0.45521(12)	0.72007(4)	0.48010(13)	0.94(3)
Ca2B[e]	0.00155(13)	0.78166(5)	0.50022(14)	1.27(3)
NaA	0.23539(28)	0.99102(11)	0.86794(34)	2.49(7)
NaB	0.26104(29)	0.50234(12)	0.13576(36)	2.84(8)
Si1A	0.20870(16)	0.93103(6)	0.35569(17)	0.81(3)
Si1B	0.30739(16)	0.56807(6)	0.65542(18)	0.79(3)
Si2A	0.48573(16)	0.87795(6)	0.21377(17)	0.80(4)
Si2B	0.02460(16)	0.61933(6)	0.79397(17)	0.75(4)
Si3A	0.16705(16)	0.08998(6)	0.33394(17)	0.78(3)
Si3B	0.67404(16)	0.59022(6)	0.34109(17)	0.75(3)
Si4A	0.48619(16)	0.87771(6)	0.77347(18)	0.80(4)
Si4B	0.02139(16)	0.61974(6)	0.23430(18)	0.72(4)
FA	0.7607(4)	0.7610(2)	0.1268(5)	2.7(1)
FB	0.2353(4)	0.2451(2)	0.3595(5)	2.5(1)
O1A	0.3493(4)	0.9351(2)	0.6138(5)	1.3(1)
O1B	0.1641(4)	0.5639(2)	0.3974(5)	1.3(1)
O2A	0.1028(4)	0.0048(1)	0.3023(5)	1.1(1)
O2B	0.5891(4)	0.5065(1)	0.2960(5)	1.0(1)
O3A	0.3483(4)	0.9352(2)	0.2356(5)	1.2(1)
O3B	0.1722(4)	0.5640(2)	0.7804(5)	1.3(1)
O4A	0.0620(4)	0.8634(2)	0.2822(5)	1.3(1)
O4B	0.4543(4)	0.6355(1)	0.7256(5)	1.1(1)
O5A	0.3938(4)	0.7990(1)	0.1901(5)	1.1(1)
O5B	0.1102(4)	0.6991(2)	0.8169(5)	1.4(1)
O6A	0.5130(4)	0.9064(1)	0.0072(4)	1.1(1)
O6B	0.9958(4)	0.5913(2)	0.0012(5)	1.2(1)
O7A	0.7013(4)	0.8924(2)	0.4117(5)	1.6(1)
O7B	0.8136(4)	0.6001(2)	0.5964(5)	1.5(1)
O8A	0.9743(4)	0.1295(2)	0.2368(5)	1.1(1)
O8B	0.4984(4)	0.6382(2)	0.2562(5)	1.2(1)
O9A	0.7019(4)	0.8922(2)	0.7911(5)	1.6(1)
O9B	0.8079(4)	0.6032(2)	0.2180(5)	1.5(1)
O10A	0.3947(4)	0.7986(1)	0.7067(5)	1.3(1)
O10B	0.1082(4)	0.6993(1)	0.2962(5)	1.2(1)

[a] MoKα, $R = 0.045$ (5343 refl.).
[b] Ca1A: 0.8534Ca + 0.1466(6)R.
[c] Ca1B: 0.978Ca + 0.022(2)R.
[d] Ca2A: 0.993Ca + 0.007(2)R.
[e] Ca2B: 0.985Ca + 0.015(2)R.

TABLE 113
Interatomic distances for agrellite in Å.

Ca1A–F A	2.400(4)	Ca1B–F A	2.201(3)	Ca2A–F B	2.192(3)	Ca2B–F A	2.444(3)
Ca1A–F B	2.409(3)					Ca2B–F B	2.464(4)
mean	2.405					mean	2.454
Ca1A–O4A	2.309(3)	Ca1B–O4B	2.326(3)	Ca2A–O4B	2.346(3)	Ca2B–O4A	2.337(4)
Ca1A–O8A	2.395(4)	Ca1B–O8B	2.338(3)	Ca2A–O8B	2.350(4)	Ca2B–O8A	2.430(4)
Ca1A–O10B	2.476(3)	Ca1B–O10A	2.376(3)	Ca2A–O10A	2.392(4)	Ca2B–O10B	2.532(4)
Ca1A–O5B	2.495(4)	Ca1B–O5A	2.387(4)	Ca2A–O10B	2.407(3)	Ca2B–O5B	2.562(3)
Ca1A–O5A	2.708(3)	Ca1B–O5B	2.408(3)	Ca2A–O5A	2.408(3)	Ca2B–O10A	2.720(3)
Ca1A–O9A	3.066(3)	mean	2.367	mean	2.381	Ca2B–O7A	3.107(4)
mean	2.575					mean	2.615
NaA–O2A	2.353(4)	NaB–O2B	2.270(4)				
NaA–O6A	2.501(3)	NaB–O6B	2.408(4)				
NaA–O3A	2.568(4)	NaB–O3B	2.564(4)				
NaA–O1A	2.571(5)	NaB–O1B	2.578(5)				
NaA–O8A	2.603(4)	NaB–O6B	2.597(4)				
NaA–O6A	2.606(4)	NaB–O7B	2.897(4)				
NaA–O7A	3.102(4)	NaB–O8B	2.937(4)				
NaA–O9A	3.102(4)	NaB–O9B	3.011(4)				
mean	2.676	mean	2.658				
Si1A–O4A	1.568(3)	Si1B–O4B	1.567(3)	Si2A–O5A	1.583(3)	Si2B–O5B	1.583(3)
Si1A–O2A	1.633(3)	Si1B–O1B	1.637(3)	Si2A–O7A	1.625(3)	Si2B–O7B	1.613(3)
Si1A–O1A	1.634(3)	Si1B–O3B	1.637(4)	Si2A–O3A	1.630(4)	Si2B–O6B	1.642(4)
Si1A–O3A	1.639(4)	Si1B–O2B	1.638(3)	Si2A–O6A	1.634(4)	Si2B–O3B	1.643(4)
mean	1.619	mean	1.620	mean	1.618	mean	1.620
Si3A–O8A	1.585(3)	Si3B–O8B	1.580(3)	Si4A–O10A	1.585(3)	Si4B–O10B	1.582(3)
Si3A–O7A	1.623(3)	Si3B–O7B	1.621(3)	Si4A–O9A	1.624(4)	Si4B–O9B	1.615(4)
Si3A–O9A	1.629(4)	Si3B–O9B	1.625(4)	Si4A–O1A	1.631(3)	Si4B–O6B	1.637(4)
Si3A–O2A	1.637(3)	Si3B–O2B	1.645(3)	Si4A–O6A	1.639(4)	Si4B–O1B	1.638(3)
mean	1.619	mean	1.618	mean	1.620	mean	1.618

TABLE 114
Atomic parameters of gadolinite-(Y)[a].

	x	y	z	B_{eq} (Å^2)
R[b]	0.32854(2)	0.10828(2)	0.00013(3)	0.62
Si	0.07822(6)	0.27850(9)	0.5192(1)	0.52
Be	0.3355(3)	0.4143(4)	0.4642(6)	0.52
Fe[c]	0	0	0	0.67
O1	0.0303(2)	0.4131(2)	0.7607(4)	0.76
O2	0.4518(2)	0.2871(2)	0.3248(4)	0.71
O3	0.1954(2)	0.3476(3)	0.3089(4)	0.73
O4	0.1419(2)	0.1065(2)	0.6847(4)	0.72
O5[d]	0.3329(2)	0.4126(3)	0.7979(4)	0.80

[a] MoKα, $R = 0.029$, $R_w = 0.034$ (2790 refl.).
[b] R: 0.647Y + 0.353Ln.
[c] Fe: 0.864Fe.
[d] O5: 0.864O + 0.136(OH).

HINGGANITE-(Y) (xinganite, yttroceberysite, yberisilite)
$YBeSiO_4(OH)$
$Y_2(\square,Fe)Be_2Si_2O_8(OH,O)_2$

Sys. monoclinic	$a =$ 9.888(5) Å	source: Kola Peninsula, Russia
S.G. $P2_1/a$	$b =$ 7.607(3) Å	Ref.: Yakubovich et al. (1983)
$Z =$ 2	$c =$ 4.740(2) Å	JCPDS: #26-0812
Dx = 4.2 g/cm^3	$\beta = 90.45(4)°$	
Dm = 4.08 g/cm^3		
AP: table 116	ID: table 117	IL: fig. 52

HINGGANITE-(Yb)
$YbBeSiO_4(OH)$
$Yb_2(\square,Fe)Be_2Si_2O_8(OH,O)_2$

Sys. monoclinic	$a =$ 9.888(5) Å	source: Kola Peninsula, Russia
S.G. $P2_1/a$	$b =$ 7.607(3) Å	Ref.: Voloshin et al. (1983b)
$Z =$ 2	$c =$ 4.740(2) Å	JCPDS: #35-0705
Dx = 4.83 g/cm^3	$\beta = 90.45(4)°$	

hingganite-(Ce)
$CeBeSiO_4(OH)$
$Ce_2(\square,Fe)Be_2Si_2O_8(OH,O)_2$

Sys. monoclinic	$a =$ 9.996(10) Å	source: Tahara, Hirukawa, Ena, Gifu, Japan
S.G. $P2_1/a$	$b =$ 7.705(7) Å	Ref.: Miyawaki et al. (1987)
$Z =$ 2	$c =$ 4.792(4) Å	JCPDS: #40-1452
	$\beta = 90.06(4)°$	

TABLE 115
Interatomic distances for gadolinite-(Y) in Å.

R–O1	2.329(2)	Si–O1	1.612(2)
R–O1	2.335(2)	Si–O3	1.632(2)
R–O4	2.381(2)	Si–O2	1.641(2)
R–O2	2.392(2)	Si–O4	1.648(2)
R–O5	2.397(2)	mean	1.633
R–O3	2.473(2)		
R–O5	2.497(2)	Be–O5	1.592(3)
R–O3	2.691(2)	Be–O4	1.634(4)
mean	2.437	Be–O2	1.651(3)
		Be–O3	1.660(3)
Fe–O5	2.035(2) ×2	mean	1.634
Fe–O4	2.224(2) ×2		
Fe–O2	2.288(2) ×2		
mean	2.182		

TABLE 116
Atomic parameters of hingganite-(Y)[a].

	x	y	z	B (Å^2)
R[b]	0.33301(9)	0.1089(1)	0.9987(2)	0.80(1)
Si	0.0791(3)	0.2763(4)	0.5190(7)	0.33(4)
Be	0.335(1)	0.413(2)	0.448(3)	0.1(2)
□,Fe[c]	0	0	0	0.9(3)
O1	0.1950(8)	0.347(1)	0.300(2)	0.5(1)
O2	0.1485(8)	0.109(1)	0.687(2)	0.6(1)
O3	0.0332(8)	0.412(1)	0.764(2)	0.5(1)
O4	0.4499(8)	0.284(1)	0.326(2)	0.5(1)
OH,O	0.3305(8)	0.412(1)	0.786(2)	0.5(1)

[a] MoKα, $R = 0.0659$ (1345 refl.).
[b] R: 0.51Y + 0.23Yb + 0.13Ca + 0.09Er + 0.04Dy.
[c] □,Fe: 0.13Fe.

calciogadolinite
$CaRFe^{3+}Be_2Si_2O_{10}$
$CaRFe^{3+}Be_2Si_2O_{10}$

Sys. monoclinic	$a = 9.988(2)$ Å	source: synthetic $CaYFe^{3+}Be_2Si_2O_{10}$
S.G. $P2_1/a$	$b = 7.566(2)$ Å	Ref.: Ito and Hafner (1974)
$Z = 2$	$c = 4.696(1)$ Å	
	$\beta = 90°01(2)'$	

TABLE 117
Interatomic distances for hingganite-(Y) in Å.

R–O3	2.284(8)	Si–O3	1.618(8)
R–O3	2.291(8)	Si–O4	1.633(9)
R–O2	2.339(8)	Si–O1	1.641(9)
R–O4	2.344(8)	Si–O2	1.648(9)
R–OH,O	2.432(8)	mean	1.635
R–O1	2.460(8)		
R–OH,O	2.519(8)	Be–OH,O	1.60(1)
R–O1	2.686(8)	Be–O4	1.61(2)
mean	2.419	Be–O1	1.63(2)
		Be–O2	1.63(2)
□,Fe–OH,O	2.063(8) ×2	mean	1.62
□,Fe–O2	2.253(8) ×2		
□,Fe–O4	2.308(8) ×2		
mean	2.208		

CALCYBEBOROSILITE-(Y) (=erdmannite)
$(Y,Ca)(Be,B)SiO_4(OH)$
$YCaBeBSi_2O_8(OH)_2$

Sys. monoclinic	$a = 9.86$ Å	source: Alaisk Ridge, Tadzhikistan
S.G.	$b = 7.48$ Å	Ref.: Semenov et al. (1963)
$Z = 2$	$c = 4.66$ Å	
$Dm = 3.78$ g/cm^3	$\beta = 88°30'$	

MINASGERAISITE-(Y)
$(Y,Bi)_2CaBe_2Si_2O_{10}$
$(Y,Bi)_2CaBe_2Si_2O_{10}$

Sys. monoclinic	$a = 9.833(2)$ Å	source: Jaguaracu, Timoteo, Minas Gerais, Brazil
S.G. $P2_1/a$	$b = 7.562(1)$ Å	Ref.: Foord et al. (1986)
$Z = 2$	$c = 4.702(1)$ Å	JCPDS: #39-0344
$Dx = 4.90$ g/cm^3	$\beta = 90.46(6)°$	
$Dm > 4.25$ g/cm^3		

Gadolinite-(Y), -(Ce), hingganite-(Y), -(Yb), -(Ce), calciogadolinite, calcybeborosilite-(Y), and minasgeraisite-(Y) are members of the datolite–gadolinite group with general formula: $A_2BC_2D_2O_8X_2$; A = R, Ca, Bi; B = Fe^{2+}, Fe^{3+}, Mn, Ca, □; C = Be, B; D = Si, P, As; X = O, OH, F. Ito and Mori (1953) proposed that the crystal structure of gadolinite-(Y) can be derived from that of datolite, $CaBSiO_4(OH)$, by a simple replacement of atoms, based on their analysis of the crystal structure of datolite and on the examination of the X-ray powder patterns of both minerals. Pavlov and Belov (1959) analyzed the crystal structure of gadolinite-(Y) using two-dimensional photographic data. Foit and Gibbs (1975) reported a refinement of the crystal structure of synthetic $Yb_2NiBe_2Si_2O_{10}$. Miyawaki et al. (1984) refined the crystal structure of gadolinite-(Y) using a natural non-metamict sample. On the other

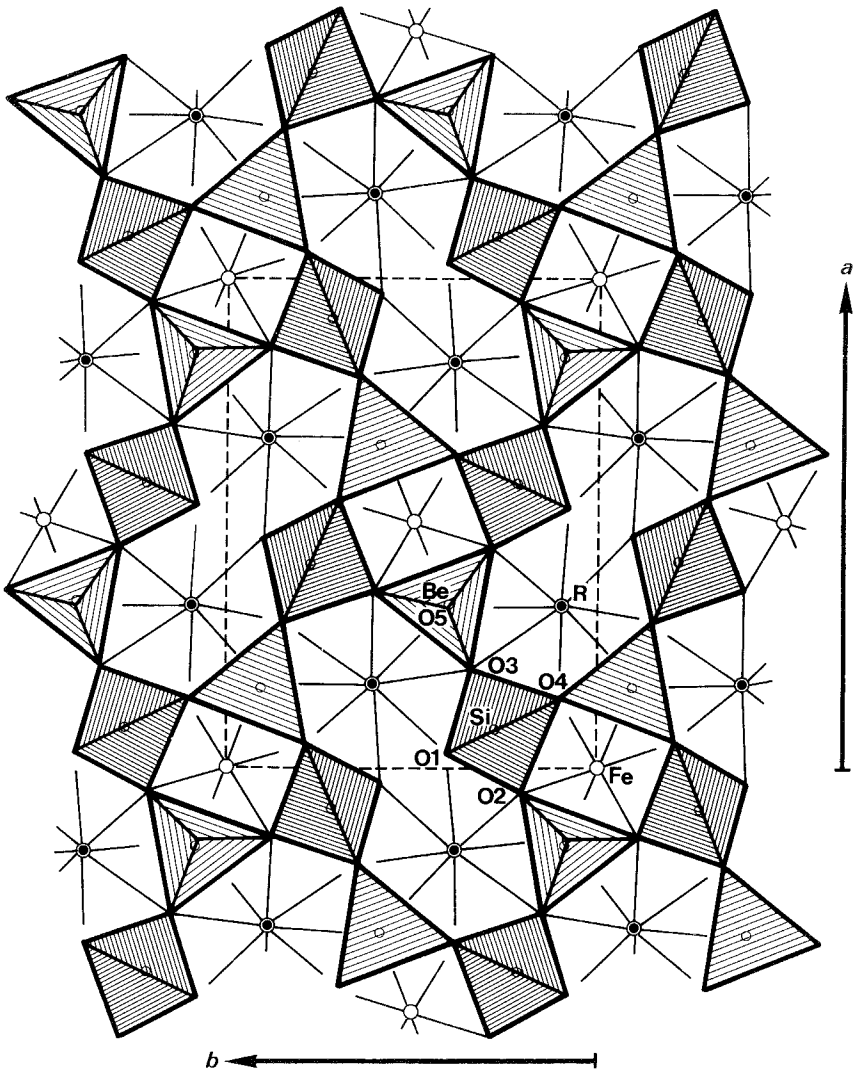

Fig. 51. The crystal structure of gadolinite-(Y).

hand, Yakubovich et al. (1983) determined the crystal structure of hingganite-(Y)*. As can be seen from figs. 51 and 52, the crystal structures of gadolinite-(Y) and hingganite-(Y) are isostructural. The structures consist of sheets parallel to the (001) plane which was formed by the corner-sharing linkages of SiO_4 and BeO_4 tetrahedra. In both structures, two rare earth atoms are situated between the eight-membered rings of the tetrahedra forming eight-coordinated square antiprisms. The iron atoms

* Although they described their specimen as hingganite-(Yb), the predominant rare earth is yttrium in the specimen. Therefore, it is hingganite-(Y). Hingganite-(Yb) was reported by Voloshin et al. (1983b).

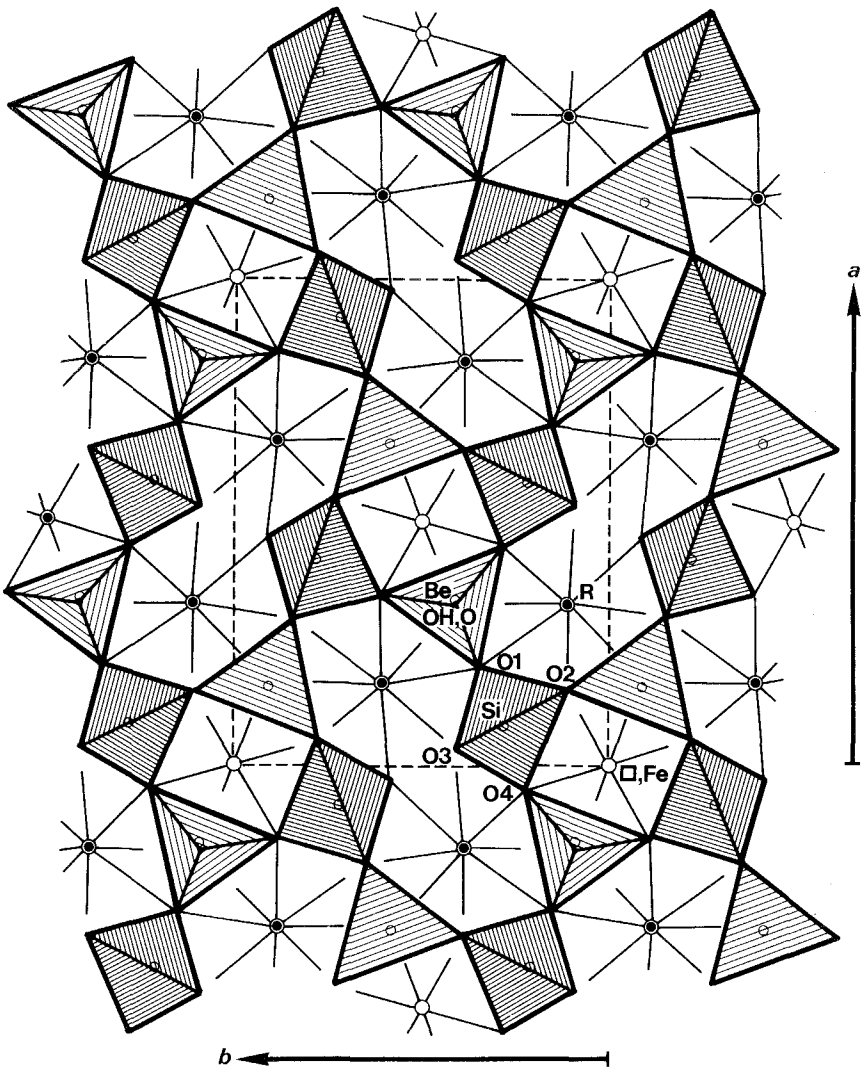

Fig. 52. The crystal structure of hingganite-(Y).

are at the origins of the unit cells. A characteristic difference between the structure of hingganite-(Y) and that of gadolinite-(Y) is that the Fe site is almost vacant and one of the corners of the BeO_4 tetrahedra is mainly occupied by a hydroxyl ion in hingganite-(Y).

Calciogadolinite was described by Nakai (1938). Ito and Hafner (1974) proposed that calciogadolinite is one of the three end-members of a solid solution observed in natural gadolinite samples: the other two end-members are of the type gadolinite-(Y) and hingganite-(Y). The solid solution of the latter two is based on the coupled isomorphous substitution $Fe^{2+} + 2O^{2-} \leftrightarrows \square + 2OH^-$ observed in the crystal struc-

ture of the natural gadolinite-(Y) sample (Miyawaki et al. 1984) and that of hingganite-(Y) (Yakubovich et al. 1983). In addition, it was reported that the coupled substitution $R^{3+} + Be^{2+} \rightleftarrows Ca^{2+} + B^{3+}$ was observed in natural samples of gadolinite-(Y) (Miyawaki et al. 1984) and homilite, $Ca_2Fe^{3+}B_2Si_2O_{10}$ (Miyawaki et al. 1985). It is of great interest to determine the crystal structure of calciogadolinite, which would make it possible to reveal a complete mechanism of isomorphous substitution among the solid solution series in the gadolinite group minerals. Unfortunately, however, the type specimen of calciogadolinite from Tadachi, Nagano, Japan, was lost during World War II.

Calcybeborosilite-(Y) is the intermediate phase between hingganite-(Y) and datolite. This mineral was described as erdmannite by Doelter (1912). Semenov et al. (1963) described a mineral corresponding to calcybeborosilite-(Y) from Tadzhikstan. The space group of this mineral has not been reported. If the space group is $P2_1$, the same as that of an unknown mineral, $YCaFe^{3+}_{0.33}Be_2Si_2O_8(OH)_2$, from Tahara, Gifu, Japan (Miyawaki et al. 1987), there is a possibility of ordering of Y–Ca and Be–B in calcybeborosilite-(Y).

Minasgeraisite-(Y) was described by Foord et al. (1986) as a new mineral from Minas Gerais, Brazil. X-ray powder diffraction data showed that the mineral is isostructural with gadolinite-(Y). However, minasgeraisite-(Y) has a peculiar chemical composition and includes significant amounts of Bi and Ca (Foord et al. 1986). It is unusual from the viewpoint of crystal chemistry that the calcium atom with a large ionic radius occupies the relatively small octahedral site which is occupied by Fe in the case of gadolinite-(Y).

The name "xinganite" used by Ximen and Peng (1985b) is a misprint of hingganite that occurred in the translation from Chinese to English. The chemical and crystallographic data of yttroceberysite described by Ding et al. (1981) suggest it to be a member of the gadolinite group. The mineral should be called hingganite-(Y) rather than gadolinite-(Y) because of its lower content of Fe and higher H content.

NORDITE-(La)
$(La,Ca)(Sr,Ca)Na_2(Na,Mn)(Zn,Mg)Si_6O_{17}$
$(La,Ca)(Sr,Ca)Na_2(Na,Mn)(Zn,Mg)Si_6O_{17}$

Sys. orthorhombic	$a = 14.27 \pm 0.03$ Å	source: Lovozero, Kola Peninsula, Russia
S.G. Pcca	$b = 5.16 \pm 0.01$ Å	Ref.: Bakakin et al. (1970)
$Z = 4$	$c = 19.45 \pm 0.15$ Å	JCPDS: #27-0672
$Dm = 3.48$ g/cm^3		
AP: table 118	ID: table 119	IL: fig. 53

NORDITE-(Ce)
$(Ce,Ca)(Sr,Ca)Na_2(Na,Mn)(Zn,Mg)Si_6O_{17}$
$(Ce,Ca)(Sr,Ca)Na_2(Na,Mn)(Zn,Mg)Si_6O_{17}$

Sys. orthorhombic	$a =$	source:
S.G. Pcca	$b =$	Ref.: Levinson (1966)
$Z = 4$	$c =$	

TABLE 118
Atomic parameters of nordite-(La)[a].

	x	y	z	B (Å²)
R	0.25	0	0.3194	0.39(3)
Sr,Ca	0.25	0	0.0217(2)	0.06(5)
Na	0.0696(10)	0.0125(81)	0.1693(8)	2.10(26)
Na,Mn	0	0	0	2.05(36)
M	0.25	0.5	0.1687(3)	0.91(7)
Si1	0.0980(7)	0.4542(23)	0.0623(4)	0.61(14)
Si2	0.1019(7)	0.5433(23)	0.2747(4)	0.46(13)
Si3	0.1116(5)	0.5516(17)	−0.0819(4)	0.31(11)
O1	0.9955(16)	0.3389(53)	0.0811(14)	0.84(10)
O2	0.1701(18)	0.2995(71)	0.1101(12)	0.70(10)
O3	0.1172(18)	0.3537(59)	−0.0131(12)	1.49(46)
O4	0.1019(16)	0.7640(68)	0.0672(12)	1.64(45)
O5	0	0.6366(96)	0.25	1.28(58)
O6	0.1783(18)	0.7090(69)	0.2321(12)	0.83(33)
O7	0.1221(19)	0.6503(58)	0.3532(13)	1.00(37)
O8	0.1178(18)	0.2392(58)	0.2714(12)	1.26(40)
O9	0.1857(15)	0.2226(58)	0.4173(14)	1.11(33)

[a]Mo, $R = 0.122$ (1335 refl.).

TABLE 119
Interatomic distances for nordite-(La) in Å[a].

R–O9	2.41 ×2	Sr,Ca–O9	2.51 ×2
R–O8	2.44 ×2	Sr,Ca–O2	2.58 ×2
R–O6	2.48 ×2	Sr,Ca–O4	2.59 ×2
R–O7	2.65 ×2	Sr,Ca–O3	2.71 ×2
mean	2.50	mean	2.60
Na–O2	2.36	Na,Mn–O4	2.30 ×2
Na–O8	2.40	Na,Mn–O1	2.35 ×2
Na–O4	2.41	Na,Mn–O3	2.49 ×2
Na–O8	2.47	mean	2.38
Na–O6	2.52		
Na–O1	2.63	Si2–O8	1.58
Na–O5	2.68	Si2–O5	1.61
mean	2.50	Si2–O6	1.61
		Si2–O7	1.65
M–O2	1.91 ×2	mean	1.61
M–O6	1.93 ×2		
mean	1.92	Si3–O9	1.57
		Si3–O1	1.63
Si1–O3	1.58	Si3–O7	1.64
Si1–O2	1.60	Si3–O3	1.68
Si1–O4	1.60	mean	1.63
Si1–O1	1.62		
mean	1.60		

[a]Estimated standard errors are 0.03 Å.

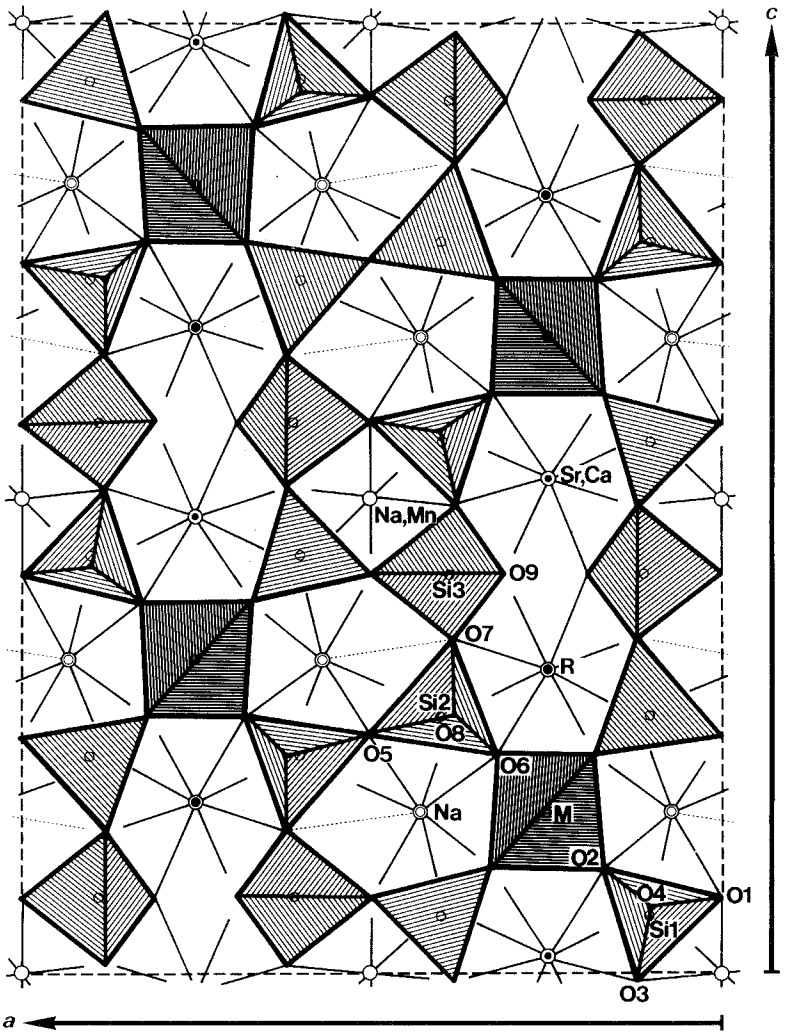

Fig. 53. The crystal structure of nordite-(La).

SEMENOVITE-(Ce)

$Ce_2Na_{0-2}(Fe,Mn,Zn,Ti)(Ca,Na)_8(Si,Be)_{20}(O,OH,F)_{48}$

$(Ce,Na,\square)_2(Na,\square,Ce)_2(Fe,Mn,\square)(\square,Fe,Mn)(Ca,Na)_8Si_8(Si,Be)_6(Si,Be)_6O_{40}(OH,O)_2(OH,F)_6$

Sys.	orthorhombic	$a = 13.879(5)$ Å	source: Ilimaussaq, Greenland
S.G.	Pmnn	$b = 13.835(5)$ Å	Ref.: Mazzi et al. (1979)
$Z =$	2	$c = 9.942(6)$ Å	JCPDS: #25-0699
Dx =	3.17 g/cm^3		
Dm =	3.14 g/cm^3		
AP:	table 120	ID: table 121	IL: fig. 54

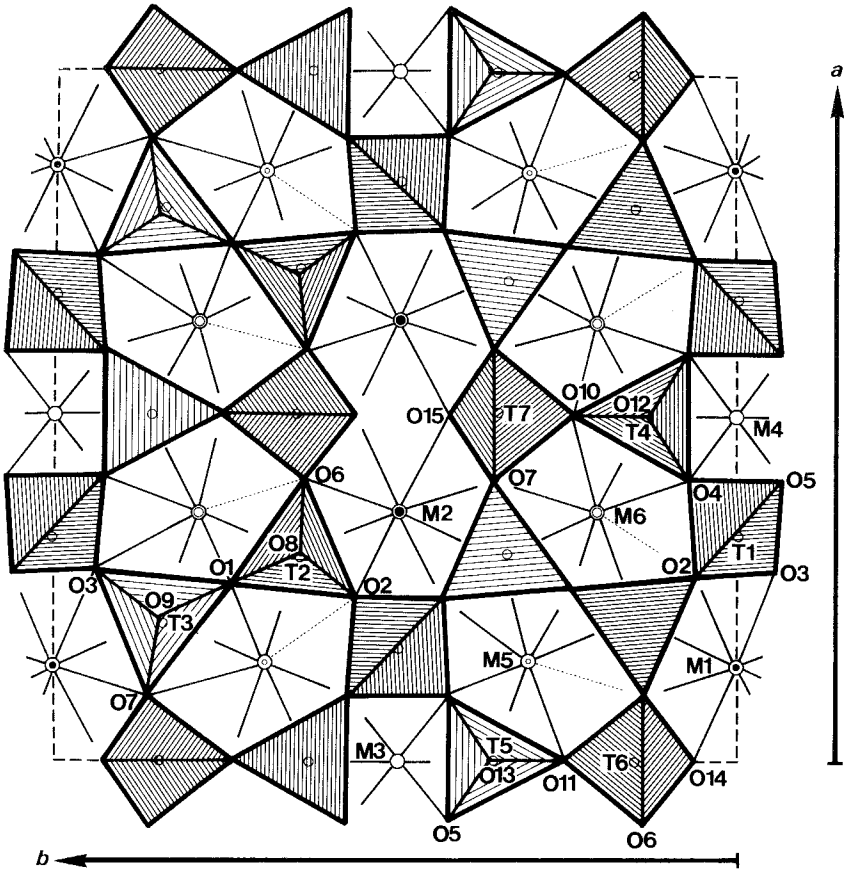

Fig. 54. The crystal structure of semenovite-(Ce).

The crystal structure of nordite-(La) was determined by Bakakin et al. (1970), and that of semenovite-(Ce) was determined by Mazzi et al. (1979). These structures (figs. 53 and 54) consist of sheets made up of tetrahedra of Si, B, and Be similar to those in the datolite–gadolinite group and the melilite group. The sheet structures are connected by cation polyhedra, R, Na, and Ca antiprisms and Fe and Mn octahedra. Mazzi et al. (1979) suggested that the crystal structure of hellandite-(Y) (Mellini and Merlino 1977) (fig. 55) can be transformed from a chain structure to a two-dimensional sheet structure comparable to the crystal structure of gadolinite-(Y), semenovite-(Ce), etc., by assuming imaginary tetrahedra at the O3, O5, O10, and O11 sites.

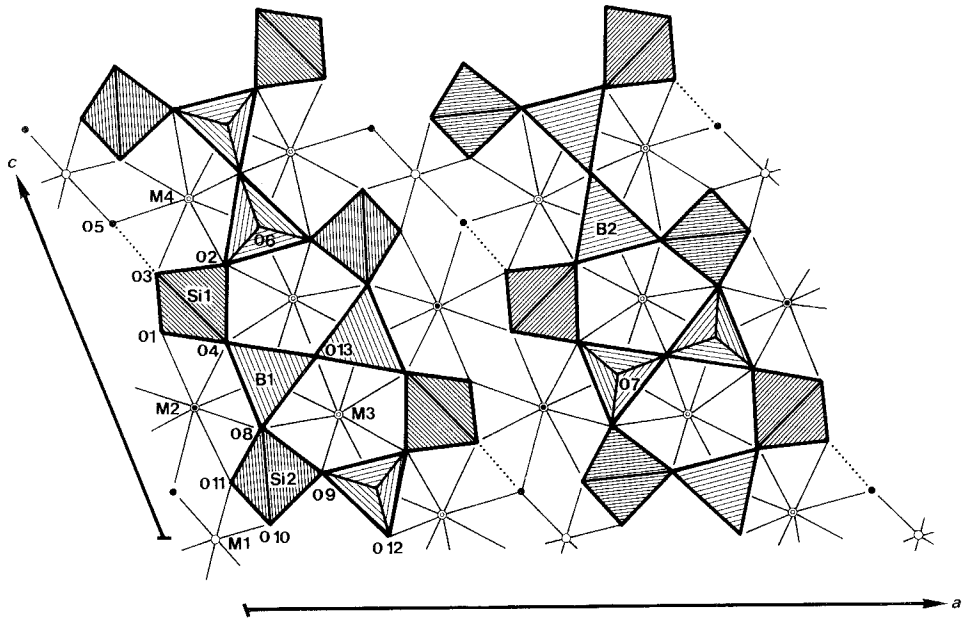

Fig. 55. The crystal structure of hellandite-(Y).

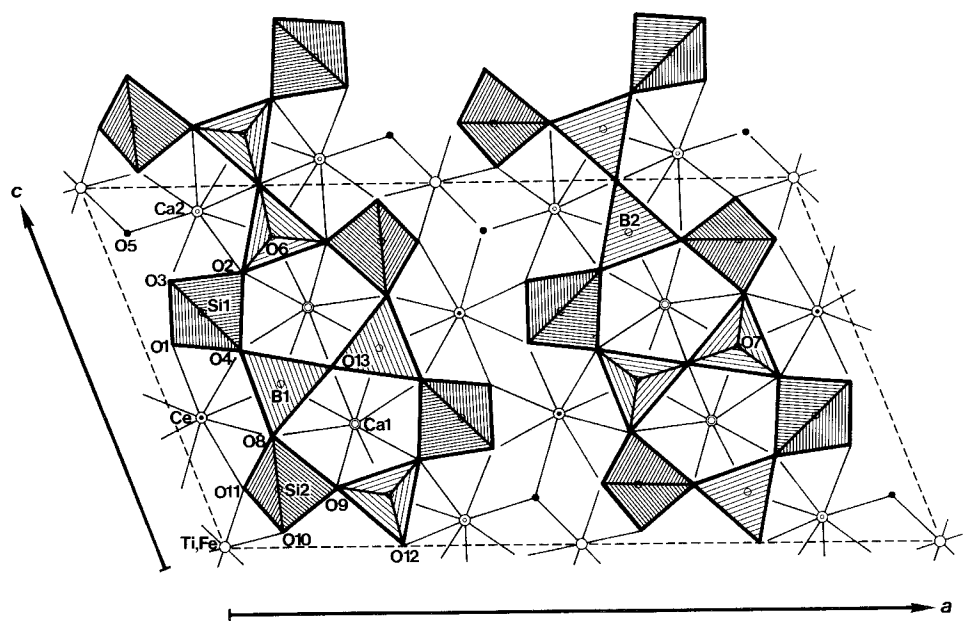

Fig. 56. The crystal structure of tadzhikite-(Ce).

TABLE 120
Atomic parameters of semenovite-(Ce)[a].

	x	y	z	B_{eq} (Å^2)
M1	0.1390(0)	0	0	1.05
M2	0.1349(2)	0	0.5	4.22
M3	0.5	0	0.5	1.59
M4	0.5	0	0	1.69
M5	0.1385(1)	0.2907(1)	0.0128(2)	1.26
M6	0.1431(2)	0.3060(2)	0.5053(3)	1.94
T1	0.3373(1)	−0.0044(2)	0.2532(2)	1.32
T2	0.2045(2)	0.1509(2)	0.2789(2)	0.73
T3	0.2043(5)	0.1547(5)	0.7769(7)	1.80
T4	0.5	0.1297(3)	0.2364(3)	0.86
T5	0.5	0.1388(8)	0.7289(10)	1.98
T6	0	0.1493(3)	0.2350(3)	1.31
T7	0	0.1513(3)	0.7466(3)	1.76
O1	0.2490(5)	0.2473(4)	0.3393(5)	1.49
O2	0.2668(4)	0.0627(4)	0.3473(5)	1.60
O3	0.2703(4)	0.0649(4)	0.8477(5)	1.34
O4	0.4061(4)	0.0737(4)	0.1713(5)	1.46
O5	0.4065(4)	0.0742(4)	0.6567(5)	1.43
O6	0.0940(4)	0.1379(5)	0.3375(5)	1.64
O7	0.0963(4)	0.1395(5)	0.8393(5)	1.83
O8	0.2023(4)	0.1449(4)	0.1172(5)	1.23
O9	0.2066(4)	0.1547(4)	0.6208(5)	1.42
O10	0.5	0.2397(6)	0.1699(8)	1.52
O11	0.5	0.2450(6)	0.6648(8)	1.65
O12	0.5	0.1328(6)	0.3934(7)	1.65
O13	0.5	0.1361(7)	0.8857(8)	1.92
O14	0	0.0619(6)	0.1234(8)	1.55
O15	0	0.0756(6)	0.6209(9)	2.33

[a] MoKα, $R = 0.050$ (1366 refl.).
M1: 0.80R + 0.14Na. T1: 1.00Si.
M2: 0.20R + 0.56Na. T2: 0.80Si + 0.20Be.
M3: 0.80(Mn,Fe). T3: 0.20Si + 0.80Be.
M4: 0.20(Mn,Fe) T4: 0.80Si + 0.20Be.
M5: 0.52Ca + 0.48Na. T5: 0.20Si + 0.80Be.
M6: 0.13Ca + 0.87Na. T6: 1.00Si.
T7: 1.00Si.

HELLANDITE-(Y)
$(Ca,Y)_4Y_2(Al,Fe)B_4Si_4O_{20}(OH)_4$
$(Ca,Y,\square)_4(Y,\square)_2(Al,Fe)B_4Si_4O_{18}(OH,O)_4(OH)_2$

Sys. monoclinic	$a = 18.99 \pm 0.01$ Å	source: Predazzo, Italy
S.G. P2/a	$b = 4.715 \pm 0.005$ Å	Ref.: Mellini and Merlino (1977)
$Z = 2$	$c = 10.30 \pm 0.01$ Å	JCPDS: #25-0184
Dx = 3.645 g/cm^3	$\beta = 111.4 \pm 0.1°$	
Dm = 3.63 g/cm^3		
AP: table 122	ID: table 123	IL: fig. 55

TABLE 121
Interatomic distances for semenovite-(Ce) in Å.

M1–O14	2.442(5) ×2	M2–O15	2.458(6) ×2
M1–O8	2.479(5) ×2	M2–O2	2.531(6) ×2
M1–O3	2.534(5) ×2	M2–O6	2.563(6) ×2
M1–O7	2.575(6) ×2	M2–O9	2.649(5) ×2
mean	2.508	mean	2.550
M3–O12	2.121(8) ×2	M4–O13	2.200(9) ×2
M3–O5	2.273(5) ×4	M4–O4	2.375(5) ×4
mean	2.222	mean	2.317
M5–O1	2.385(6)	M6–O1	2.355(6)
M5–O5	2.434(5)	M6–O4	2.441(6)
M5–O8	2.436(5)	M6–O13	2.450(5)
M5–O11	2.495(5)	M6–O8	2.511(6)
M5–O12	2.495(5)	M6–O9	2.544(6)
M5–O9	2.518(6)	M6–O10	2.649(6)
M5–O7	2.775(7)	M6–O3	2.663(6)
M5–O2	2.924(6)	M6–O6	2.942(6)
mean	2.558 [2.505][a]	mean	2.569 [2.516][a]
T1–O3	1.603(5)	T2–O1	1.588(6)
T1–O5	1.630(5)	T2–O8	1.610(5)
T1–O2	1.642(6)	T2–O2	1.642(6)
T1–O4	1.656(6)	T2–O6	1.651(5)
mean	1.633	mean	1.624
T3–O9	1.552(8)		
T3–O1	1.627(9)		
T3–O7	1.636(8)		
T3–O3	1.697(8)		
mean	1.628		
T4–O12	1.562(8)	T5–O13	1.559(12)
T4–O4	1.648(6) ×2	T5–O11	1.601(12)
T4–O10	1.655(9)	T5–O5	1.731(10) ×2
mean	1.629	mean	1.656
T6–O11	1.620(9)	T7–O7	1.631(5) ×2
T6–O14	1.641(8)	T7–O15	1.631(9)
T6–O6	1.663(5) ×2	T7–O10	1.691(8)
mean	1.647	mean	1.646

[a][ ]: mean after exclusion of the last distance.

TABLE 122
Atomic parameters of hellandite[a].

	x	y	z	B_{eq} (Å^2)
M1[b]	0	0	0	1.29
M2[c]	0.04179(4)	0.01878(14)	0.35996(7)	0.94
M3[d]	0.24771(8)	0.00225(37)	0.65957(16)	0.93
M4[e]	0.15428(6)	−0.03944(26)	0.92862(12)	1.02
Si1	0.0999(1)	0.4851(6)	0.6468(6)	1.10
Si2	0.1112(1)	0.4966(6)	0.1616(3)	1.31
B1	0.1708(5)	0.5344(18)	0.4510(9)	0.25(4)[f]
B2	0.2544(4)	0.4527(17)	0.1375(8)	0.18(4)[f]
H	0.047	0.04	0.92	4[f]
O1	0.0408(4)	0.2436(14)	0.5635(7)	1.36
O2	0.1757(4)	0.3127(14)	0.7556(7)	1.50
O3	0.0698(4)	−0.3003(15)	0.7357(7)	1.63
O4	0.1312(4)	−0.3268(14)	0.5404(7)	1.42
O5	0.0373(4)	0.1926(13)	0.8669(7)	1.37
O6	0.2457(4)	−0.2345(14)	0.8605(7)	1.46
O7	0.1665(4)	0.2219(13)	0.4475(6)	1.22
O8	0.1303(4)	0.6744(15)	0.3085(7)	1.89
O9	0.1872(4)	0.3281(15)	0.1633(8)	1.96
O10	0.0848(4)	0.7286(15)	0.0388(7)	1.62
O11	0.0526(4)	0.2484(15)	0.1576(7)	1.68
O12	0.25	0.3267(21)	0	1.64
O13	0.25	0.6515(20)	0.5	1.31

[a] MoKα, $R = 0.05$ (1480 refl.).
[b] M1: 0.55Al + 0.45Fe.
[c] M2: 0.87(Y,Ln).
[d] M3: 0.752Ca + 0.108(Y,Ln).
[e] M4: 0.556Ca + 0.334(Y,Ln).
[f] B(iso).

TADZHIKITE-(Ce)
$(Ca,Ce)_4Ce_2(Ti,Fe,Al)B_4Si_4(O,OH)_2O_{22}$
$(Ca,Ce)_4Ce_2(Ti,Fe,Al)B_4Si_4(O,OH)_2O_{22}$

Sys. monoclinic	$a = 18.946 \pm 0.004$ Å	source: Turkestan-Alai: alkalic province,
S.G. P2/a	$b = 4.714 \pm 0.004$ Å	Tadzhikistan
$Z = 2$	$c = 10.302 \pm 0.002$ Å	Ref.: Chernitsova et al. (1982)
Dx = 3.77 g/cm^3	$\beta = 111.58 \pm 0.02°$	JCPDS: #24-0137
Dm = 3.73 g/cm^3		
AP: table 124	ID: table 125	IL: fig. 56

CAPPELENITE-(Y)
$BaY_6Si_3B_6O_{24}F_2$
$BaY_6Si_3B_6O_{24}F_2$

Sys. trigonal (hex.)	$a = 10.67(2)$ Å	source: Lille-Arø, Langesundfjord, Norway
S.G. P3	$c = 4.680(2)$ Å	Ref.: Shen and Moore (1984)
$Z = 1$		JCPDS: #39-1349, #27-0042
AP: table 126	ID: table 127	IL: fig. 57

TABLE 123
Interatomic distances for hellandite in Å.

M1–O11	1.954(6) ×2	M2–O1	2.348(8)
M1–O5	1.979(8) ×2	M2–O1	2.355(7)
M1–O10	1.980(7) ×2	M2–O3	2.388(7)
		M2–O7	2.405(6)
mean	1.971	M2–O11	2.423[a]
		M2–O5	2.479(6)
		M2–O8	2.529(8)
		M2–O4	2.586(6)
		mean	2.439
M3–O13	2.343(7)	M4–O6	2.289(8)
M3–O9	2.360(7)	M4–O10	2.306(8)
M3–O6	2.364(8)	M4–O5	2.346(7)
M3–O7	2.400(6)	M4–O3	2.389(6)
M3–O2	2.445(8)	M4–O12	2.419(7)
M3–O7	2.500(8)	M4–O6	2.482(6)
M3–O4	2.613(6)	M4–O2	2.574(8)
M3–O8	2.703(8)	M4–O9	2.852(8)
mean	2.466	mean	2.457
Si1–O3	1.603(9)	Si2–O11	1.605(8)
Si1–O1	1.609(7)	Si2–O10	1.608(7)
Si1–O2	1.676(6)	Si2–O9	1.642(8)
Si1–O4	1.678(8)	Si2–O8	1.650(7)
mean	1.641	mean	1.626
B1–O7	1.476(11)	B2–O6	1.475(11)
B1–O13	1.506(9)	B2–O12	1.509(10)
B1–O4	1.531(13)	B2–O9	1.514(12)
B1–O8	1.535(10)	B2–O2	1.530(9)
mean	1.512	mean	1.507

[a]Calculated by RM.

Tadzhikite-(Ce) is a rare earth borosilicate described by Efimov et al. (1970) and it is chemically and structurally related to hellandite-(Y). Tadzhikite-(Ce) (fig. 56) is isostructural with hellandite-(Y) (fig. 55) and, therefore, it can be said that the mineral is a Ti-analogue of hellandite-(Y) (Chernitsova et al. 1982). The crystal structure of cappelenite-(Y) (Shen and Moore 1984) (fig. 57) is also a sheet structure of tetrahedra.

In these structures, large cations such as rare earths, calcium, sodium, barium and iron are situated between the sheets, which are connected by them. The intervals of the sheets are within the range 4.6–5.2 Å, and correspond to the lengths of the cell dimensions perpendicular to the sheets or to a half of them. In each sheet, the tetrahedra form four-, five-, six-, or eight-membered rings; in the structure of cappelenite-(Y) imaginary tetrahedra at the F1 and F2 sites are necessary to complete the eight-membered rings. It can be seen that the kinds of cations occupying the sites between the rings depend on the volume of the rings: i.e., large barium atoms occupy the sites between the six-membered rings, while rare earth, calcium, strontium and sodium atoms occupy the sites between the five- or eight-membered rings, and the relatively small space between the four-membered rings is mainly occupied by relatively small atoms such as iron, manganese, aluminum, or, rarely, sodium atoms.

TABLE 124
Atomic parameters of tadzhikite-(Ce)[a].

	x	*y*	*z*	*B*
Ti,Fe	0	0	0	1.14(8)
Ce	0.0421(1)	0.0194(4)	0.3595(2)	1.02(2)
Ca1	0.2518(2)	0	0.3399(4)	0.99(6)
Ca2	0.3450(2)	0.9616(7)	0.0708(3)	0.99(4)
Si1	0.1015(4)	0.488(2)	0.647(1)	0.84(8)
Si2	0.3871(4)	0.496(2)	0.837(1)	0.84(9)
B1	0.171(2)	0.523(7)	0.448(3)	0.32(31)
B2	0.244(2)	0.460(7)	0.861(3)	1.12(40)
O1	0.460(1)	0.244(4)	0.439(2)	1.10(30)
O2	0.323(1)	0.319(4)	0.243(2)	0.90(30)
O3	0.070(1)	0.706(4)	0.730(2)	1.30(30)
O4	0.131(1)	0.667(4)	0.538(2)	1.00(30)
O5	0.462(1)	0.192(4)	0.132(2)	1.00(30)
O6	0.255(1)	0.759(4)	0.140(2)	1.20(30)
O7	0.166(1)	0.229(4)	0.447(2)	0.50(20)
O8	0.132(1)	0.676(4)	0.310(2)	1.00(30)
O9	0.312(1)	0.330(4)	0.838(2)	1.40(30)
O10	0.086(1)	0.733(4)	0.042(2)	1.00(30)
O11	0.055(1)	0.255(4)	0.159(2)	1.60(30)
O12	0.25	0.331(6)	0	0.30(30)
O13	0.25	0.652(6)	0.5	0.70(40)

[a] MoKα, $R = 0.072$ (1004 refl.).

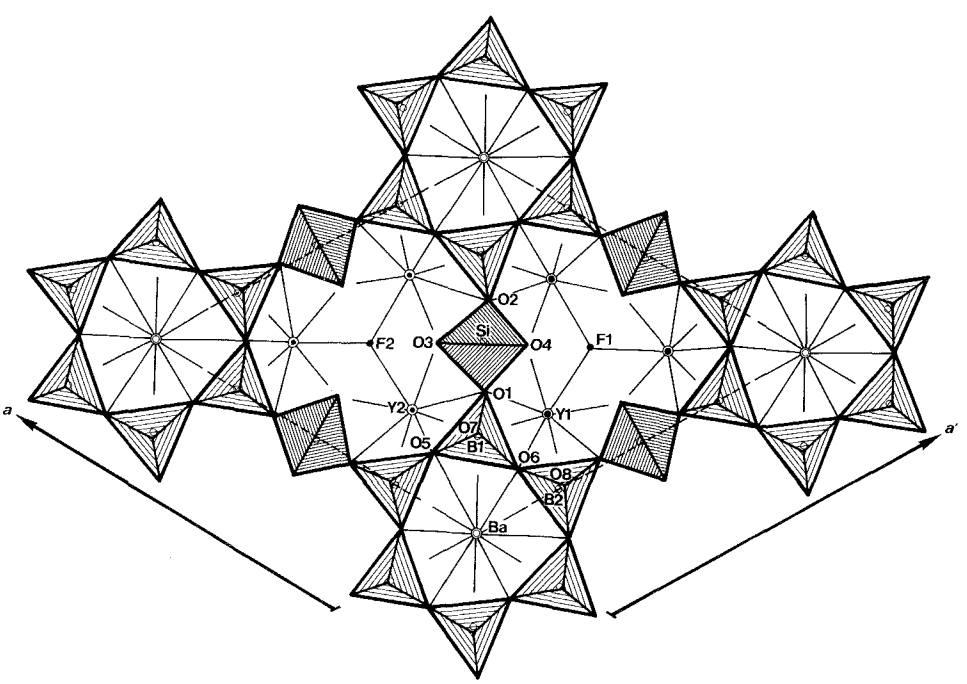

Fig. 57. The crystal structure of cappelenite-(Y).

TABLE 125
Interatomic distances for tadzhikite-(Ce) in Å[a].

Ti,Fe–O5	1.98(2) ×2	Ce–O1	2.34(2)
Ti,Fe–O10	1.98(2) ×2	Ce–O1	2.36(2)
Ti,Fe–O11	1.99(2) ×2	Ce–O3	2.37(2)
mean	1.98	Ce–O7	2.40(2)
		Ce–O11	2.44(2)
		Ce–O5	2.48(2)
		Ce–O8	2.53(2)
		Ce–O4	2.59(2)
		mean	2.44
Ca1–O13	2.34(2)	Ca2–O6	2.29(2)
Ca1–O9	2.37(2)	Ca2–O10	2.31(2)
Ca1–O6	2.37(2)	Ca2–O5	2.34(2)
Ca1–O7	2.43(2)	Ca2–O3	2.41(2)
Ca1–O2	2.46(2)	Ca2–O12	2.42(2)
Ca1–O7	2.52(2)	Ca2–O6	2.49(2)
Ca1–O4	2.63(2)	Ca2–O2	2.59(2)
Ca1–O8	2.66(2)	Ca2–O9	2.84(2)
mean	2.47	mean	2.46
Si1–O3	1.59(2)	Si2–O11	1.57(2)
Si1–O1	1.65(2)	Si2–O10	1.61(2)
Si1–O4	1.66(2)	Si2–O9	1.63(2)
Si1–O2	1.67(2)	Si2–O8	1.66(2)
mean	1.64	mean	1.62
B1–O7	1.39(4)	B2–O6	1.41(4)
B1–O13	1.52(4)	B2–O2	1.48(3)
B1–O8	1.52(3)	B2–O12	1.52(3)
B1–O4	1.55(4)	B2–O9	1.52(4)
mean	1.50	mean	1.48

[a]Calculated by RM.

SAZHINITE-(Ce)
$Na_2Ce[Si_6O_{14}(OH)] \cdot nH_2O$ ($n \geqslant 1.5$)
$Na_2Ce[Si_6O_{14}(OH)] \cdot nH_2O$ ($n \geqslant 1.5$)

Sys. orthorhombic	$a = 7.50 \pm 0.03$ Å	source: Lovozero, Kola Peninsula, Russia
S.G. Pmm2	$b = 15.62 \pm 0.06$ Å	Ref.: Shumyatskaya et al. (1980)
$Z = 2$	$c = 7.35 \pm 0.03$ Å	JCPDS: #30-1176
AP: table 128	ID: table 129	IL: fig. 58

The structure of sazhinite-(Ce) (fig. 58) is based on infinite corrugated networks formed by four-, six:-, and eight-membered rings of Si tetrahedra (Shumyatskaya et al. 1980), in contrast to the flat networks in the crystal structure of gadolinite-(Y) (fig. 51). Cerium atoms are located between the networks forming seven-coordinated monocapped octahedra. The Na1 atoms lie in distorted tetragonal pyramids with a

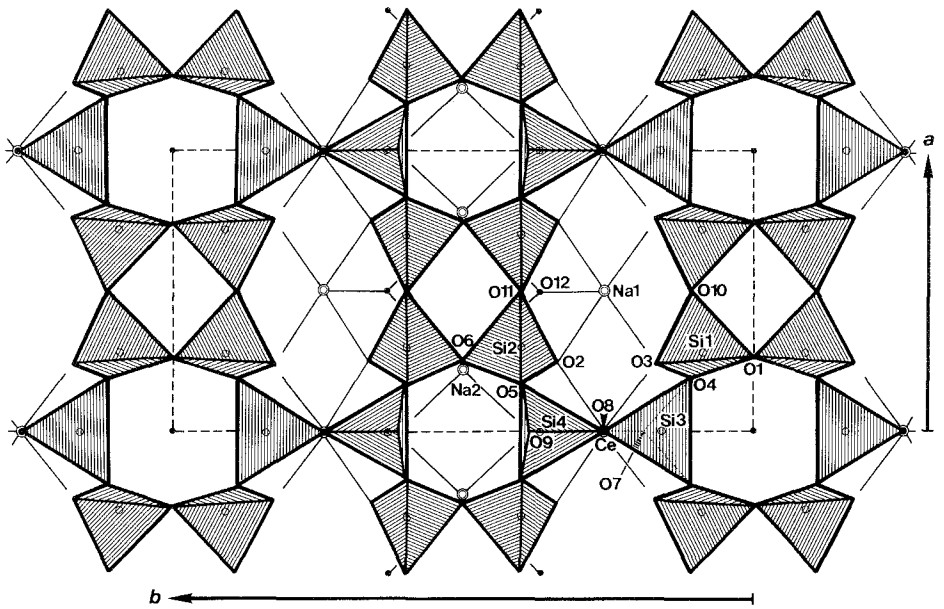

Fig. 58. The crystal structure of sazhinite-(Ce).

coordination number 5, while the Na2 atoms are surrounded by three O atoms at distances of 2.45–2.63 Å, and two water molecules at distances of about 3 Å. This coordination number of the Na2 is rather small and some anions might still be missing. Shumyatskaya et al. (1980) pointed out that the crystal structures of sazhinite-(Ce), dalyite, $K_2ZrSi_6O_{15}$, armstrongite, $CaZrSi_6O_{15} \cdot 2.5H_2O$, and the two artificial compounds $K_3NdSi_6O_{15}$ and $K_2Be_2Si_6O_{15}$, are made up of corrugated networks of "xonotlite bands of dalyite type". However, each structure can be distinguished by the arrangements of the four-, five-, six-, and eight-membered rings.

MONTEREGIANITE-(Y)
$Na_4K_2Y_2Si_{16}O_{38} \cdot 10H_2O$
$(Na,Ca,\square)_2(\square,Na)_2K_2Y_2Si_{16}O_{38} \cdot 12(H_2O,\square)$

Sys.	monoclinic	$a = 9.512(2)$ Å	source: Mont St. Hilaire, Que., Canada
S.G.	$P2_1/n$	$b = 23.956(4)$ Å	Ref.: Ghose et al. (1987)
$Z =$	2	$c = 9.617(2)$ Å	JCPDS: #31-1087
Dx =	2.41 g/cm^3	$\beta = 93.85(1)°$	
Dm =	2.42 g/cm^3		
AP:	table 130	ID: table 131	IL: fig. 59

Monteregianite-(Y) was described by Chao (1978) to be orthorhombic and a member of the macdonaldite, $BaCa_4Si_{16}O_{36}(OH)_2 \cdot 10H_2O$, group. Ghose et al.

TABLE 126
Atomic parameters of cappelenite-(Y)[a].

	K	x	y	z
Y1	1.225(6)	0.2155(2)	0.4311(2)	0.9401(6)
Y2	1.160(6)	0.4320(2)	0.2161(2)	0.9722(9)
Ba	1	0	0	0
Si	1	0.0088(7)	0.5049(7)	0.4100(14)
B1	1	0.255(2)	0.255(2)	0.474(4)
B2	1	0.003(3)	0.254(2)	0.475(4)
O1	1	0.371(2)	0.387(2)	0.630(3)
O2	1	0.018(2)	0.387(2)	0.631(3)
O3	1	0.572(2)	0.428(1)	0.236(3)
O4	1	0.426(2)	0.573(2)	0.197(3)
O5	1	0.281(2)	0.140(2)	0.600(3)
O6	1	0.112(2)	0.227(2)	0.619(3)
O7	1	0.260(1)	0.262(1)	0.186(3)
O8	1	0.001(2)	0.265(2)	0.188(3)
F1	1	0.3333	0.6667	0.735(4)
F2	1	0.6667	0.3333	0.783(4)

[a] MoKα, $R = 0.063$ (1450 refl.).

TABLE 127
Interatomic distances for cappelenite-(Y) in Å.

Y1–O4	2.32	Y2–O5	2.23
Y1–O4	2.32	Y2–O3	2.34
Y1–O7	2.38	Y2–O3	2.34
Y1–O8	2.38	Y2–O7	2.34
Y1–O2	2.40	Y2–O8	2.34
Y1–O6	2.41	Y2–O1	2.73
Y1–O1	2.42	Y2–O2	2.75
mean	2.38	mean	2.44
Y1–F1	2.38	Y2–F2	2.34
Ba–O6	2.75 ×3	Si–O3	1.62
Ba–O7	2.92 ×3	Si–O4	1.62
Ba–O8	2.95 ×3	Si–O1	1.65
Ba–O5	3.20 ×3	Si–O2	1.66
mean	2.96	mean	1.64
B1–O7	1.35	B2–O8	1.35
B1–O5	1.50	B2–O6	1.50
B1–O1	1.52	B2–O5	1.51
B1–O6	1.55	B2–O2	1.53
mean	1.48	mean	1.47

TABLE 128
Atomic parameters of sazhinite-(Ce)[a].

	x	y	z	B (Å^2)
Ce	0	0.260	0.004	3.55
Na1	0.5	0.261	0.005	3.86
Na2	0.222	0.5	0.875	6.87
Si1	0.284	0.094	0.760	3.29
Si2	0.298	0.402	0.295	2.88
Si3	0	0.164	0.496	4.39
Si4	0	0.365	0.592	3.74
O1	0.257	0	0.823	3.69
O2	0.245	0.335	0.139	5.18
O3	0.241	0.171	0.916	3.58
O4	0.192	0.114	0.565	2.56
O5	0.171	0.398	0.487	5.69
O6	0.254	0.5	0.232	3.95
O7[b]	0	0.189	0.276	4.56
O8	0	0.259	0.604	4.57
O9	0	0.392	0.789	6.36
O10	0.5	0.113	0.688	4.45
O11	0.5	0.402	0.377	5.18
O12[c]	0.5	0.373	0.766	4.22
O13[c]	0	0	0.138	10.02

[a] Mo, $R = 0.119$ (394 refl.).
[b] (OH).
[c] H_2O.

TABLE 129
Interatomic distances for sazhinite-(Ce) in Å.

Ce–O7	2.29		Na1–O2	2.44 ×2
Ce–O3	2.36 ×2		Na1–O3	2.48 ×2
Ce–O2	2.40 ×2		Na1–O12	2.48
Ce–O9	2.60		mean	2.46
Ce–O8	2.94			
mean	2.48		Na2–O9	2.45 ×2
			Na2–O6	2.63
			mean	2.51
Si1–O1	1.56		Si2–O2	1.61
Si1–O4	1.62		Si2–O6	1.63
Si1–O3	1.69		Si2–O11	1.63
Si1–O10	1.72		Si2–O5	1.71
mean	1.65		mean	1.65
Si3–O7	1.66		Si4–O9	1.51
Si3–O8	1.68		Si4–O5	1.58 ×2
Si3–O4	1.72 ×2		Si4–O8	1.66
mean	1.70		mean	1.58

TABLE 130
Atomic parameters of monteregianite-(Y)[a].

	x	y	z	U_{eq}[b]
Y[c]	−0.25645(4)	0.49845(2)	0.74445(4)	0.00432(9)
K1[d]	0.0685(8)	0.2488(3)	0.5702(9)	0.042(2)
K2[e]	0.541(1)	0.2478(5)	0.47(1)	0.036(2)
Na1[f]	0.3713(3)	0.4991(1)	0.6312(3)	0.0180(7)
Na2a[g]	0.5	0.5	0	0.017(1)
Na2b[h]	0	0.5	0.5	0.018(1)
Si1	−0.2661(2)	0.18159(6)	0.7344(2)	0.0072(4)
Si2a	−0.4972(2)	0.38752(7)	0.2288(2)	0.0073(4)
Si2b	0.2275(2)	0.38831(7)	−0.4931(2)	0.0078(4)
Si3	−0.4548(2)	0.38870(7)	0.5524(2)	0.0077(4)
Si4	−0.2553(2)	0.31464(7)	0.7465(2)	0.0067(4)
Si5a	0.2269(2)	0.11133(7)	−0.4953(2)	0.0081(4)
Si5b	0.4979(2)	0.11160(7)	0.2246(2)	0.0082(4)
Si6	−0.4521(2)	0.10614(7)	0.5519(2)	0.0083(4)
O1	−0.2588(5)	0.2481(2)	0.7358(5)	0.015(1)
O2a	−0.6183(4)	0.3414(2)	0.1882(5)	0.015(1)
O2b	0.2029(5)	0.3384(2)	−0.6097(5)	0.020(1)
O3	−0.3907(5)	0.1646(2)	0.6230(5)	0.019(1)
O4a	0.1264(4)	0.1277(2)	−0.3711(4)	0.012(1)
O4b	−0.3769(4)	0.1272(2)	0.1274(5)	0.012(1)
O5a	−0.4349(5)	0.3718(2)	0.3891(5)	0.017(1)
O5b	0.3827(4)	0.3798(2)	−0.4176(5)	0.021(1)
O6a	0.4517(4)	0.4501(2)	0.2176(5)	0.015(1)
O6b	0.2110(5)	0.4491(2)	0.4465(5)	0.017(1)
O7	−0.4038(5)	0.4494(2)	0.5892(5)	0.015(1)
O8	−0.3758(5)	0.3390(2)	0.6428(5)	0.020(1)
O9a	−0.2757(5)	0.3320(2)	0.9063(5)	0.019(1)
O9b	0.8934(5)	0.3343(2)	−0.2989(6)	0.024(1)
O10a	−0.4379(5)	0.1155(3)	0.3852(5)	0.027(2)
O10b	0.3843(4)	0.1067(2)	−0.4185(5)	0.018(1)
O11a	0.6829(5)	0.4428(2)	−0.0799(5)	0.015(1)
O11b	−0.0778(5)	0.4450(2)	0.6889(5)	0.019(1)
O12	−0.3704(5)	0.0540(2)	0.6113(6)	0.027(2)
W1	0.8428(7)	0.4480(4)	0.3443(9)	0.059(3)
W2	0.3238(8)	0.4521(4)	0.8570(7)	0.051(2)
W3[i]	0.622(1)	0.2492(4)	0.359(1)	0.059(3)
W4[j]	0.891(1)	0.187(1)	0.356(2)	0.105(8)
W5[k]	0.382(2)	0.182(1)	0.865(2)	0.08(1)
W6[l]	0.633(3)	0.750(1)	−0.610(3)	0.09(1)

[a] MoKα, $R = 0.059$ (4877 refl.).
[b] $U_{eq} = \frac{1}{3}$ trace of orthogonalized u tensor.
[c] Y: 0.60Y + 0.40Ce. [d] K1: 0.62K. [e] K2: 0.38K. [f] Na1: 0.95Na.
[g] Na2a: 0.47Na. [h] Na2b: 0.45Na. [i] W3: $0.95H_2O$. [j] W4: $0.46H_2O$.
[k] W5: $0.35H_2O$. [l] W6: $0.37H_2O$.

TABLE 131
Interatomic distances for monteregianite-(Y) in Å[a].

Y–O12	2.217(5)	K1–W3	2.761(12)	K2–W4	2.726(23)	Na1–W1	2.442(8)
Y–O11b	2.235(5)	K1–W6	2.866(31)	K2–W5	2.732(28)	Na1–O7	2.469(6)
Y–O11a	2.245(5)	K1–O9a	2.955(9)	K2–O9b	2.886(13)	Na1–O6a	2.473(5)
Y–O6b	2.276(5)	K1–W4	2.956(20)	K2–W3	3.017(15)	Na1–W2	2.495(8)
Y–O6a	2.295(5)	K1–O9b	2.978(10)	K2–O2b	3.034(13)	Na1–O7	2.523(6)
Y–O7	2.300(5)	K1–O4a	2.998(9)	K2–O9a	3.044(13)	Na1–O6b	2.557(6)
mean	2.261	K1–W5	3.049(27)	K2–O4b	3.076(12)	mean	2.493
		K1–O4b	3.059(9)	K2–O2a	3.077(13)		
		K1–O2a	3.069(9)	K2–W6	3.144(32)		
		K1–O2b	3.084(9)	K2–O4a	3.176(12)		
		mean	2.978	mean	2.991		
Na2a–O11a	2.393(5) ×2	Na2b–O11b	2.389(5) ×2				
Na2a–W2	2.394(5) ×2	Na2b–W1	2.395(5) ×2				
Na2a–O6a	2.461(5) ×2	Na2b–O6b	2.450(5) ×2				
mean	2.416	mean	2.411				
Si1–O1	1.594(5)	Si2a–O6b	1.579(5)	Si2b–O6b	1.569(5)	Si3–O7	1.568(5)
Si1–O3	1.598(5)	Si2a–O4a	1.613(5)	Si2b–O4b	1.617(5)	Si3–O5b	1.621(5)
Si1–O2b	1.605(5)	Si2a–O2a	1.633(5)	Si2b–O5b	1.625(5)	Si3–O8	1.627(5)
Si1–O2a	1.612(5)	Si2a–O5b	1.644(5)	Si2b–O2b	1.637(5)	Si3–O5a	1.629(5)
mean	1.602	mean	1.617	mean	1.612	mean	1.611
Si4–O8	1.582(5)	Si5a–O11a	1.570(5)	Si5b–O11b	1.565(5)	Si6–O12	1.562(5)
Si4–O9b	1.592(5)	Si5a–O4a	1.624(5)	Si5b–O4b	1.611(5)	Si6–O10a	1.616(5)
Si4–O1	1.598(5)	Si5a–O10b	1.640(4)	Si5b–O10a	1.611(5)	Si6–O10b	1.617(5)
Si4–O9a	1.600(5)	Si5a–O9a	1.649(5)	Si5b–O9b	1.645(6)	Si6–O3	1.647(5)
mean	1.593	mean	1.621	mean	1.608	mean	1.611

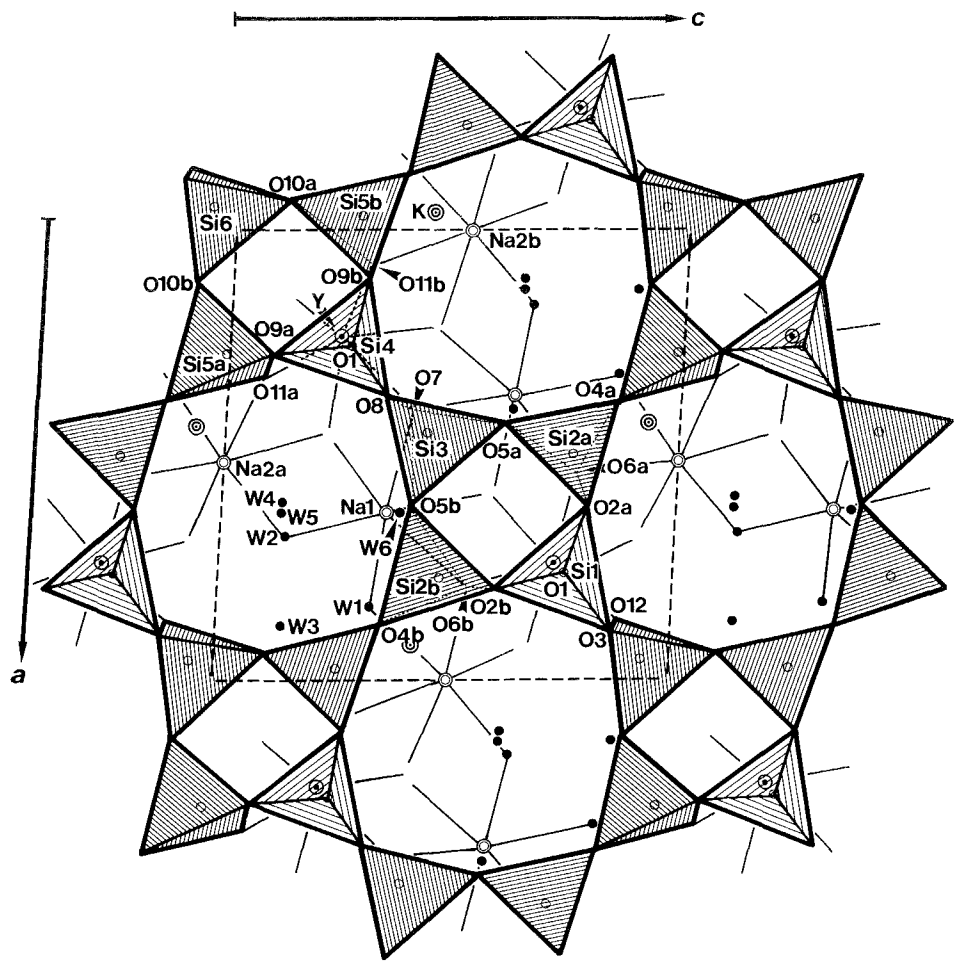

Fig. 59. The crystal structure of monteregianite-(Y).

(1987) analyzed the crystal structure of monteregianite-(Y) and revealed the true symmetry to be monoclinic. The structure (fig. 59) consists of double apophyllite-type silicate sheets with four- and eight-membered rings, and open octahedral sheets composed of $[YO_6]$ and $[NaO_4(H_2O)_2]$ octahedra. The potassium atoms are located inside the large channels of the silicate sheets, with a coordination number of ten. The six water molecules (three in partially occupied sites) are located within large channels formed by the planar eight-membered silicate rings.

Ghose et al. (1987) pointed out that the crystal structure of monteregianite-(Y) and that of rhodesite, $K_2Ca_4Na_2Si_{16}O_{38} \cdot 12H_2O$, are related by the substitution $(Na_4Y_2) \rightleftarrows (Ca_4Na_2)$. Furthermore, they pointed out the inadequacy of the description of rhodesite (Gard and Tayler 1957, Mountain 1957) and the necessity for reexamination of its chemical composition, symmetry, unit-cell dimensions and the crystal structure.

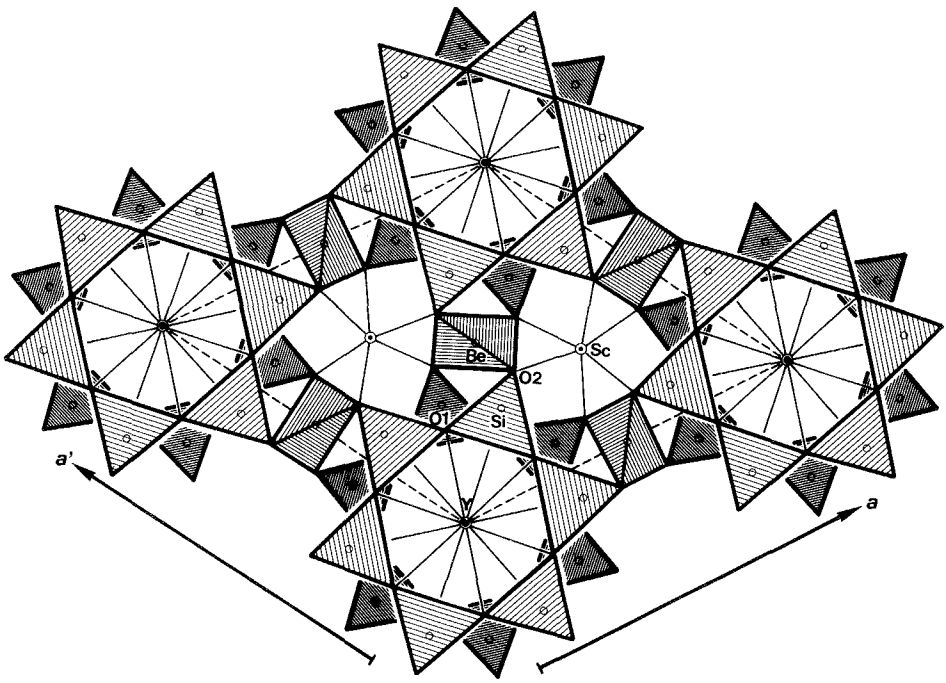

Fig. 60. The crystal structure of bazzite.

BAZZITE
$Be_3(Sc,Fe)_2Si_6O_{18}$
$[Na,Ca,K,(H_2O),Y](Si,Be)_3(Sc,Fe,Al,Mg,Mn,Ti,Sn,Y)_2Si_6O_{18}$

Sys. hexagonal	$a = 9.51 \pm 0.01$ Å	source: Baveno, Italy
S.G. P6/mcc	$c = 9.11 \pm 0.01$ Å	Ref.: Peyronel (1956)
$Z = 2$		JCPDS: #20-0165
Dx = 2.809–2.825 g/cm^3		
Dm = 2.819 ± 0.002 g/cm^3		
AP: table 132	ID: table 133	IL: fig. 60

MILARITE
$(K,Na)_xK(Ca,Y)_2(Be,Al)_3Si_{12}O_{30}(H_2O)_z$
$(Na,H_2O,\square)_2(K,Na,Ba)(Ca,Y,Na)_2(Be,Al)_3Si_{12}O_{30}$

Sys. hexagonal	$a = 10.342(2)$ Å	source: Jaguaraçú, Minas Gerais, Brazil
S.G. P6/mcc	$c = 13.777(6)$ Å	Ref.: Hawthorne et al. (1991)
$Z = 2$		JCPDS: #35-0459, #12-0450
AP: table 134	ID: table 135	IL: fig. 61

The crystal structure of bazzite was determined using X-ray photographic data by Peyronel (1956). Bazzite has a beryl ($Be_3Al_2Si_6O_{18}$)-type structure with two (Si_6O_{18}) rings at $z = 0$ and $\frac{1}{2}$, and with cations distributed at $z = \frac{1}{4}$ and $\frac{3}{4}$ in three special positions (fig. 60). Peyronel (1956) evaluated the probable distribution of qualitatively recognized cations for each special positions from the observed interatomic distances and the total electron contents of the special positions. He reported that Sc atoms

TABLE 132
Atomic parameters of bazzite[a].

	x	y	z
Sc[b]	2/3	1/3	1/4
Y[c]	0	0	1/4
Be[d]	1/2	0	1/4
Si	0.367	0.095	0
O1	0.294	0.214	0
O2	0.489	0.128	0.139

[a]FeKα, $R_{hki0} = 0.1719$ (25 refl.), $R_{h0\bar{h}l} = 0.15$ (25 refl.).
[b]Sc: Sc Fe,Al,Mg,Mn,Ti,Sn,Y.
[c]Y: Na,Ca,K,(H_2O),Y.
[d]Be: Si,Be.

TABLE 133
Interatomic distances for bazzite in Å.

Y–O1	2.70 ×12	Sc–O2	2.10 ×6
Si–O1	1.59 ×2	Be–O2	1.62 ×4
Si–O2	1.64 ×2		
mean	1.62		

TABLE 134
Atomic parameters of yttrian milarite[a].

	x	y	z	U_{eq}
A[b]	1/3	2/3	0.23572(7)	0.0046(3)
B[c]	1/3	2/3	0.0499(13)	0.0602(62)
C[d]	0	0	1/4	0.0193(7)
T1[e]	0.08132(8)	0.33844(9)	0.11249(5)	0.0087(3)
T2[f]	0	1/2	1/4	0.0097(21)
O1	0.0946(4)	0.3873(4)	0	0.0205(14)
O2	0.1959(3)	0.2779(3)	0.1333(2)	0.0180(9)
O3	0.1158(2)	0.4751(2)	0.1821(1)	0.0118(7)

[a]MoKα, $R = 0.033$ (561 refl.).
[b]A: Ca,Y,Ln. [c]B: Na,H_2O,□. [d]C: K. [e]T1: Si. [f]T2: Be,Al.

TABLE 135
Interatomic distances for yttrian milarite in Å.

A–O3	2.253(2) ×3	B–O1	2.790(5) ×3
A–O3	2.411(2) ×3	B–O3	2.801(11) ×3
mean	2.332	mean	2.796
T1–O3	1.594(2)	C–O2	3.021(2) ×12
T1–O1	1.614(1)	T2–O3	1.638(3) ×4
T1–O2	1.618(4)		
T1–O2	1.619(4)		
mean	1.611		

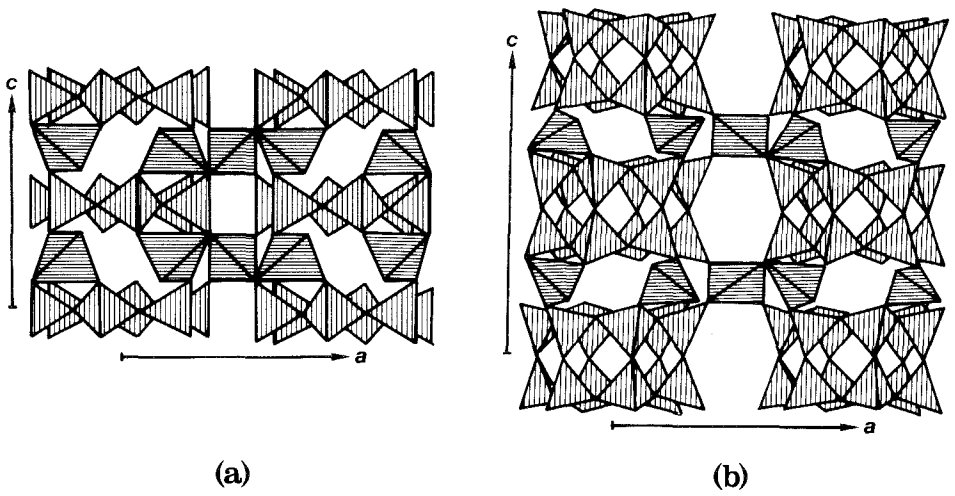

Fig. 61. Schematic illustrations of the crystal structures of bazzite (a) and milarite (b).

occupy the six-coordinated (c) site with Fe, Al, Mg, Mn, and small amounts of Ti, Sn, Y and Yb. The twelve-coordinated (a) site is occupied by Na, Ca, and K atoms, water molecules and small quantities of rare earth atoms, Y and Yb. The tetrahedral (f) site is occupied by Be and Si. Later, Nowacki and Phan (1964) and Chistyakova et al. (1966) independently made quantitative analyses of bazzite from Val Strem, Switzerland and the CIS, respectively. Their analyses revealed that bazzite is an Sc-analogue of beryl, but not a scandian beryl. The analysis by Chistyakova et al. (1966) gave the following formula: $Be_{3.06}[(Sc_{1.26}Fe^{3+}_{0.17}Al_{0.03})(Fe^{2+}_{0.31}Mn_{0.13}Mg_{0.12})]$-$(Na_{0.55}K_{0.03}Cs_{0.01})[(Si_{5.93}Be_{0.07})O_{18}] \cdot 0.87H_2O$. This formula corresponds well with the formula derived from the structure analysis by Peyronel (1956).

Cerny et al. (1991) described yttrian milarite from Minas Gerais, Brazil, which contains up to 7.90 wt% of Y_2O_3. Hawthorne et al. (1991) analyzed crystal structures of six milarite specimens, including yttrian milarite. They gave the general formula $A_2B_2C[T2_3T1_{12}O_{30}](H_2O)_x$ (A: Al, Fe^{3+}, Sn^{4+}, Mg, Zr, Fe^{2+}, Ca, Na, Y, Ln; B: Na, H_2O, □, Ca?, K?; C: K, Na, Ba, □, Ca?; T1: Si, Al; T2: Li, Be, B, Mg, Al, Si, Mn^{2+}, Zn) for milarite after their structure analyses. The crystal structure of milarite is close to that of bazzite (beryl). The difference in the crystal structures between milarite and bazzite is the numbers of the (Si_6O_{18}) rings. In contrast to the single (Si_6O_{18}) ring in the structure of bazzite (fig. 61a), the crystal structure of milarite consists of double (Si_6O_{18}) rings (fig. 61b). The A, C, T1 and T2 sites in milarite correspond to the Sc, Y, Si and Be sites in bazzite, respectively. Hawthorne et al. (1991) reported that the important substitutions in milarite are $Na + Be \rightleftarrows \square + Al$ and $Y + Be \rightleftarrows Ca + Al$. They also pointed out that the cations in the A and B sites always show positional disorder at the central position, and that the splitting distance is a function of the Be/(Be + Al) ratio.

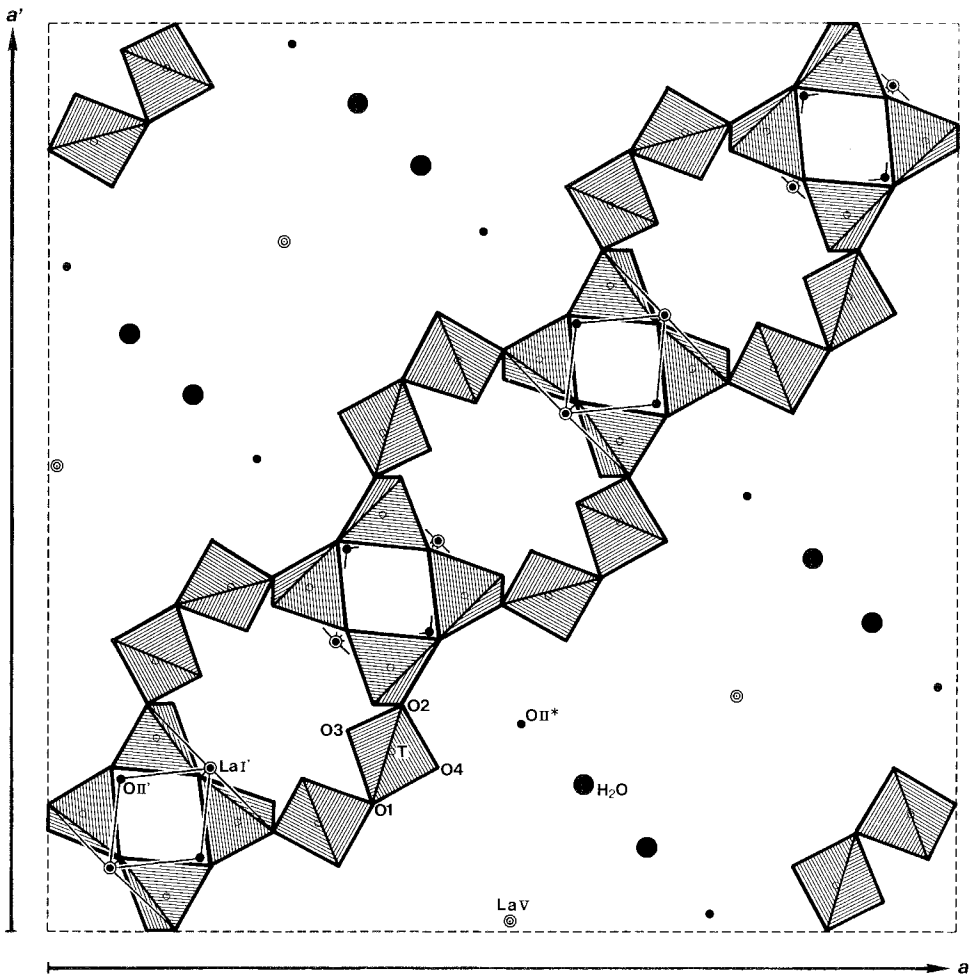

Fig. 62. The crystal structure of La-exchanged faujasite. A part of the structure (atoms at $z = 0$) is drawn.

TABLE 136
Atomic parameters of La-exchanged faujasite[a].

	x	y	z	B (Å^2)	Occ.[b]
La I′	0.0693(5)	0.0693	0.0693	3.1(6)	0.103(9)
La V	0.4907(2)	0.4907	0.4907	6.0(3)	0.322(9)
T	0.9637(1)	0.8745(1)	0.0535(1)	1.13(7)	1 (Si,Al)
O1	0.1057(3)	0.8943	0	2.3(2)	1
O2	0.0028(3)	0.0028	0.8580(4)	2.1(2)	1
O3	0.9239(3)	0.9239	0.0329(4)	1.8(2)	1
O4	0.9292(3)	0.9292	0.6772(4)	2.0(2)	1
O II′	0.1667(6)	0.1667	0.1667	2.9(8)	0.884(78)
O II*	0.2718(2)	0.2718	0.2718	6.4(10)	0.444(56)
H_2O	0.338	0.338	0.338	10.0	0.138(72)

[a]MoKα, $R = 0.12$ (426 refl.). [b]Occupancy.

TABLE 137
Interatomic distances for La-exchanged faujasite in Å.

La I′–O II′	2.45(1)	T–O2	1.632(4)
La I′–O3	2.53(1)	T–O1	1.643(4)
La I′–O2	3.09(1)	T–O3	1.647(4)
La I′–O II′	4.17(1)	T–O4	1.648(4)
		mean	1.643

La-exchanged FAUJASITE*
$La_x(Si,Al)_6O_{12} \cdot nH_2O$
$(\square,La)_3(Si,Al)_6O_{12} \cdot nH_2O$

Sys. cubic	$a = 24.69$ Å	source: synthetic $La_x(Si,Al)_6O_{12} \cdot nH_2O$
S.G. Fd3m		Ref.: Bennett and Smith (1969)
$Z = 32$		
AP: table 136	ID: table 137	IL: fig. 62

*Not natural but artificial. An example of zeolite containing rare earths.

Bennett and Smith (1969) determined the crystal structure of La-exchanged faujasite. In the structure (fig. 62), lanthanum atoms and water molecules are located in the large spaces between framework structures of zeolitic type, with partial occupancies. However, they mentioned that the electron density was insufficient to account for all the cations and water molecules, implying that they might move frequently from site to site. The R factor of their analysis was high, i.e. 0.15 for all reflections, and further analysis of the structure is necessary.

IRAQITE-(La)
$K(La,Th)_2(Ca,Na)_4(Si,Al)_{16}(O,F)_{40}$
$(La,Th,U,Pb)(K,\square)(Ca,La,Na)_2(Si,Al)_8(O,F)_{20}$

Sys. tetragonal	$a = 7.61 \pm 0.01$ Å	source: Shakhi-Rash Mt. Hero, Qala-Diza, Iraq
S.G. P4/mcc	$c = 14.72 \pm 0.02$ Å	Ref.: Livingstone et al. (1976)
$Z = 2$		JCPDS: #29-0995
$Dx = 3.28$ g/cm^3		
$Dm = 3.27$ g/cm^3		

Livingstone et al. (1976) described iraqite as a member of the ekanite, $ThCa_2Si_8O_{20}$, group. Although the crystal structure is unknown, iraqite-(La) may be isostructural with ekanite and steacyite, $K_{0.3}(Na,Ca)_2ThSi_8O_{20}$ (Perrault and Szymanski 1982).

ROWLANDITE-(Y)
$(Y,Ca,Na,Th)_4(Fe,Mn,Mg)[(Si,Al)_2O_7][F,(OH),Cl]_2$ (?)
$(Y,Ca,Na,Th)_4(Fe,Mn,Mg)[(Si,Al)_2O_7][F,(OH),Cl]_2$ (?)

Sys. ? (metamict)	$a =$	source: Barringer Hill, Llano Co., TX, USA
S.G.	$b =$	Ref.: Peacor et al. (1982)
$Z =$	$c =$	JCPDS: #13-0565

Crook et al. (1978) gave for rowlandite-(Y) the chemical formula (Y,Ln,Fe,Mn,Mg, Ca,Na,K,Th)$_3$[(Si,Al)O$_4$]$_2$(F,OH,Cl), after their chemical analysis. However it is unreasonable to consider that both larger ions, such as Y, Ln, Ca, and smaller ions, Fe, Mn, Mg, occupy the same site in the crystal structure. The chemical formula $(Y,Ca,Th,Na,K)_4(Fe,Mn,Mg)(SiO_4)_2[SiO_3(F,OH,Cl)]_2$ is recalculated by the present authors from the viewpoint of crystal chemistry of rare earth ions, using the result of Crook et al. (1978). It suggests the isomorphous substitutions $2R^{3+} \rightleftarrows Th^{4+}Ca^{2+}$. However, Peacor et al. (1982) pointed out errors in the calculation of the empirical formula, and unsuitabilities of the analytical standards and accelerating voltage in the electron microprobe analysis for rare earths used by Crook et al. (1978). Therefore, the validity of the above chemical formula is under question.

The similarity between the X-ray diffraction patterns of rowlandite-(Y) and yttrialite-(Y) heated under identical conditions suggests only that the phase assemblages that result from recrystallization are similar, not that the rowlandite-(Y) and yttrialite-(Y) structures are similar. The crystal structure of rowlandite-(Y) has never been analyzed because it occurs in the metamict state.

MAGBASITE
$KBa(Mg,Fe)_6(Al,Sc)Si_6O_{20}F_2$
$KBa(Mg,Fe)_6(Al,Sc)Si_6O_{20}F_2$

Sys. ?	$a =$	source: Asia of CIS
S.G.	$b =$	Ref.: Semenov et al. (1965)
$Z =$	$c =$	JCPDS: #18-0766
Dm ≈3.41 g/cm^3		

Semenov et al. (1965) described magbasite, $KBa(Mg,Fe)_6(Al,Sc)Si_6O_{20}F_2$. The chemical formula indicates an isomorphous substitution of Al with Sc. Although they gave X-ray powder diffraction data, crystallographic data were not given.

2.3. *Class 3: structures with tetrahedral and octahedral anionic groups – aluminosilicates and titanosilicates*

The crystal structures of this class contain tetrahedra of silicon, aluminum, and octahedra of aluminum, titanium, etc. These tetrahedra and octahedra form infinite anionic groups in their crystal structures.

TUNDRITE-(Ce)
$Na_2Ce_2TiO_2[SiO_4](CO_3)_2$
$Na_2Ce_2TiO_2[SiO_4](CO_3)_2$

Sys. triclinic	$a =$ 7.560 ± 0.002 Å	source: Khibinsk, CIS
S.G. $P\bar{1}$	$b =$ 13.957 ± 0.003 Å	Ref.: Shumyatskaya et al. (1976)
$Z = 2$	$c =$ 5.040 ± 0.001 Å	JCPDS: #25-1188, #18-1413
	$\alpha = 101°07' \pm 10'$	
	$\beta = 70°52' \pm 10'$	
	$\gamma = 100°01' \pm 10'$	
AP: table 138	ID: table 139	IL: fig. 63

TUNDRITE-(Nd)
$Na_2Nd_2TiO_2[SiO_4](CO_3)_2$
$Na_2Nd_2TiO_2[SiO_4](CO_3)_2$

Sys. triclinic	$a =$ 7.54 Å	source: Ilímaussaq, Greenland
S.G. $P\bar{1}$	$b =$ 13.98 Å	Ref.: Semenov et al. (1967)
$Z = 2$	$c =$ 5.02 Å	
	$\alpha = 101°30'$	
	$\beta = 70°25'$	
	$\gamma = 101°30'$	

The crystal structure of tundrite-(Ce) was first reported by Shumyatskaya et al. (1969) with the chemical formula $Na_3Ce_3Ti_2(SiO_4)_2(O,OH)_8 \cdot 8H_2O$. A revised formula, $(Na,K)_{3-x}(R,Ca)_4(Ti,Nb)_2(SiO_4)_2(CO_3)_3(OH) \cdot 2H_2O$, was proposed by

TABLE 138
Atomic parameters of tundrite-(Ce)[a].

	x	y	z	B (Å²)
Ce1	0.6565	0.7787	0.5923	0.83
Ce2	0.2181	0.7776	0.3103	1.04
Ti	0.6100	0.9997	0.1947	0.10
Si	0.9610	0.8578	0.9115	0.37
Na1	0	0	0.5	1.82
Na2	0.1405	0.4747	0.1748	2.08
Na3	0.5	0.5	0.5	3.26
C1	0.7914	0.3534	0.2433	1.22
C2	0.5993	0.6535	0.0623	0.71
O1	0.9335	0.7563	0.7068	0.66
O2	0.7925	0.9172	0.9089	0.81
O3	0.1613	0.9167	0.7245	0.70
O4	0.9563	0.8430	0.2243	0.88
O5	0.4053	0.9185	0.0677	0.81
O6	0.5504	0.9189	0.4993	0.74
O7	0.8735	0.3813	0.9915	0.01
O8	0.8096	0.4043	0.4623	2.41
O9	0.3343	0.3761	0.7702	1.46
O10	0.4046	0.3923	0.1771	1.37
O11	0.3076	0.7558	0.7489	1.24
O12	0.5458	0.7415	0.1339	0.91

[a]X-ray is not specified, $R = 0.070$ (3700 refl.).

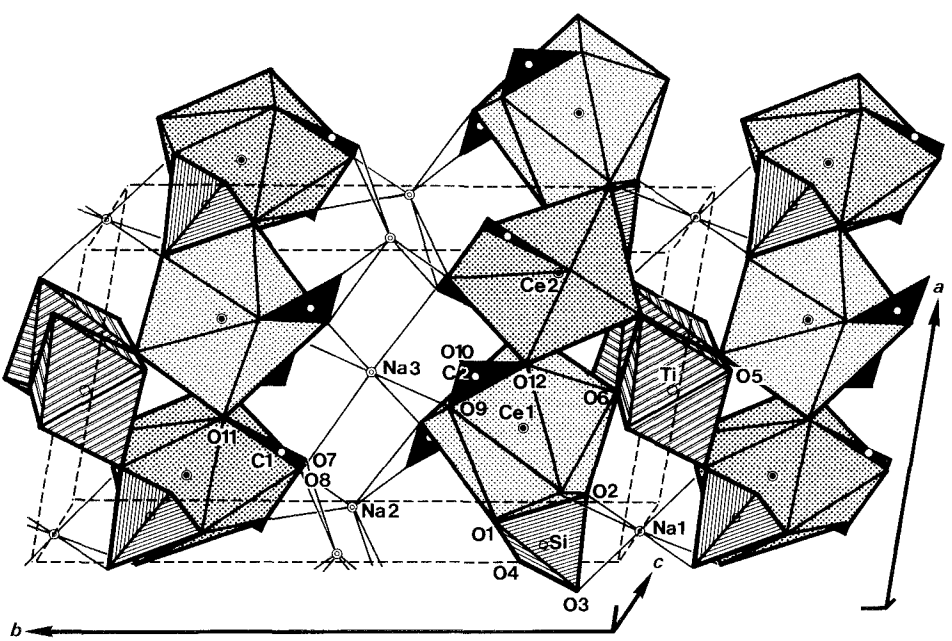

Fig. 63. Illustration of the crystal structure of tundrite-(Ce) showing the arrangement of the three kinds of layers.

TABLE 139
Interatomic distances for tundrite-(Ce) in Å.

Ce1–O6	2.42	Ce2–O1	2.42
Ce1–O1	2.43	Ce2–O5	2.45
Ce1–O11	2.48	Ce2–O12	2.46
Ce1–O4	2.54	Ce2–O4	2.52
Ce1–O2	2.56	Ce2–O3	2.58
Ce1–O9	2.57	Ce2–O7	2.58
Ce1–O12	2.64	Ce2–O11	2.67
Ce1–O12	2.69	Ce2–O11	2.70
Ce1–O10	2.73	Ce2–O8	2.91
mean	2.56	mean	2.59
Na1–O4	2.41 ×2	Na2–O7	2.34
Na1–O3	2.45 ×2	Na2–O8	2.34
Na1–O2	2.46 ×2	Na2–O9	2.46
mean	2.44	Na2–O10	2.49
		Na2–O7	2.53
Na3–O10	2.22 ×2	Na2–O8	2.55
Na3–O9	2.30 ×2	mean	2.45
Na3–O8	2.85 ×2		
mean	2.46		
Ti–O5	1.93	Si–O4	1.61
Ti–O6	1.95	Si–O1	1.62
Ti–O5	1.95	Si–O2	1.65
Ti–O6	1.96	Si–O3	1.65
Ti–O2	2.01	mean	1.63
Ti–O3	2.01		
mean	1.97		
C1–O8	1.24	C2–O9	1.27
C1–O7	1.31	C2–O10	1.27
C1–O11	1.32	C2–O12	1.32
mean	1.29	mean	1.29

Shlyukova et al. (1973). Later, Shumyatskaya et al. (1976) made a refinement of the crystal structure and established the chemical formula as $Na_2Ce_2TiO_2(SiO_4)(CO_3)_2$, which has neither water molecules nor hydroxyl ions.

The crystal structure of tundrite-(Ce) consists of three kinds of layers parallel to the *ac*-plane: a layer composed of two crystallographically independent Ce polyhedra and carbonate triangles, a layer of Ti octahedra, Na octahedra and Si tetrahedra, and a layer of Na octahedra and Na trigonal pyramids (fig. 63). In the Ce layer, nine-coordinated Ce polyhedra share their edges and corners, forming a layer which is connected to other Ce layers by the Ti, Si, Na layer at one side and by the Na, Na layer at the other side. In the Ti, Si, Na layer, the Ti octahedra share edges forming a zigzag chain parallel to the *c*-axis, and the chains are pinned by the Si orthotetrahedra forming a wall with channels. The Na1 atoms are located in the channels with octahedral coordination. Shumyatskaya et al. (1976) suggested that the perfect cleavage along (010) of tundrite-(Ce) can be attributed to the weak bond strengths of the Na–O bonds in the Na, Na layer.

TABLE 140
Atomic parameters of yttrium aluminum garnet[a].

	x	y	z	B (Å²)
Y	1/8	0	1/4	0.42(10)
				0.68(10)
Al1	0	0	0	0.21(13)
Al2	3/8	0	1/4	0.34(14)
O	−0.02985(23)	0.05056(25)	0.14878(17)	

[a]Neutron ($\lambda = 1.07$ Å), $R = 0.077$ (99 refl.).

TABLE 141
Interatomic distances for yttrium aluminum garnet in Å.

Y–O	2.303(5) ×4	Al1–O	1.921(4) ×6
Y–O	2.438(5) ×4	Al2–O	1.775(5) ×4
mean	2.371		

They also suggested the presence of the isomorphous substitution $Ce^{3+} + Ti^{4+} \rightleftarrows Ca^{2+} + Nb^{5+}$, and recognized the addition of Ca and Nb in the formula reported by Shlyukova et al. (1973), giving the formula $Na_2(Ce,Ca)_2(Ti,Nb)O_2(SiO_4)(CO_3)_2$.

Although Shumyatskaya et al. (1976) mentioned that the crystal structure of tundrite-(Ce) represented a "completely" new type, never before encountered among natural minerals, they pointed out the following structural relationship to carbocernaite. The Ce-layers in tundrite-(Ce) and the corrugated sheets of the B polyhedra in carbocernaite are practically equivalent, and this reflects on the closeness of their lattice parameters parallel to the layers of the sheets, namely, $a = 7.56$, $c = 5.04$ Å for tundrite-(Ce) and $b = 7.30$, $c = 5.23$ Å for carbocernaite.

GARNET group
$(Ca,Fe,Mg,Mn,R)_3(Al,Cr,Fe,Mn,Ti,V,Zr)_2(Si,Al)_3O_{12}$
$(Ca,Fe,Mg,Mn,R)_3(Al,Cr,Fe,Mn,Ti,V,Zr)_2(Si,Al)_3O_{12}$

Sys. cubic	$a = 12.008 \pm 0.005$ Å	source: synthetic $Y_3Al_5O_{12}$
S.G. Ia3d		Ref.: Emiraliev et al. (1976)
$Z = 8$		
AP: table 140	ID: table 141	IL: fig. 64

In the crystal structure of garnet, with the general formula $A_3B_2C_3O_{12}$ [A = Ca, Fe^{2+}, Mg, Mn^{2+}, R; B = Al, Cr^{3+}, Fe^{3+}, Mn^{3+}, Ti, V^{3+}, Zr; C = Si (including H_4 instead of Si) Al, Ti], there are three types of sites which are filled with metal ions; tetrahedrally coordinated sites filled with C cations, octahedrally coordinated sites

for the B cations, and dodecahedrally coordinated sites for the A cations. The rare earth elements in a natural garnet may occupy the "A" site owing to their large ionic radii.

A number of artificial rare earth garnets have been synthesized: e.g., $Y_3Al_5O_{12}$, known as YAG (yttrium aluminum garnet), $Y_3Fe_5O_{12}$, known as YIG (yttrium iron garnet), $Gd_3Ga_5O_{12}$, known as GGG (gadolinium gallium garnet), etc., and the crystal structures of rare earth garnets have been studied by many investigators: YIG by Geller and Gilleo (1957), YIG and YAG by Prince (1957), $Gd_3Fe_5O_{12}$ by Weidenborner (1961), $Y_3(Al,Ga)_5O_{12}$ by Marezio et al. (1968), YAG by Emiraliev et al. (1976), and so on.

Figure 64 is a projection of the crystal structure of YAG, drawn on the basis of the atomic parameters reported by Emiraliev et al. (1976). The Y dodecahedra are located at the spaces in the three-dimensional framework formed by the corner sharing linkages of the Al tetrahedra and Al octahedra.

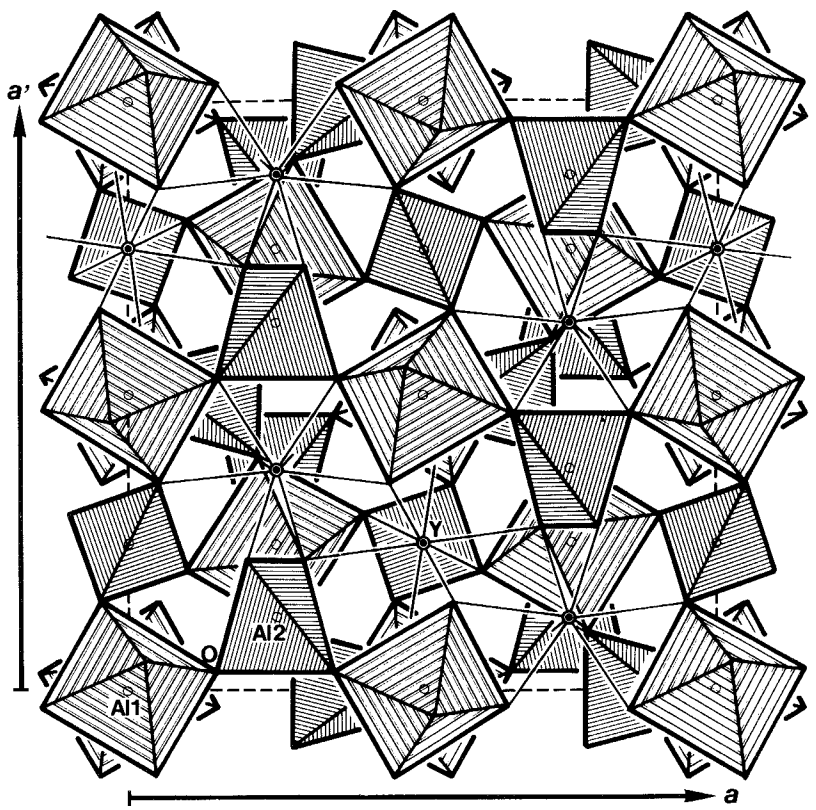

Fig. 64. The crystal structure of yttrium aluminum garnet.

ALLANITE-(Ce) (=orthite, treanorite)
$Ca(Ce,Ca)(Al,Fe)_3(Si_2O_7)(SiO_4)O(OH)$
$Ca(Ce,Ca)Al(Al,Fe)(Fe,Al)(Si_2O_7)(SiO_4)O(OH)$

Sys. monoclinic	$a =$ 8.927(8) Å	source: Pacoima Canyon, Los Angeles Co., CA, USA
S.G. $P2_1/m$	$b =$ 5.761(6) Å	
$Z = 2$	$c =$ 10.150(9) Å	Ref.: Dollase (1971)
	$\beta = 114.77(5)°$	JCPDS: #25-0169, #9-0474
AP: table 142	ID: table 143	IL: fig. 65

ALLANITE-(Y) (=yttro-orthite)
$Ca(Y,Ca)(Al,Fe)_3(Si_2O_7)(SiO_4)O(OH)$
$Ca(Y,Ca)Al(Al,Fe)(Fe,Al)(Si_2O_7)(SiO_4)O(OH)$

Sys. monoclinic	$a =$	source:
S.G. $P2_1/m$	$b =$	Ref.: Levinson (1966)
$Z = 2$	$c =$	
	$\beta =$	

TABLE 142
Atomic parameters of allanite-(Ce)[a].

	x	y	z	B (Å^2)
Ce[c]	0.5936(1)	0.75	0.4286(1)	0.7[b]
Ca[d]	0.7585(4)	0.75	0.1517(4)	1.0[b]
Al1[e]	0	0	0	0.6(1)
Al2[f]	0	0	0.5	0.6(1)
Fe[g]	0.3030(3)	0.25	0.2148(3)	0.9[b]
Si1	0.3389(5)	0.75	0.0369(5)	0.7(1)
Si2	0.6866(5)	0.25	0.2799(5)	0.7(1)
Si3	0.1880(5)	0.75	0.3240(5)	0.6(1)
O1	0.2339(10)	0.9892(18)	0.0263(9)	1.3(2)
O2	0.3109(9)	0.9679(18)	0.3630(8)	1.1(1)
O3	0.7962(9)	0.0144(17)	0.3376(8)	1.0(1)
O4	0.0561(15)	0.25	0.1306(13)	1.2(2)
O5	0.0494(15)	0.75	0.1529(13)	1.2(2)
O6	0.0674(14)	0.75	0.4119(12)	0.9(2)
O7	0.5070(14)	0.75	0.1779(13)	1.0(2)
O8[h]	0.5396(15)	0.25	0.3314(14)	1.5(2)
O9	0.6134(16)	0.25	0.1037(14)	1.7(2)
O10[i]	0.0858(15)	0.25	0.4280(13)	1.2(2)

[a] Mo, $R = 0.062$ (846 refl.).
[b] B_{eq}.
[c] Ce: 0.74R + 0.26Ca.
[d] Ca: 1.00Ca.
[e] Al1: 0.66Al + 0.34Fe.
[f] Al2: 1.00Al.
[g] Fe: 0.83Fe + 0.17Al.
[h] O8: (O,OH), recalculated by RM.
[i] O10: (OH,O), recalculated by RM.

TABLE 143
Interatomic distances for allanite-(Ce) in Å[a].

Ce–O7	2.33(1)	Ca–O3	2.34(1)
Ce–O2	2.52(1)	Ca–O3	2.34(1)
Ce–O2	2.52(1)	Ca–O1	2.37(1)
Ce–O10	2.61(1)	Ca–O1	2.37(1)
Ce–O2	2.64(1)	Ca–O7	2.37(1)
Ce–O2	2.64(1)	Ca–O5	2.59(2)
Ce–O3	2.80(1)	Ca–O6	2.91(1)
Ce–O3	2.80(1)	Ca–O9	3.11(1)
mean	2.61	Ca–O9	3.11(1)
Ce–O8	3.02(1)	mean	2.61
Ce–O8	3.02(1)		
Ce–O8	3.03(2)		
Al1–O4	1.878(8)	Al2–O3	1.876(6)
Al1–O4	1.878(8)	Al2–O3	1.876(6)
Al1–O1	1.992(9)	Al2–O10	1.91(1)
Al1–O1	1.992(9)	Al2–O10	1.91(1)
Al1–O5	2.026(9)	Al2–O6	1.920(9)
Al1–O5	2.026(9)	Al2–O6	1.920(9)
mean	1.965	mean	1.90
Fe–O8	1.94(1)	Si1–O7	1.58(1)
Fe–O4	2.00(1)	Si1–O1	1.64(1)
Fe–O2	2.20(1)	Si1–O1	1.64(1)
Fe–O2	2.20(1)	Si1–O9	1.65(2)
Fe–O1	2.30(1)	mean	1.63
Fe–O1	2.30(1)		
mean	2.16		
Si2–O8	1.60(2)	Si3–O2	1.60(1)
Si2–O9	1.63(1)	Si3–O2	1.60(1)
Si2–O3	1.632(9)	Si3–O5	1.66(1)
Si2–O3	1.632(9)	Si3–O6	1.66(2)
mean	1.62	mean	1.63

[a]Recalculated by RM.

ALLANITE-(La)
$Ca(La,Ca)(Al,Fe)_3(Si_2O_7)(SiO_4)O(OH)$
$Ca(La,Ca)Al(Al,Fe)(Fe,Al)(Si_2O_7)(SiO_4)O(OH)$

Sys. monoclinic	$a =$	source:
S.G. $P2_1/m$	$b =$	Ref.: Levinson (1966)
$Z = 2$	$c =$	
	$\beta =$	

DOLLASEITE-(Ce)
$CaCeMg_2Al(Si_2O_7)(SiO_4)(OH)F$
$(Ca,Ce)(Ce,Ca)(Mg,Fe)_2(Al,Fe)(Si_2O_7)(SiO_4)(OH)F$

Sys.	monoclinic	$a =$ 8.934(18) Å	source: Ostanmossa, Norberg, Sweden
S.G.	$P2_1/m$	$b =$ 5.721(7) Å	Ref.: Peacor and Dunn (1988)
$Z =$	2	$c =$ 10.176(22) Å	
Dm =	3.9 g/cm^3	$\beta =$ 114.31(12)°	
AP:	table 144	ID: table 145	

DISSAKISITE-(Ce)
$CaCeMgAl_2(Si_2O_7)(SiO_4)O(OH)$
$CaCeMgAl_2(Si_2O_7)(SiO_4)O(OH)$

Sys.	monoclinic	$a =$ 8.916(20) Å	source: Balchen Mt., Antarctica
S.G.	$P2_1/m$	$b =$ 5.700(8) Å	Ref.: Grew et al. (1991)
$Z =$	2	$c =$ 10.140(25) Å	
Dx =	3.97–4.02 g/cm^3	$\beta =$ 114.72(14)°	
Dm =	3.75(15) g/cm^3		

TABLE 144
Atomic parameters of dollaseite-(Ce)[a].

	x	y	z
A1[b]	0.7627(2)	3/4	0.1480(1)
A2[c]	0.5932(1)	3/4	0.4261(1)
M1[d]	0	0	0
M2[e]	0	0	1/2
M3[f]	0.3155(2)	1/4	0.2127(2)
Si1	0.3439(2)	3/4	0.0427(2)
Si2	0.6912(2)	1/4	0.2784(2)
Si3	0.1877(2)	3/4	0.3220(2)
O1	0.2450(4)	0.9917(5)	0.0369(3)
O2	0.3120(4)	0.9743(5)	0.3615(3)
O3	0.8020(4)	0.0153(5)	0.3336(3)
O4[g]	0.0607(5)	1/4	0.1457(4)
O5	0.0455(5)	3/4	0.1564(5)
O6	0.0768(6)	3/4	0.4172(5)
O7	0.5174(5)	3/4	0.1806(5)
O8	0.5474(6)	1/4	0.3324(5)
O9	0.6154(6)	1/4	0.1008(5)
O10	0.0917(6)	1/4	0.4342(5)
H	0.068(10)	1/4	0.333(10)

[a] MoKα, $R = 0.032$, $R_w = 0.025$ (1367 refl.).
[b] A1: 0.943(3)Ca + 0.057Ce.
[c] A2: 0.020(6)Ca + 0.980Ce.
[d] M1: 1.005(1)Mg − 0.005Fe.
[e] M2: 0.985(7)Al + 0.015Fe.
[f] M3: 0.872(8)Mg + 0.128Fe.
[g] O4: 0.87(9)F + 0.13O.

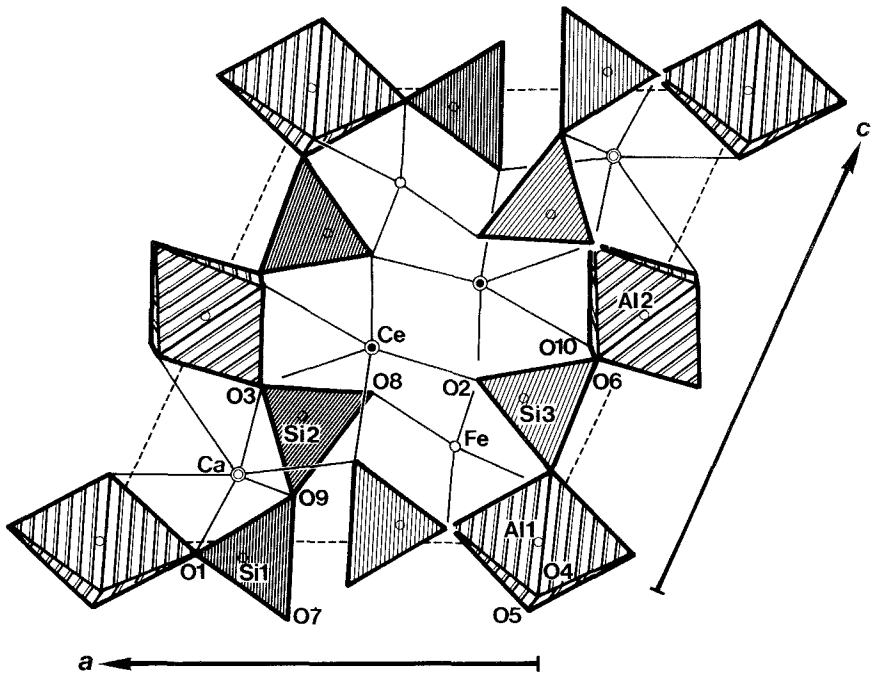

Fig. 65. The crystal structure of allanite-(Ce).

R-bearing PIEMONTITE
$Ca_2(Mn,Fe)Al_2(Si_2O_7)(SiO_4)O(OH)$
$(Ca,Mn)(Ca,Sr,La)(Al,Mn,Fe,Mg)Al(Mn,Fe)(Si_2O_7)(SiO_4)O(OH)$

Sys. monoclinic	$a =$ 8.881(1) Å	source: Monte Brugiana, Alpi Apuane, Italy
S.G. $P2_1/m$	$b =$ 5.683(1) Å	Ref.: Bonazzi et al. (1992)
$Z = 2$	$c =$ 10.150(2) Å	
	$\beta = 114.99(2)°$	
AP: table 146	ID: table 147	

Allanite-(Ce) and -(Y) are members of the epidote group, $A_2B_3(Si_2O_7)(SiO_4)$-O(OH) (A = Ca, Ce, Pb, Sr, Y; B = Al, Fe^{3+}, Mn^{3+}, V^{3+}). The crystal structure of allanite-(Ce) was determined by Pudovkina and Pyatenko (1963). Dollase (1971) refined the structure, together with those of epidote, $Ca_2Al(Al,Fe)(Fe,Al)(OH)$, and hancockite, Ca(Pb,Sr,Ca)Al,(Al,Fe)(Fe,Al)(OH). The crystal structure of allanite-(Ce) (fig. 65) contains chains of edge-sharing octahedra of two types: a single chain of Al2 octahedra and a multiple or zigzag chain of Al1 octahedra and Fe octahedra. The diortho (Si_2O_7) groups of the Si tetrahedra (Si1 and Si2) and isolated tetrahedra of Si3 crosslink the chains forming a three-dimensional framework having large spaces for the calcium and rare earth atoms.

TABLE 145
Interatomic distances for dollaseite-(Ce) in Å.

A1–O3	2.334(3) ×2	A2–O7	2.204(7)
A1–O7	2.348(6)	A2–O2	2.524(3) ×2
A1–O1	2.371(3) ×2	A2–O10	2.579(7)
A1–O5	2.493(7)	A2–O2	2.652(3) ×2
mean	2.375	A2–O3	2.849(5) ×2
		A2–O8	2.990(4) ×2
Si1–O7	1.607(5)	mean	2.523
Si1–O1	1.629(4) ×2		
Si1–O9	1.644(7)	M1–O4	1.969(4) ×2
mean	1.627	M1–O5	2.052(5) ×2
		M1–O1	2.063(4) ×2
Si2–O8	1.592(7)	mean	2.028
Si2–O3	1.625(4) ×2		
Si2–O9	1.648(6)	M2–O3	1.881(5) ×2
mean	1.623	M2–O10	1.902(5) ×2
		M2–O6	1.924(5) ×2
Si3–O2	1.635(4) ×2	mean	1.902
Si3–O5	1.640(6)		
Si3–O6	1.646(7)	M3–O8	1.952(7)
mean	1.639	M3–O4	2.056(7)
		M3–O2	2.185(4) ×2
H–O10	0.96(10)	M3–O1	2.205(5) ×2
H–O4	1.88(10)	mean	2.131
O4–O10	2.833(9)		

Dollase (1971) reported that all the atoms replacing calcium atoms, e.g., rare earths in allanite-(Ce) and lead and strontium atoms in hancockite, occupy only the A2 site of the two calcium sites, A1 and A2, in epidote. The A2 site is larger and has a higher coordination number than the A1 site even when both are completely occupied by calcium atoms. Dollase (1971) reported that the Ce site in the crystal structure of allanite-(Ce) is coordinated by ten oxygen atoms, as are the corresponding sites in the structures of other members of the epidote group. An additional eleventh neighboring oxygen atom at a distance of 3.13 Å, was also included in the coordination of the Ce site by Dollase (1971). However, the interatomic distances between Ce and the O8 sites (3.02 × 2 and 3.13 Å) are too long for the Ce–O distance. Therefore, the coordination number of the Ce site must be 8 (see table 143).

Although the hydrogen atoms of the hydroxyl ions were not located in the crystal structure of allanite-(Ce), Dollase (1971) assumed that the hydrogen atoms occupy positions analogous to those found in the crystal structure of clinozoisite, $Ca_2Al_3(Si_2O_7)(SiO_4)(O,OH)_2$ (Dollase 1968), and piemontite, $Ca_2(Al,Mn,Fe)_3(Si_2O_7)(SiO_4)(O,OH)_2$ (Dollase 1969), which are also members of the epidote group. This was confirmed by the bond-valence sums calculated by the present authors following the method of Donnay and Allmann (1970) using the atomic parameters given by Dollase (1971). The result suggests that the O10 site is occupied by the (OH) ion.

TABLE 146
Atomic parameters of R-bearing piemontite[a].

	x	y	z	U_{eq}
A1[b]	0.7575(3)	0.7500	0.1517(3)	0.0085(9)
A2[c]	0.5953(2)	0.7500	0.4261(2)	0.0117(6)
M1[d]	0	0	0	0.0080(9)
M2[e]	0	0	0.5	0.0071(13)
M3[f]	0.2991(2)	0.2500	0.2192(2)	0.0065(8)
Si1	0.3415(4)	0.7500	0.0432(4)	0.0071(11)
Si2	0.6875(4)	0.2500	0.2758(4)	0.0069(11)
Si3	0.1874(4)	0.7500	0.3217(4)	0.0043(10)
O1	0.2363(7)	0.9916(9)	0.0353(6)	0.0143(18)
O2	0.3090(7)	0.9778(9)	0.3569(6)	0.0081(18)
O3	0.7985(7)	0.0155(9)	0.3375(6)	0.0093(20)
O4	0.0555(9)	0.2500	0.1303(9)	0.0068(17)
O5	0.0447(9)	0.7500	0.1499(9)	0.0081(21)
O6	0.0714(9)	0.7500	0.4108(9)	0.0065(20)
O7	0.5141(9)	0.7500	0.1823(9)	0.0110(20)
O8	0.5335(9)	0.2500	0.3200(9)	0.0193(28)
O9	0.6186(9)	0.2500	0.1004(9)	0.0204(25)
O10	0.0871(9)	0.2500	0.4321(9)	0.0053(25)
H	0.04(2)	0.2500	0.36(2)	0.02

[a] MoKα, $R = 0.042$, $R_w = 0.037$ (748 refl.).
[b] A1: $0.78Ca + 0.22Mn^{2+}$
[c] A2: $0.69Ca + 0.03Sr + 0.28R$.
[d] M1: $0.61Al + 0.31M^{3+} + 0.08Mg$.
[e] M2: 1.00Al.
[f] M3: $0.72M^{3+} + 0.20M^{2+} + 0.08Al$.

Dollaseite-(Ce) was originally described by Geijer (1927) as "magnesium orthite", but Peacor and Dunn (1988) recently redefined it with the new name dollaseite-(Ce). The mineral belongs to the epidote group. The crystal structure of dollaseite-(Ce) (Peacor and Dunn 1988) is isostructural with that of allanite-(Ce) (Dollase 1971), and the chemical formula of dollaseite-(Ce) can be derived from that of allanite-(Ce) by the isomorphous substitution $2Mg^{2+} + F^- \rightleftarrows Fe^{2+} + Al^{3+} + O^{2-}$. Other phases isostructural with allanite-(Ce) include epidote, hancockite (Dollase 1971) and piemontite (Dollase 1969). In the crystal structure of dollaseite-(Ce), rare earth atoms occupy the larger A2 site, as in the structure of allanite-(Ce). Dollase (1971) pointed out that substitution of Ca by larger rare earth atoms selectively occurs in the A2 site rather than the A1 site because that site has the larger radius in epidote-type structures that contain only Ca. Furthermore, Peacor and Dunn (1988) suggested that the substitution of Fe^{2+} in M3 is balanced by that of R^{3+} for Ca^{2+} in the A2 site, because A2 and M3 are linked through O8, and particularly O2, and substitution of rare earths in A2 provides a more satisfactory local charge balance for O2 and O8.

Dissakisite-(Ce) is a new member of the epidote group from Antarctica and a Mg-analogue of allanite-(Ce) (Grew et al. 1991). The number of octahedral Mg sites, one,

TABLE 147
Interatomic distances for R-bearing piemontite in Å.

A1–O7	2.310(9)	A2–O7	2.266(9)
A1–O3	2.321(7) ×2	A2–O2	2.527(6) ×2
A1–O1	2.419(7) ×2	A2–O10	2.569(8)
A1–O5	2.558(9)	A2–O2	2.669(6) ×2
A1–O6	2.914(7)	A2–O3	2.777(7) ×2
A1–O9	3.054(3) ×2	A2–O8	3.006(3) ×2
mean	2.597	mean	2.679
Si1–O7	1.586(7)	M1–O4	1.860(6) ×2
Si1–O9	1.639(9)	M1–O1	1.975(6) ×2
Si1–O1	1.644(7) ×2	M1–O5	1.995(6) ×2
mean	1.628	mean	1.943
Si2–O8	1.609(9)	M2–O3	1.854(5) ×2
Si2–O3	1.618(6) ×2	M2–O10	1.882(7) ×2
Si2–O9	1.620(9)	M2–O6	1.930(7) ×2
mean	1.616	mean	1.889
Si3–O2	1.626(6) ×2	M3–O8	1.892(9)
Si3–O6	1.633(9)	M3–O4	1.961(8)
Si3–O5	1.667(8)	M3–O2	2.062(6) ×2
mean	1.638	M3–O1	2.252(6) ×2
		mean	2.080

in dissakisite-(Ce) is different from that in dollaseite-(Ce), which has two independent octahedral Mg sites.

Bonazzi et al. (1992) found R-rich piemontite and analyzed its crystal structure. The substitution of Ca with R takes place in the A2 site, as in allanite-(Ce) and dollasite-(Ce), while the A1 site is interesting because of the entry of Mn^{2+} substitution for Ca. The M2 site is fully occupied by Al while the heavier cations (Mn + Fe) are ordered mainly in M3 but also, to a minor amount, in M1. Bonazzi et al. (1992) pointed out that the O2 site in R-bearing piemontite moves towards the A2 site in comparison to R-free piemontite. Two of the four interatomic distances between A2 and O2 in the R-rich minerals, dollasite-(Ce), 2.652 Å, allanite-(Ce), 2.642 Å, and R-bearing piemontite, 2.669 Å, are shorter than those in R-free piemontite, 2.714 Å.

CHEVKINITE-(Ce) (= tscheffkinite)
$(Ce,Ca,Th)_4(Fe,Mg)(Ti,Mg,Fe)_4Si_4O_{22}$
$(Ce,Ca,Th)_4(Fe,Mg)(Ti,Mg,Fe)_4Si_4O_{22}$

Sys. monoclinic	a = 13.328(10) Å	source: synthetic $Nd_4Mg(Ti,Mg)_4Si_4O_{22}$
S.G. $P2_1/a$	b = 5.727(4) Å	Ref.: Calvo and Faggiani (1974)
Z = 2	c = 10.971(8) Å	JCPDS: #21-1015, #20-0265
Dm = 4.98 g/cm³	β = 100.91(6)°	
AP: table 148	ID: table 149	IL: fig. 66

TABLE 148
Atomic parameters of chevkinite[a].

	x	y	z	U (Å^2)
Nd1	0.35442(4)	0.02260(7)	0.23312(4)	0.0095(1)
Nd2	0.07127(4)	−0.03662(7)	0.24017(4)	0.0094(2)
Mg	0	1/2	0	0.0078(7)
M1[b]	0.2434(2)	0.2466(3)	0.5000(2)	0.0082(3)
M2a[c]	0	1/2	1/2	0.0111(5)
M2b[d]	1/2	1/2	1/2	0.0093(4)
Si1	0.2015(2)	0.4972(3)	0.2306(2)	0.0069(4)
Si2	0.3596(2)	0.5019(3)	0.0470(2)	0.0076(4)
O1	0.2393(5)	−0.2098(9)	0.3133(5)	0.0075(10)
O11	0.2170(5)	0.2527(9)	0.3130(5)	0.0081(10)
O2	−0.0247(5)	−0.2527(9)	0.3742(5)	0.0085(10)
O21	−0.0214(5)	0.2448(10)	0.3736(5)	0.0093(10)
O3	0.4131(5)	−0.2493(10)	0.0946(5)	0.0093(10)
O31	0.4437(5)	0.2947(10)	0.0931(5)	0.0107(11)
O4	0.1457(6)	−0.0104(10)	0.4757(5)	0.0106(11)
O5	0.1511(6)	0.5044(10)	0.5099(5)	0.0105(11)
O6	0.0866(6)	0.5469(10)	0.1686(5)	0.0113(11)
O7	0.2741(6)	0.4477(10)	0.1307(6)	0.0151(12)
O8	0.3132(6)	0.4892(9)	0.9015(5)[e]	0.0074(10)

[a] MoKα, $R = 0.043$ (1913 refl.).
[b] M1: 0.680Ti + 0.320Mg.
[c] M2a: 0.807(7)Ti + 0.193Mg.
[d] M2b: 0.834(9)Ti + 0.166Mg.
[e] In original paper, $z(O8) = 1 - z(O8)$.

STRONTIO-CHEVKINITE
$(Sr,Ce,Ca)_4(Fe,Mn)(Ti,Zr)_4Si_4O_{22}$
$(Sr,Ce,Ca)_4(Fe,Mn)(Ti,Zr)_4Si_4O_{22}$

Sys. monoclinic	$a =$ 13.56 Å	source: Sarambi, Paraguay
S.G. $P2_1/a$	$b =$ 5.70 Å	Ref.: Haggerty and Mariano (1983)
$Z =$ 2	$c =$ 11.10 Å	JCPDS: #38-0443
Dx = 5.44 g/cm^3	$\beta = 100.32°$	

PERRIERITE
$(Ca,Ce,Th)_4(Mg,Fe)(Ti,Mg,Fe)_4Si_4O_{22}$
$(Ca,Ce,Th)_4(Mg,Fe)(Ti,Mg,Fe)_4Si_4O_{22}$

Sys. monoclinic	$a =$ 13.818(4) Å	source: synthetic $La_4Mg(Ti,Mg)_4Si_4O_{22}$
S.G. $P2_1/a$	$b =$ 5.677(2) Å	Ref.: Calvo and Faggiani (1974)
$Z =$ 2	$c =$ 11.787(6) Å	JCPDS: #19-0302
Dm = 4.94 g/cm^3	$\beta = 113.85(3)°$	
AP: table 150	ID: table 151	IL: fig. 67

The crystal structures of chevkinite-(Ce) and perrierite were determined in space group C2/m by Pen and Pan (1964) and Gottardi (1960), respectively. Calvo and

TABLE 149
Interatomic distances for chevkinite in Å[a].

Nd1–O3	2.407		Nd2–O8	2.391	
Nd1–O21	2.434		Nd2–O2	2.459	
Nd1–O8	2.441		Nd2–O31	2.525	
Nd1–O2	2.537		Nd2–O6	2.531	
Nd1–O1	2.538		Nd2–O11	2.581	
Nd1–O11	2.557		Nd2–O4	2.591	
Nd1–O31	2.627		Nd2–O1	2.600	
Nd1–O7	2.807		Nd2–O21	2.636	
Nd1–O5	2.836		Nd2–O3	2.688	
mean	2.576		mean	2.556	
Mg–O6	2.003	×2	M1–O5	1.938	
Mg–O3	2.177	×2	M1–O4	1.951	
Mg–O31	2.216	×2	M1–O5	1.992	
mean	2.132		M1–O4	2.009	
			M1–O11	2.015	
			M1–O1	2.020	
			mean	1.988	
M2a–O2	1.961	×2	M2b–O21	1.955	×2
M2a–O21	1.997	×2	M2b–O2	1.984	×2
M2a–O5	1.998	×2	M2b–O4	2.011	×2
mean	1.985		mean	1.983	
Si1–O6	1.580		Si2–O8	1.602	
Si1–O7	1.618		Si2–O7	1.623	
Si1–O11	1.636		Si2–O3	1.633	
Si1–O1	1.639		Si2–O31	1.644	
mean	1.618		mean	1.626	

[a]Errors are of the order of 0.007 Å for Nd–O, 0.008 Å for Mg,M–O, and are 0.010 Å or less for Si–O.

Faggiani (1974) successfully refined the two structures using synthetic samples in space group $P2_1/a$ as suggested by Ito and Arem (1971). The crystal structure of synthetic chevkinite-(Ce) (fig. 66) is essentially the same as that of synthetic perrierite (fig. 67). The origin of the unit cell is located at the Mg site in the former and at the M1 site in the latter. They are made up of two kinds of sheet structures, one is a sheet of M1 and M2 octahedra and the other is a sheet of diortho groups of Si tetrahedra and Mg octahedra, both of them being parallel to the *ab*-plane. The two kinds of sheets alternate and form a three-dimensional framework. The rare earth atoms lie in cavities of the framework forming nine-coordinated polyhedra.

Strontio-chevkinite is an Sr-analogue of chevkinite-(Ce) and was described by Haggerty and Mariano (1983). They proposed the chemical formula $(Sr,Ce,Ca)_4$-$(Fe^{2+},Fe^{3+})(Ti,Zr)_2Ti_2Si_4O_{22}$ for strontio-chevkinite after consideration of the distribution of the cations based on the ionic radii. However, the crystal structure analysis of artificial chevkinites (Calvo and Faggiani 1974) indicated that there are three Ti sites occupied by both Ti and Mg in the structures. Therefore, the

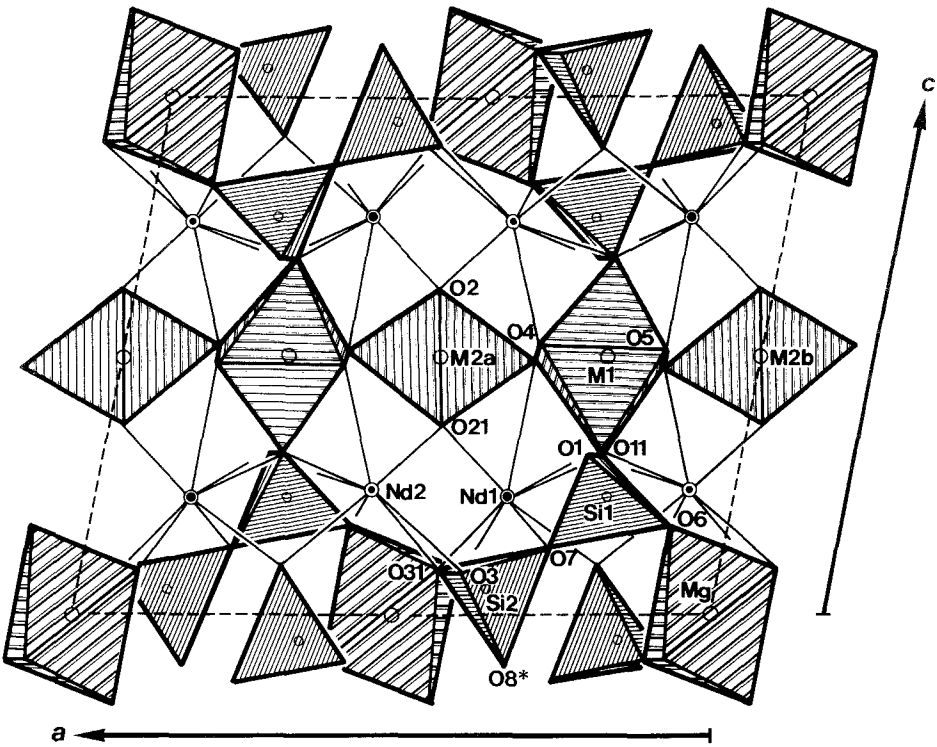

Fig. 66. The crystal structure of synthetic chevkinite, $Nd_4Mg(Ti,Mg)_4Si_4O_{22}$.

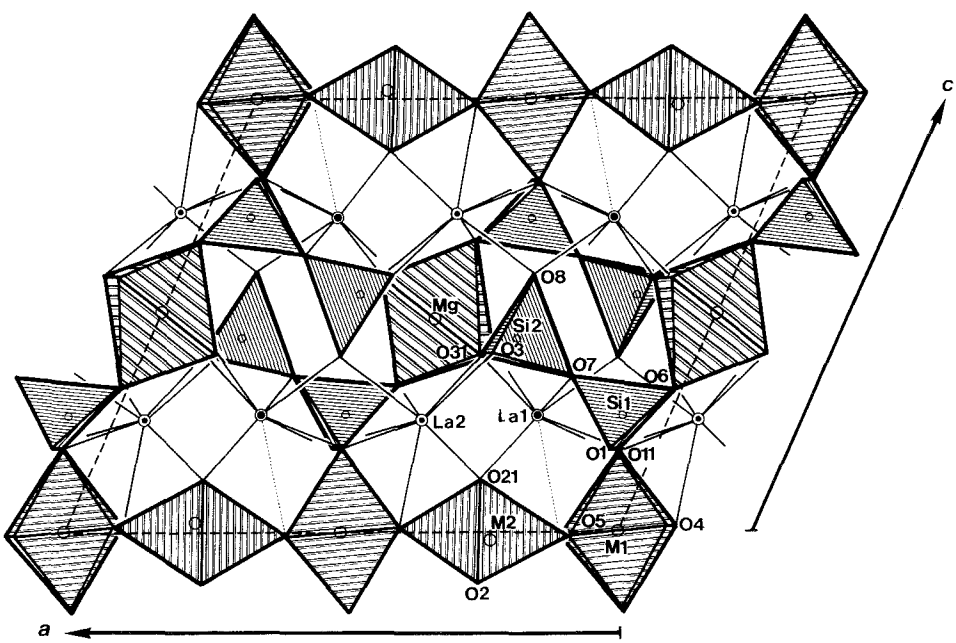

Fig. 67. The crystal structure of synthetic perrierite, $La_4Mg(Ti,Mg)_4Si_4O_{22}$.

TABLE 150
Atomic parameters of perrierite[a].

	x	y	z	U (Å^2)
La1	0.23756(5)	0.0198(1)	0.26687(6)	0.0078(3)
La2	0.04897(5)	0.0265(1)	0.7432(6)	0.0087(3)
Mg	0	1/2	1/2	0.0047(9)
M1[b]	−0.0039(2)	0.2385(6)	0.0004(3)	0.0105(6)
M2[c]	0.2749(2)	0.0071(4)	0.017(2)	0.0068(4)
Si1	0.4123(2)	−0.0001(5)	0.7322(3)	0.0057(6)
Si2	0.1624(2)	0.0027(5)	0.5489(3)	0.0069(6)
O1	0.0794(6)	−0.2597(14)	0.1864(7)	0.0091(14)
O11	0.0652(6)	0.2556(14)	0.1858(7)	0.0103(14)
O2	0.2899(6)	0.2606(15)	0.1229(7)	0.0128(15)
O21	0.2875(6)	−0.2401(14)	0.1225(7)	0.0105(15)
O3	0.3736(6)	−0.2511(14)	0.4058(7)	0.0123(15)
O31	0.3920(6)	0.2862(15)	0.4066(8)	0.0139(15)
O4	0.0957(7)	0.0077(14)	0.9894(8)	0.0114(15)
O5	0.4067(7)	−0.0041(14)	0.0089(8)	0.0110(15)
O6	0.4932(7)	0.0328(15)	0.6667(8)	0.0150(16)
O7	0.2884(7)	−0.0337(16)	0.6366(8)	0.0176(17)
O8	0.1384(6)	−0.0036(14)	0.4042(7)	0.0115(15)

[a] MoKα, $R = 0.046$ (1878 refl.).
[b] M1: 0.616(6)Ti + 0.384Mg.
[c] M2: 0.884Ti + 0.116Mg.

chemical formula for chevkinite-(Ce) must be written as $(Ce,Ca,Th)_4(Fe,Mg)(Ti,Mg,Fe)_4Si_4O_{22}$.

Recently, Yang et al. (1991) investigated the space group of natural chevkinite-(Ce) from Mianxi, Sichuan Province, China, by transmission electron microscopy. Their selected-area electron diffraction and convergent-beam electron diffraction patterns proved that the space group is C2/m, and not $P2_1/a$. Their result confirms the space group given by Pen and Pan (1964), and is not in agreement with that by Calvo and Faggiani (1974). Yang et al. (1991) pointed out the possibility of a difference in space groups between natural chevkinite-(Ce) and synthetic $Nd_4Mg(Ti,Mg)_4Si_4O_{22}$. This may arise from the difference in chemical compositions: the Ce sites in natural chevkinite-(Ce) are completely replaced by Nd and the Fe^{2+} sites by Mg or Co in the synthetic samples.

TÖRNEBOHMITE-(Ce)
$Ce_2Al(SiO_4)_2(OH)$
$Ce_2Al(SiO_4)_2(OH)$

Sys. monoclinic	$a = 7.383(3)$ Å	source: Bastnäs, Riddarhyttan, Västmanland, Sweden
S.G. $P2_1/c$	$b = 5.673(3)$ Å	
$Z = 4$	$c = 16.937(6)$ Å	Ref.: Shen and Moore (1982)
Dx = 5.12 g/cm^3	$\beta = 112.04(2)°$	JCPDS: #34-0160, #14-0257
Dm = 4.94 g/cm^3		
AP: table 152	ID: table 153	IL: fig. 68

TABLE 151
Interatomic distances for perrierite in Å[a].

La1–O3	2.468	La2–O8	2.470
La1–O2	2.503	La2–O21	2.544
La1–O8	2.511	La2–O1	2.603
La1–O21	2.549	La2–O31	2.610
La1–O1	2.553	La2–O11	2.612
La1–O11	2.556	La2–O2	2.624
La1–O31	2.591	La2–O6	2.666
La1–O7	2.860	La2–O4	2.707
mean	2.574	La2–O3	2.711
(La1–O5	3.452)	mean	2.616
Mg–O6	2.014 ×2		
Mg–O3	2.179 ×2		
Mg–O31	2.179 ×2		
mean	2.212		
M1–O4	1.924	M2–O5	1.789
M1–O4	1.942	M2–O21	1.956
M1–O5	1.978	M2–O2	1.963
M1–O11	2.002	M2–O2	1.979
M1–O5	2.018	M2–O21	1.982
M1–O1	2.023	M2–O4	2.421
mean	1.981	mean	2.015
Si1–O6	1.605	Si2–O8	1.601
Si1–O7	1.636	Si2–O31	1.635
Si1–O1	1.645	Si2–O7	1.639
Si1–O11	1.646	Si2–O3	1.643
mean	1.633	mean	1.630

[a]Errors are of the order of 0.007 Å for La–O, 0.008 Å for Mg, M–O, and are 0.010 Å or less for Si–O.

TÖRNEBOHMITE-(La)
$La_2Al(SiO_4)_2(OH)$
$La_2Al(SiO_4)_2(OH)$

Sys. monoclinic	$a=$	source: Ural, Russia
S.G.	$b=$	Ref.: Levinson (1966)
$Z=$	$c=$	
	$\beta=$	

The crystal structure of törnebohmite-(Ce) (fig. 68) contains linear chains of Al octahedra running parallel to [010]. Insular $[SiO_4]$ tetrahedra, which corner-link to the octahedral chains, are arranged in trans-configuration to these chains (Shen and Moore 1982). The rare earth atoms are located between the chains forming a serrated wall of linked polyhedra with ten-coordination parallel to the {001} plane.

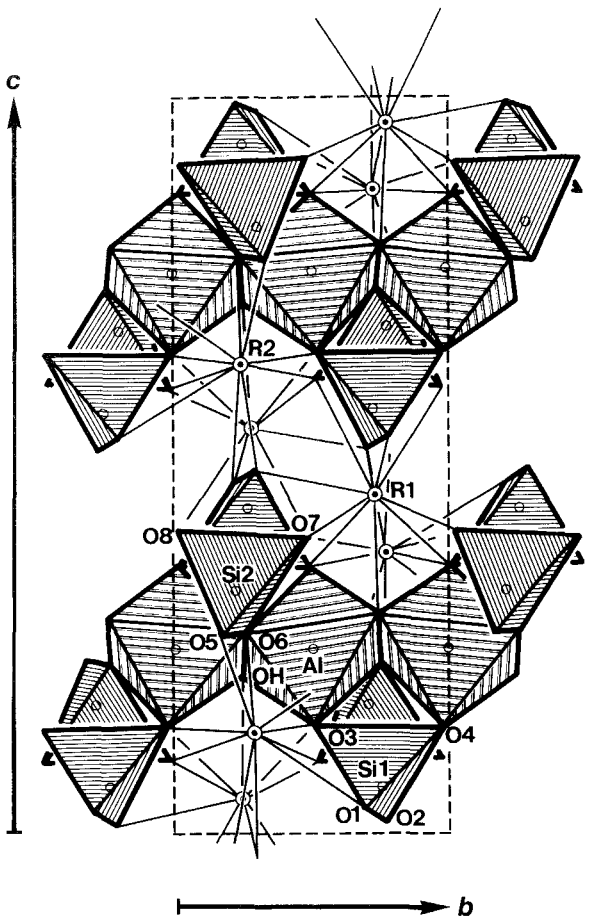

Fig. 68. The crystal structure of törnebohmite-(Ce).

Shen and Moore (1982) suggested that such a straight chain motif can be seen in the crystal structures of rare earth silicates, e.g., allanite-(Ce) (Dollase 1971), perrierite and chevkinite-(Ce) (Calvo and Faggiani 1974). Törnebohmite-(Ce) is isostructural with fornacite, $Pb_2Cu(AsO_4)(CrO_4)(OH)$ (Cocco et al. 1967), and is structurally related to goedkenite, $Sr_2Al(PO_4)_2(OH)$, based on the following isomorphism: $R^{3+} + Si^{4+} \rightleftarrows Ca(Sr)^{2+} + P^{5+}$. This type of isomorphism is observed between some (OH)-bearing rare earth silicates and (OH)-bearing alkaline earth phosphate analogues (Moore et al. 1975), e.g., between törnebohmite-(Ce), $Ce_2Al(OH)(SiO_4)_2$, and goedkenite, $(Sr,Ca)_2Al(OH)(PO_4)_2$; britholite-(Ce), $Ce_3Ce_2(OH)(SiO_4)_3$, and hydroxylapatite, $Ca_5(OH)(PO_4)_3$; cerite-(Ce), $Ce_{14}Ca_4Mg_2(SiO_4)_{12}[SiO_3(OH)]_2$, and whitlockite, $Ca_{14}Ca_4Mg_2(PO_4)_{12}[PO_3(OH)]_2$.

TABLE 152
Atomic parameters of törnebohmite-(Ce)[a].

	x	y	z	B_{eq} (Å^2)
R1	0.81254(4)	0.73320(5)	0.45628(2)	0.58(1)
R2	0.21935(5)	0.78459(6)	0.36951(2)	0.78(1)
Si1	0.5286(2)	0.2507(3)	0.4187(1)	0.49(4)
Si2	0.9312(2)	0.2389(3)	0.3381(1)	0.50(4)
Al	0.4929(3)	0.5008(3)	0.2503(1)	0.34(4)
O1	0.3822(8)	0.2133(10)	0.4665(3)	1.68(15)
O2	0.7488(6)	0.2851(8)	0.4845(3)	1.01(13)
O3	0.5083(6)	0.0120(7)	0.3614(3)	0.58(15)
O4	0.4791(6)	−0.5097(7)	0.3600(3)	0.67(13)
O5	0.0406(6)	0.1733(8)	0.2739(3)	0.90(13)
O6	0.6939(6)	0.2561(7)	0.2765(2)	0.63(12)
O7	0.9988(6)	0.4764(7)	0.3943(3)	0.65(14)
O8	0.9811(6)	0.0234(7)	0.4057(3)	0.96(17)
OH	0.3239(6)	0.2450(7)	0.2144(2)	0.60(11)

[a] MoKα, $R = 0.033$ (2586 refl.).

TABLE 153
Interatomic distances for törnebohmite-(Ce) in Å.

R1–O1	2.298(4)	R2–O2	2.427(4)
R1–O8	2.407(4)	R2–O8	2.473(4)
R1–O7	2.490(4)	R2–O7	2.530(4)
R1–O8	2.649(4)	R2–O3	2.540(4)
R1–O2	2.661(4)	R2–O5	2.546(4)
R1–O7	2.667(4)	R2–O4	2.593(4)
R1–OH	2.683(4)	R2–O5	2.761(4)
R1–O3	2.724(4)	R2–O6	2.782(4)
R1–O4	2.758(4)	R2–O1	2.929(4)
R1–O2	3.011(4)	R2–O1	3.199(4)
mean	2.635	mean	2.678
Si1–O1	1.590(5)	Si2–O7	1.616(4)
Si1–O2	1.601(4)	Si2–O8	1.620(4)
Si1–O3	1.640(4)	Si2–O5	1.622(4)
Si1–O4	1.643(4)	Si2–O6	1.672(4)
mean	1.619	mean	1.632
Al–OH	1.861(4)		
Al–OH	1.871(4)		
Al–O3	1.890(4)		
Al–O4	1.900(4)		
Al–O6	1.935(4)		
Al–O6	1.954(4)		
mean	1.902		

TABLE 154
Atomic parameters of hibonite[a].

	x	y	z
Ca	2/3	1/3	1/4
Al1	0	0	0
Al2	0	0	0.25771(7)
Al3	1/3	2/3	0.02808(3)
Al4	1/3	2/3	0.19102(3)
Al5	0.16855(3)	0.33710(7)	−0.10914(1)
O1	0	0	0.14907(5)
O2	2/3	1/3	0.05461(5)
O3	0.18107(10)	0.36214(19)	1/4
O4	0.15505(7)	0.31010(13)	0.05213(3)
O5	0.50325(7)	1.00650(14)	0.14912(3)

[a]MoKα, $R = 0.025$ (1492 refl.).

HIBONITE
$(Ca,Ce)(Al,Ti,Mg)_{12}O_{19}$
$(Ca,Ce)(Al,Ti,Mg)_{12}O_{19}$

Sys.	hexagonal	$a = 5.5587(1)$ Å	source: synthetic $CaAl_{12}O_{19}$
S.G.	$P6_3/mmc$	$c = 21.8929(3)$ Å	Ref.: Utsunomiya et al. (1988)
$Z =$	2		JCPDS: #38-0469, #38-0470
Dx =	3.79 g/cm^3		
AP:	table 154	ID: table 155	IL: fig. 69

The crystal structure of synthetic hibonite, $CaAl_{12}O_{19}$, was determined by Kato and Saalfeld (1968) and was refined by Utsunomiya et al. (1988). Since anharmonicity of the thermal vibration of the Al2 atom was observed, refinement of the temperature factors including anharmonic terms up to the fourth order was done (Utsunomiya et al. 1988). The result supports a split atom model where Al^{3+} statistically occupies one of the two equivalent Al2 sites at room temperature.

Hibonite has the magnetoplumbite structure (fig. 69). It consists of three kinds of units: (1) triplet layers of the β-Al_2O_3-type formed by the octahedra of Al1 and Al5 and tetrahedra of Al3, (2) columns composed of trigonal bi-pyramids of Al2 and twelve-coordinated Ca polyhedra, and (3) columns consisting of Al4 octahedra adjoining the Al2 and Ca columns. The rare earth atoms contained in natural specimens may replace the calcium atoms accompanying the charge compensation by the substitution of Mg^{2+} for Al^{3+} at the Al2, Al4 or Al5 sites which share the oxygen atoms with the Ca polyhedra.

MOSANDRITE (=rinkite, rinkolite, johnstrupite)
$Na(Na,Ca)_2(Ca,Ce)_4(Ti,Nb,Zr)(Si_2O_7)_2(O,F)_2F_2$
$Na(Na,Ca)_2(Ca,Ce)_4(Ti,Nb,Zr)(Si_2O_7)_2(O,F)_2F_2$

Sys.	monoclinic	$a = 5.679(3)$ Å	source: Hibbing, CIS
S.G.	$P2_1$	$b = 7.412(3)$ Å	Ref.: Rastsvetaeva et al. (1991)
$Z =$	2	$c = 18.835(6)$ Å	JCPDS: #31-0313
Dx =	3.36 g/cm^3	$\alpha = 101.26(3)°$	
Dm =	3.29(3) g/cm^3		
AP:	table 156	ID: table 157	IL: fig. 70

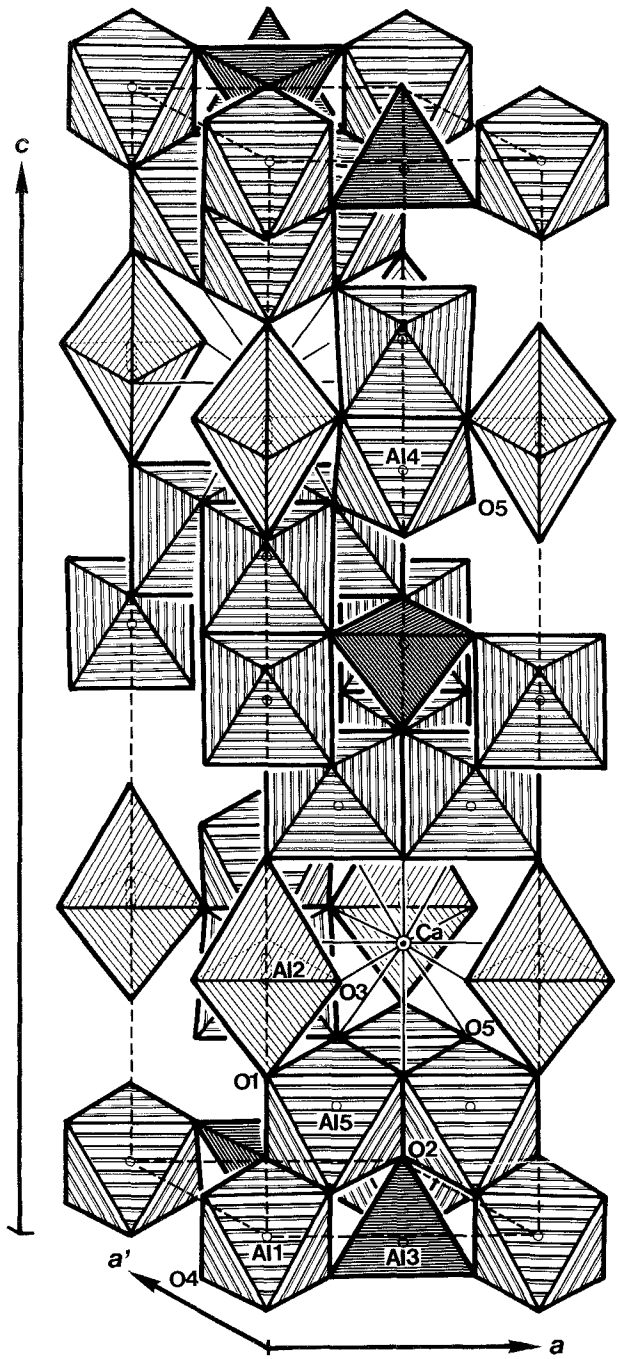

Fig. 69. The crystal structure of synthetic hibonite, $CaAl_{12}O_{19}$.

TABLE 155
Interatomic distances for hibonite in Å[a].

Ca–O5	2.7117(7) ×6	Al1–O4	1.8791(6) ×6
Ca–O3	2.7828(8) ×6	Al2–O3	1.7515(9) ×3
mean	2.7473	Al2–O1	2.0409(19)
Al3–O4	1.7955(6) ×3	Al2–O1	2.3784(19)
Al3–O2	1.8103(13)	mean	1.9348
mean	1.7992	Al4–O5	1.8756(7) ×3
Al5–O5	1.8062(5) ×2	Al4–O3	1.9536(8) ×3
Al5–O1	1.8433(6)	mean	1.9146
Al5–O2	1.9855(7)		
Al5–O4	1.9993(6) ×2		
mean	1.9066		

[a]Recalculated by RM.

NACARENIOBSITE-(Ce)
$Na_3[Ca_3Ce](Nb,Ti,Ta)(Si_2O_7)_2OF_3$
$(Na,\square)_3[(Ca,Sr)_3Ce](Nb,Ti,Ta)(Si_2O_7)_2OF_3$

Sys. monoclinic	$a = 18.901 \pm 0.005$ Å	source: Kvanefjeld, Ilímaussaq, Greenland
S.G. $P2_1/a$	$b = 5.683 \pm 0.003$ Å	Ref.: Petersen et al. (1989)
$Z = 2$	$c = 7.462 \pm 0.002$ Å	
$Dx = 3.43$ g/cm^3	$\beta = 101.29 \pm 0.04°$	
$Dm = 3.45$ g/cm^3		

The crystal structure of mosandrite was studied by many workers (Kheirov et al. 1963, Li et al. 1965, Simonov and Belov 1968). Galli and Alberti (1971) analyzed the crystal structure of mosandrite from Greenland using the space group $P2_1/c$. Later, Rastsvetaeva et al. (1991) refined the structure, using a specimen from the CIS, revealed the ordering of calcium, sodium and rare earth atoms, and concluded that the space group for mosandrite is $P2_1$. The basic feature of the crystal structure of mosandrite from Rastsvetaeva et al. (1991) is the same as that given by Galli and Alberti (1971), except for the occupancies of the large-cation sites for R, Ca and Na. The structure (fig. 70) consists of sheets of Na, M1 and M2 octahedra with diortho Si_2O_7 groups, parallel to the (001) plane. The M3, M4, M5 and M6 sites are occupied by calcium, and cerium-group rare earth atoms are located between the sheets with seven- and eight-coordination, and connect the sheets. Rastsvataeva et al. (1991) reported that the occupancy factor of rare earth atoms for the M4 site, 0.3, is greater than those for the M3, M4 and M5 sites, 0.2, indicating cation ordering among the large-cation sites.

Petersen et al. (1989) found a new Na–Ca–R–Nb silicate mineral with $Nb/Ti > 1$, nacareniobsite-(Ce), which corresponds to the Nb-dominant of mosandrite $(Na,Ca)_3(Ca,Ce)_4(Ti,Nb,Al,Zr)(Si_2O_7)_2(O,F)_4$ ($Nb/Ti < 1$). Although the structure of nacareniobsite-(Ce) has not yet been solved, the similarity of the crystal data of the two minerals indicates that nacareniobsite-(Ce) may be isostructural with mosandrite.

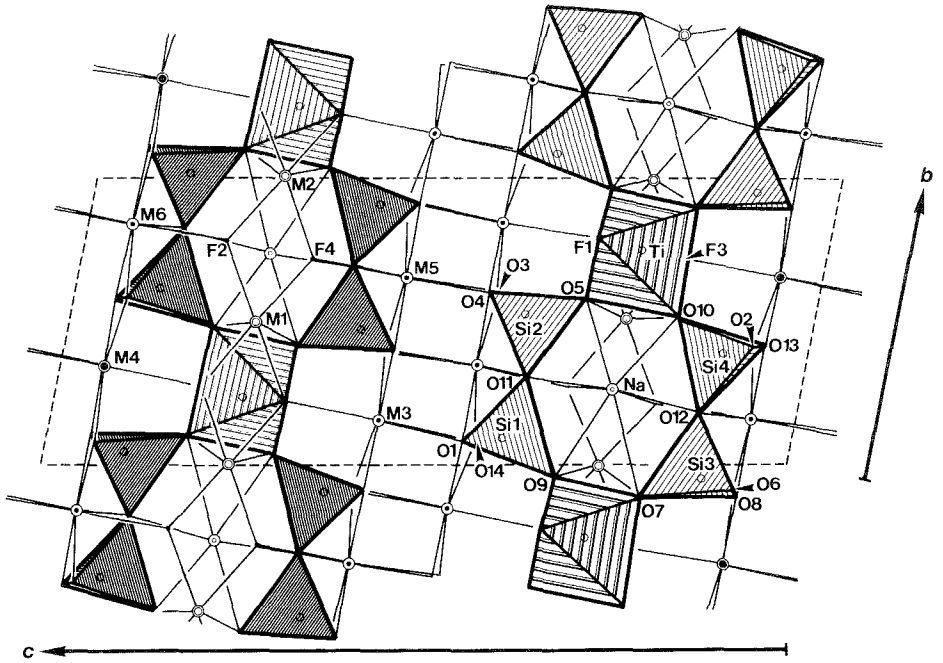

Fig. 70. The crystal structure of mosandrite.

Petersen et al. (1989) pointed out a problem in the nomenclature of Na–Ca–R–(Ti,Nb) silicate minerals named "mosandrite", "rinkite", "johnstrupite", "rinkolite", and "lovchorrite". They mentioned that mosandrite has a distinctly lower Na and higher H_2O content than the other minerals, whereas Fleischer and Mandarino (1991) described "rinkolite" to be a synonym of "rinkite", and "mosandrite" to be an alteration product of "rinkite". Nacareniobsite-(Ce) clearly differs from the other minerals in the Nb:Ti ratio. The ideal chemical formula of nacareniobsite-(Ce) is $Na_3Ca_3CeNb(Si_2O_7)_2OF_3$. Petersen et al. (1989) reported that the Nb-free end-member obtained by a $Nb^{5+} + Na^+ \rightleftarrows Ti^{4+} + Ca^{2+}$ substitution has the formula $Na_2Ca_4CeTi(Si_2O_7)_2OF_3$ and is the dominant component in "rinkite" and "rinkolite". An isomorphous substitution involving rare earth elements, $2Ca^{2+} \rightleftarrows R^{3+} + Na^+$, is also suggested for these minerals.

JOAQUINITE-(Ce)
$NaFe^{2+}Ba_2Ce_2Ti_2Si_8O_{26}(OH)\cdot H_2O$
$NaFe^{2+}Ba_2Ce_2Ti_2Si_8O_{26}(OH)\cdot H_2O$

Sys. monoclinic	$a = 10.516 \pm 0.003$ Å	source: San Benito Co., CA, USA
S.G. C2	$b = 9.686 \pm 0.003$ Å	Ref.: Dowty (1975)
$Z = 2$	$c = 11.833 \pm 0.004$ Å	JCPDS: #36-0385
	$\beta = 109.67 \pm 0.03°$	
AP: table 158	ID: table 159	IL: fig. 71

TABLE 156
Atomic parameters of mosandrite[a].

	x	y	z	B_{eq}
Ti	0.5083(7)	0.7480(3)	0.2512(1)	2.32(3)
Na	0.5069(13)	0.2642(7)	0.2519(3)	1.67(5)
M1[b]	0.0083(9)	0.5044(6)	0.2505(2)	1.80(5)
M2[c]	0.0062(10)	0.9977(7)	0.2516(2)	2.09(6)
M3[d]	0.8424(1)	0.8468(1)	0.4421(1)	1.24(2)
M4[e]	0.1652(1)	0.6514(1)	0.0581(1)	1.41(2)
M5[f]	0.8395(3)	0.3456(1)	0.4410(1)	1.72(3)
M6[g]	0.1674(3)	0.1580(1)	0.0598(1)	1.76(2)
Si1	0.3502(6)	0.0934(2)	0.3879(1)	0.99(4)
Si2	0.3490(9)	0.5271(4)	0.3891(1)	2.43(6)
Si3	0.6584(6)	0.9528(2)	0.1102(7)	0.73(3)
Si4	0.6580(8)	0.3856(3)	0.1126(1)	1.94(5)
O1	0.566(1)	0.0859(8)	0.4403(3)	1.8(2)
O2	0.897(1)	0.4146(7)	0.0684(3)	1.5(2)
O3	0.108(2)	0.599(1)	0.4319(4)	3.1(2)
O4	0.571(1)	0.603(1)	0.4421(2)	1.0(1)
O5	0.353(2)	0.578(1)	0.3109(3)	2.0(1)
O6	0.898(1)	0.905(1)	0.0648(3)	1.4(2)
O7	0.648(2)	0.893(1)	0.1897(3)	2.1(1)
O8	0.436(2)	0.889(1)	0.0606(6)	4.2(4)
O9	0.368(2)	0.961(1)	0.3078(3)	2.4(2)
O10	0.654(2)	0.512(1)	0.1918(3)	1.9(1)
O11	0.366(2)	0.300(1)	0.3684(4)	3.1(2)
O12	0.646(2)	0.177(1)	0.1298(4)	2.4(1)
O13	0.433(2)	0.413(1)	0.0594(4)	2.7(2)
O14	0.098(2)	0.085(1)	0.4238(5)	4.0(3)
F1	0.793(1)	0.776(1)	0.3112(2)	2.2(2)
F2[h]	0.158(1)	0.215(1)	0.1889(3)	3.0(2)
F3[i]	0.197(1)	0.717(1)	0.1901(3)	3.4(2)
F4	0.848(2)	0.278(1)	0.3132(3)	3.5(2)

[a] MoKα, $R = 0.0502$ (2681 refl.).
[b] M1: 0.7Na + 0.3Ca.
[c] M2: 0.7Na + 0.3Ca.
[d] M3: 0.8Ca + 0.2R.
[e] M4: 0.7Ca + 0.3R.
[f] M5: 0.8Ca + 0.2R.
[g] M6: 0.8Ca + 0.2R.
[h] F2: O,F.
[i] F3: O,F.

TABLE 157
Interatomic distances for mosandrite in Å.

Ti–O9	1.896(7)	Na–F4	2.249(10)
Ti–O7	1.900(8)	Na–O11	2.301(11)
Ti–F1	1.961(7)	Na–F2	2.303(9)
Ti–O5	2.047(8)	Na–O12	2.399(9)
Ti–O10	2.056(6)	Na–O10	2.483(9)
Ti–F3	2.098(8)	Na–O5	2.527(8)
mean	1.993	Na–O9	2.778(10)
		Na–O7	2.889(8)
		mean	2.491
M1–O5	2.274(9)	M2–F2	2.339(9)
M1–O10	2.305(10)	M2–F4	2.353(8)
M1–F3	2.374(9)	M2–O9	2.354(10)
M1–F2	2.388(8)	M2–O7	2.398(10)
M1–F4	2.407(9)	M2–F3	2.427(8)
M1–F1	2.442(7)	M2–F1	2.476(8)
mean	2.365	mean	2.391
M3–O3	2.358(8)	M4–O8	2.329(11)
M3–O14	2.362(10)	M4–O13	2.335(8)
M3–O1	2.373(6)	M4–O2	2.362(5)
M3–O4	2.375(5)	M4–O6	2.404(5)
M3–F1	2.434(5)	M4–F3	2.445(6)
M3–O1	2.518(6)	M4–O13	2.541(6)
M3–O14	2.839(10)	M4–O2	2.682(5)
mean	2.465	mean	2.442
M5–F4	2.362(7)	M6–F2	2.387(5)
M5–O14	2.401(9)	M6–O13	2.419(8)
M5–O4	2.438(5)	M6–O2	2.427(5)
M5–O3	2.449(8)	M6–O6	2.429(6)
M5–O1	2.472(6)	M6–O8	2.512(11)
M5–O4	2.530(5)	M6–O8	2.586(11)
M5–O3	2.691(9)	M6–O6	2.648(6)
M5–O11	3.007(12)	M6–O12	3.015(10)
mean	2.544	mean	2.553
Si1–O1	1.580(7)	Si2–O5	1.590(8)
Si1–O14	1.588(11)	Si2–O3	1.623(9)
Si1–O9	1.636(7)	Si2–O4	1.638(6)
Si1–O11	1.647(7)	Si2–O11	1.654(7)
mean	1.612	mean	1.626
Si3–O8	1.590(11)	Si4–O10	1.600(6)
Si3–O6	1.611(6)	Si4–O2	1.626(7)
Si3–O12	1.634(5)	Si4–O12	1.639(6)
Si3–O7	1.644(7)	Si4–O13	1.661(9)
mean	1.620	mean	1.631

TABLE 158
Atomic parameters of joaquinite-(Ce)[a].

	x	y	z	B (Å²)
R	0.1667(1)	0.7467(1)	0.4518(1)	1.17(2)[d]
Ba	0.2366(1)	0	0.0058(1)	0.94(2)[d]
Na[b]	0	0.054(3)	0.5	5.9(8)[d]
Fe[c]	0	0.3694(6)	0.5	0.6(1)[d]
Ti	0.0490(3)	0.7369(5)	0.1276(3)	0.36(4)[d]
Si1	0.3773(5)	0.7343(7)	0.2426(4)	0.66(8)[d]
Si2	0.3085(5)	0.2674(7)	0.2432(5)	0.91(9)[d]
Si3	0.1206(6)	0.0375(7)	0.2917(5)	0.80(9)[d]
Si4	0.0929(6)	0.4365(6)	0.2709(6)	0.68(9)[d]
O1	0	0.867(2)	0	0.6(3)
O2	0	0.606(2)	0	0.8(3)
O3	0.116(2)	0.881(2)	0.251(1)	1.2(2)
O4	0.188(1)	0.385(2)	0.191(1)	0.9(2)
O5	0.226(2)	0.115(2)	0.237(1)	1.3(3)
O6	0.233(1)	0.715(1)	0.133(1)	0.7(2)
O7	0.472(2)	0.605(2)	0.299(2)	1.6(3)
O8	0.086(2)	0.604(2)	0.268(1)	1.0(2)
O9	0.371(1)	0.737(2)	0.375(1)	1.0(2)
O10	0.412(1)	0.303(2)	0.372(1)	1.5(3)
O11	0.144(2)	0.368(2)	0.403(1)	1.4(3)
O12	0.173(2)	0.044(2)	0.443(1)	1.7(3)
O13	0.367(1)	0.254(2)	0.133(1)	0.8(2)
O14	0.439(2)	0.880(2)	0.203(2)	1.7(3)
OH	0	0.576(4)	0.5	5.0(9)
H_2O	0	0.199(3)	0	2.6(5)

[a]X-ray is not specified, $R = 0.086$, $R_w = 0.075$ (2630 refl.).
[b]Na: 0.75Na + 0.25Fe.
[c]Fe: 0.79Fe + 0.21Na.
[d]B_{eq}.

STRONTIOJOAQUINITE
$(Na,Fe)_2Ba_2(Sr,Ce)_2Ti_2Si_8O_{24}(O,OH)_2 \cdot H_2O$
$(Na,Fc,\square)_2Ba_2(Sr,Ce)_2Ti_2Si_8O_{24}(O,OH)_2\square \cdot 0.8H_2O$

Sys. monoclinic	$a = 10.516(6)$ Å	source: San Benito Co., CA, USA
S.G. P2, Pm or P2/m	$b = 9.764(5)$ Å	Ref.: Wise (1982)
$Z = 2$	$c = 11.87(1)$ Å	JCPDS: #36-0384
$Dx = 3.68$ g/cm³	$\beta = 109°17(4)'$	

ORTHOJOAQUINITE-(Ce)
$NaFe^{2+}Ba_2Ce_2Ti_2Si_8O_{26}(OH) \cdot H_2O$
$NaFe^{2+}Ba_2Ce_2Ti_2Si_8O_{26}(OH) \cdot H_2O$

Sys. orthorhombic	$a = 10.48$ Å	source: San Benito Co., CA, USA
S.G. Cc2m	$b = 9.66$ Å	Ref.: Dowty (1975)
$Z = 4$	$c = 22.26$ Å	JCPDS: #26-1034

TABLE 159
Interatomic distances for joaquinite-(Ce) in Å.

R–O8	2.48(2)	Ba–O6	2.74(1)
R–O10	2.55(2)	Ba–O1	2.78(1)
R–O10	2.58(2)	Ba–O14	2.82(2)
R–O9	2.60(1)	Ba–O13	2.89(2)
R–O11	2.60(1)	Ba–O4	2.93(1)
R–O3	2.60(2)	Ba–O13	2.97(2)
R–O12	2.61(2)	Ba–O2	2.98(1)
R–OH	2.61(3)	Ba–O5	3.00(2)
R–O12	2.89(2)	Ba–O7	3.07(2)
mean	2.62	Ba–H_2O	3.13(2)
		Ba–O6	3.15(1)
Na–O12	2.14(6) ×2	mean	2.95
Na–O9	2.41(3) ×2		
Na–O10	2.85(3) ×2	Ti–O1	1.90(1)
mean	2.47	Ti–O2	1.90(2)
		Ti–O6	1.92(1)
Fe–OH	2.00(4)	Ti–O13	1.95(1)
Fe–O9	2.07(2) ×2	Ti–O3	1.97(2)
Fe–O11	2.19(2) ×2	Ti–O8	2.03(2)
mean	2.10	mean	1.94
Si1–O9	1.59(1)	Si2–O10	1.58(2)
Si1–O6	1.64(1)	Si2–O13	1.62(1)
Si1–O7	1.64(2)	Si2–O4	1.66(2)
Si1–O14	1.68(2)	Si2–O5	1.70(2)
mean	1.64	mean	1.64
Si3–O3	1.59(2)	Si4–O11	1.61(2)
Si3–O7	1.62(2)	Si4–O8	1.62(2)
Si3–O5	1.64(2)	Si4–O14	1.64(2)
Si3–O12	1.69(2)	Si4–O4	1.66(2)
mean	1.63	mean	1.63

BARIO-ORTHOJOAQUINITE
$(Fe^{2+},Mn)_2(Ba,Sr)_4(Ti,Al)_2Si_8O_{26}\cdot H_2O$
$(Fe^{2+},Mn)_2Ba_2(Ba,Sr)_2(Ti,Al)_2Si_8O_{26}\square\cdot H_2O$

Sys. orthorhombic	$a = 10.477(5)$ Å	source: San Benito Co., CA, USA
S.G. Ccmm, Cc2m or $Ccm2_1$	$b = 9.599(1)$ Å	Ref.: Wise (1982)
$Z = 4$	$c = 22.59(1)$ Å	JCPDS: #36-0386
Dx = 3.962 g/cm^3		
Dm = 3.959(2) g/cm^3		

BYELORUSSITE-(Ce)
$(Na,K)(Mn,Zn,Fe,Mg)(Ba,Sr)_2Ce_2Ti_2Si_8O_{26}[F,(OH)] \cdot H_2O$
$(Na,K)(Mn,Zn,Fe,Mg)(Ba,Sr)_2Ce_2Ti_2Si_8O_{26}[F,(OH)] \cdot H_2O$

Sys. orthorhombic	$a = 10.57(6)$ Å	source: Zhitkovitschskij horst,
S.G. $P2_12_12_1$	$b = 9.69(6)$ Å	Homel, Byelorussia
$Z = 4$	$c = 22.38(10)$ Å	Ref.: Shpanov et al. (1989)
Dx = 4.09 g/cm^3		
Dm = 3.92 g/cm^3		

Joaquinite-(Ce) had been believed to have an orthorhombic lattice due to the polysynthetic twinning. Cannillo et al. (1972) revealed the crystal system to be monoclinic, and assigned the space group as C2/m after a crystal structure analysis of joaquinite-(Ce). Dowty (1975) refined the structure, giving the space group as C2 instead of C2/m, revealing several additional atoms (Na, OH, H_2O) and proposing the ideal chemical formula to be $NaFe^{2+}Ba_2Ce_2Ti_2Si_8O_{26}(OH) \cdot H_2O$, in agreement with the results of the chemical analyses.

The structure (fig. 71) is characterized by four-membered rings of Si tetrahedra, which are connected by Ti octahedra forming sheets parallel to the *ab*-plane. The sheets are held together by Ba, Na, Fe and R atoms between the sheets. The R site is surrounded by eight oxygen atoms and an (OH) ion, and the Ba site is coordinated by ten oxygen atoms and a water molecule. The Na atom forms a distorted octahedron with six oxygen atoms. The Fe site has unusual five-coordination with four oxygen atoms and an (OH) ion.

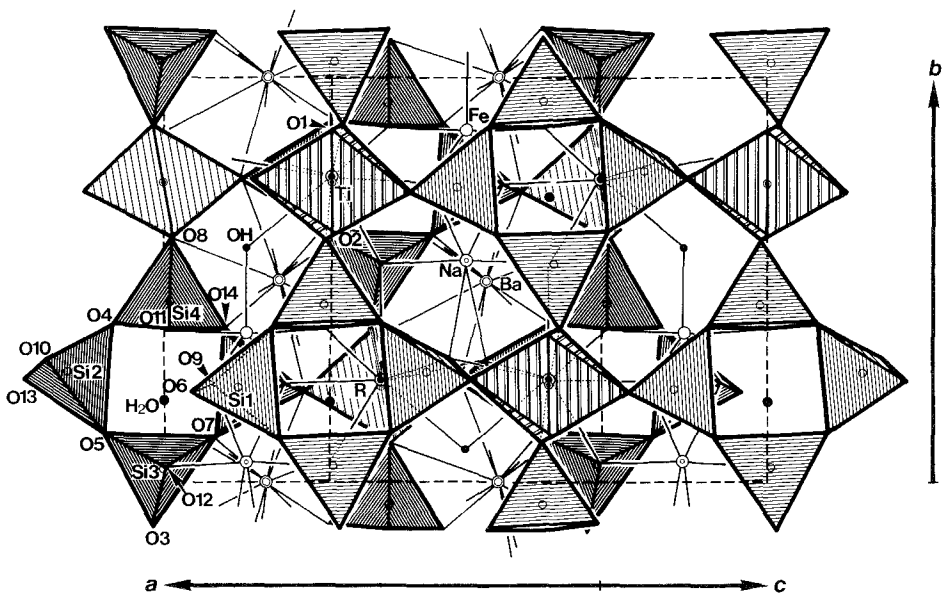

Fig. 71. The crystal structure of joaquinite-(Ce).

TABLE 160
Atomic parameters of R-bearing vesuvianite[a].

	x	y	z	U_{iso} (Å^2)		x	y	z	U_{iso} (Å^2)
Si1a	−1/4	1/4	1/2	0.008(1)	Feb2[p]	1/4	1/4	−0.4574(6)	0.022(2)
Si1b	−1/4	1/4	0	0.010(1)	O1a	−0.2245(4)	0.1739(4)	0.0852(6)	0.012(2)
Si2a	−0.0404(2)	0.3187(2)	0.1279(2)	0.010(1)	O1b	−0.2786(5)	0.1731(4)	0.4143(6)	0.015(2)
Si2b	−0.0408(2)	0.1812(1)	0.3726(2)	0.012(1)	O2a	−0.1171(5)	0.1626(4)	0.2821(6)	0.014(2)
Si3a	0.0848(2)	0.1507(2)	0.6375(2)	0.010(1)	O2b	−0.1169(5)	0.3372(4)	0.2183(6)	0.014(2)
Si3b	0.0851(2)	0.3489(2)	−0.1371(2)	0.010(1)	O3a	−0.0448(4)	0.2244(4)	0.0710(6)	0.013(2)
Ca1a	−1/4	1/4	0.2496(3)	0.014(1)	O3b	−0.0469(4)	0.2767(4)	0.4264(6)	0.012(2)
Ca2a	0.1893(1)	−0.0477(1)	0.6219(2)	0.012(1)	O4a	−0.0594(4)	0.1045(4)	0.4690(6)	0.012(2)
Ca2b	−0.0474(1)	0.1893(1)	−0.1220(2)	0.013(1)	O4b	−0.0592(4)	0.3925(4)	0.0330(6)	0.012(2)
Ca3a[c]	0.1784(1)	0.3985(1)	0.1094(1)	0.014	O5a	−0.0087(4)	0.3272(4)	−0.1805(6)	0.014(2)
Ce3a[d]	0.1784(1)	0.3985(1)	0.1094(1)	0.012(1)	O5b	−0.0103(4)	0.1723(4)	0.6797(6)	0.014(2)
Ca3b[e]	0.3219(1)	0.3988(1)	−0.6087(1)	0.014	O6a	0.1209(5)	0.2755(5)	−0.0584(7)	0.020(2)
Ce3b[f]	0.3219(1)	0.3988(1)	−0.6087(1)	0.013(1)	O6b	0.1225(4)	0.2224(5)	0.5534(6)	0.017(2)
Cac1[g]	1/4	1/4	−0.3530(8)	0.033(2)	O7a	0.0554(4)	0.1757(5)	0.3227(7)	0.016(2)
Cac2[h]	1/4	1/4	−0.1453(8)	0.015(2)	O7b	0.0573(4)	0.3242(4)	0.1777(6)	0.015(2)
Mg1a[i]	0.38[b]	−0.1108(1)	0.1197(2)	0.014	O8a	0.0937(5)	0.4390(5)	−0.0733(6)	0.014(2)
Fe1a[j]	0.38[b]	−0.1108(1)	0.1197(2)	0.005(1)	O8b	0.0953(4)	0.0594(4)	0.5730(6)	0.013(2)
Mg1b[k]	−0.1204(1)	0.1114(1)	0.6266(2)	0.014	O9a	0.1474(4)	0.1475(4)	0.7500(6)	0.014(2)
Fe1b[l]	−0.1204(1)	0.1114(1)	0.6266(2)	0.007(1)	O10a[q]	1/4	1/4	0.1397(18)	0.037(5)
Ala1[m]	0	0	1/2	0.018(1)	O10b[r]	−1/4	−1/4	−0.3603(21)	0.036(6)
Ala2[n]	0	1/2	0	0.023(1)	O11a[s]	−0.0019(4)	0.0630(5)	0.1366(7)	0.016(2)
Feb1[o]	1/4	1/4	−0.0511(7)	0.019(2)	O11b[t]	−0.0625(4)	0.0011(4)	0.6352(6)	0.015(2)

[a] Mokα, $R = 0.0664$, $R_w = 0.0722$ (2874 refl.).
[b] Calculated by RM using the (Mg,Fe)1a–O distances given in the original paper. The (Mg,Fe)1a–O distances calculated using the reported x coordinate for the Mg1a and Fe1a sites, 0.0002(1), are inconsistent with the distances given in the original paper, and are unreasonable (see the following table of interatomic distances).
[c] Ca3a: 0.64Ca. [d] Ce3a: 0.42Ce. [e] Ca3b: 0.31Ca. [f] Ce3b: 0.51Ce. [g] Cac1: Ca. [h] Cac2: Ca. [i] Mg1a: not given. [j] Fe1a: not given. [k] Mg1b: not given. [l] Fe1b: not given. [m] Ala1: Al. [n] Ala2: Al. [o] Feb1: Fe + minor Cu. [p] Feb2: Fe + minor Cu. [q] O10a: (OH). [r] O10b: (OH). [s] O11a: 0.5O + 0.5(OH). [t] O11b: 0.5O + 0.5(OH).

TABLE 161
Interatomic distances for R-bearing vesuvianite in Å[a].

Ca1a–O1a	2.334(8) ×2			Ca2a–O8b	2.326(7)	Ca2b–O8a	2.356(8)
Ca1a–O1b	2.352(8) ×2			Ca2a–O5b	2.367(7)	Ca2b–O3a	2.366(8)
Ca1a–O2b	2.541(7) ×2			Ca2a–O3b	2.391(8)	Ca2b–O5a	2.368(7)
Ca1a–O2a	2.543(7) ×2			Ca2a–O2a	2.430(7)	Ca2b–O2b	2.439(7)
				Ca2a–O5a	2.448(7)	Ca2b–O5b	2.450(7)
mean	2.443			Ca2a–O1b	2.470(7)	Ca2b–O1a	2.458(7)
				Ca2a–O4a	2.488(7)	Ca2b–O4b	2.500(7)
				mean	2.417	mean	2.420
Ca,Ce3a–O7b	2.388(7)	Ca,Ce3b–O7a	2.411(7)	Cac1–O6b	2.344(8) ×4	Cac2–O6a	2.323(9) ×4
Ca,Ce3a–O3a	2.466(7)	Ca,Ce3b–O11b	2.459(7)	Cac1–O9a	2.599(8) ×4	Cac2–O9a	2.609(8) ×4
Ca,Ce3a–O11a	2.469(7)	Ca,Ce3b–O3b	2.482(7)	mean	2.472	mean	2.466
Ca,Ce3a–O6a	2.539(8)	Ca,Ce3b–O6b	2.513(8)				
Ca,Ce3a–O7b	2.541(7)	Ca,Ce3b–O7a	2.555(8)				
Ca,Ce3a–O10a	2.630(3)	Ca,Ce3b–O8b	2.615(7)				
Ca,Ce3a–O8a	2.634(8)	Ca,Ce3b–O10b	2.637(4)				
Ca,Ce3a–O7a	2.645(8)	Ca,Ce3b–O7b	2.639(7)				
Ca,Ce3a–O6a	2.933(8)	Ca,Ce3b–O6b	2.858(8)				
mean	2.583	mean	2.574				

Mg,Fe1a–O11a	1.944(8)[b]	Mg,Fe1b–O2b	1.968(7)	Mg,Fe1a–O8a	1.146(8)[c]		
Mg,Fe1a–O2a	1.967(8)[b]	Mg,Fe1b–O11b	1.971(7)	Mg,Fe1a–O4b	2.146(7)		
Mg,Fe1a–O1a	2.053(8)[b]	Mg,Fe1b–O1b	1.988(8)	Mg,Fe1a–O5b	2.585(7)[c]		
Mg,Fe1a–O3a	2.068(7)[b]	Mg,Fe1b–O3b	2.020(7)	Mg,Fe1a–O11a	2.753(8)[c]		
Mg,Fe1a–O5a	2.106(7)[b]	Mg,Fe1b–O5b	2.086(7)	Mg,Fe1a–O2b	2.827(7)[c]		
Mg,Fe1a–O4b	2.138(7)[b]	Mg,Fe1b–O4a	2.114(7)	Mg,Fe1a–O9a	2.861(7)[c]		
mean	2.035[b]	mean	2.025	mean	2.386[c]		
Al1–O11b	1.890(7) ×2	Al2–O11a	1.908(8) ×2	Fe1–O6a	2.081(8) ×4	Fe2–O6b	2.065(6) ×4
Al1–O4a	1.935(6) ×2	Al2–O8a	1.971(8) ×2	Fe1–O10a	2.274(23)	Fe2–O10a	2.172(26)
Al1–O8b	1.976(6) ×2	Al2–O4b	1.978(6) ×2	mean	2.120	mean	2.086
mean	1.934	mean	1.952				
Si1a–O1b	1.650(7) ×4	Si1b–O1a	1.624(7) ×4				
Si2a–O3a	1.638(7)	Si2b–O7a	1.634(7)	Si3a–O5b	1.621(7)	Si3b–O6a	1.595(9)
Si2a–O2b	1.645(9)	Si2b–O3b	1.642(7)	Si3a–O6b	1.626(8)	Si3b–O5a	1.607(7)
Si2a–O4b	1.651(7)	Si2b–O2a	1.644(8)	Si3a–O8b	1.643(7)	Si3b–O8a	1.620(8)
Si2a–O7b	1.656(9)	Si2b–O4a	1.696(7)	Si3a–O9a	1.667(7)	Si3b–O9a	1.669(7)
mean	1.648	mean	1.654	mean	1.639	mean	1.623

[a] Recalculated by RM.
[b] Values given in the original paper.
[c] Values calculated by RM using the original x coordinates for the (Mg,Fe)1a site, 0.0002(1), which are strange for (Mg,Fe)–O distances.

Dowty (1975) also reported on orthojoaquinite-(Ce), an orthorhombic dimorph of joaquinite-(Ce) found during his study, and revealed the structural relationship between the monoclinic and orthorhombic phases. Wise (1982) described new members of the joaquinite group, strontiojoaquinite and bario-orthojoaquinite, after the nomenclature of this group. He suggested that a vacancy was present at the Na and Fe sites as well as at the OH site, which had already been pointed out by Dowty (1975), and that the Na and Fe atoms substituted for each other. Furthermore, he reported that the rare earth atoms can be completely replaced by divalent cations such as Sr and Ba. A combination of the result of the crystal structure analysis by Dowty (1975) and the formulae given for the new members by Wise (1982) enables us to express the general formula for joaquinitie as $(Na,Fe,\square)(Fe,Na,\square)$-$(Ba,Sr)_2(R,Sr,Ba)_2Ti_2Si_8O_{24}(O,OH)_2[(OH),\square]\cdot H_2O$.

Byelorussite-(Ce) is a new mineral of the joaquinite group (Shpanov et al. 1989). Although it is chemically an Mn-analogue of orthojoaquinite-(Ce), the space group, $P2_12_12_1$, given by Shpanov et al. (1989) is different from that of orthojoaquinite-(Ce), Cc2m, given by Dowty (1975).

R-bearing VESUVIANITE
$(Ca,R)_{19}Al_4Fe(Mg,Al)_8(SiO_4)_{10}(Si_2O_7)_4(OH)_{10}$
$Ca_{12}(Ca,Ce)_8(Al,Fe)_4(Fe,Cu)_2(Mg,Ti,Fe)_8[(Si,Al)O_4]_{10}[(Si,Al)_2O_7]_4(OH)_2[(OH),O]_8$

Sys. tetragonal	$a = 15.799(3)$ Å	source: San Benito Co., CA, USA
S.G. P4/n	$c = 11.917(3)$ Å	Ref.: Fitzgerald et al. (1987)
$Z = 2$		JCPDS: #38-0473, #38-0474
AP: table 160	ID: table 161	IL: fig. 72

The crystal structure of R-bearing vesuvianite was determined by Fitzgerald et al. (1987). In the structure (fig. 72), Si2 and Si3 independently form Si_2O_7 groups, whereas Si1 atoms are at the center of isolated tetrahedra. Mg, Fe, and Al atoms are coordinated by six oxygen atoms, and the polyhedra of Feb1 and Feb2 are square pyramids with five-coordination. Rare earth atoms selectively occupy parts of the nine-coordinated Ca3 site, but do not occupy the eight-coordinated Ca1, Cac sites or the seven-coordinated Ca2 site. R-bearing vesuvianite shows complex coupled substitutions: R for Ca, Ti for Al, Mg for Al and OH^- for O^{2-}.

---

yftisite
$Y_4TiSi_2O_9F_6$
$Y_4TiSi_2O_9F_6$

Sys. orthorhombic	$a = 14.949(4)$ Å	source: Kola Peninsula, Russia
S.G. Cmcm	$b = 10.626(2)$ Å	Ref.: Balko and Bakakin (1975)
$Z = 4$	$c = 7.043(2)$ Å	JCPDS: #33-1462
AP: table 162	ID: table 163	IL: fig. 73

The mineral name "yftisite" was recently discredited by the IMA Commission on New Minerals and Mineral Names due to its incomplete chemical analysis (Nickel and Mandarino 1987, Fontan and Pierrot 1982).

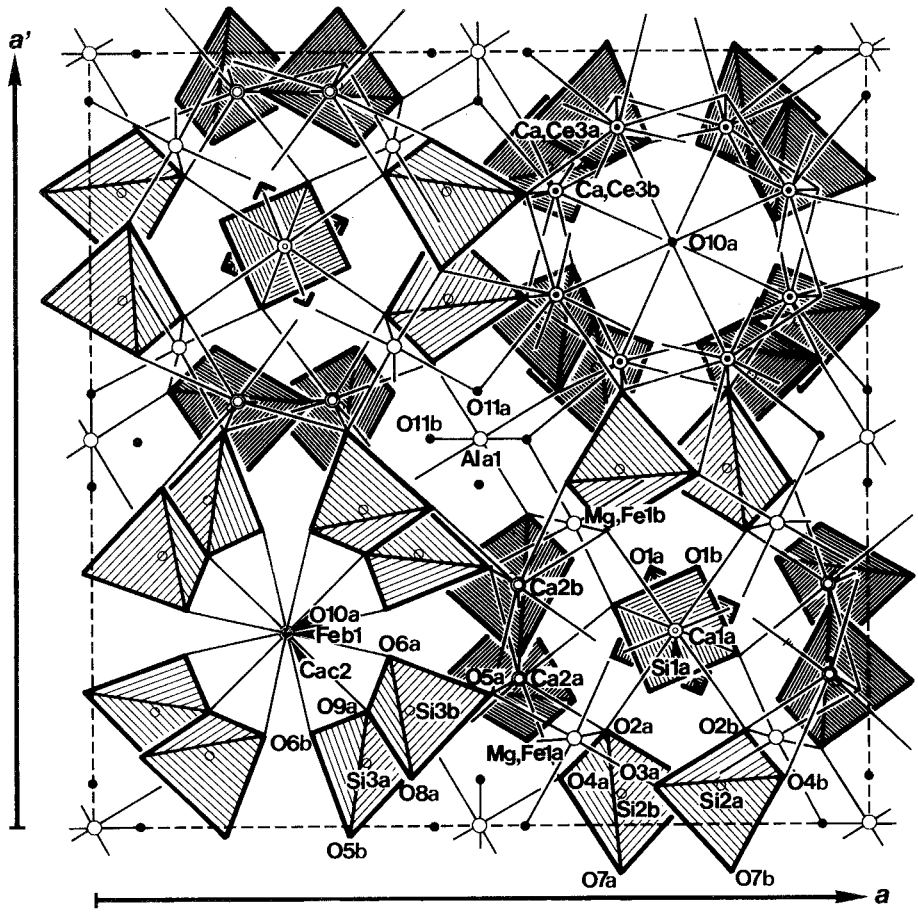

Fig. 72. The crystal structure of R-bearing vesuvianite.

TABLE 162
Atomic parameters of yftisite[a].

	x	y	z	B (Å^2)
Y1	0.1464(2)	0.4368(1)	0.25	1.2
Y2	0.1313(1)	0.7933(3)	0.25	1.0
Ti	0	0	0.5	1.3
Si	0.1559(4)	0.1200(4)	0.25	0.2
O1	0.0954(4)	0.1262(5)	0.0553(10)	1.0
O2	0.2952(5)	0.4854(8)	0.25	0.7
O3	0.2201(4)	0.2487(5)	0.25	0.7
O4	0.5	0.4337(5)	0.25	0.7
F1	0.3582(5)	0.1181(5)	0.0610(18)	0.9
F2	0	0.4204(6)	0.25	4.2
F3	0	0.6987(6)	0.25	1.9

[a] MoKα, $R = 0.067$ (385 refl.).

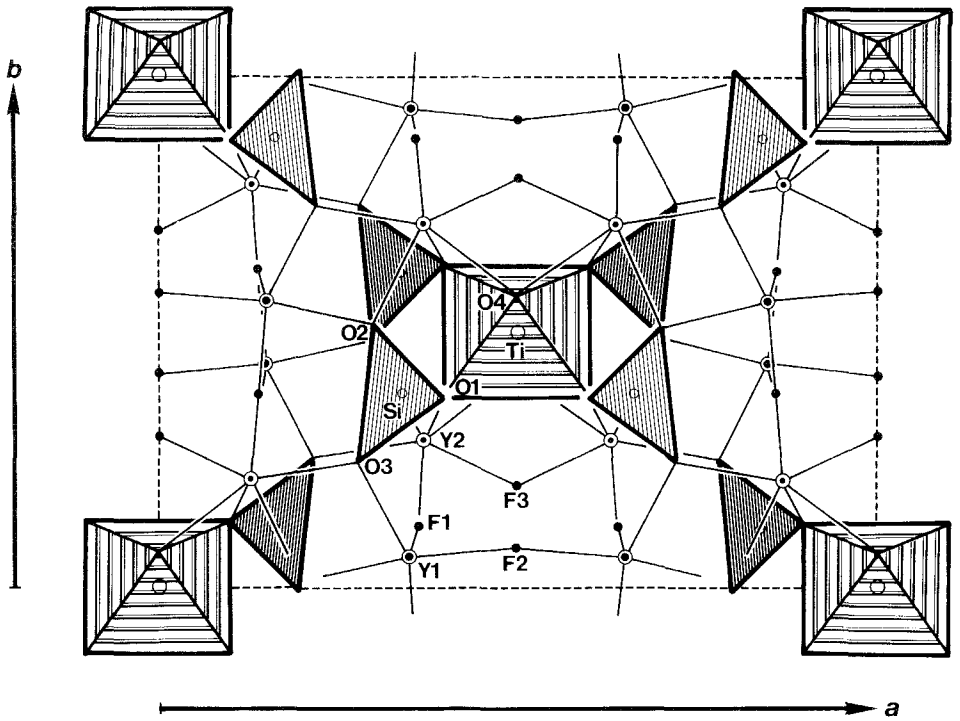

Fig. 73. The crystal structure of yftisite.

TABLE 163
Interatomic distances for yftisite in Å.

Y1–O3	2.282	Y2–O3	2.272
Y1–O2	2.285	Y2–O2	2.323
mean	2.284	Y2–O1	2.376 ×2
		Y2–O4	2.466
Y1–F2	2.195	mean	2.363
Y1–F1	2.268 ×2		
Y1–F1	2.343 ×2	Y2–F3	2.205
mean	2.283	Y2–F1	2.293 ×2
[mean]	2.283	mean	2.264
Ti–O4	1.896 ×2	[mean]	2.326
Ti–O1	1.996 ×4	Si–O2	1.602
mean	1.963	Si–O1	1.643 ×2
		Si–O3	1.671
		mean	1.640

However, the crystal structure of this mineral had been reported by Balko and Bakakin (1975). The structure (fig. 73) consists of infinite columns of Ti octahedra and Si tetrahedra, parallel to the *c*-axis. The columns are linked by two independent seven- and eight-coordinated Y polyhedra.

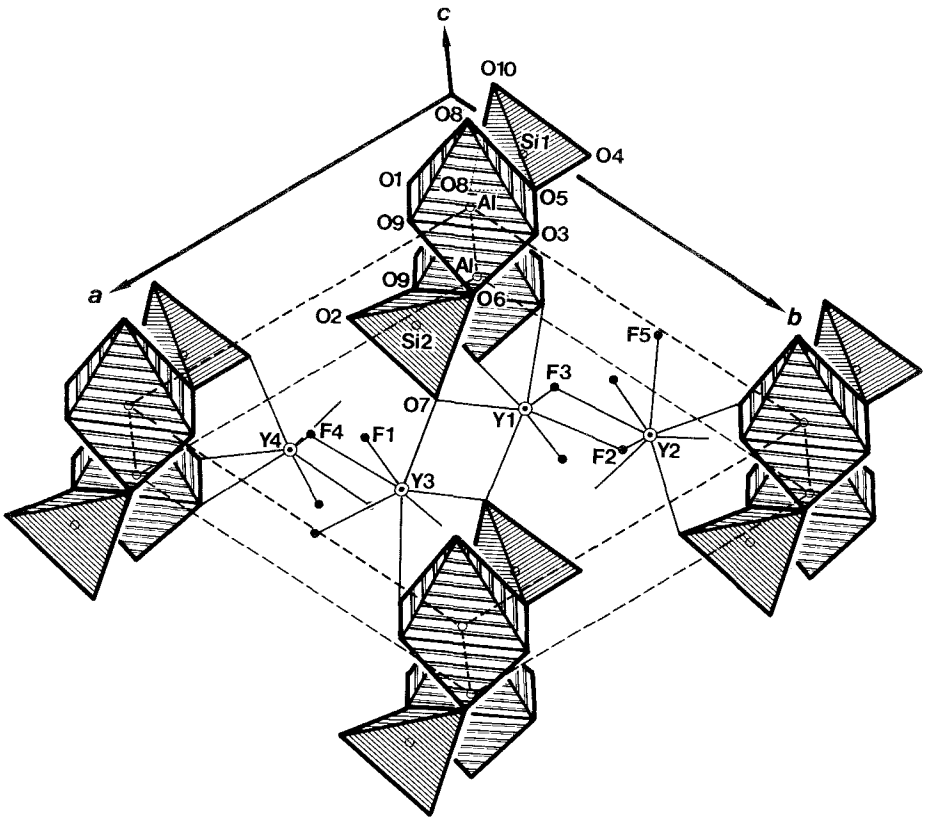

Fig. 74. The crystal structure of kuliokite-(Y).

KULIOKITE-(Y)			
$Y_4Al(SiO_4)_2(OH)_2F_5$			
$Y_4Al(SiO_4)_2(OH)_2F_5$			
Sys. triclinic	$a =$ 8.606(6) Å		source: Kola Peninsula, Russia
S.G. P1	$b =$ 8.672(8) Å		Ref.: Sokolova et al. (1986)
$Z =$ 1	$c =$ 4.317(3) Å		JCPDS: #40-0467
Dx = 4.38 g/cm^3	$\alpha = 102.79(6)°$		
Dm = 4.3 g/cm^3	$\beta = 97.94(5)°$		
	$\gamma = 116.66(6)°$		
AP: table 164	ID: table 165		IL: fig. 74

The crystal structure of kuliokite-(Y) was determined by Sokolova et al. (1986). The crystal structure (fig. 74) consists of columns of Al–O octahedra and Si–O tetrahedra, which are parallel to the *c*-axis. The columns are connected by Y–O,F "Thomson cubes". Sokolova et al. (1986) described the structure as a three-dimensional framework of Y polyhedra with cavities, in which Al–Si strips are

TABLE 164
Atomic parameters of kuliokite-(Y)[a].

	x	y	z	B_{iso} (Å^2)
Y1	0.2938(5)	0.4489(5)	0.3180(9)	0.61(6)
Y2	0.2614(5)	0.8030(5)	0.9857(9)	0.64(6)
Y3	0.7405(5)	0.5424(5)	0.7237(9)	0.45(5)
Y4	0.7098(5)	0.1575(5)	0.0266(9)	0.46(5)
Al	0	0	0	0.1(2)
Si1	0.691(1)	0.842(2)	0.352(2)	0.3(2)
Si2	0.311(1)	0.150(1)	0.660(3)	0.2(2)
O1[b]	0.002(4)	0.808(4)	0.704(8)	0.4(4)
O2	0.421(4)	0.064(4)	0.843(7)	0.5(5)
O3[b]	0.007(3)	0.213(3)	0.298(7)	0.5(5)
O4	0.562(4)	0.898(4)	0.168(8)	1.0(6)
O5	0.814(4)	0.003(3)	0.705(7)	0.6(5)
O6	0.185(4)	0.190(3)	0.899(7)	0.5(5)
O7	0.440(3)	0.343(4)	0.623(7)	0.5(5)
O8	0.820(4)	0.818(3)	0.121(8)	0.5(5)
O9	0.182(3)	0.002(3)	0.315(6)	0.4(5)
O10	0.580(4)	0.644(4)	0.435(7)	0.4(5)
F1	0.732(3)	0.436(3)	0.170(5)	0.7(4)
F2	0.261(3)	0.704(3)	0.461(6)	0.6(4)
F3	0.277(3)	0.532(4)	0.848(6)	1.0(4)
F4	0.716(3)	0.249(3)	0.572(6)	0.7(4)
F5	0.001(4)	0.558(4)	0.910(4)	2.0(6)

[a] MoKα, $R = 0.066$ (975 refl.).
[b] (OH).

located. They pointed out the presence of hydrogen bonds between O1(OH)–O8, –O9 and O3(OH)–O5, –O6, based on interatomic distances. They also suggested a structural relationship between kuliokite-(Y), kainosite-(Y) and borcarite, $Ca_4MgB_4O_6(CO_3)_2(OH)_6$.

ILMAJOKITE
$(Na,Ce,Ba)_{10}Ti_5(Si,Al)_{14}O_{22}(OH)_{44} \cdot nH_2O$
$(Na,Ce,Ba)_{10}Ti_5(Si,Al)_{14}O_{22}(OH)_{44} \cdot nH_2O$

Sys. monoclinic (?)	$a \approx 23$ Å	source: Lovozero, Tundra, Kola Peninsula, Russia
S.G.	$b \approx 24.4$ Å	
$Z =$	$c \approx 37$ Å	Ref.: Bussen et al. (1972)
Dm = 2.20 ± 0.02 g/cm^3	$\beta = ?$	JCPDS: #25-0783

Ilmajokite was described by Bussen et al. (1972) as having a monoclinic lattice, but accurate lattice parameters were not given.

TABLE 165
Interatomic distances for kuliokite-(Y) in Å.

Y1–O10	2.17(3)	Y2–F3	2.21(3)
Y1–O6	2.25(3)	Y2–F2	2.24(3)
Y1–F3	2.29(3)	Y2–O4	2.29(4)
Y1–O7	2.30(3)	Y2–O2	2.34(3)
Y1–F3	2.31(3)	Y2–F3	2.36(3)
Y1–O3	2.37(3)	Y2–O9	2.39(3)
Y1–F2	2.37(3)	Y2–F2	2.40(3)
mean	2.29	Y2–O1	2.42(3)
		mean	2.33
Y3–F5	2.21(4)	Y4–O2	2.20(3)
Y3–O7	2.28(3)	Y4–O5	2.26(3)
Y3–F1	2.31(2)	Y4–F1	2.27(2)
Y3–O10	2.31(3)	Y4–F4	2.27(3)
Y3–F1	2.34(2)	Y4–F4	2.30(2)
Y3–O8	2.35(3)	Y4–O4	2.30(3)
Y3–F4	2.39(3)	Y4–O3	2.44(3)
Y3–O1	2.42(3)	mean	2.29
mean	2.33		
A1–O1	1.87(3)		
A1–O8	1.88(3)		
A1–O6	1.91(2)		
A1–O5	1.92(3)		
A1–O9	1.92(3)		
A1–O3	1.98(3)		
mean	1.91		
Si1–O4	1.59(4)	Si2–O9	1.59(3)
Si1–O5	1.64(3)	Si2–O7	1.60(3)
Si1–O8	1.64(4)	Si2–O2	1.66(3)
Si1–O10	1.70(3)	Si2–O6	1.69(3)
mean	1.64	mean	1.64

LAPLANDITE-(Ce)
$(Na,K,Ca)_4(Ce,Th)(Ti,Mg,Al,Nb)PSi_7O_{22} \cdot 5H_2O$
$(Na,K,Ca)_4(Ce,Th)(Ti,Mg,Al,Nb)PSi_7O_{22} \cdot 5H_2O$

Sys. orthorhombic	$a = 7.27$ Å	source: Mt. Karnasurt, Lovozero, Kola Peninsula, Russia
S.G. Pmmm	$b = 14.38$ Å	
$Z = 4$	$c = 22.25$ Å	Ref.: Eskova et al. (1974)
$Dm = 2.83$ g/cm^3		JCPDS: #27-0673

The crystal structure of laplandite is unknown.

TRANQUILLITYITE
$Fe_8(Zr,Y)_2Ti_3Si_3O_{24}$
$Fe_8(Zr,Y)_2Ti_3Si_3O_{24}$

Sys. rhombohedral (cubic)	$a = 9.486(10)$ Å	source: Sea of Tranquillity, Moon
S.G.	$(a = 4.85(3)$ Å)	Ref.: Gatehouse et al. (1977)
$Z = 2$	$\alpha = 88.57(6)°$	JCPDS: #26-1143
$Dx = 4.83$ g/cm^3		

Tranquillityite is from the Sea of Tranquillity on the moon (Lovering et al. 1971). The chemical formula suggests an interesting substitution between zirconium and yttrium. The crystal structure is unknown. Gatehouse et al. (1977) found that tranquillityite has a fluorite-related structure from their single crystal work using reconstituted samples in both air and vacuum, and that the structure is related to the structure of a MnZrTi-silicate synthetic phase.

TRIMOUNSITE-(Y)
$Y_2Ti_2SiO_9$
$Y_2Ti_2SiO_9$

Sys. monoclinic	$a = 12.299(2)$ Å	source: Trimouns, Ariège, France
S.G. $P2_1/c$	$b = 11.120(2)$ Å	Ref.: Piret et al. (1990)
$Z = 4$	$c = 4.858(1)$ Å	
$Dx = 4.85$ g/cm^3	$\beta = 95.62(1)°$	
$Dm = 5.0$ g/cm^3		

Trimounsite-(Y) is a new rare earth silicotitanate mineral described by Piret et al. (1990). They reported that it is nesosilicate, $Y_2Ti_2(O_5/SiO_4)$, and that the crystal structure is not really similar to that of any known mineral. They also reported that the yttrium atom is surrounded by seven oxygen atoms and the Ti octahedra form a $(Ti_2O_6)_n$ double chain. They mentioned that the detailed description of the crystal structure will appear elsewhere.

2.4. *Class 4: structures with octahedral anionic groups – complex oxides containing octahedrally coordinated titanium, niobium, tantalum*

The crystal structures of the minerals belonging to this group consist of columns, sheets or three-dimensional frameworks of octahedra of Tb, Nb, Ta, and so on.

FERGUSONITE-β-(Y)
$YNbO_4$
$YNbO_4$

Sys. monoclinic	$a = 5.243$ Å	source: synthetic $YbNbO_4$
S.G. I2/a	$b = 10.841$ Å	Ref.: Kinzhibalo et al. (1982)
$Z = 4$	$c = 5.046$ Å	JCPDS: #23-1486
	$\beta = 94.50°$	
AP: table 166	ID: table 167	IL: fig. 75

FERGUSONITE-β-(Ce) (=brocenite)
$CeNbO_4$
$CeNbO_4$

Sys. monoclinic	$a = 5.569$ Å	source: synthetic $LaNbO_4$
S.G. I2/a	$b = 11.529$ Å	Ref.: Kinzhibalo et al. (1982)
$Z = 4$	$c = 5.206$ Å	JCPDS: #33-0332, #29-0402
	$\beta = 94.00°$	
AP: table 168	ID: table 169	

TABLE 166
Atomic parameters of fergusonite-β-(Y)[a].

	x	y	z
Yb	0.25	0.62170(1)	0
Nb	0.25	0.14315(4)	0
O1	0.08920(50)	0.46130(20)	0.24960(50)
O2	−0.00190(50)	0.71880(20)	0.28750(50)

[a] MoKα, $R = 0.030$, $R_w = 0.038$ (831 refl.).

TABLE 167
Interatomic distances for fergusonite-β-(Y) in Å.

Yb–O1	2.282(3) ×2	Nb–O1	1.850(3) ×2
Yb–O2	2.293(3) ×2	Nb–O2	1.932(3) ×2
Yb–O1	2.342(3) ×2	Nb–O2	2.396(4) ×2
Yb–O2	2.379(3) ×2	mean	2.059(3)
mean	2.324(3)		

TABLE 168
Atomic parameters of fergusonite-β-(Ce)[a].

	x	y	z
La	0.25	0.62083(3)	0
Nb	0.25	0.14160(0)	0
O1	0.10090(70)	0.45370(30)	0.26090(80)
O2	−0.01270(70)	0.71810(40)	0.30150(80)

[a] MoKα, $R = 0.042$, $R_w = 0.056$ (789 refl.).

TABLE 169
Interatomic distances for fergusonite-β-(Ce) in Å.

La–O1	2.454(7) ×2	Nb–O1	1.848(7) ×2
La–O2	2.488(7) ×2	Nb–O2	1.923(7) ×2
La–O1	2.531(6) ×2	Nb–O2	2.523(7) ×2
La–O2	2.538(7) ×2	mean	2.098(7)
mean	2.503(6)		

FERGUSONITE-β-(Nd)
$NdNbO_4$
$NdNbO_4$

Sys. monoclinic	$a = 5.4753(19)$ Å	source: synthetic $NdNbO_4$
S.G. I2/c	$b = 11.2905(48)$ Å	Ref.: Tsunekawa and Takei (1978)
$Z = 4$	$c = 5.1493(32)$ Å	JCPDS: #35-0703
	$\beta = 94.578(35)°$	
AP: table 170	ID: table 171	

FERGUSONITE-(Y)
$YNbO_4$
$YNbO_4$

Sys. tetragonal	$a = 5.16$ Å	source: Central Urals, Russia
S.G. $I4_1/a$	$c = 10.89$ Å	Ref.: Komkov (1959)
$Z = 4$		JCPDS: #9-0443
AP: table 172	ID: table 173	IL: fig. 76

fergusonite-(Ce)
$CeNbO_4$
$CeNbO_4$

Sys. tetragonal	$a = 5.17$ Å	source: Novopoltavsk, CIS
S.G.	$c = 5.30$ Å	Ref.: Kapustin (1986)
$Z =$		
$Dm = 5.48$ g/cm^3		

TABLE 170
Atomic parameters of fergusonite-β-(Nd)[a].

	x	y	z
Nd	0	0.6293(1)	1/4
Nb	0	0.1039(1)	1/4
O1	0.2398(15)	0.0323(7)	0.0446(16)
O2	0.1515(15)	0.2068(7)	0.4906(16)

[a] MoKα, $R = 0.0342$ (458 refl.).

TABLE 171
Interatomic distances for fergusonite-β-(Nd) in Å.

Nd–O2	2.405(8) ×2	Nb–O2	1.847(8) ×2
Nd–O1	2.424(9) ×2	Nb–O1	1.928(9) ×2
Nd–O2	2.464(8) ×2	mean	1.888
Nd–O1	2.498(8) ×2		
mean	2.448		

TABLE 172
Atomic parameters of fergusonite-(Y)[a].

	x	y	z
Y,Yb[b]	0	0	1/2
Nb	0	0	0
O	0.185 ± 0.01	0.25 ± 0.01	0.092

[a]Mo, (19 0*kl*, 15 *hk*0 refl.).
[b]$0.85Y + 0.15Yb$.

TABLE 173
Interatomic distances for fergusonite-(Y) in Å.

Y–O	2.30 ×4	Nb–O	1.89 ×4
Y–O	2.34 ×4	Nb–O	[2.35 ×4][b]
mean	2.32	mean	2.12

[a][ ]: recalculated by RM.

fergusonite-(Nd)
$NdNbO_4$
$NdNbO_4$

Sys. tegragonal — $a =$ — source: Baiyun Obo, Inner Mongolia, China
S.G. — $c =$
$Z =$ — Ref.: Zhang and Tao (1987)

FORMANITE-(Y)
$YTaO_4$
$YTaO_4$

Sys. tetragonal — $a = 7.75$ Å — source: synthetic $YTaO_4$
S.G. P4/m, $P4_2/m$, P4/n or $P4_2/n$ — $c = 11.41$ Å — Ref.: Palache et al. (1944)
JCPDS: #26-1478
$Z =$
$Dx = 7.03$ g/cm^3

FORMANITE-(Y) (?)
$YTaO_4$
$YTaO_4$

Sys. monoclinic — $a = 5.292$ Å — source: synthetic $YTaO_4$
S.G. P2/a — $b = 5.451$ Å — Ref.: Wolten (1967)
$Z = 2$ — $c = 5.110$ Å — JCPDS: #26-1478
$\beta = 96.44°$
AP: table 174 — ID: table 175 — IL: fig. 77

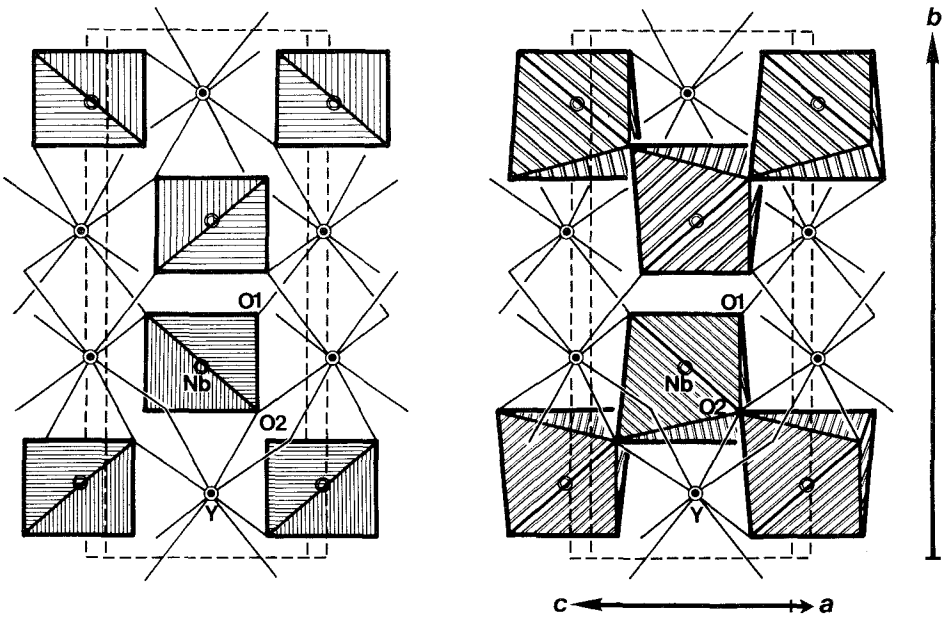

Fig. 75. The crystal structure of fergusonite-β-(Y). The coordination polyhedra of Nb atoms are drawn as tetrahedra (left) and octahedra (right), respectively.

Two phases, a high-temperature (fergusonite-(Y)) T-phase with tetragonal symmetry and a low temperature M-phase (fergusonite-β-(Y)) with monoclinic symmetry, are known for fergusonite. Komkov (1959) determined the crystal structures of both phases. Later, the crystal structure of the M-phase was refined independently by Weitzel and Schröcke (1980) and by Trunov et al. (1981). Their unit cells were different from those of Kinzhibalo et al. (1982): $a = 7.037$, $b = 10.945$, $c = 5.298$ Å, $\beta = 134.07°$ (Trunov et al. 1981).

Kinzhibalo et al. (1982) did a series of crystal structure analyses of synthetic fergusonite-β, $LaNbO_4$, $SmNbO_4$, $GdNbO_4$, $HoNbO_4$ and $YbNbO_4$. The crystal structure of fergusonite-β consists of zigzag chains of distorted Nb octahedra running parallel to the c-axis (fig. 75 right). The chains are connected by eight-coordinated Y polyhedra. Another expression of the crystal structure of fergusonite-β with tetrahedral Nb-coordinations (fig. 75 left) shows a close relationship to that of scheelite, $CaWO_4$, and its structure can be regarded as a distorted form of the scheelite-type structure. Kinzhibalo et al. (1982) suggested that the coordination number of Nb atoms should be considered as six, after consideration of valence forces. They reported that not only the mean R–O distances in RO_8 dodecahedra, but also the mean Nb–O distances in NbO_6 octahedra increase with an increase in the ionic radii of the rare earth ions, although the shortest four Nb–O distances practically do not change. The breakdown of the bonds between Nb and the outermost O atoms causes a destruction of the infinite chain of NbO_6 octahedra, resulting in a tetragonal structure of the scheelite type. They found that the transition energy between the monoclinic β-phase and the tetragonal phase (scheelite-type structure) depends on the lengths

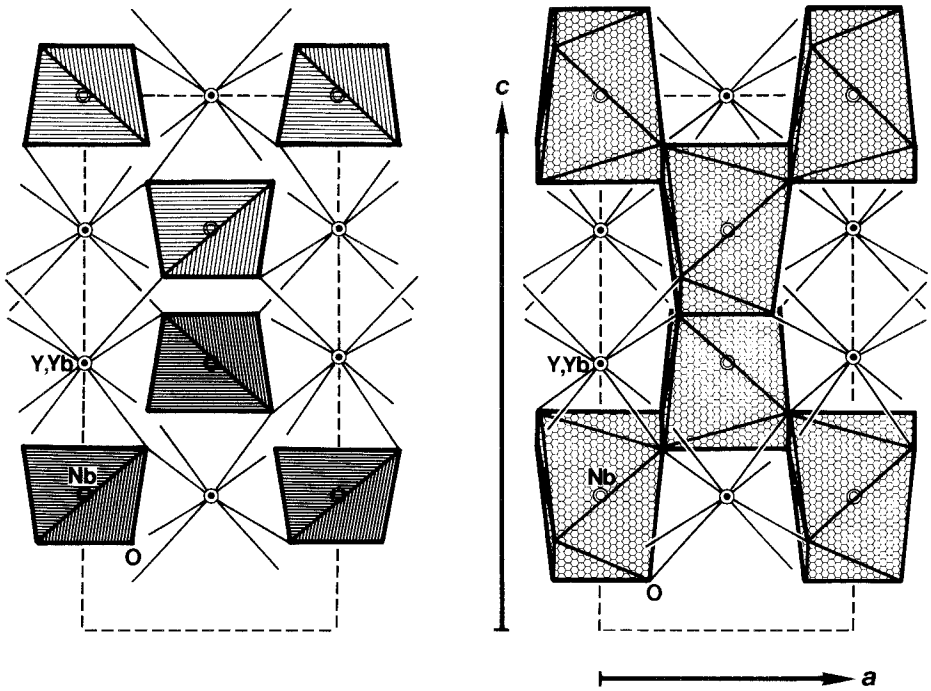

Fig. 76. The crystal structure of fergusonite-(Y). The coordination polyhedra of Nb atoms are drawn as tetrahedra (left) and eight-coordinated polyhedra (right), respectively.

of the fifth and sixth Nb–O distances, i.e., the transition energy depends on the ionic radii of the rare earth ions.

Tsunekawa and Takei (1978) reported the crystal structures of synthetic $LaNbO_4$ and $NdNbO_4$. They also clarified a new kind of twinning structure, i.e. a rotation about the *b*-axis normal to the (010) plane of shear.

Although the structural features of fergusonite-(Y) (T-phase) (fig. 76) are basically identical with those of fergusonite-β (M-phase), the arrangement of atoms in fergusonite-(Y) is more symmetrical than in fergusonite-β. Komkov (1959) reported that fergusonite-(Y) is isostructural with the scheelite group of minerals, and may be considered as a representative of the group. He also suggested that fergusonite-(Y) is a salt of the acid H_3NbO_4, and not a complex oxide. The coordination numbers of the Y and Nb sites were reported as 8 and 4, respectively, by Komkov (1959) (fig. 76 left). However, the four next-nearest oxygen atoms are located at a distance of 2.35 Å from the Nb site, and these oxygen atoms may be included in the coordination of the Nb atoms (fig. 76 right).

Formanite-(Y) is a Ta-analogue of fergusonite-(Y) (T-phase). The crystal structure has not been reported yet, but it is very likely that it is isostructural with fergusonite-(Y). On the other hand, Wolten (1967, 1968) reported the crystal structure of $YTaO_4$ as fergusonite-M′, the third fergusonite polymorph (fig. 77). He found the M′-phase for $YTaO_4$ and the tantalates of lanthanides from Sm through Yb during the course of his synthetic study. The structure of the M′-modification of fergusonite is similar to that of wolframite, $(Fe,Mn)WO_4$ (Weitzel and Schröcke 1980).

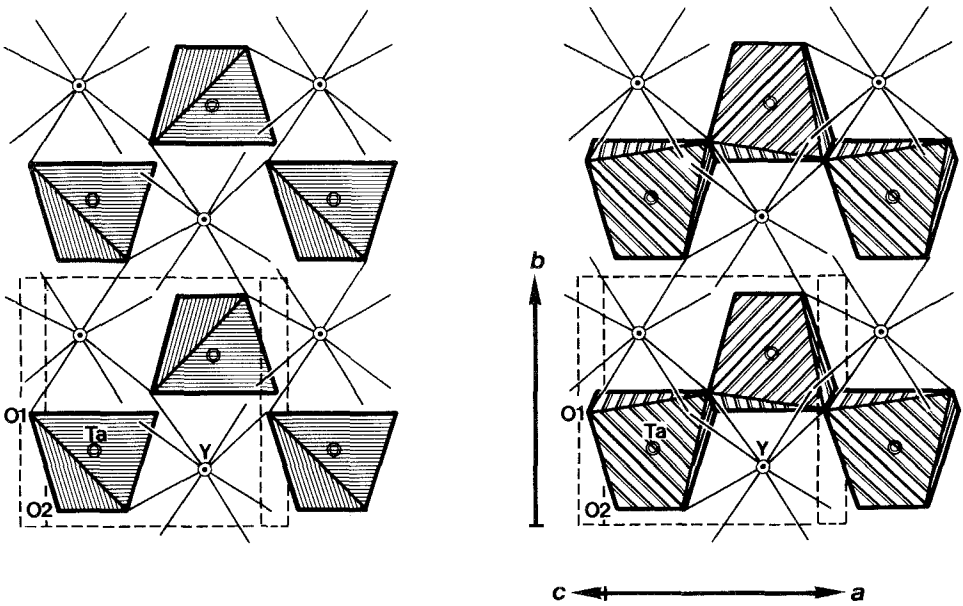

Fig. 77. The crystal structure of $YTaO_4$.

TABLE 174
Atomic parameters of formanite-(Y) (?), $YTaO_4$[a].

	x	y	z	B (Å^2)
Y	1/4	0.7694(6)	0	
Ta	1/4	0.3056(3)	1/2	
O1	0.490(6)	0.462(4)	0.226(4)	0.59(30)
O2	0.081(12)	0.069(8)	0.258(7)	3.12(75)

[a] AgKα, $R = 0.149$ (729 refl.).

TABLE 175
Interatomic distances for formanite-(Y) (?), $YTaO_4$, in Å.

Y–O2	2.25 ×2	Ta–O2	1.94 ×2
Y–O2	2.34 ×2	Ta–O1	2.03 ×2
Y–O1	2.40 ×2	Ta–O1	[2.14 ×2][a]
Y–O1	2.42 ×2	mean	2.04
mean	2.35		

[a] [ ]: recalculated by RM.

LUCASITE-(Ce)
$CeTi_2(O,OH)_6$
$CeTi_2(O,OH)_6$

Sys. monoclinic	$a = 5.178(1)$ Å	source: Argyle Akl, Kimberley, Australia
S.G. I2/a	$b = 8.756(4)$ Å	Ref.: Nickel et al. (1987)
$Z = 4$	$c = 9.768(5)$ Å	JCPDS: #40-1455
$Dx = 5.00$ g/cm^3	$\beta = 93.52(4)°$	
AP: table 176	ID: table 177	IL: fig. 78

The crystal structure of lucasite-(Ce) (fig. 78) is related to the $PbSb_2O_6$-type, with ordering of Ce and Ti atoms in alternate {001} cation layers in a hexagonal closest-packed anion arrangement (Nickel et al. 1987). The $TiO_4(OH)_2$ octahedra share edges forming gibbsite-like fused hexagonal rings. The Ce atoms are sandwiched between pairs of hexagonal rings and are in eight-fold coordination. Although the chemical formula of lucasite-(Ce) is related to that of aeschynite-(Ce), their structures are quite different.

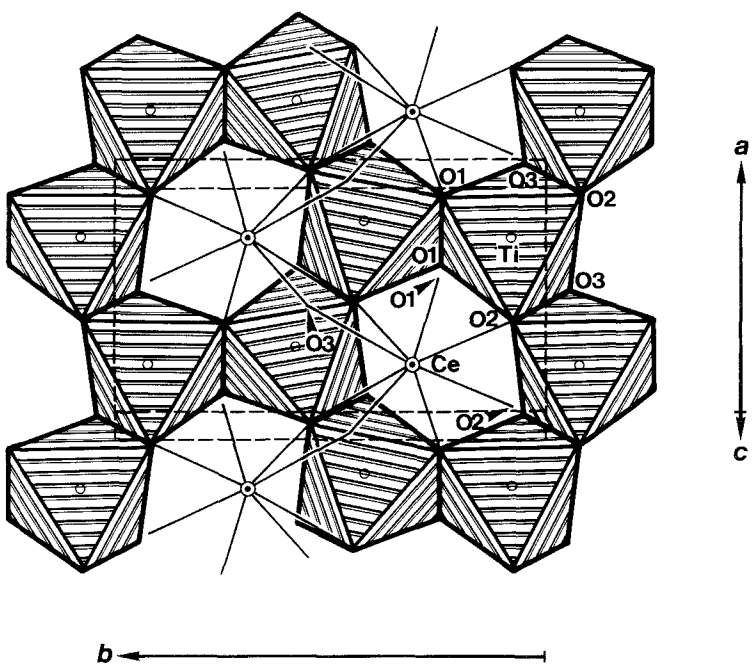

Fig. 78. The crystal structure of lucasite-(Ce).

TABLE 176
Atomic parameters of lucasite-(Ce)[a].

	x	y	z
Ce	1/4	0.1894(1)	0
Ti	0.2187(3)	0.9154(2)	0.2651(2)
O1	0.6007(13)	0.2541(8)	0.1411(7)
O2	0.4083(13)	0.0799(8)	0.3692(8)
O3	0.9976(13)	0.0450(8)	0.1402(7)

[a] MoKα, $R = 0.054$ (977 refl.).

TABLE 177
Interatomic distances for lucasite-(Ce) in Å.

Ce–O1	2.283(7) ×2	Ti–O1	1.898(7)
Ce–O3	2.324(7) ×2	Ti–O2	1.954(7)
Ce–O2	2.552(7) ×2	Ti–O3	1.977(7)
Ce–O3	2.741(7) ×2	Ti–O3	1.979(7)
mean	2.475	Ti–O2	1.987(7)
		Ti–O1	1.988(7)
		mean	1.964

TABLE 178
Atomic parameters of euxenite-(Y)[a].

	x	y	z	B (Å²)
Y	0	0.2447(7)	0.25	1.05(6)
Nb,Ti	0.1628(6)	0.2965(13)	0.8186(16)	−0.33(18)
O1	0.0963(2)	0.4425(5)	0.5365(4)	0.42(7)
O2	0.0849(2)	0.0842(5)	0.9193(5)	0.09(7)
O3	0.2596(2)	0.1437(5)	0.6474(5)	0.34(6)

[a] Neutron ($\lambda = 1.069$ Å) (powder data), $R = 0.033$, $R_p = 0.083$.

TABLE 179
Interatomic distances for euxenite-(Y) in Å.

Y–O2	2.300 ×2	Nb,Ti–O2	1.722
Y–O1	2.326 ×2	Nb,Ti–O3	1.876
Y–O2	2.378 ×2	Nb,Ti–O1	1.973
Y–O1	2.497 ×2	Nb,Ti–O3	2.078
mean	2.375	Nb,Ti–O1	2.081
		Nb,Ti–O3	2.408
		mean	2.023

EUXENITE-(Y)
$(Y,Ca,U,Th)(Nb,Ti)_2O_6$
$(Y,Ca,U,Th)(Nb,Ti)_2O_6$

Sys. orthorhombic	$a = 14.6432(20)$ Å	source: synthetic $YNbTiO_6$
S.G. Pbcn	$b = 5.5528(6)$ Å	Ref.: Weitzel and Schröcke (1980)
$Z = 4$	$c = 5.1953(7)$ Å	JCPDS: #14-0643, #9-0442, #5-0603
AP: table 178	ID: table 179	IL: fig. 79

TANTEUXENITE-(Y) (= delorenzite)
$(Y,Ca)(Ta,Nb,Ti)_2[O,(OH)]_6$
$(Y,Ca)(Ta,Nb,Ti)_2[O,(OH)]_6$

Sys. orthorhombic	$a = 14.57$ Å	source: Pilbara, Australia
S.G. Pbcn	$b = 5.56$ Å	Ref.: Strunz (1978); Hölzel (1989);
$Z = 4$	$c = 5.18$ Å	Nickel and Nichols (1991)
$Dm = 5.68$ g/cm^3		JCPDS: #31-1434

FERSMITE
$(Ca,R,Na)(Nb,Ta,Ti)_2[O,(OH),F]_6$
$(Ca,R,Na)(Nb,Ta,Ti)_2[O,(OH),F]_6$

Sys. orthorhombic	$a = 14.926 \pm 0.004$ Å	source: synthetic $CaNb_2O_6$
S.G. Pbcn	$b = 5.752 \pm 0.004$ Å	Ref.: Cummings and Simonsen (1970)
$Z = 4$	$c = 5.204 \pm 0.004$ Å	JCPDS: #39-1392
$Dx = 4.78$ g/cm^3		The unit cell the latter used was different:
$Dm = 4.70$ g/cm^3		
AP: table 180	ID: table 181	IL: fig. 80

POLYCRASE-(Y)
$(Y,Ca,U,Th)(Ti,Nb,Ta)_2O_6$
$(Y,Ca,U,Th)(Ti,Nb,Ta)_2O_6$

Sys. orthorhombic	$a = 5.54$ Å	source: Boise, ID; Llano, TX, USA, etc.
S.G. Pcan (?)	$b = 14.59$ Å	Ref.: Roberts et al. (1974)
$Z = 4$ (?)	$c = 5.18$ Å	
$Dm = 4.30$–5.87 g/cm^3		

TABLE 180
Atomic parameters of fersmite[a].

	x	y	z	B
Ca	0	0.2244(6)	0.75	
Nb	0.1653(1)	0.3166(2)	0.2987(2)	
O1	0.0893(6)	0.0997(14)	0.4040(18)	1.4988
O2	0.1003(6)	0.4280(14)	0.0056(18)	1.8431
O3	0.2576(6)	0.1351(14)	0.1266(17)	0.4638

[a] MoKα, $R = 0.067$ (618 refl.).

TABLE 181
Interatomic distances for fersmite in Å.

Ca–O2	2.319(9) ×2	Nb–O1	1.774(9)
Ca–O2	2.322(9) ×2	Nb–O2	1.919(9)
Ca–O1	2.353(9) ×2	Nb–O3	1.947(9)
Ca–O1	2.427(8) ×2	Nb–O2	2.065(9)
mean	2.355	Nb–O3	2.077(9)
		Nb–O3	2.342(8)
		mean	2.021

yttrocrasite-(Y)
$(Y,Th,Ca,U)(Ti,Fe)_2[O,(OH)]_6$
$(Y,Th,Ca,U)(Ti,Fe)_2[O,(OH)]_6$

Sys. orthorhombic	$a=$	source: Burnet Co., TX, USA
S.G.	$b=$	Ref.: Crook (1976);
$Z=$	$c=$	Nickel and Nichols (1991)
$Dm = 4.80$ g/cm^3		

yttrocolumbite
$(Fe,Mn,Y)(Nb,Ta)_2O_6$
$(Fe,Mn,Y)(Nb,Ta)_2O_6$

Sys. orthorhombic	$a=$	source: Mozambique
S.G.	$b=$	Ref.: Lepierre (1937);
$Z=$	$c=$	Nickel and Nichols (1991)

YTTROTANTALITE-(Y)
$(Y,U,Ca)(Ta,Nb,Fe)_2[O,(OH)]_6$
$(Y,U,Ca)(Ta,Nb,Fe)_2[O,(OH)]_6$

Sys. orthorhombic	$a:b:c = 2.695:1:0.929$	source:
S.G.	$= 14.82:5.5:5.11$	Ref.: Strunz (1978)
$Z=$		

loranskite-(Y)
$(Y,Ca)ZrTaO_6$ (?)
$(Y,Ca)ZrTaO_6$ (?)

Sys.	$a=$	source: Impilahti, Erajarvi, Finland
S.G.	$b=$	Ref.: Nikolaeeff (1897)
$Z=$	$c=$	

Ewing (1976) reported a numerical approach to the classification of complex orthorhombic rare earth, AB_2O_6-type Nb–Ta–Ti oxides, based on published chemical data. He concluded that these minerals can be chemically classified in the following three groups: "aeschynite, $Ce(Nb,Ti)_2O_6$", "euxenite, $Y(Nb,Ti)_2O_6$" and "polycrase,

$Y(Ti,Nb)_2O_6$". However, as he mentioned, the classification cannot be used directly to ascertain the chemical and structural relations of the members, because it was derived from a statistical analysis of published data in the absence of structural or morphological data. The minerals cited above usually occur in the metamict state, and the crystallographic data of these minerals are often ambiguous.

The crystal structure of euxenite-(Y) was determined by Weitzel and Schröcke (1980) using a synthesized crystal of $Y(Nb,Ti)_2O_6$. The structure (fig. 79) is identical to the columbite, $(Fe,Mn)Nb_2O_6$, structure (Bordet et al. 1986), if the degree of distortion of the coordination polyhedra is neglected. The basic unit of the structure is a chain of (Nb,Ti) octahedra which are connected to each other along the shortest edges. These chains are oriented along the *c*-axis. Adjacent chains are connected to each other by the vertices of the octahedra in "two-layered parcels" which are perpendicular to the *b*-axis. The chains of each "layer" are not directly connected to each other, but only through the chains of adjacent "layers". The "two-layered parcels" of niobium octahedra are connected to each other by Y atoms. The Y atoms is in eight-fold coordination with a distorted cubic shape. The Y polyhedra share two O atoms. They are connected to some of the (Nb,Ti) octahedra by edges, and to others by vertices.

Aleksandrov (1960) determined the crystal structure of fersmite using an annealed natural sample which had been partially metamict. The structure (fig. 80) is isostructural with that of euxenite-(Y) (fig. 79). Aleksandrov (1960) assumes that the O1 atoms are partially replaced by (OH) ions, based on the consideration of interatomic distances and charge balance.

Cummings and Simonsen (1970) refined the structure using a synthetic crystal of $CaNb_2O_6$. The mean Ca–O distance, 2.355 Å for rare earth free synthetic fersmite,

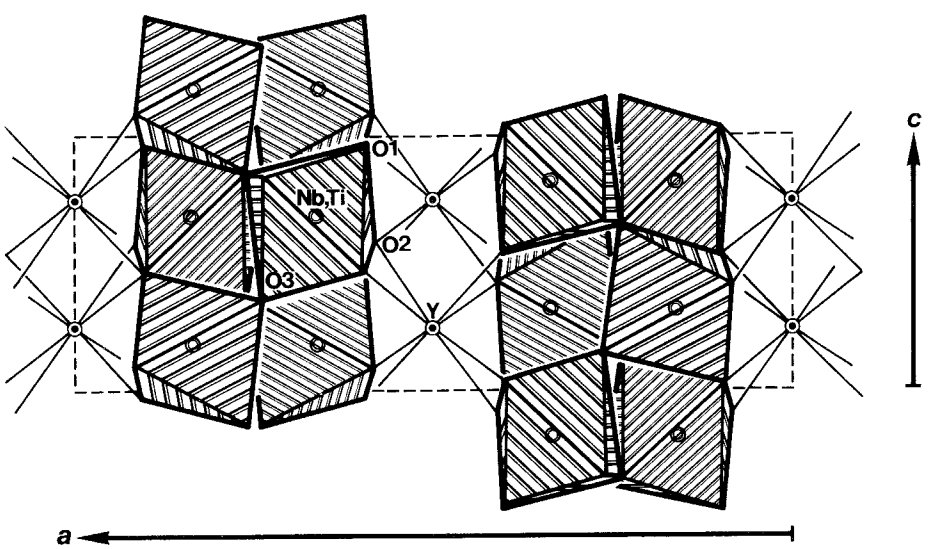

Fig. 79. The crystal structure of euxenite-(Y).

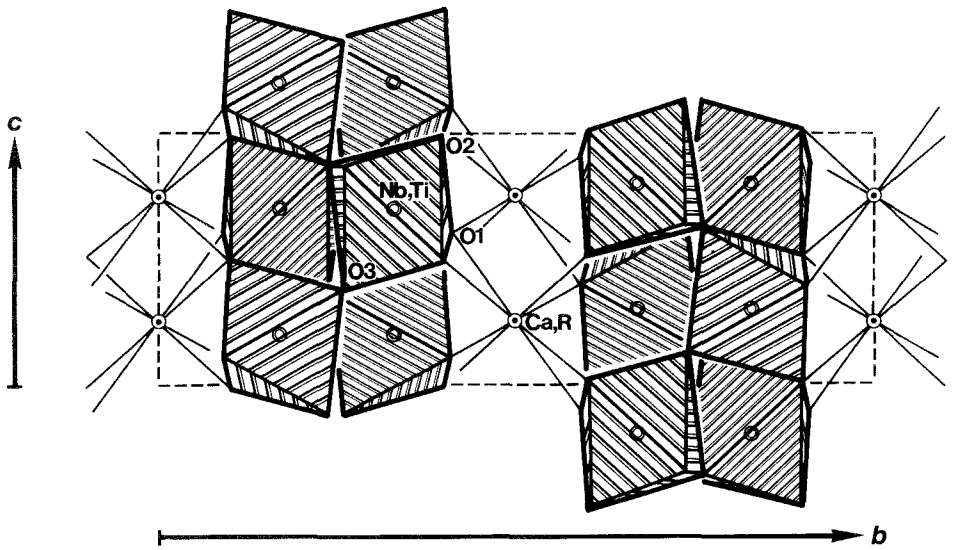

Fig. 80. The crystal structure of fersmite.

is considerably shorter than the mean Ca,R–O distance, 2.48 Å, of natural fersmite reported by Aleksandrov (1960).

The crystal structure of tantalite, $(Fe,Mn)Ta_2O_6$, (Grice et al. 1976) is isostructural with that of columbite, $(Fe,Mn)Nb_2O_6$, which is α-type. Yttrocolumbite-(Y) and yttrotantalite-(Y) may be Y-analogues of columbite and tantalite, respectively. The crystallographic data for yttrotantalite-(Y) and polycrase are close to those for euxenite-(Y).

Loranskite-(Y) is an inadequately described mineral. Roberts et al. (1974) suggested that the mineral may be a variety of euxenite-(Y).

SAMARSKITE-(Y) (=ampangabeite, nuevite)
$(Y,U,Ca,Pb)Fe_2(Nb,Ta,Ti,Sn)_5O_{16}$
$(Y,U,Ca,Pb)Fe_2(Nb,Ta,Ti,Sn)_5O_{16}$

Sys. monoclinic	$a =$ 5.66(1) Å	source: Mitchell, NC, USA
S.G.	$b =$ 4.910(6) Å	Ref.: Akimoto et al. (1986)
$Z =$	$c =$ 5.19(1) Å	JCPDS: #39-0361, #2-0717
	$\beta = 90.4(2)°$	

Samarskite-(Y) is a complex oxide of rare earths, uranium, calcium, niobium, tantalum and other elements; it always occurs in the metamict state. This characteristic has been an obstruction to the study of the chemistry and crystal structure of this mineral. Although many chemical formulae and crystallographic data for samarskite-(Y) have been proposed, no complete chemical or structural understanding of samarskite-(Y) has been achieved.

Sugitani et al. (1984) reported that recrystallization of natural samples by annealing

in a reducing atmosphere produced a low-temperature phase and a high-temperature phase. The cell dimensions of these phases are consistent with the axial ratio of the natural sample determined from morphological measurements (Palache et al. 1944). They also synthesized compounds having X-ray powder diffraction patterns similar to those of the phases recrystallized in a reducing atmosphere, and gave as ideal formula $YFe_2Nb_5O_{16}$, after the chemical analysis of the synthetic sample (Sugitani et al. 1985). Furthermore, Akimoto et al. (1986) revealed that the phases reported by Sugitani et al. (1984) can be obtained by annealing the natural samples both in a reducing atmosphere and in air under limited temperature conditions; otherwise the mineral decomposes into several phases.

Nakai et al. (1987) revealed that the local structure around Nb in metamict samarskite-(Y) is similar to that in euxenite-(Y), based on the result of Nb K-edge EXAFS and XANES analyses.

---

ishikawaite
$(U,Fe,Y,Ca)(Nb,Ta)O_4$
$(U,Fe,Y,Ca)(Nb,Ta)O_4$

Sys. orthorhombic	$a =$	source: Ishikawa, Iwaki, Japan
S.G.	$b =$	Ref.: Kimura (1922)
$Z =$	$c =$	

Ishikawaite was originally described by Kimura (1922). The mineral differs from samarskite in composition: it contains more UO_2 and less rare earths than samarskite-(Y) Ohashi (1924) suggested crystallographic similarity between ishikawaite, samarskite and yttrotantalite. Makarochkin (1972) described ishikawaite from the CIS. The chemical composition of this material is found to be close to $(U,La)(Fe,Al)_2(Nb,Ti)_5O_{16}$. The same relation can be found in the original analysis too, affording the room of creation of ishikawaite as a discrete species from samarskite-(Y) as its U-dominant member. Detailed compositional and structural data are lacking for this mineral.

AESCHYNITE-(Ce)
$(Ce,Ca,Fe,Th)(Ti,Nb)_2[O,(OH)]_6$
$(Ce,Ca,Fe,Th)(Ti,Nb)_2[O,(OH)]_6$

Sys. orthorhombic	$a =$ 7.538 Å	source: synthetic $CeTiNbO_6$
S.G. Pmnb	$b =$ 10.958 Å	Ref.: JCPDS #15-0864
$Z =$ 4	$c =$ 5.396 Å	JCPDS: #15-0864
$Dx = 5.617$ g/cm^3		

AESCHYNITE-(Y) (= blomstrandine, priorite, taiyite)
$(Y,Ca,Fe,Th)(Ti,Nb)_2[O,(OH)]_6$
$(Y,Ca,Fe,Th)(Ti,Nb)_2[O,(OH)]_6$

Sys. orthorhombic	$a = 5.37 \pm 0.01$ Å	source:
S.G. Pbnm	$b = 11.08 \pm 0.02$ Å	Ref.: Aleksandrov (1962)
$Z =$ 4	$c = 7.56 \pm 0.02$ Å	JCPDS: #20-1401
$Dm = 4.96 \pm 0.05$ g/cm^3		
AP: table 182	ID: table 183	IL: fig. 81

TABLE 182
Atomic parameters of aeschynite-(Y)[a].

	x	y	z
Y	0.042	0.458	0.25
Nb,Ti	0.040	0.144	0.008
O1	0.378	0.210	0.567
O2	0.264	0.477	0.538
O3	0.167	0.105	0.25
O4	0.375	0.355	0.25

[a] Mo, $R_{hk0} = 0.125$ (74 refl.), $R_{0kl} = 0.165$ (56 refl.).

TABLE 183
Interatomic distances for aeschynite-(Y) in Å.

Y–O4	2.12	Nb,Ti–O1	1.90
Y–O3	2.24	Nb,Ti–O3	1.99
Y–O2	2.43 ×2	Nb,Ti–O2	2.00
Y–O2	2.44 ×2	Nb,Ti–O1	2.02
Y–O1	2.46 ×2	Nb,Ti–O2	2.13
mean	2.38	Nb,Ti–O4	2.14
		mean	2.03

aeschynite-(Nd)
$(Nd,Ca)(Ti,Nb)_2[O,(OH)]_6$
$(Nd,Ca)(Ti,Nb)_2[O,(OH)]_6$

Sys. metamict	$a =$	source: Baiyun Obo, Inner Mongolia, China
S.G.	$b =$	Ref.: Zhang and Tao (1982)
$Z =$	$c =$	JCPDS: #38-0480
Dx = 4.60–5.04 g/cm^3		

NIOBO-AESCHYNITE-(Ce)
$(Ce,Ca,Th)(Nb,Ti)_2[O,(OH)]_6$
$(Ce,Ca,Th)(Nb,Ti)_2[O,(OH)]_6$

Sys. orthorhombic	$a =$ 5.396(1) Å	source: Tofty, AK, USA
S.G. Pbnm	$b =$ 11.085(2) Å	Ref.: Rosenblum and Mosier (1975)
$Z =$ 4	$c =$ 7.585(3) Å	JCPDS: #29-0311
Dm = 5.04 g/cm^3		

niobo-aeschynite-(Nd)
$Nd(Nb,Ti)_2[O,(OH)]_6$
$Nd(Nb,Ti)_2[O,(OH)]_6$

Sys. orthorhombic	$a =$	source:
S.G.	$b =$	Ref.: Fleischer and Mandarino (1991)
$Z =$	$c =$	

TANTALAESCHYNITE-(Y)
$(Y,Ca,Th)(Ta,Nb,Ti)_2O_6$
$(Y,Ca,Th)(Ta,Nb,Ti)_2O_6$

Sys. orthorhombic	$a = 5.34(2)$ Å	source: Raposa, São José do Sabugí, Paraíba, Brazil
S.G.	$b = 10.97(2)$ Å	
$Z = 4$	$c = 7.38(2)$ Å	Ref.: Adusumilli et al. (1974)
Dx = 6.39 g/cm^3		JCPDS: #26-0001
Dm = 5.75–6.13 g/cm^3		

VIGEZZITE
$(Ca,Ce)(Nb,Ta,Ti)_2O_6$
$(Ca,Ce)(Nb,Ta,Ti)_2O_6$

Sys. orthorhombic	$a = 11.065(2)$ Å	source: Vigezzo Valley, Novara, Italy
S.G. Pnma	$b = 7.527(1)$ Å	Ref.: Giuseppetti and Tadini (1990)
$Z = 4$	$c = 5.343(1)$ Å	JCPDS: #34-1316
AP: table 184	ID: table 185	

TABLE 184
Atomic parameters of vigezzite[a].

	x	y	z	B_{eq}
Ca,Ce	0.4565(1)	1/4	0.0391(1)	0.94(2)
Nb,Ta,Ti	0.3587(0)	0.5061(0)	0.5382(0)	0.95(1)
O1	0.2875(3)	0.4390(4)	0.8722(6)	1.09(6)
O2	0.5251(3)	0.4583(4)	0.7300(5)	1.02(6)
O3	0.6223(4)	1/4	0.3345(8)	1.07(9)
O4	0.3545(4)	1/4	0.4485(8)	1.05(8)

[a] MoKα, $R = 0.019$ (488 refl.).

TABLE 185
Interatomic distances for vigezzite in Å.

Ca,Ce–O2	2.401 ×2	Nb,Ta,Ti–O1	1.890
Ca,Ce–O3	2.420	Nb,Ta,Ti–O2	1.944
Ca,Ce–O4	2.461	Nb,Ta,Ti–O3	1.969
Ca,Ce–O1	2.513 ×2	Nb,Ta,Ti–O4	1.987
Ca,Ce–O2	2.526 ×2	Nb,Ta,Ti–O1	2.015
mean	2.470	Nb,Ta,Ti–O2	2.138
		mean	1.991

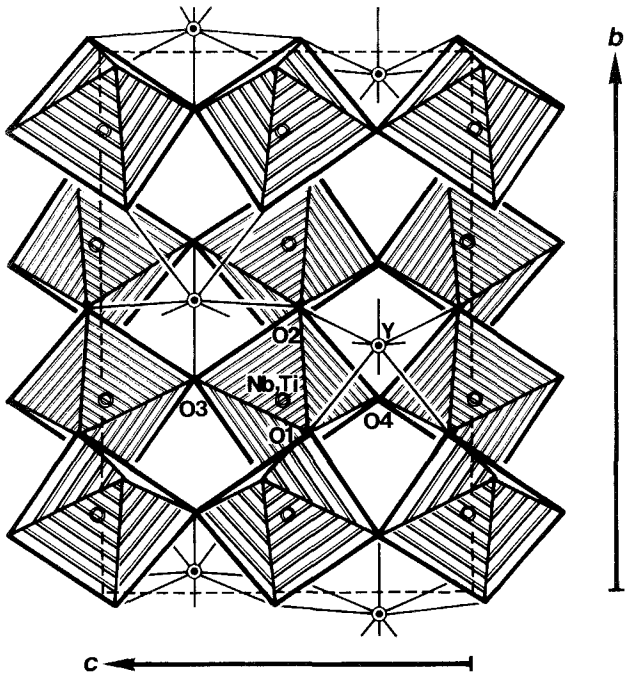

Fig. 81. The crystal structure of aeschynite-(Y).

The structural features of aeschynite-(Y) (Aleksandrov 1962) (fig. 81) are different from those of euxenite-(Y) despite the fact that both minerals can be expressed as AB_2O_6. In the crystal structure, (Nb,Ti) octahedra form a three-dimensional framework by corner sharing and edge sharing linkages; this distinguishes aeschynite-(Y) from the other niobates and titanoniobates of composition AB_2X_6 – columbite, fersmite and euxenite-(Y), in which these octahedra form isolated two-dimensional groups. The rare earth atoms in aeschynite-(Y) are situated in the tunnel-like spaces of the framework parallel to the *c*-axis, and form distorted eight-coordinated square antiprisms.

Niobo-aeschynite-(Ce), -(Nd) and tantalaeschynite-(Y) are the Nb and Ta-analogues, respectively. Vigezzite (Graeser et al. 1979) is a Ca-dominant species of niobo-aeschynite-(Ce) or -(Nd).

Giuseppetti and Tadini (1990) determined the crystal structure of non-metamict vigezzite. Vigezzite is isostructural with aeschynite-(Y) (Aleksandrov 1962). In the puckered pseudo-hexagonal packing of oxygens the (Nb,Ta,Ti) cations occupy all the octahedral sites. The octahedra form chains parallel to the *b*-axis, and the chains are connected along the *a*-axis by the shared edges with the shortest O–O distance. Zigzag strips of the octahedral double chains are parallel to the *b*-axis. On the other hand, the large (Ca,Ce) cations lie in the tunnel of broad holes of the network centered by the screw diad axes, forming a distorted eight-coordinated polyhedron, which is ideally comparable with the polyhedron C_{2v} or square antiprism.

BRANNERITE (=absite)
$(U,Th,Ca,Y)(Ti,Fe)_2O_6$
$(U,Th,Ca,Y)(Ti,Fe)_2O_6$

Sys.	monoclinic	$a =$ 9.8123(15) Å	source: synthetic UTi_2O_6
S.G.	C2/m	$b =$ 3.7697(6) Å	Ref.: Szymanski and Scott (1982)
$Z =$	2	$c =$ 6.9253(9) Å	JCPDS: #12-0477, #8-0002
Dx =	6.37 g/cm^3	$\beta = 118.957(6)°$	
Dm =	6.35 g/cm^3		
AP:	table 186	ID: table 187	IL: fig. 82

Ruh and Wadsley (1966) determined the crystal structure of an artificial $ThTi_2O_6$ crystal, whose correct mineral name is thorutite, under the name of brannerite. The crystal data are: $ThTi_2O_6$ monoclinic, C2/m, $a = 9.822$, $b = 3.824$, $c = 7.036$ Å, $\beta = 118.84°$. Szymanski and Scott (1982) refined the crystal structure using synthetic brannerite, UTi_2O_6, and found that UTi_2O_6 (brannerite) is isostructural with $ThTi_2O_6$ (thorutite). Figure 82 shows the structure of $ThTi_2O_6$, which contains zigzag sheets of Ti–O octahedra of the anatase, TiO_2, type. The sheets are joined through Th ions in interlayer octahedral positions. There are two Th–O distances of 2.36 Å and four of 2.35 Å, but the octahedron is slightly flattened; two more oxygen atoms at 2.96 Å are probably unbonded, because Pauling's electrostatic bond length criterion precludes bonding between them (Ruh and Wadsley 1966). The corresponding distances for UTi_2O_6 are as follows: two O at 2.252 Å, four O at 2.296 Å, and two further O at 2.824 Å. The rare earth atoms found in the chemical analysis of natural brannerite must occupy the U site because of their relatively large ionic radii.

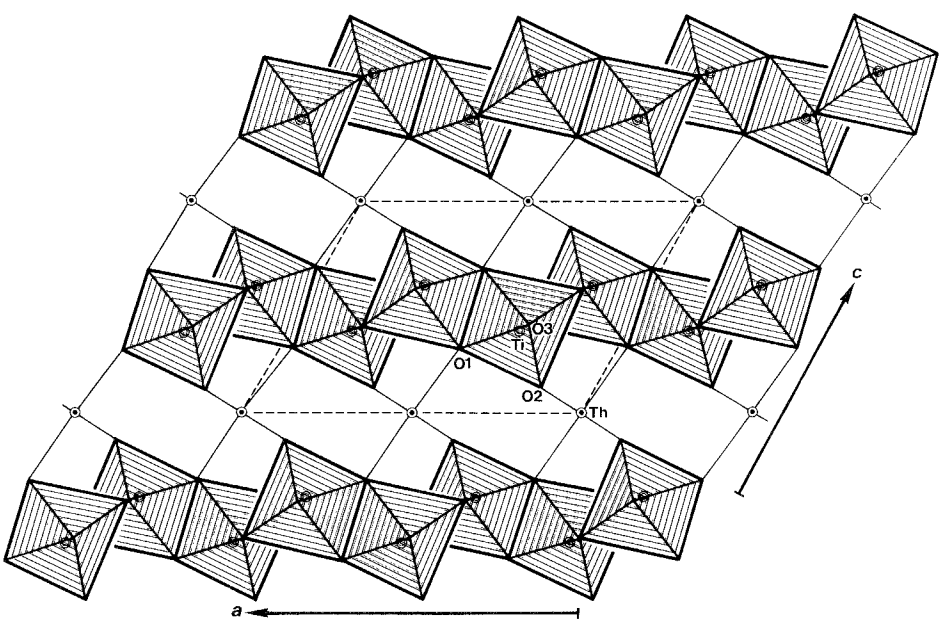

Fig. 82. The crystal structure of synthetic $ThTi_2O_6$, which is isostructural with brannerite, UTi_2O_6.

TABLE 186
Atomic parameters of brannerite[a].

	x	y	z
U	0	0	0
Ti	0.82356(4)	0	0.39107(6)
O1	0.97718(22)	0	0.30828(31)
O2	0.65272(24)	0	0.10530(33)
O3	0.28053(26)	0	0.40531(38)

[a] MoKα, $R = 0.0223$ (1845 refl.).

TABLE 187
Interatomic distances for brannerite in Å.

U–O1	2.252(2) ×2	Ti–O1	1.854(3)
U–O2	2.296(1) ×4	Ti–O2	1.875(2)
mean	2.281	Ti–O3	1.944(1) ×2
		Ti–O1	2.053(2)
		Ti–O3	2.104(3)
		mean	1.962

CERIOPYROCHLORE-(Ce) (=marignacite)
$(Ce,Ca)_2(Nb,Ta)_2O_6(OH,F)$
$(Ce,Ca)_2(Nb,Ta)_2O_6(OH,F)$

Sys. cubic	$a =$	source:
S.G. Fd3m		Ref.: Hogarth (1977)
$Z =$		

YTTROPYROCHLORE-(Y) (=obruchevite)
$(Y,Na,Ca,U)_2(Nb,Ta,Ti)_2O_6(O,OH)$
$(Y,Na,Ca,U)_2(Nb,Ta,Ti)_2O_6(O,OH)$

Sys. cubic	$a = 10.0$–10.34 Å	source: Alakurtt, Karelia, Russia
S.G. Fd3m		Ref.: Kalita (1957)
$Z = 8$		JCPDS: #25-1015, #18-0765

PLUMBOPYROCHLORE
$(Pb,Y,U,Ca)_2Nb_2O_6(OH)$
$(Pb,Y,U,Ca)_2Nb_2O_6(OH)$

Sys. cubic	$a = 10.534 \pm 0.05$ Å	source: Urals, Russia
S.G.		Ref.: Skorobogatova et al. (1966)
$Z = 8$		JCPDS: #25-0453

strontiopyrochlore
$(Sr,R,Ca,Ba,K,Na)_{0.66}(Nb,Fe,Al,Ta)_2(O,OH)_{7.06}$
$(Sr,R,Ca,Ba,K,Na)_{0.66}(Nb,Fe,Al,Ta)_2(O,OH)_{7.06}$

Sys. cubic	$a = 10.53$ Å	source: Yenisei Ridge, Russia
S.G.		Ref.: Lapin et al. (1986)
$Z = 8$		
$Dm = 3.80$ g/cm^3		

URANMICROLITE (=djalmaite)
$(U,Ca,Ce)_2(Ta,Nb)_2O_6(OH,F)$
$(U,Ca,Ce)_2(Ta,Nb)_2O_6(OH,F)$

Sys. cubic	$a = 10.40$ Å	source:
S.G.		Ref.: Strunz (1978)
$Z = 8$		

YTTROBETAFITE-(Y)
$(Y,U)_2(Ti,Nb,Ta)_2O_6(OH)$
$(Y,U)_2(Ti,Nb,Ta)_2O_6(OH)$

Sys. cubic	$a =$	source:
S.G. Fd3m		Ref.: Hogarth (1977)
$Z = 8$		

CALCIOBETAFITE
$(Ca,Na,Ce,Th)_2(Ti,Nb,Ta)_2O_6(O,F)$
$(Ca,Na,Ce,Th)_2(Ti,Nb,Ta)_2O_6(O,F)$

Sys. cubic	$a = 10.2978(5)$ Å	source: Monte di Procida, Campania, Italy
S.G. Fd3m		Ref.: Mazzi and Munno (1983)
$Z = 8$		JCPDS: #13-0197
AP: table 188	ID: table 189	IL: fig. 83

TABLE 188
Atomic parameters of calciobetafite[a].

	x	y	z	B_{eq} (Å^2)
M8[b]	0	0	0	0.77(1)
M6[c]	0.5	0.5	0.5	0.94(1)
O	−0.1771(4)	0.125	0.125	0.87(5)
O,F	0.125	0.125	0.125	1.77(6)

[a] MoKα, $R = 0.019$ (75 refl.).
[b] M8: 0.761(2)(Ca,Na) + 0.239(R,Th,U).
[c] M6: 0.535(6)Ti + 0.465(Nb,Ta).

TABLE 189
Interatomic distances for calciobetafite in Å.

M8–O,F	2.2295 ×2	M6–O	1.969(3) ×6
M8–O	2.577(3) ×6		
mean	2.490		

ZIRCONOLITE-*3O* (=polymignite,polymignyte)*
$(Ca,Fe,Y,Th)_2Fe(Ti,Nb)_3Zr_2O_{14}$
$(Ca,Na,Ce,Th)_2Zr_2(Ti,Nb,Ta)_3(\square,Fe)_4O_{14}$

Sys. orthorhombic	$a = 10.148(4)$ Å	source: Monte di Procida, Campania, Italy
S.G. Acam	$b = 14.147(5)$ Å	Ref.: Mazzi and Munno (1983)
$Z = 4$	$c = 7.278(3)$ Å	JCPDS: #38-0450
AP: table 190	ID: table 191	IL: fig. 84

ZIRCONOLITE-*3T* (=zirkelite)*
$(Ca,Na,Ce)Zr(Ti,Nb,Ta,Fe)_2O_7$
$(Ca,Na,Ce)_2Zr_2(Ti,Nb,Ta)_3(Fe,\square)_2O_{14}$

Sys. trigonal (hex.)	$a = 7.287(2)$ Å	source: Monte di Procida, Campania, Italy
S.G. $P3_121$	$c = 16.886(9)$ Å	Ref.: Mazzi and Munno (1983)
$Z = 3$		
AP: table 192	ID: table 193	IL: fig. 85

TABLE 190
Atomic parameters of zirconolite-*3O*[a].

	x	y	z	B_{eq} (Å^2)
M8[b]	0.75	0.11594(4)	0.25	0.63(1)
M7[c]	0.01505(6)	0.23319(4)	0.5	0.55(1)
M61[d]	0	0	0	0.79(2)
M62[e]	0.25	0.13323(7)	0.25	0.56(2)
M4[f]	0	0	0.4306(6)	1.97(10)
M5[g]	0.039(5)	0.015(2)	0.5	0.3(9)
O1	0.1259(3)	0.0333(3)	0.1903(5)	0.96(7)
O2	0.1197(3)	0.2331(2)	0.2104(5)	0.92(7)
O3	−0.1007(5)	0.1089(4)	0.5	0.97(11)
O4	−0.0904(5)	0.1295(4)	0	0.84(10)
O5	0.1799(5)	0.1396(4)	0.5	0.94(10)

[a] MoKα, $R = 0.025$ (743 refl.).
[b] M8: 0.574(7)(Ca,Na) + 0.426(R,Th).
[c] M7: 1.000Zr.
[d] M61: 0.517(8)Ti + 0.483(Nb,Ta).
[e] M62: 0.878(11)Ti + 0.122(Nb,Ta).
[f] M4: 0.462(6)Fe.
[g] M5: 0.029(4)Fe.

TABLE 191
Interatomic distances for zirconolite-*3O* in Å.

M8–O3	2.370(4)	M7–O4	2.088(5)
M8–O3	2.370(4)	M7–O2	2.108(4)
M8–O4	2.443(4)	M7–O2	2.108(4)
M8–O4	2.443(4)	M7–O3	2.115(5)
M8–O1	2.498(4)	M7–O5	2.133(5)
M8–O1	2.498(4)	M7–O2	2.360(4)
M8–O2	2.529(4)	M7–O2	2.360(4)
M8–O2	2.529(4)	mean	2.182
mean	2.460		
M61–O1	1.942(4)	M62–O1	1.942(4)
M61–O1	1.942(4)	M62–O1	1.942(4)
M61–O1	1.942(4)	M62–O5	1.956(2)
M61–O1	1.942(4)	M62–O5	1.956(2)
M61–O4	2.049(5)	M62–O2	1.956(3)
M61–O4	2.049(5)	M62–O2	1.956(3)
mean	1.978	mean	1.951
M4–O3	1.916(5)	M5–O3	1.86(3)
M4–O3	1.916(5)	M5–O3	1.95(3)
M4–O1	2.217(5)	M5–O5	2.26(4)
M4–O1	2.217(5)	M5–O1	2.43(2)
mean	2.067	M5–O1	2.43(2)
		mean	2.19

ZIRCONOLITE-*2M* (=zirconolite)*
$(Ca,Na,Ce)Zr(Ti,Nb,Ta,Fe)_2O_7$
$(Ca,Th,U,Ce)_2(Zr,Ti)_2(Ti,Nb,Zr,Fe)_2(\square,Fe,Ti)_2(Ti,Nb)O_{14}$

Sys. monoclinic	$a = 12.431(1)$ Å	source: Kaiserstuhl, Germany
S.G. C2/c	$b = 7.224(1)$ Å	Ref.: Sinclair and Eggleton (1982)
$Z = 4$	$c = 11.483(3)$ Å	JCPDS: #34-0167, #17-0495
$Dx = 4.9$ g/cm^3	$\beta = 100.33(1)°$	
AP: table 194	ID: table 195	IL: fig. 86

ZIRKELITE
$(Ti,Ca,Zr)O_{2-x}$
$(Ti,Ca,Zr)O_{2-x}$

Sys. cubic	$a = 5.02$ Å	source:
S.G.		Ref.: Bayliss et al. (1989)
$Z =$		

TABLE 192
Atomic parameters of zirconolite-$3T$[a].

	x	y	z	B (Å^2)
M81[c]	0.8324(7)	0	0.3333	1.0(1)[b]
M82[d]	0.3295(7)	0	0.3333	0.9(1)[b]
M7[e]	0.1653(6)	0.6676(8)	0.0166(1)	0.7(1)[b]
M61[f]	0.333(2)	0	0.8333	1.1(2)[b]
M62[g]	0.497(1)	0.334(2)	0.1640(1)	0.7(1)[b]
M5[h]	0.044(3)	0.894(2)	0.169(1)	3.0(6)[b]
O1	0.595(2)	0.634(3)	0.1428(7)	1.0(2)
O2	0.010(2)	0.820(2)	0.0579(5)	0.7(2)
O3	0.527(2)	0.314(2)	0.0488(7)	1.5(3)
O4	0.202(3)	0.227(2)	0.1442(7)	1.4(2)
O5	0.532(2)	0.890(2)	0.0536(6)	1.2(2)
O6	0.947(2)	0.312(2)	0.0540(6)	0.7(2)
O7	0.207(2)	0.616(2)	0.1425(7)	1.2(2)

[a] MoKα, $R = 0.063$ (659 refl.).
[b] B_{eq}.
[c] M81: 0.64(1)(Ca,Na) + 0.36(R,Th).
[d] M82: 0.50(1)(Ca,Na) + 0.50(R,Th).
[e] M7: 1.00Zr.
[f] M61: 0.78(1)Ti + 0.22(Nb,Ta).
[g] M62: 0.69(1)Ti + 0.31(Nb,Ta).
[h] M5: 0.5Fe.

kobeite-(Y)
$Y(Zr,Nb)(Ti,Fe)_2O_7$
$Y(Zr,Nb)(Ti,Fe)_2O_7$

Sys. trigonal (hex.)	$a =$ 7.241 Å	source: Paringa, South Westland, New Zealand
S.G.	$c =$ 16.571 Å	Ref.: Kato (1989); Hutton (1957)
$Z = 6$		JCPDS: #11-0259

scheteligite
$(Ca,Fe,Mn,Sb,Bi,Y)_2(Ti,Ta,Nb,W)_2[O,(OH)]_7$
$(Ca,Fe,Mn,Sb,Bi,Y)_2(Ti,Ta,Nb,W)_2[O,(OH)]_7$

Sys. orthorhombic (?)	$a =$	source: Kragerø, Norway
S.G.	$b =$	Ref.: Bjørlykke (1937)
$Z =$	$c =$	

The pyrochlore group consists of a series of oxides of niobium, tantalum or titanium. The minerals crystallize in a cubic lattice and are expressed by the general formula, $A_{2-x}B_2O_6(O,OH,F)_{1-y} \cdot zH_2O$ (A = R, U, K, Ba, Pb, ...; B = Nb, Ta,

TABLE 193
Interatomic distances for zirconolite-*3T* in Å.

M81–O2	2.41(2)	M82–O2	2.36(2)
M81–O2	2.41(2)	M82–O2	2.36(2)
M81–O3	2.42(3)	M82–O3	2.41(3)
M81–O3	2.42(3)	M82–O3	2.41(3)
M81–O4	2.46(1)	M82–O5	2.45(3)
M81–O4	2.46(1)	M82–O5	2.45(3)
M81–O6	2.50(2)	M82–O1	2.46(1)
M81–O6	2.50(2)	M82–O1	2.46(1)
mean	2.45	mean	2.42
M61–O7	1.89(3)	M62–O4	1.92(3)
M61–O7	1.89(3)	M62–O1	1.96(3)
M61–O6	1.93(1)	M62–O1	1.96(3)
M61–O6	1.93(1)	M62–O3	1.97(1)
M61–O4	2.01(3)	M62–O5	1.98(1)
M61–O4	2.01(3)	M62–O7	2.00(3)
mean	1.94	mean	1.96
M7–O2	2.06(1)	M5–O2	1.89(2)
M7–O5	2.10(1)	M5–O2	1.93(2)
M7–O6	2.13(1)	M5–O4	2.14(2)
M7–O3	2.14(1)	M5–O1	2.32(2)
M7–O7	2.21(1)	M5–O4	2.44(2)
M7–O6	2.35(3)	mean	2.14
M7–O5	2.42(3)		
mean	2.20		

Ti, ...). The IMA Subcommittee on Nomenclature of the Pyrochlore Group has established the classification and nomenclature of the group (Hogarth 1977). According to the nomenclature, the pyrochlore group minerals can be classified into three groups based on their atomic ratios of Nb, Ta and Ti at the B site using the following criteria: i.e., "pyrochlore": $Nb + Ta > 2Ti$ and $Nb > Ta$; "microlite": $Nb + Ta > 2Ti$ and $Ta \geqslant Nb$; and "betafite": $2Ti \geqslant Nb + Ta$. Ceriopyrochlore-(Ce) and yttropyrochlore-(Y) are pyrochlores containing rare earths. These two minerals differ in their compositions of the rare earth elements. Plumbopyrochlore is a pyrochlore of Pb which usually contains considerable amounts of rare earths. Uranmicrolite is a microlite of U showing substitution of Ca and Ce for U at the A site. Lapin et al. (1986) reported an occurrence of strontiopyrochlore. The structure of strontiopyrochlore is not reported; it may be isostructural with pyrochlore, but it has a slightly larger unit cell. It appears that the mineral has not yet been approved by the IMA commission. Yttrobetafite-(Y) is an Y-group dominant betafite.

Mazzi and Munno (1983) described a new member of this group, calciobetafite, and determined its crystal structure. They also analyzed the crystal structures of

TABLE 194
Atomic parameters of zirconolite-*2M*[a].

	x	*y*	*z*	B_{eq} (Å^2)
M1[b]	0.3752(1)	0.1245(3)	0.4971(1)	1.78
M2[c]	0.1210(1)	0.1261(2)	−0.0239(1)	1.36
M3[d]	0.2500(1)	0.1252(3)	0.7450(1)	1.50
M4[e]	0.4788(8)	0.0892(6)	0.2509(5)	3.42
M5[f]	0	0.1279(5)	0.25	1.60
O1	0.3087(7)	0.1243(13)	0.2864(6)	3.10
O2	0.4693(6)	0.1373(14)	0.0891(7)	2.75
O3	0.2070(8)	0.0857(12)	0.5687(8)	2.84
O4	0.3957(8)	0.1665(13)	0.7151(7)	2.97
O5	0.7121(8)	0.1700(11)	0.5821(7)	2.51
O6	−0.0024(7)	0.1157(14)	0.4189(6)	2.42
O7	0.1086(8)	0.0653(13)	0.7917(7)	2.98

[a] MoKα_1, $R = 0.052$, $R_w = 0.035$ (949 refl.).
[b] M1: 0.87Ca + 0.13(Th,U,R).
[c] M2: 0.85Zr + 0.15Ti.
[d] M3: 0.125Fe + 0.375Ti + 0.35Nb + 0.15Zr.
[e] M4: 0.33Fe + 0.17Ti.
[f] M5: 0.72Ti + 0.28Nb.

TABLE 195
Interatomic distances for zirconolite-*2M* in Å.

M1–O2	2.326(8)	M2–O3	2.051(8)
M1–O2	2.371(9)	M2–O6	2.066(8)
M1–O3	2.391(9)	M2–O5	2.107(8)
M1–O3	2.396(10)	M2–O2	2.108(10)
M1–O1	2.412(7)	M2–O7	2.141(9)
M1–O5	2.486(9)	M2–O5	2.314(10)
M1–O4	2.490(8)	M2–O6	2.340(9)
M1–O6	2.532(9)	mean	2.161
mean	2.426		
M3–O4	1.927(10)	M4–O2	1.867(10)
M3–O1	1.960(9)	M4–O2	1.873(10)
M3–O1	1.970(9)	M4–O4	2.120(11)
M3–O7	1.975(9)	M4–O1	2.239(13)
M3–O5	1.983(8)	M4–O4	2.404(12)
M3–O3	2.019(9)	mean	2.10
mean	1.972		
M5–O7	1.941(9) ×2		
M5–O6	1.947(7) ×2		
M5–O4	1.965(9) ×2		
mean	1.951		

TABLE 196
New mineral nomenclature of $CaZrTi_2O_7$ (zirconolite) group minerals.

New name	Discredited name	Formula	Crystal system	S.G.	Lattice parameters
zirconolite		$CaZrTi_2O_7$	non-crystalline	(metamict)	
zirconolite-*3O*	polymingnite	$CaZrTi_2O_7$	orthorhombic	Acam	$a = 10.148(4)$, $b = 14.147(5)$, $c = 7.278(3)$ Å
zirconolite-*3T*	zirkelite	$CaZrTi_2O_7$	trigonal	$P3_121$	$a = 7.287(2)$, $c = 16.886(9)$ Å
zirconolite-*2M*	zirconolite	$CaZrTi_2O_7$	monoclinic	C2/c	$a = 12.431(1)$, $b = 7.224(1)$, $c = 11.483(3)$ Å, $\beta = 100.33(1)°$
zirkelite		$(Ti,Ca,Zr)O_{2-x}$	cubic		

zirconolite-*3O* ("polymignite")* and zirconolite-*3T* ("zirkelite"). They revealed that zirconolite-*2M* ("zirconolite") is an independent mineral species, and the name is not a synonym of zirconolite-*3T* ("zirkelite"), after comparison of the crystal structure of zirconolite-*2M* ("zirconolite") (Sinclair and Eggleton 1982) with that of zirconolite-*3T* ("zirkelite"). Thus the mineral name "zirkelite" used in the paper by Sinclair and Eggleton (1982) should be replaced by "zirconolite".

Mazzi and Munno (1983) clarified the structural relationships between calciobetafite (pyrochlore), zirconolite-*3O* ("polymignite"), zirconolite-*3T* ("zirkelite"), and zirconolite-*2M* ("zirconolite"). They concluded that zirconolite-*3O* ("polymignite"), zirconolite-*3T* ("zirkelite"), and zirconolite-*2M* ("zirconolite") are polymorphs of the same compound, $(Ca,Na,R,Th,\ldots)_2^{VIII}Zr_2^{VII}(Ti,Nb,\ldots)_3^{VI}(Fe,Ti)^{V,IV}O_{14}$.

Projections of the crystal structures of calciobetafite, zirconolite-*3O* ("polymignite"), zirconolite-*3T* ("zirkelite") and zirconolite-*2M* ("zirconolite") are given in figs. 83, 84, 85, and 86, respectively. The structures comprise sheets of six- and three-membered rings of octahedra of niobium, tantalum or titanium. In the crystal structure of zirconolite-*3O* ("polymignite"), seven-coordinated Zr polyhedra are inserted in the sheets. Between the sheets, eight-coordinated polyhedra of calcium, rare earth, sodium and so on (in all cases), seven-coordinated polyhedra of zirconium or titanium [zirconolite-*3O* ("polymignite"), zirconolite-*3T* ("zirkelite"), and zirconolite-*2M* ("zirconolite")], and octahedra of niobium, tantalum or titanium [calciobetafite and zirconolite-*3O* ("polymignite")] form another kind of sheet. In all the structures, except that of calciobetafite, four- or five-coordinated sites partially occupied by iron are situated in the cavities of the six-membered rings of the octahedra, and this is the characteristic difference between zirconolite-*3O* ("polymignite"), zirconolite-*3T*

* Recently, Bayliss et al. (1989) revised the mineral nomenclature of zirconolite-related minerals (table 196). Zirconolite is the noncrystalline (metamict) mineral or mineral with undetermined polytypoid of $CaZrTi_2O_7$. Zirconolite-*3O*, zirconolite-*3T* and zirconolite-*2M* are the three-layered orthorhombic polytypoid, the three-layered trigonal polytypoid, and the two-layered monoclinic polytypoid of $CaZrTi_2O_7$, respectively. Polymignite (metamict) is discarded as equivalent to zirconolite. Zirkelite is the cubic mineral with formula $(Ti,Ca,Zr)O_{2-x}$. This revision was approved by the IMA Commission on New Minerals and Mineral Names. We have used both new and old (given in " ") nomenclature in the text, because the new nomenclature is not yet popular and may cause confusion.

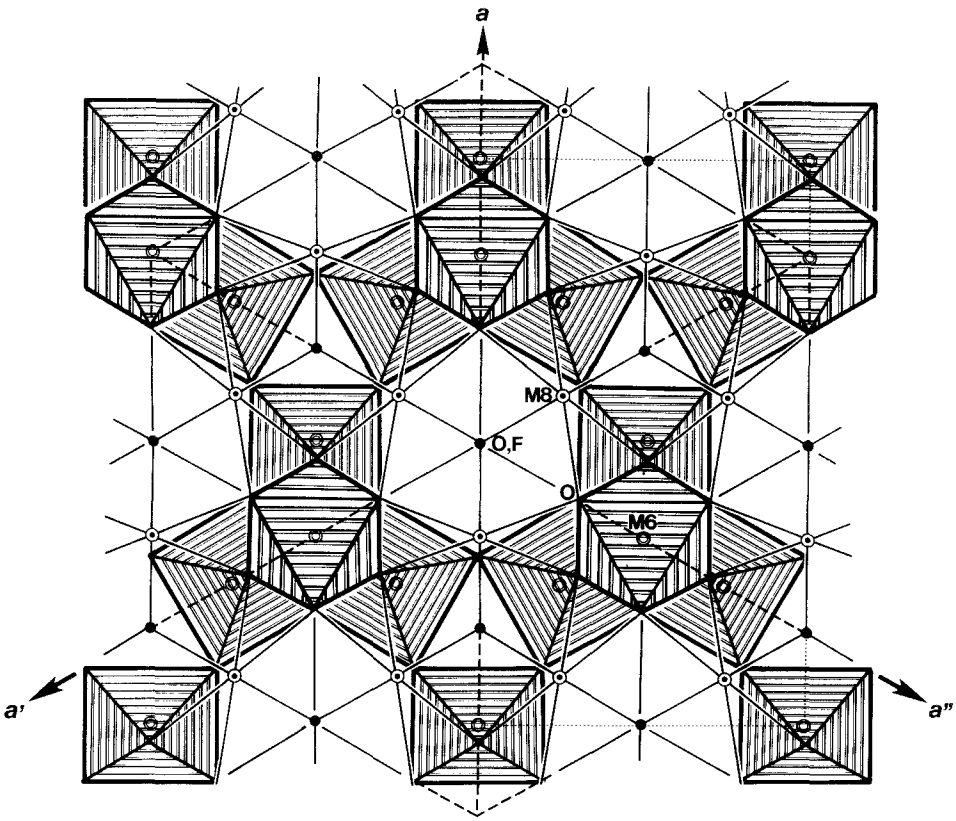

Fig. 83. The crystal structure of calciobetafite. The light broken lines indicate one half of the "multiple cell'.

("zirkelite") and zirconolite-*2M* ("zirconolite"), on the one hand, and calciobetafite (pyrochlore) on the other. The crystal structures of the former three minerals may be derived from that of pyrochlore. Chains, formed by distorted (Ca,R, ...) cubes alternating with (Ti,Nb, ...) octahedra in pyrochlore, are replaced in the remaining minerals either by chains of Zr polyhedra with seven vertices or chains in which (Ti,Nb, ...) octahedra alternate with distorted (Fe,Ti, ...) tetrahedra or trigonal bipyramids. The different arrangement of these chains gives rise to the different symmetries of the three phases. The crystal structures of zirconolite-*3T* ("zirkelite"; fig. 85) and zirconolite-*2M* ("zirconolite"; fig. 86) are very similar to each other, since they differ only in the stacking of identical pairs of layers of polyhedra.

The similarity of these structures can be clearly represented using the C-centered orthorhombic "multiple cells" proposed by Mazzi and Munno (1983). They are drawn with light broken lines in the figures: the cell parameters are $a = 12.61$, $b = 7.28$, $c = 17.84$ Å for calciobetafite (fig. 83), $a = 2 \times 12.37$, $b = 7.28$, $c = 17.41$ Å for zirconolite-*3O* ("polymignite"; fig. 84), $a = 12.62$, $b = 7.29$, $c = 16.89$ Å for zirconolite-

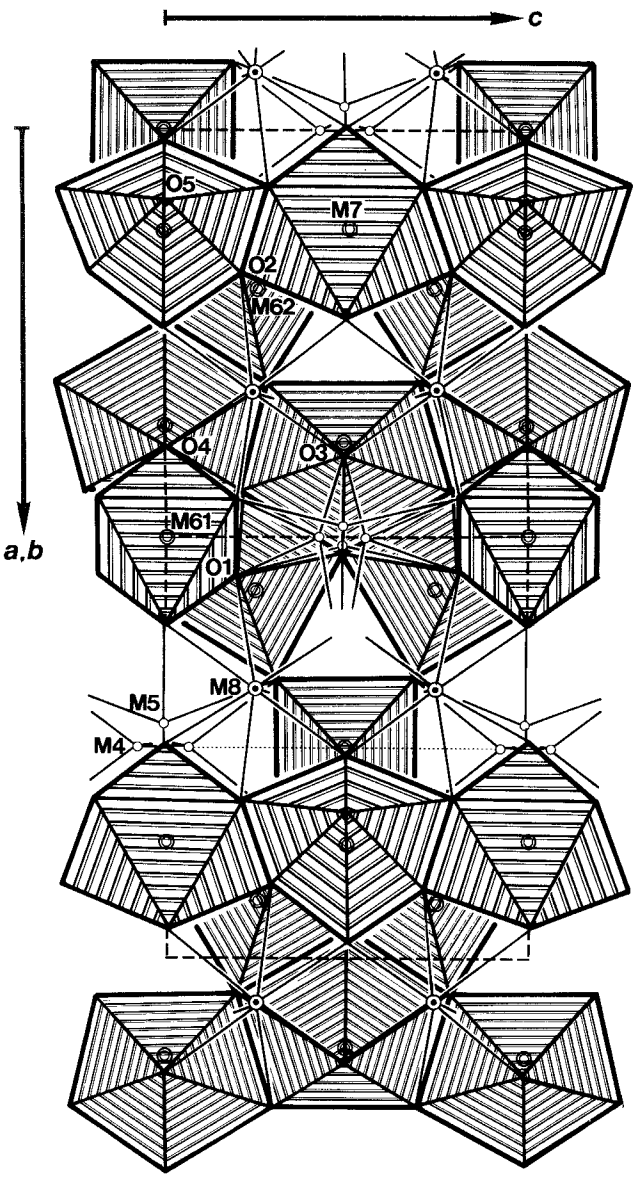

Fig. 84. The crystal structure of zirconolite-*3O* ("polymignite"). The light broken lines indicate one half of the "multiple cell'.

3T ("zirkelite"; fig. 85), and $a = 12.61$, $b = 7.31$, $c = 4 \times 16.88$ Å for zirconolite-*2M* ("zirconolite"; fig. 86).

Roberts et al. (1974) suggested that scheteligite may be a member of the pyrochlore group. This mineral was classified in the section of the pyrochlore group by Strunz (1978) and by Palache et al. (1944). However, Hogarth (1977) proposed that scheteligite may possibly belong to the betafite subgroup, with complex substitution by Y, Mn, Sb, W, Bi and that the mineral name was doubtful. Consequently, scheteligite

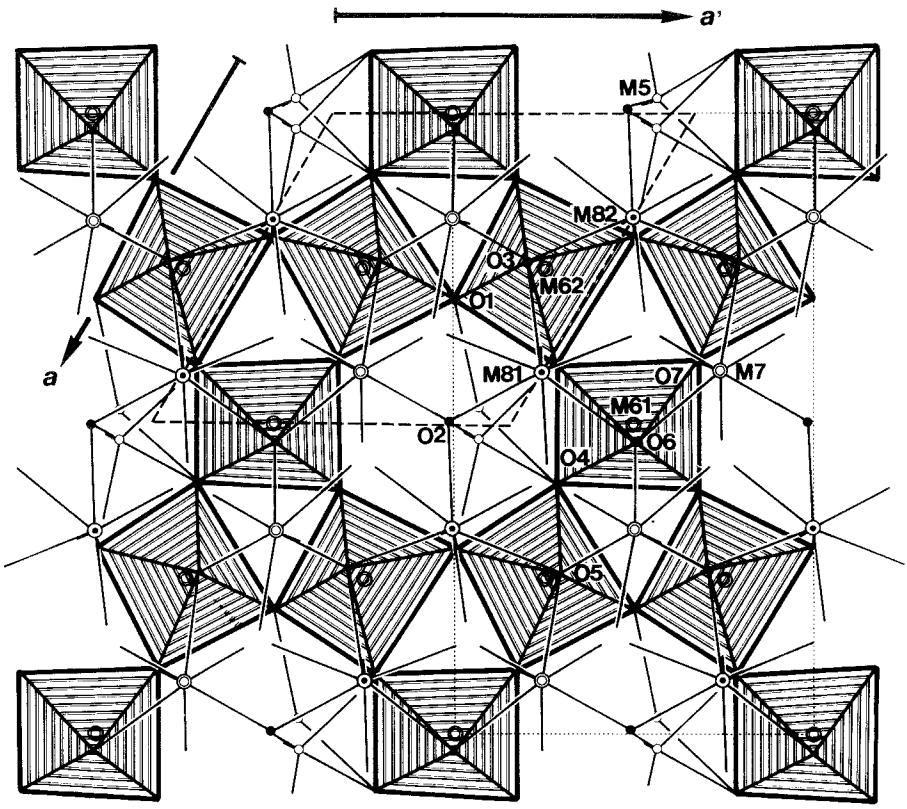

Fig. 85. The crystal structure of zirconolite-*3T* ("zirkelite"). The light broken lines indicate one half of the "multiple cell'.

was discredited by the IMA Commission on New Minerals and Mineral Names (Nickel and Mandarino, 1987).

Kobeite-(Y) occurs in the metamict state. Only qualitative chemical tests were done. Although the unit cell, cubic, $a = 5.02$ Å, given by Hutton (1957), is similar to that of murataite, the X-ray powder pattern of heated kobeite-(Y) is quite different from that of murataite (Hutton 1957). In the JCPDS card (#11-259), different crystallographic data are given: orthorhombic, $a = 5.753$, $b = 14.758$, $c = 4.985$ Å, which are close to those of euxenite-(Y).

Kato (1989) pointed out that a trigonal system with lattice parameters $a = 7.241$, $c = 16.751$ Å is in accordance with the X-ray powder diffraction pattern of kobeite-(Y) heated to 1200°C (Hutton 1957), and with the morphology of the original specimen. These cell dimensions are very close to those of zirconolite-*3T* ("zirkelite") given by Mazzi and Munno (1983). Kato (1989) suggested that kobeite-(Y) is an Y-dominant analogue of zirconolite-*3T* ("zirkelite") with the ideal formula $Y(Zr,Nb)(Ti,Fe^{2+})_2O_7$, and concluded that kobeite-(Y) and zirconolite-*3T* ("zirkelite") form isostructural series.

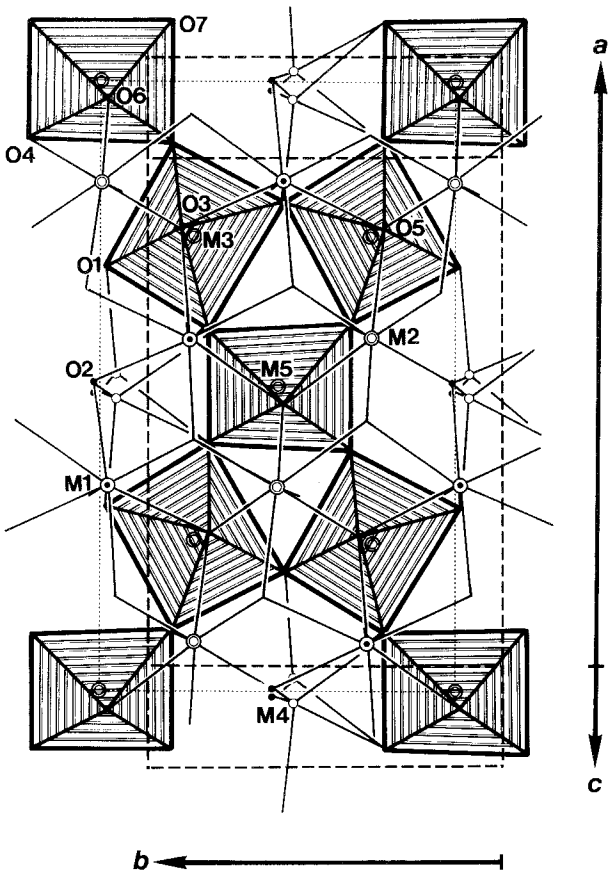

Fig. 86. The crystal structure of zirconolite-*2M* ("zirconolite"). The light broken lines indicate one half of the "multiple cell'.

DAVIDITE-(La) (=ferutite, ufertite)
$(La,Ca,Th)(Y,U,Fe)(Ti,Fe)_{20}(O,OH)_{38}$
$(La,Ca,Th,\square)(U,Y)(Fe,Mg,\square)_2(Fe,Ti,\square)_6Ti_{12}O_{38}$

Sys.	trigonal (rhomb.)	$a =$ 9.190(3) Å	source: Pandora Prospect, Pima Co., AZ, USA
S.G.	$R\bar{3}$	$\alpha = 68.73(1)^\circ$	Ref.: Gatehouse et al. (1979)
$Z =$	1		JCPDS: #13-0505, #8-0305
Dx =	4.72 g/cm^3		
Dm =	4.42 g/cm^3		
AP:	table 197	ID: table 198	IL: fig. 87

DAVIDITE-(Ce)
$(Ce,Ca,Th)(Y,U,Fe)(Ti,Fe)_{20}(O,OH)_{38}$
$(Ce,Ca,Th,\square)(U,Y)(Fe,Mg,\square)_2(Fe,Ti,\square)_6Ti_{12}O_{38}$

Sys.	trigonal (rhomb.)	$a =$	source: Norway
S.G.	$R\bar{3}$	$\alpha =$	Ref.: Gatehouse et al. (1979)
$Z =$			JCPDS: #8-0291

TABLE 197
Atomic parameters of davidite-(La)[a].

	x	y	z	B (Å^2)
M0[b]	0	0	0	1.17(2)
M1[c]	0.5	0.5	0.5	0.53(2)
M2[d]	0.3090(1)	0.3090(1)	0.3090(1)	0.47(2)
M3[e]	0.3474(1)	0.1269(1)	0.0184(1)	0.51(2)
M4[f]	0.3086(1)	0.7218(1)	0.1448(1)	0.34(2)
M5[g]	0.4749(1)	0.0775(1)	0.6444(1)	0.30(2)
O1	0.2999(5)	0.6300(5)	0.3765(5)	0.54(5)
O2	0.1486(5)	0.2347(5)	0.9391(5)	0.49(6)
O3	0.9192(5)	0.4574(5)	0.3025(5)	0.43(5)
O4	0.1446(5)	0.5137(5)	0.9897(5)	0.55(5)
O5	0.3891(5)	0.4869(5)	0.1345(5)	0.52(5)
O6	0.7131(5)	0.2404(5)	0.0688(5)	0.48(5)
O7	0.2134(4)	0.2134(4)	0.2134(4)	0.59(9)

[a] MoKα, $R = 0.045$ (1200 refl.).
[b] M0: 0.20Ca + 0.54Ln + 0.09(Sr,Th,Pb).
[c] M1: 0.33U + 0.30Y + 0.37Ln.
[d] M2: 0.12Mg + 0.79Fe.
[e] M3: 0.11Ti + 0.76Fe + 0.03Cr.
[f] M4: 1.00Ti.
[g] M5: 1.00Ti.

TABLE 198
Interatomic distances for davidite-(La) in Å.

M0–O2	2.745(4) ×6	M1–O1	2.243(4) ×6
M0–O6	2.794(4) ×6		
		M3–O4	1.951(4)
mean	2.769(4)	M3–O3	1.976(4)
		M3–O2	1.995(4)
M2–O5	1.975(4) ×3	M3–O7	2.020(4)
M2–O7	2.000(4)	M3–O4	2.024(4)
mean	1.981(4)	M3–O2	2.093(4)
		mean	2.010(4)
M4–O2	1.871(4)	M5–O4	1.839(4)
M4–O6	1.937(4)	M5–O1	1.887(4)
M4–O3	1.962(4)	M5–O3	1.923(4)
M4–O1	1.968(4)	M5–O5	1.968(4)
M4–O5	2.038(4)	M5–O6	2.037(4)
M4–O6	2.075(4)	M5–O5	2.180(4)
mean	1.975(4)	mean	1.972(4)

DAVIDITE-(Y)
$Y(Ti,Fe)_{21}O_{38}$
$Y(Ti,Fe)_{21}O_{38}$

Sys. trigonal (rhomb.)	$a =$	source: Vishnevye Gory, Ural Mts., Russia
S.G. $R\bar{3}$	$\alpha =$	Ref.: Levinson (1966)
$Z =$		

LOVERINGITE
$(Ca,Ce)(Ti,Fe,Cr,Mg)_{21}O_{38}$
$(Ca,Ce,Th)(Zr,Mg,Ce)(Fe,Mg,\square)_2(Cr,Fe,Ti,V,\square)_6(Ti,Al)_{12}O_{38}$

Sys. trigonal (rhomb.)	$a =$ 9.117(4) Å	source: Jimberlana, Australia
S.G. $R\bar{3}$	$\alpha = 69.07(1)^\circ$	Ref.: Gatehouse et al. (1978)
$Z = 1$		JCPDS: #30-0263
AP: table 199	ID: table 200	

TABLE 199
Atomic parameters of loveringite[a].

	x	y	z	B (Å^2)
M0[b]	0	0	0	2.11(11)
M1[c]	0.5	0.5	0.5	0.77(7)
M2[d]	0.31090(15)	0.31090(15)	0.31090(15)	0.69(8)
M3[e]	0.34754(34)	0.12318(33)	0.02156(34)	0.72(5)
M4[f]	0.30841(36)	0.72081(33)	0.14588(37)	0.63(5)
M5[g]	0.47612(38)	0.08155(35)	0.63977(37)	0.75(5)
O1	0.3058(13)	0.6269(13)	0.3801(13)	0.92(19)
O2	0.1523(14)	0.2378(14)	0.9393(13)	1.14(21)
O3	0.9211(12)	0.4571(12)	0.3002(13)	0.47(15)
O4	0.1427(14)	0.5149(14)	0.9908(14)	1.16(17)
O5	0.3901(14)	0.4896(14)	0.1345(14)	1.11(18)
O6	0.7104(12)	0.2410(12)	0.0699(13)	0.55(16)
O7	0.2120(8)	0.2120(8)	0.2120(8)	0.55(33)

[a] MoKα, $R = 0.043$ (398 refl.).
[b] M0: 0.72Ca + 0.23Ln + 0.05(Y,Th,U,Pb).
[c] M1: 0.58Zr + 0.1Ln + 0.32Mg.
[d] M2: 0.30Mg + 0.62Fe.
[e] M3: 0.37Cr + 0.36Fe + 0.14Ti + 0.03V.
[f] M4: 0.97Ti + 0.03Al.
[g] M5: 0.97Ti + 0.03Al.

TABLE 200
Interatomic distances for loveringite in Å.

M0–O2	2.772(11) ×6	M1–O1	2.166(11) ×6
M0–O6	2.807(11) ×6	M3–O4	1.935(11)
mean	2.790	M3–O3	1.972(11)
M2–O5	1.977(11) ×3	M3–O2	1.973(11)
M2–O7	2.047(11)	M3–O4	1.987(11)
mean	1.995	M3–O7	1.990(11)
		M3–O2	2.039(11)
		mean	1.983
M4–O2	1.878(11)	M5–O4	1.877(11)
M4–O6	1.934(11)	M5–O1	1.895(11)
M4–O3	1.960(11)	M5–O3	1.908(11)
M4–O1	1.992(11)	M5–O5	1.984(11)
M4–O5	2.000(11)	M5–O6	2.038(11)
M4–O6	2.060(11)	M5–O5	2.120(11)
mean	1.971	mean	1.970

CRICHTONITE (plumboan- =mohsite)
$(Sr,La)(Ti,Fe,Mn)_{21}O_{38}$
$(Sr,La,Pb,\square)(Mn,Fe)Fe_2(Fe,Ti)_6Ti_{12}O_{38}$

Sys. trigonal (rhomb.)	$a = 9.148(2)$ Å	source: Dauphiné, France
S.G. $R\bar{3}$	$\alpha = 69.078(6)°$	Ref.: Grey et al. (1976)
$Z = 1$		JCPDS: #22-1121
$Dx = 4.54$ g/cm^3		
AP: table 201	ID: table 202	

Davidite-(La) (Gatehouse et al. 1979), loveringite (Gatehouse et al. 1978), and crichtonite (Grey et al. 1976) belong to the crichtonite group, and are isostructural. Figure 87 was drawn using the atomic parameters of davidite-(La). The structures are based on a close-packed anion framework with a nine-layer stacking sequence (hhc...) in which the large cations, Ca, Sr, R, and Pb atoms occupy one of the anion sites M0 with coordination number 12 in the cubic layers (fig. 87a). The small cations are ordered into both tetrahedral and octahedral interstices between the close-packed anion layers. There are two types of cation layers, which are drawn in figs. 87b and c. The metal atoms M1 and M3 occupy octahedral sites between pairs of the hexagonally stacked anion layers, i.e. h–M–h (fig. 87b). The $M3O_6$ octahedra occupied by iron, titanium, and chromium articulate by edge-sharing forming interconnected twelve-membered hexagonal rings, with an isolated $M1O_6$ octahedron of uranium, zirconium or manganese at the center of each ring. The h–M–c metal-

TABLE 201
Atomic parameters of crichtonite[a].

	x	y	z	B (Å²)
M0[b]	0	0	0	0.622(4)
M1[c]	0.5	0.5	0.5	0.085(6)
M2[d]	0.31002(15)	0.31002(15)	0.31002(15)	0.305(5)
M3[e]	0.34821(18)	0.01996(18)	0.12540(18)	0.303(4)
M4[f]	0.30861(21)	0.15018(21)	0.71802(21)	0.388(4)
M5[g]	0.47337(20)	0.64054(21)	0.08370(20)	0.334(4)
O1	0.30300(77)	0.37824(77)	0.62878(77)	1.00(1)
O2	0.15029(76)	0.93711(75)	0.23654(75)	0.88(1)
O3	0.91852(73)	0.30110(72)	0.45916(73)	0.63(1)
O4	0.14475(75)	0.98866(74)	0.51544(74)	0.75(1)
O5	0.39014(73)	0.13445(75)	0.48615(74)	0.64(1)
O6	0.70853(72)	0.07152(74)	0.24216(73)	0.61(1)
O7	0.21402(50)	0.21402(50)	0.21402(50)	0.71(2)

[a] MoKα, $R = 0.040$ (505 refl.).
[b] M0: 0.7Sr + 0.2(Pb,R).
[c] M1: 0.7Mn + 0.3Fe.
[d] M2: 1.0Fe.
[e] M3: 0.73Fe + 0.27Ti.
[f] M4: 1.0Ti.
[g] M5: 1.0Ti.

TABLE 202
Interatomic distances for crichtonite in Å.

M0–O2	2.753(7) ×6	M1–O1	2.205(7) ×6
M0–O6	2.831(7) ×6	M3–O4	1.940(7)
mean	2.792(7)	M3–O3	1.976(7)
M2–O5	1.966(7) ×3	M3–O2	1.999(7)
M2–O7	1.991(7)	M3–O4	2.017(7)
mean	1.972(7)	M3–O7	2.019(7)
		M3–O2	2.086(7)
		mean	2.006(7)
M4–O2	1.873(7)	M5–O1	1.860(7)
M4–O1	1.937(7)	M5–O4	1.864(7)
M4–O2	1.949(7)	M5–O3	1.930(7)
M4–O6	1.982(7)	M5–O5	2.000(7)
M4–O5	2.023(7)	M5–O6	2.013(7)
M4–O6	2.050(7)	M5–O5	2.136(7)
mean	1.969(7)	mean	1.967(7)

atom layers, two per unit cell, contain metals in both octahedral and tetrahedral sites (fig. 87c). The octahedrally coordinated M4 and M5 atoms of titanium join by edge-sharing into six-membered hexagonal rings, which are interlinked via corner-sharing with the basal oxygen of the $M2O_4$ tetrahedra of iron and magnesium.

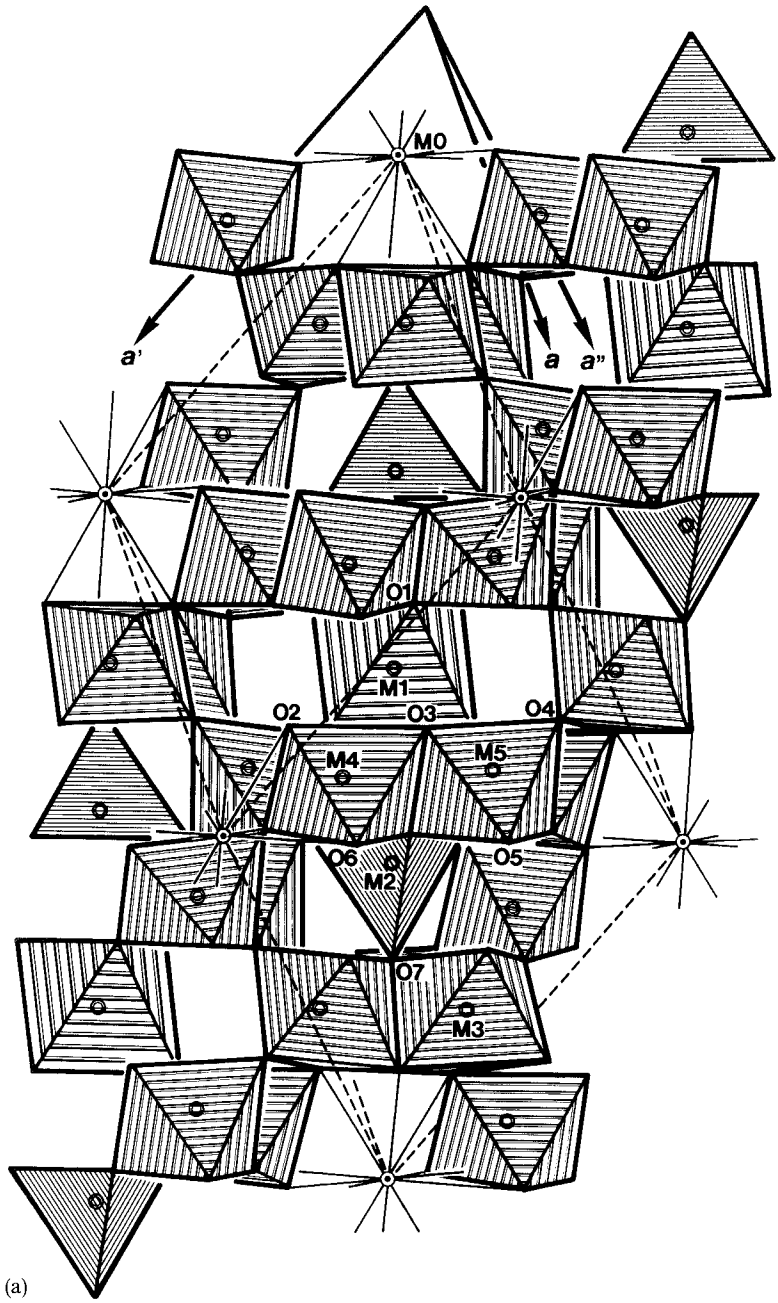

Fig. 87. The crystal structure of davidite-(La), which is isostructural with loveringite and crichtonite. The illustration (a) shows the arrangement of the two kinds of layers shown in (b) and (c).

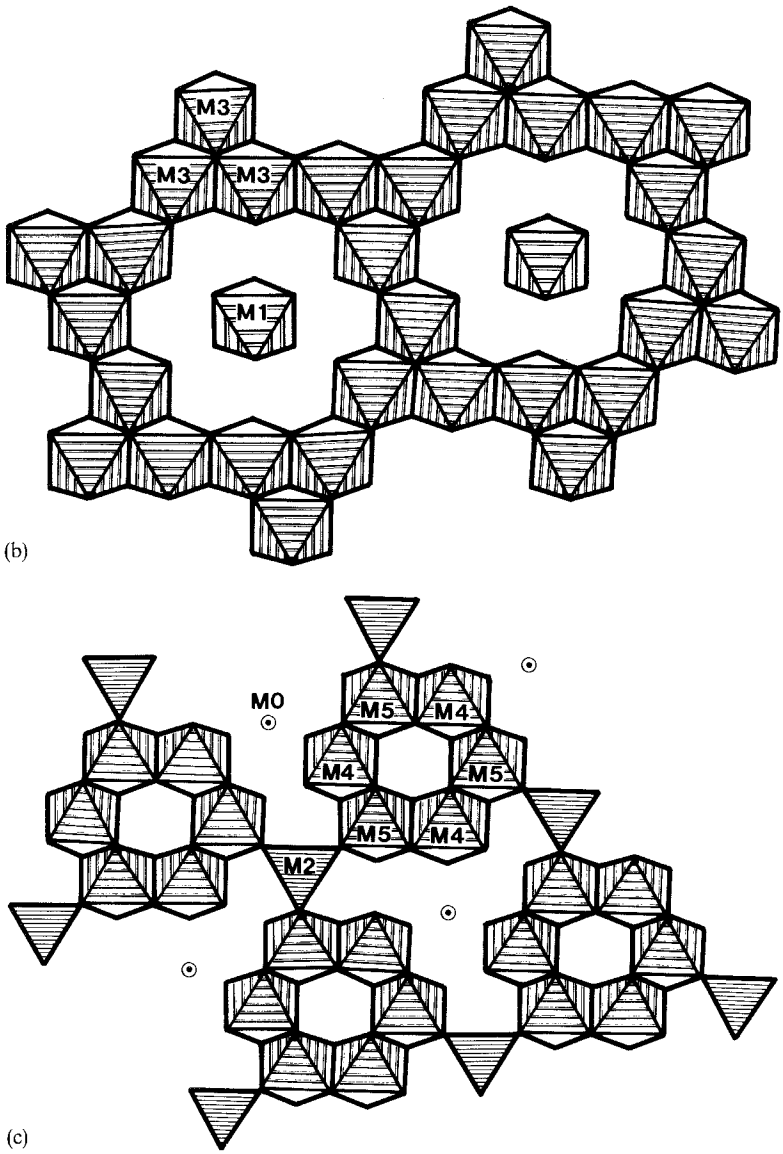

Fig. 87. (b) and (c).

Gatehouse et al. (1979) reported that uranium and the Ce-group rare earth atoms independently occupy the M1 and M0 sites in the crystal structure of davidite-(La), and that Y-group rare earth atoms with smaller ionic radii substitute for the uranium atoms at the M1 site. They also explained the low uranium content with high cerium and yttrium content in the sample of davidite from Norway, by the presence of the tetravalent Ce^{4+} ion with relatively small size at the M1 site. Gatehouse et al. (1979)

pointed out that the M1–O bond length and the unit cell edge, a, show a linear relationship in the crichtonite-group minerals, and concluded that the cell dimensions depend on the size of M1.

YTTROTUNGSTITE-(Y)
$(Y,Ca,Mg)(W,Al,Si,Ti,Fe)_2(O,OH)_7(OH)\cdot H_2O$
$(Y,Ca,Mg)(W,Al,Si,Ti,Fe)_2(O,OH)_7(OH)\cdot H_2O$

Sys. monoclinic	$a =$ 6.954(6) Å	source: Kramat Pulai mine, Perak, Malaysia
S.G. $P2_1/m$	$b =$ 8.637(9) Å	Ref.: Davis and Smith (1971)
$Z =$ 4	$c =$ 5.771(6) Å	JCPDS: #26-1396
Dm = 5.96 g/cm^3	$\beta = 104°56(4)'$	
AP: table 203	ID: table 204	IL: fig. 88

TABLE 203
Atomic parameters of yttrotungstite-(Y) in Å[a].

	x	y	z
Y	0.724(4)	1/4	
	0.719(7)		0.248(8)
W	0.186(2)	0.064(1)	
	0.182(2)		0.212(2)
O1	0.14(2)	1/4	
	0.15(1)		0.97(2)
O2	0.14(2)	1/4	
	0.18(3)		0.41(4)
O3	0.45(2)	0.08(1)	
	0.40(1)		0.20(1)
O4	0.85(1)	0.06(1)	
	0.85(1)		0.03(2)
O5	0.85(1)	0.06(1)	
	0.82(3)		0.59(4)
O6	0.52(2)	1/4	
	0.60(1)		0.80(1)

[a] CuKα, $R_{hk0} = 0.14$ (49 refl.), $R_{h0l} = 0.17$ (40 refl.). Atomic coordinates are calculated for each reflection data set: (xy) for ($hk0$) and (xz) for ($h0l$).

TABLE 204
Interatomic distances for yttrotungstite-(Y) in Å.

Y–O4	2.4 ×2	W–O3	1.5
Y–O5	2.4 ×2	W–O4	2.2
Y–O6	2.5		
Y–O3	2.7 ×2		
mean	2.5		

CEROTUNGSTITE-(Ce)
$(Ce,Ca)(W,Al)_2O_6(OH)_3$
$(Ce,Ca)(W,Al)_2O_6(OH)_3$

Sys. monoclinic	$a = 5.874 \pm 0.005$ Å	source: Nyamulilo mines, Kigezi, Uganda
S.G. $P2_1$ or $P2_1/m$	$b = 8.700 \pm 0.005$ Å	Ref.: Sahama et al. (1970)
$Z = 2$	$c = 7.070 \pm 0.005$ Å	JCPDS: #25-0193
	$\beta = 105°27' \pm 0.05'$	

The crystal structure of yttrotungstite-(Y) was analyzed by Davis and Smith (1971) using photographic data with intensities obtained by visual estimation. The structure (fig. 88) consists of a zigzag chain of WO_6 octahedra running parallel to the *b*-axis. One of the six corners of the WO_6 octahedra is occupied by an (OH) ion (O1 or O2). The yttrium atom is coordinated by six oxygen atoms of the WO_6 octahedra in a trigonal prismatic form, and additionally, by one water molecule (O6) forming a distorted monocapped trigonal prism.

The crystal data of cerotungstite-(Ce) suggest that this mineral is a Ce-analogue of yttrotungstite-(Y). In addition, the chemical formula reported by Sahama et al. (1970) corresponds well with that of yttrotungstite-(Y) derived from the structure analysis.

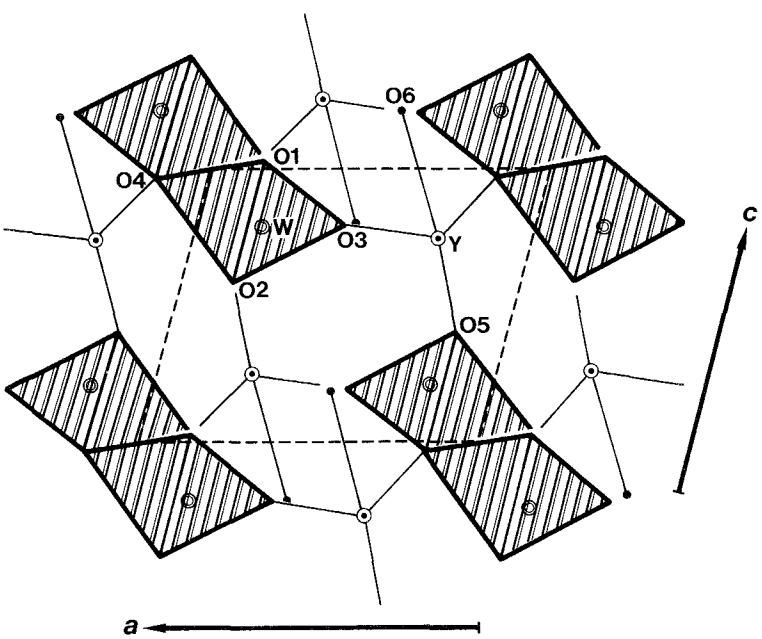

Fig. 88. The crystal structure of yttrotungstite-(Y).

MURATAITE
$(Na,Y)_4(Zn,Fe)_3(Ti,Nb)_6O_{18}(F,OH)_4$
$(Na,Y)_4(Zn,Fe)_3(Ti,Nb)_6O_{18}(F,OH)_4$

Sys. cubic	$a = 14.863(5)$ Å	source: El Paso Co., CO, USA
S.G. F432, Fm3m or Fm3		Ref.: Adams et al. (1974)
$Z = 8$		JCPDS: #26-1383
Dx = 4.64 g/cm^3		
Dm = 4.69 g/cm^3		

The crystal structure of murataite has not yet been reported.

LOPARITE-(Ce)
$(Ce,Sr,Na,Ca)(Ti,Nb,Fe)O_3$
$(Ce,Sr,Na,Ca)(Ti,Nb,Fe)O_3$

Sys. cubic	$a = 3.886(1)$ Å	source: Sarambi, Paraguay
S.G. Pm3m		Ref.: Haggerty and Mariano (1983)
$Z = 1$		JCPDS: #35-0618, #20-0272
Dx = 5.26(5.14) g/cm^3		

nioboloparite
$(Na,Ce,Ca)(Ti,Nb)O_3$
$(Na,Ce,Ca)(Ti,Nb)O_3$

Sys. pseudo-cubic (?)	$a = 3.905 \pm 0.005$ Å	source: Khibina Tundra, Kola Peninsula, Russia
S.G.		Ref.: Tikhonenkov and Kazakova (1957)
$Z = 1$		
Dm = 4.657 g/cm^3		

Loparite-(Ce) is a member of the perovskite-group, and may be isostructural with cubic perovskite, $CaTiO_3$, and tausonite, $SrTiO_3$. The loparite-(Ce) sample from South America (Haggerty and Mariano 1983) contains considerable amounts of strontium, showing a solid solution series between loparite-(Ce) and tausonite. Haggerty and Mariano (1983) suggested that Sr, Na, and R may occupy the A site in the cubic perovskite-type structure, with Ti + Nb dominantly occupying the B site. Because of charge balance, a phase with the chemical formula $CeTiO_3$ could not exist as an end-member of the solid solution. Therefore, the isomorphous substitution of Sr, Ca, Na, or K for R in the A site and Fe^{3+} for Ti in the B site may be essential in the crystal structure of loparite-(Ce).

Niobloparite, described by Tikhonenkov and Kazakova (1957), contains considerable amounts of niobium and sodium. However, the Ti content is still greater than the Nb content. Therefore, the specimen should be named as a Nb-rich Na-analogue of loparite, and not "niobloparite".

2.5. *Class 5: structures without anionic groups – fluorides and simple oxides*

A few fluoride minerals of rare earths are known, but none for chlorides, bromides and iodides. Simple oxides of the rare earths are very rare in nature and no rare earth sulfide mineral is known.

FLUOCERITE-(Ce) (=tysonite)
CeF_3
CeF_3

Sys. trigonal (hex.)	$a = 7.030(2)$ Å	source: synthetic NdF_3
S.G. $P\bar{3}c1$	$c = 7.200(2)$ Å	Ref.: Kondratyuk et al. (1988)
$Z = 6$		JCPDS: #38-0452
AP: table 205	ID: table 206	IL: fig. 89

FLUOCERITE-(La)
LaF_3
LaF_3

Sys. trigonal (hex.)	$a = 7.185$ Å	source: synthetic LaF_3
S.G. $P\bar{3}c1$	$c = 7.351$ Å	Ref.: Cheetham et al. (1976)
$Z = 6$		JCPDS: #32-0483

Three space groups for fluocerite-(Ce) or the isostructural synthetic RF_3 phases have been proposed, and their crystal structures have been analyzed based on the following space groups: $P6_3/mcm$ (Oftedal 1931c, Afanasiev et al. 1972), $P\bar{3}c1$ (Mansmann 1965, Zalkin et al. 1966) and $P6_3cm$ (de Rango et al. 1966). Cheetham et al. (1976) analyzed the crystal structures of LaF_3 and CeF_3 in a powder neutron diffraction study, and reexamined the three space groups. They were able to eliminate the space group $P6_3/mcm$, and found that the disordered structure proposed by Afanasiev et al. (1972) was unsatisfactory. Although their study did not discriminate

TABLE 205
Atomic parameters of fluocerite-(Ce)[a].

	x	y	z	B
Nd	0.3414(1)	0	1/4	0.23(2)
F1	0	0	1/4	1.17(3)
F2	1/3	2/3	0.3145(2)	0.70(3)
F3	0.3104(1)	−0.0579(1)	0.5805(1)	0.93(3)

[a] Neutron ($\lambda = 1.1105$ Å), $R = 0.0191$, $R_w = 0.0211$ (385 refl.).

TABLE 206
Interatomic distances for fluocerite-(Ce) in Å[a].

Nd–F2	2.362(1) ×2
Nd–F1	2.400(1)
Nd–F3	2.406(1) ×2
Nd–F3	2.424(1) ×2
Nd–F3	2.579(1) ×2
Nd–F3	2.967(1) ×2
mean	2.534

[a] Recalculated by RM.

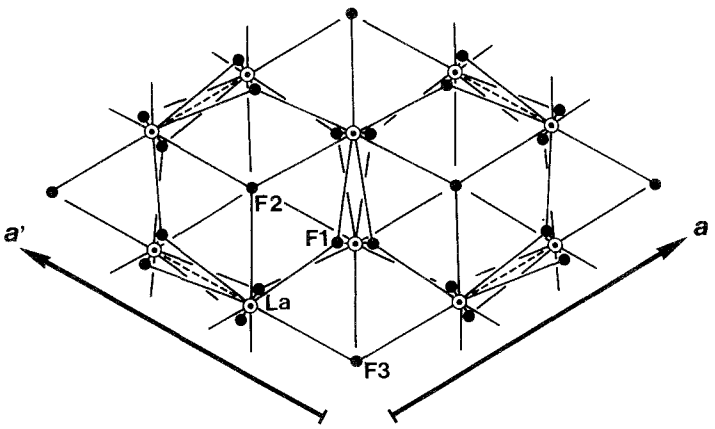

Fig. 89. The crystal structure of LaF_3.

between $P\bar{3}c1$ and $P6_3cm$, they suggested that the true space group is $P\bar{3}c1$ based on the indirect evidence of NMR.

Gregson et al. (1983) asserted that their neutron diffraction data demonstrated that the space group of fluocerite, LaF_3, was not $P\bar{3}c1$. However, Zalkin and Templeton (1985) again refined the crystal structure of fluocerite in the space group $P\bar{3}c1$ with a model which accounts for the effects of twinning and disproved this assertion.

Kondratyuk et al. (1988) examined the crystal structure of NdF_3 using a sample showing merohedric twinning, by neutron diffraction analysis. They analyzed the structure based on the two different space groups $P6_3cm$ and $P\bar{3}c1$, and compared the results. Their results showed that NdF_3 has space group $P\bar{3}c1$, which gave not only lower R_w and R values, but also physically more significant thermal vibration parameters and clearer differential nuclear-density synthesis than the $P6_3cm$ model. This result confirms the analysis of the crystal structure of CeF_3 by Zalkin and Templeton (1985).

In the structure of LaF_3 (fig. 89), the La atom is coordinated by nine F atoms at distances between 2.417 and 2.638 Å, with two more distant neighbors at 3.002 Å (Zalkin and Templeton 1985). NdF_3 is isostructural with LaF_3, with nine F atoms at distances between 2.362 and 2.579 Å and two more distant F atoms at 2.967 Å (Kondratyuk et al. 1988).

GAGARINITE-(Y)
$YCaNaF_6$
$(Y,Ca)_2(Na,\square)F_6$

Sys. trigonal (hex.)	$a = 5.99 \pm 0.03$ Å	source: Kazakhstan
S.G. $P\bar{3}$	$c = 3.53 \pm 0.02$ Å	Ref.: Voronkov et al. (1962)
$Z = 1$		JCPDS: #15-0069
$Dm = 4.21$ g/cm^3		
AP: table 207	ID: table 208	IL: fig. 90

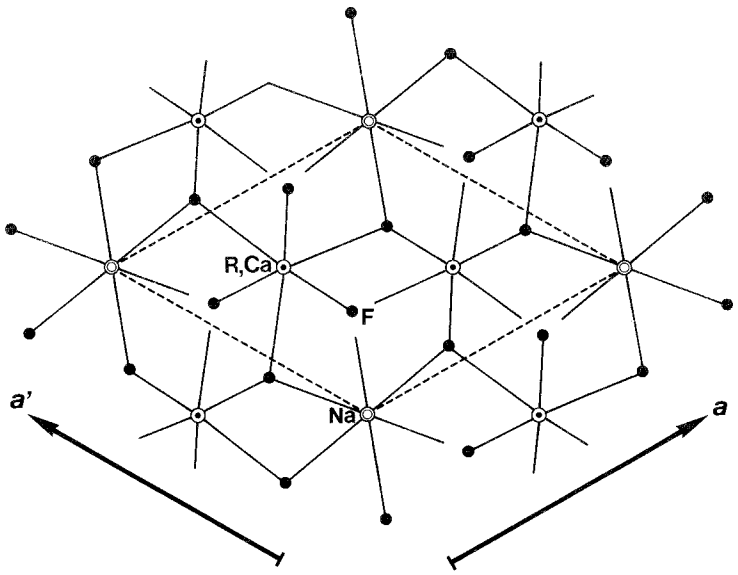

Fig. 90. The crystal structure of gagarinite-(Y).

The crystal structure of gagarinite-(Y) (fig. 90) consists of nine-coordinated (R,Ca) polyhedra and partially occupied Na sites with octahedral coordination (Voronkov et al. 1962). This structure may be considered as derived from that of UCl_3; the symmetry changes from $P6_3/m$ (UCl_3) to $P\bar{3}$ [gagarinite-(Y)]. The Na atoms are the extra ones; they have flattened octahedra as their coordination polyhedra, and these lie alternately with empty polyhedra of the same shape on the three-fold axes along

TABLE 207
Atomic parameters of gagarinite-(Y)[a].

	x	*y*	*z*
R,Ca[b]	2/3	1/3	0.25
Na[c]	0	0	0
F	0.318	0.393	0.25

[a] Mo, $R_{hk0} = 0.093$, $R_{h0l} = 0.082$.
[b] R,Ca: 0.6R + 0.4Ca.
[c] Na: 0.8Na.

TABLE 208
Interatomic distances for gagarinite-(Y) in Å.

R,Ca–F	2.30 ×3	Na–F	2.33 ×6
R,Ca–F	2.39 ×6		
mean	2.36		

c. The shape of the (R,Ca) polyhedron is a tricapped trigonal prism. The (R,Ca) prisms share their top and bottom triangular faces forming infinite columns parallel to the *c*-axis. These columns are analogous to those for calcium in apatite. This mineral shows a substitution of an unique type: $R^{3+} + \square \rightleftarrows Ca^{2+} + Na^{+}$.

TVEITITE-(Y)
$Ca_{14}Y_5F_{43}$
$Ca_{14}Y_5F_{43}$

Sys. trigonal (hex.)	$a = 16.6920 \pm 0.0009$ Å	source: Høydalen, Tørdal, Norway
S.G. $R\bar{3}$	$c = 9.6664 \pm 0.0008$ Å	Ref.: Bevan et al. (1982)
$Z = 3$		JCPDS: #29-0363
AP: table 209	ID: table 210	IL: fig. 91

FLUORITE, YTTRIAN (= yttrofluorite)
$(Ca,Y)F_2$
$Ca_{1-x}Y_xF_{2+x}$

Sys. cubic	$a = 5.489(2)$ Å	source: synthetic $Ca_{0.90}Y_{0.10}F_{2.10}$
S.G. Fm3m		Ref.: Otroshchenko et al. (1988)
$Z = 4$		JCPDS: #31-0293
AP: table 211	ID: table 212	IL: fig. 92

The crystal structure of tveitite-(Y) (Bevan et al. 1982) is closely related to fluorite and is the $n = 19$ member of a homologous series of fluorite-related compounds, M_nX_{2n+5}, which occur in the system CaF_2–YF_3 (Gettmann and Gries 1978). In the structure (fig. 91), the formation of three-dimensional clusters of thirteen cubic close-packed F anions is observed. These clusters have the form of filled cuboctahedra with F8 being the center, and are ordered in the structure. The Y ions of M_6X_{37} clusters have an 8 + 1 coordination by F in the form of a monocapped square

TABLE 209
Atomic parameters of tveitite-(Y)[a].

	x	*y*	*z*	*B*
Y	0.0169(1)	0.1489(1)	0.1786(2)	0.60(6)
Ca1	0	0	0.5353(6)	2.8(5)
Ca2	0.2654(3)	0.2348(3)	0.1557(4)	0.1(5)
Ca3	0.1749(3)	0.4059(3)	0.1672(4)	1.2(3)
F1	0.1958(7)	0.0831(7)	0.0040(11)	1.0(2)
F2	0.1102(8)	0.0975(8)	0.2349(12)	1.4(3)
F3	0.0190(6)	0.1495(6)	0.4146(10)	0.1(5)
F4	0.2702(6)	0.1024(6)	0.2573(11)	0.3(2)
F5	0.1576(6)	0.2686(6)	0.2515(11)	0.2(2)
F6	0.0324(6)	0.2842(6)	0.0971(11)	0.4(2)
F7	0.2955(6)	0.3838(6)	0.0744(11)	0.3(2)
F8	0	0	0.060(9)	1.4(8)

[a] MoKα, $R = 0.122$ (1164 refl.).

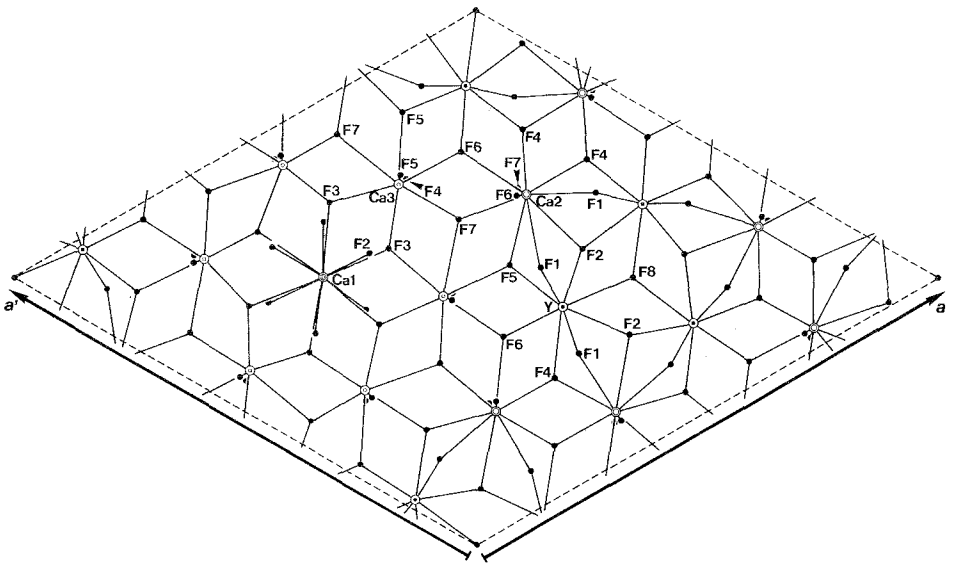

Fig. 91. The crystal structure of tveitite-(Y).

TABLE 210
Interatomic distances for tveitite-(Y) in Å.

Y–F2	2.218(8)	Ca2–F5	2.361(8)
Y–F2	2.223(9)	Ca2–F4	2.386(8)
Y–F1	2.249(8)	Ca2–F7	2.444(8)
Y–F1	2.257(9)	Ca2–F7	2.449(8)
Y–F3	2.281(8)	Ca2–F6	2.463(9)
Y–F6	2.314(8)	Ca2–F4	2.489(8)
Y–F4	2.329(9)	Ca2–F6	2.516(9)
Y–F5	2.338(7)	Ca2–F2	2.609(10)
Y–F8	2.654(29)	Ca2–F1	2.670(8)
mean	2.318	Ca2–F1	2.796(9)
		mean	2.518
Ca1–F3	2.440(8) ×3	Ca3–F3	2.293(8)
Ca1–F3	2.661(8) ×3	Ca3–F3	2.317(8)
Ca1–F2	2.841(8) ×3	Ca3–F5	2.343(8)
Ca1–F2	3.402(9) ×3	Ca3–F4	2.356(8)
mean	2.836	Ca3–F6	2.360(9)
		Ca3–F5	2.401(8)
		Ca3–F7	2.424(8)
		Ca3–F7	2.429(9)
		mean	2.365

antiprism, the F8 atom in the cuboctahedron being the common cap for all six square antiprisms of the cluster. These clusters are distributed along the three-fold symmetry axes so that their centers occupy the positions 0, 0, 0; $\frac{1}{3}, \frac{2}{3}, \frac{2}{3}$; $\frac{2}{3}, \frac{1}{3}, \frac{1}{3}$; with symmetry $\bar{3}$. Between each pair of clusters lying one above the other along the hexagonal *c*-axis, there is generated a somewhat distorted icosahedron of twelve F atoms, within which the atom Ca1 is found, and these [001] columns of alternating M_6X_{37} clusters and CaF_{12} icosahedra, fused together, are embedded in a matrix of virtually unmodified fluorite-type structure, where the Ca3 atom is coordinated by eight F atoms in the form of an almost undistorted cube. The Ca2 atoms occur in the boundary region between the fluorite-type matrix and the columns. The Ca2 atoms are ten-coordinated, and the coordination polyhedron can be described as the combination of half a cube and half an icosahedron. Bevan et al. (1982) proposed the probable ideal formula $Ca_{14}Y_5F_{43}$, which means partial occupancies at the Y and F sites.

Yttrian fluorite is considered as a solid solution of CaF_2 and YF_3, both of which have very similar X-ray powder diffraction patterns (Uetani et al. 1968). Otroshchenko et al. (1988) analyzed the crystal structure of synthetic $Ca_{0.90}Y_{0.10}F_{2.10}$ using neutron diffraction data of the single crystal. $Ca_{0.90}Y_{0.10}F_{2.10}$ is one of the disordered solid solutions $M_{1-x}R_xF_{2+x}$ (M = Ca, Sr, Ba) with the fluorite structure, and $Ca_{1-x}Y_xF_{2+x}$ has been described as fluorite, yttrian (yttrofluorite), having an X-ray powder diffraction pattern very similar to synthetic fluorite, by Uetani et al. (1968). The heterovalent isomorphism in the fluorite-type structure, together with filling by F^- ions of the additional positions, is accompanied by the formation of vacancies at the basic position of the F ions. The probable position for the interstitial F atoms is 32f (*xxx*) or 48i ($\frac{1}{2}yy$) (Maksimov et al. 1968). Otroshchenko et al. (1988) revealed that the additional atoms are in the latter position (fig. 92).

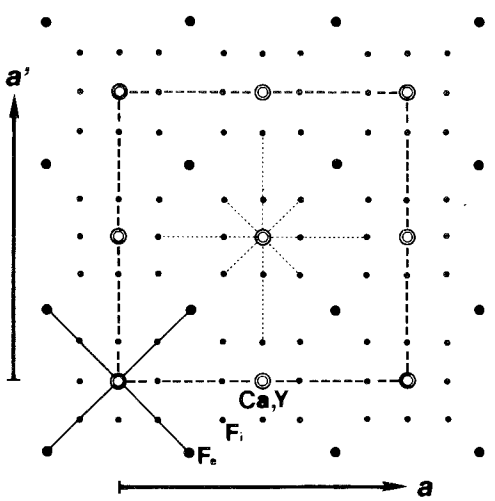

Fig. 92. The crystal structure of fluorite, yttrian.

TABLE 211
Atomic parameters of fluorite, yttrian[a].

	Occupancy	x	y	z	Temperature factor
Ca,Y	4/4	0	0	0	$B = 0.73(2)$
F_c	7.55(2)/8	1/4	1/4	1/4	$B = 0.79(1)$
F_i	0.85/48	1/2	0.366(2)	0.366(2)	$B_{11} = 3.2(2)$, $B_{22} = B_{33} = 0.6(1)$, $B_{23} = 0.1(1)$

[a]Neutron ($\lambda = 1.167$ Å, Cu monochromator), $R = 0.010$, $R_w = 0.008$ (33 refl.).

TABLE 212
Interatomic distances (Å) for fluorite, yttrian[a].

Ca,Y–F_i	2.14 ×12
Ca,Y–F_c	2.38 ×8
Ca,Y–F_i	2.94 ×8
mean[b]	2.14

[a]Calculated by RM.
[b]Weighted.

CERIANITE-(Ce)
$(Ce,Th)O_2$
$(Ce,Th)O_2$

Sys. cubic — $a = 5.42 \pm 0.01$ Å — source: Sudbury, Ont., Canada
S.G. Fm3m — Ref.: Graham (1955)
$Z = 4$ — JCPDS: #34-0394
$Dm > 3.21$ g/cm^3

Cerianite-(Ce) is a solid solution resulting from isomorphous substitution among CeO_2, ThO_2 and UO_2 and has the fluorite-type structure.

3. Some crystal-chemical aspects of rare earth minerals

3.1. *Structural differences between Y-group and Ce-group rare earths*

The coordination numbers of the rare earth atoms are generally high, and their coordination polyhedra are as large as those of sodium, calcium, thorium ions and so on. It is found that Y-group rare earths and Ce-group rare earths show a difference in their coordination numbers (table 213). The coordination numbers of the Y-group rare earths range from 6 to 11, and the most frequently observed number is 8. On the other hand, those of the Ce-group rare earths range from 7 to 12, but the most frequently observed number is again 8. The coordination numbers of calcium resemble those of the Ce-group, hence isomorphous substitution between calcium and Ce-group rare earths has been often observed.

The differences in coordination numbers and sizes of coordination polyhedra between the two groups are reflected in the crystal structures of the carbonates and

TABLE 213

Coordination number and coordination polyhedra of rare earths at respective rare earth (metal) sites.

C.N.	Y-site	Ce-site	(Ca,Y)-site	(Ca,Ce)-site	Others
6	oct. [2b] YTTRIALITE-(Y)*		[2b] AGRELLITE*	[2b] EUDIALYTE*	oct. [4] BRANNERITE*(U,Y)-site
	oct. [2b] THORTVEITITE			[2b] AGRELLITE*	oct. [4] LOUVERINGITE*(Zr,Ce)-site
	oct. [2b] KEIVIITE-(Y)			[3] DOLLASEITE-(Ce)*	
	oct. [2b] KEIVIITE-(Yb)				
	oct. [2b] HIORTDAHLITE II				
	oct. [2b] MISERITE				
	oct. [2b] MONTEREGIANITE-(Y)				
	oct. [4] DAVIDITE-(Ce)*				
	oct. [4] DAVIDITE-(La)				
7	mtp. [2b] THALENITE-(Y)	[2a] lessingite-(Ce)*	[2a] APATITE*	mo'. [3] MOSANDRITE*	
	mtp. [2b] F-anal. THALENITE-(Y)	[2a] BRITHOLITE-(Ce)*	[2a] chukhrovite-(Ce)*	mo'. [2a] chukhrovite-(Ce)*	
	[3] yftisite	moc. [2b] SAZHINITE-(Ce)			
	[3] KULIOKITE-(Y)				
	mtp. [4] YTTROTUNGSTITE-(Y)*				
8	dod. [2a] XENOTIME-(Y)	[1] CEBAITE-(Ce)	btp. [2b] AGRELLITE*	[2b] AGRELLITE*	
	[2a] WAKEFIELDITE-(Y)	[1] CEBAITE-(Nd)	sap. [2b] HELLANDITE-(Y)*	[3] PERRIERITE*	
	sap. [2a] VYUNTSPAKHKITE-(Y)	[2a] WAKEFELDITE-(Ce)	cub. [4] FERSMITE*	cub. [4] FERSMITE*	
	dod. [2b] KAINOSITE-(Y)	[2a] MONAZITE-(Ce)		sap. [4] VIGEZZITE	
	dod. [2b] CAYSICHITE-(Y)	[2a] MONAZITE-(La)		cub. [4] CALCIOBETAFITE*	
	[2b] THALENITE-(Y)	[2a] MONAZITE-(Nd)		cub. [4] ZIRCONOLITE-*3O**	
	[2b] F-anal. THALENITE-(Y)	boc. [2a] VITUSITE-(Ce)		cub. [4] ZIRCONOLITE-*3T**	
	dod. [2b] ASHCROFTINE-(Y)*	sap. [2a] RETZIAN-(Ce)		cub. [4] ZIRCONOLITE-*2M**	
	btp. [2b] ASHCROFTINE-(Y)*	sap. [2a] RETZIAN-(La)			
	sap. [2b] GADOLINITE-(Y)*	sap. [2a] RETZIAN-(Nd)			
	sap. [2b] HINGGANITE-(Y)*	dod. [2a] RHABDOPHANE-(Ce)			

sap. [2b] HINGGANITE-(Yb)*
sap. [2b] CAPPELENITE-(Y)
sap. [2b] HELLANDITE*
sap. [3] GARNET
[3] ALLANITE-(Y)*
cub. [3] yftisite
[3] KULIOKITE-(Y)
cub. [4] FERGUSONITE-β-(Y)
cub. [4] FERGUSONITE-(Y)
cub. [4] EUXENITE-(Y)
sap. [4] AESCHYNITE-(Y)

dod. [2a] RHABDOPHANE-(La)
dod. [2a] RHABDOPHANE-(Nd)
dod. [2b] CERITE-(Ce)
[2b] PHOSINAITE
sap. [2b] GADOLINITE-(Ce)*
sap. [2b] NORDITE-(La)*
sap. [2b] NORDITE-(Ce)*
sap. [2b] SEMENOVITE-(Ce)*
sap. [2b] TADZHIKITE-(Ce)*
[3] ALLANITE-(Ce)*
cub. [4] FERGUSONITE-β-(Ce)
cub. [4] FERGUSONITE-β-(Nd)
boc. [4] LUCASITE-(Ce)
sap. [4] AESCHYNITE-(Ce)
sap. [4] aeschynite-(Nd)

9 [1] TENGERITE-(Y)
[1] MOYDITE-(Y)
ttp. [2a] BRITHOLITE-(Y)
ttp. [2a] AGARDITE-(Y)*
ttp. [5] GAGARINITE-(Y)*
msa. [5] TVEITITE-(Y)

mcu. [1] SAHAMALITE-(Ce)
ttp. [2a] BELOVITE-(Ce)
ttp. [2a] lessingite-(Ce)*
ttp. [2a] BRITHOLITE-(Ce)
ttp. [2a] FRANÇOISITE-(Nd)
ttp. [2a] AGARDITE-(La)*
[2a] STILLWELLITE-(Ce)
[2b] STEENSTRUPINE-(Ce)
[3] JOAQUINITE-(Ce)
[3] TUNDRITE-(Ce)
[3] TUNDRITE-(Nd)

ttp. [2a] Ca-anal. AGARDITE*

[3] CHEVKINITE*
[3] PERRIERITE*
[3] R-VESUVIANITE*

[2a] CHERALITE*(Zr,Y)-site

10

bap. [1] LANTHANITE-(La)
bap. [1] LANTHANITE-(Ce)
bap. [1] LANTHANITE-(Nd)
163. [1] HUANGHOITE-(Ce)

[1] CALCIOANCYLITE-(Nd)*
154. [1] BURBANKITE*
qtp. [1] CARBOCERNAITE*

C.N.	Y-site	Ce-site	(Ca,Y)-site	(Ca,Ce)-site	Others
		163. [1] baiyuneboite-(Ce)			
		[1] CEBAITE-(Ce)			
		[1] CEBAITE-(Nd)			
		[1] ANCYLITE-(Ce)*			
		[1] CALCIOANCYLITE-(Nd)*			
		[1] GYSINITE-(Nd)*			
		[1] REMONDITE-(Ce)			
		163. [1] DAQINGSHANITE-(Ce)			
		[3] DOLLASEITE-(Ce)*			
		[3] TORNEBOHMITE-(Ce)			
		[3] TORNEBOHMITE-(La)			
11	ptp. [1] BASTNÄSITE-(Y)	ptp. [1] BASTNÄSITE-(Ce)			
		ptp. [1] BASTNÄSITE-(La)			
		[5] FLUOCERITE-(Ce)			
12		363. [4] DAVIDITE-(Ce)*		363. [3] HIBONITE*	
		363. [4] DAVIDITE-(La)*		363. [4] LOVERINGITE*	
				363. [4] CRICHTONITE*	

Numbers in brackets are the class of the mineral groups.
oct.: octahedron (see fig. 94a). moc. monocapped octahedron (fig. 94c). mo'.: monocapped octahedron (fig. 94e). mtp.: monocapped trigonal prism (fig. 94d). dod.: dodecahedron (fig. 94h). sap.: square antiprism (fig. 94i). cub.: cube (fig. 94g). btp.: bicapped trigonal prism (fig. 94j). boc.: bicapped octahedron (fig. 94f). ttp.: tricapped trigonal prism (fig. 94m). msa.: monocapped square antiprism (fig. 94l). mcu.: monocapped cube (fig. 94k). bap.: bicapped square antiprism (fig. 94o, p). 163.: 163-type polyhedron (fig. 94q). 154.: 154-type polyhedron (fig. 94r). qtp.: quadcapped octahedron (fig. 94n). ptp.: pentacapped octahedron (fig. 94s). 363.: 363-type polyhedron (fig. 94t).
*The asterisks indicate the site where the substitutions between rare earths and heterovalent foreign ions are observed.

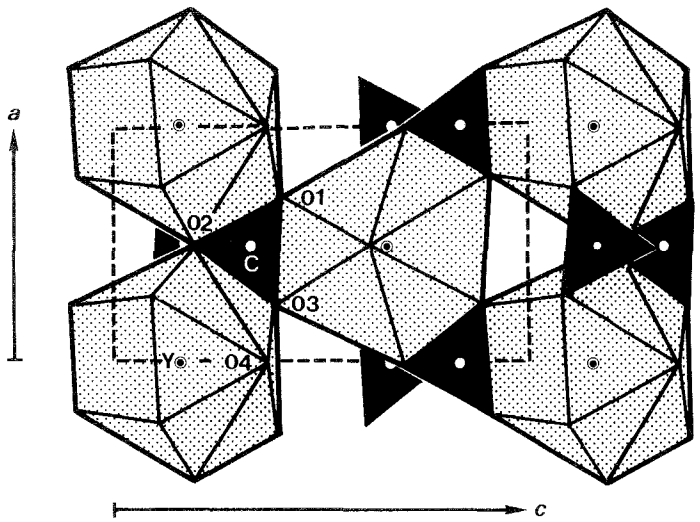

Fig. 93. The crystal structure of $Y(CO_3)(OH)$.

phosphates: e.g., "tengerite-(Y), $Y_2(CO_3)_3 \cdot nH_2O$ ($n = 2$–3) (fig. 1) – lanthanite-(La), $La_2(CO_3)_3 \cdot 8H_2O$ (fig. 4)", "xenotime-(Y), YPO_4 (fig. 19) – monazite-(Ce), $CePO_4$ (fig. 21)", and "ancylite-(Ce) (fig. 13) – the synthetic substance, $Y(CO_3)(OH)$ (Beall and Milligan 1976) (fig. 93)". These minerals do not have infinite framework structures, and the anionic groups in the structures are isolated from each other and are connected by rare earth atoms forming three-dimensional structures. Therefore, the size of the R polyhedron affects the whole structure. In the case of tengerite-(Y) and lanthanite-(La) the difference between the degree of hydration is due to the difference between Y and La.

On the other hand, structures having a tight framework, as seen in the structures of gadolinite-(Y) (fig. 51), allanite-(Ce) (fig. 65) and aeschynite-(Y) (fig. 81), are not affected by the sizes of the R polyhedra, because they can accept R polyhedra of various sizes without rearrangement of the structure.

In addition, the coordination numbers of rare earth atoms tend to increase in the order -silicate, -phosphate, -carbonate. This is explained by a decrease in the bond strengths of the oxygen atoms in SiO_4^{4-}, PO_4^{3-}, and CO_3^{2-} ions, which have average negative charges of -1, $-\frac{3}{4}$, and $-\frac{2}{3}$ per oxygen atom, respectively.

3.2. *Isomorphous substitutions between rare earth ions and non-rare-earth ions, Ca^{2+}, Na^{+}, Th^{4+}, etc.*

As can be seen in table 213, isomorphous substitutions are more frequently observed in minerals rich in Ce-group rare earths than in those rich in Y-group rare earths. This can be explained by the similarity of the ionic radii and coordination numbers of the Ce-group rare earth ions and the calcium and sodium ions, as mentioned in section 3.1. On the other hand, thorium ions tend to be substituted by

Y-group rare earth ions rather than by Ce-group ones in the octahedral sites, as observed in brannerite and davidite-(La).

The mutual substitution of heterovalent ions must be accompanied by compensation of their charge differences. The charge compensation mechanisms found in the structures of rare earth minerals were classified into the following four types:

(1) Substitution accompanying vacancies.

(1.1) $3Ca^{2+} \leftrightarrows 2R^{3+} + \square$.

(1.2) $R^{3+} + \square \leftrightarrows Ca^{2+} + Na^{+}$.

(2) Coupled substitution within a rare earth site.

(2.1) $2R^{3+} \leftrightarrows Ca^{2+} + Th^{4+}$.

(2.2) $2Ca^{2+} \leftrightarrows R^{3+} + Na^{+}$.

(3) Coupled substitution of two independent sites.

(3.1) $R^{3+} + Na^{+} \leftrightarrows Ca^{2+} + Ca^{2+}$.

(3.2) $R^{3+} + Si^{4+} \leftrightarrows Ca^{2+} + (P,As)^{5+}$.

(3.3) $R^{3+} + Al^{3+} \leftrightarrows Ca^{2+} + Si^{4+}$.

(3.4) $R^{3+} + Be^{2+} \leftrightarrows Ca^{2+} + B^{3+}$.

(3.5) $R^{3+} + Be^{2+} \leftrightarrows Ca^{2+} + Al^{3+}$.

(3.6) $R^{3+} + Ti^{4+} \leftrightarrows Ca^{2+} + (Nb,Ta)^{5+}$.

(3.7) $R^{3+} + Mg^{2+} \leftrightarrows Ca^{2+} + Al^{3+}$.

(3.8) $R^{3+} + (OH)^{-} \leftrightarrows Ca^{2+} + H_2O$.

(3.9) $R^{3+} + O^{2-} \leftrightarrows Ca^{2+} + (OH,F)^{-}$.

(4) Substitution accompanying valence variation.

(4.1) $R^{3+} + Fe^{2+} \leftrightarrows Ca^{2+} + Fe^{3+}$.

In almost all rare earth minerals, complex solid solutions result from these isomorphous substitutions. Type (1.1) can be observed in hellandite-(Y) and semenovite-(Ce) combined with type (3.9). Although the range of solid solution is not narrow, a mineral with an end-member composition has not yet been observed. Type (1.2) has been observed only in gagarinite-(Y). Such a substitution accompanying a vacancy site may occur only in crystal structures having tight frameworks formed by covalent bonding, because the number of atoms changes before and after the substitution.

Types (2.1) and (2.2) are the simple ones occurring at an independent site. They are the most common substitutions observed in the crystal structures of rare earth minerals because they do not require any other concomitant substitution. Such examples are observed in aeschynite-(Y), ewaldite and apatite. Although the solid-solution range of type (2.1) is, in general, wide, this type is rarely observed in the case of sesqui-type carbonates.

Type (3.1) is a coupled substitution occurring at two independent sites and is different from type (2.1). This substitution can be observed at the (R,Sr) and (Na,Ca) sites in the crystal structure of carbocernaite.

Types (3.2), (3.3), (3.4) and (3.5) are coupled substitutions, where one of the substitutions occurs at the tetrahedral site. Type (3.2) can be seen in britholite-(Ce) and tritomite-(Ce), and type (3.3) in chukhrovite-(Y). Type (3.4) can be observed in gadolinite-(Y) and homilite, although the ranges of solid solutions are very narrow. Type (3.5) can be observed in yttrian milarite.

In contrast to types (3.2), (3.3), (3.4) and (3.5), types (3.6) and (3.7) are coupled

substitutions occurring at octahedral sites and R-sites. Many titanates, such as polycrase-(Y), euxenite-(Y) and aeschynite-(Y), contain complex solid solutions of type (3.6) and others. The complex solid solutions with combinations of (3.6), (2.1), and (3.8) or (3.9) make it especially difficult to study their chemical compositions and crystal structures. A comparison of the chemical formula of many hibonite samples (Fleischer and Mandarino 1991) with the crystal structure of synthetic $CaAl_{12}O_{19}$ (Utsunomiya et al. 1988) suggests that hibonite may contain a solid solution of type (3.7).

Types (3.8) and (3.9) accompany isomorphous substitutions at the anion sites. The coupled substitution of type (3.8) can be observed only in ancylite-(Ce), while that of type (3.9) is frequently observed in many minerals such as Ca-rich agardite and fersmite. The former can occur in crystal structures containing isolated hydroxyl ions, which are rarely seen.

Type (4.1) is a substitution proposed by Ito and Hafner (1974) for solid solutions of the gadolinite series.

3.3. *Coordination polyhedra of rare earth atoms*

As mentioned in section 3.1, the rare earth atoms exhibit seven kinds of coordination numbers with anions, from 6 to 12. The shapes of the coordination polyhedra of rare earth atoms are, in almost all cases, not regular polyhedra, but rather distorted polyhedra, except for the cases in which rare earth atoms lie in highly symmetric special positions of a space group, because bonds between rare earth atoms and anions are ionic rather than covalent, and their coordination numbers are high. Considering the distortion of the polyhedra, the coordination polyhedra composed of rare earths (R) and surrounding anions (X) may be classified into the following 21 groups, from form (a) to form (u), including some imaginary forms [the numbers in parentheses are the number of vertices in a plane at each horizontal level, e.g., 1 is point (•), 2 is line (——), 3 is triangle (▲) and 4 is square (■)]; a trigonal prism is defined by two triangular planes, thus, it is expressed by (33), and the prime " ′ ", means "anti-" situation:

(1) RX_6	(a)	octahedron (trigonal antiprism)	(33′) or (141),
	(b)	trigonal prism	(33),
(2) RX_7	(c)	monocapped octahedron	(133′),
	(d)	monocapped trigonal prism	(313) or (142),
	(e)	distorted monocapped trigonal prism	(142),
(3) RX_8	(f)	bicapped octahedron	(3113′),
	(g)	cube	(44),
	(h)	dodecahedron	(22′22′),
	(i)	square antiprism	(44′),
	(j)	bicapped trigonal prism	(323),
(4) RX_9	(k)	monocapped cube	(144),
	(l)	monocapped square antiprism	(144′),
	(m)	tricapped trigonal prism	(333),

(5) RX_{10}	(n)	tetracapped trigonal prism	(13231),
	(o)	bicapped square antiprism	(144′1),
	(p)	bicapped dodecahedron	(22′42′),
	(q)	hexagonal pyramid with triangle	(163),
	(r)	pentagonal pyramid with square	(154),
(6) RX_{11}	(s)	pentacapped trigonal prism	(13331),
(7) RX_{12}	(t)	tetracapped cube	(444) or (363),
	(u)	icosahedron	(3333).

Illustrations of these polyhedra are given in fig. 94.

The octahedron (a) is a typical coordination polyhedron for six-coordinated rare earths. Examples of this coordination are yttrium-group rare earth sites in yttrialite-(Y), thortveitite, keiviite-(Y), -(Yb), miserite and monteregianite-(Y). Although octahedral calcium sites partially substituted by Ce-group rare earths are found in agrellite and dollaseite-(Ce), no octahedral site dominantly occupied by Ce-group rare earths has been reported. An octahedral site would be too small for the larger Ce-group rare earths to compensate their trivalent charge. It is worth noting that no trigonal prism (b) has been reported as the coordination polyhedron of a rare earth atom.

Two kinds of polyhedra have been reported for seven-coordinated rare earth atoms, the monocapped octahedra (c) and the monocapped trigonal prisms (d). These coordination polyhedra can be derived from an octahedron (a) and a trigonal prism (b), respectively, by the addition of one vertex on a face. Coordinations of rare earth atoms in sazhinite-(Ce) and chukhrovite-(Ce) were described as monocapped octahedra (Shumyatskaya et al. 1980, Mathew et al. 1981), and that of yttrotungstite-(Y) was described as a monocapped trigonal prism (Davis and Smith 1971). Thalenite-(Y) and its F-analogue have three Y sites in their structures, of which two are seven-coordinated and one is eight-coordinated. Kornev et al. (1972) reported that the coordination polyhedra of the seven-coordinated Y2 sites in thalenite-(Y) exhibit a trigonal prism plus a semi-octahedron (d). Yakubovich et al. (1988) reported that the polyhedra of the two independent seven-coordinated Y sites in the F-analogue of thalenite are a trigonal prism with a semi-octahedron on a side face and an octahedron with a pyramid on one of the faces, i.e. a monocapped octahedron (c). A distorted trigonal prism with a semi-octahedron corresponds to the form (e), a square with one vertex on one side and two on another side, which was used in the description of the seven-coordinated (Ca,Ce) site in mosandrite by Galli and Alberti (1971). Distorted polyhedra of these three types, (c), (d), (e), resemble each other, and are often difficult to distinguish clearly.

The eight-coordination polyhedra include a bicapped octahedron (f), a cube (g), a D_{2d} (or Δ)-dodecahedron (h), a square antiprism (i) or a bicapped trigonal prism (j). The bicapped octahedron (f) is found in the structures of vitusite-(Ce) and lucasite-(Ce). Fergusonite-β-(Y), euxenite-(Y), fersmite and the zirconolite-group minerals have distorted cubic coordinations of the rare earth sites in their structures. The cube (g) can be derived from a distorted bicapped octahedron (f) by flattening the six pairs of triangles to squares. The D_{2d} (or Δ)-dodecahedron (h) is one of the most

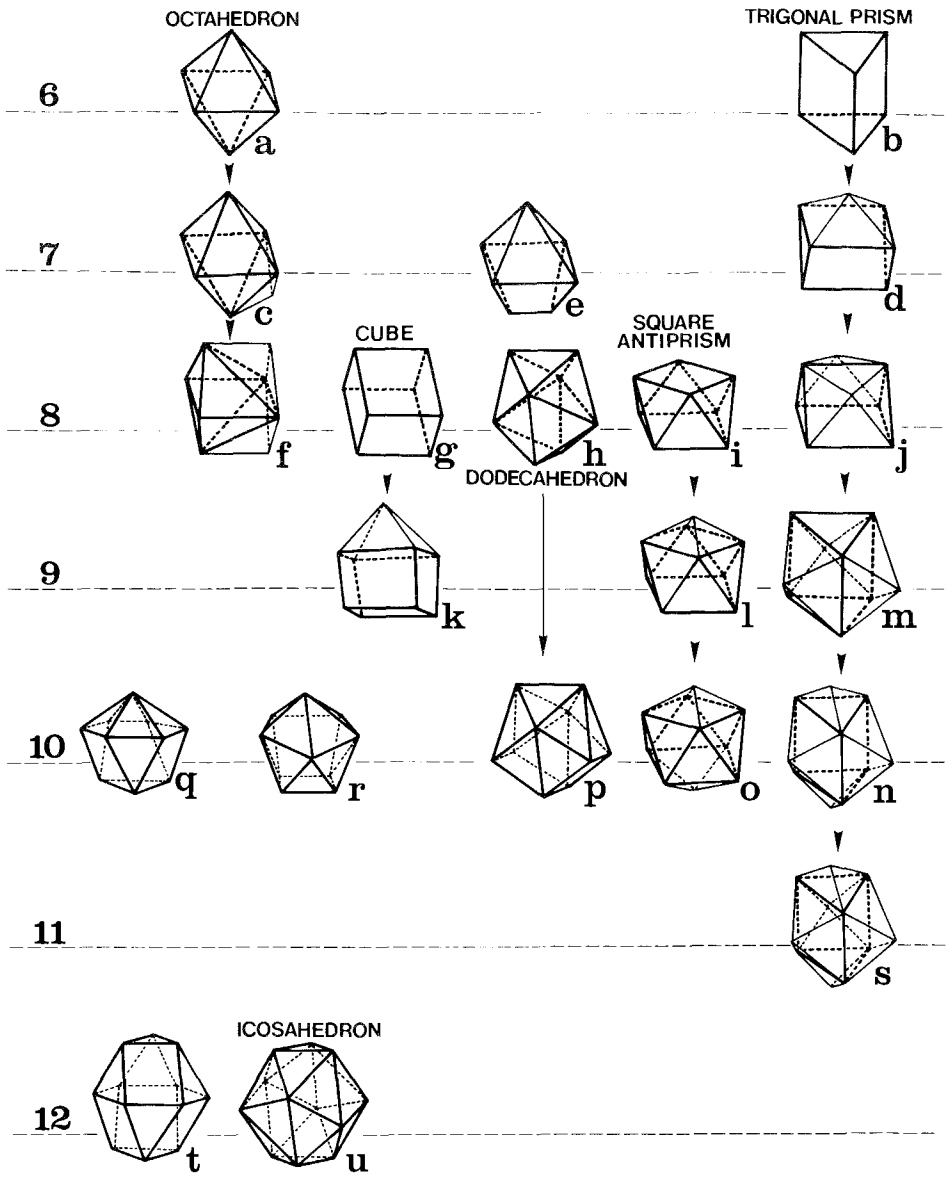

Fig. 94. The coordination polyhedra of rare earth atoms in the crystal structures of rare earth minerals.

frequently observed polyhedra of eight-coordinated rare earth sites. The crystal structures of kainosite-(Y), xenotime-(Y), cerite-(Ce) and so on, contain this type of polyhedron. Ghose and Wan (1979) described the irregular coordination polyhedra of (Ca,R) sites in agrellite as a square pyramid with a triangle above the equatorial

plane, which corresponds to type (143) according to the rule mentioned above. This type of polyhedron can also be described as a distorted bicapped trigonal prism (j); a square in the equatorial plane of a square pyramid and two vertices of a triangle form a trigonal prism, and the top of the pyramid and one vertex of the triangle form two caps. Ashcroftine-(Y) (Moore et al. 1987) has two Y-sites in the structure. One of them is a D_{2d}-dodecahedron (h), and the other is an eight-coordinated bicapped trigonal prism (j) if we assume that the occupancies of the distorted anion sites are full in all of them. The bicapped trigonal prism (j) can be converted to a square antiprism (i) by flattening the pair of triangles of the two caps (upper triangles in fig. 94j) to a square. The square antiprisms (i) are often found in rare earth minerals, such as gadolinite-(Y), nordite-(Ce), hellandite-(Y) and aeschynite-(Ce). Coordination polyhedra of D_{2d}-dodecahedron (h), square antiprism (i) and cube (g) are found in both Y- and Ce-group rare earth sites.

Tricapped trigonal prisms (m) are frequently found in the nine-coordinated rare earth sites. A typical example is the $YO_6(OH)_3$ polyhedron in agardite-(Y). This type of polyhedron is also found in the structures of belovite-(Ce), françoisite-(Nd) and gagarinite-(Y). The crystal structure of tveitite-(Y) contains monocapped square antiprisms (l), and that of sahamalite-(Ce) contains monocapped cubes (k).

The pentacapped trigonal prism (n) can be derived from a bicapped trigonal prism (j) by addition of two vertices on the top and bottom triangular faces, and is observed in the crystal structure of carbocernaite. Dal Negro et al. (1977) reported that the shape of the R polyhedra in lanthanite-(La) can be approximately described as a distorted Archimedean antiprism whose square faces are replaced by pyramids. This shape can be described, in other words, as a bicapped square antiprism (o). However, Shinn and Eick (1968) described the lanthanum polyhedra in their synthetic lanthanite-(Y) as a polyhedron which is derived from a D_{2d}-dodecahedron by splitting two vertices to form a pair of neighboring square faces (fig. 94p). The rare earth polyhedron in huanghoite-(Ce) and daqingshanite-(Ce) is a hexagonal pyramid with a triangle (q). Effenberger et al. (1985) reported that the B site in burbankite occupied with Ca and R atoms, forms a combination of a pentagonal pyramid and a square (r).

The coordination polyhedron of the Ce site in bastnäsite-(Ce) is a pentacapped trigonal prism (s). This polyhedron can be derived from a tricapped prism (m) by the addition of two vertices on the two triangular faces of the prism.

A twelve-coordination polyhedron which consists of a hexagon and two triangles (t) was reported for the Ce site in davidite-(Ce) and the (Ca,Ce) sites in loveringite and hibonite. This polyhedron is closely related to the icosahedron (u).

4. Summary and conclusion

About one hundred crystal structures of rare earth minerals are described, classified, and discussed in this review. In addition, all known rare earth minerals are included in the list. Brief comments on the isomorphous substitutions between rare earth atoms and other ions and coordination polyhedra of rare earth atoms are given from the viewpoint of crystal chemistry.

The rare earth minerals were classified in the following five classes with a few exceptions:

(1) Minerals with crystal structures containing isolated triangular anionic groups: for example, bastnäsite-(Ce), ancylite-(Ce).
(2) Minerals with crystal structures containing tetrahedral anionic groups: for example, monazite-(Ce), gadolinite-(Y).
(3) Minerals with crystal structures containing anionic groups of tetrahedral and octahedral ions: for example, allanite-(Ce), mosandrite.
(4) Minerals with crystal structures containing anionic groups of octahedral ions: for example, fergusonite-(Y), euxenite-(Y).
(5) Minerals with crystal structures without anionic groups: for example, fluocerite-(Ce).

The coordination numbers of the Ce-group rare earths are similar to those of calcium and are generally higher than those of Y-group rare earths. Consequently, the isomorphous substitution between Ce-group rare earths and calcium is more commonly observed than that between Y-group rare earths and calcium. The structures of Y-group rare earth minerals are different from those of Ce-group rare earth minerals when these structures belong to classes 1 and 2(*a*) owing to the difference in the ionic radii between the two groups, even if the chemical formulae of the two minerals are similar.

The isomorphous substitutions between rare earths and the other heterovalent ions found in the crystal structures of rare earth minerals can be summarized as in the following four groups: (1) substitution accompanying vacancies, (2) coupled substitution within a rare earth site, (3) coupled substitution at two independent sites and (4) substitution accompanying valence variations.

The rare earth atoms exhibit seven kinds of coordination numbers, from 6 to 12, in the crystal structures of rare earth minerals. The coordination polyhedra were classified in 21 subgroups from form (a) to form (u), including some imaginary forms, and graphical depictions and mineralogical examples of each form have been given.

Acknowledgments

We dedicate this work to the late Prof. Kozo Nagashima, a pioneer of the chemistry of rare earth minerals in Japan.

The authors wish to express their sincere thanks to Dr. Akira Kato, Dr. Ernest H. Nickel, Prof. Donald M. Burt and Prof. LeRoy Eyring for their review of the manuscript. Their kind suggestions and important information are quite useful to complete this manuscript. Special thanks are extended to Prof. Zhang Pei-shan, Prof. Josef Zemann, Prof. Peter Bayliss, Dr. Roy Kristiansen, Prof. Kichiro Koto, Prof. Hiroshi Takeda, and Prof. Yoshinori Sugitani for their helpful and important information concerning literature on rare earth minerals.

We are indebted to Prof. Jiro Shiokawa, Prof. Gin-ya Adachi, Dr. Shozo Shibata and Dr. Shinji Tomura for their encouragement.

References

Adams, J.W., T. Botinelly, W.N. Sharp and K. Robinson, 1974, Am. Mineral. **59**, 172.

Adusumilli, M.S., C. Kieft and E.A.J. Burke, 1974, Mineral. Mag. **39**, 571.

Afanasiev, M.L., S.P. Habuda and A.G. Lundin, 1972, Acta Crystallogr. B **28**, 2903.

Akimoto, J., A. Uejima and Y. Sugitani, 1986, J. Mineral. Soc. Jpn. **17**, 159.

Aleksandrov, V.B., 1960, Dokl. Akad. Nauk SSSR **132**, 597.

Aleksandrov, V.B., 1962, Dokl. Akad. Nauk SSSR **142**, 107.

Armbruster, T., C. Bühler, S. Graeser, H.A. Stalder and G. Amthauer, 1988, Schweiz. Mineral. Petrogr. Mitt. **68**, 125.

Aruga, A., and I. Nakai, 1985, Acta Crystallogr. C **41**, 161.

Bakakin, V.V., N.V. Belov, S.V. Borisov and L.P. Solovyeva, 1970, Am. Mineral. **55**, 1167.

Balko, V.P., and V.V. Bakakin, 1975, Zh. Strukt. Khim. **16**, 837.

Batalieva, N.G., and Yu.A. Pyatenko, 1967, Zh. Strukt. Khim. **8**, 548.

Batalieva, N.G., and Yu.A. Pyatenko, 1972, Sov. Phys. Crystallogr. **16**, 786.

Batalieva, N.G., G.K. Krivokoneva, I.A. Bondar' and G.A. Sidorenko, 1969, Dokl. Akad. Nauk SSSR **189**, 615.

Baudracco-Gritti, C., S. Quartieri, G. Vezzalini, F. Permingeat, F. Pillard and R. Rinaldi, 1987, Bull. Minéral. (France) **110**, 657.

Bayliss, P., and A.A. Levinson, 1988, Am. Mineral. **73**, 422.

Bayliss, P., F. Mazzi, R. Munno and T.J. White, 1989, Mineral. Mag. **53**, 565.

Beall, G.W., and W.O. Milligan, 1976, Acta Crystallogr. B **32**, 3143.

Bennett, J.M., and J.V. Smith, 1969, Mater. Res. Bull. **4**, 343.

Bevan, D.J.M., J. Strähle and O. Greis, 1982, J. Solid State Chem. **44**, 75.

Bevins, R.E., G. Rowbothan, F.S. Stephens, S. Turgoose and P.A. Williams, 1985, Am. Mineral. **70**, 411.

Bianchi, R., T. Pilati, V. Diella, C.M. Gramaccioli and G. Mannucci, 1988, Am. Mineral. **73**, 601.

Bjørlykke, H., 1937, Nor. Geol. Tidsskr. **17**, 47.

Boggs, R.C., 1980, Am. Mineral. **65**, 1138.

Bonazzi, P., C. Garbarino and S. Menchetti, 1992, Eur. J. Mineral. **4**, 23.

Bordet, P., A. Mchale, A. Santoro and R.S. Roth, 1986, J. Solid State Chem. **64**, 30.

Borisov, S.V., and R.F. Klevtsova, 1963, J. Struct. Chem. **4**, 575.

Bowles, J.F.W., and D.J. Morgan, 1984, Mineral. Mag. **48**, 146.

Bowles, J.F.W., E.A. Jobbins and B.R. Young, 1980, Mineral. Mag. **43**, 885.

Bulakh, A.G., V.V. Kondrat'eva and E.N. Baranova, 1961, Zap. Vses. Mineral. Ova. **90**, 42.

Burt, D.M., 1989, Reviews in Mineralogy, Vol. 21 (Mineralogical Society of America, Washington, DC) pp. 259.

Bussen, I.V., L.F. Gannibal, E.A. Goiko, A.N. Mer'kov and A.P. Nedorezova, 1972, Zap. Vses. Mineral. Ova. **101**, 75.

Calvo, C., and R. Faggiani, 1974, Am. Mineral. **59**, 1277.

Calvo, C., and R. Gopal, 1975, Am. Mineral. **60**, 120.

Cannillo, E., F. Mazzi and G. Rossi, 1972, Tschermaks Mineral. Petrogr. Mitt. **17**, 233.

Carron, M.K., C.R. Naeser, H.J. Rose Jr and F.A. Hildebrand, 1958, Geol. Surv. Bull. **1036**, 253.

Cerny, P., F.C. Hawthorne, J.L. Jambor and J.D. Grice, 1991, Can. Mineral. **29**, 533.

Cesbron, F., C. Gilles, P. Pelisson and J.-C. Saugues, 1988, C.R. Hebd. Séances Acad. Sci. C (Paris) **307**, 915.

Chabot, B., and H. Sarp, 1985, Z. Kristallogr. **171**, 155.

Chao, G.Y., 1978, Can. Mineral. **16**, 561.

Chao, G.Y., P.R. Mainwaring and J. Baker, 1978, Can. Mineral. **16**, 335.

Cheetham, A.K., B.E.F. Fender, H. Fuess and A.F. Wright, 1976, Acta Crystallogr. B **32**, 94.

Chemical Abstracts, Chemical Abstracts Service, 2540 Olentangy River Road, P.O. Box 3012, Columbus, OH 43210.

Chen, T.T., and G.Y. Chao, 1975, Can. Mineral. **13**, 93.

Chernitsova, N.M., Z.V. Pudovkina and Yu.A. Pyatenko, 1982, Sov. Phys.-Dokl. **27**, 367.

Chistyakova, N.B., V.A. Moleva and Z.P. Razmanova, 1966, Dokl. Akad. Nauk SSSR **169**, 1421.

Christensen, A.N., 1973, Acta Chem. Scand. **27**, 2973.

Church, A.H., 1865a, Chem. News **12**, 121.

Church, A.H., 1865b, J. Chem. Soc. London **3**, 259.

Claringbull, G.F., and M.H. Hey, 1953, Mineral. Mag. **30**, 211.
Cocco, G., L. Fanfani and P.F. Zanazzi, 1967, Z. Kristallogr. **124**, 385.
Crook III, W.W., 1976, Mineral. Rec., p. 182.
Crook III, W.W., R.C. Ewing and A.J. Ehlmann, 1978, Am. Mineral. **63**, 754.
Cruickshank, D.W.J., H. Lynton and G.A. Barclay, 1962, Acta Crystallogr. **15**, 491.
Cummings, J.P., and S.H. Simonsen, 1970, Am. Mineral. **55**, 90.
Dal Negro, A., G. Rossi and V. Tazzoli, 1975, Am. Mineral. **60**, 280.
Dal Negro, A., G. Rossi and V. Tazzoli, 1977, Am. Mineral. **62**, 142.
Davis, R.J., and G.W. Smith, 1971, Mineral. Mag. **38**, 261.
De Rango, C., G. Tsoucaris and C. Zelwer, 1966, C.R. Hebd. Séances Acad. Sci. C (Paris) **263**, 64.
Deliens, M., and P. Piret, 1977, Bull. Soc. Fr. Mineral. Cristallogr. **100**, 39.
Deliens, M., and P. Piret, 1982, Can. Mineral. **20**, 231.
Deliens, M., and P. Piret, 1986a, Bull. Minéral. (France) **109**, 305.
Deliens, M., and P. Piret, 1986b, Bull. Minéral. (France) **109**, 643.
Deliens, M., and P. Piret, 1989, Eur. J. Mineral. **1**, 85.
Deliens, M., and P. Piret, 1990, Eur. J. Mineral. **2**, 407.
Desautels, P.E., 1967, Am. Mineral. **52**, 860.
Dexpert, H., M. Lemaitre-Blaise and P. Caro, 1972, Reactivity of Solids (Chapman and Hall, London).
Dietrich, J.E., M. Orliac and F. Permingeat, 1969, Bull. Soc. Fr. Mineral. & Cristallogr. **92**, 420.
Ding, X., G. Bai, Z. Yuan and L. Sun, 1981, Geol. Rev. China **27**, 459.
Doelter, C., 1912, Handbuch der Mineralchemie, Band II (Theodor Steinkopff, Dresden und Leipzig) p. 191.
Dollase, W.A., 1968, Am. Mineral. **53**, 1882.
Dollase, W.A., 1969, Am. Mineral. **54**, 710.
Dollase, W.A., 1971, Am. Mineral. **56**, 447.
Donnay, G., 1953, Am. Mineral. **38**, 868.
Donnay, G., and R. Allmann, 1970, Am. Mineral. **55**, 1003.
Donnay, G., and J.D.H. Donnay, 1953, Am. Mineral. **38**, 932.
Donnay, G., and H. Preston, 1971, Tschermaks Mineral. Petrog. Mitt. **15**, 201.
Dowty, E., 1975, Am. Mineral. **60**, 872.
Dunn, P.J., 1985, Am. Mineral. **70**, 1333.
Dunn, P.J., and B.D. Sturman, 1982, Am. Mineral. **67**, 841.
Dunn, P.J., D.R. Peacor and W.B. Simmons, 1984, Mineral. Mag. **48**, 533.
Effenberger, H., F. Kluger, H. Paulus and E.R. Wölfel, 1985, Neues. Jahrb. Miner. Monatsh. **1985**, 161.
Efimov, A.F., V.D. Dusmatov, V.Yu. Alkhazov, Z.G. Pudovkina and M.E. Kazakova, 1970, Dokl. Akad. Nauk SSSR **195**, 1190.
Embrey, P.G., and J.P. Fuller, 1980, A Manual of New Mineral Names 1892–1978. British Museum, Natural History (Oxford University Press, London).
Emiraliev, A., A.G. Kocharov, R.V. Bakradze, I. Karimov and Z.I. Akhmedzhanov, 1976, Sov. Phys. Crystallogr. **21**, 112.
Eremenko, G.E., and V.A. Bel'ko, 1982, Zap. Vses. Mineral. Ova. **111**, 321.
Ermilova, L.P., V.A. Moleva and R.F. Klevtsova, 1960, Zap. Vses. Mineral. Ova. **89**, 15.
Eskova, E.M., E.I. Semenov, A.P. Khomyakov, M.E. Kazakova and O.V. Sidorenko, 1974, Zap. Vses. Mineral. Ova. **103**, 571.
Ewing, R.C., 1976, Can. Mineral. **14**, 111.
Farkas, L., Z. Maksimović and Gy. Pantó, 1985, Neues. Jahrb. Mineral. Monatsh. **1985**, 298.
Fehr, T., and R. Hochleitner, 1984, Lapis **1/84**, 22, 37.
Feldman, L.G., S.Sh. Sarkisian, V.P. Boriskin, S.P. Purusova, N.V. Khoay and C.C. Ben, 1987, Mineral. Zh. **9**, 78.
Felsche, J., 1970, Naturwissensch. **57**, 127.
Finger, L.W., and E. Prince, 1975, Nat. Bur. Stand. US Tech. Note **854**, 54.
Finney, J.J., and N.N. Rao, 1967, Am. Mineral. **52**, 13.
Fisher, F.G., and R. Meyrowitz, 1962, Am. Mineral. **47**, 1346.
Fitzgerald, S., P.B. Leavens, A.L. Rheingold and J.A. Nelen, 1987, Am. Mineral. **72**, 625.
Fitzpatrick, J., 1986, Powder Diffraction, **1**, 330.
Fitzpatrick, J., and A. Pabst, 1986, Am. Mineral. **71**, 188.
Fleischer, M., and J.A. Mandarino, 1991, Glossary of Mineral Species, 1991 (The Mineralogical Record Inc., Tucson, AZ).
Foit Jr, F.F., and G. Gibbs, 1975, Z. Kristallogr. **141**, 375.
Fontan, F., and R. Pierrot, 1982, Bull. Minéral. (France) **105**, 701.

Foord, E.E., M.H. Staatz and N.M. Conklin, 1984, Am. Mineral. **69**, 196.
Foord, E.E., R.V. Gaines, J.G. Crock, W.B. Simmons Jr and C.P. Barbosa, 1986, Am. Mineral. **71**, 603.
Frondel, C., 1961, Can. Mineral. **6**, 576.
Fu, P., and X. Su, 1987, Acta Mineral. Sin. **7**, 289.
Fu, P., Y. Kong, G. Gong, M. Shao and J. Qian, 1987, Acta Mineral. Sin. **7**, 298.
Galli, E., and A. Alberti, 1971, Acta Crystallogr. B **27**, 1277.
Gard, J.A., and H.F.W. Taylor, 1957, Mineral. Mag. **31**, 611.
Gatehouse, B.M., I.E. Grey, J.F. Lovering and D.A. Wark, 1977, Proc. 8th Lunar Science Conference (U.S.A.), p. 1831.
Gatehouse, B.M., I.E. Grey, I.H. Campbell and P. Kelly, 1978, Am. Mineral. **63**, 28.
Gatehouse, B.M., I.E. Grey and P.R. Kelly, 1979, Am. Mineral. **64**, 1010.
Gay, P., 1957, Mineral. Mag. **31**, 455.
Geijer, P., 1927, Sver. Geol. Unders. Arsb. **20**, 1.
Geller, S., and M.A. Gilleo, 1957, Acta Crystallogr. **10**, 787.
Genkina, E.A., Yu.A. Malinovskii and A.P. Khomyakov, 1991, Sov. Phys. Crystallogr. **36**, 19.
Gettmann, W., and O. Gries, 1978, J. Solid State Chem. **26**, 255.
Ghose, S., and C. Wan, 1979, Am. Mineral. **64**, 563.
Ghose, S., P.K. Sen Gupta and C.F. Campana, 1987, Am. Mineral. **72**, 365.
Ghouse, K.M., 1968, Indian J. Pure Appl. Phys. **6**, 265.
Ginderow, P.D., 1989, Acta Crystallogr. C **45**, 185.
Giuseppetti, G., and C. Tadini, 1990, Neues Jahrb. Mineral. Monatsh. **1990**, 301.
Giuseppetti, G., F. Mazzi and C. Tadini, 1971, Tschermaks Mineral. Petrogr. Mitt. **16**, 105.
Giuseppetti, G., C. Tadini and M. Oddone, 1989, Neues Jahrb. Mineral. Monatsh. **1989**, 153.
Golyshev, V.M., V.I. Simonov and N.V. Belov, 1971, Sov. Phys. Crystallogr. **16**, 70.
Golyshev, V.M., V.I. Simonov and N.V. Belov, 1973, Sov. Phys. Crystallogr. **17**, 993.
Gottardi, G., 1960, Am. Mineral. **45**, 1.
Graeser, S., and H. Schwander, 1987, Schweiz. Mineral. Petrogr. Mitt. **67**, 103.
Graeser, S., H. Schwander and H.A. Stalder, 1974, Mineral. Mag. **39**, 145.
Graeser, S., H. Schwander, H. Hänni and V. Mattioli, 1979, Mineral. Mag. **43**, 459.
Graham, A.R., 1955, Am. Mineral. **40**, 560.
Gregson, D., C.R.A. Catlow, A.V. Chadwick, G.H. Lander, A.N. Cormack and B.E.F. Fender, 1983, Acta Crystallogr. B **39**, 687.
Grew, E.S., E.J. Essene, D.R. Peacor, S.-C. Su and M. Asami, 1991, Am. Mineral. **76**, 1990.
Grey, I.E., D.J. Lloyd and J.S. White Jr, 1976, Am. Mineral. **61**, 1203.
Grice, J.D., and T.S. Ercit, 1986, Can. Mineral. **24**, 675.
Grice, J.D., and G. Perrault, 1975, Can. Mineral. **13**, 209.
Grice, J.D., R.B. Ferguson and F.C. Hawthorne, 1976, Can. Mineral. **14**, 540.
Grice, J.D., J. van Velthuizen, P.J. Dunn, D.E. Newbury, E.S. Etz and C.H. Nielsen, 1986, Can. Mineral. **24**, 665.
Guillemin, C., and R. Pierrot, 1957, Bull. Soc. Fr. Mineral. Crystallogr. **80**, 549.
Haggerty, S.E., and A.N. Mariano, 1983, Contrib. Mineral. Petrol. **84**, 365.
Hak, J., Z. Johan, M. Kuacek and W. Liebscher, 1969, Neues Jahrb. Mineral. Monatsh. **1969**, 201.
Harkins, W.D., 1917, J. Am. Chem. Soc. **39**, 856.
Hawthorne, F.C., and H.D. Grundy, 1973, Acta Crystallogr. B **29**, 2615.
Hawthorne, F.C., M. Kimata, P. Černý, N. Ball, G.R. Rossman and J.D. Grice, 1991, Am. Mineral. **76**, 1836.
Hess, H., 1983, Neues Jahrb. Mineral. Monatsh. **1983**, 385.
Hey, M.H., C. Milton and E.J. Dwornik, 1982, Mineral. Mag. **46**, 493.
Hogarth, D.D., 1977, Am. Mineral. **62**, 403.
Hogarth, D.D., and N. Miles, 1969, Can. Mineral. **10**, 136.
Hölzel, A.R., 1989, Systematics of Minerals (Mainz, Germany).
Hughes, J.M., M. Cameron and A.N. Mariano, 1991, Am. Mineral. **76**, 1165.
Hutton, C.O., 1957, Am. Mineral. **42**, 342.
Ito, J., 1968, Am. Mineral. **53**, 890.
Ito, J., and J.E. Arem, 1971, Am. Mineral. **56**, 307.
Ito, J., and S.S. Hafner, 1974, Am. Mineral. **59**, 700.
Ito, J., and H. Johnson, 1968, Am. Mineral. **53**, 1940.
Ito, T., and H. Mori, 1953, Acta Crystallogr. **6**, 24.
Jaffe, H.W., and V.J. Molinski, 1962, Am. Mineral. **47**, 9.
Jaffe, H.W., R. Meyrowitz and H.T. Evans Jr, 1953, Am. Mineral. **38**, 741.

Kalita, A.P., 1957, Dokl. Akad. Nauk SSSR **17**, 120.

Kalsbeek, N., S. Larsen and J.G. Rønsbo, 1990, Z. Kristallogr. **191**, 249.

Kapustin, Yu.L., 1986, Nov. Dannye Mineral. **33**, 43.

Karpov, O.G., D.Yu. Pushcharovskii, A.P. Khomyakov, E.A. Pobedimskaya and N.V. Belov, 1980, Sov. Phys. Crystallogr. **25**, 650.

Kato, A., 1989, Abstracts 1989 Annual Meeting, Mineral. Soc. Jpn., pp.103.

Kato, A., and K. Nagashima, 1970, Introduction to Japanese minerals, Geol. Surv. Jpn. pp. 39, 85 and 86.

Kato, K., and H. Saalfeld, 1968, Neues Jahrb. Mineral. Abh. **109**, 192.

Kheirov, M.B., Kh.S. Mamedov and N.V. Belov, 1963, Dokl. Akad. Nauk SSSR **150**, 103.

Kimura, K., 1922, J. Geol. Soc. Tokyo **29**, 316.

Kinzhibalo, L.N., V.K. Trunov, A.A. Evdokimov and V.G. Krongauz, 1982, Sov. Phys. Crystallogr. **27**, 22.

Kirillov, A.S., 1964, Dokl. Akad. Nauk SSSR **159**, 1048.

Klevtsova, R.F., and S.V. Borisov, 1964, J. Struct. Chem. **5**, 137.

Kokkoros, M.P., 1942, Prakt. Akad. Athenon **17**, 163.

Komkov, A.I., 1959, Sov. Phys. Crystallogr. **4**, 796.

Kondratyuk, I.P., A.A. Loshmanov, L.A. Muradyan, B.A. Maksimov, M.I. Sirota, E.A. Krivandina and B.P. Sobolev, 1988, Sov. Phys. Crystallogr. **33**, 57.

Kornev, A.N., N.G. Batalieva, B.A. Maksimov, V.V. Ilyukhin and N.V. Belov, 1972, Sov. Phys. Dokl. **17**, 88.

Kostov, I., 1968, Mineralogy (Oliver and Boyd, Edinburgh).

Krol, O.F., V.I. Chernov, Yu.V. Shipovalov and G.A. Khan, 1964, Zap. Vses. Mineral. Ova. **93**, 147.

Krstanović, I., 1965, Z. Kristallogr. **121**, 315.

Krutik, V.M., D.Yu. Pushcharovskii, A.P. Khomyakov, E.A. Pobedimskaya and N.V. Belov, 1981, Sov. Phys. Crystallogr. **26**, 679.

Kuz'menko, M.V., and S.I. Kozhanov, 1959, Tr. Inst. Mineral. Geokhim. & Kristallokhim. Redk. Elem. **2**, 95.

Lapin, A.V., A.A. Malyshev, V.V. Ploshko and G.Ye. Cherepivskaya, 1986, Dokl. Akad. Nauk SSSR **290**, 1212.

Laubmann, H., 1923, Geol. Landesunters. München **35**, 193.

Lefebvre, J.-J., and C. Gasparrini, 1980, Can. Mineral. **18**, 301.

Lepierre, C., 1937, Mem. Acad. Cien. Lisboa, Cl. Cien. **1**, 361, 374.

Levinson, A.A., 1966, Am. Mineral. **51**, 152.

Li, D., P. Wang and J. Liu, 1981, J. Chin. Silicate Soc. **9**, 422.

Li, F.H., and H.J. Fan, 1982, Acta Phys. Sin. **31**, 1206.

Li, F.H., and H. Hashimoto, 1984, Acta Crystallogr. B **40**, 454.

Li, T., V.I. Simonov and N.V. Belov, 1965, Dokl. Akad. Nauk SSSR **162**, 1288.

Lima de Faria, J., 1964, Estud. Ensaios Doc. **112**, 33.

Livingstone, A., D. Atkin, D. Hutchison and H.M. Al-Hermezi, 1976, Mineral. Mag. **40**, 441.

Lovering, J.F., et al., 1971, Proc. 2nd Lunar Science Conf. Vol. 1, p. 39.

Makarochkin, B.A., 1972, Zap. Vses. Mineral. Ova. **101**, 474.

Maksimov, B.A., L.A. Muradyan and V.I. Simonov, 1986, Crystallography and Crystal Chemistry (Nauka, Moscow) p. 215. In Russian.

Maksimović, Z., and Gy. Pantó, 1983, Trav. Com. Int. Etude Bauxites, Oxydes & Hydroxydes Alum. **13**, 191.

Maksimović, Z., and Gy. Pantó, 1985, Mineral. Mag. **49**, 717.

Mansmann, M., 1965, Z. Kristallogr. **122**, 375.

Marezio, M., J.P. Remeika and P.D. Dernier, 1968, Acta Crystallogr. B **24**, 1670.

Mathew, M., S. Takagi, K.R. Waerstad and A.W. Frazier, 1981, Am. Mineral. **66**, 392.

Mayer, H.J., 1969, Z. Kristallogr. **128**, 183.

Mazzi, F., and R. Munno, 1983, Am. Mineral. **68**, 262.

Mazzi, F., L. Ungaretti, A. Dal Negro, O.V. Petersen and J.G. Rønsbo, 1979, Am. Mineral. **64**, 202.

Mellini, M., and S. Merlino, 1977, Am. Mineral. **62**, 89.

Mellini, M., and S. Merlino, 1978, Can. Mineral. **16**, 81.

Mellini, M., and S. Merlino, 1982, Am. Mineral. **67**, 604.

Mellini, M., S. Merlino, P. Orlandi and R. Rinaldi, 1982, Am. Mineral. **67**, 599.

Merlino, S., and N. Perchiazzi, 1985, Tschermaks Mineral. Petrogr. Mitt. **34**, 297.

Merlino, S., and N. Perchiazzi, 1987, Mineral. & Petrology, **37**, 25.
Milton, C., B. Ingram, J.R. Clark and E.J. Dwornik, 1965, Am. Mineral. **50**, 593.
Milton, D.J., and H. Bastron, 1971, Mineral. Rec. **9**, 166.
Mineev, D.A., T.I. Lavrishcheva and A.V. Bykova, 1970, Zap. Vses. Mineral. Ova. **99**, 328.
Mineralogical Abstracts, Mineral. Soc. Great Brit. and Mineral. Soc. America.
Miyawaki, R., and I. Nakai, 1987, Rare Earths **11**, 1.
Miyawaki, R., and I. Nakai, 1988, Rare Earths **13**, 1.
Miyawaki, R., and I. Nakai, 1989, Rare Earths **15**, 1.
Miyawaki, R., and I. Nakai, 1990, Rare Earths **17**, 1.
Miyawaki, R., and I. Nakai, 1991, Rare Earths **19**, 1.
Miyawaki, R., I. Nakai and K. Nagashima, 1984, Am. Mineral. **69**, 948.
Miyawaki, R., I. Nakai and K. Nagashima, 1985, Acta Crystallogr. C **41**, 13.
Miyawaki, R., I. Nakai, K. Nagashima, A. Okamoto and T. Isobe, 1987, J. Mineral. Soc. Jpn. **18**, 17.
Miyawaki, R., J. Takase and I. Nakai, 1993, Am. Mineral., in press.
Mooney, R.C.L., 1948, J. Chem. Phys. **16**, 1003.
Mooney, R.C.L., 1950, Acta Crystallogr. **3**, 337.
Moore, P.B., 1967, Am. Mineral. **52**, 1603.
Moore, P.B., and J. Shen, 1983a, Am. Mineral. **68**, 996.
Moore, P.B., and J. Shen, 1983b, Tschermaks Mineral Petrogr. Mitt. **31**, 47.
Moore, P.B., A.J. Irving and A.R. Kampf, 1975, Am. Mineral. **60**, 957.
Moore, P.B., P.K. Sen Gupta, E.O. Schlemper and S. Merlino, 1987, Am. Mineral. **72**, 1176.
Mountain, E.D., 1957, Mineral. Mag. **31**, 607.
Murgoci, G., 1922, C.R. Hebd. Séances Acad. Sci. C (Paris) **175**, 372, 426.
Muto, T., R. Meyrowitz, A.M. Pommer and T. Murano, 1959, Am. Mineral. **44**, 633.
Nadezhina, T.N., D.Yu. Pushcharovskii and A.P. Khomyakov, 1987, Mineral. Zh. **9**, 45.
Nagashima, K., R. Miyawaki, J. Takase, I. Nakai, K. Sakurai, S. Matsubara, A. Kato and S. Iwano, 1986, Am. Mineral. **71**, 1028.
Nakai, I., J. Akimoto, M. Imafuku, R. Miyawaki, Y. Sugitani and K. Koto, 1987, Phys. Chem. Minerals **15**, 113.
Nakai, T., 1938, Bull. Chem. Soc. Jpn. **13**, 591.
Neumann, H., and B. Nilssen, 1968, Lithos **1**, 113.
Nickel, E.H., and J.A. Mandarino, 1987, Am. Mineral. **72**, 1031.
Nickel, E.H., and M.C. Nichols, 1991, Mineral Reference Manual (Van Nostrand Reinhold, New York).
Nickel, E.H., and J.E. Temperly, 1987, Mineral. Mag. **51**, 605.
Nickel, E.H., I.E. Grey and I.C. Madsen, 1987, Am. Mineral. **72**, 1006.
Nikolaeeff, P.D., 1897, Verh. k. russ. min. Ges., XXXV Protocolle, p. 11.
Nowacki, W., and K.D. Phan, 1964, Bull. Soc. Fr. Mineral. Cristallogr. **87**, 453.
Nurlybayev, A.N., 1962, Dokl. Akad. Nauk SSSR **147**, 152.
Oddo, G., 1914, Z. Anorg. Allg. Chem. **87**, 253.
Oftedal, I., 1929, Z. Kristallogr. **72**, 239.
Oftedal, I., 1931a, Z. Kristallogr. **78**, 462.
Oftedal, I., 1931b, Z. Kristallogr. **79**, 437.
Oftedal, I., 1931c, Z. Phys. Chem. **13**, 190.
Ohashi, R., 1924, J. Geol. Soc. Tokyo **31**, 166.
Orlandi, P., M. Pasero and G. Vezzalini, 1990, Eur. J. Mineral. **2**, 413.
Otroshchenko, L.P., V.B. Aleksandrov, N.N. Bydanov, V.I. Simonov and B.P. Sobolev, 1988, Sov. Phys. Crystallogr. **33**, 449.
Palache, C., H. Berman and C. Frondel, 1944, Dana's System of Mineralogy, 7th Ed. (Wiley, New York).
Pavlenko, A.S., L.P. Orlova, M.V. Akhmanova and K.I. Tobelko, 1965, Zap. Vses. Mineral. Ova. **94**, 105.
Pavlov, P.V., and N.V. Belov, 1959, Kristallographiya **4**, 324.
Peacor, D.R., and P.J. Dunn, 1982, Am. Mineral. **67**, 1039.
Peacor, D.R., and P.J. Dunn, 1988, Am. Mineral. **73**, 838.
Peacor, D.R., W.B. Simmons Jr, E.J. Essene and E.Wm. Heinrich, 1982, Am. Mineral. **67**, 156.
Pecora, W.T., and J.H. Kerr, 1953, Am. Mineral. **38**, 1169.
Pen, C., and C. Pan, 1964, Sci. Sin. **13**, 1539.
Perrault, G., and J.T. Szymanski, 1982, Can. Mineral. **20**, 59.
Pertlik, F., and A. Preisinger, 1983, Tschermaks Mineral. & Petrogr. Mitt. **31**, 39.
Petersen, O.V., J.G. Rønsbo and E.S. Leonardsen, 1989, Neues Jahrb. Mineral. Monatsh. **1989**, 84.
Peyronel, G., 1956, Acta Crystallogr. **9**, 181.
Piret, P., and M. Deliens, 1982, Bull. Mineral. (France) **105**, 225.

Piret, P., M. Deliens and J. Piret-Meunier, 1988, Bull. Mineral. (France) **111**, 443.

Piret, P., M. Deliens and M. Pinet, 1990, Eur. J. Mineral. **2**, 725.

Podporina, Ye., V. Burkov and K. Danilova, 1983, Dokl. Akad. Nauk SSSR **268**, 139.

Prince, E., 1957, Acta Crystallogr. **10**, 787.

Proshchenko, E.G., 1962, Zap. Vses. Mineral. Ova. **91**, 260.

Pudovkina, Z.V., and Yu.A. Pyatenko, 1963, Dokl. Akad. Nauk SSSR **153**, 146.

Qian, J., P. Fu, Y. Kong and G. Gong, 1982, Acta Phys. Sin. **31**, 577.

Raade, G., and K. Brastad, 1992, Eur. J. Mineral. **4**, in press.

Rastsvetaeva, R.K., and V.I. Andrianov, 1987, Sov. Phys. Dokl. **32**, 252.

Rastsvetaeva, R.K., B.E. Borutskii and A.I. Gusev, 1988, Sov. Phys. Crystallogr. **33**, 207.

Rastsvetaeva, R.K., M.N. Sokolova and B.E. Borutskii, 1990, Sov. Phys. Crystallogr. **35**, 814.

Rastsvetaeva, R.K., B.E. Borutskii and Z.V. Shlyukova, 1991, Sov. Phys. Crystallogr. **36**, 349.

Raup, O.B., A.J. Gude III, E.J. Dwornik, F. Cuttitta and H.J. Rose Jr, 1968, Am. Mineral. **53**, 1081.

Ren, Y., L. Ximen and Z. Peng, 1983, Geochemistry (China) **2**, 180.

Roberts, A.C., G.Y. Chao and F. Cesbron, 1980, Geol. Surv. Canada, Paper 80-1C, p. 141.

Roberts, W.L., G.R. Rapp Jr and J. Weber, 1974, Encyclopedia of Minerals (Van Nostrand Reinhold, New York).

Rømming, C., A.K. Kocharian and G. Raade, 1992, Eur. J. Mineral. **4**, in press.

Rose, D., 1980, Neues Jahrb. Mineral. Monatsh. **1980**, 247.

Rosenblum, S., and E.L. Mosier, 1975, Am. Mineral. **60**, 309.

Rouse, R.C., D.R. Peacor and R.L. Freed, 1988, Am. Mineral. **73**, 168.

Ruh, R., and A.D. Wadsley, 1966, Acta Crystallogr. **21**, 974.

Rumanova, I.M., G.F. Volodina and N.V. Belov, 1967, Sov. Phys. Crystallogr. **11**, 485.

Sahama, Th.G., O. von Knorring and M. Lehtinen, 1970, Bull. Geol. Soc. Finland **42**, 223.

Sawyer, J., P. Caro and L. Eyring, 1973, Rev. Chim. Miner. **10**, 93.

Scharm, B., and P. Kühn, 1983, Neues Jahrb. Mineral. Monatsh. **1983**, 201.

Scott, J.D., 1976, Can. Mineral. **14**, 515.

Segalstad, T.V., and A.O. Larsen, 1978, Am. Mineral. **63**, 188.

Semenov, E.I., V.D. Dusmatov and N.S. Samsonova, 1963, Kristallographiya **8**, 677.

Semenov, E.I., A.P. Khomyakov and A.V. Bykova, 1965, Dokl. Akad. Nauk SSSR **163**, 718.

Semenov, E.I., M.E. Kazakova and R.A. Aleksandrova, 1967, Medd. Groenl. **181**, 1.

Semenov, E.I., M.E. Kazakova and V.J. Bukin, 1968, Medd. Groenl. **181**, 3.

Shen, J., and P.B. Moore, 1982, Am. Mineral. **67**, 1021.

Shen, J., and P.B. Moore, 1984, Am. Mineral. **69**, 190.

Shi, N., Z. Ma and Z. Peng, 1982, Kexue Tongbao **27**, 76.

Shinn, D.B., and H.A. Eick, 1968, Inorg. Chem. **7**, 1340.

Shlyukova, Z.V., E.V. Vlosova, M.E. Kazakova, G.O. Piloyan, N.G. Shumyatskaya and B.E. Borutskii, 1973, Dokl. Akad. Nauk SSSR **211**, 426.

Shpanov, E.P., G.N. Netschelyustov, S.V. Baturin and L.S. Solntseva, 1989, Zap. Vses. Mineral. Ova. **118**, 100.

Shumyatskaya, N.G., A.A. Voronkov, V.V. Ilyukhin and N.V. Belov, 1969, Sov. Phys. Dokl. **14**, 304.

Shumyatskaya, N.G., A.A. Voronkov, V.V. Ilyukhin and N.V. Belov, 1976, Sov. Phys. Crystallogr. **21**, 399.

Shumyatskaya, N.G., A.A. Voronkov and Yu.A. Pyatenko, 1980, Sov. Phys. Crystallogr. **25**, 419.

Simonov, V.I., and N.V. Belov, 1968, Sov. Phys. Crystallogr. **12**, 740.

Sinclair, W., and R.A. Eggleton, 1982, Am. Mineral. **67**, 615.

Skorobogatova, N.V., G.A. Sidorenko, K.A. Dorofeeva and T.I. Stolyarova, 1966, Geol. Mestorozhd. Redk. Elem. **30**, 84.

Smith, W.L., J. Stone, D.R. Ross and H. Levine, 1960, Am. Mineral. **45**, 92.

Smolin, Yu.I., Yu.F. Shepelev and A.P. Titov, 1973, Sov. Phys. Crystallogr. **17**, 749.

Sokolova, E.V., Yu.K. Egorov-Tismenko, A.V. Voloshin and Ya.A. Pakhomovskii, 1986, Sov. Phys. Dokl. **31**, 601.

Strada, M., and G. Schwendiman, 1934, Gazz. Chim. Ital. **64**, 662.

Structure Reports, International Union of Crystallography (Reidel, Dordrecht).
Strunz, H., 1942, Naturwissenschaften **30**, 64.
Strunz, H., 1978, Mineralogische Tabellen, 7th Ed. (Akademische Verlagsgesellschaft Geest & Portig, Leipzig).
Sugitani, Y., Y. Suzuki and K. Nagashima, 1984, Am. Mineral. **69**, 377.
Sugitani, Y., Y. Suzuki and K. Nagashima, 1985, Am. Mineral. **70**, 856.
Szymanski, J.T., and J.D. Scott, 1982, Can. Mineral. **20**, 271.
Tarkhanova, G.A., G.A. Sidorenko and N.N. Kuznetsova, 1964, Zap. Vses. Mineral. Ova. **93**, 106.
Taylor, G.F., 1975, Am. Mineral. **60**, 690.
Tikhonenkov, I.P., and M.E. Kazakova, 1957, Zap. Vses. Mineral. Ova. **86**, 641.
Trunov, V.K., V.A. Efremov, Yu.A. Velikopodnyi and I.M. Averina, 1981, Sov. Phys. Crystallogr. **26**, 35.
Tsunekawa, S., and H. Takei, 1978, Phys. Status Solidi a **50**, 695.
Ueda, T., 1953, Mem. Coll. Sci. Univ. Kyoto B **20**, 227.
Ueda, T., 1967, J. Jpn. Assoc. Mineral. Petrol. Econ. Geol. **58**, 170.
Uetani, K, Y. Ogimura, A. Kato and K. Nagashima, 1968, Bull. Chem. Soc. Jpn. **41**, 603.
Utsunomiya, A., K Tanaka, H. Morikawa, F. Marumo and H. Kojima, 1988, J. Solid State Chem. **75**, 197.
Vaes, J.F., 1947, Ann. Soc. Geol. Belg. **70**, B233.
Vegard, L., 1927, Philos. Mag. **4**, 511.
Vlasov, K., 1966, Geochemistry and Mineralogy of Rare Elements, p. 301.
Vlasov, K.A., M.V. Kuz'menko and E.M. Es'kova, 1959, Akad. Nauk SSSR **1959**, 423.
Volodina, G.F., I.M. Rumanova and N.V. Belov, 1963, Dokl. Akad. Nauk SSSR **149**, 109.
Voloshin, A.V., Ya.A. Pakhomovskii and F.N. Tyusheva, 1983a, Mineral. Zh. **5**, 94.
Voloshin, A.V., Ya.A. Pakhomovskii, Yu.P. Men'shikov, A.S. Povarennykh, E.N. Matvienko and O.V. Yakubovich, 1983b, Dokl. Akad. Nauk SSSR **270**, 1188.
Voloshin, A.V., Ya.A. Pakhomovskii and F.N. Tyusheva, 1985, Mineral. Zh. **7**, 79.
Voronkov, A.A., and Yu.A. Pyatenko, 1967a, J. Struct. Chem. SSSR **8**, 835.
Voronkov, A.A., and Yu.A. Pyatenko, 1967b, Sov. Phys. Crystallogr. **12**, 214.
Voronkov, A.A., and N.G. Shumyatskaya, 1968, Sov. Phys. Crystallogr. **13**, 192.
Voronkov, A.A., N.G. Shumyatskaya and Yu.A. Pyatenko, 1962, J. Struct. Chem. SSSR **3**, 665.
Voronkov, A.A., N.G. Batalieva and Yu.A. Pyatenko, 1965, Sov. Phys. Crystallogr. **9**, 461.
Walenta, K., 1978, Chem. Erde **38**, 331.
Wang, H., H. Shu, C. Kuo, S. Li and C. Wang, 1973, Ti Ch'iu Hua Hsueh (Geochimica) **1**, 31.
Wang, X., 1978, Kexue Tongbao **23**, 743.
Weidenborner, J.E., 1961, Acta Crystallogr. **14**, 1051.
Weitzel, H., and H. Schröcke, 1980, Z. Kristallogr. **152**, 69.
White Jr, J.S., and J.E. Nelen, 1987, Mineral. Rec. **18**, 203.
Williams, C.G., 1865, Chem. News **12**, 183.
Wise, W.S., 1978, Am. Mineral. **63**, 704.
Wise, W.S., 1982, Am. Mineral. **67**, 809.
Wolten, G.M., 1967, Acta Crystallogr. **23**, 939.
Wolten, G.M., 1968, Acta Crystallogr. B **24**, 463.
Ximen, L., and Z. Peng, 1985a, Geochemistry (China) **4**, 89.
Ximen, L., and Z. Peng, 1985b, Acta Mineral. Sin. **5**, 289.
Yakubovich, O.V., E.N. Matvienko, A.V. Voloshin and M.A. Simonov, 1983, Sov. Phys. Crystallogr. **28**, 269.
Yakubovich, O.V., M.A. Simonov, A.V. Voloshin and Ya.A. Pakhomovskii, 1984, Sov. Phys. Crystallogr. **29**, 141.
Yakubovich, O.V., M.A. Simonov, A.V. Voloshin and Ya.A. Pakhomovskii, 1986, Sov. Phys. Dokl. **31**, 930.
Yakubovich, O.V., A.V. Voloshin, Ya.A. Pakhomovskii and M.A. Simonov, 1988, Sov. Phys. Crystallogr. **33**, 356.
Yang, G., Z. Pan, X. Wu and X. Liu, 1991, J. China Univ. Geosciences **2**, 75.
Zachariasen, W.H., 1930, Z. Kristallogr. **73**, 1.
Zalkin, A., and D.H. Templeton, 1985, Acta Crystallogr. B **41**, 91.
Zalkin, A., D.H. Templeton and T.E. Hopkins, 1966, Inorg. Chem. **5**, 1466.
Zhang, P., and K. Tao, 1981, Sci. Geol. Sin. 195.
Zhang, P., and K. Tao, 1982, Sci. Geol. Sin. **1982**(4), 424.
Zhang, P., and K. Tao, 1983, Sci. Geol. Sin. **1983**(4), 409.
Zhang, P., and K. Tao, 1986, Bayan Obo Mineral (Science Publisher, Beijing, China) 208pp.
Zhang, P., and K. Tao, 1987, Zhongguo Xitu Xuebao **5**, 1.
Zoltai, T., 1960, Am. Mineral. **45**, 960.

Handbook on the Physics and Chemistry of Rare Earths, Vol. 16
edited by K.A. Gschneidner, Jr. and L. Eyring

Chapter 109

APPEARANCE POTENTIAL SPECTROSCOPY OF LANTHANIDES AND THEIR INTERMETALLICS

D.R. CHOPRA
Department of Physics, East Texas State University, Commerce, TX 75429, USA

Contents

List of symbols

BE	binding energy
E_F	Fermi energy
XAS	X-ray absorption spectroscopy
BIS	Bremsstrahlung isochromat spectroscopy
IPE	inverse photoemission spectroscopy
APS	appearance potential spectroscopy
AES	Auger electron spectroscopy
XPS	X-ray photoelectron spectroscopy
$\hbar\omega_0$	quantum energy
SXAPS	soft X-ray appearance potential spectroscopy
AEAPS	Auger electron appearance potential spectroscopy
DAPS	disappearance potential spectroscopy
DOS	density of states
LEED	low-energy electron diffraction
CEELS	core-level electron energy-loss spectroscopy
FRESCA	Fermi-level reference electron spectroscopy for chemical analysis
XANES	X-ray absorption near-edge spectroscopy
EAPFS	extended appearance potential fine structure
EXAFS	extended X-ray absorption fine structure

1. Introduction

The valence band states near the Fermi level (E_F) yield vital information for understanding physical and chemical properties of materials. During the past decades, the field of materials characterization has grown significantly and a host of new techniques have been developed to analyze the atomic structures of the surfaces (Tong et al. 1984). Most of these techniques (such as Auger electron and X-ray photoelectron spectroscopies) have been devoted to spectroscopic investigation of the electronic density of occupied states in solids. From such studies on the binding energy (BE) of core electrons, in particular, important information on the electronic structure of a material can be obtained. This, in turn, permits determination of the effective charges on the atoms and the polarity of the bonds between atoms of different types in alloys or compounds (Jørgensen and Berthou 1972). Comparatively few experiments have been carried out to measure the density of unoccupied electronic states. Appropriate experimental methods have been discussed by Nagel (1973). Among the techniques used to probe the density of unoccupied electronic states, X-ray absorption (XAS), Bremsstrahlung isochromat (BIS), inverse photoemission (IPE), and appearance potential (APS) spectroscopies have proved to be the most promising approaches.

In XAS the incident X-rays traverse through the sample. X-rays of appropriate energy are absorbed by the atoms and, as a result, a core electron is excited to an unoccupied state above the Fermi energy, E_F. The decrease in the transmitted X-ray intensity is measured. However, in this spectroscopy selection rules are rigorously obeyed and all symmetries must be considered to interpret the spectral features. The schematic diagram, in the one-electron approximation, of the X-ray excitation of a core state is shown in fig. 1.

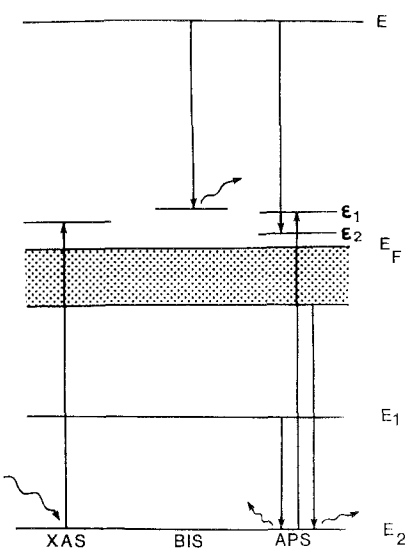

Fig. 1. A schematic diagram showing electron excitation of a core state in X-ray absorption (left), Bremsstrahlung emission (middle) and appearance potential (right) spectroscopies.

In BIS, the sample to be investigated serves as the anode of an X-ray tube. An X-ray spectrometer, tuned to a fixed quantum energy $\hbar\omega_0$, records the Bremsstrahlung yield as a function of the accelerating voltage across the tube. Those electrons with initial energy E with respect to E_F of the anode, which undergo radiative transitions with emission of a quantum of energy $\hbar\omega_0$, show up in final states in the conduction band of the sample at an energy $E - \hbar\omega_0$. Assuming a constant radiative matrix element, the transition probability will be proportional to the density of the final unfilled states. The measured yield will, therefore, directly reflect the density of empty one-electron states. The corresponding schematic diagram is also shown in fig. 1. Inverse photoemission (IPE) spectroscopy represents an important and growing area of the present-day surface analysis (Drube et al. 1987). Measurements in it are carried out in a manner very similar to those done with the BIS technique. In this spectroscopy, the energy of incident electrons is no more than a few tens of electron volts. This technique is, therefore, sensitive to the surface region because of the finite path length of low-energy electrons. The simple model stated above has been shown to be valid for isochromat results in the X-ray energy range, where the method can be regarded as inverse to XPS (Himpsel and Fauster 1984, Ludeke et al. 1986) and hence the name inverse photoemission.

Appearance potential spectroscopy measures the probability for electronic excitation of a core level as a function of incident electron energy. Unlike photoemission techniques, which utilize one-electron excitation processes to give the density of occupied states, APS is based on a two-electron excitation/relaxation process and spectra contain the information on the convoluted density of *unoccupied* states. The experiment consists of a simple triode arrangement. The energy of the incident electrons is gradually increased, and the dependence of the total signal strength on this energy is measured. As the incident-electron energy crosses the excitation threshold of a core level, the incident electron imparts its energy to the core-level electron as a result of an inelastic collision. Both the incident and core electrons are scattered to unoccupied states above E_F, with the creation of an inner hole. The excitation process is followed by the filling of the core hole which causes X-rays or Auger electrons to be emitted. The yield (X-rays or Auger electrons) of the relaxation process is measured as a function of incident-electron energy. When the intensity of the emitted X-rays is measured, the method is called soft X-ray APS (SXAPS). Measuring the total secondary electron current is called Auger electron APS (AEAPS). In another modification of the technique, the current of elastically reflected electrons is measured. At the threshold energy of core-level excitation the number of electrons that undergo inelastic scattering disappear from the measured current. The method is appropriately called disappearance potential spectroscopy (DAPS). In SXAPS and AEAPS the intensity depends upon the fluorescence and Auger yields, respectively, which, in turn, depend on the type of electron shell, on the BE, and on the atomic environment. These methods give results based on the details of the relaxation mechanism, whereas DAPS is free of these complications. The corresponding transitions in the one-electron approximation are included in fig. 1. As a tool for chemical analysis APS has its merits when compared with other techniques, especially when applied to multiple component alloys (Wandelt and Ertl 1976a, Dose and Haertl

1981). APS has also been shown to be sensitive to adsorption phenomena (Ertl and Wandelt 1974, Andersson and Nyberg 1975, Nyberg 1979). Since spectra representing adsorbed oxygen and a metal oxide, respectively, exhibit marked differences, chemisorption and oxidation phases can be distinguished (Nyberg 1975). The special advantages of APS over other spectroscopies are that it is a non-dispersive technique and the peaks in the spectrum are specific to a single element. This makes it experimentally simple and allows one to separately examine the states accessible to core electrons of different elements on the same surface. A very appealing feature of APS is that only one core level is involved in the measured signal. Assuming a monochromatic projectile electron beam, this leads to the presence of relatively sharp lines in the APS spectrum. It is also possible to investigate the excitation probability for particular sublevels by means of DAPS where no relaxation is involved. Another important aspect of APS is that it reveals a localized density of states (DOS) because the matrix element governing the core-hole production involves the very short-range wave function of the initial core-electron state. Since electronic excitation does not obey selection rules, APS reveals information regarding the total DOS. As compared to this, XAS measures only specific symmetry characteristics. The form of the signal is, in principle, determined by the self-convolution of the density of conduction band states near the E_F of metals. The intensity of the signal, therefore, depends on the density of conduction band states. If the density of states is low or of disadvantageous character, APS cannot be utilized as a universal analytical technique. This limited scope explains the scant utilization of the technique relative to that of AES or XPS. Nevertheless, APS has the potential for providing interesting results which cannot be obtained by other techniques. Mainly three groups of elements provide a strong signal: 3d transition metals, alkaline earths and rare earths. In this respect, APS, AES, and XPS are complementary techniques. As stated above, APS does not require a dispersive analyzer in contrast to other techniques. It thus measures energy rather than momentum. This accounts for the extreme simplicity of the APS spectrometer. APS complements the information regarding the elemental identification, chemical bonding, density of unoccupied states, near-neighbor configuration in the surface layer, and the mechanism of excitation and transport processes inside the target.

2. Theoretical processes

A simple model to describe the APS was successfully used by Park and Houston (1972) to interpret their experimental results. In APS, the surface of a solid is bombarded with monochromatic electrons of energy, E, in the range of 0 to 2000 eV. The total intensity of X-ray emission consists of a linearly increasing Bremsstrahlung background superimposed by characteristic radiation. It is feasible to suppress the background and enhance the onset of characteristic radiation. If the incident electron is captured by a state ε_1 above E_F, the energy may be conserved by the excitation of a core electron into a state ε_2 as shown in fig. 2, and is given by

$$\varepsilon_2 = eV + e\phi_c + kT - \varepsilon_1 - E_b, \tag{1}$$

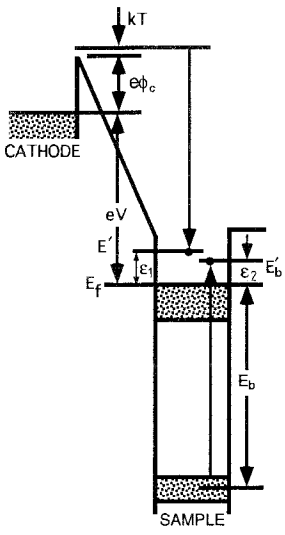

Fig. 2. Electron excitation in APS. The core electron may scatter into a state $\varepsilon_2 = eV + e\phi_c + kT - \varepsilon_1 - E$. The core hole may subsequently decay by the emission of characteristic X-rays or Auger electrons.

where V is the potential applied between a thermionic emitter and the anode, $e\phi_c$ is the emitter work function, kT is the average thermal energy of the emitted electrons and E_b is the BE of the core electron relative to E_F. Here we assume that only one-electron processes are involved and the core-level density of states is represented by a Dirac delta function. The final state must take all possible combinations of energetic positions of both electrons (incident and core electrons) into consideration. The characteristic emission has a distinct threshold given by

$$E = E_b = eV + e\phi_c + kT. \tag{2}$$

It is evident that the minimum energy of an incident electron (appearance potential) for the excitation of a core electron of BE E_b will occur at $E = E_b$ resulting in the transfer of both the incident and core electrons to E_F. The excitation probability, $P(E, E_b)$ of the process at a given incident energy E is given by

$$P(E, E_b) \propto \int_0^{E-E_b} P_1(E \to \varepsilon_1)\, P_2(E_b \to \varepsilon_2)\, N(\varepsilon_1) N(\varepsilon_2)\, \delta(\varepsilon_1 + \varepsilon_2 - E + E_b)\, d\varepsilon_1\, d\varepsilon_2. \tag{3}$$

The energy conservation is expressed by a δ-function. The factors $P_1(E \to \varepsilon_1)$ and $P_2(E_b \to \varepsilon_2)$ representing the transition probabilities, may depend on selection rules and are unknown. If these factors are assumed to be independent of E over a small range of E values above the threshold E_b, then they can be taken as simply proportional to the one-electron DOS $N(\varepsilon_1)$ and $N(\varepsilon_2)$, respectively, and the equation simplifies to

$$P(E, E_b) \propto \int_0^{E-E_b} N(E - E_b - \varepsilon_2)\, N(\varepsilon_2)\, d\varepsilon_2, \tag{4}$$

which is simply the self-convolution of the density of the conduction band states. In APS, the derivative, APS(E) of $P(E, E_b)$ is determined experimentally and is represented by

$$\mathrm{APS}(E) \propto \int_0^{E-E_b} N(\varepsilon_2) \frac{\mathrm{d}}{\mathrm{d}E} N(E - E_b - \varepsilon_2)\, \mathrm{d}\varepsilon_2. \tag{5}$$

The characteristic features of this model in the case of simple and 3d transition metals consist of a peak which is followed by a undershoot and then a step-like increase. For a simple step-like density of unoccupied states at E_F, APS(E) is approximated by $N^2_{E_F}$, i.e. the height of the APS peak above the background is proportional to the square of the DOS at E_F. The core-level BE is determined from the threshold of the APS peak. Neglecting the other broadening effects, the width of the positive peak should resemble the width of the unfilled DOS.

APS is very sensitive to DOS at E_F. Thus elements having low DOS give a weak signal in the spectrum. In fig. 3 is shown the schematic representation of the DOS for the transition and noble metals (Park 1975). The Fermi energy, E_F, in the case of transition metals lies in a narrow, partially filled d-band as shown in fig. 3a. The one-electron density of states is given by $N(E)$. The two-electron density of conduction states $N_{2c}(E)$ is given by the self-convolution of $N(E)$ above E_F. The dotted curve is the derivative of this function and is characterized by a negative dip. For metals having filled d-bands the situation is shown in fig. 3b. The derivative of $N_{2c}(E)$ is a step-like function and is shown dotted in the figure. In actual practice, the APS spectrum looks like the dotted curves but broadened by the core-level lifetime width and the instrument response function. It is further important to note that APS probes the local density of states in the vicinity of atoms whose core electrons are excited.

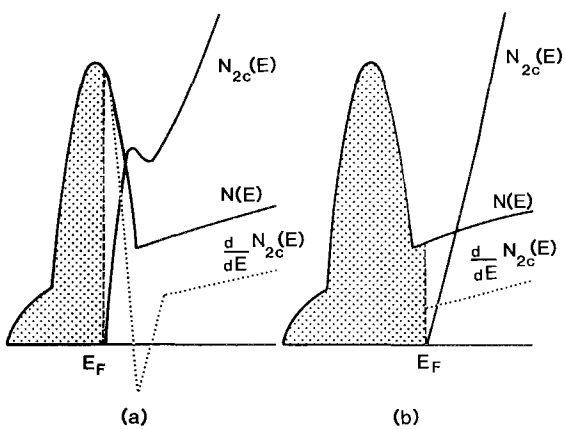

Fig. 3. A schematic representation of the DOS in APS. (a) A partially filled d-band for transition metals. $N(E)$ is the one-electron DOS. The two-electron density of conduction states $N_{2c}(E)$ is given by the self-convolution of $N(E)$ above E_F. The derivative of this function is the dotted curve and is characterized by a sharp peak at E_F followed by a negative dip. (b) The d-band is just filled for noble metals. The derivative of $N_{2c}(E)$ is a step-like function (Park 1975).

The degree of localization depends upon the character of the particular state to be excited.

The BEs of the core levels are determined from the corresponding appearance potential peaks simply from the intersection of the extrapolated projection of the background and the positive going low-energy slope of the peak. As core BEs are characteristic of specific elements, chemical analysis of the surface is feasible. Since the APS yield is proportional to the self-convolution of the density of the final electron states broadened by the finite lifetime of the core hole and by the finite experimental resolution, precise knowledge about the BE can be obtained by using deconvolution techniques. Successful deconvolution techniques have been developed by Fukuda et al. (1977), Dose and Fauster (1979b), Dose et al. (1981), and Schulz et al. (1984). As an alternative to avoid the uncertainty introduced due to this correction in the BE measurements, Fukuda et al. (1977) have used a field-emission electron source. In this the field-emitted electrons tunnel through the potential barrier at the emitter surface. Therefore, no correction for the work function is required. Using such an electron source, absolute $2p_{3/2}$ core-level BEs have been determined for 3d transition metals from their APS spectra corrected for the lifetime broadening of the core state (Fukuda et al. 1977). There are two different approaches that are utilized in the study of DOS in APS (Eckertova 1988). In the first one the calculated DOS was used to determine the shape of the APS spectrum and then compared with experimental results obtained by SXAPS. In the second approach the experimentally obtained spectrum was used to derive the density of states. However, both approaches do not lead to agreement between the theory and the experiment. In some cases, the assumptions of the theory are not considered valid and the one-electron model cannot be used.

3. Experimental technique

In SXAPS the total soft X-ray intensity emitted by a sample under electron bombardment is measured as a function of incident-electron energy. The schematic of this spectrometer is shown in fig. 4. Electrons from a tungsten filament, F, impinge on the sample, S, to be studied. A grid electrically separates the filament–target and the detector assemblies. The entire system is enclosed in a stainless-steel chamber and is maintained under UHV conditions. X-rays passing through the grid strike the walls of the chamber which act as a photocathode. The resulting photoelectrons are collected on an electrode which is biased at $+300$ V. The filament is biased positive with respect to the chamber walls in order to prevent the primary electrons from reaching the collector. The extraction of the signal in the first-derivative mode is accomplished by the modulation technique. The accelerating voltage is modulated by a small sinusoidal signal. The output is synchronously detected and amplified with the help of a phase-lock amplifier. Details of the experimental technique are available elsewhere (Chopra et al. 1976, Park and Houston 1974).

An AEAPS spectrometer is similar to an SXAPS except for some minor changes. The spectrometer fabricated in our laboratory (Grolemund and Chopra 1983) consists

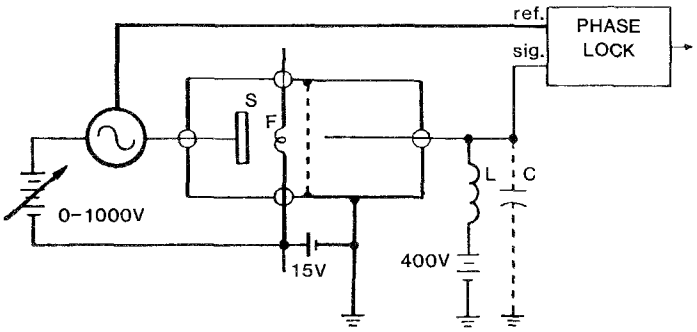

Fig. 4. A simplified schematic of the soft X-ray appearance potential spectrometer. S is the sample and F is the filament.

of a triode arrangement and is shown in fig. 5. The anode completely surrounds the filament except for a 1 mm exit aperture in the top of the anode as shown. The target sample is mounted directly above the aperture. Electrons emitted from the filament are accelerated to the anode by a constant potential. The target is also at a positive potential but this one is linearly varied by a programmable ramp generator. The anode potential is held at a voltage that is higher than the maximum voltage of the ramp for a certain core state; therefore the anode serves as a collector of back-scattered electrons. The current in the anode–sample circuit is then

$$I = I_p - I_s, \tag{6}$$

where I_p is the primary-electron current and I_s is the secondary-electron current. The I_s arises as a result of the interaction of primary electrons and the sample. Because the anode potential is kept constant, the primary current remains constant. Variations in I then reflect changes in the secondary current only. An increase in I_s due to the emission of Auger electrons accompanying the onset of a core-level excitation will indicate a sudden decrease in I. Extraction of this information is accomplished by differentiating the secondary current with respect to the target voltage. This is done by superimposing a small signal with frequency ω_0 in the filament circuit. The secondary current in the anode–sample circuit that varies at

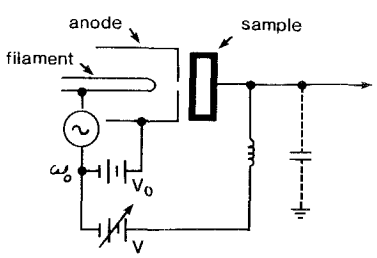

Fig. 5. A schematic diagram of the Auger electron appearance potential spectrometer. Field-emitted electrons passing through an aperture in the anode impinge on the sample. The signal is extracted by the potential-modulation technique.

this frequency is then synchronously detected with a phase-lock amplifier. Because the secondary electron emission does not exhibit a linear dependence on incident-electron energy, it is generally advantageous to make measurements in the second-derivative mode. The increase of inelastically scattered electrons at the threshold energy is accompanied by a decrease of elastically scattered electrons, because of the opening of new inelastic channels when ionization is possible. The decrease in elastically scattered electrons cannot be observed in the sample current because of the complications due to the increase in the inelastically scattered electrons. However, the elastic and inelastic contributions can be separated with a LEED optics system, or cylindrical mirror analyzer (Kirschner and Staib 1975), or other high-pass filter arrangements (Kirschner and Losch 1977). By measuring the decrease in elastic reflected current at the threshold energy, DAPS detection is accomplished.

Single-crystal materials exhibit complicated AEAPS spectra at low energies (Park et al. 1974). In fact, the APS structure is completely masked by a low-energy electron diffraction (LEED) structure. This structure is formed only by elastically scattered electrons. To separate the elastic and inelastic contributions to the APS spectra, Eckertova and Pavluch (1984) and Pavluch and Eckertova (1985) have devised a new spectrometer. The advantages of such a spectrometer are that it reduces the effect of the primary current on the spectra and also reduces the non-linearity of the electron gun. With these modifications the signal-to-background ratio is considerably enhanced, thus facilitating good interpretation of the spectra, especially in the case of single crystals. Due to the smooth background the fine structure appearing on the high-energy side of a particular core-level spectrum can be easily detected and analyzed to obtain important information regarding the nearest-neighbor configuration in the surface layer.

The major problem encountered in APS is the signal-to-noise ratio. In the SXAPS broad-band noise is present due to Bremsstrahlung photons, and this increases steadily with the primary-electron energy (Tracy 1972). In AEAPS, the yield of low-energy secondary electrons is not a simple function of the primary-electron energy and depends sensitively on the surface conditions. In DAPS, the back-scattering cross section of the electrons in a solid is low. This makes the total reflection coefficient rather small (of the order of 10^{-3} to 10^{-2}) which in turn reduces the signal-to-noise ratio. Andersson et al. (1974) have designed a low-noise SXAPS spectrometer to improve the signal-to-noise ratio. It utilizes a silicon surface-barrier diode detector cooled with liquid nitrogen. They have used an Al window to filter out low-energy photons. Replacing the W cathode by a LaB_6 emitter which operates at $\sim$1000 K and using an emission current of $\leqslant$100 μA, thermal effects can be neglected. Lee (1977) has discussed the signal-to-noise performance of an SXAPS spectrometer in the cases of quantum and energy detectors. He found that in the useful electron-energy range, the sensitivity of energy detectors is superior to that of quantum detectors using an X-ray filter. Padalia et al. (1991) have reported a significant improvement in the sensitivity of SXAPS using a Cu–BeO photoelectron multiplier for the detection of soft X-rays.

The resolution of the spectrometer depends on several factors, such as the voltage drop across the filament, the thermal energy spread of the incident-electron energy

and the amplitude of the modulation voltage. Taking such factors into consideration, the resolution in SXAPS can be kept below 0.5 eV, making it the highest resolution core-level spectroscopy available (Park and Houston 1974).

4. Applications

We will discuss applications of the APS technique to simple as well as multicomponent systems. The results of the applications cited are compared with those from other techniques wherever available. The derivation of the DOS directly from the APS spectrum of 3d transition metals has been dealt with by various authors (Dose et al. 1981). The one-electron theory explains satisfactorily the 3d transition metal spectra, but fails when applied to the lanthanide metals. The electronic structures of the lanthanide metals and their intermetallics as obtained from APS spectra are also discussed.

4.1. *Transition metals*

Core-level BE data are used in a number of surface spectroscopies. It is usually assumed that BEs determined by one technique are the same as those determined by others. It has, however, been shown that small but significant differences do exist in BEs measured by different methods (Anderson et al. 1982, Esteva et al. 1983). Fundamental differences have been found between the BEs measured by APS and XPS. X-ray photoelectron spectroscopy values generally appear to be larger than those measured by APS. This may result from the substantial difference in final states in the two types of spectroscopies (Gadzuk and Sunjic 1975). APS normally measures the BE of negative ions whereas XPS values are characteristic of positive ions. Webb and Williams (1974) have found close agreement between APS and XPS values for Fe and Ni. They suggested that the core-level widths and surface chemical shifts contribute to the differences between BEs obtained with the two techniques. A series of measurements of the L_3-shell BEs of six 3d transition metals by XPS, AEAPS, and core-level electron energy-loss spectroscopy (CEELS) were made with the same specimen materials and the same reference power supplies (Erickson and Powell 1984). This study indicates that BE differences up to about 1.5 eV can occur.

Anderson et al. (1982) have made use of a new photoelectron spectroscopic technique to carry out a meaningful comparison of XPS and APS BEs. This technique is called Fermi-level referenced electron spectroscopy for chemical analysis (FRESCA). It has the principal advantage of yielding absolute measurements of the energy of photoelectrons. It also eliminates most of the inherent sources of error in XPS and does not require BE standards to relate the measurements to an absolute energy scale. The FRESCA technique utilizes a standard XPS spectrometer which compares the energy of the photoelectrons with the reference electron energies from a field emitter. The BEs measured with FRESCA and APS agree very well at lower energies in the case of transition metals. At energies above 600 eV significant differences are observed. Anderson et al. (1982) suggest that this effect may be primarily

related to the filling of the d-band rather than to the energy of the exciting photoelectrons. In reality there can be different final states and a varying screening response of the solid for each type of excitation. Until these effects are clearly understood, accurate BE data for one spectroscopy should not be assumed to be applicable to other spectroscopies with the same accuracy.

Overall, the BEs of the L_2, L_3 core levels of transition metals derived from APS spectra are in all cases lower than the literature values (Bearden and Burr 1967). Dev and Brinkman (1970) correlated these surface chemical shifts to the reduced coordination of the surface atoms resulting from the low penetration depths of incident electrons. It is important to note that the measurement of energy-level differences is simpler and more precise because these are not affected by the distribution of valence electrons. The observed APS spectral peaks show excellent agreement with the L_3–L_2 spin–orbit intervals for the 3d transition elements. Park and Houston (1972) have determined the width of the unfilled d-band of 3d transition metals and found reasonable agreement with the theoretical values.

4.2. *Lanthanide metals*

The theory that relates the SXAPS line shapes to the self-convolution of the one-electron density of states above E_F has worked well for the 3d transition metals and some of the simple metals (Nilsson and Kanski 1972, 1973, Park and Houston 1972). The basic assumption of the theory is that both the excited core electron and the scattered projectile electron are implanted in the spatially extended states in the conduction band. However, for lanthanides the self-convolution model fails. Considerable discrepancies between theory and experiment have appeared. The breakdown of the one-electron model occurs because the excited core electron may occupy a 4f orbital which is quite localized about the excited ion. An interpretation of the SXAPS line shapes in terms of the atomic-like transitions, including exchange interaction, rather than in terms of continuous interband transitions, violates the fundamental assumption on which the one-electron model is based. To explain the SXAPS of lanthanides, Wendin (1974) has proposed a two-densities-of-states model: one for the scattered projectile electron and the other for the excited ion with an electron–hole pair. The two densities of states may be interacting or non-interacting with each other. For the projectile electron the DOS is proportional to the conduction band states generally represented by the Bremsstrahlung isochromat data. The DOS for the core electron is localized and approximated with the soft X-ray absorption measurements. One or both of these may contain highly localized states. This model is no longer appropriate when both the projectile electron and excited core electron occupy 4f orbitals on the same excited ion of $4d^9 4f^{N+2}$ configuration, where N varies from 0 for La to 14 for Yb. Smith et al. (1976) have found an apparent relationship between the portions of SXAPS spectra and the soft X-ray absorption data for rare earths.

Chopra and Martin (1982) have made a comparative study of $M_{4,5}$-levels SXAPS of lanthanides (fig. 6) to understand the trends across the series. The spectra have been aligned for purposes of making a comparison. The peak intensities are not

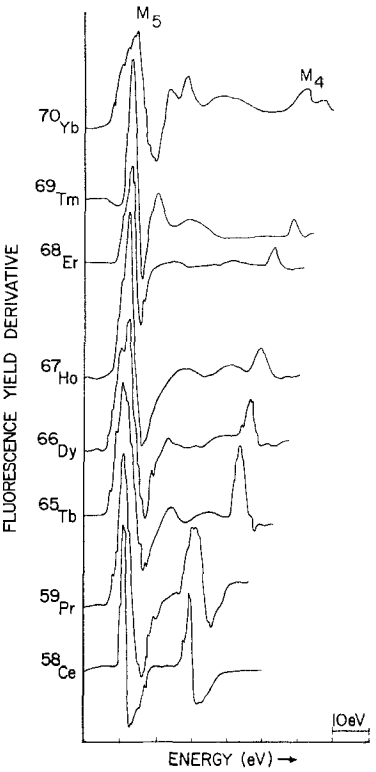

Fig. 6. $M_{4,5}$-levels SXAPS spectra of the lanthanides. The spectra are aligned for the purpose of making a comparison. The complexity of the secondary structure is seen to be rich for medium lanthanides and decreases for light and heavy lanthanides (Chopra and Martin 1982).

normalized. The M_4 and M_5 spectral region consists of two main peaks superimposed with a secondary structure. The complexity of this structure is rich for medium lanthanides and decreases for light and heavy lanthanides. The intensity of the M_4 peak decreases with Z. According to one-electron theory the intensity ratio of M_5 to M_4 peaks is computed by the statistical weighting of $2j + 1$. For lanthanides this ratio is predicted to be 1.5. The systematic study of the SXAPS of lanthanides indicates a significant increase of M_5/M_4 intensity ratio towards the end of the series, reaching a maximum with Tm ($Z = 69$) and then tending to decrease. The trend is consistent with the j–j coupling transition rates in lanthanides. As the 4f levels are progressively filled, the radiative probability of the $3d_{3/2} \rightarrow 4f_{5/2}$ transition decreases without affecting the $3d_{5/2} \rightarrow 4f_{7/2}$ transition probability significantly. The intensity ratio of M_5 to M_4 peaks is predicted to be 1.5 as stated earlier. The deviation of this ratio in the case of the lanthanide series from the statistically weighting of 1.5 implies an anomaly in the excitation probability. We have also recorded the M_2- and M_3-levels SXAPS of the same elements and found these to be more than an order of magnitude weaker than the M_4 and M_5 peaks. This indicates that lanthanides exhibit intense SXAPS structures for those core levels which have proper symmetry to satisfy the dipole selection rules for transitions to the final states.

Any explanation of the SXAPS of lanthanides must take into account the local

character of the atoms. Some authors (Harte and Szcezepanek 1978, Smith et al. 1976) have proposed the resonant scattering interaction in which both the incident and 3d core electrons occupy the atomic 4f orbitals according to the $3d^{10}4f^N + e \rightarrow 3d^9 4f^{N+2}$ transition. This implies that SXAPS are not predicted for lanthanides with less than two 4f vacancies. However, SXAPS spectra of lanthanides with less than two 4f vacancies have been observed by Chopra and Martin (1982). The systematic investigations of the lanthanides (Chopra and Martin 1982, Harte and Szcezepanek 1978) also reveal some clues regarding the excitation probabilities of various transition channels. $_{69}$Tm (ground state $3d^{10}4f^{12}$) may assume either of the final state configurations: $3d^9 4f^{14}$ or $3d^9 4f^{13}\varepsilon f$ (where εf is the continuum state), depending on the scattering modes of the incident and excited core electrons. Tm SXAPS yields a strong M_5 peak which is not rich in complex line structure. The next element $_{70}$Yb is divalent and has no 4f vacancy. However, Yb_2O_3 has been reported to be trivalent with $4f^{13}$ configuration. The measured M_5-level SXAPS from an oxidized Yb surface is quite broad and complex, and has an intensity approximately 15 to 20% relative to the Tm peak. It is obvious that the resonant process which scatters both electrons into the 4f state is not valid in Yb_2O_3, which has only a single 4f vacancy. The SXAPS spectrum of Yb_2O_3, therefore, results from the second resonant process of the scattering of two electrons to the final state configuration $4f^{14}\varepsilon f$. From the comparison of the M_5-level SXAPS peaks of Yb_2O_3 with those of Tm, it is estimated that the oscillator strengths of the M_5- or M_4-level peaks is divided between the $3d^9 4f^{N+2}$ and $3d^9 4f^{N+1}\varepsilon f$ configuration states in the ratio of 5 : 1, based on the peak intensities.

The exchange interaction between the 4f electrons and 3d hole splits the final state configuration into a multiplet. The multiplicity of these levels, however, depends entirely on the number of 4f electrons and shows a maximum when the 4f levels are half full. The exchange interaction in the case of the 3d levels of the lanthanides is weaker than the spin–orbit interaction. The observed line structure is, therefore, grouped around the spin–orbit components and constitutes a small fraction of the total oscillator strength of the 3d excitation. The line structure is then expected to get quite complex for medium lanthanides and then tends to decrease towards the extreme ends of the series. This is, indeed, demonstrated by the data of the above investigation.

Hinker et al. (1989) have given a new interpretation of the fine structure of APS spectra of light lanthanides La^{3+}, Ce^{3+} and Ce^{4+} systems. La is considered the simplest case for analysis since the La^{3+} ion is described by a noble-gas configuration with empty 4f levels and the La 5d and 6s valence electrons are forming the conduction band. Ce offers the advantage of covering a range of 0 and 1 f counts in the Ce^{3+} and Ce^{4+} ground-state configurations. Thus the comparison of the corresponding spectra is expected to yield detailed information about the influence of the 4f occupation number on the fine structure of the APS spectra. The authors explicitly use a two-step model of the APS process – the excitation step followed by the decay step (fig. 7). The excitation process is the same for all APS spectra. It seems that the differences in the decay step are responsible for the spectral differences among SXAPS, AEAPS and DAPS. In terms of this model, DAPS gives information directly

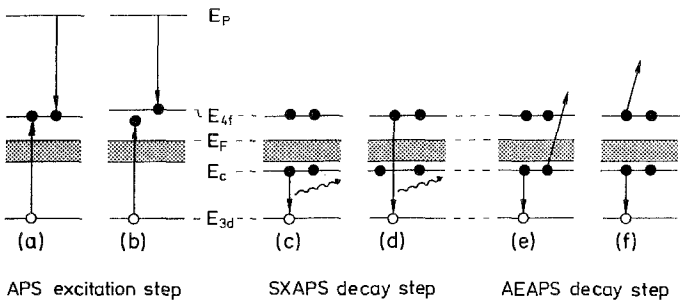

Fig. 7. An energy-level diagram for the APS two-step model, describing the different excitation channels [(a), (b)] and decay channels for SXAPS [(c), (d)] and AEAPS [(e), (f)] schematically. In the excitation step a 3d electron is excited near the Fermi energy, E_F, by an incident electron with energy E_p. Only transitions with at least one electron being excited to the 4f level are considered here. Due to correlation effects the energy E_{4f} of the 4f level depends on the number of 4f electrons. For the decay step a distinction is made between two basically different decay channels: one describing characteristic X-ray emission in the case of SXAPS (c) and Auger emission in the case of AEAPS (e) and the other one describing processes with the excited 4f level being actively involved in the decay processes [(d), (f)]. The occupied parts of the band structure (shaded areas) and a second core level with energy E_c, which is actively involved in the decay processes, are included. (Hinker et al. 1989).

about the excitation process, whereas SXAPS and AEAPS include additional information about the different decay steps. The 3d–4f excitation by electron impact is resonantly enhanced near the excitation threshold due to the formation of quasi-discrete states of the $3d^9 4f^{n+2}$ configuration with both the incident and the excited core electron captured by the 4f level. The second excitation channel leads to a $3d^9 4f^{n+1} \varepsilon^1$ configuration with one electron excited to the 4f level and the other one to a continuum state. In the interpretation of spectra, it is noted that X-ray excited transitions are governed by dipole selection rules whereas in electron excited spectra these restrictions are weakened. It will, therefore, be pertinent to compare APS spectra with core-level electron energy-loss spectra (CEELS) instead of with XAS data. It is also important to distinguish between the dominant decay steps for SXAPS and AEAPS. The former describes the "ordinary" characteristic X-ray emission and Auger emission processes without the direct involvement of excited 4f electrons. The latter describes "recombination" processes with the excited 4f electrons being actively involved in the transitions.

This comparison is shown in fig. 8a for the La $3d_{5/2}$ and $3d_{3/2}$ levels of LaB_6. Analogous results for Ce in CeB_6 are shown in fig. 8b. The authors chose DAPS as the adequate APS version since DAPS is assumed to probe the excitation step in the most direct way. In accordance with the La XAS results of Kanski et al. (1976) the leading peaks A and A′ of the APS spectrum coincide in energy with the $3d^{10}4f^0 \rightarrow 3d^9 4f^1$ dipole allowed transitions peaks C and C′ of the CEELS spectrum. The important fact of the present investigation is that the CEELS main lines (C, C′) clearly have no counterparts in DAPS. It was therefore concluded that the DAPS spectrum exhibits no $3d^9 4f^1$ features that may be associated with non-dipole excitations and the low-energy APS peaks, A and A′ are caused by a $3d^9 4f^2$ configuration.

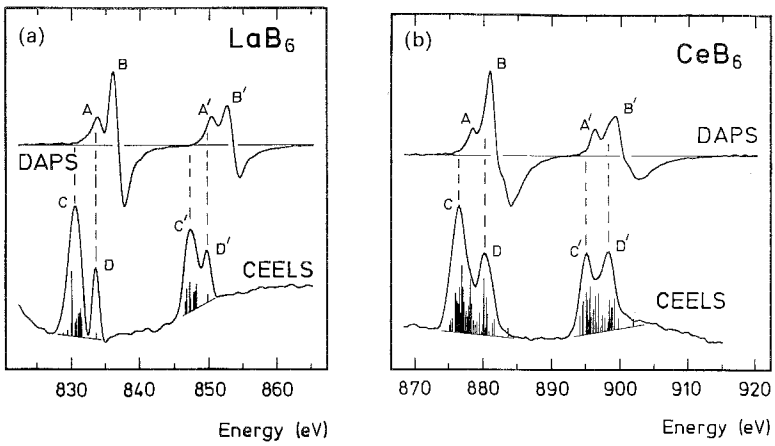

Fig. 8. (a) DAPS and CEELS of the La $3d_{3/2,5/2}$ levels in LaB_6. The spectra are presented on a common energy scale with DAPS given as a function of incident energy and CEELS as a function of loss energy. DAPS is given in derivative form and CEELS in non-derivative form. The La $3d^9 4f^1$ multiplet structure (bar diagram) has been taken from Thole et al. (1985). Dashed lines indicate the energy positions of the CEELS line structures. (b) DAPS and CEELS of the Ce $3d_{3/2,5/2}$ levels in CeB_6 (Hinker et al. 1989). The Ce $3d^9 4f^2$ multiplet structure (bar diagram) has been taken from Thole et al. (1985).

The correspondence between the APS and CEELS features in the case of CeB_6 is rather poor. In particular the low-energy peaks of the two spectra do not coincide in energy but are located at markedly higher energies in APS as compared with CEELS.

Overall, both La and Ce results indicate that the $3d^9 4f^{n+2}$ configuration is responsible not only for the APS main peaks but also for the low-energy peaks. Excitations to $3d^9 4f^{n+1} \varepsilon^1$ (ε denotes itinerant electron state) seem to have no significant influence on the APS spectral features. In AEAPS the excited $3d^9 4f^{n+2}$ configuration predominantly decays via ordinary Auger transitions in which the 4f electrons act as spectators. From the competing recombination and ordinary (with and without the involvement of excited 4f electrons) X-ray emission processes in SXAPS, the recombination process $3d^9 4f^{n+2} \rightarrow 3d^{10} 4f^{n+1} + \hbar\omega$ has been found to be the dominating decay process. The APS fine structure is determined by the multiplet structure of the excited $3d^9 4f^{n+2}$ configuration; the major part of which is suppressed by the state selective excitation and decay probabilities. As a consequence, differences are observed in the fine structures of SXAPS and DAPS or AEAPS. The SXAPS intensity of the $3d_{3/2}$ peak is reduced due to the recombination Auger transition $3d^9_{3/2} 4f^{n+2} \rightarrow 3d^9_{5/2} 4f^{n+1} + \bar{e}$ (involving excited 4f electrons), which converts the $3d_{3/2}$ hole to a $3d_{5/2}$ hole.

Hinker et al. (1987) have also investigated the oxidation of Ce using SXAPS with a view to determine the electron occupation number of the 4f level in the ground state of CeO_2. Schneider et al. (1985) have proposed a model for the electronic structure of CeO_2 in order to explain a variety of spectroscopic results. According to this model CeO_2 in the ground state possesses two types of 4f states. The first

one is itinerant and forms part of the valence band of the insulator. These states have an occupation number of 0.5 electrons/Ce atom. The second kind of 4f states, which have nearly pure $4f^1$-character, are found in the band gap of the insulator. These states are not occupied in the ground state. According to their two-step model of 3d-level SXAPS of lanthanide compounds, the excitation step near the threshold causes the promotion of both the incident electron and the excited core electron into empty 4f states as a result of the $3d^{10}4f^N + \bar{e} \rightarrow 3d^9 4f^{N+2}$ transition, N being the number of 4f-electrons in the ground state. A transition of the type $3d^{10}4f^N + \bar{e} \rightarrow 3d^9 4f^{N+1}\varepsilon^1$ involving itinerant or extended states is not expected to contribute to the intensity of the main SXAPS features. Only the transition $3d^{10}4f^0 + \bar{e} \rightarrow 3d^9 4f^2$ is allowed in tetravalent CeO_2 whereas the transition $3d^{10}4f^1 + \bar{e} \rightarrow 3d^9 4f^3$ reflects the multiple splitting of trivalent γ-Ce and Ce_2O_3. The SXAPS fine structures of CeO_2 and γ-Ce or Ce_2O_3 should, therefore, reflect the differences in multiplet splitting of their respective excited configurations, $3d^9 4f^2$ and $3d^9 4f^3$. Hinker et al. (1987) have carried out APS measurements on γ-Ce and Ce oxides. The 3d-SXAPS spectra are shown in the derivative mode in fig. 9. The energy positions of the $3d^9 4f^N$ ($N = 2, 3, 4$, for γ-Ce and $N = 1, 2, 3$, for CeO_2) configurations were calculated from the uncoupled version of the Gunnarsson and Schonhammer (1983) model and are indicated. From fig. 9 it is evident that there are significant differences between this spectra of Ce and Ce_2O_3 due to the differences in the coupling strength of the 4f states to itinerant states. On the other hand, the CeO_2 spectrum seems to be dominated by the $3d^9 4f^2$ configuration since both neighboring configurations $3d^9 4f^1$ and $3d^9 4f^3$ are well separated from $3d^9 4f^2$. Hinker et al. (1987) have correlated the changes in 3d-level APS spectral features in terms of the 4f count

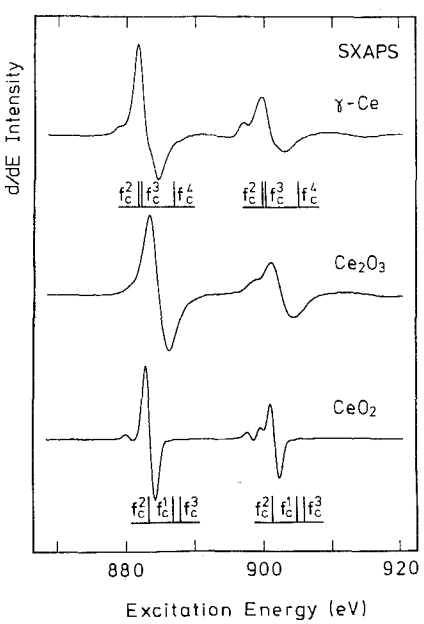

Fig. 9. SXAPS of γ-Ce and Ce oxides (Hinker et al. 1987). The bars give the energy positions of the different configurations (c indicates the presence of the 3d hole).

of γ-Ce, Ce_2O_3 and CeO_2, and derived values between 0 and 0.7 in overall agreement with the model of Schneider et al. (1985). SXAPS has thus been found to be an appropriate method for the investigation of valences and valence changes in Ce compounds.

The exchange interaction plays a more dominant role in the 4d–4f transitions for the lanthanides. The spin–orbit splitting is rather weak. The multiplet splitting is expected to be more pronounced when the 4d level is excited. As a result of the strong exchange interaction between the 4d vacancy and 4f electrons, the final state splits into a multiplet spread over 20 eV. Each of the final-state configurations consists of a large number of terms, and the number of possible transitions to these terms is large. The observed SXAPS spectra for $N_{4,5}$ levels of lanthanides are, therefore, quite complex (Chopra 1987). Detailed theoretical calculations of the convoluted bands with multiple splitting due to exchange interactions in the presence of an extra electron are needed for more plausible interpretation of these spectra.

Shulakov et al. (1985) have studied in the La $N_{4,5}$-region the ultrasoft X-ray emission spectra of lanthanum oxidized in vacuum. The spectra were taken at various incident-electron energies. New structural features appeared in the spectrum with increasing electron energy. Based on dipole selection rules, the various peaks in the radiation spectrum have been attributed to the radiative decay via the new states formed for X-ray emission. They have compared these features with those in the isochromat spectra of La_2O_3. The integrated Bremsstrahlung intensity was found to increase monotonically with the electron energy. This variation in the intensity is responsible for the structure of the APS spectrum and may arise near the thresholds because of anomalies in the cross section for the inelastic scattering of electrons into free electron states of the target. They conclude that the main contribution to the fine structure of the La $N_{4,5}$ APS spectrum comes from the characteristic 5d–5p and Bremsstrahlung channels. The resonance lines in the 4d emission spectrum of La are usually associated with transitions to the ground state from highly localized excited states below the threshold. The features observed in the $N_{4,5}$ APS spectrum have been very well accounted for by the principal channels of radiative decay of a 4d vacancy in the X-ray emission spectrum. This study demonstrates that the X-ray emission spectrum of La can very well be used to explain the structures associated with its APS spectrum.

4.3. *Correlation of APS spectroscopies*

SXAPS and AEAPS, respectively, measure the differential of the total fluorescence and secondary-electron yield as a function of the incident-electron energy. Thus AEAPS is complementary to SXAPS and a good correlation in their spectral features is expected. Hatwar and Chopra (1985a) have compared the $N_{4,5}$-level SXAPS and AEAPS spectra of La, Ce, Pr, Nd and Sm metals and their oxides. The $N_{4,5}$-level APS spectra for La and Ce are shown in fig. 10a and b, respectively. The SXAPS and AEAPS spectra show a strong resemblance. The spectra of Ce shown in fig. 10a exhibit multiplet structure below the expected 4d excitation threshold and a broad 10–20 eV wide peak above the threshold, followed by small peaks of decreasing

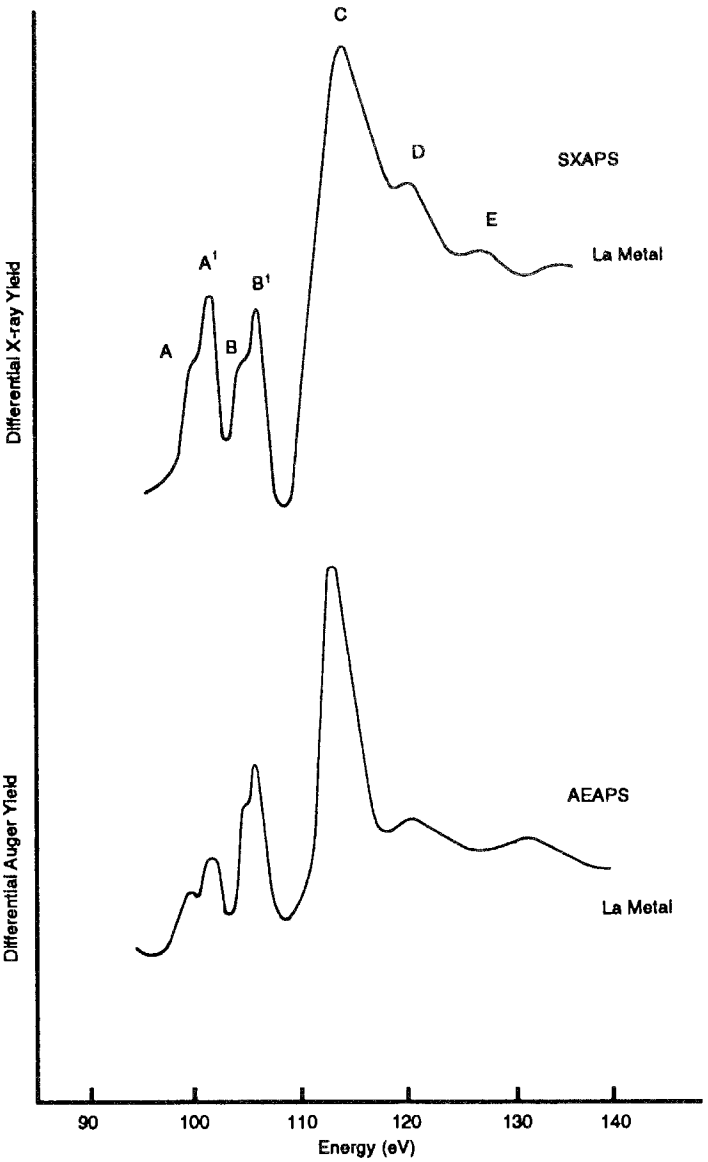

Fig. 10. (a) The SXAPS and AEAPS spectra of pure La metal. The SXAPS curves were recorded with an excitation current of 2.5 mA and with a modulation amplitude of 1.0 eV_{p-p}. The AEAPS spectra were recorded with an emission current of 2.0 mA. The time constant in both cases was 30 s.

intensity. The multiplet structures are similar to those observed in other core-level spectroscopies such as XAS and CEELS. Relative to SXAPS peaks the AEAPS peaks are consistently narrower, better resolved and more intense by an order of magnitude when referred to the same current and signal-to-background ratio. This is due to the

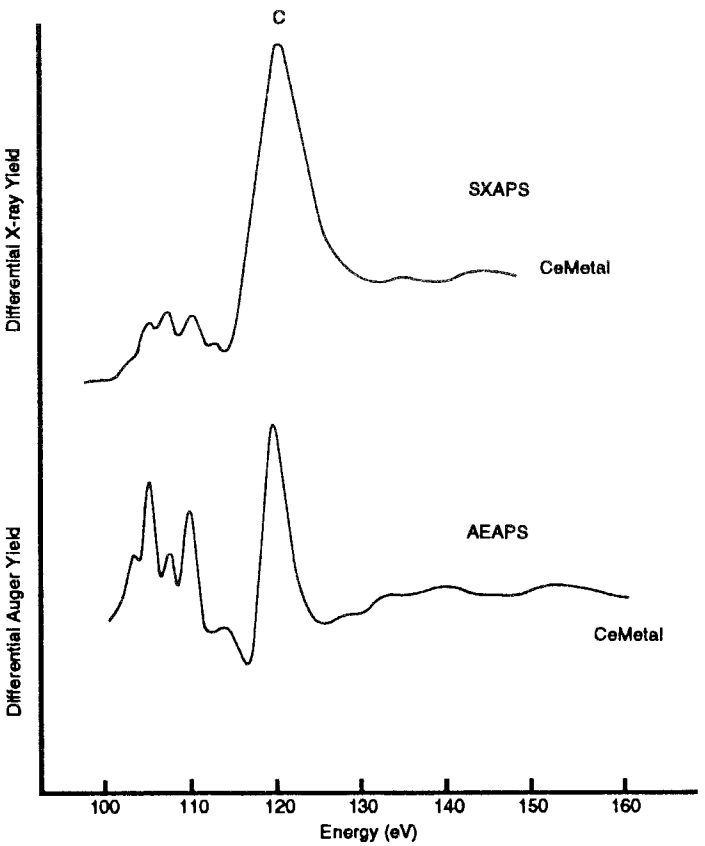

Fig. 10. (b) The SXAPS and AEAPS spectra of pure Ce metal (Hatwar and Chopra 1985a). Conditions for recording the data were as given in (a).

fact that in the soft X-ray region, a core hole is more likely to decay by non-radiative recombination. In AEAPS with the ejection of the Auger electron, screening of the core hole is reduced, and correspondingly there is an increase in the exchange interaction, enhancing the intensity of pre-threshold multiplet peaks. From the comparison of spectra it is possible to obtain information about the decay mechanism following the excitation of a core electron in the lanthanides. The SXAPS technique makes us aware of the fact that the total electron-induced fluorescence of a material shows abrupt changes at the appearance potential of characteristic X-rays. On the other hand, Leifeld et al. (1974) have interpreted the variation in X-ray emission in the La 3d region as due to the huge resonance in the Bremsstrahlung background rather than to the onset of characteristic X-ray emission. In SXAPS one just measures the X-ray yield non-dispersively, and from this experiment one cannot distinguish between the mechanism leading to the characteristic emission and Bremsstrahlung. In Bremsstrahlung an incident electron falls into a discrete empty state above E_F with energy conserved by emission of a photon. The final state is basically a negative

ion with an electronic configuration of $4f^{N+1}$. In AEAPS the final state has one electron in the empty conduction band accompanied by a core hole. Thus the final electron state in AEAPS differs from that of Bremsstrahlung in the form of a core hole. If Bremsstrahlung plays an overriding role in APS, then SXAPS and AEAPS will be expected to have notably different line shapes. If, on the other hand, the characteristic decay mechanism scheme dominates, then the two spectroscopies should give similar results. The overall resemblance regarding the number and shapes of the peaks between SXAPS and AEAPS spectra suggests that characteristic emission plays a dominant role in determining the line shapes of the $N_{4,5}$-levels SXAPS and AEAPS of lanthanides and Bremsstrahlung makes a minimal contribution to the spectral features of these elements. The $N_{4,5}$-level SXAPS and AEAPS spectra of Ce metal surfaces exposed to oxygen showed no major changes in the fine-structure region except for a chemical shift of about 0.5 eV. The number of five peaks below the threshold remains the same and is indicative of a tripositive Ce ion in the oxide as in pure metal. The decrease in the intensity of the main peak is obviously due to the decreased atomic concentration of Ce ions in the oxide surface. Similar results regarding the SXAPS study of Ce and its oxides have been reported. Plateau and Karlsson (1978) have shown that the oxide phase formation depletes the Ce 5d band but does not affect the 4f level apart from a small chemical shift. Sm metal spectra also do not indicate any changes in the spectral features while going from metal to oxide except for a chemical shift of 2.5 eV towards higher energy. This shift is comparatively larger than those of oxides of the other light lanthanides studied, where the shifts are less than 1.0 eV. The 150 eV valence band spectra of Sm by Allen et al. (1980) do not show any significant changes in the spectra due to oxygen exposure. Wertheim and Crecelius (1978) have shown from the XPS data that the first few atomic layers of trivalent metallic Sm contain about 20% divalent component (Sm fractional valence 2.6) due to surface relaxation effects. When Sm metal forms oxide, the Sm ions have the same surface and bulk valency. The shift of 2.5 eV from metal to oxide seems too large to be accounted for by the contribution of 20% divalent component in the metal. It is well known that the core-level shifts are affected by the extra-atomic relaxation effects (Watson and Perlman 1976). The larger shift in Sm oxide may be due to a decrease in relaxation effects in Sm_2O_3. The interpretation of SXAPS spectra from oxidized surfaces of lanthanides is consistent with the data from other core-level spectroscopies. It may be noted that the similarity between the spectra of metal and oxide is perhaps not unexpected since the relevant transitions are shielded from their environment by the centrifugal potential barrier and the other shells. As a matter of fact the APS line shape can be interpreted in terms of the atomic-like transitions, including exchange interactions, rather than in terms of continuum interband transitions (Smith et al. 1976).

As the most important result, APS has proven to be an appropriate technique for the investigation of the electronic structure of lanthanide compounds in a way similar to other core-level spectroscopies such as XPS, XAS and CEELS, with the advantage of a rather simple experimental setup. Furthermore, when applied to 4f systems, APS offers the potential of studying correlation effects directly because of the allowed addition of two electrons to the partially occupied 4f level.

4.4. *Lanthanide intermetallics*

Valence band spectroscopies (AES and XPS) are practically limited to binary alloys because of the complications encountered with an increase in the number of alloy constituents. In contrast with AES and XPS, which probe the occupied DOS of the sample, SXAPS measures the unoccupied conduction band DOS. An important aspect of SXAPS should be pointed out in the present context. Since the matrix element governing the core-hole creation involves the very short-range wave function of the initial core electron state, the technique is expected to reveal a localized DOS. Since the spectra of different constituents are well separated in energy, the application of SXAPS is by no means limited to binary alloys. The changes in SXAPS spectral features and shifts in BE which accompany alloy formation will better characterize the alloys.

Hatwar and Chopra (1985a, b) have utilized the SXAPS technique to study the rare earth–transition metal intermetallics. Most of the La–Ni intermetallics are found to be paramagnetic. The paramagnetic susceptibility can be accounted for solely in terms of the La component, while Ni is assumed to be non-magnetic. Alloying Ni with electron-rich La diminishes the Ni magnetic moment progressively as the La content increases. Traditionally, this has been ascribed to the filling of the Ni d-band by extra electrons supplied by La. XPS studies, however, indicate that despite band filling, there is no evidence of large charge transfer (Hillebrecht et al. 1983). Ni has only 0.6 d vacancies, and the Ni spectra should reflect complete filling of the 3d band with increased La concentration as a result of charge transfer. Hatwar and Chopra (1985a) have investigated the SXAPS of La–Ni intermetallics (fig. 11). Since SXAPS probes the local density of unfilled states, any vacant d-states in the Ni band of the intermetallics will be reflected in the Ni SXAPS spectra. The changes in spectral features of SXAPS will give information about the charge transfer and hybridization of the valence bands of the constituents. Since La $3d_{3/2}$ and Ni $2p_{3/2}$ have nearly the same energy and their SXAPS peaks overlap, the Ni L_2 peak was used to gain information regarding the electronic structure of these intermetallics. The spectra of $LaNi_x$ ($x = 1$ to 5) were investigated and are shown in fig. 11.

The intensity of the Ni L_2 peak decreases as the concentration of La increases (i.e. going from $LaNi_5$ to LaNi). The band structure calculations of $LaNi_5$ indicate the transfer of 1.5 electrons per La atom to Ni (Malik et al. 1982). The 1.5 electrons will be sufficient to fill the 0.6 d hole of Ni in LaNi and 1.2 d holes of Ni in $LaNi_2$. As a result, Ni L_2 SXAPS in these intermetallics is not expected. However, in no case is a complete disappearance of the Ni L_2 peak observed. The appearance of a Ni L_2 peak consistently in all the La–Ni intermetallics indicates the presence of 3d unoccupied states in the conduction band of Ni. The mere charge transfer is, therefore, not considered adequate to explain the present SXAPS results. The BIS of pure La shows a peak at ~ 5 eV above E_F, corresponding to 4f states (Lang et al. 1981). At this energy the variation in DOS of Ni is minimal (Speier et al. 1984). According to the joint density of states model the APS spectra of Ni (as well as of La) would show, apart from the threshold peak, a structure for the peak in DOS at ~ 5 eV above E_F. Since no such structure has been observed in SXAPS spectra of La and Ni in the

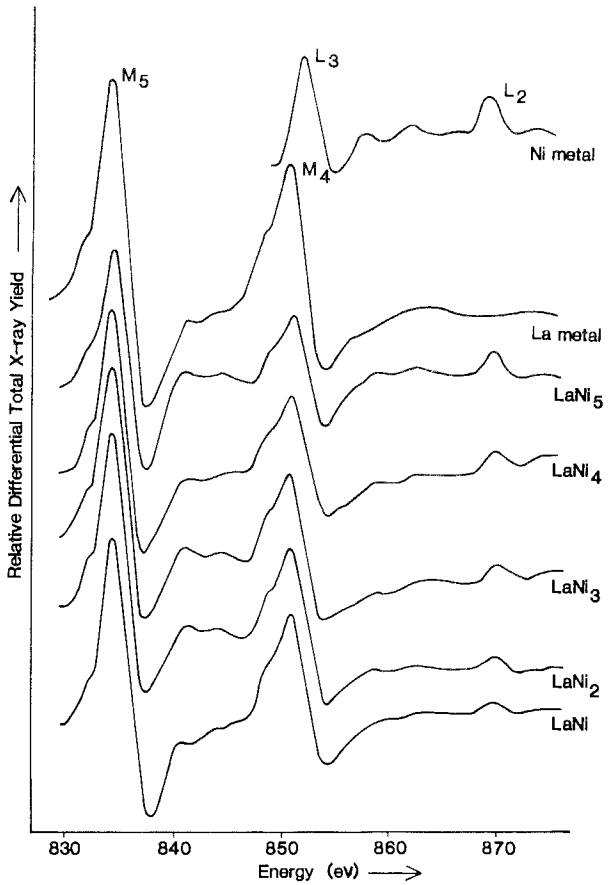

Fig. 11. $M_{4,5}$-levels of La and $L_{2,3}$-levels of Ni SXAPS spectra in pure metals and their intermetallics (Hatwar and Chopra 1985b).

La–Ni system, it is logical to conclude that the joint density of states model fails to account for the bonding in these intermetallics. As an alternative explanation, the effect of hybridization of La and Ni wave functions needs to be considered in explaining the partial filling of the 3d band. The hybridization of La and Ni bands results in the consequent filling of the band without appreciably changing the d count of Ni. In conclusion, the observation of the Ni L_2 peak in all La–Ni intermetallics indicates that the hybridization of La and Ni bands is more important for filling the 3d band of Ni than charge transfer. Dose et al. (1984) have considered the effect of hybridization in a glassy $Cu_{60}Zr_{40}$ sample studied by SXAPS. The pure Cu spectra show a nearly step-like behavior superimposed with some oscillatory structure. The Cu spectrum in the glass resembles that of partially filled d-shell transition metals. They interpreted these SXAPS spectra of Cu as a result of hybridization of Cu d-states with the p-states of Zr.

Horn et al. (1988) have compared the electronic structure of several superconducting copper oxide perovskites with closely related non-superconductors using several spectroscopic techniques including APS. Using XPS, a number of workers have

shown that the Cu valence is +2 in most superconducting materials. Within the resolution of the XPS technique, there is no evidence of Cu being in other oxidation states. The spectra of non-superconductors resemble in energy and shape those of Cu^+ as in Cu_2O. There has been considerable interest in comparing the superconducting compounds with analogous non-superconducting compounds with a view to isolating those features of the electronic properties which are crucial to the superconducting behavior. X-ray absorption near-edge spectroscopy (XANES) results show that the Cu 1s edge is displaced some 10 eV to higher energy in divalent compounds relative to monovalent compounds. Based on this argument Cu is found to be divalent in superconducting Eu and Y compounds. However, in non-superconducting Ce- and Pr-based compounds the Cu 1s edge is slightly shifted to lower energy, indicating substantial Cu^{2+} behavior, in contrast with XPS results. It is important to determine whether the differences result from different excitation processes in XPS and XANES. APS, which sensitively probes the local density of unoccupied states, has been used to resolve the problem. It is known that Cu^{2+} implies Cu in a $3d^9$ configuration and Cu^+ implies Cu in a $3d^{10}$ configuration with a filled 3d band. Their APS spectra, shown in fig. 12, clearly indicated that in the non-superconducting $YBa_2Cu_3O_7$ the Cu d-band is essentially filled, confirming a Cu^+ ($3d^{10}$) configuration. Only the superconducting Y compound shows empty hybridized states of the $3d^9$ (Cu^{2+}) configuration. The APS spectrum of Pr is found to be void of Cu 2p features relating to the $3d^9$ configuration. The spectrum of $PrBa_2Cu_3O_7$ in the Cu 2p region is partially obscured by Pr 3d peaks. Evidently, if the Cu 2p features were as large as in superconducting $YBa_2Cu_3O_7$, they would be markedly visible. The different values of the Cu valence, +2 by bulk technique

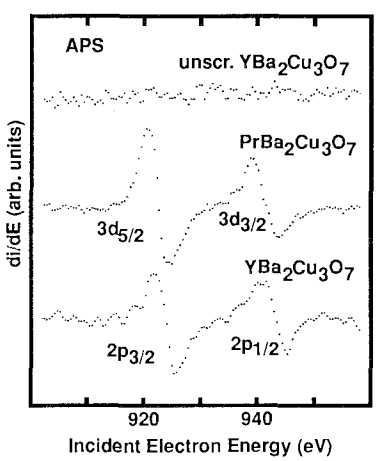

Fig. 12. The appearance potential spectra in the vicinity of the Cu 2p core levels for samples as indicated (Horn et al. 1988). Plotted is the derivative of the total secondary-electron yield as a function of incident electron energy. (i) The non-superconducting $YBa_2Cu_3O_7$ does not give any signature of Cu^{2+} ($3d^9$) configuration in Cu 2p region. (ii) The spectrum of $PrBa_2Cu_3O_7$ is partially obscured by Pr 3d peaks, but it is evident that if Cu 2p features were as large as in superconducting $YBa_2Cu_3O_7$ they would be visible. (iii) The $YBa_2Cu_3O_7$ exhibits characteristic 2p APS peaks of Cu^{2+} ($3d^9$) configuration.

(XAS) and +1 by surface sensitive techniques (XPS and APS), must be due to surface effects. A possible reason for this discrepancy is a loss of oxygen from the surface region under UHV conditions, a hypothesis supported by other measurements. Different spectroscopic techniques, emission and absorption, therefore give the same results for the electronic state of Cu. APS is, thus, found to be more suitable for the study of intermetallics and compounds, especially the multicomponent systems.

5. Concluding remarks and prospects

In this review paper we have discussed some applications of APS to modern science and technology and highlighted its importance relative to other available techniques. In this section, we discuss the relative strengths and limitations of APS.

The intensity of a signal in an APS spectrum is determined by the transition of a core electron to the unoccupied states above E_F. The strength of the signal, therefore, depends upon the density of these unoccupied states. For simple metals, the 3d transition metals, the lanthanides, etc., having high density of unoccupied states at E_F, this technique is particularly suitable for studying them. Noble metals, such as Au, having very low DOS, give a very weak signal in the spectrum. This is the reason why APS cannot be used as a common analytical tool. For the elements to which it is sensitive, the spectra are much simpler and easier to interpret. Moreover, APS is a non-dispersive technique and requires only a relatively simple and inexpensive apparatus. These are the special advantages of APS over other techniques.

The one-electron theory, discussed previously, explains satisfactorily the features observed in the spectra of simple and 3d transition metals. The theory is valid for systems having a continuous DOS above E_F. Discrepancies between theory and experiment were observed for lanthanides. The breakdown of the one-electron model occurs because the excited core electron and/or projectile electron may occupy 4f orbitals, which are quite localized about the excited ion. Wendin (1974) has made an attempt to explain the spectral features on the basis of a two densities of states model: one for the scattered projectile electron and the other for the excited ion with an electron–hole pair. This model is able to explain some of the spectral features. More theoretical work, taking into account the core-level widths, core-hole lifetime broadening, many-body and other effects contributing to the spectrum, is needed to provide a more plausible explanation for the APS spectra.

An interesting application of APS is the derivation of the density of states from the signal shape. In their work Dose and Scheidt (1979, 1981) have described the technique to extract the surface density of unoccupied states from measured SXAPS spectra. Results for 3d and 5d metals have been found in excellent agreement with theoretical calculations. On the other hand, BIS offers the possibility of relating directly the experimentally determined spectral features to the theoretical DOS. APS is found more suitable to the study of intermetallics, especially to multicomponent systems. Another important application of APS is to the study of the adsorption phenomenon. From the work of Andersson et al. (1974) it is seen that K-level spectra of various adsorbates, such as C, N, O and S, at transition metal surfaces can be

measured even in the sub-monolayer region. Moreover spectra from adsorbed oxygen and metal oxide, respectively, exhibit marked differences.

The extended X-ray absorption fine structure (EXAFS) associated with an absorption discontinuity gives information regarding the interatomic distance, coordination number and degree of disorder in a solid system. In contrast to bulk information available from EXAFS measurements, the fine structure in the APS spectrum [extended appearance potential fine structure (EAPFS)], gives information about the surface structure since it employs a low-energy electron beam for excitation. The structure occurs on the high-energy side of a particular core-level appearance-potential edge and extends over several hundred eV. The maxima of the fine structure that originates from the interference of the outcoming spherical wave scattered on the neighboring atoms in the surface region, provide information on the surface structure without the need of long-range order necessary for LEED (Cohen et al. 1978). Because of the low fluorescence yield of SXAPS, AEAPS has been found more efficient in determining the surface structure of simple and 3d transition metals (Konishi et al. 1986, Mehl et al. 1984). The analysis of EAPFS can be done on similar lines as with EXAFS. Unlike EXAFS, which requires high-intensity sources such as those from a synchrotron or rotating anode tubes, EAPFS makes use of an experimental setup commonly available in any surface analysis laboratory. Since APS suffers from a high background and a low signal-to-noise ratio, microanalysis or fast scanning/analysis modes, which are presently available for other surface analytical techniques, are not feasible (Ertl and Kuppers 1985). For the elements to which APS is applicable, the sensitivity of APS is considered higher than that of AES. The strength of the APS method lies in the simplicity of the spectra, permitting discrimination of neighboring elements for which the Auger signals overlap (Sundgren et al. 1983, Dawson and Tzatzov 1985). Attempts of quantitative analysis have been made using SXAPS (Ertl and Wandelt 1972, Wandelt and Ertl 1976b, c). Limited results for quantitative evaluation using AEAPS and DAPS have been reported (Kirschner and Staib 1975). For the analysis of 3d transition metals the sensitivity of SXAPS has been claimed to be $\sim 1\%$ (Engelmann et al. 1974). SXAPS has the lowest sensitivity of all APS methods due to the low fluorescence yield, but its Bremsstrahlung background is linear and can be easily excluded. Additionally, the SXAPS signal is practically free of transport complications since X-rays do not undergo any absorption in the surface layer. In the case of AEAPS and DAPS the low energy of primary electrons does not prolong the excitation process (in comparison with AES), so that the processes connected with the relaxation of a given primary excitation can be studied.

The present experience with the APS technique is quite limited. The experimental work has been narrowed down due to the non-availability of sufficient theoretical data. The main difficulty is the extraction of relevant information from the experimental data in order to correlate with the existing theoretical models. A wide scope exists for the theoretical and experimental work in this field. When the different aspects of APS are fully exploited, this spectroscopy will be accepted as a popular technique for material characterization of surfaces.

Acknowledgments

The author feels pleasure in acknowledging stimulating discussions with Anil R. Chourasia and T.K. Hatwar. He also wishes to thank Teresa Fisher and Mona Towne for their help during the preparation of the article. The work was supported by grants from the Robert A. Welch Foundation and East Texas State University.

References

Allen, J.W., L.I. Johansson, I. Lindau and S.B. Hagstrom, 1980, Phys. Rev. B **21**, 1335.

Anderson, C.R., R.N. Lee, J.F. Morar and R.L. Park, 1982, J. Vac. Sci. Technol. **20**, 617.

Andersson, S., and C. Nyberg, 1975, Surf. Sci. **52**, 489.

Andersson, S., H. Hammarquist and C. Nyberg, 1974, Rev. Sci. Instrum. **45**, 877.

Bearden, J.A., and A.F. Burr, 1967, Rev. Mod. Phys. **39**, 125.

Chopra, D.R., 1987, J. Less-Common Met. **127**, 373.

Chopra, D.R., and G. Martin, 1982, Study of $M_{4,5}$-level soft X-ray appearance potential of selected rare earths, in: The Rare Earths in Modern Science and Technology, Vol. 3, eds B.M. McCarthy, H.B. Silber and J.J. Rhyne (Plenum, New York) p. 131.

Chopra, D.R., H. Babb and R. Bhalla, 1976, Phys. Rev. B **14**, 5231.

Cohen, P.I., T.L. Einstein, W.T. Elam, Y. Fukuda and R.L. Park, 1978, Appl. Surf. Sci. **1**, 538.

Dawson, P.T., and K.K. Tzatzov, 1985, Surf. Sci. **149**, 105.

Dev, B., and H. Brinkman, 1970, Ned. Tijdschr. Vacuumtech. **8**, 176.

Dose, V., and Th. Fauster, 1979a, Appl. Phys. **20**, 299.

Dose, V., and Th. Fauster, 1979b, Appl. Phys. **20**, 1.

Dose, V., and A. Haertl, 1981, Phys. Rev. Lett. **47**, 132.

Dose, V., and H. Scheidt, 1979, Appl. Phys. **19**, 19.

Dose, V., and H. Scheidt, 1981, Phys. Status Solidi **103**, 47.

Dose, V., Th. Fauster and H. Grossman, 1981, J. Comp. Phys. **41**, 34.

Dose, V., G. Reusing and H.J. Guntherodt, 1984, Solid State Commun. **49**, 1081.

Drube, W., F.J. Himpsel and R. Ludeke, 1987, J. Vac. Sci. & Technol. B **5**, 930.

Eckertova, L., 1988, Surf. Sci. **200**, 490.

Eckertova, L., and J. Pavluch, 1984, Czech. J. Phys. B **34**, 622.

Engelmann, H.J., K. Brandt and J.E. Houston, 1974, J. Vac. Sci. & Technol. **11**, 227.

Erickson, N.E., and C.J. Powell, 1984, J. Vac. Sci. & Technol. A **2**, 840–841.

Ertl, G., and J. Kuppers, 1985, Low Energy Electrons and Surface Chemistry, Monographs in Modern Chemistry, 2nd Ed. (Verlag Chemie, Weinheim) p. 157.

Ertl, G., and K. Wandelt, 1972, Phys. Rev. Lett. **29**, 218.

Ertl, G., and K. Wandelt, 1974, Z. Naturforsch. a **29**, 768.

Esteva, J.M., R.C. Karnatak, J.C. Fuggle and G.S. Sawatzky, 1983, Phys. Rev. Lett. **50**, 910.

Fukuda, Y., W.T. Elam and R.L. Park, 1977, Phys. Rev. B **16**, 3322.

Gadzuk, J.W., and M. Sunjic, 1975, Phys. Rev. B **12**, 524.

Grolemund, D.L., and D.R. Chopra, 1983, IEEE Trans. Nucl. Sci. **NS-30**, 934.

Gunnarsson, O., and K. Schönhammer, 1983, Phys. Rev. B **28**, 4315.

Harte, W.E., and P.S. Szeczepanek, 1978, Jpn. J. Appl. Phys. **17-2** (Suppl.) 305.

Hatwar, T.K., and D.R. Chopra, 1985a, Lanthanide Actinide Res. **1**, 135.

Hatwar, T.K., and D.R. Chopra, 1985b, J. Electron. Spectrosc. & Relat. Phenom. **35**, 77.

Hillebrecht, F.U., J.C. Fuggle, P.A. Bennett, Z. Zonierek and Ch. Freiburg, 1983, Phys. Rev. B **27**, 2179.

Himpsel, F.J., and Th. Fauster, 1984, J. Vac. Sci. & Technol. A **2**, 815.

Hinker, H., C. Westphal and H. Merz, 1987, J. Phys. Colloq. (Paris) **48**, C12-1041.

Hinker, H., R. Stiller and H. Merz, 1989, Phys. Rev. B **40**, 10594.

Horn, S., X. Cai, T. Guo, C.L. Chang and M.L. den Boer, 1988, Electron spectroscopy of

high-temperature and superconductors, in: Topical Conference on Film Processing and Characterization of High-Temperature Superconductors, Anaheim, California, 1987, Vol. 165, pp. 311–322.
Jorgensen, C.K., and H. Berthou, 1972, Mat.-Fys. Medd. Dan. Vidensk. Selsk. **38**, 15.
Kanski, J., P.O. Nilsson and I. Curelaru, 1976, J. Phys. F **6**, 1973.
Kirschner, J., and W. Losch, 1977, J. Vac. Sci. & Technol. **14**, 1173.
Kirschner, J., and P. Staib, 1975, Appl. Phys. **6**, 99.
Konishi, R., H. Tanigawa and H. Sasakuna, 1986, Jpn. J. Appl. Phys. **25**, 1616.
Lang, J.K., Y. Baer and P.A. Cox, 1981, J. Phys. F **22**, 121.
Lee, R.N., 1977, Rev. Sci. Instrum. **48**, 1603.
Leifeld, R.J., A.F. Burr and M.B. Chamerlain, 1974, Phys. Rev. A **9**, 316.
Ludeke, R., D. Straub, F.J. Himpsel and G. Landgren, 1986, J. Vac. Sci. & Technol. A **4**, 874.
Malik, S.K., F.J. Arlinghaus and W.E. Wallace, 1982, Phys. Rev. B **25**, 6488.
Mehl, M.J., T.L. Einstein and G.W. Bryant, 1984, J. Vac. Sci. & Technol. A **2**, 862.
Nagel, D.J., 1973, X-ray probes of vacant energy bands, in: Band Structure Spectroscopy of Metals and Alloys, eds D.J. Fabian and L.M. Watson (Academic Press, New York) pp. 457–489.
Nilsson, P.O., and J. Kanski, 1972, Phys. Lett. A **41**, 217.
Nilsson, P.O., and J. Kanski, 1973, Surf. Sci. **37**, 700.
Nyberg, C., 1975, Surf. Sci. **52**, 1.
Nyberg, C., 1979, Surf. Sci. **82**, 165.
Padalia, B.D., P.S. Shinde, A.V. Kargaonkar and W.C.J. Carvalho, 1991, Rev. Sci. Instrum. **62**, 1109.
Park, R.L., 1975, Surf. Sci. **48**, 80.
Park, R.L., and J.E. Houston, 1972, Phys. Rev. B **6**, 1073.
Park, R.L., and J.E. Houston, 1974, J. Vac. Sci. & Technol. **11**, 1.
Park, R.L., M.L. den Boer and Y. Fukuda, 1974, in: Proc. 6th Czech. Conf. Electronics and Vacuum Physics, Bratislava, Vol. 4, p. 53–59.
Pavluch, J., and L. Eckertova, 1985, Czech. J. Phys. B **35**, 630.
Plateau, A., and S.K. Karlsson, 1978, Phys. Rev. B **18**, 3820.
Schneider, W.-D., B. Delley, E. Wuilloud, J.M. Imer and Y. Baer, 1985, Phys. Rev. B **32**, 6819.
Schulz, S.W., K.T. Schleidcher, D.M. Ruck and H.V. Chun, 1984, J. Vac. Sci. & Technol. A **2**, 822.
Shulakov, A.S., T.M. Zimkina and A.P. Stepanov, 1985, Sov. Phys.-Solid State **27**, 65.
Smith, R.J., M. Piacentini, J.L. Wolf and D.W. Lynch, 1976, Phys. Rev. B **14**, 3419.
Speier, W., J.C. Fuggle, R.C. Zeller, B. Ackermann, K. Czet, F.U. Gillebrecht and M. Capagna, 1984, Phys. Rev. B **30**, 6921.
Sundgren, J.E., B.O. Johansson and S.E. Karlsson, 1983, Surf. Sci. **128**, 265.
Thole, B.T., G. van der Laan, J.C. Fuggle, G.S. Sawatzky, R.C. Karnatak and J.M. Esteva, 1985, Phys. Rev. B **32**, 5107.
Tong, S.Y., 1984, Phys. Today **37**, 50.
Tracy, J.C., 1972, J. Appl. Phys. **43**, 4164.
Wandelt, K., and G. Ertl, 1976a, Surf. Sci. **53**, 403.
Wandelt, K., and G. Ertl, 1976b, J. Phys. F **6**, 1607.
Wandelt, K., and G. Ertl, 1976c, Z. Naturforsch. A **31**, 205.
Watson, R.E., and R.L. Perlman, 1976, Photoelectron Spectroscopy, Structure and Bonding, Vol. 24 (Springer, Berlin) p. 83.
Webb, C., and P.N. Williams, 1974, Phys. Rev. Lett. **33**, 824.
Wendin, G., 1974, Localized excitations in appearance potential spectra in barium, in: Proc. Int. Conf. on Vacuum-Ultraviolet Radiation in Physics, Hamburg (Vieweg-Pergamon, Braunschweig) pp. 252–254.
Wertheim, G.K., and G. Crecelius, 1978, Phys. Rev. Lett. **40**, 813.

SUBJECT INDEX